Dynamics of Molecules and Chemical Reactions

edited by

Robert E. Wyatt
University of Texas at Austin
Austin, Texas

John Z. H. Zhang
New York University
New York, New York

MARCEL DEKKER, INC. NEW YORK · BASEL · HONG KONG

Start of Citation[PU]Marcel Dekker, Inc.[/PU][DP]1996[/DP]End of Citation

Library of Congress Cataloging-in-Publication Data

Dynamics of molecules and chemical reactions / edited by Robert E. Wyatt,
John Z.H. Zhang.
p. cm.
Includes index.
ISBN 0-8247-9538-5 (alk. paper)
1. Chemical kinetics. 2. Molecular dynamics. I. Wyatt, Robert E.
(Robert Eugene) II. Zhang, John Z.H.
QD502.D96 1996
541.39'4—dc20 96-18104
CIP

Marcel Dekker, Inc.
270 Madison Avenue, New York, New York 10016

Current printing (last digit):
10 9 8 7 6 5 4 3 2 1

PRINTED IN THE UNITED STATES OF AMERICA

Start of Citation[PU]Marcel Dekker, Inc.[/PU][DP]1996[/DP]End of Citation

Preface

During the past 10 to 15 years, tremendous progress has been made in the development and application of theoretical approaches to the study of energy transfer in excited molecules (intramolecular dynamics), and in the study of reactive collisions. These developments in theoretical dynamics have proceeded with advances in computer technology and with the implementation of powerful experimental techniques. The availability of powerful workstations, vector supercomputers, and massively parallel computers has drastically changed the landscape of research in theoretical chemistry. Perhaps the most significant result of this is that theoretical chemists are no longer satisfied with qualitative models of chemical phenomena. The current trend emphasizes detailed dynamical information, including rigorous calculations of cross sections and state-to-state transition probabilities. This progress has been made possible by the development of effective analytical and computational techniques coupled with the availability of powerful computational resources. In addition, the availability of experimental results, frequently obtained using new laser techniques, has stimulated theoreticians to produce results that can be used to interpret and analyze these experiments.

The subject material in the 16 chapters of this volume falls into the broad area of research in chemical dynamics. Chapters 1 to 4 deal with intramolecular dynamics and spectroscopy. Chapter 5, on grid methods, then serves as a bridge to Chapters 6 to 12, which are concerned with quantum mechanical approaches to reaction dynamics. Chapters 13 to 15 deal with semiclassical and classical approaches to reaction dynamics, and the volume concludes with a chapter on activated rate processes. The authors were selected because of their expertise in the areas described in their chapters.

The theoretical methods described here encompass most of the promising approaches that have been developed since 1980. Included in the list of methods described are both time-dependent and time-independent approaches, variational and perturbative methods, iterative and direct methods, and approaches based on the use of physical grids or finite sets of basis functions. Some of the methods are still in the process of development. In this sense, the computational foundations of this field are themselves rather dynamic. Although there are many viable approaches to dynamical problems involving 2 to 3 atoms and up to about 5000 coupled states, it is very important to develop and apply methods that can be extended to moderately sized polyatomic molecules (5 to 12 atoms) with, say, 10^4 to 10^5 (or even more) states. For the intramolecular dynamics problem, at least in some cases, this is now possible. Polyatomic reactions with this degree of complexity are currently beyond the scope of rigorous quantum mechanical methods, but significant progress is being made in 4-atom reaction dynamics. However,

Start of Citation[PU]Marcel Dekker, Inc.[/PU][DP]1996[/DP]End of Citation

it may be that some methods (for example, those involving iteration of matrix-vector products) will be applicable to these problems.

In order to assist both graduate students and researchers to grasp recent significant developments in intramolecular dynamics and reaction dynamics, we have tried to provide in this volume a broad spectrum of topics and detailed expositions of many of the current methodologies in chemical dynamics, as well as extensive discussions of applications of these methods to problems of current experimental interest. In addition to providing the latest methods for the active researcher, each chapter was written with the graduate student in mind. For this purpose, the beginning sections of each chapter contain introductory material, although the amount of this material varies from chapter to chapter.

Perhaps we are now at a crossroads (hopefully not a dead end) in the development and application of theoretical methods to problems in intramolecular dynamics and reaction dynamics. Because of the efforts of many research groups, a number of the "easier" but challenging problems (such as the low-energy $H + H_2$ reaction) have now been satisfactorily solved. Where should we go from here and which routes will be the most fruitful ones to follow? We hope that this volume will be useful to those scientists who will be charting the future paths in this exciting field.

ROBERT E. WYATT
JOHN Z. H. ZHANG

Start of Citation[PU]Marcel Dekker, Inc.[/PU][DP]1996[/DP]End of Citation

Contents

Start of Citation[PU]Marcel Dekker, Inc.[/PU][DP]1996[/DP]End of Citation

Start of Citation[PU]Marcel Dekker, Inc.[/PU][DP]1996[/DP]End of Citation

Contributors

Thomas C. Allison, Ph.D. Department of Chemistry, Chemical Physics Program and Supercomputer Institute, University of Minnesota, Minneapolis, Minnesota

N. Balakrishnan, Ph.D. Department of Chemistry, H. C. Ørsted Institute, University of Copenhagen, Copenhagen, Denmark

Gert D. Billing, Ph.D. Department of Chemistry, H. C. Ørsted Institute, University of Copenhagen, Copenhagen, Denmark

David C. Chatfield, Ph.D.* Department of Chemistry, Chemical Physics Program and Supercomputer Institute, University of Minnesota, Minneapolis, Minnesota

Ronald S. Friedman, Ph.D.** Department of Chemistry, Chemical Physics Program and Supercomputer Institute, University of Minnesota, Minneapolis, Minnesota

David K. Hoffman, Ph.D. Department of Chemistry and Ames Laboratory, Iowa State University, Ames, Iowa

Youhong Huang, Ph.D. Departments of Chemistry and Physics, University of Houston, Houston, Texas

John S. Hutchinson, Ph.D. Department of Chemistry, Rice University, Houston, Texas

Christophe Iung, Ph.D. Laboratory of Structure and Dynamics of Molecular Systems and Solids, University of Science and Technology, Montpellier, France

Ronnie Kosloff, Ph.D. The Fritz Haber Research Center for Molecular Dynamics, The Hebrew University of Jerusalem, Jerusalem, Israel

Donald J. Kouri, Ph.D. Departments of Chemistry and Physics, University of Houston, Houston, Texas

**Current affiliation:* Florida International University, Miami, Florida

***Current affiliation:* Indiana University-Purdue University, Fort Wayne, Indiana

Start of Citation[PU]Marcel Dekker, Inc.[/PU][DP]1996[/DP]End of Citation

Aron Kuppermann, Ph.D. Department of Chemistry, California Institute of Technology, Pasadena, California

Raphael D. Levine, Ph.D. The Fritz Haber Research Center for Molecular Dynamics, The Hebrew University of Jerusalem, Jerusalem, Israel

Gillian C. Lynch, Ph.D. Department of Chemistry, Chemical Physics Program and Supercomputer Institute, University of Minnesota, Minneapolis, Minnesota

Vladimir A. Mandelshtam, Ph.D. Department of Chemistry, University of Southern California, Los Angeles, California

Nikola Markovic, Ph.D. Department of Physical Chemistry, Göteborg University, Göteborg, Sweden

Howard R. Mayne, Ph.D. Department of Chemistry, University of New Hampshire, Durham, New Hampshire

Anne B. McCoy, Ph.D. Department of Chemistry, The Ohio State University, Columbus, Ohio

Steven L. Mielke, Ph.D. Department of Chemistry, Chemical Physics Program and Supercomputer Institute, University of Minnesota, Minneapolis, Minnesota

William H. Miller, Ph.D. Department of Chemistry, University of California and the Chemical Sciences Division, Lawrence Berkeley National Laboratory, Berkeley, California

Hiroki Nakamura, Ph.D. Department of Theoretical Studies, Institute for Molecular Science, Myodaiji, Okazaki, Japan

Eli Pollak, Ph.D. Chemical Physics Department, Weizmann Institute of Science, Rehovot, Israel

Françoise Remacle, Ph.D. Department of Chemistry, University of Liège, Liège, Belgium

Sarah A. Schofield, Ph.D. Department of Chemistry and Biochemistry, University of Texas at Austin, Austin, Texas

David W. Schwenke, Ph.D. NASA Ames Research Center, Moffett Field, California

Edwin L. Sibert III, Ph.D. Department of Chemistry, University of Wisconsin-Madison, Madison, Wisconsin

Howard S. Taylor, Ph.D. Department of Chemistry, University of Southern California, Los Angeles, California

Start of Citation[PU]Marcel Dekker, Inc.[/PU][DP]1996[/DP]End of Citation

Donald G. Truhlar, Ph.D. Department of Chemistry and Supercomputer Institute, University of Minnesota, Minneapolis, Minnesota

Peter G. Wolynes, Ph.D. Department of Chemistry, Noyes Laboratory, University of Illinois at Urbana-Champaign, Urbana, Illinois

Robert E. Wyatt, Ph.D. Department of Chemistry and Biochemistry and Institute for Theoretical Chemistry, University of Texas at Austin, Austin, Texas

Dong H. Zhang, Ph.D. Department of Chemistry, New York University, New York, New York

John Z. H. Zhang, Ph.D. Department of Chemistry, New York University, New York, New York

Start of Citation[PU]Marcel Dekker, Inc.[/PU][DP]1996[/DP]End of Citation

1

Spectra, Rates, and Intramolecular Dynamics

FRANÇOISE REMACLE
University of Liège, Liège, Belgium

RAPHAEL D. LEVINE
The Fritz Haber Research Center for Molecular Dynamics, The Hebrew University of Jerusalem, Jerusalem, Israel

I. INTRODUCTION

This book is about the intermolecular and intramolecular motion of atoms at energies sufficiently high that changes of chemical interest can take place. The problem that this chapter and indeed the entire first part of this book deals with arises because there are two very useful views of vibrationally excited molecules, two views which at first sight are in a very real conflict. At lower energies we have the description provided by many years of study of infrared and Raman spectroscopy (1–4). The motion of the atoms in the excited molecule can be described by normal modes where in each such mode all the atoms move coherently. A typical case, that of the DCCH molecule, is shown in Fig. 1. Normal modes retain their identity and hence their energy content for a long time. The atoms can vibrate in a given mode for more periods than the earth has, so far, revolved around the sun, a time sufficient to observe the decay of the excited vibrational state by the (very slow, often submillisecond) emission of infrared light. In space where, due to the low density, molecules are only slowly deactivated by collisions, radio astronomy uses this infrared emission to detect many unexpected species (5). The other point of view, which has been developed to describe the process of bond breaking (or of bond rearrangements as in isomerization) is just as old (6). In this picture, the energy is delocalized and moves from one mode of motion to another on a time scale short compared to the scale of the chemical event of interest. There have been many attempts to prepare and/or to probe such energy rich molecules on ever shorter time scales. The

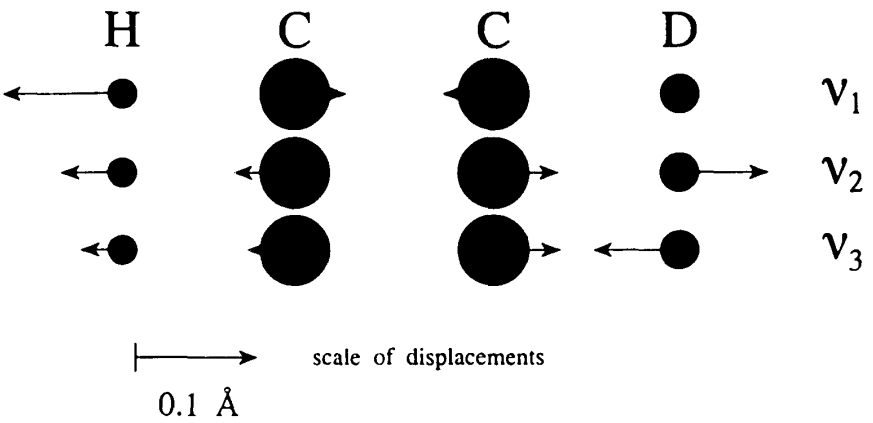

Figure 1 The normal modes of motion for the three stretch modes of DCCH. (Adapted from T. A. Holme and R. D. Levine, *Chem. Phys. Lett. 150*: 393 (1988).) The displacement of the atoms in each mode is shown by an arrow. Note that while all atoms contribute to all modes, the respective contributions do vary and the ν_1 mode is almost a localized CH stretch. For recent studies of the overtone spectroscopy of HCCH and its isotopomers see J. Liévin, M. Abbouti Temsamani, P. Gaspard, and M. Herman, *Chem. Phys. Lett. 190*: 419 (1995); M. J. Bramley, S. Carter, N. C. Handy, and I. M. Mills, *J. Mol. Spectrosc. 160*: 181 (1993); B. C. Smith and J. S. Winn, *J. Chem. Phys. 89*: 4638 (1988); K. Yamanouchi, N. Ikeda, S. Tuschiya, D. M. Jonas, J. K. Lundberg, G. W. Abramson, and R. W. Field, *J. Chem. Phys. 95*: 6330 (1991).)

available evidence is that typically the mode mixing is very fast (7). A classic example is outlined in Fig. 2, which shows two distinct dissociation paths of a molecule where the initial activation is quite localized and hence is expected to very much favor one path over the other. The energy rich molecule can be deactivated by collisions with a buffer gas and once it is cooled down, the reaction is quenched. Increasing the buffer gas pressure decreases the time an energy rich molecule survives after it is formed. Up to quite high pressures one could not detect a difference in the branching fraction between the two paths shown in Fig. 2.

The two paradigms, the spectroscopic and the kinetic one, cannot be simultaneously right. Either the vibrational energy stays put in a given mode or it very rapidly dissipates. Of course, the answer is that both descriptions have limited ranges of validity. The spectroscopic one is appropriate at lower energies and the kinetic one at higher levels of excitation. Much of our concern in the first part of this book is in the intermediate regime where neither description is quite appropriate. We find this worthy of a detailed examination because we understand so well the two extremes that it is time that we close the gap. This is made possible and timely since experimental and theoretical techniques for probing this intermediate region are becoming available. Much interesting chemistry occurs in the intermediate region so that intellectual curiosity is only a part of the answer. Equally important is that an understanding of this region is essential if we are to control the dynamics via the preparation of the system. This is the simplest notion of control and one that is most reasonable for deterministic systems: the way to specify where the system will end up is to send it on its way in the right direction. The very foundation of the kinetic point of view denies that this is possible. If the system rapidly dissipates any selective initial excitation then the final outcome cannot be determined by a choice of initial conditions and this is the very point of the experiment outlined in Fig. 2. Both

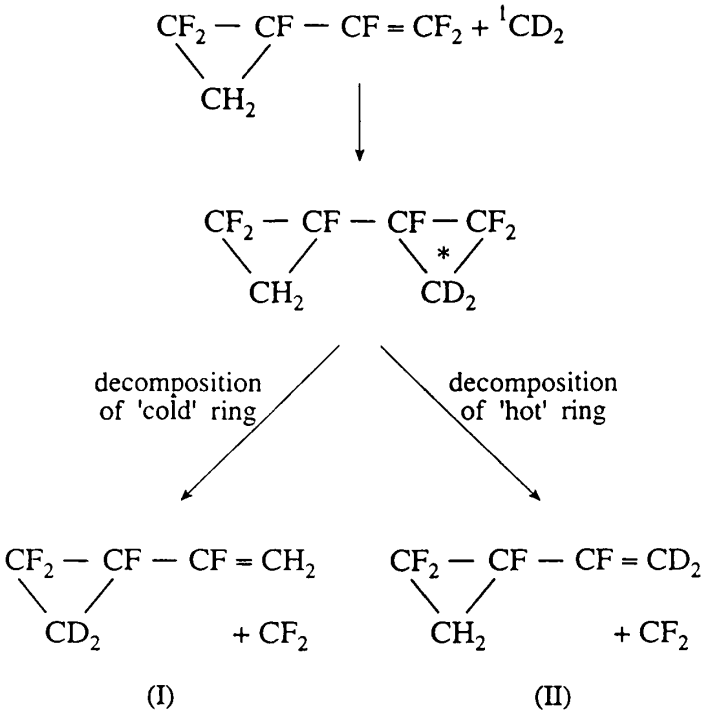

Figure 2 Two competing decay modes of a "chemically activated" molecule. The excess energy is initially localized in the ring containing the two newly formed C—C bonds (indicated by a star). Yet the experiment (by J. D. Rynbrandt and B. S. Rabinovitch, *J. Phys. Chem.* 75: 2164 (1971)) failed to detect a difference in the two alternative decays. The standard overview of the implications drawn from these experiments is (7).

experimentalists and theorists regard this apparent loss of the ability to control* (via initial preparation) as a challenge to their ingenuity and schemes for recovering it are the subject of frequent discussions (8–10). There is also a question of principle that is involved. For many purposes one can regard energy rich isolated molecules as closed mechanical systems. (This is not quite right because, e.g., they can emit infrared light but this is a rather slow process.) A mechanical system is not supposed to ever lose track of its initial conditions. One can even put it in a stronger (but equivalent) way: the initial conditions are constants of the motion. Yet the kinetic point of view claims that the memory of the initial excitation very rapidly erodes. Why do molecules forget?

It has been very fashionable to blame the kinetic behavior on "chaos," which for our introductory purpose we can think of as the sensitivity to the precise initial conditions. If the initial conditions are fully and tightly specified (i.e., when one excites an eigenstate) then indeed the isolated system cannot forget. But in reality one can seldom excite a molecule to a fully specified initial state and if one did, then there would only be the spectroscopic mode of behavior. Otherwise, the point is that even quite simple mechanical systems but of realistic complexity (e.g., allowing for anharmonicity) exhibit sensitivity to initial conditions by which one means that two rather similar initial states follow quite diverging trajectories. If the initial state is not sharply defined then its subsequent evo-

*A somewhat different notion of control, one that is receiving considerable current attention (10,11), is by tailoring the laser pulse to direct the evolution of the molecule.

lution will be not unlike the spreading of cream in a coffee cup: pretty soon the cream appears to us to be uniformly distributed and this uniformity is irrespective of how we poured the cream in. Excellent technical discussions of chaos (12–14) and its implications for energy rich molecules (15–17) are available. Our purpose however is to understand the dynamics on shorter time scales during which the system is amenable to being controlled and to find out how this period can be extended.

The evidence that one has a reason to look for a merging of the spectroscopic and the kinetic points of view, a regime where important elements of both approaches survive and coexist comes from studies at the boundaries of this regime where the archetypal behavior is more extreme. Figure 3 shows (bottom panel) the HF product vibrational state distribution from the H atom abstraction reaction of an F atom with $(CH_3)_4C$. The reaction satisfies those criteria that we have come to recognize (18), as typical of the kinetic regime: the energy is high and the reaction proceeds through a polyatomic transition state yet the HF vibrational energy disposal is quite specific and, as shown in Fig. 3, is qualitatively different from what it would be if the energy was randomized. The reason is that the abstraction reaction is a direct one (18), proceeding within one or a few vibrational periods. On such a short time scale, there is no time for intramolecular processes to take place so that the excitation energy does not delocalize and is carried away as internal energy of HF. This behavior is unlike that for the indirect bimolecular reaction as shown in Fig. 2, where an energy-rich intermediate is formed and remains stable for at least hundreds of vibrational periods before the reaction occurs. The boundary between the spectroscopic and kinetic regimes is thus not simply a matter of energy content nor that of the number of available states. Accessibility of these states (denied for the reaction shown in Fig. 3 by the fast time scale) is also important.

A similar conclusion emerges also from spectroscopic studies of very energy rich states recently made possible both by the ability to monitor the very weak absorption of light from the ground to these high up states and by the development of special methods for accessing them (19–23). As one goes up in energy and/or in the size of the molecule the gradual breakdown in the strict spectroscopic paradigm becomes increasingly evident (24). The long-known phenomenon of "perturbations" in the spectrum (1), an interesting but unusual occurrence at lower energies, becomes increasingly more common as the energy is higher up. What happens is clear from perturbation theory: the extent of mixing of two states is inversely proportional to their energy difference. At lower energies a vibrational state is, barring an accident of nature, far removed from any neighboring states. Because the density of vibrational states increases rapidly (approximately as the energy to the power, s, of vibrational modes, $s = 3N - 6$, where N is the number of atoms), the states are increasingly closer as the energy goes up so much so that for molecules larger than triatomics one speaks of the onset of the vibrational quasicontinuum of states (18) well below the dissociation threshold. The natural reaction is then to say that this onset is the transition from the spectroscopic to the kinetic regime. That will however be somewhat too facile because a closer examination reveals that things are not quite that simple. For one thing, and as already noted, accessibility is important, which here means that no, the spectrum of a molecule at high energies is not uniform. On the contrary, it reveals a rich structure.

An important characteristic of a moderate resolution vibrational spectra of isolated molecules at higher excitation is its "clump" or bumpy structure (19). A computer generated example of what we mean is shown in Fig. 4. The spectrum consists of broad characteristic clumps or "features." The breadth of the clumps is not due to experimental

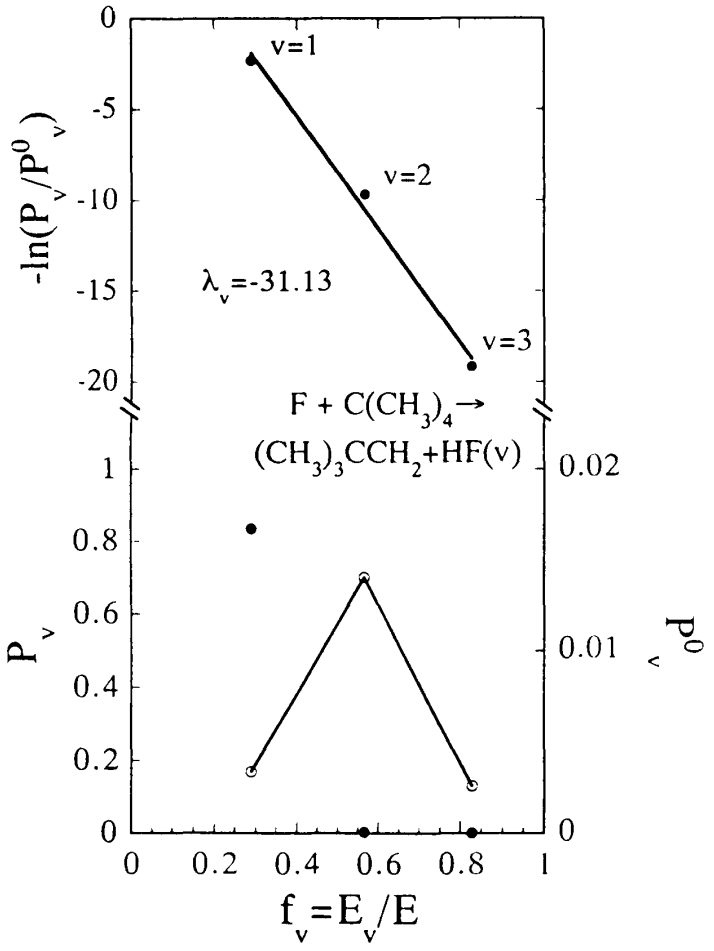

Figure 3 Surprisal plots (18) for the HF vibrational state distribution from the exoergic H atom abstraction reaction F + $(CH_3)_4C$ → $(CH_3)_3CCH_2$ + HF(v). (Bottom panel) The observed (by D. J. Bogan and D. W. Setser, *J. Chem. Phys. 64*: 586 (1976)) distribution, $P(v)$, open dots connected by a line, and the (so called, prior) distribution, $P^0(v)$ full symbols, vs. the HF vibrational energy. The prior distribution is the one expected when all products' final states are equally probable (18). The observed distribution is qualitatively different from the prior one and their deviance, the surprisal, $-\ln(P(v)/P^0(v))$ is plotted vs. E/E_v, where E_v is the HF vibrational energy and E is the total energy, in the upper panel. One can interpret the linear dependence of the surprisal on the HF vibrational energy as reflecting the presence of a quantity which is conserved by the dynamics. (See, for example, ref. (108)). In this sense, surprisal analysis is analogous to the search for quantum numbers that are not destroyed by the intramolecular couplings.

imperfections; in particular it is neither due to superposition of spectra of different initial states (known as an inhomogeneous broadening) or to collisional or other environmental effects nor is it due to the width of the frequency resolution. Such problems can, of course, degrade spectra but we assume that they have been overcome so that the clumps are an inherent property of the molecule. Examination of the spectral range which spans a clump at a much higher resolution then reveals that each clump is, in fact, a series of clumps, Fig. 4. When it can be done, an even much finer resolution reveals that each later clump may in fact be a series of congested clumps. When should we expect the process to converge—when the density of clumps along the frequency axis equals the

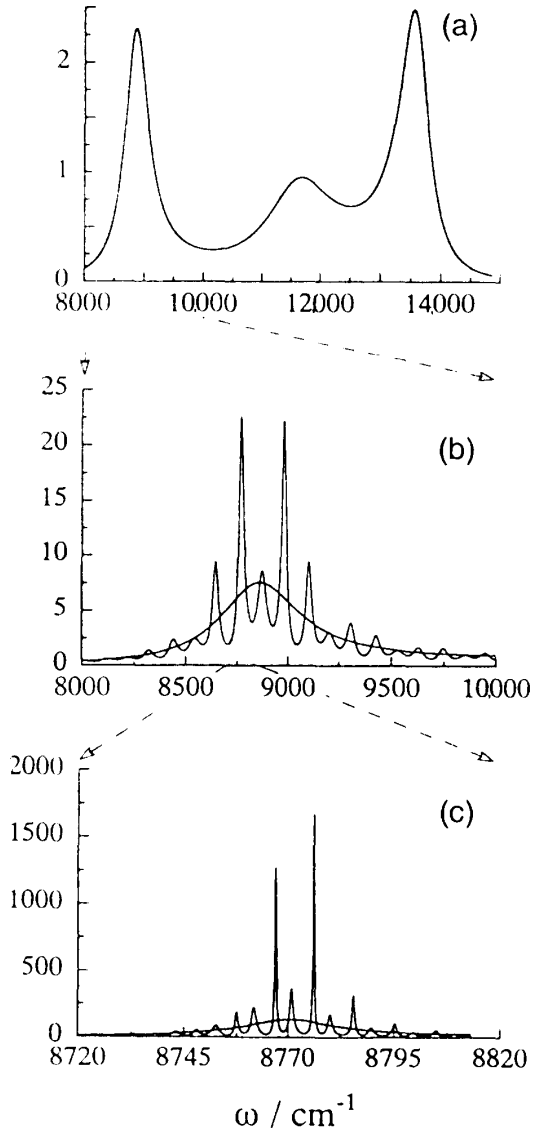

Figure 4 Three spectra at increasing levels of resolution. A computational example using the method of Sec. IV.B (Eq. (101) in particular), with three different time scales. The plot is adapted from F. Remacle and R. D. Levine, (102). (a) The broad envelope, determined by the shortest time scale. (b) The leftmost broad feature (smooth curve) shown under an intermediate resolution, revealing a nested structure. (c) One feature of the intermediate resolution (smooth curve) shown at high resolution. The point is that what appears as a single feature under a given resolution is found, at a higher resolution, to be a clump of several transitions. The unfolding process will converge when the density of transitions equals the density of (symmetry allowed) states at the given energy. It may converge earlier if there are strict selection rules that limit the range of accessible final states.

density of (allowed by symmetry) vibrational quantum states. In other words, ultimately we expect that, at least in the strict kinetic limit, every final state that can be accessed in principle will be observed. (Albeit the intensity may be so very small as to cause real experimental problems of signal to noise.) But what are the intermediate resolution clumps? We shall come to recognize them as the signature of the transition from the spectroscopic to the kinetic scheme of things.

A constant of the motion is a mechanical quantity (the energy being the most familiar one) that is conserved during the time evolution. This conservation necessarily restricts the motion of the molecule. Consider a nonrotating molecule. In the spectroscopic regime there is one constant of motion (typically taken to be the vibrational quantum number) per vibrational mode. In the kinetic regime there is only the total (vibrational) energy. If the molecule is a diatomic, the two regimes coincide. But for any bigger molecule, one can think of the transition as the erosion of the good spectroscopic constants of the motion. The point made in Fig. 4 is that this erosion is gradual rather than sudden. That constants of the motion can remain de facto effective for longer or shorter times and that these times can be quite different. Some constants can survive for very long while others fade very quickly. We shall argue that the observation of different spectra at different resolutions is a direct experimental evidence bearing on this point.

As chemists, we should be quite comfortable with the notion of "almost good" constants of the motion. Our very science hinges on this concept. The foremost example is the routine drilling we give students in balancing equations that represent chemical reactions. What do we teach them—that the number of atoms of any given kind must be the same on the left and right sides of the equation. Why do we teach it—because on any reasonable chemical time scale the number of atoms of a given kind is conserved. Yet, on an astrophysical time scale this is not the case. There are many other chemical examples, and all depend on the available energy, the lower it is, the more readily can we identify conserved quantities. The "number of bonds" is perhaps a simple one: At lower energies we expect only such chemical reactions where the number of bonds is conserved. Dissociation reactions, where this is not the case, are either typical of higher temperatures or require special circumstances. It was not only reactionary attitudes that made the examiners critical of Mr. (as he then was) Arrhenius' thesis work in which he argued that salts dissociated in water.

In what follows we shall cover some of the technical theoretical machinery that enables us to be more specific and detailed. Other particularly relevant chapters in this volume include Chap. 2 (Wyatt and Iung), Chap. 3 (Schofield and Wolynes), and Chap. 4 (McCoy and Sibert). Our discussion begins with the spectrum as source of information on intramolecular dynamics. Nowadays, when direct experimental monitoring of the time evolution of a molecule of a femtosecond time scale is a reality (25–28), the need for the frequency domain information is less obvious. Yet a conceptual and a technical understanding of intramolecular dynamics requires that the nature of the bridge linking the time and the frequency domains be well at hand and much of the recent progress has come about from a judicious combination of insights provided by both domains.

II. THE TIME-DEPENDENT VIEW OF SPECTROSCOPY

That the time and frequency variables are conjugate in the same sense that the position and momentum variables are, was in principle clear in both classical and quantum mechanics. It is even possible to take the usual notion of the phase space, whose dimension equals twice the number of mechanical degrees of freedom and to add two more, those of time and energy, and this is possible also in quantum mechanics (29,30). The advantage of doing so in practice was first realized in the so called, linear response regime (31,32), where the change in the state of the system is linear in the perturbation. Spectroscopy with weak (i.e., ordinary) fields is a clear example and for reasons which we intend to discuss, the early applications were to simple molecules (typically diatomic)

perturbed by their surroundings (32–34). We shall be primarily concerned with isolated and bigger molecules where it is the rest of the molecule that serves as the "bath." The very fact that we shall be able to make such an analogy shows that the distinction between intra- and intermolecular dynamics is at least in part a matter of convenience and not an essential one. One can think of a molecule and its environment as one supramolecule and one can equally regard the localized optically prepared initial state as being coupled to an environment provided by the rest of the molecule.

The technical discussion begins with a case that is convenient for an introductory presentation, that of vibrational dynamics in an excited electronic state. Experiments of this kind have been extensively pursued in both the frequency (35) and the time (36) domains. The formalism can be generalized to include the higher-order processes, such as two-photon spectroscopies (Raman (23,37–42), stimulated emission spectroscopy (20,22), and higher-order ones (23,43)). At the heart of the formalism is the notion of a nonstationary state which evolves in time. Our point of view, which follows Heller (44) can therefore be usefully applied to other aspects of dynamics, including photodissociation (45) and reactive collisions (46).

A. The Time Autocorrelation Function

We consider a one-photon excitation from the ground electronic state $|g\rangle$ to an electronically excited state $|e\rangle$. In the absence of the light the Hamiltonian H written within the Born-Oppenheimer approximation is diagonal in the electronic quantum numbers and can be symbolically written as

$$H = |g\rangle H_g \langle g| + |e\rangle H_e \langle e| \tag{1}$$

Here H_g and H_e are the Hamiltonians for the nuclear motion on the ground and on the excited electronic states, respectively. Each of these two Hamiltonians contains the kinetic energy operator for the motion of the atoms, which has the same form for the two states and a potential energy function which can be quite different. It is the difference in the two potential functions which implies that a stationary state for the nuclei on the ground electronic state will not be stationary for the excited state Hamiltonian. All the rest are details. Note that no coupling between the two electronic states is allowed for in Eq. (1) and while we shall assume this to be a good approximation, there will clearly be exceptions and these can be quite interesting in their own right (35,47–49) as they will allow for another type of intramolecular decay, known as radiationless transitions. Also in Eq. (1) we disregard the role of any other electronically excited states. One can disregard any optical transitions in the infrared by taking the dipole transition operator T to be strictly off diagonal in the electronic quantum numbers. The only allowed transitions are therefore those which promote an initial state $|i\rangle$ of the ground electronic state to a final state $|f\rangle$ of the excited electronic state. The set of quantum numbers needed to specify these states includes both the specification of the electronic state and those for the motion of the nuclei but from now on, the electronic quantum numbers of $|i\rangle$ and $|f\rangle$ are implicitly implied but not written explicitly. Then the fully resolved one-photon electronic absorption spectrum is, up to overall factors,

$$S(\varpi) = \sum_f |\langle i| T |f\rangle|^2 \delta(\varpi_i + \varpi - \varpi_f) \tag{2}$$

where ϖ_i and ϖ_f are the energies of the eigenstates $|i\rangle$ and $|f\rangle$ of the Hamiltonians H_g and H_e in frequency units $\varpi = E/\hbar$ respectively. Our purpose is to show that one can

discuss the time evolution that gives rise to the spectrum as generated from an optically bright state on the upper electronic potential which at time $t = 0$ is given by

$$|\psi_i(0)\rangle = T|i\rangle \tag{3}$$

and which evolves under the action of the excited state Hamiltonian. Typically $|\psi_i(0)\rangle$ is not an eigenstate of H_e and is therefore nonstationary. In particular, if, as is often the case, the initial state $|i\rangle$ on the ground potential energy surface is localized in the nuclear configuration, the initial state on the upper surface $|\psi_i(0)\rangle$ is also localized. If the dependence of the transition operator T on the nuclear coordinates is taken into account then the two states are not quite on top of one another, but the localized character, which we typically refer to as the Franck-Condon region, will remain.

By using closure over all final states of the upper electronic state, the spectrum Eq. (2) can be expressed as an expectation value over the bright state

$$\begin{aligned} S(\varpi) &= \sum_f \langle iT^\dagger|f\rangle\delta(\varpi_i + \varpi - \varpi_f)\langle f|T|i\rangle \\ &= \langle i|T^\dagger\delta\left(\varpi_i + \varpi - \frac{H_e}{\hbar}\right)T|i\rangle \\ &= \langle\psi_i(0)|\delta\left(\varpi_i + \varpi - \frac{H_e}{\hbar}\right)|\psi_i(0)\rangle \end{aligned} \tag{4}$$

The Fourier transform of the spectrum

$$C(t) = \int_{-\infty}^{+\infty} S(\varpi)\exp(-i\varpi t)\, d\varpi \tag{5}$$

is found to be determined by the time propagation of the initial state $|\psi_i(0)\rangle$ (44,50):

$$\begin{aligned} C(t) &= \langle i|T^\dagger \left[\int_{-\infty}^{+\infty} \delta\left(\varpi_i + \varpi - \frac{H_e}{\hbar}\right)\exp(i\varpi t)\, d\varpi\right] T|i\rangle \\ &= \langle i|T^\dagger \exp(i\varpi_i t)\exp\left(-\frac{iH_e t}{\hbar}\right)T|i\rangle \\ &= \exp(i\varpi_i t)\,\langle\psi_i(0)|\psi_i(t)\rangle \end{aligned} \tag{6}$$

In Eq. (6), $|\psi_i(t)\rangle$ is the initial state propagated up to time t on the upper electronic state. (Recall that since the transition dipole operator T is strictly off-diagonal in the electronic quantum numbers, the optically bright initial state, defined by Eq. (3), is only on the excited state.) Explicitly

$$|\psi_i(t)\rangle = \exp(\varpi_i t)\,\exp\left(-\frac{iH_e t}{\hbar}\right)|\psi_i(0)\rangle \tag{7}$$

Note the value of $C(t)$ at $t = 0$ is given by the normalization of the initial state $|\psi_i(0)\rangle$ and corresponds to the area under $S(\varpi)$

$$C(t = 0) = \langle\psi_i(0)|\psi_i(0)\rangle = \int_{-\infty}^{+\infty} S(\varpi)\, d\varpi \tag{8}$$

It is convenient to scale the area of the spectrum to unity, so that, using the Cauchy-Schwarz inequality (51), $|C(t)| \leq 1$. Equality is possible if (and only if) the initial state

recurs, i.e., if at some time t the state $|\psi_i(t)\rangle$ equals the initial bright state. Since the spectrum is real, one can define the time auto correlation function $C(t)$ for negative values of time by $C^*(t) = C(-t)$.

Equation (6), which expresses the frequency spectrum as the Fourier transform of the time autocorrelation of the initial state, is the central result of this section. It shows how to relate to the observed one-photon spectrum, determined in the frequency domain, to the time evolution of a nonstationary state on the excited electronic state. It is possible to obtain similar results for other spectroscopies. For example, the Raman excitation spectrum is determined by a time cross-correlation function between two different states. This is useful to know because the time autocorrelation function, while quite informative, really only tells us where the initial state is not, while the cross-correlation function tells where the initial state is. Before we turn to these considerations in detail, we should take advantage of what is already implied by the time autocorrelation function itself.

The essential point is the complementary nature of the descriptions in the time and frequency domains, a complementarity most familiar to us in the form of the time energy uncertainty principle. For our purpose we want a somewhat more detailed statement, a statement whose physical content can be loosely stated as "the overall shape of the spectrum is determined by very short time dynamics, higher resolution corresponds to longer time evolution. A fully resolved spectrum is equivalent to a complete knowledge of the dynamics." We now proceed to make this into a technical statement by an appeal to the convolution theorem for the Fourier transform (51). A preliminary requirement for this development is the definition of the operation of smoothing. To erase details in a function (in our case, the spectrum) we convolute it with a localized window function. A convolution operation is defined by

$$S(\varpi) * W(\varpi) \equiv \int_{-\infty}^{+\infty} S(\varpi')W(\varpi - \varpi')\, d\varpi' \tag{9}$$

and is symmetric in the two functions. The simplest example of smoothing of a function is by taking an average of the function over an interval and this is equivalent to taking the window function, $W(\varpi)$ in (9), to be of unit area over the interval $-\Omega$ to Ω. Convoluting the spectrum with such a window function $W_\Omega(\varpi)$ (Fig. 5) leads to

$$S_\Omega(\varpi) \equiv S(\varpi) * W_\Omega(\varpi) = (2\Omega)^{-1} \int_{\varpi-\Omega}^{\varpi+\Omega} S(\varpi')\, d\varpi' \tag{10}$$

Other localized window functions will lead to somewhat different detailed smoothing but the essential point remains—smoothing is achieved by convoluting with a localized window function. The other point, illustrated in Fig. 5, is that the Fourier transform of a function localized in frequency is a function localized in time, where the two widths are inverse to one another: A broad window function has a transform which is tightly localized about the origin of the time axis, and vice versa. This is a mathematical property of the Fourier transform relation between two functions, familiar in its implication as the energy-time uncertainty principle.

The convolution theorem (51) is the statement that the Fourier transform of a convolution of two functions is given as the product of their respective Fourier transforms. In symbolic form, the theorem states that

$$S(\varpi) * W(\varpi) \leftrightarrow C(t) \cdot W(t) \tag{11}$$

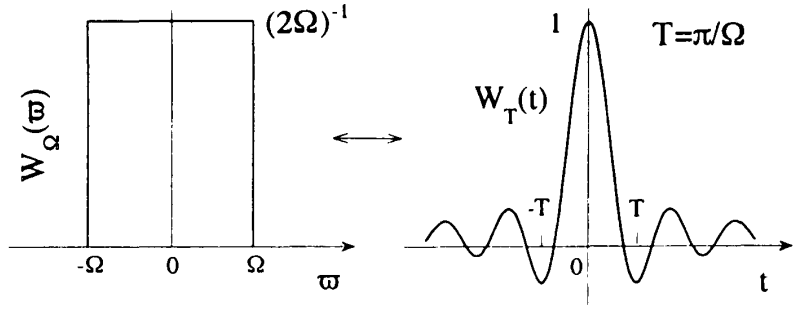

Figure 5 The unit window function in frequency, $W_\Omega(\varpi)$ and its Fourier transform in the time domain, $W_I(t)$. The widths of the transform pair are inverse to one another, and this mathematical result is true in general (51). (The physical implication of this theorem is, of course, the time-frequency uncertainty principle. In the present context, this theorem implies that short time dynamics determines the broad features of the spectrum, and vice versa). Convoluting the spectrum with the unit window function is the simplest form of coarse graining; cf. Eq. (10).

where the double-headed arrow denotes the Fourier transform pair; e.g., Eq. (5) reads $S(\varpi) \leftrightarrow C(t)$ and we use the notation $W(\varpi) \leftrightarrow W(t)$. It follows from Eq. (11) that the Fourier transform $C_I(t)$, $C_I(t) \leftrightarrow S_\Omega(\varpi)$, of a smoothed spectrum is simply given as the product of $C(t)$ by a localized window function $W_I(t)$. It is seen from Fig. 5 that the range of the window function in time is $T = \pi/\Omega$, where Ω is the resolution of the smoothed spectrum. Equation (11) is the technical statement of the qualitative idea of the correspondence in resolutions between the frequency and the time domains.

To return to chemistry, Fig. 6 shows schematic potential energy curves for an electronic spectrum of a cold isolated diatomic molecule. There is no possibility for IVR, but the spectrum (Fig. 7) clearly has a broad envelope which, judging from the spacings,

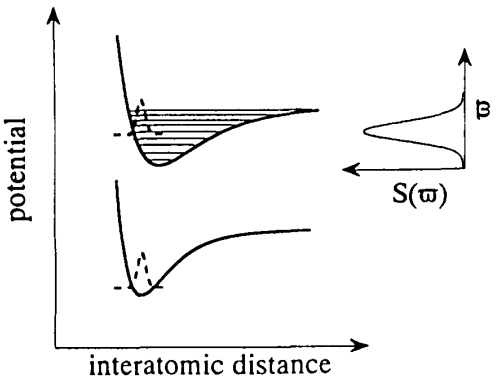

Figure 6 Potential energy curves for a ground and an electronically excited state. The coordinate dependence of the ground state wave function and the corresponding bright state, $|\psi(0)\rangle$ on the upper surface are shown as dashed curves. The shift of the equilibrium position of the excited with respect to the ground state potential implies that the bright state is not stationary and will evolve in time with a change in its shape. In a frequency-resolved language, the shift in equilibrium position means that several vibrational states on the excited curve are within the Franck-Condon region. The corresponding spectrum is shown in Fig. 7.

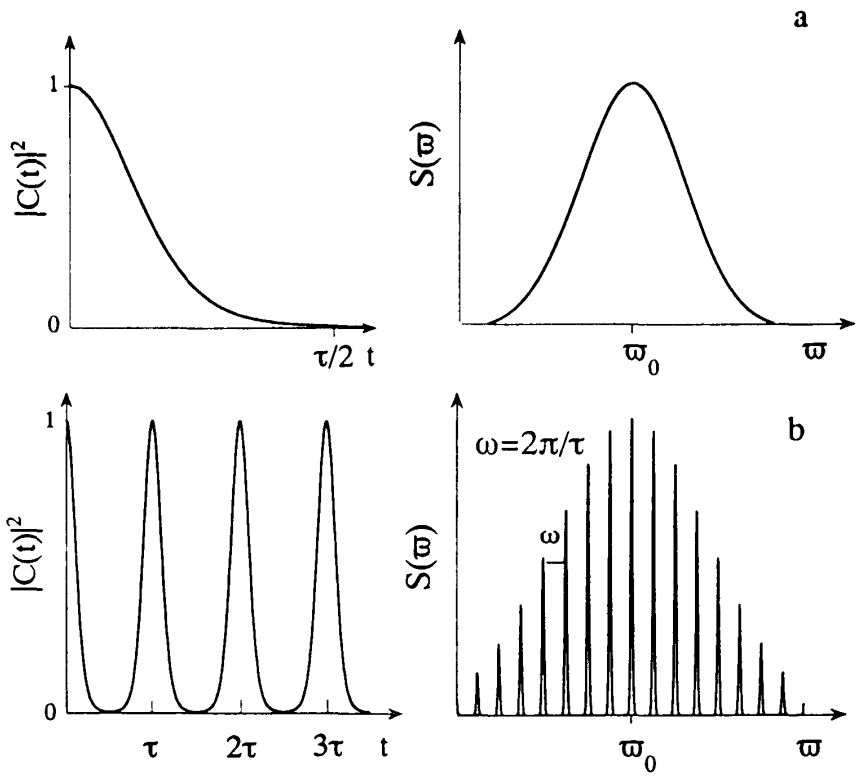

Figure 7 The time auto correlation function and the corresponding spectrum for a Gaussian wave packet propagating on an excited harmonic potential energy surface. (a) The short time decay of $C(t)$ (cf. Eq. (17)) and the broad spectrum (= the Franck Condon envelope (cf. (18)). (b) The longer time dependence of $C(t)$ and the corresponding, vibrationally resolved, spectrum.

spans a number of vibrational transitions. That several vibrational states of the upper electronic state can be accessed is to be expected if, as is often the case, the potential energy function for the excited state is shifted with respect to that of the ground state: There are several final vibrational states in the Franck-Condon region and the range of final states determines the width in frequency of the absorption. Now consider the same description in the time domain. The optically bright state is a nonstationary state localized in the Franck-Condon region, Fig. 6. It evolves by moving out of this region toward the outer turning point of the excited state potential. In so doing, the time autocorrelation function first decreases, Fig. 7, and this rapid time dependence determines the envelope of the frequency spectrum. Since we are dealing with a diatomic molecule, then at times of the order of a vibrational period, the wave packed $|\psi_i(t)\rangle$ will return to the Franck-Condon region. These returns, clearly evident in Fig. 7, help build up the structure of the spectrum. Forgetting the role of the rotation we have the simple expressions

$$|\psi_i(t)\rangle = \sum_n a_n \exp(-i\varpi_n t)|n\rangle \qquad C(t) = \sum_n |a_n|^2 \exp(-i\varpi_n t) \tag{12}$$

where the a_n's are the amplitudes of the different final vibrational states indexed by n where in our earlier notation $a_n = \langle e, n|T|g, 0\rangle$. As is to be expected, the Fourier transform of such a time autocorrelation function will clearly give rise to a series of spikes with the intensities $|a_n|^2$ at the frequencies ϖ_n. So far, this is a complicated derivation of an

expected result. Say, however, we examine $C(t)$ at times short compared to a vibrational period. Then the rapid (Gaussian-like, see below) decline determines the envelope of the spectrum. We make a detour to show this.

1. Intermezzo on the Harmonic Spectrum

It is instructive to compute the time correlation function in the simple case that the ground and excited state potentials are harmonic but differ in their equilibrium position and frequency. This is particularly simple if the initial vibrational state is the ground state (or, in general, a coherent state (52)) so that its wave function is a Gaussian. We shall also use the Condon approximation where the transition dipole is taken to be a constant, independent of the nuclear separation, but explicit analytical results are possible even without this approximation. A quick derivation which uses the properties of coherent states (52) is as follows. The initial state on the upper approximation is, in the Condon approximation, a coherent state, $|\psi_i(0)\rangle = |\alpha\rangle$. The value of the parameter α is determined by the initial conditions which, if we start from a stationary state, are that there is no mean momentum and that the mean displacement $\langle x\rangle$ is the difference in the equilibrium position of the two potentials. In general, using m and ω to denote the mass and the vibrational frequency

$$\langle x\rangle = \left(\frac{2\hbar}{m\omega}\right)^{1/2} \mathrm{Re}(\alpha) \qquad \langle p\rangle = (2m\hbar\omega)^{1/2}\,\mathrm{Im}(\alpha) \tag{13}$$

it follows that the initial value of α is real and is determined by the shift δx_{eq} in equilibrium positions,

$$|\alpha|^2 = \frac{m\omega}{2\hbar}(\delta x_{eq})^2 \tag{14}$$

For a coherent state [52]

$$|\psi_i(t)\rangle = \exp\left(-\frac{i\omega t}{2}\right)|\alpha(t)\rangle \tag{15}$$

where $\alpha(t) = \alpha\exp(-i\omega t)$ and using the overlap integral of two coherent states [52]

$$\langle\alpha|\alpha'\rangle = \exp\left(-\frac{|\alpha|^2}{2}\right)\exp\left(-\frac{|\alpha'|^2}{2}\right)\exp(\alpha^*\,\alpha') \tag{16}$$

one obtains for the time autocorrelation function, shown in Fig. 7,

$$\begin{aligned} C(t) &\equiv \langle\psi_i(0)|\psi_i(t)\rangle \\ &= \exp\left(-\left(\frac{|\alpha|^2}{2}\right)\left(1 - \exp(-i\omega t) - \frac{i\omega t}{2}\right)\right) \\ &\xrightarrow{t\to 0} \exp(-|\alpha|^2\,\omega^2 t^2 - i\varpi_0 t) \end{aligned} \tag{17}$$

The short time limit is Gaussian and determines the envelope of the spectrum, shown in Fig. 6. Since the Fourier transform of a Gaussian in time is a Gaussian in frequency and since a phase factor corresponds to a shift in the frequency, the frequency ϖ_0 corresponds to the center of the Franck-Condon band (it is the frequency of the transition turning

point). Explicitly, the envelope of the spectrum is

$$S(\varpi) \propto \exp\left(- \frac{(\varpi - \varpi_0)^2}{2\sigma^2} \right) \tag{18}$$

The width, σ of the spectrum is as determined from the reflection approximation (1) which relates the width to the slope F of the upper potential energy curve at the center of the band,

$$\sigma = |\alpha|\omega = \frac{F}{(2\hbar\omega)^{1/2}}, \qquad \text{where } F = m\omega^2\delta x_{eq} \tag{19}$$

Equation (18) is a very simple example of how the very short time dynamics determines the low-resolution (i.e., the envelope) spectrum. The details of the intensities of individual transitions require a longer time propagation and result in the resolved spectrum shown in Fig. 7. The envelope is however given by Eq. (18) and what the longer time dynamics reveals are the details which make up this envelope. A subsidiary lesson is that a broad envelope is not necessarily a signature of IVR. In the present example, and this carries over to the polyatomic case as well, the broad envelope is determined by inertia i.e., by the acceleration of the position of the oscillator. (To quantitatively show this, take α in Eq. (13) to be a function of time. It is the first deviation of $x(t)$ from its initial value that gives rise to the Gaussian approximation. We reiterate that this can be shown in the multidimensional case as well (53).)

The next section introduces many of the methods available for computing $C(t)$ and other correlation functions. Much additional material will be found in the following chapters. In particular, the notion of the coherent state can be effectively generalized both to the multidimensional case and also for potentials which while not quite harmonic can be well approximated locally by a Taylor expansion up to second order. Heller (37,44,50), in particular, has championed this point of view. Another important lesson is that one only needs to propagate the initial state for very short times in order to generate a fairly resolved frequency spectrum. The reason is the value of the velocity of light which means that in frequency (i.e., cm $^{-1}$) units, a spectral resolution of $\Delta\nu$ requires a propagation time of $1/cT$ (cf. Fig. 5, noting that ϖ is an angular frequency, $\varpi = 2\pi\nu$). A 3-ps propagation is thus sufficient to resolve spectral features which are 10 cm $^{-1}$ apart. What this means is that even exact propagation schemes (See, e.g., Chapters 2 and 3) can be practical because one need not propagate for a very long time.

B. The Dipole Time Correlation Function

The time autocorrelation function can be written as a transition dipole correlation function, a form that is equally useful for an inhomogeneously broadened spectrum. This is the form that is extensively used to discuss the spectral effects of the environment (32–34). The dipole correlation function also provides for the novice an intuitively clear prescription as to how to compute a spectrum using classical dynamics. For the expert it points out limitations of this, otherwise very useful, approximation. The required transformation is to rewrite the spectrum so that the time evolution is carried by the dipole operator rather than by the bright state wave packet. The conceptual advantage is that it is easier to imagine what the classical limit will be because what is readily provided by classical mechanics trajectory computations is the time dependence of the coordinates and momenta and hence, of functions thereof. In other words, in our mind it is easier to

transcribe between quantum and classical dynamics using the Heisenberg picture in which it is the quantum mechanical operators that carry the time evolution.

The derivation begins with the expression of the transition operator in the Heisenberg picture $T(t)$:

$$\begin{aligned} T(t) &\equiv \exp\left(\frac{iHt}{\hbar}\right) T \exp\left(-\frac{iHt}{\hbar}\right) \\ &= \exp\left(\frac{iH_e t}{\hbar}\right) T \exp\left(-\frac{iH_g t}{\hbar}\right) + \text{H.c.} \end{aligned} \tag{20}$$

where H.c. stands for Hermitian conjugate. To make the transition from the Schroedinger picture, in which it is the wave functions that carry the time evolution, note that an equivalent form for $|\psi_i(t)\rangle$ in Eq. (7) is

$$|\psi_i(t)\rangle = T(-t)|\psi_i\rangle \tag{21}$$

Then, using Eq. (21), the Fourier transform $C(t)$ of the absorption spectrum is expressed as the transition dipole correlation function

$$C(t) = \langle i|T^{\dagger}T(-t)|i\rangle = \langle i|T^{\dagger}(t)T|i\rangle \tag{22}$$

The advantage of expressing the correlation function as an expectation value over the initial state is that, if the actual state is not sharply selected but is a mixture of states then (22) can be readily generalized

$$C(t) = \sum_i p_i \langle i|T^{\dagger}(t)T|i\rangle \tag{23}$$

Here p_i is the weight of the ith initial state and a more compact notation is to write (23) as

$$C(t) = \text{Tr}(\rho T^{\dagger}(t)T) \tag{24}$$

where the trace is over the density matrix ρ of the system

$$\rho = \sum_i p_i|i\rangle\langle i| \tag{25}$$

We now discuss two ways of taking a classical limit by replacing the quantum mechanical trace operation by an integral over the classical phase space, leading to a classical correlation function

$$C_{\text{cl}}(t) = (2\pi\hbar)^{-s} \int\int d\mathbf{p}\, d\mathbf{x}\, \rho(\mathbf{p}, \mathbf{x}) T(\mathbf{x}(t)) T(\mathbf{x}(0)) \tag{26}$$

The integral is written for a system of s degrees of freedom and $\mathbf{x}(t)$ is a classical trajectory with the initial conditions $\mathbf{x}(0)$, $\mathbf{p}(0)$. The averaging is over the distribution of initial conditions and we wrote the transition operator as a function of the coordinates alone. In the more general case it will be a function of both position and momentum coordinates. The route leading to the semiclassical Franck-Condon principle is taken up in connection with Eq. (33). Here, we continue in a different vein.

By making an ergodic assumption, the computation of Eq. (26) can be simplified. This assumption is familiar in the theory of stochastic processes (54). The sufficient con-

ditions are, as far as we understand them, making the average in Eq. (26) over a stationary distribution in phase space, which in our case of a sharp initial energy, means a microcanonical distribution. Using such an initial distribution is equivalent to a time auto correlation function (Eq. (24)), which is the Fourier transform not of the spectrum of a sharply defined initial state as given by Eq. (2) but of the averaged spectrum

$$S(\varpi) = \sum_i \sum_f |\langle i|T|f\rangle|^2 \delta(\varpi' + \varpi - \varpi_f)\delta(\varpi' - \varpi_i) \tag{27}$$

The averaging in Eq. (27) is over all possible initial states at the initial energy. For this spectrum it is possible to replace the ensemble average in Eq. (26) by the time average along a trajectory (55)

$$S_{cl}(\varpi) = \left| T_{cl}\left(\varpi = \frac{E_i - E_f}{\hbar}\right)\right|^2 \tag{28}$$

Here $T_{cl}(\varpi)$ is the Fourier transform of the time-dependent transition dipole, computed along the trajectory

$$T_{cl}(\varpi) = \int dt\ T_{cl}(\mathbf{x}(t))\exp(-i\varpi t) \tag{29}$$

The procedure is therefore very straightforward. A classical trajectory is computed and at every time step along the trajectory, the value of the transition dipole (or any other operator of interest) is determined. If the time points have been a priori specified to be equally spaced, the integral in (29) can be computed using a fast Fourier transform (FFT) algorithm. If, as will often be the case, the trajectory integration uses a variable time step then the integral can be done numerically and the simplest is to evaluate it piecewise as the trajectory propagates. Strictly speaking, the ergodic assumption implies that a single trajectory, if run for a sufficiently long time, suffices because, by assumption, it will representatively sample all the available phase space. A multitude of considerations (an important practical one being the stability of the integrator) factors however running several trajectories for a finite time and averaging the result. Hence, as a practical prescription one often writes Eq. (28) as

$$S_{cl}(\varpi) = \left\langle \left| T_{cl}\left(\varpi = \frac{E_i - E_f}{\hbar}\right)\right|^2 \right\rangle \tag{30}$$

where the averaging is over the initial conditions of the trajectories.

Other practical considerations include the duration of integration of the trajectory. As discussed in connection with Eq. (11), putting a finite upper limit T on the time integration in Eq. (29) is equivalent to keeping an infinite upper limit but multiplying the integrand by a unit step function (cf. Fig. 5). This means that the result is not $T_{cl}(\varpi)$ but its convolution with a window function whose width in frequency units is $1/cT$. The duration of integration is therefore determined by the required frequency resolution. The one additional complication is near the origin of the frequency scale where a finite peak due to the window function occurs. If the low-frequency range is of interest one can overcome this by noting that Eq. (29) implies that

$$i\varpi T_{cl}(\varpi) = \int dt \left(\frac{dT_{cl}(x|t))}{dt}\right)\exp(-i\varpi t) \tag{31}$$

known as the time differentiation theorem of the Fourier transform (51) (proven by writing the inverse transform or by integration by parts). The trick is then to transform not the dipole directly but its time derivative. If the dipole function is linear in the coordinate then this is sometimes known in quantum mechanics as the dipole velocity form of the spectrum. Obviously, if the problem is very severe one can use the second time derivative which will yield $\varpi^2 T_{cl}(\varpi)$. While we are on the subject of practical aspects, a trivial mistake is to overlook the distinction between the absolute atom-atom distance and the displacement of this distance from its equilibrium value. In many places it makes no real difference but in computing the spectrum it does. Two serious problems are (i) for many polyatomic molecules we do not know the realistic dependence of the transition dipole on the interatomic distances. The evidence from diatomic molecules is that for large vibrational amplitudes (and these, after all, are the motions that concern us) the dependence is definitely not linear. (ii) As we shall further discuss below, but as is already implied by the notation in Eq. (30), strictly speaking one should compute a separate trajectory (or, in practice, a separate ensemble of trajectories) for each particular $i \rightarrow f$ transition. If we use a trajectory (or an ensemble) at a fixed energy what we obtain is the power spectrum which, for an anharmonic system, is not quite the optical spectrum. This point is further discussed below.

Figure 8 is an example of a classical power spectrum $S_{cl}(\varpi)$ for an energy-rich molecule. The different panels show spectra computed using different dipole functions. Each such function is taken to be linear in the displacement of a particular coordinate. One might think that at the higher energy, all vibrational modes will be coupled so that each power spectrum will span the same range of frequencies. This clearly does not happen. The different spectra are fairly distinct even though the energy is high enough to be above the barrier to isomerization.

It is important to recognize that the computation of the spectrum from a single (or, in practice, a few) classical trajectory(ies) yields the power spectrum $S_{cl}(\varpi)$ which is not quite the same as an approximate quantum spectrum Eq. (2) where the approximation is that each transition matrix element is evaluated semiclassically. The latter has been thoroughly discussed (56,57) and, strictly speaking, requires running a separate trajectory for each transition of interest. The point is the choice of the energy at which the trajectory is computed which, for accurate results, needs to be midway between the energy of the initial and final states and the reason is that in anharmonic systems the frequency is a function of the energy. Since a spectrum can span final states of very different energies, one trajectory will not be enough to generate the entire spectrum. A simple concrete example is that of the Morse oscillator (58). The analytical solution for the trajectory, written as a Fourier series so that its transform can be obtained by inspection, is

$$x = x_{eq} + \delta + \beta^{-1} \sum_n \frac{h^n}{n} \{1 - \cos[n\omega_0(1 - \rho)^{1/2} t]\} \tag{32}$$

Here δ is the initial displacement of the oscillator from equilibrium which we take to be at the left turning point. β is the range parameter of the Morse potential and ω_0 is the harmonic frequency. The actual frequency is $\omega_0(1 - \rho)^{1/2}$, where ρ is the energy of the oscillator in units of the well depth $\rho = E/D$, $h = \sqrt{\rho}/[1 + \sqrt{1 - \rho}]$, $0 \leq h < 1$, so that the weight of the terms in the Fourier series increases with the energy of the trajectory.

In the example, we consider infrared vibrational transitions with a dipole which is linear in the displacement of the oscillator. Such a system will exhibit a mechanical

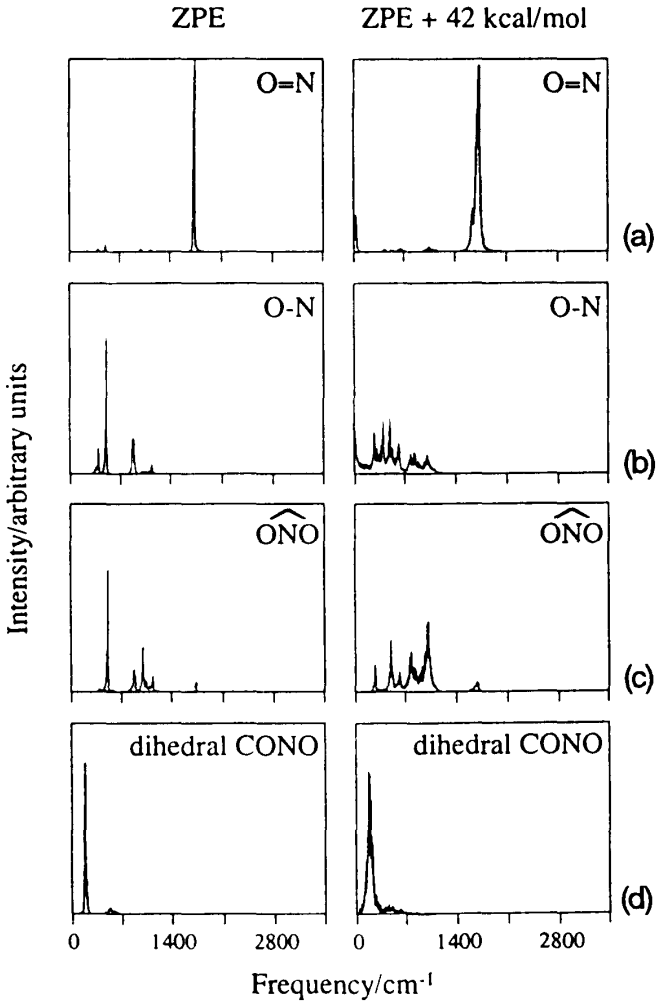

Figure 8 The computed power spectrum of different modes of CH_3ONO at the zero-point energy content (left) and at an energy higher by 42 kcal mol $^{-1}$ (right). The higher energy is well above the barrier for the *cis* to *trans* isomerization of the molecule. The computations of the trajectories lasted for 10 ps, which is much longer than the 0.7-ps lifetime for isomerization at that energy. (Adapted from T. D. Sewell, D. L. Thompson and R. D. Levine, *J. Phys. Chem. 96*: 8006 (1992).) The four rows correspond to four different modes which are involved in the isomerization. (a) The O=N stretch, which is a high-frequency mode. (b) The O—N stretch which is a lower-frequency mode and at the higher energy is significantly perturbed. The same is true for (c) the ONO angle. The latter two modes are significantly mixed as can be seen from the spectrum. (d) The CONO dihedral angle which is essentially the reaction coordinate for the isomerization.

anharmonicity in that there can be vibrational overtone transitions due to the anharmonicity of the potential. The spectrum is determined, cf. Eq. (28), by a Fourier transform of Eq. (32) which results in a series of equispaced spikes of decreasing height. The amplitude of the overtone transitions h''/n, decreases exponentially with the order, n, of the transition, as is to be expected. What is not quite correct are the frequencies. The different overtones are equally spaced, at the frequencies $n\omega_0(1 - \rho)^{1/2}$, whereas the correct quantal result is that the spacing between the successive overtones decreases due to the anharmonicity of the level structure. One can obtain the right spacings and the

right intensities by using a different trajectory for each overtone, a trajectory whose vibrational quantum number is the average of those for the initial and final states of the transition (56).

We close this section by discussing a practical way of computing electronic spectra from classical trajectories using the semiclassical Franck-Condon principle (59). Assuming that the dipole transition operator T commutes with the kinetic energy operator of the Hamiltonians H_e and H_g and that the kinetic and potential energies commute with one another, Eqs. (23) and (20) lead to the following expression of the autocorrelation function $C(t)$:

$$C(t) = \left\langle |T_{cl}(x(t))|^2 \exp\left[- \frac{i\Delta V(x(t))t}{\hbar} \right] \right\rangle \tag{33}$$

where

$$\Delta V(x(t)) = V_e(x(t)) - V_g(x(t)) \tag{34}$$

is the difference between the ground and excited potential energies along the trajectory. The averaging in Eq. (33) is taken over an ensemble of initial conditions.

The classical Franck-Condon principle is the two results: (i) the transition is possible when the frequency equals $\Delta V(x(t))$ which means that there is no change in the momenta of the nuclei during the transition and (ii) the transition occurs preferentially near the classical turning points of the vibrational motion. We now recover these conclusions from Eq. (33).

The semiclassical spectrum $S(\varpi)$ is obtained as the Fourier transform of $C(t)$ (Eq. (5)), which gives using Eq. (33):

$$S_{cl}(\varpi) = \left\langle \int_{-\infty}^{+\infty} |T_{cl}(x(t))|^2 \exp[-i\Delta V(x(t))] \exp(i\varpi t)\, dt \right\rangle \tag{35}$$

Equation (35) is the practical result. Assuming that $|T_{cl}(x(t))|^2$ is slowly varying one gets

$$S_{cl}(\varpi) \cong \left\langle |T_{cl}(x(t))|^2 \right\rangle \left\langle \int_{-\infty}^{+\infty} \mathrm{dt} \exp\left[i\varpi t \left(1 - \frac{\Delta V(x(t))}{\hbar\varpi} \right) \right] \right\rangle \tag{36}$$

or in an explicit form that shows where the transition takes place

$$S_{cl}(\varpi) \cong \left\langle |T_{cl}(x(t))|^2 \right\rangle \left\langle \delta\left[\varpi - \frac{\Delta V(x(t))}{\hbar} \right] \right\rangle \tag{37}$$

That the transition occurs preferentially at the classical turning point can be demonstrated if the integral in Eq. (36) (or better yet Eq. (35)) is evaluated using the stationary phase approximation (51). The points of stationary phase precisely occur at the classical turning points at which the momentum is zero. These expressions can also be generalized to the multidimensional case (59).

1. Moments and Sum Rules

For a very short time interval, one can determine the time evolution of the correlation function by a Taylor expansion. This is an application of the time differentiation theorem already mentioned in connection with Eq. (31). What the theorem provides is a relation between the coefficients in the Taylor expansion and the frequency moments of the

spectrum:

$$\langle \varpi^p \rangle = \int_{-\infty}^{+\infty} \varpi^p S(\varpi)\, d\varpi \tag{38}$$

Standard manipulations relate the frequency moments of the spectrum to the time derivatives of $C(t)$ at the origin

$$\langle \varpi^p \rangle = (i)^p \frac{d^p C(t=0)}{dt^p} \tag{39}$$

Below we provide the relation of the pth moment to the pth-order commutator of H and T. In particular, we shall argue that the $p = 0$ moment, i.e., the normalization of the spectrum corresponds to the limiting short time information on the dynamics. Higher-order moments are seldom sufficient as the Taylor expansion

$$C(t) = \sum_{p=0} \left(\frac{\langle \varpi^p \rangle}{p!} \right) (-it)^p \tag{40}$$

when truncated at a finite (and, in practice, necessarily low) order is not convergent. To characterize the dynamics one needs the values of $C(t)$ at finite times.

2. The Raman Wave Function

$C(t)$, the Fourier transform of the spectrum, can also be explicitly written as an autocorrelation function in the sense used in the theory of stochastic processes (54).

$$C(t) = \lim_{T \to \infty} \frac{1}{2T} \int_{-T}^{+T} \langle \psi_i(\tau) | \psi_i(t + \tau) \rangle\, d\tau \tag{41}$$

To prove Eq. (41) one expands $|\psi_i(t)\rangle$ as given in Eq. (7) in the eigenstates of H_c

$$|\psi_i(t)\rangle = \exp(i\varpi_i t) \sum_f |f\rangle\langle f|\psi_i\rangle \exp(-i\varpi_f t) \tag{42}$$

Using Eq. (42) in Eq. (41) gives

$$C(t) = \exp(i\varpi_i t) \sum_f |\langle f|\psi_i\rangle|^2 \exp(-i\varpi_f t) = \langle \psi_i | \psi_i(t) \rangle \tag{43}$$

The wave function $|\psi_i(t)\rangle$ is nonzero only for $t > 0$. One can therefore write for its frequency components

$$|\psi_i(\varpi)\rangle = \lim_{T \to \infty} \frac{1}{T} \int_{-T}^{+T} \theta(t) \exp(i\varpi t) |\psi_i(t)\rangle\, dt \tag{44}$$

where $\theta(t)$ is the unit step function. Using the form of Eq. (7) for $|\psi_i(t)\rangle$ and replacing $1/T$ by ε, so that the limiting form is $\varepsilon \to 0$ through positive values,

$$\begin{aligned} |\psi_i(\varpi)\rangle &= \lim_{\varepsilon \to 0^+} \varepsilon \left(\varpi + \varpi_i - \frac{H_c}{\hbar} + i\varepsilon \right)^{-1} |\psi_i\rangle \\ &= \lim_{\varepsilon \to 0^+} \varepsilon G^+(\varpi) |\psi_i\rangle \end{aligned} \tag{45}$$

The amplitude $|\psi_i(\varpi)\rangle$ has been previously defined in the theory of resonant Raman scattering (37) and referred to as "the Raman wave function." In the present approach,

the one-photon absorption cross section is the power spectrum (54) of the frequency dependence of $|\psi_i(\varpi)\rangle$. The absorption spectrum, as the Fourier transform of the convolution integral Eq. (41) can be written as

$$S(\varpi) = \lim_{T\to\infty} \frac{1}{T}\left[\int_{-T}^{+T} \theta(t)\exp(i\varpi t)|\psi_i(t)\rangle\, dt\right]^{\dagger}\left[\int_{-T}^{+T} \theta(t)\exp(i\varpi t)|\psi_i(t)\rangle\, dt\right] \tag{46}$$

which upon using Eq. (45) leads to

$$\begin{aligned} S(\varpi) &= \lim_{\varepsilon\to 0^+} \varepsilon\langle\psi_i|G^-(\varpi)G^+(\varpi)|\psi_i\rangle \\ &= \lim_{\varepsilon\to 0^+} \varepsilon\left\langle\psi_i\left|\frac{1}{(\varpi_i + \varpi - H_e/\hbar)^2 + \varepsilon^2}\right|\psi_i\right\rangle \\ &= \left\langle\psi_i\left|\delta\left(\varpi_i + \varpi - \frac{H_e}{\hbar}\right)\right|\psi_i\right\rangle \end{aligned} \tag{47}$$

This completes the demonstration of the formal equivalence of the Raman and the absorption spectroscopies.

3. Raman Excitation Profiles

The one photon absorption spectrum directly determines the time autocorrelation function, which in the notation of this subsection is $C_{ii}(t)$. It is of interest to also determine the time cross-correlation function $C_{fi}(t)$ which is the overlap of the time-evolved bright state with some different probe state

$$C_{fi}(t) \equiv \langle\psi_f|\psi_i(t)\rangle \tag{48}$$

This is the correlation function which determines the Raman amplitude for the transition $i \to f$ as a function of frequency.

$$\alpha_{fi}(\varpi) = -(i\hbar)\int_0^{\infty} C_{fi}(t)\exp(i\varpi t)\, dt \tag{49}$$

Here, as in the case of the one-photon spectrum, $|\psi_f\rangle$ is the bright state on the upper electronic potential energy surface which corresponds to the final state f on the ground electronic state. Equation (49) is a "half" Fourier transform in that it is limited to positive values of the time. One can regard it as an ordinary Fourier transform by defining the cross-correlation function to equal zero for negative times. Such a function is called causal in the theory of Fourier transform (51) and this puts conditions on the analytic properties of the Raman amplitude. These will be further discussed in Sec. IV.

The Raman excitation profile is proportional to $|\alpha_{fi}(\varpi)|^2$ which means that one cannot determine the time cross-correlation function directly from the observed Raman excitation profile. The indirect route is to first build a model potential energy surface for both the ground and the excited electronic states. The overlap $\langle\psi_f|\psi_i(t)\rangle$ is calculated by propagating the initial wave packet $|\psi_i\rangle$ on the upper electronic state and a computed resonance Raman excitation profile is obtained using Eqs. (48) and (49). The parameters of the potential energy surfaces can then be adjusted in order to get a good fit of the experimental excitation profile. In Sec. IV we shall discuss a method for a direct inversion. Another approach which has been discussed is the use of the transform theory (38,41).

III. METHODOLOGIES

The computation of spectra relies on two types of methodologies, those which determine the energetics (including the dependence of the dipole operator on the vibrational coordinates) and those which carry out the time propagation. The former is largely outside the scope of this volume. Yet one must recognize that without the energetic input one can not proceed. The energetic situation is nowadays making a very satisfactory progress and working procedures which determine the potential energy for the ground state of a polyatomic molecule to a spectroscopic level of accuracy are becoming available. The same is essentially the case also for any expectation value over the ground state wave function. However, this is not quite the case for electronically excited states. One result is that we definitely do not yet have the quantitative knowledge of how the transition dipole function varies with the nuclear coordinates even for small polyatomics. The situation is definitely improving. One important approach, driven by the needs of dynamics, is to give up the traditional demarcation between energetics and dynamics and to carry out both in the same computation. The energetic input is thereby generated where it is needed. In other words, the potentials, etc., are determined at the point where the trajectory is, at the current time step. It then is moved to the next step and the required energetics are determined and so on. This is made possible by the refinement of the so-called gradient techniques (60) which determine not only the local energy but also its derivatives (or even second derivatives). It is thereby possible to specify where the trajectory is to go to in the next time step using the forces computed at the current position. For motion confined to the ground potential energy surface, such methods can already be applied to systems of considerable complexity (61). A related development is the refinement of density functional theory (62) to a level which might be accurate enough for dynamical computations.

The other part, that of computing the dynamics, is covered in many chapters of this book. Our purpose is not to preview the material but rather to note what procedures are available with reference to the computations of spectra and of intramolecular dynamics in general. Other sources for this overview include (63). A rather schematic outline is provided in Fig. 9. The figure does not cover the earlier point, that of combining the energetics with the dynamics but it should be clear that some methods are inherently more suitable for this purpose. In particular, classical dynamics, which requires only a local input, has an advantage in thinking about the implementation of such an approach. The advantage is however not absolute. For example, there is a formulation of quantal propagation where the coupling is needed piecewise, step by step, rather than globally (64). The essence of the method is to introduce a progress variable q (which need not be one-dimensional) such that the problem is assumed solved for $q < q_0$. Now increment q_0 to a new value, $q_0 + \delta q_0$. Since the increment is small, it is easy to compute the resulting change in the wave function to first order in δq_0 (65). One thereby obtains an equation for propagating the wave function (or other quantities) as a function of q_0, where the input at any step is the change in the potential between the two points. Other methods for integration of the Schrödinger differential equation (66) can also be adapted to using only local input about the potential. It is also possible to develop methods (67) which do not introduce the distinction between energetics and dynamics and solve the entire problem as one whole from the very beginning.

We turn now to a brief and not exhaustive discussion of specific classes of methods. The entire discussion is based on the assumption that the required potentials, couplings,

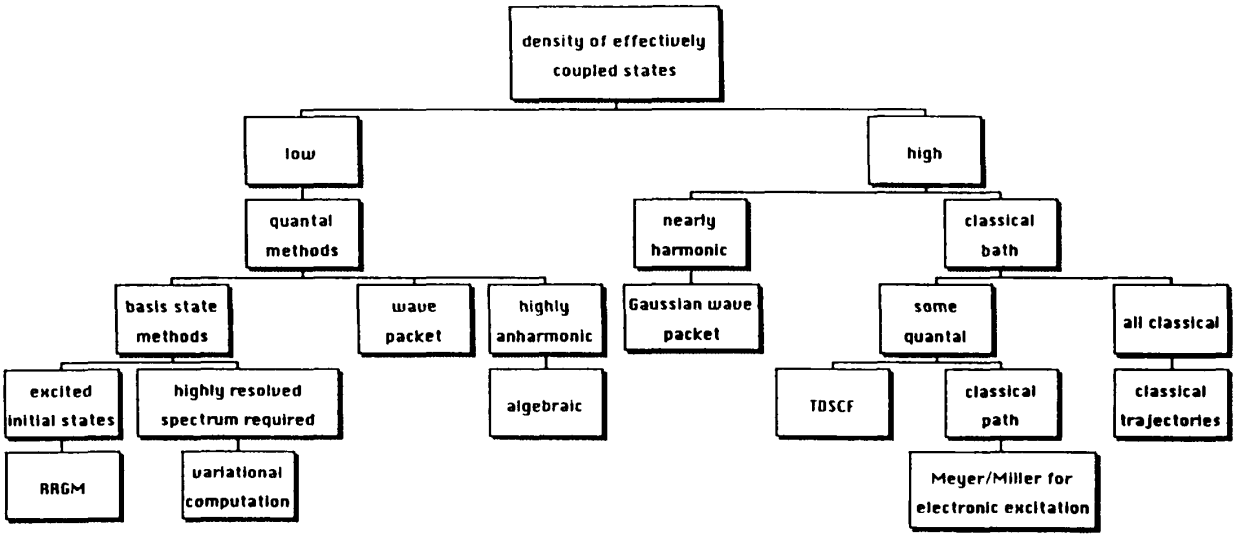

Figure 9 A schematic guide to method selection.

etc., are available. For the reasons discussed above, often these will be empirical or "realistic" but not exact. On the other hand, empirical force fields often combine much chemical insights and systematics and can provide a very valuable guide to what can happen during the dynamics.

A. Classical Dynamics

Computing classical trajectories (68) is no longer limited by the size of the system (69). Even on a workstation one can, nowadays, run trajectories for systems with hundreds of atoms, and run enough trajectories to be able to Monte Carlo average over the initial conditions. (Recall that for systems larger than triatomics, the number of trajectories that are needed is determined by the resolution required in the results and not by the number of atoms (66)). Of course, the exponential divergence of nearby trajectories implies that a rather small time step must be used and even then the results are only reasonably accurate for very short times. People do very much differ in their detailed attitude on this point. We prefer to restrict running the trajectories to such time intervals that the integration is time reversible, that is, that upon reversal of the final values of the momenta, computing back will recover the initial condition of the trajectory to within some acceptable tolerance. (The conservation of the total energy, while a necessary condition is a far weaker indicator of the stability of the integrator.) When one needs dynamical information for longer times and the integration is too unstable it seems to us to be the signature of the need for other methods. It is, however, possible, and not uncommon, to argue otherwise. The arguments are of two sorts. The first one is that the necessarily more approximate alternative methods simply try to mimic the inherent instability of the dynamics. Why not let the integrator do that? Surely it is the best way to mimic the instability. We regard this as a reasonable but expensive (in computer time) attitude. The more approximate procedures typically center attention on a subsystem of interest and represent the rest of the system as a "bath" to which the subsystem is dissipatively coupled (70–74). The computational effort is thereby much reduced and such methods can, with due care, compare favorably with a full dynamical computation (74). The other

rationale for integrating even when microscopic reversibility does not hold is sometimes based on the shadowing theorem. Loosely stated, the theorem says that during most any portion of an unstable trajectory, what one is computing is a segment of an exact trajectory, but a trajectory which need not have the same initial conditions as the one that the integrator started with.

One reason why integration of a classical trajectory is so unstable is that the coordinates and momenta continue to change in time even when the degrees of freedom are uncoupled. When a mode is a high frequency vibration, this change can be quite rapid (a vibrational period of <20 fs is common for strong bonds or for hydrides). If there are time intervals during which the modes are uncoupled, one can change variables to action angle variables. The action variable is the classical analog of the quantum mechanical quantum number and the angle variable evolves linearly with time when there is no coupling. (See (75) for the definition of these variables and (76) for an example.) Even if the modes are not vibrations and even if the coupling does not cease, one can still define modes (the dressed variables (77)) that only change in a localized region. Another approach, which is very useful in the quite common situation that different modes have rather different time scales, is to take explicit advantage of this separation by de facto freezing the slow modes while the fast ones propagate for a few steps, adjusting the slow modes, freezing them again, etc. (78).

An important limitation on the use of classical evolution for intramolecular dynamics is the problem of the zero-point energy. A molecule of reasonable complexity can have a quite high zero-point energy, often high enough to isomerize or even fragment the molecule, while the other modes go down in energy toward the very bottom of the well. In reality this does not happen because the zero-point energy is not available for transfer from one mode to another. Nor will it happen in a strictly harmonic molecule. The zero-point energy is however available in classical mechanics since, for realistic potentials, the anharmonicity is large enough that such an energy exchange is possible. The power spectrum of a classically cold large molecule and of the same molecule with its zero-point energy can be quite different, Fig. 10. The exchange of the zero point energy between the different vibrational modes is manifested by a broadening of the lines, which are far sharper for the classically cold molecule. Not evident on the scale of the figure is that the vibrational frequencies of the classically cold molecule are a shade too low. This is because of the dependence of the vibrational frequency on the energy content of the mode. There have been a number of prescriptions (79–81) for avoiding the problem. In the final analysis such corrections are a "fix" rather than a real solution. Figure 11 is an illustration of the problem and how it can be avoided.

Having emphasized what can go wrong, we should reiterate that classical mechanics is a readily available tool which can address a variety of systems which are not easily simulated otherwise. Foremost is the problem of many degrees of freedom, as is the case for a molecule perturbed by its environment. Figure 12 shows the power spectrum of the coordinate. In this computation the Fourier transform of the dipole function (cf. Eq. (28)) is taken for different finite time segments along the trajectory. One cannot take these intervals to be too short as otherwise the spectrum will be too broad to be useful. A 1-ps time span appears in the case shown to provide a practical compromise. A solvent is only one form of an external perturbation. Another is an external field, most typically, the field of a high-intensity laser, a field which is too strong to be treated in perturbation theory. One includes coupling to the field as part of the Hamiltonian and computes trajectories in the presence of the field (82). Another important application to systems of

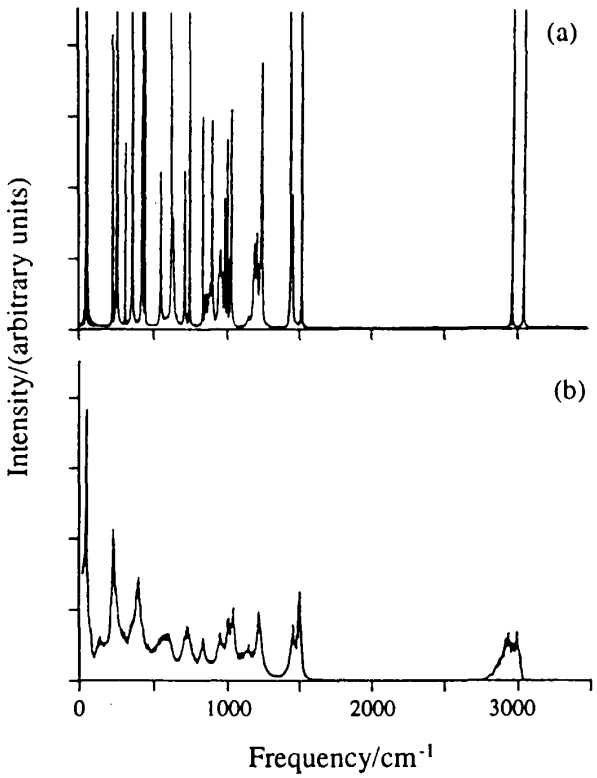

Figure 10 The classical power spectrum of a large molecule (RDX, hexahydro-1,3,5-trinitro-1,3,5-triazine) at a very low energy (a) and at its zero-point energy content (78 kcal mol $^{-1}$) (b). Already at the zero point there is extensive classical mode mixing. (Adapted from T. D. Sewell, C. C. Chambers, D. L. Thompson, and R. D. Levine, *Chem. Phys. Lett. 208*: 125 (1993).)

many degrees of freedom is the vibrational spectroscopy of polymers (83) and biomolecules (84).

B. Wave Packets

The solution of the time-dependent Schrödinger equation is both a practical approach (see Chap. 5) and a useful conceptual tool. The inherent advantage is that one can choose that initial state which is of interest (most typically, the optically bright state) and that the time evolution need only be determined up to the required frequency resolution. A concrete example where this advantage is very clear is shown in the two panels of Fig. 13.

The numerical solution of the Schrödinger equation (whether in its time-dependent form or by other methods) has the additional advantage that changes in the electronic state of the system can be allowed for. What this means is that one can, for example consider the dynamics in the presence of strong laser fields where processes which are not first order in the field are possible. These include a stimulated emission back to the ground state (possibly followed by excitation back to the excited state, etc.) or further absorption to higher excited states. The higher order processes can be of interest for diagnostic purposes (as in a pump and probe experiment) or can be the unavoidable result of a high-power laser pulse. Another class of problems where the interstate couplings are of central interest is when the Born-Oppenheimer approximation breaks down. The radiationless transitions of low-lying excited states is one notable example (35,47–

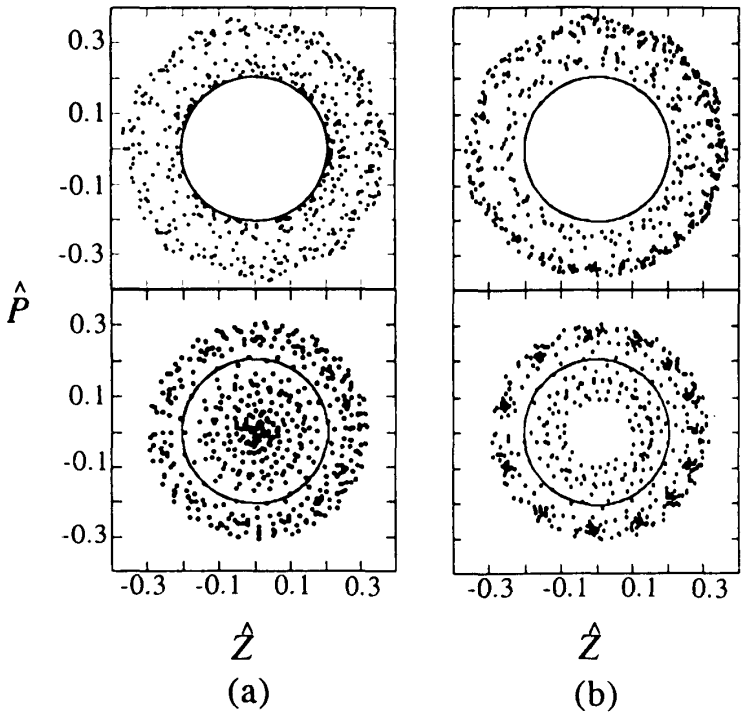

Figure 11 The region in phase space sampled by the vibrational motion of one of the two HF molecules in the HF dimer. (Lower panel) The results of an ordinary classical trajectory computation. (Upper panel) A classical computation which enforces conservation of the zero-point energy (zpe) of each mode. The trajectory is plotted for every time step of integration, in the $(\hat{Z}, \hat{P})$-plane. $\hat{E} \equiv E/D_e = \hat{P}^2 + \hat{Z}^2$, $\hat{Z}^2 = V(R)/D_e$, and $\hat{P}$ is the dimensionless momentum. The inner circle (in both panels) marks the zpe boundary; i.e., any point inside corresponds to the molecule vibrational energy dropping below the zpe. Each of the two HF molecules is given, at $t = 0$, one quantum of energy and the points are sampled at equal time intervals during 1 ps of integration. (a) This specific trajectory spent a considerable time in the quantum forbidden region and, in particular, near the origin, i.e., with practically no internal energy. A similar study of the second HF molecule shows that the energy lost by the first is essentially entirely gained by the second and the intermolecular energy does not change appreciably. (b) For a different trajectory where some energy is always left in the reference HF molecule. (Adapted from Ref. 81.)

49, 85,86). What wave packet methods enable one to do is to simultaneously examine the role of both interstate and of intrastate dynamics. This is important because of the increasing attention that is given to electronically nonadiabatic processes in photodissociation (87,88) and other experiments where the motion of the atoms is also of prime interest.

Special mention needs to be given to an approximation that has had an important influence not only on how one computes but also on how one thinks about wave packets (44,53). The essence of the point is the notion of a coherent state already briefly discussed in Sec. II.A.1. For the limited purpose of our discussion we consider a wave function to be a coherent state if it is specified as a function of one or more parameters and its time dependence is fully contained in the way that these parameters depend on time. What this means is that as the wave function evolves in time, its functional form is unchanged. It remains the same function of the parameters as it was, but the actual shape of the

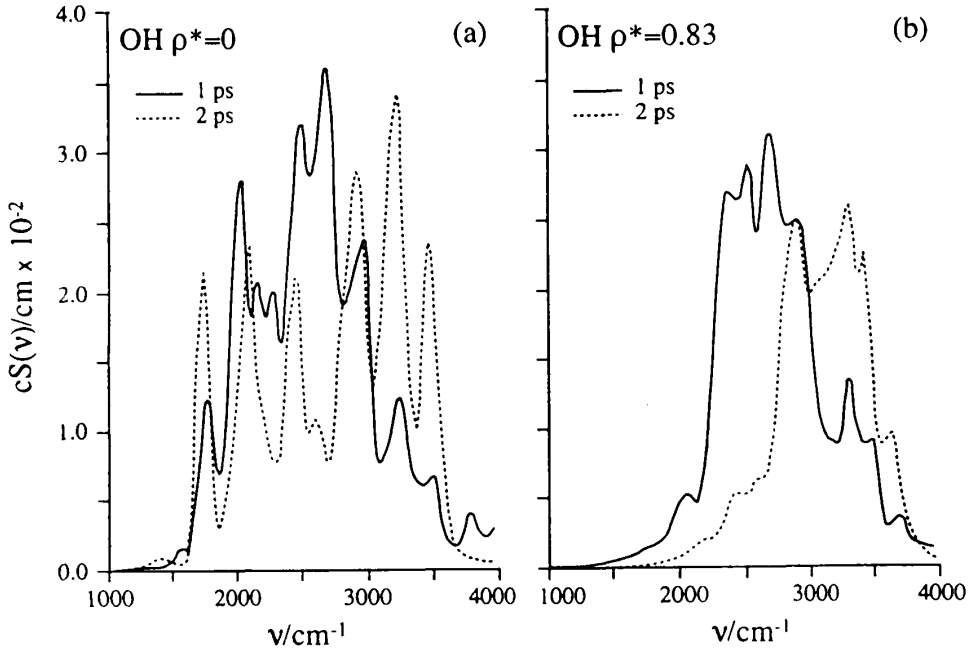

Figure 12 The classical power spectrum of the OH stretch of OHCl initially excited to the $v = 6$ overtone of the OH mode. This provides enough energy to dissociate the weak O—Cl bond but the two modes, which very much differ in their frequency, are not effectively coupled. Two power spectra are shown corresponding to propagating classical trajectories for the first ps after excitation and for the time interval between 1 and 2 ps after excitation. (a) Computation for the isolated molecule. (b) Computations for the molecule in liquid Ar at the (quite high) reduced density of 0.83. Note the solvent induced changes in the spectrum showing that the environment can affect the course of IVR. (Adapted from Y. S. Li, R. W. Whitnell, K. R. Wilson, and R. D. Levine, *J. Phys. Chem.* 97: 3647 (1993).)

wave function will change because the parameters can change with time. A simple and most familiar such form is that of a Gaussian. In one dimension, this is

$$\psi(x, t) = \exp\left\{\frac{-\Sigma_t^{-1}(x - x_t)^2 - ip_t(x - x_t) - s_t}{\hbar}\right\} \tag{50}$$

Since both Σ_t and s_t can be complex, the function in Eq. (50) is specified by six time-dependent parameters, which one can think of as the two first moments and three second moments of the position and momenta and the condition of normalization:

$$\begin{aligned} x_t &\equiv \langle\psi(x, t)|x|\psi(x, t)\rangle \\ p_t &\equiv \langle\psi(x, t)|p|\psi(x, t)\rangle \\ (x^2)_t &\equiv \langle\psi(x, t)|x^2|\psi(x, t)\rangle \\ (xp + px)_t &\equiv \langle\psi(x, t)|xp + px|\psi(x, t)\rangle \\ (p^2)_t &\equiv \langle\psi(x, t)|p^2|\psi(x, t)\rangle \end{aligned} \tag{51}$$

What this means is that the function really represents a Gaussian in phase space. The label "coherent state" is often reserved for the special case when x and p are uncorrelated, which corresponds to a state of "minimum uncertainty," i.e., one for which the

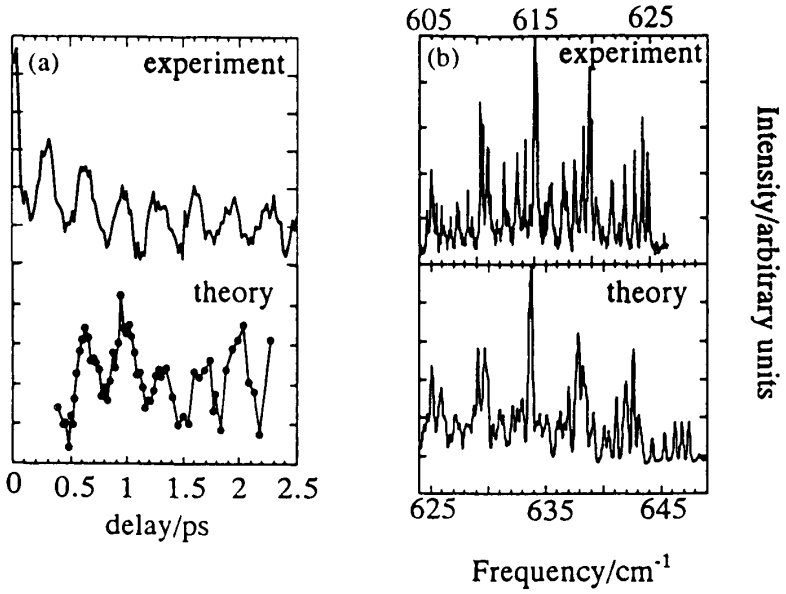

Figure 13 Comparison of the experimental and a quantum mechanically computed (by exact wave packet propagation using an ab initio computed potential energy) spectrum of a nonrotating Na_3 molecule pumped to its B electronic state. (Courtesy of Experiment by S. Rutz, E. Schreiber, and L. Wöste; Computations by B. Reischl, all of the Free University of Berlin) (a) The short time dynamics: Shown is the population of the excited state vs. time as determined by a pump-probe experiment and by the computation (points connected by a straight-line segments). The periodicity (about 320 fs) is due to the symmetric stretch motion. (b) A frequency spectrum. The long time dynamics (as reflected in the well-resolved spectrum) show the contribution of a different set of vibrational modes. The dominant peaks can be identified as the radial pseudorotation motion of $Na_3(B)$ while the splittings are due to the angular pseudorotational motion. (Adapted from B. Reischl, *Chem. Phys. Lett.*, *239*: 173 (1995) and V. Bonacic-Koutecky, J. Gaus, J. Manz, B. Reischl, and R. de Vivie-Riedle, to be published.)

uncertainty product, $\Delta x \Delta p$, is minimal. In this case Σ_t is real and is the measure of the width in coordinate space, and this form of Eq. (50) is the one often quoted in textbooks (52). For the coherent state Σ_t is the width $\hbar/2m\omega$ of the ground state of the oscillator, and is time independent. In the more general case, in which the position and momentum are correlated, the transcription between the second moments as given in Eq. (51) and the parameters in the wave function is

$$\begin{aligned} \Sigma_t &\equiv \frac{a + ib}{2\hbar} \\ s_t &= ip_t x_t + \frac{1}{4}\ln(2\pi\Sigma_t) \\ (\Delta x^2)_t &\equiv \langle (x - x_t)^2 \rangle = \frac{\hbar}{2a} \\ (\Delta p^2)_t &\equiv \langle (p - p_t)^2 \rangle = \frac{\hbar(a^2 + b^2)}{2a} \\ (\Delta x \Delta p)_t &\equiv \langle (x - x_t)(p - p_t) \rangle = \frac{2b}{\hbar a} \end{aligned} \tag{52}$$

That $a > 0$ and that $b = 0$ only in the absence of correlations is clear from Eq. (52). The Gaussian distribution in phase space which is specified by the five moments is the so-called Wigner function (89) that corresponds to the wave function given in Eq. (50) (50).

The advantages of the Gaussian approximation are very clear. Computationally, instead of solving for the time-dependent wave function, which even in one dimension satisfies a partial differential equation, we only need to determine five functions of time. As we shall shortly show, these satisfy ordinary differential equations. The conceptual advantage is that the shape of the wave function is transparent. It is a Gaussian centered about the mean position. Since in the Gaussian approximation the mean position is simply a classical trajectory for the given potential, one can readily visualize how the wave function evolves in time. Many useful insights based on this approach will be found in (44).

There are two ways to determine the parameters that enter into the specification of the wave function. The long (and more correct) way is via a variational principle (53, 90–94). For our purpose it is sufficient to require that the ansatz (Eq. (50)) (50) for the wave function satisfies the time-dependent Schrödinger equation. To do so consider the equation of motion for the moments:

$$\begin{aligned} M_{nm} &= x^n p^m, \qquad n, m = 0, 1, 2, \qquad n + m \leq 2 \\ \frac{d\langle M_{nm}\rangle}{dt} &= \left\langle \frac{d\psi(t)}{dt} \middle| M_{nm} \middle| \psi(t) \right\rangle + \text{c.c.} \\ &= (i\hbar)^{-1}\langle\psi(t)|[M_{nm}, H]|\psi(t)\rangle \end{aligned} \tag{53}$$

where the square brackets denote the commutator. There is no problem with the position which only fails to commute with the kinetic energy. The momentum operator leads to the derivative of the potential energy, $[p, V(x)] = -i\hbar dV(x)/dx$, i.e., to the force. To evaluate the expectation value of the force one makes the approximation*

$$\langle\psi(t)\left|\frac{dV(x)}{dx}\right|\psi(t)\rangle = \frac{dV(x_t)}{dx_t} \tag{54}$$

In other words, the mean value of the force is approximated as the value of the force at the mean position. This is clearly not an approximation if the potential is harmonic so that the force is linear. The Gaussian form of the wave function is thus exact for a harmonic potential. For other potentials we note that almost everywhere a reasonable potential can be locally approximated as harmonic by which we mean that the force is linear. In the general case, the value of the force does change from one point to the next and the Gaussian approximation neglects this variation which is reasonable except where the force is a rapidly changing function of position. Two such danger regions are near the classical turning points of the motion and, at higher energies, where the curvature of the potential changes sign.

The Gaussian approximation yields a set of closed equations of motion for the moments. What we mean by closed is that the time derivative of the five moments are expressed only in terms of the five moments themselves, so that, for given initial conditions, the equations can be solved. The solution specifies the wavefunction at all times,

*The careful reader will point out that since we know the variance of x, one could have kept the third derivative of the potential and thereby obtain a better approximation. That is correct, but it is not a consistent approximation because one cannot keep this derivative in the equation of motion for p^2.

given its initial (Gaussian) form. In the multidimensional case, using (2) **G** for the inverse mass matrix and **F** for the force matrix (which here is a function of the position) one finds

$$\frac{d\mathbf{x}_t}{dt} = \mathbf{G}\mathbf{p}_t, \qquad \frac{d\mathbf{p}_t}{dt} = \mathbf{F}(\mathbf{x}_t) \tag{55}$$

One can (at one's peril) freeze the elements of the cross correlation matrix at their initial value (which is the frozen Gaussian approximation) or evaluate their time dependence from the closed set of equations of motion

$$\frac{d\mathbf{A}}{dt} = \mathbf{GB} + \mathbf{BG}^T, \quad \frac{d\mathbf{B}}{dt} = \mathbf{GC} - \mathbf{AK}(\mathbf{x}_t), \quad \frac{d\mathbf{C}}{dt} = -\mathbf{K}(\mathbf{x}_t)\mathbf{B} - \text{H.c.} \tag{56}$$

where **K** is the force constant matrix. The elements of the covariance matrix **S** are defined by

$$\begin{aligned}
\mathbf{S} &= \begin{pmatrix} \mathbf{A} & \mathbf{B} \\ \mathbf{B}^T & \mathbf{C} \end{pmatrix} \\
\mathbf{A} &\equiv ((\mathbf{x} - \mathbf{x}_t)(x - \mathbf{x}_t)^T) \\
\mathbf{B} &\equiv \frac{1}{2}((\mathbf{x} - \mathbf{x}_t)(\mathbf{p} - \mathbf{p}_t)^T + (\mathbf{p} - \mathbf{p}_t)(\mathbf{x} - \mathbf{x}_t)^T) \\
\mathbf{C} &\equiv ((\mathbf{p} - \mathbf{p}_t)(\mathbf{p} - \mathbf{p}_t)^T)
\end{aligned} \tag{57}$$

C. Energy-Domain Methods

Methods based on diagonalizing the Hamiltonian have their own advantages and are particularly suitable for higher resolution. All that we need to point out here is that one can view such methods also as stemming from a variational principle except that the trial wave function depends linearly on the variational parameters (95). Another variational ansatz is that of self-consistency (96,97) in which one writes the trial wave function as a product of unknown functions, each a function of one coordinate. The equation for the unknown functions is obtained from the variational principle. The applications to vibrations is simpler than the corresponding electronic problem in that there is no need to account for the exchange. Otherwise it is similar in that each mode moves in an effective potential determined by all the other modes. The advantage is that each equation is for one mode but, of course, the solution need to be done self-consistently. At higher energies, it is not always easy to decide which coordinates provide the best choice for building a product wave function. However, and as in the electronic problem, one can improve upon the first approximation by configuration interaction, that is, by writing the wave function as a linear combination of products.

1. The Algebraic Approach

An approach which is rather different than those so far discussed is the algebraic one (98). In a well-defined sense which is discussed below, the algebraic approach is a generalization of the symmetry group of the Hamiltonian. The approach is meant to address up front some rather general characteristics of intramolecular dynamics. These include (i) At least for short times, vibrationally excited molecules do seem to have a good, full, set of quantum numbers. (ii) The spectrum corresponding to these good quantum numbers

is typically anharmonic. (iii) When the good quantum numbers fail, they typically do not all fail together but rather sequentially (where by sequentially one can mean going up in energy or going longer in time or both). For some molecules, the good quantum numbers do persist. This is essentially the concept of a tier structure as discussed in the chapter by McCoy and Sibert. (iv) At higher energies it is sometimes the case that new conserved quantum numbers appear.

The algebraic approach begins with the notion of a zeroth-order description based on a dynamical symmetry, a concept which is a generalization of the usual definition of the symmetry group of the Hamiltonian. What a dynamical symmetry means in practice is that one constructs a zeroth-order Hamiltonian for which there is a full set of quantum numbers for labeling the eigenstates and that the energy is an analytical function of these quantum numbers. In the infrared or Raman spectroscopy of polyatomic molecules (1) one knows that to zeroth order it is practical to represent the spectrum by a Dunham-type formula

$$G(v_1, v_2, \ldots) = \sum_i \omega_i\left(v_i + \frac{1}{2}\right) + \sum_{i,j} x_{ij}\left(v_i + \frac{1}{2}\right)\left(v_j + \frac{1}{2}\right) \tag{58}$$

where the v_i's are the vibrational quantum numbers and the spectroscopic constants (the frequencies ω_i and the self- and cross-anharmonicities x_{ij}) are determined by a fit to the observed spectrum. For higher accuracy cubic terms may be added. The algebraic approach begins with a zeroth-order Hamiltonian which has a similar spectrum where the (linear) spectroscopic parameters are fitted to the experiment, just as is done for (58). The practical difference with the Dunham formula is that fewer parameters are needed, or, in other words, the parameters in (58) are not all independent. Much more important is the difference of principle: the algebraic approach starts with a Hamiltonian and therefore one has wave functions which can be used to compute other expectation values. Furthermore, the procedure used to provide the zeroth-order Hamiltonian is such that it also suggests the higher-order corrections.

The technique is based on a choice of a Lie algebra. Empirical experience suggests that the same algebra is to be used for an entire class of molecules. The choice of the algebra is based on the following requirement: The operators of the algebra, called the generators, must be sufficient to connect all the states in the spectrum. In a language which may be familiar from the theory of symmetry, all the states must belong to one irreducible representation of the algebra. It is in this aspect that the algebraic approach differs from the familiar set of symmetry operators. The latter only connect degenerate states. This difference arises because, by definition, the familiar symmetry operators commute with the Hamiltonian.

Given the algebra G, a Hamiltonian with a dynamical symmetry is constructed as follows. Arrange the subalgebras of G such that they are nested within one another

$$G \supset G_1 \supset G_2 \supset \cdots \supset G_n \tag{59}$$

This is called a chain. Each subalgebra has one (or more) Casimir operator(s) $C(G_i)$ which commute with all the operators of that subalgebra. The Casimir operator is usually bilinear in the generators and the number of linearly independent Casimir operators is the rank of the algebra. In (59) the Casimir operator of the last subalgebra necessarily commutes with all the Casimir operators of the earlier subalgebras. The Hamiltonian is given as a linear combination of the Casimir operators for the chain of Eq. (59).

$$H = \sum_i A_i C(G_i) \tag{60}$$

The coefficients A_i are the analog of the spectroscopic parameters in the Dunham formula and are to be fitted to the observed spectrum. The eigenvalues of a Hamiltonian of the form of (60) can be usually be written down by inspection because the eigenvalues of the Casimir operators of the relevant Lie algebras are known explicitly as functions of the label(s) of the irreducible representations. Because typically the Casimir operators are bilinear in the generators, their eigenvalues are quadratic functions of the labels ≡ quantum numbers. Hence the eigenvalues of (60) are typically of the Dunham form given in Eq. (58).

The subgroup G_n, the last one in the chain of Eq. (59) is the only algebra whose generators commute with the Hamiltonian. The quantum numbers of its Casimir operators will be conserved even as one progressively breaks the other quantum numbers. In applications (98) this last subgroup is usually the rotation (in physical space) algebra. The dynamical symmetry of the Hamiltonian is broken in a systematic fashion by mixing in other symmetries which stem from alternative chains of the group G. Thus Eq. (59) is replaced by

$$G \supset \begin{Bmatrix} G_1 \\ G_1' \end{Bmatrix} \supset G_2 \supset \cdots \supset G_n \tag{61}$$

If the Hamiltonian now contains the Casimir operators of both G_1 and G_1', which do not commute, then the labels of neither provide good quantum numbers. Of course, in general such a Hamiltonian has to be diagonalized numerically. In this way one can proceed to break the dynamical symmetries in a progressive fashion. In (61) all the quantum numbers of G_2 up to G_n remain good. If we add another subalgebra beside G_2 only those quantum numbers provided by G_3 on will be conserved, etc. In applications, the different chains are found to correspond to different limiting cases such as the normal versus the local mode limits for coupled stretch vibrations (99).

The primary shortcoming of the algebraic approach is that the Hamiltonian is not expressed in the geometrical variables that one is used to. It is therefore useful to note that one can obtain a classical limit which is of the familiar form. By first determining the parameters in the algebraic Hamiltonian from a fit to the spectrum one can obtain quite realistic potential energies in this fashion (100).

IV. SPECTRA OF MAXIMAL ENTROPY

In this section we present a point of view that provides a convenient parametrization of the spectrum and apply it to discuss three aspects: (i) the different frequency scales in the spectra and the interpretation in terms of the sequential exploration of phase space, (ii) the fluctuation of spectral intensities, and (iii) the extraction of the time cross-correlation function from observed Raman excitation profiles. For the convenience of the reader we first summarize the practical results so that one can skip Sec. IV.A.1–3 and proceed directly to the applications in Sec. IV.B. The derivation of the parametrization, in Sec. IV.A.2, uses the maximal entropy formalism in the manner of (101) and further details can be found in (102,103). Two extensive reviews are (104,105). Section IV.A.1 is a brief discussion of why we use the maximum entropy formalism. The discussion is brief and cannot replace the more detailed presentations available (e.g., (55,101,107,108)) in the literature.

A. Formalism

The spectrum of maximal entropy is of the functional form

$$S(\varpi) = 1 \Big/ \sum_{r=0}^{M} \lambda_r \exp(-i\varpi t_r) \tag{62}$$

The spectrum is parametrized by the numerical values of the $M + 1$ multipliers λ_r. In principle, their values are determined by the values of the Fourier transform $C(t)$ at the times t_r, $r = 0, 1, \ldots, M$, $t_0 = 0$. The separation of time scales in the exploration of phase space is equivalent to a specification of times t_r such that the later times differ by an order of magnitude or more from the earlier ones. Times which are comparable will correspond to the spectral structure at a given level of resolution. If the times fall into three distinct groups (early, intermediate, and late) then the resulting spectrum will have three levels of clumps as in Fig. 4.

The spectrum is real so that it is specified by $2M + 1$ real numbers. It follows from (62) that λ_0 is real while $\lambda_r^* = \lambda_{-r}$. The latter condition is equivalent to $C^*(t) = C(-t)$. The form that is manifestly real is therefore

$$S(\varpi) = 2 \Big/ \sum_{r=-M}^{M} \lambda_r \exp(-i\varpi t_r), \qquad \lambda_r = \lambda^*_{-r},\ t_r = -t_{-r} \tag{63}$$

For the inversion of the Raman spectrum it is useful to rewrite the spectrum as an amplitude squared:

$$S(\varpi) = |\alpha(\varpi)|^2 = 1 \Big/ \left| \sum_{r=0}^{M} \gamma_r \exp(-i\varpi t_r) \right|^2 \tag{64}$$

where the complex parameters γ_r are an alternative set to the λ_r's. It is sometimes advantageous to regard the denominator in (64) as a polynomial in the complex variable $z = \exp(-i\varpi\delta t)$ so that $\exp(-i\varpi t_r) = z^{n_r}$, $n_r = t_r/\delta t$ where δt is a common time unit. It is then possible to parameterize the spectrum by the roots, z_k, of this polynomial

$$|\alpha(\varpi)|^2 = 1 \Big/ \left| \prod_{k=1}^{K} (z - z_k) \right|^2, \qquad K = \frac{t_M}{\delta t} \tag{65}$$

where the order of the polynomial is determined by the longest time in the spectrum.

The numerical value of the parameters in the spectrum is determined either as a fit to an observed spectrum or from given values of the time correlation function. Either procedure is best implemented by seeking the (unique, global) minimum of the Lagrangian introduced in Sec. IV.A.3. The subroutine UMIAH of the IMSL library (106) is convenient for this purpose. Other numerical aspects are discussed in (105). Note however that much of the discussion therein applies to the special case when the time points t_r are equally spaced in which case Eq. (62) is referred to as the Burg spectrum.

The rest of this section provides the details of how the functional form given in Eq. (62) is derived and with the practical aspect of how to determine the values of the Lagrange multipliers λ_r, $r = 0, 1, \ldots, M$. The reader interested in applications can proceed directly to Sec. IV.B.

1. Why Maximum Entropy

The amplitudes of the different lines in the spectrum can be regarded as the components of the optically prepared bright state in the basis of the eigenstates of the system, cf. Eqs. (2)–(3). Already in Sec. II we had several occasions to note that the bright state behaves not unlike a random vector. One can therefore ask what the spectrum will be if we make the approximation that these components are truly random. This requires us to specify, in a technical sense, what we mean by random. This is where entropy comes in. By random we will mean that the distribution of the amplitudes be as uniform as possible and, as such, be a distribution of maximal entropy.

The case of a truly random bright state is likely to be a limiting one. In reality, the dynamics do constrain the time evolution of the bright state. What one therefore needs is a prescription for dealing with situations which are not fully random. Entropy continues to provide a convenient tool because rather than look for that distribution which is as random as possible one can instead specify that distribution which is as uniform as it can be subject to the input from the dynamics. In technical terms, we seek that distribution of amplitudes whose entropy is maximal, but the maximum is subject to auxiliary conditions. These additional conditions (or constraints) are to be provided by the dynamics. The result is a spectrum that is consistent with the given dynamical input and is otherwise the result of a maximally uniform set of amplitudes. Section IV.A.2 provides a more technical version of these considerations.

One important point that can be obscured by the technical details is the following: The functional form of the spectrum is identified quite readily; in fact, as soon as the nature of the input from the dynamics is specified. This functional form, e.g., Eq. (62), contains a number of parameters, as many as the number of constraints. The work is to determine the values of these parameters. But for many purposes the functional form of the spectrum is all that one really needs. The numerical value of the parameters can be determined, e.g., by a fit to an observed spectrum. The parameters can also be varied so as to explore the possible spectra that can be generated, etc. For completeness (and, in practice, for the inversion of Raman spectra) one needs to know how to determine the value of the parameters and we will discuss this in some detail. But for many purposes the parametrized form of the spectrum is sufficient.

2. Derivation

For a spectrum of N lines we consider a vector $\mathbf{x}$, of N components $\mathbf{x}_f$, where $\mathbf{x}_f$ is the complex amplitude of the transition $i \rightarrow f$, $f = 1, \ldots, N$. We write $\mathbf{x}_f$ as a vector since as a complex number it itself has two components. By a distribution of amplitudes we mean a probability density function $P(\mathbf{x})$ (107), such that the observed value of the transition intensity is $\langle |x_f|^2 \rangle$:

$$\langle y_f \rangle = \langle |x_f|^2 \rangle = \int |x_f|^2 \, P(\mathbf{x}) \, d\mathbf{x} \tag{66}$$

As such, $P(\mathbf{x})$ is not directly observable.* What can be measured are various reduced distributions such as the distribution of line intensities irrespective of line positions. It

*$P(\mathbf{x})$ is the analog of the distribution of velocities of all N molecules in the container. For any given container, one cannot observe a distribution. What is observable is the distribution in velocity of molecules, i.e., how many molecules, out of N, have velocities in the range v to $v + \Delta v$.

is the latter quantity that is typically analyzed (55) and is further discussed in Sec. IV.A.3.

The constraints imposed on $P(\mathbf{x})$ are the values, $C(t_r)$ of the Fourier transform of the spectrum Eq. (5) at the times t_r, $r = 0, \ldots, M$, $t_0 = 0$.

$$\begin{aligned} C(t_r) &= \sum_{f=1}^{N} \langle y_f \rangle \exp(-i\varpi_f t_r) \\ &= \int d\mathbf{x}\, P(\mathbf{x}) \left[\sum_{f=1}^{N} \langle |x_f|^2 \rangle \exp(-i\varpi_f t_r) \right] \end{aligned} \tag{67}$$

For $r > 0$, the M members $C(t_r)$ are complex so that there are $2M + 1$ real parameters. Our purpose is to use as few as possible parameters with $2M + 1 < N$. Equation (67) do therefore not suffice to determine a unique $P(\mathbf{x})$.

The functional form of the (unique (108)) distribution $P(\mathbf{x})$ which is (i) normalized

$$\int d\mathbf{x}\, P(\mathbf{x}) = 1 \tag{68}$$

(ii) correctly yields the $M + 1$ values for the constraints $C(t_r)$, and (iii) is of maximal entropy, is of the standard (108) form

$$P(\mathbf{x}) = \mathbf{Z}^{-1} \exp\left[- \sum_{r=0}^{M} \lambda_r C_r(\mathbf{x}) \right] \tag{69}$$

where we define, cf. Eq. (67),

$$C_r(\mathbf{x}) \equiv \sum_{f=1}^{N} |x_f|^2 \exp(-i\varpi_f t_r) \tag{70}$$

so that

$$C(t_r) = \langle C_r(\mathbf{x}) \rangle \tag{71}$$

and $\mathbf{Z}$ ensures the normalization of $P(\mathbf{x})$.

We do not prove here that Eq. (69) is that distribution whose entropy is maximal, nor that the maximum is unique. Instead we refer to Ref. 108 or to any of the other general references.

The Lagrange multipliers in the distribution given in Eq. (69) are to be determined, as usual, in terms of the values of the constraints $C(t_r)$. We shall provide a more direct route from the spectrum to the Lagrange multipliers. That route will not only provide $P(\mathbf{x})$ but also explicit results for the frequency dependence of $S(\varpi)$ and, equivalently, of the entire time dependence of $C(t)$.

It is often convenient to rewrite $P(\mathbf{x})$, Eq. (69), as

$$\begin{aligned} P(\mathbf{x}) &= Z^{-1} \exp\left[- \sum_{r=0}^{M} \lambda_r \sum_{f=1}^{N} |x_f|^2 \exp(-i\varpi_f t_r) \right] \\ &= Z^{-1} \exp\left[- \sum_{f=1}^{N} |x_f|^2 \sum_{r=0}^{M} \lambda_r \exp(-i\varpi_f t_r) \right] \\ &= Z^{-1} \exp\left(- \sum_{f=1}^{N} \mu_f |x_f|^2 \right) \end{aligned} \tag{72}$$

The N real parameters μ_f defined by the last line of Eq. (72), i.e.,

$$\mu_f = \sum_{r=0}^{M} \lambda_r \exp(-i\varpi_f t_r) \tag{73}$$

are not all independent but can be expressed in terms of the $2M + 1$ real parameters λ_r, $r = 0, \ldots, M$. That the parameters μ_f are real, follows from the spectrum $S(\varpi)$, and hence $\langle |x_f|^2 \rangle$ being real. It is also possible to impose this explicitly, as follows: Since $S(\varpi)$ is real, its Fourier transform $C(t)$ must satisfy the time cross-symmetry property.

$$C(t) = C^*(-t) \tag{74}$$

If we define $t_{-r} \equiv -t_r$, then $C(t_{-r}) = C^*(t_r)$, and the same is true for their conjugate Lagrange multipliers,

$$\lambda_{-r} = \lambda_r^* \tag{75}$$

The expression given in Eq. (73) for μ_f can thus be equivalently written in the manifestly real form

$$\mu_f = \frac{1}{2} \sum_{r=-M}^{M} \lambda_r \exp(-i\varpi_f t_r) \tag{76}$$

with λ_0 being twice its value in Eq. (73).

It follows from Eq. (72) that even when dynamical information is included as constraints, the distribution of amplitudes of different lines remain uncorrelated:

$$P(\mathbf{x}) = \prod_{f=1}^{N} P(\mathbf{x}_f) \tag{77}$$

$$P(\mathbf{x}_f) = \exp(-\lambda_{0f} - \mu_f |x_f|^2) \tag{78}$$

Here, λ_{0f} ensures normalization

$$\exp(\lambda_{0f}) = \int d\mathbf{x}_f \exp(-\mu_f |x_f|^2) \tag{79}$$

The distribution function $P(\mathbf{x}_f)$ of a given line amplitude is itself two-dimensional because the amplitude $\mathbf{x}_f$ is, in general, complex. Since only the modulus of $\mathbf{x}_f$ is constrained by the data on one-photon absorption, the real and imaginary parts of $\mathbf{x}_f$ are independently and identically distributed.

Any other dynamical information derivable using only the one-photon spectrum for a cw source will equally depend only on the transition intensities and hence invariably will lead to Gaussian uncorrelated fluctuations, of the type of Eq. (72), when used in a maximum entropy formalism.

3. The Distribution of Spectral Intensities

The probability density function $P(y_f)$, of the intensity $y_f = |x_f|^2$ is readily derived from that of $P(\mathbf{x}_f)$. For a complex variable $\mathbf{x}_f$, $\mathbf{x}_f \equiv |x_f| \exp(i\theta_f)$, $d\mathbf{x}_f = (1/2)\, dy_f\, d\theta_f$. Hence,

$$P(y_f) = \int_0^{2\pi} \frac{P(\mathbf{x}_f)\, d\theta_f}{2} = \pi \exp(-\lambda_{0f} - \mu_f y_f) \tag{80}$$

where, from Eq. (79),

$$\exp(\lambda_{0f}) = \frac{1}{2}\int\int dy_f\, d\theta_f \exp(-\mu_f|x_f|^2) = \pi\int_0^\infty dy_f \exp(-\mu_f y_f) = \frac{\pi}{\mu_f} \tag{81}$$

so that, in general,

$$P(y_f) = \langle y_f\rangle^{-1} \exp\left(-\frac{y_f}{\langle y_f\rangle}\right) \tag{82}$$

where

$$\langle y_f\rangle = \frac{1}{\mu_f} \tag{83}$$

In the special case when x_f is real, we have from Eq. (78)

$$P(x_f) = \langle 2\pi\langle x_f^2\rangle\rangle^{-1/2} \exp\left(-\frac{x_f^2}{2\langle x_f^2\rangle}\right) = (\pi\langle y_f\rangle)^{-1/2} y_f^{-1/2} \exp\left(-\frac{y_f}{2\langle y_f\rangle}\right) \tag{84}$$

Equations (82) and (84) are both of the form of a distribution known as chi-square. This distribution is characterized by the number, ν, of degrees of freedom,

$$P(y) = \left(\frac{\nu y}{\langle y\rangle}\right)^{\nu/2-1} \exp\left(-\frac{\nu y}{2\langle y\rangle}\right) \Big/ 2^{\nu/2}\Gamma\left(\frac{\nu}{2}\right) \tag{85}$$

The cases of a real and a complex amplitude correspond to $\nu = 1$ and 2, respectively, and these two distributions are shown in Fig. 14. In the general case, the number of

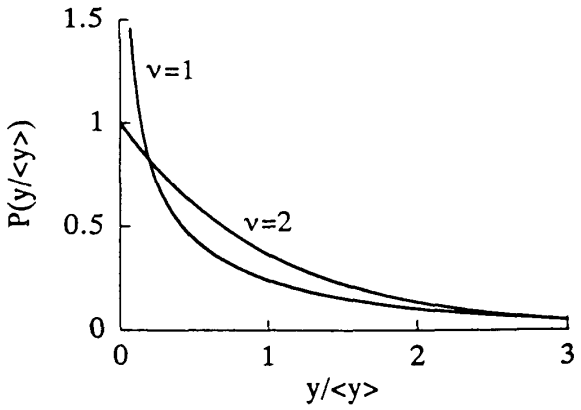

Figure 14 The chi-square distribution for one and two degrees of freedom. The lower the number, ν of degrees of freedom, the higher the fraction of low-intensity transitions. At a higher number of degrees of freedom the function becomes localized in a Gaussian-like fashion.

degrees of freedom determines the width of the chi-square distribution:

$$\langle (y - \langle y \rangle)^2 \rangle = \frac{2}{\nu} \langle y \rangle^2 \tag{86}$$

The observed value, $\langle |x_f|^2 \rangle$, of the strength of the $i \rightarrow f$ transition is given, using Eq. (66) and the distribution $P(\mathbf{x})$ of maximum entropy, Eq. (77), by

$$\begin{aligned} \langle |x_f|^2 \rangle &= \frac{1}{\mu_f} \\ &= \left(\sum_{r=0}^{M} \lambda_r \exp(-i\varpi_f t_r) \right)^{-1} \\ &= 2 \Big/ \sum_{r=-M}^{M} \lambda_r \exp(-i\varpi_f t_r) \end{aligned} \tag{87}$$

where the second form is explicitly real (cf. Eq. (76)), using the crossing symmetry, $\lambda_{-r} = \lambda_r^*$, Eq. (75), when $t_{-r} = -t_r$.

We now show how Eq. (87) provides a practical algorithm for the determination of the Lagrange multipliers λ_r and, at the same time for the optimal selection of the times t_r at which the constraints are imposed. We do so by comparing the spectrum of maximal entropy

$$S^{ME}(\varpi) = 2 \Big/ \sum_{r=-M}^{M} \lambda_r \exp(-i\varpi t_r) \tag{88}$$

$$S^{ME}(\varpi) = \langle |x_f|^2 \rangle \tag{89}$$

to the observed (or computed) spectrum.

The first step is to express the entropy of the distribution of amplitudes*

$$\mathbf{S}[\mathbf{x}] = -\int d\mathbf{x}\, P(\mathbf{x}) \ln P(\mathbf{x})$$

in terms of the observed spectrum. First, note that since $P(\mathbf{x})$ factorizes, cf. Eq. (77), $\mathbf{S}[\mathbf{x}]$ for the distribution of maximal entropy is the sum of contribution of individual lines

$$\begin{aligned} \mathbf{S}^{ME}[\mathbf{x}] &= -\sum_f \int d\mathbf{x}_f\, P(\mathbf{x}_f) \ln P(\mathbf{x}_f) \\ &= -\sum_f \mathbf{S}^{ME}[\mathbf{x}_f] \end{aligned} \tag{90}$$

Next, using Eqs. (78) and (81), we get

$$\mathbf{S}^{ME}[\mathbf{x}_f] = \lambda_{0f} + \mu_f \langle |x_f|^2 \rangle = \ln(\langle |x_f|^2 \rangle) + 1 \tag{91}$$

---

*It is here, or equivalently in Eq. (69), that it is matters that we use $P(\mathbf{x})$. The reason is that the entropy can only be written as in Eq. (90) when in the absence of any constraints beyond normalization, $P(\mathbf{x})$ is uniform (7). Note that if $P(\mathbf{x})$ is uniform, $P(\mathbf{y})$ is not, and vice versa.

or

$$\mathbf{S}^{ME}[\mathbf{x}] = \sum_{f=1}^{N} \ln(\langle |x_f|^2 \rangle) + N \tag{92}$$

A shortcut "derivation" of Eq. (87) is to seek the maximum of Eq. (89) subject to the $M + 1$ constraints given by Eq. (67). The independent variations of the $\langle |x_f|^2 \rangle$'s lead to Eq. (87).

When Eq. (87) is used in Eq. (91), the entropy is expressed in terms of the Lagrange multipliers λ_r. Using the approach of Agmon et al. (109), one can now regard the entropy as a function of trial values of the Lagrange multipliers, and seek its optimal value

$$\mathbf{S}^{ME}[\mathbf{x}^T] = -\sum_{f=1}^{N} \ln\left[\sum_{r=0}^{M} \lambda_r^T \exp(-i\varpi_f t_r)\right] + N \tag{93}$$

Here, the superscript T designates a trial value.

To seek the maximum of (93) under variation of the Lagrange multipliers λ_r, it is convenient to seek the (unique and only) extremum of the Lagrangian

$$\begin{aligned} L = &\int \ln[S^{ME}(\varpi)]^T \, d\varpi + \frac{1}{2}\sum_{r=-M}^{M} \lambda_r^T \langle \exp(-i\varpi t_r) \rangle \\ &- \frac{1}{2}\sum_{r=-M}^{M} \lambda_r^T \langle \exp(-i\varpi t_r) \rangle^T - \int \ln S(\varpi) \, d\varpi \end{aligned} \tag{94}$$

with

$$\langle \exp(-i\varpi t_r) \rangle = \int S(\varpi) \exp(-i\varpi t_r) \, d\varpi$$

$$\langle \exp(-i\varpi t_r) \rangle^T = \int [S^{ME}(\varpi)]^T \exp(-i\varpi t_r) \, d\varpi$$

and, from (87)

$$[S^{ME}(\varpi)]^T = 2 \Big/ \sum_{r=-M}^{M} \lambda_r^T \exp(-i\varpi t_r) \tag{95}$$

defined by

$$\frac{\partial L}{\partial \lambda_r^T} = 0 \tag{96}$$

Here, $S(\varpi)$ is the input spectrum and $[S^{ME}(\varpi)]^T$ is its ME estimate using the trial values of the λ's. We find it convenient to do so using the subroutine UMIAH of the IMSL Library (106). Other algorithms are also possible since the Lagrangian L has no secondary extrema. On the other hand, it is very useful to have good initial guesses for the λ_r^T's. The reason is that while the second derivative of L is guaranteed to be mathematically definite, it can be numerically quite shallow (109) (as a function of the λ_r^T's), particularly so if the constraints $f_r(\mathbf{x})$ are not numerically linearly independent.

A practical route to an initial estimate of the Lagrange multipliers λ_r^T's is via the Burg algorithm (104,105). This generates a spectrum of maximum entropy provided the times t_r are equally spaced, $t_r = r\delta t$. In many applications (see Sec. IV.B), there are specific reasons to preferring unequally spaced time intervals. One option is to use the

Burg algorithm so as to generate trial Lagrange multipliers, which do lead to a maximal value of the entropy for equally spaced t_r's. Then one seeks to lower this maximal value of the entropy by varying the t_r's. One converges to this point by seeking the extremum of L with respect to variations of the t_r's. At the minimum, the initial trial values of the λ_r's are no longer optimal and a new extremum of L with respect to the λ_r's is sought. This min-max algorithm has been found to converge quite effectively.

Another practical aspect is that the form of Eq. (95) for μ_f, $\langle|x_f|^2\rangle = 1/\mu_f$ can be conveniently rewritten as the explicitly positive form

$$\langle|x_f|^2\rangle = 1 \Big/ \left|\sum_{r=0}^{M} (a_r + ib_r) \exp(-i\varpi t_r)\right|^2 \tag{97}$$

Here, the a_r's and b_r's are real coefficients such that the (complex valued) Lagrange multipliers are bilinear forms in the a's and b's. We find it more convenient to vary the Lagrangian L with respect to these real coefficients. One can show analytically that this is equivalent to varying the λ_r^T's.

We remark in Sec. IV.B that the real and imaginary parts of the λ_r's are both important for describing the fluctuations in the intensities. Starting with a given spectrum $S(\varpi)$ minimizing L yields a spectrum of maximum entropy

$$S^{ME}(\varpi) = 2 \Big/ \sum_{r=-M}^{M} \lambda_r \exp(-i\varpi t_r) \tag{98}$$

The quality of fit of $S(\varpi)$ by $S^{ME}(\varpi)$ is the value of L at the minimum. When the fit is tight, one has a good set of Lagrange multipliers for describing the fluctuations of the intensities, using Eq. (84) with $\langle y_f\rangle$ given by Eq. (87).

B. Applications

The spectrum of maximum entropy provides an explicit and concrete expression of the complementarity of the frequency- and time-domain descriptions. The short time constraints delineate the broad spectral features while the long time constraints govern the fine structure. To show this explicitly, suppose that there is a separation of time scales so that one can specify a frequency interval $\Delta\varpi$ such that the times t_r at which the constraints are imposed can be grouped as

$$\begin{aligned} &0 \le r \le M_1, \qquad \Delta\varpi t_r << 2\pi \\ &M_1 \le r \le M, \qquad \Delta\varpi t_r >> 2\pi \end{aligned} \tag{99}$$

Then the envelope of the spectrum is specified by the first M_1 constraints and the additional, $M - M_1$ constraints determine the finer structure seen only at resolution better than $\Delta\varpi$. This is seen by coarse graining the spectrum (Eq. (62)) over $\Delta\varpi$. As discussed in Sec. II, the convolution theorem implies that the corresponding Fourier transform satisfies $C(t_r) \cong 0$, $r \ge M_1$. This can also be seen directly from Eq. (67). Hence the Lagrange multipliers, Eq. (76) satisfy

$$\begin{aligned} \mu_f &= \frac{1}{2}\sum_{r=-M}^{M} \lambda_r \exp(-i\varpi_f t_r), \qquad \text{higher resolution} \\ &= \frac{1}{2}\sum_{r=-M_1}^{M_1} \lambda_r \exp(-i\varpi_f t_r), \qquad \text{lower resolution} \end{aligned} \tag{100}$$

Since $1/\mu_f$ is the intensity of the spectrum at the frequency ϖ_f it takes fewer terms to represent the spectrum at the lower resolution. Indeed, it follows from Eq. (98) that the high-resolution spectrum can be written as

$$S(\varpi) = \left\{ \left[\frac{1}{S_1(\varpi)} \right] + \sum_{r=1+M_1}^{M} \lambda_r \exp(-i\varpi t_r) \right\}^{-1} \tag{101}$$

where $S_1(\varpi)$ is the envelope of the spectrum. Figure 4 is an illustration of this point. Three different frequency ranges are included: a short time range which gives the overall broad spectrum, an intermediate time regime and a long time scale. Within each time scale one may need one or more terms in the spectrum, depending on the extent of structure. This brings us to the second topic, the fluctuations of intensities.

In the regime of well-defined quantum numbers, the density of states in a given energy range is far higher than the density of spectral features. The reason is that many final states are simply not accessible from the initial state. The corresponding intensities are identically zero and the spectrum contains a few, but strong, lines. As we go up in energy, more and more final states can be reached and the spectrum becomes more "grassy"; there are more and more weak transitions. What does one expect in the limit—that all states will appear with equal (and, hence, necessarily low) intensity? The answer is no. Even if there are no constraints imposed by the dynamics the spectrum will not appear to be gray. Rather, what one expects is that even in that limit the distribution of intensities will remain quite uneven and, its general quantitative form will be a chi-square distribution with one or two degrees of freedom (one if the amplitudes can be taken to be real, two otherwise).

By a distribution of intensities we mean that one bins all transitions in accordance to the magnitude of the intensity, irrespective of the position of the transition along the frequency axis. (For the joint distribution of line spacings and intensity see (Ref. 110).) The distribution under discussion is the histogram resulting from this binning procedure. In symbolic form this is

$$P(y) = N^{-1} \sum_{f=1}^{N} \int dy_f \, P(y_f) \delta(y - y_f) \tag{102}$$

Consider first the limit where no dynamical input is given. Then only the value of $C(t)$ at $t = 0$ is imposed as a constraint in determining $P(y_f)$ by the procedure of maximal entropy. In this case all the Lagrange multipliers μ_f have exactly the same value, namely $\mu_f = 1/\lambda_0$ and so all the distributions $P(y_f)$ are the same. One can therefore explicitly carry out the sum over final states in (102), with the result

$$P(y) = \begin{cases} \langle y \rangle^{-1} \exp\left(-\dfrac{y}{\langle y \rangle} \right), & \nu = 2, \quad \text{complex transition amplitudes} \\ (\pi \langle y \rangle)^{-1/2} y^{-1/2} \exp\left(-\dfrac{y}{2\langle y \rangle} \right), & \nu = 1, \quad \text{real transition amplitudes} \end{cases} \tag{103}$$

These two distributions were already shown in Fig. 14. As is clear, the hallmark of this limiting situation is a quite broad distribution, with predominately weak transitions.

In the general case, when each line has its own distribution, we cannot evaluate the sum in (102) explicitly. What one can show (103) is that dynamical information

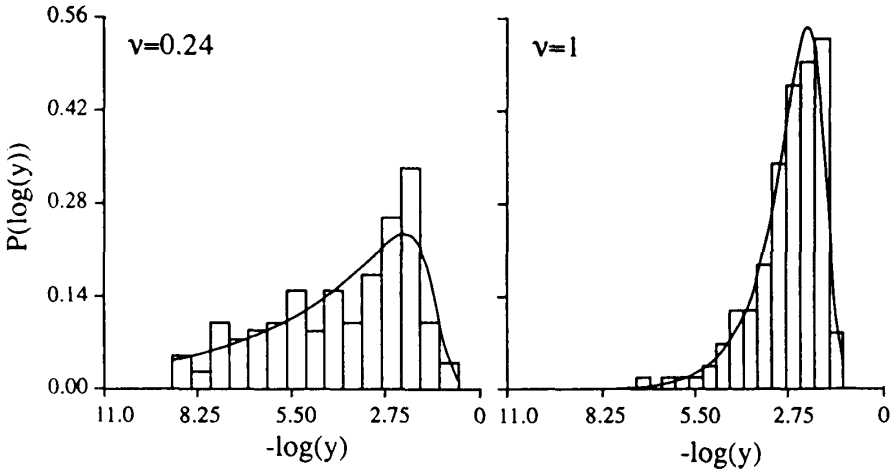

Figure 15 The distribution of intensities for a quantum mechanically computed (by an energy domain diagonalization method) spectrum for a very anharmonic two-vibrational-mode potential and the fit by a chi-square distribution. (Left panel) A lower energy initial state so that mode mixing is very incomplete. There are many weak transitions and the number of degrees of freedom is low. (Right panel) At a high energy where the fit suggests that the mixing is complete (ν = 1 since the wave functions are real). The plot is vs. the logarithm of the intensity so as to emphasize the low intensities region. (Adapted from J. Brickmann, Y. M. Engel, and R. D. Levine, *Chem. Phys. Lett. 137*: 441 (1987).)

reduces the value of the number ν of degrees of freedom. In other words, there are more weaker transitions. Explicit computations of spectra verify this expectation (Fig. 15). The same result is obtained if one uses in Eq. (102) distributions $P(y_f)$ of maximal entropy (Fig. 16).

While imposing finite time constraints reduces the number of degrees of freedom, any averaging tends to increase them. In other words, if the intensity is really a sum of

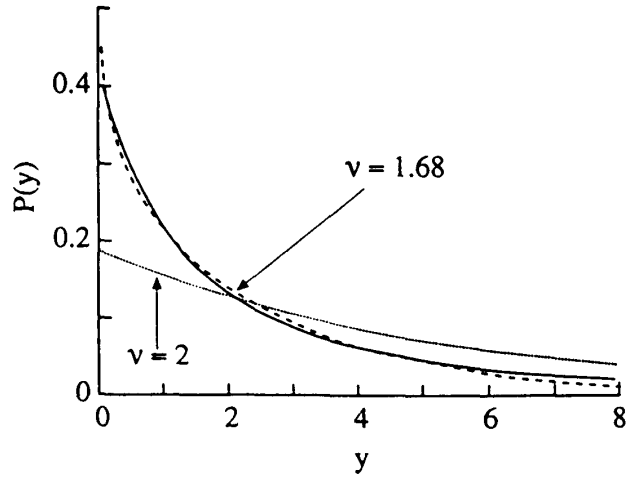

Figure 16 The distribution of intensities determined by binning, as in Eq. (102) of a spectrum which has two time scales, solid line, and the fit by a chi-square distribution with ν = 1.68 degrees of freedom, dashed line. Shown for comparison is the chi-square distribution with two degrees of freedom. (From Ref. (103).)

n terms, the number of degrees of freedom is correspondingly higher by n. This can be understood from the general expectation that averaging reduces fluctuations and that the chi-square distribution for larger than two degrees of freedom is a localized, Gaussian-like distribution, whose width, cf. Eq. (86), decreases with increasing ν.

The final application we discuss is one where the maximum entropy formalism is used not only to fit the spectrum but also to extract new results. Specifically we discuss the determination of the time cross-correlation function, $C_{fi}(t)$ (Eq. (43)), which is the Fourier transform of the Raman scattering amplitude $\alpha_{fi}(\varpi)$ (Eq. (44)) when what is measured is the Raman scattering cross section $\sigma_{fi}(\varpi) \propto |\alpha_{fi}(\varpi)|^2$. The problem is that the experiment does not appear to determine the phase of the amplitude. The application proceeds in two stages: (i) Representing the Raman spectrum as one of maximal entropy, using as constraints the Fourier transform of the observed spectrum. At the end of this stage one has a parametrization of $|\alpha_{fi}(\varpi)|^2$ whose accuracy can be determined by how well it fits the observed frequency dependence. (ii) The fact that the Raman spectrum can be written as a square modulus as in Eq. (97) implies that it can be uniquely factorized into a minimum phase function

$$\alpha_{fi}(\varpi) = 1 \Big/ \sum_{r=0}^{M} (a_r + ib_r)\exp(-i\varpi t_r) \tag{104}$$

and its Fourier transform $C_{fi}(t)$ can now be computed.

The proof that Eq. (97) implies (104) requires an appeal to the Fejer-Riesz theorem (111). By a minimum phase function, we mean that when compared to any other function $\beta_{fi}(\varpi)$ such that $|\alpha_{fi}(\varpi)| = |\beta_{fi}(\varpi)|$, the phase $\varphi_\alpha(\varpi)$ of the function $\alpha_{fi}(\varpi)$ that we recover satisfies the relation

$$\frac{d\varphi_\alpha(\varpi)}{d\varpi} > \frac{d\varphi_\beta(\varpi)}{d\varpi} \tag{105}$$

It can be shown (111) that the two functions $\alpha_{fi}(\varpi)$ and $\beta_{fi}(\varpi)$ differ by an all-pass function $\alpha_0(\varpi)$, which is such that

$$|\alpha_0(\varpi)| = 1 \tag{106}$$

and possesses a monotonically decreasing phase $\varphi_0(\varpi)$; $d\varphi_0(\varpi)/d\varpi < 0$. Therefore, one obtains the inequality Eq. (105)

$$\varphi_\beta(\varpi) = \varphi_\alpha(\varpi) + \varphi_0(\varpi) \tag{107}$$

Another numerical procedure for a direct inversion of $|\alpha_{fi}(\varpi)|^2$ to the causal cross-correlation function $C_{fi}(t)$ is via the use of the dispersion relation between the modulus and the phase of $\alpha_{fi}(\varpi)$ (102,111). This route also leads to a minimum phase polarizability $\alpha_{fi}(\varpi)$.

The practical implementation of the direct ME inversion outlined above is to the Raman excitation of the C–I stretching mode ν_{11} of the iodobenzene molecule to a final state with one, two, and three vibrational quanta respectively. The input Raman excitation profiles are computed using the harmonic model of Ref. 112. The total cross-correlation function is written as the product of two single harmonic correlation functions (for the Raman active C–I stretching mode ν_{11} and a ring mode ν_7) times a bath function. The bath function stands for the global autocorrelation function of the remaining modes and it is responsible for the internal damping. As in Ref. 112, it is a Blackman-Harris window

function (113) whose effect is merely to limit the range of the total correlation function to 120 fs and thus to coarse grained the spectrum (cf. Sec. II.A). The spectra are then fitted to a ME form (stage (i), Eq. (97)). As an example of a ME fit, we show in Fig. 17 the input spectra for the 0-1 transition and its fit to Eq. (97) using nine nearly equally spaced time values t_r (a good fit with equally spaced times values t_r is possible here since there is basically one kind of spacing in the input spectrum). The cross-correlation functions $C_{fi}(t)$ are then obtained as the Fourier transform of $\alpha_{fi}(\varpi)$ using Eqs. (104) and (64) (stage (ii)). Figure 18 compares the three input cross-correlation functions computed using the model of Ref. 112 (left column) to the results of the ME inversion (right column). The ME inversion keeps reasonable track of the systematic changes in the cross-correlation function of the final states, and the relative heights and positions of the main features are well reproduced. Note however that a good reproduction of the very short time dynamics requires an accurate representation of the asymptotic (high and low ϖ) shape of $\alpha_{fi}(\varpi)$ (cf. Sec. II.A). This is noticeable in the bottom panel of Fig. 18 for the 0-1 transition where the asymptotic behavior of the input $|\alpha_{fi}(\varpi)|^2$ has been intentionally truncated to mimic realistic data.

The second example deals with an anharmonic model of two coupled Morse oscillators plus a bath. Details about the computation of the cross-correlation functions $C_{fi}(t)$ can be found in Appendix D of Ref. 102. In this example, the bath function is a Blackman-Harris function whose width is 600 fs, which results in a more resolved spectrum, as can be seen from the bottom panel of Fig. 19. The spectrum essentially exhibits two kinds of spacings: two wide peaks are separated by about 3600 cm^{-1} while within each clump, the spacing between resolved features is about 170 cm^{-1}. Due to the disparities of the frequency spacings, the time cross-correlation (plotted in the upper panel a of Fig. 19) has a nested structure: a short time beating frequency (whose period is 9 fs and which corresponds to the large spacing between the two peaks in the spectrum) is embedded in a long time envelope (whose period is 200 fs and which corresponds to the spacing between resolved features within a clump of peaks). The input spectrum is

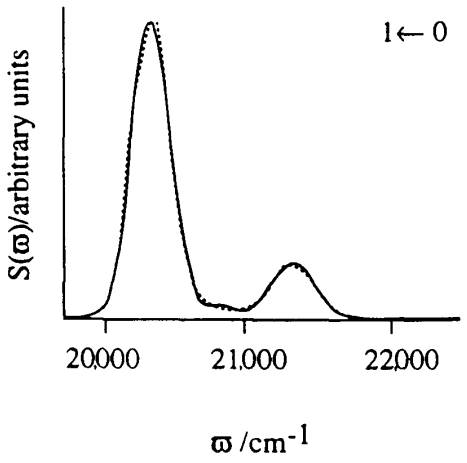

Figure 17 The Raman excitation spectrum for a transition to the $\tilde{B}$ electronic state of iodobenzene with one quantum of vibrational excitation in the ν_{11} vibrational mode. (Solid line) computed in the harmonic approximation for the motion in the $\tilde{B}$ state. (Dotted line) The maximal entropy fit of this spectrum obtained using Eq. (97). This fit is used to determine the cross-correlation function as shown in Fig. 18. (From Ref. (102).)

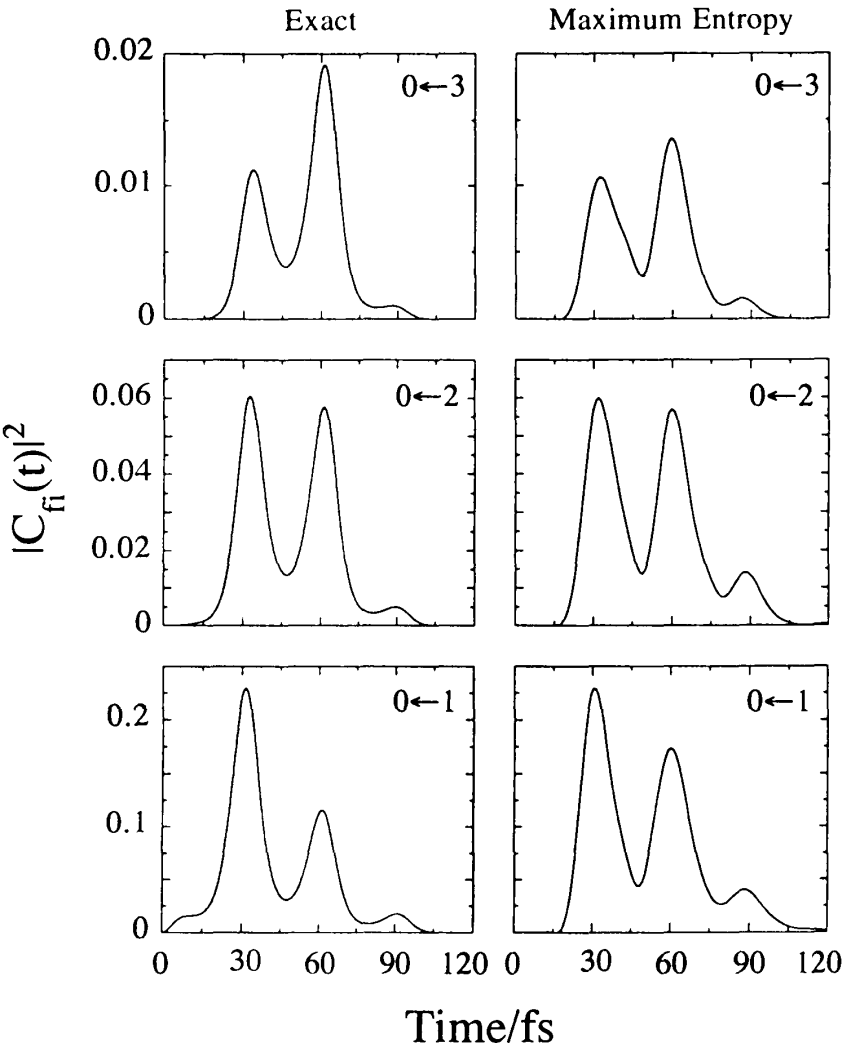

Figure 18 Time cross-correlation functions for three Raman transitions in iodobenzene (from the ground state to the $\tilde{B}$ excited electronic state with ν = 1, 2, 3 quanta in the ν_{11} vibrational mode. (Left) Computed for a harmonic $\tilde{B}$ state potential and convoluted with a 125-fs-wide window function. The spectrum is computed from this cross-correlation function. (Right) The time correlation function determined from the Raman frequency spectrum (the excitation profile) via the maximum entropy formalism, as discussed in the text, using nine Lagrange multipliers λ_i. (From Ref. (102).)

fitted using 11 unequally spaced time values t_i. Note that in this case, a satisfactory fit cannot be obtained with equally spaced time values due to the different orders of magnitude of the spacings in the input spectrum. The time cross-correlation function resulting from the direct ME inversion is plotted in upper panel b. The different time scales of the input cross-correlation are recovered and, but for the short time rise, the result of the ME procedure agrees reasonably well with the input function.

The direct determination of time cross correlation functions from experiments is thus possible and reasonably accurate. Typically, experimental resonant Raman excitation profiles exhibits broad features (112), and the time cross-correlation function therefore provides short time information (for about the first 100 fs) on the excursion of the wave packet out of the Franck-Condon region. This information is complementary to that

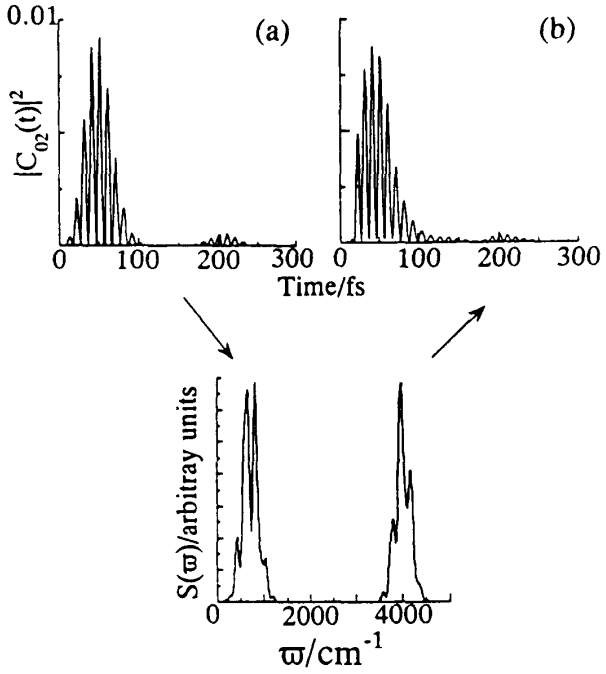

Figure 19 The Raman spectrum and time cross correlation function when the motion on the excited electronic state potential is anharmonic, compare to Figs. 17 and 18, which are for a harmonic approximation. (Top, a) Computed time correlation function using a wide window function; (b) The maximal entropy representation of this function, determined from the spectrum. Note the clear separation of time scales due to the anharmonicity (cf. Fig. 20). (Bottom) The Raman excitation spectrum obtained from the computed time correlation function (a). The arrows are the sequence of computations: (a) is determined from the dynamics. The spectrum is determined from (a). The maximum entropy cross-correlation function (b) uses only the spectrum as input.

obtained from absorption spectroscopy which probes the region in phase space initially accessed by the nonstationary initial state. More insight is thus gained on the short time delocalization of the initial state, which is a crucial step in the understanding of the control of chemical reactions via selective excitation (114).

V. KINETICS AND THE EXPLORATION OF PHASE SPACE

The motivation for much of our interest in the exploration in phase space is provided by the hope that a better understanding will pave the way for a control of the chemical act by proper selection of initial conditions. What have we learned that is useful in this respect? The shortest time scales that one uncovers are indeed quite short, of the order of a vibrational period or less. In a homogeneously broadened spectrum, these short times determine the broad spectral envelopes. The good news is that it is not necessary to beat these fast time scales in order to achieve selectivity. The time scale in question is the time it takes for an extended bond to contract, or vice versa. It is a time scale on which the harmonic approximation and, therefore, the spectroscopic paradigm are valid. In this regime one can write the displacement x_j of the jth bond as a linear combination of normal modes

$$x_j = \sum_i a_{ji} \cos(\omega_i t + \phi_i) \tag{108}$$

Here ϕ_i is the initial phase of the ith normal modes of frequency ω_i. Say now the initial phases of the normal modes are such that the bond is stretched. The differences between the vibrational frequencies means that quite rapidly the terms in Eq. (108) will get out of synch and the bond will contract. This, however, is not IVR, although it is true that in a large harmonic molecule it may take quite a while before the same bond is again extended.

The molecule is not quite harmonic and its energy levels are more accurately given by the Dunham type expression given in Eq. (58). But both the cross- and the self-anharmonicity terms, the x_{ij}'s, are smaller than the harmonic frequencies by more than an order of magnitude. What this means is that following the first time scale there is a quiescent period during which the system hardly explores its phase space. Figure 20 is a schematic illustration of this point. The very same point is made by the observations of nested spectra. By the end of the second period the volume sampled in phase space is still quite restricted, provided that, as we have tacitly assumed, the initial excitation was selective.

The onset of a defacto kinetic behavior typically occurs from the second period on. Since for typical molecular parameters the second period is very roughly of the order of a ps or even less, that is not necessarily good news. Depending on the nature of the anharmonicities, on the available energy, and on the state which was initially accessed, it may already occur during the second period or it may be delayed. It is from here on that individual differences between molecules have a significant effect. Thus, while it can be possible, in special cases, to maintain complete selectivity over even longer periods, at the higher energies which are of interest for chemistry, one must assume that selectivity will be eroded beyond the second period. Eroded but not completely lost. The reason is that a truly statistical behavior implies that the system representatively sampled all of its available phase space before the onset of the dissociation or isomerization or any other chemical change. If there are restrictions on the volume of phase space sampled

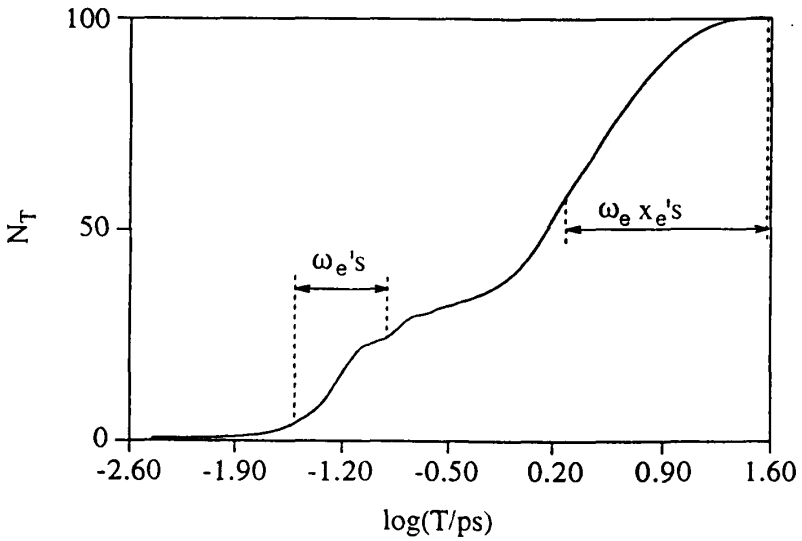

Figure 20 The volume sampled in phase space vs. time on a logarithmic scale. The logarithmic scale is needed to show different time scales in the same plot. The two regimes shown (indicated by arrows) correspond to the range of vibrational frequencies and the range of anharmonicities (cf. Eq. (58)). (Adapted from J. C. Lorquet, Y. M. Engel, and R. D. Levine, *Chem. Phys. Lett. 175*: 461 (1990).)

by the system then that is already a nonstatistical behavior. All the available evidence is that such restrictions persist beyond the second period. One expects that modes of comparable frequencies, such as the bond stretches, will mix, but that otherwise selectivity will be maintained. The results of Fig. 8 show that even at chemical energies selectivity can be maintained for times comparable to the scale of the chemical change.

The reaction coordinate for dissociation must be some linear combination of stretch modes. If the energy remains localized in the stretch modes then the actual rate of dissociation will be much faster than that expected from statistical considerations. The latter assume that energy is fully shared over all modes prior to dissociation. Specifically, the RRK (115) unimolecular reaction rate at the energy E is given by

$$k(E) = \frac{N^*(E - E_0)}{\hbar\rho(E)} \tag{109}$$

In modern terminology, $N^*(E - E_0)$ is the number of states at the transition state* which is at an energy E_0 above the bottom of the well so that the energy available at the transition state is $E - E_0$. The denominator in (109), $\rho(E)$, is the density of states of the energy rich molecule. This comes about because one *assumes* that all these states are accessible. But if the volume actually sampled in phase space is lower, then the actual rate will be higher. To achieve significant enhancement of the rate it is necessary that the actual volume is much smaller. As an example, consider a large molecule. The number s of vibrational modes increases with the number N of atoms as $s = 3N - 6$. But the number of high-frequency stretch modes increases more slowly. Hence, large molecules with initial excitation in their stretch modes could dissociate faster than expected (116). The point is that one beats dissipation by preparing the excited molecule with energy in the modes which become the reaction coordinate (117). We turn next to a Hamiltonian model which exhibits this aspect very clearly.

A. The Trapping Model

We consider an analytically tractable quantum mechanical model on the basis of which we show that one can prepare a molecule so that it will dissociate (or isomerize) promptly even though other preparations will lead to a much slower reaction. Moreover, the model clearly identifies which modes need to be excited and, as expected from our considerations above, these will turn out to be the modes which are directly connected to the transition state.

To make the model as simple as possible we consider N degenerate states which can dissociate. In general, there can be K, $K \geq 1$, dissociation continua. These will in general be distinct continua because there can be different possible internal states of the products. A useful way to think about K is as the number $N^*(E - E_0)$ of states at the transition state. If we uniquely correlate the states at the transition state with the states of the products (118) then this identification is obvious. Otherwise, we recall that there is no obvious way to specify the location of the transition state except for its property of being the bottleneck for the reactive events. It follows from this (known as the "variational transition state" (119)) point of view that the transition state is to be located where $N^*(E - E_0)$ is minimal (120).

*Recall that this is the number of energetically accessible states in all the other degrees of freedom excluding the motion along the reaction coordinate.

The full Hamiltonian of the system includes both the bound states and the continua. It is however possible (65,121) to write down an "effective Hamiltonian" **H**, which is the full Hamiltonian as far as the bound states are concerned, but which makes no explicit reference to the continua. Instead, the effective Hamiltonian incorporates a rate operator Γ which describes the dissociation of the bound states due to their coupling to the continua. In the model we assume that the rate operator is purely imaginary so that there is no shift in the energy of the bound states due to the coupling to the continua. Under this assumption, the matrix elements of the rate operator are of the form

$$\Gamma_{n',n} \equiv \langle n'|\Gamma|n\rangle = \pi \sum_{k=1}^{K} \langle n'|V|k\rangle\langle k|V|n\rangle \tag{110}$$

where the states $|k\rangle$ are energy eigenstates of the different continua at the same energy as the bound states. In matrix notation, Eq. (110) is of the form

$$\Gamma = \mathbf{V}\mathbf{V}^{\dagger} = \sum_{k=1}^{K} \mathbf{v}_k \mathbf{v}_k^{\dagger} \tag{111}$$

where

$$\mathbf{v}_k^{\dagger} \cdot \mathbf{v}_k \equiv \pi \sum_{n=1}^{N} \langle k|V|n\rangle\langle n|V|k\rangle$$

To simplify some algebra that will be needed later, we take the vectors $\mathbf{v}_k$ to be orthogonal

$$\mathbf{v}_k^{\dagger} \cdot \mathbf{v}_l = \sum_{n=1}^{N} (\mathbf{v}^{\dagger}k)_n(\mathbf{v}k)_n = \Gamma_k \delta_{k,l} \tag{112}$$

and to be normalized as shown.

The effective Hamiltonian is

$$\mathbf{H} = E\mathbf{I} - i\Gamma \tag{113}$$

Here E is the energy of the degenerate bound states and **I** is the unit matrix. The second term describes the loss of population of the bound space due to dissociation. We know it is a loss term because Eq. (111) implies that the rate matrix Γ is (semi)positive definite, i.e., the eigenvalues λ_n of the effective Hamiltonian must have a nonpositive imaginary part or that $\exp(-i\lambda_n t/\hbar) = \exp(-i(E_n - i\Gamma_n)t/\hbar) = \exp(-iE_n t/\hbar)\exp(-\Gamma_n t/\hbar)$ so that the states do decay in time because $\Gamma_n \geq 0$. To determine the eigenvalues we need to diagonalize Eq. (113). The assumption of Eq. (112) implies that there are K eigenvectors which can be explicitly written down:

$$|n_k\rangle = \frac{1}{\sqrt{\Gamma_k}} \sum_{n=1}^{N} (\mathbf{v}_k)_n |n\rangle = \frac{1}{\sqrt{\Gamma_k}} \sum_{n=1}^{N} |n\rangle\langle n|V|k\rangle \equiv \frac{1}{\sqrt{\Gamma_k}} QV|k\rangle, \qquad k = 1, \ldots, K \tag{114}$$

where **Q** is the projection operator on the subspace of bound states, $\mathbf{Q} = \Sigma_{n=1}^{N} |n\rangle\langle n|$. The corresponding eigenvalues are

$$\lambda_k = E - i\Gamma_k, \qquad k = 1, \ldots, K \tag{115}$$

In addition, there are $N - K$ other, degenerate, eigenvectors whose eigenvalues are all E. That the latter eigenvectors are stable (i.e., that their energy is real) is a direct consequence of the initial assumption that the bound states are exactly degenerate. If they are not, but their spacings are small compared to the Γ_k's then the imaginary part of the other, $N - K$, eigenvalues is finite but small (122). That almost degenerate, and hence densely spaced, states should have low dissociation rates also follows directly from the RRK result, Eq. (109), since the density $\rho(E)$ of bound states is the inverse of the mean spacing of states.

To prove that Eq. (114) is an eigenvector of Eq. (113), one uses the orthogonality condition given by Eq. (112). The normalization determines the eigenvalue. The other $N - K$ eigenvectors are degenerate and are any linear combination of the $N - K$ vectors that are orthogonal to the K vectors $\mathbf{v}_k$.

What have we shown? That for a bound subspace with a high $N > K$ density of states and with K states at the transition state, there will be K states that will dissociate promptly and other, $N - K$, states whose decay is much slower. The states that promptly decay are equal in number to the number of states at the transition state and are formally defined by analogy to the optically bright states, cf. Eq. (23), i.e., by the action of the intramolecular coupling on the states at the transition state.

If one excites any of the promptly dissociating states then it will proceed to dissociate with a fast rate without any sampling of the rest of the energetically available phase space. In general, for an energy-rich polyatomic molecule one expects a high density of bound states and the slow RRK dissociation rate is physically understood as due to the low probability (i.e., K/N) for the required energy to be localized along the reaction coordinate. What the model showed is that, in addition, there are far fewer states which promptly dissociate. These are the K states which are directly coupled to the transition state.

B. The Fluctuations in Rate Constants

The RRK rate monotonically increases with increasing energy of the molecule. On a state-by-state basis the rate of dissociation shows much more irregularity (123,124), in a manner similar to that discussed in Sec. IV for the spectral intensities (which are the rates of transition induced by the light). What the RRK rate provides is the mean about which the fluctuations occur. Hence, as in Eq. (86) one can write

$$\langle (k - k_{\mathrm{RRK}})^2 \rangle = \left(\frac{2}{\nu}\right) k_{\mathrm{RRK}}^2 \tag{116}$$

where ν is the number of degrees of freedom. In the present context one can provide a physical interpretation for this number on the basis of the analogy between the states at the transition state and the initial states in spectroscopy. In Sec. IV.A.2 we have shown that if there are several initial states, then ν increases by the corresponding number. Since in general there are up to two degrees of freedom per state (see, e.g., Fig. 4.1.), $2/\nu \geq 1/K$, so that large fluctuations are less likely at higher energies when K is higher and are more probable when the number of degrees of freedom per state is below 2. The more regular is the dynamics, the more the latter is the case.

C. Probing the Products' States

One way of probing the fluctuations in rate constants is to sharpen the definition of the event. This is obvious on rather general grounds but the typical pump probe experiment

provides a practical way of realizing this goal. The dissociation rate constant that the kinetics textbooks discuss and which is the subject of the RRK theory and its refinements is the rate of *dissociation* by which one means the rate of decrease in the number of reactants, irrespective of the specific state of the products. In a typical pump-probe experiment where the detection is products' state specific, one measures not quite this rate. Rather, one measures the rate of appearance of products in a particular state (or group of states). If one assumes that phase space has been representatively sampled then the rise time of the signal into any final state is the same and is given by $1 - \exp(-kt)$, where k is the rate of dissociation. What is different for different final states is then the amplitude of the signal, $k(\rightarrow \text{final state } f)/k$ ($k = \Sigma_f k(\rightarrow \text{final state } f)$), also known as the branching fraction. There are two implicit assumptions in this familiar result. The first, which we already mentioned, is that the very same population of reactant states gives rise to all possible final states so that different final states are in competition with one another. The second, and less obvious, assumption is that the same transition state configuration determines both the overall rate of dissociation and also the rate of appearance of specific states of products.* Much of the evidence is to the contrary so much so that it is customary to speak of "exit valley interactions." These are the forces that operate past the bottleneck to reaction, en route to the products, and which determine the final state distribution. Chemical intuition would even suggest that different attributes of the products are determined in different regions. An obvious example are the rotations which remain coupled by the long-range forces even as the products are already otherwise quite separated.

In conclusion, probing products' states (125,126) can provide evidence for selectivity not available from examination of the overall rate of dissociation. It is possible, for example, for the bound phase space prior to the bottleneck for reaction, to be well sampled (either because of the preparation itself and/or through the subsequent intramolecular dynamics) yet for the products to be nonstatistical, Fig. 21, in the same manner as shown for a direct reaction in Fig. 3. In this figure the final states are grouped into very broad bins. At a higher resolution of the final states it is also possible to discern fluctuations as discussed in the case of the spectrum in Sec. IV. This is particularly the case if the initial state is well defined. Averaging over a distribution of initial states results in the averaging over the fluctuations (127). One can indeed argue that the practical success of the RRK expression for the rate constants owes much to the inherently large volume in the reactants' phase space which is accessed by an initial nonselective preparation.

VI. CONCLUDING REMARKS

There are two clear directions of further progress. One needs to sharpen the theoretical tools, and this volume contains the building blocks for doing so, and further experiments which close the gap between the spectroscopic and the kinetic regime are needed. (The commercial availability of femtosecond lasers will surely encourage more participants to

*If this was the case one could generalize transition state theory to apply also to state specific rates. This is seen by application of detailed balance. If there is a transition state for each state of the products then, for the reversed reaction, each state of the reactants (i.e., the products of the forward reaction) will correlate to its own transition state.

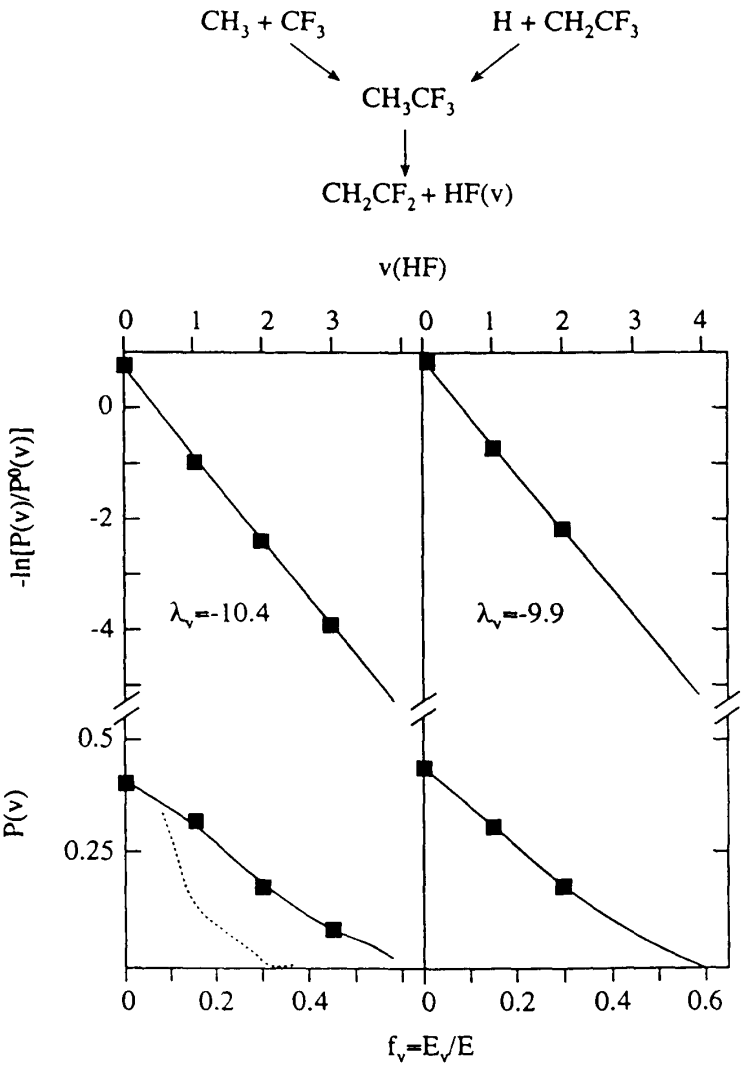

Figure 21 Surprisal plot for the vibrationally hot HF product from the four-center elimination reaction $CH_3CF_3 \rightarrow CH_2{=}CF_2 + HF$. The energy rich, long living, CH_3CF_3 is produced via two routes as shown. The HF vibrational distribution is rather nonstatistical, but is almost the same for both routes. (Adapted from E. Zamir and R. D. Levine, *Chem. Phys. 52*: 253 (1980).) For recent experimental studies of elimination reactions see E. Arunan, S. J. Wategaonker, and D. W. Setser, *J. Phys. Chem. 95*: 1539 (1991); T. R. Fletcher and R. Leone, *J. Chem. Phys. 88*: 4720 (1988).)

probe molecules on their inherent time scale (128). There is, however, at least one additional direction where progress is possible. This is in bringing the new theoretical and experimental capabilities to bear on systems of real chemical interest. In saying this we most certainly do not wish to de-emphasize the importance of understanding of intra/intermolecular dynamics for its own sake (and a complete understanding includes the comparison of experiment and theory at the highest possible level of resolution). Nor do we expect that industrial applications are around the corner. It took many years and the valiant efforts of many people until electronic structure theory became a practical research tool of the chemist. But now it is, and we look forward to a similar development in molecular reaction dynamics.

REFERENCES

1. G. Herzberg, *Molecular Spectra and Molecular Structure*. Vol. II. *Infrared and Raman Spectra of Polyatomic Molecules*, Van Nostrand, Princeton, 1960.
2. E. B. Wilson Jr., J. C. Decius, and P. C. Cross, *Molecular Vibrations*, McGraw-Hill, New York, 1954.
3. I. N. Levine, *Molecular Spectroscopy*, Wiley, New York, 1975.
4. W. H. Flygare, *Molecular Structure and Dynamics*, Prentice-Hall, New Jersey, 1978.
5. B. H. Andrew (ed.), *Interstellar Molecules*, Reidel, Dordrecht, 1980.
6. O. K. Rice and H. C. Rampsperger, Theories of unimolecular gas reactions at low pressures, *J. Am. Soc. 49*: 1617 (1927); L. S. Kassel, Studies in homogeneous gas reactions, *J. Phys. Chem. 32*: 225 (1928); F. A. Lindeman, The radiation theory of chemical reactions, *Trans. Faraday Soc. 17*: 598 (1922).
7. I. Oref and B. S. Rabinovitch, Ergodicity of excited polyatomics, *Acc. Chem. Res. 12*: 166 (1979).
8. J. C. Whitehead (ed.), *Selectivity in Chemical Reactions*, NATO ASI Series C, Vol. 245, Kluwer, Dordrecht, 1987; J. Manz and C. S. Parmenter (eds.), *Mode Selective Unimolecular Reactions*, *Chem. Phys. 139*: 1 (1989); J. Jortner, R. D. Levine, and B. Pullman (eds.), *Mode Selective Chemistry*, Kluwer, Dordrecht, 1991.
9. F. F. Crim, Vibrationally mediated photodissociation: exploring excited-state surfaces and controlling decomposition pathways, *Ann. Rev. Phys. Chem. 44*: 397 (1993).
10. P. Brumer and M. Shapiro, Laser control of molecular processes, *Ann. Rev. Phys. Chem. 43*: 257 (1992).
11. D. Neuhauser and H. Rabitz, Paradigms and algorithms for controlling molecular motion, *Acc. Chem. Res. 26*: 496 (1993); W. S. Warren, H. Rabitz, and M. Dahleh, Coherent control of quantum dynamics: the dream is alive, *Science 259*: 1581 (1993); S. A. Rice, New ideas for guiding the evolution of a quantum system, *Science 247*: 1317 (1990); B. Kohler, J. L. Krause, F. Raski, K. R. Wilson, V. V. Yakovlev, R. M. Whitnell, and Y. Yan, Controlling the future of matter, *Acc. Chem. Res. 28*: 133 (1995).
12. M. Tabor, *Chaos and Integrability in Nonlinear Dynamics*, Wiley, New York, 1989.
13. A. J. Lichtenberg and M. A. Lieberman, *Regular and Stochastic Motion*, Springer, New York, 1983.
14. L. E. Reichl, *The Transition to Chaos in Conservative Classical Systems: Quantum Manifestations*, Springer-Verlag, New York, 1992.
15. S. A. Rice, Overview of the dynamics of intramolecular transfer of vibrational energy, *Adv. Chem. Phys. 47*: 117 (1981); P. Brumer, Intramolecular energy transfer: theory for the onset of statistical behavior, *Adv. Chem. Phys. 47*: 202 (1981); P. Brumer and M. Shapiro, Chaos and reaction dynamics, *Adv. Chem. Phys. 70*: 365 (1988).
16. E. B. Stechel and E. J. Heller, Quantum ergodicity and spectral chaos, *Ann. Rev. Phys. Chem. 35*: 563 (1984).
17. T. Uzer, Theory of intramolecular vibrational energy transfer, *Phys. Rep. 199*: 73 (1991).
18. R. D. Levine and R. B. Bernstein, *Molecular Reaction Dynamics and Chemical Reactivity*, Oxford University Press, New York, 1989.
19. C. E. Hamilton, J. L. Kinsey, and R. W. Field, Stimulated emission pumping: new methods in spectroscopy and molecular dynamics, *Ann. Rev. Chem. Phys. 37*: 493 (1986).
20. M. Quack, Spectra and dynamics of coupled vibrations in polyatomic molecules, *Ann. Rev. Phys. Chem. 41*: 839 (1990).
21. K. K. Lehmann, G. Scoles, and B. H. Pate, Intramolecular dynamics from eigenstate-resolved infrared spectra, *Ann. Rev. Phys. Chem. 45*: 241 (1994).
22. F. J. Northup and T. J. Sears, Stimulated emission pumping: applications to highly vibrationally excited transition molecules, *Ann. Rev. Chem. Phys. 43*: 127 (1992).
23. W. T. Pollard and R. A. Mathies, Analysis of femtosecond dynamic absorption spectra of nonstationary states, *Ann. Rev. Phys. Chem. 43*: 497, (1992).

24. M. J. Berry, Vibrational photochemistry and photophysics, *Proc. Robert A. Welch Foundation Conf. on Chemical Research, XXVIII*, Welch Foundation, 1984, p. 133.
25. A. H. Zewail and R. B. Bernstein, Real-time laser femtochemistry: viewing the transition from reagents to products, *Chem. Eng. News 66(45)*: 24 (1988).
26. L. R. Khundar and A. H. Zewail, Ultrafast molecular reaction dynamics in real time: progress over a decade, *Ann. Rev. Phys. Chem. 41*: 15 (1990).
27. J. Manz and A. W. Castelman (eds.), *Femtosecond Chemistry, J. Phys. Chem.* 97(48) (1993).
28. J. Manz and L. Woste (eds.), *Femtosecond Chemistry*, VHC Verlag, Weinhein, 1995.
29. P. Pfeifer and R. D. Levine, A stationary formulation of time-dependent problems in quantum mechanics, *J. Chem. Phys. 79*: 5512 (1983).
30. G. Yao and R. E. Wyatt, Stationary approaches for solving the Schroedinger equation with time-dependent Hamiltonians, *J. Chem. Phys. 101*: 1904 (1994).
31. R. Kubo, The fluctuation-dissipation theorem, *Rep. Prog. Phys. 29*: 255 (1966).
32. R. G. Gordon, Correlation functions for molecular motion, *Adv. Magn. Reson. 3*: 1 (1968).
33. W. G. Rothschild, *Dynamics of Molecular Liquids*, Wiley, New York, 1984.
34. M. W. Evans, G. J. Evans, W. T. Coffey, and P. Grigolini, *Molecular Liquids*, Wiley, New York, 1982.
35. J. Jortner and R. D. Levine, Photoselective chemistry, *Adv. Chem. Phys. 47*: 1 (1981).
36. P. M. Felker and A. H. Zewail, Picosecond time-resolved dynamics of vibrational energy redistribution and coherence in beam isolated molecules, *Adv. Chem. Phys. 70*: 265 (1988).
37. S. Y. Lee and E. J. Heller, Time-dependent theory of Raman scattering, *J. Chem. Phys. 71*: 4777 (1979); E. J. Heller, R. L. Sundberg, and D. Tannor, Simple aspects of Raman scattering, *J. Phys. Chem. 86*: 1822 (1982).
38. B. R. Stallard, P. M. Champion, P. R. Callis, and A. C. Albrecht, Advances in calculating Raman excitation profiles by means of the transform theory, *J. Chem. Phys. 78*: 712 (1983).
39. M. O. Hale, G. E. Galica, S. G. Glovoger, and J. L. Kinsey, Emission spectroscopy of photodissociating CH_3I and CD_3I, *J. Phys. Chem. 90*: 4997 (1986).
40. M. Shapiro, Real-time dependence of photodissociation and continuum Raman experiments, *J. Phys. Chem. 97*: 7396 (1993).
41. A. C. Albrecht, R. J. H. Clark, D. Oprescu, S. J. R. Owens, and C. Svendsen, Overtone resonance Raman scattering beyond the Condon approximation: transform theory and vibronic properties, *J. Chem. Phys. 101*: 1890 (1994).
42. L. D. Ziegler, Y. C. Chung, P. G. Wang, and Y. P. Zhang, The resonance rotational Raman effect: a probe of excited-state short-time dynamics, *J. Phys. Chem. 94*: 3394 (1990).
43. S. Mukamel, Solvatation effects in four-wave mixing and spontaneous Raman and fluorescence lineshapes of polyatomic molecules, *Adv. Chem. Phys. 70*: 165 (1988).
44. E. J. Heller, The semiclassical way to molecular spectroscopy, *Acc. Chem. Res. 14*: 368 (1981).
45. R. Schinke, *Photodissociation Dynamics*, Cambridge University, Cambridge, 1993.
46. D. E. Weeks and D. J. Tannor, A time-dependent formulation of the scattering matrix using Moller operators, *Chem. Phys. Lett. 207*: 301 (1993); D. J. Tannor and D. E. Weeks, Wave packet correlation function formulation of scattering theory: the quantum analog of classical *S*-matrix theory, *J. Chem. Phys. 98*: 3884 (1993).
47. K. F. Freed, The theory of radiationless processes in polyatomic molecules, *Top. Curr. Chem. 31*: 105 (1972).
48. H. Köppel, W. Domcke, and L. S. Cederbaum, Multimode molecular dynamics beyond the Born-Oppenheimer approximation, *Adv. Chem. Phys. 57*: 59 (1984).
49. R. L. Whetten, G. S. Ezra, and E. R. Grant, Molecular dynamics beyond the adiabatic approximation: new experiments and theory, *Ann. Rev. Phys. Chem. 36*: 277 (1985).
50. E. J. Heller, Quantum corrections to classical photodissociation models, *J. Chem. Phys. 68*: 2066 (1978).
51. A. Papoulis, *The Fourier Integral and Its Applications*, McGraw-Hill, New York, 1962.
52. C. Cohen-Tannoudji, B. Diu, and F. Laloë, *Quantum Mechanics*, Wiley, New York, 1977.

53. D. P. Huber and E. J. Heller, Generalized Gaussian wavepacket dynamics, *J. Chem. Phys. 87*: 5302 (1987).
54. A. Papoulis, *Probability, Random Variables and Stochastic Processes*, McGraw-Hill, New York, 1991.
55. R. D. Levine, Fluctuations in spectral intensities and transition rates, *Adv. Chem. Phys. 70*: 53 (1987).
56. D. W. Noid, M. L. Koszykowski, and R. A. Marcus, Spectral analysis method of obtaining molecular spectra from classical trajectories, *J. Chem. Phys. 67*: 404 (1977); M. L. Koszykowski, D. W. Noid, and R. A. Marcus, Semiclassical theory of intensities of vibrational fundamentals, overtones, and combination bands, *J. Phys. Chem. 86*: 2113 (1982); D. W. Noid, M. L. Koszykowski, and R. A. Marcus, Quasiperiodic and stochastic behavior in molecules, *Ann. Rev. Phys. Chem. 32*: 267 (1981).
57. J. M. Gomez-Llorentez, and E. Pollak, Classical dynamics methods for high energy vibrational spectroscopy, *Ann. Rev. Phys. Chem. 43*: 91 (1992).
58. W. C. De Marcus, Classical motion of a morse oscillator, *Am. J. Phys. 46*: 733 (1978).
59. M. Lax, The Franck-Condon principle and its application to crystal, *J. Chem. Phys. 20*: 1752 (1952).
60. P. Pulay, *Modern Theoretical Chemistry*, Vol. 4 (H. F. Schaefer, ed.), Plenum Press, New York, 1977; B. H. Lengsfield III and D. R. Yarkony, Nonadiabatic interactions between potential energy surfaces: theory and applications, *State Selected and State-to-State Ion-Molecule Reaction Dynamics*. Part 2: *Theory* (M. Baer and C.-Y. Ng, eds.), *Adv. Chem. Phys. 82*: 1 (1992).
61. R. Car and M. Parrinello, Unified approach for the molecular dynamics and density-functional theory, *Phys. Rev. Lett. 55*: 2471 (1985); M. E. Tuckerman and M. Parrinello, Integrating the Car-Parrinello equations. I: Basic integration techniques, *J. Chem. Phys. 101*: 1302 (1994).
62. R. G. Parr and W. Yang, *Density-Functional Theory of Atoms and Molecules*, Oxford University Press, New York, 1989.
63. R. B. Bernstein (ed.), *Atom-Molecule Collision Theory*, Plenum, New York, 1979; J. Broeckhove and L. Lathouwers (eds.), *Time Dependent Quantum Molecular Dynamics*; NATO ASI Series B, Vol. 299, Plenum Press, New York, 1992; R. Kosloff, Propagation methods for quantum molecular dynamics, *Ann. Rev. Phys. Chem. 45*: 145 (1994); E. Deumens, A. Diz, R. Longo, and Y. Öhrn, Time-dependent theoretical treatments of the dynamics of electrons and nuclei in molecular systems, *Rev. Mod. Phys. 66*, 917 (1994).
64. R. D. Levine, Molecular collisions and reactive scattering, *MTP International Review of Science*. Vol. 1: *Theoretical Chemistry* (A. D. Buckingham, ed.), Butterworths, London, 1972.
65. R. D. Levine, *Quantum Mechanics of Molecular Rate Processes*, Clarendon, Oxford, 1969; R. D. Levine, An extended Hellman-Feynman theorem, *Proc. Roy. Soc. A294*: 467 (1966).
66. W. A. Lester, Jr., The *N* coupled-channel problem, *Modern Theoretical Chemistry*, Vol. I (W. H. Miller, ed.), Plenum Press, New York, 1976, p. 1; D. Secrest, Rotational excitation I: The quantal treatment, in *Atom-Molecule Collision Theory* (R. B. Bernstein, ed.), Plenum Press, New York, 1979.
67. J. Broeckhove, L. Lathouwers, and P. Van Leuven, The generator coordinate approximation for molecules: a review, *J. Math. Chem. 6*: 207 (1991).
68. D. G. Truhlar and J. T. Muckerman, Reactive scattering cross sections. III: Quasiclassical and semiclassical methods, *Atom-Molecule Collision Theory* (R. B. Bernstein, ed.), Plenum, New York, 1979; L. M. Raff and D. L. Thompson, The classical approach to reactive scattering, *Theory of Chemical Reaction Dynamics* (M. Baer, ed.), CRC, Boca Raton, FL, 1985.
69. M. P. Allen and D. J. Tildesley, *Computer Simulations of Liquids*, Clarendon, Oxford, 1987.
70. S. A. Adelman and J. D. Doll, Brownian motion and chemical dynamics on solid surfaces, *Acc. Chem. Res. 10*: 378 (1977); S. A. Adelman, Chemical reaction dynamics in liquid solution, *Adv. Chem. Phys. 53*: 61 (1983).

71. J. W. Gazduk, The semiclassical way to molecular dynamics at surfaces, *Ann. Rev. Phys. Chem. 39*: 395 (1988).
72. S. Mukamel, Reduced equations of motion for collisionless molecular multiphoton processes, *Adv. Chem. Phys. 47*: 509 (1981).
73. C. B. Harris, D. E. Smith, and D. J. Russel, Vibrational relaxation of diatomics molecules in liquids, *Chem. Rev. 90*: 481 (1990).
74. I. Benjamin, L. L. Lee, Y. S. Li, and K. R. Wilson, Generalized Langevin model for molecular dynamics of an activated reaction in solution, *Chem. Phys. 152*: 1 (1991).
75. M. S. Child, *Semiclassical Mechanics with Molecular Applications*, Clarendon, Oxford, 1991.
76. D. E. Weeks and R. D. Levine, Dynamics of non-rigid molecules: the exploration of phase space via resonant and sub-resonant coupling, *Structures and Dynamics of Non-Rigid Molecular Systems* (Y. G. Smeyers, ed.), Kluwer, Dordrecht, 1995.
77. D. M. Charutz and R. D. Levine, The dynamics of dressed variables, *Chem. Phys. 159*: 321 (1992).
78. M. Tuckerman, G. J. Martyna, and B. J. Berne, Reversible multiple time scale molecular dynamics, *J. Chem. Phys. 97*: 1990 (1992).
79. W. H. Miller, W. L. Hase, and L. Darling, A. simple model for correcting the zero point energy problem in classical trajectory simulations of polyatomic molecules, *J. Chem. Phys. 91*: 2863 (1989).
80. J. Bowman, B. Gazdy, and Q. Sun, A. method to constrain vibrational energy in quasiclassical trajectory calculations, *J. Chem. Phys. 91*: 2859 (1989); R. Alimi, A. Garcia-Vela, and R. B. Gerber, A remedy for zero-point energy problems in classical trajectories: a combined semiclassical/classical molecular dynamics algorithm, *J. Chem. Phys. 96*: 2034 (1992).
81. M. Ben-Nun and R. D. Levine, Conservation of zero-point energy in classical trajectory computations by a simple semiclassical correspondence, *J. Chem. Phys. 101*: 8768 (1994).
82. D. Permann and I. Hamilton, Energy stepping close to dissociation for HF in a moderate laser field, *J. Chem. Phys. 97*: 3865 (1992); P. S. Dardi and S. K. Gray, Classical and quantum mechanical studies of HF in an intense laser field, *J. Chem. Phys. 77*: 1345 (1982).
83. C. E. Wozny, B. G. Sumpter, and D. W. Noid, Calculating the vibrational spectra of linear polymers from molecular dynamics trajectories, *Trends Polym. Sci. 2*: 375 (1994); B. G. Sumpter and D. W. Noid, Computational experiments on the migration of internal energy in macromolecular systems, *Chem. Phys. 186*: 323 (1994).
84. J. A. McCammon and S. C. Harvey, *Dynamics of Proteins and Nucleic Acids*, Cambridge University Press, 1987; C. L. Brooks, M. Karplus, and B. M. Pettitt, *Proteins: A Theoretical Perspective of Dynamics, Structure and Thermodynamics*, Wiley, New York, 1988.
85. G. Stock and W. H. Miller, Classical formulation of the spectroscopy of nonadiabatic excited-state dynamics, *J. Chem. Phys. 99*: 1545 (1993).
86. C. Woywod, W. Domcke, A. L. Sobolewski, and H-J Werner, Characterization of the S_1–S_2 conical intersection in pyrazine using ab initio multiconfiguration self-consistent-field and multireference configuration-interaction methods, *J. Chem. Phys. 100*: 1400 (1994); G. Stock and W. Domcke, Femtosecond spectroscopy of ultrafast nonadiabatic excited-state dynamics on the basis of ab initio potential-energy surfaces: the S_2 state of pyrazine, *J. Phys. Chem. 97*: 12466 (1993).
87. G. C. Waschewsky, P. W. Kash, T. L. Myers, D. C. Kitchen, and L. J. Butler, What Woodward and Hoffmann didn't tell us: the failure of the Born-Oppenheimer approximation in competing reaction pathways, *J. Chem. Soc. Faraday Trans. 90*: 1581 (1994).
88. J. J. Valentini, D. P. Gerrity, D. L. Phillips, J.-C. Nieh, and K. D. Tabor, CARS spectroscopy of $O_2(^1\Delta_g)$ from the Hartley band photodissociation of O_3: dynamics of the dissociation, *J. Chem. Phys. 86*: 6745 (1987).
89. M. Hillery, R. F. O'Connell, M. O. Scully, and E. P. Wigner, Distribution functions in physics: fundamentals, *Phys. Rep. 106*: 121 (1984).

90. A. K. Kerman and S. E. Koonin, Hamiltonian formulation of time-dependent variational principles for the many-body system, *Ann. Phys. 100*: 332 (1976).
91. R. Heather and H. Metiu, An efficient procedure for calculating the evolution of the wave function by fast Fourier transform methods for systems with spatially extended wave function and localized potential, *J. Chem. Phys. 86*: 5009 (1987).
92. R. G. Littlejohn, The semiclassical evolution of wave packets, *Phys. Rep. 138*: 193 (1986).
93. K. J. Kay, Improved semiclassical propagation of wave packets, *J. Chem. Phys. 91*: 170 (1989).
94. P. Kramer and M. Saraceno, *Geometry of the Time-Dependent Variational Principle*, Springer-Verlag, Berlin, 1981.
95. Z. Bacic and J. C. Light, Theoretical methods for rovibrational states of floppy molecules, *Ann. Rev. Phys. Chem. 40*: 469 (1989); J. M. Bowman (ed.), Molecular vibrations, *Comp. Phys. Comm. 51* (1983).
96. J. M. Bowman, The self-consistent-field approach to polyatomic vibrations, *Acc. Chem. Res. 19*: 202 (1986).
97. R. B. Gerber and M. Ratner, Self-consistent-field methods for vibrational excitation in polyatomic molecules, *Adv. Chem. Phys. 70*: 97 (1988).
98. F. Iachello and R. D. Levine, *Algebraic Theory of Molecules*, Oxford University Press, New York, 1995.
99. O. S. van Roosmalen, I. Benjamin, and R. D. Levine, A unified algebraic model description of interacting vibrational modes in ABA molecules, *J. Chem. Phys. 81*: 5986 (1984).
100. I. L. Cooper and R. D. Levine, Construction of triatomic potential from algebraic Hamiltonians which represent stretching vibrational overtones, *J. Mol. Struct. 191*: 201 (1989).
101. R. D. Levine, An information theoretical approach to inversion problems, *J. Phys. A 13*: 91 (1980).
102. F. Remacle and R. D. Levine, Time domain information from resonant Raman excitation profiles: a direct inversion by maximum entropy, *J. Chem. Phys. 99*: 4908 (1993).
103. F. Remacle and R. D. Levine, Maximal entropy spectral fluctuations and the sampling of phase space, *J. Chem. Phys. 99*: 2383 (1993).
104. R. Roy, B. G. Sumpter, G. A. Pfeiffer, S. K. Gray, and D. W. Noid, Novel methods for spectral analysis, *Phys. Rep. 205*, 109 (1991).
105. W. H. Press, B. P. Flannery, S. A. Teukolsky, and W. T. Vetterling, *Numerical Recipes: The Art of Scientific Computing*, Cambridge University Press, Cambridge, 1986.
106. Math/Library, *User's Manual*, IMSL, 1987.
107. R. D. Levine, The statistical wave function, *J. Stat. Phys. 52*: 1203 (1988).
108. R. D. Levine, Statistical dynamics, *Theory of Reactive Collisions* (M. Baer, ed.), CRC, Boca Raton, FL, 1985.
109. N. Agmon, Y. Alhassid, and R. D. Levine, An algorithm for finding the distribution of maximal entropy, *J. Comput. Phys. 30*: 250 (1979).
110. R. D. Levine and J. L. Kinsey, On the repulsion of energy eigenstates in the time domain, *Proc. Natl. Acad. Sci. USA 88*: 11133 (1991).
111. A. Papoulis, *Signal Analysis*, McGraw-Hill, New York, 1977.
112. S. C. O'Brien, C. Kittrel, J. L. Kinsey, and B. R. Johnson, Spectroscopy and dynamics of resonance Raman scattering by iodobenzene excited in the *B* continuum, *J. Chem. Phys. 96*: 67 (1992).
113. F. J. Harris, On the use of windows for harmonic analysis with discrete Fourier transform, *Proc. IEEE 66*: 51 (1978).
114. P. J. Reid, M. K. Lawless, S. D. Wickham, and R. A. Mathies, Determination of pericyclic photochemical reaction dynamics with resonance Raman spectroscopy, *J. Phys. Chem. 98*: 5597 (1994).
115. P. J. Robinson and K. A. Holbrook, *Unimolecular Reactions*, Wiley, New York, 1972; R. G. Gilbert and S. C. Smith, *Theory of Unimolecular Recombination Reactions*, Blackwell, Oxford, 1990.

116. E. W. Schlag and R. D. Levine, On the unimolecular dissociation of large molecules, *Chem. Phys. Lett. 163*: 523 (1989).
117. F. Remacle, J. C. Lorquet, and R. D. Levine, Unimolecular dissociation of selectively excited polyatomic molecules, *Chem. Phys. Lett. 209*: 315 (1993).
118. M. Quack and J. Troe, Specific rate constants of unimolecular processes. II: Adiabatic channel model, *Ber. Besung. Phys. Chem. 78*: 240 (1974).
119. D. G. Trulhar, W. L. Hase, and J. T. Hynes, Current status of transition-state theory, *J. Phys. Chem. 87*: 2664 (1983).
120. W. H. Wong and R. A. Marcus, Concept of minimum state density in the activated complex theory of bimolecular reactions, *J. Chem. Phys. 55*: 5625 (1971).
121. S. Nordholm and S. A. Rice, A quantum ergodic theory approach to unimolecular fragmentation, *J. Chem. Phys. 62*: 157 (1975).
122. F. Remacle, M. Desouter-Lecomte, and J. C. Lorquet, Extracting laws of decay in the femto-picosecond range from autocorrelation functions, *J. Chem. Phys. 91*: 4155 (1989).
123. R. D. Levine, Quantal fluctuations in unimolecular rate constants, *Ber. Bunsenges. Phys. Chem. 92*: 222 (1988).
124. W. H. Miller, Effects of fluctuations in state-specific unimolecular rate constants on the pressure dependence of the average unimolecular reaction rate, *J. Phys. Chem. 92*: 4261 (1988).
125. S. A. Reid, J. T. Brandon, M. Hunter, and H. Reisler, *J. Chem. Phys. 99*: 4860 (1993); S. A. Reid, D. C. Robie, and H. Reisler, *J. Chem. Phys. 100*: 4256 (1994); S. A. Reid and H. Reisler, *J. Chem. Phys. J. Chem. Phys. 101*:5683 (1994).
126. N. Changlong, L. Hua, and J. Pfab, Photodissociation of jet-cooled NO_2 at 355 nm: strong alignment and oscillations in the rotational state distributions of the NO ($v'' = 1$) fragment, *J. Phys. Chem. 97*: 7458 (1993).
127. F. Remacle and R. D. Levine, Does a dissociating molecule sample the available phase space, *J. Phys. Chem. 95*: 7124 (1991).
128. K. L. Kompa and R. D. Levine, A new look at laser chemistry, *Acc. Chem. Res. 27*: 91 (1994).

2

Quantum Mechanical Studies of Molecular Spectra and Dynamics

ROBERT E. WYATT

University of Texas at Austin, Austin, Texas

CHRISTOPHE IUNG

University of Science and Technology, Montpellier, France

I. INTRODUCTION

A. Intramolecular Dynamics and Spectra

One of the central goals of chemical physics is to understand the nature of *intramolecular energy flow*. Starting from a well defined initial excitation, we seek answers to questions such as: Where does the energy go? How long does it take to get there? To what extent is this flow state- or mode-specific? What is the detailed mechanism leading to the flow? What features of the potential energy surface are most important in determining the time scales and destination for the energy lost from the initial "hot spot"? How do spectral *features* measured in the frequency domain relate to *events* occurring in the time domain? During the past decade, considerable progress toward answering questions of this type has been made from both the experimental and theoretical directions. An excellent review of the experimental situation, with references to the literature through 1994, was recently presented by Lehman et al. (1). An outstanding review of the theoretical studies, including work published through 1990, was presented by Uzer (2). An earlier review by Quack (3) covers theoretical and experimental studies on several molecules.

Understanding intramolecular dynamics requires more than just applying simplistic (but sometimes very useful) ideas, such as the Fermi golden rule (FGR). Among other things, the FGR states that the rate of energy transfer out of the initial state should be proportional to the total density of states. The implication, for example, is that a $v = 2$

overtone, because it is embedded in a region of higher state density, should relax much faster than the $v = 1$ state. This is certainly correct in some cases. However, recent experimental results (1) on the lifetimes of acetylenic CH stretch states in the molecules $(CY_3)_3XCCH$ (X = C, Si, Sn and Y = H, D) show some surprising features which indicate violation of the FGR. For example, in the molecule for which Y = H and H = Si, the CH lifetime for $v = 2$ is a factor of 2 *longer* than for $v = 1$, even though the density of states (of A_1 symmetry which can couple with the stretch) *increases* by a factor of 3000. Detailed quantum mechanical calculations by Stuchebrukhov, Mehta, and Marcus (4,5) have shown that a subset of coupled states in the first few tiers of background states coupled to the initial CH stretch controls the dynamics; the total state density does not play a significant role. This example, and others mentioned later in this chapter, point to the need for quantum dynamical calculations to assist with the interpretation and correlation of experimental data. In addition, the dynamical calculations can provide insights which would be impossible to glean from limited sets of experimental data.

The most commonly used experimental techniques probe molecules in the *frequency domain* rather than in the time domain. As emphasized recently (1) "the increased level of detail provided by frequency-domain methods produces a more complete picture of the vibrational energy redistribution process, invalidating frequently made claims that time domain techniques, being more direct, are somehow superior." The "molecular eigenstate" spectra provided by high-resolution experiments currently provide the most complete picture of molecular dynamics. Of course, the frequency-domain and time-domain viewpoints are complementary and we frequently obtain enhanced understanding by considering both viewpoints.

In this chapter, we will discuss theoretical and computational developments in intramolecular dynamics and vibrational spectroscopy which have occurred since the early 1980s. Emphasis will be placed upon the results arising from a long standing collaboration between research groups at The University of Texas at Austin and the University of Paris-Orsay (and more recently, at the University of Montpellier). The computational methods that were used and developed have resulted in the most detailed studies ever to be reported on the spectra and dynamics of moderate-sized molecules. Because of the very large number of available quantum states, frequently $>10^6$, a number of new methods were developed, tested, and then incorporated into the production codes.

In the next section, we will begin by discussing some conventional viewpoints of intramolecular dynamics and spectroscopy. This will permit us to define a number of terms that will play a key role in the later sections. Then, in Section II, we will describe the computational methods that have made it possible to perform very large scale quantum mechanical calculations on selected molecules. Section II.A begins with a statement of the strategy that we have used, while Section II.B describes techniques that can be used for the contraction of very large basis sets. Section II.C then proceeds into computational methods for computing spectra and time-dependent energy flow. Through the use of these computational techniques we will then present, in Sections III and IV, many results on the spectra and dynamics for 9-mode CD_3H and 21-mode planar benzene. Finally, Section V presents a summary of these methods and results and then lists some topics for future research.

B. Spectrum, Survival, and Transition Probabilities

One of the goals of the calculations that we will be describing in later sections is to obtain the *lineshape function*, the *survival probability* and *transition probabilities* asso-

ciated with the initial state $|\psi_i\rangle$. First, the lineshape function associated with transitions from the ground state $|\psi_g\rangle$ is defined by

$$S(E) = \sum_{\alpha} |\langle\psi_g|\mu|\psi_\alpha\rangle|^2 L(E - E_\alpha) \tag{1}$$

where $|\psi_\alpha\rangle$ is the eigenfunction corresponding to the eigenvalue E_α. The quantity $\langle\psi_g|\mu|\psi_\alpha\rangle$ is the *dipole matrix element* linking the ground state with eigenstate $|\psi_\alpha\rangle$; the absolute square of this quantity is the *line intensity*. The lineshape function for each spectral line is frequently assumed to be given by the normalized *Lorentzian*,

$$L(E - E_\alpha) = \frac{1}{\pi} \frac{\Gamma}{(E - E_\alpha)^2 + \Gamma^2} \tag{2}$$

where Γ is the *linewidth* (the linewidth could depend upon the eigenstate). We note that when $E = E_\alpha$, $L = 1/\pi\Gamma$, and when $E = E_\alpha \pm \Gamma$, $L = 1/2\pi\Gamma$; as a result, Γ is the half-width at half-maximum for this spectral line. Finally, the Lorentzian is normalized in the sense

$$\int_{-\infty}^{\infty} L(E - E_\alpha)\, dE = 1 \tag{3}$$

When the function $S(E)$ in Eq. (1) is plotted versus E, the resulting curve is *the absorption spectrum* associated with the transitions from the ground state. When Γ is very small, the lines do not overlap and we obtain the *stick spectrum*.

In discussions of molecular vibrational spectroscopy, the two viewpoints expressed in Figure 1 are frequently invoked (6). The upper part of the figure shows the zero-order states involved in the *mode picture*. The ground state is linked to the *bright state* $|\phi\rangle$ (which is one of the zero-order states) by a nonzero dipole matrix element and the bright state in turn is linked to a set of *background states* $|\chi_i\rangle$ by intramolecular vibrational matrix elements, $\langle\phi|V|\chi_i\rangle$. The background states (dark states) are not directly linked to the ground state and can only be populated in an absorption experiment by receiving amplitude from the bright state. In contrast, in the eigenstate picture shown in the lower part of this figure, transitions from the ground state can populate a number of eigenstates. An illustrative absorption spectrum is shown to the right of the upper set of eigenvalues. In order to establish the relationship between these two pictures, imagine that we diagonalize the vibrational Hamiltonian operator in the basis set provided by the bright state and the background states. Each of the resulting eigenstates may then be written

$$|\psi_\alpha\rangle = c_{b,\alpha}|\phi\rangle + \sum_i c_{i,\alpha}|\chi_i\rangle \tag{4}$$

where $c_{b,\alpha} = \langle\phi|\psi_\alpha\rangle$ and $c_{i,\alpha} = \langle\chi_i|\psi_\alpha\rangle$. The amplitude $c_{b,\alpha}$ measures the extent to which the bright state is found in this eigenstate. The bright state amplitudes $\{c_{b,\alpha}\}$ will play a major role in the later sections of this chapter. (We are assuming that a single bright state, which is one of the zero-order states, is mixed into the eigenstate).

Returning to the dipole amplitude linking the ground state with eigenfunction $|\psi_\alpha\rangle$, we will substitute the expansion of the eigenfunction given in Eq. (4) into the transition amplitude

$$\langle\psi_g|\mu|\psi_\alpha\rangle = \langle\psi_g|\mu|\phi\rangle c_{b,\alpha} \tag{5}$$

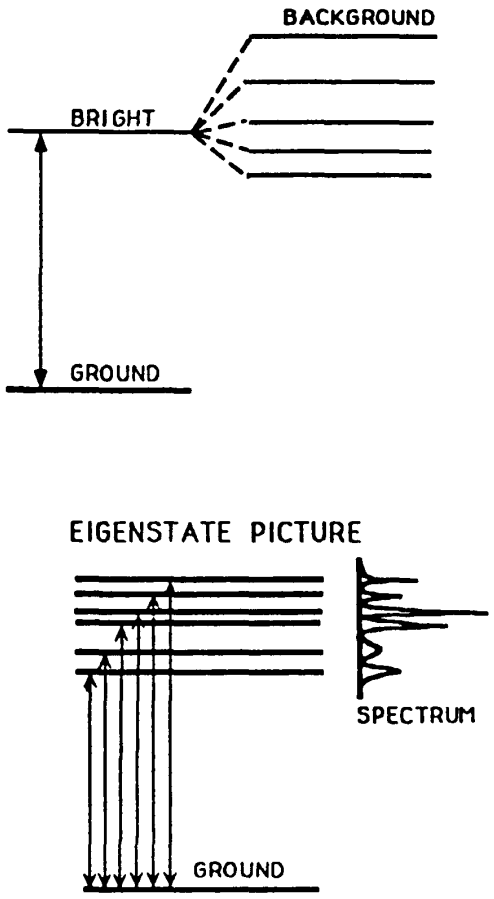

Figure 1 The mode picture (upper half) and the eigenstate picture (lower half) in molecular spectroscopy. In the mode picture, a radiative transition can occur between the ground state and the single bright state. The bright state is shown linked to five background or dark states. In the eigenstate picture, the dipole strength is shared among six eigenstates, leading to the representative spectrum shown to the right of the upper set of eigenstates.

where we have used the assumption that the background states are not linked to the ground state by dipole matrix elements, $\langle\psi_g|\mu|\chi_i\rangle = 0$. The significant result expressed in Eq. (5) is that the amplitudes $c_{b,\alpha}$ determine the variation of the spectral intensity when the light source scans the region of frequencies where the bright state $|\phi\rangle$ dominates the spectrum. We note that the matrix element $\langle\psi_g|\mu|\phi\rangle$ is constant in this frequency region. The spectral intensities $|\langle\psi_g|\mu|\psi_\alpha\rangle|^2$ are thus measures of the probabilities of finding the bright state in the various eigenstates. After factoring out these constant terms, the re-normalized spectrum can be written directly in terms of the amplitudes $c_{b,\alpha}$:

$$S(E) = \sum_{\alpha} |c_{b,\alpha}|^2 L(E - E_\alpha) \tag{6}$$

A plot of the probabilities $|c_{b,\alpha}|^2$ versus the energies E_α is also referred to as a *stick spectrum.*

The *bright state* $|\phi\rangle$ is frequently referred to as the *doorway state* which leads to the sea of background states. We will also refer to this state as the *initial state* and we will use the notation $|i\rangle = |\psi_i\rangle = |\phi\rangle$. A broadband short-time laser pulse whose frequency spectrum encompasses this spectral band could, at least in principle, be used to create

this state at a specific time, say $t = 0$. A good discussion of this point was presented by Brumer and Shapiro in their 1992 review article (7).

The *survival probability* $S(t)$ associated with the initial state is the absolute square of the *survival amplitude*, $S(t) = |A(t)|^2$. The survival amplitude $A(t)$ is the overlap between the state that evolves in time from this initial state and the initial state

$$A(t) = \langle\psi(0)|\psi(t)\rangle = \langle i|i(t)\rangle \tag{7}$$

where $|\psi(0)\rangle = |\psi_i\rangle$ and $|\psi(t)\rangle = |i(t)\rangle$ is the time evolving wave packet which develops out of the initial state. If we expand $|i\rangle$ in terms of the (usually unknown) eigenstates

$$|i\rangle = \sum_{\alpha} c_{\alpha}|\psi_{\alpha}\rangle \tag{8}$$

then the time-evolving state is

$$|i(t)\rangle = \sum_{\alpha} c_{\alpha}e^{(-iE_{\alpha}t)}|\psi_{\alpha}\rangle \tag{9}$$

so that the survival amplitude is then

$$A(t) = \langle i|i(t)\rangle = \sum_{\alpha} |c_{\alpha}|^2 e^{(-iE_{\alpha}t)} \tag{10}$$

(The amplitudes on the right side of Eq. (10) are actually the same as the amplitudes in Eq. (6), $c_{\alpha} = c_{b,\alpha}$.) Further details concerning the calculation of the important amplitude $A(t)$ will be presented in Section II.

As time advances from $t = 0$, the survival probability starts at the value 1, then (at least in many cases) gradually decreases. There are frequently a number of oscillations superimposed upon the declining function $S(t)$; these are due to *partial recurrences* of the time evolving wave packet upon the starting wave packet. The relationship between the survival amplitude and the lineshape function will be described in Section II. Examples of survival probability plots will be shown later in Sections III and IV.

In addition to the survival probability of the initial state, we will also be interested in time-dependent *transition probabilities*. The transition probability at time t between the time-evolving state $|\psi(t)\rangle$ and another zero-order state $|\xi\rangle$ is the absolute square of the transition amplitude

$$P(t) = |\langle\xi|\psi(t)\rangle|^2 \tag{11}$$

Later, in Section II.C, we will describe computational methods for generating these probabilities. We note that these probabilities are not directly related to the absorption spectrum described in the first part of this section. However, the importance of these probabilities is that they will permit us to develop the mechanistic details of the energy transfer process.

II. THE LARGE QUANTUM DYNAMICAL PROBLEM

A. Strategy

In this section, we will describe, in considerable detail, the computational approach that has made it possible to perform large-scale quantum mechanical calculations on molecules such as CD_3H and C_6H_6. We begin with a very large direct product basis set, the elements of which span the *primitive space*. The dimension of this space is so large,

frequently $>10^9$, that direct dynamical studies are precluded. Using one of several types of *contraction algorithm*, we then search this space to extract the most important basis elements for the spectral or dynamical process under consideration. These elements become members of an exclusive "club," which is referred to as the *active space*. The active space is much smaller than the primitive space and may contain from 10^3 up to possibly 10^6 elements. Two contraction algorithms are described later in this section. These are the *artificial intelligence tree-pruning algorithm* and the recently developed *wave operator sorting algorithm*.

Once the active space has been constructed, we then begin the more interesting task of computing very accurate spectral and dynamical information. Two complementary approaches are possible depending upon both the type of information and the level of detail that is desired. If the goal is to obtain the spectrum, the survival probability of the initial state, or restricted dynamical information related to this state (such as the rate of exploration of phase space), then the *recursive residue generation method* (RRGM) offers the most efficient route. For more detailed information, including state-to-state time-dependent transition amplitudes, it is necessary to follow the time development of the wave packet after it is launched from the initial state. For this purpose, the *expansion of the propagator in Chebyshev polynomials* provides an efficient computational approach. From the detailed dynamical information so obtained, it is possible to analyze the dynamics and thus elucidate the mechanism for the energy flow out of the initial state. In a relatively fast *Lanczos recursion sequence*, the RRGM provides the spectrum and the survival, while in a much longer calculation, the *Chebyshev propagator* provides very detailed state-to-state information. Results obtained with both of these approaches will be described later for CD_3H and C_6H_6.

B. Construction of the Active Space

1. Artificial Intelligence Tree-Pruning Algorithm

The first method that we will consider for constructing the active space is based upon the use of artificial intelligence tree pruning algorithms. In textbooks on AI (8) this subject usually falls under the general topic concerned with "choosing among alternatives." We will first consider the main steps involved in performing an AI selection, and then we will review a number of studies which have used these techniques.

The key steps in the AI approach are *search, evaluate, and select*. When the desired number of states has been selected, the search terminates and in a sense we have pruned the search tree by not exploring and generating the rest of the tree. In order to get started, we imagine construction of the decision tree, which shows the multitude of available choices, as shown in Figure 2. We begin with the *parent node* (or state, in the quantum mechanical application), and show the various alternatives available. These alternatives, which are the states linked to the parent by nonzero matrix elements, form the first tier of nodes. These nodes are shown connected to the parent by short line segments (which represent the links or couplings). The concept of tiers of connected states has been used for a number of years in chemical dynamics (9–12). Then, the possibilities available to each of these first-tier nodes are shown as the set of second tier nodes. This process then continues, with the tier t nodes shown connected to the tier $t + 1$ nodes by short line segments. The resulting tree structure shows each successive generation of "children," "grandchildren," etc. branching away from the parent. Although Figure 2 shows a tree through the third generation of descendents, the entire tree is usually not constructed

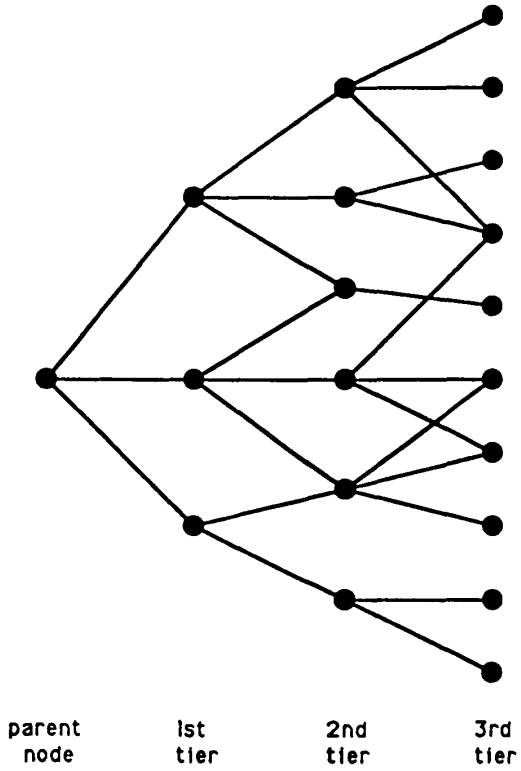

Figure 2 The first three tiers of states that develop from the parent node are shown. The nonzero matrix elements are shown as lines linking the states. Note that there may be several paths from the parent node to each descendent node.

before the search begins. Rather, we stand at a node, expand it, select the most important descendents, jump to one of the selected nodes, and then start the whole expand-select process again.

This brings up two important issues: first, the criterion by which the most important nodes are selected, and second, the order in which the nodes are expanded. Let us consider the first issue. There are two aspects to the selection process, one concerning tactics (which is concerned with the *local search*), the other concerning strategy (which is concerned with *entire paths* through the state space). If a node has, for example, six descendents, how can we select the most important two or three of these? In many cases, entire paths through state-space are desired; the states lying along these paths will eventually form the active space.

Concerning tactics, in many cases, heuristic devices or "rules of thumb" are used. For the intramolecular dynamics problem, low-order (meaning usually first-order) perturbation theory is frequently used in the tactical search. Imagine that we begin with state $|j\rangle$ in tier t. This state has the zero-order energy E_j^0. We compute the first-order coupling strength to the candidate state $|k\rangle$ in tier $t + 1$:

$$S_{jk} = \frac{\langle j|H|k\rangle}{E_j^0 - E_k^0} \tag{12}$$

Clearly, this coupling strength, and the "importance" of state $|k\rangle$, increases as the matrix element $V_{jk} = \langle j|H|k\rangle$ linking the two states increases, and as the energy detuning between

them decreases. A problem may arise when the two states become nearly degenerate in energy; this forces S_{jk} to become very large, with the result that the search may take off in a less beneficial segment of the tree. This problem can be at least partially circumvented by resetting the value of S_{jk} to unity whenever $|S_{jk}| > 1$.

The process of listing all states $|k\rangle$ that are linked to a parent state $|j\rangle$ through Hamiltonian matrix elements is referred to as *expanding the node*. In AI terminology, the *successor operator* applied to state $|j\rangle$ yields all states which can be reached in one step. Next comes *pruning*; the less useful nodes are eliminated according to prespecified criteria. One way in which this may be accomplished is as follows. The local coupling strength is used to construct the performance indicator, PI, for the path through state space:

$$\left(\frac{\text{tier } 0}{\text{state } i}\right) \rightarrow \left(\frac{\text{tier } 1}{\text{state } m}\right) \rightarrow \cdots \left(\frac{\text{tier } t}{\text{state } j}\right) \rightarrow \left(\frac{\text{tier } t+1}{\text{state } k}\right) \tag{13}$$

If the PI for the segment of the path from $|i\rangle$ to $|j\rangle$ is denoted $W_j^{(t)}$, then the updated PI for the path from $|i\rangle$ to $|k\rangle$ is constructed from both $W_j^{(t)}$ and the local coupling strength S_{jk}. Possibly the simplest way to do this is to form the product, $W_k^{(t+1)} = W_j^{(t)} S_{jk}$. The candidate state $|k\rangle$ in tier $t + 1$ is then retained if $|W_k^{(t+1)}| \rangle W_{\min}$. As an alternative, the top several states could be selected.

There are many ways to pick routes through state space. Textbooks on AI normally describe some of these strategies (8). Some procedures (depth-first, hill climbing, breadth search, beam search, etc.) seek *satisfactory paths*, other procedures seek an *optimal path* (branch and bound, dynamic programming, etc.), while still others, called game strategies, add an *adversarial relationship* (these include minimax, alpha-beta pruning, progressive deepening, etc.). Some of these procedures will be described below in the context of the intramolecular dynamics problem. Associated with each path through state space is a quantitative measure of its "goodness," this is the PI introduced earlier.

As a result of applying the AI search and select strategy, we have selected a set of states in tier 1, denoted $S^{(1)}$, and a set of states in tier 2, denoted $S^{(2)}$, and so on through the various tiers. With the initial state in tier 0 now denoted $S^{(0)}$, the set of selected states is denoted

$$S = S^{(0)} \oplus S^{(1)} \oplus S^{(2)} \cdots \tag{14}$$

This set of states now constitutes the active space, so that $A = S$. If the primitive space is made up of both active states and inactive or background states, the AI selection procedure may be denoted $P = A \oplus B \overset{\text{AI}}{\rightarrow} A$.

The values for several parameters are usually chosen before the search begins. These parameters limit the depth and width of the search tree and the size of the active space. These are (1) the number of tiers to search, N_t; (2) a window size Δ, such that states whose zero-order energies deviate more than this value from the energy of the initial state are automatically rejected; (3) a selection threshold $W_{\min}$, such that states whose performance indicators fall below this value are rejected; (4) the number of states selected for the active space, N_a.

There are many ways to select what we hope will be the best paths through the state space. Let us go back in history and examine some of these. First, back in 1983, Tietz and Chu (13) introduced the *most probable path approximation*, MPPA, in their study of the absorption of infrared laser photons by SO_2. In this example, the various tiers correspond to the number of photons absorbed. Thus the states in tier 1 lie $\hbar\omega$ above the initial state, states in tier 2 lie $\hbar\omega$ above those in tier 1, and so on. The PI for the

path $i \rightarrow j \rightarrow k \rightarrow l \ldots$ through state space was chosen as follows:

$$\frac{\langle i|H|j\rangle}{E_j^0 - (E_i^0 + \hbar\omega)} \cdot \frac{\langle j|H|k\rangle}{E_k^0 - (E_i^0 + 2\hbar\omega)} \cdot \frac{\langle k|Hl|\rangle}{E_l^0 - (E_i^0 + 3\hbar\omega)} \cdots \tag{15}$$

We note that the detuning of the state from the energy of the "dressed" initial state energy appears in the denominator for each tier. In addition, there are no tactical terms of the type S_{jk} in Eq. (12), although the numerators in Eqs. (15) and (12) are the same. As a result, the energy of a state is never compared with that of states in the preceding tier; all comparisons are made with the dressed initial state energies, $E_i^0 + n\hbar\omega$. As we mentioned earlier, there are many ways to construct performance indicators. In the MPPA, a specified number of paths, N_p, are chosen at each step. All couplings are examined when the nodes in tier t are expanded, but only the most important ones producing N_p paths are stored for later use. It is clear that the name MPPA is well chosen.

The AI technique introduced by Tietz and Chu was developed further by Chang and Wyatt (14,15) in their studies of the multiphoton excitation of degenerate anharmonic oscillator-rigid rotor systems (such as tetrahedral and octahedral molecules). Two search strategies were used in these studies. In the first, the *best-first strategy*, only the most important nodes in each tier are expanded. For example, nodes 1 and 2 in tier 1 of Figure 3 are expanded, yielding nodes 5, 6, and 7 from node 1 and nodes 6 (a repeat) and 8

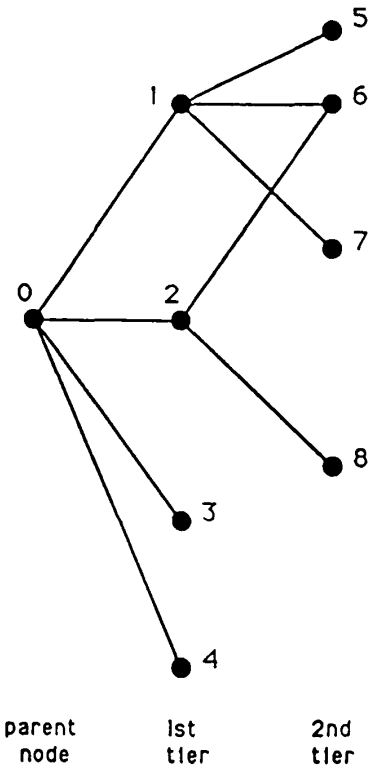

Figure 3 An illustration of the *best-first strategy*; only the most important nodes in each tier are expanded. For example, nodes 1 and 2 in tier 1 are expanded, yielding nodes 5, 6, and 7 from node 1 and nodes 6 (a repeat) and 8 from node 2. If nodes 5 and 8 have the highest values for S_{jk}, then these two nodes are added to the running candidate list, which now includes nodes 3, 4 from tier 1, along with the newcomers 5 and 8. The four nodes in this list are expanded, and the top few nodes are selected. Nodes from several tiers may be present in the candidate list.

from node 2. If nodes 5 and 8, for example, have the highest values for S_{jk}, then these two nodes are added to the running candidate list, which now includes nodes 3, 4 from tier 1, along with the newcomers 5 and 8. The four nodes in this list are expanded, and the top few nodes are selected. Note that nodes from several tiers may be present in the candidate list. However, usually only a tactical evaluation function, such as S_{jk}, was used in the selection process. As such, the best-first search does not take into account the entire path leading from the initial state. A better strategy is *branch-and-bound*, in which the PI along a *complete path* from the initial state is used in the selection process. In practice, the single state with the highest PI is selected from the running candidate list, and if several paths lead to the same state, the states along the path with the highest PI are selected (this latter feature is referred to as *dynamic programming*). In their study of multiphoton excitation, Chang and Wyatt found that branch-and-bound with dynamic programming led to converged results, while the best-first strategy sometimes did not find states along the optimal paths.

Several search algorithms and a number of performance indicators were compared in the 1988 study by Lederman and Marcus (16,17). They considered five PIs, which differ in how the energy detunings are used as penalties along the search paths. For this purpose, two types of detunings were used: the local energy detuning for states in adjacent tiers, and the nonlocal detuning of a candidate state from the energy of the initial state. For the path $i \rightarrow j \rightarrow k \rightarrow l$, these PIs are as follows.

1. Each energy denominator involves the arithmetic average of the local detuning and the detuning from the energy of the initial state:

$$\mathrm{PI}_1 = V_{ij} \cdot \frac{V_{jk}}{(\Delta E_{jk} + \Delta E_{ik})/2} \cdot \frac{V_{kl}}{(\Delta E_{kl} + \Delta E_{il})/2} \tag{16}$$

2. The same as PI_1, except that the geometric average is used:

$$\mathrm{PI}_2 = V_{ij} \cdot \frac{V_{jk}}{(\Delta E_{jk} \cdot \Delta E_{ik})^{1/2}} \cdot \frac{V_{kl}}{(\Delta E_{kl} \cdot \Delta E_{il})^{1/2}} \tag{17}$$

3. A sequence of independent hops, with a penalty for the detuning of the final state energy from that of the initial state:

$$\mathrm{PI}_3 = V_{ij} \cdot \frac{1}{\Delta E_{il}} \cdot \frac{V_{jk}}{\Delta E_{jk}} \cdot \frac{V_{kl}}{\Delta E_{kl}} \tag{18}$$

4. A penalty for detuning from the energy of the initial state at each step, but no penalty for local detuning:

$$\mathrm{PI}_4 = V_{ij} \cdot \frac{V_{jk}}{\Delta E_{ik}} \cdot \frac{V_{kl}}{\Delta E_{il}} \tag{19}$$

5. A sequence of independent hops, with only local detunings, as in Eq. (12):

$$\mathrm{PI}_5 = V_{ij} \cdot \frac{V_{jk}}{\Delta E_{jk}} \cdot \frac{V_{kl}}{\Delta E_{kl}} \tag{20}$$

These performance indicators were used in conjunction with two search algorithms. These algorithms have the following features:

1. *Best complete paths.* All states are accepted along paths to one or more goal *states.* In this case, a goal state is one whose detuning from the initial state is within $\pm\Delta$ and whose PI is above a minimum value.
2. *Best incomplete paths.* As in the first search algorithm, all states along the path to a goal state are accepted. In this case, a goal state has the best PI *at each step* of the search. As a result, the most promising path is accepted through each tier. In AI, this is referred to as a best-first search.

These PI's and search procedures were used to study vibrational energy transfer from one ligand across a heavy metal to another ligand (the heavy metal blocking effect). For this problem, the best incomplete paths search algorithm with PI_3 gave results in good agreement with those from direct matrix diagonalization in the full space. However, different applications may require different PIs and search algorithms.

We will conclude this section by mentioning several other recent studies which have employed AI selection procedures. Colbert and Sibert (18) used an AI selection scheme in their investigation of the OH (v = 4) overtone in HOOH. Zhang and Marcus (19) have developed a sophisticated AI selection scheme for use in their studies of the CH(v) benzene overtones. In their studies of overtone relaxation from the acetylenic CH stretch in molecules of the type $(CH_3)_3C{-}CC{-}H$, Stuchebrukhov and Marcus (4) have used a performance indicator similar to PI_4 described above. The best-incomplete paths search algorithm with essentially PI_5 was used by Iung and Leforestier (20,21) for their studies of the overtone spectra and IVR in CD_3H (more about this in Sec. III).

2. Wave Operator Sorting Algorithm

One of the main drawbacks with the AI tree pruning algorithm presented in the previous section arises from the imposition of an energy criterion to reduce the dimension of the active space. Computational studies have shown that such an approximation can lead to erroneous results (20). Consequently, other methods which are more flexible and do not use an arbitrary energy cutoff should be used to construct the active space. For this reason, it will be productive to focus on algorithms which are rigorously based on the use of perturbation theory. In this approach, the full Hamiltonian, H, is subdivided into two different operators: H^0 and W. The first operator, the zero-order Hamiltonian, is assumed to describe the system in an approximate but satisfactory way. The coupling operator W is assumed to be "not too strong."

In the remainder of this section, the Bloch formalism (22) of the effective Hamiltonian (23) will be first presented and then applied to the construction of an active space (24) without using arbitrary selection criteria.

Wave operator definition. In many situations, one would like to extract a set of eigenvalues from the complete spectrum. These interesting eigenvalues are usually quite far above the ground state energy. We will define S as the subspace generated by the set of N eigenvectors, $\{|\Psi_n\rangle, n = 1, N\}$ that play an important role in our problem. Of course, these states satisfy the Schrödinger equation:

$$H|\Psi_n\rangle = E_n|\Psi_n\rangle \tag{21}$$

How can we obtain good approximations to these eigenstates?

We will now define S^0 as the *model space* generated by the zero-order description of the states $|\Psi_n\rangle$. These states are denoted $|\Psi_n\rangle^0$ and are eigenvectors of the H^0 operator. The basic functions $\{|\Psi_n\rangle^0, n = 1, N\}$ form an orthonormal basis set. We will now define

the operator P^0 as the *projection operator* into this N-dimensional subspace. As a result, we can also consider a new basis set $\{|n\rangle^0,\ n = 1, N\}$ which contains the projection into the model space of the eigenvectors $|\Psi_n\rangle$:

$$P^0|\Psi_n\rangle = |n\rangle^0 \tag{22}$$

In general, we will have to assume that the S and S^0 spaces are *not* orthogonal. This means that there does not exist a vector in the S-space which is orthogonal to all of the vectors of the S^0-space (22). In addition, the states $|n\rangle^0$ constitute a nonorthonormal basis set for the model space, S^0. From a physical point of view, it is important to have a one-to-one correspondence between the exact eigenvectors, $|\Psi_n\rangle$, and the vectors $|n\rangle^0$. However, another basis set, denoted $\{|\overline{n}\rangle^0,\ n = 1, N\}$, biorthogonal to the previous one $\{|n\rangle^0,\ n = 1, N\}$ has to be defined and used in Bloch's formulation. These vectors satisfy the following equations:

$${}^0\langle\overline{m}|n\rangle^0 = \delta_{mn} \qquad \text{and} \qquad P^0 = \sum_{m=1}^{N} |m\rangle^0\,{}^0\langle\overline{m}| \tag{23}$$

It will be useful to keep in mind the definitions of the three basis sets which span the same model space. First, the basis sets, $\{|n\rangle^0,\ n = 1, N\}$ and $\{|\overline{m}\rangle^0,\ m = 1, N\}$, will be used in developing Bloch's theory. The nonorthogonal basis set, $\{|n\rangle^0,\ n = 1, N\}$, is built from the projections of the exact eigenstates [Eq. (22)] into the model space. The other nonorthogonal basis set, $\{|\overline{m}\rangle^0,\ m = 1, N\}$, is the biorthogonal basis set of the previous one (see Eq. (23)). By contrast, the orthonormal basis set, $\{|\Psi_n\rangle^0,\ n = 1, N\}$, will be used in the computational applications discussed at the end of the section.

We will now define the *wave operator* Ω as the operator which maps vectors in the model space into the exact eigenvectors. This operator is given by the relations

$$\Omega|n\rangle^0 = |\Psi_n\rangle \quad \text{and} \quad \Omega|\alpha\rangle = 0 \qquad \text{if } P^0|\alpha\rangle = 0 \tag{24}$$

This definition is consistent with the following expansion:

$$\Omega = \sum_{m=1}^{N} |\Psi_m\rangle^0\langle\overline{m}| \tag{25}$$

It is straightforward to show that this operator also satisfies the following equations:

$$\Omega^2 = \Omega, \quad P^0\Omega = P^0, \quad \text{and} \quad \Omega P^0 = \Omega \tag{26}$$

The main question now is: How can we approximate this powerful operator which allows us to generate the exact eigenvectors? The aim of the Bloch formalism presented below is to develop a perturbative expansion for the wave operator.

Effective Hamiltonian theory. Following the formalism developed by Bloch, we will define a new operator called the *effective Hamiltonian*, H_{eff}, given by

$$H_{\text{eff}} = P^0 H \Omega \tag{27}$$

Notice that this operator acts on the model space to give a state which also belongs to this subspace, S^0. However, this operator does take into account the full Hamiltonian of the system. Substituting Eq. (25) into Eq. (27) and also using the Schrodinger equation

satisfied by the eigenvectors $|\Psi_n\rangle$, the effective Hamiltonian can be expressed as

$$H_{\text{eff}} = P^0 H \sum_{m=1}^{N} |\Psi_m\rangle^0 \langle\overline{m}| = P^0 \sum_{m=1}^{N} |\Psi_m\rangle (E_m)^0 \langle\overline{m}| \tag{28}$$

Finally, we obtain

$$H_{\text{eff}} = \sum_{m=1}^{N} |m\rangle^0 (E_m)^0 \langle\overline{m}| \tag{29}$$

Using this equation, the action of the effective Hamiltonian on a vector in the S^0-space is

$$H_{\text{eff}}|m\rangle^0 = E_m|m\rangle^0 \tag{30}$$

Consequently, the eigenvalues and eigenvectors of this operator are equal to the exact eigenvalues and to the projection into the model space of the eigenvectors of the exact Hamiltonian, respectively. *The effective Hamiltonian is an operator on the zero-order space, but its eigenvalues are equal to the exact ones.* However, it is important to note that its eigenvectors are usually nonorthogonal. In fact, the effective Hamiltonian is non-Hermitian.

Before considering approximations for the wave operator, we will establish an important equation. We will show that the operator $H\Omega$ can be expressed in terms of the effective Hamiltonian. First, we note that

$$H\Omega = H \sum_{m=1}^{N} |\Psi_m\rangle^0 \langle\overline{m}| = \sum_{m=1}^{N} |\Psi_m\rangle E_m{}^0 \langle\overline{m}| \tag{31}$$

Consequently, the effective Hamiltonian satisfies the fundamental equation

$$H\Omega = \Omega H_{\text{eff}} \tag{32}$$

This equation can be considered as a generalization of the ordinary Schrodinger (23) equation for one eigenvector to an operator equation for simultaneously handling N states. By using the definition of the effective Hamiltonian, Eq. (27), and Eq. (26), the previous equation becomes

$$H\Omega = \Omega H\Omega \tag{33}$$

We are now ready to develop approximate solutions for the wave operator using this later equation, appropriately called the *Bloch equation.*

Perturbative solution of the Bloch equation. We will first introduce the *reduced wave operator* X by assuming intermediate normalization for the exact wave function and writing Ω as

$$\Omega = (P^0 + Q^0)\Omega = P^0 + X \tag{34}$$

where Q^0 is the projector into the *complementary space* associated with the model space S^0, i.e.,

$$Q^0 = I - P^0 \tag{35}$$

X is a *transition operator* which couples the model space, S^0 to the Q^0 space orthogonal to S^0. This new operator X satisfies the following relations:

$$X = Q^0 X P^0, \quad Q^0 X = X, \quad \text{and} \quad X P^0 = X \tag{36}$$

We can now rewrite Eq. (24) by using the reduced wave operator:

$$|\Psi_n\rangle = |n\rangle^0 + X|n\rangle^0 \tag{37}$$

By first writing $H = H^0 + W$, and $\Omega = P^0 + X$, and then multiplying both sides of Eq. (33) by Q^0, we obtain

$$Q^0(H^0 + W)(P^0 + X) = Q^0(P^0 + X)(H^0 + W)(P^0 + X) \tag{38}$$

If all terms depending on the zero-order Hamiltonian H^0 are then collected on the right side of the equality, we obtain, by using Eq. (36),

$$[X,H^0] = Q^0(I - X)W(1 + X)P^0 \tag{39}$$

where I represents the identity operator.

This later equation can be "solved" to give an explicit equation for X:

$$X = \sum_{m=1}^{N} \frac{Q^0}{E_m^0 - H^0}(I - X)W(I + X)P_m^0 \tag{40}$$

where $P_m^0 = |\Psi_m\rangle^0\,{}^0\langle\Psi_m|$ is the projector associated with an eigenvector of the zero-order Hamiltonian. We must remember that this basis set does not coincide with the non-orthogonal basis set $\{|n\rangle^0, n = 1, N\}$. These states, $|n\rangle^0$, span the same model space but are not eigenvectors of the zero-order Hamiltonian. These states are only defined as the projection into the model space of the exact eigenvectors, $|\Psi_n\rangle$, of the full Hamiltonian H.

Equation (40) can now be solved by successive iterations, a procedure which provides the perturbative expansion of the reduced wave operator in powers of the perturbation W.

$$X = \sum_k X^{(k)} \tag{41a}$$

where

$$X^{(0)} = 0$$

$$X^{(1)} = \sum_{m=1}^{N} \frac{Q^0}{E_m^0 I - H} WP_m^0 \tag{41b}$$

$$X^{(2)} = \sum_{m=1}^{N} \frac{Q^0}{E_m^0 I - H^0} W \frac{Q^0}{E_m^0 I - H^0} WP_m^0$$

$$\sum_{m=1}^{N}\sum_{m'=1}^{N} \frac{Q^0}{(E_m^0 I - H^0)(E_{m'}^0 I - H^0)} WP_m^0 WP_m^0 + \cdots \tag{41c}$$

This development leads to the perturbative expansion of the effective Hamiltonian given by

$$H_{\text{eff}} = \sum_k H_{\text{eff}}^{(k)} \tag{42a}$$

$$H_{\text{eff}}^{(0)} = P^0 H^0, \qquad H_{\text{eff}}^{(1)} = P^0 WP, \qquad H_{\text{eff}}^{(2)} = P^0 WX^{(1)} \tag{42b}$$

This original approach, first proposed by Bloch (22) in 1958, follows a pedagogical approach to obtain both the wave operator and the effective Hamiltonian. However, from a computational point of view, the perturbative expansion [Eq. (41)] frequently diverges and the first few terms give only an approximation to the exact solution. In vibrational

problems for which the state density is very high near the eigenvalues studied, it is also the case that this procedure will quickly diverge because of the near degeneracy of many states.

Recursive distorted wave approximation. Several linear and quadratic methods have been proposed to obtain the wave operator by limiting the divergence of Eq. (40) (23,25–30). In the applications presented below, a recursive treatment, proposed by Jolicard (31–33) and called the *recursive distorted wave approximation* (RDWA) has been used. Such an approach leads to the equations:

$$X = \lim_{N\to\infty} X^N; \qquad H_{\text{eff}} = \lim_{N\to\infty} H^N \tag{43}$$

with

$$X^N = X^{N-1} + \sum_{\alpha\notin S^0} \sum_{i\in S^0} |\alpha\rangle^0\, {}^0\langle i| \, \frac{{}^0\langle\alpha|H^N|i\rangle^0}{{}^0\langle i|H^N|i\rangle^0 - {}^0\langle\alpha|H^N|\alpha\rangle^0} \tag{44}$$

$$H^{N=0} = H, \qquad H^N = (1 - X^{N-1})H(1 + X^{N-1}) \quad \text{and} \quad X^0 = 0 \tag{45}$$

The states $|i\rangle^0$ and $|\alpha\rangle^0$ represent the eigenvectors of the zero-order Hamiltonian belonging to the S^0-space and to its orthogonal complement, respectively. Consequently, the zero-order Hamiltonian can be written

$$H^0 = \sum_{i\in S^0} |i\rangle^0 (E_i^0)\, {}^0\langle i| + \sum_{\alpha\notin S^0} |\alpha\rangle^0 (E_\alpha^0)\, {}^0\langle\alpha| \tag{46}$$

At each iteration step, this procedure involves the evaluation of X^N and the effective Hamiltonian H^{N+1} which is then used to calculate X^{N+1}, and so on. The originality of this iteration method comes from the presence of the perturbed diagonal elements (i.e., ${}^0\langle i|H^N|i\rangle^0$, ${}^0\langle\alpha|H^N|\alpha\rangle^0$) rather than their zero-order expressions [see Eq. (41)] in Bloch's perturbative expression. The study of simple systems (31,32) has shown that this procedure may accelerate the convergence of the series.

The wave operator sorting algorithm. Now consider the special case where the model space S^0 is generated by only one zero-order vector $|i\rangle^0$. Consequently, the eigenvector $|\Psi_i\rangle$ obtained by applying the wave operator on this state is given by using Eq. (34):

$$|\Psi_i\rangle = |i\rangle^0 + \sum_{\alpha\neq i} |\alpha\rangle^0 X_{\alpha i} \qquad \text{where } X_{\alpha i} = {}^0\langle\alpha|X|i\rangle^0 \tag{47}$$

Usually, because of near degeneracies, some of the $X_{\alpha i}$ matrix elements obtained by using Eqs. (43)–(45) diverge. Practically, this means that these matrix elements are larger than unity. Consequently, the algorithm does not converge to the state which corresponds to the zero-order state $|i\rangle^0$. To overcome this divergence, all contributions to $X_{\alpha i}$ larger than a given value (32–34) (for instance unity) are reset automatically to one. In applications to CD_3H and C_6H_6, we did not attempt to converge the perturbative expansion for the X operator because of many near degeneracies. Consequently, the reduced wave operator is used to provide a first estimate of the magnitude of the different zero-order states, $|\alpha\rangle^0$, in the expression for the eigenvector studied, i.e., $|\Psi_i\rangle$.

Assume now that N_i iterations of the X operator have been performed. As a result, a large number of nonzero matrix $X_{\alpha i}$ elements have been generated. The states $|\alpha\rangle^0$ are then reordered such that those having the largest magnitudes of $X_{\alpha i}$ are up near the top

of the list. Then, from this reordered list, the top N_a states are selected; the remaining $N_a + 1, \ldots, N$ states are discarded. This means that the transition operator considered for the following recursions is equal to

$$X^N = X^{N-1} + \sum_{\alpha=1}^{N_a} |\alpha\rangle^0 \, {}^0\langle i| \frac{{}^0\langle\alpha|H^N|i\rangle^0}{{}^0\langle i|H^N|i\rangle^0 - {}^0\langle\alpha|H^N|\alpha\rangle^0} \tag{48}$$

Then, the effective Hamiltonian H^{N+1} is estimated by using this expression, and so on. After usually three or four iterations, the iterative calculation is terminated. As already mentioned, from the reordered list, the top N_a states are selected to form the active space in which the dynamics will be studied.

In order to use the wave operator pruning algorithm, two parameters must be specified: N_i the number of X-operator iteration steps; and N_a, the number of retained states. One feature that the wave operator selection algorithm shares with the AI tree pruning algorithm is that successive tiers of states are generated. However, the selection criteria are quite different in the two methods. For example, the wave operator algorithm does not use an energy window. In practice, some states with large detunings from the initial state are selected for inclusion in the active space by the wave operator approach. Applications and comparisons between the two selection methods will be given in Section III.

C. Dynamics in the Active Space

1. Recursive Residue Generation Method

Introductory remarks. In this section, application of the recursive residue generation method to the computation of overtone spectra and survival probabilities will be described. Given the Hamiltonian and the initial state wave function, the RRGM (35,36) focuses upon computation of the residues and eigenvalues which are required to compute spectra and survival probabilities. We will begin by defining the term *residue*. Then, in order to establish some of the notation, the standard matrix diagonalization approach will be reviewed. Next, we will proceed to the RRGM. Applications to overtone dynamics will be presented later in Sections III and IV.

A major goal of the RRGM is the "direct" computation of the residues $\{r_\alpha\}$, *without computing the eigenvectors*. The residue r_α is the probability of finding an initial state $|\psi_i\rangle$ overlapping eigenvector α, $r_\alpha = |\langle\psi_i|\psi_\alpha\rangle|^2$. The initial state could refer to a prepared *doorway state* or to the normalized product of the dipole function times the ground state eigenvector, $|\psi_i\rangle = N\mu|\psi_0\rangle$. The term residue arises in the following way. *If* we did know the eigenvalues and eigenvectors of the Hamiltonian operator, then the spectral resolution of the identity, Hamiltonian and Green operators could be written

$$\begin{aligned} I &= \sum_\alpha |\psi_\alpha\rangle\langle\psi_\alpha| \\ H &= \sum_\alpha |\psi_\alpha\rangle E_\alpha \langle\psi_\alpha| \\ G(E) &= (E - H)^{-1} = \sum_\alpha |\psi_\alpha\rangle (E - E_\alpha)^{-1} \langle\psi_\alpha| \end{aligned} \tag{49}$$

The matrix element of the *Green operator* (referred to as the *Green function*) over the initial state is then

$$G_{ii}(E) = \langle\psi_i|G(E)|\psi_i\rangle = \sum_\alpha \frac{\langle\psi_i|\psi_\alpha\rangle\langle\psi_\alpha|\psi_i\rangle}{E - E_\alpha} = \sum_\alpha \frac{r_\alpha}{E - E_\alpha} \tag{50}$$

From the last expression, it is apparent that r_α is the "strength" or intensity of the Green function at the pole E_α on the energy axis.

The core of the RRGM utilizes the Lanczos algorithm (37–42) for transforming a matrix into a smaller tridiagonal form. The first application of the algorithm was by Lanczos himself in 1951; a "difficult" 8×8 eigenproblem was solved in 100 h on a mechanical calculator (42). Since then, many large-scale eigenproblems have been solved with this algorithm. The algorithm has been described in detail in a number of textbooks, monographs, and conference proceedings (43–48). A comprehensive history of the Lanczos algorithm covering the period 1948–1976, including both formal developments and applications, has been presented by Golub and O'Leary (46). In December 1993, an international conference was held in remembrance of the 100th anniversary of the birth of Cornelius Lanczos (48).

One of the best references to learn about the Lanczos algorithm continues to be Volume 35 of the series *Solid State Physics* (47). Recent (1985 and thereafter) applications have been made in a number of fields, including molecular electronic structure (49), densities of electronic states (50), resolvent operator calculations (51), resonance eigenvalues (52), bound state eigenvalues (53), atom-molecular reactive scattering (54), molecule-surface scattering (55), vibronic coupling (56), intramolecular dynamics (4,57), dynamics for explicit time-dependent problems (58), molecular vibration-rotation spectroscopy (59), survival probabilities (60), ESR relaxation (61), and lattice gauge theory (62). The RRGM itself was reviewed (36) in 1989. In addition to the overtone studies of C_6H_6 and CD_3H described in this chapter, the RRGM has been used (63) to compute stimulated emission pumping (SEP) spectra for HCN, the photodissociation spectrum and survival probability (64) for O_3, the absorption spectrum (65) for H_2O, and the photodissociation spectrum and survival probability for H atoms in intense electric and magnetic fields (66).

Direct matrix diagonalization. The time-honored way to compute a spectrum is worth a brief review. Assume that we begin with a real-valued orthonormal basis set with dimension N, $\{|j\rangle, j = 1, 2, \ldots, N\}$, where each member could represent a multimode function. We assume that this basis is sufficient to represent both the initial state $|\psi_i\rangle$ and the eigenstates $|\psi_\alpha\rangle$ that make a major contribution to the spectrum. The expansion coefficients of the initial state in this basis set,

$$|\psi_i\rangle = \sum_{j=1}^{N} d_j|j\rangle \tag{51}$$

can be represented by the column vector **d**:

$$\mathbf{d} = \begin{vmatrix} d_1 \\ d_2 \\ \vdots \\ d_N \end{vmatrix} \tag{52}$$

In order to generate eigenvectors of the Hamiltonian matrix, we follow the two-step procedure: (1) Compute the matrix elements of the Hamiltonian operator in the basis set, $H_{ij} = \langle i|H|j\rangle$. (2) Using standard direct diagonalization algorithms, compute the eigenvalues and eigenvectors of the $N \times N$ real symmetric matrix **H**,

$$\mathbf{HC} = \mathbf{CE} \tag{53}$$

where **E** is the diagonal eigenvalue matrix. (We note that direct diagonalization algorithms actually use a finite sequence of transformations to generate **C** and **E**.) Column number α in the $N \times N$ eigenvector matrix **C** is then

$$\mathbf{c}_\alpha = \begin{vmatrix} c_{1\alpha} \\ c_{2\alpha} \\ \vdots \\ c_{N\alpha} \end{vmatrix} \tag{54}$$

This corresponds to the expansion of the eigenvector in the basis set. The amplitude for finding the doorway state localized on eigenvector α is then given by the inner product,

$$\langle \psi_i | \psi_\alpha \rangle = \mathbf{d}^t \mathbf{c}_\alpha = \sum_{j=1}^{N} d_j c_{j,\alpha} \tag{55}$$

where the superscript t denotes the transpose of the column vector **d**. (If **d** contains complex-valued elements, then we would use the adjoint, transpose-complex conjugate, instead of the transpose in Eq. (55). The lineshape function and the survival probability can then be computed from the eigenvalues and the residues, $r_\alpha = |\langle \psi_i | \psi_\alpha \rangle|^2$.

In spite of its apparent simplicity, the direct method has several major shortcomings. First, the computational effort involved in solving the matrix eigenproblem in Eq. (53) scales as $O(N^3)$. This feature, along with the storage requirements, which scale as N^2, for **H**, **C**, and the required workspace, limit N in practice to no more than several thousand. The recursive approach described below is designed to overcome these unfavorable characteristics.

General aspects of the recursion method. The recursive residue generation method provides a computationally efficient way to compute spectra and survival probabilities in large multistate systems. Before presenting any details, we will first review some of the basic features of the method. In order to make a link between the lineshape function and the term "residue," we will rewrite Eq. (6) in Section I.B as

$$S(E) = \sum r_\alpha L(E - E_\alpha) \tag{56}$$

where r_α again denotes a residue. As mentioned above, the primary output from an RRGM calculation is the set of residues $\{r_\alpha\}$ and the eigenvalues $\{E_\alpha\}$. Computation of the eigenvectors $|\psi_\alpha\rangle$ is avoided. The recursion sequence that eventually leads to these residues and the eigenvalues is initiated with the normalized starting vector $|\psi_i\rangle$. The idea is then, in stepwise fashion, to develop an $M \times M$ tridiagonal matrix **T**, in which M, the number of recursion steps required for convergence, is frequently much smaller than the dimension of the vector space, N. This process is accomplished by the Lanczos algorithm (37–47), which involves the construction of the sequence of $N \times 1$ column vectors $\mathbf{U}_0$, $\mathbf{U}_1, \ldots, \mathbf{U}_{M-1}$, in which $\mathbf{U}_0$ represents $|\psi_i\rangle$, the starting vector. All of these vectors are not stored; it is possible to develop **T** by storing only two vectors (see p. 260 in Parlett (40)). We will return to this point when the Lanczos algorithm is described.

After performing M Lanczos recursion steps, we will have computed the diagonal and off-diagonal elements in the $M \times M$ tridiagonal matrix **T**. From **T**, we can then quickly compute M eigenvalues and residues. This, in turn, permits an M-term approximation to the lineshape function in Eq. (56):

$$S(E) \approx \sum_{\alpha=1}^{M} r_\alpha L(E - E_\alpha) \tag{57}$$

Of course, it is necessary to verify convergence by examining the spectra for several values of M.

Lanczos recursion algorithm. We have mentioned that the Lanczos recursion algorithm plays a key role in the RRGM. This algorithm has the following goal: given the starting vector $\mathbf{U}_0$, and the $N \times N$ matrix $\mathbf{H}$, construct the $M \times M$ *tridiagonal matrix representation* of the Hamiltonian, denoted $\mathbf{T}$. At each step, we generate a new recursion vector, along with a pair of diagonal and off-diagonal elements of $\mathbf{T}$. These diagonal and off-diagonal elements are denoted $\{a_0, a_1, \ldots\}$ and $\{b_0, b_1, \ldots\}$, respectively. These matrix elements form the *chain representation*, or *ball and spring model*, of the Hamiltonian for this problem. Figure 4 displays the chain developed by the Lanczos algorithm. We begin (recursion step $M = 0$) with the $\mathbf{U}_0$ and the first diagonal element, $a_0 = \mathbf{U}_0^{\dagger}\mathbf{H}\mathbf{U}_0$. This diagonal element is represented by the first ball in the chain. In the first recursion step, we generate the next diagonal element, a_1, and the first off-diagonal element, b_1. These two elements are portrayed as the first spring and the second ball in Figure 4. The process then continues; each recursion step develops a new ball or *self-energy*, representing a_n, and a new spring, representing b_{n-1}. (In Figure 4, the radius of each ball corresponds to the magnitude of the diagonal element, a_n.) The resulting Huckel-like one-dimensional lattice is *disordered* in the sense that all of the diagonal and off-diagonal elements are different from one another. This 1D chain that we have developed is the most compact representation of the problem, except for the fully diagonal (eigenvector) representation.

The Lanczos algorithm is very simple and can be written in just a few lines of computer code. At the start of step n, we have available $\mathbf{U}_{n-1}$, $\mathbf{U}_n$, and b_n. We then

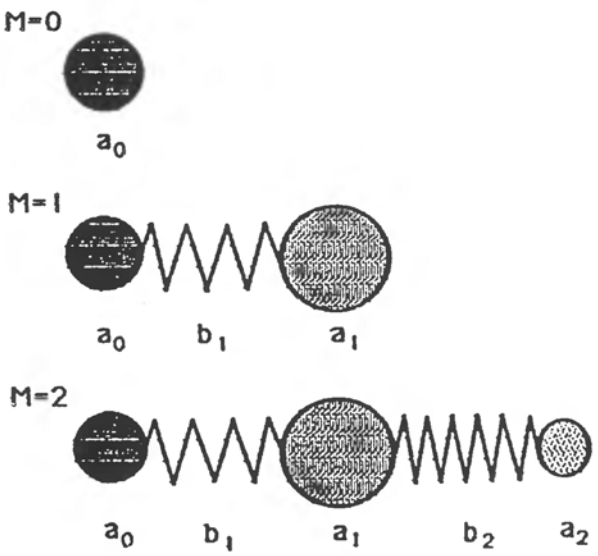

Figure 4 The ball and spring representation of the first three steps in the Lanczos recursion. At the start, $M = 0$, we compute the self-energy of the initial state. This is represented by the first ball in the chain. In step $M = 1$, we then compute the first off-diagonal element and the second diagonal element; these are shown as the spring and ball connected to the first ball. Then for $M = 2$, we compute the next spring and ball. Each successive step adds a ball and spring to the chain. The chain is thus built a link at a time.

compute the matrix-vector product $\mathbf{HU}_n$ and use the three-term recurrence equation

$$\mathbf{HU}_n = a_n\mathbf{U}_n + b_{n+1}\mathbf{U}_{n+1} + b_n\mathbf{U}_{n-1} \tag{58}$$

where a_n, b_{n+1}, and $\mathbf{U}_{n+1}$ are to be found. The recursion vectors are orthonormal by design, $\mathbf{U}_m^t\mathbf{U}_n = \delta_{mn}$, so multiplying Eq. (58) by $\mathbf{U}_n$ gives the new diagonal element $a_n = \mathbf{U}_n^t\mathbf{HU}_n$. We now write Eq. (58) as

$$\mathbf{U}_{n+1} = \frac{1}{b_{n+1}}\{\mathbf{HU}_n - a_n\mathbf{U}_n - b_n\mathbf{U}_{n-1}\} \tag{59}$$

where each term within the brackets is now known. Forcing the normalization of $\mathbf{U}_{n+1}$ then gives the new off-diagonal element

$$b_{n+1} = \|\mathbf{HU}_n - a_n\mathbf{U}_n - b_n\mathbf{U}_{n-1}\|^{1/2} \tag{60}$$

This completes step n; we now have the next recursion vector $\mathbf{U}_{n+1}$, along with the two new elements of the tridiagonal matrix, a_n, and b_{n+1}. From this point onward, the recursion method just loops over the same steps. After M recursion steps, we have the $M \times M$ tridiagonal matrix $\mathbf{T}$. In the next step, we will extract the residues and eigenvalues from $\mathbf{T}$.

After M Lanczos recursion steps, we have generated the M Lanczos vectors $\{\mathbf{U}_n\}_0^{M-1}$. These vectors are said to span (form a basis set for) the M-dimensional *Krylov subspace*. Another viewpoint is obtained if we start with the vector $\mathbf{U}_0$ and the matrix $\mathbf{H}$ and then keep "hitting" $\mathbf{H}$ onto $\mathbf{U}_0$ to form the *power vectors* $\mathbf{HU}_0, \mathbf{H}^2\mathbf{U}_0, \ldots, \mathbf{H}^{M-1}\mathbf{U}_0$. These vectors span the same M-dimensional subspace, now denoted $K\{\mathbf{U}_0, \mathbf{H}, M\}$. If we apply the Gram-Schmidt orthonormalization algorithm to the power vectors, starting with $\mathbf{U}_0$, then we will develop the Lanczos vectors. The sets of vectors $\{\mathbf{H}^j\mathbf{U}_0\}$ and $\{\mathbf{U}_n\}$ are thus two different bases for the same subspace. We also observe that the tridiagonal matrix $\mathbf{T}$ will be different for different choices of the starting vector $\mathbf{U}_0$.

Finally, we note that the Hamiltonian matrix enters only through the matrix-vector products, $\mathbf{HU}_{\text{old}} = \mathbf{U}_{\text{new}}$, so that $\mathbf{H}$ itself is not modified. For large basis sets where the storage of $\mathbf{H}$ in central memory would be prohibitive, it may be possible to compute the matrix-vector product "on-the-fly," using properties of the Hamiltonian and the basis set. In our production code, we have used properties of the anharmonic potential and the basis set to compute $\mathbf{HU}_{\text{old}}$. In addition, Bramley and Carrington (59) have used properties of DVR grids and basis sets in their Lanczos applications. In their studies of H_3^+ and other molecules, the computational effort scaled between N log N and N^2.

Green function and lineshape function. In order to compute residues and eigenvalues from the chain parameters, we will carry out some formal manipulations on the Green function in Eq. (49). Some readers may want to skip to the end, where the main result is given by Eq. (71).

In matrix notation, we can rewrite Eq. (50) for the Green function as

$$G(E) = G_{ii}(E) = \mathbf{U}_0^t(\mathbf{H} - \mathrm{E}\mathbf{1}_N)^{-1}\mathbf{U}_0 \tag{61}$$

where $\mathbf{H}$ and $\mathbf{1}_N$ are the $N \times N$ Hamiltonian and unit matrices. Next, after M recursion steps, imagine that we stack the recursion vectors (each $N \times 1$) side by side to build the $N \times M$ matrix $\mathbf{Q}$ (this is not actually done in the computer):

$$\mathbf{Q} = [\mathbf{U}_0, \mathbf{U}_1, \ldots, \mathbf{U}_{M-1}] \tag{62}$$

The matrix **Q** formally brings **H** into tridiagonal form,

$$\mathbf{Q}^t\mathbf{H}\mathbf{Q} = \mathbf{T} \tag{63}$$

where **T**, an $M \times M$ matrix, is the restriction of **H** to the subspace spanned by the M recursion vectors. Also, **Q** is an orthogonal matrix since the recursion vectors themselves are orthonormal, $\mathbf{Q}\mathbf{Q}^t = \mathbf{1}_N$. As a result,

$$\mathbf{H} - E\mathbf{1}_N = \mathbf{Q}\mathbf{T}\mathbf{Q}^t - E\mathbf{Q}\mathbf{Q}^t = \mathbf{Q}(\mathbf{T} - E\mathbf{1}_M)\mathbf{Q}^t \tag{64}$$

where $\mathbf{1}_M$, an $M \times M$ unit matrix, was inserted in the last step. The inverse matrix is then

$$(\mathbf{H} - E\mathbf{1}_N)^{-1} = \mathbf{Q}(\mathbf{T} - E\mathbf{1}_M)^{-1}\mathbf{Q}^t \tag{65}$$

With these preliminaries now completed, we are ready to return to Eq. (61):

$$G(E) = \mathbf{U}_0^t\mathbf{Q}(\mathbf{T} - E\mathbf{1}_M)^{-1}\mathbf{Q}^t\mathbf{U}_0 \tag{66}$$

Now, because the recursion vectors are orthonormal, the matrix product $\mathbf{U}_0^t\mathbf{Q}$ has the simple form

$$\mathbf{U}_0^t\mathbf{Q} = \mathbf{U}_0^t[\mathbf{U}_0, \mathbf{U}_1, \ldots, \mathbf{U}_{M-1}] = [1, 0, 0, \ldots, 0] = \mathbf{e}_1^t \tag{67}$$

The result is just the first unit row vector, $\mathbf{e}_1^t$, a very simple result indeed ($\mathbf{e}_1$ itself is the first unit column vector). Consequently, the Green function can be written

$$G(E) = \mathbf{e}_1^t(\mathbf{T} - E\mathbf{1}_M)^{-1}\mathbf{e}_1 = (\mathbf{T} - E\mathbf{1}_M)_{11}^{-1} \tag{68}$$

The final step arises from the matrix product $\mathbf{e}_1^t\mathbf{A}\mathbf{e}_1 = A_{11}$, where **A** is an $M \times M$ matrix. This operation selects the 1,1 (upper-left) element from matrix **A**. As a result, $G(E)$ is the 1,1 element of the inverse of $(\mathbf{T} - E\mathbf{1}_M)$.

The quantity $(\mathbf{T} - E\mathbf{1}_M)^{-1}$ can be evaluated directly in terms of the chain parameters, $\{a_i\}$ and $\{b_i\}$, using continued fraction techniques. However, it is more convenient for our purposes to consider the diagonalization of **T**, where **S** and **E** are both $M \times M$ matrices:

$$\mathbf{S}^t\mathbf{T}\mathbf{S} = \mathbf{E} \tag{69}$$

The 1,1 element of $(\mathbf{T} - E\mathbf{1}_M)^{-1}$ is then

$$\mathbf{e}_1^t\mathbf{S}(\mathbf{E} - E\mathbf{1}_M)^{-1}\mathbf{S}^t\mathbf{e}_1 \tag{70}$$

but since $(\mathbf{E} - E\mathbf{1}_M)$ is a diagonal matrix, with elements $E - E_\alpha$, we finally obtain for the Green function

$$G(E) = \sum_{\alpha=1}^{M} \frac{S_{1\alpha}^2}{E - E_\alpha} \tag{71}$$

This is the result that we have been striving for: *only the elements in the first row of the eigenvector matrix S are needed to compute* $G(E)$. This equation shows that the residues are given by $r_\alpha = S_{1,\alpha}^2$ so that the lineshape function is

$$S(E) = \sum_{\alpha=1}^{M} S_{1\alpha}^2 L(E - E_\alpha) \tag{72}$$

It is significant that all spectral intensity information is contained within the *first row* of the eigenvector matrix associated with the tridiagonal matrix **T**. We will now show that it is possible to evaluate the survival amplitude in terms of the same quantities.

Survival amplitude and the chain propagator. The *time-development operator*, $U(t)$, also referred to as the *propagator*, associated with the Hamiltonian operator is given by

$$|\Psi(t)\rangle = e^{-iHt}|\Psi(0)\rangle \tag{73}$$

An extension of this result is provided by the propagation matrix, $\mathbf{U}(t)$, which advances the column vector $\mathbf{C}(t)$ representing $|\Psi(t)\rangle$:

$$\mathbf{C}(t) = \mathbf{U}(t)\mathbf{C}(0) = \exp[-i\mathbf{H}t]\mathbf{C}(0) \tag{74}$$

The *survival amplitude* for the initial state $|\Psi_i\rangle$, which is represented by the column vector $\mathbf{C}(0) = \mathbf{U}_0$, is then

$$A(t) = \mathbf{U}_0^t \exp[-i\mathbf{H}t]\mathbf{U}_0 \tag{75}$$

Recall that the *survival probability* is the absolute square of the survival amplitude, $S(t) = |A(t)|^2$.

Equation (75) for the survival amplitude may also be expressed in terms of the *chain propagator*. From Eq. (67), we may express **H** in terms of the chain Hamiltonian matrix **T**, $\mathbf{H} = \mathbf{QTQ}^t$. Using this result in Eq. (75) then gives

$$A(t) = \mathbf{U}_0^t\mathbf{Q} \exp[-i\mathbf{T}t]\mathbf{Q}^t\mathbf{U}_0 \tag{76}$$

Using an earlier result in Eq. (19), $\mathbf{U}_0^t\mathbf{Q} = \mathbf{e}_1^t$, then gives

$$A(t) = \mathbf{e}_1^t \exp[-i\mathbf{T}t]\mathbf{e}_1 = (\exp[-i\mathbf{T}t])_{1,1} \tag{77}$$

This equation states that the survival amplitude is the 1,1 "upper-left" element of the matrix representation of the chain propagator. This result is analogous to Eq. (68), which expresses the Green function in terms of the 1,1 element of the inverse of the matrix $(\mathbf{T} - E\mathbf{1}_M)$.

The $M \times M$ matrix $\exp[-i\mathbf{T}t]$ is referred to as the *chain propagator*; the tridiagonal matrix **T** is the representation of the chain Hamiltonian in the Lanczos basis, $\{\mathbf{U}_0, \ldots, \mathbf{U}_{M-1}\}$. Referring to the ball and spring representation shown in Figure 4, imagine that we start at $t = 0$ with unit amplitude in state $\mathbf{U}_0$, on the left ball. As time advances, amplitude flows down the chain (due to the off-diagonal couplings b_n) and populates balls 2, 3, ..., $M - 1$. The amplitude for occupying the first ball at this later time is then given by Eq. (77). It is evident that the chain must be made long enough so that reflections from the end ball do not have time to reflect back toward the left and spoil the amplitude on the first ball.

In order to evaluate the right side of Eq. (77), we return to Eq. (69) and express **T** in terms the eigenvalue matrix **E**, $\mathbf{T} = \mathbf{SES}^t$. Substituting this result into Eq. (77) then yields

$$A(t) = \mathbf{e}_1^t\mathbf{S} \exp[-i\mathbf{E}t]\mathbf{S}^t\mathbf{e}_1 \tag{78}$$

However, since **E** is diagonal, Eq. (78) is easily evaluated:

$$A(t) = \sum_{\alpha=1}^{M} S_{1,\alpha}^2 e^{-iE_\alpha t} \tag{79}$$

Comparing this result to Eq. (72) for the lineshape function, we note that both of these quantities can be evaluated in terms of the eigenvalues of the tridiagonal matrix $\{E_\alpha\}$ and the squares of the elements in the first row of the eigenvector matrix, $\{S_{1,\alpha}^2\}$. The QL algorithm, described next, provides an efficient way to compute these quantities.

The QL algorithm. The standard technique for computing all of the eigenvalues of a symmetric matrix is to use a finite sequence of orthogonal similarity transforms to tridiagonalize the matrix, followed by use of the QL (or the closely related QR) algorithm (67,68). The QL algorithm, developed by Francis (67) in 1961, uses a theoretically infinite sequence of orthogonal similarity transformations which preserves the tridiagonal form and converges to a diagonal matrix. The resulting eigenvector matrix is the product of all of the transformation matrices. If the eigenvectors are desired, then these transformations can be accumulated *as they are applied* to the matrix (69). The QL algorithm costs $O(M^2)$ to compute the eigenvalues but also costs $O(M^3)$ if *all* of the eigenvectors are computed.

In our context, the matrix $\mathbf{T}$ is already tridiagonal and only the first row of the eigenvector matrix [S in Eq. (69)] is needed. Fortunately, it is possible to obtain the first row of the eigenvector matrix of $\mathbf{T}$ for $O(M^2)$ operations. To initiate the QL algorithm, we first factor $\mathbf{T}$ (now relabeled $\mathbf{T}_1$) into an orthogonal matrix and a lower triangular matrix (with nonnegative diagonal elements):

$$\mathbf{T}_1 = \mathbf{Q}_1\mathbf{L}_1 \rightarrow \mathbf{Q}_1^t\mathbf{T}_1 = \mathbf{L}_1 \tag{80}$$

When these factors are *multiplied in reverse order*, the next tridiagonal matrix in the sequence is formed:

$$\mathbf{T}_2 = \mathbf{L}_1\mathbf{Q}_1 = \mathbf{Q}_1^t\mathbf{T}_1\mathbf{Q}_1 \tag{81}$$

The process is continued by "doggedly iterating" (40). At step k, we first factor

$$\mathbf{T}_k = \mathbf{Q}_k\mathbf{L}_k \tag{82}$$

and then reverse multiply:

$$\begin{aligned}\mathbf{T}_{k+1} &= \mathbf{L}_k\mathbf{Q}_k = \mathbf{Q}_k^t\mathbf{T}_k\mathbf{Q}_k \\ &= (\mathbf{Q}_k^t \cdots \mathbf{Q}_2^t\mathbf{Q}_1^t)\mathbf{T}_1(\mathbf{Q}_1\mathbf{Q}_2 \cdots \mathbf{Q}_k) = \mathbf{S}_k^t\mathbf{T}_1\mathbf{S}_k\end{aligned} \tag{83}$$

There are several significant features about this iterative process:

1. The tridiagonal form is preserved in the sequence of $\mathbf{T}$ matrices.
2. The sequence $\mathbf{T}_1, \mathbf{T}_2, \ldots, \mathbf{T}_k$ converges to a *diagonal* (eigenvalue) matrix

$$\mathbf{T}_1 \rightarrow \mathbf{T}_2 \rightarrow \cdots \mathbf{T}_k = \text{diag}(E_1, E_2, \ldots, E_M) \tag{84}$$

3. As $\mathbf{T}_k$ becomes diagonal, $\mathbf{S}_k$ simultaneously converges to the eigenvector matrix of $\mathbf{T}$:

$$\mathbf{S}_k^t\mathbf{T}_1\mathbf{S}_k = \mathbf{E} = \text{diag}(E_1, E_2, \ldots, E_M) \tag{85}$$

We emphasized that only the top row $(S_{11}, S_{12}, \ldots, S_{1M})$ of the eigenvector matrix of $\mathbf{T}$ is needed in order to compute the residues. The QL algorithm, as normally implemented, computes *all eigenvectors* of $\mathbf{T}$; the converged $M \times M$ matrix $\mathbf{S}_k$ is generated. However, Scott and Wyatt have shown that the algorithm may be modified (69) to produce *only the first row* of $\mathbf{T}$. The key observation is the fact that each new transformation

is applied *on the right* of the current approximation to the eigenvector matrix. That is, if $\mathbf{Q}_1, \mathbf{Q}_2, \ldots, \mathbf{Q}_k$ are the transformations used so far, then the approximation to the eigenvector matrix is

$$\mathbf{S}_k = \mathbf{Q}_1\mathbf{Q}_2 \cdots \mathbf{Q}_k \tag{86}$$

with the $\mathbf{Q}$'s multiplied in that order. Formally, the first row of the eigenvector matrix is

$$\mathbf{e}_1^t\mathbf{S}_k = \mathbf{e}_1^t\mathbf{Q}_1\mathbf{Q}_2 \cdots \mathbf{Q}_k \tag{87}$$

where $\mathbf{e}_1^t = (1, 0, 0, \ldots, 0)$. Thus, to obtain the desired row, it is only necessary to obtain a *single vector* by operating on the right by each transformation matrix as it is generated. The only extra storage needed is the vector of length M, which will hold the final result.

Computation of transition probabilities. In addition to survival amplitudes, the RRGM can also be used to compute state-to-state *time-dependent transition amplitudes*. If we denote the initial state at $t = 0$ as $|i\rangle$, then the state that evolves from this initial state is $|i(t)\rangle = U(t)|i\rangle$, where $U(t)$ is again the evolution operator. At time t, the amplitude for finding state $|f\rangle$ in this evolved state is given by $A_{if}(t) = \langle f|U(t)|i\rangle$. If we know the eigenvectors, $|\psi_\alpha\rangle$, and eigenvalues, E_α, for this Hamiltonian, then the transition amplitude can be written

$$A_{if}(t) = \sum_\alpha \langle f|\psi_\alpha\rangle\langle\psi_\alpha|i\rangle \exp(-iE_\alpha t) \tag{88}$$

We will now recast this amplitude into a form that is more convenient for RRGM calculations. It may not be obvious, but *this transition amplitude can be written in terms of the difference between two survival amplitudes*. This result can be shown as follows. If we define two orthonormal transition vectors, $|u_0\rangle = [|i\rangle + |f\rangle]/\sqrt{2}$, and $|v_0\rangle = [|i\rangle - |f\rangle]/\sqrt{2}$, then the transition amplitude can be expresed as

$$\begin{aligned} A_{if}(t) &= \frac{1}{2}\sum_\alpha \{|\langle u_0|\psi_\alpha\rangle|^2 - |\langle v_0|\psi_\alpha\rangle|^2\}\exp(-iE_\alpha t) \\ &= \frac{1}{2}[A_u(t) - A_v(t)] \end{aligned} \tag{89}$$

where $A_u(t)$ and $A_v(t)$ are the survival amplitudes associated with the two initial states $|u_0\rangle$ and $|v_0\rangle$. In order to compute these amplitudes, the RRGM now enters the story. We initiate two Lanczos recursion sequences: the first develops the U-chain (with Lanczos vectors $\mathbf{U}_0, \mathbf{U}_1, \ldots$) from the starting vector $|u_0\rangle$ and the other develops the V-chain (with Lanczos vectors $\mathbf{V}_0, \mathbf{V}_1, \ldots$) starting from $|v_0\rangle$. The two resulting survival amplitudes, when subtracted, yield the desired transition amplitude. This method permits the computation of a small number of transition amplitudes in very large multistate systems, without knowing the eigenvectors. However, when many transition amplitudes are required, then the Chebyshev expansion of the propagator provides an efficient computational route (see Sec. II.C.3).

RRGM summary. In this section, we have reviewed the recursive residue generation method for the computation of the lineshape function and the transition probabilities. The RRGM aims at computation of the set of residues and eigenvalues $\{r_\alpha, E_\alpha\}$. The steps are summarized as follows:

a. The normalized initial state $|\psi_i\rangle$ is expanded in the basis set used to represent the Hamiltonian. This expansion provides the elements of the starting vector $\mathbf{U}_0$.
b. Given $\mathbf{U}_0$ and a subroutine for computing the matrix-vector product, $\mathbf{HU}_{old} = \mathbf{U}_{new}$, we perform M Lanczos recursion steps. This generates the set of diagonal $\{a_i\}$ and off-diagonal $\{b_i\}$ elements of the $M \times M$ tridiagonal matrix $\mathbf{T}$. These elements are referred to as the chain parameters.
c. Given the chain parameters, the QL algorithm is used to compute the eigenvalues $\{E_\alpha\}$ of $\mathbf{T}$. In addition, the elements $S_{1,\alpha}$ in the first row of the eigenvector matrix $\mathbf{S}$ associated with $\mathbf{T}$ are also computed.
d. The lineshape function and the survival probability are then computed from these eigenvalues and the squares of the elements in the first row of $\mathbf{S}$.
e. Convergence is checked by recurring to a higher value of M, and then steps (c) and (d) are repeated.

The most time consuming step in this algorithm is the series of matrix-vector products involved in step (b).

2. Filtered Lanczos Algorithm

The conventional Lanczos algorithm begins with the Hamiltonian matrix $\mathbf{H}$ and a starting vector $\mathbf{U}_0$ and builds, step by step, a relatively small $M \times M$ tridiagonal matrix $\mathbf{T}$. Diagonalization of $\mathbf{T}$ then yields approximations to some of the eigenvalues of $\mathbf{H}$. These approximations are excellent for eigenvalues on the extreme edges of the spectrum, and are frequently very good for interior eigenvalues in the sparse region where there are relatively large gaps between the adjacent eigenvalues. However, in the dense interior region where the gaps may be very small, the conventional Lanczos algorithm converges so slowly that it ceases to be a viable approach.

This somewhat pessimistic view of the Lanczos algorithm as a procedure for tackling the interior eigenproblem changes completely when the iteration is driven not by $\mathbf{H}$ itself but with a *spectral filter*, a specially designed function of $\mathbf{H}$, denoted $f(\mathbf{H})$. This function generates a transformed spectrum, which we will try to compute, but what do we desire of this new spectrum? We want the eigenvalues of $f(\mathbf{H})$ to be well separated from the others (we want to improve the gap distribution). Also, we should be able to invert the computed spectrum of the filter to obtain uniquely and exactly the desired eigenvalues of $\mathbf{H}$. A many-one map is fine until we need to do the inverse operation.

Several filters have been used with the Lanczos algorithm; these are described below.

1. The first Lanczos filter was suggested by Ericsson and Ruhe (70) (ER) in 1980. Their method, appropriately termed *shift and invert*, uses the filter $(E\mathbf{1}_N - \mathbf{H})^{-1}$. This has the highly desirable effect of throwing the eigenvalues of $\mathbf{H}$ that lie near E to the extreme edges of the spectrum. The Lanczos algorithm shows its appreciation of this shift and invert strategy by converging these eigenvalues very quickly.

2. An exponential filter, $f(\mathbf{H}) = \exp[-\beta\mathbf{H}]$ was used by Webster et al. (71) to extract the lower eigenvalues of $\mathbf{H}$ in studies of the spectroscopy of the $e^- + H_2O$ system.

3. Recently, Kono (72) suggested use of the Gaussian derivative filter,

$$f(\mathbf{H}) = (\mathbf{H} - E\mathbf{1})\exp[-\beta(\mathbf{H} - E\mathbf{1})^2] \tag{90}$$

where E is chosen in the middle of the interesting part of the spectrum and where β controls the width of the filter. The Kono filter has recently been used by Iung and

Leforestier (73) in studies of the overtone spectroscopy of CD_3H. Some of these results will be described later in Section III.D.2.

In many respects, the best filter to use in the Lanczos algorithm is the Green function, $f(\mathbf{H}) = (E\mathbf{1} - \mathbf{H})^{-1}$. The gap separations near energy E that result from the use of this filter are more extreme and therefore better than those produced by the Kono filter. The result of using the Green function filter is that the eigenvalues of $\mathbf{H}$ that are far from the input value E are mapped to a cluster near the value 0, while the desired eigenvalues near E are mapped to very large positive or negative values. One excellent feature of the conventional Lanczos algorithm is that convergence is improved for well separated eigenvalues and for eigenvalues at the extreme edges of the spectrum. The hyperbolic map achieves these very desirable features and, works extremely well for eigenstates in the dense interior region of the spectrum.

In a recent study, Wyatt has developed a two-layer iteration scheme for computing interior eigenstates of large Hamiltonian matrices (74). Instead of *factoring* the shifted operator, as suggested by Ericcson and Ruhe and subsequently implemented this way in almost all applications, *iterative methods* were used for applying $f(\mathbf{H})$ to a vector. Factorization usually requires that the matrix and the factor, denoted $\mathbf{L}$, fit in the central memory, but this new iterative algorithm works effectively on platforms that have relatively modest central memory (i.e., typical workstations) as well as supercomputers. The overall algorithm involves two iteration loops. The *outer Lanczos loop* develops a small subspace in terms of which the filter $f(\mathbf{H})$ is tridiagonal. Direct diagonalization of the small tridiagonal matrix yields excellent approximations for some of the eigenvalues of $f(\mathbf{H})$. Inversion of these eigenvalues then gives the desired eigenvalues of $\mathbf{H}$. The *inner Green function loop* applies the Green function to a Lanczos vector. There are two distinct ways to do this. In the *direct method*, we expand the $f(\mathbf{H})$ operator, and then apply the terms in the series expansion one-by-one to the "old" vector. In the *indirect method*, we iteratively solve the linear algebra problem $f(\mathbf{H})^{-1}\mathbf{V}_{new} = \mathbf{V}_{old}$. There are several effective ways to do this. As expected, the direct and indirect methods are closely related, but they do *not* have the same convergence characteristics. Further details and computational results are presented elsewhere (74).

3. Chebyshev Expansion of the Propagator

In the previous section, we showed that the RRGM can be used to calculate individual state-to-state transition probabilities, $P_{if}(t)$. Another way of studying the IVR processes involves the explicit calculation of the time evolution of the initial state $|i\rangle$ (75,76). We will begin by recalling that the solution to the Schrodinger time-dependent equation can be written in terms of the evolution operator (propagator)

$$U(t)|i\rangle = |i(t)\rangle \qquad \text{where } U(t) = \exp(-iHt) \quad \text{and} \quad |i(t=0)\rangle = |i\rangle \tag{91}$$

In order to compute the evolving state $|i(t)\rangle$, Tal-Ezer and Kosloff (77) were the first to propose an expansion of the evolution operator in terms of Chebyshev polynomials. They initially developed this method for wavepacket calculations on spatial grids. More recently, this procedure has been adapted and applied to bound systems (20). It involves breaking the total integration time (for instance 2 ps) into smaller time steps Δt (each about 25 fs), and using a polynomial expansion of the evolution operator $U(\Delta t)$ over each small time step. This efficient method provides all the transition probabilities $P_{if}(t)$ from initial state $|i\rangle$ in one calculation because it directly provides the evolving state $|i(t)\rangle$.

Chebyshev expansion of a real function $f(x)$. We will first define the Chebyshev polynomial of degree n ($n = 0, 1, 2, \ldots$) denoted $T_n(x)$,

$$T_n(x) = \cos(n \arccos(x)) \tag{92}$$

where x is a real variable belonging to the interval $[-1, 1]$. This family of polynomials satisfies the recurrence relation (78)

$$T_{n+1}(x) = 2xT_n(x) - T_{n-1}(x) \qquad \text{with } T_0(x) = 1 \quad \text{and} \quad T_1(x) = x \tag{93}$$

It is straightforward to verify that the polynomial $T_n(x)$ has n zeros and $n + 1$ extrema corresponding either to $T_n(x) = 1$ or $T_n(x) = -1$. The Chebyshev polynomials are orthogonal over the weight function $(1 + x^2)^{-1/2}$, i.e.,

$$\int_{-1}^{1} \frac{T_i(x)T_j(x)}{\sqrt{1 - x^2}}\, dx = \delta_{ij} \frac{\pi}{2} (1 + \delta_{i0}) \tag{94}$$

Consequently, a function $f(x)$ defined in the interval $[-1, 1]$, can be approximated by a finite development in terms of the Chebyshev polynomials:

$$f(x) \approx \sum_{n=0}^{N} a_n T_n(x) \qquad \text{with } a_n = \frac{2 - \delta_{n0}}{\pi} \int_{-1}^{1} \frac{f(x)T_n(x)}{\sqrt{1 - x^2}}\, dx \tag{95}$$

Since the $T_n(x)$'s are all bounded between -1 and 1, the difference between the estimated function and the function $f(x)$ can be no larger than the sum of the absolute values of neglected coefficients, $|a_k|$ ($k > N$). In fact, these coefficients usually decrease rapidly. As a result, the error is dominated by the first omitted term $a_{N+1}T_{N+1}(x)$, which is a small oscillatory function with $N + 2$ extrema (equal in absolute value) distributed uniformly over the interval $[-1, +1]$. Because of the uniform character of the Chebyshev expansion, the error usually decreases exponentially once N is large enough.

Chebyshev expansion of the propagator. First consider the function of energy, $f(E) = \exp(-iE\Delta t)$, in which E is an energy belonging to the interval $[E_{\min}, E_{\max}]$, and where Δt represents a small time interval. In order to perform a Chebyshev expansion, we need to define a function restricted to the interval $[-1, 1]$. We will define the new variable ε:

$$\varepsilon = \frac{\langle E \rangle - E}{R} \qquad \text{in which } R = \frac{E_{\max} - E_{\min}}{2} \quad \text{and} \quad \langle E \rangle = \frac{E_{\max} + E_{\min}}{2} \tag{96}$$

The two quantities R and $\langle E \rangle$ correspond to the half-width and average energy of the energy spectrum, respectively. The new variable, ε, does belong to the interval $[-1, 1]$. Consequently, the function $f(E)$ can be now written as a new function $g(\varepsilon)$:

$$g(\varepsilon) = \exp(-i\langle E \rangle \Delta t)\exp(iR\Delta t\varepsilon) \approx \sum_{n=0}^{N} a_n T_n(\varepsilon)$$

with

$$a_n = \frac{2 - \delta_{n0}}{\pi} \int_{-1}^{1} \frac{g(\varepsilon)T_n(\varepsilon)}{\sqrt{1 - \varepsilon^2}}\, d\varepsilon$$

$$= \frac{2 - \delta_{n0}}{\pi} \exp(-i\langle E \rangle \Delta t) \int_{-1}^{1} \frac{\exp(iR\Delta t\varepsilon)T_n(\varepsilon)}{\sqrt{1 - \varepsilon^2}}\, d\varepsilon \tag{97}$$

Consequently, by using the definition of the Chebyshev polynomials and by defining an angle $q = \arccos(\varepsilon)$, Eq. (97) becomes

$$a_n = \frac{2 - \delta_{n0}}{\pi} \exp(-i\langle E\rangle \Delta t) \int_0^{\pi} \exp(iR\Delta t \cos\theta)\cos(n\theta)\, d\theta \tag{98}$$

This latter integral is related to one of the integral representations of the Bessel function of the first kind of order n, $J_n(x)$ (79).

$$J_n(x) = \frac{i^{-n}}{\pi} \int_0^{\pi} \exp(ix \cos\theta)\cos(n\theta)\, d\theta \tag{99}$$

Consequently, the coefficients in the Chebyshev development of $f(x)$ are given by using Eqs. (95) and (99):

$$a_n = c_n i^n \exp(-i\langle E\rangle \Delta t) J_n(R\Delta t), \qquad \text{with } c_n = 2 \text{ if } n > 0,\ c_0 = 1 \tag{100}$$

Propagating the state vector. Assume at time t that we know the expansion of the evolving state $|i(t)\rangle$ in the zero-order basis set. How can we obtain the time advanced state $|i(t + \Delta t)\rangle$? In order to do this, the evolution operator $U(\Delta t)$ will be expanded in terms of Chebyshev polynomials. To apply the scheme described above, it is necessary to have accurate estimates of the extreme eigenvalues of the Hamiltonian operator, denoted $E_{\min}$ and $E_{\max}$. Experience has shown that a wrong estimate of these values can lead to propagation errors. This problem can be efficiently solved by means of the Lanczos algorithm, which has been shown to quickly converge eigenvalues on both the edges of the spectrum (38). Application of about 100 Lanczos recursion steps on a starting vector $|u_0\rangle$ gives excellent estimates of these extreme eigenvalues.

The expansion of the evolution operator in terms of Chebyshev polynomials is then utilized. Tal-Ezer and Kosloff have shown (77) that the degree of the expansion (N) has to be at least 40. How can we now efficiently apply the evolution operator to the state $|i(t)\rangle$ to obtain the new state $|i(t + \Delta t)\rangle$? This latter state is equal to

$$|i(t + \Delta t)\rangle = \sum_{n=0}^{N} a_n T_n(\varepsilon)|i(t)\rangle \tag{101}$$

in which the operator ε is related to the Hamiltonian operator H by a relation similar to Eq. (96), i.e.,

$$\varepsilon = \frac{\langle E\rangle - H}{R} \tag{102}$$

It is useful to define the following intermediate states $|j^m\rangle$:

$$|j^m\rangle = T_m(\varepsilon)|i(t)\rangle \tag{103}$$

These states obey the same recursion relation as the Chebyshev polynomials:

$$|j^{m+1}\rangle = 2\varepsilon|j^m\rangle - |j^{m-1}\rangle \tag{104}$$

Consequently, the calculation of $|i(t + \Delta t)\rangle$ requires that we act with the Hamiltonian operator N times on a vector known in the zero-order basis set. In our applications, N is about 150 and $\Delta t = 25$ fs. Consequently, a dynamical calculation in the interval time [0, 2 ps] requires about 10,000 multiplications of the Hamiltonian matrix on a vector

$|j^m\rangle$. By contrast, a Lanczos calculation requires only about 1000 multiplications by this Hamiltonian. Consequently, the Chebyshev and Lanczos methods are complementary approaches for calculating transition probabilities. The Chebyshev method yields all transition amplitudes in a rather long calculation, while the RRGM calculation provides a few specific transition amplitudes (for instance, the survival) in a much shorter calculation.

III. SPECTROSCOPY AND DYNAMICS OF CD_3H

A. Introduction

This section will emphasize quantum mechanical studies of the CD_3H molecule, including all nine vibrational degrees of freedom. This molecule constitutes a very interesting candidate to which we will apply the different methods proposed in Section II. The CH stretch fundamental spectroscopy of the CX_3H compounds has been extensively studied (80–97), and has revealed the existence of a large effective potential energy coupling between the CH stretching and bending motions. Energy initially localized in a CH stretch overtone, which carries the oscillator strength, can thus be expected to rapidly undergo relaxation. The CD_3H molecule is the first in the CX_3H series, and displays the lowest density of states. Its experimental spectrum, which is well resolved up to about 16,000 cm^{-1}, is quite different from those of the other CX_3H compounds. A theoretical investigation, based on a two-mode description (CH stretch and DCH bend modes), has been realized by Quack and co-workers (91,94). Iung and Leforestier (95) have determined an empirical potential energy surface for the CD_3H molecule including all nine vibrational degrees of freedom, which leads to good agreement with the experimental absorption line positions up to the fifth overtone (error within a few wavenumbers). This surface is used for the computations reported later in this section. First, a brief review of the previous experimental and theoretical results on the CH chromophore will be presented. Then, we will describe how the Hamiltonian operator is implemented in the computer code used in the two applications presented later in this chapter (i.e., applications to the CD_3H and C_6H_6 molecules). This major production code has been written by Claude Leforestier (20). Then, computational results on overtone spectra and the mechanism for energy transfer will be presented in Sections III.D, E, and F.

B. CH Overtone Spectroscopy

In this section, we will review previous studies of the CH overtone spectroscopy of CD_3H. There exist high-resolution, rotationally resolved, experimental data for the first three CH overtones ($|nv_1\rangle$ with n = 2, 3, 4) in the infrared and near infrared region (91,94). In the visible region, there also exists data from photoacoustic laser spectroscopy (96,97) and from the intracavity laser absorption spectroscopy (ICLAS) technique, which provides absolute intensities (85,86). Compared to methane, analysis of the spectra is much easier for CD_3H, because of the relatively isolated CH chromophore.

The CH chromophore is composed of mode 1 (CH stretch) and mode 5 (HCD bend) whose fundamental frequencies are 2,990 cm^{-1} and 1,293 cm^{-1}, respectively. The remaining four modes are called *bath modes*. (These modes are described further in Ref. 95.) The fundamental energies of the CH stretch and CH bend allow a strong Fermi resonance between the $|nv_1\rangle^0$ and $|(n - m)v_1 + 2mv_5\rangle^0$ zero-order states. If n is larger than 4, the difference in the energies of the zero-order states, i.e., $|nv_1\rangle^0$ and $|(n - m)v_1$

$+ 2mv_5\rangle^0$ ($m = 1, \ldots, n$), becomes rather small because of the strong anharmonicity of the CH stretch. Consequently, this Fermi resonance is more efficient for high values of n. For this reason, we will later focus on the fifth overtone.

Quack's group (91,94) has proposed an elegant model for the CH overtone bands up to $n = 6$ by considering only modes 1 and 5. In this approach, *only the DCH bending motion is assumed to interact with the CH stretch mode.* The other four vibrational modes are neglected. In fact, they showed that the states $|(n - m)v_1 + 2mv_5\rangle^0$ of roughly the same energy and the same symmetry are strongly coupled in *Fermi polyads* characterized by the same value of the *chromophore quantum number N*, defined by

$$N = n_1 + 2n_5 \tag{105}$$

These chromophore states will be denoted $|n_1, n_5\rangle^0$. We will now focus on the polyad associated with an integer value for N. This polyad contains $N + 1$ states. For instance, Fermi resonance for the fifth CH overtone results in mixing among the following seven states: $|0, 12\rangle^0$, $|1, 10\rangle^0$, $|2, 8\rangle^0$, $|3, 6\rangle^0$, $|4, 4\rangle^0$, $|5, 2\rangle^0$, $|6, 0\rangle^0$.

The band centers for these polyads have been described by an *effective spectroscopic Hamiltonian* (91,94). Its diagonal and off-diagonal elements are given by Eqs. (106) and (107), respectively:

$$^0\langle n_1, n_5, l_5|\hat{H}_{\text{eff}}|n_1, n_5, l_5\rangle^0 = + n_5^2x'_{55} + n_1n_5x'_{15} + l_5^2g'_{55}\, n_1\nu'_1 + n_5\nu'_5 + n_1^2x'_{11} \tag{106}$$

$$^0\langle n_1, n_5, l_5|k'_{sbb}q_1(q_{5x}^2 + q_{5y}^2)|n_1 - 1, n_5 + 2, l_5\rangle^0$$
$$= -\frac{1}{2}k'_{sbb}\sqrt{\frac{1}{2}n_1(n_5 - l_5 + 2)(n_5 + l_5 + 2)} \tag{107}$$

where the fundamental frequencies (ν'_1, ν'_5) and the anharmonicities (x'_{11}, x'_{55}, x'_{15}, g'_{55}) have their usual spectroscopic meaning. In addition, n_1 and n_5 are the stretching and bending quantum numbers, respectively. The last quantum number, l_5, refers to the vibrational angular momentum quantum number for the degenerate CH bending vibration (98). The coordinates q_1 and (q_{5x}, q_{5y}) correspond to the dimensionless normal coordinates for modes 1 and 5, respectively. All of these parameters have been fitted to reproduce the overtone spectrum up to $N = 6$. This fit is easily possible with a root mean square deviation of less than 2 cm^{-1}, which is larger than experimental uncertainties (at most 0.1 cm^{-1}), but well within the accuracy expected for such a simple model (94). However, there are a large uncertainties in the spectroscopic parameters obtained (86). For example, Quack et al. have proposed $k'_{sbb} = 30 \pm 15$ cm^{-1}. Such an approach has been applied to several CX_3H compounds which also exhibit a strong Fermi resonance between the stretch and bend modes (92). Quack's group has also fitted from the spectrum a potential surface which represents very accurately the experimental data. This surface will be described later.

C. Hamiltonian and Basis Sets

1. The Vibrational Hamiltonian

The description of the Hamiltonian operator has to be quite general in order to be applicable to any molecule with N_m vibrational modes. It is assumed that the total Hamil-

tonian H can be split into a zero-order Hamiltonian H^0 and a coupling operator W:

$$H = H^0 + W \tag{108}$$

The zero-order Hamiltonian will be written as the sum of zero-order Hamiltonians, h_i^0, each referring to one given mode i. The coupling operator W is the sum of N_t *terms* T_t which can be expressed as a product of single-mode operators:

$$H^0 = \sum_{i=1}^{N_m} h_i^0 \quad \text{and} \quad W = \sum_{t=1}^{N_t} T_t \tag{109}$$

where

$$T_t = C_t\{A^{(t,1)} + B^{(t,1)} + \cdots\} \times \{A^{(t,2)} + (B^{(t,2)} + \cdots\} \times \cdots \times \{(A^{(t,N_m)} + B^{(t,N_m)} + \cdots\}$$

in which the operators $A^{(t,j)}$, $B^{(t,j)}$, . . . depend only on the jth mode. The sum of operators within each bracket $\{\cdots\}$ refers to a *step*, so that each term is written as a product of steps.

The total Hamiltonian can thus be written in the more compact form

$$H = H^0 + \sum_t C_t\left\{\prod_s \left[\sum_p C_{t,s,p} O^{(t,s,p)}\right]\right\} \tag{110}$$

where t refers to a term and s to a step. In fact, this representation is close to the usual Taylor expansion of a potential surface in terms of normal or local coordinates.

We will take as an example a single coupling term: $C_k q_3(a_1 q_1 + a_2 q_1^2 + a_3 q_1^3)$. In this case, the input file would be coded as follows:

TERM 1 C_k

STEP 1 $C_{111}O^{(1,1,1)} = q_3$

STEP 2 $C_{121}O^{(1,2,1)} = a_1 q_1$

$C_{122}O^{(1,2,2)} = a_2 q_1^2$

$C_{123}O^{(1,2,3)} = a_3 q_1^3$

A typical input data set may contain hundreds of terms, each coded this way, line by line.

The wave operator sorting algorithm, the RRGM, and the Chebyshev propagator never require the construction of the full Hamiltonian matrix. Instead, these algorithms are based upon the feature that one is able to calculate the matrix elements ${}^0\langle m|H|n\rangle^0$ between two arbitrary zero-order basis states or to act with the Hamiltonian operator H on any wave function known in this zero-order basis set. These calculations require the storage in high-speed memory of only the single-mode matrices $\mathbf{O}^{(t,s,p)}$ [Eq. (110)] which are part of the Hamiltonian operator. Furthermore, only the nonzero elements of these sparse matrices are stored. *Within this formulation, there is no upper limit on the molecular complexity or the basis set size that can be considered.* The reason is that any coupling matrix elements can be assembled from the single-mode matrices (95).

2. Primitive Basis Set

The zero-order vibrational basis set B used to describe the vibrational dynamics is built as the tensor product of single-mode bases:

$$B = B^{(1)} \times B^{(2)} \times \cdots \times B^{(N_m)} \tag{111}$$

in which $B^{(i)}$ is spanned by the eigenvectors of the single-mode Hamiltonian $h_i^{(i)}$:

$$B^{(i)} = \{|n_i\rangle^{(i)},\ n \in [N_{\min}^{(i)}, N_{\max}^{(i)}]\} \qquad \text{with } h_i^{(i)}|n_i\rangle^{(i)} = E_i^{(i)}|n_i\rangle^{(i)} \tag{112}$$

For nondegenerate modes, the zero-order states $|n_i\rangle^{(i)}$ can be defined analytically as harmonic oscillator eigenstates or numerically as solutions of the eigenequation:

$$\left(-\frac{1}{2m}\frac{d}{dq}g(q)\frac{d}{dq} + V(q)\right)|n\rangle^{(i)} = E^{(i)}|n\rangle^{(i)} \tag{113}$$

In the later case, this equation can be solved by using the discrete variable representation (100).

3. Merged Basis Sets

Owing to the tensor product definition in Eq. (111), the basis set contains some very high energy states, such as $|N_{\max}^1, \ldots, N_{\max}^{N_m}\rangle^{(i)}$. In order to reduce the overall basis set size, we will define combination (merged) modes by retaining only the combined states $|\nu_{ij}\rangle^{(i)} = |n_i, m_j\rangle^{(i)}$ whose energies are below a given energy threshold $E^{(i,j)}$. This mode merging procedure is shown schematically in Figure 5. As will be seen later, the actual combined $\{|n_i, m_j\rangle^{(i)}\}$ basis set, and thus the $E^{(i,j)}$ value, depends on the process under consideration. The merging of modes can proceed recursively. That is, an already combined mode ν_{ij} can be merged with another mode, say k, to define a new combined mode ν_{ijk}. One could thus in principle end up with a unique combined mode. But, such a procedure would necessitate the explicit construction of the Hamiltonian matrix in the merged basis set, and this would usually be too large to fit in the high-speed memory. Some applications of the mode merging procedure are presented below.

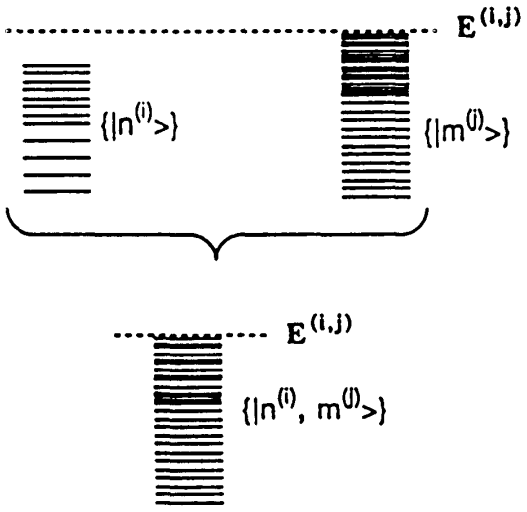

Figure 5 Merging of two modes n_i and n_j in order to reduce the overall zero-order basis set size. Only the combined states $|n_i, n_j\rangle^{(i)}$ located below a given energy threshold $E^{(i,j)}$ are retained.

4. Application to CD_3H

The CD_3H molecule has six vibrational modes, three of which are doubly degenerate. The primary zero-order description used in these calculations consists of the direct product of the single-mode basis sets,

$$\begin{aligned}\{|n^{(1)}, n^{(2)}, n^{(3)}, n^{(4)}, l^{(4)}, n^{(5)}, l^{(5)}, n^{(6)}, l^{(6)}\rangle^0\} \\ = \{|n^{(1)}\rangle\} \times \{|n^{(2)}\rangle\} \times \{|n^{(3)}\rangle\} \times \{|n^{(4)}, l^{(4)}\rangle\} \\ \times \{|n^{(5)}, l^{(5)}\rangle\} \times \{|n^{(6)}, l^{(6)}\rangle\}\end{aligned} \tag{114}$$

where the states $|n^{(i)}\rangle$ (i = 1, 2, 3) are Morse eigenstates and the states $|n^{(i)}, l^{(6)}\rangle$ (i = 4, 5, 6) correspond to doubly degenerate harmonic oscillator eigenstates associated with the bending modes.

In accord with Eqs. (108)–(109), the full vibrational Hamiltonian H will be decomposed into the sum of a zero-order Hamiltonian and a coupling operator W. In the expression for the zero-order Hamiltonian (Eq. (109)), i refers to one nondegenerate normal or local mode Q_i or to a pair of normal modes (Q_{ix}, Q_{iy}) for a doubly degenerate mode. In the case of a nondegenerate mode, h_i^0 represents a Morse oscillator. For the doubly degenerate mode, h_i^0 is a 2D harmonic oscillator Hamiltonian (i.e., $h_i^0 = h_{ix}^0 + h_{iy}^0$). We have used for the coupling operator an expansion in terms of dimensionless reduced normal mode coordinates $\{q_i\}$. This operator has been split into three terms:

$$W(q) = W(q_1, q_5) + W(\text{chromophore-bath}) + W(\text{bath}) \tag{115}$$

Experience on the calculation of the fifth CH overtone has shown that a very accurate description of the chromophore coupling is required. Consequently, an eighth-order description of the coupling between the chromophore modes, $W(q_1, q_5)$, has been used in order to represent the CH chromophore accurately. This potential operator, determined by Quack and colleagues (91), very accurately reproduces the chromophore spectrum through $N = 6$.

By contrast, the bath is composed of modes 2, 3, 4, and 6 which are weakly coupled to the CH stretch. Their fundamental energies are equal to 2,162, 1,007, 2,248 and 1,037 cm^{-1}, respectively. The W(chromophore-bath) and W(bath) operators have been estimated (95) empirically in order to reproduce the Gray and Robiette spectroscopic Hamiltonian (99,101). Finally, the Hamiltonian used in this study can be written (91,95)

$$\begin{aligned}W(q) = &\sum_{i=1}^{3} M_i(q_i) + \sum_{i=4}^{6} F_{ii} \cdot (q_{ix}^2 + q_{iy}^2) \\ &+ \sum_{n=1}^{6} \sum_{m=1}^{8} C_{nm} q_1^n \cdot (q_{5x}^2 + q_{5y}^2)^m \\ &+ \sum_{i<j=1}^{3} F_{ij} \cdot q_i \cdot q_j^2 + \sum_{i=1}^{3} \sum_{j=4}^{6} F_{ijj} \cdot q_i \cdot (q_{jx}^2 + q_{jy}^2) \\ &+ \sum_{i=4}^{6} F_{iij}(q_{ix}^2 q_{jx} - 2q_{ix}q_{iy}q_{jy} - q_{iy}^2 q_{jx}) \\ &+ \sum_{i<j=1}^{3} F_{iij} \cdot q_i^2 q_j^2 + \sum_{i<j=4}^{6} F_{iijj}(q_{ix}^2 + q_{iy}^2)(q_{jx}^2 + q_{jy}^2)\end{aligned} \tag{116}$$

in which the F_{ijk} and F_{ijkl}, and the C_{nm} parameters come from Refs. 95 and 91, respectively. Notice in the previous equation that F_{155} and F_{1155} has been set to zero because these terms correspond to chromophore coupling already included in Quack's chromophore potential.

Because we will focus on the fifth CH overtone in CD_3H, the range on the quantum numbers for the individual modes has been chosen as

$$\begin{aligned} &n^{(1)} \in [0, 9]; \quad n^{(5)} \in [0, 12]; \quad l^{(5)} \in [-n^{(5)}, n^{(5)}] \\ &\quad \text{for the chromophore modes} \\ &n^{(i)} \in [0, 3] \quad \text{if } i = 2, 3, 4, 6 \qquad \text{and} \qquad l^{(j)} \in [-n^{(j)}, n^{(j)}] \quad \text{if } j = 4, 6 \\ &\quad \text{for the bath modes} \end{aligned} \tag{117}$$

The primitive basis set can be reduced by merging modes 1 and 5 (chromophore modes), modes 2 and 4 (intermediate energy modes), and modes 3 and 6 (lower energy modes). The following energy criteria were used:

$$\begin{aligned} &0 \le E_1^0 + E_5^0 \le 26{,}500 \text{ cm}^{-1}; \; 0 \le E_2^0 + E_4^0 \le 7{,}000 \text{ cm}^{-1}; \\ &0 \le E_3^0 + E_6^0 \le 3{,}500 \text{ cm}^{-1} \end{aligned} \tag{118}$$

This results in an overall merged basis set of 207,000 states. The energy thresholds (26,500, 7000, 3500 cm^{-1}) used in Eq. (118) were specially selected for the study of the CH chromophore states.

D. Calculation of the Overtone Spectrum

1. Wave Operator Contraction

The general methods described in Section II (i.e., the wave operator contraction algorithm, and the Lanczos and filtered Lanczos algorithms for computing spectra) will now be applied to CD_3H. The results obtained by these different approaches will be compared to exact ones obtained in filtered Lanczos calculations performed in large active spaces. We will first apply the wave operator contraction algorithm presented in Section II.B.2. Recall that the wave operator is defined to map the initial state, $|i\rangle^0$, into the corresponding eigenvector $|\psi_i\rangle$.

A natural way to calculate a CH eigenvector $|nv_1\rangle$ consists in applying the wave operator to the initial zero-order state $|nv_1\rangle^0$. In order to illustrate this point, we have performed four iterations of the wave operator scheme on the zero-order states $|nv_1\rangle^0$ (n = 2, 3, 4, 5 and 6). Consequently, we have obtained a first approximation to the $|nv_1\rangle$ eigenvectors (n = 2, 3, 4, 5 and 6). The results obtained this way are compared to the exact ones in Table 1.

When the exact eigenvector $|nv_1\rangle$ is not very different from its zero-order description, $|nv_1\rangle^0$, the wave operator expansion very quickly converges to the correct eigenvector. This ideal behavior occurs for the first, second, and fourth overtones. An attractive feature is that this method does not require very much CPU time (at least 10 times less than an exact calculation). However, for the third overtone, this scheme dramatically diverges after three iterations. Phenomena such as this have been intensively studied in the past (22–30) and are caused by near degeneracy between the perturbed energies. In the present case, an accidental degeneracy during the iteration occurs between the perturbed energies of the $|4v_1\rangle^0$ and $|2v_1 + 2v_5 + v_3\rangle^0$ states. This state does not play an important role in the exact expression for the third overtone. Anomalies such as this are

Table 1 Energies Associated with the Eigenvectors Obtained from the Initial State $|nv_1\rangle^0$ Either by Performing Four Iterations of the Wave Operator Contraction Algorithm or by Performing an Exact Calculation (based upon filtered Lanczos calculations).

	Wave operator results after *four iterations*[a]	Exact energies and eigenvectors
$2\nu_1$		
Energy[b]	5865.4	5865.5
Eigenvector	$0.97\ \|2\nu_1\rangle^0 + 0.21\ \|\nu_1 + 2\nu_5\rangle^0$	$0.97\ \|2\nu_1\rangle^0 + 0.22\ \|\nu_1 + 2\nu_5\rangle^0$
$3\nu_1$		
Energy[b]	8623.9	8624.0
Eigenvector	$0.95\ \|3\nu_1\rangle^0 - 0.29\ \|2\nu_1 + 2\nu_5\rangle^0$	$0.95\ \|3\nu_1\rangle^0 - 0.29\ \|2\nu_1 + 2\nu_5\rangle^0$
$4\nu_1$		
Energy[b]	*3 iterations*: 11267.2	11267.7
Eigenvector	$0.91\ \|4\nu_1\rangle^0 + 0.35\ \|3\nu_1 + 2n_5\rangle^0 - 0.13\ \|2\nu_1 + 4\nu_5\rangle^0$	$0.92\ \|4\nu_1\rangle^0 + 0.37\ \|3\nu_1 + 2\nu_5\rangle^0 - 0.13\ \|2\nu_1 + 4\nu_5\rangle^0$
Energy[b]	*4 iterations*: 11266.8	
Eigenvector	$0.69\ \|4\nu_1\rangle^0 + 0.27\ \|3\nu_1 + 2\nu_5\rangle^0 - 0.09\ \|2\nu_1 + 4\nu_5\rangle^0 + 0.65\ \|2\nu_1 + 2\nu_2 + \nu_3\rangle^0 - 0.08\|\nu_1 + 3\nu_5 + 2\nu_4\rangle^0$	
$5\nu_1$		
Energy[b]	13794.8	13798.7
Eigenvector	$0.85\ \|5\nu_1\rangle^0 - 0.47\ \|4\nu_1 + 2\nu_5\rangle^0 - 0.20\ \|3\nu_1 + 4\nu_5\rangle^0 + 0.10\ \|2\nu_1 + 6\nu_5\rangle^0$	$0.84\ \|5\nu_1\rangle^0 - 0.47\ \|4\nu_1 + 2\nu_5\rangle^0 - 0.23\ \|3\nu_1 + 4\nu_5\rangle^0 + 0.09\ \|2\nu_1 + 6\nu_5\rangle^0$
$6\nu_1$		
Energy[b]	16214.3	16152.1
Eigenvector	$0.67\ \|6\nu_1\rangle^0 - 0.61\ \|5\nu_1 + 2\nu_5\rangle^0 + 0.27\ \|3\nu_1 + 6\nu_5\rangle^0 - 0.084\ \|2\nu_1 + 8\nu_5\rangle^0$	$-0.66\ \|6\nu_1\rangle^0 + 0.34\ \| - 3\nu_1 + 6\nu_5\rangle^0 + 0.35\ \|4\nu_1 + 4\nu_5\rangle^0 - 0.27\ \|2\nu_1 + 8\nu_5\rangle^0 + 0.12\ \|12\nu_5 + \nu_3\rangle^0 + 0.11\ \|\nu_1 + 8\nu_5 + \nu_3\rangle^0 + 0.26\|\nu_1 + 10\nu_5 + \nu_3\rangle^0 + -0.12\ \|3\nu_1 + 6\nu_5 + \nu_3\rangle^0 - 0.12\|2\nu_1 + 8\nu_5 + \nu_3\rangle^0 + 0.10\|10\nu_1 + \nu_3\rangle^0$
Energy[b]		16234.0
Eigenvector		$0.53\ \|6\nu_1\rangle^0 - 0.57\ \|5\nu_1 + 2\nu_5\rangle^0 + 0.47\ \|4\nu_1 + 4\nu_5\rangle^0 + 0.30\ \|3\nu_1 + 6\nu_5\rangle^0 - 0.16\ \|2\nu_1 + 8\nu_5\rangle^0 - 0.09\ \|\nu_1 + 10\nu_5\rangle^0$

[a]For the third overtone, the wave operator method diverges after three iterations. For this reason, the results obtained after either three or four iterations are provided.

[b]The energies are expressed in cm^{-1}.

expected to arise in vibrational problems because the state density can be large. This is the reason why we do not perform more than four iterations of the wave operator scheme and why we reset the transition operator X_{ki} matrix elements equal to unity when they become larger than unity.

In the calculation of the eigenvector for the fifth overtone, this scheme does not diverge, but it does not converge at all! For example, after four iterations the wave operator gives a vector whose components on the $|6\nu_1\rangle^0$ and $|5\nu_1 + 2\nu_5\rangle^0$ basis states are similar while the exact eigenstate $|6\nu_1\rangle$ (E = 16,152 cm^{-1}) has a large amplitude on the $|6\nu_1\rangle^0$ state but a very small amplitude (less than 0.075) on the $|5\nu_1 + 2\nu_5\rangle^0$ state. In fact, two different eigenvectors have a large projection (larger than 0.4) on the initial $|6\nu_1\rangle^0$ state. It is also difficult to identify the $|6\nu_1\rangle$ state. Is it the eigenvector associated with the eigenvalue equal to 16,152 cm^{-1} or to 16,234.0 cm^{-1}? Different states of the chromophore are so strongly coupled that two eigenstates have a large projection on the basis state $|6\nu_1\rangle^0$. The wave operator gives a combination of these two states after four iterations. *This is the reason why the perturbative expansion of the wave operator cannot be used to directly compute the eigenvectors but can be effectively used to define an active space.*

In a previous study (102), we have analyzed the capability of the wave operator algorithm to extract from a huge primitive space an active space containing all of the zero-order states which play a significant role in determining the spectrum of a given CH overtone. We have also analyzed the broad energy distribution of states in the active space. For instance, the interval containing the zero-order states which are retained in the active space built to study the fifth overtone was [11,000 cm^{-1}, 26,000 cm^{-1}], while the energy of the initial state was about 16,200 cm^{-1}. *We have observed that the nonresonant states retained in the active space collectively play a crucial role; omission of these secondary nonresonant states leads to erroneous results.*

Finally, we have shown that *the wave operator sorting algorithm builds a far more efficient active space than the more traditional intelligence AI tree pruning procedure.* We have compared spectra obtained in a direct exact Lanczos calculation in the primitive basis set with spectra obtained with either the wave operator sorting algorithm or the AI tree-pruning procedure. It was found that the dimension of the active space built with the wave operator is smaller than that obtained using the AI tree-pruning algorithm. Also, one of the main advantages of the wave operator sorting algorithm is that it does not require the use of arbitrary parameters. Parameters such as these are very difficult to assign confidently and to generalize to other systems.

2. Spectral Calculations Using Lanczos Methods

Traditional RRGM calculations. In the previous subsection, we showed that the wave operator does not generally give an accurate expression for an eigenstate, although it does efficiently build an active space. We now need to extract from the active space (containing several thousand states) the spectral information associated with various CH overtones, $|n\nu_1\rangle$, with n = 1, 2, . . . , 6. All of the calculations presented in this section were obtained using a 207,000 state primitive basis set.

First, an active space containing 4000 states was built by applying the wave operator to the zero-order state $|6\nu_1\rangle^0$. Calculation of the spectrum in this active space then proceeded using the RRGM. We will first focus on the convergence of the energy of the chromophore states with respect to the number of Lanczos recursion steps. Given this initial state, all of the chromophore eigenvectors $|n\nu_1\rangle$ (n = 2, 3, 4, 5, 6) can be obtained

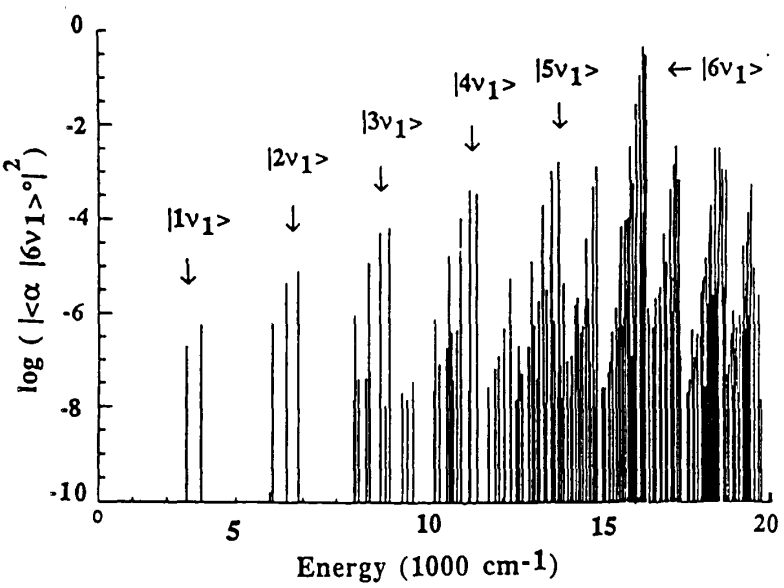

Figure 6 Residues $|^0\langle 6\nu_1|\alpha\rangle|^2$ and energies of the eigenstates $|\alpha\rangle$ obtained using the RRGM (3000 recursions) in an active space containing 4000 states.

in one calculation (95). Here, $|n\nu_1\rangle$ refers to the eigenvector whose projection on the zero-order CH stretch state $|n\nu_1\rangle^0$ is the largest one. Figure 6 shows the results obtained after performing 3000 Lanczos recursions. Table 2 provides the energy and the residue ($|^0\langle 6\nu_1|n\nu_1\rangle|^2$) associated with the chromophore states $|n\nu_1\rangle$ (n = 2, 3, 4, 5) obtained after performing 1000, 2000, or 3000 Lanczos recursions. For n = 6, all of the energies associated with the eigenvectors whose residue is larger than 0.1, are provided. In these calculations, it was found that 2000 recursions were required to obtain converged energies and residues.

Table 2 Overtone Energies (cm $^{-1}$) Obtained with the Direct Lanczos Method as a Function of the Number of Lanczos Recursions

$n\nu_1$	1000 iterations	1500 iterations	2000 iterations	3000 iterations	Exact results
$2\nu_1$	5865.5 (0.77 10^{-5})	converged			5865.5
$3\nu_1$	8624.0 (0.65 10^{-4})	converged			8624.0
$4\nu_1$	11267.7 (0.34 10^{-3})	converged			11267.7
$5\nu_1$	13800.2 (0.19 10^{-5})	13798.8 (0.42 10^{-5})	13798.7 (0.42 10^{-5})	converged	13798.7
$6\nu_1$	16046.5 (0.11)	16046.6 (0.11)	16046.7 (0.11)	converged	16046.8 (0.11)
	16152.7 (0.40)	16152.1 (0.43)	16152.1 (0.43)	converged	16152.1 (0.43)
	16163.9 (0.11)	16168.6 (0.11)	16167.9 (0.10)	16168.1 (0.11)	16169.1 (0.05)
					16168.5 (0.06)
	16234.0 (0.28)	converged			16234.0 (0.28)

The initial state of the recursion $|u_0\rangle$ was defined as the zero-order state $|6\nu_1\rangle^0$. Eigenvalues for the states $|n\nu_1\rangle$ are given for n = 2,...,6. For n = 6, energies are given for the eigenvectors whose residue on the initial state $|u_0\rangle = |6\nu_1\rangle^0$ is larger than 0.1. The last column gives the exact results. An energy is considered as exact if it is known with an error of 0.1 cm^{-1} and a residue if it is known to three significant digits.

It is surprising that the first eigenstates which converge are the *lower overtone states associated with the smaller residues.* Intuitively, one may expect that the main lines (16,152 cm^{-1} and 16,234 cm^{-1}) would converge first because the new basis set built by the Lanczos algorithm explores the space spanned by the $|6\nu_1\rangle^0$ state. In fact, *the Lanczos algorithm first converges energies located in the energy domain where the state density is low.* Figure 6 illustrates this fundamental property of the Lanczos algorithm. The lower overtones converge first because states which are close to them are associated with residues which are almost 100 times smaller than the residues near 16,200 cm^{-1}. By contrast, the main line (16,152 cm^{-1}) converges more slowly because the close lines near 16,169 cm^{-1} and 16,234 cm^{-1} have equivalent residues.

From these calculations, we notice the nonconvergence of the secondary line near 16,168 cm^{-1}. This line position is only known within ± 0.5 cm^{-1}. Usually, such a precision would be very satisfactory because the potential surface used is quite approximate. But if we would like to access the eigenvector, this slow convergence becomes a critical problem. If we compare this Lanczos calculation with an exact one, we conclude that the energy near 16,168 cm^{-1} converges slowly because it corresponds to two very close eigenenergies equal to 16,168.5 and 16,169.1 cm^{-1}.

This analysis illustrates the critical role played by the state density on the convergence of a Lanczos calculation. Eigenvectors associated with the larger residues and relatively far from the other eigenvalues whose residue is nonnegligible converge first. However, if a few lines are very close together, the convergence is slow. In such a case, it is advantageous to use the filtered version of the Lanczos algorithm.

Filtered Lanczos calculations. This new method involves application of the Lanczos recursion scheme with the Gaussian derivative operator (see Sec. II.C.2). This operator has the same eigenvectors as the Hamiltonian, but the spectral density is smaller near the test input energy. The part of the spectrum near this test energy is dilated while the remaining part is compressed to the value zero. Only one preselected energy window is explored in such a filtered Lanczos calculation. This energy window is defined by the parameters E^0 and ΔE, the first of which defines the center of the window while the second defines its width. The following results have been obtained by using the filter function $(\mathbf{H} - E^0)\exp(-(\mathbf{H} - E^0)^2/\Delta E)$. As a result, the spectrum of the Hamiltonian is dilated in the interval $[E^0 - \frac{2}{3}\Delta E, E^0 + \frac{2}{3}\Delta E]$.

The eigenvalues of the states whose chromophore character is significant are spread over a large energy interval, [15,100 cm^{-1}, 16,230 cm^{-1}]. Consequently, in order to explore this interval, the ΔE and E^0 parameters of the Gaussian filter function must be assigned to about 1,000 cm^{-1} and 15,700 cm^{-1}, respectively. The filtered Lanczos method has been applied in a 6000 state active space built from the $|3\nu_1 + 6\nu_5\rangle^0$ zero-order state. This zero-order state was chosen because it provides nonnegligible projections on all of the chromophore eigenstates. Table 3 gives the number of Lanczos recursions required in order to obtain converged eigenvalues. As expected, the larger the residue and the smaller the state density, the faster the convergence. Consequently, the more isolated state (15,103 cm^{-1}) converges first. On the contrary, it is more difficult to converge the lines near 16,200 cm^{-1}. The four eigenvalues (16,047, 16,152, 16,169, and 16,234 cm^{-1}) are satisfactorily obtained in the large basis set (207,000 states) after performing about 300 Lanczos recursions. To rapidly converge the important eigenvalues located near 16,200 cm^{-1}, we can use a more selective filter whose slope near these eigenvalues is higher. This will provide a greater dilation of the spectrum in this region. A calculation was then

Table 3 Number of Filtered Lanczos Recursion Steps Required to Obtain an Energy with an Error Smaller than 0.1 cm^{-1} and a Residue Known with Three Significant Digits

	Number of filtered Lanczos recursions required	
Eigenvalues	E^0 = 15700 cm^{-1} ΔE = 1000 cm^{-1}	E^0 = 16200 cm^{-1} ΔE = 150 cm^{-1}
15102 (0.017)	125	x
15333 (0.017)	225	x
15482 (0.261)	175	x
15752 (0.014)	275	x
15937 (0.137)	200	50
16047 (0.484)	250	25
16169 (0.036)	275	100
16152 (0.116)	250	75
16234 (0.096)	225	50

The number given in parentheses after the energy is the residue of the eigenvector on the $|3\nu_1 + 6\nu_5\rangle^0$ zero-order state. The first energy window ΔE = 1000 cm^{-1} allows convergence of all chromophore eigenstates with less than 300 recursions. The second energy window, ΔE = 200 cm^{-1}, allows convergence of one part of the spectrum by performing less than 100 iterations. An energy is considered to be exact if it is known with an error of 0.1 cm^{-1} and a residue if it is known with three significant digits.

performed by fixing ΔE and E^0 to 200 and 16,200 cm^{-1}, respectively. All of the spectral lines within the interval explored by the new Gaussian filter were converged after 100 recursions. The other eigenstates cannot be obtained because they do not belong to this energy interval.

Consequently, this study shows that the choice of the parameters in the spectral filter depends upon the density of the spectrum. This density is not the full state density but only the density of states whose projection on the initial state is nonnegligible. When this density is high, a more selective filter must be used. This new approach leads to an accurate expression for the eigenvector and constitutes a very useful and powerful tool for computing spectra.

3. Analysis of the Fifth Overtone

The $|6\nu_{CH}\rangle$ chromophore space will be defined to contain all of the zero-order states $|(6 - m)\nu_1 + 2m\nu_5\rangle^0$ (m = 0, 1, . . . , 6). We have performed a series of filtered Lanczos calculations in several 6000 state active spaces built by applying the wave operator to different zero-order states $|(6 - m)\nu_1 + 2m\nu_5\rangle^0$. Table 4 provides the expressions for the eigenvectors whose projections on at least one zero-order chromophore state is larger than 0.1. First, we note that the energies and the eigenvector expressions do not depend on the nature of the chromophore state used to build the active space. This means that the wave operator procedure extracts from the 207,000-state primitive basis set a satisfactory active space independent of the zero-order chromophore states selected to build the active space. Secondly, the chromophore character of the different eigenstates has been estimated. The chromophore character of a given eigenvector, $|\Psi\rangle$, is defined as

$$C(\text{chromo}) = \sum_{n^{(1)}n^{(5)}l^{(5)}} |^0\langle n^{(1)}, 0, 0, 0, 0, n^{(5)}, l^{(5)}, 0, 0|\Psi\rangle|^2 \qquad (119)$$

Table 4 Analysis of the Fifth Overtone Eigenstates for CD_3H

Eigenvalues (cm^{-1})	Projection on the zero-order chromophore states $\|6 - m, 2m\rangle''$ of the chromophore eigenvector							Chromophore character	Assignment	Eigenvalues obtained by neglecting the bath modes (cm^{-1})
	0	1	2	3	4	5	6			
15102	—	—	—	−0.13	−0.38	0.56	0.26	55%	$\|1, 10\rangle$	15097
15333	—	—	—	−0.13	—	—	—	2%	bath	—
15482	—	—	−0.28	0.51	0.30	0.34	0.32	65%	$\|3, 6\rangle$	15456
15752	—	0.30	0.50	−0.12	0.40	0.11	0.38	67%	$\|14, 4\rangle$	15715
15937	0.16	0.47	0.22	0.37	—	0.24	−0.60	85%	$\|0, 12\rangle$	15905
16047	0.33	0.49	−0.18	0.22	−0.40	−0.30	0.37	82%	chromophore	16048
16169	0.32	—	0.12	−0.19	—	0.31	−0.21	29%	bath	—
16152	−0.66	—	0.35	0.34	−0.27	—	—	75%	$\|6, 0\rangle$	16160
16234	0.53	−0.57	0.47	0.30	−0.16	−0.09	—	95%	$\|5, 2\rangle$	16233

Column 1 gives the eigenenergies of all eigenstates which have a projection larger than 0.1 on the initial state. Columns 2–7 give the projection of the different eigenstates on the zero-order chromophore states. Column 8 gives the chromophore character of each eigenstate (see Eq. (119)). Column 9 proposes an assignment of each state. Column 10 gives the energies obtained for the chromophore states if the coupling with the bath modes is neglected.

Seven eigenstates exhibit a chromophore character larger than 50%. This result can be analyzed as follows: The zero-state $|6\nu_1\rangle^0$ is strongly coupled to six other chromophore states, i.e., $|(6 - m)\nu_1 + 2m\nu_5\rangle^0$ ($m = 1, \ldots, 6$), belonging to the same polyad ($n = 6$) and this state is very weakly coupled to the chromophore states belonging to the other polyads ($n \neq 6$). If the bath modes are neglected, this coupling scheme results in seven eigenvectors, each of which is a combination of the different zero-order states, $|(6 - m)\nu_1 + 2m\nu_5\rangle^0$ ($m = 0, \ldots, 6$). Consequently, our six mode calculation shows that the CH chromophore can be separated in a first approximation from the other modes, even at this high excitation energy (about 16,000 cm^{-1}).

However, in a more quantitative description, the bath modes cannot be neglected. For instance, two bath states (15,333 cm^{-1} and 16,169 cm^{-1}) have a nonnegligible chromophore character. The analysis of the eigenvector has shown that the 15,333 cm^{-1} band is essentially a combination of states $|n_1\nu_1 + n_5\nu_5 + n_2\nu_2 + n_3\nu_3\rangle^0$ and that the band near 16,169 cm^{-1} can be assigned to a combination of the states $|n_1\nu_1 + n_5\nu_5 + n_3\nu_3\rangle^0$. As a result, the eigenvector $|6\nu_1\rangle$ (E = 16,152 cm^{-1}) located near 16,169 cm^{-1} also has a nonnegligible projection on the states $|n_1\nu_1 + n_5\nu_5 + n_3\nu_3\rangle^0$. We can estimate the character of the eigenstate denoted $|6\nu_1\rangle$ (E = 16,152 cm^{-1}) on the states $|n_1\nu_1 + n_5\nu_5 + n_3\nu_3\rangle^0$:

$$C(\text{chromo} + \text{mode } 3) = \sum_{n^{(1)}n^{(3)}n^{(5)}l^{(5)}} |^0\langle n^{(1)}, 0, n^{(3)}, 0, 0, n^{(5)}, l^{(5)}, 0, 0|6\nu_1\rangle|^2 \qquad \text{with } n^{(3)} \neq 0 \quad (120)$$

The character, C(chromo + mode 3), of this state $|6n_1\rangle$ is about 14%. The same calculation for the eigenstate located near 16,169 cm^{-1} gives 55%. This analysis shows that these bands result from a small but not negligible coupling between the chromophore and mode 3. As a result, the bath modes do play a secondary but nonnegligible role in the chromophore spectrum.

In Table 4, the eigenvalues obtained by neglecting the bath mode couplings in Eq. (115) (i.e., W(chromophore − bath) + W(bath) = 0) are provided. The comparison between the first and last columns shows that several energies are shifted significantly (±40 cm^{-1}) by the couplings between the bath modes and the chromophore.

Finally, it is not easy to confidently assign each chromophore line to a single zero-order state $|(6 - m)\nu_1 + 2m\nu_5\rangle^0$ because the chromophore states are a combination of several different zero-order states. For instance, the 16,047 cm^{-1} eigenvector is a combination of seven zero-order states associated with the $n = 6$ polyad. The assignment proposed in Table 4 is quite artificial because all the eigenvectors have a large projection on essentially two zero-order states. Finally, we notice that these CH chromophore eigenenergies belong to a rather large energy interval, i.e., [15,100 cm^{-1}, 16,234 cm^{-1}]. This confirms that no energy criteria should be used in order to build the active space. For instance, the $|3\nu_1 + 6\nu_5\rangle^0$ basis state enters significantly in the composition of nine eigenvectors whose associated energies are spread over the interval [15,100 cm^{-1}, 16,234 cm^{-1}].

This application to CD_3H confirms that the computational methods described in Section II are capable of providing converged energies and eigenvectors for a given basis set. This new approach leads to the exact expression for the eigenvectors and should constitute in the future a helpful and powerful tool for analyzing vibrational spectra.

E. Intramolecular Dynamics

A time-dependent study of IVR from the initial local mode $|6\nu_1\rangle^0$ will now be presented. In order to calculate the time-evolving state $|6\nu_1(t)\rangle$, the evolution operator was expanded

in terms of Chebyshev polynomials (see Sec. II.C.3). The result is that this evolving state is known in terms of an expansion in zero-order states $|n\rangle^0$:

$$|6\nu_1(t)\rangle = \sum_{|n\rangle^0} c_n(t)|n\rangle^0 \tag{121}$$

The results obtained with this method are displayed in Figure 7. In this figure, we have displayed, as a function of time, the survival probability $P_{6\nu_1}(t)$,

$$P_{6\nu_1}(t) = |^0\langle 6\nu_1|6\nu_1(t)\rangle|^2 \tag{122}$$

the overall population $P_{CH}(t)$ of the chromophore,

$$P_{CH}(t) = \sum_{n^{(1)}n^{(5)}l^{(5)}} |^0\langle n^{(1)}, 0, 0, 0, 0, n^{(5)}, l^{(5)}, 0, 0|6\nu_1(t)\rangle|^2 \tag{123}$$

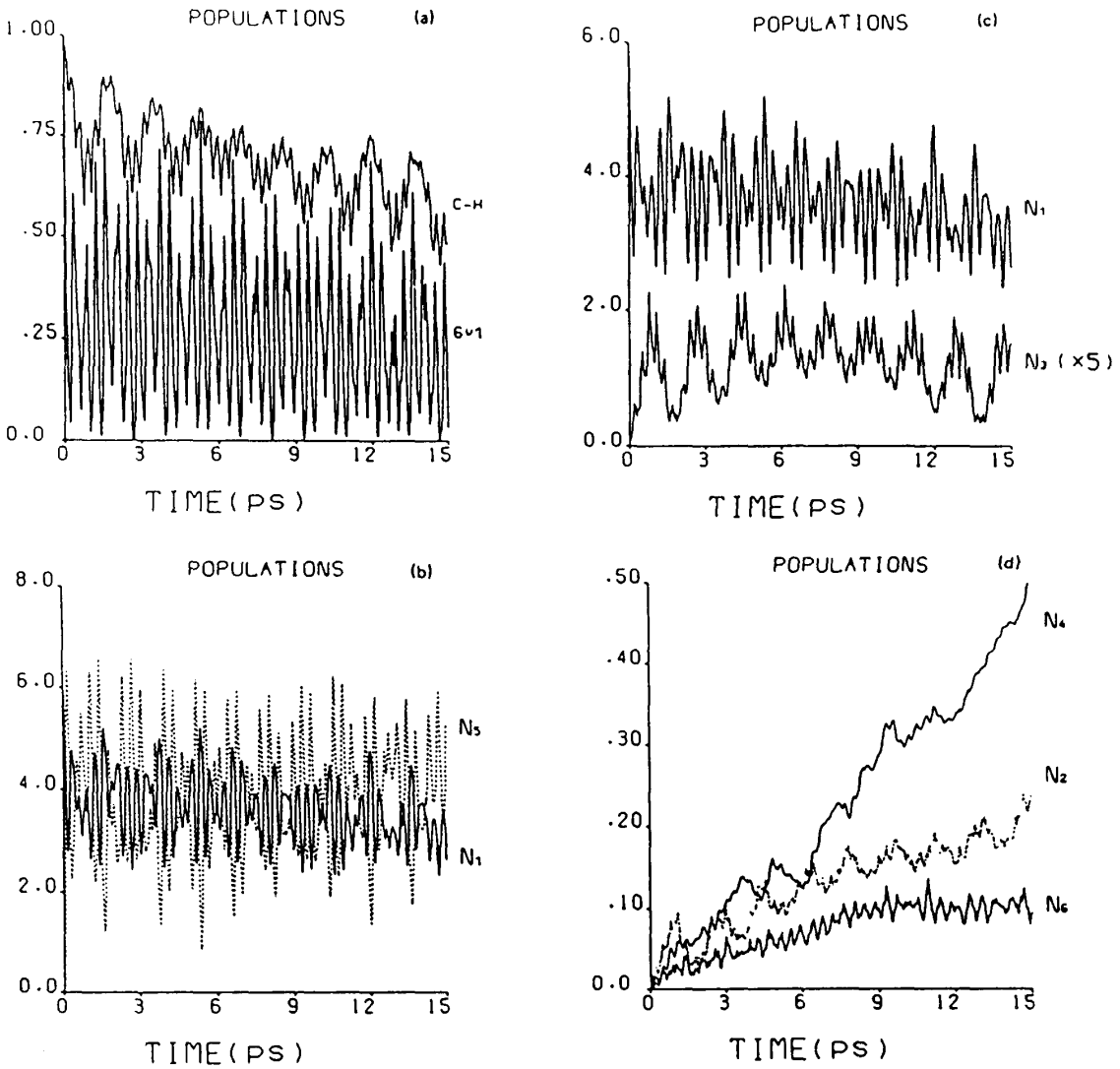

Figure 7 Time evolution of the initial $|6\nu_1\rangle^0$ state, computed using the Chebyshev propagation scheme: (a) survival probability (lower curve) and overall chromophore population (upper curve, defined in Eq. (123). (b), (c), and (d) Vibrational mode populations, defined in Eq. (124).

as well as the average quantum number $N_i(t)$ of each mode

$$N_i(t) = \sum_{|n\rangle^0} |{}^0\langle n|6\nu_1(t)\rangle|^2 \times n^{(i)} \tag{124}$$

where the summation is over all states on the right side of Eq. (121) and where $|n\rangle^0$ is a nine-mode basis function, $|n^{(1)}, n^{(2)}, \ldots, n^{(9)}\rangle^0$.

One striking feature observed in Figure 7a concerns the very slow relaxation out of the CH chromophore over this 15-ps time interval. Although the survival probability displays a fast initial decay on a time scale of about 0.1 ps, the energy leaks very slowly out of the chromophore, on a time scale greater than 15 ps. In fact, Figure 7b shows that the CH stretch and bend populations vary in opposite directions, a maximum in N_1 always corresponding to a minimum in N_5, and reciprocally. The CH bending mode thus acts as an energy buffer for the stretching mode. The time scale (about 0.33 ps) for the energy exchange between the ν_1 and ν_5 modes can be related to the 2:1 Fermi resonance between the $|6\nu_1\rangle$ and $|5\nu_1 + 2\nu_5\rangle$ states. Table 4 gives the energies of these states as 16,152 and 16,234 cm^{-1}, respectively. This 82-cm^{-1} energy separation leads to quantum beats associated with a period of 2 ps/ΔE = 0.4 ps, in good agreement with the observed value.

Figure 7a shows that there exists a longer time modulation (about 2 ps) in the chromophore population. The origin of this modulation can be directly traced to the n_3 mode, the population of which displays the same evolution pattern as shown in Figure 7c. In this figure, we have compared the N_1 and N_3 average quantum numbers. It can be seen that these populations vary out of phase, indicating a resonance between the ν_1 and ν_3 modes. From the quantum beat period, we expect a resonance between two states separated by 15 cm^{-1}; as we noticed previously, the states with energies 16,169 cm^{-1} and 16,152 cm^{-1} have an important contribution from the n_3 mode. Finally the N_2, N_4, and N_6 populations, shown in Figure 7d, display a monotonic increase over the 15-ps interval, apart from modulations due to the N_1–N_5 and N_1–N_3 resonances. The overall relaxation from the $|6\nu_1\rangle^0$ mode is displayed in Figure 8.

IV. SPECTROSCOPY AND DYNAMICS FOR C_6H_6

A. Introduction

A very demanding application of the computational methods discussed in Section II concerns the overtone spectroscopy and dynamics of energy flow in benzene. This section

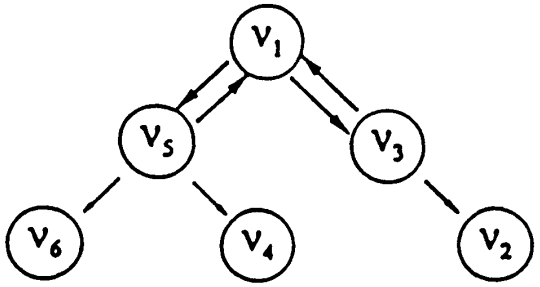

Figure 8 Overall relaxation behavior of the $|6\nu_1\rangle^0$ local mode. The arrow intensities reflect the energy exchange rate. Double arrows indicate a quasi-reversible exchange.

will emphasize quantum mechanical studies of 21-mode planar benzene (103–108,34). These studies began in 1990 and continued through 1994 in both Austin and Orsay. Starting with the five- and nine-mode benzene fragments C_3H and C_3H_3, these studies then went on to consider 16- and full 21-mode models. We will begin by reviewing previous experimental and theoretical studies in Section IV.B. The Hamiltonian and basis sets will be described in Section IV.C. Then, computational results on overtone spectra and the mechanism for energy transfer will be presented in Sections IV.D–F.

B. Previous Benzene Studies

1. Experimental Overtone Spectroscopy

We will begin by briefly reviewing the experimental studies of benzene overtones. Later, in Section IV.D, we will compare the computed spectrum for the second CH overtone with the results from supersonic expansion experiments. The interpretation of the overtone spectrum of benzene in terms of anharmonic CH stretch vibrations goes back to the experimental studies of Ellis (109) reported in 1929. A significant feature is that the frequencies of the overtone spectral peaks follow the Birge-Sponer relationship (110), $\omega_{peak} = A\nu - B\nu^2$ (ν = 1, 2, 3, . . .). This is the same frequency relationship that one obtains for a Morse oscillator. A more extensive analysis in terms of local modes of vibration was developed by Henry (111–112) starting in 1968. An excellent review (113) describing the use of local modes to interpret the spectra of highly vibrationally excited molecules was presented in 1977. A number of other studies have also focused on the local mode model (114–119).

In more recent times, during the mid-1970s, Albrecht and co-workers developed the thermal lens technique and used it to study the absorption spectrum of liquid benzene (120–123). In important studies during the late 1970s and early 1980s, Berry and co-workers recorded ν = 1 to 9 overtone spectra of room temperature gas phase benzene using the intracavity cw dye laser technique with optoacoustic detection (124). They reported broad absorption features; for ν = 3, the roughly 100-cm^{-1} FWHM asymmetric absorption feature had a broad shoulder on the red side of the main feature.

The experimental situation advanced significantly when Page, Shen, and Lee (6,125,126) reported results using the supersonic molecular beam technique. The benzene molecules were rotationally cooled to 5 K by the supersonic expansion, which eliminated much of the rotational broadening in the room temperature experiments of Berry et al. The ν = 1 fundamental, and the ν = 2 and 3 overtones created by a tunable IR laser were detected by monitoring $C_6H_6^+$ ions created through resonant enhanced two-photon ionization (R2PI) produced by a UV laser. In these experiments, the most intense peak of the ν = 3 overtone was centered at 8827 cm^{-1} with a FWHM of <10 cm^{-1}. Recently, Scotoni et al. (127,128) reported additional supersonic molecular beam results for both the ν = 3 and ν = 4 overtones. However, instead of R2PI detection, they used a cryogenically cooled bolometer. Under these beam conditions, the 20 K rotational temperature molecules also exhibited in the ν = 3 spectrum a main peak at 8827 cm^{-1}, but with at least five less prominent bands on the "red" side of the main peak. Comparisons between these experimental spectra and computed overtone spectra will be described in Section IV.D. Although not directly related to the computational studies described later, we note that Chernoff et al. (129) recorded high, relatively harmonic, *normal mode overtones* of the C—C ring breathing mode up to 10,000 cm^{-1}.

2. Computational Studies of Spectra and Dynamics

We will now review the classical and quantal studies of benzene spectra and dynamics. Using both classical and quantum mechanical models, Sibert et al. (130) made detailed comparisons with the experimental results of Berry et al. Their model involved only *kinetic energy coupling* in curvilinear coordinates, the most important of which was between the CH stretch (a Morse oscillator) and the contiguous CCH in-plane wag (other smaller kinetic coupling terms were also included). All anharmonic potential energy coupling terms were neglected. An important theoretical construction used in these studies was that of *tiers* of quantum states; successive tiers were coupled by anharmonic terms in the Hamiltonian. In these quantum mechanical studies, about 700 states in three tiers were used and a phenomenological relaxation parameter was introduced to mimic the effect of neglected additional tiers. The spectra predicted by this model appeared to be in good agreement with the experimental data that was available in 1982. Shi and Miller (131) have used a semiclassical model with kinetic coupling in internal curvilinear coordinates to predict correlation functions and spectra for local mode relaxation in benzene. Their results were also in good agreement with the experimental results of Berry et al. Buck et al. (132) also used the kinetic coupling model with a statistical wave function approximation to predict overtone widths in benzene.

In addition to our recent studies on the benzene overtones, Zhang and Marcus (ZM) (133–135) have computed spectra and survival probabilities for CH (ν = 1, 2, and 3). There are some similarities and a number of differences in formulation and methodology between our work and that of ZM; these aspects were discussed in Benzene V. Comparisons between our computed overtone spectra and those of ZM were also presented in Benzene V (106).

Hase and co-workers (136–140) have reported an extensive series of trajectory studies on overtone relaxation in benzene. Comparisons between our quantum studies for the five- and nine-mode benzene fragments of C_5H and C_5H_5 and the trajectory results were presented in Benzene I (103). Further comparisons for 16-mode and 21-mode benzene were presented in Benzene II and III (104,105). Clarke and Collins (141) also used classical trajectories to study overtone relaxation in benzene. Finally, Thompson et al. have also used trajectory methods to study energy flow from excited CH overtones (142,143) and from various excited CC stretch, CCH wag, and CCC bend normal modes. Several potential surfaces with varying degrees of anharmonicity were used.

Gomez-Llorente et al. (144) presented a critique on the use of classical trajectories to study overtone relaxation in planar benzene. Their conclusion is

> . . . because some of the trajectories used to simulate the quantum flow from the local mode region are blocked and redirected back into the region, and the remainder (the majority) are outside the region and do not feel it, *standard studies* of the flow of ensembles of trajectories designed to mimic packet flow *cannot be used to compute local mode IVR rates of benzene*'' (italics added for emphasis).

The term ''standard studies'' refers to those based upon tracking the time evolution of swarms of trajectories, so that correlation functions and spectra can be computed. Instead, it is recommended that the analysis be based upon stability parameters of trajectories. Stability analysis of the CH periodic orbit, as a function of stretch-wag coupling, was the subject of an earlier study by Garcia-Ayllon et al. (145).

3. Development of Force Fields

Since about 1980, considerable computational effort has been devoted to the determination of an accurate force field for benzene (146–157). Although detailed analyses of the experimental data go back 60 years (158), even the harmonic force field is not known to high accuracy from the experimental data. One reason for this situation is that benzene has five spectroscopically inactive vibrational modes and the number of independent quadratic force constants (34 for nonplanar benzene and 26 for the planar molecule) is too large to be determined by experimental information alone. Even establishing the harmonic frequencies has required considerable effort, because anharmonic corrections must be estimated for the measured fundamental frequencies. Recently, after years of detailed experimental and theoretical studies, Goodman and co-workers (149–152) have established a benchmark *harmonic force field* by combining all currently available IR, Raman, and one- and two-photon electronic excitation information from four isotopomers with theoretical calculations. This set of quadratic force constants and harmonic frequencies provides an important database for comparison with future theoretical studies.

We will now comment briefly on the force fields that have been computed for benzene. The first one to incorporate both harmonic and anharmonic force constants (some cubic force constants) was reported by Pulay et al. (146) in 1981. This force field was determined with the 4-21P basis set at the SCF level. The computed harmonic force constants, as expected, were larger than the empirical values, so Pulay et al. developed a scaled quadratic force field. The scale factors were adjusted so that the computed frequencies agreed well with the *experimental fundamental frequencies.*

The more recent 1992 Maslen et al. force field for benzene (153) was computed by evaluating *analytic derivatives* through quartic terms at the SCF level. The DZP basis set was used in these studies. The derivatives were evaluated at the equilibrium geometry determined at the MP2 (Moller-Plesset second-order pertubation theory) level using a larger basis set, TZ2P (triple-zeta plus double polarization). It is significant that a complete ab initio force field at the quartic level has been computed for benzene.

Following a procedure similar to that of Pulay et al. (146), we have developed a scaled quadratic force field (106) based upon the Maslen et al. force field. The scale factors were obtained by adjusting the force constants so that the resulting harmonic frequencies agreed well with the empirical harmonic frequencies. In the resulting force field, the scaled frequencies deviate from the empirical harmonic frequencies from 0.2 to 9.2 cm^{-1}. We note that diagonal elements in the scaled DZP force field are larger than those in the scaled force field of Pulay et al. because the latter was determined by fitting to experimental *fundamental frequencies* rather than to *harmonic frequencies.*

These comparisons, and additional comparisons with other ab initio calculations, indicate that the harmonic frequencies for benzene have not been pinned down at the $\pm 10-20$ cm^{-1} level by the previously mentioned ab initio calculations. In order to reduce inaccuracies in the harmonic force field, we have performed relatively large scale calculations using a valence triple zeta plus polarization basis set (pVTZ) in coupled-cluster calculations with single and double excitations (CCSD). These results, as well as comparisons with previous ab initio and recent density functional (156–157) results, are described elsewhere (108).

A significant reason for determining accurate *anharmonic force fields* for benzene is that they serve as input into dynamical studies of overtone spectra and intramolecular energy transfer. In previous studies, we have used the force fields developed by Pulay et

al. (146) and by Maslen et al. (153). In related studies, Zhang and Marcus (133–135) used the Goodman et al. harmonic force field (152) as part of the input.

C. Hamiltonian and Basis Sets

1. Coordinate Systems for Dynamics

The vibrational anharmonic Hamiltonian for benzene may be formulated in either internal curvilinear coordinates or internal rectilinear coordinates. For example, the quantum mechanical studies of Sibert et al. (130) and Zhang et al. (133) employed curvilinear coordinates, whereas the classical mechanical studies of Hase et al. (136–140) have employed rectilinear coordinates. There are advantages and disadvantages connected with either formulation. For curvilinear coordinates, the G-matrix elements which enter the kinetic energy are functions of the coordinates, so that the quantum mechanical kinetic energy operator is quite complex. Usually, the G-matrix elements are Taylor expanded about the equilibrium geometry and only the lowest orders are retained in the dynamics. On the other hand, in rectilinear coordinates, the G-matrix elements are constant, independent of geometry, and the kinetic energy operator has a simple form. However, the potential surface or force field is usually formulated as a series expansion in curvilinear coordinates because of the relatively small number of terms involved. Conversion of this potential to rectilinear coordinates is quite complicated and many terms may be required for convergence.

Recently, the dynamical formulations in these two coordinate systems were compared (159) for the nine-mode CD_3H molecule. This study focused upon the validity of the *kinetic approximation* in curvilinear coordinates; the Hamiltonian contained the kinetic energy operator, which could be truncated, and *only* harmonic potential terms. The kinetic energy operator was expanded to high order, with up to 140 terms. Low-order expansions, particularly first or second order, gave a poor description of both the spectroscopic and dynamic features. It thus appears, from a computational point of view, that the curvilinear description may not give a simpler approach than one based upon rectilinear coordinates.

For the studies on benzene described in the following sections, the Hamiltonian was formulated in rectilinear coordinates. The "pure vibrational" kinetic energy operator was treated exactly (but nonquadratic vibrational angular momentum terms $\pi_i\pi_j$, Coriolos, and rotational terms were neglected), but the price to be paid is that the anharmonic potential contains a large number of terms. Development of the vibrational anharmonic Hamiltonian is described in the next three sections.

Before specifying the form for the kinetic energy operator, we will comment on the various coordinate systems that are used in studies of molecular dynamics. Four coordinate systems are frequently used; they are defined as follows for 21-mode planar benzene:

d_i: (i = 1, 2, . . . , 24), *Cartesian* (x, y) *displacements* of the atoms from their equilibrium positions.

$\Re_i$: (i = 1, 2, . . . , 21), *internal curvilinear displacement coordinates*, defined in Table 3 of Pulay et al. (146).

R_i: (i = 1, 2, . . . , 21), *internal rectilinear displacement coordinates*, labeled by analogy to the curvilinear coordinates.

Q_i: (i = 1, 2, . . . , 21), *normal coordinates*.

Conversions between these four coordinate systems are defined by the following tensorial or linear transformations (160):

$$\mathfrak{R} = \mathbf{B}^*\mathbf{d} = \mathbf{L}^*\mathbf{Q} = \mathbf{T}^*\mathbf{R} \tag{125}$$

$$\mathbf{R} = \mathbf{L}_1\mathbf{Q} = \mathbf{B}_1\mathbf{d} \tag{126}$$

where $\mathbf{B}^*$, $\mathbf{L}^*$, and $\mathbf{T}^*$ are *nonlinear tensor transformations* from $\mathbf{d}$, $\mathbf{Q}$, or $\mathbf{R}$ to curvilinear coordinates, while $\mathbf{L}_1$ and $\mathbf{B}_1$ are *linear transformations* from $\mathbf{Q}$ and $\mathbf{d}$ to rectilinear coordinates. For example, the tensor transformation from Cartesian to curvilinear coordinates is

$$\mathfrak{R}_i = \sum_p B_i^p \delta_p + \frac{1}{2}\sum_{p,q} B_i^{pq}\delta_p\delta_q + \frac{1}{6}\sum_{p,q,r} B_i^{pqr}\delta_p\delta_q\delta_r + \cdots \tag{127}$$

The successive sets of coefficients defining this transformation are denoted $\mathbf{B}_1$, $\mathbf{B}_2$, $\mathbf{B}_3$, ... The coefficients $\mathbf{B}_i$ and the coefficients $\mathbf{L}_i$ in the $\mathbf{L}^*$ transformation are defined elsewhere (160).

2. Potential for CH Chromophore

Because of the relatively high energy of the initial CH overtone excited state, the stretch-wag potential for the overtone excited CH bond requires special consideration. The stretch-wag potential, through cubic terms, in the input force field in curvilinear coordinates is

$$V_c(\rho, \beta) = \frac{1}{2}k_2\rho^2 + \frac{1}{6}k_3\rho^3 + \frac{1}{2}k_2'\beta^2 + \frac{1}{6}k_3'\rho\beta^2 \tag{128}$$

where k_3' is the cubic interaction constant. In order to extend this potential to higher vibrational energies, the two pure stretch terms were replaced by the Morse potential

$$V_c(\rho, \beta) = V_m(\rho) + \frac{1}{2}k_2'\beta^2 + \frac{1}{6}k_3'\rho\beta^2 \tag{129}$$

We mentioned that the dynamical calculations will be performed in rectilinear coordinates. The potential in these coordinates is expressed as the sum of a Morse potential in the rectilinear stretch coordinate r, plus the harmonic bend potential in the rectilinear bend coordinate b, and a correction potential,

$$V_r(r, b) = V_m(r) + \frac{1}{2}k_2'b^2 + \Delta(r, b) \tag{130}$$

The correction potential is expressed as a power series in the two rectilinear coordinates:

$$\Delta(r, b) = \sum_{m,n} c_{mn} r^m b^{2n} \tag{131}$$

The expansion coefficients c_{mn} were determined by linear least squares fitting of $\Delta(r, b)$ to the ab initio force field values at a number of grid points (106).

3. The Hamiltonian in Rectilinear Coordinates

Because we will use rectilinear coordinates $\{R_i\}$ and normal coordinates $\{Q_i\}$ to formulate the Hamiltonian operator, it is necessary to convert the input force field in curvilinear coordinates to a force field in rectilinear coordinates. After using the transfor-

mations in Section IV.C.1, the resulting force field in normal coordinates becomes

$$V = \frac{1}{2}\sum_{r} \lambda_r Q_r^2 + \frac{1}{6}\sum_{r,s,t} \Phi^{rst} Q_r Q_s Q_t + \frac{1}{24}\sum_{r,s,t,u} \Phi^{rstu} Q_r Q_s Q_t Q_u + \cdots \tag{132}$$

This force field may also be expressed in rectilinear coordinates by first inverting the matrix $\mathbf{L}_1$ in Eq. (126); this gives

$$Q_r = \sum_{i} (\mathbf{L}_1)^{-1}_{ri} R_i \tag{133}$$

When this transformation is used for each normal coordinate appearing in Eq. (132), the result is

$$V = \frac{1}{2}\sum_{i,j} F^{ij} R_i R_j + \frac{1}{6}\sum_{i,j,k} F^{ijk} R_i R_j R_k + \cdots \tag{134}$$

This expansion of the potential in rectilinear coordinates is analogous to Eq. (132) for normal coordinates.

The Hamiltonian will now be summarized for one overtone excited CH oscillator interacting with the $N - 1$ *ring modes*. Normal coordinates for the ring $\{Q_2, \ldots, Q_N\}$ and for the overtone excited oscillator $\{Q_1\}$ are defined by uncoupling the overtone excited oscillator from the ring. The final form for the Hamiltonian then contains terms (both potential and kinetic) which couple the CH stretch mode to the ring modes. The derivation of the vibrational Hamiltonian was presented in Section II.C of Benzene I (103), and we will only summarize the final result here. The vibrational Hamiltonian may be partitioned into the terms

$$H = H_{\text{CH}} + H^0_{\text{ring}} + T_{\text{CH-ring}} + V^0_{\text{CH-ring}} + V^a_{\text{CH-ring}} + V^a_{\text{ring-ring}} \tag{135}$$

where the CH oscillator and ring Hamiltonians and the two quadratic CH-ring coupling terms are

$$\begin{aligned}
H_{\text{CH}} &= \frac{1}{2}P_1^2 + V_m(Q_1) \\
H^0_{\text{ring}} &= \frac{1}{2}\sum_{j=2}^{N} (P_j^2 + \lambda_j Q_j^2) \\
T_{\text{CH-ring}} &= P_1 \sum_{j=2}^{N} G_{1j} P_j \\
V^0_{\text{CH-ring}} &= Q_1 \sum_{j=2}^{N} F_{1j} Q_j,
\end{aligned} \tag{136}$$

In addition, $V^a_{\text{CH-ring}}$ and $V^a_{\text{ring-ring}}$ are anharmonic CH stretch-ring interactions and cubic plus quartic ring-ring interactions, respectively. Note that three terms in Eq. (135) provide chromophore-ring coupling; these are the two quadratic kinetic and potential coupling terms, and the anharmonic potential coupling terms.

4. Primitive Vibrational Basis Set

The primitive (or uncontracted) basis set for the vibrational dynamics consists of the direct product of harmonic oscillator functions for all ring normal modes times Morse oscillator functions for the overtone excited CH stretch. Thus for 21-mode planar ben-

zene, the basis functions are denoted

$$|\nu_1\rangle|\nu_2\rangle \cdots |\nu_{20}\rangle|\nu_{21}\rangle = |\nu_1, \nu_2, \ldots, \nu_{20}, \nu_{21}\rangle^0 \tag{137}$$

where modes 16 through 21, labeled in order of increasing energy, are the six high-frequency CH modes. (The vibrational modes for planar benzene are described further in Refs. 103–105.) For mode i, the vibrational quantum number can range from 0 to $\nu^i_{\max}$. As a result, the dimension of the primitive direct product space is (M is the number of modes),

$$d = \prod_{i=1}^{M} (\nu^i_{\max} + 1) \tag{138}$$

The value of d is frequently $>10^6$, so the wave operator contraction algorithm, described earlier in Section II.B.2, was used to select functions from the primitive space to build the active space.

D. Overtone Spectrum and Survival Probability

The CH ($\nu = 3$) overtone spectrum and survival probability for 21-mode planar benzene were computed using both the Pulay et al. (146) and the Maslen et al. (153) force fields. However, only results from calculations using the more recent DZP/SCF force field will be reviewed here. Results obtained using the Pulay et al. force field were presented in Benzene I–IV (103–105,34).

The primitive basis set was specified with the following values for the $\nu_{\max}$ parameters (mode 19 corresponds to the initially excited CH stretch): (15×3, 3×1, 3, 2×1), resulting in a basis set dimension of 1.37×10^{11}. Note that the CH modes which are not overtone excited at $t = 0$ each have two basis functions, with $\nu_i = 0$ or 1. The wave operator sorting algorithm with three iterations was then used to construct several active spaces with dimensions d_a varying from 1000 to 4500. It was found that the main features in the spectrum were approximately converged (intensities converged to ~10%) for $d_a = 4000$, consequently this value was used for all further comparisons. The necessary residues and eigenvalues were then computed with the RRGM. (For this value of d_a, 3500 Lanczos recursion steps were used; this number of steps converges the survival probability to at least 1.2 ps.)

The computed overtone spectrum is shown in Figure 9a (solid curve) and the survival probability is shown in Figure 9b. These results were obtained with the anharmonic scaling parameters $a = 0.95$ and $b = 0.90$. (The parameter a multiplies the CH-ring anharmonic interaction terms, while parameter b scales the ring-ring anharmonic terms.) The spectrum shows several secondary features near -80, -50, 20, 40, and 60 cm^{-1} relative to the central peak. The survival probability in Figure 9b exhibits rapid initial falloff, with $S(t)$ declining below 0.025 by $t = 10{,}000$ au (0.12 ps). After this time, the survival probability shows a series of low-amplitude (<0.05) recurrence oscillations extending to $t = 50{,}000$ au (1.2 ps) and beyond.

Alterations in the overtone spectrum and survival probability with respect to the anharmonic scaling parameters (a, b) was explored for the Pulay et al. force field in our earlier studies, Benzene II (104) and Benzene III (34). In the present studies based upon the Maslen et al. force field, only a limited exploration of the (a, b) parameter space was attempted. The overtone spectrum for another set of values, $a = b = 1.0$ (which corresponds to the unscaled anharmonic potential) are also shown in Figure 9a (dashed curve).

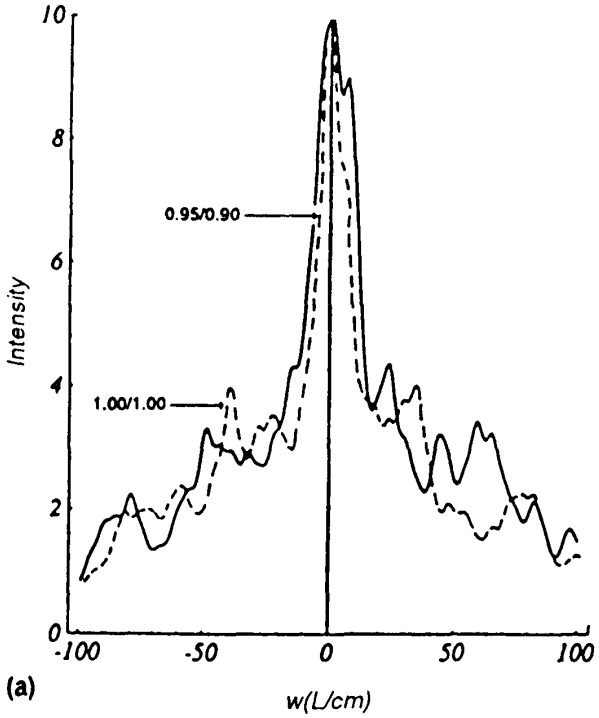

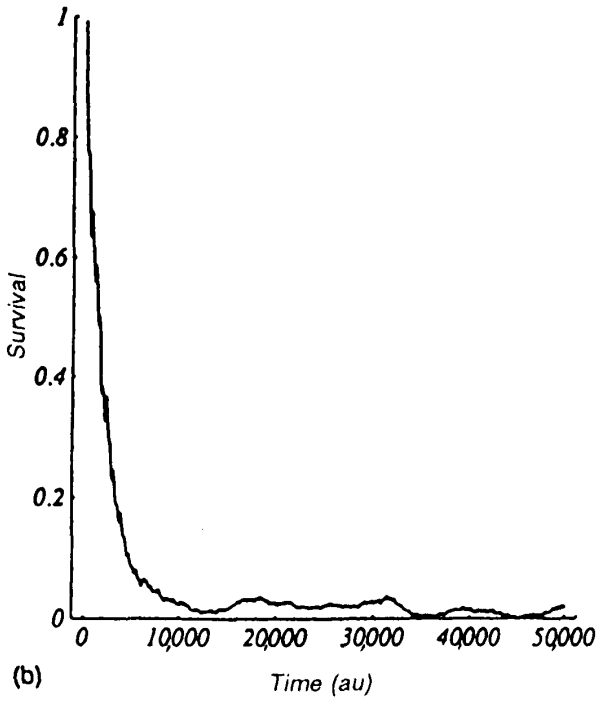

Figure 9 Smoothed CH (v = 3) overtone spectrum (a) and survival probability (b) computed from the DZP/SCF quartic force field. In (a), the peak intensity has been scaled to the value 10. Also in (a), spectra are shown for two values of the anharmonic scaling parameters: continuous curve, a = 0.95, b = 0.90; dashed curve, a = b = 1.0.

The spectral envelopes and the features in the vicinity of the main peak are similar, but some secondary features (for example, near -30 cm^{-1} and near $+60$ cm^{-1}) are shifted or altered in intensity.

E. Comparison with Experiment

We mentioned in Section IV.B.1 that two groups (6,125–127) have recently measured CH ($v = 3$) overtone spectra in benzene. The experimental overtone spectra from both of these groups were reconstructed with a set of Lorentzian line shapes centered at frequencies $\{\omega_j\}_1^N$,

$$I(\omega) = \sum_{j=1}^{N} \frac{A_j \Gamma^2}{(\omega - \omega_j)^2 + \Gamma^2} \tag{139}$$

where Γ is the common HWHM of each Lorentzian. Reconstructions of the two experimental spectra are shown in Figure 10a. Note that the frequency axis actually shows the frequency change from the position of the spectral peak. Also, we note that the Page et al. spectrum was reported over a slightly different frequency range [8727, 8927 cm^{-1}] than the Scotoni et al. spectrum [8700, 8900 cm^{-1}]. Differences in these two spectra apparently reflect different beam and detector conditions in the two experiments.

The Fourier transform of the frequency spectrum yields the survival amplitude. We define the limited Fourier transform in the frequency window $[\omega_1, \omega_2]$ as

$$s(t) = \left| \int_{\omega_1}^{\omega_2} I(\omega) e^{i\omega t} \, d\omega \right|^2 \tag{140}$$

so that the survival probability, normalized to unity at $t = 0$, is $S(t) = s(t)/s(0)$. The two survival probabilities computed in this manner are displayed in Figures 10b and 10c. In both survival plots, we note rapid falloff of $S(t)$ by $t = 10{,}000$ au, and recurrence phenomena at later times. In these two figures, the short-time decay, for $t < 10{,}000$ au, is probably too slow since addition of more states in a broader frequency window would decrease the lifetime of the initial state.

The CH ($v = 3$) spectrum and survival probability computed with the Maslen et al. force field will now be compared with the experimental results. The computed overtone spectra in Figure 9a have a slightly higher intensity over the interval -50 to $+70$ cm^{-1} when compared with the experimental spectrum of Scotoni et al. (127). The Scotoni et al. spectrum shows several absorption features in the interval -60 to -90 cm^{-1}, the most intense of which is about 40% of the peak intensity. The computed spectrum shows a secondary structure near -80 cm^{-1} with an intensity that is about 25% of the peak intensity. The overtone spectrum of Page et al. (6,125,126) has a lower intensity over the interval -30 to -100 cm^{-1} compared with either the computed spectrum or the experimental spectrum of Scotoni et al.

The computed survival probability shown in Figure 9b may be compared with the absolute square of the Fourier transform of the experimental overtone spectrum. Compared with the experimental results, the survival probability shown in Figure 9b shows more rapid falloff at short times, $t < 5000$ au. This is expected, since the experimental spectra are available over a limited (~200 cm^{-1}) frequency window. After $t = 20{,}000$ au (0.5 ps), the computed survival shows a sequence of low-amplitude recurrence oscillations; this amplitude agrees qualitatively with the experimental results.

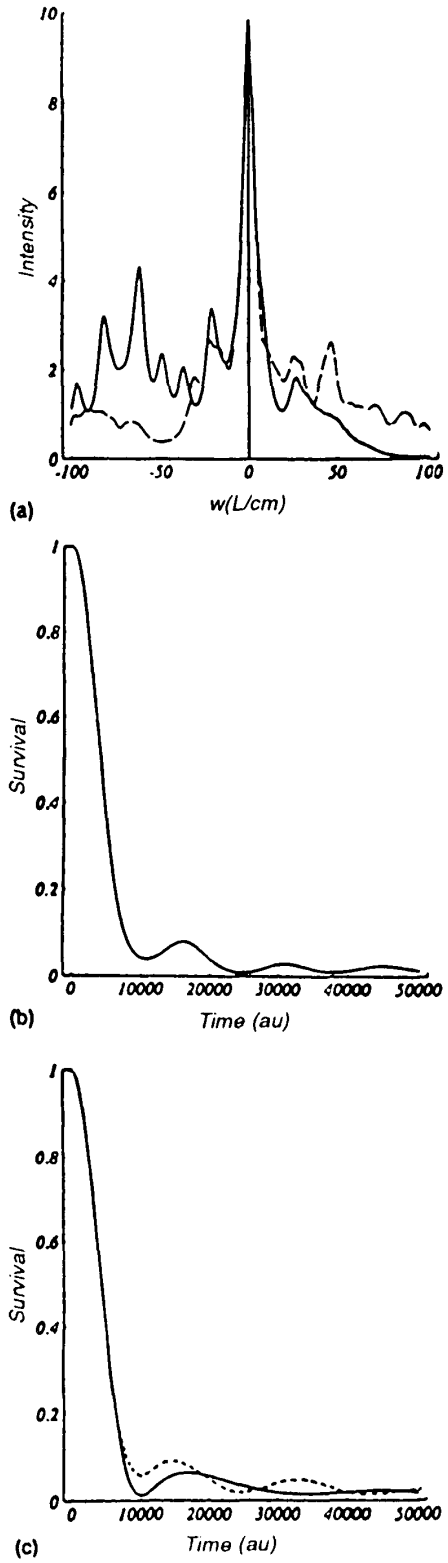

Figure 10 Reconstructions of the experimental $\nu = 3$ overtone spectra. (a) Reconstruction of the spectrum of Page et al. using 27 Lorentzians (dashed curve). Reconstruction of the spectrum of Scotoni et al. using 25 Lorentzians (continuous curve). This experimental data extends to about $+40\ cm^{-1}$ from the central peak. In both spectra, the central peak occurs at $8827\ cm^{-1}$. (b) Survival probability computed from the reconstruction of the spectrum of Page et al. (c) Survival probability computed from the reconstruction of the spectrum of Scotoni et al. When the absorption peak about $-70\ cm^{-1}$ from the central peak is artificially eliminated, the resulting survival probability (dashed curve) closely resembles the result shown in (b).

F. Time-Dependent Study of Energy Flow

A number of questions arise concerning IVR in a molecule like benzene: In terms of local modes, how rapidly does energy leave the initial state, where is the energy deposited, and how long does it take to get there? Does the energy spread over all of the initially unexcited vibrational modes in accord with a statistical theory? Does the energy in each mode approach a steady-state value, and if so, how long does it take to reach this state? Can sequential energy flow be observed in the bonds or local modes that are increasingly removed from the initially excited bond? In order to answer these basic questions, a time-dependent internal mode analysis must be performed (107).

The initial condition for the dynamics at $t = 0$ was again chosen to be a $v = 3$ overtone excited CH oscillator. The subsequent dynamics was then generated by propagating the time-dependent wave function in the active space. If we let $\mathbf{C}(t)$ denote the column vector of the expansion coefficients of the various basis functions at time t, then this state vector evolves according to the equation $\mathbf{C}(t) = \mathbf{U}(t)\mathbf{C}(t)$, where $\mathbf{U}(t) = \exp[-i\mathbf{H}t]$ is the time propagator associated with the vibrational Hamiltonian matrix $\mathbf{H}$. In order to evaluate the propagator, we used the Chebyshev expansion (Sec. II.C.3).

We will now develop the equations used to compute the local mode energies. After defining the local mode Hamiltonian, we will convert it into the normal coordinates that were used to define the basis sets used for the dynamical calculations. The local mode Hamiltonian, for mode i, is defined in terms of the harmonic oscillator potential (except for the initially excited stretch, as described later)

$$H_i^{(l)} = T_i^{(l)} + V_i^{(l)} = \frac{1}{2}(g_{ii}P_i^{(l)2} + k_{ii}R_i^2) \tag{141}$$

where R_i and $P_i^{(l)}$ are the local coordinate and conjugate momentum, and g_{ii} and k_{ii} and the appropriate diagonal G-matrix element and force constant, respectively. In order to begin the conversion to normal coordinates, we will use the relation $\mathbf{R} = \mathbf{LQ}$, where $\mathbf{L}$ converts from the column vector of normal coordinates to that of local coordinates. From this equation, we obtain

$$R_i = \sum L_{ij}Q_j \tag{142}$$

The conversion of the momentum operator is slightly more complicated, and begins as follows:

$$\frac{\partial}{\partial Q_i} = \sum \left(\frac{\partial R_j}{\partial Q_j}\right)\frac{\partial}{\partial R_j} = \sum L_{ji}\frac{\partial}{\partial R_i} \tag{143}$$

from which $\mathbf{P}^{(n)} = \mathbf{L}^t\mathbf{P}^{(l)}$, or $\mathbf{P}^{(l)} = (\mathbf{L}^t)^{-1}\mathbf{P}^{(n)}$. From the last of these equations, we obtain

$$P_i^{(l)} = \sum (L^t)_{ij}^{-1}P_j^{(n)} \tag{144}$$

When R_i and $P_i^{(l)}$ from Eqs. (142) and (144) are then substituted into Eq. (141), we obtain the desired local mode Hamiltonian expressed in terms of normal coordinates:

$$H_i^{(l)} = \frac{1}{2}\sum (P_j^{(n)}A_{jk}P_k^{(n)} + Q_jB_{jk}Q_k) \tag{145}$$

where the matrix elements are defined by

$$A_{jk} = (L^t)_{ij}^{-1}(L^t)_{ik}^{-1}g_{ii} \quad \text{and} \quad B_{jk} = L_{ij}L_{ik}k_{ii} \tag{146}$$

Equations (145) and (146) constitute the operational equations used to compute the local mode energies.

When considering the energy of the initially excited CH oscillator, the only difference from the above treatment is that we assume a Morse oscillator Hamiltonian. As mentioned earlier, the basis functions are products of a Morse oscillator function for the initially excited oscillator times harmonic oscillator functions for each of the 20 ring modes. As a result, the average energy for the initially excited oscillator is easily evaluated.

The average energy for local mode i at time t is then

$$\langle E_i(t)\rangle = \langle\psi(t)|H_i^{(l)}|\psi(t)\rangle \tag{147}$$

where $|\psi(t)\rangle$ is the wave function at time t. Using the expansion of the wave function in terms of the basis functions, $\{|n\rangle\}$, we obtain

$$\langle E_i(t)\rangle = \sum c^*_n c_m \langle n|H_i^{(l)}|m\rangle \tag{148}$$

where the time-dependent coefficients, as mentioned previously, were obtained through the Chebyshev propagation of the state vector $\mathbf{C}(t)$.

Figures 11 and 12 show the average local bond energies as a function of time during energy transfer from the CH (v = 3) overtone. This 2-ps time interval corresponds to about 200 CH or to about 80 CC or CCH harmonic vibrational periods. Figure 11 shows the decline in energy of the initially excited CH stretch, along with the growth in energy of the initially unexcited CH stretches, CH wags, and CC stretches. The energy variation of the three CCC ring modes is nearly "flat" on the scale of this figure (only 250 cm^{-1} at t = 2 ps). At short times, the initially unexcited modes *simultaneously* gain energy, but the *rate of energy uptake* follows the ordering: CH wags > CC stretches > CH stretches > CCC bends. The largest amount of energy goes into the six low-frequency CH wags (3200 cm^{-1} at 2 ps), followed by the six CC stretches (2500 cm^{-1} at 2 ps). In addition, about 600 cm^{-1} is acquired by the five initially unexcited CH stretches. We

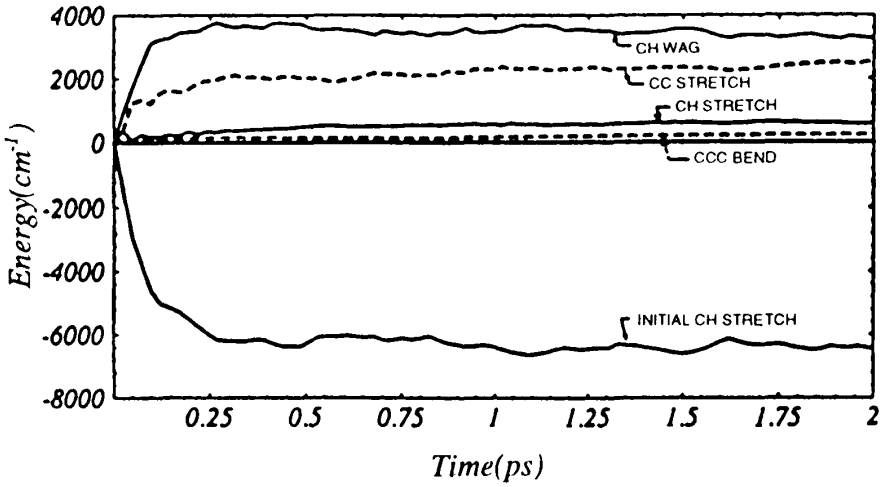

Figure 11 Variation in average vibrational energy (cm^{-1}) vs. time (ps) for relaxation from the CH (v = 3) overtone. The energy lost from the initially excited CH stretch, and the energy gain for the other local modes are shown. Total energies are shown for 6 CH stretch, 6 CC stretch, 6 CCH wag, and 3 CCC bend modes.

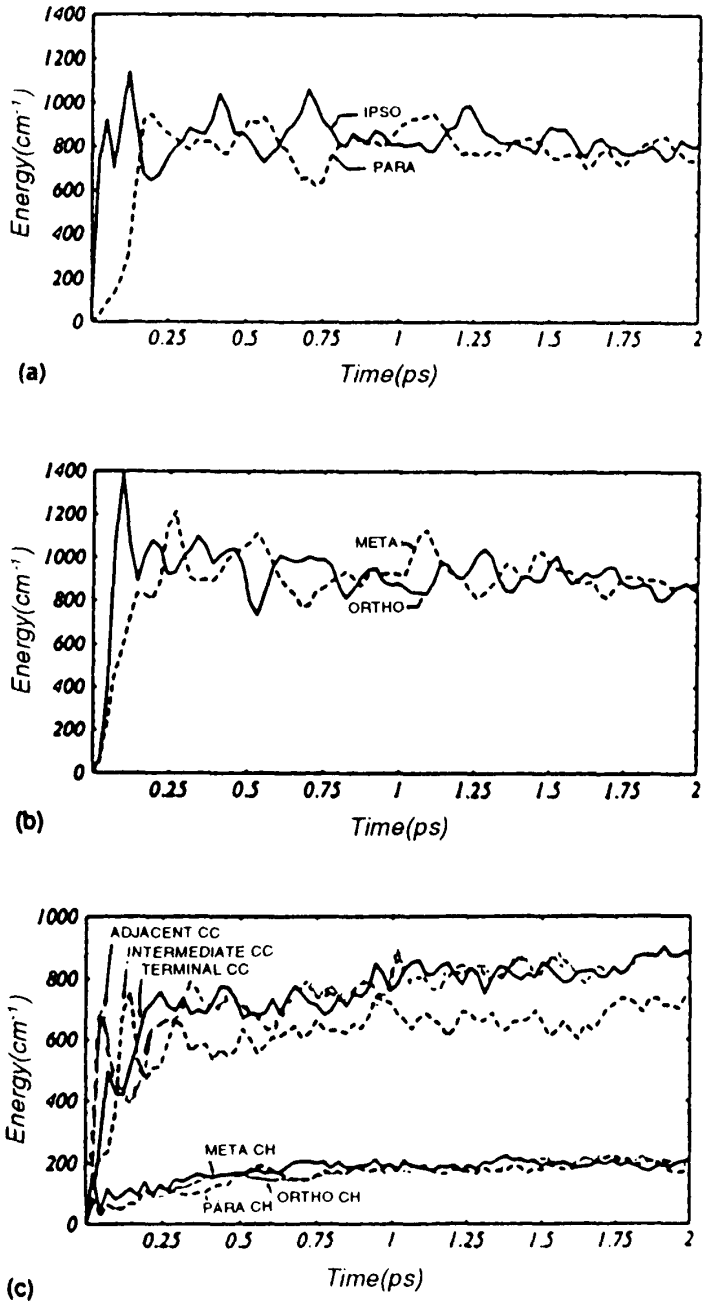

Figure 12 Average local mode vibrational energy (cm^{-1}) vs. time (ps) for relaxation from the CH (v = 3) overtone. The energy growth for three types of local mode are shown: (a) Energy in the *ipso* and *para* CCH wags. (b) Energy in the two *ortho* and the two *meta* wags. (c) Energy in the pairs of adjacent, central, and terminal CC stretches. The energies in the pair of *ortho* and *meta* CH stretches are also shown, along with the energy of the single *para* stretch.

also note that the energy in the CH wags and the CC stretches reaches an approximate steady-state value after about 1.0 ps, while the energy of the unexcited CH stretches and the CCC bends continues to slowly increase.

Figures 12a–c provide a more detailed view of the energy transfer. First, Figures 12a and b show the energy in the four types of CH wag motion, while Figure 12c shows

the energy in the three different types of CC stretches and the initially unexcited CH stretches. At short times, $t < 0.2$ ps, the energy goes first into the *ipso* CH wag, then into the adjacent CC stretches, then into both the central CC stretches and the *ortho* CH wags, then into both the terminal CC stretches and the *meta* CH wags, and finally into the *para* wag at about $t = 0.20$ ps. During the next 0.2 ps, part of the energy returns to the *ipso* CH wag. During the next 0.2 ps, the energies of the CH wags and the CC stretches approach their average steady-state values. *Then, for $t > 0.6$ ps, we note an important coherent oscillation involving wag (or CC motion) at opposite ends of the molecule: the wag (or CC stretch) energy oscillates between the ipso and para positions.* For example, at $t = 1.10$ ps and $t = 1.40$ ps, the *ipso* energy is relatively high, while the *para* energy is relatively low. At later times, this internal clock continues to beat with a period of about 0.3 ps, which can be considered as the time required to go from the *ipso* to the *para* position and then to return to the *ipso* position. These oscillations represent a relatively long distance correlation between local modes at opposite ends of the molecule. We also note that the *ortho* and *para* wag energies oscillate about 180° out of phase. Similar oscillations are observed between the adjacent and terminal CC stretches. Finally, Figure 12c also shows the time dependence of energy transfer into the five initially unexcited CH stretches. For $t < 2$ ps, these modes play a relatively secondary role. However, their energies increase slowly over the entire time interval.

In summary, this internal coordinate analysis of time-dependent energy flow leads to the following *relaxation mechanism*: (1) For $t < 0.05$ ps, energy lost from the CH stretch quickly excites the contiguous wag. (2) During the next 0.1 ps, the *ortho*, *meta*, and *para* CH wags each acquire about 450 cm^{-1} and the adjacent, central, and terminal CC stretches each acquire about 250 cm^{-1}. (3) After about 1 ps, the energies in the CH wags and CC stretches reach approximate steady-state values, but the energies in the initially unexcited CH stretches and in the CCC bends continue to slowly increase. (4) Superimposed upon the steady-state energies are coherent oscillations that involve energy flow between opposite ends of the molecule. (5) At $t = 2$ ps, about 37% of the energy released from the initially excited CH stretch ends up in the CCH wag motions, 29% goes to the CC stretches, 7% to the initially unexcited CH stretches, and 3% in the CCC bends. About 24% of the energy still remains in the initially excited CH stretch.

It is likely that the symmetrical cyclic structure of benzene plays an important role in the energy oscillations, except at short times ($t < 0.1$ ps) when the dynamics is principally localized within the overtone excited chromophore. We note that, after 1 ps, the energy of either the *ipso* or *para* wag is roughly equal to the energy of the two *meta* or two *ortho* wags, while the energy of the initially unexcited *para* CH stretch is similar to the energy of the two *meta* or two *ortho* CH stretches. This nonstatistical energy distribution is certainly influenced by the symmetry of the molecule.

V. CONCLUSIONS AND FUTURE DIRECTIONS

In this chapter, we began by describing a strategy for the computational investigation of both spectra and intramolecular dynamics in moderate-sized molecules. This strategy is based upon first contracting the very large primitive basis set to form the active space. Then, two approaches were described for extracting spectroscopic and dynamical information from the active space. The RRGM, possibly using a spectral filter to drive the Lanczos recursion algorithm, is an efficient approach for computing spectroscopic infor-

mation. Detailed time-dependent dynamical information can be computed through use of the Chebyshev expansion of the propagator.

These methods were then applied to two multimode systems. Applications to CD_3H emphasized the influence of the six background modes upon the dynamics of the three-mode CH chromophore. Particular emphasis was placed upon the fifth CH overtone near 16,000 cm^{-1}. In addition to detailed spectroscopic analysis, the IVR was studied by showing plots of chromophore populations and average mode populations for times up to 15 ps. Our applications to 21-mode planar benzene have emphasized the spectra and intramolecular dynamics associated with the second CH overtone near 9000 cm^{-1}. The computed spectra were compared with data from two experimental groups. Detailed time-dependent studies have elucidated the mechanism for energy flow from the initial hot spot. Plots of local mode energies for times less than 2 ps allowed us to assess the role of the CH wags, CC stretches, and CH stretches in the energy transfer process.

There are a number of remaining *theoretical and computational issues* to explore in intramolecular dynamics and spectroscopy. We will list some of these:

1. It will be important to continue the investigation of perturbative approaches for constructing active spaces, including the further development and application of the multilevel Bloch space S^0 in the production codes.
2. It would be interesting to establish the possible relationships between the Bloch formalism for constructing effective Hamiltonians and other perturbative approaches, including Van Vleck perturbation theory (161).
3. There is considerable interest in the development and testing of spectral filters for use in Lanczos recursion procedures. Although progress has been made in the testing of a Green function filter for incorporation in Lanczos codes (74), it remains to be seen how well this will perform in difficult molecular problems having many coupled states (such as the benzene overtones).
4. It will be important to continue the development of the effective Hilbert space formalism (58) for converting problems with explicitly time-dependent Hamiltonians to stationary problems in an extended Hilbert space. This feature will permit the use of propagation algorithms now used for problems with time-independent Hamiltonians to also be used for pulsed laser-molecule interactions. Peskin and Moiseyev (162) have recently developed and applied a version of the extended space formalism (they refer to it as the (t, t') formalism).
5. It will be of interest to explore the connections between scaling theories (163) of energy flow in quantum number state-space with detailed computational results on specific systems. Interesting results have recently been obtained for model lattices (164), but the question remains as to how useful these approaches will be for more complex multimode systems.

With respect to *computational studies* of the spectra and intramolecular dynamics in interesting molecules, there are many interesting possibilities, including the following:

1. Time-dependent studies of the benzene isotopomers (165), such as C_6H_5D and $C_6H_3D_3$. These molecules have different sequences of vibrational resonances compared to C_6H_6, which should strongly influence the energy flow.
2. Intramolecular dynamics in S_1 *p*-fluorotoluene. The availability of considerable experimental information on this electronically excited molecule and the availability of an approximate force field suggests that this would be an interesting

system to investigate. We have made comparisons between quantum calculations and previous classical trajectory calculations (166).

3. Overtone spectroscopy and dynamics in fluoroform, CF_3H. This molecule has been the focus of many experimental studies (3). Computational studies on the influence of the background modes on the CH chromophore dynamics are now underway on a new ab initio force field (167).
4. Overtone spectroscopy and dynamics in CH_4. The availability of new ab initio force field information (168) and the possibility of new experiments suggest that quantum dynamical studies of this molecule would be both timely and interesting.

ACKNOWLEDGMENTS

These studies at the University of Texas were supported in part by the National Science Foundation and the Robert Welch Foundation. We wish to thank Prof. Claude Leforestier for his many contributions to our work, particularly for his development of the major production code which was used in all of these computational studies.

REFERENCES

1. K. K. Lehman, G. Scoles, and B. H. Pate, *Ann. Rev. Phys. Chem. 45*: 241 (1994).
2. T. Uzer, *Phys. Rep., 199*: 73 (1991).
3. M. Quack, *Ann. Rev. Phys. Chem., 41*: 839 (1990).
4. A. A. Stuchebrukhov and R. A. Marcus, *J. Chem. Phys., 98*: 6044 (1993).
5. A. A. Stuchebrukhov, A. Mehta, and R. A. Marcus, *J. Phys. Chem., 97*: 12491 (1993).
6. R. H. Page, Y. R. Shen, and Y. T. Lee, *J. Chem. Phys., 88*: 4621 (1988).
7. P. Brumer and M. Shapiro, *Ann. Rev. Phys. Chem., 43*: 257 (1992).
8. P. H. Winston, *Artificial Intelligence*, Addison-Wesley, Reading, MA, 1984, Ch. 4.
9. P. R. Stannard and W. M. Gelbart, *J. Phys. Chem., 85*: 3592 (1981).
10. E. L. Sibert III, W. P. Reinhardt, and J. T. Hynes, *J. Chem. Phys., 81*: 1115 (1984).
11. J. S. Hutchinson, J. T. Hynes, and W. P. Reinhardt, *Chem. Phys. Lett., 108*: 35 (1984).
12. J. S. Hutchinson, *J. Chem. Phys., 82*: 22 (1985).
13. J. V. Tietz and S.-I. Chu, *Chem. Phys. Lett., 101*: 446 (1983).
14. J. Chang and R. E. Wyatt, *Chem. Phys. Lett., 121*: 307 (1985).
15. J. Chang and R. E. Wyatt, *J. Chem. Phys., 85*: 1826 (1986).
16. S. M. Lederman and R. A. Marcus, *J. Chem. Phys., 88*: 6312 (1988).
17. S. M. Lederman, S. J. Klippenstein, and R. A. Marcus, *Chem. Phys. Lett., 146*: 7 (1988).
18. D. T. Colbert and E. L. Sibert III, *J. Chem. Phys., 94*: 6519 (1991).
19. Y. Zhang and R. A. Marcus, *J. Chem. Phys., 96*: 6065 (1992).
20. C. Iung and C. Leforestier, *Comp. Phys. Comm., 63*: 135 (1991).
21. C. Iung and C. Leforestier, *J. Chem. Phys., 97*: 2481 (1992).
22. C. Bloch, *Nucl. Phys., 6*: 329 (1958).
23. P. Durand and J. P. Malrieu, *Ab initio Methods in Quantum Chemistry* (K. P. Lawley, ed.), Wiley, New York, 1987.
24. R. E. Wyatt, C. Iung, and C. Leforestier, *J. Chem. Phys., 97*: 3458 (1992).
25. B. H. Brandow, *Rev. Mod. Phys., 39*: 771 (1967).
26. B. H. Brandow, *Adv. Quantum Chem., 10*: 187 (1977).
27. P. O. Lowdin, *Int. J. Quantum Chem., 2*: 867 (1968).
28. L. Lindgren, *J. Phys., B7*: 2441 (1974).
29. D. J. Klein, *J. Chem. Phys., 61*: 786 (1974).

30. J. P. Malrieu, P. Durand, and J. P. Daudey, *J. Phys.*, *A18*: 809 (1985).
31. G. Jolicard, *Chem. Phys.*, *127*: 31 (1988).
32. G. Jolicard and J. Perié, *Adv. Mult. Proc. Spec.*, *8*: 1 (1993).
33. G. Jolicard and A. Grosjean, *J. Chem. Phys.*, *95*: 1920 (1991).
34. R. E. Wyatt and C. Iung, *J. Chem. Phys.*, *98*: 5191 (1993).
35. A. Nauts and R. E. Wyatt, *Phys. Rev. Lett.*, *81*: 2238 (1983).
36. R. E. Wyatt, *Adv. Chem. Phys.*, *73*: 231 (1989).
37. C. Lanczos, *J. Res. Nat. Bur. Stand.*, *45*: 58 (1950).
38. J. K. Cullum and R. A. Willoughby, *Lanczos Algorithms for Large Symmetric Eigenvalue Computations*, Birkhauser, Boston, 1985.
39. G. H. Golub and C. F. Van Loon, *Matrix Computations*, Johns Hopkins, Baltimore, 1989, Chap. 9.
40. B. N. Parlett, *The Symmetric Eigenvalue Problem*, Prentice-Hall, Englewood Cliffs, N.J., 1980, Chap. 13.
41. Y. Saad, *Numerical Methods for Large Eigenvalue Problems*, Halsted, New York, 1992, Chap. VI.
42. J. B. Rosser, C. Lanczos, M. R. Hestenes, and W. Karush, *J. Res. Nat. Bur. Stand.*, *47*: 291 (1951).
43. G. Strang, *Introduction to Applied Mathematics*, Wellesley-Cambridge, Wellesley, 1986, pp. 389–392.
44. D. G. Pettifor and D. L. Weaire (eds.), *The Recursion Method and Its Applications*, Springer, Berlin, 1985.
45. N. S. Sehmi, *Large Scale Structural Eigenanalysis Techniques*, Wiley, New York, 1989.
46. G. H. Golub and D. P. O'Leary, *SIAM Rev.*, *31*: 50 (1989).
47. H. Ehrenreich, F. Seitz, and D. Turnbull (eds.), *Solid State Physics*, Vol. 35, Academic, New York, 1980.
48. Proceedings of the Cornelius Lanczos International Centenary Conference, North Carolina State University, 1993.
49. R. Riedinger and M. Benard, *J. Chem. Phys.*, *94*: 1222 (1991).
50. H. O. Karlsson, G. L. Bendazzoli, O. Goscinski, and S. Evangelisti, to appear.
51. H. D. Meyer and S. Pal, *J. Chem. Phys.*, *91*: 6195 (1989); T. J. Godin and R. Haydock, *Comp. Phys. Comm.*, *64*: 123 (1991).
52. K. F. Milfeld and N. Moiseyev, *Chem. Phys. Lett.*, *130*: 145 (1986).
53. M. Kaluza, *Comp. Phys. Comm.*, *79*: 425 (1994); G. C. Groenboom and H. M. Buck, *J. Chem. Phys.*, *92*: 4374 (1990).
54. M. D'Mello, C. Duneczky, and R. E. Wyatt, *Chem. Phys. Lett.*, *148*: 169 (1988); C. Duneczky and R. E. Wyatt, *J. Phys. B*, *21*: 3727 (1988).
55. O. Kolin, C. Leforestier, and N. Moiseyev, *J. Chem. Phys.*, *89*: 6836 (1988).
56. E. Haller, H. Koppel, and L. S. Cederbaum, *J. Mol. Spec.*, *111*: 377 (1985).
57. K. Marshall and J. Hutchinson, *J. Phys. Chem.*, *91*: 3219 (1987); *J. Chem. Phys.*, *95*: 3232 (1991).
58. G. Yao and R. E. Wyatt, *J. Chem. Phys.*, *101*: 1904 (1994).
59. G. Charron and T. Carrington, Jr., *Mol. Phys.*, *79*: 13 (1993); A. McNichols and T. Carrington, Jr., *Chem. Phys. Lett.*, *202*: 464 (1993); M. J. Bramley and T. Carrington, Jr., *J. Chem. Phys.*, *99*: 8519 (1993); M. J. Bramley, J. W. Tromp, T. Carrington, Jr., and G. C. Corey, *J. Chem. Phys.*, *100*: 6175 (1994).
60. N. Ben-Tal and N. Moiseyev, *J. Phys. A*, *24*: 3593 (1991).
61. K. V. Vasavada and J. H. Freed, *Comp. Phys. Sept./Oct.*, *61*: (1989); D. J. Schneider and J. H. Freed, *Adv. Chem. Phys.*, *73*: 387 (1989).
62. I. M. Barbour, N. E. Behilil, P. E. Gibbs, M. Rafig, K. J. M. Moriarty, and G. Schierholz, *J. Comp. Phys.*, *68*: 227 (1987); A. N. Burkitt and A. C. Irving, *Comp. Phys. Comm.*, *59*: 447 (1990); A. Duncan and R. Roskies, *Phys. Rev. D*, *31*: 364 (1985); J.-W. Choe, A.

Duncan, and R. Roskies, *Phys. Rev. D, 37*: 472 (1988); J. R. Hiller, *Phys. Rev. D, 43*: 2418 (1991); M. Kaluza and H. C. Pauli, *Phys. Rev. D, 45*: 2968 (1992).
63. J. P. Brunet, R. A. Freisner, R. E. Wyatt, and C. Leforestier, *Chem. Phys. Lett., 153*: 425 (1988); C. Leforestier and R. E. Wyatt, in H. L. Dai and R. W. Field (eds.), *Molecular Dynamics and Spectroscopy by Stimulated Emission Pumping*, World Scientific, River Edge, New Jersey, 1995, p. 755.
64. F. LeQuere and C. Leforestier, *J. Chem. Phys., 92*: 247 (1990); *Chem. Phys. Lett., 189*: 537 (1992).
65. N. Martin Poulin, M. J. Bramley, and T. Carrington, Jr., Abstract, Second Canadian Conference on Computational Chemistry, 1994.
66. H. O. Karlsson and O. Goscinski, *J. Phys. B, 25*: 5015 (1992).
67. J. G. F. Francis, *Comp. J., 4*: 265 (1961/62).
68. B. Parlett, *SIAM Rev., 6*: 275 (1964); G. W. Stewart, *Introduction to Matrix Computations*, Academic, New York, 1973, Chap. 7.
69. R. E. Wyatt and D. Scott, in *Large Eigenvalue Problems* (J. Cullum and R. Willoughby, eds.), North-Holland, Amsterdam, 1986, p. 67.
70. T. Ericsson and A. Ruhe, *Math. Comp., 35*: 1251 (1980).
71. F. Webster, P. J. Rossky, and R. A. Friesner, *Comp. Phys. Comm., 63*: 494 (1991).
72. H. Kono, *Chem. Phys. Lett., 214*: 137 (1993).
73. C. Iung and C. Leforestier, *J. Chem. Phys. 102*:8453 (1995).
74. R. E. Wyatt, *J. Chem Phys. 103*:8433 (1995).
75. R. Kosloff, *J. Phys. Chem., 92*: 2087 (1988).
76. R. C. Mowrey and D. J. Kouri, *J. Chem. Phys., 84*: 6466 (1986).
77. H. Tal-Ezer and R. Kosloff, *J. Chem. Phys., 81*: 3967 (1984).
78. W. J. Thompson, *Comp. Phys., 8*: 161 (1994).
79. *Handbook of Mathematical Functions* (M. Abramowitz and I. Stegun, eds.), Dover, New York, 1972.
80. M. S. Child and L. Halonen, *Adv. Chem. Phys., 57*: 1 (1984).
81. G. A. Voth, R. A. Marcus, and A. H. Zewail, *J. Chem. Phys., 81*: 5494 (1984).
82. J. W. Perry, D. J. Moll, A. Kuppermann, and A. H. Zewail, *J. Chem. Phys., 82*: 1195 (1985).
83. W. H. Green, W. D. Lawrance and C. B. Moore, *J. Chem. Phys., 86*: 6000 (1987).
84. J. Segall, R. N. Zare, H. R. Dübal, M. Lewerenz, and M. Quack, *J. Chem. Phys., 86*: 634 (1987).
85. A. Campargue, F. Stoeckel, M. Chenevier, and H. Ben Kraiem, *J. Chem. Phys., 87*: 5598 (1987).
86. A. Campargue and F. Stoeckel, *J. Chem. Phys., 85*: 1220 (1986).
87. E. Kauppi and L. Halonen, *J. Chem. Phys., 90*: 6980 (1989).
88. D. T. Colbert and E. L. Sibert, *J. Chem. Phys., 91*: 350 (1989).
89. L. Halonen and E. Kauppi, *J. Chem. Phys., 92*: 3278 (1990).
90. H. Hollenstein, M. Lewerenz, and M. Quack, *Chem. Phys. Lett., 165*: 175 (1990).
91. M. Lewerenz and M. Quack, *J. Chem. Phys., 88*: 5408 (1988).
92. H. R. Dübal, T. K. Ha, M. Lewerenz, and M. Quack, *J. Chem. Phys., 91*: 6698 (1989).
93. R. Marquardt and M. Quack, *J. Chem. Phys., 95*: 4854 (1991).
94. H. R. Dübal and M. Quack, *J. Chem. Phys., 81*: 3779 (1984).
95. C. Iung and C. Leforestier, *J. Chem. Phys., 90*: 3198 (1989).
96. G. J. Scherer, K. K. Lehmann, and W. Klemperer, *J. Chem. Phys., 81*: 5319 (1984).
97. G. A. Voth, R. A. Marcus, and A. H. Zewail, *J. Chem. Phys., 82*: 1195 (1985).
98. P. Barchewitz, *Spectroscopie Atomique et Moleculaire*, Vol. 2, Masson, Paris, 1971.
99. D. L. Gray and A. G. Robiette, *Mol. Phys., 37*: 1901 (1979).
100. J. C. Light, I. P. Hamiltonian, and J. V. Lill, *J. Chem. Phys., 82*: 1400 (1985).
101. D. L. Gray and A. G. Robiette, *Mol. Phys., 37*: 1901 (1979).
102. C. Iung, C. Leforestier, and R. E. Wyatt, *J. Chem. Phys., 98*: 6722 (1993).

103. R. E. Wyatt, C. Iung, and C. Leforestier, *J. Chem. Phys.*, *97*: 3458 (1992).
104. R. E. Wyatt, C. Iung, and C. Leforestier, *J. Chem. Phys.*, *97*: 3477 (1992).
105. R. E. Wyatt and C. Iung, *J. Chem. Phys.*, *98*: 3577 (1993).
106. R. E. Wyatt and C. Iung, *J. Chem. Phys.*, *98*: 6758 (1993).
107. C. Iung and R. E. Wyatt, *J. Chem. Phys.*, *99*: 2261 (1993).
108. L. J. Brenner, J. Senekowitsch, and R. E. Wyatt, *Chem. Phys. Lett.*, *215*: 63 (1993).
109. J. W. Ellis, *Trans. Farad. Soc.*, *25*: 888 (1929).
110. R. T. Birge and H. S. Sponer, *Phys. Rev.*, *28*: 259 (1926).
111. B. R. Henry and W. Siebrand, *J. Chem. Phys.*, *49*: 5369 (1968).
112. R. J. Hayward and B. R. Henry, *Chem. Phys.*, *12*: 387 (1976).
113. B. R. Henry, *Acc. Chem. Res.*, *10*: 207 (1977).
114. R. Wallace, *Chem. Phys.*, *11*: 189 (1975).
115. M. L. Sage, *J. Phys. Chem.*, *83*: 1455 (1979).
116. D. F. Heller, *Chem. Phys. Lett.*, *61*: 583 (1979).
117. E. J. Heller and W. M. Gelbart, *J. Chem. Phys.*, *73*: 626 (1980).
118. M. E. Kellman, *Chem. Phys. Lett.*, *94*: 331 (1983).
119. L. Halonen, *Chem. Phys. Lett.*, *87*: 221 (1987).
120. D. F. Heller and S. Mukamel, *J. Chem. Phys.*, *70*: 463 (1979).
121. R. L. Swofford, M. E. Long, and A. C. Albrecht, *J. Chem. Phys.*, *65*: 179 (1976),.
122. R. L. Swofford, M. S. Burberry, J. A. Morrell, and A. C. Albrecht, *J. Chem. Phys.*, *66*: 664 (1977).
123. M. E. Long, R. L. Swofford, and A. C. Albrecht, *Science*, *191*: 183 (1976).
124. K. V. Reddy, D. F. Heller, and M. J. Berry, *J. Chem. Phys.*, *76*: 2814 (1982).
125. R. H. Page, Y. R. Shen, and Y. T. Lee, *J. Chem. Phys.*, *88*: 5362 (1988).
126. R. H. Page, Y. R. Shen, and Y. T. Lee, *Phys. Rev. Lett.*, *59*: 1293 (1987).
127. M. Scotoni, A. Boschetti, N. Oberhofer, and D. Bassi, *J. Chem. Phys.*, *94*: 971 (1991).
128. M. Scotoni, C. Leonardi, and D. Bassi, *J. Chem. Phys.*, *95*: 8655 (1991).
129. D. A. Chernoff, J. D. Meyers, and J. G. Pruett, *J. Chem. Phys.*, *85*: 3732 (1986).
130. E. L. Sibert, W. P. Reinhardt, and J. T. Hynes, *J. Chem. Phys.*, *81*: 1115, 1135 (1984).
131. S. Shi and W. H. Miller, *Theor. Chim. Acta*, *68*: 1 (1985).
132. V. Buck, R. B. Gerber, and M. A. Ratner, *J. Chem. Phys.*, *81*: 3393 (1984).
133. Y. Zhang, S. J. Klippenstein, and R. A. Marcus, *J. Chem. Phys.*, *94*: 7319 (1991).
134. Y. Zhang and R. A. Marcus, *J. Chem. Phys.*, *96*: 6065 (1992).
135. Y. Zhang and R. A. Marcus, *J. Chem. Phys.*, *97*: 5283 (1992).
136. P. J. Nagy and W. L. Hase, *Chem. Phys. Lett.*, *54*: 73 (1978).
137. D. H. Lu, W. L. Hase, and R. J. Wolf, *J. Chem. Phys.*, *85*: 4422 (1986).
138. R. J. Wolf, D. S. Bhatia, and W. L. Hase, *Chem. Phys. Lett.*, *132*: 493 (1986).
139. D. H. Lu and W. L. Hase, *Chem. Phys. Lett.*, *142*: 187 (1987).
140. D. H. Lu and W. L. Hase, *J. Phys. Chem.*, *92*: 3217 (1988); *J. Chem. Phys.*, *89*: 6723 (1988); *91*: 7490 (1989).
141. D. L. Clarke and M. A. Collins, *J. Chem. Phys.*, *86*: 6871 (1987); *87*: 5912 (1987).
142. K. L. Bintz, D. L. Thompson, and J. W. Brady, *J. Chem. Phys.*, *85*: 1848 (1986); *86*: 4411 (1987); *Chem. Phys. Lett.*, *131*: 398 (1986).
143. Y. Guan and D. L. Thompson, *J. Chem. Phys.*, *88*: 2355 (1988).
144. J. M. Gomez-Llorente, O. Hahn, and H. S. Taylor, *J. Chem. Phys.*, *92*: 2762 (1990).
145. A. Garcia-Ayllon, J. Santamaria, and G. S. Ezra, *J. Chem. Phys.*, *89*: 801 (1988).
146. P. Pulay, G. Fogarasi, and J. E. Boggs, *J. Chem. Phys.*, *74*: 3999 (1981).
147. P. Pulay, *J. Chem. Phys.*, *85*: 1703 (1986).
148. H. Guo and M. Karplus, *J. Chem. Phys.*, *89*: 4235 (1988).
149. A. G. Ozkabak and L. Goodman, *J. Chem. Phys.*, *87*: 2564 (1987).
150. L. Goodman, A. G. Ozkabak, and K. B. Wiberg, *J. Chem. Phys.*, *91*: 2069 (1989).
151. A. G. Ozkabak, L. Goodman, and K. B. Wiberg, *J. Chem. Phys.*, *92*: 4115 (1990).

152. L. Goodman, A. G. Ozkabak, and S. N. Thakur, *J. Phys. Chem.*, *95*: 9044 (1991).
153. P. E. Maslen, N. C. Handy, R. D. Amos, and D. Jayatilaka, *J. Chem. Phys.*, *97*: 4233 (1992).
154. N. C. Handy, P. E. Maslen, R. D. Amos, J. S. Andrews, C. W. Murray, and G. J. Laming, *CHem. Phys. Lett.*, *197*: 506 (1992).
155. E. Albertazzi and F. Zerbetto, *Chem. Phys.*, *164*: 91 (1992).
156. A. Berces and T. Ziegler, *Chem. Phys. Lett.*, *203*: 592 (1993).
157. A. Berces and T. Ziegler, *J. Chem. Phys.*, *98*: 4793 (1993).
158. E. B. Wilson, Jr., *Phys. Rev.*, *45*: 706 (1934).
159. C. Iung and C. Leforestier, *Chem. Phys.*, *155*: 369 (1991).
160. M. A. Parasieu, I. Suzuki, and J. Overend, *J. Chem. Phys.*, *42*: 2335 (1965); A. R. Hoy, I. M. Mills, and G. Strey, *Mol. Phys.*, *24*: 1265 (1972).
161. E. L. Sibert III, *J. Chem. Phys.*, *88*: 4378 (1988); *Int. Rev. Phys. Chem.*, *9*: 1 (1990).
162. U. Peskin and N. Moiseyev, *J. Chem. Phys.*, *99*: 4590 (1993).
163. S. A. Schofield and P. G. Wolynes, *J. Chem. Phys.*, *98*: (1993).
164. S. A. Schofield, P. G. Wolynes, and R. E. Wyatt, *Phys. Rev. Lett. 74*:3720 (1995).
165. R. E. Wyatt and C. Iung, to appear.
166. C. S. Parmenter, *J. Phys. Chem.*, *86*: 1735 (1982); D. M. Moss and C. S. Parmenter, *J. Chem. Phys.*, *98*: 6897 (1993).
167. A. Maynard, R. E. Wyatt and C. Iung, *J. Chem. Phys. 103*:8372 (1955).
168. T. Lee, J. M. L. Martin, and P. R. Taylor, *J. Chem. Phys.*, *102*: 254 (1995).

in terms of Chebyshev polynomials (see Sec. II.C.3). The result is that this evolving state is known in terms of an expansion in zero-order states $|n\rangle^0$:

$$|6\nu_1(t)\rangle = \sum_{|n\rangle^0} c_n(t)|n\rangle^0 \tag{121}$$

The results obtained with this method are displayed in Figure 7. In this figure, we have displayed, as a function of time, the survival probability $P_{6\nu_1}(t)$,

$$P_{6\nu_1}(t) = |^0\langle 6\nu_1|6\nu_1(t)\rangle|^2 \tag{122}$$

the overall population $P_{CH}(t)$ of the chromophore,

$$P_{CH}(t) = \sum_{n^{(1)}n^{(5)}l^{(5)}} |^0\langle n^{(1)}, 0, 0, 0, 0, n^{(5)}, l^{(5)}, 0, 0|6\nu_1(t)\rangle|^2 \tag{123}$$

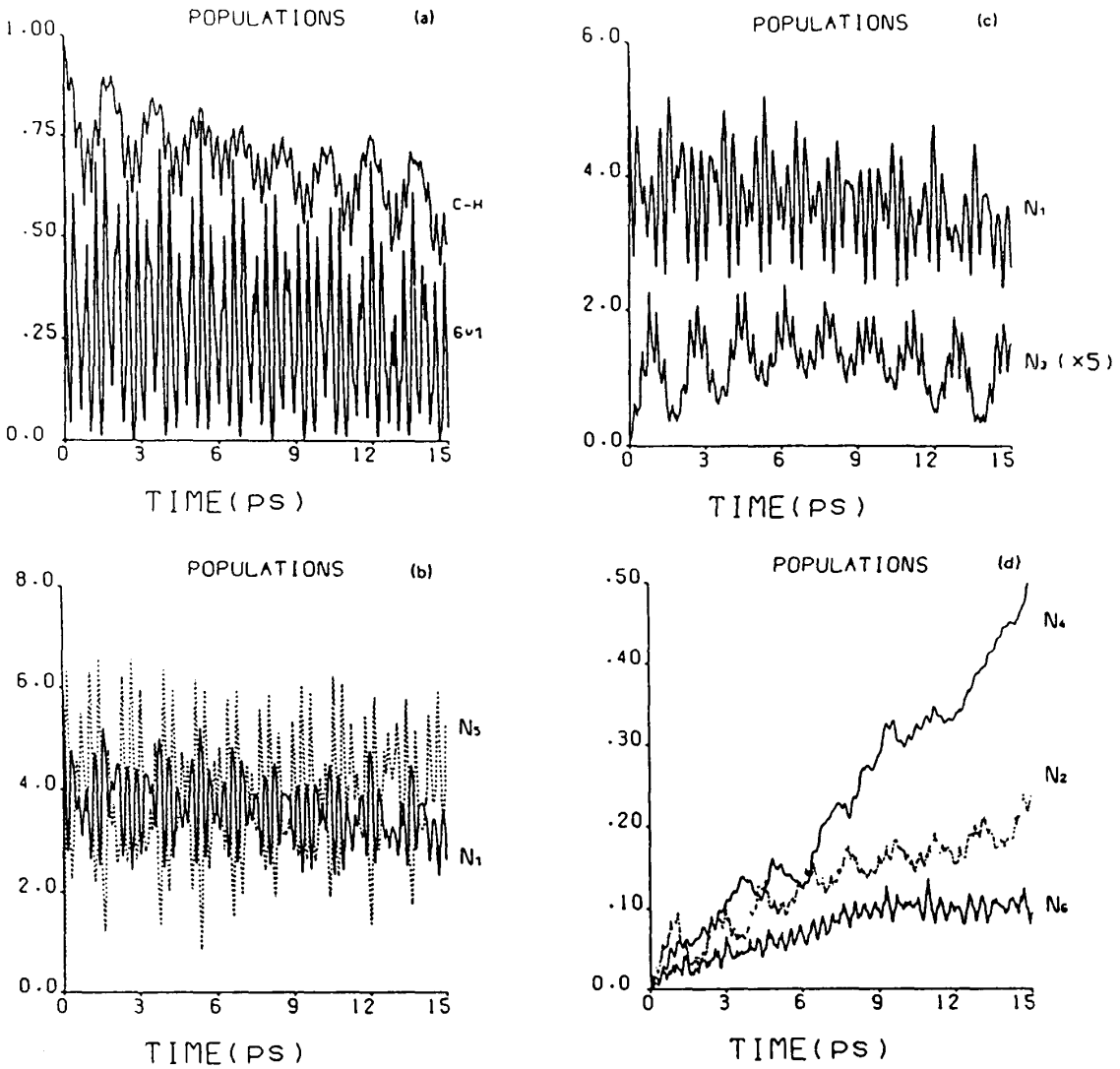

Figure 7 Time evolution of the initial $|6\nu_1\rangle^0$ state, computed using the Chebyshev propagation scheme: (a) survival probability (lower curve) and overall chromophore population (upper curve, defined in Eq. (123). (b), (c), and (d) Vibrational mode populations, defined in Eq. (124).

3

Picturing Quantized Intramolecular Vibrational Energy Flow: Action Diffusion, Localization, and Scaling

SARAH A. SCHOFIELD

University of Texas at Austin, Austin, Texas

PETER G. WOLYNES

University of Illinois at Urbana-Champaign, Urbana, Illinois

1. INTRODUCTION

Interest in how quantum mechanics affects vibrational energy flow within a single molecule predates the discovery of the Schrödinger equation (1). Nevertheless, understanding intramolecular vibrational energy redistribution (IVR) remains an area of investigation in chemical physics today (2). How can a problem have such longevity? Clearly it must be both important, so that interest remains sustained, and either very difficult, so that no approach makes much headway, or very rich in complexity, so there is much to do. Intramolecular vibrational energy flow shares all three of these features.

IVR is important because it is an issue in understanding all chemical change. It was quite clear to the early theoretical chemical kineticists that a molecule must be energetically activated in order to decompose unimolecularly (3). It was equally clear that the activation of the molecule need not be too specific since rates of decomposition seemed to depend primarily on the temperature of the reaction. Thus how energy deposited in one mode of motion within a molecule was transmuted into energy in a reactive mode was clearly of interest. In the early days it was not clear how complete energy flow would be. Indeed, just as Planck believed that quantum laws of blackbody radiation might be the result of limitations on the way in which energy was transferred between light and matter, such limitations were thought to be a possibility within the molecules

themselves. The great success of completely statistical theories of unimolecular decomposition took quite some time to emerge, but the remarkable achievements of the quantum mechanical Rice-Ramsperger-Kassel-Marcus (RRKM) theory (3) eventually led those motivated to study intramolecular energy flow to question whether it ever was a significant limiting process. The ongoing quest for controlling chemical reactions via laser pulses (4) is therefore considered quixotic by some but, nevertheless, it provides the motive for much of the current interest.

The problem of understanding quantum intramolecular vibrational energy flow has also proved to be quite difficult. One fundamental difficulty plaguing both theory and experiment is that even a moderate-sized molecule possesses a huge multidimensional state-space describing how vibrational energy is partitioned between many different modes of motion of the molecule. Most experiments are not simultaneously equally sensitive to all modes. Similarly, because a molecule is a quantum mechanical object, it is hard to devise experiments that, without violating the Heisenberg uncertainty principle, tell us that energy goes here first, then there, and so on. The high dimensionality of the state-space also makes difficult the direct solution of the Schrödinger equation for IVR problems. Indeed, this has become practical only in recent years.

The IVR problem can be intricate. There are several reasons why we should expect a rich variety of situations in the intramolecular energy flow problem. One sign is that even an individual physical chemist often holds contradictory views on the nature of energy flow itself. These views have grown up from examining different classes of experimental results. When thinking as chemical kineticists we are surprised by the idea of limited energy flow and almost immediately jump to a belief in a kind of global statistical chaos. On the other hand, as spectroscopists we expect nearly every spectral line to be classified and given a specific name. This argues against chaos and for a great regularity of motion. The reconciliation of these two views clearly involves some kind of transition between the two regimes. The correspondence principle also suggests a richness of mechanism. Both few- and many-dimensional classical mechanical problems involving flow of energy between different modes of motion have been seriously investigated in many fields, ranging from astronomy to plasma physics (2,5). An amazingly rich picture involving the possibility of sometimes coexisting perfectly regular motions, and extraordinarily stochastic and irregular motions applies in low-dimensional systems. There have been proposed a variety of mechanisms for slow diffusional change of near constants of the motion which can be seen in high-dimensional systems. Many of these mechanisms are known to be possible in macroscopic situations. Thus at least this same range of mechanisms must be contemplated as possible in the quantum mechanical case which we study in molecules, even if we subscribe to the notion that $\hbar$ can limit the complexity of classical mechanics.

Much progress has been made in other areas of quantum physics earlier in the absence of complete solutions of the many-body Schrödinger equation. In our view, until recently the lack of direct experimental information and direct unambiguous computational results have conspired with the high dimensionality and richness of mechanism in the IVR problem to inhibit the development of simple pictures of quantum intramolecular vibrational energy flow.

In this chapter we review some pictures of quantized intramolecular vibrational energy flow which we have studied in recent years. These pictures are attempts toward quantizing the phenomenological pictures of diffusion in action space that describe some classical many-dimensional energy flow problems (5,6). Classically, in these pictures,

weakly coupled systems of oscillators undergo chaotic motion in which the amount of action, or excitation, in each mode executes a random walk. This random walk underlies diffusion (7) in action space, that is the spreading out of the probability of observing a particular set of actions in the different modes, as time progresses. Quantizing diffusive dynamics suggests an analogy to the Anderson localization problem which describes quantum transport of an electron in disordered solid-state systems (8), whose classical transport is diffusive. The main focus of this article consists of presenting two ways of making this connection. One approach uses a phenomenological scaling picture of quantum diffusion and was proposed for IVR by Schofield and Wolynes (9). The other approach, due to Logan and Wolynes, is a "first principles" approximate treatment of energy flow which suggests an analogy between Anderson localization and transport through Fermi resonances in a system of coupled anharmonic oscillators (10).

Both of these approaches highlight the importance of understanding the transition between the regime of global energy flow and the regime of localization where highly restricted dynamics allows energy to remain primarily in a few modes. Thus these pictures of quantum intramolecular energy flow help in reconciling the standard conceptions about energy flow in molecules. The pictures, however, have some rather unusual consequences that have not been traditionally expected. For example, they yield the possibility of strongly nonexponential decays of the survival probability. They also lead to unusual behavior of intramolecular vibrational energy flow rates with coupling strengths. Recently, the advances in direct solution of the Schrödinger equation for models exhibiting intramolecular vibrational energy flow have made possible a test of these possibilities. We describe some of the results of a model study by Schofield et al. (11) that addresses these questions and mention work of Bigwood and Gruebele (12) on more detailed models of actual molecules that leads to similar results.

Finally, we discuss the way in which these pictures of energy flow within molecules modify our expectations about unimolecular reaction rates. Both the simple pictures and approximate calculational methods discussed here, as well as the detailed calculations, are still in a very early stage of development. In the last section we mention some of the open problems facing those who wish to picture quantized intramolecular energy flow.

2. ORIENTATION

Energy flow in molecules occurs as a result of coupling between the nuclear motions. The energy flow we consider involves randomization of energy in the different modes of motion while maintaining constant total energy. Although both rotational and vibrational motion can occur, the present discussion will focus on the vibrational motion.

Typically, molecules vibrate anharmonically. A vibration is anharmonic when the frequency of oscillation depends on the level of excitation. The classical Morse oscillator, with energy

$$\epsilon = \frac{p^2}{2m} + D_e(1 - \exp(-aq))^2 \tag{1}$$

is an example of a nonlinear oscillator. D_e is the dissociation energy. The action, defined as $J = (1/2\pi)\oint p\, dq$, is an integral of the motion. That is, $\dot{J} = 0$. Its conjugate variable is the angle, whose variation with time, $\dot{\theta} = \partial\epsilon(J)/\partial J$, is the nonlinear frequency. Ex-

pressed in these coordinates, the Morse oscillator has energy

$$\epsilon = D_e\left(1 - \left(1 - \frac{J}{J_{\max}}\right)^2\right) \tag{2}$$

and frequency

$$\omega = \omega_0 \frac{J_{\max} - J}{J_{\max}} \tag{3}$$

$J_{\max} = 2D_e/\omega_0$ is the maximum level of excitation that is bound and $\omega_0 = a\sqrt{2D_e/m}$ the harmonic frequency. Bohr-Sommerfeld quantization gives the quantum number n, where $n + 1/2 = J/\hbar$. The nonlinearity of the quantum Morse oscillator is $\omega' = \partial\omega/\partial n = -\hbar a^2/m$. The quantum Morse oscillator often provides a reasonable model for the vibrations of a dissociative bond. In describing the vibrations, different sets of coordinates may be used, for example either local bond coordinates or approximately normal coordinates. Here, we consider coupling between anharmonic normal coordinates.

The anharmonicity of the vibrations leads to a mechanism of energy flow among coupled vibrations (2,5,13,14). It is well known that classically energy flows due to the existence of overlapping nonlinear resonances. A nonlinear resonance between two vibrations occurs when

$$m_1\omega_1(J_1) = m_2\omega_2(J_2) \tag{4}$$

with m_1 and m_2 integers. This resonance creates a zone in action space within which energy transfers locally between the two modes. Action space is the space of action coordinates $\vec{J} = (J_1, J_2, \ldots, J_s)$, where s is the number of oscillators. When resonance zones overlap energy flows within the union of the two zones, if the coupling strength is sufficiently strong. The Kolmogorov-Arnol'd-Möser theorum and the Chirikov criterion give a quantitative meaning to sufficiently strong (2,13). Physically, energy flows rapidly when the energy in coupling exceeds the variation of energy within the resonance. Many overlapping nonlinear resonances in a system with multiple modes of vibration lead to energy flow throughout the whole action space, consistent with conservation of total energy. Quantum mechanical studies have also pointed to the importances of nonlinear, Fermi resonances, although the description becomes more complex (10,15).

The central role of Fermi resonances in energy flow illustrates the importance of the locality of the coupling between vibrational states. The quantum states may be described, for example, by the set of quantum numbers giving the degree of excitation in the individual modes, $|j\rangle = |\{n_\alpha^{(j)}\}\rangle$. j serves as a state label and $n_\alpha^{(j)}$ is the number of quanta in oscillator α in state $|j\rangle$. For example, in a two-mode system we could have $|0\rangle = |0, 0\rangle$, $|1\rangle = |0, 1\rangle$, $|2\rangle = |1, 0\rangle$, $|3\rangle = |1, 1\rangle$, $|4\rangle = |0, 2\rangle$, etc. A Fermi resonance might connect, using the two-mode example, state $|2\rangle$ to state $|4\rangle$, for a total change of one quantum in mode 1 and two quanta in mode 2. Since neither n_1 nor n_2 change by much in this interaction, the interaction is local. A measure of the locality is the vector distance between two coupled sites in state-space. For the two states in the example this distance is $L_{2,4} = (|n_1^{(4)} - n_1^{(2)}|^2 + |n_2^{(4)} - n_2^{(2)}|^2)^{1/2} = \sqrt{5}$. In a system with local coupling, if L_{ij} is large, then the coupling matrix element V_{ij} is small to vanishing, where $H = H_0 + V$, and H_0 is diagonal in the basis $|\{n_\alpha^j\}\rangle$.

General properties common to systems with similar symmetries may be described using random matrix methods. In this approach complex functions of the quantum num-

bers, such as the unperturbed energies, are replaced by elements chosen from a random distribution. Random matrix methods for global Hamiltonians (16), applying to systems in which all states couple, have been useful previously in theories of reaction rates (17,18) and in interpreting experimental spectra (19). Local random matrix methods provide an appropriate means of addressing questions of energy flow in systems in which the locality of the coupling and the concomitant near selection rules play an important role. These methods allow for analytical solution for such quantities as the typical rate of decay of the amplitude to occupy a site in state-space. The following two sections will discuss analytical results of two different local random matrix approaches to the problem of energy flow in molecules. Then Section V describes computations designed to test these predictions.

The central theme of the following sections is the existence of a localization transition in many-dimensional quantum systems described by local random matrix models. An exact molecular eigenstate is said to be localized in the space of the quantum numbers of the approximate normal modes when its amplitude falls off exponentially from a peak, as $e^{-1/\xi}$. This defines the localization length ξ. The localization transition occurs when the coupling energy is comparable to the energy difference between unperturbed states. The location of the transition at this point is supported by a simple perturbation argument. Starting with a zeroth-order state localized on one site in quantum number space, the perturbed wavefunction contains contributions from other states that depends on the matrix elements of the coupling divided by the energy difference. The contributions become significant, causing the wave function to delocalize, when the ratio is of order unity. The locality of the coupling is important to the existence of the transition, as is the randomness of the energy differences. Not all those states nearby in state-space will have similar energy and those states which do have similar energy may be too far away to couple effectively. In order to couple effectively states both must be near to each other in state space and must have an accidental similarity in energy, in addition to having a large enough coupling strength. Therefore a localization transition exists at a critical coupling strength.

The description of the localization transition in molecules has been approached with success by making use of an analogy with the problem of Anderson localization in metals (9,10). In metals the electronic wave functions can localize in the space of sites in the crystal lattice (8). This phenomenon was first predicted theoretically by Anderson using a model with random site energies and a coupling interaction between sites that falls off with the distance, r, between sites (20). For the localization to occur the falloff must be faster than r^{-3}. The same analytical methods that have been used to describe Anderson localization can be applied to the problem of localization of molecular eigenstates in the quantum number space. Two methods in particular, a finite size scaling approach (9) and a self-consistent probabilistic mean field approach (10), led to the results delineated in the next two sections. The two approaches give complementary results, as can be seen in Section V. The scaling approach, presented in Section III, addresses the determination of the survival probability, the probability for a time-evolving wave function to overlap its initial condition, averaged over initial conditions of similar total energy. It is found that the average survival probability decays as a power law with time, with an exponent that depends on the proximity to the transition. The results are general for local random matrix systems. The self consistent field approach, presented in Section IV, addresses the determination of the self energy which results from the introduction of coupling between states, in particular the imaginary part of the self energy, focusing on

the most probable value. For strongly delocalized states the most probable value of the imaginary part of the self energy, Δ_{mp}, increases linearly with coupling strength. At a critical value of the coupling strength Δ_{mp} vanishes in an isolated system of infinite size, signalling the localization transition. The results are presented for a Fermi resonance system of anharmonic oscillators. Calculations performed for a similar Fermi resonance system (11) are presented in Section V.

3. SCALING

The original finite-size approach to Anderson localization, which we borrow for intramolecular vibrational energy localization, was introduced by Thouless, who made the following argument (21). Imagine two separate segments of space of linear dimension L in which the wave functions are delocalized. They are brought together, allowing the wave functions to interact at the boundaries. Will the new wave function in the new segment of space of linear dimension $2L$ be localized or delocalized? Thouless argued that the new wave functions will be delocalized when a characteric number $g > 1$ and localized when $g < 1$. The quantity

$$g = \frac{\hbar \rho_L(E)}{t(L)} \tag{5}$$

is the Thouless number. $\rho_L(E)$ is the local density of states in a segment of size L. $\Delta E \sim 1/\rho_L(E)$ is the typical spacing between two energy levels. This energy difference must be overcome for the states in the two segments of size L to effectively couple, creating a state delocalized over the combined segment of size $2L$. This is accomplished through the coupling at the boundaries caused by the uncertainty in energy arising from transport along a segment of length L. This uncertainty is $\Delta E \sim \hbar/t(L)$, where $t(L)$ is the transport time over length L. Hence, the localization transition occurs at $g_c \sim 1$. In the electronic problem the transport is the spatial diffusion of electrons. In the IVR problem this transport is the energy flow through quantum state-space. The Thouless number is a measure of the number of states in a segment of size L which have energies falling within the energy uncertainty of a given state. This finite size procedure could be carried out with succeedingly larger segments to find the function $g(L)$. Carried out for a particular system this would constitute a renormalization group calculation. Here we present a simplified version of the structure expected of the results of such a calculation.

The finite-size scaling approach to localization assumes that there is a unique function describing the length scaling of the renormalization transformation which is universal for systems of the same symmetry and dimension and that depends only on the Thouless number (22). This function is $\beta(g)$, where (for L' a small multiple of L)

$$g(L') \sim g(L)\left(\frac{L}{L'}\right)^{\beta(g(L))} \tag{6}$$

The function $\beta(g)$ can be determined in both the localized and delocalized limits, using the definition of g, together with models for the transport time in the two limits. In either limit

$$\frac{\rho_{L'}(E)}{\rho_L(E)} \sim \left(\frac{L'}{L}\right)^d \tag{7}$$

That is, the local density of states is proportional to the volume, which in turn scales geometrically with the length with exponent d, the number of dimensions. In the electronic problem this is the number of spatial dimensions. In the delocalized limit, a transport model which supposes an uncorrelated random walk from lattice site to lattice site gives (21,23)

$$\frac{t(L')}{t(L)} \sim \left(\frac{L'}{L}\right)^2 \tag{8}$$

This is simply diffusive motion (9). Therefore, in the delocalized limit

$$\frac{g(L')}{g(L)} \sim \left(\frac{L'}{L}\right)^{d-2} \tag{9}$$

giving $\beta = d - 2$, a constant depending on the dimension. In the localized limit

$$\frac{t(L')}{t(L)} \sim \exp\left(\frac{L'}{L}\right) \tag{10}$$

reflecting the fact that transport occurs via a tunneling mechanism. By noting that $\beta(g) = d \ln(g)/d \ln(L)$, this gives $\beta \sim \ln(g)$. Interpolation gives a function of the form shown in Figure 1. The localization transition occurs when $\beta = 0$ and $g = g_c$. In a renormalization calculation this would be an unstable fixed point. That is, on the side $\beta > 0$, increasing L leads towards the delocalized limit, whereas, on the side $\beta < 0$, increasing L leads toward the localized limit. In metals, g is related to the conductance and is therefore a directly measurable quantity. For molecules, however, some translation

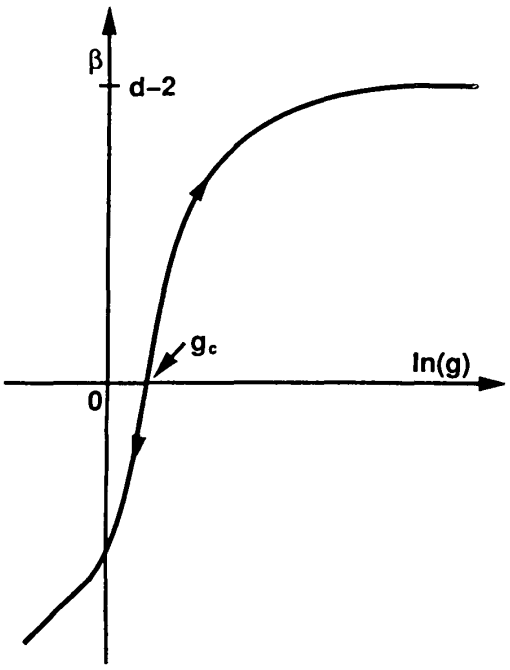

Figure 1 Scaling function for the renormalization transformation. The critical value, which is an unstable fixed point for the transformation, is indicated by g_c. d is the number of dimensions. β, the scaling function, and g, the Thouless number, are defined fully in the text.

is necessary to determine the measurable quantity of interest here, the average survival probability.

In applying the finite size scaling analysis to molecular energy flow one must first translate from crystal lattice sites in metals to sites in the space of the quantum numbers giving the excitation in approximate normal modes of vibration (7). Since we are interested here in isolated molecules the total energy must be conserved, confining motion to a $d = (s - 1)$-dimensional surface in quantum number space, where s is the number of vibrational modes. $t(L)$ is then the transport time across a distance L on the constant-energy surface in quantum number space. Using the same type of model of transport in the strongly delocalized limit as is used in the Anderson localization problem leads to a model of quantum number diffusion on the constant energy surface. This is reasonable, using the following semiclassical argument. Using a perturbation method one begins with a classical system with zeroth-order Hamiltonian $H_0(\{J\})$, where the J are the classical actions, invariants of periodic motion. The addition of a perturbation $\lambda H'(\{J\}, \{\theta\})$ strong enough to break up periodic orbits causes diffusion in the action space, after averaging over the more rapidly varying conjugate angles θ. Using the Bohr-Sommerfeld quantization $n \sim J/\hbar$, if one looks only at scale of $J \gg \hbar$, then n may be treated as a continuous variable, giving a semiclassical picture of diffusion in quantum number space.

In a quantum system which localizes the diffusion picture generalizes to a random walk in quantum number space. Inverting $t(L)$ then enables the determination of the average survival probability via the ansatz

$$P(t) \sim L^{-d}(t) \tag{11}$$

Here we have assumed that the geometrical scaling is governed by the dimensionality of the energy surface, d. In general, d could be replaced by a fractal (24) dimension $d_f < d$ (9). Individual states may show oscillations in the survival probability superposed on an overall decay. The averaging over initial conditions isolates the overall decay. The ansatz follows from first assuming that the average survival probability decays inversely with the "volume" (hypersurface area) explored by the random walk. Then the random walk is assumed to be isotropic. This leads to the geometric scaling of the survival probability with the length L. L is, for example, the root mean square displacement of the random walk. An isotropic system is considered here to simplify the explanation. Anisotropy may be incorporated without great difficulty (25).

The ansatz for the survival probability must be supplemented by conditions on its time range of applicability. More completely, then,

$$P(t) \approx \begin{cases} 1, & t < t_0 \\ L^{-d}(t), & t_0 < t < t_\infty \\ P_\infty, & t > t_\infty \end{cases} \tag{12}$$

where t_0 and t_∞ are found from $L(t_0) = 1$ and $L^d(t_\infty) = 1/P_\infty$. P_∞ is the long-time value of the average survival probability, either N, the number of quantum number states, if the eigenstates are delocalized, or ξ^d, with ξ the localization length, if the eigenstates are localized. In actuality, $P(t)$ will be a smooth function and may decay to some $P < 1$ before the scaling behavior sets in, but the above serves as a useful approximation.

Near the transition the function $\beta(g)$ can be used to determine $P(t)$. Actually, only the knowledge that $g = g_c$ is a fixed point, with $\beta = 0$, is needed, together with the

definitions of β and g. The definition of the Thouless number gives

$$\frac{g(L')}{g(L)} \sim \left(\frac{L'}{L}\right)^d \frac{t(L)}{t(L')} \tag{13}$$

Then the definition of the scaling function gives

$$\beta = d - \frac{d \ln t}{d \ln L} \tag{14}$$

Therefore, when $\beta = 0$

$$\frac{d \ln t}{d \ln L} = d \tag{15}$$

Solving this equation leads to the random walk dynamics

$$t \sim L^d \tag{16}$$

Inverting this equation gives the desired $L(t)$, which in turn determines $P(t)$ via the ansatz.

The results of the analysis of the random walk dynamics in the different regimes is summarized in Table 1. In the strongly localized limit we have neglected the exponential decay of the eigenfunction, essentially treating the length ξ as a "brick wall." This is sufficient for the present purposes. The main conclusion of the scaling analysis is the prediction of dynamical scaling of the average survival probability, that is the survival probability decays as a power law with time, with an exponent that depends on the proximity to the localization transition. In the strongly delocalized limit the decay follows the diffusion prediction. Near the localization transition the decay of $P(t)$ is independent of dimension and simply depends inversely on time. For a large dimensionality this is a much weaker decay than that resulting from the diffusion in quantum number space which occurs when the eigenstates are strongly delocalized. For a computational test of the dynamical scaling see Section V.

Now we address the possible concern the reader may have at this point regarding why power law decays result in this model when the common view in the literature of intramolecular vibrational redistribution (IVR) is one of exponential decay of survival probabilities (26). Power law and exponential decays are different limits of the same phenomenon. Early literature on IVR clearly noted that decays could be nonexponential (27). All treatments start from the idea that some state, not an exact eigenstate, has been excited. This state is coupled to other states of similar energy. Energy then flows from the initial state. Differences result from assumptions regarding the equivalence of states and regarding the topology of the couplings. Exponential decays can result when special bottlenecks to energy flow, dominating the dynamics, are present or when a special initial

Table 1 The Scaling Analysis, as Used to Obtain the Average Survival Probability P

Regime	g	β	L	P
Strongly delocalized	$\gg g_c$	>0	$t^{1/2}$	$t^{-d/2}$
Critical	g_c	0	$t^{1/d}$	t^{-1}
Strongly localized	$\ll g_c$	<0	ξ	ξ^{-d}

g is the Thouless number, β the scaling function, and L the average distance in quantum number space.

(bright) state decays due to direct coupling with all other (dark) states of similar energy. Power law decays result when the initial state is coupled locally to other statistically equivalent states. In addition, examining the local resonances distinguishes the situations. The exponential case is the appropriate situation when the initial quantum state is far from resonance from any states to which it is directly coupled but where states of nearly the same energy exist, very distant in quantum number space. This corresponds to the "superexchange mechanism" described by Mehta et al. (28). It is also likely to be a situation that is relevant in the semiclassical limit where the initial state corresponds with a Bohr orbit that is also a KAM torus. This is the situation envisioned by Davis and Heller in their work on "dynamical tunneling" (29). A more general model would, of course, allow for a mixture of both superexchange and quantized action diffusion pictures.

Finally, we add rate parameters to the scaling analysis. Up to this point the fact that time has dimension has been ignored, since the scaling approach predicts only exponents, not rates. In the strongly delocalized limit the relevant rate is the coefficient of diffusion D in quantum number space. Thus in this limit,

$$P(t) \sim (Dt)^{-d/2} \tag{17}$$

For an individual system D depends on the parameters in the Hamiltonian. One expects D to increase with increasing coupling strength between the molecular modes, all else being the same. The relevant rate near the transition is a microscopic frequency of local motion, ω, that depends on the local density of states. Thus in this regime,

$$P(t) \sim (\omega t)^{-1} \tag{18}$$

ω will also depend on the coupling strength, as does the ratio D/ω. The *weak* dependence on time of the average survival probability near the transition in no way implies a *slow* rate scale $\omega < D$ near the transition. In fact, the reverse is expected to be true near and on the delocalized side of the transition. Both D and ω characterize the decay of the average survival probability. The statistics of the decay of individual states is addressed by the self-consistent probabilistic mean field analysis that is the subject of the following section.

4. MANY FERMI RESONANCE SYSTEM

Consider a many Fermi resonance system of coupled anharmonic oscillators (10). In an analytical treatment of the energy flow, it is convenient to use an algebraic representation for the Hamiltonian. The Hamiltonian $H = H_0 + V$ consists of an unperturbed portion,

$$H_0 = \sum_{\alpha=1}^{s} \epsilon(\hat{n}_\alpha) \tag{19}$$

and a coupling

$$V = \frac{1}{3!} \sum_{\alpha,\beta,\gamma} \phi_{\alpha\beta\gamma}(b_\alpha^\dagger + b_\alpha)(b_\beta^\dagger + b_\beta)(b_\gamma^\dagger + b_\gamma) \tag{20}$$

$\hat{n}_\alpha = b_\alpha^\dagger b_\alpha$ is the number operator and $b_\alpha^\dagger$ and b_α are creation and annihilation operators, respectively. The oscillators have frequencies $\omega_\alpha(n_\alpha) = \hbar^{-1}\partial\epsilon_\alpha/\partial n_\alpha$, with small local nonlinearity $\omega'_\alpha(n_\alpha) = \partial\omega_\alpha/\partial n_\alpha$. That is, $|\omega'_\alpha(n_\alpha)| \ll \omega_\alpha(n_\alpha)$. The sum in the equation for V does not include $\alpha = \beta = \gamma$. The conversion between the algebraic representation and

the (position, momentum) coordinate representation for the particular case of a Morse oscillator is discussed in Section V.

The zero-order states may be described by the set of quanta in the individual oscillators. This gives states $|i\rangle = |\{n_\alpha\}\rangle$, of the same general form as introduced in Section II. In this basis the Hamiltonian is written

$$H = \sum_i \epsilon_i |i\rangle \langle i| + \sum_{i,j} V_{i,j} |i\rangle \langle j|, \tag{21}$$

a tight-binding form. The second sum does not include $i = j$. Simplifying the mathematical analysis, the states are coupled with the topology of a Cayley tree with connectivity K, as illustrated in Figure 2. The connectivity is the number of sites one level further down the tree coupled to a site at a given level. In a Cayley tree the connectivity is constant and each site in a lower level is coupled to only one site in the higher level. As will be seen in Section V, the Cayley tree assumption does not appear to be a serious limitation to the application of the results which appear below. The energy of a given initial state $|j\rangle$ is specified by $\epsilon_j = \Sigma_\alpha \epsilon_\alpha(n_\alpha^{(j)})$. However the energies

$$\epsilon_k = \epsilon_j + \zeta_k \tag{22}$$

of the K states $|k\rangle$ to which state $|j\rangle$ is directly connected are distributed randomly about ϵ_j. Specific results were obtained using the simple Lorentzian distribution

$$P(\zeta) = \frac{\lambda\pi^{-1}}{\lambda^2 + \zeta^2} \tag{23}$$

for purposes of illustration. The half-width of the distribution is λ. This completes the description of the model. Now we present the method of analysis.

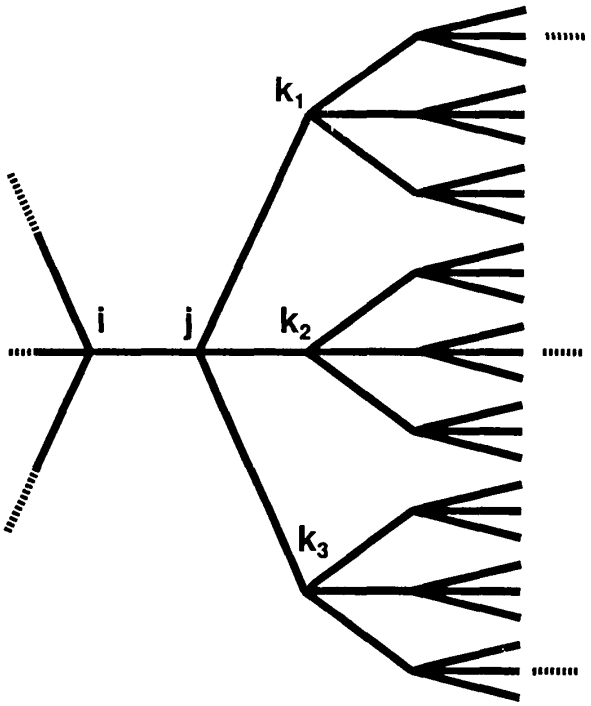

Figure 2 Section of a Cayley tree coupling topology, illustrated for site connectivity $K = 3$. In practice one is concerned with much larger values of K.

The evolution of the wave function

$$|\Psi(t)\rangle = i \sum_k G_{kj}(t)|k\rangle \tag{24}$$

can be determined from the Green functions

$$G_{kj}(t) = -\frac{i}{\hbar} \langle k|e^{-iHt/\hbar}|j\rangle \tag{25}$$

which simply depend on the matrix elements of the propagator $e^{-iHt/\hbar}$. It is generally easier to determine the energy-dependent Green function

$$G_{kj}(E) = \lim_{\eta \to 0+} \int_0^\infty dt\, e^{i(E+i\eta)t} G_{kj}(t) \tag{26}$$

The self-energy $S_j(E)$ is defined by

$$G_{jj}(E) = [g_{jj}^{-1}(E) - S_j(E)]^{-1} \tag{27}$$

with

$$g_{jj}(E) = [E + i\eta - \epsilon_j]^{-1} \tag{28}$$

the Green function for the unperturbed system with Hamiltonian H_0. The self-energy accounts for corrections due to the addition of the coupling V in the full Hamiltonian H. It has both real and imaginary parts:

$$S_j(E) = E_j - i\Delta_j(E) \tag{29}$$

Combining the last five equations, it can be shown that the asymptotic value of the time averaged survival probability,

$$\bar{P}_{jj}(t) = t^{-1} \int_0^t dt'\, |\langle j|e^{-iHt'/\hbar}|j\rangle|^2 \tag{30}$$

depends on the imaginary part of the self-energy,

$$\bar{P}_{jj}(t = \infty) = \sum_\lambda \left[1 + \frac{\Delta_j(E_\lambda)}{\eta}\right]^{-2} \tag{31}$$

where E_λ is an exact eigenenergy. In an infinite-sized isolated system $\eta \to 0$ and $\bar{P}_{jj}(t \to \infty)$ vanishes unless $\Delta_j(E_\lambda) \sim \eta$. This is precisely what happens when the eigenstates are localized, as is found below. Thus the imaginary part of the self-energy determines the extent of the exact eigenstates in the space of the basis states.

The self-energy of each site in the Cayley tree depends on the self-energy of states farther down in the Cayley tree. Therefore the distribution of self-energies at one site arises from the distribution $P(\zeta)$ of site energy differences and the distribution of the self-energies of locally coupled sites which therefore must be solved for self consistently. The Logan-Wolynes analysis utilizes the approximation that these distributions are independent of location in the Cayley tree to solve the probabilistic self-consistency equations (10). In the treatment of Logan and Wolynes the self-energy at a site j was computed

in second-order perturbation theory:

$$S_j(E) = \sum_{k \neq j} \frac{V_{jk}^2}{E - \epsilon_k + S_k(E) + i\eta} \tag{32}$$

We note that for a specific set of site energies this yields an enormous set of simultaneous equations. In fact, just this set for a particular realization was solved later by Stuchebrukhov and Marcus in discussing a solvable Green function tier model for the lineshape of some large polyatomic molecules (30). The approximate statistical solution of the coupled equation carried out by Logan and Wolynes (which is patterned after earlier work on the Anderson problem by Abou-Chacra et al. (31)) gives other insights. A main point is that we expect the probability distribution of the local linewidths Δ_j to have a very peculiar form. In the weak coupling limit of a localized eigenstate of energy E which overlaps site j, the distribution of the imaginary part of the self energy can be computed, assuming the imaginary part of the self-energies of the coupled sites are very small:

$$f(\Delta_j) = \left(\frac{3\Delta_{mp}}{2\pi}\right)^{1/2} \Delta_j^{\,3/2} \exp\left(\frac{-3\Delta_{mp}}{2\Delta_j}\right) \tag{33}$$

Δ_{mp} is the most probable, or typical, value of Δ_j. Since $f(\Delta_j)$ is an asymmetric distribution, with a long tail for large Δ_j, as can be seen in Figure 3, the most probable value differs from the mean, or average value, of Δ_j, which is strictly infinite for this $f(\Delta_j)$. Notice that Δ_{mp} rather than the mean, reveals the scale of the distribution. Traditional approaches to IVR address the average (26), obtaining $\Delta_{gr} = \langle \Delta_j^0 \rangle$, the average of the imaginary part of the self-energy which results when just one tier of coupled states is considered. The inadequacy of the average in systems in which the eigenstates becomes localized results from the fact that the only significant contributions to the average result from the tail of the distribution, that is from those rare occurrences where an exact resonance occurs. We expect the solution of the self-consistent equations for the probability distribution of Δ to also reflect this peculiarity arising from the statistical resonance. The distribution will,

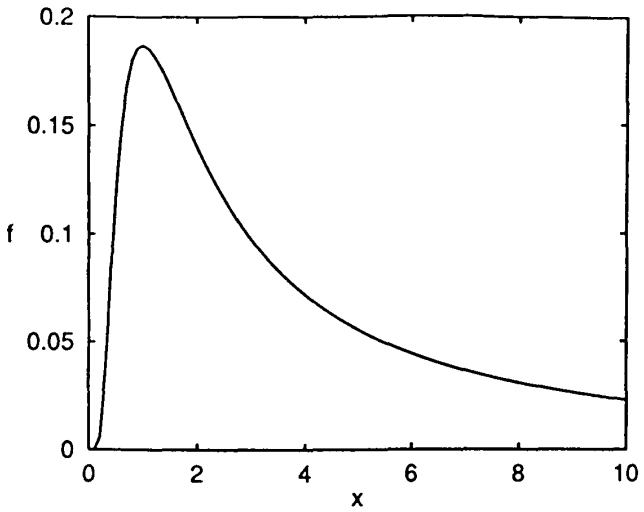

Figure 3 The distribution of local linewidths in the weak coupling limit, $f(x)$, where $x = \Delta/\Delta_{mp}$. (See Eq. (33).)

however, be cutoff at large Δ since eventually even the exact and distant resonances have some finite width. This means that different moments of the probability distribution $f(\Delta)$ may be quite different in their scaling with input parameters (32). This is sometimes termed a "multifractal" (24,33) situation. Logan and Wolynes untie the Gordian knot of probabilistic self-consistency by actually replacing the self-energies of the immediate target sites by their most probable value and requiring only self-consistency of that most probable value. The self-consistency equations now show the possibility of a transition that resembles the spread of a disease in an orchard. If there is a site (A) nearly in resonance with another more distant site, this original site (A) will have a large linewidth which in turn makes it easier for its neighbors to flow to it. If there is a sufficient probability of a chain of resonances the probability amplitude on any site can flow very far away.

The self-consistency condition can be expressed graphically, as in Figure 4. Here the most probable value of the site linewidth, $\Delta_{mp}^{(j)}$, is expressed in terms of the most probable value of its target site linewidth, $\Delta_{mp}^{(k)}$, and the imaginary energy which is also the dephasing rate η. The overall magnitude of the curve depends on how many sites can come into resonance on the average. When $\eta \to 0$, the graphical treatment gives

$$\Delta_{mp} = \begin{cases} \eta \dfrac{T(E;\ \epsilon_j)}{1 - T(E;\ \epsilon_j)}, & T < 1 \\ (K\langle |V|^2 \rangle)^{1/2} \left[\dfrac{T(E;\ \epsilon_j) - 1}{T(E;\ \epsilon_j)} \right]^{1/2} & T > 1 \end{cases} \tag{34}$$

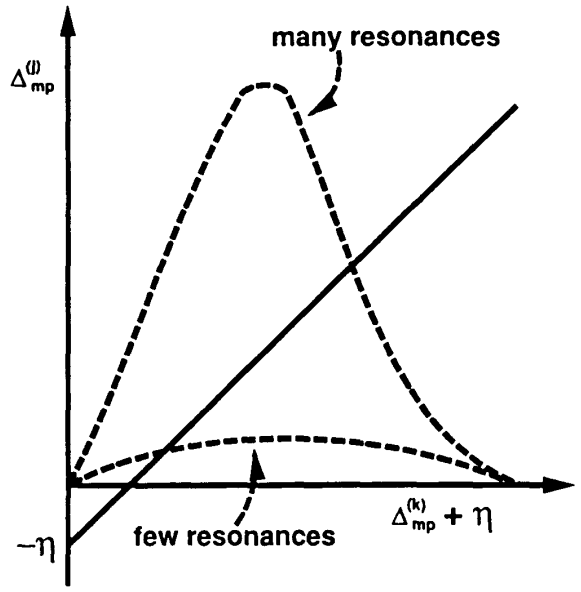

Figure 4 Schematic illustration of self-consistent solution for Δ_{mp}, the most probable value of imaginary part of the self-energy. The dashed lines indicated the dependence of the most probable value at level j in the Cayley tree on the most probable value at the next level k. η is the dephasing rate. The self-consistent value of Δ_{mp} is obtained from the intersection with the solid line. For many overlapping resonances, when the Thouless number g appearing in Figure 1 is large, this yields a finite, nonvanishing value, even for vanishing η. However, there are few overlapping resonances, when the Thouless number g is small, the intersection occurs for a value that vanishes as $\eta \to 0$.

where

$$T(E;\ \epsilon_j) = \frac{2\pi}{3}\,[K\langle|V|\rangle D_L(E;\ \epsilon_j)]^2 \tag{35}$$

is a parameter measuring whether the coupling can bring levels into resonance. $D_L(E;\ \epsilon_j)$ is the local density of states. The localization transition occurs when $T = 1$. Notice that for large coupling Δ_{mp} increases *linearly* with increasing magnitude of the coupling. This is in contrast to the golden rule result for the one tier mean, which contains a quadratic dependence on the magnitude of the coupling, $\Delta = \pi K\langle|V|^2\rangle P(E - \epsilon_j)$. Here $P(E - \epsilon_j)$ is the average unperturbed density of states, which does not include the broadening effects of coupling between states. The quadratic dependence arises from the existence of just one tier, that is from global coupling. With local rather than global couplings, a renormalized golden rule estimate is obtained by replacing $P(E - \epsilon_j)$ by $D_L(E;\ \epsilon_j)$. This renormalized result has an asymptotic linear dependence on the magnitude of the coupling, since $D_L(E;\ \epsilon_j)$ varies inversely with large coupling strength. These results are independent of the detailed form of the distribution of site energy differences.

More specific results are obtained using a Lorentzian distribution of site energy differences. It is convenient to introduce a new variable,

$$y = K^{1/2}\bar{V}/\lambda \sim K^{1/2}\phi M^{3/2}/\lambda \tag{36}$$

linear in the coupling magnitude $\bar{V} \approx \langle|V^2|\rangle^{1/2} \approx \langle|V|\rangle$. M is the level of excitation of individual oscillators, K the connectivity, λ the half-width of the distribution, and ϕ the cubic coupling constant. Use of the Lorentzian distribution of site energy differences to evaluate the local density of states $D_L(E;\ \epsilon_j)$, then gives the result

$$\Delta_{mp} = \lambda y\left[1 - \frac{3\pi}{8}\,\frac{(1 + [1 + 4y^2]^{1/2})^2}{Ky^2}\right]^{1/2}, \qquad y \geq y_c \tag{37}$$

where y_c is the value of y at the localization transition,

$$y_c = \frac{2\beta K^{1/2}}{\beta^2 K - 4} \tag{38}$$

with $\beta = (8/3\pi)^{1/2}$. In the strong coupling limit

$$\Delta_{mp} \sim \lambda y(1 - 3\pi/2K)^{1/2}, \qquad y \gg y_c \tag{39}$$

Thus if M, λ, and K are fixed and known and ϕ is varied, the value of ϕ_c and the proportionality factor Δ_{mp}/ϕ for large ϕ can be determined. This has in fact been done for a similar Fermi resonance system as described in the following section. Section V describes the results of calculations designed to test the predictions both of Sections III and IV.

5. CALCULATIONS

Here we describe exact quantum calculations on a model many-dimensional Fermi resonance system, using the methods explained in Chapters 1 and 3 (11). As in the previous section of this chapter, the Hamiltonian $H = H_0 + V$ consists of an unperturbed portion and a coupling term. As a simple means to model $s = 6$ anharmonic oscillators the normal

modes in H_0 are chosen to be Morse oscillators. In mass-scaled coordinates,

$$H_0 = \sum_{\alpha}^{\lambda} \left[\frac{1}{2} P_\alpha^2 + D_e(1 - e^{-a_\alpha Q_\alpha})^2 \right] \tag{40}$$

The a_α are chosen so that the harmonic frequencies $\nu_\alpha = a_\alpha \sqrt{2D_e}/2\pi$ fall randomly in the interval [1000 cm^{-1}, 1004.4 cm^{-1}]. Note that $\nu_\alpha = \omega_\alpha/2\pi$. Many molecular vibrations have frequencies on the order of 1000 cm^{-1}. The anharmonic oscillators are coupled through cubic interaction terms. In the same mass-scaled coordinates

$$V = \frac{\phi}{3!} \sum_{\alpha,\beta,\gamma \in n.n.} Q_\alpha Q_\beta Q_\gamma \tag{41}$$

The triple sum is over all nearest-neighbor combinations, with modes 1 and 6 coupled. For example the term $Q_5Q_6Q_1$ is included, but $Q_1Q_2Q_5$ is not, because mode 5 is not a nearest neighbor to mode 2. The calculations are carried out using a direct product basis

$$|j\rangle = \prod_{\alpha=1}^{\lambda} |n_\alpha^{(j)}\rangle \tag{42}$$

of Morse oscillator functions. Note that, as for the last section, the basis states are specified by the set of quanta in the approximate normal modes of vibration. In the calculations, it was desired to have enough excitation in the oscillators so that the diffusion picture might hold. However it was necessary to have a small enough product basis as to make the calculations tractable. A compromise was reached by choosing as initial conditions the 252 states created by distributing five quanta among the six oscillators. That is, $\Sigma_\alpha n_\alpha^{(j)} = 5$ for all $|j\rangle$. These states all have similar, though not identical, energy. The energy differences are randomly distributed as a result of the randomness in a_α, with a width $\lambda = 13.2$ cm^{-1}. Therefore a localization transition is expected to exist at a critical value, ϕ_c, of the coupling strength.

To estimate the value of ϕ_c, using the results of the previous section, it is necessary to compare the form of the present Hamiltonian, written in a coordinate representation, to that in the previous section, written in an algebraic representation. Facilitating the comparison, the creation and annihilations operators for the Morse oscillator are known to satisfy (34)

$$b_\alpha^\dagger + b_\alpha = (2n_{\max})^{1/2}(1 - \exp(-a_\alpha Q_\alpha)) \tag{43}$$

$n_{\max} = (2D_e/h\nu_\alpha)^{1/2}$ is the quantum number of the highest bound excitation. At first glance the two Hamiltonians differ. However in the present case, the average level of excitation of an individual oscillator is $M = 1.6$. For such a moderate level of excitation low-amplitude oscillations occur. Therefore

$$b_\alpha^\dagger + b_\alpha \approx \left(\frac{2\nu_\alpha}{h}\right)^{1/2} Q_\alpha \tag{44}$$

Because the ν_α are randomly distributed, but in both cases under comparison, there is no off-diagonal randomness, we replace ν_α with the value specified by the average harmonic frequency ν. This gives

$$V = \frac{\phi'}{3!} \sum_{\alpha\beta\gamma \in n.n.} (b_\alpha^\dagger + b_\alpha)(b_\beta^\dagger + b_\beta)(b_\gamma^\dagger + b_\gamma) \tag{45}$$

where

$$\phi' = \left(\frac{h}{2\nu}\right)^{3/2} \phi \tag{46}$$

and the sum is restricted to nearest-neighbor combinations. The topology of the coupling differs from that in the previous section, because different sites couple directly to a varying number of other sites and because, starting at a given site and tracing the coupling through levels, a site at a lower level can connect to more than one site at a higher level. However, an average connectivity K can be estimated from the number of states directly coupled to an initial state, averaging over initial states. This gives $K = 17$. Application of the localization criterion of the previous section then gives

$$\phi_c' = 1.2 \text{ cm}^{-1} \tag{47}$$

The diffusion coefficient in the strongly delocalized limit can be estimated by identifying it with the most probable value of the imaginary part of the self energy and using the results of the previous section. This gives the estimate

$$D \approx \frac{11\phi'}{\hbar} \tag{48}$$

This prediction is then tested by the calculations, in addition to the criterion for the localization transition.

The model we have chosen is expected to exhibit dynamical scaling since it is a local random matrix model. It satisfies the assumption of an isotropic statistically homogeneous state-space used in deriving the results of Section III. Since there are six modes, the dynamics occur on the five-dimensional constant-energy surface in quantum number space. Therefore the scaling analysis gives

$$P(t) = L^{-5}(t) = (Dt)^{-5/2} \tag{49}$$

in the limit of strongly delocalized states, and

$$P(t) = L^{-5}(t) = (\omega t)^{-1} \tag{50}$$

near the transition to localized eigenstates.

The calculations were aimed at testing the previous four equations. The survival probability for an individual state is computed from

$$S(t) = |\langle \Psi(t) | \Psi(0) \rangle|^2 \tag{51}$$

The distance in quantum number space is measured from the extent of the spread of the wave function:

$$R(t) = \langle \Psi(t) | (n - n_0)^2 | \Psi(t) \rangle^{1/2} \tag{52}$$

where n gives the location in quantum number space. The desired averages over initial conditions are

$$P(t) = \langle S(t) \rangle; \qquad L(t) = \langle R(t) \rangle \tag{53}$$

Calculations were carried out for nine values of the coupling strength at logarithmic intervals from $\phi'/\phi_c' = 6350$–0.635 cm^{-1}. (Throughout this section, logarithms are base 10.) Ideally one method would be used to compute $|\Psi(t)\rangle$, enabling the calculation of $S(t)$ and $R(t)$ for every initial condition. In practice, the computation of $R(t)$ requires more information, needing the full evolution of $|\Psi(t)\rangle$, and is therefore more computationally expensive than the calculation of $S(t)$. $S(t)$ was easily obtained for all 252 initial condi-

tions, using the RRGM method (35) described in the chapter by Wyatt and Iung. $R(t)$ was obtained using the Chebyshev method (36), described in the chapter by Leforestier and Kosloff, for a randomly chosen subset of 18 initial conditions. The reduced set averages for $P(t)$ obtainable from the Chebyshev calculations were compared to the full averages $P(t)$ obtained from the RRGM calculations, giving reasonable agreement, in support of the reduced set average for $L(t)$. In the calculations, the maximum quantum number in an individual oscillator was 6, giving a direct product space of dimension 117,649. A contracted basis of 3136 states was obtained by merging modes 1–3 with an energy cutoff of 5921 cm^{-1} and merging modes 4–6 with the same energy cutoff. In the calculations of $S(t)$, 700–2500 Lanczos recursions were used in the RRGM algorithm, depending on the coupling strength. In the calculations of $R(t)$, 40–440 terms were used in the Chebyshev expansion of the propagator, depending on the time step. The total time ranged from 10 fs to 125 ps, depending on the coupling strength. The calculations took a total of about 400 CPU hours on the IBM RS6000/370 workstation, the bulk of it for the determination of $L(t)$ at the lowest coupling strength.

The results of the calculations support the predictions based on the application of the analysis of both the previous sections to the model system studied. The dramatic change from $L_{max} > 1$ to $L_{max} \leq 1$ in Figure 5 as the coupling strength is lowered from

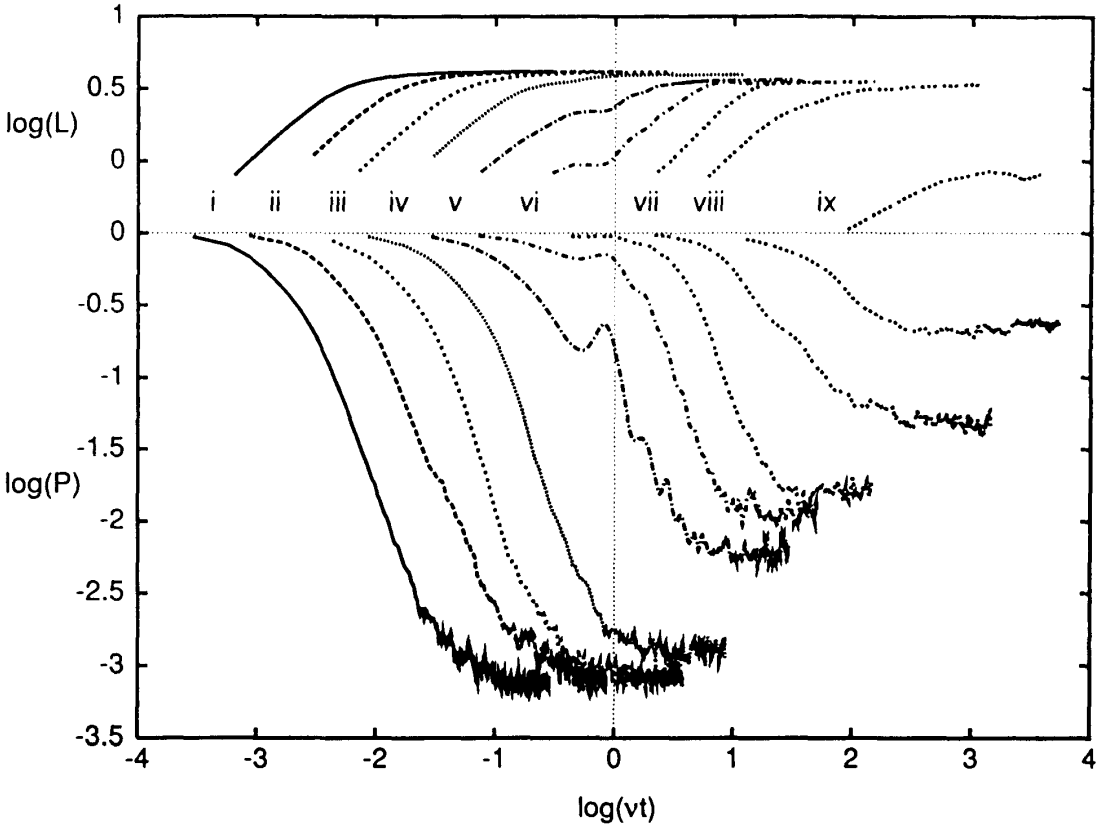

Figure 5 Computational results. The average survival probability, P, and the average wavefunction extent, L, as a function of time, on a log/log scale, for different coupling strength ϕ'. Note that the scale for $\log(L)$ is offset by 0.5. The labels on the plot indicate the following values of $\log(\phi'/\phi_c')$: (i) 3.8; (ii) 3.3; (iii) 2.8; (iv) 2.3; (v) 1.8; (vi) 1.3; (vii) 0.8; (viii) 0.3; (ix) −0.2. For each curve the time has been multiplied by the harmonic frequency ν.

$\phi' > \phi_c$ (case viii) to $\phi' < \phi_c'$ (case ix) supports the predicted location of the transition. Figure 6 shows a fit to the scaling predictions in the delocalized limit, using $D = 14\phi'/\hbar$ over a range of coupling strengths. This is close to the prediction of $D = 11\phi'/\hbar$. Excellent agreement is seen with the scaling prediction over 1.5 decades in Figure 6. Figure 7 shows a fit to the dynamical scaling of $P(t)$ predicted near the localization transition. The agreement is excellent over one decade. However, the simple geometrical scaling $P(t) \sim L^{-5}(t)$ is not supported by the calculations near the localization transition. This may reflect multifractal critical eigenstates, as have been found in Anderson localization systems (33) and as would be expected by the treatment of Logan and Wolynes (10). The more detailed investigation of the connection provides a promising avenue of further research.

Similar calculational methods can be applied to models aimed at describing particular molecules. Bigwood and Gruebele have developed a flexible but detailed calculational model for intramolecular vibrational energy flow in which accurate harmonic frequencies of specific modes, as well as generic information about local anharmonicities, are used as input (12). Therefore the local density of states is reasonably well modeled. Rather than invoking specific Fermi resonance mechanisms, they argue for a general form of nonlinear coupling which decays exponentially with unperturbed quantum number differences between coupled states. In this respect their model resembles Heller's

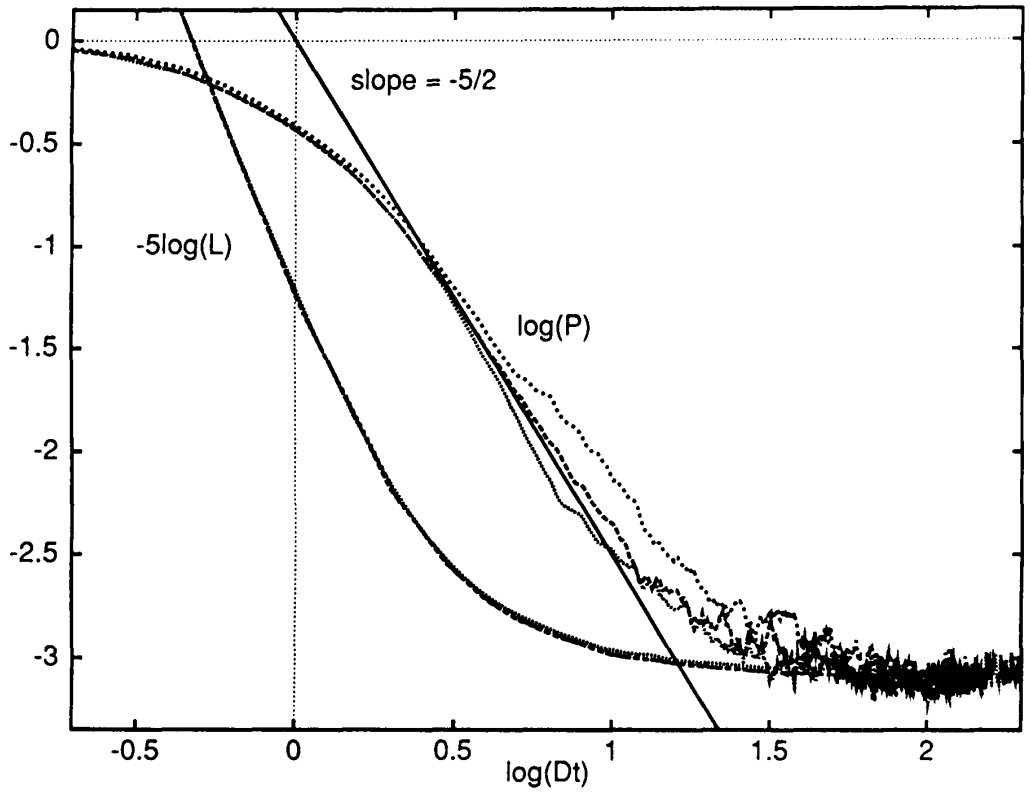

Figure 6 Diffusional scaling. Shown as a function of time are P, the average survival probability, and L^{-5}, L the average wavefunction extent, on a log/log scale, as computed for three values of the coupling strength in the strongly delocalized limit, $\log(\phi'/\phi_c') = 2.8$, 3.3, and 3.8. The straight line with slope indicated on the figure shows the power law fit to $P(t)$. For each curve showing computational results the time has been multiplied by $D = 11\phi'/\hbar$.

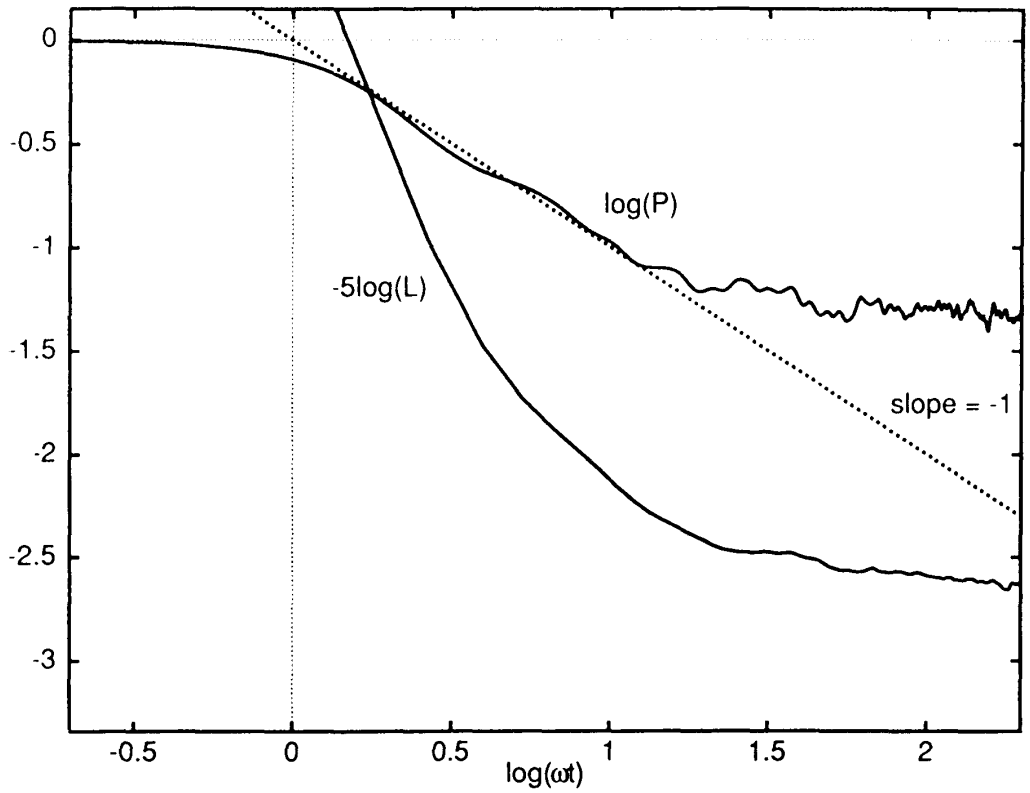

Figure 7 Critical scaling. Shown as a function of time are P, the average survival probability, and L^{-5}, L the average wave function extent, on a log/log scale, as computed for $\log(\phi'/\phi_0') = 0.3$. The straight line with slope indicated on the figure shows the power law fit to $P(t)$. For each curve showing computational results the time has been multiplied by $\omega = 28$ cm^{-1}.

model of dynamical tunneling. In its behavior, this model is basically close to the local random matrix coupling discussed if the exponential fall off rate is large. Their computational studies also show the existence of nonexponential decays resembling power laws and the linear dependence of the average energy flow rate on nonlinear coupling predicted from the pictures discussed for local random matrix models in this chapter. In addition, they have shown how their computational model can give impressively good renditions of the actual IVR seen in specific molecules such as 1-propyne. Their work also points out very clearly the difference between the superexchange mechanism and the one involving nearby resonances which is most discussed in the action diffusion-based pictures. The Bigwood-Gruebele model shows much promise for unifying the pictures of energy flow discussed here and detailed molecular spectroscopic investigations.

6. APPLICATION TO REACTION RATES

In this section we describe the influence of the localization transition on the dynamics of unimolecular dissociation of isolated molecules. These molecules are constrained to constant total energy. For a moderate sized molecule there will be many quantum eigenstates consistent with this constraint. A molecule typically dissociates from a reactive state quite different from an initially excited state, with neither being an exact eigenstate. There may be many reactive states. They might be characterized, for example, by the

existence of sufficient energy in a stretch vibration so as to be above the dissociation energy of that bond. In order for reaction to occur after initial excitation, energy must be transferred from the initial state to a reactive state. Thus the reaction dynamics depend in general on whether energy flows and on the rate of energy flow if it occurs. That is, the reaction dynamics depend on the degree of localization of the exact eigenstates.

If the exact eigenstates are localized not all initial conditions lead to eventual reaction. If the distance in quantum number space between the initial state and any reactive state is larger than the localization length, then the rate of reaction is vanishingly small. Other initial states nearby to reactive states may react rapidly. Under these conditions the reaction dynamics are highly nonuniform. The average rate of reaction does not give a fair indication of how rapidly reaction occurs from any given initial state.

If the eigenstates are delocalized any reactive state is potentially accessible from any initial state. Under these conditions it is valid to employ statistical measures of reaction dynamics, such as the average rate of dissociation, the average being over initial conditions. In general, this average reaction rate depends on the rate of energy flow. However, if the rate of energy flow is neither too fast nor too slow, a quasiequilibrium approach may be used. In the RRKM theory (3), the assumption of a quasiequilibrium between the reactive states, which collectively form an activated complex, or transition state, and all the states of the reactant molecule consistent with the total energy gives the result

$$k_{\mathrm{RRKM}} = \frac{N^{\ddagger}(E)}{h\rho(E)} \tag{54}$$

$N^{\ddagger}(E)$ is the number of states of the activated complex at total energy E consistent with the restriction of energy $\epsilon^{\ddagger}$, and $\rho(E)$ is the total density of states. The transition state is defined by the restriction of energy $\epsilon^{\ddagger}$ to critical motions. In the Kassel picture of the transition state the energy $\epsilon^{\ddagger}$ is in a critical bond extension. In the Marcus picture of the transition state, the energy $\epsilon^{\ddagger}$ is the energy at the saddle point on the molecular potential energy surface in configuration space. The Kassel picture lends itself more easily to the present extension accommodating energy flow in quantum number space. The picture of the transition state we will use is that of a region of contiguous reactive states in the quantum number space of vibrational basis states, as illustrated in Figure 8. This space is the same as used in previous sections.

A dependence of the reaction dynamics on the energy flow dynamics causes deviations from the RRKM prediction for the average rate of unimolecular dissociation. If energy flows slowly compared to the rate of dissociation directly from a reactive state the reactive state can fail to equilibrate with the other states rapidly enough to validate the quasiequilibrium assumption. In this case, the average reaction rate should increase with increasing rate of energy flow. In Sections II and III it was demonstrated that the rate of energy flow depends on the proximity to the transition to localized eigenstates, slowing with the approach to the transition from the delocalized side. Near the transition equilibration occurs slowly and the average reaction rate is expected to depend crucially on the rate of energy flow. In addition, as the localization transition is approached from the delocalized side the individual rates of reaction from different initial states should fluctuate increasingly about the average reaction rate. In this section we describe a method for quantifying the effects of the approach to the localization transition on both the average rate of unimolecular dissociation and on the fluctuations about the average. First

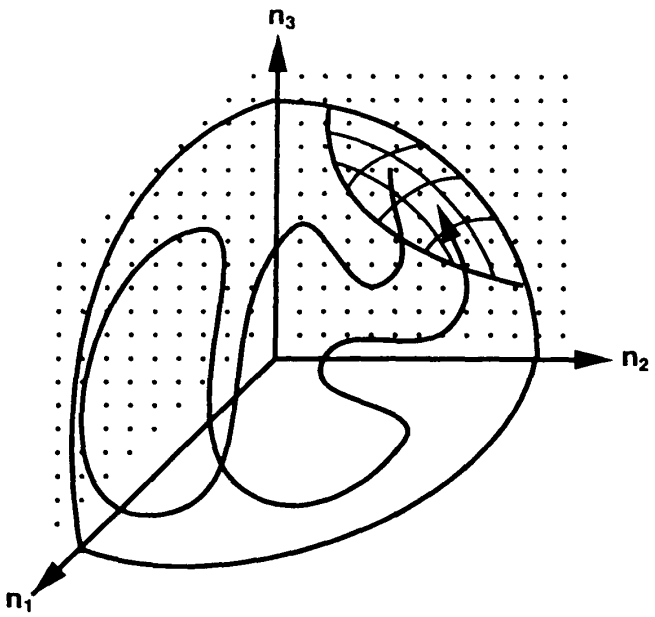

Figure 8 Schematic of the reaction model, for an $s = 3$ mode system. The axes indicate the level of excitation in the approximate normal modes. Vibrational motion is confined to the $(s - 1)$-dimensional constant energy surface. The transition region of reactive states is indicated by the crosshatching. A random walk on the constant energy surface originating in and returning to this region is illustrated. In practice, one is concerned with systems with larger values of s.

we show the relationship between the average and the fluctuations using a renormalized perturbation expansion for the average rate. We then discuss the dependence of the average reaction rate and the rate fluctuations on the probability to remain in or return to the transition region of reactive states. Finally we evaluate this dependence using a dynamical model based on the scaling perspective described in Section II.

In order to evaluate the effects of the approach to the localization transition upon the reaction rate we first define the rate quantum mechanically using the dynamics of the density matrix (37). Following Zwanzig's method (38) one can partition the space into reactant states, indicated by a and product states, indicated by b (39,40). Then a projector

$$\mathcal{P} = |\rho_a^{eq} aa\rangle\rangle\langle\langle aa| + |\rho_b^{eq} bb\rangle\rangle\langle\langle bb| \tag{55}$$

is defined that isolates population dynamics. $|aa\rangle\rangle$, and $|bb\rangle\rangle$, are reactant and product Liouville states, which arise in considering the dynamics of the density matrix. The Liouville states $|jj\rangle\rangle = |j\rangle\langle j|$ are the basis states for the density matrix, in the same way that the Hamiltonian states $|j\rangle$ are basis states for the wave function. Both $|aa\rangle\rangle$ and $|bb\rangle\rangle$ can contain many substates. ρ_a^{eq} and ρ_b^{eq} are the reactant and product equilibrium density matrices, respectively. Operating with the projector $\mathcal{P}$ on the density matrix and solving for the reactant population then gives an integrodifferential equation. This can be solved via the Laplace-Fourier transform, giving an exponential decay of the population $p_a(t)$, with a rate that depends on the matrix elements of the frequency-dependent rate operator,

$$\mathcal{K}(\omega) = \mathcal{L}'[-i\omega + i\mathcal{Q}\mathcal{L}]^{-1}\mathcal{Q}\mathcal{L}' \tag{56}$$

$\mathcal{Q} = \mathcal{I} - \mathcal{P}$ is the correlation projector and $\mathcal{L}'$ is the part of the Liouvillian, $\mathcal{L} = \hbar^{-1}[H,]$, which is not diagonal in a and b. For dissociation the b states approach a continuum

leading to negligible back-reaction. In this case, the average rate satisfies

$$k = <\mathcal{K}_{jjjj}(\omega \rightarrow ik)> \tag{57}$$

with the subscript j referring to a reactant substrate and $\langle\ \rangle$ denoting the microcanonical average over all of these states consistent with the total energy E. The matrix elements are computed as follows:

$$\langle\langle ij|\mathcal{K}|kl\rangle\rangle = \mathrm{Tr}\{|i\rangle\langle j|(\mathcal{K}|k\rangle\langle l|)\} \tag{58}$$

$\mathcal{K}(\omega)$ may be evaluated using a perturbation expansion in the coupling $\mathcal{L}'$. A simple resummation of the perturbation series is accomplished by neglecting connected dynamical processes of higher than fourth order (41). At large coupling a more accurate result obtains from first taking the limit of large coupling in the simple resummed result and then renormalizing by replacing the rate operator evaluated to second order in the coupling with the full rate operator. This gives

$$k = <\langle\langle jj|\mathcal{K}(ik)[k + i\mathcal{L}_\alpha]^{-1}\mathcal{Q}\mathcal{K}(ik)|jj\rangle\rangle> \tag{59}$$

Taking the zero frequency limit on the right-hand side of this equation enables the use of the identity

$$|jj\rangle\rangle\langle\langle jj| = [ih\rho(E)\mathcal{L}_\alpha]^{-1} \tag{60}$$

The factor of $h\rho(E)$ assures normalization. The result for the average rate can be written

$$k = \frac{N_{\mathrm{eff}}(E)}{h\rho(E)} \tag{61}$$

where

$$N_{\mathrm{eff}}(E) = <[(\mathcal{K}_{jjjj} - k)/k]^2>^{-1} \tag{62}$$

N_{eff} is just the inverse of the rate fluctuation. This is the traditional definition of the number of effective decay, or reaction, channels in the random matrix approach to the statistics of decay rates. This approach has been used both in nuclear (16) and chemical (17) physics. Comparing this result with the RRKM prediction, one can see that $N_{\mathrm{eff}}(E)$ replaces $N^{\ddagger}(E)$. One can use either a vibrationally adiabatic tunneling model (17) or a model of hopping between two electronic surfaces in the Condon approximation (40) to show that, when a global random matrix model is used for the Hamiltonian, $N_{\mathrm{eff}} = N^{\ddagger}$ in the classical limit.

In a system described by a local random matrix model there can be corrections to the RRKM prediction for the average reaction rate. Assuming that the total reaction time is the sum of the RRKM contribution and a correction, and using $[i\mathcal{L}_\alpha]^{-1} = \int dt\ e^{-i\mathcal{L}_\alpha t}$, the number of effective reaction channels satisfies

$$\frac{1}{N_{\mathrm{eff}}} = \frac{1}{N^{\ddagger}} + \frac{k_{\mathrm{RRKM}}}{P_r^{\mathrm{eq}}}\int_0^\infty dt\ [P_r(t) - P_r^{\mathrm{eq}}] \tag{63}$$

$P_r(t)$ is the average probability to remain at or return to the transition region of reactive states

$$P_r(t) = <\langle\langle\phi_j|e^{-i\mathcal{L}_\alpha t}|\phi_j\rangle\rangle> \tag{64}$$

due to non-RRKM dynamics. The state $|\phi_j\rangle\rangle$ is defined by the action of the rate operator,

$$|\phi_j\rangle\rangle = c\mathcal{K}|jj\rangle\rangle \tag{65}$$

with c a constant that normalizes the states such that $P_r(0) = 1$. Thus the corrections to the RRKM prediction depend on the probability to return to the reactive region.

To evaluate the corrections to the RRKM result for the average reaction rate, a model for the probability to return to the region of reactive states is needed. Consider a random walk through quantum number space beginning at a reactive state within the transition region, as illustrated in Figure 8. While the random walk remains in the transition region $P_r(t) = 1$. However, after escaping the transition region at time $t^\ddagger$, the random walk may wander among nonreactive states before returning to a reactive state. There are $N^\ddagger$ of these states. Thus a simple approximation to $P_r(t)$ is

$$P_r(t) = \begin{cases} 1, & t < t^\ddagger \\ N^\ddagger P(t), & t > t^\ddagger \end{cases} \tag{66}$$

$P(t)$ is the average survival probability of an individual state in the transition region. This has been evaluated for systems described by a local random matrix model using the scaling perspective on energy flow and localization described in Section II (42). The results are illustrated in Figure 9. In the limit of strongly delocalized eigenstates, for a large number of dimensions

$$\frac{N_{\text{eff}}}{N^\ddagger} \approx \left[1 + \frac{\omega_0}{D}\right]^{-1} \tag{67}$$

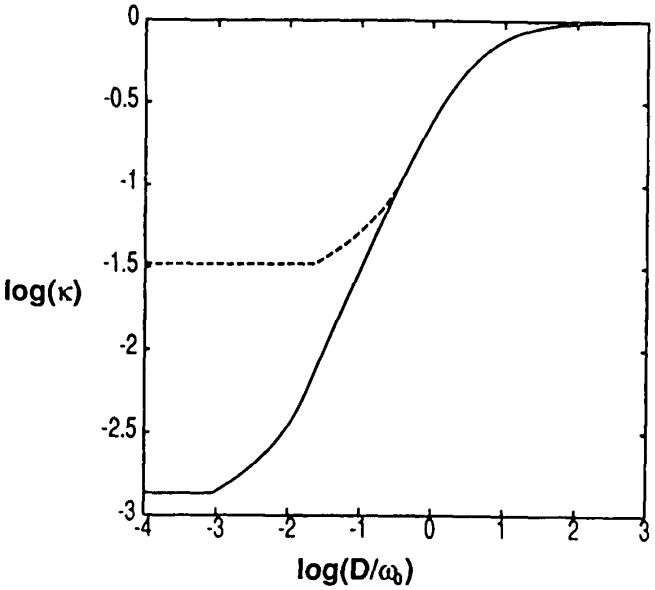

Figure 9 Corrections to the RRKM reaction rate. The ration $\kappa = N_{\text{eff}}/N^\ddagger = k/k_{\text{RRKM}}$ is shown as a function of D/ω_0 (D the diffusion coefficient and ω_0 the RRKM frequency) for $N^\ddagger = 10^3$, $N = 10^6$, $d = 14$. Two values of $C = \omega/\omega_0$ (ω the frequency characterizing critical dynamics near the localization transition) are shown: 10 (solid line); 50 (dashed line). In generating this figure, using a connection procedure between the regime of critical dynamics and the regime of strongly delocalized dynamics described in Ref. 39, typical values of $N^\ddagger$ and N were used, as determined with the aid of Table 11-3 for CH_3NC on p. 367 of Ref. 3.

where $\omega_0 = N(E)/h\rho(E)$ is the RRKM frequency. Here the reaction rate increases with increasing diffusion coefficient D until the RRKM result is reached for larger D. When D is much larger than ω, of course the whole picture of a well-defined quantum number space probably breaks down so this trend may only be valid up to moderate levels of stochasticity. At the opposite extreme, near the transition to localized eigenstates,

$$\frac{N_{\text{eff}}}{N^{\ddagger}} \approx \left[1 + \frac{N^{\ddagger}}{C}\right]^{-1} \tag{68}$$

where $C = \omega/\omega_0$, ω the microscopic frequency characteristic of dynamics near the localization transition. This means that near the transition to localized eigenstates $N_{\text{eff}} \approx 1$. That is, at the transition there is effectively only one channel open to reaction. This is the main result of the application of the scaling analysis to determining corrections to the RRKM prediction to the microcanonical average rate of unimolecular dissociation due to energy flow and localization. This approach has been extended to include the effects of external dephasing on the energy flow (25).

The fact that at the localization transition there is effectively only one reaction channel points to a breakdown of the utility of the average reaction rate at the transition. At the transition, not only are the fluctuations of order unity, since the fluctuation is the inverse of N_{eff}, but the average reaction rate is of order the inverse of the Poincaré time. The Poincaré time, $h\rho(E)$ is the time for recurrences to individual energy eigenstates. After the Poincaré recurrence time average rate behavior is not meaningful. The magnitude of the fluctuations points to the necessity of obtaining the full distribution of reaction rates from different initial states, for an accurate description of the statistics of reaction. Thus a different approach, more along the lines of that taken in Section III for unreacting systems, is necessary for the description of the unimolecular decay of molecules with localized eigenstates.

7. CONCLUDING REMARKS

The pictures of IVR which we have reviewed in this chapter are still quite primitive. Since they attempt to quantize a model resembling diffusive dynamics of local actions which we expect for some systems in the classical correspondence limit, they really attempt only to quantize the simplest caricature of irregular dynamics. There is a great need for quantizing models in which regular motions coexist with irregular motions in the classical limit. This could unify the mechanism describing dynamical tunneling with the quantum diffusion effects discussed here. Similarly we know of several cases where the quantum mechanically regular motion of collective coordinates arises and can exist in the face of underlying chaos of the complete trajectory. The area where this is most well known, of course, is nuclear physics where the single-particle states can be described by Gaussian orthogonal ensemble statistics simplifying high irregular motion, but where in a similar energy range there are collective dipole states (16); similar situations may apply for molecules.

In the quantum realm we see both from theory and detailed calculations that there is a hint of multifractality. Thus the scaling analysis discussed so far must be oversimplified and an important goal will be the development of a scaling picture which can accommodate the multifractality. Detailed calculations will doubtless help in this. There are many interesting questions relating to how to estimate parameters for individual molecules and how to observe the consequences of the different types of intramolecular

vibrational energy flow. Many of the previous computational analyses of IVR start from detailed potential energy models which are hard to manipulate. An intermediate level modeling effort using directly spectroscopic observables seems to be a more promising alternative. The Bigwood-Gruebele model is most exciting in this regard (12).

Can the detailed scaling phenomena at the transition between localization and energy flow be seen in individual molecules? The difficulty here is twofold. First, for the small molecules which have mostly been studied in IVR, only special modes have been looked at. These "bright states" may often be bright simply because they correspond to largely isolated nearly regular motions. Thus they may not describe at all the typical way in which energy flows in the many-dimensional state-space. More experiments on different parts of quantum number space involving combination bands (44) will definitely help. Second, of course, focusing on a transition usually requires experimentally achieving tunability and this is difficult when one uses small molecules since even substituting a single atom can give a very different behavior as in the various studies of the heavy atom effect by Marcus and co-workers and by Uzer and Hynes (43). Studying environmental effects on energy flow in condensed phases or varying the size of small nanoclusters where lower levels of excitation in a many-body system are relevant, may be places where tunability can be most easily introduced. If the dream of laser control of quantum motions is achieved, it will, of course, be easy to test these ideas and, indeed, they will probably be essential to understanding control. If molecules are, as many expect, largely delocalized in the energy flow, as we begin to control them, they will approach the transition to localization. While the engineering goal may be to localize eigenstates entirely, it certainly will not hurt to study the transition along the way.

ACKNOWLEDGMENTS

This work has been supported by grants from the National Science Foundation the University of Illinois and at the University of Texas. We have enjoyed conversations over the years with Martin Grubele, Eric Heller, David Leitner, David Logan, Nancy Makri, and Bob Wyatt about intramolecular vibrational energy flow. We thank them.

REFERENCES

1. R. C. Tolman, *Phys. Rev.*, *11*: 261 (1918); *J. Am. Chem. Soc.*, *42*: 2506 (1920); *47*: 2654 (1925).
2. For a review, see T. Uzer, *Phys. Rep.*, *199*: 73 (1991).
3. J. I. Steinfeld, J. S. Francisco, and W. L. Hase, *Chemical Kinetics and Dynamics*. Prentice Hall, Englewood Cliffs, NJ, 1989, Chap. 11.
4. W. Warren, H. Rabitz, and M. Dahleh, *Science*, *259*: 1581 (1993); W. S. Warren, *Science*, *262*: 1008 (1993); S. A. Rice, *Science*, *258*: 412 (1992).
5. A. J. Lichtenberg and M. A. Lieberman, *Regular and Stochastic Motion*, Springer, New York, 1983.
6. A. N. Kaufman, *Phys. Rev. Lett.*, *27*: 376 (1971).
7. P. W. Atkins, *Physical Chemistry*, W. H. Freeman, New York, 1994, Chap. 24.
8. For a review, see P. A. Lee and T. V. Ramakrishnan, *Rev. Mod. Phys.*, *57*: 287 (1985).
9. S. A. Schofield and P. G. Wolynes, *J. Chem. Phys.*, *98*: 1123 (1993).
10. D. E. Logan and P. G. Wolynes, *J. Chem. Phys.*, *93*: 4994 (1990).
11. S. A. Schofield, P. G. Wolynes, and R. E. Wyatt, *Phys. Rev. Lett.*, *74*: 3720 (1995).
12. B. Bigwood and M. Gruebele, *Chem. Phys. Lett.*, *235*: 604 (1995).

13. B. V. Chirikov, *Phys. Rep.*, *52*: 263 (1979).
14. R. Z. Sagdeev, D. A. Usikov, and G. M. Zavlavsky, *Nonlinear Physics*, Harwood Academic, New York, 1988; D. W. Oxtoby and S. A. Rice, *J. Chem. Phys.*, *65*: 1676 (1976).
15. G. A. Voth, R. A. Marcus, and A. H. Zewail, *J. Chem. Phys.*, *81*: 5494 (1984); E. L. Sibert, J. T. Hynes, and W. Reinhardt, *J. Phys. Chem.*, *87*: 2032 (1983); G. A. Voth, *J. Chem. Phys.*, *88*: 5547 (1988); B. Ramachandran and K. G. Kay, *J. Chem. Phys.*, *99*: 3659 (1993) and references therein; K. M. Atkin and D. E. Logan, *Phys. Lett. A*, *162*: 255 (1992).
16. M. L. Mehta, *Random Matrices*, Academic, Boston, 1991; T. A. Brody et al., *Rev. Mod. Phys.*, *53*: 385 (1981); *Statistical Theories of Spectra*: *Fluctuations* (C. E. Porter, ed.), Academic, New York, 1965.
17. W. H. Miller, R. Hernandez, and C. B. Moore, *J. Chem. Phys.*, *93*: 5657 (1990).
18. E. J. Heller and S. A. Rice, *J. Chem. Phys.*, *61*: 936 (1974); W. M. Gelbart, S. A. Rice, and K. F. Freed, *J. Chem. Phys.*, *57*: 4699 (1972).
19. E. Abramson, R. W. Field, D. Imre, K. K. Innes, and J. L. Kinsey, *J. Chem. Phys.*, *80*: 2298 (1984).
20. P. W. Anderson, *Phys. Rev. B*, *36*: 4135 (1958).
21. D. J. Thouless, *Phys. Rev. Lett.*, *39*: 1167 (1977).
22. E. Abrahams et al., *Phys. Rev. Lett.*, *42*: 673 (1979).
23. E. W. Montroll and M. F. Shlesinger, in *Nonequilibrium Phenomena II. From Stochastics to Hydrodynamics* (J. L. Leibewitz and W. W. Montroll, eds.), North-Holland, New York, 1984.
24. M. Schroeder, *Fractals, Chaos, and Power Laws*, W. H. Freeman, New York, 1991.
25. S. A. Schofield and P. G. Wolynes, *J. Phys. Chem.*, *99*: 2753 (1995).
26. P. M. Felker and A. H. Zewail, *Adv. Chem. Phys.*, *70*: 265 (1988); J. D. McDonald, *Ann. Rev. Phys. Chem.*, *30*: 29 (1979).
27. M. Bixon and J. Jortner, *J. Chem. Phys.*, *50*: 3284 (1969).
28. A. Mehta, A. A. Stuchebrukhov, and R. A. Marcus, *J. Phys. Chem.*, *99*: 2677 (1995).
29. M. Davis and E. J. Heller, *J. Phys. Chem.*, *85*: 307 (1981).
30. A. A. Stuchebrukhov and R. A. Marcus, *J. Chem. Phys.*, *98*: 6044 (1993).
31. R. Abou-Chacra, P. W. Anderson, and D. J. Thouless, *Phys. Rev. B*, *36*: 4135 (1987).
32. A. D. Mirlin and Y. V. Fyodorov, *Phys. Rev. Lett.*, *72*: 526 (1994).
33. H. Grussbach and M. Schreiber, *Phys. A*, *191*: 394 (1992); U. Fastenrath, M. Janßen, and W. Pook, *ibid.*, p. 401; B. Huckenstein and L. Schweitzer, *ibid.*, p. 406.
34. R. D. Levine, in *Mathematical Frontiers in Computational Chemical Physics* (D. G. Truhlar, ed.), Springer, New York, 1988.
35. A. Nauts and R. E. Wyatt, *Phys. Rev. Lett.*, *81*: 2238 (1983); R. E. Wyatt, *Adv. Chem. Phys.*, *73*: 231 (1989).
36. H. Tal-Ezer and R. Kosloff, *J. Chem. Phys.*, *81*: 3967 (1984); R. Kosloff, *J. Phys. Chem.*, *92*: 2087 (1988).
37. D. A. McQuarrie, *Statistical Mechanics*, Harper and Row, New York, 1976, p. 574.
38. R. Zwanzig, *Physica*, *30*: 1109 (1964); *J. Chem. Phys.*, *33*: 1338 (1960).
39. M. Sparpaglione and S. Mukamel, *J. Chem. Phys.*, *88*: 3263 (1988).
40. S. A. Schofield and P. G. Wolynes, *J. Chem. Phys.*, *100*: 350 (1994).
41. R. D. Mattuck, *A Guide to Many-Body Feynman Diagrams*, Dover, New York, 1992.
42. S. A. Schofield and P. G. Wolynes, *Chem. Phys. Lett.*, *217*: 497 (1994).
43. For example, T. Uzer and J. T. Hynes, *Chem. Phys.*, *139*: 163 (1989); S. M. Lederman et al., *Chem. Phys.*, *139*: 171 (1989).
44. E. R. Th. Kerstel et al., *J. Chem. Phys.*, *100*: 2588 (1994).

4

Canonical Van Vleck Perturbation Theory and Its Application to Studies of Highly Vibrationally Excited States of Polyatomic Molecules

ANNE B. McCOY

The Ohio State University, Columbus, Ohio

EDWIN L. SIBERT III

University of Wisconsin-Madison, Madison, Wisconsin

I. INTRODUCTION

A long-standing goal of physical chemists is to draw connections between the simple electrostatic interactions between nuclei and electrons that comprise molecules and the observed chemical reactivity and dynamics displayed by these systems. This is a daunting task when one considers the number of interacting particles that comprise even the simplest of triatomic molecules. Instead of performing these calculations strictly ab initio, considerable progress can be made by invoking the Born-Oppenheimer approximation (1). This remarkable approximation leads naturally to the concept of chemical bonds as it allows one to treat the molecule as if it consisted of a group of point masses connected by springs.

In spite of recent advances in computer technology and electronic structure theory, only for the simplest molecules can potential energy surfaces be calculated with spectroscopic accuracy by employing purely ab initio approaches (2). For more complicated systems, empirical approaches are often used to invert spectra from experimental observables (3–10). This process is shown schematically by following the arrows up in Fig. 1. This new potential can then be used to predict the spectroscopy and dynamics for previously unobserved states and thereby help direct future experiments (11,12). This latter process corresponds to following the down arrows in Fig. 1.

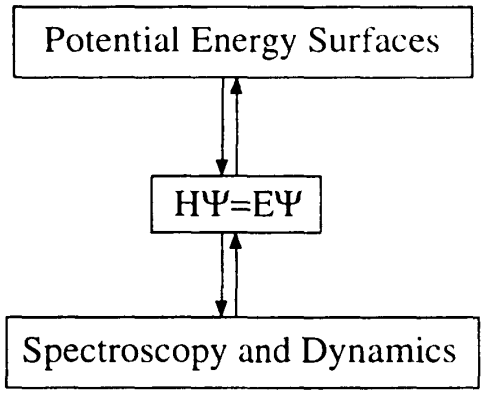

Figure 1 Schematic picture of the relationship between Born-Oppenheimer potential energy surfaces, the rotation-vibration Hamiltonian, and the observed spectroscopy and dynamics.

One way to probe experimentally the potential energy surface is through studies of states with large amounts of vibrational energy, since the corresponding wave functions extend over a large range of molecular geometries. Recent advances in experimental approaches and technologies have enabled workers to probe just such states for a variety of polyatomic molecules. In particular, several groups have investigated the spectroscopy and dynamics of highly vibrationally excited states ($E_{vib} \approx 8000-20{,}000$ cm^{-1}) of HCN, H_2O, H_2CO, and C_2H_2 (13–20). These molecules are of interest due to the fact that highly excited vibrational states are accessible through several experimental techniques. For example, direct single-photon excitation in this energy regime selectively excites states of the molecule with predominately XH stretching character (X = C,N,O) (21). In contrast, dispersed fluorescence and stimulated emission pumping (SEP) experiments are typically sensitive to states with energy in the bending or low-frequency stretching degrees of freedom (22,23). Using both of these experimental approaches to study the spectroscopy and dynamics, one can probe a large portion of the ground state Born-Oppenheimer potential energy surface and, thus, determine the strength of the intramolecular forces for a wide range of molecular geometries.

To fully illuminate the nature of the vibrational states being probed by these experiments, theoretical approaches are required that describe the energy flow. This flow has long been understood for molecules at low levels of vibrational excitation where the vibrational motions are approximated well by a set of uncoupled harmonic oscillators (24,25). In this limit, the flow of energy between the internal degrees of freedom is a consequence of the phasing and dephasing of the normal mode oscillations. In another limiting case, which typically occurs at high energies, the zero-order states are strongly mixed, and energy flows freely between all of the modes of the molecule on the time scales of most experiments. Here the observed dynamics and spectroscopy are found to be described well by statistical models (26,27). The experiments, in which we are interested, probe the energy regime that falls between these two limits. To illuminate the nature of the vibrational states being probed in this regime, it is desirable to develop computational methods with which one can compute the relevant observables and make comparisons with experiment. Consequently a great deal of interest has been directed toward the development of new methods (11,12,28–30) for obtaining vibrational eigenvalues and eigenfunctions. The most powerful of these approaches is based on the vari-

ational principle (12,28–30). Here the eigenfunctions are constructed from linear combinations of zero-order basis states. By systematically increasing the size of this basis, the calculated eigenfunctions and eigenvalues converge to the true solutions of the Schrödinger equation. These "exact" quantum mechanical approaches for calculating highly excited vibrational states are extremely demanding computationally for systems with more than three degrees of freedom (31) or for systems in which many rotational levels are populated (32). Here, alternative routes to their solutions are required (11,28,33,34).

One approach that has been long used to study systems with low to moderate levels of vibrational excitation is second-order canonical Van Vleck pertubation theory, hereafter referred to as CVPT (35–37). Many groups have used CVPT to study molecular vibrations (8,35,38–42). A full review of all the recent applications therefore is beyond the scope of this chapter, and we discuss, instead, the work in our group. In a series of studies, we developed FORTRAN programs to implement CVPT up to eighth order and applied this method to studies of highly excited vibrational states in H_2O, HCN, SO_2, CO_2, C_2H_2, C_2D_2, H_2CO, D_2CO, and CHD_3 (43–54).

The beauty of CVPT is that it provides a simple and rapid method whereby one can transform the Hamiltonian from an initial representation to a final one, where the molecular properties of interest are more readily calculated in the final representation than they are in the initial one. In traditional perturbative approaches, one represents the Hamiltonian in some well-known zero-order representation, this yielding a Hamiltonian matrix. One then uses the perturbative analysis to generate a matrix **T**, such that when one carries out the similarity transformation (cf. the top panel of Fig. 2) *all* of the contributions to the off-diagonal elements of the Hamiltonian matrix that were of order λ before the transformation are of order λ^2 after the transformation. Although one can then proceed to higher order, here we consider a single transformation in order to obtain results of order λ^2. The contribution of Van Vleck was to develop his perturbative expressions in terms of **S** where $\mathbf{T} = \exp(i\lambda\mathbf{S})$ rather than work directly with the matrix **T**.

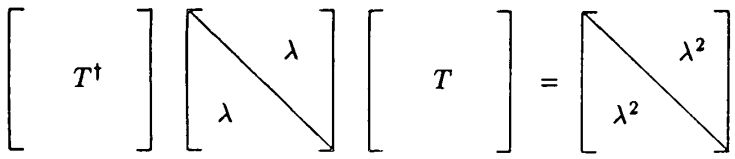

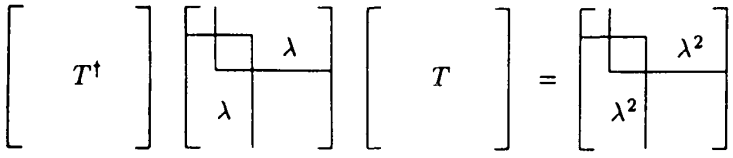

Figure 2 A schematic of the Van Vleck perturbation theory in a matrix representation. Each pannel represents the similarity transform $\mathbf{T}^\dagger\mathbf{H}\mathbf{T} = \mathbf{K}$, where $\mathbf{T} = \exp(i\lambda\mathbf{S})$. In the upper pannel **K** is transformed to a diagonal representation. In lower pannel **K** is transformed to a block-diagonal representation. This latter transformation allows intrinsically coupled zero-order states to remain coupled in the final representation.

This has the advantage that, so long as **S** is Hermitian, **T** is unitary. Furthermore Van Vleck formulated his theory so that rather than trying to remove all of the off-diagonal terms of order λ, one could chose **S** so that only select off-diagonal terms of order λ in the original representation do not appear in the transformed representation. The bottom panel of Fig. 2 shows an example where perturbation theory is used to construct a block-diagonal Hamiltonian. The λ^0 and λ^1 contributions to the terms within the blocks are unaltered by the transformation. In this manner one can carry out perturbation theory even when several zero-order states strongly mix among themselves. The disadvantage of this approach is that, after applying the perturbation theory, one then needs to individually diagonalize each block of the block-diagonal Hamiltonian. If the zero-order representation consists of harmonic oscillators, it is possible to carry out the exact same transformations as described above using an operator framework. Rather than perform matrix multiplications, one performs operator algebra. The results are the same, however, the operator algebra offers significant time savings. All of our work has taken advantage of the operator approach.

As would be expected of a perturbative approach, CVPT does a good job of describing the rotation-vibration spectra of molecules, like SO_2, in which the heavy masses lead to motions that are nearly harmonic over large ranges of the vibrational quantum numbers (41,55). It is less obvious that it should provide nearly as good an approximation for molecules containing anharmonic XH stretching modes or for molecules in which the vibrational states are highly mixed. Nonetheless, we have found that with a careful selection of coordinates and proper treatment of resonance interactions between nearly degenerate states we can achieve accurate perturbative expansions even at relatively high levels of rotation-vibrational excitation.

When CVPT converges, it provides significant savings in computer time and memory over variational approaches. The difference in the computational requirements of these two approaches is particularly impressive for molecules containing more than three atoms or for molecules with substantial rotational excitation (31,32,49,56). For example, in calculating the vibrational states of H_2CO up to 9000 cm^{-1} using the variational approach we needed to use a basis of at least 2000 carefully constructed nonseparable functions. In contrast, results with comparable accuracy were obtained by applying fourth-order CVPT to the vibrational Hamiltonian. This transformation required less than 1 min of computer time on an IBM 6000/340, and the transformed Hamiltonian is block diagonal with fewer than 66 states per block at energies below 10,000 cm^{-1}. The inclusion of molecular rotations increases the computation time by less than a factor of 3. For both the variational and the perturbative calculations, the size of the basis required to obtain converged energies increases by a factor of approximately $2J$, where J is the quantum number associated with the total angular momentum of the system. Whereas this makes variational calculations prohibitively expensive for J much above two, CVPT has been used to calculate H_2CO states with $J = 12$. Therefore, CVPT allows us to study systems at energies that would otherwise be computationally inaccessible.

The organization of the remainder of this chapter is as follows. We begin with a description of rotation-vibration Hamiltonians, discussing how they are derived and what form they take. This is followed by a brief description of canonical Van Vleck perturbation theory. Our focus here is not so much in describing the theory per se, since the theory is well known. Instead, it is to give an indication of how the perturbative results can be implemented on computers. The remainder of the chapter consists of results. We begin by examining the results of eigenvalue calculations, paying attention to the role of

coordinates and level of perturbative treatment. We then present select results of perturbation theory for calculating rotation-vibration mixing, calculating dipole induced rotation-vibration spectra, and iteratively improving potential energy surfaces by fitting to experimental observables.

II. ROTATION-VIBRATION HAMILTONIANS

The best-known Hamiltonian for describing the rotation-vibration motions of polyatomic molecules is based on rectilinear normal coordinates. The quantum mechanical version of this Hamiltonian was derived by Wilson and Howard (24,57). It was subsequently simplified by Watson for both nonlinear (58) and linear molecules (59). Although this Hamiltonian is excellent for treating small-amplitude vibrations, it has notable shortcomings when used to calculate large-amplitude vibrational motion. For this reason, many investigators have employed Hamiltonians based on alternative coordinate systems (28,30). For the general case of bond-angle coordinates, the derivation of the Hamiltonian is nontrivial. Handy and co-workers (60–62) have developed an approach for deriving the kinetic energy operator. They use the chain rule to transform the Cartesian coordinate kinetic energy operator, to a representation in which it is written in terms of the three Euler angles, a set of $3n - 6$ internal coordinates and their conjugate momenta. Although this process only requires that one can calculate the derivatives of internal vibrational coordinates and the three Euler angles with respect to the $3n$ Cartesian coordinates, the resulting algebra is sufficiently complicated that computer algebra systems are essential.

Although analytic expressions have been obtained using this approach for specific molecular systems, the resulting Hamiltonians are very complex. Moreover one does not have the flexibility of readily changing the choice of embedding or redefining the internal coordinates. For this reason we prefer to make use of an alternative approach. We use the method of Pickett (63), who, following the work of Meyer and Günthard (64), transformed the classical rotation-vibration Hamiltonian, expressed as a function of the angular momenta, $3n - 6$ internal coordinates and their conjugate momenta, to its quantum mechanical form following standard procedures (65). Pickett's treatment is general. The form of the Hamiltonian is the same regardless of the choice of embedding and choice of internal coordinates. As a result there is considerable flexibility in the choice of both internal coordinates and embedding of the body-fixed axis system.

In order to evaluate these expansion coefficients, one needs only to be able to transform between the curvilinear internal coordinates and the Cartesian coordinates and back to the internal coordinates. We now outline the central steps in this procedure.

A. The Pickett Hamiltonian

The quantum mechanical rotation-vibration Hamiltonian (63) takes the form

$$H = H_v + \frac{1}{2}\mathbf{J}^T(\mu + \Lambda)\mathbf{J} - \frac{1}{2}[\mathbf{P}^T\mathbf{A}^T\mathbf{J} + \mathbf{J}^T\mathbf{A}\mathbf{P}] \tag{1}$$

The first contribution is the ($J = 0$) vibrational Hamiltonian

$$H_v = \frac{1}{2}\mathbf{P}^T\mathbf{G}\mathbf{P} + V + V' \tag{2}$$

The kinetic energy contribution is expressed in terms of the internal coordinates, R_t, and their conjugate momenta, $P_t = -i\hbar\ \partial/\partial R_t$. Here t takes on any value between 1 and $3n - 6$. If the internal coordinates are the usual stretch-bend extensions, then the **G**-matrix elements, which are functions of R_t, are those of Wilson et al. (24). The terms that depend solely on the coordinates are the Born-Oppenheimer potential V and a mass dependent contribution V', this latter term resulting from the noncommunitivity of P_t and R_t.

In our perturbative treatment, we do not require an analytical form for **G** or V'. Instead we expand these coordinate-dependent terms, just as we do the potential V, in a Taylor series expansion about the equilibrium configuration (45,46,49). In order to evaluate the expansion coefficients we use finite difference techniques. The advantage of this strategy is that it only requires the evaluation of **G** and V' at specific molecular configurations. These contributions are evaluated by noting that $\mathbf{G} = \mathbf{B}\mathbf{B}^T$ and that V' is a function of the **G**-matrix elements. Here **B** is the $(3n - 6) \times 3n$ **B**-matrix, whose elements are

$$B_{tk} = \frac{\partial R_t}{\partial \xi_k} \tag{3}$$

The mass-weighted Cartesian coordinates are denoted ξ_k. Using Eq. (3), the numerical value of the B_{tk} matrix elements are determined for any value of the internal coordinates via a finite difference scheme. Once the **B**-matrix is constructed, expansions for G_{ij} and V', about the equilibrium configuration of the molecule, can be evaluated using higher-ordering differencing techniques.

Evaluation of the remaining contributions to the Hamiltonian is a bit more complicated. The matrices μ, Λ, and **A** are all solely functions of the internal coordinates. In contrast to **G**, however, the functional form depends on the criterion used for embedding the body-fixed reference frame. For example, evaluation of Λ and **A** requires knowledge of how the internal coordinates depend on the body-fixed Cartesian coordinates, as well as the inverse relationship $\partial\xi_k/\partial R_t$. These derivatives are obtained by inversion of the $3n \times 3n$ **B**-matrix, where the additional six rows are used to define the origin and embedding of the body-fixed axis system. There are a variety of possible embeddings. Eckart (66) has supplied a simple algorithm that will minimize Coriolis interactions at the molecular equilibrium configuration. This criterion is equivalent to finding an embedding such that $\mathbf{A} = 0$ at the equilibrium configuration. The final term, μ, is the instantaneous inverse moment of inertia tensor whose components are defined with respect to the body-fixed frame. Taylor series expansions of these terms about the molecular equilibrium configuration are again obtained by employing finite difference schemes.

To understand the various contributions to the rotation-vibration Hamiltonian, we rewrite the Hamiltonian in Eq. (1) as

$$H = H_v + H_r + H_{vr} \tag{4}$$

The vibrational contribution to this Hamiltonian is that given by Eq. (2), and the pure rotational contribution is

$$H_r = \frac{1}{2}\,\mathbf{J}^T(\mu^0 + \Lambda^0)\mathbf{J} \tag{5}$$

Here J_α are the components of the total angular momentum along the body-fixed axes. They obey the commutation relations

$$[J_\alpha, J_\beta] = -i\hbar\epsilon_{\alpha\beta\gamma}J_\gamma \tag{6}$$

The matrices μ^0 and Λ^0 are the equilibrium values of these matrices. It should be noted that in an Eckart frame $\Lambda^0 = 0$. Moreover, if the Eckart frame corresponds to the principal axis frame in the equilibrium configuration, then H_r takes the familiar form of a Hamiltonian for rigid-body motion:

$$H_r = \frac{1}{2}\left[\mu^0_{xx}J_x^2 + \mu^0_{yy}J_y^2 + \mu^0_{zz}J_z^2\right] \tag{7}$$

The vibrations and rotations are coupled via the H_{vr} term in Eq. (4). This coupling can be divided into two contributions. The first includes those terms that are proportional to $J_\alpha J_\beta$, which is the difference between the second term in Eq. (1) and H_r. These are referred to as centrifugal coupling. The second includes those terms that are linear in J_α. These contributions are referred to as α-axis Coriolis coupling and consist of the third term in Eq. (1).

B. Choice of Coordinates

In most of our calculations, it is computationally convenient to carry out the above derivations in terms of curvilinear normal coordinates Q_t and their conjugate momenta instead of R_t and their conjugate momenta. This distinction between curvilinear and rectilinear normal coordinates has been discussed in some detail in the work of Hoy et al. (6) and Quade (67). Here we briefly review the essential differences as they relate to the current discussion.

To understand the differences between curvilinear and rectilinear normal coordinates it is useful to consider the extension coordinates, **S**, which are linearly related to the mass-weighted Cartesian coordinates, ξ, by the **B**-matrix, i.e.,

$$S_t = \sum_{k=1}^{3n} B^0_{tk}\xi_k, \qquad t = 1, 2, \ldots, 3n - 6 \tag{8}$$

Here B^0_{tk} is the **B** matrix of Eq. (3) evaluated at the equilibrium configuration. In the limit of small-amplitude vibrations the internal coordinates **S** are equivalent to the bond-angle extension coordinates **R**. This is demonstrated in Fig. 3, where the angle extension in HCN is compared to the corresponding extension of S_t. The internal coordinates **S** are also related to the rectilinear normal coordinates via the linear transformation

$$S_t = \sum_{j=1}^{3n-6} L_{tj}q_j \tag{9}$$

A central advantage of the **q** representation is that these coordinates are related to the mass-weighted Cartesian coordinates *via* an orthogonal transformation.

Since the **S** are only equivalent to the **R** in the limit of small extensions, the **q** are related to the bond-angle coordinates, **R**, by a *nonlinear* transformation. Nonetheless, one can define a set of coordinates that are linearly related to the bond-angle coordinates as

$$R_t = \sum_{j=1}^{3n-6} L_{tj}Q_j \tag{10}$$

where both Eqs. (9) and (10) use the same transformation matrix. In the harmonic oscillator limit the **q** and the **Q** representations lead to identical Hamiltonians. We will

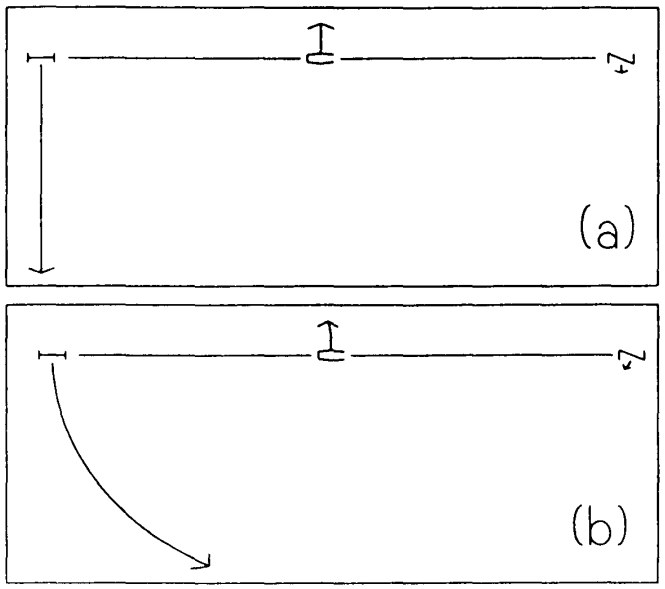

Figure 3 The internal bend extension coordinate for HCN is displayed pictorially for (a) the rectilinear, S, and (b) the curvilinear R coordinate representations. (From Ref. 47.)

refer to the **Q** as *curvilinear* normal coordinates and **q** as the *rectilinear* normal coordinates. These coordinates are defined to be the linear combination of the internal coordinates that leads to a separable harmonic oscillator Hamiltonian to lowest order.

Since this transformation to normal coordinates is invertible, one can readily determine the functional dependencies of the terms in Eq. (1) using either the normal or internal coordinates. Interestingly, in our study of vibrational states of the well-known local mode molecule H_2O and its deuterated analogs we found only minor differences between the results of CVPT in the internal and normal mode representations (46). The normal mode calculations, however, required significantly less computer time to run, since many terms in the Hamiltonian are constrained to zero by symmetry. For this reason we chose to use the normal mode coordinates for all subsequent studies.

Finally, the normal coordinates need not be linear combinations of the internal extension coordinates. In the results reported in this chapter, we use Simons-Parr-Finlan (SPF) (68) or Morse coordinates (2) for describing the stretching degrees of freedom. The normal coordinates are then defined as the appropriate linear combination of these coordinates. When we expand the coordinate dependent terms of the Hamiltonian in a Taylor series to a given order, the normal coordinates based on the SPF or Morse coordinates lead to a more accurate representation of *both* the model potential and the **G** matrix elements than do expansions based on the usual internal extension coordinates. In the case of the SPF coordinates, these expansions are exact at fourth order. Likewise, an appropriate choice of bending coordinates can also provide a more rapid convergence of these terms (49).

With the above approach we can combine the use of curvilinear normal coordinates with the Eckart frame. When we do so, the harmonic oscillator, rigid rotor, and, to lowest order, the Coriolis and centrifugal coupling contributions to H have exactly the same form as those found for the more commonly used Watson Hamiltonian (58).

III. CANONICAL VAN VLECK PERTURBATION THEORY

Although CVPT has long been recognized as a powerful and elegant perturbative approach (65), it has been found to be particularly useful in the theoretical treatment of rotation-vibration motions of polyatomic molecules where it has played an historic role (37). The traditional implementation of this approach, however, covered in some detail in the work of Amat et al. (36), has the serious drawback that as one goes beyond second order in the perturbative expansions, the resulting expressions for the energy levels become horrendously complex. Furthermore, if there is a resonance interaction, the equations have to be rewritten in order to correctly deal with the problem of small denominators. In order to address the shortcomings of the perturbative approach, over the last several years we have implemented a perturbative treatment of molecular rotations and vibrations that take advantage of the fact that the perturbative results are obtained through a series of canonical transformations. The commutator algebra involved in each individual canonical transformation is relatively trivial and can be carried out using FORTRAN codes (43,44). Combining the myriad of transformations to obtain the final perturbative expressions requires extensive bookkeeping, but this is a task that is easily left to the computer.

In this section we describe the required contact transformations. The section is structured in the following manner. It begins with a description of the perturbative transformations as they apply to the (J = 0) vibrational Hamiltonian. Select results are given for CO_2 and H_2CO. The section concludes with a brief overview of how these ideas are extended to include rotations. Here results will be presented for H_2O, H_2CO, and SO_2. More detailed accounts of these studies can be found elsewhere (43,44,47,49).

A. Molecular Vibrations

To obtain the perturbative solutions for the (J = 0) Hamiltonian we take as our starting point the vibrational Hamiltonian of Eq. (2), where the coordinate-dependent terms G_{ij}, V, and V' are expanded in a Taylor series in the dimensionless normal coordinates. The coordinates Q_i and corresponding momenta P_i are reexpressed in terms of harmonic oscillator raising and lowering operators $a_i^\dagger$ and a_i, where

$$a_i^\dagger|n_i\rangle = (n_i + 1)^{1/2}|n_i + 1\rangle; \qquad a_i|n_i\rangle = (n_i)^{1/2}|n_i - 1\rangle \tag{11}$$

Following Nielsen (35), this Hamiltonian is then reexpressed in the form

$$H = H^{(0)} + \lambda H^{(1)} + \lambda^2 H^{(2)} + \cdots + \lambda^n H^{(n)} \tag{12}$$

where λ is the perturbation parameter. We take $H^{(0)}$ to be N uncoupled harmonic oscillators with frequencies ω_j. Terms that are cubic in coordinates and momenta are included in $H^{(1)}$; quartic terms are included in $H^{(2)}$, and so forth. The expansion includes terms through nth order, the order to which the perturbative analysis is to be carried out. An exception is made for the partitioning of V' (cf. Eq. (2)). Here the constant term is put in $H^{(2)}$, the linear term in $H^{(3)}$, etc. With this choice of ordering, all the terms in $H^{(l)}$ are proportional to $\hbar^{(l+2)/2}$.

The transformations are accomplished via a succession of canonical transformations,

$$K = \exp[i\lambda^n[S^{(n)},]] \cdots \exp[i\lambda^2[S^{(2)},]] \exp[i\lambda[S^{(1)},]]H \tag{13}$$

A subtle point is that both the original and the transformed Hamiltonians are written as a function of the raising and lowering operators, $a_i^\dagger$ and a_i. Nonetheless the original operators are the raising and lowering operators for the normal modes, whereas the final raising and lowering operators are those for the final representation in which we wish to represent the Hamiltonian. One does not need to know the relationship between the original and final sets of raising and lowering operators if one is only interested in calculating the energy. The important fact is that the commutation relation between the raising and the lowering operators is preserved by the canonical transformations; hence this transformation is said to be canonical. As the form of these transformations implies, one first transforms H to an intermediate Hamiltonian

$$K_1 = \exp[i\lambda[S^{(1)},]]H \tag{14}$$

where

$$\exp[i\lambda[S^{(1)},]]H = H + i\lambda[S^{(1)}, H] - \frac{\lambda^2}{2!}[S^{(1)},[S^{(1)}, H]] + \cdots \tag{15}$$

Expanding H and K_1 in powers of λ and then equating powers of λ one obtains

$$K_1^{(0)} = H^{(0)} \tag{16}$$

$$K_1^{(1)} = H^{(1)} + i[S^{(1)}, H^{(0)}] \tag{17}$$

$$K_1^{(2)} = H^{(2)} + i[S^{(1)}, H^{(1)}] - \frac{1}{2!}[S^{(1)}, [S^{(1)}, H^{(0)}]] \tag{18}$$

and so forth. If $H^{(1)}$ is written in the normal form

$$H^{(1)} = \sum_{\mathbf{m}} \sum_{\mathbf{n}} C_{\mathbf{m},\mathbf{n}} \prod_{j=1}^{N} (a_j^\dagger)^{m_j}(a_j)^{n_j} \tag{19}$$

then a choice of

$$S^{(1)} = \sum_{\mathbf{m}}{}' \sum_{\mathbf{n}}{}' C_{\mathbf{m},\mathbf{n}} \frac{\Pi_{j=1}^{N} (a_j^\dagger)^{m_j}(a_j)^{n_j}}{i \sum_{j=1}^{N} (m_j - n_j)\hbar\omega_j} \tag{20}$$

can be shown, using the commutation relation $[a_i, a_j^\dagger] = \delta_{ij}$ and Eq. (17), to lead to

$$K_1^{(1)} = \sum_{\mathbf{m}}{}'' \sum_{\mathbf{n}}{}'' C_{\mathbf{m},\mathbf{n}} \prod_{j=1}^{N} (a_j^\dagger)^{m_j}(a_j)^{n_j} \tag{21}$$

The primes and double primes refer to restricted summations; a term in $H^{(1)}$ will not appear in $K_1^{(1)}$ if the corresponding term is included in $S^{(1)}$. In this way $K_1^{(1)}$ can be designed to include just those terms that lead to significant resonant coupling. Although K_1 is calculated through nth order, it is constructed to have the desired form only through first order.

In order to obtain a Hamiltonian that has the correct form through λ^2, a second transformation must be carried out. In analogy to the first

$$K_2 = \exp[i\lambda[S^{(2)},]]K_1 \tag{22}$$

In general, the operator $S^{(n)}$ can be chosen such that, through order λ^n, K_n contains only those terms that couple degenerate or nearly degenerate states.

There are many different forms that the transformed Hamiltonian K may take (43). A particularly convenient form is one where the Hamiltonian is block-diagonal. We have found this form to be an efficient approach for describing the triatomic molecules CO_2, HCN, H_2O, D_2O, and SO_2. It has also proven effective for the tetraatomics HCCH, DCCD, H_2CO and D_2CO and well as for the pentaatomic CHD_3 (43,45–47,49). This structure is also the basis of the construction of the polyad phase spheres of Kellman and co-workers (69–71).

The CO_2 molecule provides a simple example. The CO symmetric stretch frequency is twice that of the bend. This leads to the well-known 2:1 Fermi resonance (cf. Table 1). If this resonance were the only signficant resonance, then K in Eq. (21) could be constructed so that it contains, in addition to the diagonal contributions, all off-diagonal coupling terms that satisfy $2(m_1 - n_1) + (m_2 - n_2)$. The term $a_1a_2^\dagger a_2^\dagger + a_1^\dagger a_2 a_2$ is an example of such a term. At higher energies there is also a near 2:4 resonance between the symmetric and asymmetric stretching modes, hence better results are obtained when we do not decouple these states. As such there are two linearly independent resonances in this three-degree-of-freedom system. Consequently there remains the single good quantum number

$$N_t = 2n_1 + n_2 + 4n_3 \tag{23}$$

where n_i = number of quanta in the ith normal mode. Given that the states within each block are coupled by multiple resonance interactions, we will refer to N_t as the super-polyad quantum number as opposed to the polyad number.

Table 2 contains selected eigenvalues obtained from diagonalizing the individual blocks of the matrix representation of K. One can see that whereas the second-order results lead to errors of 20 cm^{-1} for excitation energies as low as 4218 cm^{-1}, the fourth-

Table 1 Calculated Harmonic Frequencies, ω_j, of CO_2, HCN, H_2CO, and SO_2

Molecule	Mode	Symmetry	$\omega_j/(cm^{-1})$	Motion
CO_2	1	Σ_g^+	1351.97[a]	CO symmetric stretch
	2	Π_u	671.99	OCO bend
	3	Σ_u^+	2393.37	CO asymmetric stretch
HCN	1	A_1	3440.09[b]	CH stretch
	2	A_1	2126.85	CN stretch
	3	E_1	726.97	HCN bend
H_2CO	1	a_1	2937.4[c]	CH symmetric stretch
	2	a_1	1777.8	CO stretch
	3	a_1	1544.0	HCH bend
	4	b_1	1188.3	Out-of-plane bend
	5	b_2	3012.0	CH asymmetric stretch
	6	b_2	1269.4	In-plane wag
SO_2	1	a_1	1664.7[d]	SO symmetric stretch
	2	a_1	519.5	OSO bend
	3	b_2	1380.4	SO asymmetric stretch

[a]Calculated from the potential in Ref. 8.
[b]Calculated from the potential in Ref. 72.
[c]Calculated from the potential in Ref. 74.
[d]Calculated from the potential in Ref. 82.

Table 2 Vibrational Energies for CO_2, Calculated at Various Orders of CVPT

		Curvilinear			Rectilinear			
State	N_i^{ab}	D_2	D_4	E_6	D_2^c	D_4	E_6	E_v
0, 2, 0	2	1.08	0.00	1283.65	1.68	−0.04	1283.64	1283.65
1, 0, 0	2	−1.61	0.01	1386.27	−2.21	0.05	1386.27	1386.27
1, 2, 0	4	3.64	0.02	2544.63	6.13	−0.24	2544.60	2544.63
2, 0, 0	4	−0.98	0.02	2667.16	−0.82	0.01	2667.16	2667.16
1, 2, 0	4	−5.78	0.02	2793.04	−8.43	0.29	2793.06	2793.03
1, 4, 0	6	8.12	0.06	3786.62	14.18	−0.80	3786.52	3786.60
3, 0, 0	6	0.19	0.07	3936.16	2.13	−0.12	3936.13	3936.15
3, 0, 0	6	−5.04	0.08	4057.67	−6.32	0.18	4057.68	4057.66
1, 4, 0	6	−13.50	0.08	4218.40	−20.22	1.00	4218.50	4218.40
0, 0, 4	16	0.51	0.22	9234.94	0.44	0.15	9234.87	9234.92
1, 6, 2	16	25.56	−0.01	9507.41	32.07	−2.13	9506.99	9507.40
3, 2, 2	16	7.98	0.05	9685.58	10.76	−0.61	9685.42	9685.59
2, 12, 0	16	64.42	1.75	9810.62	118.84	−17.99	9806.69	9810.02
4, 0, 2	16	−3.52	−0.10	9820.07	−2.94	−0.23	9820.01	9820.10
3, 2, 2	16	−15.73	−0.24	9955.52	−17.66	0.21	9955.58	9955.48
5, 6, 0	16	30.76	1.99	10048.18	71.18	−10.34	10045.68	10047.88
2, 4, 2	16	−33.37	−0.40	10135.90	−40.55	1.82	10136.24	10136.02
6, 4, 0	16	5.82	1.95	10258.13	32.08	−4.88	10256.68	10257.91
8, 0, 0	16	−10.09	1.57	10430.10	2.82	−1.74	10429.30	10429.90
8, 0, 0	16	−22.70	1.78	10576.85	−18.69	−0.18	10576.35	10576.55
7, 2, 0	16	−41.97	2.48	10756.75	−47.87	3.15	10756.88	10756.25
6, 4, 0	16	−66.39	2.77	10976.48	−87.74	8.66	10977.76	10975.82
5, 6, 0	16	−95.04	2.61	11226.88	−137.10	16.32	11229.87	11226.23
3, 10, 0	16	−127.56	1.90	11503.78	−195.72	26.34	11509.11	11502.27

[a] $N_i = 2n_1 + n_2 + 4n_3$.
[b] Normal mode labels correspond to leading component in wave function expansion.
[c] $D_n = E_6 - E_n$, where E_n is result of nth-order CVPT.

order curvilinear results are very accurate up to 11,500 cm^{-1}. When the Hamiltonian for CO_2 is expanded in rectilinear normal coordinates, the convergence is much slower, and the sixth-order results are in poorer agreement with the variational energies. This is a consequence of the slower convergence of the expansion of the Hamiltonian in terms of the rectilinear normal coordinates, compared to the analogous expansion in terms of curvilinear normal coordinates. It is important to note that when there are no near degeneracies in a system, as is the case for HCN (cf. Table 1), and K in Eq. (21) contains only diagonal terms, the curvilinear and rectilinear normal coordinate expansions of the Hamiltonian yield identical expressions for K. This is a consequence of the fact that K is expanded in powers of $\delta = \hbar^{1/2}$ with terms in K_l containing only terms of $O(\delta^{l+2})$. Therefore, mathematically, this expansion must be independent of the underlying coordinates.

Formaldehyde represents a molecule that lies somewhere between CO_2 and HCN in terms of the importance of resonances in the Hamiltonian. We will therefore report only the curvilinear normal coordinate results. For the calculations on H_2CO we use the potential of Harding and Ermler (73) as modified by Bowman and co-workers (74).

H_2CO has C_{2v} symmetry and therefore four point-group representations: a_1, a_2, b_1, b_2. In order to understand how the blocks are defined one can inspect the fundamental frequencies of Table 1. This table shows that there are two high-frequency modes with similar frequencies (ω_1 and ω_5). These frequencies are, in turn, approximately twice the frequency of the remaining four modes. Consequently, there are several likely candidates for 2:1 Fermi resonance interactions. In addition, there is a strong Darling-Dennison resonance between the two high-frequency CH stretches. We expect that the lower-frequency modes may also be coupled by Darling-Dennison resonances. Despite all these resonances there remains a single constant of the motion,

$$N_t = 2n_1 + n_2 + n_3 + n_4 + 2n_5 + n_6 \tag{24}$$

For $J = 0$ and with this choice of N_t, the magnitude $|E_6 - E_4|$, where E_n is the result of nth-order perturbation theory, is less than 1 cm^{-1} for all the states up to 10,000 cm^{-1} above the zero-point energy (cf. Fig. 4). This difference, which we take to be roughly a measure of convergence, is about the same magnitude as $|E_v - E_6|$ where E_v are the eigenvalues obtained from a variational calculation (49). Higher J results were found to display similar convergence.

The existence of the superpolyad quantum number is not simply based on energy considerations. We have found, in fact, that there is considerable overlap in the spectrum between states of differing superpolyad numbers. For example, many states with $N_t = 7$ have a greater energy than states with $N_t = 8$. The additional considerations for constructing the superpolyad quantum number involve the connectivity of states. The magnitude of matrix elements between two vibrational normal-mode zero-order states $|\mathbf{n}\rangle$ and

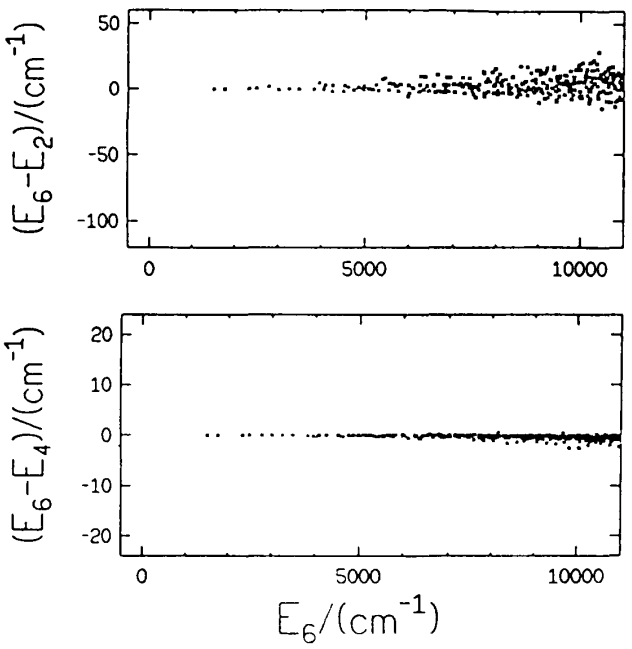

Figure 4 Convergence plots of perturbative energies for the $J = 0$ curvilinear normal coordinate Hamiltonian of H_2CO. The energy difference $E_6 - E_n$ is plotted as a function of E_6 for the energy eigenstates with a_1 symmetry and $N_t \leq 8$. Note the difference in the scales of the y-axis. (From Ref. 49.)

$|\mathbf{n}'\rangle$ falls off rapidly as the difference in the quanta in the two states

$$\Delta = \sum_{i=1}^{6} |n_i - n_i'| \tag{25}$$

increases. At the vibrational energies considered in this paper, the magnitude of coupling terms with $\Delta \geq 5$ are typically much less than the inverse of the density of states. This is not true of the lower-order resonances. Therefore, the consideration of *low-order* resonances ($\Delta = 3$ or 4) are crucial for determining the superpolyad structure (53).

B. Molecular Rotations

In order to extend these ideas to include rotation we cannot simply express the full rotation-vibration Hamiltonian in the form of Eq. (19) and apply the transformations of Eq. (13). If we did so, we run into difficulties; the coefficients $C^{(l)}_{\mathbf{m},\mathbf{n}}$ no longer commute, as they are now functions of the angular momentum operators. Analytical expansions for K_1 and K_2 through fourth order in rectilinear normal coordinates are given by Amat et al. (36), but in order to implement high-order CVPT additional modifications are necessary.

To remove the operator dependence of the $C^{(l)}_{\mathbf{m},\mathbf{n}}$, while maintaining the simple form of H given in Eq. (19), we reexpress the rotation operators in terms of the raising and lowering operators for two coupled, degenerate harmonic oscillators. Following Schwinger (75), in a body-fixed coordinate system, the rotation operators are redefined as

$$\begin{aligned}
J_x &= \frac{1}{2}\left(a_{r1}^{\dagger}a_{r2} + a_{r1}a_{r2}^{\dagger}\right) \\
J_y &= \frac{i}{2}\left(a_{r1}^{\dagger}a_{r2} - a_{r1}a_{r2}^{\dagger}\right) \\
J_z &= \frac{1}{2}\left(a_{r1}^{\dagger}a_{r1} - a_{r2}^{\dagger}a_{r2}\right) \\
J^2 &= J_x^2 + J_y^2 + J_z^2 \\
&= \frac{1}{2}\left(a_{r1}^{\dagger}a_{r1} + a_{r2}^{\dagger}a_{r2}\right) \times \left[\frac{1}{2}\left(a_{r1}^{\dagger}a_{r1} + a_{r2}^{\dagger}a_{r2}\right) + 1\right]
\end{aligned} \tag{26}$$

These definitions have been used by several groups (76–79) to gain insights into the properties of two harmonically coupled degenerate anharmonic oscillators.

In contrast to the work of Nielsen (35) we introduce the rotation terms at higher orders in the perturbative expansion. In expanding $\mathbf{A}$, $H^{(1)}$ includes constant terms, $H^{(2)}$ includes linear terms and so forth. In expanding μ and Λ, $H^{(2)}$ includes constant terms, $H^{(3)}$ includes linear terms, and so forth. Once again, with this choice of ordering, all the terms in $H^{(l)}$ are proportional to $\hbar^{(l+2)/2}$. When taking the perturbation theory to high orders, it is not crucial to introduce the rotational couplings in $H^{(0)}$ because these terms are much smaller than the corresponding contributions to the vibrational Hamiltonian.

In order to take advantage of the molecular symmetry, the rotational contribution to the full-wave function must be symmetry adapted. This is accomplished by transforming to the Wang basis (80). Second, the Hamiltonian matrix representation of K is not, in general, real symmetric. Huber (81) has discussed a rotational basis that is both sym-

metry adapted and that leads to a real symmetric Hamiltonian matrix. Following his approach, the rotation basis is expressed as linear combinations of the harmonic oscillator basis vectors $|n_{r1}, n_{r2}\rangle$ as

$$|J, K^+\rangle = \frac{1}{\sqrt{2}} [|n_{r1}, n_{r2}\rangle + (-1)^{J+K}|n_{r2}, n_{r1}\rangle]$$

$$|J, K^-\rangle = \frac{1}{i\sqrt{2}} [|n_{r1}, n_{r2}\rangle - (-1)^{J+K}|n_{r2}, n_{r1}\rangle] \tag{27}$$

if $n_{r1} \neq n_{r2}$; otherwise

$$|J, 0\rangle = |n_{r1}, n_{r1}\rangle \tag{28}$$

The harmonic oscillator labels n_{ri} are related to J and K by $n_{r1} = J + K$ and $n_{r2} = J - K$, where J and K are the quantum numbers associated with the total angular momentum and the projection of the angular momentum onto the molecular z-axis, respectively. As shown by Huber (81), these basis vectors lead to the relations

$$J^2|J, K^\pm\rangle = J(J + 1)\hbar^2|J, K^\pm\rangle \tag{29}$$

and

$$J_z|J, K^\pm\rangle = \pm iK\hbar|J, K^\mp\rangle \tag{30}$$

Combining these rotation functions with the usual vibrational basis functions provides a symmetry-adapted rotation-vibration basis.

With this basis the Hamiltonian matrix for K is block-diagonal, where each block contains states of the same Γ, J, and N_t quantum numbers, where Γ refers to the molecular symmetry. Since CVPT is performed in an operator framework, the perturbative transformations to determine K are performed only once.

Figure 5 illustrates the convergence for the $J = 6$ states of SO_2. For these calculations we use the potential of Carter et al. (82) expanded through fourth order in SPF coordinates for the stretches and $\Delta z = \cos\theta - \cos\theta_e$ for the bend coordinate. For SO_2, the superpolyad number,

$$N_t = 2(n_1 + n_3) + n_2 \tag{31}$$

where the normal modes are defined in Table 1. By comparing Fig. 5a, b, noting that the scale of the ordinates differs by a factor of 10, it is clear that the energy levels are well converged at sixth order. Where possible, we have tested this convergence by comparing our results to variational calculations. We find that $|E_n - E_{n-2}| \sim |E_v - E_n|$ (46).

Calculations of bend states in H_2O provide a rigorous test of perturbation theory. This is evident in the results of Fig. 6. There, the energy difference ΔE_{rot} between pure bending states with $J = 2$, and $K = 2$ and the corresponding $J = 0$ states is plotted as a function of the number of quanta in the bend. The five lines represent, from top to bottom, the results of a variational calculation and the results of eighth-, sixth-, fourth-, and second-order perturbation theory. The perturbative results are clearly approaching the variational results, albeit slowly. This slow convergence can also be seen in the results of Fig. 5. Here the states with largest $|E_8 - E_6|$ are those in which most of the vibrational excitation is in the bend.

The poor agreement between variational and perturbative results that is observed for large values of the bend quantum numbers is a consequence of the fact that the

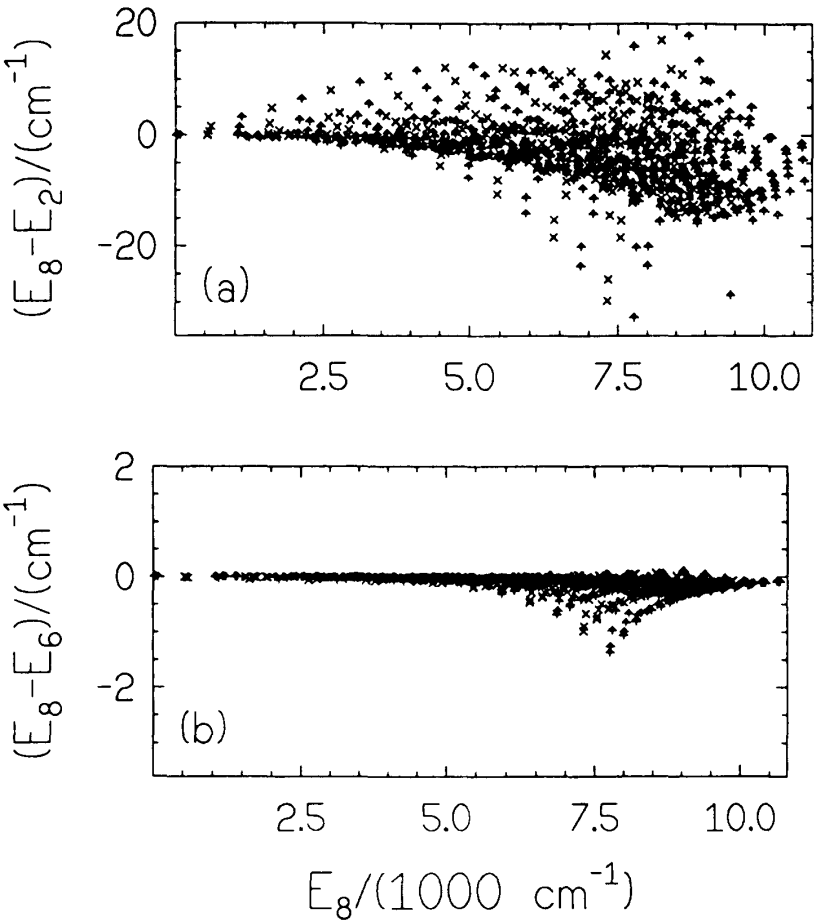

Figure 5 Convergence plot (cf. Fig. 4) of the a_1 symmetry states of SO_2 with $J = 6$ and $N_t \leq 16$. To show the superpolyad structure, states with even and odd values of N_t are represented by $\triangle$ and $\times$, respectively. (From Ref. 49.)

functional form of ΔE_{rot}, observed for the variational results in Fig. 6, cannot be modeled as a low-order expansion in the bend quantum numbers. There are two reasons for this behavior. The first occurs for $J = 0$, when the molecule has four or more quanta of excitation in the bend the wavefunction has nonzero amplitude at $\theta = \pi$. The zero-order harmonic oscillator description of the bending motions is expected to diverge at these energies. Second, as the molecule becomes linear, the moment of inertia along the molecular axis approaches zero and therefore the corresponding rotational constant approaches infinity. Clearly this term cannot be represented well by a low-order Taylor series expansion in the bend coordinate. In spite of these difficulties, the results in Fig. 6 demonstrate that CVPT is converging toward the variational results.

IV. APPLICATIONS OF CVPT

The discussion to this point has focused on applications of CVPT to calculate transition frequencies. In the remainder of this chapter we will discuss three applications of CVPT that involve the determination of other properties of the wave function. We will present select results of calculations of rotation-vibration mixing (49), calculation of rotation-vibration dipole induced transitions (48), and iterative refinement of potential energy

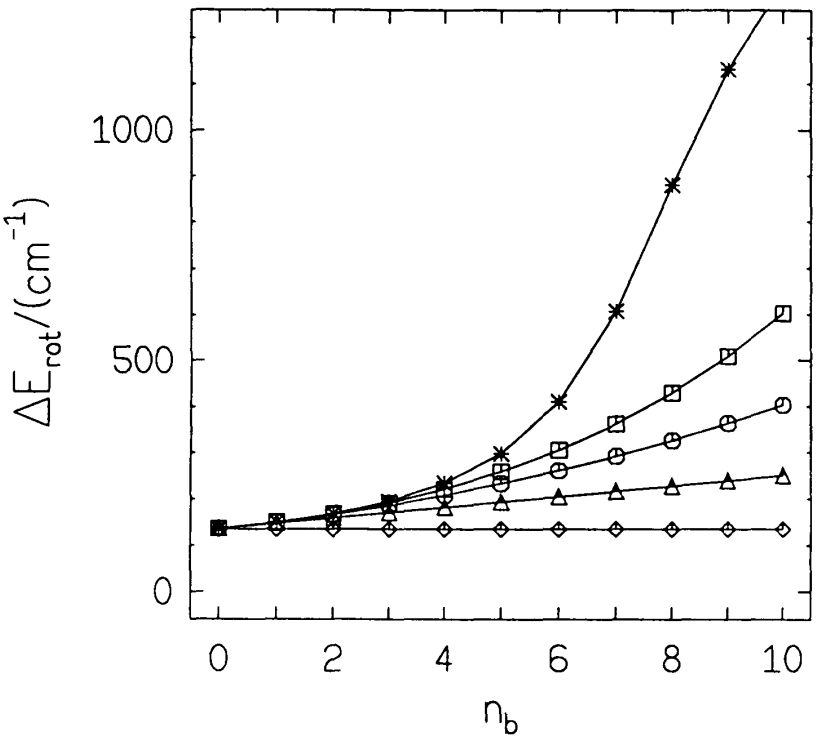

Figure 6 The differences between energies of bend overtones in H_2O with $J = 2$ and $K = 2$ and the energies of the corresponding $J = 0$ states are plotted as a function of the number of quanta in the bend. The results of variational, eighth, sixth, fourth, and second-order perturbative calculations are denoted by *, □, ○, △, and ◇ respectively. The perturbative results model the rotation-vibration coupling as a polynomial expansion in the bend quantum number. Given the actual form of this coupling, as obtained from the variational calculation, the slow convergence of CVPT is not surprising. (From Ref. 49.)

surfaces with the goal of obtaining improved agreement between theoretically calculated and experimental measured observables (51,54). In variational and perturbative methods, errors in the wave function of $O(\lambda^n)$ produce energies with corrections on the order of $O(\lambda^{2n})$. Other observables will be sensitive to different features of the wave function and calculation of these properties provides a stringent test of the perturbative methods presented above.

A. Rotation-Vibration Mixing

It is well recognized that rotation-vibration interactions play a crucial role in the spectroscopy and dynamics of many polyatomic systems. The H_2CO molecule, for which Coriolis interactions have been well characterized at low levels of vibrational excitation (83), provides an excellent example. At vibrational energies as low as 7500 cm^{-1} above the zero-point energy, Dai et al. (13) have demonstrated clearly that rotation has a profound effect on the nature of molecular vibrations; their results indicate a breakdown in the separability of the rotational and vibrational degrees of freedom. While Frederick et al. have shown that rotation-vibration mixing is prevalent in the classical dynamics of SO_2 at energies near the threshold to dissociation (84), they have found little rotation-vibration mixing for energies less than 15,000 cm^{-1}.

In order to quantify the degree of rotation-vibration mixing we examine the "goodness" of the rotational energy as a constant of the motion, this being just one of the several possible measures of rotation-vibration mixing (49). In the first row of Fig. 7 we plot the standard deviation of the symmetric top energy ΔE_S as a function of its expectation value $\langle E_S \rangle$ for the $J = 12$ states of SO_2 with A_1 symmetry. Here E_S is defined to be the symmetric top energy. The associated Hamiltonian is (85)

$$H_S = \frac{1}{2}\left[\frac{\mu^0_{xx} + \mu^0_{yy}}{2}(J^2 - J_z^2) + \mu^0_{zz}J_z^2\right] \tag{32}$$

where $\mu^0_{\alpha\alpha}$ are the inverse moment of inertia tensor elements of Eq. (7). Each column in the figure corresponds to increasing values of N_t, the largest being $N_t = 16$. With the trivial exception that the number of states increases as N_t increases, the plots are quantitatively similar. This similarity indicates that the nature of the rotational states is insensitive to the amount of vibrational energy. We have tested the sensitivity of these results to the order of perturbation theory. These displayed results were obtained by applying sixth-order CVPT to the rotation-vibration Hamiltonian; they are quantitatively similar to the fourth-order results.

That ΔE_S is nonzero is not so much a result of rotation-vibration mixing, as it is a result of SO_2 being an asymmetric top. This conjecture is verified by plotting ΔE_A as a function of the expectation value of the rigid asymmetric top Hamiltonian given by Eq. (7). These results are displayed in the second row of Fig. 7. We find that ΔE_A is

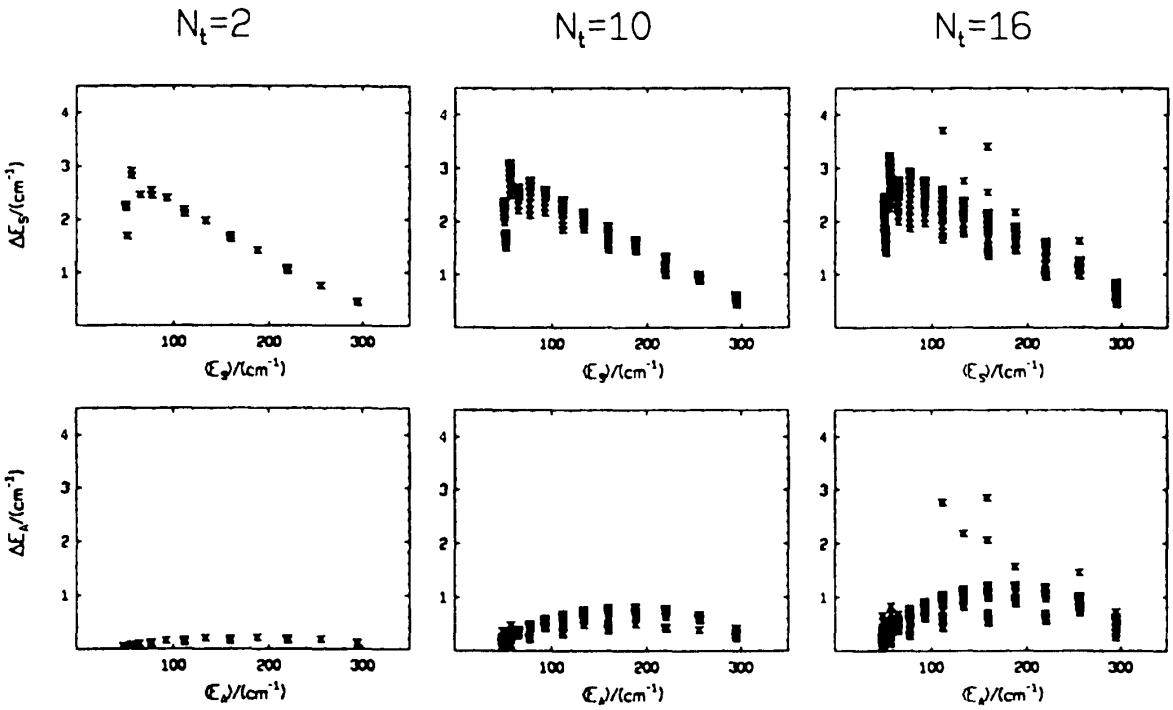

Figure 7 Rotation-vibration mixing in SO_2 for states of a_1 symmetry and $J = 12$. The columns correspond to $N_t = 2$, 10, 16 (cf. Eq. (31)). The standard deviation of the symmetric and asymmetric top energies are plotted against the expectation value of the corresponding energies in the upper and lower row, respectively. (From Ref. 49.)

extremely small over a wide range of vibrational energies and that the few exceptions result from accidental degeneracies.

Neither of the above results include the effects of the instantaneous distortion of the molecule, as the $\mu^0_{\alpha\alpha}$ are taken to be constants. In both these calculations we neglect the coordinate dependence of the inverse moment of inertia tensor in Eq. (5) and evaluate μ in the equilibrium configuration. This definition was the one of several definitions considered by Frederick et al. (84) that leads to the smallest standard deviation. If we were to include the coordinate dependence of μ in our definition of the rotational energy operators, then both ΔE_S and ΔE_A would be substantially larger.

The rotation-vibration interactions for H_2CO provide a striking contrast to those found for SO_2. For the calculation on H_2CO we used the same potential as was used for the $J = 0$ calculation. The Eckart conditions were used to embed the body-fixed axes. The convergence in the perturbative energies for $J \leq 12$ was similar to that found for $J = 0$ (cf. Fig. 4). As was found for SO_2, the rotation-vibration mixing results are similar for the fourth- and sixth-order effective Hamiltonians K; the results we present are fourth order. The breakdown in the "goodness" of the K quantum number is evident in Fig. 8, where we have plotted ΔE_S as function of $\langle E_S \rangle$. The first four panels correspond to the $N_t = 0$, 2, 4, and 6 blocks respectively. These N_t blocks roughly correspond to states with energies of 0, 3000, 6000, and 9000 cm^{-1}. Only for $N_t = 0$ does it appear that K is a good quantum number. The little mixing that occurs here, in contrast to the higher N_t blocks (note the change in the scale of the y-axis), is a result of H_2CO being an asymmetric top. The separability between the rotational and vibrational degrees of freedom observed for $N_t = 0$ diminishes dramatically with increasing vibrational energy. At vibrational energies near 9000 cm^{-1} above the zero-point energy (cf. Figs. 8d–f), the mixing is pronounced.

B. Dipole Intensities

The second application of CVPT we will investigate is the calculation of dipole intensities. As was alluded to above, these calculations provide a stringent test of our perturbative methods. To understand this, consider the zero-order picture we are using to describe molecular vibrations. It consists of N uncoupled harmonic oscillators. To lowest order, the dipole moment operator consists of a constant and linear term. Therefore in the harmonic limit, only transitions with $\Delta v = 1$ are allowed, where v is the number of quanta in a particular mode. At higher-order perturbation theory, the order of the perturbation theory determines the maximum value of Δv. For example, at fourth-order perturbation theory, only $\Delta v \leq 4$ transitions can be calculated. The predicted intensities for transitions with $\Delta v > 4$ will be zero. Also, studies on one-dimensional systems have shown that the predicted value of the transition intensity is highly sensitive to features of the inner wall of the potential (86,87). As we are interested in studying the nature of highly excited vibrational states, the calculation of the intensity of transitions to these states should provide a rigorous test of the accuracy of the CVPT results.

1. Calculation of IR Intensities

Many of the insights into the nature of highly excited vibrational states have been gleaned from the energies and intensities of molecular transitions. For example, our understanding of the coupling of "bright," local mode stretch states with nearly degenerate "dark," background states is based on intensity borrowing arguments. The contribution to the

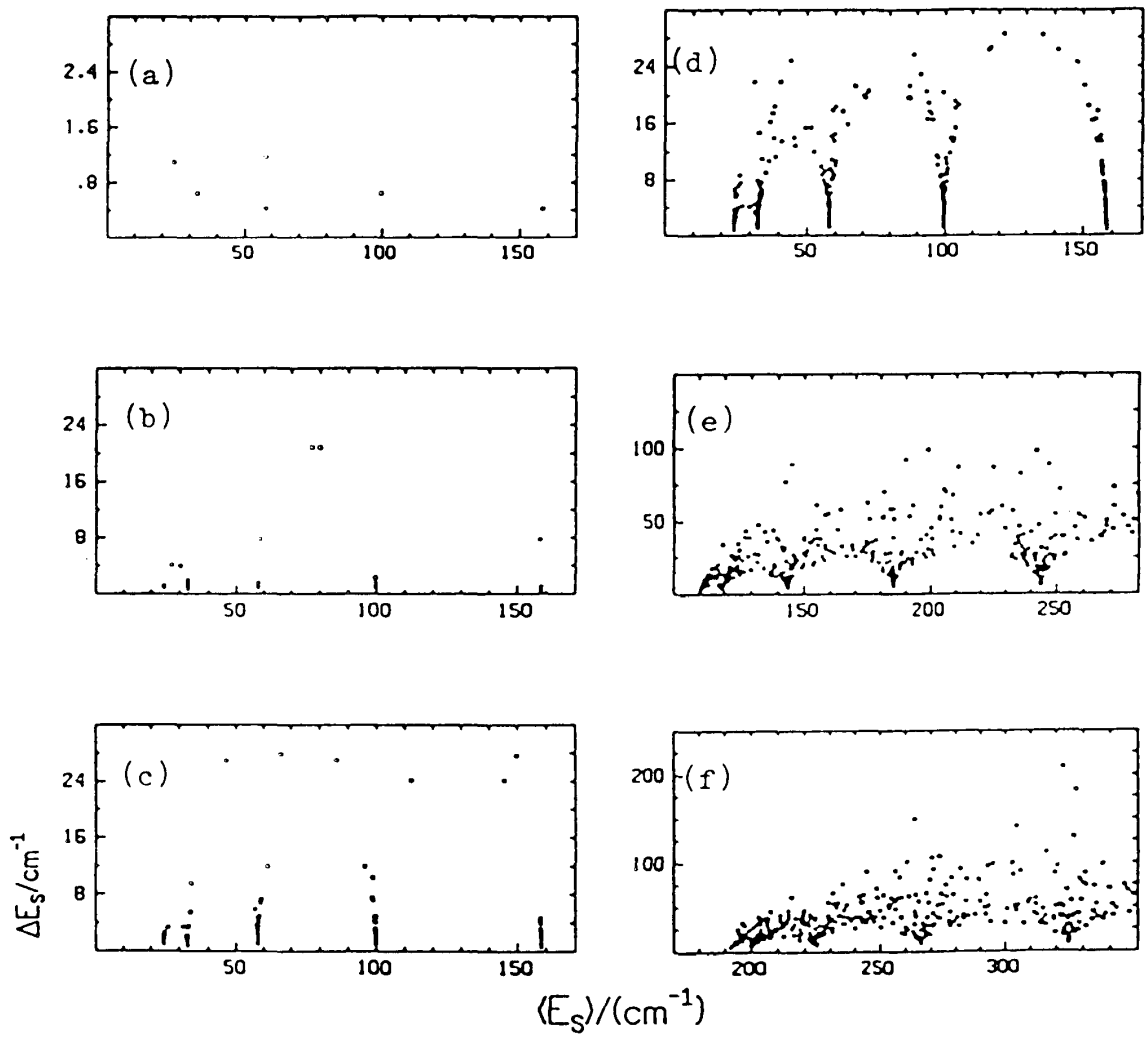

Figure 8 The standard deviations of the symmetric top energies, plotted as a function of the corresponding expectation values for H_2CO for (a) $J = 4$, $N_t = 0$, (b) $J = 4$, $N_t = 2$, (c) $J = 4$, $N_t = 4$, (d) $J = 4$, $N_t = 6$, (e) $J = 9$, $N_t = 6$, $E_v \leq 350$ cm^{-1}, and (f) $J = 12$, $N_t = 6$, $E_v \leq 350$ cm^{-1}. The approximate energy for a given N_t block is $N_t \times 1500$ cm^{-1}. (From Ref. 49.)

transition intensity between vibrational eigenstates $|v\rangle$ and $|v'\rangle$ that results from the α component of the dipole moment operator μ_α along the body-fixed α-axis is

$$I_{v,v'} \propto |\langle v|\mu_\alpha|v'\rangle|^2 \tag{33}$$

Here μ_α is a function of the vibrational coordinates. The proportionality constant involves the summation over all possible transitions out of populated ro-vibrational states. Determination of this constant will be discussed in more detail in Sec. IV.B.3. To evaluate the matrix element in Eq. (33) using CVPT, we apply the same transformation to μ_α as was used to transform H to K (cf. Eq. (13)):

$$\mu_\alpha^{\text{eff}} = \exp[i\lambda^n[S^{(n)},]] \cdots \exp[i\lambda^2[S^{(2)},]]\exp[i\lambda[S^{(1)},]]\mu_\alpha \tag{34}$$

If K has only diagonal contributions, then $I_{v,v'}$ is given by the square of the v, v' element of the μ_α^{eff} matrix. If K includes resonance interactions, then the procedure is slightly more complicated. We will return to this latter situation later in this section.

To illustrate this procedure and to evaluate the utility of CVPT for determining intensities of transitions, we will consider two models of a CH stretch potential. The first potential is the one-dimensional contribution to the ab initio HCN stretch surface calculated by Botschwina (88). The second surface (GM1), developed by Baggott (89), is expressed as a quartic expansion in the Morse coordinate, $y = (1 - \exp\{\alpha(r - r_e)\})$. These two potentials and the difference between them are plotted in Fig. 9. In addition to appearing very similar, the overlap of the lowest seven eigenstates, calculated on these two potentials, is larger than 0.98 (90). In contrast, the calculated intensities of the $0 \rightarrow 6$ transition differ by nearly a factor of 5, thereby demonstrating that transitions *intensities* can be sensitive to very different features of the wave function than are transition *frequencies*.

The calculated intensities for these two potentials are plotted in Fig. 10. Converged variational results, obtained by Smith and Lehmann (86), are compared to our results calculated using second- through eighth-order CVPT. For these states, the results of CVPT are in good agreement with the variational intensities. This result is quite remarkable. As stated, CVPT is based on a zero-order harmonic oscillator, linear dipole ap-

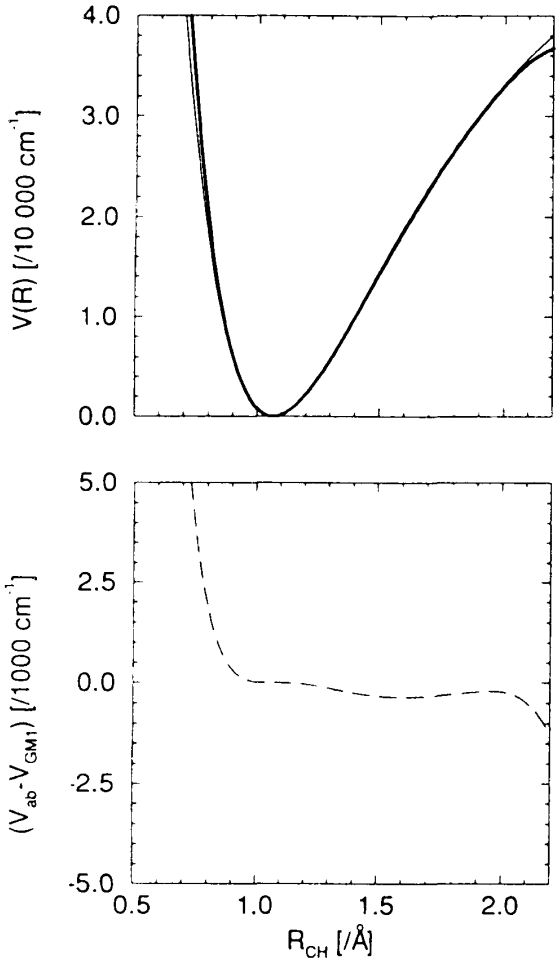

Figure 9 Plot of two representations of the CH stretch potential in HCN. The bold line represents the ab initio surface and the thin line gives the GM1 surface. The dashed line provides the difference between the two surfaces. This third quantity is plotted on the enlarged scale.

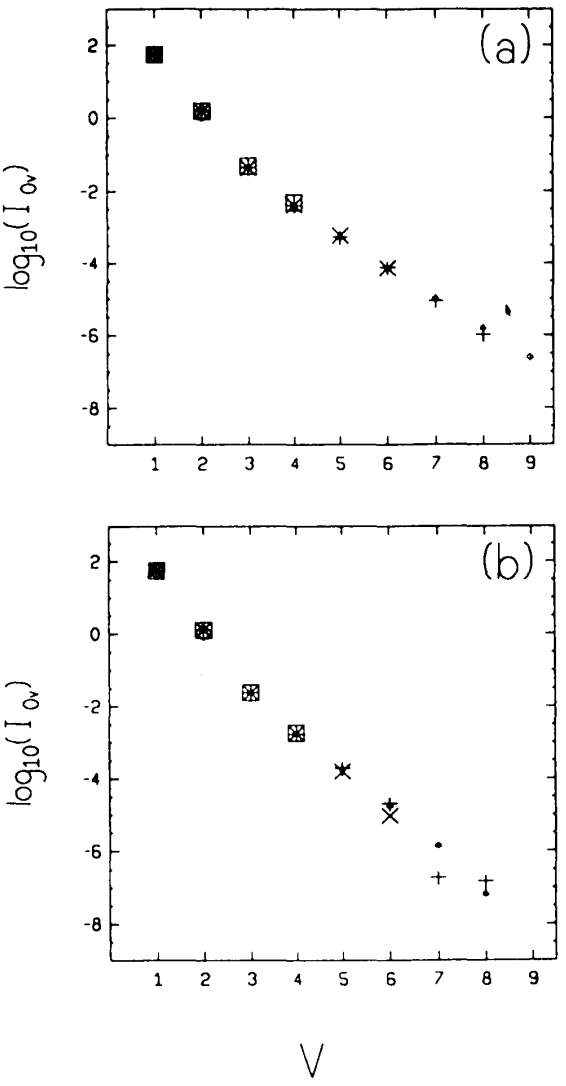

Figure 10 Transition intensities, I_{0v}, calculated using second, fourth, sixth, and eighth-order CVPT, denoted by ◇, □, X and +, respectively, are compared to transition intensities, denoted by *, obtained variationally (86) for transitions on (a) ab initio and (b) general Morse (GM1) CH stretch potentials. Only nonzero intensities are included in the plots. (From Ref. 48.)

proximation, and within this approximation only transitions with $\Delta v = 1$ are allowed. At nth order in perturbation theory, the effective dipole moment operator will only contain terms through $(a^\dagger)^n$ and transitions with $\Delta v > n$ are predicted to have zero intensity. In spite of this limitation, the fourth order, $\Delta v = 4$ intensities are predicted to be 4.83 and 1.86 m/mol, compared to variational results of 4.07 and 1.76 m/mol, respectively. By eighth order, the errors in the perturbative intensities are smaller than 1%.

2. The Spectrum for HCN

Having demonstrated that CVPT can accurately predict the differences in transition intensities on two one-dimensional potentials, we will investigate the sensitivities of the predicted intensities to the choice of off-diagonal coupling terms that are to be included in K. In Fig. 11, the perturbatively obtained stretch spectrum for HCN in the region from

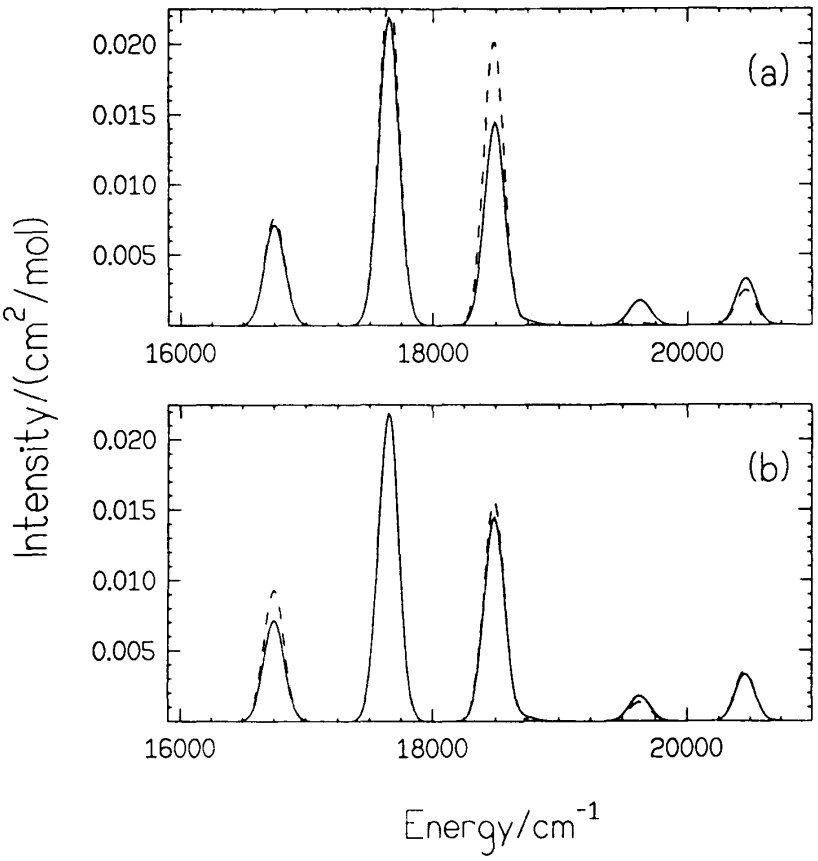

Figure 11 The perturbative vibrational spectrum of HCN (---) is compared to the variational spectrum (——). Both have been calculated using the two-dimensional potential and dipole moment surfaces of Botschwina (88). The transition energies have been artificially broadened using Gaussians with FWHM of 112 cm^{-1}. The five prominent peaks in the spectrum, in increasing energy, correspond to the (4,2), (5,1), (6,0), (5,2), and (6,1) states. The effective Hamiltonian, K, is diagonal in (a) and block-diagonal in (b). The improved results of (b) are a result of allowing terms in the K, that couple the state (v, 0) with the states ($v - j$,j). (From Ref. 48.)

16,000–21,000 cm^{-1} is compared to the variational spectrum. For these calculations, the two-dimensional stretch potential and dipole moment surfaces, calculated by Botschwina (88), are used.

The spectrum in Fig. 11a was obtained having transformed K to a form where it contains no resonance interactions. These results, in comparison to variational results (48), are improved (cf. Fig. 11b) when K is constructed so that it contains terms that couple the CH and CN stretch modes. The most important coupling terms between the stretches are the n:n resonance terms, e.g., $a_1^\dagger a_1^\dagger a_2 a_2 + a_1 a_1 a_2^\dagger a_2^\dagger$. The subscripts 1 and 2 denote the CH and CN stretching modes respectively. These terms contribute to the Hamiltonian at second and higher orders.

Calculating the dipole intensities, with resonances included, requires one step in addition to the procedure described above. After the matrix representation of the effective dipole moment operator is calculated, in the same basis as was used to set up the block-diagonal Hamiltonian matrix, the similarity transformation that diagonalizes the Hamiltonian matrix is applied to the dipole moment matrix. The intensity of the transition

between the v and v' state is given by the square of the v, v' element of the resulting matrix.

In addition to the 1:1 resonance discussed above, Smith et al. (15) have found that in certain regions of the spectrum there is a strong 2:3 resonance between the CH and CN stretches. To investigate the quantitative effects of these two resonances, we examine the states (2,4), (4,1), and (5,0), the notation being (n_1, n_2). While the inclusion of either or both of these resonances shifts the transition frequencies by less than 3 cm $^{-1}$, the inclusion leads to dipole intensities that are in much better agreement with those obtained variationally (cf. Table 3). The calculated intensity of the transition to the (2,4) state is found to range over three orders of magnitude depending on which resonances are included in K. When both resonances are included, there is only a 5% difference between the perturbative and the variational intensities.

This result demonstrates a very important issue in using CVPT to compute spectra. The quality of the approximation is sensitive to the choice of resonances included in K. Even for molecules, like HCN, where the vibrational spectrum is extremely well reproduced when K in Eq. (21) contains only diagonal terms (47), intensity studies can provide important insights into what resonances may be important in at least small regions of the potential.

3. Intensities of Transitions between Rotational States

The discussion has focused on calculations of the band intensities for various transitions between vibrational states in HCN. While these studies provide insights into the nature of the mixing between states as well as information about the effectiveness of CVPT for computing these quantities, this is a system where other methods can be used to calculate more accurately the quantities of interest. In this section we will investigate a system where exact variational calculations are prohibitively expensive. Computation of the full rotation-vibration spectrum of H_2CO at 10 K requires the ability to calculate rotation-vibration states up to $J = 8$. Variational calculations of the vibrational band origins up to 9000 cm $^{-1}$ are computationally demanding due to the large number of states that must be included to converge the calculation. At $J = 8$ the number of states increases by about a factor of 17, putting these calculations outside of the range of those that can be attempted using exact variational approaches.

As we demonstrated above, CVPT can be used to compute properties of rotation-vibration states of H_2CO. To calculate the rotation-vibration spectrum, we must also be able to calculate the intensity of the transition between the energy eigenstate $|v'\Gamma'M'J'\rangle$ and $|v\Gamma MJ\rangle$. Here the eigenstates are defined in terms of their total angular momentum

Table 3 Calculated Intensities (cm/mol) for the (2,4), (4,1), and (5,0) States in HCN, Obtained by Including Different Resonances between CH and CN Stretching Normal Modes

Resonance	(2,4)	(4,1)	(5,0)	$E_{2,4}$	$E_{4,1}$	$E_{5,0}$
Diag	0.043	28.84	32.95	14717.53	14741.47	15644.87
1:1	0.024	28.08	29.16	14717.31	14740.90	15646.29
3:2	3.06	25.79	32.83	14715.22	14743.79	15644.54
3:2 & 1:1	2.70	25.34	29.01	14714.97	14743.19	15645.82
Exact[a]	2.85	25.11	27.91	14715.00	14743.83	15646.99

[a]Results of variational calculation discussed in Ref. 47.

J, the projection of the angular momentum onto the space-fixed Z-axis M and the point group symmetry Γ. The label v serves to enumerate the rotation-vibration states whose Γ, M, and J labels are the same. The contribution to the intensity, due to the F component of the space-fixed dipole moment operator μ is obtained by evaluating (85)

$$I_{v,v'} = \frac{4\pi^2 N_0}{3\hbar c Q} g_v \exp\left(\frac{-E_v}{k_b T}\right) \times \sum_F \sum_{M,M'=-J}^{J} |\langle v\Gamma JM|\mu_F^{\text{eff}}|v'\Gamma' J'M'\rangle|^2 \tag{35}$$

Nuclear spin weightings are given by g_v. For H_2CO states that are symmetric with respect to a rotation by π about the symmetry axis, $g_v = 0.25$; for the antisymmetric states $g_v = 0.75$. Here we will be considering the 10 K spectrum for H_2CO, where only the ground vibrational state is populated. For this vibrational state, the symmetric and antisymmetric rotation-vibration states are those for which K is even and odd, respectively (91). The effective dipole moment operator μ_F^{eff} is obtained from μ_F via the transformation of Eq. (34). To transform μ_F, we first reexpress it in terms of the body-fixed dipole moment operators μ_α, described above, by

$$\mu_F = \sum_\alpha \mu_\alpha \lambda_{F\alpha} \tag{36}$$

This expression separates the vibrational dependence, incorporated in μ_α from the rotational dependence in the direction cosine matrix elements $\lambda_{F\alpha}$. Our ability to apply the transformation of Eq. (34) lies in our ability to rewrite both the vibrational contributions μ_α and the rotational contributions $\lambda_{F\alpha}$ to the right side of Eq. (36) in terms of raising and lowering operators (50).

We have used this approach to calculate the spectrum of H_2CO at 10 K. For these calculations we used a linear approximation to the 6-31ext MP2 dipole surface of Simandiras et al. (92). Spectra, calculated using fourth-order CVPT, are shown in Fig. 12. At this level, only the vibrational structure is apparent for the overtone states. This spectrum contains much information about the potential and dipole surfaces from which it was generated and the ability to calculate both of these properties will aide in the development and refinement of potential surfaces. Also, at higher rotational temperatures, the spectrum for H_2CO is extremely congested. We believe that the ability to calculate spectra for this molecule, including all of the relevant Fermi and Coriolis couplings, will provide a powerful tool in the assignment of these spectra.

C. Fitting Spectra

Thus far we have focused on using CVPT to follow the arrows down in Fig. 1. In other words, given a potential and dipole moment operator, expanded in a Taylor series about the equilibrium geometry of the molecule, we have calculated a variety of observables. It should be stressed that CVPT will not provide accurate results for all molecules. In particular, if the molecule is undergoing large-amplitude motion about multiple minima, our approach is not recommended.

In this section, we will discuss how we have used CVPT to follow the arrows up through Fig. 1—that is, how we have used CVPT to fit potential energy surfaces using CVPT. After presenting the general approach, we will discuss potentials for HCN and

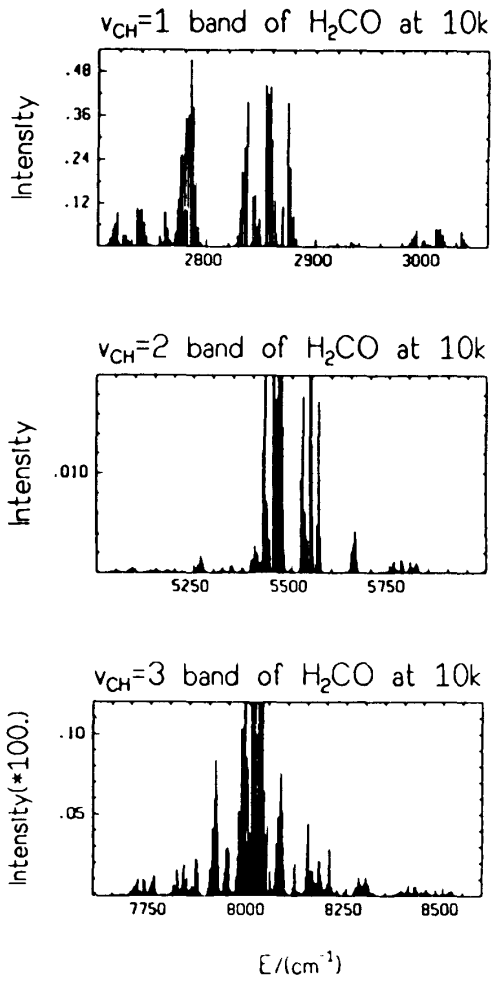

Figure 12 The theoretical spectrum of H_2CO at 10 K, calculated at fourth-order perturbation theory. The reported intensities are in units of km/mol. (From Ref. 50.)

H_2CO that we have fit using this method. More detailed accounts of these studies have been presented elsewhere (51,54).

1. Methods

A common approach for fitting a potential to the observed transition frequencies is as follows. First, one calculates the transition energies and any other observables that are to be fit from an initial guess of the potential. This potential may have been obtained from an ab initio calculation or it may be an earlier empirical potential. Next, these results are compared to the observed quantities and

$$\chi^2 = \sum_i \frac{(E_i^{\text{calc}} - E_i^{\text{obs}})^2}{\sigma_i^2} \tag{37}$$

is constructed. For simplicity, we will assume that only energies are to be fit. Other observables may be incorporated into χ^2 by adding appropriate terms to the summation. Finally the force constants are varied to improve the agreement between calculated and observed results. This translates to finding a minimum in χ^2.

The key to being able to minimize χ^2 is having an efficient and accurate method for calculating the energies. In our studies we have used fourth-order perturbation theory. For H_2CO, we have fit states with $E_{vib} < 7600$ cm^{-1}. Here, the fourth-order energies are converged to within approximately 1 cm^{-1}, this being approximately the experimental uncertainty (20). For HCN, we have considered a larger energy range, and the agreement at fourth order is not nearly as good as for H_2CO. In this case we scaled the fourth-order energies to agree with the result of a converged variational calculation. This scaling factor needed to be calculated fewer than five times during the optimization of the force field.

Before we can undertake fitting a potential, we must determine an appropriate initial form for the potential. For both of these systems, we use a truncated Taylor series expansion of the potential in the internal coordinates

$$V = \sum_{i \geq j} F_{ij} S_i S_j + \sum_{i \geq j \geq k} F_{ijk} S_i S_j S_k + \sum_{i \geq j \geq k \geq l} F_{ijkl} S_i S_j S_k S_l + \cdots \tag{38}$$

The bend dependence is expanded in terms of the bend extension coordinates, and the stretch dependence is expanded in terms of Morse coordinates (2) for the HCN potential and in terms of Simons-Parr-Finlan (SPF) coordinates (68) for the H_2CO potential. Potentials of this form have been long recognized to provide a good approximation to the potential in the region of the minimum. Using the SPF or Morse coordinates in place of the usual bond extension coordinates, extends the range of validity of these low-order expansions of the potential.

Given an initial form for the potential, we use the Marquardt algorithm (93,94) to minimize χ^2. This algorithm requires the evaluation of terms such as $\partial E_i^{calc}/\partial F_{lmn}$. Such derivatives can be readily calculated using Hellmann-Feynman theory, which states that

$$\frac{\partial E_i^{calc}}{\partial F_{lmn}} = \left\langle \frac{\partial H}{\partial F_{lmn}} \right\rangle = \langle S_l S_m S_n \rangle = \langle A_{lmn} \rangle \tag{39}$$

where the averages are over the ith eigenstate of H. Using the same procedures as were used to evaluate the dipole moment matrix elements (cf. Eq. (34)), A_{lmn} is transformed to A_{lmn}^{eff}. This procedure will only work for cubic and higher-order terms in the potential. When necessary, the quadratic terms are varied manually.

2. Results for HCN

The first potential we fit using CVPT was a sixth-order expansion to the HCN surface. HCN provides an attractive molecule for several reasons. First, the transition frequencies of this molecule can be obtained using a diagonal form for the effective Hamiltonian. Second, this molecule has been studied by direct absorption experiments and by SEP studies. The absorption spectrum was obtained by Lehmann and Klemperer and coworkers (15,19), who have observed transitions to states with up to eight quanta of excitation in the CH stretch. The SEP studies were performed in by Wodtke and coworkers (16). They were able to observe states with up to 7 quanta of excitation in the CN stretch and 14 quanta of excitation in the bend. As HCN was the first molecule for which we fit a potential, we performed three fits in order to characterize the method as well as to obtain an optimal fit to the potential.

For the first fit, we start with a sixth-order expansion of the HCN potential. This potential, which Carter, Handy, and Mills fit to the energies of 31 $l = 0$ states reported by Smith et al. (15) with a mean absolute deviation $\Sigma_{i=1}^{n} |E_i^{obs} - E_i^{calc}| = 0.67$ cm^{-1} (72), provides an excellent starting point for our fits to the above $l = 0$ states as well as 40

additional states. The differences between the observed and calculated transition energies for this potential are plotted in Fig. 13. This figure demonstrates an important issue when fitting potentials. The quality of the fit is only as good as the sensitivity of the observables to all of the features of the molecular potential. Here the agreement for the overtone states (represented by +) is excellent, but large deviations are observed for the states observed in the SEP experiments (represented by ◇). We have iteratively improved this force field using the above methods to obtain a set of force constants denoted by $\{f_{ijk}\}$ and energies with a mean absolute difference of 0.69 cm^{-1}. The results are plotted in Fig. 14.

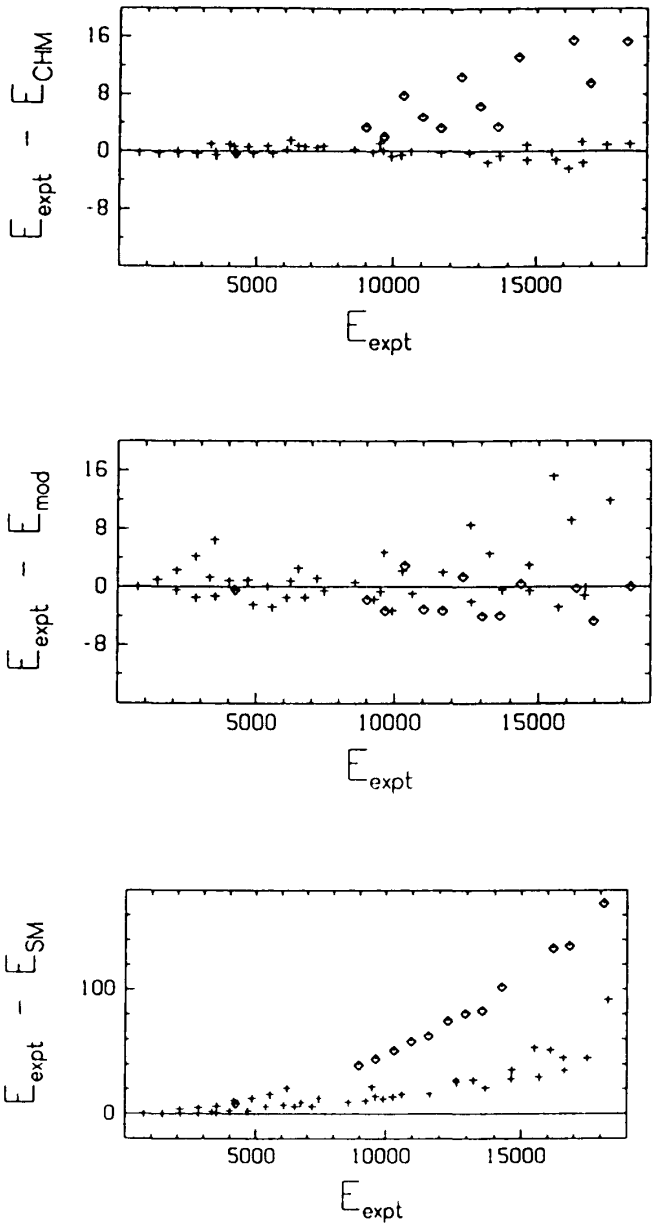

Figure 13 The agreement between observed and calculated transition energies for three representations of the HCN potential. Pluses are used to denote states that were observed by absorption experiments (15), and diamonds denote those observed in SEP studies (16). The three potentials represent the three initial set of parameters for our fits. (From Ref. 50.)

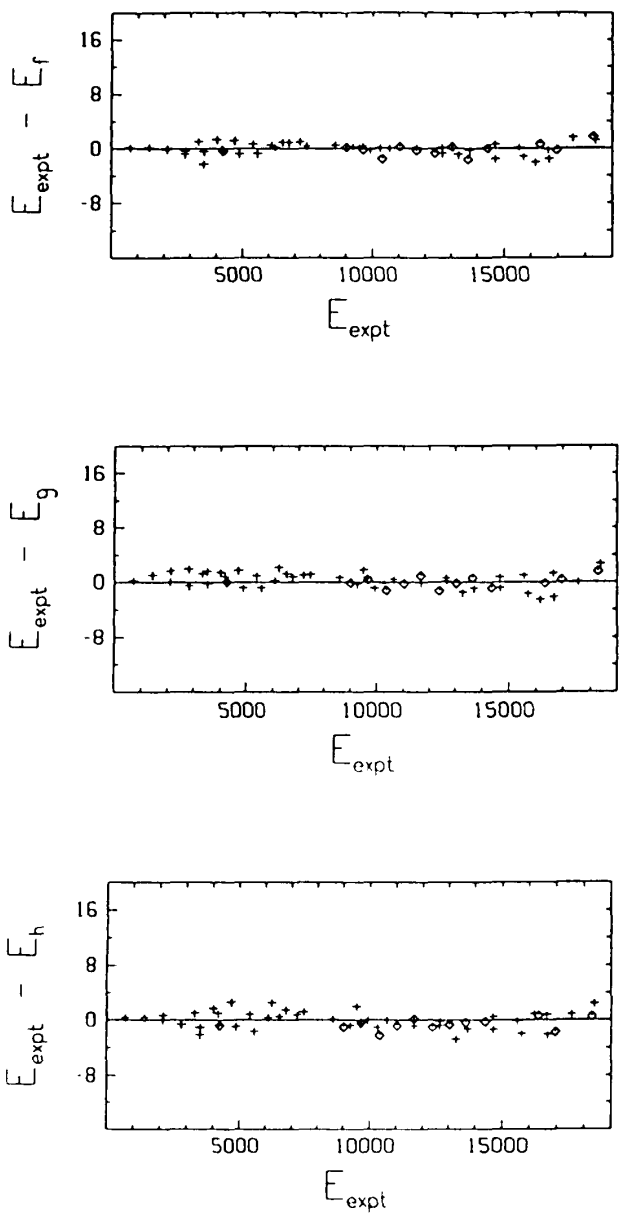

Figure 14 The same as Fig. 13, except for the potentials that resulted from fitting this set of transition energies. (From Ref. 51.)

While the results are very encouraging, the Carter, Handy, and Mills potential was previously refined to fit much of the data included here, making this fit a poor test of the robustness of the method. We have therefore fit the same set of states, starting from two modified versions of the potential derived by Strey and Mills (95). The differences between the calculated and observed energies of the transitions in HCN included in the fit are plotted in Fig. 13. Starting from these potential, we were able to fit the same set of states with a mean absolute deviation of 1.25 and 1.00 cm^{-1}. The resulting potentials are denoted by $\{g_{ijk}\}$ and $\{h_{ijk}\}$, respectively.

Having obtained three sets of force constants, an interesting and important question is how different these potentials are. To simplify the following discussion we focus on

the results of the surfaces defined by the f and g sets of force constants. While both of these fit potentials do an excellent job of reproducing the observed energies, some of the force constants differ by as much as a factor of 10. These differences raise the question of the uniqueness of the final set of parameters obtained by fitting a set of experimental observables. In an ideal situation, a set of observables would lead to a surface for χ^2 with a single, global minimum. In reality, χ^2 often has multiple minima as well as multidimensional regions in which it remains nearly constant. To begin to investigate the topology of χ^2 in the region of the two fit potential surfaces, we take the line in parameter space that connects the f_{ijk} to the g_{ijk} and calculate χ^2 at several points along this line. Any potential corresponding to a point on this line can be defined by a set of force constants $\{F_{ijk}\}$, where

$$F_{ijk} = \beta(f_{ijk} - g_{ijk}) + g_{ijk} \tag{40}$$

The results are shown in the top panel of Fig. 15. In this plot, the lines denote the results of scaled fourth-order perturbation theory, where the scaling factors were computed for the reference potentials. In the actual fit, these factors would be updated after each optimization of the parameters. The x's denote the exact values of χ^2 for that set of parameters. This figure demonstrates that χ^2 varies little with β in spite of the fact that some of the individual force constants change substantially. These values for χ^2 support the fact that both of these potentials are in a region where χ^2 is insensitive to particular changes in the force constants. Further, the scaled perturbation theory appears to do a good job of reproducing the true values of χ^2 for changes in $\beta \leq 1/3$ and gives qualitative agreement for larger changes of β.

3. Results for Formaldehyde

Another molecule for which a large fraction of the vibrational states have been observed is H_2CO. Very recently, Bouwens et al. (20) assigned band origins of 198 new vibrational

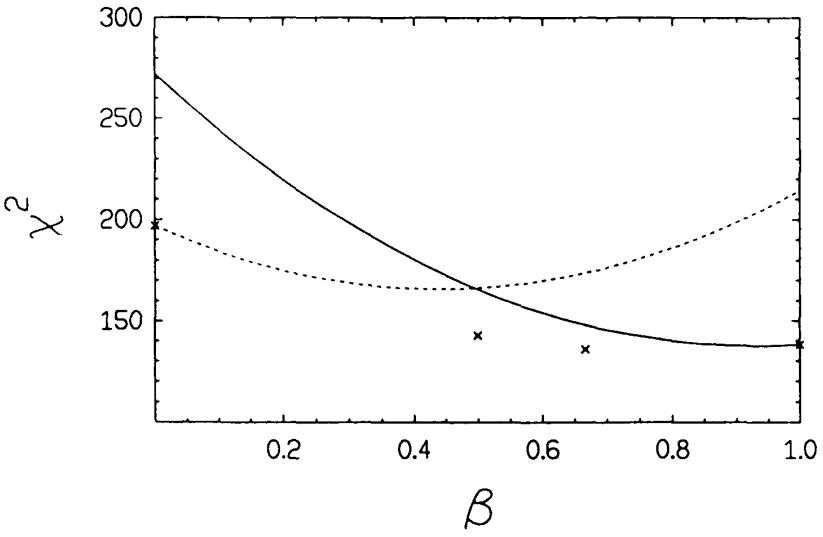

Figure 15 The topology of χ^2 along the line (cf. Eq. (40)) connecting the two fit potentials. The dashed and solid curves represent the results of perturbation theory scaled by energies and rotational constants calculated using the potentials that correspond to $\beta = 0$ and 1, respectively. The x's give the exact values of χ^2 for that set of parameters. (From Ref. 51.)

states with energies up to 12,500 cm^{-1}. This substantially increased the number of observed transitions in this molecule. In our work, we have fit the vibrational energies of 138 vibrational states with $E_{vib} \leq 7600$ cm^{-1}.

The procedure we followed is basically the same as that used to fit the HCN surface. Here we started with an ab initio quartic force field, calculated by Martin et al. (96). The fit from this potential proceeded in two steps. First we varied six of the quadratic force constants. Because these force constants determine $H^{(0)}$, these constants could not be optimized using the approaches detailed above. Instead, we fit these constants to the six harmonic frequencies in H_2CO. This modification leads to a mean absolute difference for the 138 observed states included in the fits of 4.9 cm^{-1}. Following the procedures outlined above, we were able to further refine the potential to obtain a final mean absolute deviation of 1.5 cm^{-1} for these states.

There has been considerable prior work on calculating H_2CO potential energy surfaces, and it is useful to compare our results to these earlier studies. The work of Martin et al. (96) provides a good overview, which we will not reproduce here except to report a few key results. In that work the agreement between theory and experiment (as it stood before the work of Polik and co-workers (20)) is examined for those states with two or less quanta of excitation. Using 20 of the 21 observed states, they compared their work to earlier theoretical work. With their best "adjusted" potential they found an absolute mean difference of 4.2 cm^{-1}. This can be compared to the 6.7 cm^{-1} difference found for the Martin, Lee, and Taylor surface, 5.7 cm^{-1} found for the "adjusted" potential of Romanowski et al. (74), and 18.9 cm^{-1} for the "best" empirical potential of Maessen and Wolfsberg (97). In the present study, we find a 0.9 cm^{-1} absolute mean difference between the 27 calculated transition energies and the more recent set of experimentally determined transition energies to those states with two or less quanta of excitation (20).

There are three reasons for this improvement. First the 1_2 state was misassigned (20). Second, much of the earlier work used an approximation to the force field in order to simplify the calculation of the vibrational states. In particular, the internal coordinate force field was reexpressed as a low-order expansion in terms of the rectilinear normal coordinates (96,74). The final reason for the improvement is a result of the quality of the fit potential energy surface which we have obtained. The earlier adjusted force fields were obtained by changing only the diagonal quadratic force constants.

The 0.9 cm^{-1} mean absolute deviation found at low energies is similar to the 1.5 cm^{-1} mean absolute deviation (2.1 cm^{-1} root mean squared deviation) found for the 138 states included in our fit. The quality of the fit can be further judged by examining its quality for those states not included in the fit. Bouwens et al. (20), using our E_6 results, report a 2.7 cm^{-1} mean absolute deviation (4.1 cm^{-1} root mean squared deviation) between our calculated transitions and the nearly 280 currently assigned transitions in H_2CO. These states have energies up to 12,500 cm^{-1} of excitation.

V. SUMMARY

In this chapter, we have reviewed the work in our group in which we have used high-order CVPT to study the nature of vibrationally excited states of polyatomic molecules. Most of the previous applications of CVPT to molecular systems focused on the energy regime over which molecular vibrations are nearly harmonic. Clearly there are many molecules, particularly those containing one or more hydrogen atoms, for which this energy regime is quite small. However, if we use sixth-order perturbation theory to

calculate the energies, rotational constants and transition intensities of the vibrational states of these molecules, we find that our results are in excellent agreement with those calculated variationally over a wide range of energies. The power of the CVPT comes from the fact that it requires only a fraction of the computer time and memory of variational calculations.

One of the important ingredients to being able to use CVPT to study molecular vibrations and rotation-vibration interactions is the expansion of the Hamiltonian. In our work, we follow the work of Pickett (63) and use very general expressions for the terms in the Hamiltonian. The evaluation of these terms requires simply the ability to convert from Cartesian to internal coordinates and back to Cartesian coordinates. Given an expansion of the Hamiltonian, about the potential minimum, in some appropriate set of coordinates, CVPT can be applied to this Hamiltonian in a straightforward manner. This is one of the advantages of this approach. The actual transformations required to obtain the effective Hamiltonian are independent of the details of the molecular Hamiltonian.

Having developed the theory, we discussed several applications of CVPT to molecular problems. The first was the use of CVPT to investigate rotation-vibration mixing in H_2CO and SO_2. In the second we calculated transition strengths of overtone excitations in HCN and H_2CO. This provided a stringent test of the quality of the wave functions obtained from CVPT. When we were able to make direct comparisons to variational calculations, the perturbation theory did remarkably well. In addition, transition intensities are sensitive to different regions of the potential than are transition frequencies. Together, these two quantities provide valuable information for fitting potential energy surfaces.

In the final section, we employed CVPT to fit expansions of the Born-Oppenheimer potentials for HCN and H_2CO. Preliminary work has also been performed for fitting a potential for C_2H_2 using CVPT (52). While workers are beginning to use variational approaches to fit potentials for tetraatomic molecules, these approaches are much more limited in terms of the energy ranges that can be computed as accurately as low-order perturbation theory. This is particularly notable for H_2CO where fourth-order perturbation theory provides energies that are within 1.5 cm^{-1} of the variational results for energies up to 7600 cm^{-1} above the zero point energy. To conclude, we believe that CVPT provides an extremely general and powerful approach for studying highly excited states of polyatomic molecules.

REFERENCES

1. M. Born and J. R. Oppenheimer, *Ann. Phys.*, *84*: 527 (1927).
2. W. Meyer, P. Botschwina, and P. Burton, *J. Chem. Phys.*, *84*: 891 (1986).
3. A. S. Coolidge, H. M. James, and E. L. Vernon, *Phys. Rev.*, *54*: 726 (1938).
4. Y. P. Varshni, *Rev. Mod. Phys.*, *29*: 664 (1957).
5. A. Abel and D. M. Dennison, *Phys. Rev.*, *43*: 716 (1933).
6. A. R. Hoy, I. M. Mills, and G. Strey, *Mol. Phys.*, *24*: 1265 (1972).
7. K. S. Sorbie and J. N. Murrell, *Mol. Phys.*, *29*: 1387 (1975).
8. A. Chédin, *J. Mol. Spec.*, *76*: 430 (1979).
9. L. Halonen and T. Carrington, *J. Chem. Phys.*, *88*: 4171 (1988).
10. P. Jensen, *J. Mol. Spec.*, *133*: 438 (1989).
11. *Comp. Phys. Comm. 51* (1988). Thematic issue on molecular vibrations.
12. J. M. Bowman (Ed.), *Advances in Molecular Vibrations and Collision Dynamics*, JAI, Greenwich, CT, 1991.

13. H. L. Dai, C. L. Korpa, J. L. Kinsey, and R. W. Field, *J. Chem. Phys.*, *82*: 1688 (1985).
14. B. C. Smith and J. S. Winn, *J. Chem. Phys.*, *89*: 4638 (1988).
15. A. M. Smith, S. L. Coy, W. Klemperer, and K. K. Lehmann, *J. Mol. Spec.*, *134*: 134 (1989).
16. X. Yang, C. A. Rogaski, and A. M. Wodtke, *J. Opt. Soc. Am. B*, *7*: 1835 (1990).
17. K. Yamanouchi, S. Takeuchi, and S. Tsuchiya, *J. Chem. Phys.*, *92*: 4044 (1990).
18. D. M. Jonas, S. A. B. Solina, B. Rajaram, R. J. Silbey, R. W. Field, K. Yamanouchi, and S. Tsuchiya, *J. Chem. Phys.*, *99*: 7350 (1993).
19. D. Romanini and K. K. Lehmann, *J. Chem. Phys.*, *99*: 6287 (1993).
20. R. J. Bouwens, J. A. Hammerschmidt, M. M. Grzeskowiak, T. A. Stegink, P. M. Yorba, and W. F. Polik, *J. Chem. Phys.*, *104*: 460 (1996).
21. F. F. Crim, *Annu. Rev. Phys. Chem.*, *35*: 657 (1984).
22. *J. Opt. Soc. Am. B 7*: No. 9 (1990). Thematic issue on molecular spectroscopy and dynamics by stimulated-emission pumping.
23. R. Field and H. Dai (Eds.), *Molecular Dynamics and Spectroscopy by SEP*, Scientific Monograph., 1995.
24. E. B. Wilson, J. C. Decius, and P. C. Cross, *Molecular Vibrations*, McGraw-Hill, New York, 1955.
25. G. Herzberg, *Molecular Spectra and Molecular Structure, Vol. II*, Krieger, Malabar, FL, 1991.
26. P. J. Robinson and K. A. Holbrook, *Unimolecular Reactions*, Wiley Interscience, New York, 1972, Ch. 4 and references therein.
27. T. A. Brody, J. Flores, J. B. French, A. P. Mello, A. Pandey, and S. S. M. Wong, *Rev. Mod. Phys.*, *7*: 385 (1982).
28. G. D. Carney, L. L. Sprandel, and C. W. Kern, *Adv. Chem. Phys.*, *37*: 305 (1978).
29. Z. Bačić and J. C. Light, *Annu. Rev. Phys. Chem.*, *40*: 469 (1989).
30. E. L. Sibert, *Int. Rev. Phys. Chem.*, *9*: 1 (1990).
31. M. Aoyagi and S. K. Gray, *J. Chem. Phys.*, *94*: 195 (1991).
32. S. Carter and N. C. Handy, *J. Chem. Phys.*, *87*: 4294 (1987).
33. R. E. Wyatt, C. Iung, and C. Leforestier, *J. Chem. Phys.*, *97*: 3458 (1992).
34. J. Antikainen, R. Friesner, and C. Leforestier, *J. Chem. Phys.*, *102*: 1270 (1995).
35. H. H. Nielsen, *Rev. Mod. Phys.*, *23*: 90 (1951).
36. G. Amat, H. H. Nielsen, and G. Tarago, *Rotation-Vibration Spectra of Molecules*, Marcel Dekker, New York, 1971.
37. D. Papoušek and M. R. Aliev, *Molecular Vibrational-Rotational Spectra*, Elsevier, New York, 1982.
38. J. E. Baggott, *Mol. Phys.*, *62*: 1019 (1987).
39. L. E. Fried and G. S. Ezra, *J. Chem. Phys.*, *90*: 6378 (1989).
40. A. Willetts, N. C. Handy, W. H. Green, Jr., and D. Jayatilaka, *J. Phys. Chem.*, *94*: 5608 (1990).
41. E. Kauppi and L. Halonen, *J. Chem. Phys.*, *96*: 2933 (1992).
42. R. Hernandez, *J. Chem. Phys.*, *101*: 9534 (1994).
43. E. L. Sibert, *J. Chem. Phys.*, *88*: 4378 (1988).
44. E. L. Sibert, *Comp. Phys. Comm.*, *51*: 149 (1988).
45. E. L. Sibert, *J. Chem. Phys.*, *90*: 2672 (1989).
46. A. B. McCoy and E. L. Sibert, *J. Chem. Phys.*, *92*: 1893 (1990).
47. A. B. McCoy and E. L. Sibert, *J. Chem. Phys.*, *95*: 3476 (1991).
48. A. B. McCoy and E. L. Sibert, *J. Chem. Phys.*, *95*: 3488 (1991).
49. A. B. McCoy, D. C. Burleigh, and E. L. Sibert, *J. Chem. Phys.*, *95*: 7449 (1991).
50. A. B. McCoy and E. L. Sibert, *Mol. Phys.*, *77*: 697 (1992).
51. A. B. McCoy and E. L. Sibert, *J. Chem. Phys.*, *97*: 2938 (1992).
52. A. B. McCoy, Ph.D. thesis, University of Wisconsin-Madison, 1992.
53. D. C. Burleigh and E. L. Sibert, *J. Chem. Phys.*, *98*: 8419 (1993).
54. D. C. Burleigh, A. B. McCoy, and E. L. Sibert, *J. Chem. Phys.*, *104: 480 (1996).*

55. L. E. Fried and G. S. Ezra, *J. Chem. Phys.*, *86*: 6270 (1987).
56. B. H. Chang and D. Secrest, *J. Chem. Phys.*, *94*: 1196 (1991).
57. E. B. Wilson and J. B. Howard, *J. Chem. Phys.*, *4*: 260 (1936).
58. J. K. G. Watson, *Mol. Phys.*, *15*: 479 (1968).
59. J. K. G. Watson, *Mol. Phys.*, *19*: 465 (1970).
60. M. J. Bramley, W. H. Green, and N. C. Handy, *Mol. Phys.*, *73*: 1183 (1991).
61. N. C. Handy, *Mol. Phys.*, *61*: 207 (1987).
62. A. G. Császár and N. C. Handy, *J. Chem. Phys.*, *102*: 3962 (1995).
63. H. M. Pickett, *J. Chem. Phys.*, *56*: 1715 (1972).
64. R. Meyer and Hs. H. Günthard, *J. Chem. Phys.*, *49*: 1510 (1968).
65. E. C. Kemble, *The Fundamental Principles of Quantum Mechanics*, McGraw-Hill, New York, 1937, p. 394.
66. C. Eckart, *Phys. Rev.*, *47*: 552 (1935).
67. C. R. Quade, *J. Chem. Phys.*, *64*: 2783 (1976).
68. G. Simons, R. G. Parr, and J. M. Finlan, *J. Chem. Phys.*, *59*: 3229 (1973).
69. L. Xiao and M. E. Kellman, *J. Chem. Phys.*, *90*: 6086 (1989).
70. L. Xiao and M. E. Kellman, *J. Chem. Phys.*, *93*: 5805 (1990).
71. M. E. Kellman, *J. Chem. Phys.*, *93*: 6630 (1990).
72. S. Carter, N. C. Handy, and I. M. Mills, *Philos. Trans. R. Soc. London, Ser. A*, *332*: 309 (1990).
73. L. B. Harding and W. C. Ermler, *J. Comput. Chem.*, *6*: 13 (1985).
74. H. Romanowski, J. M. Bowman, and L. B. Harding, *J. Chem. Phys.*, *82*: 4155 (1985).
75. J. Schwinger, *Quantum Theory of Angular Momentum* (L. C. Biedenharn and H. van Dam, eds.), Academic, New York, 1965, p. 229.
76. D. K. Sahm, R. V. Weaver, and T. Uzer, *J. Opt. Soc. Am. B*, *9*: 1865 (1990).
77. D. Farrelly, *J. Chem. Phys.*, *85*: 2119 (1986).
78. M. E. Kellman, *J. Chem. Phys.*, *76*: 4528 (1982).
79. K. K. Lehmann, *J. Chem. Phys.*, *79*: 1098 (1983).
80. S. C. Wang, *Phys. Rev.*, *34*: 243 (1929).
81. D. Huber, *Int. J. Quantum Chem.*, *28*: 245 (1985).
82. S. Carter, I. M. Mills, J. N. Murrell, and A. J. C. Varandas, *Mol. Phys.*, *45*: 1053 (1982).
83. M. Allegrini, J. W. C. Johns, and A. R. W. McKellar, *J. Mol. Spec.*, *67*: 476 (1977).
84. J. H. Frederick, G. M. McClelland, and P. Brumer, *J. Chem. Phys.*, *83*: 190 (1985).
85. J. D. Graybeal, *Molecular Spectroscopy*, McGraw-Hill, New York, 1988.
86. A. M. Smith, W. Klemperer, and K. K. Lehmann, *J. Chem. Phys.*, *94*: 5040 (1991).
87. E. E. Nikitin, C. Noda, and R. N. Zare, *J. Chem. Phys.*, *98*: 46 (1993).
88. P. Botschwina, *Faraday Trans. 2*, *84*: 1263 (1988).
89. J. E. Baggott, G. L. Caldow, and I. M. Mills, *Faraday Trans. 2*, *84*: 1407–1422, 1604–1607 (1988).
90. K. K. Lehmann and A. M. Smith, *J. Chem. Phys.*, *93*: 6140 (1990).
91. G. Herzberg, *Molecular Spectra and Molecular Structure*, Vol. II, Krieger, Malabar FL, 1991.
92. E. D. Simandiras, R. D. Amos, and N. C. Handy, *J. Chem. Phys.*, *82*: 4155 (1987).
93. D. W. Marquardt, *J. Soc. Ind. Appl. Math.*, *11*: 431 (1963).
94. In the present study, we used the nonlinear least squares routine written by W. C. Ehrhardt, Department of Chemistry, University of Wisconsin-Madison, 1977.
95. G. Strey and I. M. Mills, *J. Mol. Spec.*, *26*: 129 (1973).
96. J. M. L. Martin, T. J. Lee, and P. R. Taylor, *J. Mol. Spec.*, *160*: 105 (1993).
97. B. Maessen and M. Wolfsberg, *J. Phys. Chem.*, *88*: 6420 (1984).

5

Quantum Molecular Dynamics on Grids

Ronnie Kosloff
The Fritz Haber Research Center for Molecular Dynamics, The Hebrew University of Jerusalem, Jerusalem, Israel

I. INTRODUCTION

Molecular dynamics is the study of basic principles of chemical change. Its underlying theory is either classical or quantum mechanics. Much of the original insight into molecular encounters stemmed from a classical picture where the atoms were imagined to be positioned in three-dimensional coordinate space. This picture is in conflict with the quantum mechanical viewpoint that particles do not possess a definite position. A true quantum image of the particle is now understood as a blurred object able to interfere with itself.

The traditional development of quantum mechanics has been heavily influenced by the work of Hilbert, describing the wave function Ψ by a functional expansion $\Psi = \Sigma_n a_n \phi_n$. This formulation created a powerful theory which has been translated into an effective computational scheme based on linear algebraic methods. These algebraic methods have become the main agents of quantum molecular dynamical computations, but have blurred the image of the molecular encounter. The algebraic approach has created a new language in which, for example, a chemical reaction is described by a matrix quantity, the state-to-state transition amplitude S_{ij}.

The lack of a clear image in quantum molecular dynamics has been a handicap for most researchers. This is in comparison to classical molecular dynamics which is strongly linked to the notion of a trajectory, a causal path leading from reactants to products. Imaging the flow of a trajectory constitutes one of the main sources of insight on classical molecular dynamics.

The historical development of quantum molecular dynamics abandoned the causal framework based on time-dependent formalism and adopted a time-independent frame-

work. This was despite the fact that causal interpretation of events, where a cause in the past leads to a result in the future is strongly imprinted in human thought. In the time-independent formalism the stationary currents become the source of imagery, a tool which has rarely been used. As a result, molecular dynamics has had to face the problem that intuitive insight has been heavily based on classical mechanics, while quantitative predictions have been based on quantum dynamics.

One way out of the discrepancy has been to augment the classical description with quantum corrections. This has been the motivation for the large effort put into developing semiclassical methods in molecular dynamics (1–5). Such a line of thought has not been followed in this chapter. Instead a bolder approach, based on quantum methods in the time domain where the wave function is represented directly in configuration space, is attempted. Two questions are raised by this endeavor:

a. Can new insight on molecular encounters be gained from a quantum coordinate representation in the time domain?
b. Can an efficient and accurate computational method be developed based on these representations?

The purpose of this chapter is to show that these two questions can be answered positively based on a grid description and computation scheme.

The historical development of grid methods in molecular dynamics can be traced to the early work of McCullough and Wyatt (6,7), who used a direct finite differencing (FD) scheme to solve the collinear $H + H_2$ reactive scattering problem. Their work then utilized two important imaging tools: snapshots of contour plots of the absolute value of the wave function and flux maps. Numerical improvement of the original method was introduced by Askar (8), who suggested a replacement of the Crank-Nicholson propagator by the second-order differencing scheme (SOD). At the time, the numerical accuracy and efficiency of the FD method was not sufficient to compete with the time-independent spectral quantum methods for reactive scattering. As a result, the FD methods were almost abandoned. (As an exception FD methods became popular in the calculations of above threshold ionization ATI due to their ability to tolerate the Coulomb singularity without contaminating the rest of the wave function (9). In Section III an analysis of why finite difference methods are hard to converge will be presented.

It was the introduction of the Fourier based pseudospectral methods (10–12) which created a grid based method with high accuracy and efficiency. This development was supplemented by the more general pseudospectral methods introduced into molecular dynamics by Light et al. (13) which greatly increased the applicability of grid based methods. Another important development was the Chebychev-based propagator (14) which became the base for the development of spectral and pseudospectral methods in the time-energy phase space. Recent developments in implementing propagator techniques have made the distinction between time-dependent and time-independent methods almost vanish (15). Currently, due to the efforts of many people, time-dependent and time-independent grid based methods are able to create imagery as well as high-quality, first-principle simulations, of molecular encounters.

II. GENERAL SETUP OF GRID METHODS

When simulating a molecular encounter experiment, it is wise to define the framework of the simulation before attempting to perform it. The duration of the experiment will

be limited by the patience of the experimentalist of course, but more precisely a typical molecular encounter is completed in a few femtoseconds up to a few picoseconds. The next task in setting the simulation is to count the number of particles or the number of degrees of freedom in the problem. Each particle is to be contained in a finite volume which for a typical encounter is between 10 to 1000 $^{\circ}A^3$. Finally, the energy range of a molecular encounter ΔE is to be set, typically in the range of 0–10 eV. Once this arena of the simulation has been worked out, its computational feasibility can be determined.

The next step is to realize that the arena of molecular change is the phase space $\{p, q\}$, which is true for both classical and quantum mechanics. The "volume" of the position-momentum phase space containing the encounter can be estimated from the range of position and momentum. The maximum momentum can be determined from the energy range $|P_{max}| < \sqrt{2mE_{max}}$. This estimate has to be repeated for each degree of freedom. The range of position is also determined by a condition on the potential $V(q_{max}) < E_{max}$. The molecular encounter takes place in a volume that is a direct product of the position momentum phase space $\{p, q\}$ of all degrees of freedom and of the time-energy phase space $\{t, E\}$.

Figure 1 shows the volume containing the molecular encounter and its projections on the $\{q, p\}$ phase space and the $\{t, E\}$ phase space. In classical mechanics, the encounter is described by a thread running through the volume $\{q, p\} \otimes \{t, E\}$. In quantum mechanics, a global description of this "volume" is required. From quantum statistical mechanics it can be concluded that a sufficient sampling is obtained if this "volume" is divided by h for each spatial and time dimension. This leads to the number of grid points necessary for sufficient sampling $N_g \approx \mathcal{V}/h^N$ for N spatial dimensions, and $N_t \approx \Delta E \cdot T/\hbar$ (see Fig. 1).

Representing the wave function on a grid can be formally symbolized as $\Psi(q, t) \rightarrow \Psi(q_i, t_j)$. It will be shown that grid methods are able to reach a sampling efficiency which is very close to the estimates of h per unit of occupied phase space.

From the estimate of the number of grid points in space, N_g and in time, N_t it can be concluded that any effort that reduces the represented "volume" should be attempted. The influence of "empty volume" increases with the dimensionality of the problem. In one and two-dimensional problems one can afford to be sloppy in the representation, but in a high-dimensional problem, sloppiness can eliminate the ability to simulate the problem at all. The way to eliminate empty phase space "volume" is to correlate the representation as much as possible. An extreme example of a correlated state is an energy eigenstate which occupies exactly $\mathcal{V} = h^{N+1}$, or one pixel in hyperspace.

To follow the molecular dynamics means following the evolution of the wave function through time $\Psi(q, t + T) = \mathbf{U}(T)\Psi(q, t)$. In the discrete representation this evolution is manifested as a discrete mapping of the wave function $\Psi(q, t_j)$ into the same discrete space: $\Psi(q_j, t_l + T)$. This goal will be obtained in two stages: the first is the study of the discrete mapping produced by the Hamiltonian operator: $\Phi = \mathbf{H}\Psi$, i.e., obtaining $\Phi(q_j)$ from $\Psi(q_i)$. The second stage is implementing the evolution operator based on this mapping. The development of these steps will be described in Sections III and V.

III. REPRESENTATION OF THE WAVE FUNCTION Ψ ON A SPATIAL GRID

The discrete representation of the wavefunction can be imagined as viewing the world through a set of portholes. Since we know that the viewed wavefunction is continuous,

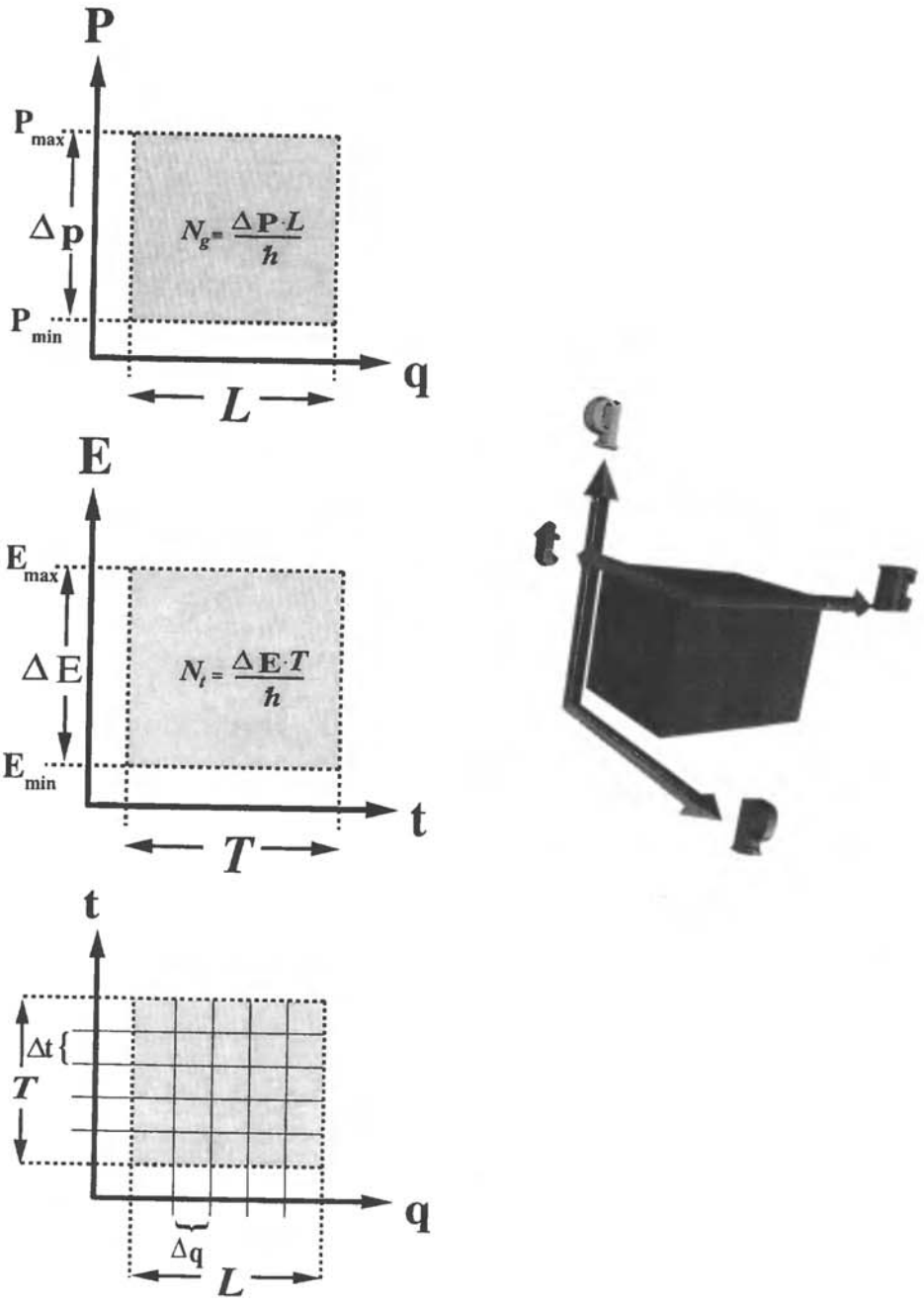

Figure 1 A schematic description of the arena of a molecular encounter. The "volume" on the right represents a three-dimensional projection of the four-dimensional phase space volume $\mathcal{V} = \{q, p\} \otimes \{t, E\}$. Each degree of freedom can be projected onto the three left panels. The lower left panel shows the arena represented directly by the grid.

by interpolating between the individual pictures the global landscape can be reconstructed. This concept, which forms the basis of representation theory, enables the reconstruction of the full position-momentum phase space.

There are two approaches to such interpolation, a local and a global one. The local approach is based on a set of piecewise-continuous functions, usually polynomials. These functions are designed to interpolate locally between the grid points. The interpolation

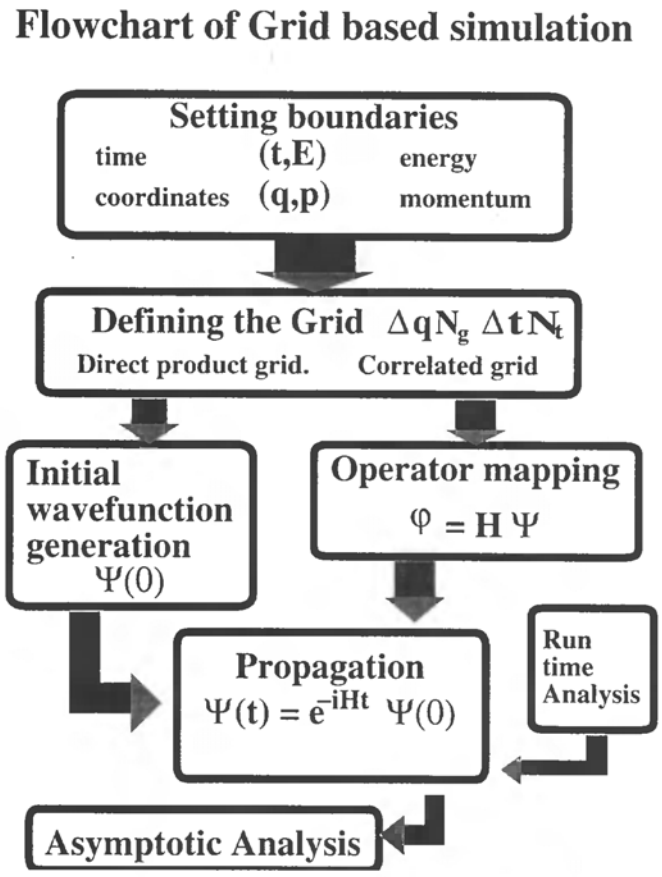

Figure 2 Flowchart of the generic simulation of a molecular dynamical event based on grid schemes.

process allows the derivatives on the points to be defined since it is based on analytically continuous functions. This local interpolation is the basis of the finite difference method (FD).

The global approach uses an interpolation based on a family of global functions which span all the sampled space with appropriate boundary conditions. This approach which is due to Gauss, is termed collocation (Sec. III.A). In a more elaborate form, based on orthogonal functions it is termed *pseudospectral representation* (Sec. III.B) (16). Since any local method is global within a small interval we will start by analyzing global approaches.

A global approximation of a wave function $\psi(q)$ by a finite set of N_f functions $g_n(q)$ becomes

$$\psi(q) \approx \overline{\psi}(q) = \sum_{n=0}^{N_f-1} a_n g_n(q) \tag{1}$$

where $g_n(q)$ are analytic functions in the domain of interest, obeying the appropriate boundary conditions. The finite representation problem is recast as a method of obtaining the expansion coefficients a_n once the functions $g_n(q)$ are known.

A. General Collocation Method

In mathematical terms, the collocation method determines the expansion coefficients by matching the approximate solution to the true solution on a set of $N_g = N_f$ grid points,

$$\psi(q_j) \equiv \bar{\psi}(q_j) = \sum_{n=0}^{N_g-1} a_n g_n(q_j) \tag{2}$$

where the q_j are the collocation points. These are the sampling points shown in Figure 3. Equation (2) is equivalent to a set of coupled linear equations. In matrix form they become

$$\psi = \mathbf{G}\mathbf{a} \tag{3}$$

where $\psi_j = \psi(q_j)$ and the matrix $G_{nj} = g_n(q_j)$. Provided that the $g_n(q_n)$ are linearly independent, the solution of Eq. (3) becomes

$$\mathbf{a} = \mathbf{G}^{-1}\psi \tag{4}$$

The functional basis that supplies the global picture is connected through the expansion coefficients a_n to the spatial grid. This provides the ability to define the scalar product of two functions. If

$$\psi(q) = \sum_n a_n g_n(q) \tag{5}$$

and

$$\phi(q) = \sum_m b_m g_m(q) \tag{6}$$

then

$$\langle\psi|\phi\rangle \equiv \sum_{nm} S_{nm} a_n^* b_m \tag{7}$$

where S_{nm} is the overlap matrix

$$S_{nm} = \int_D dq\; g_n(q)^* g_m(q) \tag{8}$$

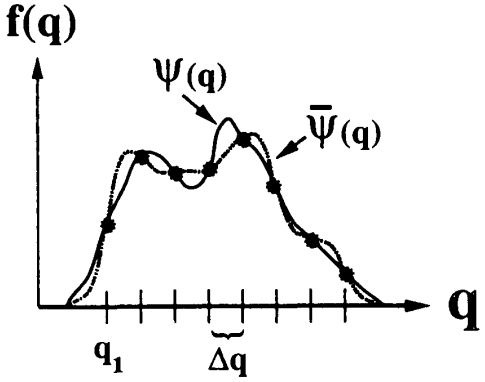

Figure 3 An interpolation of the wave function ψ (solid) by its approximation $\bar{\psi}$ (dashed). The approximate and the original functions are identical on the sampling points q_i.

and the integration is carried out over the domain D.

Primitive collocation methods, based on general expansion functions g_n, have been developed. An attractive idea has been to distribute localized functions in regions where the wavefunction is expected to have a high probability. Such a method, using a set of distributed Gaussian functions, has been developed by Hamilton and Light (17). Attempts to use wavelets as a localized base have also been reported. Nevertheless the numerical experience with these methods has not been satisfactory. The main drawback of primitive collocation schemes is overcompleteness of the representation which leads to a reduction in the rank of the overlap matrix S. This problem causes numerical singularities in the inversion of the **G** matrix. Such a phenomenon can also be understood from the perspective of Gram-Schmidt orthogonalization. Functions which have nearly complete overlap will cause extreme numerical sensitivity upon orthogonalization.

This problem can be overcome by the use of orthogonal expansion functions (the subject of Sec. III.B). Another possible numerical fix is to use more sampling points than functions. The overdetermination of the inversion is overcome by a least squares procedure (18).

B. Orthogonal Collocation Schemes

A great simplification in the collocation scheme is achieved if the set of expansion functions $g_n(q)$ obey the orthogonality relation

$$\sum_{n=0}^{N_g-1} g_n^*(q_i)g_n(q_j) = \delta_{ij} \tag{9}$$

allowing a direct inversion for the expansion coefficients a_n in Eq. (3):

$$a_n = \sum_{j=0}^{N_g-1} \psi^*(q_j)g_n(q_j) \tag{10}$$

This means that the expansion coefficients a_n are the discrete functional transform of the function ψ. On the other hand, if

$$\langle g_n|g_m\rangle = \int_D dq\ g_n^*(q)g_m(q) = \delta_{nm} \tag{11}$$

then the scalar product in Eq. (7) is greatly simplified, leading to

$$\langle\psi|\phi\rangle = \sum_n a_n^* b_n \tag{12}$$

which, using Eq. (9), becomes

$$\langle\psi|\phi\rangle = \sum_{j=0}^{N_g-1} \psi^*(q_j)\phi(q_j) \tag{13}$$

A consequence of the orthogonality relations is that the collocation functional expansion scheme becomes a discrete vector space with a unitary transformation between the discrete sampling points q_j and the discrete functional base a_n. The matrix **G** is then unitary.

At this point, it is appropriate to compare the collocation method with the traditional variation approach to the functional expansion problem. The variational approach

minimizes the functional

$$\mathcal{J} = \int_D d\mathbf{q}\, |\psi(q) - \bar{\psi}(q)|^2 \tag{14}$$

Here, $\mathcal{J}$ is the averaged squared difference between the function ψ and its approximation $\bar{\psi}$, and D is the domain of interest, leading to the determination of a_n by the relation $\delta\mathcal{J} = 0$. If the expansion functions are orthogonal, $\langle g_n|g_m\rangle = \delta_{nm}$, then the expansion coefficients become the functional transform of ψ:

$$\bar{a}_n = \langle\psi|g_n\rangle = \int_D dq\, \psi^*(q)g_n(q) \tag{15}$$

This method will be referred to as the variational spectral method (19). At this point one can approximate the integral in Eq. (15) by a Gaussian quadrature of N points:

$$\bar{a}_n \approx \sum_{l=0}^{N-1} \psi^*(q_l)g_n(q_l)W(q_l) \tag{16}$$

Based on the Christoffel-Darboux formula (20) it can be shown that this procedure leads to a functional expansion which becomes an interpolation formula on the integration points, $\bar{\psi}(q_k) \equiv \psi(q_k)$. As an example consider an expansion by the Chebychev orthogonal polynomials $g_n(q) = T_n(q)$ with the constant weights $W(q_l) = 2/\pi$. The quadrature points q_l are the zeros of the Chebychev polynomial of degree $N + 1$. On inserting Eq. (16) into the functional expansion Eq. (2) becomes

$$\begin{aligned}\sum_{n=0}^{N-1} \bar{a}_n T_n(q_k) &= \frac{2}{\pi}\sum_{n=0}^{N-1}\sum_{l=0}^{N-1} \psi(q_l)T_n(q_l)T_n(q_k) \\ &= \sum_{l=0}^{N-1} \psi(q_l)\frac{2}{\pi}\sum_{n=0}^{N-1} T_n(q_l)T_n(q_k) = \psi(q_k)\end{aligned} \tag{17}$$

and therefore $\bar{\psi}(q_k) \equiv \psi(q_k)$. The last equation is because of changing the order of summation and the Christoffel-Darboux formula (20), which for the Cheychev polynomials reads $(2/\pi)\ \Sigma_{n=0}^{N-1}\ T_n(q_l)T_n(q_k) = \delta_{lk}$. From Eq. (17), it can be concluded that the Chebychev variational expansion is equivalent to a polynomial interpolation when the sampling points are the zeros of the $N + 1$ Chebychev polynomial and the expansion coefficients are calculated using the Gauss-Chebychev quadrature scheme of order N (see also Sec. III.E). In general this means that the variational and the collocation methods based on orthogonal expansion functions are closely related and therefore their quality of representation is numerically equivalent.

Section III.D will elaborate on a particular choice of orthogonal functions, the Fourier set.

C. Direct Grid Collocation Methods

A direct inversion of the collocation representation Eq. (1) where the expansion coefficients a_n become the values of the function at the interpolation points $a_n = \psi(q_n)$ can be

obtained with a proper choice of expansion functions $g_n(q)$. This representation is generated by a global function $U_{N_g}(q)$ which has N_g simple zeros at the interpolation points: $U_{N_g}(q_j) = 0$ for all grid points j. Then

$$\bar{\psi}(q) = \sum_{j=0}^{N_g-1} \psi(q_j) \frac{U_{N_g}(q)}{(q - q_j)U'_{Ng}(q_j)} \tag{18}$$

is an interpolation formula (21), where $U'_{Ng}(q_j)$ is the derivative of $U_{N_g}(q)$ at the interpolation point q_j. The structure of the expansion functions, $g_n(q) = U_{N_g}(q)/(q - q_j)U'_{N_g}(q_n)$, is responsible for the direct inversion property. The value of the function is one on grid point q_n and zero on all other grid points (see Fig. 4)

Choosing the generating function U_{N_g} as the polynomial, $U_{N_g}(q) = (q - q_1)(q - q_2) \cdots (q - q_j) \cdots (q - q_{N_g})$ leads to the well-known Lagrange interpolation formula. Figure 4 shows the expansion function $g_n(q)$ which is based on the zeros of the Chebychev orthogonal polynomial of order N_g. Another choice appropriate for evenly distributed sampling points is based on the global function $N_{N_g}(q) = \sin(2\pi q/\Delta q)$. It is closely related to the Fourier method described in the next section.

D. The Fourier Method

An examination of the Fourier method, which is a special case of an orthogonal collocation representation, elucidates the main considerations of representation theory. It will be shown that by optimizing the representation the quantum limit of one point per unit phase space volume of h can be obtained. Moreover, the Fourier method has great numerical advantages because of the "fast" nature of the algorithm (22–26). This means that the numerical effort scales semilinearly with the represented volume of phase space (27).

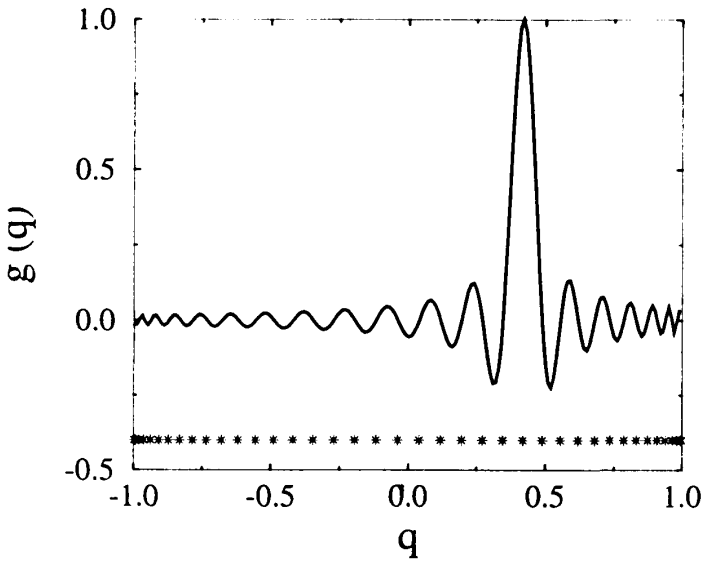

Figure 4 Direct grid interpolation function $g_n(q)$ ($n = 15$, $N_g = 40$) for Chebychev interpolation points. The function $g_n(q)$ equals one on grid point $n = 15$ and zero at all other grid points. The 40 interpolation points are shown as stars at the bottom of the plot.

In the Fourier method, the orthogonal functions $g_n(q)$ are chosen as (12,28,27)

$$g_k(q) = e^{i2\pi kq/L}, \qquad k = -(N_g/2 - 1), \ldots, 0, \ldots, N_g/2 \tag{19}$$

leading to N_g equally spaced sampling points where $q_j = (j - 1)\Delta q$ ($j = 1, \ldots N_g$) and L is the length of the interval. Using the relation $L = N_g\Delta q$, the completeness relations of the Fourier expansion functions become

$$\begin{aligned}\sum_{k=-N_g/2+1}^{N_g/2} g_k(q_n)g_k^*(q_m) &= \sum_{k=-(N_g/2-1)}^{N_g/2} e^{i2\pi kq_n/L} e^{-i2\pi kgm/L} \\ &= \sum_{k=-(N_g/2-1)}^{N_g/2-1} e^{i2\pi kn/N_g} e^{-i2\pi km/N_g} \\ &= e^{-i2\pi(n-m)/N_g} \frac{1 - e^{i2\pi(n-m)}}{1 - e^{i2\pi(n-m)/N_g}} = \delta_{nm}N_g\end{aligned} \tag{20}$$

where the summation can be carried out explicitly because it is a geometric series. The fourth equality in Eq. (20) follows because if $n = m$ the summation is trivial. Otherwise, $|n - m|$ ranges from 1 to $N_g - 1$ and is never an integral multiple of N_g. Thus the denominator never vanishes while the numerator is identically zero. This is the first orthogonality relation, Eq. (9).

The second orthogonality relation equivalent to Eq. (11) becomes

$$\frac{1}{2\pi}\int_{-\pi}^{\pi} e^{imq'} e^{-inq'}\, dq' = \frac{1}{2\pi}\left[\frac{1}{i(m-n)} e^{i(m-n)q}\right]_{-\pi}^{\pi} = \delta_{nm} \tag{21}$$

where $q' = \pi(q/L - 1)$, $0 \le q \le L$. These relationships imply that the domain D has periodic boundary conditions. The symmetry between n and k in Eq. (20) leads to the discrete version of Eq. (21):

$$\sum_{j=1}^{N_g} g_k(q_j)qe(q_j) = \delta_{kl}N_g, \qquad |k - j| < N_g \tag{22}$$

The Fourier expansion of a wave function $\psi(q)$ is next explored:

$$\psi(q) \approx \sum_{k=-(N_g/2-1)}^{N_g/2} a_k e^{i2kq/L} \tag{23}$$

The expansion coefficients a_k become the discrete Fourier expansion coefficients. The orthogonality of the Fourier functions with equidistant sampling points can be used to invert the relation, giving

$$a_k = \frac{1}{N}\sum_{j=1}^{N_g} \psi(q_j)e^{-i2\pi kq_j/L} \tag{24}$$

Thus, the adjoint relationship, expressed by the matrix G, is particularly simple. In quantum mechanics the coefficients a_k have an important interpretation since they represent the amplitude of the wave function in momentum space. Equations (23) and (24) are direct analogues to the continuous Fourier transformation, which changes a coordinate

representation to a momentum representation:

$$\begin{cases} \psi(q) = \dfrac{1}{\sqrt{2\pi}} \displaystyle\int_{-\infty}^{\infty} e^{ikq}\bar{\psi}(k)\, dk \\ \bar{\psi}(k) = \dfrac{1}{\sqrt{2\pi}} \displaystyle\int_{-\infty}^{\infty} e^{-ikq}\psi(q)\, dq \end{cases} \tag{25}$$

This means that the expansion coefficient a_k can be interpreted as the value of the wave function in the momentum representation at the discrete point k: $a_k = \bar{\psi}(p_k)$, and a momentum evenly spaced grid is automatically constructed with the grid spacing $\Delta p = 2\pi/L$.

1. Phase Space Representation of the Fourier Method

The phase space representation of the Fourier method is of a rectangular shape. The volume in phase space covered by the Fourier representation is calculated as follows: The length of the spatial dimension in phase is **L**, and the maximum momentum is $\mathbf{p}_{max}$. Therefore, the represented volume becomes $\mathcal{V} = 2\mathbf{L}\cdot\mathbf{p}_{max}$, where the factor of two appears because the momentum range is from $-\mathbf{p}_{max}$ to $+\ \mathbf{p}_{max}$. Using the fact that $\mathbf{p} = \hbar\mathbf{k}$, the phase space volume can be expressed as

$$\mathcal{V} = 2\hbar\mathbf{L}\cdot\mathbf{k}_{max} = N_g h \tag{26}$$

where N_g is the number of sampling points. Equation (26) is the desired link between the sampled phase space volume and the number of grid points N_g. Since $L = N\Delta q$, it follows that the sampling spacing Δq is related to the maximum wave vector via

$$\Delta q = \frac{\pi}{|\mathbf{k}_{max}|} \tag{27}$$

The computational scaling properties of the Fourier method are a result of the scaling properties of the FFT algorithm which scales as $O(N_g \log N_g)$. As a result the phase space volume determines the scaling of the computational effort: $O(\mathcal{V} \log \mathcal{V})$.

A function that is compact in momentum space is equivalent to the band-limited Fourier transform of the function. Confinement of such a function to a finite volume in phase space is equivalent to a band-limited function with finite support. (The support of a function is the set for which the function is nonzero.) The accuracy of a representation of this function is assured by the Whittaker-Kotel'nikov-Shannon sampling theorem (29–31). It states that a band-limited function with finite support is fully specified, if the functional values are given by a discrete, sufficiently dense set of equally spaced sampling points. The number of points is determined by Eq. (26). This implies that a value of the function at an intermediate point can be interpolated with any desired accuracy. This theorem also implies a faithful representation of the nth derivative of the function inside the interval of support. In other words, a finite set of well-chosen points yields arbitrary accuracy.

Since the wave functions are band limited, Eq. (23) equals the sum of sinc functions: $\psi(q) = \sum_{n=-(N_g/2-1)}^{N_g/2} \psi(n\Delta q)\mathrm{sinc}[k_{max}(q - n\Delta q)]$. The relation is a consequence of the fact that the sinc function is the Fourier transform of a band (rectangle). See also Eq. (18).

For unbounded problems, such as occur in quantum mechanics, the wave function cannot be confined in both coordinate and momentum space. In principle, no wave func-

tion is strictly band limited with finite support. The idea of a wave packet, a wave function that is almost band limited, is central to the use of the discrete representation.

The most well-studied example of a wave packet is the Gaussian wave function [1]. Although its wave function is not confined to a finite volume, the amplitude outside this volume in phase space converges exponentially to zero in either coordinate or momentum space. This exponential convergence is typical of a good representation of phase space. A counterexample is supplied by a rectangular packet. In coordinate space the wave function is well confined, but in momentum space the rectangular wave function is transformed to $\bar{\psi}(k) = A[\sin(a(k - k_0))/a(k - k_0)]$, which has only a linear convergence rate with the size of the grid in k space (see Fig. 5). This point is central to the use of the Fourier method which balances the coordinate and momentum representations. For a time dependent calculation, a phase space box has to be large enough to keep the wave function localized at all times or using the above concept conserves the wave packet property.

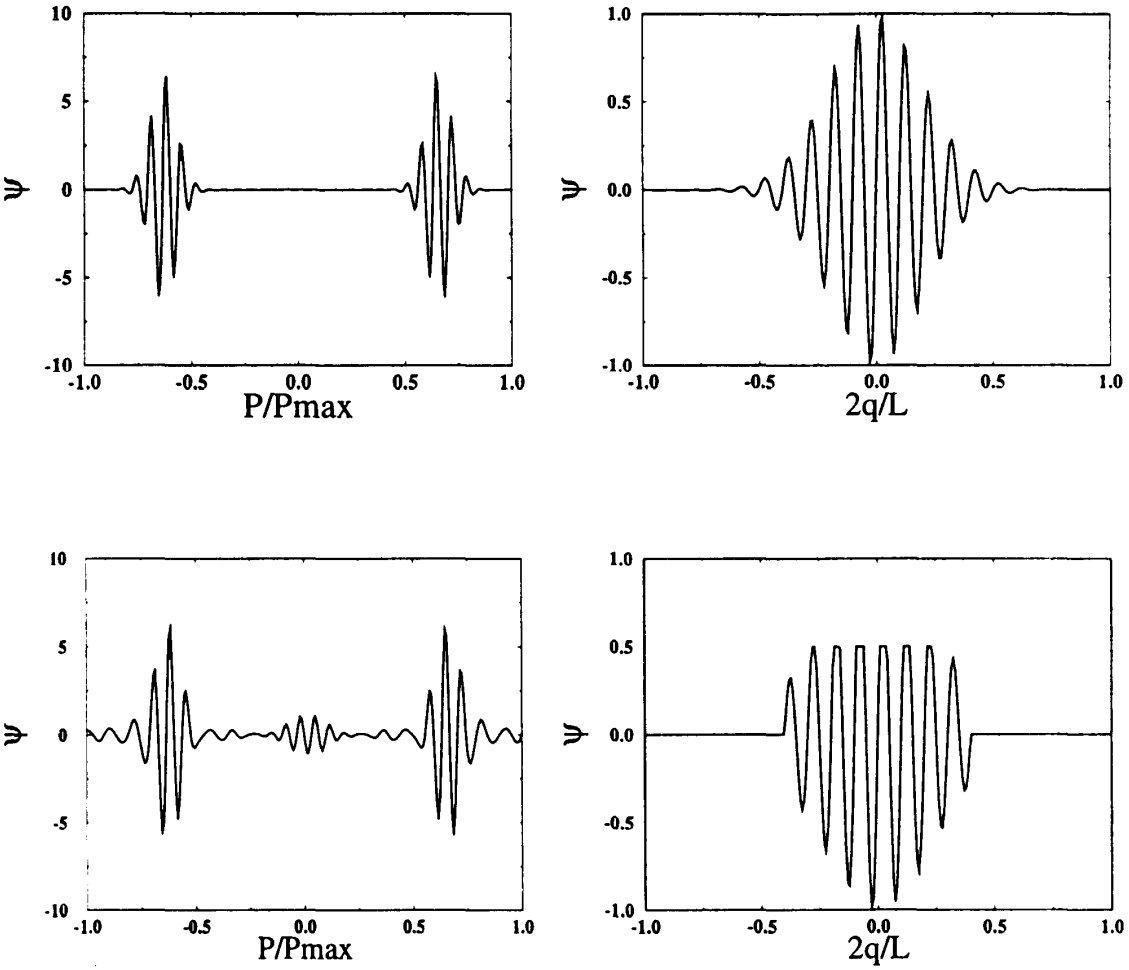

Figure 5 (Upper panel) A wave packet, a semilocalized wave function in coordinate space (right panel) and in momentum space (left panel) where $P_{max} = \pi/\Delta q$, L is the interval length: $L = N_g \Delta q$). For the wave packet the convergence of the expansion (23) with respect to N_g is exponential: $O(e^{-\alpha N_g})$. (Lower panel) A localized wave function in coordinate space but due to the sharp cutoff it is not localized in momentum space (left lower panel). Convergence with respect to N_g is only $O(1/N_g)$.

E. Collocation by Orthogonal Polynomials

Orthogonal polynomials are a very useful set of expansion functions on grids. The simplest case is to define $g_n(q)$ as $w(q)P_n(q)$, where $P_n(q)$ is a member of the set of orthogonal polynomials, and $w(q)$ is a weight function. These functions obey the continuous orthogonal relation defined in the domain D:

$$\int_D w(q)P_n^*(q)P_m(q)\,dq = \delta_{nm} \tag{28}$$

If the sampling points q_j are chosen as zeros of the $P_{N_g}(q)$ polynomials; $O_{N_g}(q_j) = 0$, then the theory of Gaussian integration leads to

$$\sum_{j=0}^{N_g-1} W_j P_n^*(q_j)P_m(q_j) = \delta_{mn} \tag{29}$$

where W_j are point weights. Equation (29) is used to invert the collocation relation (32), leading to (33–35)

$$a_n = \sum_{j=0}^{N_g-1} W_j P_n^*(q_j)\psi(q_j) \tag{30}$$

The grid points which are the Gauss integration quadrature points can be calculated by diagonalizing the position operator in the collocation basis (36). Figure 4 shows the sampling points of the $P_{40}(q)$ Chebychev polynomial ($P_n(q) = \cos(n\ \cos^{-1}(q))$). The method can be supplemented by including the end points in the grid, thus using Gauss Radau or Gauss Labato quadratures (37,38). The orthogonal polynomials can also be used as a basis for a direct grid representation by choosing $g_j(q) = w_j^{1/2} \sum_{n=0}^{N_g-1} P_n(q_j)P_n(q)$ (39,40).

Part of these ideas are well discussed in the work of Gottlieb and Orszag (19) and are known as the pseudospectral method. In molecular dynamics this approach is known as DVR (36).

F. Operators Represented by Grid Methods

Operators in quantum mechanics are determined by their consequences. Operators map the wave function ψ into a new state vector:

$$\phi = \mathbf{A}\psi \tag{31}$$

This elementary relation has a direct consequence in the discrete representation on the grid:

$$\phi(q_i) = \sum_{j}^{N_g} A_{ij}\psi(q_j) \tag{32}$$

Equation (32) states that in the discrete world the mapping induced by the operator has to be recast into the original grid representation.

In general, the application of an operator to a state vector will scale as $O(N_g^2)$. For large grid applications, this scaling becomes prohibitively expensive, and much effort must be dedicated to reduce this computation scaling law.

1. Application of Local Operators

In coordinate space local operators are analytic functions of the coordinate q; i.e, $\mathbf{A} = f(\mathbf{q})$. The mapping induced by local operators on a coordinate-based grid is straightforward. For example, the application of the potential operator (Fig. 6):

$$\phi = \mathbf{V}\psi \Rightarrow \phi(q_i) = V(q_i)\psi(q_i) \tag{33}$$

This means that the operator $\mathbf{V}$ is diagonal in the grid representation. The application of local operators reduces the operation count of the operator mapping from $O(N_g^2)$ to $O(N_g)$.

From a different perspective the matrix elements of $\mathbf{V}$: $\langle\psi|\mathbf{V}|\phi\rangle$ are calculated by a quadrature formula where the grid points become sampling points. If the potential operator has discontinuous derivatives, its mapping will reduce a wavepacket to a wave function possessing a nonlocal representation in momentum space; i.e, if ψ is a band-limited function then $\phi = \mathbf{V}\psi$ is not. A typical example is a particle in a box.

2. Mapping Induced by Differential Operators

Differential operators constitute the most important class of nonlocal operators. The mapping of the momentum operator $\mathbf{P} = -i\hbar(\partial/\partial_q)$, and the kinetic energy operator $\mathbf{T} = \mathbf{p}^2/2M = -(\hbar^2/2M)(\partial^2/\partial q^2)$ are of special interest.

The calculation of the derivatives is based on the analytic properties of the interpolation functions $g_n(q)$. This means that they can be differentiated at any point:

$$\frac{\partial\psi}{\partial q} = \sum_{n=1}^{N_g} a_n \frac{\partial}{\partial q} g_n(q) \tag{34}$$

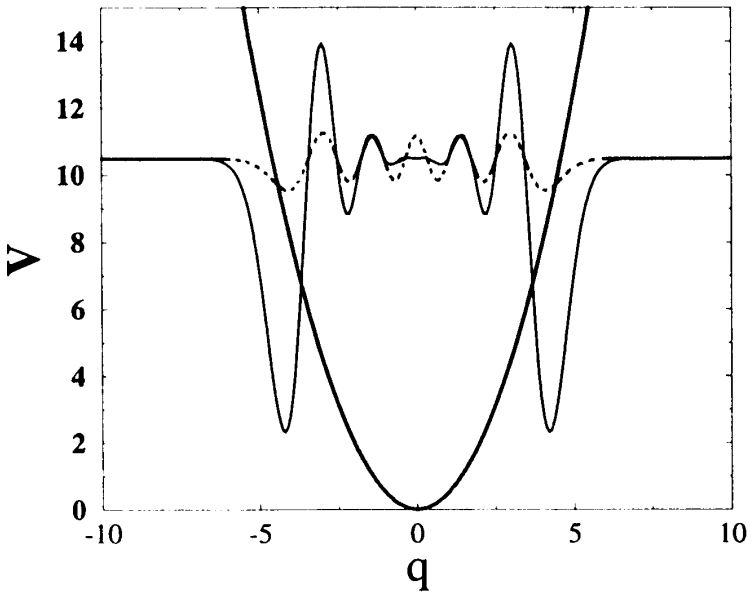

Figure 6 The mapping created by the potential operator: The wave function $\psi(q_i)$ (dashed) the potential function $V(q_i)$, and the mapped wave function $\phi(q_i) = V(q_i)\psi(q_i)$ (solid). Notice that the potential amplifies certain parts of the wave functions ψ. (The $n = 10$ eigenstate of the harmonic oscillator is shown.)

and in particular on the grid points:

$$\frac{\partial \psi}{\partial q}\Big|_{q_i} = \sum_{n}^{N_g} \frac{\partial}{\partial q} g_n(q_i) \sum_{j=1}^{N_g} G_{nj}^{-1} \psi_j \tag{35}$$

Defining the derivative operator matrix

$$\frac{\partial \psi}{\partial q_i} = \sum_{j=1}^{N_g} D_{ij} \psi(q_j)$$

it becomes

$$D = FG^{-1} \tag{36}$$

where the matrix F becomes $F_{nj} = \partial g_n(q_j)/\partial q$ and the matrix G is defined in Eq. (3). In a similar fashion, higher-order derivative operators can be defined. This general formula is very flexible but may lead to an operator representation of the momentum and the kinetic energy operators which are not hermitian. The derivative operator can also be obtained by differentiating the direct grid interpolation formula (18) on the grid points.

An improved derivative formula can be obtained if the derivative of the basis functions can be recast into the original set; i.e.,

$$\frac{\partial}{\partial q} g_n(q) = \sum_{m=1}^{N_g} d_{nm} g_m(q) \tag{37}$$

or in matrix form: $\partial/\partial q\ \mathbf{g} = \mathbf{dg}$. Then the derivative operator has the simple form

$$D = GdG^{-1} \tag{38}$$

If the expansion functions are derived from orthogonal polynomials, the matrix **d** can be obtained from the recursion relation for the orthogonal polynomials (32). If there is a fast transform for G (which is true for the Chebychev polynomial expansion), then applying Eq. (38) will scale as $O(N_g \log N_g)$.

3. Derivatives in the Fourier Representation

In the Fourier representation, the transformation matrix $G = U_f$, $((U_f)_{jk} = (1/\sqrt{N_g}\ e^{i2\pi jk/N_g})$ is unitary and supplies the means to transform the wave function from coordinate to momentum space. Moreover, the expansion functions $g_k(q) = e^{i2\pi kq/L}$ are eigenvalues of the derivative matrix. Therefore, $d_{kk'} = (i2\pi k/L)\delta_{kk'}$ which leads to the Fourier derivative formula for order n:

$$\frac{\partial^n \psi}{\partial q^n} = U_f d^n U_f^{\dagger} \tag{39}$$

This formula is analogous to the continuous version of the Fourier derivative formula:

$$\frac{\partial^n \psi(q)}{\partial q^n} = \frac{1}{2\pi} \int_{-\infty}^{\infty} (ik)^n e^{ikq} \bar{\psi}(k)\, dk \tag{40}$$

A physical interpretation of the Fourier derivative formula Eq. (39) is obtained by noticing the analogy between the discrete Fourier transform $\mathbf{U}_f$ and the unitary transformation from coordinate to momentum space in quantum mechanics $\langle p|q\rangle$. In the momentum

representation, the momentum operator and kinetic energy operators become local operators. Therefore the generated mapping is just a multiplication, leading to the algorithm for calculating the kinetic energy operator on the grid representation. The first step in the operation is to Fourier transform $\psi(q)$ from coordinate space to $\tilde{\psi}(p)$ in momentum space. (**A** → **B** in Fig. 7). The second step is to multiply the wave function by the kinetic energy operator:

$$T(k) = \frac{\mathbf{p}^2}{2m} = \frac{\hbar^2 k^2}{2m} \tag{41}$$

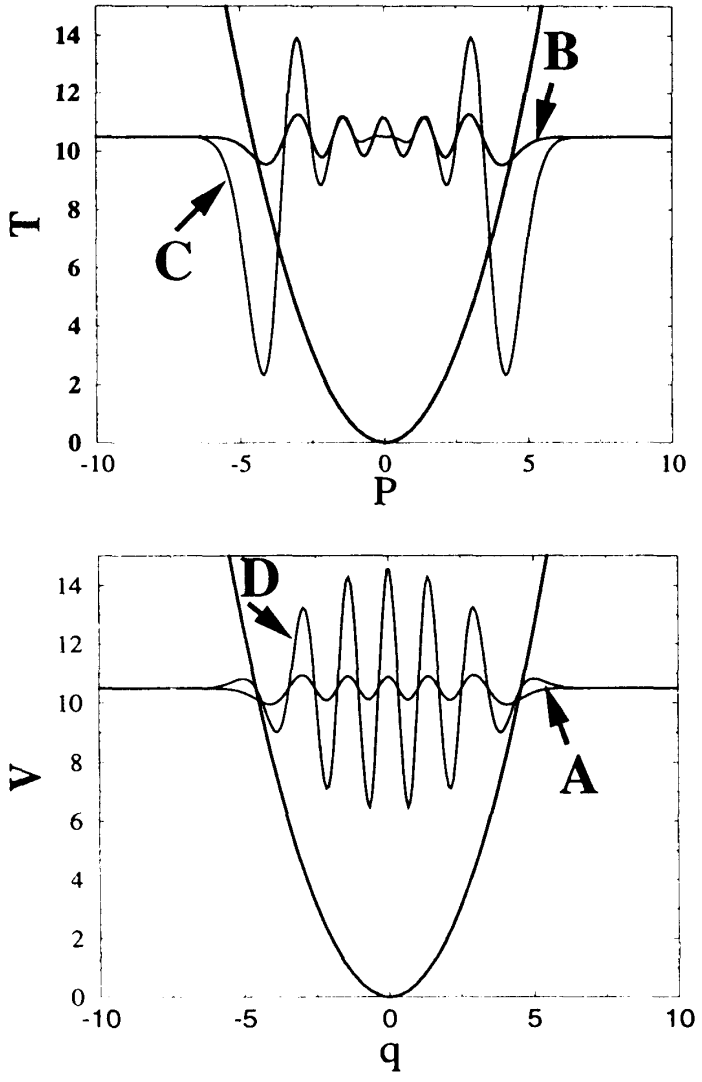

Figure 7 The four steps in the application of the kinetic energy operator by the Fourier method (A → B → C → D): (lower panel) coordinate space; (upper panel) momentum space. A is the original wave function $\psi(q)$. B represents the wave function in momentum space $\tilde{\psi}(p)$ obtained by Fourier transform of $\psi(q)$. C is the application of the kinetic energy operator in momentum space. $\tilde{\phi}(p) = p^2/2M \cdot \tilde{\psi}(p)$ where $T = p^2/2M$ is also shown. D is $\phi(q) = T\psi(q)$. It is the final result obtained by a Fourier transform of C.

The operation on a component of the wave function represented in momentum space becomes

$$\frac{\mathbf{p}^2}{2m}\bar{\psi}(k) = \frac{\hbar^2 k^2}{2m} a_k \tag{42}$$

(designated by **C** in Fig. 7). The operation is completed by an inverse Fourier transform (**C** → **D** in Fig. 7).

The operation scaling law of the Fourier method is determined by the forward and reverse unitary transformations from coordinate to momentum space. In general, they scale as $O(N_g^2)$ but with the use of the fast Fourier transform (FFT) algorithm this scaling is reduced to $O(N_g \log N_g)$.

The result of Eqs. (41) and (42) can be generalized for any local operator in momentum space. The algorithm for calculating the mapping of such operators is as follows: (a) calculate the expansion coefficients a_k by the discrete Fourier transform; (b) multiply each point in k space by the value of the operator at that point; (c) transform the result back to the coordinate sampling space by an inverse Fourier transform.

The convergence of the operator mapping $\phi = \hat{\mathbf{O}}\psi$ is determined by the wave packet nature of the wave function ϕ. The quantum mechanical nature of the approximation depends on the ability to represent the position momentum commutation relation $[\hat{\mathbf{X}}, \hat{\mathbf{P}}] = i\hbar$. A close examination reveals that the function $f(q) = q$ is not band limited on the interval $[0, L]$ because it is discontinuous at the end of the interval $q = L$. Now if $f(q) = q$ is replaced by a periodic function $f(q + L) = f(q)$, then

$$[f(\mathbf{q}), \mathbf{p}] = i\hbar f'(\mathbf{q}) \tag{43}$$

since the Fourier method differentiates exactly periodic functions (12). This means that the Fourier method fulfills the quantum mechanical commutation relations for periodic potentials and compact wave functions. Practically this means that converged results are obtained when the wave function is effectively zero at the boundaries of the phase space box; i.e., it is a wave packet.

4. Convolution Operators

Another important operator which is local in momentum space is the unitary translation operator defined by

$$\hat{\mathbf{U}}_t(y)\psi(x) = \psi(x + y) \tag{44}$$

which becomes a phase shift in momentum space:

$$\hat{\mathbf{U}}_t(y)\bar{\psi}(k) = e^{iky} a_k \tag{45}$$

The efficient numerical ability to translate the wave packet in coordinate space has important consequences. With no loss of accuracy the wave packet can be centered in the middle of the grid. This can be done either continuously, resulting in a dynamical grid, or sequentially at predetermined intervals. Such a process can be accompanied by a shift in momentum

$$\hat{\mathbf{U}}_p(k')\bar{\psi}(k) = \bar{\psi}(k + k') \tag{46}$$

which becomes a phase shift in the coordinate space:

$$\hat{\mathbf{U}}_p(k')\psi(x) = e^{ik'x}\psi(x) \tag{47}$$

The two shift operator equations (44) and (46) can reduce significantly the effective volume represented in phase space by matching the grid to regions where the wave function has significant amplitude. One should remember that when shifting the wave function the potential has to be shifted in the opposite direction and the kinetic energy operator shifts to $\hat{\mathbf{T}}(k) = (\hbar^2/2m)(k - k')^2$. Another use of the shift operator is to interpolate the wave function to points which are not represented on the grid. An example of the use of an interpolation procedure is when there is a sudden change of the potential. In photodissociation, for example, the ground state wave function is placed on an excited electronic potential which undergoes a rapid momentum increase. To guarantee convergence, the sampling density has to be increased from its value in the ground electronic state.

One simple scheme to effect this interpolation is as follows. Consider a wave function which is sampled by N points. It is first transformed to momentum space. Then the wave function is cast onto a larger grid of M points by adding $M - N$ zeros to the momentum values for $|k| > \pi N/L$. A back transform will increase the density of points without adding any new information to the wave function.

5. Comparison of Different Derivative Operators

The simple implementation of the translation operator is a consequence of a general property of the Fourier transform that a convolution of two functions in coordinate space becomes a multiplication of the transform function in momentum space. This fact can be used to study local implementations of the differential operators. In all local methods the derivative matrix D is a banded matrix. For example, consider the mapping of the fourth-order finite difference (FD) kinetic energy operator:

$$\hat{\mathbf{T}}^4_{\mathrm{FD}}\psi(q_j) = -\frac{\hbar^2}{2m}\frac{\psi(q_{j+1}) + \psi(q_j - 1) - 2\psi(q_j)}{\Delta q^2} \tag{48}$$

Examining Eq. (48), it is obvious that it is a member of the family of convolution operators and therefore is diagonal in **k** space. Performing a Fourier transform, the spectrum in **k** space of the FD kinetic energy operator is obtained:

$$T^4_{FD}(k) = -\frac{\hbar^2}{2m}\frac{2(\cos(k\Delta q) - 1)}{(\Delta q)^2} = \frac{\hbar^2}{2m}\left(\frac{2\sin(k\Delta q/2)}{\Delta q}\right)^2 \tag{49}$$

Likewise, the sixth-order finite difference operator has spectrum

$$T^6_{FD}(k) = -\frac{\hbar^2}{2m}\frac{2\cos(2k\Delta q) - 32\cos(k\Delta q) + 30}{12(\Delta q)^2} \tag{50}$$

Figure 8 compares the different spectra.

It is apparent that as the momentum **p** increases, the finite difference spectrum deviates more and more from the correct value. It is usually assumed that acceptable accuracy with the FD method is obtained when at least 10 points are used per wave period. This means also using 10 points per unit volume in phase space. The finite difference algorithms are based on a local polynomial approximation of the wave function and therefore the convergence of the method follows a power law of the form $(\Delta q)^n$, where n is the order of the finite difference approximation. This semilocal description leads to a poor spectral representation of the kinetic energy operator, which will be true as well, for other banded representations of the kinetic energy operator such as the

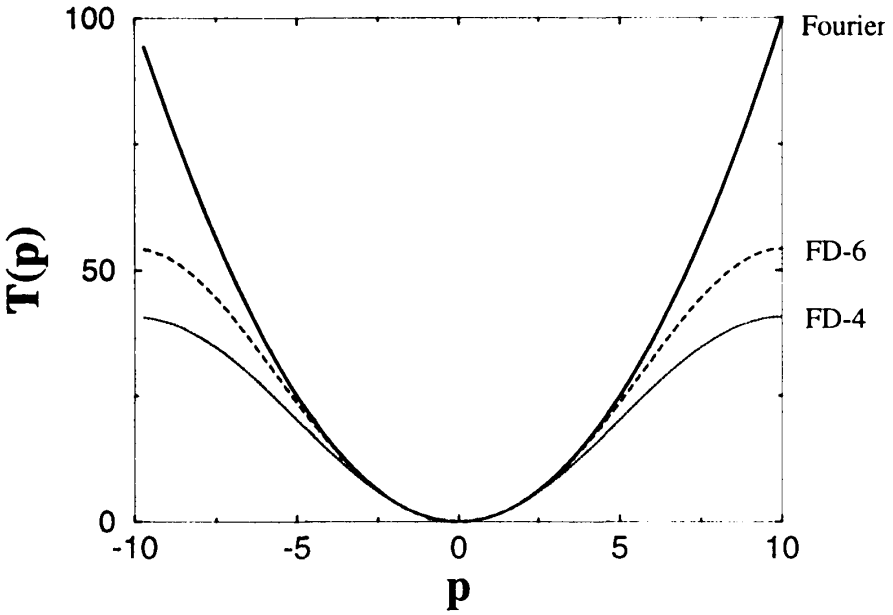

Figure 8 Comparison of the kinetic energy operator spectrum for the Fourier method (solid) with the fourth- (FD-4) and sixth-order (FD-6) finite difference method.

recently developed DAF-based operator (41). A general consequence is that a semilocal representation of the momentum operator does not obey the commutation relations of quantum mechanics. This fact, combined with an iterative use of the operator, leads to an exponential accumulation of errors. Propagation with a Hamiltonian based on these operators leads to anomalous dispersion of the wave function.

G. The Harmonic Oscillator Example

After viewing the wealth of considerations used to set up a grid and define the mapping generated by the operators on the grid, a specific example will serve as a summary. The goal is to find the optimal representation of the Hamiltonian operator for the harmonic oscillator $\mathbf{H} = 1/2m\mathbf{P}^2 + m\omega^2 q^2$. Figure 9 displays the phase-space picture of the $n = 10$ eigenstate of the harmonic oscillator. It is apparent that the amplitude of the wave function outside the circle $(\frac{1}{2}(q^2 + p^2) = 10 + \frac{1}{2}$ becomes exponentially small, thus, the wave function is a wave packet. Therefore, a finite representation based on a Fourier grid will have exponential convergence.

In constructing an optimal grid, the first step is to set the energy cutoff of the system. For a symmetric grid of length L the maximum value of the potential energy is determined by the extreme points on the grid:

$$V_{\max} = \frac{m\omega^2}{2}\left(\frac{L}{2}\right)^2 = \frac{m\omega^2 \Delta q^2 N_g^2}{8} \tag{51}$$

where N_g is the number of sampling points and the grid is centered at about zero. The maximum kinetic energy is limited by the maximum momentum which can be represented on the grid, leading to

$$T_{\max} = \frac{P_{\max}^2}{2m} = \frac{\hbar^2}{2m}\left(\frac{2\pi}{2\Delta q}\right)^2 = \frac{\hbar^2 \pi^2}{2m\Delta q^2} \tag{52}$$

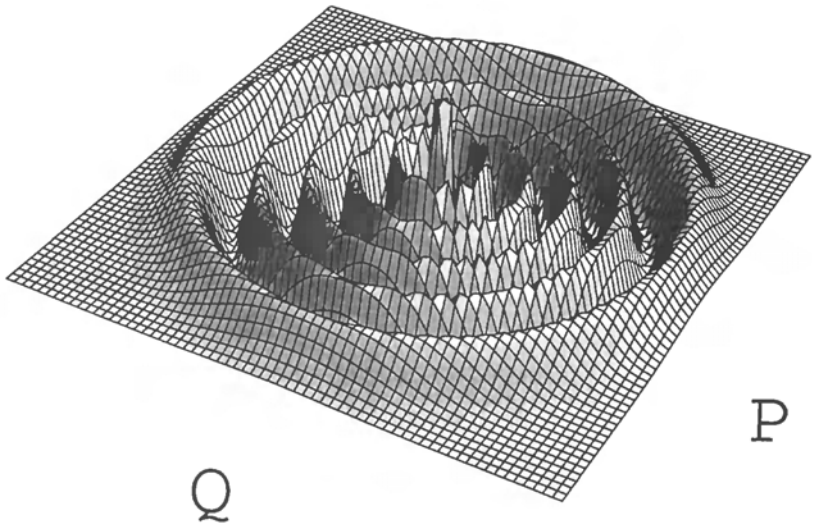

Figure 9 Wigner distribution function of the $n = 10$ eigenfunction of the harmonic oscillator. The picture shows the extent of the wave function in phase space which has nearly optimal sampling due to the balance between the representation of the kinetic and potential energy.

Equations (51) and (52) represent an energy cutoff due to the discrete representation of the Hilbert space. The optimal representation balances the kinetic and potential energy. Using the viral theorem for the harmonic oscillator, the cutoff in the potential energy should match the cutoff in the kinetic energy, with the resulting optimal grid spacing

$$\Delta q_{\text{opt}} = \left(\frac{h}{m\omega N_g}\right)^{1/2} \tag{53}$$

Figure 10 shows a schematic representation of the phase space representation imposed by the optimal and suboptimal grids.

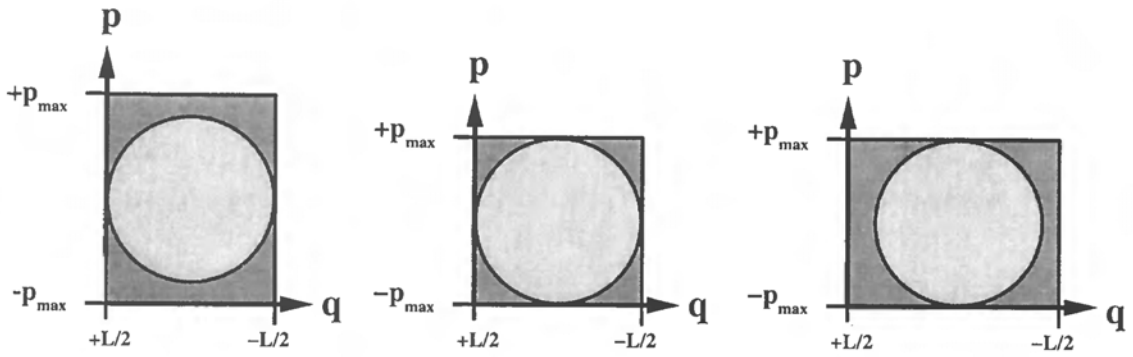

Figure 10 Schematic representation of the phase space "volume" represented by the Fourier grid. Superimposed is the maximum energy cutoff circle. The grid representation on the left is suboptimal due to an oversampling of the kinetic energy (Δq is too small), and the grid phase space on the right over samples the potential energy (L is too large). The grid in the center shows optimal sampling efficiency of $\pi/4$ which is the ratio of the area of the energy conservation disk to the area of the phase space square.

To illustrate these considerations, a grid is constructed using the functions $\psi(q_j) = \delta(q_i - q_j) = 1/\pi \operatorname{sinc}(2\pi(q_i - q_j)/\Delta q)$ ($\operatorname{sinc}(z) = \sin(z)/z$). This basis function is zero on all other grid points except j, where its value is 1. The Hamiltonian matrix in this base is calculated as follows: The potential energy matrix is diagonal: $V_{jj} = V(q_j)$. To calculate the kinetic energy matrix elements, a discrete Fourier transform is applied to the expansion function ψ_j, then multiplied by $\hbar^2k^2/2m$ and back-transformed. The resulting vector becomes the matrix element T_{ji}. At this stage the Hamiltonian matrix $\hat{\mathbf{H}} = \hat{\mathbf{T}} + \hat{\mathbf{V}}$ is diagonalized and the eigenvalues of the discrete representation are compared to the exact results.

Table 1 shows the calculated eigenvalues using 8, 16, and 32 sampling points with the optimal grid spacing Δq_{opt} for $\omega = 1$, $m = 1$, and $\hbar = 1$.

When the results for eight sampling points are compared with 16 sampling points, the exponential convergence of the expansion is demonstrated. For the ground state energy the error decreases six orders of magnitude by only doubling the number of grid points. Other states show similar behavior. When the number of points is doubled again to 32, the error in the ground state becomes saturated because the roundoff error of the double precision arithmetic used in the calculation overcomes the representation error. For unsaturated eigenvalues doubling the number of points from 16 to 32 reduces the error another five to six orders of magnitude.

Another view on the convergence of the Fourier method can be obtained by counting the number of converged eigenvalues obtained for N_g grid points. If the convergence criterion is three significant digits, it is observed that three converged eigenvalues are obtained for $N_g = 8$, 8 for $N_g = 16$, and 20 for $N_g = 32$ grid points. This means that the fraction of significant eigenvalues increases with the number of points in the represen-

Table 1 Convergence of the Fourier Representation for the Harmonic Oscillator

N_g		8 points	16 points	32 points
Δq_{opt}	Exact	0.8862265	0.6266568	0.4431132
1	0.5	0.4999760107111692	0.4999999998715793	0.4999999999999845
2	1.5	1.500539183698194	1.500000006153576	1.499999999999986
3	2.5	2.494397791604125	2.499999857637178	2.500000000000002
4	3.5	3.534291735531325	3.500002068787167	3.499999999999993
5	4.5	4.378294841394608	4.499978178076544	4.499999999999982
6	5.5	5.960743369677700	5.500169240572392	5.500000000000130
7	6.5	6.212358517586826	6.498928884935602	6.499999999997876
8	7.5	9.976917743504451	7.505122466888302	7.500000000025498
9	8.5		8.478529454896226	8.499999999731434
10	9.5		9.567379412999802	9.500000002414588
11	10.5		10.33263329166096	10.49999998073345
12	11.5		11.95570264326039	11.50000013337068
13	12.5		12.04789296489282	12.49999916184023
14	13.5		14.56012875187433	13.50000457741937
15	14.5		15.44949561677325	14.49997680742042
16	15.5		20.69252130835984	15.50010120025324
17	16.5			16.49957859092886
18	17.5			17.50146417275678

tation. Figure 11 shows the fraction of significant eigenvalues as a function of the logarithm of the number of points.

Figure 11 shows that the converged eigenvalue fraction increases with the number of points until it reaches saturation regardless of the number of significant digits used as the convergence criterion. This asymptotic ratio can be used to define the sampling efficiency.

The saturation of the eigenvalue fraction occurs because the Fourier method constructs a rectangular phase space (see Fig. 9). Using the balanced choice of Δq_{opt}, the phase space becomes a square. On the other hand, due to energy conservation, the support for an eigenfunction in phase space up to a cutoff energy has the shape of a disk determined by the largest eigenfunction (or an ellipse in the general case). The area between the circumference of the disk and the perimeter of the square is wasted sampling space. Therefore the maximum sampling efficiency is the ratio of the area of the circle to the area of the square leading to $\pi/4 \approx 79\%$. This is the asymptotic value represented by the bold line in Figure 11.

To illustrate this point further, Figure 12 shows the converged eigenvalue fraction as a function of the grid spacing Δq. It is clear that a square in phase space offers the optimal choice where, to the left of the cusp point $\Delta q = \Delta q_{\text{opt}}$, the kinetic energy operator error dominates. To the right of the cusp point, the potential energy error dominates.

This example shows that a careful choice of grid parameters which balance the representation of the kinetic and potential energy can drastically reduce the amount of computation effort.

Table 2 shows the convergence of the first eigenvalues of the finite difference method for the same parameters as Table 1. The kinetic energy spectrum was constructed from Eq. (49). The grid spacing Δq was optimized for each case independently.

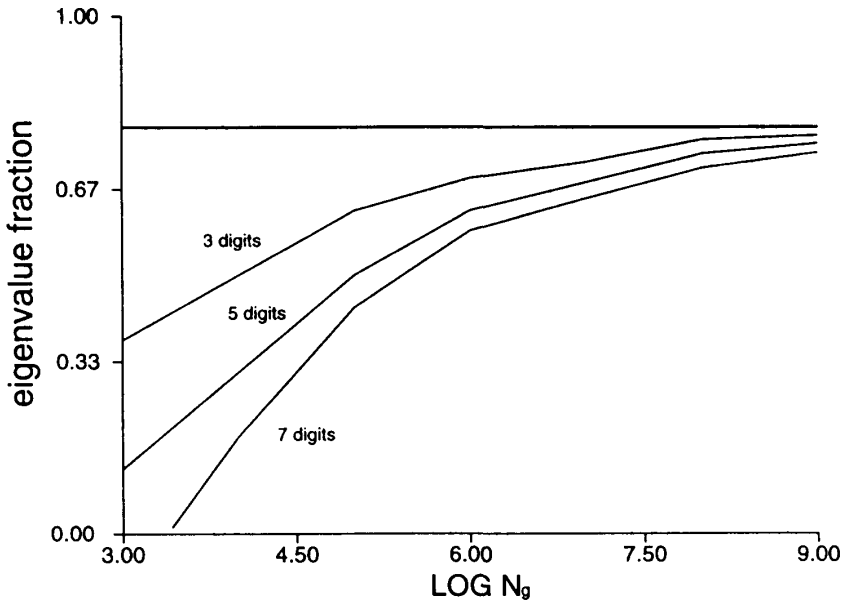

Figure 11 Sampling efficiency defined by the ratio of converged eigenvalues within a fixed number of digits to the number of sampling points, as a function of the logarithm of the number of sampling points. The heavy line represents the asymptotic value of $\pi/4$.

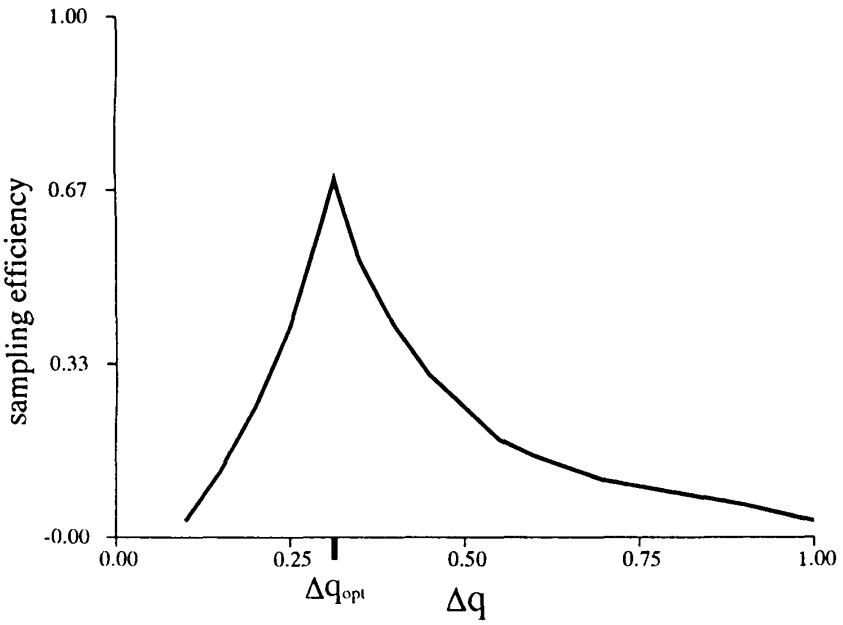

Figure 12 Sampling efficiency defined as the ratio of converged eigenvalues divided by N_g, for a fixed number of points (N_g = 64) as a function of the grid spacing Δq. The optimal sampling spacing is marked. At Δq_{opt} the sampling efficiency approaches $\pi/4$ at the cusp point Δq_{opt}.

Table 2 Convergence of the Finite Difference Representation for the Harmonic Oscillator

			Fourth-order FD		
N_g		8 points	16 points	32 points	64 points
Δq_{opt}	Exact	0.7	0.4	0.2	0.11
1	0.5	0.4825740879	0.49478668002	0.49860380104	0.499603845744
2	1.5	1.4317143539	1.47679543400	1.49594408176	1.498464505411
3	2.5	2.2214522909	2.41491682858	2.46274206266	2.490855167811
4	3.5	3.1888159106	3.43350682128	3.54493542145	3.511444750027
5	4.5	3.5308260773	4.10115403608	4.21270019153	4.381333406923
6	5.5	4.4614149311	5.56420368670	5.96798953995	5.712163111633
			Sixth-order FD		
N_g		8 points	16 points	32 points	64 points
Δq_{opt}	Exact	0.75	0.44	0.24	0.13
1	0.5	0.496832961	0.4996361441	0.4999643185	0.4999968936
2	1.5	1.485276212	1.4982057984	1.4998077039	1.4999837996
3	2.5	2.393088218	2.485823514	2.4985394570	2.4998518646
4	3.5	3.439160266	3.5084173131	3.5020862644	3.5004457190
5	4.5	3.920284648	4.3402199322	4.4695728153	4.4948505331
6	5.5		5.7031594608	5.5688982555	5.5178475240
7	6.5		6.0977450000	6.2657050814	6.4167645240

Table 1 and 2 reveal the slow convergence of the finite difference method compared to the Fourier method. Even for the sixth-order finite difference, the convergence is increased only one order of magnitude when the number of points is doubled. Also, the finite difference method uses a much smaller optimal grid spacing than the Fourier method: for $N_g = 64$, $\Delta q_{\text{opt}} = 0.313$ in the Fourier method compared to $\Delta q_{\text{opt}} = 0.11$ in the FD-4 method and $\Delta q_{\text{opt}} = 0.13$ in the FD-6 method. This means that the FD method has a much smaller sampling efficiency. These results are typical of the FD method. Moreover since grid methods are used in an iterative fashion these errors accumulate.

H. Mapped Fourier Methods

The global balancing of kinetic and potential energy was shown to be an important step in optimizing the calculation. However, even for the optimally balanced representation of the harmonic oscillator there is "air" between the rectangular "box" in phase space used by the Fourier method and the circular shape defined by the Hamiltonian. One can imagine cases where the phase space box has a more complicated shape. For example, it can be expected that the optimal sampling density of the Morse oscillator should be lower in regions of small classical kinetic energy (Fig. 13).

A solution to the balancing problem is to define a mapping transformation which correlates the position and momentum. This is achieved by transformation from the original set of coordinates q to a new set q', the curvilinear coordinate, both of dimension N:

$$\bar{q}_j = M_j(\{q_i\}, \alpha) \tag{54}$$

and the inverse transformation

$$q_j = M_j^{-1}(\{\bar{q}_i\}, \alpha) \tag{55}$$

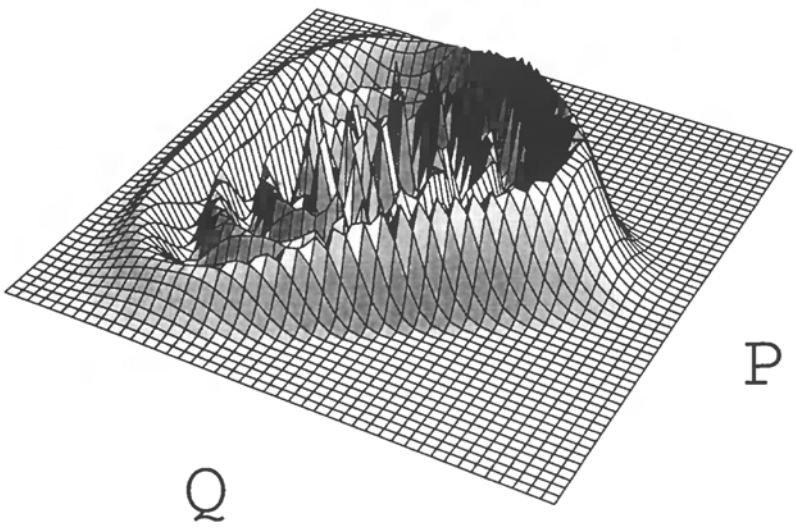

Figure 13 Phase-space representation of the $n = 8$ vibrational eigenstate of H_2. Notice that at the outer classical turning point, the momentum distribution becomes narrow due to the slowing down of the "particle" at the outer region of the potential. Notice the unused phase-space area for large p and q.

where α is a set of parameters defining the mapping function M. The result of this mapping is that a correlation is induced between the kinetic and potential operators.

The new curvilinear space is defined in terms of the Riemannian metric tensor (g_{ij}) (we use here the summation over repeated indices convention):

$$g_{ij} = \frac{\partial_q^k}{\partial \bar{q}^i} \frac{\partial q^k}{\partial \bar{q}^j} \tag{56}$$

The operator of Laplacian is

$$\nabla^2 = J^{-1} \frac{\partial}{\partial \bar{q}^j} \left(J g^{jk} \frac{\partial}{\partial \bar{q}^k} \right); \qquad J = \sqrt{|\det(g_{ij})|} \tag{57}$$

where g^{jk} is the jk matrix element of the metric tensor inverse matrix and J is the Jacobian of the transformation. The operator of integration is

$$\int \psi(\{q_i\}) \prod_{j=1}^{N} dq_j = \int \psi(\{\bar{q}_i\}) J \prod_{j=1}^{N} d\bar{q}_j \tag{58}$$

The result of this mapping is that a correlation is induced between the kinetic and potential operators. In the mapping procedure the kinetic energy operator is calculated by the chain rule:

$$\hat{\mathbf{T}} = -\frac{\hbar^2}{2m} \left(\frac{\partial M}{\partial q} \right) \frac{\partial}{\partial q'} \left(\frac{\partial M}{\partial q} \right) \frac{\partial}{\partial q'} = \frac{\hbar^2}{2m} \left(J^{-1} \frac{\partial}{\partial q'} \right)^2 \tag{59}$$

This kinetic energy operation can be implemented by a sequential evaluation of the first derivative multiplied by J^{-1}. The overall evaluation requires at least three Fourier transforms per operation compared to two Fourier transforms for the simple, rectilinear, Fourier method.

There are many examples of such mapping functions. For example, if

$$\theta = \cos^{-1}(q) \tag{60}$$

and

$$q = \cos(\theta) \tag{61}$$

then the Fourier method is transformed into a Chebychev pseudospectral representation (19). This representation which belongs to the class of orthogonal polynomial transformations is exceptional because the mapping of Eq. (61) has a fast transform implementation.

Another example is the mapping of the interval $-L/2 < q < L/2$ into itself (42):

$$q = M^{-1}(q', \alpha, \beta) = \frac{L}{2} D \left[\frac{q'}{L/2} - E\alpha \tan^{-1}\left(\frac{q'}{\alpha L/2} \right) \right] \tag{62}$$

where

$$D(\alpha, \beta) = \frac{1}{1 - (1 - \beta)\alpha \tan^{-1}(1/\alpha)} \tag{63}$$

$$E = 1 - \beta \tag{64}$$

where α and β are external parameters used to adjust the function to the problem. Figure 14 shows the mapping transformation used to enhance the sampling at the origin which is effective for a Coulombic problem.

The above mapping procedure was tested on the hydrogen atom eigenfunctions. In all cases the mapping procedure was able to enhance the convergence as is demonstrated in Fig. 15.

The mapping transformation is straightforwardly extendible to multidimensions (43). In variational calculations, for example in the finding of the ground state wave function, the optimal mapping parameters can be obtained variationally (44).

I. Non-Cartesian Grids

The concept of a functional space which contains a local representation of the kinetic energy operator can be carried beyond Cartesian coordinates. For example the kinetic energy operator in radial coordinates becomes

$$\frac{\mathbf{P}_r^2}{2m} = -\frac{\hbar^2}{2m}\left[\frac{1}{r^2}\frac{\partial}{\partial r}r^2\frac{\partial}{\partial r}\right] \tag{65}$$

In the Fourier method this kinetic energy operator is a special case of mapping as described in the Section III.H (42,45). An alternative method for the radial part is based on the fact that the Bessel function, $J_{1/2}(r)$ is an eigenfunction of the radial part of the Laplacian. This means that by using a Bessel transform, the radial part of the Laplacian becomes a local operator with the spectrum $-k^2$. This result can be generalized by using the transform with $J_{l+1/2}$. In this case a centrifugal part $k(l + 1)/r^2$, is included in the transformation (46,47).

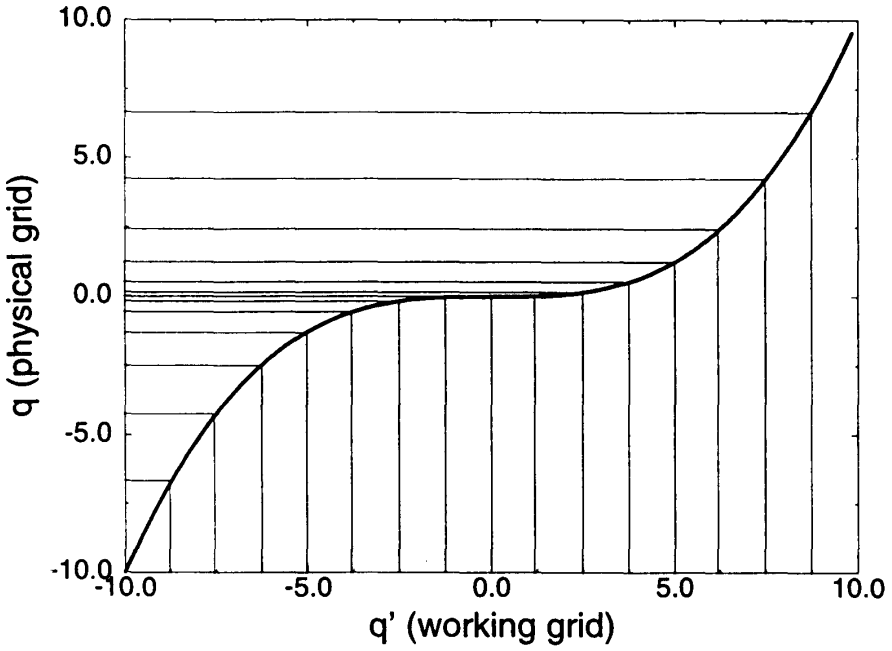

Figure 14 The mapping transformation: the relation between the physical grid and the working grid using the mapping function in Eq. (62) with parameters α = 0.00005, β = 9. Notice the congesting of sampling points near the origin which is appropriate for the Coulomb problems.

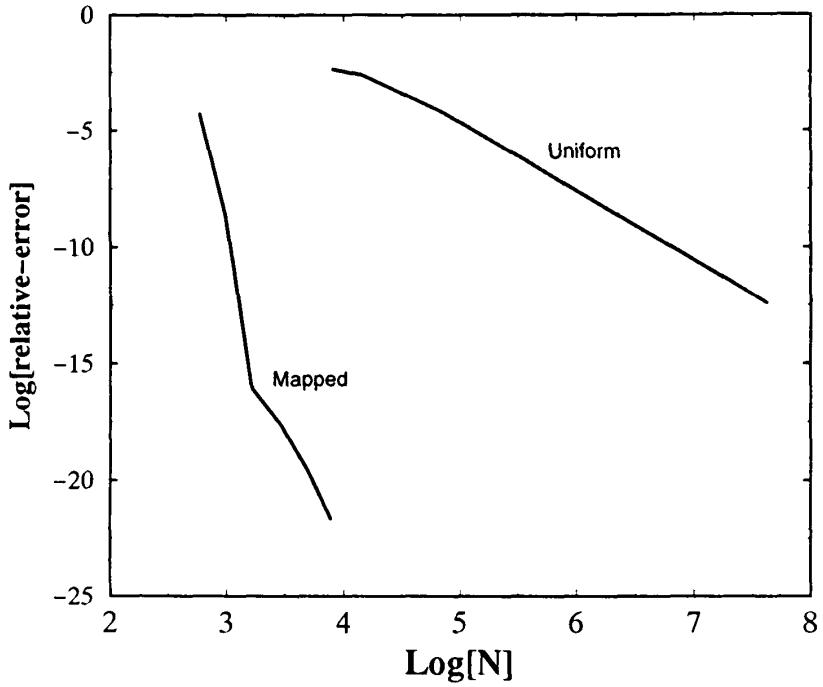

Figure 15 The convergence of the energy of the first excited state of hydrogen $\psi(r) = r^2 e^{-r/2}$, as a function of the number of grid points, N_g. It is clear that the mapped grid increases the sampling efficiency and therefore increases the energy accuracy by many orders of magnitude.

There are two approaches to this problem. The first, which is in the spirit of the DVR scheme, is to use the zeros of the Bessel function $J_\nu(r) = 0$ as collocation points. It has been shown by Lemoine (47) that this procedure leads to an almost unitary collocation transformation. The second approach is based on the fact that technically, fast Bessel transforms can be carried out by a change of variable. The transform becomes a convolution which is then carried out by means of a fast Fourier transform (48–50). The Fourier-Bessel transform of order ν is defined by

$$\hat{\psi}(k) = \int_0^\infty r\psi(r)J_\nu(kr)\,dr \tag{66}$$

for $k > 0$. The Bessel transform is its own inverse. Substituting $r = r_0 e^{-y}$ and $k = k_0 e^{x}$ in Eq. (66) and multiplying both sides by $e^{\alpha x}$ gives

$$e^{\alpha x}\hat{\psi}(k_0 e^{x}) = r_0^2 \int_{-\infty}^{\infty} e^{(\alpha-2)y}\psi(r_0 e^{-y})e^{\alpha(x-y)}j_\nu(r_0 k_0 e^{x-y})\,dy \tag{67}$$

The expression on the right-hand side is a convolution of the function $e^{(\alpha-2)y}\psi(r_0 e^{-y})$ and $r_0^2 e^{\alpha x}J_\nu(r_0 k_0 e^{x})$. The parameter α is arbitrary and therefore can be chosen to optimize the accuracy. The convolution theorem (51,24) states that the Fourier transform of the convolution of b and c, denoted $b * c$, equals the product of their Fourier transforms. Hence $b * c$ can be computed by performing an FFT on b and c, multiplying the results, and performing an inverse FFT. The use of the Fourier-Bessel transform can be viewed as a logarithmic mapping function on the coordinates r. Numerical tests show (47) that the

grid based on the zeros of the Bessel function has improved sampling efficiency over the mapping convolution transformation.

J. Symmetry Adopted Grids

An obvious solution to minimize the number of grid points N_g is to introduce symmetry. Consider for example an inversion point such as the point $x = 0$ in the harmonic oscillator. The eigenfunctions can be classified as being either even or odd with respect to parity: $\psi(q) = \pm\psi(-q)$. If one restricts the calculation to one class of functions the computational effort can be reduced by a factor of 2 by using a fast cosine transform for even functions and a fast sine transform for odd functions (52). The same symmetry considerations should work for other types of grids.

Translational symmetry of the type $\hat{\mathbf{V}}(q + nL) = \hat{\mathbf{V}}(q)$ can also be exploited. The symmetry of the potential is reflected in selection rules imposed on the momentum change. A typical example can be found in atom scattering from a crystal surface. In this case the selection rule $\Delta k = \pm n\pi/L$ is imposed. By matching the grid to the unit cell and employing the periodic boundary conditions of the Fourier representation, the selection rules are automatically fulfilled. In more than one dimension the matching of the grid to the unit cell might require a skewed grid representation. As will be seen in Section IV.C, the skewed grid has more efficient sampling. Other types of symmetry can be considered by working out the selection rules on Δk. Then the kinetic energy operator can be evaluated by shifting the spectrum in k space using Eq. (47). The details can be found in Ref. 53.

IV. MULTIDIMENSIONAL GRIDS

A. Direct Product Grids

A straightforward approach to constructing a multidimensional representation is to assemble it directly from a direct product of one-dimensional representations. On a grid this means that the position vector $\mathbf{q}$ becomes $q_{ijk\ldots} = \{q_i^1, q_j^2, q_k^3, \ldots\}$ where q_l^n is the nth one-dimensional position pointer. Such a construction has the advantage that each degree of freedom is independent thus allowing each individual representation to be optimized. Naturally, the optimization leads to different types of grids for each degree of freedom. For example, in circular coordinates, a possible choice is an evenly spaced grid in the angle ϕ and a grid in the radial coordinate r (Fig. 16).

A more elaborate example of a multidimensional representation is the grid construction in molecular surface scattering (54–59). It is constructed from a three-dimensional Fourier grid for the translational $\{x, y, z\}$ coordinates and a spectral expansion using spherical harmonics for the angular coordinates θ and ϕ and a DVR type grid for r. The translational grid spacing in the x and y coordinates is matched to the unit cell of the crystal surface (Fig. 17). Since the propagation is carried out in the global time-energy phase space, it imposes a common energy cutoff on all the individual degrees of freedom; otherwise the representation is not balanced.

The advantage of the direct product construction is the flexibility in adopting the representation to each specific degree of freedom. The drawbacks of the direct product construction are obvious. The energy range becomes N times larger for N degrees of freedom. Moreover there is more chance for empty sampling space. For example, in the $H_2 + H$ encounter once the energy band is restricted there are regions in coordinate space

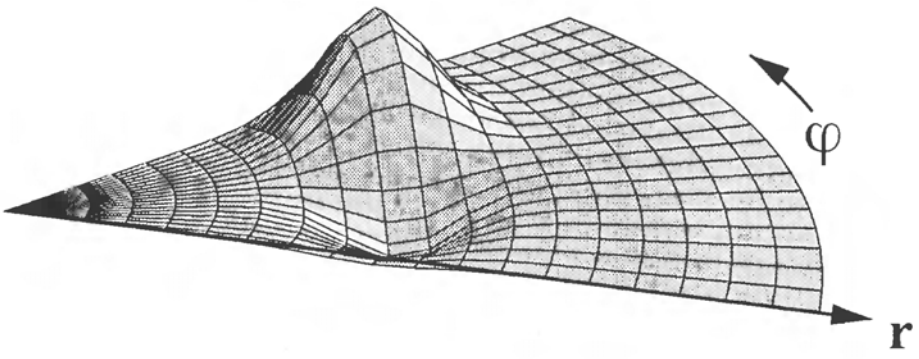

Figure 16 A direct product representation in r and ϕ coordinates of a wave function representing a collinear encounter in hyperspherical coordinates.

which are well into the classical forbidden region where the wave packet amplitude is negligible. Figure 18 shows a rectangular grid for H_2 + H encounter superimposed on the potential. This situation becomes more acute in higher dimensions.

B. Simple Correlated Grids

Representation methods are designed for wave packets. It is therefore safe to assume that the wave packet decays exponentially when entering the classical forbidden region of phase space. In the position picture, grid correlation can be obtained by eliminating grid points which are above a certain potential energy cutoff value (60). The retained points below an energy cutoff are marked in Fig. 18. In many cases this procedure can reduce the number of grid points significantly but the price will be a complicated grid topology. A compromise which allows the use of the FFT algorithm is to decompose the grid into rectangular boxes. Such a construction is represented in Fig. 18 by a thick dashed line. The values of the points between the energy restricting contour and the grid boundary can be replaced by zero, thus maintaining the ability to use the FFT algorithm while

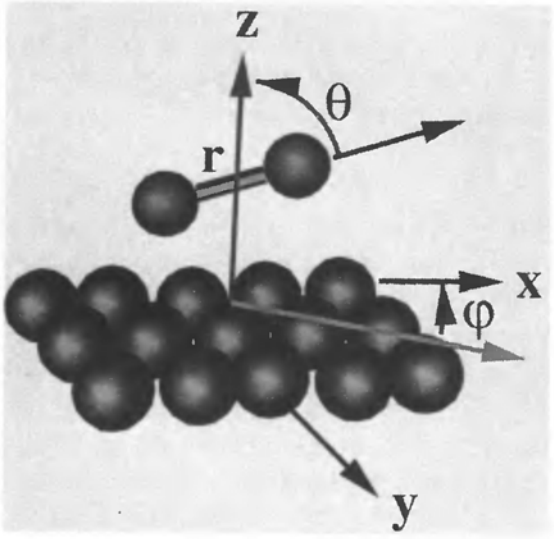

Figure 17 The grid and coordinate setup for a molecular surface scattering encounter. A Fourier grid is used for the x, y, z coordinates and a spectral expansion for the θ, ϕ coordinates.

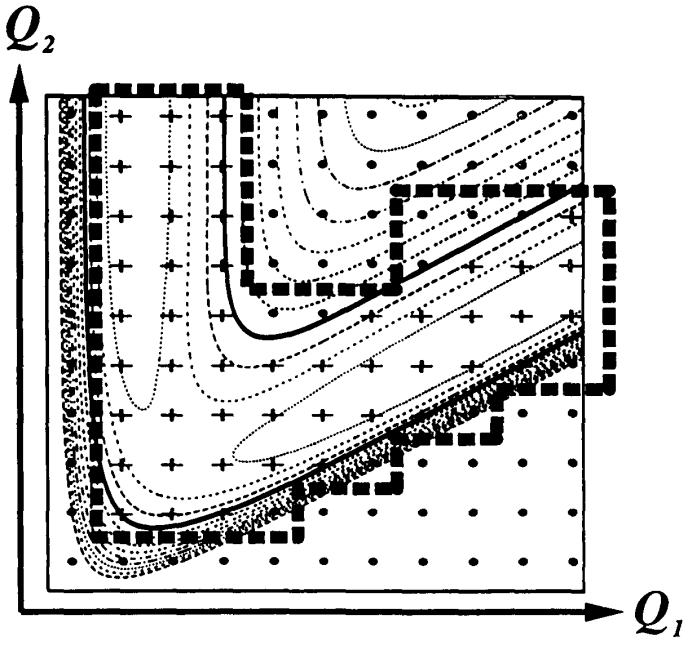

Figure 18 A two-dimensional rectangular grid for the collinear H_2 + H encounter in mass-scaled Jacobi coordinates superimposed on the potential. The thick contour line represents the potential energy cutoff. The grid points represented by + signs have potential energy less than the cutoff value. The gray grid points are in the forbidden region where the internuclear distance r_2 is negative. The dashed line represents the border of a rectangular correlated grid. The number of grid points correlated by a cutoff energy is 44% of the total number N_g and the number of correlated rectangular grid points is 53% of the total number.

minimizing the energy range. The first application of grid methods to reactive scattering (7) eliminated part of the high-energy three-body dissociation region by constructing an **L** shaped grid.

A more involved situation is found in curvilinear coordinates. For example, in circular coordinates the angular kinetic energy term $\mathbf{T} = (1/2mr^2)(\partial^2/\partial\phi^2)$ correlates the angular kinetic energy with the radial coordinate r (Fig. 19).

The above observation suggests imposing an energy cutoff on the angular momentum. As a consequence, as r approaches the origin, the number of expansion functions becomes smaller than the number of grid points in ϕ.

Grid constructions in which the number of grid points is unbalanced with the number of expansion functions is common in situations where a high degree of correlation is needed. As described above, grid points are eliminated which are deep in classically forbidden regions. This amounts to replacing the value of the wave function at these points by zero. These considerations can be applied to the momentum space, leading to the elimination of expansion functions which are above the energy cutoff, i.e., are in the classical forbidden region in momentum space. The result is a highly correlated grid. If the points and functions are related by a quadrature rule the elimination of points or functions causes no problem in principle since the transformation from the point to the functional representation is still unitary.

If the functional base is already correlated, i.e., not a direct product type, a more complicated grid construction results. An important example is the $Y_{lm}(\theta, \phi)$ functional

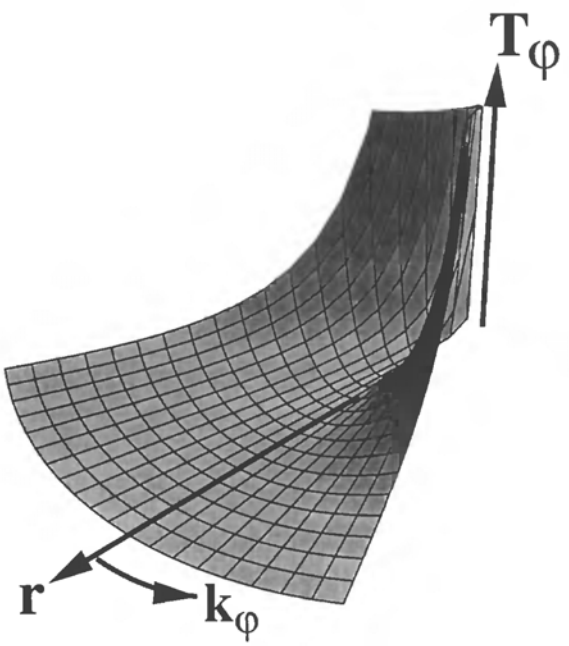

Figure 19 The kinetic energy operator $T_\phi = \hbar^2 k_\phi^2 / 2mr^2$ in angular momentum space as a function of r and k_ϕ for hyperspherical coordinates. Notice that the energy cutoff is a function of both variables.

representation in spherical coordinates where the θ expansion function is correlated with ϕ through the angular momentum projection m (61). Corey and Lemoine (62,35) have suggested use of a direct product grid in θ and ϕ where the grid points in θ are Gaussian quadrature points of Legendre polynomials of degree j_{max}. These points are able to integrate exactly the associate Legendre polynomials of order less than $2j_{max} + 1$. In such a construction there are more grid points than expansion functions, but due to the quadrature rule, there is no ambiguity in the transformation from grid points to functions and back.

The adiabatic pseudospectral method (63–65) is also based on a similar approach. First a direct product grid is constructed. Then by adiabatic reduction, the spectral functional expansion is reduced by correlating in a hierarchical form each degree of freedom successively. As a result, the number of grid points becomes larger than the number of functions. To relate the two representations, a least square procedure (18) is employed to transform from the grid to the functional representation. The result is a correlated representation which can be used to further optimize the representation by eliminating grid points which are deep in the classical forbidden region. In the next section it will be shown that a non-direct direct-product grid is able to enhance the sampling significantly.

C. The Fourier Method in Many Dimensions

For more general problems, it has been observed that the direct product representation, which for the Fourier method implies a representation by an equally spaced Cartesian grid, is not optimal. A careful analysis of the Fourier method leads to the observation that this direct product grid is not isotropic in momentum space, so that different directions have different sampling intervals. A faithful representation of a multidimensional

function by the Fourier method means that the function is band limited. The symmetric construction of the coordinate and momentum representation means that the description of the function is also periodic in momentum space. The representation therefore can be viewed as an infinite number of replicas of the original **k** space picture extending in all directions. The band-limited property of the original functions means that these replica do not overlap. If a priori there is no preferable direction in space then a cutoff in momentum can be represented as a sphere with radius p_{max}. A Cartesian grid in coordinate space is also Cartesian in momentum space. Therefore, the nonoverlapping role can be envisioned as packing spheres so that they touch their neighbors at $2D$ points for D dimensions. It is clear that the best sampled direction is along the diagonal, but for an isotropic problem the volume between the spheres becomes wasted sampling volume.

Although a completely isotropic grid is not possible, the sampling positions can be chosen to construct the optimum isotropic grid in momentum space. From the previous description it can be concluded that the optimal sampling points are equivalent to the centers of multidimensional densely packed hard spheres. (The problem of the optimal packing of hard spheres has been solved up to 23 dimensions (66).) The free volume between the spheres is wasted sampling volume. The sampling efficiency can be defined as the ratio of the volume of the space-filling spheres to the volume of the total space. Figure 20 illustrates the situation in three dimensions.

The Cartesian grid reaches a sampling efficiency of $\pi/4 \approx 79\%$, the ratio of the area of a disk to a square. Skewing the grid increases the sampling efficiency to $\pi/2\sqrt{3} \approx 91\%$ the ratio of a disk to a hexagon. In many dimensions, the limit of one sampling point per unit volume is not obtainable even for optimal packing. Table 3 compares the sampling efficiency of a cubic grid with the optimal grid as a function of dimension.

It can be deduced from Fig. 21 that the importance of optimal sampling increases with dimensionality. For calculations beyond three dimensions, optimal sampling becomes extremely important. For example, for six dimensions, 2.7 sampling points are needed per unit volume, compared to 12.4 points in the Cartesian cubic lattice. Nevertheless even the optimal sampling efficiency decreases with dimensionality. This fact poses an intrinsic limitation to the Fourier method for multidimensional calculations.

In a rectangular set of multidimensional coordinates, the kinetic energy operator is separable,

$$\hat{\mathbf{T}} = \frac{\hbar^2}{2m} \sum_{i=1}^{D} \mathbf{K}_i^2 \tag{68}$$

where $\mathbf{K}_i$ is the vector of k values in the spatial dimension i. In the case of the optimal packing or in other skewed sets of coordinates, the kinetic energy operator becomes

$$\frac{\hat{\mathbf{P}}^2}{2m} = \frac{\hbar^2}{2m} \mathbf{K}^{\dagger} \cdot \mathbf{G} \cdot \mathbf{K} \tag{69}$$

where $\mathbf{K}$ is the vector of k values for each spatial direction and $\mathbf{G}$ a positive definite matrix connecting spatial direction i with direction j. The $\mathbf{G}$ matrix can be calculated by using the knowledge of the coordinates of the centers of the optimally packed spheres (67). This correlated grid appears naturally in atom surface scattering where the grid is matched to the unit cell. It leads to the correlated kinetic energy term: $\hat{\mathbf{T}}_{xy} = (\hbar^2/2m)(k_x^2 + k_y^2 + k_x k_y \sin\theta)$. The method can be extended to molecular surface scattering with

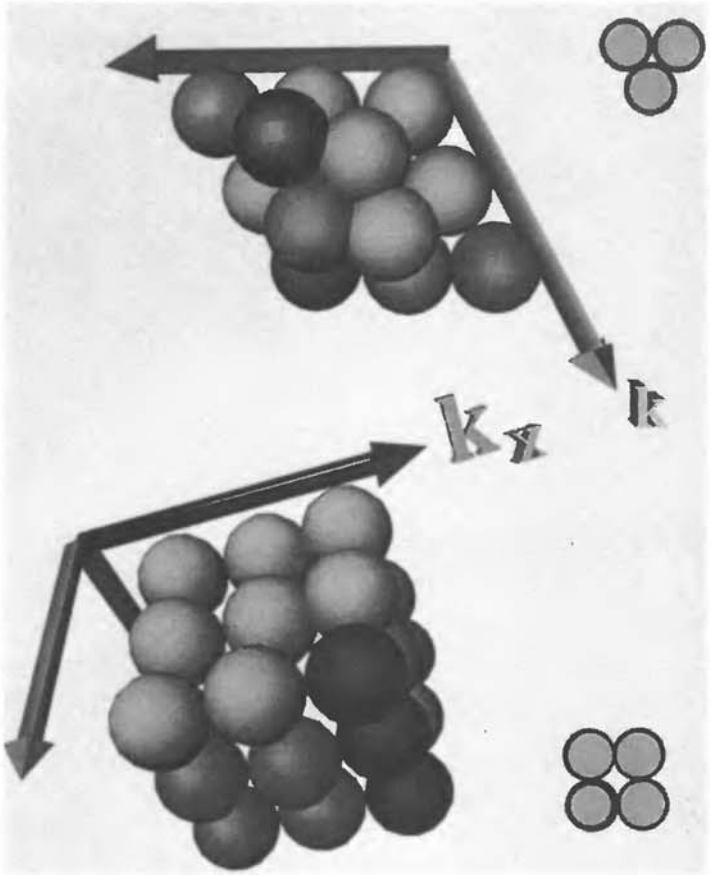

Figure 20 Schematic view of the k spectrum sampled on a three-dimensional cubic grid (bottom) and on a skewed grid (top). The Fourier transform of a function f is contained in the sphere p_0. Sampling the function f on a discrete grid produces copies of $\hat{f}(K)$, each containing a sphere with radius K_{max}. These spheres should be distinct for optimal sampling.

Table 3 Isotropic Sampling Efficiency

Dimension	Maximum efficiency η_{max} (%)	Cubic lattice η_{cub} (%)	Improvement factor η_{max}/η_{cub}
1	100.0	100.0	1.0
2	90.6	78.5	1.15
3	74.0	52.4	1.4
4	61.7	30.8	2.0
5	46.5	16.45	2.8
6	37.3	8.07	4.6
7	29.57	3.69	8.0
8	8.07	0.505	16.0

Source: From Ref. 66.

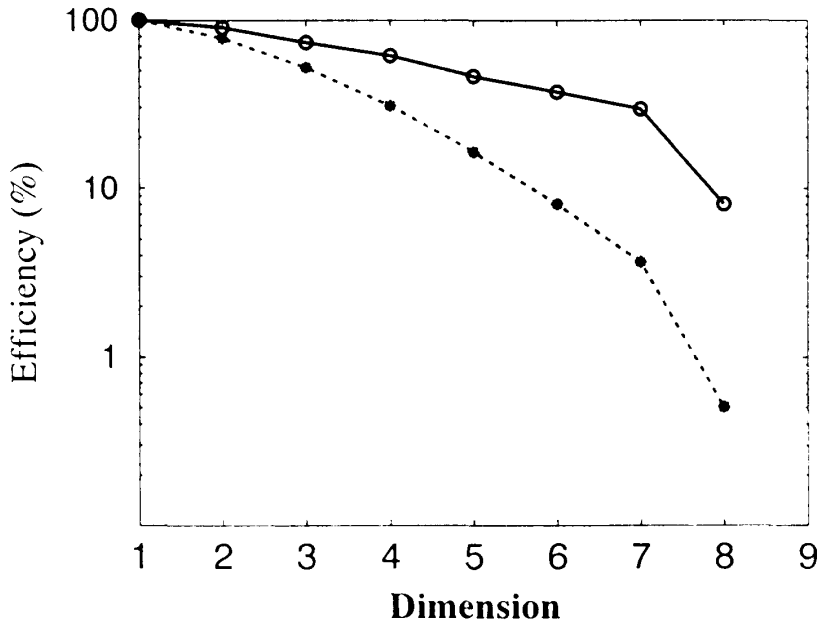

Figure 21 Comparison of sampling efficiency of a cubic to a skewed grid as a function of dimension. The stars represent the cubic grid, the open circles the skewed grid.

arbitrary angles of incidence by applying a phase shift (68). Additional correlation is possible by eliminating momentum values which are higher than an energy cutoff in Eq. (69) in the same spirit of eliminating grid points which are above a potential energy cutoff in coordinate space (59).

D. Computational Considerations

Summarizing the different approaches to grid construction, it should be emphasized that the purpose of the grid representation is to supply an effective algorithm for calculating the mapping induced by the Hamiltonian operator: $\phi = \mathbf{H}\psi$. The effectiveness of the algorithm can be judged by the operation count, i.e., by the number of floating point operations required to carry out the mapping. The most extreme case is when the Hamiltonian is represented as a full matrix. In this case the operation count scales as $O(N_g^2)$. For large multidimensional problems, this scaling relation becomes prohibitively expensive. This is in contrast to the mapping induced by the potential energy which in a grid coordinate representation is local and therefore scales linearly with N_g as $O(N_g)$. The bottleneck of computation can be identified in the kinetic energy operation. At this point one should distinguish between one- and multidimensional considerations.

1. One-Dimensional Kinetic Energy Scaling

In the general collocation representation, the kinetic energy operator Eq. (38) is a full matrix and therefore the mapping induced by it scales as $O(N_g^2)$. In the other extreme are the finite difference methods which are constructed from banded matrices and therefore scale linearly as $O(N_g)$. The linear scaling relation is at the expense of accuracy. In the Fourier method, due to the FFT algorithm, the scaling is semilinear with N_g, $O(N_g \log N_g)$ with no price in accuracy. One can view the algorithm as an efficient means of performing the unitary transformation from coordinate to momentum space. An alter-

native to the FFT algorithm is to define directly the kinetic energy operator in coordinate space

$$\hat{\mathbf{T}}(\mathbf{x}) = \mathbf{Z}^{-1}\hat{\mathbf{T}}(\mathbf{k})\mathbf{Z} \tag{70}$$

where $\mathbf{Z}_{jk} = \langle x_j|k\rangle = 1/\sqrt{2\pi}e^{ikxj}$ is the coordinate to momentum unitary transformation. The drawback to the use of Eq. (70) is that it is a full matrix operator scaling as $O(N_g^2)$. Since the FFT algorithm has an overhead of a factor of 3 to 5, there is a turnover appearing between $N_{g\text{crit}} = 32$ to $N_{g\text{crit}} = 96$ so that for $N_g < N_{g\text{crit}}$ a direct transform becomes more efficient than the FFT algorithm. This finding is very sensitive to the particular computer architecture in use (59). For example, very efficient FFT routines are available on vector and parallel computer architecture (69). The superior scaling of the Fourier method has been the motivation for searching for other fast transforms to perform the kinetic energy operator (46). Since in most of the present applications N_g is rather small, the usefulness of these transforms is marginal considering the added complications involved.

One of the recurring problems in using the Fourier method is the periodic boundary conditions. In some cases, such as scattering from a crystal surface, these boundary conditions match the physical problem. When a bound state problem is considered, the wave function at the boundary should be zero. Effectively such a condition is approximated by forcing the wave function at the boundary of the grid to be deep in the classical forbidden region. The amplitude of the wave function at the boundary can thus be made exponentially small. Practically this means devoting some sampling points to the classically forbidden region. The extent of this region can be estimated from the semiclassical tunneling formula

$$\psi(L) \approx \exp\left(-\frac{1}{\hbar}\int_{l}^{L}\sqrt{2\mu(V(x) - E)}\,dx\right) \tag{71}$$

where the buffer region extends from l to L with E as a typical energy. These boundary conditions fit the view of a wave packet which becomes exponentially close to a band-limited function with finite support. Absorbing boundary conditions are also extremely important (70–78). Like the bound state boundary conditions they reduce to zero the amplitude of the wave function at the end of the grid.

Another related method to reduce the grid requirement is based on the superposition principle. The wave function and the propagation are split between two overlapping grids (79). This method allows the separation of the asymptotic dynamics from the interaction part. Care must be taken that the transmission of amplitude from one grid to the other is gradual in space to avoid numerical problems of overflowing phase space by a sharp transmission function.

2. Multidimensional Kinetic Energy Scaling

When a direct product multidimensional grid is constructed from D one-dimensional grids: $N_g = N_1 \otimes N_2 \otimes N_3 \otimes \cdots \otimes N_D$. If the individual one-dimensional kinetic energy operation scales as $O(N_l^\alpha)$, then the total number of operations to calculate this term on all grid points becomes $N_g/N_l O(N_l^\alpha) = N_g O(N_l^{\alpha-1})$. Since the total kinetic energy operator is the sum of kinetic energy operators on each degree of freedom, the total operation count will scale linearly with the total number of grid points $O(DN_g)$. These considerations still hold for the multidimensional skewed Fourier grid and for the adiabatically

correlated grid (63). The consequence is that high-dimensional problems scale semilinearly according to the number of grid points, with small dependence on the one-dimensional scaling of the kinetic energy operator. It then becomes more important to reduce the total number of grid points than to optimize the 1D operation (60,63).

One of the methods to minimize the number of grid points is to use an adaptive grid, a grid which changes as the calculation progresses. For example, in a reactive scattering calculation for the initial state representation it is sufficient to include only the entrance channel. When the wave packet evolves to sample more of the grid then the reactive channel is included. Adaptive grids are useful also in momentum space. Consider as an example a Coulomb explosion event or any sudden change from an attractive to a repulsive potential energy surface. As time proceeds the wave packet accelerates and the momentum is shifted to higher values. Examining Figure 22, it becomes clear that a grid that follows the wave function both in coordinate space and in momentum space will reduce the number of grid points by at least a factor of 15, which is the effective area ratio of the support of the wave packet in phase space in relation to the total represented area required for the full dynamical encounter.

Optimal positioning of the wave function becomes possible provided there is an interpolation scheme which allows a grid-to-grid transfer of the wave function. The collocation method in general and the Fourier method in particular are capable of extremely accurate and efficient interpolation aside from their intrinsic advantage in the representation of nonlocal operators. An extreme case of a continuously adaptive grid is provided in the interaction picture (80–85). This representation continuously shifts the grid and therefore significantly reduces its size. The price paid is that the Hamiltonian of the problem becomes explicitly time dependent which complicates the propagation procedure.

V. PROPAGATION SCHEMES

The limelight now shifts to the time-energy phase space. A detailed description is beyond the scope of the present chapter has been recently reviewed (15). The present focus will therefore be on the interrelations between the position-momentum phase space representation and the propagator representing operators in the time-energy phase space.

Propagation methods have in common the recursive application of an elementary mapping step which for the Hamiltonian operator, becomes

$$\phi = \hat{\mathbf{H}}\psi \tag{72}$$

Since grid methods supply a very direct means to perform this mapping, the development of propagation schemes has been closely related to the development of grid methods. The propagation schemes supplement the elementary mapping by the additional operation of two vectors $\phi_3 = \phi_1 + \phi_2$. This means that the propagator scheme becomes an effective agent to calculate recursively the mapping of a polynomial on an initial wave function:

$$\phi_N = \mathcal{P}_N(\hat{\mathbf{H}})\psi \tag{73}$$

where $\mathcal{P}_N$ is a polynomial of degree N. On this basis, propagation methods can approximate the mapping of any analytic function $f(z)$ of an operator under study on a wave function $\phi = f(\hat{\mathbf{H}})\psi$. With these concepts in mind, propagation techniques can be classified according to the function $f(z)$ which is approximated. For example, the evolution

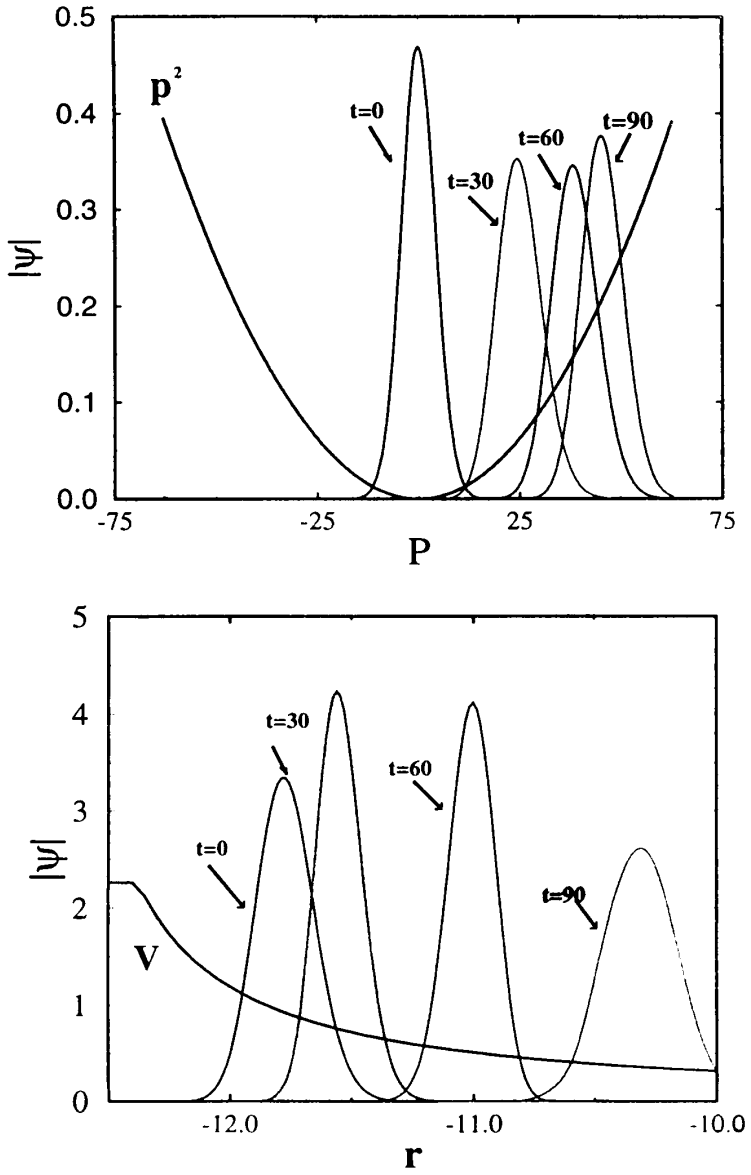

Figure 22 Wave packet propagation in a Coulomb experiment simulation of the process $D_2 \rightarrow 2D^+$. (Lower panel) Absolute value of the wave function in position space superimposed on the repulsive Coulomb potential. The wave functions are labeled by the elapsed time from the ionization in atomic units. (Upper panel) Absolute value of the wave function in momentum space superimposed on the kinetic energy term P^2. Since the wave function is compact an adaptive grid which will follow the wave packet in position and momentum space can reduce the number of grid points significantly.

operator $\hat{\mathbf{U}}(t) = \exp(-i/\hbar\hat{\mathbf{H}}t)$ is represented by the function e^{-izt}. Table 4 summarizes the classification according to the function $f(z)$. For more details see Ref. 15.

Propagation schemes can also be classified by the type of polynomial used to carry out the approximation. Four families of polynomials have been used in conjunction with grid methods. Table 5 summarizes these.

The diversity of these schemes means that when an effective grid representation is chosen a propagation scheme can be selected which will enable to calculate any observ-

Table 4 Common Functions in Propagation Schemes

	$f(z)$	Use	Reference
1	e^{-izt}	Evolution operator $\hat{U}(t)$	14,86
	$\cos(zt)$, $\sin(zt)$		87
2	$e^{-z\tau}$	Relaxation, diffusion	88,89
3	$e^{-(z-\alpha)^2\tau}$	Filtering	90,91
	$\int_0^I e^{-izt} g(t)\,dt$	Filter diagonalization	92,93
4	$\frac{i}{2\pi}\frac{1}{E-z}$	Raman spectra	94
	$\int_0^\infty e^{iEt} e^{-izt}\,dt$	Green's function	95,96,60,97
5	$\delta(z-E)$	Correlation functions	98,99
		Absorption spectra	100
	$\int_{-\infty}^{\infty} e^{iEt} e^{-izt}\,dt$	Spectral density	101

able of interest in a dynamical molecular encounter. This concludes the task of comparing simulation with experiment. In the next section, the relation of these propagation methods to a grid in the time-energy phase space will be investigated.

A. Time-Energy Grids

The description of the molecular encounter in the time-energy phase space is distinct from that in the position-momentum phase space. The first is an initial value problem while the latter is a boundary value problem. This distinction means that while in the position-momentum phase space the grid supplies a means of interpolation between the points. In contrast, in the time-energy phase space the grid is used for extrapolation. The point is illustrated by comparing the second-order differencing (SOD) time propagation scheme (8) to the finite difference (FD) scheme. The central differencing formula is used in both cases. In the second-order FD method the derivatives are calculated at a point q_j by interpolating between the two neighboring points; $\partial\psi_j/\partial q \approx (\psi_{j+1} - \psi_{j-1})/2\Delta q$. In the SOD scheme the central differencing formula is used to extrapolate to a new point in time: $\psi_{n+1} \approx \psi_{n-1} + 2\Delta t\,(\partial\psi/\partial t)$.

Table 5 Classification of Polynomials

	$\mathcal{P}_N$	Scheme	Recursion formula	Reference
1	Taylor		$\phi_n = \hat{\mathbf{H}}\phi_{n-1}$	102
	SOD		$\psi_{n+1} = \psi_{n-1} - i2\Delta t\hat{\mathbf{H}}\psi_n$	8
2	Chebychev	Spectral	$\phi_{n+1} = 2\hat{\mathbf{H}}\phi_n - \phi_{n-1}$	14
	Legendre		$(n+1)\phi_{n+1} = (2n+1)\hat{\mathbf{H}}\phi_n - n\phi_{n-1}$	96
3	Newton	Pseudospectral	$\phi_{n+1} = (\hat{\mathbf{H}} - x_n\hat{\mathrm{I}})\phi_n$	103,15,97
4	Lanczos	Krylov	$\hat{\mathbf{H}}\phi_n = \beta_{n-1}\phi_{n-1} + \alpha_n\phi_n + \beta_n\phi_{n+1}$	104–107
	Residum	$\phi_n = \hat{\mathbf{H}}^n\psi$		108–110

The drawback of any extrapolation scheme in the time domain is that errors accumulate during the propagation. By changing the primary perspective to the energy domain an interpolation in the energy spectrum can replace the extrapolation, leading to superior convergence properties. Most of the high-quality propagation schemes exploit this property. They use a spectral functional expansion in the energy variable to approximate the propagator. For example the Chebychev propagation scheme is a spectral expansion in the energy domain (15).

A representation in the energy variable can also be based on a grid construction. The Newtonian propagation methods (103,111,15) are based on such a concept. The primary interpolation grid is constructed in the energy eigenvalue domain. For example, the grid points can be chosen as the zeros of the Chebychev polynomial. This requires renormalization of the Hamiltonian so that its eigenvalues will be contained in the interpolated region (15). The grid points can also be extended into the complex plane in order to interpolate problems with complex eigenvalues (103,112,113).

Figure 23 shows an evolving wave packet on the coordinate-time grid (q, t). Due to the slight unharmonicity of the potential used, the initially compact wave packet dispersed, which means that for long enough time the wave functions fills uniformly all the available coordinate space. Two methods of propagation are compared. In the left panels

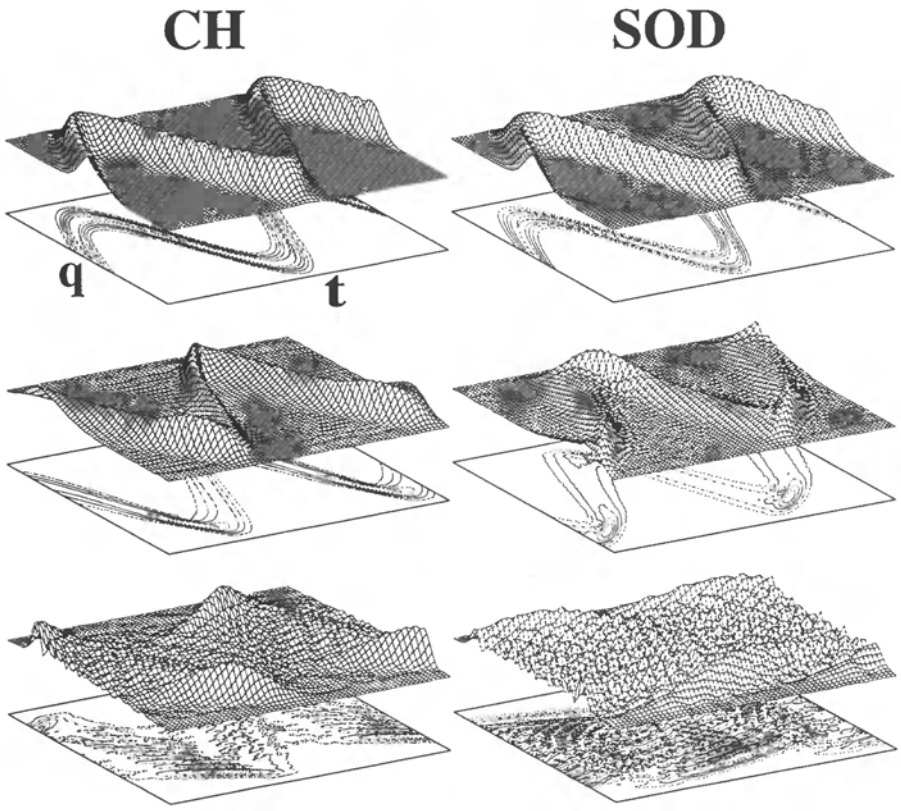

Figure 23 The evolution of an unharmonic oscillator on a position-time grid (q, t). The potential is $V(q) = q^2/2 - 2|q|/5$. Comparison between the evolution generated by the Chebychev (left) and SOD (right) propagation schemes. The interpolation grid consists of 32 Chebychev points with a time step $\Delta t = 0.05$. The propagation by the SOD scheme required the same numerical effort. The upper panel represents the first two cycles. The middle panels show the evolution after 10 cycles, and the lower panels shows the evolution after 50 cycles.

the propagation was carried out by interpolation (CH) in the energy domain while in the right panel by extrapolation (SOD). The upper panels represent the first two cycles of the oscillator wave function.

The first two cycles look quite similar although careful comparison shows that in the SOD scheme numerical dispersion appears already at this early stage. This can be seen as low-amplitude signals between the waves. After approximately 10 cycles, further degradation appears in the SOD scheme: the phase of the main oscillation lags behind and the shape of the packet deteriorates. After approximately 50 cycles, the SOD scheme has lost the majority of the phase coherence. The interpolation scheme for the same conditions is converted to eight-digit accuracy. It is important to point out that the SOD scheme preserves norm and energy to eight digits as well. This is an important observation common to many short time propagation schemes that the phase coherence is lost due to numerical dispersion much before the norm and energy show any significant error.

The number of grid points required to represent the time-energy phase space directly determines the cost of the calculation. In the SOD scheme a stability analysis (94) determines the maximum time step as $\Delta t_{\max} \leq \hbar/|E_{\max}|$, where $|E_{\max}|$ is the largest eigenvalue of the Hamiltonian $\hat{\mathbf{H}}$ represented on the spatial grid. This inequality translates to the minimum number of grid points in the time-energy phase space $N_t > \Delta E \cdot t_s/\hbar$, where ΔE is the range of eigenvalues of the Hamiltonian and t_s the total simulated time. The same minimum number of grid points in energy is found in a Chebychev-based Newtonian energy grid $N_t > \Delta E \cdot t_s/2\hbar$. The methods differ completely in their convergence rate. Another difference is that in an energy interpolation scheme evaluation of the wave function at all the intermediate time steps is carried out simultaneously as well as backward propagation.

The above result, which is a consequence of the time-energy uncertainty principle, can be generalized to all propagation schemes. The size of the time step or the order of the interpolation polynomial is directly proportional to the volume of the time-energy phase space. This observation reflects back to the grid construction in coordinate space. The energy range for optimal computational efficiency requires balancing and minimizing the energy range of each of the grid representations of the individual degrees of freedom.

B. Propagators for Explicitly Time-Dependent Operators

In many physical applications the Hamiltonian is explicitly time dependent. The common solution for propagation in these explicitly time-dependent problems is to use very small grid spacing in time, such that within each time step the Hamiltonian $\hat{\mathbf{H}}(t)$ is almost stationary. Under these semistationary conditions a short-time propagation method in the time-energy phase space is employed. The drawback of this solution is that it is based on extrapolation; therefore the errors accumulate. Moreover, time ordering errors add with the usual numerical dispersion errors (108).

A global solution to the error accumulation problem is obtained by embedding in the time-energy phase space of the system in a larger phase space where interpolation in the energy domain becomes possible (111,114). The first step is to add a grid in a new coordinate t'. The relation between the embedded wave function and the usual one subject to an initial state $\Psi(x, 0)$ is defined as

$$\Psi(x, t) = \int_{-\infty}^{\infty} dt' \, \delta(t' - t)\Phi(x, t', t) \tag{74}$$

where t' acts like an additional coordinate in the generalized Hilbert space (111) and $\Phi(x\ t', t)$ is the solution of the time dependent Schrödinger equation represented by the (t, t') formalism

$$i\hbar \frac{\partial}{\partial t} \Phi(x, t', t) = \mathcal{H}(x\ t')\Phi(x, t', t) \tag{75}$$

The $\mathcal{H}(x, t')$ operator is defined for a general time-dependent Hamiltonian by

$$\mathcal{H}(x, t') = H(x\ t') - i\hbar \frac{\partial}{\partial t'} \tag{76}$$

A simple proof has been derived by Peskin and Moiseyev (115). Since $\mathcal{H}(x, t')$ is time (i.e., t) independent, a time-dependent solution of Eq. (75) is given formally by

$$\Phi(x, t', t) = \hat{U}(x, t', t)\Psi(x, t_0) \qquad \text{where} \qquad \hat{U}(x, t', t) = e^{-i/\hbar \mathcal{H}(x,t')t} \tag{77}$$

Equation (77) is solved by constructing a grid in the eigenspace domain of $\mathcal{H}$ (113) or by a spectral expansion in the energy domain (114). Figure 24 shows such a solution for a system subject to a short pulse. The first-derivative term $-i\hbar(\partial/\partial t)$ in Eq. (76) is responsible for a unidirectional propagation of events. An excitation located at time t' only influences the wave function after $t > t'$.

The hierarchcy of grids required to represent faithfully an explicitly time-dependent problem is as follows: a grid in the coordinate q to represent the $\{p, q\}$ phase space, a grid in the t' coordinate to represent the $\{E, t'\}$ phase space, and a grid in $\mathcal{E}$ allowing propagation in the $\{\mathcal{E}, t\}$ phase space.

VI. SUMMARY

Grid methods are at their best when they are used to represent wave packets. Wave packets are wave functions which posses a finite support in phase space. That is their amplitude outside a finite "volume" in phase space becomes exponentially small when the supporting "volume" is increased. Pseudospectral representation methods for wave packets are able to obtain exponential convergence of the calculation. This exponential convergence is a consequence of the dual-representation strategy which is both pointwise on a grid as well as supported by a set of global functions. Within the pseudospectral family, the Fourier representation has particular importance since the grid and functional representation are symmetric. This symmetry enables the interpretation of the representation of the wave packet on two grids, the position grid and the momentum grid.

Since the wave packet property is crucial in maintaining a high level of accuracy, during a simulation of a molecular encounter all measures should be employed to preserve this property. A counterexample should stress the point. Coulombic wave functions are not wave packets because of the singularity of the potential. For this reason pseudospectral methods lose much of their advantage. This accounts for the popularity of the semilocal FD and finite element grid methods for simulating encounters under the influence the Coulomb potential. For other applications the accuracy of the FD methods is not sufficient.

A phase-space picture is one of the most effective ways to study the representation qualities of a grid for a particular problem. The idea is to draw an energy confining boundary in phase space. A wave function with an energy range within the restricting

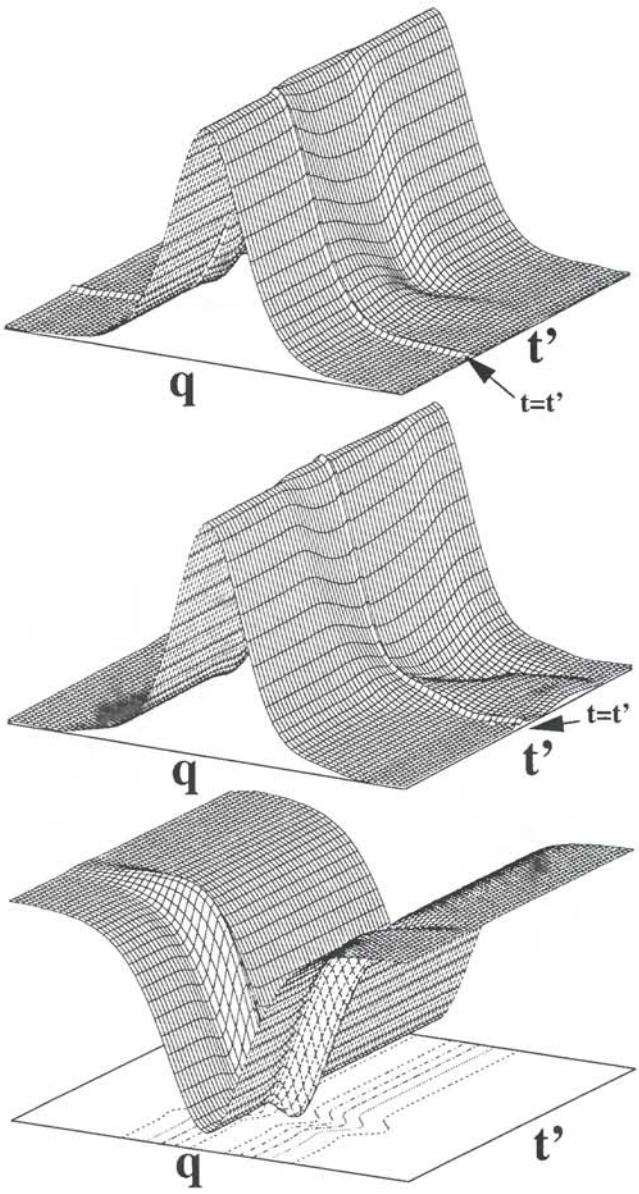

Figure 24 The wave function and the potential on an embedded representation q, t'. The lower panel displays the potential. In the q coordinate the potential has a well supporting bound states. In the t' direction the pulse appears as a hump in the potential at $t' = 24$. The upper panel shows the wave function at $t = 20$ just before the pulse. The arrow indicates the trace where $t = t'$ (enhanced in the figure). The wave function has not changed from its initial shape at $t = 0$ (a Gaussian wave function in q and a constant in t'). The middle panel displays the wave function immediately after the pulse at $t = 32$. The wave function is excited. One should notice the flow of events from past to future.

boundary, will decay exponentially in the classically forbidden regions and is therefore classified as a wave packet. Absorbing boundaries using imaginary potentials serve the same purpose of maintaining the wave packet property for scattering encounters. It should therefore be designed in a such a way that the scattering wave function is maintained as a wave packet on the grid at all stages of the propagation.

With these considerations in mind, the construction of an optimal simulation of a molecular encounter by grid methods can be rationalized. The task begins by defining the global objective which is the observation under study. This objective determines the volume of time-energy phase-space, i.e., the energy band and the time duration of the process. Once set, the energy band imposes a constraint on the position-momentum phase-space description. In the representation of each individual degree of freedom, grid points or functional basis elements which have energy outside the predetermined energy band are eliminated. After this stage, global correlations should be imposed to eliminate composite points from the grid, both in the coordinate space and in "momentum" space, outside the energy band. In a particular application the sampling efficiency can be estimated by dividing the classically allowed regions of phase space by the phase-space volume of the grid.

Different optimal representation strategies can be employed for the individual degrees of freedom depending on the number of states contained in the energy band. If only a few states are present a spectral expansion in a basis is sufficient. An extreme example are the electronic degrees of freedom, which under normal conditions of molecular encounters one wave function is enough by the Born-Oppenheimer approximation and a few more can describe complicated nonadiabatic transitions. A spectral expansion is also common in the description of inelastic scattering of hydrogen from surfaces. For a higher density of states, pseudospectral grid representations become advantageous. These can be either DVR or Fourier-based grids. The advantage of a fast transform such as the FFT is hardware dependent typically when $N_g > 50$. The duality between the pointwise base and the functional base in these methods means that the primary representation is a matter of convenience.

The representation on the spatial grid has strong influence on the volume of the time-energy phase space. This is why a global approach to the simulation is required. The most effective methods of propagation are based on the use of the energy as the primary representation. This is because the propagator can be approximated as an interpolation as opposed to an extrapolation in the time domain.

Finally, the molecular dynamical simulation is only as good as the new insight it is able to supply. This task is beyond the scope of this chapter and depends mainly on human ingenuity.

ACKNOWLEDGMENTS

I wish to thank my colleagues, Dan Kosloff, Hillel Tal-Ezer, Charley Cerjan, David Tannor, Mark Ratner, Claude Leforestier, Rich Friesner, Nimrod Moiseyev, William Miller, Don Kouri, Stephan Gray, and Daniel Neuhauser for their contributions to this work, and to my students Roi Baer, Allon Bartana, Meli Naphcha, Eyal Fattal, Uri Psekin, Nir Ben-Tal, Rob Bisseling and Audrey Dell Hammerich. This research was supported by the Binational United States–Israel Science Foundation. The Fritz Haber Research Center is supported by the Minerva Gesellschaft für die Forschung, GmbH München, FRG.

References

1. E. J. Heller, *J. Chem. Phys., 94*: 2723 (1991).
2. W. H. Miller, *J. Chem. Phys., 95*: 9428 (1991).
3. M. F. Herman and E. Kluk, *Chem. Phys., 91*: 27 (1984).

4. K. G. Kay, *J. Chem. Phys., 100*: 2250 (1994).
5. G. D. Billing, *Int. Rev. Phys. Chem., 13*: 309 (1994).
6. E. A. McCullough and R. E. Wyatt, *J. Chem. Phys., 51*: 1253 (1969).
7. E. A. McCullough and R. E. Wyatt, *J. Chem. Phys., 54*: 3578 (1971).
8. A. Askar and A. S. Cakmac, *J. Chem. Phys., 68*: 2794 (1978).
9. K. C. Kulander, K. J. Schafer, and J. L. Krause, *Atoms in Intense Radiation Fields* (M. Gavrila, ed.), Academic, New York, 1992, p. 247.
10. M. D. Feit, J. A. Fleck Jr., and A. Steiger, *J. Comp. Phys., 47*: 412 (1982).
11. M. D. Feit and J. A. Fleck Jr., *J. Chem. Phys., 78*: 301 (1983).
12. D. Kosloff and R. Kosloff, *J. Comp. Phys., 52*: 35 (1983).
13. J. C. Light, I. P. Hamilton, and J. V. Lill, *J. Chem. Phys., 82*, 1400 (1985).
14. H. Tal-Ezer and R. Kosloff, *J. Chem. Phys., 81*: 3967 (1984).
15. R. Kosloff, *Ann. Rev. Phys. Chem., 45*: 145 (1994).
16. C. Lanczos, *J. Math. Phys., 17*: 123 (1938).
17. J. C. Light and I. P. Hamilton, *J. Chem. Phys., 84*: 306 (1986).
18. R. A. Friesner, *J. Chem. Phys., 85*: 1462 (1986).
19. D. Gottlieb and S. A. Orszag, SIAM, Philadelphia, 1977.
20. M. Abramowitz and I. A. Stegun, *Handbook of Mathematical Functions*, Dover, 1972.
21. C. Schwartz, *J. Math. Phys., 26*: 411 (1985).
22. C. Lanczos, *Applied Analysis*, Prentice-Hall, Engelwood Cliffs, NJ, 1956.
23. J. W. Cooley and J. W. Tukey, *Math. Comp., 19*: 297 (1965).
24. H. J. Nussbaumer, *Fast Fourier Transform and Convolution Algorithms*, 2nd ed., Springer-Verlag, Berlin, 1982.
25. C. Temperton, *J. Comp. Phys., 52*: 1 (1983).
26. M. T. Heideman, D. H. Johnson, and C. S. Burrus, *IEEE ASSP, 4*(1): 14 (1984).
27. R. Kosloff, *Numerical Grid Methods and Their Application to Schrodinger's Equation* (C. Cerjan, ed.), Kluwer, Boston, 1993, p. 175.
28. G. G. Balint-Kurti, R. N. Dixon, and Clay Marston, *Int. Rev. Phys. Chem., 11*: 317 (1992).
29. E. T. Whittaker, *Proc. Roy. Soc. Edinburgh, 35*: 181 (1915).
30. H. Nyquist, *Trans. AIEE 1, 47*: 617 (1928).
31. C. E. Shannon, *Proc. IRE* (1949).
32. C. Canuto, M. Y. Hussaini, A. Quarteroni, and T. A. Zang, *Spectral Methods in Fluid Dynamics*, Springer, Berlin, 1987.
33. A. Bacic and J. C. Light, *J. Chem. Phys., 85*: 4594 (1986).
34. A. Bacic and J. C. Light, *J. Chem. Phys., 87*: 4008 (1987).
35. G. C. Corey, J. W. Tromp, and D. Lemoine, *Numerical Grid Methods and Their Application to Schrodinger's Equation* (C. Cerjan, ed.), Kluwer, Boston, 1993, p. 1.
36. J. C. Light, *Time Dependent Quantum Molecular Dynamics*, Vol. B 299, J. Broeckhove and L. Lathouwers (eds.), NATO ASI, 1992, p. 185.
37. D. E. Manolopolous and E. E. Wyatt, *Chem. Phys. Lett., 152*: 23 (1988).
38. D. E. Manolopoulos, *Numerical Grid Methods and Their Application to Schrodinger's Equation* (C. Cerjan, ed.), Kluwer, Boston, 1993, p. 57.
39. F. J. Lin and J. T. Muckerman, *Comp. Phys. Comm., 63*: 538 (1991).
40. R. V. Weaver, J. T. Muckerman, and T. Uzer, *Time Dependent Quantum Molecular Dynamics*, Vol. B 299 (J. Broeckhove and L. Lathouwers, eds.), NATO ASI, 1992, p. 381.
41. Y. Hoang, D. J. Kouri, and D. J. Hoffman, *J. Chem. Phys., 101*: 10493 (1994).
42. E. Fattal, R. Baer and R. Kosloff, *Phys. Rev. E* 53; (1996).
43. B. Jackson, *J. Phys. Chem., 93*: 7699 (1989).
44. F. Gygi, *Phys. Rev. B, 48*: 11692 (1993).
45. O. A. Sharfeddin, H. F. Bowen, D. J. Kouri, and D. Hoffman, *J. Comp. Phys., 100*: 294 (1992).
46. R. H. Bisseling and R. Kosloff, *J. Comp. Phys., 59*: 136 (1985).

47. D. Lemoine, *J. Chem. Phys., 101*: 4350 (1994).
48. A. E. Siegman, *Opt. Lett., 1*: 13 (1977).
49. J. D. Talman, *J. Comp. Phys., 29*: 35 (1978).
50. J. D. Talman, *Comp. Phys. Comm., 30*: 93 (1983).
51. R. N. Bracewell, *The Fourier Transform and its Applications*, McGraw-Hill, New York, 1978.
52. A. Besprozvannaya and D. Tannor, *Comp. Phys. Comm., 63*: 569 (1991).
53. Y. Shi and D. Tannor, *J. Chem. Phys., 92*: 2517 (1990).
54. R. C. Mowrey, H. F. Bowen, and D. J. Kouri, *J. Chem. Phys., 86*: 2441 (1987).
55. R. C. Mowrey and D. J. Kouri, *J. Chem. Phys., 86*: 6140 (1987).
56. R. C. Mowrey, Y. Sun, and D. J. Kouri, *J. Chem. Phys., 91*: 6519 (1989).
57. G. D. Billing, *Comp. Phys. Rep., 12*: 383 (1990).
58. G. R. Darling and S. Holloway, *J. Chem. Phys., 101*: 3268 (1994).
59. M.-N. Carre and D. Lemoine, *J. Chem. Phys., 101*: 5305 (1994).
60. D. T. Colbert and W. H. Miller, *J. Chem. Phys., 96*: 1982 (1992).
61. O. A. Schrafeddin and J. C. Light, *J. Chem. Phys., 102*: 3622 (1995).
62. G. C. Corey and D. Lemoine, *J. Chem. Phys., 97*: 4115 (1992).
63. R. A. Friesner, J. A. Bentley, M. Menou, and C. Leforestier, *J. Chem. Phys., 99*: 324 (1993).
64. C. Leforestier and R. Friesner, *Numerical Grid Methods and Their Application to Schrodinger's Equation* (C. Cerjan, ed.), Boston, 1993, p. 69.
65. J. Antikainen, R. A. Friesner, and C. Leforestier, *J. Chem. Phys., 102*: 1270 (1995).
66. D. P. Peterson and D. Midelton, *Inform. Contr., 5*: 279 (1962).
67. R. H. Bisseling and R. Kosloff, *J. Comp. Phys., 76*: 243 (1988).
68. G. J. Kores and R. C. Mowrey, *J. Chem. Phys., 101*: 805 (1994).
69. P. N. Swartztrauber, *Parallel Computation*, Academic Press, New York, 1982.
70. C. Leforestier and R. E. Wyatt, *Chem. Phys. Lett., 78*: 2334 (1983).
71. R. Kosloff and D. Kosloff, *J. Comp. Phys., 63*: 363 (1986).
72. D. Neuhauser and M. Baer, *J. Chem. Phys., 90*: 4351 (1989).
73. M. S. Child, *Mol. Phys., 72*: 89 (1991).
74. A. Vibok and G. G. Balint-Kurti, *J. Chem. Phys., 96*: 7615 (1992).
75. G. G. Balint-Kurti and A. Vibok, *Numerical Grid Methods and Their Application to Schrodinger's Equation* (C. Cerjan, ed.), Kluwer, Boston, 1993, p. 412.
76. C. W. MacCurdy and C. K. Stroud, *Comp. Phys. Comm., 63*: 323 (1991).
77. T. Seideman and W. H. Miller, *J. Chem. Phys., 97*: 2499 (1992).
78. D. Acias, S. Brouard, and J. G. Muga, *Chem. Phys. Lett., 228*: 672 (1995).
79. R. Heather and H. Metiu, *J. Chem. Phys., 86*: 5009 (1987).
80. J. Zhang, *Chem. Phys. Lett., 160*: 417 (1989).
81. J. Zhang, *J. Chem. Phys., 92*: 324 (1990).
82. J. Zhang, *Comp. Phys. Comm., 63*: 28 (1991).
83. C. J. Williams, J. Qian, and D. J. Tannor, *J. Chem. Phys., 95*: 1721 (1991).
84. D. J. Tannor, A. Besprozvannaya, and C. J. Williams, *J. Chem. Phys., 96*: 2998 (1992).
85. J. Kugar and D. H. Meyer, *J. Chem. Phys., 90*: 566 (1989).
86. T. J. Park and J. C. Light, *J. Chem. Phys., 85*: 5870 (1986).
87. S. K. Gray, *J. Chem. Phys., 96*: 6543 (1992).
88. R. Kosloff and H. Tal-Ezer, *Chem. Phys. Lett., 127*: 223 (1986).
89. N. Agmon and R. Kosloff, *J. Phys. Chem., 91*: 1988 (1987).
90. A. D. Hammerich, J. G. Muga, and R. Kosloff, *Isr. J. Chem., 29*: 461 (1989).
91. Y. Zeiri, E. Fattal, and R. Kosloff, *J. Chem. Phys., 102*: 1859 (1995).
92. D. Neuhauser, *J. Chem. Phys., 93*: 2611 (1990).
93. D. Neuhauser, *J. Chem. Phys., 100*: 5076 (1994).
94. R. Kosloff, *J. Phys. Chem., 92*: 2087 (1988).
95. W. Zhu, Y. Hoang, D. J. Kouri, M. Arnold, and D. J. Hoffman, *Phys. Rev. Lett., 72*: 1310 (1994).

96. D. J. Kouri, W. Zhu, Y. Hoang, and D. J. Hoffman, *Chem. Phys. Lett., 220*: 312 (1994).
97. S. Aurbach and C. Leforestier, *Comp. Phys. Comm., 78*: 55 (1994).
98. R. Baer and R. Kosloff, *Chem. Phys. Lett., 200*: 183 (1992).
99. R. Baer and R. Kosloff, *J. Phys. Chem., 99*: 2534 (1995).
100. Bernt Hartke, Ronnie Kosloff, and Sanford Ruhman, *Chem. Phys. Lett., 158*: 238 (1989).
101. W. Zhu, Y. Huang, D. J. Kouri, C. Chandler, and D. J. Hoffman, *Chem. Phys. Lett., 217*: 73 (1994).
102. Y. Sun, D. J. Kouri, D. W. Schwenke, and D. G. Truhlar, *Comp. Phys. Comm., 63*: 51 (1991).
103. M. Berman, R. Kosloff, and H. Tal-Ezer, *J. Phys. A, 25*: 1283 (1992).
104. G. Moro and J. H. Freed, *J. Chem. Phys., 74*: 3757 (1981).
105. H. Köpel, L. S. Cederbaum, and W. Domcke, *J. Chem. Phys., 77*: 2014 (1982).
106. A. Nauts and R. E. Wyatt, *Phys. Rev. Lett., 51*: 2238 (1983).
107. R. E. Wyatt, *Adv. Chem. Phys., 73*: 231 (1989).
108. H. Tal Ezer, R. Kosloff, and C. Cerjan, *J. Comp. Phys., 100*: 179 (1992).
109. C. Leforestier, R. Bisseling, C. Cerjan, M. Feit, R. Friesner, A. Guldberg, A. D. Hammerich, G. Julicard, W. Karrlein, H. Dieter Meyer, N. Lipkin, O. Roncero, and R. Kosloff, *J. Comp. Phys., 94*: 59 (1991).
110. C. Cerjan and R. Kosloff, *Phys. Rev. A, 47*: 1842 (1993).
111. U. Peskin, R. Kosloff, and N. Moiseyev, *J. Chem. Phys., 100*: 8849 (1994).
112. A. Bartana, R. Kosloff, and D. J. Tannor, *J. Chem. Phys., 99*: 196 (1993).
113. U. Banin, A. Bartana, S. Ruhman, and R. Kosloff, *J. Chem. Phys., 101*: 8461 (1994).
114. G. Yao and R. E. Wyatt, *J. Chem. Phys., 101*: 1904 (1994).
115. U. Peskin and N. Moiseyev, *J. Chem. Phys., 99*: 4590 (1993).

6

Time-Dependent Quantum Dynamics for Gas-Phase and Gas-Surface Reactions

DONG H. ZHANG and JOHN Z. H. ZHANG

New York University, New York, New York

I. INTRODUCTION

For the past decade, time-dependent (TD) computational methods for solving the Schrödinger equation have developed considerably, and the time-dependent approach has become an extremely important theoretical and computational tool for studying many dynamical processes in the field of chemical physics. The surge of interest in using the TD approach for dynamics studies reflects that theoretical chemists are tackling more and more complex systems of chemical interest. The TD approach has attractive features in theoretical calculations for large and complex chemical systems. Firstly, the computational time of the standard time-independent (TI) close-coupling approach scales as N^3 with the number of basis functions N. Although it is possible in many cases to employ iterative methods in the TI approach that could lower the scaling to N^2 provided that one can obtain converged results with a relatively small number of iteration steps. However, the convergence property of iterative methods is highly dependent on the specific problem on hand. Secondly, one realizes that many of the complex problems are not easily susceptible to standard TI treatments. For example, some processes involve very complicated boundary conditions and/or involve TD Hamiltonians such as those in molecule-surface reaction, breakup process, molecules in pulsed laser fields, etc. These processes either do not have well-defined boundary conditions in the traditional sense or are inherently time-dependent and thus could not be easily treated by standard TI methods. On the other hand, TD methods provide a wonderful alternative to treating these complex processes and, at the same time, provide clear and direct physical insight into the dynamics in much the same way as classical mechanics. The successful development and

application of various computational methods for solving the TD Schrödinger equation in the past decade or so, coupled with the development of fast digital computers, has significantly improved the numerical efficiency for practical applications of the TD methods to chemical dynamics problems. In particular, the relatively lower computational scaling of the TD approach with the number of basis functions (cpu time $\propto N^{\alpha}$ with $1 < \alpha < 2$) makes it computationally attractive for large scale computations. Of course, this lower computational scaling of the TD approach with the number of basis functions is a result of initial value treatment which solves for only one specific solution at a time.

II. SOLVING THE TIME-DEPENDENT SCHRÖDINGER EQUATION

A. Representation

The starting point of discussions is the TD Schrödinger equation

$$i\hbar \frac{\partial}{\partial t} |\Psi_S(t)\rangle = H|\Psi_S(t)\rangle \tag{1}$$

where H is the Hamiltonian operator, being time-dependent or time-independent, and Ψ_S is the TD wavefunction. The central task of this section is to find the numerical solution for Ψ_S which contains all the necessary dynamics information of the system. For most of our discussions, we will assume that the Hamiltonian H is time-independent, which is usually the case for a closed system, unless otherwise specified explicitly.

The wavefunction Ψ_S satisfying Eq. (1) is in the Schrödinger representation (SR), and has the formal solution (assuming H independent of time)

$$|\Psi_S(t)\rangle = e^{-(i/\hbar)Ht}|\Psi_S(0)\rangle \tag{2}$$

where the time evolution is unitary since H is Hermitian. In the Schrödinger representation, the wavefunction $\Psi_S(t)$ is time-dependent as in (1) but operators are time-independent. Sometimes, it is useful to employ the interaction representation (IR) by splitting the Hamiltonian H into two parts,

$$H = H_0 + V \tag{3}$$

where H_0 is a reference Hamiltonian and V is the residual interaction potential. H_0 is often chosen to be the asymptotic limit of H for scattering problems but the best choice generally depends on the specific problem on hand. One can then define an interaction representation which is related to the Schrödinger representation by a unitary transformation

$$|\Psi_I(t)\rangle = e^{(i/\hbar)H_0t}|\Psi_S(t)\rangle \tag{4}$$

It is relatively straightforward to derive the equation for $\Psi_I(t)$,

$$i\hbar \frac{\partial}{\partial t} |\Psi_I\rangle = V_I(t)|\Psi_I(t)\rangle \tag{5}$$

where $V_I(t)$ is the generalized interaction operator in the IR defined as

$$V_I(t) = e^{(i/\hbar)H_0t}Ve^{-(i/\hbar)H_0t} \tag{6}$$

In general, one can regard the IR as a general representation, while both Schrödinger and Heisenberger representations are special cases corresponding, respectively, to the

choice of $H_0 = 0$ for the former and $V = 0$ for the latter in (3). There are certain advantages in using the IR wavefunction for some applications as shown in Refs. 1–6.

B. Wavefunction Propagation

Solving Eq. (1) or (5) for a given initial wavefunction $\Psi(0)$ constitutes a propagation of the wavefunction, which is carried out by integrating the wavefunction in time. The propagation can be accomplished by using a variety of integration methods. The most straightforward approach is based on finite difference schemes including Runga-Kutta method, second-order difference (SOD) method, or higher-order difference methods. At present, however, more sophisticated methods, such as the split-operator (SP) method (7), Chebychev polynomial method (8), short iterative Lanczos method (9–12) as well as other methods, are often used in practical applications. Here, we briefly describe three commonly used propagators, namely, SOD, SP, and Chebychev polynomial methods.

In the SOD method, one approximates the time-derivative of the wavefunction by second-order finite differencing,

$$\frac{\partial}{\partial t}\Psi(t) = \frac{\Psi(t + \Delta) - \Psi(t - \Delta)}{2\Delta} + O(\Delta^2) \tag{7}$$

which results in the following iterative formula for the wavefunction:

$$\Psi(t + \Delta) = \Psi(t - \Delta) - {}^{i/\hbar}2\Delta H\,\Psi(t) \tag{8}$$

The wavefunction obtained by the SOD method of (8) is correct to the second order $O(\Delta^2)$. Since the iterative procedure in Eq. (8) needs wavefunctions at two prior times, Ψ_0 and Ψ_1, the SOD method requires the use of a self-starting scheme such as the Runga-Kutta method to generate Ψ_1 first. The SOD method is stable with respect to the time increment Δ below a certain critical value Δ_{max}. If the stepsize Δ is greater than Δ_{max}, the solution becomes unstable and increases exponentially (blow up). The SOD method is extremely easy to use but is not very efficient for large-scale calculations because it generally requires the use of a small time step in order to obtain stable and accurate solutions.

The split-operator (SP) method is extremely popular and has been widely used in many practical applications. It approximates the short-time propagator by the equation

$$e^{-(i/\hbar)tH\Delta} = e^{-(i/\hbar)H_0\Delta/2}\, e^{-(i/\hbar)V\Delta}\, e^{-(i/\hbar)H_0\Delta/2} + O(\Delta^3) \tag{9}$$

where the Hamiltonian H is split into two parts as in (3) and the error term is due to the noncommuting of H_0 and V. The wave function is propagated by

$$\Psi(t + \Delta) = e^{-(i/\hbar)H_0\Delta/2}\, e^{(i/\hbar)V\Delta}\, e^{-(i/\hbar)H_0\Delta/2}\,\Psi(t) \tag{10}$$

The above propagation of $\Psi(t)$ is explicitly unitary, which is a main factor contributing to the numerical stability of the SP method.

The original derivation of Eq. (9) is given by Fleck et al. (7). However, since the split-operator scheme is closely related to the interaction representation, it can be derived rather straightforwardly in IR (3). The basic approximation is the expansion of the interaction $V_I(t)$ around the middle point in the time interval $[t_0, t_0 + \Delta]$,

$$V_I(t) = V_I(\bar{t}) + (t - \bar{t})V_I'(\bar{t}) + \frac{1}{2}(t - \bar{t})^2 V_I''(\bar{t}) + O(\Delta^3) \tag{11}$$

where the prime denotes the derivative and t is the middle value in the range $[t_0, t_0 + \Delta]$, i.e., $t = t_0 + \Delta/2$. It can be shown that the contribution to Eq. (5) from the second term in (11) is zero and from the third is of the order $O(\Delta^3)$ (3). Keeping just the first term in (11), the solution to Eq. (5) then gives the solution of (10) after a uniform transformation. The reader is referred to Ref. 3 for details of the derivation using IR. Since the SP method is a short time propagator like the SOD, it can easily handle complicated Hamiltonians including time-dependent Hamiltonians and complex Hamiltonians.

Another widely used propagation scheme is the Chebychev polynomial expansion method introduced by Kosloff and Kosloff (8). This is a global propagator in the sense that it expands the propagator $e^{-(i/\hbar)Ht}$ in the interval $[0, t]$. The method is based on the Chebychev expansion relation for the function $\exp(iRX)$ ($X \in [-1, 1]$) (13),

$$e^{iRX} = \sum_n A_n(R)T_n(X) \tag{12}$$

where the coefficients A_n are given by (13)

$$A_n(R) = (2 - \delta_{n0})i^n J_n(R) \tag{13}$$

and J_n is the Bessel function of the first kind of order n. Using Eq. (12), one obtains the expansion relation for the propagator,

$$\begin{aligned} e^{-iHt} &= e^{-i(E_{max} + E_{min})t/2} e^{iR\hat{X}} \\ &= e^{-i(E_{max} + E_{min})t/2} \sum_n A_n T_n(\hat{X}) \end{aligned} \tag{14}$$

where

$$R = (E_{max} - E_{min})t/2 \tag{15}$$

$$\hat{X} = \frac{E_{max} + E_{min} - 2H}{E_{max} - E_{min}} \tag{16}$$

and E_{max} and E_{min} are, respectively, the maximum and minimum eigenvalues of the Hamiltonian operator. The propagation is usually carried out by using the recurrence relation for the Chebychev polynomial (13)

$$T_{n+1}(X) = 2XT_n(X) - T_{n-1}(X) \tag{17}$$

with $T_0 = 1$ and $T_1 = X$.

The Chebychev method converges exponentially with the number of expansion terms n for a given step size Δ and is particularly advantageous and efficient when Δ is large. However, unlike short-time propagators such as SOD or SP, the Chebychev method is not directly applicable to time-dependent or non-Hermitian Hamiltonians.

Using whatever propagation method, one has to evaluate the action of the Hamiltonian operator on the wavefunction $\Psi(t)$. This is normally carried out by expanding $\Psi(t)$ in a suitable basis set and then evaluates the operator action on basis functions. One can use the FFT (fast Fourier transform) techniques (7,14), discrete variable representation (DVR) (15,16) techniques, or simply calculate matrix elements of the operator in a given basis set.

C. Bound States

The time-dependent wave packet propagation can be employed to obtain bound state energies and bound state wavefunctions without the need to diagonalize the Hamiltonian matrix. The application of the method to bound state calculation is quite straightforward. If the Hamiltonian supports bound states Φ_n with eigenenergies E_n, one can expand any given initial wave packet in this eigenbasis set,

$$\Psi(0) = \sum_n C_n \Phi_n \tag{18}$$

and the TD wavefunction can therefore be written as

$$\Psi(t) = e^{-(i/\hbar)Ht}\Psi(0) = \sum_n C_n e^{-(i/\hbar)E_n t}\Phi_n \tag{19}$$

One can then calculate the Fourier transform of the autocorrelation function of the wavefunction as

$$\begin{aligned} S(E) &= \mathrm{Re}\left[\frac{1}{T}\int_0^T e^{(i/\hbar)Et}\,\langle\Psi(0)|\Psi(t)\rangle\,dt\right] \\ &= \sum_n |C_n|^2\,\mathrm{Re}\left[\frac{1}{T}\int_0^T e^{(i/\hbar)(E-E_n)t}\,dt\right] \\ &= \sum_n |C_n|^2\,\frac{\hbar}{(E-E_n)T}\sin\left[\frac{(E-E_n)T}{\hbar}\right] \end{aligned} \tag{20}$$

In the limit $T \to \infty$, the above expression gives rise to the stick spectrum and the height of the stick is equal to $|C_n|^2$.

Equation (20) gives the sinc spectrum which is oscillatory in E for a finite T. Due to this oscillation, there are extra peaks that do not correspond to actual eigenvalues. The use of Gaussian or Lorentzian spectra was shown to be numerically superior for eigenenergy calculations (17). Most importantly, the Gaussian or Lorentzian spectrum is "noise-free" and every single spectral peak represents an eigenvalue (17). For example, by including a weighting function $\sim \exp(-\alpha^2 t^2)$ in Eq. (20), one obtains the Gaussian spectrum

$$\begin{aligned} S_G(E) &= \frac{1}{2\pi}\int_{-\infty}^{\infty} e^{iEt}\,\langle\Psi(0)|\Psi(t)\rangle\,e^{-\alpha^2 t^2}\,dt \\ &= \frac{1}{2\alpha\sqrt{\pi}}\sum_n e^{-(E-E_n)^2/4\alpha^2}|C_n(E)|^2 \end{aligned} \tag{21}$$

which is positive definite and decays exponentially from the spectral peak. The reader is referred to Ref. 17 for detailed discussions.

Once the eigenenergy is obtained, it is straightforward to obtain the bound state wavefunction by performing a Fourier transform

$$|\Phi_n\rangle \propto \frac{1}{2\hbar T}\int_{-T}^{T} e^{(i/\hbar)E_n t}|\Psi(t)\rangle\,dt \tag{22}$$

However, in order to separate the neighboring states E_n and $E_{n'}$, the propagation time T has to be long enough such that $T >> 1/(E_n - E_{n'})$. If the bound state is degenerate, one

TD propagation from a given initial wave packet can only give one degenerate state. One needs to perform n separate propagations with n different initial wave packets in order to obtain all n degenerate states. A mixed TD/TI method was recently proposed by Neuhauser to deal with this problem which involves explicit diagonalization of some approximate eigenstates obtained from relatively short propagation. Some encouraging results have been obtained using this method (18).

D. Quasi-bound States

The similar TD approach can be applied to quasi-bound or resonance states. Of course, quasi-bound states are, rigorously speaking, continuum states and should be obtained from rigorous scattering calculations. However, since wavefunctions of quasi-bound states are highly concentrated in localized regions, they are similar to bound state wavefunctions in these regions and can therefore be calculated using bound-state-type methods, but care is required. In fact, one only needs to replace E_n by the complex energy $E_n - i\Gamma_n$ in the analysis of the previous subsection and Eq. (20) then becomes

$$\begin{aligned} S(E) &= \sum_n |C_n|^2 \, \mathrm{Re}\left[\int_0^T e^{(i/\hbar)(E - E_n + i\Gamma_n)t} \, dt\right] + A_b(E, T) \\ &= \sum_n |C_n|^2 \, \frac{\Gamma_n - \{\Gamma_n \cos[(E - E_n)T/\hbar] - E_n \sin[(E - E_n)T/\hbar]\} e^{-\Gamma_n T}}{(E - E_n)^2 + \Gamma_n^2} \\ &\quad + A_b(E, T) \end{aligned} \tag{23}$$

where $A_b(E, T)$ is the background contribution from other bound and continuum states. In the limit of $T \to \infty$ and for an isolated resonance, Eq. (23) reduces to the familiar Breit-Wigner formula,

$$S(E) = |C_n|^2 \, \frac{\Gamma_n}{(E - E_n)^2 + \Gamma_n^2} \tag{24}$$

However, in order to resolve both the resonance energy E_n and resonance width Γ_n using the Breit-Wigner formula (24), the propagation has to be carried out for a sufficiently long time so that the uncertainty relation

$$T \gg \frac{1}{\Gamma_n} \tag{25}$$

is satisfied. Thus direct application of the TD method is quite difficult to obtain accurate resonance widths, especially narrow ones. However, there are ways to overcome this problem. One simple approach is just to calculate the decay rate of the resonance wavefunction (survival probability) and extract the width from the time-dependence of the resonance wavefunction (19,20). Another adopted approach is to directly fit the autocorrelation at various propagation time T (21). Both approaches require that the background contribution to Eq. (23) be small enough such that the resonance contribution dominates the spectrum in Eq. (23). Thus it is possible to extract a narrow resonance width from only short-time propagation if the initial wave packet is chosen to have large overlap with the resonance wavefunction.

Yet another attractive approach is to artificially broaden the resonance width Γ_n by using the Lorentzian spectrum (17)

$$S_L(E) = \frac{1}{2\pi}\int_{-\infty}^{\infty} e^{iEt}\,\langle\Psi(0)|\Psi(t)\rangle\, e^{-\alpha|t|}\,dt$$

$$= \frac{1}{\pi}\frac{\alpha + \Gamma_n}{(\alpha + \Gamma_n)^2 + (E - E_n)^2}\,|C_n(E)|^2 + A_b(E) \tag{26}$$

where α is chosen to be much greater than Γ_n so that Eq. (25) is satisfied at a much shorter time for the total decay width $\Gamma = \alpha + \Gamma_n$ (17). Direct fitting of Eq. (26) will give the total width and the true width Γ_n is simply obtained by substracting out α from the total width Γ.

It is worth mentioning that one often uses an absorbing potential or optical potential in calculating resonance energies because it eliminates pseudoeigenenergies due to finite boundary reflections (22–24). This is generally necessary for calculations with a finite spacial grid.

E. Scattering States

The time-dependent wave packet approach provides an attractive alternative to the standard time-independent close-coupling (CC) approach for scattering problems. Although both approaches are formally equivalent, they are technically different and the TD approach has computational advantageous for large-scale scattering problems. The most important difference is that the TD approach solves for one column of the S-matrix at a time while the TI CC approach solves for the whole S-matrix in a single TD calculation. As a result, the computational time of each TD calculation scales less than N^2 versus N^3 scaling of the TI CC calculation, where N is the total number of basis functions. In addition, a single wave packet propagation enables one to obtain scattering information for all the energies contained in the initial wave packet. These features make the TD approach increasingly attractive for large-scale computational calculations in chemical dynamics.

The most straightforward application of the TD approach to a scattering problem is to launch an initial wave packet in a specific internal state from the asymptotic region with a positive momentum toward the interaction region. There are different ways to extract the scattering information once the time-dependent wavefunction $\Psi(t)$ is obtained. One approach is to directly project out the specific product states from the final $\Psi(t)$ using the relation (1)

$$S_{fi}(E) = \lim_{t\to\infty} \langle\Phi_{fE}|\Psi_I(t)\rangle \,/\, \langle\Phi_{iE}|\Psi_I(0)\rangle \tag{27}$$

where $|\Phi_{iE}\rangle$ and $|\Phi_{fE}\rangle$ are energy-normalized initial and final asymptotic states, respectively, and $|\Psi_I(t)\rangle$ is the IR wavefunction defined in (4). The advantage of using (27) is that one does not need to perform time to energy transform on the wave function $|\Psi_I(t)\rangle$ to obtain TI scattering information such as the S-matrix. All scattering information is contained in the final wavefunction $|\Psi_I(t = \infty)\rangle$. However, this approach requires one to calculate the overlap integral $\langle\Phi_{fE}|\Psi_I(t)\rangle$ for each energy. In addition, the handling of the boundary reflection problem is more complicated in this approach. As a result, this method is most efficient when applied to scattering processes involving only short prop-

agation during which the wave packet remains compact in configuration space such as in direct scattering or photodissociation.

A different approach is based on the time → energy transform, i.e., one transforms the TD wavefunction $|\Psi(t)\rangle$ to the energy-dependent (ED) wavefunction $|\Psi_I(E)\rangle$ which is a solution of the TI Schrödinger equation. This approach is more general because once the ED wavefunction $|\Psi_I(E)\rangle$ is obtained, it is straightforward to extract scattering information from $|\Psi_I(E)\rangle$. For example, one can carry out the asymptotic analysis by calculating the scattering amplitude or flux. More detailed discussions on this approach will be presented in subsequent sections.

III. GAS-PHASE PHOTOFRAGMENTATION DYNAMICS

Quantum mechanical calculations for unimolecular dissociation of triatomic molecules are now quite routinely carried out in many practical applications which have provided important theoretical basis for understanding the dissociation dynamics of some simple molecular systems. However, rigorous quantum mechanical calculations for systems with four or more atoms is still in its infancy. The photofragmentation study for four-atom systems is both practically important and fundamentally interesting. The fragmentation of dimers or binary complexes, for example, results in two separate monomers, each can carry excess energy in its internal degrees of freedom. This process produces a more complex yet more interesting final product state distribution than that of triatomic molecules which have only one molecular product with internal degrees of freedom.

Progress in accurate quantum dynamics study for polyatomics was first made in photofragmentation dynamics calculation for weakly bound four-atom complexes. The TI calculation by Clary (25) and TD calculation by Zhang et al. (26,27) have included explicitly four degrees of freedom for VP (vibrational predissociation) dynamics calculation of D_2HF, as well as in subsequent calculations for ArH_2O (28), H_2HF (29), HDHF (30), HOOH (31,32), and HF dimer (33–36). The photofragmentation studies for binary dimers have all used rigid bond model, in which the two intramolecular bonds are frozen while the remaining four degrees of freedom are explicitly included in the dynamics calculation. The following subsections provide general treatments for direct photodissociation and vibrational predissociation of the diatom-diatom complex.

A. Direct TD Method for Photodissociation

Photodissociation involves a direct optical excitation (usually in the UV or VUV region) from the ground (bound) electronic state to the excited (repulsive) electronic state of the molecule which then dissociates. The fundamental quantity in photofragmentation calculation is the Franck-Condon (FC) factor

$$A_n = |\langle \psi_{nE}^{(-)} | \chi \rangle|^2 \tag{28}$$

where $\psi_{nE}^{(-)}$ is an incoming scattering state and χ is the localized wave packet given by $|\chi\rangle = \mu_e|\psi_g\rangle$ where μ_e is the transition dipole and ψ_g is the ground state wavefunction. In order to calculate the FC factor, one needs to calculate both the bound wavefunction $|\psi_g\rangle$ and the scattering wavefunction $\psi_{nE}^{(-)}$, the latter calculation is the main source of difficulty. Numerous studies for the photodissociation of the triatomic molecule H_2O have been reported over the past decade (37). A review of the theoretical treatment for photodissociation was given by Balint-Kurti and Shapiro some years ago (38). A recent book

by Schinke has summarized many recent developments in this research area and the reader is referred to the Schinke's book for details (39).

The standard TD approach to photodissociation was proposed by Heller and coworkers (40). In the TD approach, one simply converts the FC factor into a TD expression (41)

$$\begin{aligned} A_n &= \langle \psi_{nE}^{(-)} | \chi \rangle \\ &= \langle \lim_{t \to \infty} e^{iHt/\hbar} e^{-iH_0 t/\hbar} \Phi_{nE} | \chi \rangle \\ &= \lim_{t \to \infty} \langle \Phi_{nE} | \Psi_I(t) \rangle \end{aligned} \tag{29}$$

where the IR wavefunction is defined by (4). The total dissociation cross section is simply proportional to

$$\begin{aligned} P_{\text{tot}} &\propto \sum_n |A_n|^2 \\ &= \langle \chi | \delta(E - H) | \chi \rangle \\ &= \frac{1}{2\pi\hbar} \int_{-\infty}^{\infty} e^{(i/\hbar)Et} \langle \chi | e^{-iHt/\hbar} | \chi \rangle \, dt \end{aligned} \tag{30}$$

where the orthogonality relation

$$\sum_n |\psi_{nE}^{(-)}\rangle\langle\psi_{nE}^{(-)}| = \delta(E - H) \tag{31}$$

has been used and bound states, if any, have been projected out from χ.

In the TD calculation for direct photodissociation, the wave packet propagation is carried out on a repulsive potential energy surface, which does not generally support any bound states and the wave packet propagation usually takes only a short time from the beginning to the end. Therefore numerical calculation of cross sections for direct photodissociations is generally quite straightforward.

1. $H_2O_2 \rightarrow OH + OH$

Since quantum dynamics calculations for photodissociation of triatomic molecules are quite routine these days but calculations for four-atom systems are scarce, we choose to present an example for photodissociation of a four-atom system—hydrogen peroxide. UV photodissociation of H_2O_2 has been extensively studied by Schinke et al. using classical trajectory method (42). Theoretical and experimental evidences suggest that this is a direct dissociation process involving a repulsive interaction between two OH fragments with little OH vibrational excitation. Therefore one can freeze both OH bonds and include only four degrees of freedom in the dynamics calculation. The four remaining degrees of freedom are shown in Fig. 1. Since this is a typical rigid bond diatom-diatom system, we present in the following a rather detailed quantum treatment.

The Hamiltonian H can be written in Jacobi coordinates shown in Fig. 1 as

$$H = -\frac{\hbar^2}{2\mu}\frac{\partial^2}{\partial R^2} + \frac{\vec{l}^{\,2}}{2\mu R^2} + B_0 \vec{j}_1^{\,2} + B_0 \vec{j}_2^{\,2} + V(\hat{r}_1, \hat{r}_2, \vec{R}) \tag{32}$$

where μ is the reduced mass of two OH diatoms, $\vec{l}$ is the orbital angular momentum operator, $\vec{j}_1$ and $\vec{j}_2$ are the rotational angular momentum operators of two OH diatoms, and B_0 is the rotation constant of OH in the ground vibrational state. The two diatomic

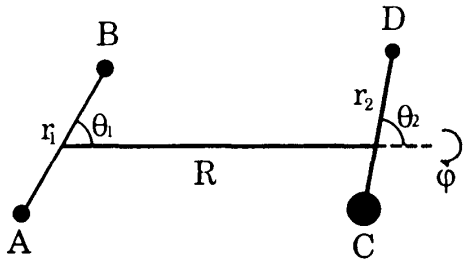

Figure 1 Jacobi coordinates for the diatom-diatom system of AB + CD. R is the distance between the center of mass of two diatoms and ϕ is the out-of-plane torsional angle.

distances, r_1 and r_2, are fixed at the equilibrium position and this treatment results in an effective four degrees of freedom quantum mechanical problem in both bound and scattering calculations.

The partial photodissociation cross section to a particular final state in the golden rule approximation is proportional to the following quantity

$$P_f \propto |\langle \psi_f^{(-)} | \chi \rangle|^2 \tag{33}$$

where $|\psi_f^{(-)}\rangle$ is an incoming continuum eigenfunction which corresponds to an asymptotic state f on the excited potential energy surface. The wavefunction χ is given by

$$|\chi\rangle = \mu_d |\phi_b\rangle \tag{34}$$

where μ_d is the transition dipole function between the ground and the excited potential energy surface, and ϕ_b is the initial bound state wavefunction on the ground PES (potential energy surface). Equation (33) is transformed into an equivalent time-dependent expression as in Eq. (29)

$$P_f \propto \lim_{t \to \infty} |\langle \phi_f | \Psi_s(t) \rangle|^2 \tag{35}$$

where ϕ_f is an eigenfunction of the asymptotic Hamiltonian H_0 in quantum state f and $\Psi_s(t)$ is the Schrödinger wavefunction $\Psi_s(t) = e^{-iHt}\Psi_s(0)$. The time-dependent wave function can be propagated using the split-operator algorithm (7)

$$\begin{aligned} \Psi_s(t + \Delta) &= e^{-iH\Delta}\Psi_s(t) \\ &= e^{-iH_0\Delta/2} e^{-iV\Delta} e^{-iH_0\Delta/2} \Psi_s(t) \end{aligned} \tag{36}$$

where $\Psi_s(0) = |\chi\rangle$. The dipole function μ_d is usually chosen to be a constant in dynamics calculations.

In quantum mechanical calculations of polyatomic systems, it is important to utilize the symmetry properties of the system to reduce the computational effort. For example, the parity of the molecular systems is always conserved and the calculation can always be done for each parity separately. In addition to conservation of parity, the H_2O_2 system possess an exchange symmetry corresponding to the invariance of the Hamiltonian with respect to the exchange of two OH diatoms. Thus the wavefunction, both bound and unbound, should be properly symmetrized. An additional symmetry involving the exchange of two H atoms alone is not important here because it requires simultaneous breaking of two OH bonds, an unlikely event. In the following, we explicitly show basic formalisms for the treatment of the continuum wavefunction with molecular exchange symmetry for HOOH. The proper treatment of exchanging symmetry for two identical

molecules has been discussed by several workers (43–47). We present in the following a summary of the main results and the working formulae.

The time-dependent wavefunction in Eq. (36) can be expanded in terms of symmetrized space-fixed (SF) angular momentum eigenfunctions as

$$\Psi^{\pm}_{JM}(\vec{R}, \hat{r}_1, \hat{r}_2, t) = \sum_{j_1,j_2,j_{12},l} F^{\pm JM}_{j_1,j_2,j_{12},l}(R, t) I^{\pm JM}_{j_{12},l,(j_1,j_2)}(\hat{R}, \hat{r}_1, \hat{r}_2) \tag{37}$$

where $I^{\pm JM}_{j_{12},l,(j_1,j_2)}$ is the exchange-invariant angular momentum eigenfunction given by (31,34)

$$I^{\pm JM}_{j_{12},l,(j_1,j_2)} = \frac{1}{\sqrt{2(1 + \delta_{j_1,j_2})}} [Y^{JM}_{j_{12},l,(j_1,j_2)} \pm (-1)^{j_1+j_2-j_{12}+l} Y^{JM}_{j_{12},l,(j_2,j_1)}] \tag{38}$$

with the restriction $j_1 \geq j_2$. Note that states with $j_1 = j_2$ and $\pm(-1)^{-j_{12}+l} = -1$ do not exist for the corresponding exchange symmetry. The unsymmetrized total angular momentum eigenfunction can be expressed in the body-fixed (BF) representation.

$$\begin{aligned} Y^{JM}_{j_{12},l,(j_1,j_2)} = \sum_{K,m_1} D^{J}_{K,M}(\Theta\Phi\Psi) \sqrt{\frac{2l + 1}{4\pi}} \langle j_{12}Kl0|JK\rangle \\ \times \langle j_1 m_1 j_2 K - m_1 | j_{12} K\rangle y_{j_1 m_1}(\theta_1, 0) y_{j_2 K - m_1}(\theta_2, \phi) \end{aligned} \tag{39}$$

where three internal angles (θ_1, θ_2, ϕ) are defined in Fig. 1. The rotation matrix $D^{J}_{K,M}$, Eular angles ($\Theta\Phi\Psi$), Clebsch-Gordon coefficients, and spherical harmonics y_{jm} follow the standard definition (48). The system parity, defined as $p = (-1)^{j_1+j_1+l}$, is a conserved quantity and there is no coupling between basis functions of different parity.

Utilizing Eq. (38) we obtain the symmetrized potential matrix elements as follows:

$$\begin{aligned} \langle I^{\pm}_{j_{12},l,(j_1,j_2)} | V | I^{\pm}_{j'_{12},l',(j'_1,j'_2)} \rangle = \frac{1}{\sqrt{(1 + \delta_{j_1,j_2})(1 + \delta_{j'_1,j'_2})}} \{ \langle Y^{JM}_{j_{12},l,(j_1,j_2)} | V | Y^{JM}_{j'_{12},l',(j'_1,j'_2)} \rangle \\ \pm (-1)^{j_1+j_2-j_{12}+l} \langle Y^{JM}_{j_{12},l,(j_2,j_1)} | V | Y^{JM}_{j'_{12},l',(j'_1,j'_2)} \rangle \} \end{aligned} \tag{40}$$

Using Eq. (39), the potential matrix elements in Eq. (40) can be explicitly evaluated as

$$\begin{aligned} \langle Y^{JM}_{j_{12},l,(j_1,j_2)} | V | Y^{JM}_{j'_{12},l',(j'_1,j'_2)} \rangle = \sum_{K} \frac{\sqrt{(2l + 1)(2l' + 1)}}{2J + 1} \\ \times \langle j_{12}Kl0|JK\rangle \langle j'_{12}Kl'0|JK\rangle \\ \times \sum_{m_1,m'_1} \langle j_1 m_1 j_2 K - m_1 | j_{12} K\rangle \langle j'_1 m'_1 j'_2 K - m'_1 | j'_{12} K\rangle \\ \times \int_0^{\pi} \sin\theta_1 \, d\theta_1 \int_0^{\pi} \sin\theta_2 \, d\theta_2 \, P_{j_1,K-m_1}(\theta_1) P_{j_2,K-m_1}(\theta_2) \\ \times V_R^{m_1,m'_1}(\theta_1, \theta_2) P_{j'_1,m'_1}(\theta_1) P_{j'_2,K-m'_1}(\theta_2) \end{aligned} \tag{41}$$

where

$$V_R^{m_1,m'_1}(\theta_1, \theta_2) = \frac{1}{\pi} \int_0^{\pi} d\phi \cos[(m_1 - m'_1)\phi] V(\theta_1, \theta_2, \phi, R) \tag{42}$$

and $P_{j,m}(\theta) = \sqrt{2\pi} y_{j,m}(\theta, 0)$.

For photodissociation of H_2O_2, the centrifugal potential is relatively small due to a large reduced mass and low rotational excitation. We thus choose the kinetic energy operator to be H_0 in Eq. (36). The R-dependent wave function $F^{\pm JM}_{j_1,j_2,j_{12},l}$ in Eq. (38) is expanded in sine functions, and the action of $e^{-iH_0\Delta/2}$ on $F^{\pm JM}_{j_1,j_2,j_{12},l}$ is done by FFT. The potential matrix $\mathbf{V(R)}$ is diagonalized at given grid points R_i in the evaluation of the exponential term $e^{-iV\Delta}$. The normalized asymptotic eigenfunction in Eq. (35) is

$$\phi_f = \sqrt{\frac{2\mu}{\pi k_{j_1,j_2}\hbar^2}}\, I^{\pm JM}_{j_{12},l,(j_1,j_2)} \sin(k_{j_1j_2}R) \tag{43}$$

where the wave number k is given by

$$k_{j_1j_2} = \sqrt{\frac{2\mu}{\hbar^2}\,[E - B_0 j_1(j_1 + 1) - B_0 j_2(j_2 + 1)]} \tag{44}$$

Some of the calculated results for photodissociation of H_2O_2 using a fit to the Schinke-Staemmler potential energy surface (42) are plotted in Figs. 2 and 3. As shown in Fig. 2, the OH rotational distribution is Gaussianlike with a maximum centered around $j = 8$ on the $\tilde{A}$ surface and $j = 9$ on the $\tilde{B}$ surface. In addition, the $|j_1 - j_2|$ distribution, where j_1 and j_2 are rotation quantum numbers of two OH fragments, is shown in Fig. 3. This quantity measures the scalar correlation of rotations of two OH fragments. Fig. 3 shows that two product rotations are highly correlated with the maximum at $j_1 \approx j_2 \pm 1$, which reflects the fact that the initial geometric positions of the two OH radicals are more or less dynamically equivalent. These quantum results are in good agreement with the classical trajectory results of Schinke and Staemmler (42).

B. TD Golden Rule Method for Vibrational Predissociation

For relatively small molecules, experimental evidence suggest that vibrational predissociation (VP) is primarily responsible for the observed linewidths, as opposed to intramolecular

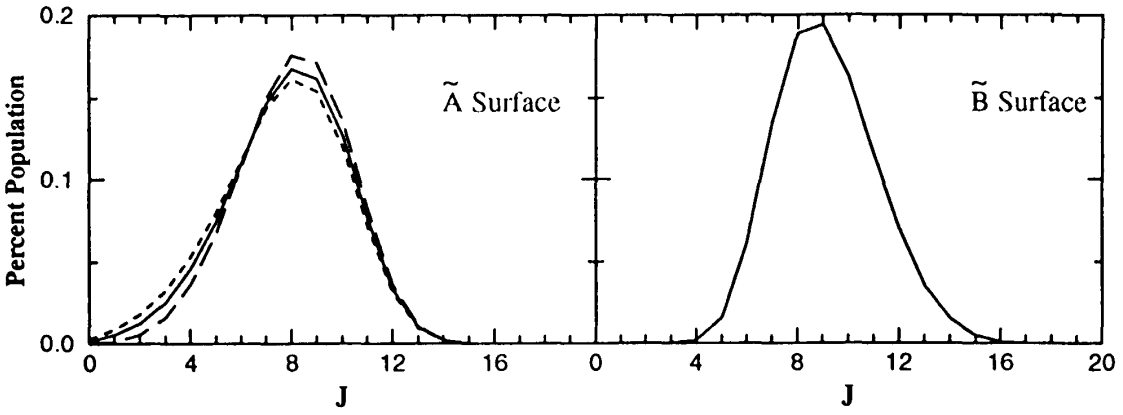

Figure 2 Rotational distributions of OH radicals in photodissociation of H_2O_2 from the lowest doublet states at 248 nm. Dashed lines denote distribution from the even-parity state, long-dashed lines, the odd-parity state, and the solid lines, the average distribution.

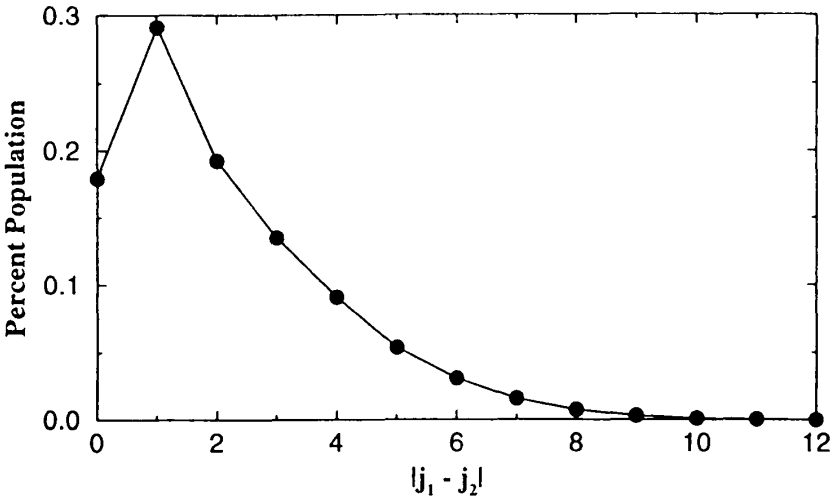

Figure 3 Distribution of $|j_1 - j_2|$ from photodissociation of HOOH at 248 nm. There is no difference between the $\tilde{A}$ and $\tilde{B}$ state.

vibrational relaxation (IVR). Recent advances in infrared laser techniques have made it now possible to experimentally prepare a well-defined excited rovibrational state and to probe individual quantum state of the fragments resulting from laser excitation. This kind of state-to-state experiment demands accurate quantum mechanical calculations for comparison in order to elucidate the underlying dynamics and the intra- and intermolecular forces. The long predissociation lifetime signals weak couplings between initial and final vibrational states which makes it ideal for the golden rule treatment.

The VP is usually induced through an infrared (IR) excitation of one of the vibrational modes of the complex which is different from UV excitation of electronic states in photodissociation. In addition, the photodissociation occurs on the excited PES which is often purely repulsive and involves only short time dynamics. However, VP occurs on the ground electronic PES which is attractive and often supports many bound and quasi-bound states. Thus VP dynamics is generally more complex than that in direct photodissociation. Most VP dynamics problems are treated by TI scattering calculations. Recently, a TD golden rule treatment was reported by Villarreal (49) for calculating the total decay width and by Zhang and Zhang (50) for calculating both the total and partial decay widths. Since the TD golden rule method is an efficient method for weakly bound systems, we present in the following the theoretical derivation and treatment for vibrational predissociation within the golden rule approximation.

Let us denote the excited state after initial excitation by $|\chi_i\rangle$ with quantum numbers denoted by the composite index i, which is assumed to be in a particular vibrational state v_i. The continuum eigenstate of the full Hamiltonian H is denoted as $|\psi_{fE}^{(-)}\rangle$, whose quantum numbers are given by the composite index f. The probability per unit energy that the system will end up in the continuous state f is given by

$$\frac{dP_{fi}}{dE} = \left| \langle \psi_{fE}^{(-)} | \chi_i \rangle \right|^2 \tag{45}$$

where $|\psi_{fE}^{(-)}\rangle$ is the full scattering wave function satisfying $(E - H)|\psi_{fE}^{(-)}\rangle = 0$. Utilizing the Möller scattering operator (41), one can write

$$\begin{aligned}|\psi_{fE}^{(-)}\rangle &= \Omega_-|\phi_{fE}^{(-)}\rangle \\ &= \lim_{t\to\infty} e^{iHt/\hbar}e^{-iH_f t/\hbar}\phi_{fE}^{(-)}\rangle \end{aligned} \tag{46}$$

where H_f is the vibrational adiabatic Hamiltonian for the vibrational state v_f, and $|\phi_{fE}^{(-)}\rangle$ is the continuum eigenstate of H_f satisfying the Schrödinger equation, $(E - H_f)|\phi_{fE}^{(-)}\rangle = 0$. Utilizing Eq. (46), one can rewrite Eq. (45) as

$$\frac{dP_{fi}}{dE} = \lim_{t\to\infty}\left|\langle\phi_{fE}^{(-)}|\Psi_I(t)\rangle\right|^2 \tag{47}$$

where

$$|\Psi_I(t)\rangle = e^{iH_f/\hbar}e^{-iHt/\hbar}|\chi_i\rangle \tag{48}$$

In the rigorous full quantum treatment (19), one solves for the full time-dependent wavefunction in Eq. (48) which can be computationally expensive. In the golden rule treatment, $\Psi_I(t = \infty)$ is obtained by a first-order approximation as follows:

$$\begin{aligned}|\Psi_I(\infty)\rangle &= |\chi_i\rangle - i\int_0^\infty dt'\, e^{i/\hbar H_f t'}Ve^{-iHt'/\hbar}|\chi_i\rangle \\ &\approx |\chi_i\rangle - i\int_0^\infty dt'\, e^{i/\hbar H_f t'}Ve^{-i(E_R - i\Gamma)t'/\hbar}|\chi_i\rangle \\ &= |\chi_i\rangle + (H_f - E_R + i\Gamma)^{-1}V|\chi_i\rangle \end{aligned} \tag{49}$$

where $V = H - H_f$ is the coupling potential that induces the dissociation and E_R and Γ are, respectively, the resonance energy and the decay width. The projection of $|\Psi_I(\infty)\rangle$ on to $|\phi_{fE}^{(-)}\rangle$ gives

$$\langle\phi_{fE}^{(-)}|\Psi_I(\infty)\rangle \approx (E_f - E_R + i\Gamma)^{-1}\langle\phi_{fE}^{(-)}|V|\chi_i\rangle \tag{50}$$

Utilizing the unitary condition

$$\sum_f P_{fi} = \sum_f \int dE_f \left|\langle\phi_{fE}^{(-)}|\Psi_I(\infty)\rangle\right|^2 = 1 \tag{51}$$

we then obtain the relation

$$\begin{aligned}1 &= \sum_f \int dE_f \frac{|\langle\phi_{fE}^{(-)}|V\chi_i\rangle|^2}{|E_f - E_R + i\Gamma|^2} \\ &\approx \sum_f |\langle\phi_{fE}^{(-)}|V|\chi_i\rangle|^2 \int dE_f \frac{1}{|E_f - E_R + i\Gamma|^2} \\ &= \frac{\pi}{\Gamma}\sum_f \left|\langle\phi_{fE_R}^{(-)}|V|\chi_i\rangle\right|^2 \end{aligned} \tag{52}$$

Equation (52) is the desired TI golden rule result for partial decay width Γ_f and total width Γ (HWHM),

$$\Gamma_f = \pi \left| \langle \phi_{fE}^{(-)} | V | \chi_i \rangle \right|^2 \tag{53}$$

$$\Gamma = \sum_f \Gamma_f \tag{54}$$

and the lifetime is given by

$$\tau = \frac{1}{2\Gamma} \tag{55}$$

If we invoke the scattering relation (46) again, Eq. (53) becomes

$$\Gamma_f = \pi \left| \langle \phi_{fE}^0 | \Phi_I(t = \infty) \rangle \right|^2 \tag{56}$$

where the TD wave function is

$$|\Phi_I(t)\rangle = e^{iH_0 t/\hbar} e^{-iH_f t/\hbar} |\phi_c\rangle \tag{57}$$

where $|\phi_c\rangle = V|\chi_i\rangle$ is the continuum portion of the initial wave packet from which all bound states of H_f have been projected out and $|\phi_{fE}^0\rangle$ is the "free" scattering state satisfying the asymptotic equation

$$(E - H_0)|\phi_{fE}^0\rangle = 0 \tag{58}$$

and the "residual" potential is given by

$$V_f = H_f - H_0 \tag{59}$$

The above treatment is equivalent to stating that $|\chi_i\rangle = |v_i\rangle|\overline{\chi}_i\rangle$ and $|\phi_{fE}^0\rangle = |v_f\rangle\,|\overline{\phi}_{fE}^0\rangle$ where "barred" states have one less vibrational degree of freedom. If we factor out the vibrational state, we then have

$$\Gamma_f = \pi \left| \langle \overline{\phi}_{fE_v}^0 | \overline{\Phi}_I(t = \infty) \rangle \right|^2 \tag{60}$$

where $\overline{\Phi}_I(t = \infty)$ is the $t = \infty$ limit of $\Phi(t)$ in Eq. (57) with one less vibrational degree of freedom and E_v is the resonance energy with the vibrational energy subtracted out, i.e., $E_v = E_r - \varepsilon_{vf}$.

1. $D_2HF(v = 1) \rightarrow D_2 + HF(v = 0)$

Equations (57) and (60) have been applied to the VP calculation for several triatomic (50,51) and tetraatomic systems (26,27,29). We show here some results for vibrational predissociation of the four-atom complex D_2HF which results from infrared excitation of the HF vibration. In this case, the product consists of two molecular fragments, D_2 and HF, and both can carry energies in rotational degrees of freedom. This feature of joint product rotation distribution is not present in triatomic systems in which only one fragment is a molecular species. The TD golden-rule calculation is carried out using the ab initio PES of Clary (25). The VP process in $D_2HF(v = 1)$ is dominated by the $V \rightarrow V$

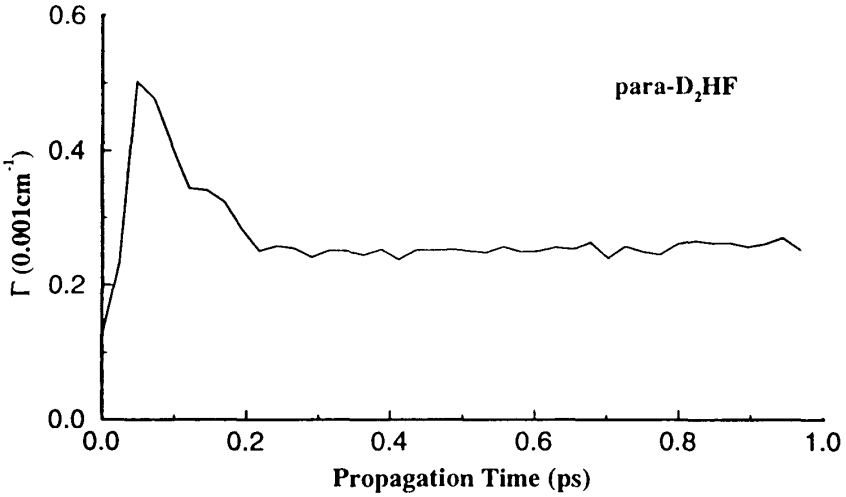

Figure 4 Decay width Γ for vibrational predissociation in *para*-$D_2(v = 0)HF(v = 1) \rightarrow D_2(v = 1) + HF(v = 0)$ (odd rotation of D_2) as a function of propagation time.

energy transfer from the $HF(v = 1)$ mode to the $D_2(v = 1)$ mode, which is the most favorable decay channel and is consistent with the "momentum gap" rule (52). Figure 4 shows the decay width for *ortho*-D_2HF (even rotation of D_2) calculated as a function of propagation time. It shows that the decay width is converged in less than 1-ps propagation while the computed VP lifetime is 1.5 ns. The joint product rotation distribution is shown in Fig. 5 for both para- and *ortho*-D_2HF where rotation quantum numbers of both fragments are determined simultaneously. These results are in good agreement with the TI calculation of Clary (25) and with experiment (53) as shown in Ref. 26.

C. TD Flux Method

Although TD golden-rule method works well for vibrational predissociation of weakly bound systems such as $HeCl_2$ (50) and D_2HF (26,27) that support only a few bound states, it can run into problems for more strongly bound systems that support many bound

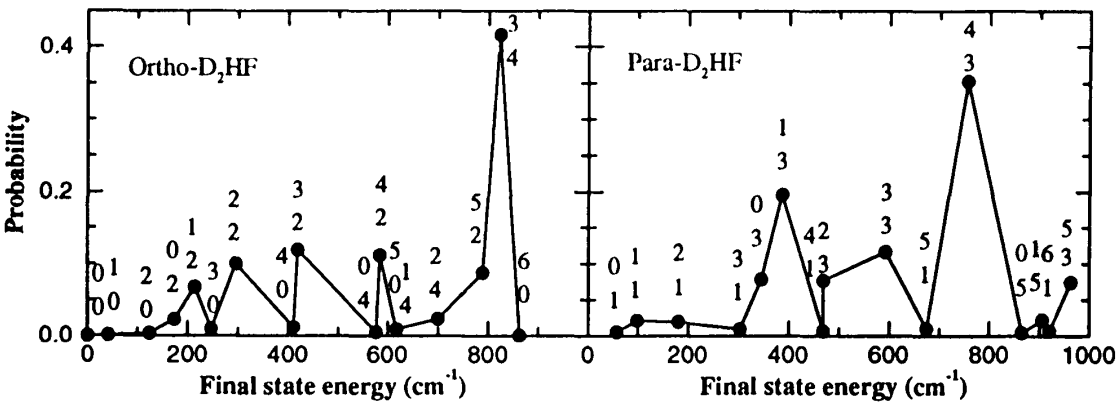

Figure 5 Rotation state distributions for *para*-$D_2HF(v = 1) \rightarrow D_2(v = 1, j_1) + HF(v = 0, j_2)$ as a function of propagation time. The upper and lower numbers refer to the rotational quantum numbers of HF and D_2, respectively. Time T is in atomic units.

states such as HF dimer. First, one needs to calculate all the bound states and project them out from the initial wave packet, which itself can be a very demanding task. Second, the wave packet propagation in a deep well system can run into numerical problems. Our study showed that direct application of the TD golden-rule method for VP of HF dimer does not produce very stable results. This is reflected in the calculated decay width being oscillatory around the correct value as a function of propagation time which results from a tiny fraction of the wavefunction that remains in the potential well region.

There are alternative approaches that could avoid this problem. One attractive method was recently proposed by Balint-Kurti and co-workers in which the photofragmentation amplitude is obtained by integrating over time the amplitude of the wave function at a large asymptotic distance (54). We recently presented a TD flux approach (35) which calculates the flux of the wavefunction instead of evaluating the overlap integral. The main advantage of the flux method or the amplitude method of Balint-Kurti et al. is that one does not need to project out the bound state components because they do not contribute to the flux or amplitude outside the interaction potential. In the following we present this TD method based on the flux formula. The discussion essentially follows that of Ref. 35.

1. Single Arrangement

To simplify the discussion, we first deal with single arrangement (nonreactive) case and further assume that χ has no bound state components. The final result can be easily generalized to the multiarrangement case and is also valid when bound states are present. Both cases will be discussed in subsequent subsections.

Under the above assumptions, $\psi_{nE}^{(-)}$ forms a complete basis set and we can expand $|\chi\rangle$ in this basis,

$$\begin{aligned} |\chi\rangle &= \sum_n \int_0^\infty dE\, |\psi_{nE}^{(-)}\rangle\langle\psi_{nE}^{(-)}|\chi\rangle \\ &= \sum_n \int_0^\infty dE\, |\psi_{nE}^{(-)}\rangle\, a_n(E) \end{aligned} \tag{61}$$

where $|\psi_{nE}^{(-)}\rangle$ is energy-normalized, i.e.,

$$\langle\psi_{mE'}^{(-)}|\psi_{nE}^{(-)}\rangle = \delta_{mn}\delta(E' - E) \tag{62}$$

and satisfies the incoming asymptotic boundary condition

$$\psi_{nE}^{(-)} \overset{R\to\infty}{\to} \sqrt{\frac{\mu}{2\pi\hbar^2}}\left[-\frac{e^{ik_nR}}{\sqrt{k_n}}|\phi_n\rangle + \sum_m S_{mn}^* \frac{e^{-ik_mR}}{\sqrt{k_m}}|\phi_m\rangle\right] \tag{63}$$

where $|\phi_n\rangle$ are channel basis functions and S_{mn} are S-matrix elements. What one needs to calculate here is the FC (Franck-Condon) factor $|a_n(E)|^2$. It is useful to point out that if χ is real, one can either use $\psi_{nE}^{(-)}$ or $\psi_{nE}^{(+)}$ equivalently to calculate the FC factor.

If we define a stationary state by

$$\begin{aligned} |A\rangle &= 2\pi\delta(E - H)|\chi\rangle \\ &= 2\pi \sum_n |\psi_{nE}^{(-)}\rangle\, a_n(E) \end{aligned} \tag{64}$$

and use the definition of the Green's function,

$$G^{\pm} = G^{P} \mp i\pi\delta(E - H) \tag{65}$$

we can write

$$|A\rangle = |A^{+}\rangle + |A^{-}\rangle \tag{66}$$

where

$$|A^{\pm}\rangle = \pm iG^{\pm}|\chi\rangle \tag{67}$$

Thus $|A^{+}\rangle$ has the outgoing boundary condition while $|A^{-}\rangle$ has the incoming boundary condition and they are called scattered waves. From Eqs. (63–67), the asymptotic boundary conditions for $|A^{\pm}\rangle$ are

$$A^{+}(R) \overset{R\to\infty}{\to} -\sqrt{\frac{2\pi\mu}{\hbar^2}} \sum_n \frac{e^{ik_nR}}{\sqrt{k_n}} |\phi_n\rangle\, a_n(E) \tag{68}$$

and

$$A^{-}(R) \overset{R\to\infty}{\to} \sqrt{\frac{2\pi\mu}{\hbar^2}} \sum_m \frac{e^{-ik_mR}}{\sqrt{k_m}} |\phi_m\rangle\, b_m(E) \tag{69}$$

where

$$b_m(E) = -\sum_n S^{*}_{mn} a_n(E) \tag{70}$$

If χ is real, A will also be real and the relation $A^{+}(R) = A^{-*}(R)$ must hold. Thus, the coefficients $a_n(E)$ and $b_n(E)$ must be complex conjugate to each other, i.e.,

$$a_n(E) = b^{*}_n(E) = -\sum_m S_{nm} a^{*}_m(E) \tag{71}$$

From Eq. (69), one can easily obtain the needed coefficients $a_n(E)$ at any given large distance R_∞ as

$$a_n(E) = -1\sqrt{\frac{\hbar^2 k_n}{2\pi\mu}}\, e^{-ik_nR_\infty} A^{+}_n(R_\infty) \tag{72}$$

where $A^{+}_n(R) = \langle R|\langle\phi_n|A^{-}\rangle$. If the asymptotic form of the scattering wavefunction is given by the spherical Bessel function or distorted wave instead of the plane wave $\exp(ikR)$ in Eq. (68), one should replace $\exp(-ikR)$ in Eq. (72) by the inverse of the appropriate asymptotic function. This result was derived before by Balint-Kurt et al. (54). Although Eq. (72) provides a convenient means for calculating the partial decay width in photofragmentation dynamics, the evaluation of $A^{+}_n(R)$ has to be carried out at large distance R_∞ in order for the plane wave representation to be valid for A^{+}_n. This will generally require the use of a large grid in numerical calculations especially when long-range potential is present. An attractive alternative approach, however, is to evaluate the flux of $|A^{+}\rangle$ which can be generally carried out at a shorter distance because it does not require any specific asymptotic representation for the stationary state $|A\rangle$ at distance R. The following is the flux treatment similar to that of Manolopoulos and Alexander (55).

From Eq. (67), it is easy to see that $|A^+\rangle$ satisfies the inhomogeneous Schrödinger equation

$$(E - H)|A^+\rangle = i|\chi\rangle \tag{73}$$

Since $\chi(R)$ is localized in the interaction region in photofragmentation, the wavefunction $A^+(R)$ satisfies the regular Schrödinger equation outside the region where χ is nonzero (outer region). Thus the flux is a constant in the outer region where χ is zero. The solution in the outer region is analogous to that of the homogeneous Schrödinger equation. This allows the calculation of the decay width to be carried out at a relatively shorter distance, and in addition, without the need to specify the asymptotic form of the wavefunction. For calculation of partial decay width using the flux method, one needs to select the surface for flux evaluation to lie outside the region beyond which inelastic scattering effect is negligible. The partial decay width can be calculated using the flux formula

$$\begin{aligned} |a_n(E)|^2 &= \frac{\hbar}{2\pi} \operatorname{Re}[A_n^{+*}(R)\hat{u}A_n^+(R)]|_{R=R_l} \\ &= \frac{\hbar^2}{2\pi\mu} \operatorname{Im}[A_n^{+*}(R) \frac{d}{dR} A_n^+(R)]|_{R=R_l} \end{aligned} \tag{74}$$

where R_l is chosen to lie outside the region of inelastic scattering. Equation (74) is valid as long as no inelastic transition is present at distance $R = R_l$ or larger even if the plane wave representation of the wavefunction is not valid in this region. Thus Eq. (74) is preferable in numerical computations. More detailed derivations and discussions of Eq. (74) can be found in Ref. 55 for photodissociation calculations by Manolopoulos and Alexander.

2. Multiarrangement

The main result—Eq. (74) from the previous section—is also valid in the multiarrangement case when properly generalized. Here we give brief derivations to generalize the results from the previous subsection to the multiarrangement case. Denote by index γ the arrangement channel, Eq. (61) can now be generalized to

$$\begin{aligned} |\chi\rangle &= \sum_{\gamma n} \int_0^\infty dE\, |\psi_{\gamma nE}^{(-)}\rangle\langle\psi_{\gamma nE}^{(-)}|\chi\rangle \\ &= \sum_{\gamma n} \int_0^\infty dE\, |\psi_{\gamma nE}^{(-)}\rangle\, a_{\gamma n}(E) \end{aligned} \tag{75}$$

where the completeness relation $\sum_{\gamma n}\int_0^\infty dE\, |\psi_{\gamma nE}^{(-)}\rangle\langle\psi_{\gamma nE}^{(-)}| = 1$ is used. The asymptotic condition for the scattering state now reads

$$\psi_{\gamma nE}^{(-)} \overset{R_\alpha\to\infty}{\to} \sqrt{\frac{\mu_\alpha}{2\pi\hbar^2}} \left[-\frac{e^{ik_{\alpha n}R_\gamma}}{\sqrt{k_{\alpha n}}} |\phi_{\alpha n}\rangle\, \delta_{\alpha\gamma} + \sum_m S^*_{\alpha m,\gamma n} \frac{e^{-ik_{\alpha m}R_\alpha}}{\sqrt{k_{\alpha m}}} |\phi_{\alpha m}\rangle \right] \tag{76}$$

Using the above relation, the asymptotic boundary condition for A^+ now reads

$$A^+ \overset{R_\alpha\to\infty}{\to} -\sqrt{\frac{2\pi\mu_\alpha}{\hbar^2}} \sum_n \frac{e^{ik_{\alpha n}R_\gamma}}{\sqrt{k_{\alpha n}}} |\phi_{\alpha n}\rangle a_{\alpha n}(E) \tag{77}$$

and

$$A^- \xrightarrow{R_\alpha \to \infty} \sqrt{\frac{2\pi\mu_\alpha}{\hbar^2}} \sum_m \frac{e^{-ik_{\alpha m}R_\gamma}}{\sqrt{k_{\alpha m}}} |\phi_{\alpha m}\rangle b_{\alpha m}(E) \tag{78}$$

where

$$b_{\alpha m}(E) = -\sum_{\gamma n} S^*_{\alpha m,\gamma n} a_{\gamma n}(E) \tag{79}$$

If χ is real, one must have

$$a_{\alpha m}(E) = b^*_{\alpha m}(E) = -\sum_{\gamma n} S_{\alpha m,\gamma n} a^*_{\gamma n}(E) \tag{80}$$

Equation (74) is now generalized to the multiarrangement case as

$$|a_{\alpha n}(E)|^2 = \frac{\hbar^2}{2\pi\mu_\alpha} \mathrm{Im}\left[A^{+*}_{\alpha n}(R) \frac{d}{dR} A^+_{\alpha n}(R)\right]\Bigg|_{R=R_{\alpha L}} \tag{81}$$

where μ_α is the reduced mass associate with the asymptotic translational motion in arrangement α.

3. Time→Energy Transform

The calculation of Eq. (74) or (81) for the partial decay width requires calculating the value of the stationary wavefunction $A^+(R)$ and its derivative $A^{+\prime}(R)$ at a given large distance R. One could, of course, directly solve the stationary Eq. (73) as pursued by Manolopoulos and Alexander (55). However, the computational time scales as N^3 with the number of channels when using stationary propagation method. An efficient alternative approach is to use the time-dependent wave packet approach. This can be accomplished through the following manipulation:

$$\begin{aligned} |A^+\rangle &= iG^+|\chi\rangle \\ &= \frac{1}{\hbar}\lim_{\epsilon\to 0}\int_0^\infty dt\, e^{i(E-H+i\epsilon)t/\hbar}|\chi\rangle \\ &= \frac{1}{\hbar}\int_0^\infty dt\, e^{iEt/\hbar}|\psi(t)\rangle \end{aligned} \tag{82}$$

where the time-dependent wave function is defined as

$$|\psi(t)\rangle = \lim_{\epsilon\to 0} e^{-i(H-i\epsilon)t/\hbar}|\chi\rangle \tag{83}$$

In principle and also in practice, the small quantity ϵ can be viewed as a legitimate means for introducing an optical potential that is used in practice to avoid the artificial boundary reflection. Such a view is promoted by Seideman and Miller (56). Thus $A^+_{\alpha n}(R_L)$ can be calculated by a half Fourier transform on the time-dependent wave function evaluated at a large distance R_L,

$$A^+_{\alpha n}(R_L) = \frac{1}{\hbar}\int_0^\infty dt\, e^{iEt/\hbar}\,\langle\phi_{\alpha n}|\psi(t, R_L)\rangle \tag{84}$$

and similarly for the derivative $A'^{+}_{\gamma n}(R_L)$

$$A'^{+}_{\alpha n}(R_L) = \frac{1}{\hbar}\int_0^\infty dt\, e^{iEt/\hbar}\langle\phi_{\alpha n}|\psi'(t, R_L)\rangle \tag{85}$$

Equations (81), (84), and (85) are the final working formulae for the dynamics calculation of photofragmentation. It involves a standard wave packet propagation in Eq. (83) and a half Fourier transform in Eq. (84) and (85) at a fixed large distance R_L.

So far we have assumed that χ has no bound state components or they have been projected out from χ if any. This is actually not necessary as long as the distance R_L is chosen to be large enough such that the bound state components of χ vanish for $R \geq R_L$. The flux calculation can be carried out without the need to project out bound state components from χ.

4. VP Lifetime of HFDF

The flux method described in the previous section has been applied to the VP dynamics study of HFDF to obtain VP lifetime from IR excitation of both HF and DF vibrations. For each excited monomer (HF or DF), there are two isomers with quite different vibrational coupling strengths depending on whether the H (or D) is "free" or "bound." It is well known that the "bound" H (or D) excitation gives rise to stronger vibrational coupling than the "free" H (or D) excitation, so we expect that the complex with "bound" H (or D) excitation has a shorter lifetime than that with "free" H (or D) excitation. Table 1 lists the lifetimes for four different combinations: HF(v = 1)–DF ("free" H excitation), HF–DF(v = 1) ("bound" D excitation), DF–HF(v = 1) ("bound" H excitation), and DF(v = 1)–HF ("free" D excitation) together with experimental results. For HF excited complex, the theoretical lifetime for "free" H excitation is 40 times longer than that for "bound" H excitation. For DF excited complex, the theoretical lifetime for "free" D excitation is about 2.5 times longer than that for "bound" D excitation. The agreement between theory and experiment is reasonably good, but the SBSQDE PES of Quack and Suhm (57) used in the quantum calculation needs further improvement in order to obtain better agreement with experiment.

Table 1 Vibrational Predissociation Lifetime for HFDF and HFHF (ns)[a]

Species	E_{ex}	E_R	τ_{exp}	τ_{theo}
HF–*DF	2838[b]	1695	1.3[b]	7.6
*DF–HF	2882[b]	1804	5.5[b]	19
DF–*HF	3868	2789	0.57[b]	4.0
*HF–DF	3927	2785	19.4[b,c]	160
HF–*HF$^{\pm}$	3868	2811	0.48[d]	3.0[e]
*HF–HF^{+}	3931	2874	24.8[d]	36.6[e]
*HF–HF^{-}	3931	2874	16.7[d]	42.0[e]

[a] E_{ex} is the excitation energy and E_R is the excess energy for dissociation, all in units of cm^{-1}.
[b] From Ref. 58.
[c] A strong J-dependence is observed for this transition and the lifetime ranges from 4.8 to 80 ns. For J = 0, the experimental lifetime is 19.4 ns.
[d] From Ref. 59.
[e] From Refs. 33 and 34.

IV. GAS-PHASE BIMOLECULAR REACTION DYNAMICS

A formidable challenge to the theory of quantum reactive scattering is to develop accurate yet practical computational methodologies to tackle chemical reactions beyond triatomic systems. One approach is to resort to the so-called reduced-dimensionality approximations to reduce the system's degree of freedom and employ the standard scattering method to treat the reduced system with only a few effective degrees of freedom (60–71). This treatment was developed by Brook and Clary for the diatom-diatom reaction H_2 + CN using the rotating bond approximation (RBA) (60), in which one bending angle and two radial coordinates are explicitly treated. Sun and Bowman and co-workers have developed an adiabatic bend approximation (ABA) to treat diatom-diatom reactions (61), which reduces the effective degrees of the system to three radial coordinates. These approximation methods are capable of producing some excellent results with a relatively small amount of computational effort when some averaged dynamical quantities are desired. There are, however, uncertainties in the dynamical results associated with these approximations, including the correct zero-point energy shifting and the lack of angular momentum coupling. Also, due to the drastic dimensionality reduction, the ABA method (61) does not provide rotation state-selected dynamics information. Recently, Echave and Clary (72) and Thompson and Miller (73) included four degrees of freedom for the H_2 + OH reaction in a planar configuration. Similar 4D planar calculation was recently reported by Goldfield et al. (74) for the more difficult HO + CO reaction. In addition, a mixed quantum/classical treatment has been presented for the H_2 + OH reactions by Balakrishnan and Billing (75). A recent review on the reduced dimensionality calculation for four-atom reactions was given by Clary (76).

Ideally, one wishes to develop accurate computational methods to study polyatomic reactions without resorting to drastic dimensionality reductions. In this regard, progress has recently been reported for rigorous quantum dynamics calculations for the four-atom reaction H_2 + OH by Zhang and Zhang (77–80), Manthe et al. (81,82), and Neuhauser (83). These dynamics studies are rigorous in the sense that the accuracy of the calculation is only limited by the accuracy of the potential energy surface. Since the first successful TD calculation for the collinear H + H_2 reaction was reported by McCullough and Wyatt (84) in 1971, tremendous progress has been made in the TD approach to gas-phase reactions (85). In particular, recent successful quantum dynamics calculations for polyatomic reactions with more than three degrees of freedom (26,27,29,31,32,35,77–80,83) have established the TD approach as an extremely important computational approach for studying complex chemical dynamics problems involving more than three degrees of freedom. The favorable computational scaling of the TD approach makes TD methods viable for some large-scale computational tasks that are difficult to handle using standard TI methods in reaction dynamics. We present in the following several examples of TD applications.

A. Atom-Diatom Reactive Scattering

We present in this subsection the TD treatment for calculating initial state-specific total reaction probabilities for the atom-diatom reaction, H + O_2 → HO + O. This is a particularly important combustion reaction (86) and it presents a real challenge to theoretical calculations because the PES has a deep well of more than 2.3 eV which supports many bound states and narrow resonances. Much progress has been made in the past few years by Neuhauser et al. in TD calculation of atom-diatom reactive scattering

(87–89). The following is a brief discussion of our TD treatment for a general atom-diatom reactive scattering system.

The Hamiltonian expressed in the reactant Jacobi coordinates for a given total angular momentum J can be written as

$$H = -\frac{\hbar^2}{2\mu_R}\frac{\partial^2}{\partial R^2} + \frac{(\vec{J} - \vec{j})^2}{2\mu_R R^2} + \frac{\vec{j}^{\,2}}{2\mu_r r^2} + V(\vec{r}, \vec{R}) + h(r) \tag{86}$$

where μ_R is the reduced mass between the center-of-mass of the atom and diatom, $\vec{J}$ the total angular momentum operator, $\vec{j}$ the rotational angular momentum operator of O_2, and μ_r the reduced mass of the diatom. The diatomic reference Hamiltonian $h(r)$ is defined as

$$h(r) = -\frac{\hbar^2}{2\mu_r}\frac{\partial^2}{\partial r^2} + V_r(r) \tag{87}$$

where V_r is a diatomic reference potential.

The time-dependent wavefunction satisfying the Schrödinger equation $i\hbar(\partial/\partial t)\Psi(t) = H\Psi(t)$ can be expanded in terms of BF (body-fixed) rovibrational eigenfunctions defined using the reactant Jacobi coordinates as

$$\Psi^{JM\epsilon}_{v_0 j_0 K_0}(\vec{R}, \vec{r}, t) = \sum_{n,v,j,K} F^{JM\epsilon}_{nvjK,v_0 j_0 K_0}(t) u^v_n(R)\phi_v(r) Y^{JM\epsilon}_{jK}(\hat{R}, \hat{r}) \tag{88}$$

where n is the translational basis label, (v_0, j_0, K_0) denotes the initial rovibrational state, and ϵ is the parity of the system defined as $\epsilon = (-1)^{j+L}$ with L being the orbital angular momentum quantum number. Since it is well known that the closed-channel components of the wavefunction are essentially zero in the asymptotic region, we only need to include "open" vibrational channels in the asymptotic region. However, both "open" and "closed" vibrational channels are needed in the interaction region. A simple way to implement this idea is to employ a nondirect product basis for the R degree of freedom and to split the whole space into two regions, the asymptotic region and the interaction region specified by R_4 and R_2, respectively (77–79). The normalized translational basis function is then defined as

$$u^{v_1}_n(R) = \begin{cases} \sqrt{\dfrac{2}{R_4 - R_1}} \sin\dfrac{n\pi(R - R_1)}{R_4 - R_1} & v_1 \le v_{\text{asy}} \\ \sqrt{\dfrac{2}{R_2 - R_1}} \sin\dfrac{n\pi(R - R_1)}{R_2 - R_1} & v_1 > v_{\text{asy}} \end{cases} \tag{89}$$

where v_{asy} is chosen to be the number of energetically open vibrational channels plus a few closed vibrational channels of the reactant diatom, and $\phi_v(r)$ is the eigenfunction of $h(r)$ in Eq. (87). Similar space-partitioning schemes were developed earlier for atom-diatom reactive scattering by Neuhauser et al. (24,90) and for gas-surface reaction by Mowrey (91). In principle, one can use different numbers of translation basis functions for each vibrational function which could result in even greater computational savings (92).

The coupled angular basis function $Y_{jK}^{JM\epsilon}$ in Eq. (88) is the BF total angular momentum eigenfunction which can be written as

$$Y_{jK}^{JM\epsilon} = (1 + \delta_{K0})^{-1/2} \sqrt{\frac{2J+1}{8\pi}} [D_{K,M}^{j} + \epsilon(-1)^{J+K} D_{-K,M}^{J}] y_{jK} \tag{90}$$

where $D_{K,M}^{J}(\Theta\Phi\Psi)$ is the Wigner rotation matrix (48) with three Euler angles $(\Theta\Phi\Psi)$ and y_{jK} are spherical harmonics.

The split-operator method of (9) was used to carry out the wave packet propagation where the reference Hamiltonian H_0 and the potential operator are defined as

$$H_0 = -\frac{\hbar^2}{2\mu_R}\frac{\partial^2}{\partial R^2} + h(r) \tag{91}$$

and

$$U = \frac{(\vec{J} - \vec{j})^2}{2\mu_R R^2} + \frac{\vec{j}^{\,2}}{2\mu_r r^2} + V(\vec{R}, \vec{r}) \tag{92}$$

The initial wave function is chosen as the product of a specific rovibrational eigenfunction and a localized translational wave packet

$$\Psi_i(0) = \varphi_{k0}(R)\phi_{v_0j_0}(r)Y_{j_0K_0}^{JM\epsilon}(\hat{R}, \hat{r}) \tag{93}$$

where the wave packet $\varphi_{k_0}(R)$ is chosen to be a standard Gaussian function:

$$\varphi_{k0}(R) = \left(\frac{1}{\pi\delta^2}\right)^{1/4} \exp\left[-\frac{(R - R_0)^2}{2\delta^2}\right] e^{-ik_0R} \tag{94}$$

The exact rovibrational function $\phi_{v_0j_0}(r)$ of the diatom is expanded in terms of the reference vibrational functions $\phi_v(r)$ to generate the coefficient vector of the wavefunction at $t = 0$.

If ψ_{iE}^{+} denotes the time-independent (TI) full scattering wave function where i and E are, respectively, initial state and energy labels, the total reaction probability from an initial state i can be obtained by the formula

$$P_i^R(E) = \sum_f |S_{fi}^R|^2 = \langle \psi_{iE}^{+} | \hat{F} | \psi_{iE}^{+} \rangle \tag{95}$$

In the above equation, $\hat{F}$ is the flux operator defined as

$$\hat{F} = \frac{1}{2}[\delta(\hat{s} - s_0)\hat{v}_s + \hat{v}_s\delta(\hat{s} - s_0)] \tag{96}$$

where s is the coordinate perpendicular to a surface in configuration space located at s_0 for flux evaluation, and $\hat{v}_s$ is the velocity operator corresponding to the coordinate s. The scattering wavefunction ψ_{iE}^{+} has the asymptotic form in the product arrangement space

$$\psi_{iE}^{+} \overset{R_f \to \infty}{\to} \sum_f S_{fi}^R \frac{e^{ik_fR_f}}{\sqrt{v_f}} \phi_f \tag{97}$$

and is normalized as $\langle\psi_{iE}^{+}|\psi_{iE'}^{+}\rangle = 2\pi\hbar\delta(E - E')$. Using (96), Eq. (95) can be simplified to yield

$$P_i^R(E) = \frac{\hbar}{\mu_s} \mathrm{Im}[\langle\psi_{iE}^{+}|\delta(s - s_0) \frac{\partial}{\partial s} |\psi_{iE}^{+}\rangle] \tag{98}$$

where μ_s is the proper mass for the coordinate s. We have chosen the reactive diatomic coordinate r to be the s coordinate and the corresponding μ_s is just the reduced mass of the reactive diatom.

Equation (95) gives the total reaction probability from a given initial state i. This quantity is easier to converge then individual reaction probabilities because one does not have to place the dividing surface for flux calculation out to the asymptotic product space. Therefore one can use a smaller numerical grid just enough to cover the reaction zone to extract the total reactive flux. In principle, the dividing surface chosen at the "transition state" will give converged result within the shortest propagation time. One could also obtain any individual reaction probability by projecting out the specific product state ϕ_f from Eq. (97) before evaluating the flux or to extract individual S-matrix element from Eq. (97). Of course, this will involve more complicated numerical calculations and require more computational resources.

The TI wave function ψ_{iE}^{+} can be obtained from the wave packet propagation by a Fourier transform. Since the TD wave function can be expanded in terms of the TI wave function which forms a complete set

$$|\psi_i(t)\rangle = e^{-i/\hbar Ht}\psi_i(0) = \frac{1}{2\pi\hbar} \int dE\, e^{-i/\hbar Et}|\psi_{iE}^{+}\rangle\, a_i(E) \tag{99}$$

the TI scattering wavefunction can be obtained by performing a Fourier transform

$$|\psi_{iE}^{+}\rangle = \frac{1}{a_i(E)} \int_{-\infty}^{\infty} e^{(i/\hbar)(E-H)t}|\psi_i(0)\rangle\, dt \tag{100}$$

The coefficient $a_i(E)$ can be easily evaluated from the free asymptotic scattering function as follows:

$$\begin{aligned} a_i(E) &= \langle 4_{iE}^{+}|\Psi_i(0)\rangle \\ &= \lim_{t\to-\infty} \langle\phi_{iE}|e^{i/\hbar H_0 t}\, e^{-i/\hbar Ht}|\varphi_i(0)\rangle \\ &= \langle\phi_{iE}|\varphi_i(0)\rangle \end{aligned} \tag{101}$$

where the free function has the same normalization as the full scattering wavefunction ψ_{iE}^{+}, namely, $\langle\phi_{iE}|\phi_{iE'}\rangle = 2\pi\hbar\delta(E - E')$.

Finally, we should mention that the time-dependent wavefunction is absorbed at the edges of the grid to avoid boundary reflections. The absorbing potential was employed in an early TD study for laser-induced dissociation by Leforestier and Wyatt (22) and for resonance studies by Jolicard and Austin (23). The use of absorbing potentials has recently been fruitfully explored and made extremely popular in quantum reactive scattering by Baer and co-workers (24,88,89). The introduction of an optical potential is straightforward using the split-operator method for time propagation which is equivalent to multiplication of the wavefunction by a decaying function $F_{\mathrm{abs}} = \exp(-(1/\hbar)V_{\mathrm{abs}}\Delta)$, where V_{abs} is the optical or absorbing potential.

1. $H + O_2 \rightarrow HO + O$

The TD method is applied to the $H + O_2$ reaction [93] using the DMBE IV PES of Pastrana et al. (94). Fig. 6 shows the total reaction probabilities for $H + O_2(v = 0, j = 1)$ at four different propagation times. As shown in Fig. 6, the reaction probabilities at high energies are converged with a relatively short propagation, while for low energies, the resonance structures grow more pronounced and more peaks appear as propagation time increases. Each curve in Fig. 6 contains reaction probabilities for several hundred energies that are obtained from a single wave packet propagation. Quantum reaction probabilities for this reaction have also been calculated using TI methods by Pack et al. (95) and cumulative reaction probabilities by Leforestier and Miller (96). The detailed aspects of the TD calculation for the $H + O_2$ reaction can be found in Ref. 93.

B. Diatom-Diatom Reactive Scattering

In this subsection, we show in detail the TD treatment for a general diatom-diatom reaction in full (6D) dimensions. We choose to present the treatment in 6D although very accurate results can be obtained by using the rigid-bond 5D (RB5D) treatment, or essentially exact results can be obtained using the potential-averaged 5D (PA5D) treatment. Both 5D treatments can result in significant savings with little loss of accuracy. These 5D treatments can be considered as special cases of the following 6D treatment.

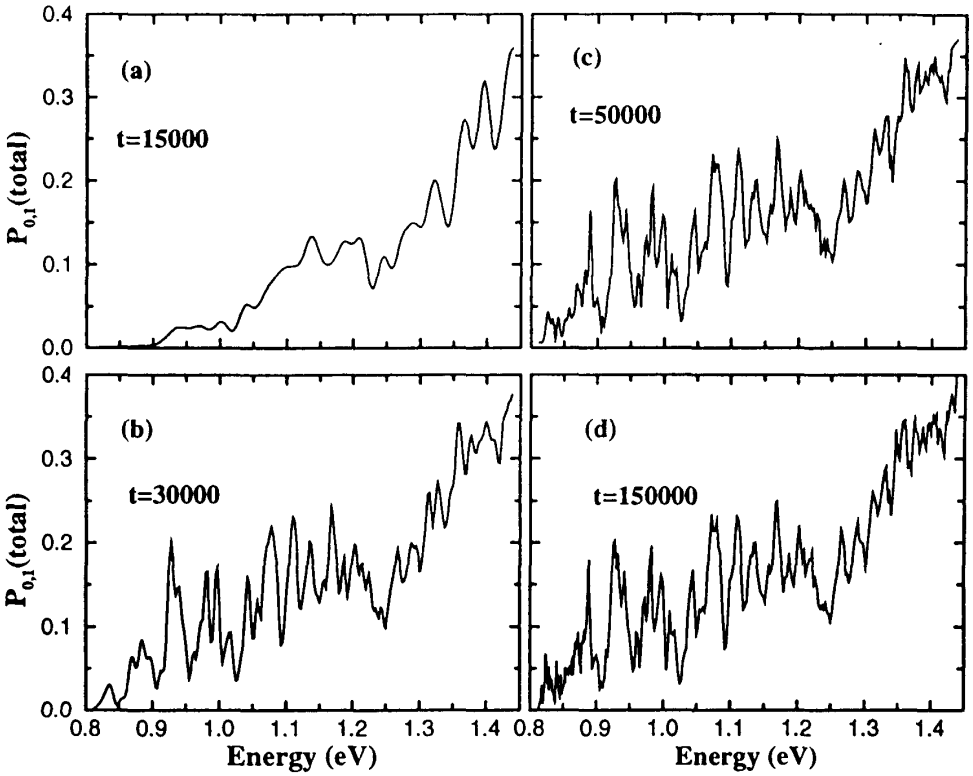

Figure 6 Total reaction probabilities from the ground state $H + O_2(v = 0, j = 1)$ for total angular momentum J = 0 as a function of scattering energy computed at different propagation times t: (a) t = 15,000; (b) t = 30,000; (c) t = 50,000; and (d) t = 150,000 a.u.

1. Full 6D Treatment

The theory presented here is for calculating the initial state-specific total reaction probabilities and cross sections for a diatom-diatom reaction AB + CD → A + BCD in full dimensions. The Hamiltonian expressed in the reactant Jacobi coordinates shown in Fig. 1 for a given total angular momentum J can be written as

$$H = -\frac{\hbar^2}{2\mu}\frac{\partial^2}{\partial R^2} + \frac{(\vec{J} - \vec{j}_{12})^2}{2\mu R^2} + \frac{\vec{j}_1^{\,2}}{2\mu_1 r_1^2} + \frac{\vec{j}_2^{\,2}}{2\mu_2 r_2^2}$$

$$+ V(\vec{r}_1, \vec{r}_2, \vec{R}) + h_1(r_1) + h_2(r_2) \tag{102}$$

where μ is the reduced mass between the center-of-mass of AB and CD, $\vec{J}$ is the total angular momentum operator, $\vec{j}_1$ and $\vec{j}_2$ are the rotational angular momentum operators of AB and CD, which are coupled to form $\vec{j}_{12}$. The reference diatomic vibrational Hamiltonian $h_i(r_i)$ $(i = 1,2)$ is defined as

$$h_i(r_i) = -\frac{\hbar^2}{2\mu_i}\frac{\partial^2}{\partial r_i^2} + V_i(r_i) \tag{103}$$

where V_i is a reference diatomic vibrational potential.

The time-dependent wavefunction satisfying the Schrödinger equation $i\hbar(\partial/\partial t)\Psi(t) = H\Psi(t)$ can be expanded in terms of the BF (body-fixed) rovibrational eigenfunctions defined in terms of the reactant Jacobi coordinates as

$$\Psi^{JM\epsilon}_{v_0 j_0 K_0}(\vec{R}, \vec{r}_1, \vec{r}_2, t) = \sum_{n,v,j,K} F^{JM\epsilon}_{nvjK,v_0 j_0 K_0}(t) u_n^{v_1}(R)\phi_{v_1}(r_1)\phi_{v_2}(r_2)Y^{JM\epsilon}_{jK}(\hat{R}, \hat{r}_1, \hat{r}_2) \tag{104}$$

where n is the translational basis label, v denotes (v_1, v_2), j denotes (j_1, j_2, j_{12}), $(v_0, j_0 k_0)$ denotes the initial rovibrational state, and ε is the parity of the system defined as $\epsilon = (-1)^{j_1+j_2+L}$ with L being the orbital angular momentum. The translational function $u_n^{v_1}(R)$ is defined as in Eq. (89) and the vibration eigenfunction $\phi_{v_i}(r_i)$ for AB or CD satisfies the equation

$$h_i(r_i)\phi_{v_i}(r_i) = \epsilon_{v_i}\phi_{v_i}(r_i) \tag{105}$$

where i refers to the reactive AB $(i = 1)$ or nonreactive CD $(i = 2)$. In particular, the reactive AB diatomic reference potential is defined to allow the vibrational function $\phi_{v_1}(r_1)$ to span a large interatomic distance r_1 to allow the reaction to occur. The reference potential $V_2(r_2)$ for the nonreactive CD bond is chosen to be the asymptotic diatomic potential of CD. In general, many more AB vibration functions ϕ_{v_1} are needed in the basis expansion than that of the nonreactive diatom CD.

The $Y^{JM\epsilon}_{jK}$ in Eq. (104) is the BF total angular momentum eigenfunction, which can be written as (79)

$$Y^{JM\epsilon}_{jK} = (1 + \delta_{K0})^{-1/2}\sqrt{\frac{2J+1}{8\pi}}\,[D^J_{K,M}Y^{j_{12}K}_{j_1 j_2} + \epsilon(-1)^{j_1+j_2+j_{12}+J}D^J_{-K,M}Y^{j_{12}-K}_{j_1 j_2}] \tag{106}$$

where $D^J_{K,M}(\Theta\Phi\Psi)$ is the Wigner rotation matrix (48) with three Euler angles $(\Theta\Phi\Psi)$ and $Y^{j_{12}K}_{j_1 j_2}$ is the angular momentum eigenfunction of j_{12} (79):

$$Y^{j_{12}K}_{j_1 j_2} = \sum_{m_1} \langle j_1 m_1 j_2 K - m_1 | j_{12} K\rangle\, y_{j_1 m_1}(\theta_1, 0) y_{j_2 K - m_1}(\theta_2, \phi) \tag{107}$$

where y_{jm} are spherical harmonics. Note in Eq. (106) the restriction $\epsilon(-1)^{j_1+j_2+j_{12}+J} = 1$ for the case of $K = 0$.

The potential matrix elements in the angular momentum basis $Y_{jK}^{JM\epsilon}$ for any fixed (R, r_1, r_2) can be calculated as

$$\begin{aligned}\langle Y_{jK}^{JM\epsilon}|V(R, r_1, r_2, \theta_1, \theta_2, \phi)|Y_{j'K'}^{JM\epsilon}\rangle &= 2\pi\delta_{KK'}\langle Y_{j_1j_2}^{j_{12}K}|V|Y_{j_1'j_2'}^{j_{12}K}\rangle \\ &= \delta_{KK'}\sum_{m_1,m_1'}\langle j_1m_1j_2K - m_1|j_{12}K\rangle\langle j_1'm_1'j_2'K - m_1'|j_{12}'K\rangle \\ &\times \int_0^\pi \sin\theta_1\, d\theta_1 \int_0^\pi \sin\theta_2\, d\theta_2\, P_{j_1m_1}(\theta_1)P_{j_2K-m_1}(\theta_2) \\ &\times V^{m_1,m_1'}(R, r_1, r_2, \theta_1, \theta_2)P_{j_1'm_1'}(\theta_1)P_{j_2'K-m_1'}(\theta_2) \end{aligned} \tag{108}$$

where

$$V^{m_1,m_1'}(R, r_1, r_2, \theta_1, \theta_2) = \frac{1}{\pi}\int_0^\pi d\phi\, \cos[(m_1 - m_1')\phi]V(R, r_1, r_2, \theta_1, \theta_2, \phi) \tag{109}$$

and $P_{jm}(\theta) = \sqrt{2\pi}y_{j,m}(\theta, 0)$. The centrifugal potential, which is not diagonal in the BF representation, is given by

$$\begin{aligned}\frac{\hbar^2}{2\mu R^2}\langle Y_{jK}^{JM\epsilon}|(\vec{J} - \vec{j}_{12})^2|Y_{j'K'}^{JM\epsilon}\rangle &= \frac{\hbar^2}{2\mu R^2}\delta_{jj'}\{[J(J+1) + j_{12}(j_{12}+1) - 2K^2]\delta_{KK'} \\ &- \lambda_{jK}^{+}\lambda_{j_{12}K}^{+}(1+\delta_{K0})^{1/2}\delta_{K+1,K'} - \lambda_{jK}^{-}\lambda_{j_{12}K}^{-}(1+\delta_{K1})^{1/2}\delta_{K-1,K'}\} \end{aligned} \tag{110}$$

and the quantity λ is defined as $\lambda_{AB}^{\pm} = [A(A+1) - B(B \pm 1)]^{1/2}$ (111)

The split-operator method is again employed to carry out the wave packet propagation,

$$\Psi^{JM\epsilon}(\vec{R}, \vec{r}_1, \vec{r}_2, t + \Delta) = e^{-iH_0\Delta/2}e^{-iU\Delta}e^{-iH_0\Delta/2}\Psi^{JM\epsilon}(\vec{R}, \vec{r}_1, \vec{r}_2, t) \tag{112}$$

where the reference Hamiltonian H_0 is defined as

$$H_0 = -\frac{\hbar^2}{2\mu}\frac{\partial^2}{\partial R^2} + h_1(r_1) + h_2(r_2) \tag{113}$$

From (102) the effective potential operator U is given by

$$U = \frac{(\vec{J} - \vec{j}_{12})^2}{2\mu R^2} + \frac{\vec{j}_1^{\,2}}{2\mu_1 r_1^2} + \frac{\vec{j}_2^{\,2}}{2\mu_2 r_2^2} + V(\vec{r}_1, \vec{r}_2, \vec{R}) \tag{114}$$

The matrix version of Eq. (112) for the expansion coefficient vector F is then given by

$$\mathbf{F}(t + \Delta) = \exp\left(-\frac{i\mathbf{H}_0\Delta}{2}\right)\mathbf{T}\,\exp(-i\mathbf{U}\Delta)\mathbf{T}\,\exp\left(-\frac{i\mathbf{H}_0\Delta}{2}\right)\mathbf{F}(t) \tag{115}$$

where $\mathbf{H}_0$ is the diagonal matrix defined as

$$[\mathbf{H}_0]_{nvjK,n'v'j'K'} = \delta_{nvjK,n'v'j'K'}(\epsilon_n^{v_1} + \epsilon_{v_1} + \epsilon_{v_2}) \tag{116}$$

where ϵ_v is obtained from solving (105) and $\epsilon_n^{v_1}$ is given by (cf. (89))

$$\epsilon_n^{v_1} = \begin{cases} \dfrac{\hbar^2}{2\mu}\left(\dfrac{n\pi}{R_4 - R_1}\right)^2 & v_1 \le v_{\text{asy}} \\ \dfrac{\hbar^2}{2\mu}\left(\dfrac{n\pi}{R_2 - R_1}\right)^2 & v_1 > v_{\text{asy}} \end{cases} \tag{117}$$

The effective potential matrix U is given by

$$[\mathbf{U}]_{lmnjK,l'm'n'j'K'} = \delta_{lmn,l'm'n'}\left\{\mathbf{V}_{jK,j'K'}(R_l, r_{1m}, r_{2n}) + \frac{\hbar^2}{2\mu R_l^2}\langle Y_{jK}^{JM\epsilon}|(\vec{-}\ \vec{j}_{12})^2|Y_{j'K'}^{JM\epsilon}\rangle + \left[\frac{\hbar^2 j_1(j_1+1)}{2\mu_1 r_{1m}^2} + \frac{\hbar^2 j_2(j_2+1)}{2\mu_2 r_{2n}^2}\right]\delta_{jK,j'K'}\right\} \tag{118}$$

where (R_l, r_{1m}, r_{2n}) is any given DVR point defined with respect to the translation and vibration basis functions of Eqs. (89) and (105). To simplify the notation, we dropped labels $JM\epsilon$ and $v_0 j_0 K_0$ with the understanding that all the equations hold for a given set of these labels.

The operation of the matrix **T** on the wave vector **F** in Eq. (115) is defined as

$$[\mathbf{TF}]_{lmnjK} = \sum_v \mathbf{C}_{n,v_2}\mathbf{B}_{m,v_1}\sum_i \mathbf{A}_{l,i}^{v_1}\mathbf{F}_{ivj} \tag{119}$$

where **A**, **B**, and **C** are orthogonal matrices that carry out the transformation between basis and DVR representations, i.e.,

$$\mathbf{A}_{l,i}^{v_1} = \langle R_l|u_i^{v_1}\rangle \tag{120}$$

$$\mathbf{B}_{m,v_1} = \langle r_{1m}|\phi_{v_1}\rangle \tag{121}$$

$$\mathbf{C}_{n,v_2} = \langle r_{2n}|\phi_{v_2}\rangle \tag{122}$$

The exponential operator $e^{-i\mathbf{U}\Delta}$ is handled by diagonalizing the matrix **U** at a given DVR point (R_m, r_{1n}, r_{2l}). We do not elaborate on how to generate DVR representations in this paper but refer the readers to Refs. 15, 16 for detailed discussions on various aspects of the DVR representation and on standard methods of generating DVR points and transformation matrix between basis and DVR representations.

The basic procedure for carrying out the wave packet propagation can be briefly summarized in three steps. (1) Generate radial basis functions $(u_n^{v_1}(R), \phi_{v_1}(r_1), \phi_{v_2}(r_2))$ in Eq. (104). (2) Generate DVR basis set $(|R_l\rangle, |r_{1m}\rangle, |r_{2n}\rangle)$ as well as transformation matrices (**A**, **B**, **C**) from a given radial basis $(|u_n^{v_1}\rangle, |\phi_{v_1}\rangle, |\phi_{v_2}\rangle)$. (3) Diagonalize the potential matrix U at all the DVR points (R_l, r_{1m}, r_{2n}) and carry out the propagation in Eq. (115). The initial wavefunction is chosen as the product of a specific rovibrational eigenfunction and a localized translational wave packet

$$\Psi_i(0) = \varphi_{k_0}(R)\phi_{v_{10}j_{10}}(r_1)\phi_{v_{20}j_{20}}(r_2)Y_{j_{10}j_{20}j_{120}K_0}^{JM\epsilon}(\hat{R}, \hat{r}_1, \hat{r}_2) \tag{123}$$

where the wave packet $\varphi_{k_0}(R)$ is chosen to be a standard Gaussian function in Eq. (94).

Once the initial state-selected total reaction probability is obtained from Eq. (95), one can calculate the integral cross section and thermal rate constant using standard

definitions. The integral cross section is obtained by summing the reaction probabilities $P^{J\epsilon}_{v_0 j_0 K_0}$ over all the partial waves (total angular momentum J):

$$\sigma_{v_0 j_0}(E) = \frac{1}{(2j_1 + 1)(2j_2 + 1)} \frac{\pi}{k^2} \sum_{J\epsilon K_0} (2J + 1) P^{J\epsilon}_{v_0 j_0 K_0}(E) \tag{124}$$

where ϵ is the parity and K_0 denotes all the initial rotation projection quantum numbers. Since the exact close-coupling calculation for $J > 0$ is extremely expensive computationally, one can employ the CS approximation (97,98) for $J > 0$ calculations in which the couplings between different K states in Eq. (110) are neglected.

The initial state-specific thermal rate constant is given by thermal averaging the kinetic energy of the flux as

$$\begin{aligned} r_{v_0 j_0}(T) &= \langle |\sigma_{v_0 j_0} v_0| \rangle \\ &= \left(\frac{8kT}{\pi\mu}\right)^{1/2} (kT)^{-2} \int_0^\infty dE_t \, E_t \exp\left(-\frac{E_t}{kT}\right) \sigma_{v_0 j_0}(E_t) \end{aligned} \tag{125}$$

where E_t is the translational energy. For the H_2 + OH reaction, an extra factor of 1/2 is needed in Eq. (125) to account for electron spin degeneracy of OH (99).

2. Rigid-Bond 5D Treatment

In this approximate treatment, one simply freezes the nonreactive or spectator bond. The 6D Hamiltonian in this case becomes the effective 5D Hamiltonian by eliminating the kinetic energy operator for the r_2 coordinate and fixed the r_2 distance in the potential energy surface. The 5D potential is simply given by

$$U_{v_2}(\vec{r}_1, \hat{r}_2, \vec{R}) = U(\vec{r}_1, \hat{r}_2, \vec{R} | r_2 = r_0) \tag{126}$$

where r_0 is either the equilibrium or averaged position of the r_2 coordinate. This treatment should be a good approximation when the influence of the nonreactive CD vibration on reaction is negligible. Of course, the accuracy of this treatment will be system-dependent. In general, the tighter the CD bond, the better the rigid bond approximation works.

3. Potential-Averaged 5D Treatment

In the PA5D treatment, one essentially treats the nonreactive bond vibration diabatically which is equivalent to including only one vibrational state in the 6D basis function expansion described previously. The net result of this treatment is a 5D Hamiltonian in which the effective 5D potential energy surface is given by averaging the 6D potential surface over the vibrational coordinate of the spectator bond. This is done by the simple procedure

$$U_{v_2}(\vec{r}_1, \hat{r}_2, \vec{R}) = \langle U \rangle_{v_2} = \langle \phi_{v_2} | U(\vec{r}_1, \vec{r}_2, \vec{R}) | \phi_{v_2} \rangle \tag{127}$$

The PA5D treatment yields essentially the same result as that given by the exact 6D treatment for the H_2 + OH reaction.

If the r_2-dependence of U in Eq. (127) is approximated by a linear expansion about the average position r_0, the PA5D potential given by (127) will be equivalent to the RB 5D potential of (126). Therefore the difference in the result of two treatments indicate the importance of the higher-order r_2-dependence of the potential.

4. $H_2 + OH \rightarrow H_2O + H$

We show in this subsection some results for the H_2 + OH reaction. First, the results using all three different treatments described above are compared in Fig. 7 for the reagent at ground state. The difference between these results is very small, and in particular, the PA5D result is essentially identical to the full 6D result within the plotting accuracy. Thus one can use the PA5D treatment for the nonreactive or spectator bond and effectively reduces the 6D dynamics problem to 5D. We note in Fig. 7 a small but sharp resonance at very low energy, which is believed to be the artifact of the Schatz-Elgersma PES (99,100) which is slightly modified by Clary (62). This artifact has negligible influence for reaction involving ground vibrational species of H_2. The reaction probability is greatly enhanced by the vibrational excitation of $H_2(v = 1)$ as shown in Fig. 8. Here, however, the resonance artifact is much more pronounced than in the ground state and it significantly influences the reaction cross section and the rate constant for reactions involving vibrationally excited H_2. The cross sections from both ground and excited vibrations of the reagents are shown in Fig. 9. The initial state-selected rate constants are also shown in Fig. 10. More detailed results can be found in Refs. 77–79.

Another interesting result comes from the study of the isotopically substituted reaction HD + OH which produces two distinguishable products, HOH + H and DOH + H. The flux calculation for the branching reaction has to distinguish the specific part of the flux that goes into a specific product. We use a simple criterion to divide the flux into two branches based on physical considerations as described in Ref. 80. Specifically at a given quadrature point in the flux evaluation, the interatomic distances between the O and the H as well as the D atom of HD are calculated. The contribution of the flux at this quadrature point is assigned to either the H-transfer reaction channel, if the OH distance is smaller than the OD distance, or vice versa (80). Figure 11 shows a contour plot of the reactive flux as a function of two bending angles θ_1 and θ_2 together with the geometry of the system. The contour plot of the reactive flux shows clear steric effect

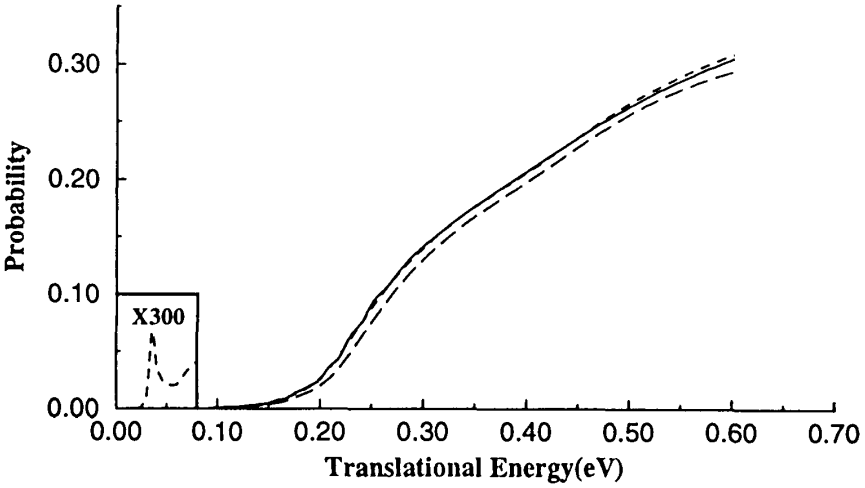

Figure 7 Total reaction probability as a function of translational energy for the reaction $H_2(00)$ + OH(00) → H + H_2O for total angular momentum $J = 0$. The solid line is the 6D result, short-dashed line the PA 5D result, and long-dashed line the RE 5D result. The reaction probability in the lower left box is enlarged by a factor of 300 before being plotted.

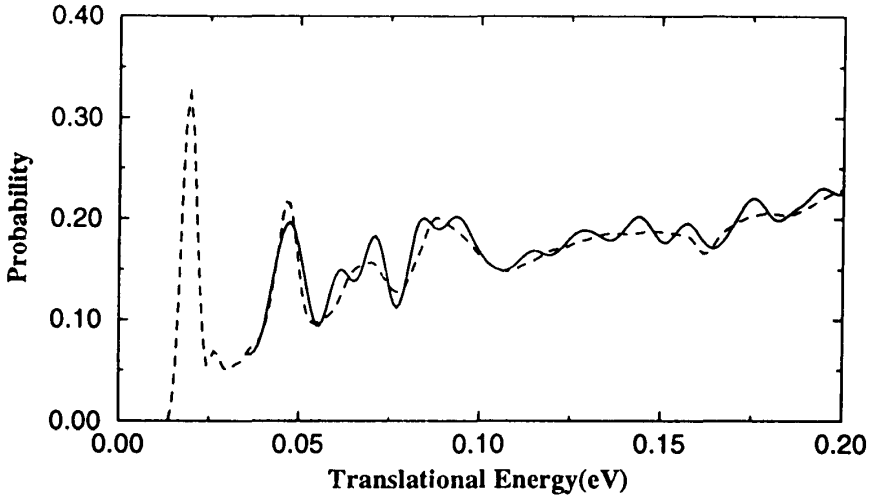

Figure 8 Total reaction probability as a function of translational energy for the reaction $H_2(10) + OH(00) \rightarrow H + H_2O$ for total angular momentum $J = 0$. Solid line is the 6D result and dashed line the PA5D result.

as illustrated in Fig. 11 where the H-transfer or D-transfer reaction can only occur when the transferring atom is nearly facing the O atom.

The reaction probabilities and cross sections are also shown in Fig. 12. The figure shows clearly that the reaction is dominated by the H-transfer channel at low collision energies but by the D-transfer channel at high collision energies. The low-energy reaction is clearly determined by tunneling which favors the H-transfer reaction. At high energy, the energetic criterion and steric effect become dominant as discussed in Ref. 80. More detailed results can be found in Ref. 101.

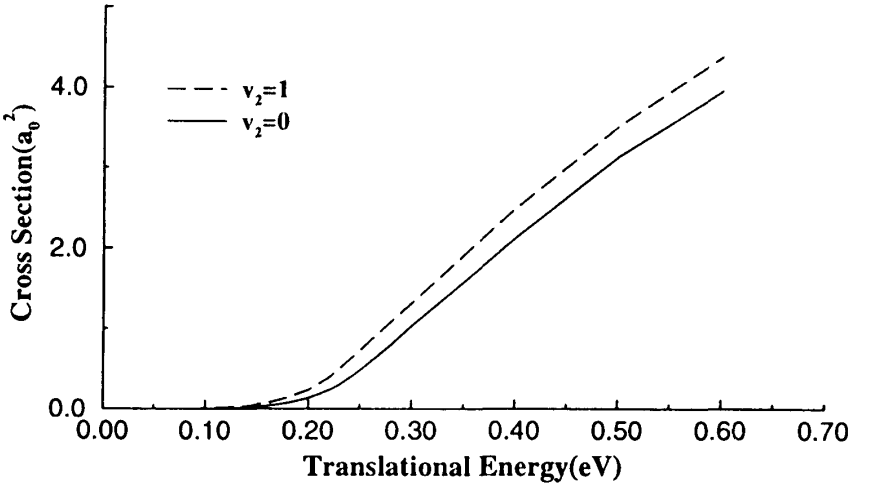

Figure 9 Integral cross sections for the reaction $H_2(00) + OH(V_20)$. The solid line is the result for $V_{2=0}$ and the long–dashed line for $v_{2=1}$.

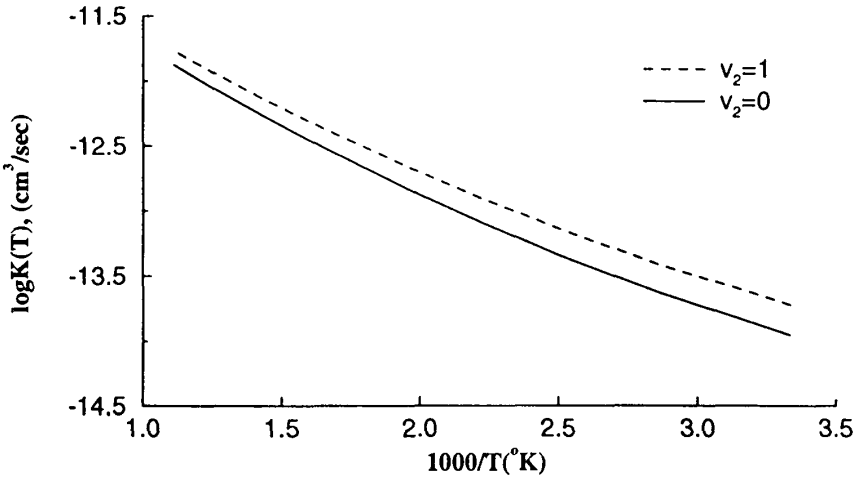

Figure 10 The rate constant for the reaction $H_2(00) + OH(v_2 0)$ as a function of temperature. Solid line is the result for $v_2 = 0$ and the dashed line $v_2 = 1$.

V. GAS-SURFACE REACTION DYNAMICS

Heterogeneous catalysis of chemical reactions on solid surfaces is of great practical importance in many areas of science and technology. A major challenge to chemists today is to understand how the structure and property of the surface of a catalyst affects the catalytic activity for a specific chemical reaction, and how the internal state of the reactant molecule influences the catalytic reaction. Although numerous studies on the kinetics of catalytic processes have been carried out in the past several decades, many detailed dynamical aspects of catalysis are far from clearly understood. A thorough understanding of the dynamics of reactions on surfaces is essential in achieving the ultimate goal of designing and controlling catalytic reaction in pollution control and other important industrial processes.

Gas-surface reaction presents another challenge to quantum dynamics theory. Current dynamics studies of gas-surface process can generally be divided into two categories according to different levels of complexity in the theoretical treatment. The first level of theory treats the solid surface as a rigid surface on which surface atoms are simply fixed

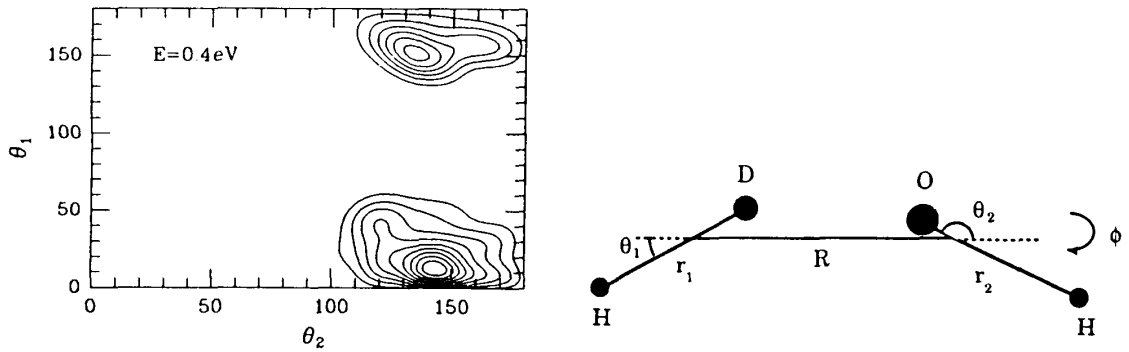

Figure 11 Reactive flux density as a function of two bending angles, θ_1 and θ_2, with all other coordinates being integrated out for the reaction HD(00) + OH(00). The insert at right shows the geometric relation.

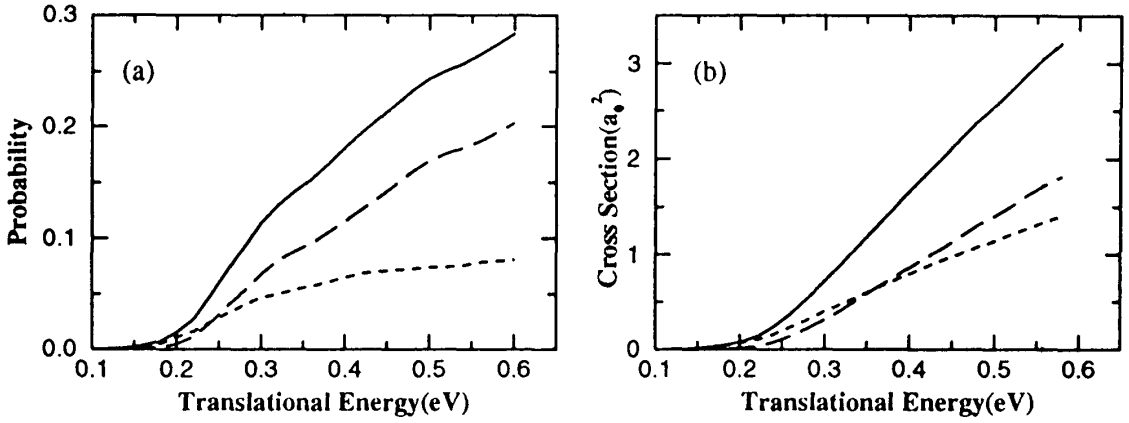

Figure 12 (a) Reaction probabilities and (b) cross sections for the HD(00) + OH(00) reaction as a function of translational energy. Dashed lines are the results for the HOH branch, long-dashed lines the DOH branch, and solid lines the total reaction.

at their equilibrium positions, or in other words, the surface is treated as "cold" surface. The next level of theory treats the motions of surface atoms explicitly but its practical implementation is significantly more complicated, if not impossible. Therefore most theoretical studies, in which surface motion is explicitly included, are classical. Although one can include surface motions either explicitly such as in molecular dymamics, or implicitly such as in Langevin dynamics, the outcome of such a classical treatment is not always clear. On the other hand, the rigid-surface theory, although approximate, is clearly defined and physically transparent, and is susceptible to the treatment of high-level dynamical theories such as quantum mechanics. Thus it is possible to develop rigorous theoretical methodologies to treat molecular reactions on rigid surfaces and to provide accurate predictions for surface reaction processes in which the effect of surface motion, often manifested by surface temperature effect, is negligible.

The last several years have seen rapid progress in quantum dynamical calculation for dissociative adsorption of hydrogen on Cu and Ni surfaces (102–120). Since the early work of Jackson and Metiu (102), who employed a collinear 2D model to simulate the dissociation process of H_2 on Ni, dynamics calculations are now routinely carried out in 3D space (104,112–118). The works in Refs. 118 and 119 have further extended diatomic dissociation on surface to 4D with local surface corrugation effect explicitly included in the quantum dynamics calculation. In addition, a mixed quantum/classical treatment for a diatom on surface has also been carried out to treat all six degrees of freedom explicitly (three quantum and three classical) (120). In the following we present TD quantum mechanical treatments for dissociative adsorption of a diatomic molecule on a rigid surface using the 3D flat-surface model, the 4D fixed-site model, and the full 6D model. The prototypical system—hydrogen dissociation on Cu(111)—is discussed and some theoretical results, especially the rotational orientation effect of H_2 on dissociation, are given.

A. Three-Dimensional Flat-Surface Model for Diatom on Surface

In the 3D flat-surface model, the molecule-surface interaction potential energy surface (PES) is constructed for a chosen dissociation site, and is assumed to be dependent only

on three degrees of freedom, the diatomic distance r, perpendicular distance from the center of the diatom to the surface Z, and the polar angle θ as shown in Fig. 13. In this model, the potential is independent of the azimuthal angle ϕ and the lateral coordinates of the center of mass of the diatom (X, Y). It is worth mentioning, however, that the name of "flat-surface" approximation is somehow misleading because although the dynamics calculation does not include the corrugation explicitly, the effect of surface corrugation is implicitly incorporated in the PES which is constructed for a specific surface site.

The 3D Hamiltonian can be written in terms of the coordinates defined in Fig. 13:

$$H = H_0 + U \tag{128}$$

with

$$H_0 = -\frac{\hbar^2}{2M}\frac{\partial^2}{\partial Z^2} - \frac{\hbar^2}{2\mu}\frac{\partial^2}{\partial r^2} + V_d(r) \tag{129}$$

$$U = \frac{\vec{j}^2}{2\mu r^2} + V(Z, r, \theta) \tag{130}$$

where M is the diatomic center-of-mass, μ is the reduced mass, and $\vec{j}$ is the angular momentum operator. The quantum mechanical treatment for diatomic dissociation on a flat-surface is essentially similar to that of atom-diatom reaction. Therefore many of the theoretical treatments are similar to those described in the previous section. In the coupled-channel wave packet approach (121,122), the time-dependent wavefunction satisfying the Schrödinger equation $i\hbar(\partial/\partial t)\Psi(t) = H\Psi(t)$ can be expanded in diatomic rovibrational eigenfunctions as

$$\Psi^m_{v_0 j_0}(Z, r, \theta, t) = \sum_{i,n,j} F^m_{inj,v_0 j_0}(t) u^n_i(Z) P^m_j(\theta) \chi_n(r) \tag{131}$$

where $(v_0 j_0 m)$ denotes the initial rovibrational state, $u^n_i(Z)$ is the translational basis function, $P^m_j(\theta)$ is the normalized associated-Legendre polynomial, and $\chi_n(r)$ is the vibrational basis function. We note here that the rotation projection quantum number m is a con-

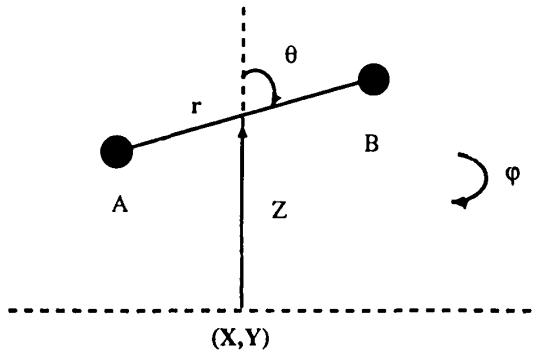

Figure 13 Molecular coordinates for diatom-surface collision where (X, Y, Z) are the center-of-mass coordinates of the diatom, r is the diatomic distance, θ is the polar angle, and ϕ is the azimuthal angle. The lateral coordinates (X, Y) is fixed in 3D and 4D fix-site model calculations.

served quantum number in the flat-surface model because the PES is independent of the azimuthal angle ϕ.

A nondirect product basis expansion method described in the previous section on gas-phase reaction, similar to the spirit of "L-shaped" grid method proposed by Mowrey (91), is also used in gas-surface reactions. This method is actually ideal for gas-surface reaction because the skewing angle of the PES is strictly 90° (see Fig. 14). A collinear model study showed explicitly that the required number of quasiadiabatic diatomic vibrational function is only larger near the potential saddle point region (92). Based on the treatment of non-direct product basis described in the previous section (Eq. 89), the translation basis function is given by

$$u_i^n(Z) = \begin{cases} \sqrt{\dfrac{2}{Z_4 - Z_1}} \sin \dfrac{i\pi(Z - Z_1)}{Z_4 - Z_1} & n \leq n_{\text{asy}} \\ \sqrt{\dfrac{2}{Z_2 - Z_1}} \sin \dfrac{i\pi(Z - Z_1)}{Z_2 - Z_1} & n > n_{\text{asy}} \end{cases} \tag{132}$$

where n_{asy} is chosen to be the number of energetically open vibrational channels plus a few closed vibrational channels of the diatom AB. The vibration eigenfunction $\chi_n(r)$ of the diatom AB satisfies

$$\left[-\frac{\hbar^2}{2\mu} \frac{\partial^2}{\partial r^2} + V_d(r) \right] \chi_n(r) = \epsilon_n \chi_n(r) \tag{133}$$

where the diatomic reference potential $V_d(r)$ is defined to allow the vibrational function $\chi_n(r)$ to span a large interatomic distance r in order to allow diatomic dissociation to occur.

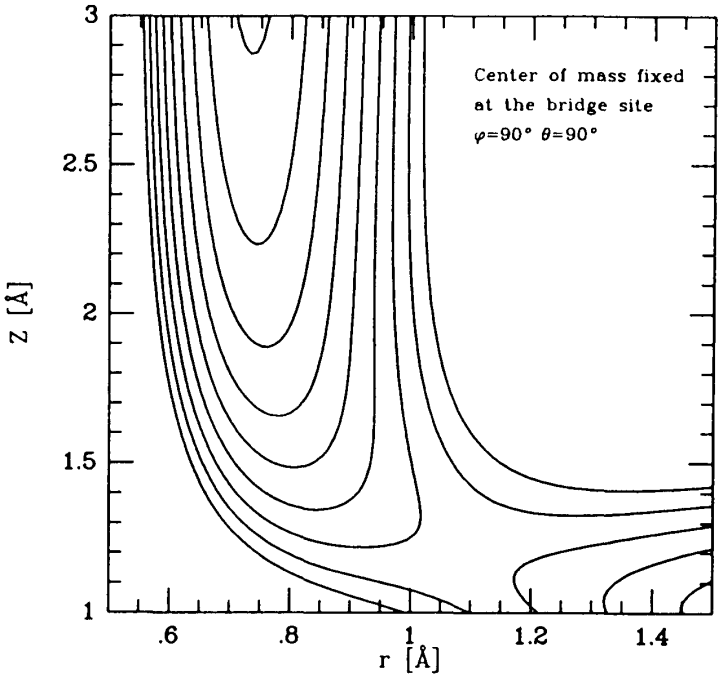

Figure 14 Contour plot of the H_2/Cu(111) PES showing the minimum-energy path.

The split-operator method is employed to carry out the wave packet propagation,

$$\Psi(Z, r, \theta, t + \Delta) = e^{-iH_0\Delta/2} e^{-iU\Delta} e^{-iH_0\Delta/2} \Psi(Z, r, \theta, t) \tag{134}$$

where H_0 and U are defined in Eqs. (128), (129), and (130). Since the total number of vibration basis functions n_{max} is much larger than n_{asy}, the computationally intensive part of the calculation is limited to the interaction region $Z \in [Z_1, Z_2]$ where reaction occurs. In the asymptotic region, the amount of computation is more or less similar to that for inelastic scattering. The procedure for wave packet propagation is essentially identical to that of gas-phase reaction described in the previous section and will not be detailed here. It should be mentioned here that the time-dependent wavefunction is absorbed at the edges of the grid to avoid boundary reflections.

The initial state-selected total dissociation probability of the diatom is obtained by projecting out the energy-dependent reactive flux. If ψ^+_{iE} denotes the time-independent (TI) full scattering wavefunction, where the labels i and E denote the initial state and energy, the total dissociation probability from an initial state i can be obtained by the flux formula (95). We choose the diatomic distance r to be the s coordinate in Eq. (96). The full TI scattering wave function is normalized as $\langle \psi^+_{iE} | \psi^+_{iE'} \rangle = 2\pi\hbar\delta(E - E')$. The total dissociation probability, according to Eq. (98), is given by

$$P_i^R(E) = \frac{\hbar}{m_r} \operatorname{Im}\left[\langle \psi^+_{iE} | \delta(r - r_0) \frac{\partial}{\partial r} | \psi^+_{iE} \rangle \right] \tag{135}$$

Since the TD wavefunction can be expanded in terms of the TI wavefunction which forms a complete set

$$|\psi_i(t)\rangle = e^{-i/\hbar H t} \psi_i(0) = \frac{1}{2\pi\hbar} \int dE \; e^{-i/\hbar E t} |\psi^+_{iE}\rangle \; a_i(E) \tag{136}$$

$$|\psi^+_{iE}\rangle = \frac{1}{a_i(E)} \int_{-\infty}^{\infty} e^{(i/\hbar)(E - H)t} |\psi_i(0)\rangle \; dt \tag{137}$$

The coefficient $a_i(E)$ can be easily evaluated from the free asymptotic function as follows:

$$\begin{aligned} a_i(E) &= \langle \psi^+_{iE} | \psi_i(0) \rangle \\ &= \lim_{t \to -\infty} \langle \phi_{iE} | e^{i/\hbar H_0 t} e^{-i/\hbar H t} | \psi_i(0) \rangle \\ &= \langle \phi_{iE} | \psi_i(0) \rangle \end{aligned} \tag{138}$$

where the last equation holds because the initial wave packet $\psi_i(0)$ is located in the asymptotic region with incoming wave only.

B. Four-Dimensional Fixed-Site Model for Diatom on Surface

So far the 3D flat-surface model has been quite successful in providing qualitative and even some quantitative dynamics information for hydrogen dissociation on metals such as the role of hydrogen vibration and rotation in dissociative adsorption on Cu(111) (104,114,117–119). However, the inherent limitation of the flat-surface model dictates that it cannot provide information on surface corrugation and its effect on molecular adsorption. One would like to investigate the effect of rotational orientation of diatomic molecules on chemisorption in the *presence* of surface corrugation. In order to obtain

this information, one needs to go beyond the flat-surface model and to include surface corrugation explicitly.

It is relatively straightforward to extend the 3D flat-surface model to the 4D fixed-site model which includes local surface corrugation explicitly. This has recently been done by Darling and Holloway (119) and Dai and Zhang (118) for the H_2/Cu(111) system. In the 4D fixed-site model, the azimuthal angle ϕ is explicitly included while the lateral coordinates of the center of mass of the diatom is still fixed at a given site, usually at a symmetric site. The inclusion of the azimuthal angle ϕ in the dynamics calculation is a natural extension of the 3D "flat-surface" model and it enables us to treat both local surface corrugation and surface site-specificity explicitly. This 4D model should provide a reasonable description for normal incidence of hydrogen over the symmetric sites of metal surfaces.

Equation (131) is now generalized to include the ϕ-dependence explicitly:

$$\Psi_{v_0 j_0 m_0}(Z, r, \theta, \phi, t) = \sum_{i,n,j,m} F^m_{injm,v_0 j_0 m_0}(t) u^n_i(Z) Y^m_j(\theta, \varphi) \chi_n(r) \tag{139}$$

and the remaining treatment is essentially identical to that of the flat-surface model described in the previous subsection. At this stage, important differences from the flat-surface treatment emerged. First, the m quantum number is no longer conserved and the allowed Δm transitions are determined by the symmetry of the chosen site (112,114,117). As shown in the appendix of Ref. 117, the allowed Δm transition is given by $\Delta m = \pm Nk$ (k = 0, 1, 2, . . .) where N is the rotation symmetry of the impact site with the possible values of N = 1,2,3,4, and 6 for a crystal surface (117). Second, the 4D model describes the migration of the diatoms through the potential valleys correctly which shows explicitly the dissociation path and adsorption sites. Neither of these two phenomena can be observed from the flat-surface model. In fact, in the flat-surface model one has to artificially cut off the potential after the molecule passes through the reaction barrier in order to avoid the artificial boundary reflection from diffusion barriers. Thus the 4D fixed-site model provides a much more realistic description of the chemisorption process. We note here that we use the word "local" surface corrugation because the center of mass of the diatom is not allowed to move on the crystal surface.

C. Full-Dimensional (6D) Model for Diatom on Surface

Ultimately, the exact dynamics study for dissociative adsorption of a diatomic molecule on a corrugated, static surface should include the lateral motion of the center of mass of the diatom, i.e., include six degrees of freedom. The 6D Hamiltonian could be written in terms of the gas-phase Jacobi coordinates (molecular coordinates) as

$$-\frac{\hbar^2}{2M}\left[\frac{\partial^2}{\partial X^2}+\frac{\partial^2}{\partial Y^2}+\frac{\partial^2}{\partial Z^2}\right]-\frac{\hbar^2\partial^2}{2\mu\partial_\gamma^2}+\frac{\vec{J}^2}{2\mu r^2}+V(X, Y, Z, r, \theta, \phi) \tag{140}$$

where (X, Y) are the lateral Cartesian coordinates of the center of mass (COM) of the diatom.

This Hamiltonian is natural for describing inelastic scattering of a diatom from the surface, and is also suitable for describing the process of dissociative adsorption. However, this set of molecular coordinates is not very suitable when the diatomic distance r is very large because the wavefunction is highly peaked around $\theta = 90°$. One alternative is to simply use the atomic coordinates which is obviously ideal for describing the dif-

fusion process, and the Hamiltonian is simply expressed in atomic Cartesian coordinates. However, atomic coordinates are not very efficient for describing gas-phase process. One compromise is to use a set of coordinates intermediate between the molecular and atomic coordinates described below. We denote this set by (X, Y, Z, z, ρ, ϕ) where (z, ρ, ϕ) is the cylindrical coordinate of the interatomic vector $\vec{r}$. Using the substitution

$$\Psi = \rho^{-1/2}\psi \tag{141}$$

one arrives at the Schrödinger equation $i\hbar(\partial/\partial t)\psi(t) = H'\psi(t)$ where

$$H' = -\frac{\hbar^2}{2M}\left[\frac{\partial^2}{\partial X^2} + \frac{\partial^2}{\partial Y^2} + \frac{\partial^2}{\partial Z^2}\right] - \frac{\hbar^2}{2\mu}\left[\frac{\partial^2}{\partial \rho^2} + \frac{1}{\rho^2}\left(\frac{1}{4} + \frac{\partial^2}{\partial \phi^2}\right) + \frac{\partial^2}{\partial z^2}\right] + V(X,Y,Z,\rho,\phi,z) \tag{142}$$

The wavefunction ψ can be expanded in basis functions of the coordinates (X,Y,Z,z,ρ,ϕ) and DVR representation can be used for all the coordinates.

So far, no exact 6D quantum dynamics calculation has been reported for diatomic dissociation on surface. But with modern computer power, such numerical endeavor will undoubtly be realized soon. We also note here recent mixed quantum/classical studies of Jackson who treated three COM coordinates classically and three internal molecular coordinates quantum mechanically for H_2/Cu(100) (120). Such treatment seems quite promising for more complex systems.

D. The H_2/Cu(111) System

1. Three-Dimensional Flat-Surface Result

We show in this subsection some calculational results for the H_2/Cu(111) system which has become the prototype for studying dissociative chemisorption on surfaces. The results presented in this subsection are obtained from calculations at the 3D flat-surface level using a LEPS PES (117). We are interested in rovibrational effect of hydrogen on dissociation. In particular, we will present some interesting results showing the effect of molecular orientation and homonuclear symmetry on dissociative chemisorption of hydrogen on Cu(111).

The 3D flat-surface results show strong vibrational effects. Although the enhancement of hydrogen dissociation by vibration is well established, its quantitative description in the interpretation of the adsorption experiment of Anger et al. (123) was controversial. The theoretical results of Ref. 114 provided strong support for the conjecture that the hydrogen dissociation on Cu is dominated by vibrationally excited component of H_2 at low energy but by ground vibration species at high energies, in good agreement with recent experimental findings (124,125,126,127).

In contrast to the vibrational effect, the rotational effect on hydrogen dissociation on Cu is much less understood, until very recently. Most 3D quantum calculations have used the plane rotor model, which is not appropriate for studying rotational effects. The studies of Refs. 113, 114, and 117 using the spherical rotor treatment have obtained important results on the effect of rotational orientation and the nuclear symmetry. The rotational orientational effect is clearly shown in Fig. 15, where reaction probabilities for different initial rotational orientation states are plotted as a function of kinetic energy. Significant enhancement of reaction probability is seen for the state with $j = m$ (''helicopter'' mode) while the m = o (''cartwheel'' mode) is least effective for dissociation.

In a nonpolarized experiment, only the degeneracy-averaged dissociation probability could be measured. One needs to average the dissociation probability $P(jm)$

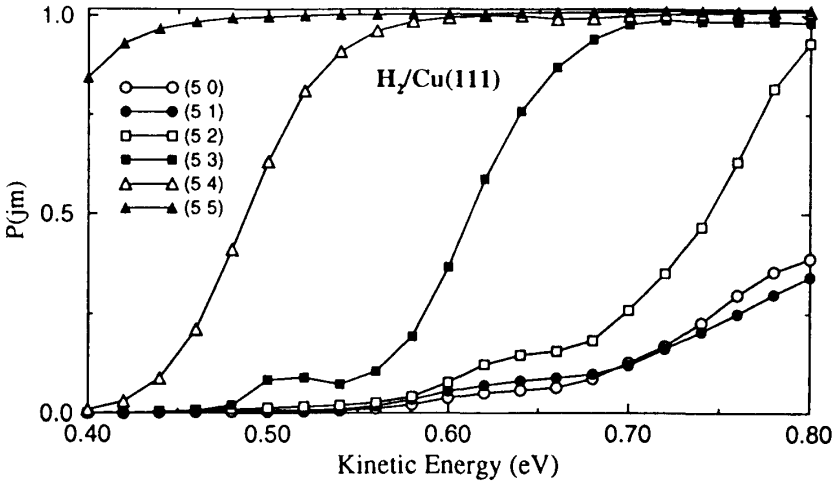

Figure 15 Dissociation probabilities of $H_2(jm)$ on Cu(111) as a function of the translation energy from initial rotational states $j = 5$ and $m = 0-5$.

over the $2j + 1$ degeneracy. We therefore define the degeneracy-averaged dissociation probability for a given j by

$$\bar{P}(j) = \frac{1}{2j + 1} \sum_{m=-j}^{m=j} P(jm) \tag{143}$$

Figure 16 plots the j-dependence of $P(j)$ at several energies for H_2/Cu(111). At low kinetic energies, $P(j)$ *increases* monotonically as j increases, as shown in the figure at $E_k = 0.44$ eV. However, as the E_k increases, $P(j)$ initially *decreases* as j increases and levels off at around $j = 5$ before moves upward as j increases further. The latter behavior is consistent with a recent experimental measurement by Michelsen et al. (127) of the mean kinetic energy of the rotational states of D_2 desorbed from Cu(111).

Another effect found in the flat-surface study of Refs. 113, 114 and 117 is the nuclear symmetry effect which states that for initial rotation states satisfying $j + m =$

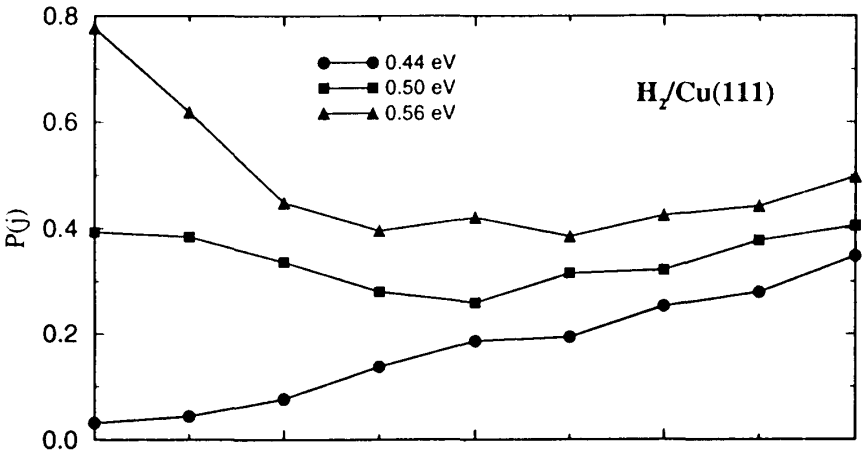

Figure 16 Degeneracy-averaged dissociation probability $P(j)$ for H_2 on Cu(111) plotted as a function of the rotation quantum number j at kinetic energies $E_k = 0.44$, 0.50, and 0.56 eV.

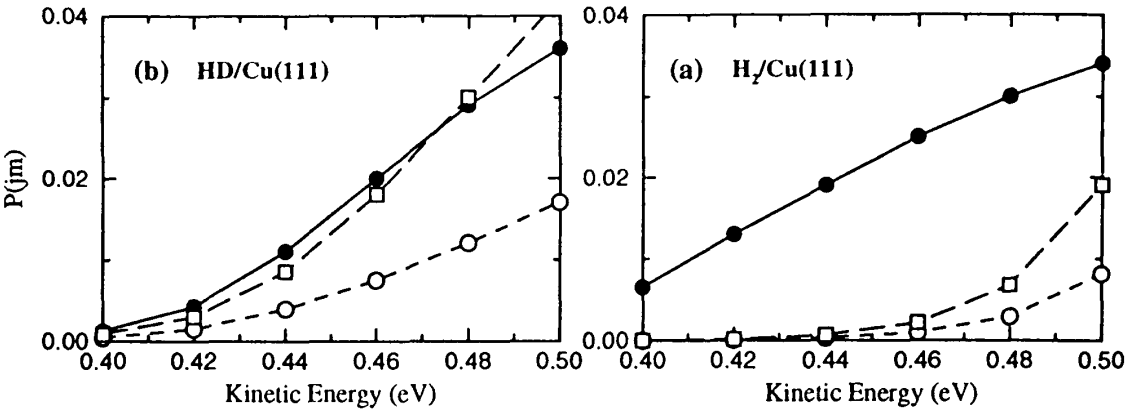

Figure 17 Dissociation probabilities $P(jm)$ for $j = 3$, $m = 0-2$ as a function of kinetic energy for (a) H_2/Cu(111) and (b) HD/Cu(111). Circles denote $P(30)$, filled circles $P(31)$, and squares $P(32)$.

odd, the reaction probability is essentially forbidden at low energies because the atom-surface states (CVV) are symmetry forbidden (114,117). This selection rule is rigorous for the flat-surface model in which m is a good quantum number (113,114,117). At very low energies, this symmetry restriction will exclude the only energetically accessible (00) atom-surface vibrational state from being populated. The exclusion of the product (vv) states will severely limit the energy flow into the product channels at low energies for rotational states with symmetry $j + m$ = odd. However, if the molecule-surface reaction is a highly exoergic process, or when the total energy is high, the closing of the product (vv) states due to the selection rule will not have a significant effect on the dissociation probability because there are sufficient number of allowed product channels for energy flow. This symmetry effect is displayed quite clearly in Fig. 17. Here the dissociation probability $P(jm)$ ($j = 3$) is plotted for three values of m ($m = 0, 1, 2$) for both H_2 and DH. For H_2 dissociation, the probabilities $P(30)$ and $P(32)$ are orders of magnitude smaller and essentially negligible compared to $P(31)$ for energies below 0.46 eV. This symmetry effect diminishes rather quickly as the energy increases and the reason for this is discussed above. However, for the heteronuclear HD on Cu, the even and odd probabilities are of similar magnitude as shown in Fig. 17.

2. Four-Dimensional Fixed-Site Result

The dynamics study for the H_2/Cu(111) system has recently been extended to 4D by Darling and Holloway (119) and by Dai and Zhang (118) in which the azimuthal angle ϕ is included in the dynamics calculation. Our 4D fixed-site calculation with explicit corrugation in the ϕ angle shows interesting results. The 4D calculation still employs the LEPS type PES with parameters fitted to available experimental and theoretical data including some new ab initio data for this system (128). Details on the PES in our 4D study is given in (118).

The 4D study of Ref. 118 observes the following. (1) The strong rotational orientation effect observed in 3D flat-surface studies is unaffected by local surface corrugation. Local surface corrugation does not change the essential characteristics of the strong dependence of the PES on the polar angle θ, which is the main reason for the orientational effect. (2) Inelastic Δm transition can be neglected for impact over high-symmetry site, such as the sixfold atop site on Cu(111), but such transition is significant

for impact over low-symmetry site, such as the bridge site. (3) The nuclear symmetry effect remains at low energy for dissociation over high-symmetry site, but is significantly diminished for dissociation over low-symmetry site. This is consistent with the rule of Δm transition over symmetry sites. These findings show that the 3D flat-surface model should be able to describe chemisorption process over high-symmetry site reasonably well, but is inadequate for chemisorption over low-symmetry site in which the corrugation effect plays an important role (118).

Future study is needed to further extend the 4D model to a full-dimensional (6D) one for this benchmark system in order to completely determine and understand the dynamics of this system and to establish the validity of the fixed-site model.

VI. CONCLUSIONS

The main purpose of this chapter is to show and demonstrate how the use of TD quantum mechanics enables one to develop versatile and powerful computational methods to treat a variety of quantum dynamics problems and to perform large-scale quantum mechanical calculations that are otherwise difficult or impractical to do using other theoretical methods. To achieve that purpose, the general time-dependent approaches to specific quantum dynamics problems in gas-phase and gas-surface are presented in detail. Efficient numerical methods for treating the scattering, photofragmentation, bimolecular reactive scattering, and molecule-surface reaction are shown and discussed in detail, together with their applications to practical chemical systems.

In gas-phase dynamics, the discussion is focused on the TD quantum wave packet treatment for tetraatomic systems. This is further divided into two different but closed related areas: molecular photofragmentation or half-collision dynamics and bimolecular reactive collision dynamics. Specific methods and examples for treating the dynamics of direct photodissociation of tetraatomic molecules and of vibrational predissociation of weakly bound dimers are given based on different dynamical characters of these two processes. TD methods such as the direct projection method for direct photodissociation, TD golden rule method and the flux method for predissociation are presented. For bimolecular reactive scattering, the use of nondirect product basis and the computation of the initial state-selected total reaction probabilities by flux calculation are discussed. The descriptions of these methods are supported by concrete numerical examples and results of their applications.

For the dissociation dynamics of diatom on rigid surface, the TD treatment is discussed using models ranging from the crude 3D flat-surface model to the exact 6D model with full inclusion of the surface corrugation effect. The H_2/Cu system is used as an benchmark system and the theoretical results obtained from several model calculations are presented for H_2 and HD dissociation on Cu(111) surface. Interesting dynamical effect, such as the steric effect in molecular-surface reaction, is discussed and comparison of theoretical predictions with experiment is also made.

We hope that this chapter will provide a useful guide for researchers in the field of theoretical chemical dynamics who wish to study these and related subjects and to further develop methodologies for studying more complex dynamical systems. Some of the rigorous quantum dynamics calculations for several prototype systems presented in this chapter could serve as benchmark results against which future development of approximate but more efficient methods could be tested.

ACKNOWLEDGMENT

We thank Jiqiong Dai and Qian Wu, who are responsible for some of the work presented in this chapter. This work is supported in part by the National Science Foundation and the Petroleum Research Fund.

REFERENCES

1. J. Z. H. Zhang, *J. Chem. Phys. 92*: 324 (1990).
2. J. Z. H. Zhang, *Chem. Phys. Lett. 160*: 417 (1989).
3. J. Z. H. Zhang, *Comput. Phys. Commun. 63*: 28 (1991).
4. S. Das and D. J. Tannor, *J. Chem. Phys. 92*: 3403 (1990).
5. C. J. Williams, J. Qian and D. J. Tannor, *J. Chem. Phys. 95*: 1721 (1991).
6. M. Founargiotakis and J. C. Light, *J. Chem. Phys. 93*: 633 (1990).
7. (a) J. A. Fleck, Jr., J. R. Morris, and M. D. Feit, *Appl. Phys. 10*: 129 (1976); (b) M. D. Feit, J. A. Fleck, Jr., and A. Steiger, *J. Comput. Phys. 47*: 412 (1982).
8. H. Tal-Ezer and D. Kosloff, *J. Chem. Phys. 81*: 3967 (1984).
9. C. Lanczos, *J. Res. Natl. Bur. Stand. 45*: 255 (1950).
10. T. J. Park and J. C. Light, *J. Chem. Phys. 85*: 5870 (1986).
11. C. Leforestier, R. Bisseling, C. Cerjan, M. D. Feit, R. Friesner, A. Guldberg, A. Hammerich, G. Jolicard, W. Karrlein, H. D. Meyer, N. Lipkin, O. Roncero, and R. Kosloff, *J. Comput. Phys. 94*: 59 (1991).
12. S. K. Gray, *J. Chem. Phys. 96*: 6543 (1992).
13. M. Abramowitz and I. A. Stegun (eds.), *Handbook of Mathematical Functions*, Dover, New York.
14. R. Kosloff and D. Kosloff, *J. Chem. Phys. 79*: 1823 (1983).
15. J. V. Lill, G. A. Parker, and J. C. Light, *Chem. Phys. Lett. 89*: 483 (1982).
16. Z. Bacic and J. C. Light, *Annu. Rev. Phys. Chem. 40*: 469 (1989).
17. J. Dai and J. Z. H. Zhang, *J. Chem. Phys., 103*: 1491 (1995).
18. D. Neuhauser, *J. Chem. Phys. 100*: 5076 (1994).
19. S. K. Gray and C. E. Wozny, *J. Chem. Phys. 91*: 7671 (1989); *94*: 2817 (1991).
20. A. Isele, C. Meier, V. Engel, N. Fahrer, and Ch. Schlier, *J. Chem. Phys. 101*: 5919 (1994).
21. J. Dai and J. Z. H. Zhang, unpublished results.
22. C. Leforestier and R. E. Wyatt, *J. Chem. Phys. 78*: 2334 (1983).
23. G. Jolicard and E. J. Austin, *J. Chem. Phys. 103*: 295 (1986).
24. D. Neuhauser and M. Baer, *J. Chem. Phys. 91*: 4651 (1989).
25. D. C. Clary, *J. Chem. Phys. 96*: 90 (1992).
26. D. H. Zhang, J. Z. H. Zhang, and Z. Bacic, *J. Chem. Phys. 97*: 927 (1992).
27. D. H. Zhang, J. Z. H. Zhang, and Z. Bacic, *Chem. Phys. Lett. 194*: 313 (1992).
28. C. Bissonnette and D. C. Clary, *J. Chem. Phys. 97*: 8111 (1992).
29. D. H. Zhang, J. Z. H. Zhang, and Z. Bacic, *J. Chem. Phys. 97*: 3149 (1992).
30. D. H. Zhang and J. Z. H. Zhang, *Chem. Phys. Lett. 199*: 187 (1992).
31. D. H. Zhang and J. Z. H. Zhang, *J. Chem. Phys. 98*: 6276 (1993).
32. Z. T. Cai, D. H. Zhang, and J. Z. H. Zhang, *J. Chem. Phys. 100*: 5631 (1994).
33. D. H. Zhang and J. Z. H. Zhang, *J. Chem. Phys. 98*: 5978 (1993).
34. D. H. Zhang and J. Z. H. Zhang, *J. Chem. Phys. 99*: 6624 (1993).
35. D. H. Zhang, Q. Wu, and J. Z. H. Zhang, *J. Chem. Phys. 102*: 124 (1995).
36. M.v. Dirke, Z. Bacic, D. H. Zhang, and J. Z. H. Zhang, *JCP, 102*: 4382 (1995).
37. See, for example, (a) P. Anderson and R. Schinke, *Molecular Photodissociation Dynamics* (M. N. R. Ashford and J. E. Baggott, eds.), Royal Society of Chemistry, London, 1987; (b) D. Imre and J. Zhang, *Chem. Phys. 139*: 89 (1989); (c) V. Engel, V. Staemmler, R. L. Vander

Wal, F. F. Crim, R. J. Sension, B. Hudson, P. Anderson, S. Hennig, K. Weide, and R. Schinke, *J. Phys. Chem. 96*: 3201 (1992).
38. G. G. Balint-Kurti and M. Shapiro, *Chem. Phys. 61*: 137 (1981).
39. R. Schinke, *Photodissociation Dynamics: Spectroscopy and Fragmentation of Small Polyatomic Molecules*, Cambridge University Press, England, 1993.
40. (a) E. J. Heller, *J. Chem. Phys. 68*: 389 (1978); K. C. Kulander and E. J. Heller, *JCP 69*: 2439 (1978).
41. J. R. Taylor, *Scattering Theory*, Wiley, New York, 1972.
42. R. Schinke and V. Staemmler, *Chem. Phys. Lett. 145*: 486 (1988).
43. W. D. Davison, *Chem. Soc. Faraday Disc. 33*: 71 (1962).
44. K. Takayanagi, *Adv. Mol. Phys. 1*: 149 (1965).
45. G. Zazur and H. Rabitz, *J. Chem. Phys. 60*: 2057 (1974).
46. S. Green, *J. Chem. Phys. 62*: 227 (1975).
47. M. H. Alexander and A. P. DePristo, *J. Chem. Phys. 66*: 2166 (1977).
48. M. E. Rose, *Elementary Theory of Angular Momentum*, Wiley, New York, 1957.
49. P. Villarreal, S. Miret-Artes, O. Roncero, G. Delgado-Barrio, J. A. Beswick, N. Halberstadt, and R. D. Coalson, *J. Chem. Phys. 94*: 42 30 (1991).
50. D. H. Zhang and J. Z. H. Zhang, *J. Chem. Phys. 95*: 6449 (1991).
51. D. H. Zhang and J. Z. H. Zhang, *J. Phys. Chem. 96*: 1575 (1992).
52. J. A. Beswick and J. Jortner, *Chem. Phys. Lett. 49*: 13 (1977); G. E. Ewing, *Chem. Phys. 29*: 253 (1978).
53. C. M. Lovejoy, D. D. Nelson, Jr., and D. J. Nesbitt, *J. Chem. Phys. 89*: 7180 (1988).
54. G. G. Balint-Kurti, R. N. Dixon, and C. C. Martson, *J. Chem. Soc. Faraday. Trans. 86*: 1741 (1990).
55. (a) D. E. Manolopoulos and M. H. Alexander, *J. Chem. Phys. 97*: 2527 (1992); (b) M. H. Alexander and D. E. Manolopoulos, *J. Chem. Phys. 97*: 4832 (1992).
56. T. Seideman and W. H. Miller, *J. Chem. Phys. 96*: 4412 (1992).
57. M. Quack and M. A. Suhm, *Mol. Phys. 69*: 791 (1990); *J. Chem. Phys. 95*: 28 (1991).
58. J. T. Farrell and D. J. Nesbitt, private communication.
59. A. S. Pine and G. T. Fraser, *J. Chem. Phys. 89*: 6636 (1988).
60. A. N. Brook and D. C. Clary, *J. Chem. Phys. 92*: 4178 (1990).
61. Q. Sun and J. M. Bowman, *J. Chem. Phys. 92*: 5201 (1990).
62. D. C. Clary, *J. Chem. Phys. 95*: 7298 (1991).
63. D. C. Clary, *J. Chem. Phys. 96*: 3656 (1992).
64. D. C. Clary, *Chem. Phys. Lett. 192*: 34 (1992).
65. G. Nyman and D. C. Clary, *J. Chem. Phys. 99*: 7774 (1993).
66. J. M. Bowman and D. Wang, *J. Chem. Phys. 96*: 7852 (1992).
67. D. Wang and J. M. Bowman, *J. Chem. Phys. 96*: 8906 (1992).
68. D. Wang and J. M. Bowman, *Chem. Phys. Lett. 207*: 227 (1993).
69. H. Szichman, I. Last, A. Baram, and M. Baer, *J. Phys. Chem. 97*: 6436 (1993).
70. D. C. Clary and G. C. Schatz, *J. Chem. Phys. 99*: 4578 (1993).
71. G. Nyman and D. C. Clary, *J. Chem. Phys. 100*: 3556 (1994).
72. J. Echave and D. C. Clary, *J. Chem. Phys. 100*: 402 (1994).
73. W. H. Thompson and W. H. Miller, *J. Chem. Phys. 101*: 8620 (1994).
74. E. Goldfield, S. Gray, and G. C. Schatz, *J. Chem. Phys., 102*: 8807 (1995).
75. Balakrishnan and G. D. Billing, *J. Chem. Phys. 101*: 2785 (1994).
76. D. C. Clary, *J. Phys. Chem. 98*: 10678 (1994).
77. D. H. Zhang and J. Z. H. Zhang, *J. Chem. Phys. 99*: 5615 (1993).
78. D. H. Zhang and J. Z. H. Zhang, *J. Chem. Phys. 100*: 2697 (1994).
79. D. H. Zhang and J. Z. H. Zhang, *J. Chem. Phys. 101*: 1146 (1994).
80. D. H. Zhang and J. Z. H. Zhang, *Chem. Phys. Lett. 232*: 370 (1995).
81. U. Manthe, T. Seideman, and W. H. Miller, *J. Chem. Phys. 99*: 10078 (1993).

82. U. Manthe, T. Seideman, and W. H. Miller, *J. Chem. Phys. 101*: 4759 (1994).
83. D. Neuhauser, *J. Chem. Phys. 100*: 9272 (1994).
84. E. A. McCullough and R. E. Wyatt, *J. Chem. Phys. 54*: 3578 (1971).
85. K. C. Kulander (ed.), *Comput. Phys. Commun. 63*, 1991.
86. J. A. Miller, R. J. Kee, and C. K. Westbrook, *Annu. Rev. Phys. Chem. 41*: 345 (1990).
87. (a) D. Neuhauser, R. S. Judson, R. L. Jaffe, M. Baer, and D. J. Kouri, *Chem. Phys. Lett. 176*: 546 (1991); (b) D. Neuhauser, R. S. Judson, D. J. Kouri, D. E. Adelman, N. E. Shafer, D. A. V. Kliner, and R. N. Zare, *Science 257*: 519 (1992).
88. D. Neuhauser and M. Baer, *J. Chem. Phys. 92*: 3419 (1990).
89. D. Neuhauser, M. Baer, R. S. Judson, and D. J. Kouri, *J. Chem. Phys. 90*: 5882 (1989).
90. D. Neuhauser, M. Baer, R. S. Judson, and D. J. Kouri, *Comput. Phys. Commun. 63*: 460 (1991).
91. R. C. Mowrey, *J. Chem. Phys. 94*: 7098 (1991).
92. O. A. Sharafeddin and J. Z. H. Zhang, *Chem. Phys. Lett. 204*: 190 (1993).
93. D. H. Zhang and J. Z. H. Zhang, *J. Chem. Phys. 101*: 3671 (1994).
94. M. R. Pastrana, L. A. M. Quintales, J. Brandas, and A. J. C. Varandas, *J. Phys. Chem. 94*: 8037 (1990).
95. T. Pack, E. A. Butcher, and G. A. Parker, *J. Chem. Phys. 99*: 9310 (1993).
96. C. Leforestier and W. H. Miller, *J. Chem. Phys. 100*: 733 (1994).
97. R. T. Pack, *J. Chem. Phys. 60*: 633 (1974).
98. P. McGuire and D. J. Kouri, *J. Chem. Phys. 60*: 2488 (1974).
99. G. C. Schatz and H. Elgersma, *Chem. Phys. Lett. 73*: 21 (1980).
100. S. P. Walch and T. H. Dunning, *J. Chem. Phys. 72*: 1303 (1980).
101. D. H. Zhang, J. Z. H. Zhang, Y. Zhang, D. Wang, and Q. Zhang, *J. Chem. Phys., 102*: 7400 (1995).
102. Jackson and H. Metiu, *J. Chem. Phys. 86*: 1026 (1987).
103. C. M. Chiang and B. Jackson, *J. Chem. Phys. 87*: 5497 (1987).
104. A. Cruz and B. Jackson, *J. Chem. Phys. 84*: 5715 (1991).
105. M. R. Hand and S. Holloway, *J. Chem. Phys. 91*: 7209 (1989).
106. H. Hand and S. Holloway, *Surf. Sci. 211/212*: 940 (1989).
107. G. R. Darling and S. Holloway, *J. Chem. Phys. 93*: 9145 (1990).
108. G. R. Darling and S. Holloway, *J. Chem. Phys. 97*: 734, 5182 (1992).
109. S. Holloway and B. Jackson, *Chem. Phys. Lett. 172*: 40 (1990).
110. U. Nielsen, D. Halstead, S. Holloway, and J. K. Norskov, *J. Chem. Phys. 93*: 2879 (1990).
111. (a) M. Assher, O. M. Becker, G. Haase, and R. Kosloff, *Surf. Sci. 206* L880 (1988): (b) G. Haase, M. Assher, and R. Kosloff, *J. Chem. Phys. 90*: 3346 (1989).
112. J. Sheng and J. Z. H. Zhang, *J. Chem. Phys. 96*: 3866 (1992).
113. J. Sheng and J. Z. H. Zhang, *J. Chem. Phys. 97*: 6784 (1992).
114. J. Sheng and J. Z. H. Zhang, *J. Chem. Phys. 99*: 1373 (1993).
115. R. C. Mowrey, *J. Chem. Phys. 99*: 7049 (1993).
116. P. Saalfrank and W. H. Miller, *J. Chem. Phys. 98*: 9040 (1993).
117. (a) J. Dai, J. Sheng, and J. Z. H. Zhang, *J. Chem. Phys. 101*: 1555 (1994): (b) J. Dai and J. Z. H. Zhang, *Surf. Sci. 319*: 193 (1994).
118. J. Dai and J. Z. H. Zhang, *J. Chem. Phys., 102*: 6280 (1995).
119. G. R. Darling and S. Holloway, *J. Chem. Phys. 101*: 3268 (1994).
120. (a) A. Gruneich, A. J. Cruz, and B. Jackson, *J. Chem. Phys. 98*: 5800 (1993): (b) S. Kumar and B. Jackson, *J. Chem. Phys. 100*: 5956 (1994).
121. G. Wolken, *J. Chem. Phys. 59*: 1159 (1973).
122. (a) D. J. Kouri and R. C. Mowrey, *Chem. Phys. Lett. 119*: 285 (1985); *J. Chem. Phys. 84*: 6466 (1986); (b) B. Jackson and H. Metiu, *J. Chem. Phys. 84*: 3535 (1986).
123. G. Anger, A. Winkler, and K. D. Rendulic, *Surf. Sci. 220*: 1 (1989).
124. H. A. Michelsen and D. J. Auerbach, *J. Chem. Phys. 94*: 7502 (1991).

125. C. T. Rettner, D. J. Auerbach, and H. A. Michelsen, *Phys. Rev. Lett. 68*: 1164 (1992).
126. D. J. Auerbach, C. T. Rettner, and H. A. Michelsen, *Surf. Sci. 283*: 1 (1993).
127. H. A. Michelsen, C. T. Rettner, D. J. Auerbach, and R. N. Zare, *J. Chem. Phys. 98*: 8294 (1993).
128. B. Hammer, Mathias Scheffler, K. W. Jacobsen, and J. K. Norskov, *Phys. Rev. Lett. 73*: 1400 (1994).

7

New Methods for Use in Scattering Calculations: The Spectral Projection Method and the Stabilization Method

VLADIMIR A. MANDELSHTAM and HOWARD S. TAYLOR
University of Southern California, Los Angeles, California

I. INTRODUCTION

Two relatively new, generic methods of implementing scattering calculations are presented. The first method (Sec. II) is called the spectral projection method and is designed to compute the scattering matrix for reactive and nonreactive processes. The method is based on the well-known fact that the S-matrix can be obtained from a complete set of finite-range solutions of the wave equation valid only inside the interaction region. Such a set can be produced by applying the operator $(E - \hat{H})^{-1}$ to vectors spanning a very short range space on the edge of the interaction region.

When the basis set representing the interacting system's potential is of a dimension that allows storage of the Hamiltonian matrix in the computer core memory, the total scattering problem can be solved easily and simultaneously at all energies by a single diagonalization of the real symmetric Hamiltonian matrix.

When the basis set is too large for the core memory, an iterative procedure based on modified Chebyshev recursion relations for the evaluation of the inverse of the operator $E - \hat{H}$ can be employed. This procedure also gives results simultaneously at many energies. The present power series expansion of $(E - \hat{H})^{-1}$ as opposed to the previously used Chebyshev expansion (1, 2) converges uniformly in energy even when "the spatial propagation range" is very short. This is achieved by using the Chebyshev recursion relations in conjunction with an absorbing potential-like damping factor. Conceptually, it is also closely analogous to time-dependent wave packet methods (3, 4) that use an absorbing potential to get rid of artificial reflections of the wave packet at the edges of

the propagation region. It differs, however, from the time-dependent approach in that it does not need to use the time-to-energy Fourier transform as it does not ever introduce time into the problem.

The above-mentioned iterative procedure can be used in different versions. There is a version which obtains the S-matrix from a complete set of solutions of the wave equation. It uses almost minimal basis set describing the interaction region plus a small edge attached to the interaction region. This edge space contains a short-range damping potential. By simply enlarging the edge (absorbing) region the modified Chebyshev recursion relations can be also used to obtain the expansion of the Green's function, G^+, satisfying proper outgoing boundary conditions. Its advantage comes in being able to compute directly the individual S-matrix elements and total reactive scattering probability out of one initial state while ignoring the details of other reactive and nonreactive channels. The price paid for such a simplification is the need to use larger basis sets that span the interaction region, the noninteracting initial (final) packet region and the long-range damping region. The Green's function version has advantages when many channels are involved or when three-or-more-body breakup occurs.

The second generic method presented here, which also can treat the full scattering problem is the stabilization method for scattering (Sec. III). The specialty of this method, which also obtains results at all energies simultaneously is its ease in finding and computing the energies and widths of scattering resonances. Diagonalization of the real symmetric Hamiltonian matrices, only for their eigenvalues in the energy range of interest, is all that is needed. The stabilization method can also most easily obtain directly (without first obtaining the S-matrix) "local properties." That is, properties that do not depend on dynamics far from a local region of the potential. Among such properties are resonance parameters, local density and total photoabsorption cross sections. The stabilization method is most impressive compared to analytic continuation methods (rotated coordinates and negative imaginary potential) when used for obtaining resonance parameters as it involves only diagonalization of real symmetric matrices (not complex matrices as analytic continuation requires).

In this chapter reactive scattering for chemical systems shall be emphasized. Though the methods developed are much more general, they can, of course, treat nonreactive scattering in such systems as well. Additionally they can be fruitfully applied to computing resonances and transmission coefficients in quantum electronic devices (5); to electron-atom (molecule) scattering; to problems involving atom (molecule) continuum processes even when they are in the presence of a laser field (6), etc.

II. THE SPECTRAL PROJECTION METHOD

A. Basic Equations

In recent paper (7) it was shown that the S-matrix can be constructed as

$$S = A^- \cdot [A^+]^{-1} \tag{1}$$

where for a number of open channels, N_o, the elements of $N_o \times N_o$ matrix A^+ are given by

$$A^+_{lp} = \pm\langle f_l^+(\hat{H} - E)|\psi_p\rangle \tag{2}$$

(For convenience we use the multi-indices l, p to take into account both channels and arrangements. The reader should observe that the vertical line between $\hat{H} - E$ and ψ_p means that the operator $\hat{H} - E$ must act to the left.) Here $\{\psi_p, p = 1, 2, \ldots, N_o\}$ is any linear independent set of solutions of the Schrödinger equation with Hamiltonian $\hat{H}$; $f_l^{\pm}$ are either the nonperturbed asymptotic channel functions

$$f_l^{\pm}(r_l, s_l) = \frac{e^{\pm ikr_l}}{\sqrt{2k_l\pi}} \Phi_l(s_l) \tag{3}$$

or their analog with distorted waves. r_l is the incident direction reaction coordinate in channel l, and s_l are the coordinates orthogonal to the reaction coordinate. By $\Phi_l(s_l)$ we define the lth target state. Note that $(\hat{H} - E)f_l^{\pm}$ is an $\mathcal{L}^2$ function equal to $V_{\text{int}}f_l^{\pm}$, V_{int} being the interaction potential. As such the integration range in (2) is effectively the interaction region. To reduce the integration volume needed to compute matrix elements by Eq. (2) it might also be convenient (but not necessary) to multiply the channel functions $f_l^{\pm}(r_l, s_l)$ by a cutoff function $g(r_l)$, which is usually chosen such that it slowly rises from zero in the interaction region approaching unity in the asymptotic region (discussion on using cutoff functions and constructing distorted waves can be found in (8)).

The derivation of Eqs. (1) and (2) will be given below. First let us make some observations. Most importantly note that the ψ_p's, from an informational point of view, at a minimum need be only point-by-point solutions inside the range of the potential. Their behavior outside is irrelevant, as is their norm. Equations similar to (1) are known to have been used to transform independent solutions of close-coupled differential equations into proper outgoing (incoming) solutions of the Schrödinger equation. In effect (as will be seen) the matrices A^{+} give the transformation from ψ_p to properly normalized ψ_j^{+} as

$$\psi_p = \sum_{j=1}^{N_o} A_{jp}^{\pm}\psi_j^{\pm} \tag{4}$$

For now obvious reasons, we refer to Eqs. (1) and (2) as a matching and renormalization process (MRP).

Equation (4) yields also an expression for the half-scattering state specific transition amplitude from initial state $\hat{\mu}\phi_o$:

$$\langle\phi_o|\hat{\mu}|\psi_j^{\pm}\rangle = \sum_{p=1}^{N_o} [A^{+}]_{pj}^{-1} \langle\phi_o|\hat{\mu}|\psi_p\rangle \tag{5}$$

There are a number of ways of extracting the S-matrix from a given set of solutions ψ_p. A flux version of the MRP exists (9, 7) (see below) as does a simple pointwise matching procedures. Although eq. (2) seems to give the most accurate results since it uses an integral property of the wave functions, for special cases it is often more practical to use a less time-consuming version of MRP involving essentially two grid points per channel just outside the interaction region (10,11).

The most elegant way to derive Eqs. (1) and (2) starts from introducing the flux operator $\hat{F}_S$ through a surface S. Matrix element of $\hat{F}S$ between any two functions Ψ and Φ can be defined by the surface integral

$$\langle\Phi|\hat{F}_S|\Psi\rangle = \int dS \left(\frac{\partial\Phi^*}{\partial n}\Psi - \frac{\partial\Psi}{\partial n}\Phi^*\right) \tag{6}$$

where n is the coordinate normal to the surface $\mathcal{S}$.

Now consider a volume Ω in configuration space where the wave function ψ_p satisfies the Schrödinger equation, i.e., $(\hat{H} - E)\psi_p = 0$; and we also assume that Ω contains the interaction region. For the closed surface S surrounding Ω the use of Gauss's theorem (integration by parts) yields a very important property of the solutions of the wave equation as

$$\langle f_l^- | (\hat{H} - E) | \psi_p \rangle = [\langle f_l^- | \hat{F}_S | \psi_p \rangle + \langle f_l^- | (\hat{H} - E)\psi_p \rangle] = \langle f_l^+ | \hat{F}_S | \psi_p \rangle = \langle f_l^- | \hat{F}_{S_l} | \psi_p \rangle \qquad (7)$$

where S_l in the last equality is a surface, blocking channel l, in the asymptotic region. This last relation is correct once the lth channel function f_l^- vanishes in all the other arrangements. This would be always true if instead of f_l^+ properly cutoff f_l^+ functions or distorted waves are used. Due to the invariant property of the flux operator the surface S_l in the lth asymptotic arrangement can be chosen arbitrarily, in particular so that $n = r_l$ allowing a trivial surface integration. Let us now prove that if the matrixes A^+ are defined as expansion coefficients in Eq. (4) then the S-matrix can be obtained using Eqs. (1) and (2). For this consider the matrix elements $\langle f_l^- | \hat{F}_{S_l} | \psi_p \rangle$. Using Eq. (4) for ψ_p and replacing the Ψ_j^+'s (or equivalently Ψ_j) by their asymptotic form

$$\Psi_j^+ = f_j^- + \sum_{n=1}^{N_o} S_{nj} f_n^+ \qquad (8)$$

we get the desired result, Eq. (1).

The problem now is to find a generic way to construct the N_o wave functions ψ_p that are correct inside the interaction region. An immediate and obvious formal choice for ψ_p inspired by, but slightly different from, the work of Kouri, Hoffman, and coworkers [2,11–14), is to write

$$\psi_p = \frac{1}{E - \hat{H}} \chi_p^{\text{ext}}, \qquad p = 1, 2, \ldots, N_o \qquad (9)$$

or in more generic way,

$$\psi_p = \frac{1}{E - \hat{H} + \hat{u}^{\text{ext}}} \chi_p^{\text{ext}}, \qquad p = 1, 2, \ldots, N_o \qquad (10)$$

where $\{\chi_p^{\text{ext}}, p = 1, 2, \ldots, N_o\}$ is a set of arbitrary $\mathcal{L}^2$ linear independent functions defined to be nonzero only in the edge of the interaction region. The "edge" is a very small region, surrounding the interaction region, where the channel functions become valid solutions. Use of the external distorting potential $\hat{u}^{\text{ext}}$ could be also beneficial in some cases (see below).

Equation (9) (or 10) is here the key equation (15) and is in fact a particular form of the time-independent wave packet Schrödinger equation (TIWSE) explored in Refs. 2,11–14. To avoid confusion at this point we notice that the operator $(E - \hat{H})^{-1}$ could be, but is not necessarily a Green's operator satisfying some particular scattering boundary conditions. What $(E - \hat{H})^{-1}$ is depends upon the basis set in which we choose to represent it and the method we use to evaluate its action on χ_p^{ext}. The simplest and probably most efficient choice (in the sense of economy of basis size) corresponds to evaluation of $(E - \hat{H})^{-1}$ using a real orthonormal basis describing only the interaction plus short-edge region in space. If the narrow wave packets χ_p^{ext} are chosen to be real the resulting wave functions ψ_p are also real. Different choices of the independent set $\{\chi_p^{\text{ext}}, p = 1, 2, \ldots, N_o\}$ give different sets $\{\psi_p, p = 1, 2, \ldots, N_o\}$ but the same S-matrix. Clearly, any desired symmetry in $\hat{H}$ can be built into the χ_p^{ext} and the ψ_p will reflect it.

As a brief aside let us show here that if an external distorting potential $\hat{u}^{\text{ext}}$ as in Eq. (10) is used, calculating the $A^{\pm}$ matrices could in some cases be simplified due to the relation reminiscent to those used in Ref. 16 for $\hat{u}^{\text{ext}}$ being the imaginary potential. Consider

$$(E - \hat{H} + \hat{u}^{\text{ext}}) \frac{1}{E - \hat{H} + \hat{u}^{\text{ext}}} = 1 \tag{11}$$

Putting (10) into (2) and using (11) yields an alternative to Eq. (2)

$$A_{lp}^{\pm} = \pm\langle f_l^{\mp} | \hat{u}^{\text{ext}} \psi_p - \chi_p^{\text{ext}} \rangle \tag{12}$$

This form of $A^{\pm}$ could have advantages relative to evaluating $A^{\pm}$ by a quadrature over the whole interaction region (Eq. (2)). The short range of $\hat{u}^{\text{ext}}$ translates in a more economical quadrature procedure. The above equation though must be used with care since it is valid only when all eigenfunctions φ_i of the distorted Hamiltonian $\hat{H} - \hat{u}^{\text{ext}}$ have no flux at the outer boundary; that is, φ_i and their first derivatives with respect to the normal coordinate vanish at the boundary.

The solution of the scattering problem, if N_o is not so large as to make even the operating with the matrices $A^{\pm}$ difficult, reduces now to evaluation of the effect of $(E - \hat{H})^{-1}$ (or, equivalently, $(E - \hat{H} + \hat{u}^{\text{ext}})^{-1}$) on the set $\{\chi_p^{\text{ext}}\}$. When the Hamiltonian matrix can be stored in the computer core memory it is possible to simply diagonalize it and to construct out of the eigenvalues E_i and eigenfunctions φ_i a solution at any desired energy from the spectral form of Eq. (9):

$$\psi_p = \sum_{i=1}^{N} \frac{\langle \varphi_i | \chi_p^{\text{ext}} \rangle}{E - E_i} \varphi_i \tag{13}$$

Here N is the size of the nearly minimal basis possible to use, namely that for the interaction region and edge. Even though this is an N^3 process the simplicity of the method and the ability to use black-box packaged programs suggest that the economy of labor time at modest cost in computer time makes this method extremely attractive. Also, when E in Eq. (13) approaches an eigenvalue E_i, numerical problems of calculating the S-matrix occur only when E equals E_i to many significant figures.

"All-energy" methods like the above and those presented in the next section significantly simplify the search for resonances, especially narrow ones. The cost of repeating calculations at different energies is minimal. The resonance energy search can be further facilitated if it is coupled with a quick and even primitive version of the stabilization method calculation (17) which uses similar diagonalization routines. As will be seen in Sec. III the narrower is the resonance the easier it is for the stabilization method to find its position. Once the resonance energy is known even roughly, the S-matrix can be computed on a dense grid about this energy. This definitely saves the effort of obtaining adequate results in the presence of narrow resonances which might be missed as they lie between the energy values chosen for the S-matrix evaluation.

For scattering results at each of a small number of energies, inversion of $E - \hat{H}$ by the LU decomposition is a method of choice.

When the problem becomes so large that the Hamiltonian matrix cannot be stored in the fast computer memory, it is no longer practical to either produce its spectral representation or invert $E - \hat{H}$ directly. In such case iterative methods should be considered as the main tool. These methods could take advantage of the real symmetric and

sparse (in discrete variable representation (DVR) (18) or distributed approximating functions (DAF) basis (19)) nature of the Hamiltonian matrix. The first such method is solving N_o sets of the simultaneous linear equations that arise from Eq. (9),

$$(E - \hat{H})\psi_p = \chi_p^{\text{ext}}, \qquad p = 1, 2, \ldots, N_o \tag{14}$$

by, say, Lanczos recursion (20), following the work of Groenenboom and Colbert (8). Recalling that an $\mathscr{L}^2$ basis is being used putting Eq. (9) into (2) shows that one could also solve

$$(E - \hat{H})y_l = (\hat{H} - E)f_l^+, \qquad l = 1, 2, \ldots, N_o \tag{15}$$

and get A^+ as

$$A_{lp}^+ = \pm\langle y_l|\chi_p^{\text{ext}}\rangle \tag{16}$$

Equation (15) is the key equation of the Kohn variational principle for the S-matrix (21). For "small" problems, when the spectral representation of $\hat{H}$ can be obtained, both methods are essentially equivalent. If the linear equations are to be solved iteratively, the present method, Eq. (14), effectively requires to solve half the number of sets of simultaneous linear equations as the basis and χ_p^{ext} can be chosen real making Eq. (14) real while (15) remains complex.

If results at many energies are needed the total effort, hidden in the number of iterations could become excessive. In the next section it will be shown that the energy-independent inhomogeneity in Eq. (14), as opposed to Eq. (15), will allow solutions for ψ_p at all energies from a single power series expansion of $(E - \hat{H})^{-1}\chi_p^{\text{ext}}$. Linear equations arising from versions of log-derivative methods (22, 23) and the extremely similar quantum transmitting boundary method (24), so favored in applications involving quantum electronic devices (25), have energy-dependent inhomogeneities and cannot take advantage of polynomial expansion.

Before proceeding to the next section where the polynomial expansion technique is described, developing a few variants of Eq. (9) will be useful in connecting to other theories.

To begin note the more usual choice of ψ_p,

$$\psi_p = \delta(E - \hat{H})(\hat{H} - E)f_p^+ \tag{17}$$

This will be used in Sec. III to connect the stabilization data to the scattering matrix. Accordingly expression (2) would take the symmetric form

$$A_{lp}^+ = \pm\langle f_l^+(\hat{H} - E)|\delta(E - \hat{H})|(\hat{H} - E)f_p^+\rangle \tag{18}$$

Equation (17) is based on the fact that the spectral density operator $\delta(E - \hat{H})$ projects any $\mathscr{L}^2$ function (or wave packet) into the space of solutions of the Schrödinger equation at the energy E. However, since the functions ψ_p are needed only inside interaction region and do not have to be properly normalized, the $\delta(E - \hat{H})$ in Eqs. (17) and, consequently, (18) can be replaced by any other projector onto the solution space inside the interaction region. A convenient form for such a spectral projector related to Eq. (9) is

$$\hat{W} = \frac{1}{E - \hat{H}}\,\hat{P}\,\frac{1}{E - \hat{H}} \tag{19}$$

where $\hat{P}$ is any projector onto the edge region. Note that using Eq. (10) would lead to a similar operator, which is not considered here. A similar idea, but in slightly different context, was used by Neuhauser in Ref. 26 who proposed to use a short-range absorbing potential in order to replace the correct Green's function by its short-range analog.

To prove that $\hat{W}$ is a projector with the desired properties it is enough to consider the action of $\hat{W}$ on any $\mathcal{L}^2$ function χ (e.g., $\chi = (\hat{H} - E)f_p^+$):

$$\hat{W}\chi = \frac{1}{E - \hat{H}} \hat{P} \frac{1}{E - \hat{H}} \chi \tag{20}$$

Now in (20) one could recognize Eq. (9) by replacing $\hat{W}\chi$ with ψ_p and $\hat{P}(E - \hat{H})^{-1}\chi$ with χ_p^{ext}, which is indeed an edge wave function even if χ is not. To make sure that the operator $\hat{W}$ projects *onto* the complete space of ψ_p's the rank of $\hat{P}$ which yields the rank of $\hat{W}$ must be at least N_o.

Note that $\hat{W}$, being a projector onto the solution space of the wave equation in a finite region, is, excluding the trivial single-channel case, not proportional to $\delta(E - \hat{H})$ in any sense.

Thus, use of the spectral projector $\hat{W}$ implies the following symmetric expression for the $A^{\pm}$ matrices:

$$A_{lp}^{\pm} = \pm\langle f_l^+(\hat{H} - E)|\hat{W}|(\hat{H} - E)f_p^+\rangle \tag{21}$$

In terms of Eq. (15) the above equation can also be written as

$$A_{lp}^{\pm} = \pm\langle y_l|\hat{P}|y_p\rangle \tag{22}$$

One way to define $\hat{P}$ is to choose it equal to multiplication operation by a function of the coordinates:

$$\langle r|\hat{P}|r'\rangle = \gamma(r)\delta(r - r') \tag{23}$$

The choice of $\gamma(r)$ can be quite arbitrary, but it should appear minimally as an edge-located barrier-like blocking potential that obstructs flow out of the interaction region. In the DVR (or DAF) representation, $\hat{P}$ has nonzero elements only on the diagonal and then only at the elements associated with the points in the edge space. (In general, $\hat{P}$ implies a matrix that only has nonzero elements in the edge-space block.) The small advantage here is that only $\gamma(r)$ need be chosen, as opposed to a linear independent set $\{\chi_p^{\text{ext}}, p = 1, 2, \ldots, N_o\}$.

In principle, for a sufficiently accurate calculation of the S-matrix the size of the edge space could be reduced to the minimum (e.g., the number of DVR points where $\gamma(r)$ is not zero can be equal to N_o).

Another way to choose the operator $\hat{P}$ in Eq. (19) in order to make it suitable for a linear equations solver is

$$\hat{P} = \sum_{j=1}^{\tilde{N}_o} |\chi_j^{\text{ext}}\rangle\langle\chi_j^{\text{ext}}| \tag{24}$$

in which case constructing the operator $\hat{W}$ operationally becomes equivalent to solving Eq. (9). When $\tilde{N}_o = N_o$, the S-matrix calculated using $\hat{W}$ should be identical to those calculated by Eqs. (9), (2), and (1). However, in practice the spectral projector $\hat{W}$ leads to a more general way to describe the solution space of the wave equation in the finite region. For instance, in some cases it might be convenient to make $\tilde{N}_o$ larger than the

number of independent solutions (e.g., $\tilde{N}_o = N_o + 1$). This, in particular, completely resolves the so-called anomaly problem caused by an accidental degeneracy of the A^+-matrices. The "accidental degeneracy" takes place basically because at some energies the set of functions $\{(E - \hat{H})^{-1}\chi_j^{\text{ext}}, j = 1, 2, \ldots, N_o\}$ may accidentally become linearly dependent. This effectively decreases the rank of $\hat{W}$. Moreover, the need to include the weakly closed channels to the MRP is satisfied by increasing the rank of $\hat{P}$. This could also be necessary because otherwise the above set might poorly represent the complete solution space.

Thus using Eq. (9) or, equivalently, Eq. (14), where ψ_p's are produced and are real functions, we evaluate A^+ from the formula

$$A_{ij}^+ = \pm \sum_{p=1}^{\tilde{N}_o} \langle f_i^+(\hat{H} - E)|\psi_p\rangle\langle\psi_p|(\hat{H} - E)f_j^+\rangle \tag{25}$$

When power series expansion are used, the ψ_p's will be complex functions having real and imaginary parts, and therefore will never cause an accidental degeneracy of A^+ matrices. As such, Eq. (9) will continue to be used in combination with Eq. (2).

We now turn to the polynomial expansion, "all-energy" method of evaluating ψ_p's from Eq. (9).

B. Iterative Calculation of $(E - \hat{H})^{-1}$ Using Modified Chebyshev Recursion Relations

As demonstrated in Refs. 1 and 2, if the inhomogeneity in Eq. (14) (χ_j^{ext} in our case) is energy independent the energy explicitly enters into the Chebyshev polynomial expansion via the energy- (here φ) dependent coefficients:

$$\psi(E) = \frac{1}{E - \hat{H} + i0}\chi^{\text{ext}} = \frac{2i}{\Delta H \sin\varphi}\left\{\frac{1}{2}\xi_0 - \sum_{n=0} e^{in\varphi}\xi_n\right\} \tag{26}$$

where the Chebyshev recursion relations for the energy-independent vectors ξ_n are given by

$$\xi_0 = \chi^{\text{ext}} \quad \xi_1 = \hat{H}_{\text{norm}}\xi_0 \quad \cdots \quad \xi_{n+1} = 2\hat{H}_{\text{norm}}\xi_n - \xi_{n-1} \tag{27}$$

The shifted Hamiltonian is

$$\hat{H}_{\text{norm}} = \frac{\hat{H} - \overline{H}}{\Delta H} \tag{28}$$

where $\overline{H} = \frac{1}{2}(H_{\max} + H_{\min})$, $\Delta H = \frac{1}{2}(H_{\max} - H_{\min})$, and $H_{\max}$ and $H_{\min}$ are respectively an upper and lower estimations of the maximum and minimum eigenvalues of the Hamiltonian matrix. The energy-dependent phase φ is defined by

$$\varphi = \arccos\left(\frac{E - \hat{H}}{\Delta H}\right) \tag{29}$$

Clearly the coefficient $2i/(\Delta H \sin\varphi)$ in Eq. (26) does not affect the result when the MRP procedure is used.

Notice, that the power series expansion of $\psi(E)$ does not involve the usual time-Fourier transform, but it does correspond to the discrete half-Fourier transform of the

sequence $\{\xi_n, n = 0, 1, 2, \ldots\}$. The difference between the present formulation and time-dependent methods is that no small numerical parameter Δt is involved here.

Special attention should be paid to the convergence issue of the Fourier transform in Eq. 26. First, the expansion will be useful only when it converges uniformly in energy. Second, if convergence is slow, the $\hat{H}$ matrix will have to be applied to the vector so many times that the method loses all advantage relative to solving linear equations by Lanczos recursion (8) where one needs a maximum of N (the basis size) iterations per channel per energy. In the power series expansion the number of iterations has no upper limit and is governed purely by numerical convergence. Here is where most of the computational advantage is won or lost.

For the Hermitian Hamiltonian $\hat{H}_{\text{norm}}$ the norm of the vectors ξ_n defined by recursion relations, Eq. (27), does not decay with the number n, and therefore the series in Eq. (26) does not converge in the usual sense. Nevertheless, it does converge in the following more general sense. One of the ways to sum such a series is to make an analytic continuation in φ by introducing a constant convergence factor $i\epsilon$:

$$\psi^{\epsilon}(E) = \frac{2i}{\Delta H \sin\varphi}\left\{\frac{1}{2}\xi_0 - \sum_{n=0} e^{-in(\varphi - i\epsilon)}\xi_n\right\} \equiv \frac{2i}{\Delta H \sin\varphi}\left\{\frac{1}{2}\xi_0^{\epsilon} - \sum_{n=0} e^{-in\varphi}\xi_n^{\epsilon}\right\} \tag{30}$$

where the second expression transfers the damping factor $i\epsilon$ to the recursion relations for ξ_n:

$$\xi_{n+1}^{\epsilon} = e^{-\epsilon}(2\hat{H}_{\text{norm}}\xi_n^{\epsilon} - e^{-\epsilon}\xi_{n-1}^{\epsilon}), \quad \xi_0^{\epsilon} = \chi^{\text{ext}}, \quad \xi_1^{\epsilon} = e^{-\epsilon}\hat{H}_{\text{norm}}\xi_0^{\epsilon} \tag{31}$$

The function $\psi^{\epsilon}(E)$ is analytic in ϵ and converges uniformly in E for any fixed positive ϵ since the norm $\|\xi_n^{\epsilon}\|$ decays exponentially with n. The desired $\psi(E)$ can then be obtained as the limit

$$\psi(E) = \lim_{\epsilon \to 0} \psi^{\epsilon}(E) \tag{32}$$

As long as the Hamiltonian matrix is defined in a minimal size (interaction plus edge) region the $\epsilon \to 0$ limit has nothing to do with the outgoing boundary conditions for the Green's function; i.e., the relation

$$\frac{1}{E - \hat{H} + i0}\chi^{\text{ext}} = \hat{G}^{+}\chi^{\text{ext}} \tag{33}$$

becomes correct only when the Hamiltonian is considered in the limit when the whole (or a very large) region of the configuration space including the asymptotic region is taken. This was done in Ref. 2. In the present approach the basis range and therefore matrix size is often much smaller. To obtain the S-matrix here we only need such solutions $\psi(E)$ which satisfy the homogeneous Schrödinger equation merely inside the interaction region and which could be anyting outside. This is why we call the method associated with Eqs. (9) and (19) the spectral projection approach.

Now, our study of the convergence of Eq. (32) in combination with Eq. (30) as a function of M, the number of iterations (terms) used shows that the convergence is not uniform in energy E (it is uniform only for finite fixed ϵ, but as ϵ gets smaller more terms in the series are needed). Quite simply the reason is that as the energy E approaches an eigenvalue of $\hat{H}$, the norm of $(E - \hat{H})^{-1}\chi^{\text{ext}}$ becomes infinitely large, and this results in a large number of iterations being needed to converge the series at such an energy.

More rapid convergence of the Fourier series can be achieved if one uses a more efficient damping factor, g_n, rather than a simple exponential damping, $e^{-n\epsilon}$,

$$\sum_{n=0}^{\infty} e^{-in\varphi}\xi_n \approx \sum_{n=0}^{M} g_n e^{-in\varphi}\xi_n \tag{34}$$

where the sequence g_n slowly decays from one to zero in the interval $n = 0, 1, \ldots, M$. The right-hand side in Eq. (34) leads to more rapid convergence when, for small n, g_n spends more time near one than the $e^{-n\epsilon}$ does and decays more rapidly at large n. The main purpose of using such damping is to get rid of (i.e., to filter) the high-frequency oscillations in φ. We will return to this question in the next section since, in general, this improvement alone does not completely resolve the nonuniform convergence problem in the sense that singularities still exist at the eigenvalues of the grid represented Hamiltonian. This will be especially bad for large systems where such singularities are dense in energy.

At this point, in analogy to the absorbing potential theory (3, 27, 16, 4), we would like to make an ansatz, to be tested empirically, that all our analysis holds if in the recursion relations, Eq. (31), we replace the constant damping factor $e^{-\epsilon}$ by a coordinate-dependent function, namely,

$$\epsilon \rightarrow \gamma(r) \tag{35}$$

This finally yields the following recursion relations:

$$\xi^{\gamma}_{n+1} = e^{-\gamma}(2\hat{H}_{\text{norm}}\xi^{\gamma}_n - e^{-\gamma}\xi^{\gamma}_{n-1}), \quad \xi^{\gamma}_0 = \chi^{\text{ext}}, \quad \xi^{\gamma}_1 = e^{-\gamma}\hat{H}_{\text{norm}}\xi^{\gamma}_0 \tag{36}$$

The desired energy-dependent solution is then obtained as

$$\psi^{\gamma}(E) = \frac{2i}{\Delta H \sin\varphi}\left\{\frac{1}{2}\xi^{\gamma}_0 - \sum_{n=0} e^{-in\varphi}\xi^{\gamma}_n\right\} \tag{37}$$

The damping factor $e^{-\gamma}$ acts on a wave function, multiplying it by the function $e^{-\gamma(r)}$. The role of $e^{-\gamma(r)}$ in the above recursion relations clearly is also analogous to that of the exponential damping factor used in conjunction with the split-operator time-propagation scheme (4).

The function $\gamma(r)$ should be considered as a convergence factor whose optimal shape and amplitude can be found by numerical experimentation. Having in mind the analogy between the present approach and the absorbing potential theory, we anticipate that the best convergence will be achieved when $\gamma(r)$ is such that it is zero in the interaction region and slowly rises in the edge region. Since so far we have not required $\psi^{\gamma}(E)$ to be the proper outgoing scattering solution, the choice of the form of $\gamma(r)$ will not be as critical as it is in the case of the well-behaved absorbing potential. That is, as before in Eqs. (23), we can still choose $\gamma(r)$, the convergence factor, to be much shorter and steeper than an absorbing potential. In fact it will resemble the blocking potential of the previous subsection. It is also important that $\gamma(r)$ does not need to vanish in the region where the edge wave packet χ^{ext} exists; that is, they can overlap as $\psi^{\gamma}(E)$ is still a solution of the homogeneous Schrödinger equation in the region where both $\gamma(r)$ and χ^{ext} are zero. Again, different choices of the functions $\gamma(r)$ and χ^{ext}_p would give different ψ_p but the same S-matrix.

The implementation of the recursion relations given by Eq. (36) needs minimal storage (two vectors at a time assuming that the matrix elements of $\hat{H}_{\text{norm}}$ are calculated

on the fly). The scattering information can be accumulated at each step using the flux (Eq. (7) or two-point version of MRP (10, 11). For example, in the flux version, having ξ_n^γ after each iteration, one would need to compute the matrix elements $\langle f_l^\mp | \hat{F}_{S_1} | \xi_n \rangle$ and update the $A_{lp}^\mp$-matrices at all energies of interest. The flux evaluation for many energies between the channel wave function $f_l^\mp$ and energy-independent ξ_n^γ is trivial since the energy dependence can be obtained analytically. Let us now point out an interesting feature of Eq. (37). Clearly if χ^{ext} is a real wave packet the wave function $\psi(E)$ as defined by Eq. (32) should be real because the converged imaginary part of $\psi^\epsilon(E)$ is proportional to the small constant ϵ. It is also clear that for any finite ϵ, Im $\psi^\epsilon(E)$ has no practical use in scattering calculations unless the Hamiltonian is represented in a very large region in configuration space. On a finite grid it gives only a stick spectra of the grid-represented Hamiltonian. When a short-range damping factor $e^{-\hat{\gamma}}$ is used problems with uniform convergence will be seen to disappear. This is because the poles of the operator implied in Eq. (37) under the action of $e^{-\hat{\gamma}}$ moved from the real axis down into the complex plane, which clearly yields the corresponding analytic continuation of the real Green's function $(E - \hat{H})^{-1}$ as represented by the Chebyshev polynomial expansion (Eq. (26)). The convergence of the series given by Eq. (37) is expected to be exponential due to the damping factor, which subtracts a portion of ξ_n^γ at each iteration step. Moreover the objection to use of Im $\psi^\epsilon(E)$ no longer holds for Im $\psi^\gamma(E)$. In fact we have observed that the imaginary part of $\psi^\gamma(E)$ as well as its real part satisfies the wave equation in the interaction region and can equivalently be used in the MRP (Eq. (2)). The "accidental" anomalies discussed in the previous subsection cannot occur when a set of complex ψ_p is used. In practice this gives much more stable uniform convergence when Eqs. (2) and (37) are implemented. All this suggests, and we anticipate, that if $\gamma(r)$ were chosen to have the extended range and soft curvature of an absorbing potential and if χ does not overlap the range of $\gamma(r)$, the relation

$$\psi^\gamma(E) \approx \hat{G}^+ \chi \tag{38}$$

would become true.

Use of Eq. (38) makes it possible to utilize a very convenient expression for the S-matrix based on the Kohn variational principle (13):

$$S_{lp} = \frac{i\sqrt{k_l k_p}}{m(2\pi)^2 \mathcal{A}(k_l)\mathcal{A}^*(k_p)} \langle \chi_l | \hat{G}^+ | \chi_p \rangle \tag{39}$$

where $\mathcal{A}(k_l)$ is the Fourier component of the incoming (outgoing) wave packet χ_l that does not overlap the interaction region and corresponds to the lth channel state.

Clearly Eq. (39) with Eq. (38) allows one to obtain a single column of the S matrix from a single $\psi^\gamma(E)$ for the price of using a much bigger basis which is, in turn, needed to describe a much longer outer absorbing region and a nonoverlapping "free" wave packet sampling region.

The flux out of any initial channel p to all states in all other arrangements would be given by the matrix element $\langle \chi_p | \text{Im } \hat{G}^+ | \chi_p \rangle$.

Interestingly, in Refs. 14 and 28 respectively the Faber and Newton polynomials of the operator $\hat{H} - i\hat{u}$ were used to expand the Green's function defined by

$$\hat{G}^+ = \frac{1}{E - \hat{H} + i\hat{u}} \tag{40}$$

Application of the present approach as envisioned in Eq. (38) would be advantageous as here the convergence problem of the Chebyshev series is solved trivially by use of the damping factor $e^{-\hat{\gamma}}$. Implementation of the Faber polynomials (14) requires the determination of a contour in the lower half of the complex plane, which includes the spectrum of the non-hermitian operator $\hat{H} - i\hat{u}$ and which at the same time has a simple shape allowing analytic evaluation of integral expressions for the energy-dependent coefficients in the Faber polynomial expansion. This might be a problem when the Green's function $(\hat{H} - i\hat{u})^{-1}$ has poles very close to the real axis (e.g., due to thresholds or narrow resonances). At the same time convergence of the Newton polynomial expansion depends on the accuracy of the estimation of the spectral domain of the non-Hermitian operator $\hat{H} - i\hat{u}$ (29); the present procedure needs only the real-valued spectral domain of the Hermitian Hamiltonian $\hat{H}$.

Equation (38) also has its own interest when applied to resonance problems which require for representation large basis sets. As discussed elsewhere (see, e.g., (30) and references therein) if a long-range absorbing potential is used the resonances can be obtained as the complex poles of the Green's function, Eq. (40)—i.e., the complex eigenvalues of $\hat{H} - i\hat{u}$. For large systems computation of these eigenvalues becomes a very difficult task. The hope is that for a large system our power series evaluation of Eq. (38) can be used to utilize a variant of Neuhauser's idea on filter diagonalization (31). Briefly, if obtaining narrow resonances (or bound states) corresponding to the real energy interval $[E_{\min}, E_{\max}]$ is of interest, a small number, K, of independent wave functions Υ_l can be constructed corresponding to an arbitrary initial wave packet χ that is assumed to have a significant overlap with the resonance states of interest:

$$\Upsilon_l = \text{Im } \hat{G}^{+}(E_l)\chi \approx \text{Im } \psi^{\gamma}(E_l), \qquad l = 1, 2, \ldots, K \tag{41}$$

where $\{E_l, l = 1, 2, \ldots, K\}$ may be chosen as a set of K equally spaced real energies in the interval $[E_{\min}, E_{\max}]$. The next step would be to use these functions as a contracted basis to diagonalize the non-Hermitian Hamiltonian $\hat{H} - i\hat{u}$. Those resulting eigenvalues which have small imaginary parts should yield the desired positions and widths of the narrow resonances. This procedure can be used to obtain the resonance wave functions as well.

C. Numerical Example: Collinear H + H_2 System

The results reported here correspond to the LSTH potential energy surface of Ref. 32. For all calculations we used the infinite-order DVR grid introduced in (33) by Colbert and Miller associated with the two normal mode coordinates. The choice of the parameters for the grid was based on the recommendations of Refs. 33 and 16. The density of DVR points n_B was varied between 3 and 4 per de Broglie wavelength corresponding to the maximum energy of interest, $E_{\max} = 1.4$ eV. The infinite grid was then truncated according to the maximum channel radius, $r_{\max}$, and cutoff criterion, $V_{\text{pot}} < E_{\text{cut}}$. We found that $n_B = 3$ and $E_{\text{cut}} = 6$ eV was sufficient to guarantee accuracy of about 0.5% or better for all channel-to-channel probabilities in the energy interval considered.

All calculations were made simultaneously for 101 equally spaced energies that adequately represent the range 0.4 to 1.4 eV. The S-matrix was first computed by direct diagonalization of the DVR Hamiltonian using for the $A^{\pm}$-matrices Eqs. (2) and (9) or Eq. (21) for many different choices of wave packets χ_p^{ext} or blocking potential $\gamma(r)$ respectively. The numerical tests showed that the results are very stable with respect to

these choices. A very high accuracy (below 1% for most energies) for the state-to-state reaction probabilities can be achieved when a blocking potential (or wave packet) in the form

$$\gamma(r) = c\frac{r - r_0}{r_{\max} - r_0} \tag{42}$$

was placed in a very short region, $r_{\max} - r_0 = 0.2$ au. Here the maximum channel radius was $r_{\max} = 5.7$ au and the density of DVR points $n_R = 3$. This corresponds to a total number of DVR points $N = 342$ including $N_P = 28$ edge grid points. Accuracy to within few percent can be achieved even when the number of DVR points in the edge region is equal to N_o, the number of open channels. No anomalies in the calculated S-matrix caused by the real eigenenergies of $\hat{H}$ or linear-dependence-type anomalies were found.

Let us now discuss the results obtained by Eq. (37). As opposed to noniterative methods (direct diagonalization of $\hat{H}$), the convergence of the expansion Eq. (37) turns out to be sensitive to the choice of the wave packets χ_P^{ext} and the damping factor $e^{-\gamma(r)}$. Namely, the smoother the wave packets and $\gamma(r)$, the faster is convergence. The choice

$$\chi_P^{\text{ext}}(r, s) = (r - r_0)\Phi_P(s) \tag{43}$$

with $\gamma(r)$ defined by Eq. (42) is certainly the smoothest choice and seems to be the best. Consequently, for better convergence the edge region should be slightly enlarged.

Even though the Fourier series in Eq. (37) converges, better results were obtained when a filtering procedure defined by Eq. (34) was also used. Such filtering is intended "to filter out" high-frequency oscillations in φ caused by the high-energy components of the Hamiltonian. With M being the number of iterations, we found that all reasonable choices of the filter g_n give satisfactory results, while the best convergence was achieved when g_n was taken in the form

$$g_n(M) = \begin{cases} 1 & \text{if } n \leq M_0 \\ \dfrac{M - n}{M - M_0} \exp\left(\dfrac{n - M_0}{M - M_0}\right) & \text{if } M_0 < n < M \end{cases} \tag{44}$$

The choice for M_0 can be somewhat arbitrary, but it should be neither too small nor too large. In all our calculations we used $M_0 = 100$.

Two sets of parameters used in the calculations of the state-to-state transition probabilities by Eqs. (37) are given in the table. The convergence rate was approximately the same when the constant c defining the amplitude of the damping potential, Eq. (42), was varied in the interval 0.1 to 0.4.

As was expected the convergence of the expansion given by Eq. (37) is uniform in energy. We found that using parameters of set I from the table a number $M = 800$

Table 1 Numerical Parameters for the H + H_2 Collinear System Used in the Calculations[a]

Set	n_b	E_{cut}	r_0	$r_{\max}$	N	N_P	c	$M_{1\%}$
I	3	6 eV	5.0 au	5.5 au	388	74	0.2	800
II	3	6 eV	5.5 au	6.0 au	314	70	0.2	600

[a]The given number of iterations, $M_{1\%}$, corresponds to roughly 1% convergence achieved for all channel-to-channel probabilities for most of 101 energy values in the interval 0.4 to 1.4 eV.

iterations provides very high accuracy, within 1%, for most energies in the energy interval considered. Set II corresponds to a smaller DVR grid and still provides high accuracy for most energies. Considerable difference between exact probabilities and those obtained using set II appears only near the resonance at the energy E = 1.3 eV. In Figs. 1 and 2 we show the reaction probability P_{00} and cumulative reaction probability $N(E) = \Sigma_{if}|S_{if}|^2$ computed using parameters of set II. Essentially converged results are achieved at most energies with M = 600, the error being generally of order of 1%. The "bad" energy regions where convergence is slower correspond to the energies near resonances, while the "flat" parts of the S-matrix elements converged much faster. This observation is consistent with those made in Ref. 28, that is, the convergence rate of a power series near a narrow resonance should be proportional to the resonance width.

Figures 1 and 2 also show that order of magnitude results can be obtained even when the number of iterations is reduced to M = 200.

It is difficult to conclude how the numerical effort grows with the size of the system from our numerical tests since there are several parameters that control the accuracy. It is also not too informative to present convergence tests for any particular energy because the convergence is different for different quantities and different energy ranges (see the figures).

When the energy interval of interest is increased and, consequently, a higher density of DVR points is used, the spectrum range ΔH becomes bigger and the convergence gets slower. Convergence of the expansion given by Eq. (37) also depends on the range of the DVR grid. The smaller the range the more rapid is convergence. This means that a bigger grid range would need more applications of $\hat{H}$ to a vector.

The number of iterations M does not critically depend on the shape of χ_p^{ext} and $\gamma(r)$ as long as they are "smooth." (The $\gamma(r)$ can be made sufficiently smooth while it is still much shorter in coordinate range than the well behaved absorbing potentials (34, 14).)

D. Discussion of the Spectral Projection Method

When the basis size is small enough to store the Hamiltonian matrix in the computer core memory, two things can be said with confidence. First, the method presented in Sec. II based on Eq. (1) and Eqs. (2) and (9) (or better to avoid anomalies, (1) and (21)) are very easy to comprehend and implement. This is especially true when the diagonalization of the full Hamiltonian is the key computational step. Second, there are many other approaches, such as the Kohn variational principle (21), the R-matrix theory (35), and the closely related, log-derivative methods (22, 23), that are easy to implement and anomaly free. The methods which use absorbing potentials clearly have a disadvantage relative to the above methods in the sense that they require larger than minimal basis sets and involve non-Hermitian matrices.

Once the problem requires a grid or basis too large for the core memory the situation changes; all the eigenvalues and eigenfunctions of $\hat{H}$ can no longer be found and the $\hat{H}$ matrix can only be available on the fly. Here solution of simultaneous linear equations, time propagation of wave packets, or power series expansions of the operator $(E - \hat{H})^{-1}$ become methods of choice. We suggest that if linear equations are to be employed the use of Eqs. (9) and (1) or (25) is economical. These methods, as do the Kohn and log-derivative methods, use a minimal basis set describing essentially the interaction region and has a sparse Hamiltonian matrix if DVR or DAF representations are employed. The approach presented here also cuts the work relative to that of the

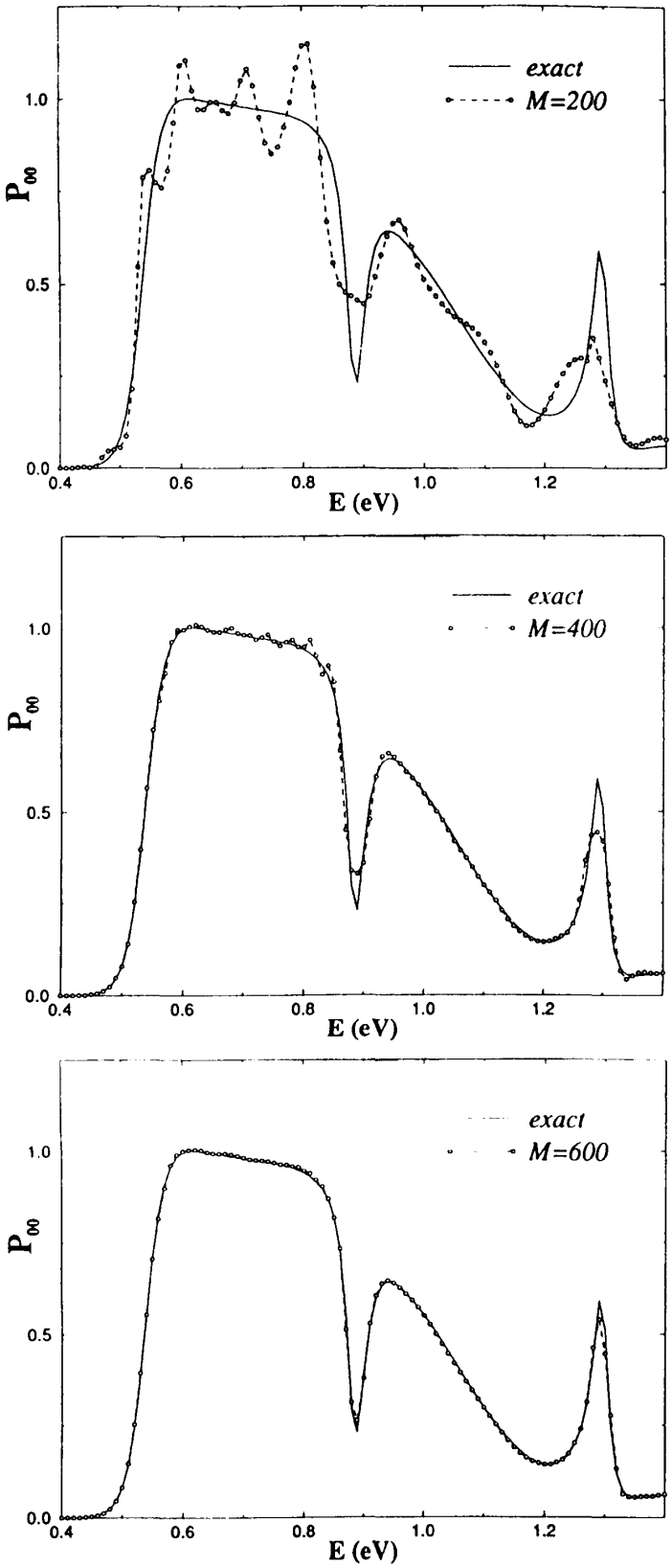

Figure 1 Reaction probability P_{00} for the collinear H + H_2 → H_2 + H exchange reaction calculated by Eqs. (37), (2), and (1). M indicates the number of iterations used in the recursion relations, Eq. (37). The calculation was done for set II of Table 1. The "exact" result corresponds to converged calculation by Eq. (21) using a very large and dense DVR grid.

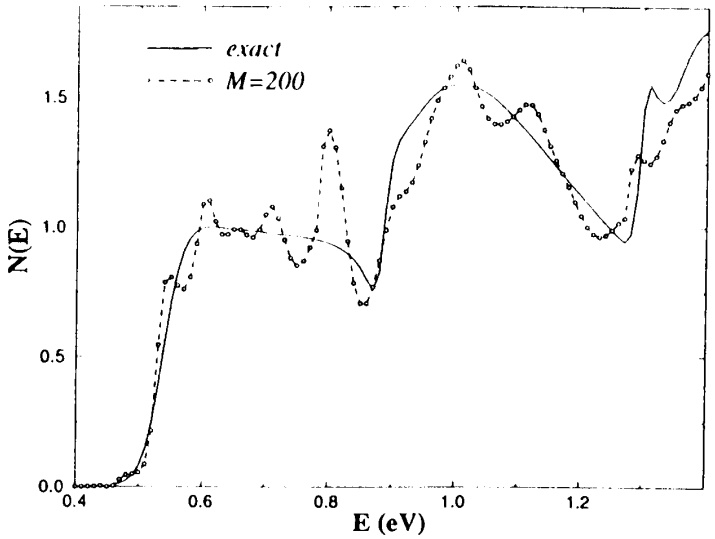

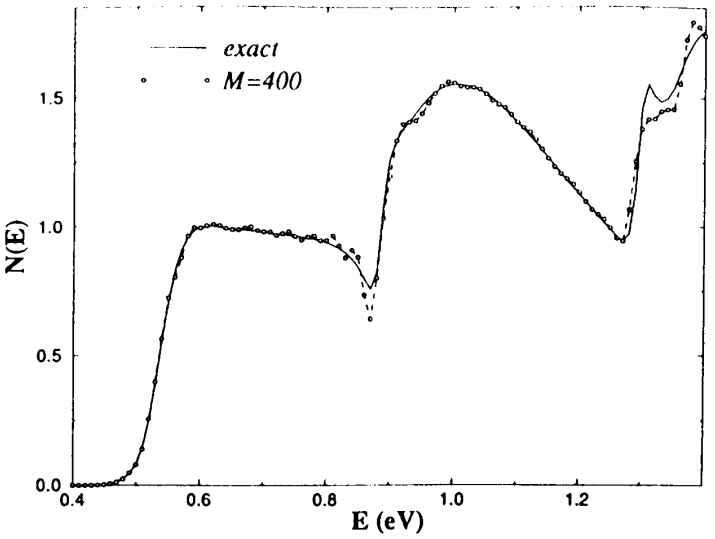

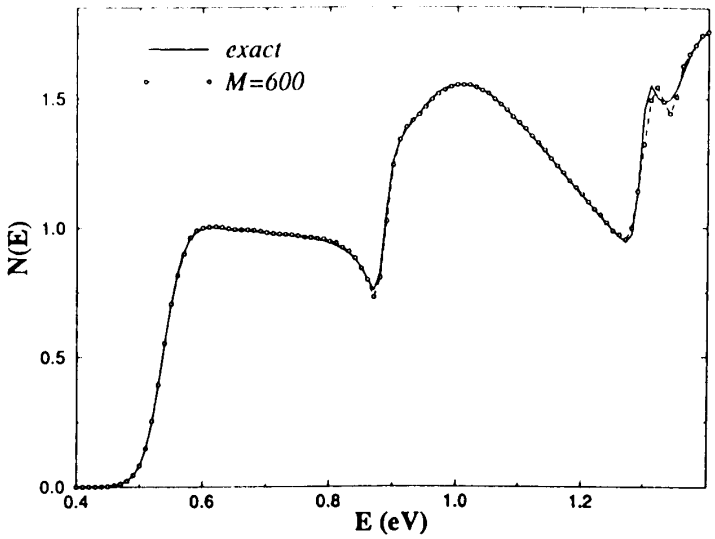

Figure 2 Same as Fig. 1 but for the cumulative reaction probability $N(E) = \Sigma_{if} |S_{if}|^2$.

Kohn variational principle for the S-matrix (21, 8) by a factor of 2. In spite of this saving it is clear from the literature that carrying out the channel-to-channel reactive scattering calculations efficiently for "big" systems by use of linear equations is still a challenge for the future (23, 8).

In Sec II, having Eq. (9), we followed the lead of Kouri, Hoffman, and co-workers (2,11–14) and turned to a time-independent, "all-energy," method using the Chebyshev polynomial expansion of the operator $(E - \hat{H})^{-1}$ represented in a small region of configuration space. We have shown a way of converging the Chebyshev series in an efficient manner, Eq. (37), whether on the small grid with short damping potential $\gamma(r)$ or on the larger grid with a well-behaved absorbing potential form of $\gamma(r)$ (to be used in Eq. (38)). The method here preserves the use of real Hamiltonians in the Chebyshev recursion relations by applying the damping factor $e^{-\gamma(r)}$ after each iteration step much like it is usually done in the wave packet time-propagation scheme. Such damping can also be interpreted as a tool to shorten the propagation range in the sense that this is always done when using an absorbing potential (3). The difference between the present and time-dependent approaches is that no Fourier transform from time to energy is needed to obtain the energy-dependent scattering solution $\psi(E)$ if Eq. (37) is used. Energy-dependent problems now can be done in the energy domain with all the advantages of the time-dependent methods.

Having pointed out the advantages of the modified Chebyshev polynomials used here, to get any results at all using Eqs. (1), (2), and (37) more input information is needed relative to the use of a properly specified initial wave packet plus absorbing potential method of Eqs. (38) and (39). This occurs when the problem, as in chemical systems (but, interestingly, not in quantum devices), has a physically separable strong interaction region and final state arrangement channel interaction region. Such separation allows one to simplify the problem by replacing the channel functions in Eq. (2) by distorted waves, effectively reducing the interaction range. This may even be a necessary procedure for large systems. As such, in Eq. (2), the input needed to get any results is the distorted waves for all arrangements. At the same time use of Eqs. (38) and (39) needs such data for only one channel to get limited results as total reaction probability out of one state; it needs distorted waves for only two channels to get an individual S-matrix element. S-matrix elements between two, out of perhaps many arrangements can be obtained without consideration of the other arrangements (27) (of course $\hat{\gamma}$ must absorb flux in all arrangements). This will allow for treatment of reactive and nonreactive scattering in the presence of three-or-more-body breakup. Equations (38) and (39) can, in principle, treat such breakup, although often breakup problems do have their own difficulties and involve strategies (36) which are beyond the scope of this chapter. The methods based on Eq. (1) get, for the S-matrix elements, "all or nothing." Additionally, if obtaining, e.g., a total reaction probability out of one state is useful, then implementation of Eqs. (38) and (39) avoids the tedious problem of having to essentially transform nonincident channel functions from a grid based on their natural coordinates to a coordinate system and grid that can represent the incident channel and interaction region. This problem, present in all methods, is here hidden in Eq. (2).

A big bonus that comes out of our work is evident, when the number of open channels N_o is not overly large (so that constructing and operating with the $A^{\pm}$-matrices is possible) and when sufficient input information, as discussed above is available. The bonus is a real shortening of basis size and a promise of the need for a small number of "$\hat{H}$-multiples." Of course, many more examples involving larger systems need be treated

before the promise of the method can be assessed. Nevertheless, the results so far, albeit on a simple system, testify to this promise.

III. THE STABILIZATION METHOD

The original version of the stabilization method (17) had as its aim the calculation of only the positions of resonances. It would do this "directly," that is, without solving the scattering problem. In fact, all it did was use the eigenenergies (no eigenfunctions needed) obtained by diagonalizing the system Hamiltonian in ever-larger enclosing boxes to construct a stabilization diagram. A "box of size L" often just means using a basis set that spans the region in the configuration space out to box length L. Having the basis end at a certain distance is equivalent to having an infinite wall at that distance.

The method first notes that each eigenvalue $E_j(L)$ must be a monotonically decreasing function of the parameter L. This is clear for instance from the fact that the density of states is always increasing as the phase space volume becomes larger which happens when the size of the system is increased.

Now in contrast to this, if a particular eigenvalue were to correspond to a resonance, its wave function would be localized in the resonance region and would be of small amplitude outside. Consequently, this root should be insensitive to the wall motion outside the resonance region. This results in the resonance root barely decreasing in energy with increasing L. Hence, in general most roots would decrease with L but one would be almost parallel to the L axis in a plot of $E_j(L)$ versus L. As such, the flat curve would intersect the decreasing ones. The theory of Hermitian matrices says that roots cannot cross; they avoid each other. The result is as seen in Fig. 3. The resonance energy is clearly noted from the sequence of avoided crossings and the flat regions on the "stabilization" graph. The narrower the resonance the more easily it is seen. For many years

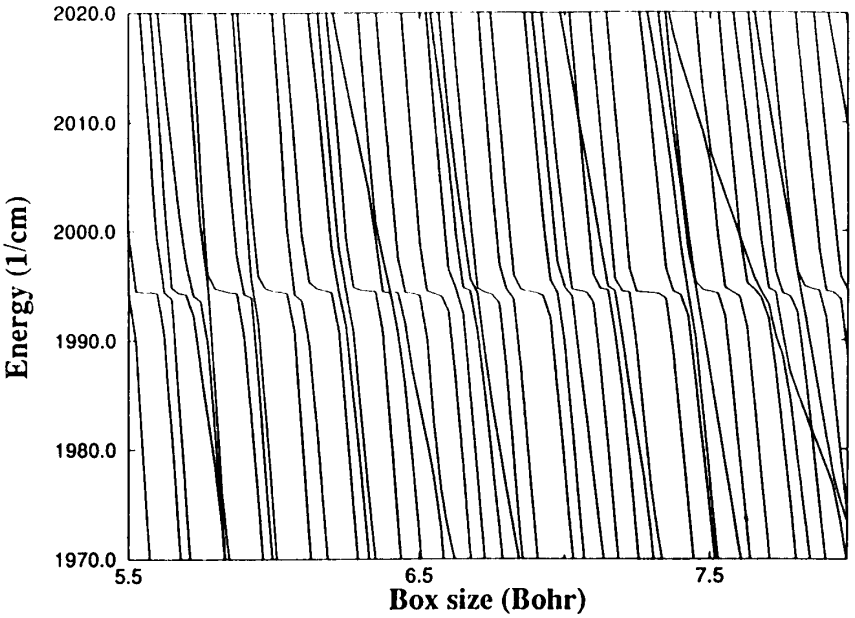

Figure 3 A typical fragment of the stabilization graph for the 3D nonrotated HCO system calculated using 100 values of the box size. The resonance at the energy E = 1994.47 cm^{-1} can be easily noted due to the flat avoided-crossings region.

the stabilization method was viewed only as a way to obtain resonance energies. Its achievement was the saving in computation relative to the historical alternative of solving the wave equation at each point of fine-energy grid and waiting for the eigenphase sum to change by π. The narrower the resonance, the harder it is to locate using such methods. Recently in Ref. 37 it was realized that the stabilization graph itself could supply both the energy and widths of resonances. Shortly after that it was further realized (7) that for a general multichannel problem if one also retains the eigenfunctions $\varphi_j(L)$ corresponding to the eigenvalues $E_j(L)$ used to plot the stabilization graph one could compute any observable, including the channel-to-channel scattering amplitudes.

In Sec. III.A the generic stabilization method is described, and it is shown that the spectral density of the system can be computed from the eigenvalues used to obtain the stabilization diagram and their corresponding eigenfunctions. Section III.B shows how to use the spectral density operator to trivially construct N_o independent solutions of the Schrödinger equation and then how to use these solutions to calculate the S-matrix and other observables. Section III.C presents illustrative results on calculation of resonances for the *HCO* formyl radical.

A. Construction of the Spectral Density

The method envisions enclosing the system in a series of boxes of increasing hyperradius L. The box converts the continuum problem into a discrete eigenvalue problem by essentially blocking all open channels. This can be accomplished, for example, by putting the Hamiltonian on a basis of box sine functions or a DVR grid based on box sine functions. For each box of size L, the eigenvalues $E_j(L)$ and unit normalized, here real, eigenfunctions $\varphi_j(L)$ are computed. This is repeated for as many values of L as is necessary to spline fit and draw a stabilization diagram of $E_j(L)$ versus L for values of L ranging from L_{inner} to L_{outer}. For scattering calculations L_{inner} is a distance just beyond the range of the potential. If resonance parameters or total photoabsorption or other short-range properties are of interest, L_{inner} is the shortest distance which is not in the resonance, photoabsorption, etc., region respectively. If distorted channel waves are used L_{inner} is just the range of the strong interaction region. L_{outer} is the shortest distance determined, by trial and error, for which the desired final quantities (S-matrix, resonance parameters, density of states, microcanonical rate, etc.) computed using the constructed spectral density converge with respect to the size of the interval $\Delta L = L_{\text{outer}} - L_{\text{inner}}$.

For convenience henceforth we will prefer to regard the energy, E, rather than the box size, L, as the independent variable. This implies using functions $L_j(E)$, that are the inverse of $E_j(L)$, and $\varphi_j(E) \equiv \varphi_j(L_j(E))$ instead of $E_j(L)$ and $\varphi_j(L)$ respectively. The $L_j(E)$ and $\varphi_j(E)$ (actually matrix elements thereof) curves up to the maximum desired energy E will be used to construct the spectral density throughout the desired energy range.

As such, we see here that full diagonalization of the Hamiltonian, whose dimension is the size of the basis, is not needed and computation saving procedures for finding only a small fraction of the eigenvalues (below the maximum desired energy) and their eigenfunctions can be employed.

For most of the observables the formulas derived and used below most often will require as input, scalar products of various functions F with eigenfunctions of the Hamiltonian in the box, $\langle F|\varphi_j(E)\rangle \equiv F_j(E)$. These will be computed only at the $(L, E_j(L))$ points that were used to construct the $L_j(E)$ versus E curves and then interpolation graphs,

for given j of $F_j(E)$ versus E are drawn to obtain the scalar products at other values of E. Now armed with the interpolated $L_j(E)$ stabilization graph and the $F_j(E)$ graphs we have sufficient information to evaluate our key formula for the spectral density. As the spectral density operator is always needed in some representation or under some integral, we evaluate it between generic testing functions α, β. Using the closure of the $\varphi_j(L)$ in a specific box of size L, we write

$$\begin{aligned}\langle\alpha|\delta(E - \hat{H})|\beta\rangle &= \lim_{L\to\infty} \langle\alpha|\delta(E - \hat{H}_L)|\beta\rangle \\ &= \lim_{L\to\infty} \sum_j \delta(E - E_j(L))\langle\alpha|\varphi_j(L)\rangle\langle\varphi_j(L)|\beta\rangle \end{aligned} \tag{45}$$

To evaluate $\delta(E - E_j(L))$ without using the histogramic method which requires evaluation of the needed high densities of spectral lines at impractically large values of L, we introduce the "averaging concept." This concept is based on the fact that the expression inside the limit in Eq. (45) can be averaged over L contained in the interval ΔL, the $L \to \infty$ limit being replaced by the limit of $\Delta L \to \infty$. Thus, using the equation

$$\int dx \left|\delta(f - f(x))g(x) = \left|\frac{df}{dx}\right|^{-1} g(x)\right|_{f(x)=f} \tag{46}$$

after integrating over L we obtain the result

$$\langle\alpha|\delta(E - \hat{H})|\beta\rangle = \frac{1}{\Delta L} \sum_j \left|\frac{dL_j(E)}{dE}\right| \alpha_j(E)\beta_j(E) \tag{47}$$

(The notation for $\alpha_j(E)$ and $\beta_j(E)$ is evident from Eq. (45).) The index j sums the summand in Eq. (47) for contributions from all $L_j(E)$ (i.e., points of intersection of the $E_j(L)$ curves and the line of constant energy E) in the interval ΔL. The slope $dL_j(E)/dE$ is read off the $L_j(E)$ versus E graph. (Alternatively the Hellman-Feynman theorem can be used to give the values of both $E_j(L)$ and its derivative at the L values emerging from the original diagonalization. This information can then be used to construct an even more accurate stabilization graph.)

Clearly $\Delta L \to \infty$ implies $L_{\text{outer}} = \infty$ in which limit the result is exact and not dependent on L_{inner}. However, in practice a better choice of L_{inner} will improve the convergence of the formula given by Eq. (47). A deeper insight into the method can be gained when L_{inner} is taken as the full range of the potential. For this consider the exact expression for the solution subspace projector for an N_o open-channel system:

$$\delta(E - \hat{H}) = \sum_{n=1}^{N_o} |\Psi_n^+\rangle\langle\Psi_n^+| \tag{48}$$

The Ψ_n^+, $n = 1, \ldots, N$, are the "exact" delta function normalized solutions of the wave equation which satisfy the standard outgoing boundary conditions. Equation (47) is seen to replace the right-hand side of Eq. (48) by the sum over different solutions at the energy E. Equation (47) is thus a projection operator made of usually more than N_o solutions of the wave equation normalized according to the boxlike density of states $|dL_j(E)/dE|$. These solutions are unacceptable as they are each zero on some finite-distance hypersurface at L and hence do not satisfy the scattering boundary conditions. Indeed they may not even be finite when they are extended numerically, using the wave equation, to infinity. Amplifying the above comments, it is seen that generically the $\varphi_j(E)$

simply cannot (except in the one-dimensional N_o open and the zero closed-channel problem) be expanded in terms of the Ψ_n^+ at a single energy, as the zero-amplitude condition at each of the infinity of points of the L hypersurface cannot be satisfied. To satisfy this condition short-range basis terms must be added which are particular to each hypersurface. Averaging causes the contributions of these terms to cancel out, allowing the implied projector in Eq. (47) to act as the projector of Eq. (48). Again the condition, $L_{\text{inner}} < L_j(E) < L_{\text{outer}}$, used to define the summation in Eq. (47) chooses independent solutions; the density given by the slope $|dL_j(E)/dE|$ renormalizes those solutions to a numerically significant amplitude as the average amplitude of the unit normalized $\varphi_j(E)$ goes to zero, while the factor $|dL_j(E)/dE|$ gets larger as $L \to \infty$.

Now, given Eq. (47) which is taken as the equivalent of Eq. (48), solutions of the wave equation must be constructed and expressions for observables derived. Equation (47) is used for calculation. Equation (48) is used to relate matrix elements of the spectral density to the more familiar matrix elements of the scattering wave functions.

B. The Extraction of Observables

Already having a procedure to compute the matrix elements of $\delta(E - \hat{H})$, we note that if X_p's are chosen as in Eq. (17) (that is, $X_p = (\hat{H} - E)f_p^+$), then insertion of Eq. (47) into Eq. (18) yields an expression for the A^+ and A^- matrices:

$$A_{lp}^{\pm} = \pm \sum_j \left| \frac{dL_j(E)}{dE} \right| \langle f_l^+(\hat{H} - E)|\varphi_j(E)\rangle\langle\varphi_j(E)|(\hat{H} - E)f_p^+\rangle \tag{49}$$

Note the similarity between the above equation and Eq. (25) originating from the spectral projection method of previous section. The symmetry of Eq. (49) which is due to the choice of X_p implies that the only integrals needed at each chosen energy are of the + or − form of

$$I_{jl}^{\pm}(E) = \langle\varphi_j(E)|(\hat{H} - E)f_l^{\pm}\rangle \tag{50}$$

The number of integrals needed in the computation procedure after each diagonalization at given L then is twice the number of open channels times the number of eigenvalues existing in the desired range of energy; values at other energies are obtained by interpolation.

Other quantities such as the total photodissociation cross section or the cumulative reaction probability can be obtained using the computed S- or A-matrices. However, we note that the quantities which are expressed in terms of matrix elements of the spectral density operator as in Eq. (45) can be calculated directly avoiding consideration of the channel-to-channel scattering, a property associated with use of the negative imaginary potential (16). Worth mentioning among these are the total photodissociation cross section (38), cumulative reaction probability (39), density of states (37), or scattering phase shift (40). The last two quantities can be used to study resonances, namely to compute their positions and widths. This application of the stabilization method which requires only the points $L_j(E)$ and *not the eigenfunctions*, $\varphi_j(E)$, seems to be the most promising especially for narrow resonances, when other nondirect methods involving calculation of the S-matrix could be difficult to implement.

The change in the density of states due to the interaction is given by

$$\Delta\rho = \text{Tr}[\delta(E - H) - \delta(E - H_0)] \tag{51}$$

where H_0 is the Hamiltonian without interaction. Using Eq. (47) this gives

$$\Delta\rho(E) = -\frac{1}{\Delta L}\sum_j \frac{dL_j(E)}{dE} - \rho_0(E) \tag{52}$$

where $\rho_0(E)$ is associated with the density of states of the noninteracting system.

To extract the resonance parameters $\Delta\rho(E)$ is approximated by a Lorentzian plus a smooth background parametric form. The method has been applied successfully in (37) to a few model problems and in (41–43) to compute the resonance parameters of more realistic and complex systems. Notably the method uses no analytic continuation nor introduces any negative imaginary absorbing potentials. Thereby, it allows us to reduce (by a factor of 2) the computer memory needed for complex diagonalizations and use very fast diagonalization codes for real symmetric matrices. Moreover, if only eigenvalues of the Hamiltonian in a small energy range are needed the diagonalization speed can be increased enormously. The latter becomes very important since the method requires multiple diagonalizations of the Hamiltonian matrices.

Equation (52) has two features that could cause problems. The first is that if a resonance overlaps a threshold, the singularity occurring as $\Delta\rho(E)$ diverges at the threshold causes the Lorentzian to be nearly unrecognizable, because of the inadequate representation of the singularity at finite L. Furthermore, near threshold the density of resonance states may not be Lorentzian at all. Resonances with this overlap property have such problems in many methods and can only be treated either by direct searches for the resonance pole of the S-matrix (44) or by an analytic continuation of the Hamiltonian (45) or by computing the collision lifetime matrix Q (46). The eigenvalues of the Q matrix as a function of energy often assign resonance and threshold effects to different eigenvalues and resolve this problem (see, e.g., Ref. 47). The few highest eigenvalues of Q as a function of energy then shows the unfettered Lorentzians shape. Since this first problem is far from generic the method remains of great use.

The second problem in using formula (52) is that since the number of $L_j(E)$ points in the finite interval ΔL is a step function of the energy, E, the calculated density of states $\Delta\rho(E)$ is discontinuous. Now this problem is purely aesthetic because one could always smooth the "jumps" and fit $\Delta\rho(E)$ to the Lorentzian with a good result for E_r and Γ.

In Ref. 40 it was shown how to avoid this second problem and an even greater computational simplification has been introduced. This simplification shows that the $L_j(E)$ *values alone* completely determine the width. To see this result let us consider the eigenphase sum, $\eta(E) = (1/2i)\log(\det S)$, which as proved in (48) can be defined by

$$\frac{\partial\eta(E)}{\partial E} = \pi\Delta\rho(E) \tag{53}$$

and, consequently,

$$\eta(E) = \varphi(E) - \varphi_0(E) = \pi\int_0^E \Delta\rho(E')\,dE' \tag{54}$$

where $\varphi_0(E)$ is the known phase shift of the noninteracting system (ΔL dependent) which by definition has no resonances. Carrying out the integration in Eq. (52) for the physically

relevant phase shift, $\varphi(E)$, we have

$$\varphi(E) = \pi N(E) + \frac{\pi}{\Delta L} \sum_j (L_0 + \Delta L - L_j(E)) \tag{55}$$

where $N(E)$ is the number of eigenvalues for which $E_j(L_0) < E$, and summation in Eq. (55) (as in Eq. (47)) is taken over all $L_j(E)$ values in the interval ΔL.

The phase shift $\varphi(E)$ has the same resonance part as the eigenphase sum $\eta(E)$ but its background phase differs. As such, after being computed it will be approximated by

$$\varphi(E) = \arctan\left(\frac{2(E - E_r)}{\Gamma}\right) + \varphi_b(E) \tag{56}$$

where the background term, $\varphi_b(E)$, is a smooth function of energy. This analysis is based on the fact that when resonance energy and lifetime can be defined the resonance term in Eq. (56) can be separated from the background.

The function $\varphi(E)$ calculated using Eq. (55) is a continuous well-behaved function of E. To see this we notice that each jth eigenvalue contributes continuously to the total phase shift, $\varphi(E)$, according to the formula

$$\varphi(E) = \sum_j \tilde{\varphi}_j(E) \tag{57}$$

where

$$\tilde{\varphi}_j(E) = \pi \begin{cases} 0 & \text{if } E < E_j(L_0 + \Delta L) \\ \dfrac{(L_0 + \Delta L) - L_j(E)}{\Delta L} & \text{if } E_j(L_0 + \Delta L) < E < E_j(L_0) \\ 1 & \text{if } E_j(L_0) < E \end{cases} \tag{58}$$

To interpret resonances and assign quantum numbers, plots of the local density are useful (42). The local density can be obtained by taking the diagonal term in the position representation of Eq. (47) to give

$$\langle x|\delta(E - \hat{H})|x\rangle = \sum_{n=1}^{N_a} |\Psi_n^+(x)|^2 = \frac{1}{\Delta L} \sum_j \left|\frac{dL_j(E)}{dE}\right| \langle x|\varphi_j(E)\rangle^2 \tag{59}$$

The method of obtaining resonances given here, for all but the very large in basis size problems which were discussed in Sec. II.B, is by far the easiest way available to obtain resonance parameters.

To obtain half-scattering quantities such as state-to-state ionization or dissociation cross section, Eq. (5) of the previous section can be used. If final channel resolution is not required and only the total dissociative absorption is wanted, a direct method of evaluation of the latter is available, namely

$$\sigma_{\text{absorp}}(E) = \langle \varphi_0 \hat{\mu}|\delta(E - \hat{H})|\hat{\mu}\varphi_0\rangle = \frac{1}{\Delta L} \sum_j \left|\frac{dL_j(E)}{dE}\right| \langle \varphi_0 \hat{\mu}|\varphi_j(E)\rangle^2 \tag{60}$$

Use of Eq. (48) for $\delta(E - \hat{H})$ gives the common form of $\sigma_{\text{absorp}}(E)$. The direct form has the advantages of not needing to know the final channel wave functions and of only having to represent the final state of the system over the position space range where $\hat{\mu}\varphi_0$ is significant. A model numerical example is not given here but is available in Ref. 38.

In Ref. 39 the Miller-Schwartz-Tromp formula (49)

$$K(E)Q = \mathrm{Tr}[\hat{F}\delta(E - \hat{H})\hat{F}\delta(E - \hat{H})] \tag{61}$$

was used to directly compute microcanonical rate for a model problem. The $\delta(E - \hat{H})$ was evaluated using Eq. (47). This was also done for H + H_2 but it was found that convergence was not satisfactory compared to the calculation of the S-matrix followed by its use to compute $N(E)$. However, if getting the S-matrix is impossible due to the enormous number of open channels, the method of Ref. 39 that uses Eq. (47) may be still very efficient for direct calculation of the microcanonical rate.

The illustrative results on scattering and resonance calculation using the stabilization method for the collinear H + $H_2 \rightarrow H_2$ + H exchange reaction had been presented in Ref. 32. This model calculation showed that the method requires a relatively modest amount of computational effort and can be used for the general case of the multichannel (arrangement) problem. In the next section we show an illustrative calculation of resonances for the 3D (J = 0) HCO formyl radical using Eq. (55).

C. Resonances of the HCO Formyl Radical

Unimolecular decay of the HCO formyl radical HCO → H + CO has been studied extensively by both experiment and theory over the last decade (see Ref. 51 and references therein). Study of resonances of this system can yield a significant insight into the decay dynamics once the latter is governed by narrow resonances.

The calculation was carried out with the same code as was previously used for the NeICl (B, v = 2) van der Waals complex (41) provided to us by Victor Ryaboy and Nimrod Moiseyev. The code had been originally made for the complex scaling calculations and then was modified for the stabilization method. The numerical procedure for the results presented below is described in Refs. 50, 41. Briefly, a primitive DVR basis for two radial coordinates, $R_{\mathrm{H-CO}}$ and R_{CO}, and one angle coordinate was used. The distance $R_{\mathrm{H-CO}}$ between H atom and the center of mass of CO was chosen as the box size parameter L. For each L the primitive basis was contracted by diagonalizing the ray Hamiltonians each having a different fixed angle configuration. The eigenfunctions of the ray Hamiltonians with eigenvalues in certain energy range were used for the part of the final contracted basis describing the radial coordinates. 100 box size values L in the interval 5.5 to 8 bohr were taken to obtain the stabilization graph.

A typical fragment of the graph is shown in Fig. 3, where a resonance can be easily noted due to the flat avoided crossings region. A graph of $\varphi(E)/\pi$ versus E computed from the data shown in Fig. 3, using Eq. (55), is given in Fig. 4, with the sudden unit rise indicating resonance. The calculated single resonant phase shift of Fig. 4 was then approximated by the form of Eq. (56) yielding the position, E = 1994.47 cm^{-1}, and width, Γ = 0.48 cm^{-1}, of the resonance. The phase shift $\varphi(E)/\pi$ for the whole energy interval, 1100 to 3200 cm^{-1}, considered in the calculation is presented in Fig. 5, where some 19 resonances cause the unit rises (some broader ones are hardly seen in the figure). For comparison the density of states computed by simply taking the energy derivative of $\varphi(E)/\pi$ is shown in Fig. 6, where all 19 resonances can be easily noted. All 13 resonances found by Wang and Bowman (51) exist in the figure. Their positions and widths are in a very good agreement except for two resonances corresponding to high CO vibrational quantum numbers. This is because the number of vibrational functions,

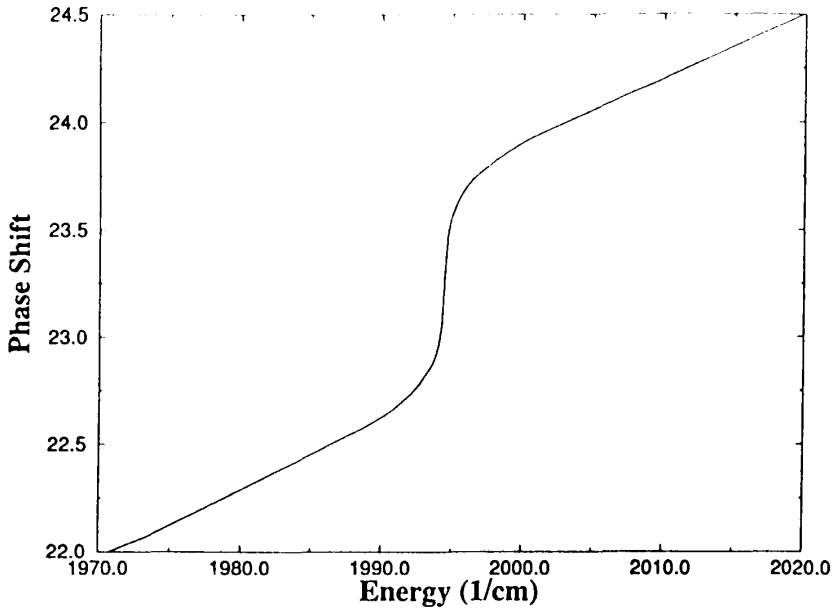

Figure 4 The phase shift $\varphi(E)/\pi$ obtained from the data shown in Fig. 3 using Eq. (55). The sudden unit rise at the energy E = 1994.47 cm^{-1} is due to the existence of an isolated narrow resonance.

N_{CO} = 7, used to describe the CO distance was not adequate for such resonances. Additionally there are six more broad resonances in Fig. 6.

D. Comments on the Stabilization Method

One of the most striking aspects of the stabilization method is that the hard-to-find narrow resonances which require repeated solutions of the fixed-energy wave equation on a dense

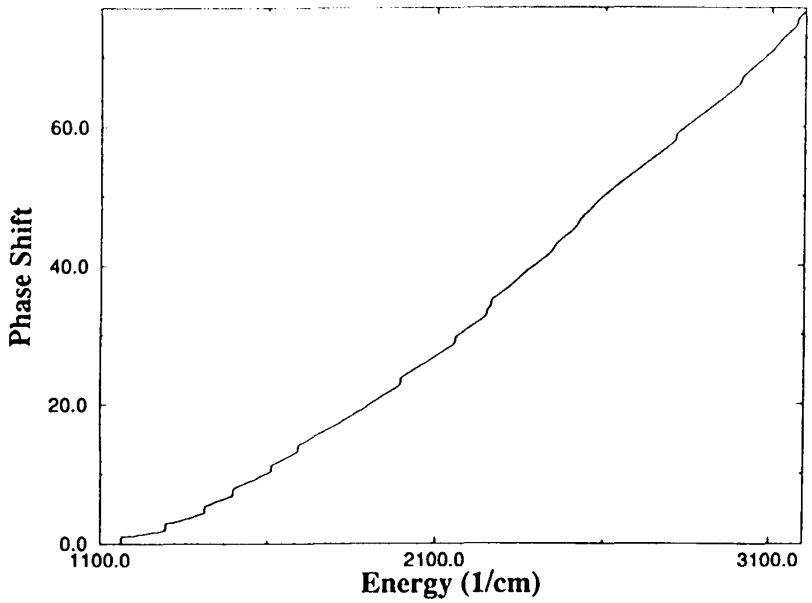

Figure 5 The same as Fig. 4 but for the whole energy range considered.

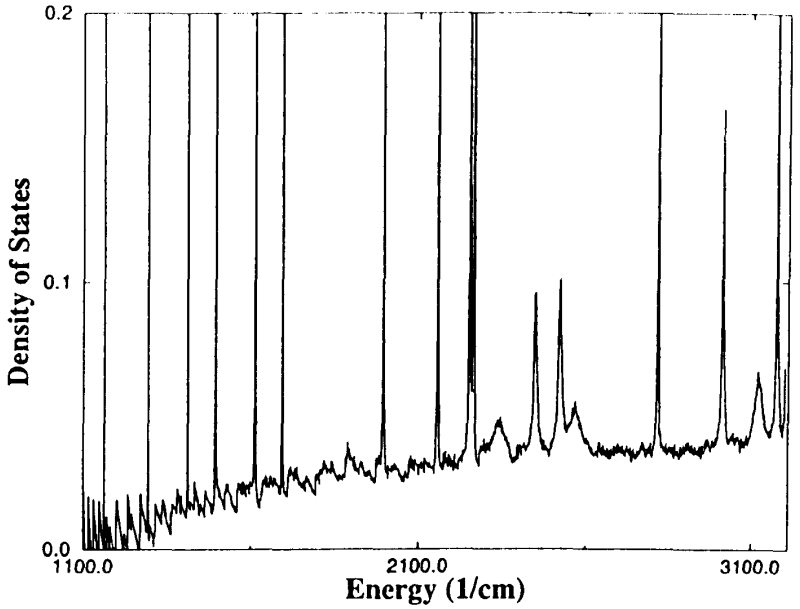

Figure 6 Density of states calculated by differentiating the data shown in Fig. 4 over the energy. Contribution to the density from each resonance can be well described by the Breit-Wigner form.

grid of energies are here trivially obvious from the flat avoided crossings seen in the diagram. Also for resonances that do not significantly overlap each other or thresholds the extraction of widths is a simple exercise (42, 41); interestingly, broad resonances can be more difficult to study (e.g., because of thresholds) than narrow ones.

The method presented here is in a sense one that changes continuously from traditional $\mathscr{L}^2$ methods that sought resonance parameters to $\mathscr{L}^2$ methods that sought scattering matices; the difference is usually only in the larger boxes needed for the latter. As such, there are three ways to get resonance parameters from the same data. The eigenphase sum can be computed from the eigenvalues (only) as done in the previous subsection or it can be gotten from parametrization of the S-matrix elements (52, 53) to the Breit-Wigner form. The former is clearly easier and requires no calculations of eigenvectors and often requires smaller boxes. The third method is to use the maximum eigenvalue of the Q-matrix (47).

How does stabilization compare to the spectral projection method of Sec. II? For problems with matrices that fit into the core memory the single diagonalization of the Hamiltonian matrix and use of Eq. (13) is extremely efficient if the S-matrix is desired. As suggested in Sec. II, combining the spectral projection method with the primitive stabilization method yields a powerful way to obtain adequate scattering information. Also note that the most difficult part of using exclusively the stabilization method for scattering calculations in a multichannel problem is the accurate interpolation of $L_j(E)$ and $I_{jl}(E)$. This step is difficult to mechanize because of the large number of avoided crossings. Although many ideas can be discussed to simplify this step the method would lose its ease and availability. Of course for direct calculations of resonances and presumably photoabsorption, it remains a superb method.

ACKNOWLEDGMENT

This work was supported by DOE grant DE-FG03-94ER14458. We wish to thank Tushar Ravuri and Professor Tasko Grozdanov for carefully reading the manuscript and making many useful remarks. Fruitful conversations with Professors Donald Kouri and Barry Schneider are also highly appreciated. We thank Professors Nimrod Moiseyev and Victor Ryaboy for help in obtaining results presented in Sec. III.C.

REFERENCES

1. B. Hartke, R. Kosloff, and S. Ruhman, Large amplitude ground state vibrational coherence induced by impulsive absorption in *CsI*. A computer simulation. *Chem. Phys. Lett. 158*:223 (1986). R. Kosloff, Time-dependent quantum-mechanical methods for molecular dynamics, *J. Phys. Chem. 92*:2087 (1988).
2. Y. Huang, W. Zhu, D. J. Kouri, and D. K. Hoffman, A general time-to-energy transform of wavepackets. Time-independent wavepacket-Schrödinger and wavepacket-Lippmann-Schwinger equations. *Chem. Phys. Lett. 206*:96 (1993).
3. R. Kosloff and D. Kosloff, Absorbing boundaries for wave propagation problems, *J. Comput. Phys. 63*:363 (1986).
4. D. H. Zhang, O. A. Sharafeddin, and J. Z. H. Zhang, Product state distribution in time-dependent quantum wave packet calculation with an optical potential. *Chem. Phys. 167*:137 (1992).
5. T. Ravuri, V. A. Mandelshtam, and H. S. Taylor, Calculation of transmission and resonance properties for quantum devices, to be published.
6. A. A. Makarov, M. Pont, and H. S. Taylor, Application of the $\mathcal{L}^2$ box-stabilization method to time-periodic systems. *Phys. Rev. A 50*:3276 (1994).
7. V. A. Mandelshtam, T. Ravuri, and H. S. Taylor, The stabilization theory of scattering, *J. Chem. Phys. 101*:8792 (1994).
8. G. C. Groenenboom and D. T. Colbert, Combining the discrete variable representation with the *S*-matrix Kohn method for quantum reactive scattering, *J. Chem. Phys. 99*:9681 (1993).
9. D. Neuhauser, Reactive scattering with absorbing potentials in general coordinate systems, *Chem. Phys. Lett. 200*:173 (1992).
10. H. W. Jang and J. C. Light, Finite range scattering wave function method for scattering and resonance lifetimes, *J. Chem. Phys. 99*:1057 (1993).
11. D. K. Hoffman, Y. Huang, W. Zhu, and D. J. Kouri, Further analysis of solutions to the time-independent wave packet equations for quantum dynamics: general initial wave packets, *J. Chem. Phys. 101*:1242 (1994).
12. D. J. Kouri, M. Arnold, and D. K. Hoffman, Time-to-energy transform of wavepackets using absorbing potentials, Time-independent wavepacket-Schrödinger and wavepacket-Lippmann-Schwinger equations. *Chem. Phys. Lett. 203*:166 (1993); W. Zhu, Y. Huang, D. J. Kouri and D. K. Hoffmann, Time-independent wavepacket forms of Schrödinger and Lippman-Schwinger equations, *Phys. Rev. Lett. 72*:1310 (1994).
13. D. J. Kouri, Y. Huang, W. Zhu, and D. K. Hoffman, Variational principles for the time-independent wave-packet-Schrödinger and wave-packet-Lippmann-Schwinger equations, *J. Chem. Phys. 100*:3662 (1994).
14. Y. Huang, D. J. Kouri, and D. K. Hoffman, A general, energy-separable polynomial representation of the time-independent full Green operator with application to time-independent wavepacket forms of Schrödinger and Lippmann-Schwinger equations, *Chem. Phys. Lett. 225*: 37 (1994).
15. This equation in its present form and the methods of Sec. II.A were first presented by V. A. Mandelshtam and H. S. Taylor at the Harvard-Smithsonian Workshop on Reactive Scattering, Cambridge, MA, June 31, 1994.

16. T. Seideman and W. H. Miller, Calculation of the cumulative reaction probability via a discrete variable representation with absorbing boundary conditions, *J. Chem. Phys. 96*:4412 (1992).
17. A. U. Hazi and H. S. Taylor, Stabilization method of calculating resonance energies—model problem, *Phys. Rev. A, A1*:1109 (1970). H. S. Taylor and J. K. Williams, Proposed theory of calculating the energy of negative-ion resonant elastic scattering states of electronic spectroscopy, *J. Chem. Phys. 42*:4603 (1965).
18. J. C. Light, I. P. Hamilton, and J. V. Lill, Generalized discrete variable approximation in quantum mechanics, *J. Chem. Phys. 82*:1400 (1985).
19. D. K. Hoffman, N. Nayar, O. A. Sharafeddin, and D. J. Kouri, Analytic banded approximation for the discretized free propagator, *J. Phys. Chem. 95*:8299 (1991).
20. C. C. Paige and M. A. Saunders, Solution of sparse indefinite systems of linear equations, *Siam J. Numer. Anal. 12*:617 (1975).
21. W. H. Miller and B. M. D. D. Jansen op de Haar, A new basis set method for quantum scattering calculations, *J. Chem. Phys. 86*:6213 (1987).
22. R. Johnson, The multichannel log-derivative method for scattering calculations, *J. Comput. Phys. 13*:445 (1973).
23. D. E. Manolopoulos, M. D'Mello, and R. E. Wyatt, Quantum reactive scattering via the log-derivative version of the Kohn variational principle: general theory for bimolecular chemical reactions, *J. Chem. Phys. 91*:6096 (1989).
24. C. S. Lent and D. J. Kirkner, The quantum transmitting boundary method, *J. Appl. Phys. 67*: 6353 (1990).
25. D. Z.-Y. Ting, E. T. Yu and T. C. McGill, Effect of band mixing on hole-tunneling times in GaAs/AlAs double-barrier heterostructures, *Phys. Rev. B 45*:3583 (1992); W. R. Frensley, Numerical evaluation of resonant states. *Supperlatt. Microstr. 11*:347 (1992).
26. D. Neuhauser, Molecular scattering–Very-short-range imaginary potentials, absorbing potentials, and flux-amplitude expressions. *J. Chem. Phys. 103*:8513 (1995).
27. D. Neuhauser and M. Baer, The application of wave packets to reactive atom-diatom systems: A new approach. *J. Chem. Phys. 91*:4651 (1989).
28. S. M. Auerbach and C. Leforestier, A new computational algorithm for Green's functions: Fourier transform of the Newton polynomial expansion, *Comp. Phys. Comm. 78*:55 (1993).
29. R. Kosloff, Propagation methods for quantum molecular dynamics, *Annu. Rev. Phys. Chem. 45*:145 (1994).
30. U. V. Riss and H-D. Meyer, Calculation of resonance energies and widths using the complex absorbing potential method, *J. Phys. B 26*:4503 (1993).
31. D. Neuhauser, Time-dependent reactive scattering in the presence of narrow resonances: avoiding long propagation times, *J. Chem. Phys. 95*:4927 (1991).
32. B. Liu, Ab initio potential energy surface for linear H_3, *J. Chem. Phys. 58*:1925 (1973); P. Siegbahn and B. Liu, An accurate three-dimensional potential energy surface for H_3, *J. Chem. Phys. 68*:2457 (1978); D. G. Truhlar and C. J. Horowitz, Functional representation of Liu and Seigbahn's accurate ab initio potential energy calculations for H + H_2, *J. Chem. Phys. 68*:2468 (1978); D. G. Truhlar and C. J. Horowitz, Erratum [*J. Chem. Phys. 68*:2466 (1978)] *J. Chem. Phys. 71*:1514(E) (1979).
33. D. T. Colbert and W. H. Miller, A novel discrete variable representation for quantum mechanical reactive scattering via the *S*-matrix Kohn method, *J. Chem. Phys. 96*:1982 (1992).
34. W. H. Thompson and W. H. Miller, State-specific reaction probabilities with a power series Green function, *Chem. Phys. Lett. 206*:123 (1993).
35. B. I. Schneider, *R*-matrix theory for electron-atom and electron-molecule collisions using analytic basis set expansions, *Chem. Phys. Lett. 31*:237 (1975); B. I. Schneider, *R*-matrix theory for electron-molecule collisions using analytic basis set expansions 2. Electron-H_2 scattering in static-exchange model. *Phys. Rev. A 11*:1957 (1975).

36. K. Kulander, Collision induced dissociation in collinear H + H_2: Quantum mechanical probabilities using the time-dependent wavepacket approach. *J. Chem. Phys. 69*:5064 (1978).
37. V. A. Mandelshtam, T. R. Ravuri, and H. S. Taylor, Calculation of the density of resonance states using the stabilization method. *Phys. Rev. Lett. 70*:1932 (1993).
38. V. A. Mandelshtam, T. R. Ravuri, and H. S. Taylor, $\mathcal{L}^2$ stabilization theory of dynamics: dissociative photoabsorption, *Phys. Rev. A 48*:818 (1993).
39. V. A. Mandelshtam and H. S. Taylor, The evaluation of microcanonical and canonical rate constants using the stabilization theory of dynamics, *J. Chem. Phys. 99*:222 (1993).
40. V. A. Mandelshtam and H. S. Taylor, V. Ryaboy, and N. Moiseyev, Stabilization theory for computing energies and widths of resonances, *Phys. Rev. A. 50*:2764 (1994).
41. V. Ryaboy and N. Moiseyev, V. A. Mandelshtam, and H. S. Taylor, Resonance positions and widths by complex scaling and modified stabilization methods: van der Waals complex NeICl, *J. Chem. Phys. 101*:5677 (1994).
42. J. Müller, X. Yang, and J. Burgdorfer, Calculation of resonances in doubly excited helium using the stabilization method, *Phys. Rev. A 49*:2470 (1994).
43. M. I. Hernandez and D. C. Clary, A study of HOCO resonances in the OH + CO → CO_2 + H reaction, *J. Chem. Phys. 101*:2779 (1994).
44. M. V. Basilevsky and V. M. Ryaboy, Direct calculation of resonant states in reactive scattering—application to linear triatomic systems. *Int. J. Quantum Chem. 19*:611 (1981); M. V. Basilevsky and V. M. Ryaboy, Decay dynamics of triatomic molecules. Quantum calculations for non-symmetric linear systems. *Chem. Phys. 86*:67 (1984).
45. V. Ryaboy and N. Moiseyev, Cumulative reaction probability from Siegert eigenvalues: model studies, *J. Chem. Phys. 98*:9618 (1993).
46. F. T. Smith, Lifetime matrix in collision theory, *Phys. Rev. 118*:349 (1960).
47. S. A. Cuccaro, P. G. Hipes, and A. Kuppermann, Symmetry analysis of accurate H+H_2 resonances for low partial waves, *Chem. Phys. Lett. 157*:440 (1989).
48. R. D. Levine, *Quantum Mechanics of Molecular Rate Processes*, Oxford University Press, 1969, chap. 2.5.3.
49. W. H. Miller, S. D. Schwartz, and J. W. Tromp, Quantum mechanical rate constants for bimolecular reactions, *J. Chem. Phys. 79*:4889 (1983).
50. N. Lipkin, N. Moiseyev, and C. Leforestier, A three-dimensional study of NeICl predissociation resonances by the complex scaled discrete variable representation method, *J. Chem. Phys. 98*:1888 (1993).
51. D. Wang and J. M. Bowman, $\mathcal{L}^2$ calculations of resonances and final rotational distributions for HCO → H + CO, *J. Chem. Phys. 100*:1021 (1994).
52. D. W. Schwenke and D. G. Truhlar, Accurate partial resonance widths for collinear reactive collisions, *J. Chem. Phys. 87*:1095 (1987).
53. J. Chang, N. J. Brown, M. D'Mello, R. E. Wyatt, and H. Rabitz, Quantum functional sensitivity analysis within the log-derivative Kohn variational method for reactive scattering, *J. Chem. Phys. 97*:6240 (1992).

8

Time-Independent Wave-Packet-Distributed Approximating Functional Approach to Quantum Dynamics

DONALD J. KOURI and YOUHONG HUANG
University of Houston, Houston, Texas

DAVID K. HOFFMAN
Iowa State University, Ames, Iowa

I. INTRODUCTION

Recently, we have developed a new general approach to treating quantum dynamics, including reactive scattering and bound states of polyatomic systems. The approach has a number of attractive features which result from combining our time-independent wave packet formulation of the Schrödinger and Lippmann-Schwinger equations (TIWSE and TIWLSE, respectively) (1–15), the distributed approximating functional (DAF) technique for representing functions and operators on a discrete grid (16–29), and the polynomial expansion of operators (PEO) (2,6,7,9,30–32). The TIW approach generalizes the usual Schrödinger equation to an inhomogeneous form. The new equation is derived by considering time-dependent wave packets, followed by a half-Fourier time-to-energy transform, so that the inhomogeneity turns out to be the $t = 0$ wave packet from the time-dependent description (1–4,8,15). Thus, we *define* the new generalized wave function $\xi^+(E)$ by

$$\xi^+(E) \equiv \frac{i}{2\pi\hbar} \int_0^\infty dt\, e^{iEt/\hbar} \chi(t) \tag{1}$$

where $\chi(t)$ is the $\mathcal{L}^2$ wave packet solution to the usual time-dependent Schrödinger equation with initial wave packet $\chi(0)$:

$$\chi(t) = e^{-iHt/\hbar}\chi(0) \tag{2}$$

The superscript + indicates a "causal"-type solution in which the time runs from $t = 0$ to plus infinity. Substituting Eq. (2) into Eq. (1) yields

$$\xi^+(E) = \frac{i}{2\pi\hbar}\int_0^\infty dt\, e^{i(E-H)t/\hbar}\chi(0) \tag{3}$$

Now if one picks a specific value of the scattering coordinate, x, and evaluates $\xi^+(E|x)$ by first computing $\chi(t|x)$ and then evaluating the time integral, the result is completely well defined and convergent. However, it should be clear that as an abstract equation, the integral operator in Eq. (3) converges only in a specialized sense. Because the integral converges for any specific value of x, we can also carry out the time integration formally by inserting a convergence factor, $+i\epsilon$, into the exponent. The resulting formal expression for the generalized state function is

$$\xi^+(E) = \frac{i}{2\pi}\frac{1}{E - H + i\epsilon}\chi(0) \tag{4}$$

which we see has some similarity to the more familiar Lippmann-Schwinger state function,

$$\psi_k^+(E) = \phi_k + \frac{1}{E - H + i\epsilon}V\phi_k \tag{5}$$

The state ϕ_k is a solution of the unperturbed Schrödinger equation,

$$(E - H_0)\phi_k = 0 \tag{6}$$

where

$$H = H_0 + V \tag{7}$$

and the wave number, k, is related to the energy E by the usual expression

$$\frac{\hbar^2k^2}{2m} = E \tag{8}$$

However, there are fundamental differences between $\xi^+(E)$ and $\psi_k^+(E)$ (which we shall discuss in more detail). This causal solution, $\xi^+(E)$, also satisfies a Schrödinger-like equation (in the limit $\epsilon \to 0$) given by

$$(E - H)\xi^+(E) = \frac{i}{2\pi}\chi(0) \tag{9}$$

where it should be clear that the factor $i/2\pi$ can also be absorbed into the definition of $\chi(0)$. In some discussions this is convenient to do. In addition, once this inhomogeneous Schrödinger equation has been derived, it possesses *infinitely* many solutions and therefore no longer necessarily has to be interpreted in terms of the time evolution used to derive it (2,5). This formulation leads to a new, general approach to quantum scattering (as well as classical scattering (15)). We note that the inhomogeneity can, but need not necessarily be interpreted as a time-dependent wave packet evaluated at time $t = 0$. Now

for E in the continuum portion of the spectrum of H, we point out that the causal and anticausal solutions of Eq. (9),

$$\xi^{+}(E) = \frac{i}{2\pi}(E - H \pm i\epsilon)^{-1}\chi(0) \tag{10}$$

are intimately connected with (but *not* identical to) the scattering states of H (4). In particular, the state $\psi(E)$ defined by

$$\psi(E) = \xi^{+}(E) - \xi^{-}(E) \tag{11}$$

is a solution of the standard time-independent Schrödinger equation (4)

$$(E - H)\psi(E) = 0 \tag{12}$$

Depending on the choice of $\chi(0)$, $\xi^{+}(E)$ and $\xi^{-}(E)$ can themselves be identified with the standard causal and anticausal scattering states, *but only in certain regions of space* (3–5,8). Indeed, it should be pointed out that the $\xi^{\pm}(E)$ in Eq. (10) do not represent the most general solutions of Eq. (9) (except in the special case that the equation has only two linearly independent solutions), since the most general solution of an inhomogeneous equation is always given by the sum of a particular solution and a general solution of the homogeneous equation (the ordinary time-independent Schrödinger equation) (33). *However, Eq. (10) gives all the solutions of interest because any scattering state, causal or anticausal, can be obtained by varying $\chi(0)$.* Thus, by varying $\chi(0)$, these two *special* solutions of the inhomogeneous equation allow one to construct the *most general* solution of the homogeneous Schrödinger equation. Said another way, the boundary conditions are transferred to the inhomogeneity of the TIWSE.

As stated above, by appropriately choosing $\chi(0)$, $\psi(E)$ as given by Eq. (12) can be made to correspond directly to a causal or anticausal scattering state, and $\xi^{+}(E)$ and $\xi^{-}(E)$ also have a direct physical interpretation. The advantage that this delivers is probably most apparent in the extraction of the desired scattering information since this can be done trivially when one constructs such states. However, one does not have to choose $\chi(0)$ so that the corresponding $\psi(E)$ is, to within a known constant, a physically meaningful scattering state. Instead, one can select a set of $\chi(0)$'s to generate a complete basis set (at the energy E) in terms of which the desired scattering state satisfying the desired boundary conditions can be expressed (4,32,34,35,9). In this case, it is immaterial what precise boundary conditions are imposed through the $\xi(E)$'s (or the $\chi(0)$'s), and hence the $\psi(E)$'s, because the latter are simply being used as a complete basis set. The most useful application of this point is the generation of such basis sets in a way that enables one to consider the smallest possible computational region (4,32,34,9). The most important drawback of this approach is that in general, one must solve linear algebraic equations to extract the scattering information. If the number of energetically accessible quantum states is large (which it certainly can be in many systems of great interest), this additional computational effort may become a major burden, thereby reducing the ability of the approach to deliver scattering information as essentially a continuous function of energy. In these circumstances, the most efficient approach would appear to us to be the original one of generating the $\xi^{+}(E)$, which by itself already incorporates the physical boundary conditions and delivers the scattering matrix as a continuous function of the energy (1,2,5–7,10). We shall elaborate more on this below.

Now the solution of the homogeneous Schrödinger equation can be constructed as (4,9)

$$\psi(E) = \delta(E - H)\chi \tag{13}$$

and the scattering information is extracted by expanding $\delta(E - H)$ formally in terms of the solutions of the Schrödinger equation with appropriate scattering boundary conditions. These can be incoming-wave, outgoing-wave, or standing-wave boundary conditions. Furthermore, the solution generated from Eq. (13) is particularly robust in that the "initial packet," χ, can be chosen to lie outside the potential, and contain negligible amounts of momentum components pointing "away" from the target, or it can be centered on top of the scattering potential (4). In the former case, either $G^+(E)\chi$ or $G^-(E)\chi$ will vanish on the "target side" of χ, so that $\delta(E - H)\chi$ generates *only* $\xi^+(E)$ or $\xi^-(E)$ in this region. It then can be shown to be, within a known constant, equal to $\psi_k^+(E)$ or $\psi_k^-(E)$ in this region (4). When χ is placed on top of the target, the superposition in terms of $\psi_k^+(E)$ and $\psi^+{}_k(E)$ (or alternatively $\psi_k^-(E)$ and $\psi^-{}_k(E)$) must be employed.

As stated above, a major reason for the attractiveness of such approaches is the fact that we have also developed robust polynomial expansions of the Green's functions and Dirac delta function in terms of polynomials of the (normalized) Hamiltonian and known, analytical coefficients containing *all* of the energy dependence (2,11,6,7,9,36). Thus,

$$\frac{1}{E - H} = \sum_n g_n(E_{\text{norm}})F_n(H_{\text{norm}}) \tag{14}$$

where the boundary conditions are reflected in the coefficients $g_n(H_{\text{norm}})$, while the $F_n(H_{\text{norm}})$ are the *same* regardless of the particular solution being constructed. Similarly,

$$\delta(E - H) = \sum_n d_n(E_{\text{norm}})F_n(H_{\text{norm}}) \tag{15}$$

and one can obtain the scattering information such that the energy dependence is analytically known (2,5,7,10,34). This is extremely useful for treating systems in which there are closely spaced resonances (10). It is clear that the expansions (14) and (15) reduce the computational problem to the repeated application of H_{norm} to a vector, according to the recursion relation defining the polynomials $F_n(H_{\text{norm}})$.

The reduction of the calculation to the repeated application of the Hamiltonian matrix to a vector suggests that computational strategies that reduce the dimensions of the Hamiltonian matrix, render it sparse and/or having a convenient structure can lead to improved efficiency. One important approach makes the required region in which the solution must be computed as small as possible by employing negative imaginary absorbing potentials (37,38). However, this makes the Hamiltonian non-Hermitian and this creates stability problems for the polynomial representation of the Green's operators or spectral density operator (39,40). We have provided a solution to this difficulty by formulating these expansions in terms of the so-called "regional" or Faber polynomials (6,7), which are developed from the theory of analytic functions. While this procedure works and leads to completely stable polynomial recursion relations, they give rise to an enlarged spectral range for the Hamiltonian, thereby requiring more terms in the polynomial expansion to converge. However, Mandelshtam and Taylor (32) have shown that rather than deal with a non-Hermitian Hamiltonian, absorbing potentials can also be introduced exactly by suitably damping the Chebychev-recursion of Huang et al. (2) and

Kosloff et al. (36). Then the Hamiltonian remains Hermitian. The result bears some similarities to the inclusion of absorbing potentials in the work of Balint-Kurti (41), Zhang and Zhang (42), and of Goldfield and Grey (43). We obtain the same results as Mandelshtam and Taylor (32), but by instead scaling the Hamiltonian with a damping factor (9).

$$H_s = D^{1/2} H_{\text{norm}} D^{1/2} \tag{16}$$

where D equals one everywhere except in a boundary region, where it attenuates smoothly to a value less than 1. Thus, eigenstates of this Hamiltonian will also satisfy the Schrödinger equation in the interior region where $D = 1$ (but outside the region where $\chi \neq 0$). However, now it is the Faber polynomial recursion which is used to generate the polynomials of this scaled Hamiltonian, and the resulting polynomials automatically decay to zero in the boundary region. To see this, we note that the Faber recursion is (6,7)

$$|\eta_0^s\rangle = |\chi_i(0)\rangle \tag{17}$$

$$|\eta_1^s\rangle = D^{1/2} H_{\text{norm}} D^{1/2} |\chi_i(0)\rangle \tag{18}$$

$$|\eta_n^s\rangle = 2D^{1/2} H_{\text{norm}} D^{1/2} |\eta_{n-1}^s\rangle - D^2 |\eta_{n-2}^s\rangle \tag{19}$$

The fact that ever higher powers of D enter as one continues the recursion causes the $|\eta_n^s\rangle$ to attenuate to zero in the boundary region as n continues to increase. Further, $D^{1/2} H_{\text{norm}} D^{1/2}$ agrees with H_{norm} in the interior region so that the solutions generated by combining Eqs. (17)–(19) with (14) or (15) must be linear combinations of solutions of the homogeneous Schrödinger equation, for energy E, in the region between the edge of the source function $|\chi_i(0)\rangle$ and the beginning of the boundary (9). It is clear that symmetric scaling of H_{norm} by $D^{1/2}$ achieves results similar to the negative imaginary absorbing potential where one replaces H by $H + V_{\text{abs}}$, and it can be shown to be equivalent to the damping of the Chebychev recursion due to Mandelshtam and Taylor (32).

Another way to take advantage of the representation of solutions to the TIWSE in terms of polynomial recursions of the Hamiltonian acting on a vector is to develop new representations of the Hamiltonian. In particular, it is convenient to employ discretizations of the coordinate representation so as to avoid having to carry out heavy calculations of matrix elements of the Hamiltonian. We have recently presented a new general approach to this based on the so-called distributed approximating functional (DAF) (16–29). Because one works in the coordinate representation, the potential is already sparse and banded (i.e., it is diagonal!) Thus, the operator which one tries to simplify is the kinetic energy portion of the Hamiltonian. However, because this operator consists of second derivatives with respect to position, and these involve limits of finite differences, one intuitively expects that they should not be too nonlocal, which translates to their discrete matrix form being highly banded. This is certainly true if one simply uses finite difference approximations for the kinetic energy operator. However, these typically require extremely small step sizes in the discretization of the coordinates to achieve the desired accuracy. The DAF representation of the kinetic energy operator is considerably more robust than finite differences, and it also provides a highly banded, sparse (and for uniform grids and Cartesian coordinates, a Toeplitz) matrix structure (16,20,1,27). The Toeplitz nature of the DAF kinetic energy implies that the matrix is constant along its diagonals, and since it is also banded, this leads to very low storage requirements for the DAF Hamiltonian. Further, one can eliminate points in the highly nonclassical regions of the potential where the wave function does not penetrate (24,26). It then results that

the matrix-vector multiplication involves on order of N multiplications, where N is the total number of grid points retained in the representation of the wave function and Hamiltonian. The combination of the DAF, TIW, and polynomial expansions of operators will be shown to lead to a highly favorable scaling of calculations with problem size.

This chapter is intended to present an integrated description of this general approach to quantum dynamics. Applications of the equations and strategies both to scattering and bound state problems will be discussed. In the next section, we begin with a detailed summary of the salient features of the DAFs as they are used to represent the Hamiltonian operator. Then in Sec. III, we discuss the TIWSE and some of the choices that can be made in solving for bound states and scattering information. Included in this is a discussion of the polynomial representations of various operators involved in the TIW form of quantum mechanics. Finally, in Sec. IV we briefly summarize some of the applications made to date of this overall approach.

II. DISTRIBUTED APPROXIMATING FUNCTIONAL REPRESENTATION OF THE HAMILTONIAN

The DAFs differ in a fundamental way from more familiar "basis-set" expansions in that

1. They do not lead to a projection of the system wave function onto a subspace (16,27).
2. In the "well-tempered regime" (for a discrete grid approximation to the system coordinates), the DAFs yield comparable accuracy for both the wave function and its derivatives (27,29).
3. The DAFs provide comparable accuracy for the wave function both on and off the discrete grid points (16,27,29).
4. The DAFs do *not* give exact values of the wave function on the grid points (16).
5. Derivatives of the wave function both on and off the grid are produced by applying the "differentiating DAF" to the values of the function on the grid (1,2,27,29).

The general structure of the *continuous* DAF associated with a set of polynomials, ϕ_n, orthogonal under weight function, w, has been shown to be (18,29)

$$I_M(x - x') = w(x - x') \sum_{n=0}^{M} \phi_n(0)\phi_n^*(x - x') \tag{20}$$

One of the most useful continuous DAFs is that based on the Hermite polynomials (20,18), in which case

$$I_M(x - x'|\sigma) = \frac{e^{-(x-x')^2/2\sigma^2}}{\sqrt{2\pi}\sigma} \sum_{n=0}^{M/2} \frac{1}{n!}\left(-\frac{1}{4}\right)^n H_{2n}\left(\frac{x - x'}{\sqrt{2}\sigma}\right) \tag{21}$$

The discretized DAFs are obtained by a quadrature approximation to the action of the continuous DAF on some function (18,20):

$$f_{\mathrm{DAF}}(x) = \int_{-\infty}^{\infty} dx'\, I_M(x - x'|\sigma) f(x') \tag{22}$$

is approximated by

$$f_{\mathrm{DAF}}(x) = \sum_j \Delta w(x - x_j) \sum_{n=0}^{M} \phi_n(0)\phi_n^*(x - x_j) f(x_j) \tag{23}$$

so the discretized DAF is (16,29)

$$I_M(x - x_j) = \Delta w(x - x_j) \sum_{n=0}^{M} \phi_n(0)\phi_n^*(x - x_j) \tag{24}$$

Again, the Hermite polynomial realization of this is (16)

$$I_M(x - x_j) = \frac{\Delta}{\sqrt{2\pi}\sigma} e^{-(x-x_j)^2/2\sigma^2} \sum_{n=0}^{M/2} \frac{1}{n!}\left(-\frac{1}{4}\right)^n H_{2n}\left(\frac{x - x_j}{\sqrt{2}\sigma}\right) \tag{25}$$

It should be clear to the reader that other Newton-Cotes quadratures can also be employed to obtain alternative expressions for discretized DAFs (44). Now note that unlike, e.g., interpolation schemes or the popular discrete variable representation (DVR) (16),

$$f_{\mathrm{DAF}}(x_k) \neq f(x_k) \tag{26}$$

since

$$I_M(x_k - x_j) \neq \delta_{kj} \tag{27}$$

To see how derivatives are computed using DAFs, we consider the continuous DAF approximation to a function (27,29):

$$f_{\mathrm{DAF}}(x) = \int dx'\, I_M(x - x') f(x') \tag{28}$$

Then

$$\frac{d}{dx} f_{\mathrm{DAF}} = \int dx'\, \frac{d}{dx} I_M(x - x') f(x') \tag{29}$$

$$= -\int dx' \left[\frac{d}{dx'} I_M(x - x')\right] f(x') \tag{30}$$

Integrating by parts (assuming that surface terms vanish, as in the case of the Hermite DAFs), we obtain

$$\frac{d}{dx} f_{\mathrm{DAF}} = \int dx'\, I_M(x - x') \frac{d}{dx'} f(x') \tag{31}$$

The equality of Eqs. (29) and (31) illustrate the property of the continuous DAF of delivering comparable accuracy for the function and its derivatives. Then the discrete DAF approximation for the derivative results from a quadrature evaluation of Eq. (29):

$$\frac{d}{dx} f_{\mathrm{DAF}} = \Delta \sum_j \frac{d}{dx} I_M(x - x_j) f(x_j) \tag{32}$$

where again, the even-spaced trapezoidal rule has been used. More sophisticated Newton-Cotes quadratures can, of course, also be employed (44).

In the case of the Hermite DAF, use of the fact that $w(x - x')$ is the generating function for the Hermite polynomials enables us to write (27,29)

$$\frac{d^p}{dx^p} f_{\mathrm{DAF}} = \frac{\Delta}{\sqrt{2\pi}\sigma(2\sigma^2)^{p/2}} \sum_j e^{-(x-x_j)^2/2\sigma^2} \sum_{n=0}^{M/2} \frac{1}{n!} \left(-\frac{1}{4}\right)^n H_{2n+p}\left(\frac{x - x_j}{\sqrt{2}\sigma}\right) f(x_j) \qquad (33)$$

It is then clear how one constructs the action of the kinetic energy and local potential energy operators on a wave function (1,2). On the grid, we have

$$H_{jk} = -\frac{\hbar^2\Delta}{4m\sqrt{2\pi}\sigma^3} e^{-(x_j - x_k)^2/2\sigma^2} \sum_{n=0}^{M/2} \frac{1}{n!} \left(-\frac{1}{4}\right)^n H_{2n+2}\left(\frac{x_j - x_k}{\sqrt{2}\sigma}\right) + \delta_{jk} V(x_j) \qquad (34)$$

This expression is easily generalized to more degrees of freedom, as well as to non-Cartesian coordinates (by making use of recursion relations satisfied by whatever polynomials are used for the particular degrees of freedom being considered) (17,23,45). It is also clear that H_{jk} is highly banded due to the Gaussian factor, and the kinetic energy portion is a function only of the difference, $x_j - x_k$. It is therefore a Toeplitz matrix (20). If the bandwidth of the H_{jk}-matrix is B, then to multiply H_{jk} with a vector having N-components will require $B \cdot N$ multiplications. Since the bandwidth B is independent of N, this implies such a product scales *linearly* with the matrix dimension N. In fact, a Toeplitz matrix-vector product can also always be done using fast Fourier transforms (FFT), leading to an overall $N \log_2 B$ scaling (24,26). Thus, one can take considerable advantage of the structure of the DAF-Hamiltonian to reduce the computational effort. We now turn to consider the time-independent wave packet formalism.

III. TIME-INDEPENDENT WAVE PACKET EQUATIONS FOR QUANTUM DYNAMICS

In the introduction we have already discussed the derivation of the time-independent wave packet (TIW) equations starting with the formal solution of the time-dependent Schrödinger equation, and then doing a half-Fourier transform from the time domain to the energy domain (1,2). We also pointed out that the resulting solutions can be used to construct other solutions of the TIW form of the Schrödinger equation besides those which are related by a constant of proportionality to the physical solution in a particular region. It was also noted that a major advantage of the TIWSE is that this makes possible the incorporation of certain aspects of the boundary conditions into the inhomogeneity (the $t = 0$ wave packet). Indeed, the TIWSE admits an infinity of solutions which fact can be used to reduce the size of the region that is required for calculations (4,9,32,34,35). This is generally done by generating a sufficient number of linearly independent numerical solutions which then can be expressed in terms of linear combinations of the linearly independent physical solutions. One thereby obtains a set of simultaneous algebraic equations for the elements of the scattering matrix or related matrices (e.g., the T- or K-matrix). Thus, the TIWSE gives one the option of generating solutions that are directly proportional, in a specific region of space, to a desired physical solution, or of generating solutions that are superpositions of the physical solutions. In this section we discuss in more detail some of the specific choices of solutions for scattering problems in order to illustrate the various sorts of approaches possible; we also discuss how the TIWSE can be used to generate an extremely efficient method for carrying out bound state calculations. We begin with the treatment of the bound states.

A. Bound State Calculations Using the Spectral Density Operator

We note first that the eigenstates of H form a complete set, so that

$$|\psi(E)\rangle = \sum_n \delta(E - E_n)|\zeta_n\rangle\langle\zeta_n|\chi_i(0)\rangle \tag{35}$$

where $|\zeta_n\rangle$ is the nth eigenstate of H. Clearly, if the projection of $|\chi_i(0)\rangle$ onto an eigenstate $|\zeta_n\rangle$ vanishes, no information about that eigenstate can be obtained. However, it is also clear that by "tuning" the energy parameter E, the operator $\delta(E - H)$ selects out those eigenstates having nonzero overlap with $|\chi_i(0)\rangle$. It is for this reason that the structure of the polynomial representation of $\delta(E - H)$ is so convenient. We consider a grid (DAF) representation of the Hamiltonian, so that H becomes a finite matrix, having a minimum and a maximum eigenvalue, $H_{\min}$ and $H_{\max}$. Then

$$H_{\text{norm}} = \frac{H - \bar{H}}{\Delta H} \tag{36}$$

$$E_{\text{norm}} = \frac{E - \bar{H}}{\Delta H} \tag{37}$$

$$\bar{H} = \frac{H_{\max} + H_{\min}}{2} \tag{38}$$

$$\Delta H = \frac{H_{\max} - H_{\min}}{2} \tag{39}$$

and

$$\delta(E - H) = \frac{1}{\pi\Delta H} \sum_n \frac{2 - \delta_{n0}}{\sqrt{1 - E_{\text{norm}}^2}} T_n(E_{\text{norm}})T_n(H_{\text{norm}}) \tag{40}$$

Here, T_n is the nth Chebychev polynomial satisfying the recursion relation

$$T_n(x) = 2xT_{n-1}(x) - T_{n-2}(x) \tag{41}$$

$$T_0(x) = 1 \tag{42}$$

$$T_1(x) = x \tag{43}$$

and also

$$T_n(x) = \cos[n \cos^{-1} x] \tag{44}$$

Now since $-1 \leq E_{\text{norm}} \leq 1$, one has

$$\sqrt{1 - E_{\text{norm}}^2} \equiv \sin\theta \tag{45}$$

$$\cos\theta = E_{\text{norm}} \tag{46}$$

Analogous matrix relations hold for $T_n(H_{\text{norm}})$. It follows that

$$\psi(E) = \frac{1}{\pi\Delta H} \sum_{n=0}^{\infty} \frac{2 - \delta_{n0}}{\sin\theta} \cos(n\theta)\eta_n \tag{47}$$

with

$$\eta_0 = \chi_i(0) \tag{48}$$

$$\eta_1 = H_{\text{norm}}\chi_i(0) \tag{49}$$

$$\eta_n = 2H_{\text{norm}}\eta_{n-1} - \eta_{n-2} \tag{50}$$

where the η_n are like a Krylov basis (11,13,14). We next define the "spectral function," $A_N(E)$, relatd to the "energy domain" autocorrelation function $A(E)$:

$$A_N(E) \equiv \langle\chi_i(0)|\psi_N(E)\rangle \tag{51}$$

$$A(E) \equiv \langle\chi_i(0)|\delta(E - H)|\chi_i(0)\rangle \tag{52}$$

$$A(E) = \lim_{N\to\infty} A_N(E) \tag{53}$$

Explicitly, we have that

$$A_N(E) = \frac{1}{\pi\Delta H}\sum_{n=0}^{N}\frac{2 - \delta_{n0}}{\sin\theta}\cos(n\theta)\langle\chi_i(0)|\eta_n\rangle \tag{54}$$

$$= \frac{1}{\pi\Delta H}\sum_{n=0}^{N}\frac{2 - \delta_{n0}}{\sin\theta}\cos(n\theta)\langle\chi_i(0)|T_n(H_{\text{norm}})|\chi_i(0)\rangle \tag{55}$$

Inserting the identity resolution in terms of the eigenstates of H_{norm},

$$1 = \sum_j |\zeta_j\rangle\langle\zeta_j| \tag{56}$$

we obtain

$$A_N(E) = \frac{1}{\pi\Delta H\sin\theta}\sum_{n=0}^{N}(2 - \delta_{n0})\cos(n\theta)\sum_j \cos(n\theta_j)|b_j|^2 \tag{57}$$

$$b_j = \langle\zeta_j|\chi_i(0)\rangle \tag{58}$$

Clearly, calculating $A_N(E)$ for a dense set of energies is very simple and inexpensive (11). Furthermore, we would expect that the $\psi_N(E)$ should yield an excellent basis for diagonalizing H_{norm} to obtain the eigenvalues and eigenfunctions within a given range of energies (13,14). Computational studies have shown that this is indeed the case, and a powerful iterative scheme can be based on using the $\psi_N(E)$ evaluated on a grid of energies to produce a relatively small basis set for subspace diagonalization of H_{norm}. A crucial aspect of the approach which can greatly affect the rate of convergence of the iterative procedure is the choice of the $\chi_i(0)$, the initial wave packet. This can be facilitated for many problems by discarding from the Hamiltonian matrix, H_{norm}, part (or all) of the off-diagonal elements. The eigenvectors and eigenvalues of $H_{\text{norm},0}$ can then be used as guides for constructing $\chi_i(0)$ and choosing the grid of energies at which to evaluate the $\psi_N(E)$ for the subspace diagonalization (14). Having improved eigenvalues and eigenvectors, one can use those which are still not accurate enough as *new* $\chi_i(0)$, and the procedure can be repeated. In addition, several tests of accuracy are available (including comparing the eigenvalue estimate to the average of H_{norm} and the square of H_{norm}) (14). Additional techniques for improving the rate of convergence, which can be added to the above basic procedure, include preconditioning the matrix, H or H_{norm} (46). If there are degeneracies, one must construct more than one initial $\chi_i(0)$ having the proper symmetry (13). Obviously, the recursion equations (48)–(50) preserve any symmetry inherent to $\chi_i(0)$.

An important variation of this procedure is to apply a window to the basic solution, $\delta(E - H)\chi_i(0)$ (47). This focuses the calculation to a very specific, finite range of energies (even without the truncation of H). It has the consequence of improving the rate of convergence of the Chebychev expansion, since the "windowed delta function" is no longer singular. As a result, the coefficients decay as the summation index increases, even for a Hermitian Hamiltonian.

B. Scattering State Calculations Using the Spectral Density Operator

The same expression that yields bound states, Eq. (47), can be used at energies E in the scattering continuum (4,48). In fact, this illustrates our earlier discussion of the construction of solutions that are linear superpositions of all possible causal (physical) solutions at a given energy. It also can be used, with the appropriate choice of $\chi_i(0)$, to generate a solution which involves only a single physical state. In order to extract the scattering information for an arbitrary choice of χ (including one sitting on top of the target), one makes use of the fact that (4)

$$\delta(E - H) = \sum_n |\zeta_n\rangle\langle\zeta_n|\delta(E - E_n) + \int_{-\infty}^{\infty} dk\, \delta\left(E - \frac{\hbar^2 k^2}{2m}\right)|\psi_k^+\rangle\langle\psi_k^+| \tag{59}$$

where the discrete sum is over any bound states of H and the integral extends over the complete set of scattering solutions (noting that for causal boundary conditions, this includes ψ_k^+ and ψ^+_{-k}, $k > 0$). Changing to an integral over dE rather than dk, and assuming we consider only scattering energies (so the discrete sum vanishes due to $\delta(E - E_n)$), we have that

$$\delta(E - H) = \frac{m}{\hbar^2}\int_0^{\infty} dE' \frac{\delta(E - E')}{k(E')}\left[|\psi_k^+\rangle\langle\psi_k^+| + |\psi^+_{-k}\rangle\langle\psi^+_{-k}|\right] \tag{60}$$

In the case of reactive scattering, the states with $-k$ correspond to the initial conditions in the other arrangements, and Eq. (60) generalizes to

$$\delta(E - H) = \frac{m}{\hbar^2}\int_0^{\infty} dE' \frac{\delta(E - E')}{k(E')}\sum_{\lambda} |\psi_\lambda^+\rangle\langle\psi_\lambda^+| \tag{61}$$

where λ is a collective index for all the quantum numbers specifying the various asymptotic arrangements and other quantum numbers (4,9). Then the solution of the homogeneous Schrödinger equation is

$$\psi_{\lambda'}(E) = \delta(E - H)\chi_{\lambda'}(0) \tag{62}$$

$$= \frac{m}{\hbar^2 k(E)}\sum_{\lambda} |\psi_\lambda^+(E)\rangle\langle\psi_\lambda^+(E)|\chi_{\lambda'}(0)\rangle \tag{63}$$

or

$$\psi_{\lambda'}(E) = \frac{m}{\hbar^2 k(E)}\sum_{\lambda} A_{\lambda\lambda'}\psi_\lambda^+(E) \tag{64}$$

By evaluating $\psi_{\lambda'}(E)$ for a complete set of λ' initial packets, at a sufficient number of grid points in the various arrangements (external to the region of scattering), one can set up linear algebraic equations which can be solved for the scattering amplitudes. Alternatively, one can "sample" the $\psi_{\lambda'}(E)$ using "final state packets," $\chi_{\lambda''}(f)$, which are

nonzero only in a finite region in one of the arrangements (9,5). Defining

$$B_{\lambda''\lambda'} \equiv \langle \chi_{\lambda''}(f)|\psi_{\lambda'}(E)\rangle \tag{65}$$

which can be evaluated knowing the $\psi_{\lambda'}(E)$, and the fact that each $\chi_{\lambda''}(f)$ is nonzero only in *one* arrangement channel (just outside the scattering potential), one again solves a linear system of algebraic equations to obtain the scattering information. In order to reduce the grid size required for such calculations, it has been common to introduce negative imaginary absorbing potentials (37,38). However, this has the drawback of making the Hamiltonian non-Hermitian. Mandelshtam and Taylor (32) have shown how one can retain the Hermitian Hamiltonian and still utilize an absorbing potential by modifying the Chebychev recursion relation. Non-Hermitian Hamiltonians can also be dealt with by appealing to the theory of analytic functions and the "regional" or Faber polynomials (6,7,9). The Chebychev polynomials have a corresponding Faber polynomial-based generalization, so that the recursion becomes (in place of Eqs. (41)–(43)) that of Eqs. (17)–(19). However, rather than use the Faber-Chebychev recursion in this manner, one can also use as the scaling D a real function which is chosen to attenuate the Hamiltonian in the "boundary region." This has the consequence of causing the polynomials η_n^s to become very small in the boundary region, as n increases. This, in turn, causes the higher contributions to the expansion of the TIW wave function to tend to zero and the expansion converges to a well-defined limit. Effectively, this implies that only a finite number of reflections occur at the boundary, and the solution in the interior region (but outside the initial packet) then is again a linear combination of the linearly independent physical solutions. The damping function, D, is chosen so that the new Hamiltonian, $D^{1/2}H_{\text{norm}}D^{1/2}$ remains Hermitian (9). In applications, we have chosen D so that it equals 1 except in a narrow boundary region, where it is attenuated smoothly to a value less than 1. Because the scaled Hamiltonian, $D^{1/2}H_{\text{norm}}D^{1/2}$, agrees with the ordinary Hamiltonian everywhere except in the boundary region, solutions of the Schrödinger equation

$$(E_{\text{norm}} - D^{1/2}H_{\text{norm}}D^{1/2})\psi = 0 \tag{66}$$

must also be expressible in the form of Eq. (64) in the region between $\chi(0)$ and the boundary. Thus, we generate a scaled Faber-Chebychev basis $|\eta_n^s\rangle$ by

$$|\eta_{\lambda 0}^s\rangle = |\chi_\lambda(0)\rangle \tag{67}$$

$$|\eta_{\lambda 1}^s\rangle = D^{1/2}H_{\text{norm}}D^{1/2}|\chi_\lambda(0)\rangle \tag{68}$$

$$|\eta_{\lambda n}^s\rangle = 2D^{1/2}H_{\text{norm}}D^{1/2}|\eta_{\lambda n-1}^s\rangle - D^2|\eta_{\lambda n-2}^s\rangle \tag{69}$$

and the spectral density solution is

$$\psi_\lambda(E_{\text{norm}}) = \frac{1}{\pi\Delta H}\sum_n \frac{2-\delta_{n0}}{\sin\theta}\cos(n\theta)\eta_{\lambda n}^s \tag{70}$$

The final state analysis behaves exactly the same as without scaling (Eqs. (64)–(65)) (4). This approach is related to that of Mandelshtam and Taylor (32) by a simple transformation, relating the damped Chebychev recursion and the Faber-Chebychev recursion with damped Hamiltonian.

Finally, we remark that one can also evaluate this expression in terms of the eigenstates, $\{|\zeta_j\rangle\}$, of $D^{1/2}H_{\text{norm}}D^{1/2}$. Then we use the resolution of the identity

$$1 = \sum_j |\zeta_j\rangle\langle\zeta_j| \tag{71}$$

to write the recursion Eq. (69) as

$$|\eta^s_{\lambda n}\rangle = 2 \sum_j E_j |\zeta_j\rangle\langle\zeta_j|\eta^s_{\lambda n-1}\rangle - D^2|\eta^s_{\lambda n-2}\rangle \tag{72}$$

We expect that for a given range of collision energies, one really only needs to include $|\zeta_j\rangle$ up to some maximum eigenenergy, rather than the entire complete set. This has been tested computationally and shown to work (49).

C. Scaling of Computational Effort with Basis Size

The key to analyzing the scaling, with basis size or matrix dimension, of these methods for solving both scattering and bound state problems is to note that the use of polynomial representations of the various operators reduces the calculations to repeated matrix-vector products. Even without any sparseness of the Hamiltonian matrix, H, this yields N^2 scaling, where H is an $N \times N$ matrix. However, the bandedness of the DAF-Hamiltonian reduces the scaling to *linear* in N, since in general, the bandwidth is independent of N. Furthermore, this is true whether one uses the Toeplitz structure of the DAF Hamiltonian to carry out the matrix-vector product using fast Fourier transforms or not (24,26). Thus, in general, the computational effort scales linearly with the vector dimension N.

However, another important fact in considering the scaling of the computational effort is that results for many energies can be obtained with very little effort beyond that required for a single energy. This suggests that the TIW approaches are likely to be especially valuable for studying systems which involve resonances, and for calculating quantities which involve energy averages. Indeed, it has been shown in actual applications that energy derivatives can be computed analytically from the TIW expressions for the S-matrix (10).

IV. APPLICATIONS

To date, the TIW approach, combined with the DAF Hamiltonian, has been applied to treat collinear reactive scattering (2,3,5,6,9,12,26) and atom-rigid rotor scattering (50). In the reactive scattering calculations, we have considered calculating both $G^+(E)\chi_i(0)$ and $\delta(E - H)\chi_i(0)$, where $\chi_i(0)$ does *not* overlap the target or strong interaction region, and $\delta(E - H)\chi_i(0)$ with $\chi_i(0)$ on top of the target or strong interaction region. Such calculations have been carried out using a region large enough so that no waves were reflected back from the boundaries. The damped Hamiltonian approach has also been used (9,32), and it is this version which is the most efficient. In addition, it is possible to eliminate from inclusion DAF grid points where the potential is significantly larger than the highest energy for which scattering information is desired (7,9). Although this destroys the Toeplitz structure of the kinetic energy matrix (thereby necessitating more storage), it decreases the size of N of the grid. It therefore can reduce the computational effort required greatly.

In carrying out calculations using either $\delta(E - H)\chi_i(0)$, where $\chi_i(0)$ overlaps the target or the damped Hamiltonian, $D^{1/2}H_{\text{norm}}D^{1/2}$, it is important to note that one must generate a sufficient number of linearly independent solutions, leading to the desired linear system of algebraic equations, to solve for the scattering information. Generally speaking, these algebraic equations are not sparse and their solution introduces a computational step scaling as the cube of the total number of internal states (channels) energetically accessible at the energy of interest. Furthermore, such equations must be

solved at each desired energy. If the number of channels is sufficiently large, this can become a computational limitation. In this circumstance, it may be more efficient to solve the equations in a large enough region that converged results (with respect to the polynomial expansion) are obtained *before* the wave encounters the boundary. Then the use of the polynomial representation of $G^+(E)$, acting on a *single* initial wave packet, will yield the appropriate column of the S-matrix without necessitating solutions of linear algebraic equations. Both types of computations have been carried out, showing that the TIW formalism is particularly robust.

Another aspect of applications which should be noted is the fact that up to the present, calculations have been carried out for systems using Cartesian-type distance variables. Thus, in the calculations of atom-rigid rotor scattering (50), the first derivative in the radial kinetic energy was eliminated by the usual substitution

$$\psi^J(j\Omega|j_0\Omega_0|R) = \frac{\mathcal{U}^J(j\Omega|j_0\Omega_0|R)}{R} \tag{73}$$

Then it is necessary to represent the operator $(-\hbar^2/2\mu)\partial^2/\partial R^2$ in terms of the DAF. The domain for R is $[0, \infty)$, rather than $(-\infty, \infty)$, and the DAF expression for the second derivative of $\mathcal{U}^J$, Eq. (33), would require values of $\mathcal{U}^J$ at negative R. However, the potential is such that the radial wave function is essentially zero before one reaches $R = 0$, so it is straightforward to simply set $\mathcal{U}^J$ equal to zero for $R < R_0$. Then the Cartesian DAF expression for the radial kinetic energy can be used without difficulty. Alternatively, one can make use of radial DAFs which have been derived specifically for treating such variables (16,23). Similarly, rather than using basis set expansions for the other variables such as angles, one can employ DAFs constructed especially for those portions of the Hamiltonian (29). Calculations making use of such DAFs, along with TIW equations, are now being initiated. We expect that a variety of state-of-the-art results will be obtained in the near future.

ACKNOWLEDGMENTS

The authors were supported by National Science Foundation grant CHE-9403416 and the R. A. Welch Foundation (DJK) and by National Science Foundation grant ASC-9310235 (Y. H.). Ames Laboratory is operated for the Department of Energy by Iowa State University under contract 2-7405-ENG82.

REFERENCES

1. D. J. Kouri, M. Arnold, and D. K. Hoffman, *Chem. Phys. Lett.* 203:166 (1993).
2. Y. Huang, W. Zhu, D. J. Kouri, and D. K. Hoffman, *Chem. Phys. Lett.* 206:96 (1993).
3. W. Zhu, Y. Huang, D. J. Kouri, M. Arnold, and D. K. Hoffman, *Phys. Rev. Lett.* 72:1310 (1994); 73:1733E (1994).
4. D. K. Hoffman, Y. Huang, W. Zhu, and D. J. Kouri, *J. Chem. Phys.* 101:1242 (1994).
5. D. J. Kouri, Y. Huang, W. Zhu, and D. K. Hoffman, *J. Chem. Phys.* 100:3662 (1994).
6. Y. Huang, D. J. Kouri, and D. K. Hoffman, *Chem. Phys. Lett.* 225:37 (1994).
7. Y. Huang, D. J. Kouri, and D. K. Hoffman, *J. Chem. Phys.* 101:10493 (1994).
8. D. J. Kouri and D. K. Hoffman, *Few Body Sys.*, 18:203 (1995).
9. Y. Huang, S. Iyengar, D. J. Kouri, and D. K. Hoffman, *J. Chem. Phys.*, submitted.
10. D. J. Kouri, W. Zhu, Y. Huang, and D. K. Hoffman, *Chem. Phys. Lett.* 220:312 (1994).

11. W. Zhu, Y. Huang, C. Chandler, and D. K. Hoffman, *Chem. Phys. Lett.*, 217:73 (1994).
12. Y. Huang, D. J. Kouri, and D. K. Hoffman, *Chem. Phys. Lett.*, 238:387 (1995).
13. D. J. Kouri, W. Zhu, G. A. Parker, and D. K. Hoffman, *Chem. Phys. Lett.*, 238:395 (1995).
14. G. A. Parker, W. Zhu, Y. Huang, D. J. Kouri, and D. K. Hoffman, *Comp. Phys. Commun.*, in press.
15. D. J. Kouri and D. K. Hoffman, *Phys. Rev. E*, submitted.
16. D. K. Hoffman, N. Nayar, O. A. Sharafeddin, and D. J. Kouri, *J. Phys. Chem.* 95:8299 (1991).
17. D. K. Hoffman and D. J. Kouri, *J. Phys. Chem.* 96:1179 (1992).
18. D. J. Kouri, W. Zhu, X. Ma, B. M. Pettitt, and D. K. Hoffman, *J. Phys. Chem.* 96:9622 (1992).
19. D. J. Kouri and D. K. Hoffman, *J. Phys. Chem.* 96:9631 (1992).
20. D. K. Hoffman, M. Arnold, and D. J. Kouri, *J. Phys. Chem.* 96:6539 (1992).
21. D. K. Hoffman, M. Arnold, and D. J. Kouri, *J. Phys. Chem.* 97:1110 (1993).
22. D. K. Hoffman, M. Arnold, W. Zhu, and D. J. Kouri, *J. Phys. Chem.* 99:1124 (1993).
23. D. K. Hoffman and D. J. Kouri, *J. Phys. Chem.* 97:4984 (1993).
24. Y. Huang, D. J. Kouri, M. Arnold, T. L. Marchioro, and D. K. Hoffman, *J. Phys. Chem.* 99: 1028 (1993).
25. T. L. Marchioro, M. Arnold, D. K. Hoffman, W. Zhu, Y. Huang, and D. J. Kouri, *Phys. Rev. E* 50:2320 (1994).
26. Y. Huang, D. J. Kouri, M. Arnold, T. L. Marchioro, and D. K. Hoffman, *Comp. Phys. Comm.* 80:1 (1994).
27. D. K. Hoffman and D. J. Kouri, *Proc. 3rd. Int. Conf. on Math. and Num. Aspects of Wave Propag. Phenom.* (G. Cohen, ed.), SIAM, 1995, pp. 56–83.
28. D. J. Kouri and D. K. Hoffman, *Time-Dep. Quant. Molec. Dynam.* (J. Broeckhove and L. Lathouwers, eds.), NATO ASI Series B 299, 1992, p. 117.
29. D. K. Hoffman, T. L. Marchioro, M. Arnold, Y. Huang, W. Zhu, and D. J. Kouri, *J. Math. Chem.*, submitted.
30. H. Tal-Ezer and R. Kosloff, *J. Chem. Phys.* 81:3967 (1984).
31. R. Kosloff, *J. Phys. Chem.* 92:2087 (1988).
32. V. A. Mandelshtam and H. S. Taylor, *J. Chem. Phys.*, 103:2903 (1995).
33. P. M. Morse and H. Feshbach, Methods of Theoretical Physics, McGraw-Hill, New York, 1953.
34. V. A. Mandelshtam and H. S. Taylor, *J. Chem. Phys.*, in press.
35. H. W. Jang and J. C. Light, *J. Chem. Phys.*, in press.
36. B. Hartke, R. Kosloff, and S. Ruhman, *Chem. Phys. Lett.* 158:223 (1986).
37. D. Neuhauser and M. Baer, *J. Chem. Phys.* 90:4351 (1989).
38. D. Neuhauser, M. Baer, and D. J. Kouri, *J. Chem. Phys.* 90:5882 (1989); 93:312 (1990).
39. M. Berman, R. Kosloff, and H. Tal-Ezer, *J. Phys. A* 25:1283 (1992).
40. S. M. Auerbach and C. Leforestier, *Comp. Phys. Comm.* 78:55 (1993).
41. G. G. Balint-Kurti and A. Vibok, *NATO ASI Series C*, 412 (1993).
42. D. H. Zhang, O. A. Sharafeddin, and J. Z. H. Zhang, *Chem. Phys.* 167:137 (1992).
43. See, *e.g.*, E. M. Goldfield, S. K. Grey, and G. C. Schatz, *J. Chem. Phys.*, in press.
44. G. A. Parker, D. J. Kouri, and D. K. Hoffman, to be published.
45. Y. Huang, D. J. Kouri, and D. K. Hoffman, in prep.
46. P. Pendergast, Z. Darakjian, E. F. Hayes, and D. C. Sorensen, *J. Comp. Phys.* 113:201 (1994).
47. D. K. Hoffman, Y. Huang, and D. J. Kouri, to be published.
48. V. A. Mandelshtam, T. Ravuri, and H. S. Taylor, *J. Chem. Phys.* 101:8792 (1994).
49. S. S. Iyengar, Y. Huang, D. J. Kouri, and D. K. Hoffman, to be published.
50. W. Zhu, Y. Huang, G. A. Parker, D. J. Kouri, and D. K. Hoffman, *J. Phys. Chem.* 98:2516 (1994).

9

Computational Spectroscopy of the Transition State

DAVID C. CHATFIELD*, RONALD S. FRIEDMAN†, STEVEN L. MIELKE, GILLIAN C. LYNCH, THOMAS C. ALLISON, and DONALD G. TRUHLAR

University of Minnesota, Minneapolis, Minnesota

DAVID W. SCHWENKE

NASA Ames Research Center, Moffett Field, California

I. INTRODUCTION

In a typical chemical reaction the ability of the atoms to rearrange themselves is controlled by one or more dynamical bottlenecks in phase space. A dynamical bottleneck may be represented by a hypersurface in phase space dividing reactants from products, and this dividing surface is called the activated complex or the transition state (1). The allowed energy levels of the transition state are not strictly quantized because they are not bound states, but they are approximately quantized (like vibrationally predissociating states in spectroscopy (2) or like collision resonances in scattering theory (3–5)), because they are fleetingly metastable. The search for these quantized energy levels is called transition state spectroscopy. Transition state spectroscopy has proved to be extremely difficult from an experimental point of view, so much so, in fact, that the term has come to be associated with any form of spectroscopy or any spectroscopic measurement that gives information about the activated complex region of the potential energy surface, even when no hint of quantized structure is present (6,7). In recent years we have learned that this structure does exist and can be uncovered by quantum reactive scattering calculations (8–16). This chapter reviews the theory behind the phenomenon and surveys recent results from our group, some (those in Secs. IV, V, and VIII) published elsewhere (8–16) and others (extensive results in Secs. VI and VII and preliminary results in Sec. IX.D) presented for the first time in this chapter. The analysis of the O + H_2 system

---

*Current affiliation: Florida International University, Miami, Florida

†Current affiliation: Indiana University–Purdue University, Fort Wayne, Indiana

includes a contribution by Bowman (13), and our work on halogen-hydrogen halide reactions is based in part on accurate scattering calculations by Schatz (17–19). We also discuss results in computational and experimental transition state spectroscopy by other groups (references in Secs. IV–IX).

II. THEORY

We focus attention on bimolecular reactions of the form A + BC → AB + C. The canonical ensemble rate coefficient $k(T)$ in the expression

$$-\frac{d[A]}{dt} = k(T)[A][BC] \tag{1}$$

can be written in terms of the microcanonical ensemble rate constant $k(E)$, T being the temperature and E being the total energy, as (8,20)

$$k(T) = \frac{\int_0^\infty \exp(-E/k_B T)\rho^R(E)k(E)\,dE}{\Phi^R(T)} \tag{2}$$

where k_B is Boltzmann's constant, $\Phi^R(T)$ is the reactants' partition function per unit volume, and $\rho^R(E)$ is the reactants' density of states per unit volume per unit energy. An exact quantum mechanical expression for $k(E)$ is given in terms of the state-to-state reaction probabilities $P_{nn'}$ by (8,21)

$$k(E) = \frac{\Sigma_n \Sigma_{n'} P_{nn'}(E)}{h\rho^R(E)} \tag{3}$$

where h is Planck's constant and $n(n')$ is an index of the quantum state of the reactants (products), and we are employing the ultimate level of state specification, in which each channel is counted as a state. For an atom-diatom reaction, $n(n')$ designates the total angular momentum J, its component M_J on an arbitrary space-fixed axis, and the set of initial (final) vibrational quantum number v (v'), rotational quantum number j (j'), and orbital angular momentum quantum number l (l'). The state-to-state reaction probability can be written in terms of elements of the scattering matrix S if desired (22):

$$P_{nn'}(E) = |S_{nn'}(E)|^2 \tag{4}$$

The double sum in Eq. (3) contains all the dynamics in both $k(T)$ and $k(E)$ and is called the cumulative reaction probability (CRP) (23) and denoted $N(E)$:

$$N(E) = \sum_n \sum_{n'} P_{nn'}(E) \tag{5}$$

The dynamical structure in $k(E)$ can be brought out most clearly by calculating the energy derivative of the CRP, the density of reactive states $\rho(E)$:

$$\rho(E) = \frac{dN(E)}{dE} \tag{6}$$

Transition state theory (TST) provides a framework for understanding the CRP and its energy derivative. The transition state theory rate constant is the value that the rate constant would have if (i) all reactant states were in local Boltzmann equilibrium and (ii) the one-way flux through a hypersurface in phase space dividing reactants from products were equal to the flux from one side to the other (24–28). In a world described by classical mechanics, the latter condition would be true if all trajectories passing through the dividing surface crossed it only once. The dividing surface in phase space has one less degree of freedom than the phase space itself, and, as mentioned in the introduction, species constrained to the dividing surface are said to be in the transition state. The missing degree of freedom, which is normal to the dividing surface, is called the reaction coordinate s.

Conditions (i) and (ii), plus the usual assumption that bound degrees of freedom have quantized energy levels, lead to the familiar expression (1,29) in which the rate constant $k(T)$ becomes proportional to a "transition state partition function," $Q^{\ddagger}(T)$, which is a sum over quantized states of an activated complex:

$$k^{\ddagger}(T) = \frac{k_B T}{h} \frac{Q^{\ddagger}(T)}{\Phi^R(T)} e^{-V^{\ddagger}/k_B T} \tag{7}$$

where $V^{\ddagger}$ is the classical potential energy at the transition state, i.e., the difference in the zeroes of energy used to compute $Q^{\ddagger}(T)$ and $\Phi^R(T)$. (Note that we take the zero of energy for partition functions to be the minimum potential energy of the species in question, *not* the lowest quantized energy level of that species.) The microcanonical ensemble version of the familiar TST expression is (30–33)

$$k^{\ddagger}(E) = \frac{N^{\ddagger}(E)}{h\rho^R(E)} \tag{8}$$

Here $N^{\ddagger}(E)$ is the number of energy states (levels) of the activated complex with energy less than or equal to E.

If we interpret the quantization of the activated complex literally, then comparison of Eqs. (3), (5), and (8) suggests that the cumulative reaction probability will increase in steps of one at the energy levels of the transition state. However, Eq. (8) neglects quantum mechanical tunneling and nonclassical reflection (diffraction by the barrier top) at energies below and above, respectively, the reaction barrier. Furthermore, it assumes that the transition state is a perfect dynamical bottleneck in the sense that all systems crossing the transition state proceed directly from reactants to products without recrossing (24–28). Several workers have proposed generalizations of transition state theory to account for quantum tunneling and recrossing effects (21,23,34,35). For example, we can account for the breakdown of these assumptions in the simplest way by replacing Eq. (8) by

$$k^{\ddagger}(E) = \frac{\sum_{\tau} \kappa_{\tau} P_{\tau}(E)}{h\rho^T(E)} \tag{9}$$

where τ is a level of the transition state, κ_{τ} is a transmission coefficient accounting for recrossing, and P_{τ} is a quantal or semiclassical transmission probability accounting for quantum mechanical tunneling and nonclassical reflection. The numerator still contains a sum over energy levels, but instead of increasing in steps of one at each new level of the transition state, it increases more gradually and by an amount governed by $\kappa_{\tau} P_{\tau}(E)$.

Note that if we set κ_τ equal to unity and $P_\tau(E)$ to a unit step function at transition state energy level E_τ, Eq. (9) reduces to (8).

If we assume that the reaction coordinate is separable, that there exists an effective potential curve $V_\tau(s)$ for passage through the transition state region in level τ, and that this potential has a parabolic form, we obtain $\kappa_\tau = 1$ and a simple form for $P_\tau(E)$. In particular, if $V_\tau(s)$ is given in terms of the reaction coordinate s by

$$V_\tau(s) = E_\tau + \frac{1}{2} k_\tau s^2 \tag{10}$$

with E_τ being the energy of the barrier maximum and k_τ being a negative force constant, then the quantum mechanical transmission probability is given by (36)

$$P_\tau(E) = \frac{1}{1 + \exp[(E_\tau - E)/W_\tau]} \tag{11}$$

where W_τ is a width parameter. The transmission probability $P_\tau(E)$ rises smoothly from zero to one. In Eq. (11), the width parameter W_τ is

$$W_\tau = \frac{\hbar|\omega_\tau|}{2\pi} \tag{12}$$

where $\hbar$ is Planck's constant divided by 2π, ω_τ is the imaginary frequency of the barrier

$$\omega_\tau = \sqrt{k_\tau/\mu} \tag{13}$$

and μ is the reduced mass. Because of Eqs. (12) and (13), W_τ is inversely related to the width of the effective potential barrier V_τ. Small values of W_τ correspond to wide barriers, for which tunneling and nonclassical reflection are less important. Inserting Eq. (11) into (9) leads to a generalized version of conventional transition state theory that incorporates quantum effects on reaction-coordinate motion and recrossing.

Equations (6), (8), (9), and (11) yield the following approximation to the density of reactive states:

$$\rho^\ddagger(E) = \sum_\tau \kappa_\tau \rho_\tau(E) \tag{14}$$

with

$$\rho_\tau(E) = \frac{\exp[(E_\tau - E)/W_\tau]}{W_\tau(1 + \exp[(E_\tau - E)/W_\tau])^2} \tag{15}$$

The function $\rho_\tau(E)$ is a symmetric bell-shaped curve centered at E_τ, and $\rho_\tau(E)$ is narrower when the effective potential barrier is wider. For an ideal dynamical bottleneck κ_τ is unity; deviations from unity indicate that recrossing or other multidimensional effects are important.

The density of reactive states $\rho(E)$ defined by Eq. (6) is the quantum mechanical analogue of the transition state theory $\rho^\ddagger(E)$ of Eq. (14). Transition state theory with quantum effects on the reaction coordinate motion and recrossing predicts that the CRP will increase in smooth steps of height κ_τ at each energy level of the transition state and that $\rho(E)$ will be a sum of bell-shaped curves, each centered at an energy E. We have found clear evidence for this prediction in the densities of reactive states $\rho(E)$ that we have calculated by accurate quantum dynamics.

Because the total angular momentum and its component are conserved during a collision, we can study the reaction dynamics for each value of J and M_J independently. Since the results are independent of M_J, we always set $M_J = 0$, and we will not mention it again (but the existence of the M_J quantum number is the reason for the factor of $2J + 1$ in the following sentence). In particular, we can study the J-specific contributions to the rate constant, $k^J(E)$ [with $k(E)$ of Eq. (3) being a $(2J + 1)$-weighted sum of individual $k^J(E)$], to the cumulative reaction probability, $N^J(E)$, and to the density of reactive states, $\rho^J(E)$. The influence of quantized transition states on chemical reactivity will be analyzed through studies of $k^J(E)$.

We can often understand the dynamics in greater detail by studying J-specific state-selected reaction probabilities $P_n^J(E)$, which are related to J-specific state-to-state reaction probabilities via

$$P_n^J(E) = \sum_{n'} P_{nn'}^J(E) \tag{16}$$

We also find it useful to define the corresponding densities of state-selected reaction probability $\rho_n^J(E)$:

$$\rho_n^J(E) = \frac{dP_n^J(E)}{dE} \tag{17}$$

A similar analysis can be made in terms of product states n' rather than initial states n:

$$P_{\rightarrow n'}^J(E) = \sum_{n} P_{nn'}^J(E) \tag{18}$$

$$\rho_{\rightarrow n'}^J(E) = \frac{dP_{\rightarrow n'}^J(E)}{dE} \tag{19}$$

The quantities $\rho_n^J(E)$ and $\rho_{\rightarrow n'}^J(E)$ are often helpful in discerning aspects of the reaction dynamics that are not apparent from $\rho^J(E)$.

We will also find it useful to present densities that result from taking the energy derivative of sums of other subsets of the state-to-state reaction probabilities. Parity-specific densities can be obtained from the derivative of the sum of $P_{nn'}$ having the same parity $P = (-1)^{j+l}$. (When $J = 0$, $j = l$, and so $P = +1$.) Furthermore, for atom-diatom reactions of the form $A + H_2 \rightarrow AH + H$, we can define a spatial permutation symmetry S, which equals $+1$ for *para* hydrogen and -1 for *ortho* hydrogen. Symmetry-specific densities are obtained by summing those $P_{nn'}$ with the same spatial permutation symmetry. Densities for a specific set (J, P, S) are denoted ρ^{JPS}; when these are summed over P and S, the above densities ρ^J are obtained.

For $H + H_2$ and $O + H_2$, the densities and CRPs to be presented result from treating the two hydrogen atoms in the initial molecule as distinguishable and presenting results for one of the two symmetry-related paths, for example, $A + H'H'' \rightarrow AH' + H''$. That is, we do not include the factor of 2 for the two products $AH' + H''$ and $AH'' + H'$. We do, however, sum over S, but ignoring nuclear spin. For $D + H_2$ and $F + H_2$, we present results for only a single symmetry S but count both product arrangements. In either of these cases, the CRP increases by about 1 at the nearly ideal transition states.

In order to separate contributions to the density of reactive states from events occurring on different time scales it is useful to introduce low-resolution convolutions of

the accurate density of reactive states. In particular we define

$$N^J(E; F) = \int_{E_i}^{E_f} dE'\ N^J(E')f(E, E'; F) \tag{20}$$

where the resolution function f is

$$f(E, E'; F) = A \exp\left\{-\left[\frac{2(E - E')}{F}\right]^2 \ln 2\right\} \tag{21}$$

and where the normalization factor A is determined by

$$A = \left(\int_{E_i}^{E_f} dE' \exp\{-[2(E - E')/F]^2 \ln 2\}\right)^{-1} \tag{22}$$

F is the full width at half maximum, and E_i and E_f are the lowest and highest energies in the convolution. The finite-resolution density of reactive states $\rho^J(E; F)$ is then defined by

$$\rho^J(E; F) = \frac{d}{dE} N^J(E; F) \tag{23}$$

Averaging over an energy width can be thought of as selecting a particular time regime for analysis. Observing the cumulative reaction probability, or any function of energy, with a finite resolution F corresponds to observing a time scale of $\Delta t = \hbar/F$ (37). In many cases, we expect total rate constants to be dominated by short-time dynamics in the vicinity of the transition state (38–42). Thus we might expect that looking at the cumulative reaction probability with a resolution broad enough to smooth over features due to longer-time dynamical effects (such as trapped-state resonances and entrance channel and exit channel couplings) will reveal broader structure due to quantized transition states.

Separating time scales in terms of energy is familiar in spectroscopy. This idea has been well expressed, for example, by Heller (43): "a spectrum taken at ultrahigh resolution (and containing long-time information) contains within it all lower-resolution information (i.e., shorter-time information). We can *choose* to examine it at lower resolution and extract the dynamics corresponding to shorter and shorter times."

III. COMPUTATIONAL METHODS

Accurate quantum mechanical cumulative reaction probabilities and densities of reactive states were obtained by carrying out converged quantum dynamics calculations for realistic potential energy surfaces. The wave function was expanded in a multiarrangement basis set (44–49), and the coefficients were found by linear algebraic methods employing a variational principle. In particular either the generalized Newton variational principle (GNVP) (50–54) or the outgoing wave variational princple (OWVP) (55–58) was used to obtain scattering matrix elements that are stationary with respect to small variations in the wave function. Full details of the basis sets and numerical methods used in these calculations are presented in previous publications from our group (53,54,58–63). One point that deserves to be emphasized though is that the method is made efficient by partitioning the Hamiltonian into distortion blocks and coupling potentials.

The reaction probabilities are well converged with respect to basis set and numerical parameters. This is extremely important since differentiation with respect to energy must yield smooth densities, and hence we give additional details of the convergence for the two new sets of calculations presented in this chapter, namely those for D + H_2 and those for F + H_2.

For the D + H_2 reaction, all calculations were carried out with the OWVP using techniques and parameters described previously (64). In particular, for the results presented here, we used parameter set *A* for $J = 12$ and 15 and parameter set *B* for $J = 0$–9. In both these parameter sets the basis functions are half-integrated Green's functions for open channels and $\mathcal{L}^2$ functions for closed channels. Specifically for the present chapter we repeated the calculations for $JPS = 3++$ with a parameter set in which all basis sets and numerical parameters were better converged as compared to set *B*. At 21 energies from 1.20–1.60 eV, the average unsigned percentage difference in the cumulative reaction probabilities from those computed with set *B* was <0.06%, and the maximum percentage difference was 0.18%. Furthermore the densities of reactive states, computed as derivatives of cubic spline fits, were almost indistinguishable when superimposed.

We also used the OWVP for the F + H_2 reaction. Two parameter sets that were used in the calculations are given in Table 1.

IV. H + H_2

In this section we discuss the quantized transition state spectra of H + H_2 with emphasis on the assignment of quantum numbers and transmission coefficients. The discussion is focused on the total CRP. Another very important aspect of the H_3 quantized transition states is their role in determining state-selected and state-to-state transition probabilities; we refer the reader to previous discussions (9,16) for that subject.

A. $J = 0$

The *J*-selected cumulative reaction probability $N^0(E)$ for the H + H_2 reaction computed (8,9) using the double many-body expansion (DMBE) potential energy surface (65) is shown versus energy as the solid line in Fig. 1a. (We will consistently use energy units of eV; 1 eV/molecule = 96.48 kJ/mol.) The CRP as a function of energy is characterized by steplike structures as predicted by transition state theory. The energy derivative of $N^0(E)$, obtained by analytically differentiating the cubic spline fit of Fig. 1a, is the density of reactive states $\rho^0(E)$, shown as the solid line in Fig. 1b. The derivative converts the steps in N^0 to peaks in ρ^0, akin to the bell-shaped curves ρ_τ of Eq. (15). The CRP reaches a value of 8.9 at 1.6 eV. Therefore, transition state theory would predict that there are nine energy levels of a quantized transition state at energies below 1.6 eV if all transmission coefficients are unity or more than nine if not all of the transition states are perfect dynamical bottlenecks. Figure 1b clearly shows seven peaks and one shoulder, and these are identified with eight transition state energy levels. The detailed analysis here suggests that there are a total of 10 quantized transition states contributing to Fig. 1b.

The density of reactive states $\rho^0(E)$ was fit by a sum of terms $\kappa_\tau\rho_\tau(E)$, as given in Eqs. (14) and (15), appropriate to scattering by parabolic potential energy barriers. (Note that the use of the parabolic barrier is the simplest barrier shape for understanding $\rho^0(E)$

Table 1 Parameter Sets for F + H_2 CRP Calculations for the 6SEC Surface

		Set A		Set B	
	Explanation	F + H_2	HF + H	F + H_2	HF + H
$j_{max}(v = 0)$	a	13	24	13	24
$j_{max}(v = 1)$	a	13	24	13	24
$j_{max}(v = 2)$	a	11	22	11	22
$j_{max}(v = 3)$	a	11	19	11	19
$j_{max}(v = 4)$	a	9	17	9	15
$j_{max}(v = 5)$	a	9	17	—	10
$j_{\alpha}^{d}(v = 0)$	b	6	13	6	13
$j_{\alpha}^{d}(v = 1-3)$	b	1	13	—	13
$j_{\alpha}^{d}(v = 4-5)$	b	1	1	—	—
$R_{\alpha 1}^{G}(a_0)(v = 0)$	c	2.85	2.4	3.85	2.94
$R_{\alpha 1}^{G}(a_0)(v = 1-3)$	c	2.85	2.4	4.2	2.94
$R_{\alpha 1}^{G}(a_0)(v \geq 4)$	c	2.85	2.4	4.2	3.3
$\Delta(a_0)(v = 0)$	d	0.25	0.18	0.25	0.27
$\Delta(a_0)(v \geq 1)$	d	0.25	0.18	0.30	0.27
$c(v = 0)$	e	1.25	0.63	1.0	0.864
$c(v \geq 1)$	e	1.25	0.63	1.2	0.864
$m^{s}(v = 0)$	f	16	18	10	8
$m^{s}(v = 1)$	f	16	18	—	8
$m^{s}(v = 2-3)$	f	16	18	—	10
$m^{s}(v \geq 4)$	f	16	18	—	—
$m^{c}(v = 0)$	g	—	—	—	—
$m^{c}(v = 1)$	g	—	—	7	—
$m^{c}(v = 2-3)$	g	—	—	7	—
$m^{c}(v \geq 4)$	g	—	—	7	8
$N_{\alpha}(HO)$	h	90	90	60	60
$N_{\alpha\alpha}^{QA}$	i	80	80	40	40
N_{12}^{QA}, N_{23}^{QA}	i	200	200	80	0
N_{α}^{QV}	j	50	50	25	25
N_{α}^{QSV}	j	25	25	25	25
N_{α}^{QGLV}	j	2	2	1	1
$r_{\alpha,min}^{QV}$	j	0.5	0.5	0.5	0.5
$r_{\alpha,max}^{QV}$	j	3.2	3.2	3.2	3.2
$N_{\alpha}(F)$	k	399	398	203	365
N_{α}^{ED}	l	13	13	13	13
$N_{\alpha,N_{\alpha}(F)}^{ED}$	l	8	8	8	8
$R_{\alpha 0}^{E}(a_0)$	m	2.3	1.5	2.3	1.5
$R_{\alpha,N_{\alpha}(F)+1}^{E}(a_0)$	m	18.0	18.0	18.0	22.0
$R_{\alpha,min}^{QR}$	n	2.3	1.5	2.8	1.75
$R_{\alpha,max}^{QR}$	n	18.0	18.0	10.0	10.0
N_{α}^{SD}	o	35	35	35	35
f_{α}^{SD}	p	0.9	0.9	0.9	0.9
n_{α}^{ER}	q	0	0	0	0
GSS_{α}	r	0	0	0	0
N_{α}^{QS}	s	52	33	24	30
N_{α}^{QGL}	s	7	11	7	11
ϵ_{χ}	t	10^{-7}		10^{-6}	

Table 1 Continued

		Set A		Set B	
	Explanation	F + H_2	HF + H	F + H_2	HF + H
ϵ_{rad}	u	10^{-5}		10^{-100}	
ϵ_t	v	10^{-8}		10^{-8}	
ϵ_W	w	10^{-7}		10^{-7}	
ϵ_B	x	10^{-5}		10^{-5}	

[a] $j_{max}(v)$ is the maximum value of the rotational quantum number in vibrational level v included in the vibrational-rotational-orbital basis. In these calculations we did not eliminate higher values of the body-frame angular momentum projection Ω.

[b] $j_\alpha^d(v)$ is the number of rotational states that are fully coupled in the distorted waves. Channels with $j \geq j_\alpha^d(v)$ are treated as uncoupled in the distorted waves, as explained in Ref. 61.

[c] $R_{\alpha 1}^G$ is the value of R_α at the center of the innermost radial Gaussian function, where R_α is the mass-scaled atom-to-diatom distance defined in Ref. 58, and radial Gaussians are used both directly as outgoing wave basis functions (in the OWVP) and to generate half-integrated Green's functions (in the GNVP and OWVP).

[d] Δ is the spacing in R_α between successive radial Gaussians.

[e] c is the radial Gaussian overlap parameter, which determines the widths of the Gaussian functions, as explained in Ref. 59.

[f] m^g is the number of radial half-integrated Green's functions per channel.

[g] m^e is the number of radial Gaussians per channel used as $\mathcal{L}^2$ basis functions for the outgoing wave.

[h] N_α(HO) is the number of harmonic oscillator functions used to expand the diatomic adiabatic vibrational eigenfunctions, which in turn are used as vibrational basis functions for the scattering calculations.

[i] $N_{\alpha\alpha}^{QA}$ and $N_{\alpha\alpha'}^{QA}$ are the number of points in the Gauss-Legendre quadrature used in the single- and multiarrangement angular quadratures, respectively. (Note that $\alpha = 1$ is F + H_2, $\alpha = 2$ and 3 are HF + H.)

[j] N_α^{QV} is the total number of points in the quadratures of the interaction potential over the vibrational coordinate. In the present calculations the quadratures are carried out by dividing the mass-scaled vibrational coordinate r_α into N_α^{QVS} segments extending from $r_{\alpha,min}^{QV}$ to $r_{\alpha,max}^{QV}$. Each segment is then integrated by a N_α^{QGLV}-point Gauss-Legendre quadrature.

[k] N_α(F) is the total number of points in the finite difference grid used for the calculation of the regular solution of the distortion problems and the half-integrated Green's functions.

[l] N_α^{FD} and $N_{\alpha,N_\alpha(F)}^{FD}$ are the number of points used in the representation of the second derivative operator in the main body of the finite difference grid and at the last grid point respectively.

[m] $R_{\alpha 0}^F$ and $R_{\alpha,N_\alpha(F)+1}^F$ are, respectively, the location of the lower and upper finite difference boundary condition points.

[n] $R_{\alpha,min}^{QR}$ and $R_{\alpha,max}^{QR}$ are the lower and upper bounds of the region of R_α over which quadratures of the variational functional are carried out.

[o] N_α^{SD} is the number of points appended to the main part of the finite difference grid with geometrically decreasing spacing.

[p] f_α^{SD} is the step-size decrease factor for the spacing of the final finite difference grid points.

[q] n_α^{FR} is the number of extra points inserted between neighboring points in the third step of the finite difference grid generation scheme explained in Ref. 61.

[r] GSS_α is the grid spacing scheme for the radial quadrature grids, as explained in Ref. 61.

[s] N_α^{QS} is the number of repetitions of N_α^{QGL}-point Gaussian quadrature used in the generation of the finite difference grid and the integrations over R_α.

[t] ϵ_χ is the vibrational screening parameter. (Screening parameters are explained in Ref. 57.)

[u] ϵ_{rad} is the radial screening parameter.

[v] ϵ_t is the translational basis screening parameter.

[w] ϵ_W is a screening parameter involving the matrix **W**.

[x] ϵ_B is a screening parameter involving the matrix **B**.

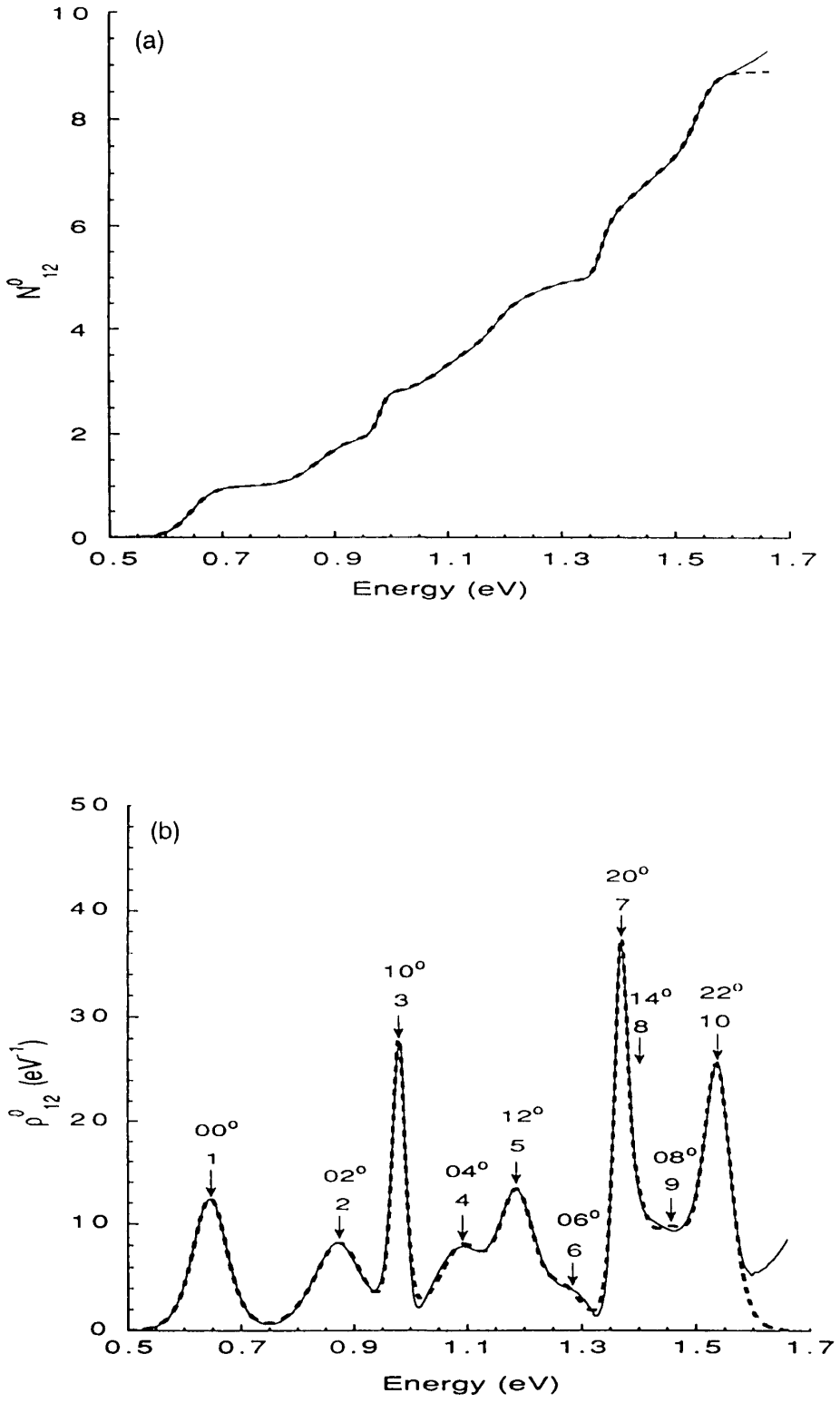

Figure 1 H + H_2, J = 0. (a) Cumulative reaction probability. The solid curve is a spline fit to the accurate quantal results, and the dashed curve was obtained by integrating the synthetic density in b. (b) Density of reactive states. The solid curve is obtained by analytically differentiating a cubic spline fit to the accurate quantum mechanical CRPs. The heavy dashed curve is the fit of Eqs. (14) and (15). The arrows are positioned at the fitted values of E_τ, and the feature numbers and assignments above the arrows correspond to Table 2. (Reprinted with permission from Ref. 8, copyright 1991, American Chemical Society.)

and does not imply that the true barriers are parabolic, just as using the harmonic oscillator model to interpret ordinary spectra does not imply that the potentials are precisely quadratic.) Each term $\kappa_\tau\rho_\tau(E)$ in the sum represents the contribution of the individual energy level of the transition state. The quantities κ_τ, E_τ, and W_τ are fitting parameters.

All of the features in the quantal $\rho^0(E)$ are fit very accurately by including 10 terms in the sum. The parameters from the fit are included in Table 2. The sum of the terms $\kappa_\tau\rho_\tau$ in the fit is shown in Fig. 1b as the dashed curve, which is nearly indistinguishable from the quantal result. By integrating the fit to the quantal density of reactive states, we obtain a synthetic curve for the CRP. This is shown in Fig. 1a as a dashed curve, which to plotting accuracy is indistinguishable from the quantal result.

The excellent agreement between the quantal and synthetic densities of reactive states in Fig. 1b demonstrates that quantized transition states globally control the chemical reactivity. All of the reactive flux, up to an energy of 1.6 eV, can be attributed to contributions from the energy levels of the transition state; i.e., there is no noticeable background. Thus, this study (and ones to follow) provides a strong validation for approximate transition state theories that postulate the existence of transition states controlling the reaction dynamics.

The value of the transmission coefficient κ_τ is shown for each feature in Table 2. (The value of κ_τ for the last feature is greater than 1 because it includes contributions from higher energy transition states that have not been included in the fit.) Many of the values of the transmission coefficients are very close to unity, suggesting that these features correspond to quantized transition states that are nearly ideal dynamical bottlenecks to the reactive flux. Several of the values of κ_τ deviate from unity; this could be the result of the assumption of parabolic effective potential barriers or from recrossing or other multidimensional effects.

Each of the 10 energy levels of the H_3 quantized transition state can be associated with a set of linear-triatomic quantum numbers (66) $[\nu_1\nu_2^K]$ where ν_1 and ν_2 are the stretch and bend quantum numbers respectively for modes orthogonal to the reaction coordinate

Table 2 Quantized Transition States for H + H_2, $J = 0$

Feature	E_τ (eV)	κ_τ	W_τ (10^{-2} eV)	Assignment	Adiabatic energy (eV)	$E(\nu_1\nu_2)$ (eV)	Δt (TSRT)[a] (fs)	Δt accurate[b] (fs)
1	0.645	1.00	2.01	$[00^0]$	0.663	0.645	10	11
2	0.872	0.97	2.95	$[02^0]$	0.909	0.872	7	10
4	1.094	0.98	3.30	$[04^0]$	1.173	1.094	6	5
6	1.286	0.18	1.48	$[06^0]$	1.452	1.309	14	
9	1.494	1.01	3.02	$[08^0]$	1.754	1.517	7	
3	0.978	0.79	0.75	$[10^0]$	0.979	0.978	28	28
5	1.192	1.02	2.17	$[12^0]$	1.173	1.192	10	8
8	1.405	0.80	2.14	$[14^0]$	1.430	1.399	10	
7	1.368	1.01	0.78	$[20^0]$	1.384	1.368	27	30
10	1.538	1.15	1.40	$[22^0]$	1.513	1.567	15	12

[a]Transition state resonance theory (TSRT) results from Eq. (29) and the W_τ values given here.
[b]From Ref. 96.

and K is the vibrational angular momentum (also the magnitude of the projection of J on the molecular axis). (Here the vibrational angular momentum is denoted K rather than ℓ, which is conventional in spectroscopy (66), but which we reserve for orbital angular momentum. For $J = 0$, K must be 0 as well.) This type of assignment corresponds to the conventional picture where the one degree of freedom corresponding to unbound motion along the reaction coordinate is "missing." (By comparison, a stable triatomic molecule like CO_2 has a "full" set of quantum numbers $(\nu_1 \nu_2^K \nu_3)$ (66), with ν_3 the asymmetric stretch quantum number. The quantum number "missing" in the transition state description will reappear when we treat the transition state as a quantum mechanical resonance.)

The lowest energy feature in $\rho^0(E)$ at 0.645 eV is easily assigned as $[00^0]$ since it is the overall reaction threshold and thus corresponds to the lowest energy level of the transition state. We are able to assign quantum numbers ν_1 and ν_2 to the other nine energy levels that affect the spectrum in this figure by using a variety of methods (8,9), but primarily by comparing the fitted values of E_τ with the barrier maxima of semiclassical vibrationally adiabatic potential energy curves. The vibrationally adiabatic curves are defined by (35,67–71)

$$V_a(\nu_1, \nu_2, K, J, s) = V_{MEP}(s) + \varepsilon_{int}(\nu_1, \nu_2, K, J, s) \tag{24}$$

where s is the distance along the reaction path ($s = 0$ at the saddle point), $V_{MEP}(s)$ is the Born-Oppenheimer potential energy along the reaction path, and $\varepsilon_{int}(\nu_1, \nu_2, K, J, s)$ is the vibrational-rotational energy of the stretch, bend, and rotational motions excluding motion along the reaction coordinate. The stretching motion (with quantum number ν_1) of the H_3 transition state correlates adiabatically with the vibrational motion (with quantum number ν) in the reactant H_2 molecule (72). The bend is doubly degenerate and—along with overall rotation—correlates to the orbital-rotational motions of the reactants (73). The vibrationally adiabatic curves (labeled by ν_1, ν_2, and K) were calculated in internal coordinates using the WKB method to treat the stretch anharmonicity (74) and a variation-perturbation treatment (75) of a quadratic-quartic potential (76) to treat bend anharmonicity. Coriolis interactions were neglected so the curves are independent of K. The energies of the maxima of these curves are in good agreement with the E_τ values obtained by fitting the density of reactive states (8,16). This comparison allows us to make the assignments shown in column 5 of Table 2. Energies of the maxima in $V_a(\nu_1, \nu_2, K, J, s)$ are shown as column 6 in that table. (For the more highly bend excited states, the semiclassical energies are less accurate, and other methods (8,9) were used to make more convincing assignments of these quantum numbers.) Notice that for $J = 0$ only even ν_2 states appear, just as in the $J = 0$ spectra of bound linear triatomics (66).

The good agreement between the energy levels of the quantized transition state obtained from the exact quantum dynamics calculations and the maxima of vibrationally adiabatic curves strongly suggests that the reactive flux is "focused" (77) in the interaction region through dynamical bottlenecks that are locally vibrationally adiabatic. The overall chemical reaction is not globally adiabatic (8,9); for example, many state-to-state reaction probabilities with $\nu \neq \nu'$ have significant magnitudes ($> 10^{-3}$). Thus we conclude that adiabaticity is a better approximation at the transition state itself than globally and that the flux passing through a particular level of the transition state may originate from a wide set of reactant states. One way to understand this is to consider that at a barrier maximum, the motion along the reaction coordinate is classically stopped. Thus the simplest criterion for vibrational adiabaticity, that vibrational motions transverse to the

reaction coordinate be fast compared to motion along the reaction coordinate, is locally satisfied.

With all of the v_1 and v_2 assignments made, some interesting trends in the fitted parameters κ_τ and W_τ appear. From Table 2, we see that the significant deviations of κ_τ from unity are generally found for the highly bend excited transition state levels. Therefore, most of the breakdown of transition state theory appears to be associated with only those few levels. In addition, we see in Table 2 that W_τ becomes larger as v_2 is increased from 0 to 2 for a given value of v_1. This is consistent with the discussion below Eq. (13) since the vibrationally adiabatic potentials become narrower as v_2 increases (8,16). This same trend in W_τ is even more apparent in the results discussed below for H + H_2, $J = 1$, where both even and odd values of v_2 are allowed.

We conclude above that the $J = 0$ cumulative reaction probability is globally controlled by quantized transition states, and we have assigned stretch (v_1) and bend (v_2) quantum numbers for the motion orthogonal to the reaction coordinate. As discussed below, similar conclusions can be reached for the $J = 1$ and $J = 4$ cumulative reaction probabilities. We have obtained spectroscopic constants for the H_3 transition state by fitting the E_τ values of [00^0], [02^0], [04^0], [10^0], [12^0], and [20^0] for $J = 0$ and [00^0] for $J = 4$ by (66)

$$\frac{E(v_1, v_2, J)}{hc} = \frac{E_0}{hc} + \omega_1(v_1 + 0.5) + \omega_2(v_2 + 1) + x_{11}(v_1 + 0.5)^2 + x_{22}(v_2 + 1)^2 + x_{12}(v_1 + 0.5)(v_2 + 1) + BJ(J + 1) \tag{25}$$

where E_0 is a constant, and ω_1, ω_2, x_{11}, x_{12}, x_{22}, and B are the usual spectroscopic fitting parameters. The fit, which reproduced the energies within about 0.02 eV, yielded values (in cm^{-1}) of $E_0 = 3061$, $\omega_1 = 2295$, $\omega_2 = 972$, $x_{11} = 227$, $x_{22} = -6$, $x_{12} = -58$, and $B = 10.6$. These parameters compare favorably with the approximate values (78) obtained by a normal modes calculation at the saddle point: $E_0 = 3372$, $\omega_1 = 2067$, $\omega_2 = 899$, and $B = 9.7$.

Energy levels $E(v_1, v_2, J = 0)$ of the transition state predicted by these spectroscopic constants are shown in Table 2 to be in good agreement with the values of E_τ obtained by fitting the density of reactive states. When Eq. (25) is applied to bound states, an implicit assumption is that the quantized states have vibrational motion about the same "equilibrium" geometry. The vibrationally adiabatic curves (8,16) suggest though that the variational transition states are found at different points along the reaction coordinate and therefore different geometries. In light of this and as the values obtained with Eq. (25) are effective values since Eq. (25) is a truncation of an infinite Taylor series, the good agreement obtained with Eq. (25) is quite remarkable.

The correspondence between the energies of the quantized transition states and the maxima of vibrationally adiabatic curves, as well as the success in using a model of transmission through effective potential energy barriers to fit the density of reactive states, both suggest that detailed explorations of the nature of scattering by one-dimensional potential barriers can provide further insight. In classical mechanics, a potential maximum is associated with metastability at the energy of the maximum and with a time delay for higher energies due to the system slowing down as it crosses the top of the barrier. In quantum mechanics, barrier passage is also associated with a time delay (79–81) manifested as an increasing phase in scattering matrix elements (relative to the background phase). In model studies of quantum mchanical transmission through and over potential barriers, it has been shown that the time delays corresponding to barrier passage are

associated with poles of the scattering matrix at complex energy (82–84). Since poles of the scattering matrix represent quantum mechanical resonances (3,5,50,85,86), we have concluded that chemical reaction thresholds associated with barriers, i.e., quantized transition states, are reactive scattering resonances. These so-called barrier resonances tend to be associated with shorter time delays than conventional resonances attributed to a particle trapped in a well between barriers. However, there is no distinction in kind between these two types of poles of the scattering matrix: barrier resonances may be transformed continuously into trapped-state resonances by varying the shape of the one-dimensional potential function (83,84). In fact, in our H + H_2 work (8,9,16) as well as our one-dimensional studies (83,84) we have found that a single resonance may partake of both barrier and trapped-state resonance characters. The identification of transition states as scattering resonances has also been made by applying a complex scaling transformation to the reaction coordinate (87).

The characterization of transition states as resonances is a useful analytical tool and provides new insights into fundamental problems of chemical reactivity. It has already been used, for example, to lead to a new computational approach for the calculation of anharmonic transition state energy levels by a reformulation of variational transition state theory (88).

Semiclassical transition state theory based on second-order perturbation theory (89) provides another way to assign quantized energy levels of the transition state, and an application (90) to the H + H_2 reaction yielded encouraging results in comparison to the full quantum (8) calculations. One difference in assignments (8,90) was later explained (88), using the resonance theory reformulation of variational transition state theory, as a consequence of the inadequacy of second-order perturbation theory.

Treatment of transition states as resonances is complicated by the fact that, in many cases, barrier resonances will not be isolated or narrow and the theory of overlapping resonances (91,92) is more complicated than the theory of isolated, narrow resonances. Analyses of the poles of the scattering matrix show that even with a simple barrier, there is more than one pole (82–84,93,94) associated with barrier passage. On the other hand, our work on H + H_2 and other systems to be described shows that in many cases the transition states are resolvable and the observable structure in the dynamical $N^J(E)$ and $\rho^J(E)$ may be correlated with one or a small number of poles. This paradoxical situation is resolved by noting that, when resonances are broad and overlapping, it is the pole nearest to the real energy axis that is useful for understanding the features of the dynamical observables. In particular, for a series of poles associated with a simple (e.g., parabolic or approximately parabolic) barrier, one can assign a new quantum number v to each member of the sequence, with $v = 0$ assigned to the pole closest to the real energy axis, $v = 1$ to the next closest pole and so on. This quantum number v is associated with the "missing" degree of freedom of the quantized transition state. The $v = 0$ transition state is used for understanding the dynamics in real time, as discussed next.

Poles in the scattering matrix occur at complex resonance energies (50,85,86)

$$\bar{E} = E_{res} - \left(\frac{i}{2}\right)\Gamma \tag{26}$$

where E_{res} is the real part of the resonance energy and Γ is the real, positive resonance width, which is related to the collision lifetime Δt by (95)

$$\Delta t = \frac{2\hbar}{\Gamma} \tag{27}$$

The complex resonance energies of the poles for the parabolic barrier of Eq. (10) are (82,93)

$$E_\nu = E_\tau - i\hbar|\omega_\tau|\left(\nu + \frac{1}{2}\right) \tag{28}$$

where ν is the analogue of the "missing" quantum number ν_3. If we assume that the pole with $\nu = 0$ dominates the behavior of the quantal reaction probability (for scattering by a parabolic barrier), then using Eqs. (12) and (26)–(28) yields

$$\Delta t = \frac{\hbar}{\pi W_\tau} \tag{29}$$

Values of Δt computed from the W_τ parameters of Table 2 are also included in Table 2, labeled TSRT (transition state resonance theory). They compare favorably with Δt values obtained (96) from accurate quantum dynamical scattering matrix elements without using transition state theory or resonance theory; these latter values are given in the last column of Table 2. It is important to note that whereas the W_τ values are obtained from fits to reaction probabilities (which contain no information about the phases of the scattering matrix elements), the direct calculation (96,97) of Δt depends explicitly on phases. Thus there is no a priori reason why the Δt values must compare favorably. The fact that they do provides further evidence of the utility of treating transition states with resonance theory.

Cuccaro et al. (96) interpreted the time delays in Table 2 as resonances and assigned a value of 0 for the third quantum number ν without explanation. We identify these resonances as quantized transition states. The analysis presented above of scattering by one-dimensional barriers, with the conclusion that the $\nu = 0$ pole is the most important because it is closest to the real energy axis, supplies a justification for the assignment of the third quantum number.

The steplike CRP originally obtained (8) from quantum mechanical scattering calculations has also been reproduced by a trace formula that avoids explicit specification of asymptotic states (98,99) and by a method based on eigenvalues of a reaction probability operator (100).

B. $J = 1$

A similar analysis of the CRP and the density of reactive states for H + H_2 with total angular momentum J equal to 1 also shows quantized transition state control of the chemical reactivity (8,16). However, the spectra are more complicated because the number of features in $N^J(E)$ and $\rho^J(E)$ increases with J. This is because both even and odd values of ν_2 are allowed for nonzero J, and states with identical ν_1 and ν_2 but different K are allowed for $J > 1$. Note that $K \leq J$ and $K = \nu_2, \nu_2 - 2, \nu_2 - 4, \ldots, 0$ or 1. The degeneracy of a state $[\nu_1\nu_2^K]$ is 2 if K is nonzero and 1 if K is zero.

A fit of the density by a sum of terms $\kappa_\tau\rho_\tau(E)$, analogous to the fit for $J = 0$, identifies 20 features up to 1.7 eV, and 15 of these are labeled in Fig. 2. Assigning transition state quantum numbers to the fitted features was simplified by analyzing each parity block separately, as described next.

For transition states, the total parity is the product of the parities of the vibrational and rotational wave functions, and it depends on both J and K. The parity of the rotational wave function is $(-1)^J$. For $K = 0$, the vibrational wave function has even parity $(+1)$.

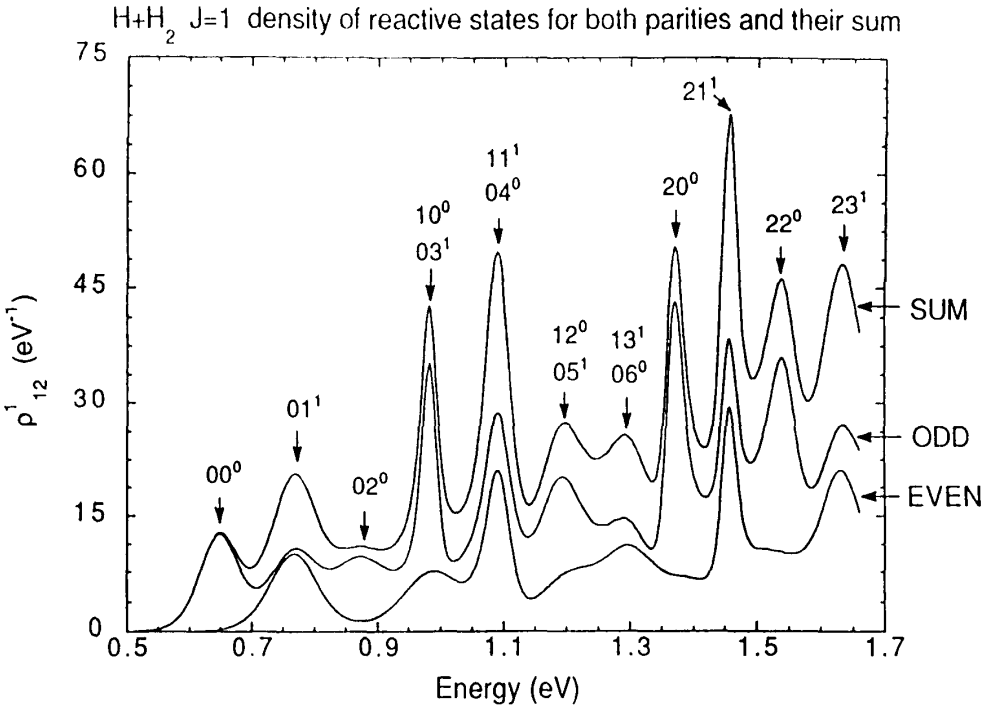

Figure 2 H + H_2, J = 1. Density of reactive states for both parities (ρ^1 labeled odd and ρ^{1-} labeled even) and their sum.

For $K > 0$, the bending mode is doubly degenerate and has one even-parity and one odd-parity component (66,96). For $JP = 1+$, then, ν_2 must be odd. Consequently, only states with $K = 1$, and hence odd ν_2, will appear in the density spectrum. For $JP = 1-$, the vibrational wave function is even, so both $K = 0$ and $K = 1$ states, and consequently both odd and even values of ν_2, are allowed. Figure 2 shows clearly that $K = 0$ states occur only in the odd parity block. The spectrum for $JP = 1+$ is similar to the spectrum for $J = 0$ in Fig. 1b, except that the $[\nu_1\nu_2^0]$ features in the $J = 0$ spectrum corresponds to $[\nu_1(\nu_2 + 1)^1]$ features in the $JP = 1+$ spectrum. All values of ν_2 are allowed for $JP = 1-$, so the spectrum for odd parity has twice as many features as that for even parity. The spectra for $JP = 1+$ and $JP = 1-$ sum to give the spectrum for $J = 1$.

Assignments and values of E_τ, κ_τ, and W_τ from a fit by a sum of terms $\kappa_\tau\rho_\tau(E)$ are given in Table 3. The parameters E_τ, W_τ, and κ_τ for $J = 1$ exhibit the same trends as those for $J = 0$. Most of the κ_τ are close to 1, indicating that the quantized transition states are good dynamical bottlenecks. Again, most of the exceptions are highly bend excited states. The quantal and fitted densities are identical to plotting accuracy (9), indicating that quantized transition states can account for all of the chemical reactivity. Table 3 also shows that fitted energies match the predictions of Eq. (25) well with the parameters given earlier, differing by only 0.018 eV on average (the larger differences are for highly bend excited states).

It was mentioned in Sec. IV.A. that the widths of features in the density of reactive states generally increase with ν_2. The density for $JP = 1-$ (Fig. 2) provides a striking demonstration of this. The first three peaks in Fig. 2 are due to states $[00^0]$, $[01^1]$, and $[02^0]$; the next four peaks are primarily due to states $[10^0]$, $[11^1]$, $[12^0]$, and $[13^1]$; and the last four peaks are primarily due to states $[20^0]$, $[21^1]$, $[22^0]$, and $[23^1]$. Inspection

Table 3 Quantized Transition States for H + H_2, $J = 1$

Assignment	$E(v_1, v_2)$ (eV)	E_τ (eV)	κ_τ $JP = 1+$	κ_τ $JP = 1-$	W_τ (10^{-2} eV)
$[00^0]$	0.647	0.647		1.00	2.04
$[01^1]$	0.762	0.767	1.00	0.97	2.53
$[02^0]$	0.875	0.875		1.01	3.06
$[03^1]$	0.986	0.990	1.01	0.96	3.29
$[04^0]$	1.096	1.088		1.00	2.16
$[05^1]$	1.205	1.205	0.81	1.00	3.07
$[06^0]$	1.311	1.290		0.79	2.30
$[07^1]$	1.416	1.388	0.55	0.09	2.74
$[08^0]$	1.520	1.498		1.21	2.89
$[09^1]$	1.622	1.560	0.27	0.27	2.15
$[0\ 10^0]$	1.722	a		a	a
$[10^0]$	0.981	0.981		0.84	0.79
$[11^1]$	1.088	1.089	0.98	0.73	1.28
$[12^0]$	1.194	1.187		1.00	2.19
$[13^1]$	1.299	1.298	1.00	0.39	2.71
$[14^0]$	1.401	1.401		1.21	2.18
$[15^1]$	1.502	1.502	1.00	0.81	2.75
$[16^0]$	1.602	a		a	a
$[17^1]$	1.700	a	a	a	a
$[20^0]$	1.371	1.370		1.03	0.80
$[21^1]$	1.471	1.456	0.74	0.77	0.82
$[22^0]$	1.570	1.540		1.01	1.28
$[23^1]$	1.667	1.633,[b] 1.639[c]	1.91[b]	2.88[c]	2.34,[b] 2.73[c]

[a]This state's contribution is believed to be included in the unresolved feature nominally assigned as $[23^1]$.
[b]Values from the $JP = 1+$ fit.
[c]Values from the $JP = 1-$ fit.

of the odd-parity curve in Fig. 2 shows that the first peak of each of these three sets of peaks is the tallest and narrowest; the others become shorter and broader as energy increases. This trend is confirmed by the fit values of W_τ (9), and it is consistent with adiabatic transition state theory. As v_2 increases for a given v_1, peaks in vibrationally adiabatic curves become higher and narrower, causing tunneling to become significant over a wider range of energies. The related effect in the fully quantum world is that abrupt steps in $N^1(E)$ become smoothed out, and peaks in $\rho^1(E)$ become broader. The broader peaks are generally associated with shorter lifetimes, as demonstrated for $J = 0$. We also note that broader features in $\rho^1(E)$ generally have smaller peak heights because the integrated area under each is approximately the same, being one for an ideal transition state ($\kappa_\tau = 1$).

C. $J = 4$

The accurate cumulative reaction probability and density of reactive states (summed over parities) for $J = 4$ are shown in Fig. 3. The nine prominent features correspond to transition states with $v_2 = 0$, 1, or 2 for $v_1 = 0$, 1, and 2, just as in the $J = 1$ spectrum (9). States with $v_2 > 2$ also occur, but they are harder to identify because they are broad and

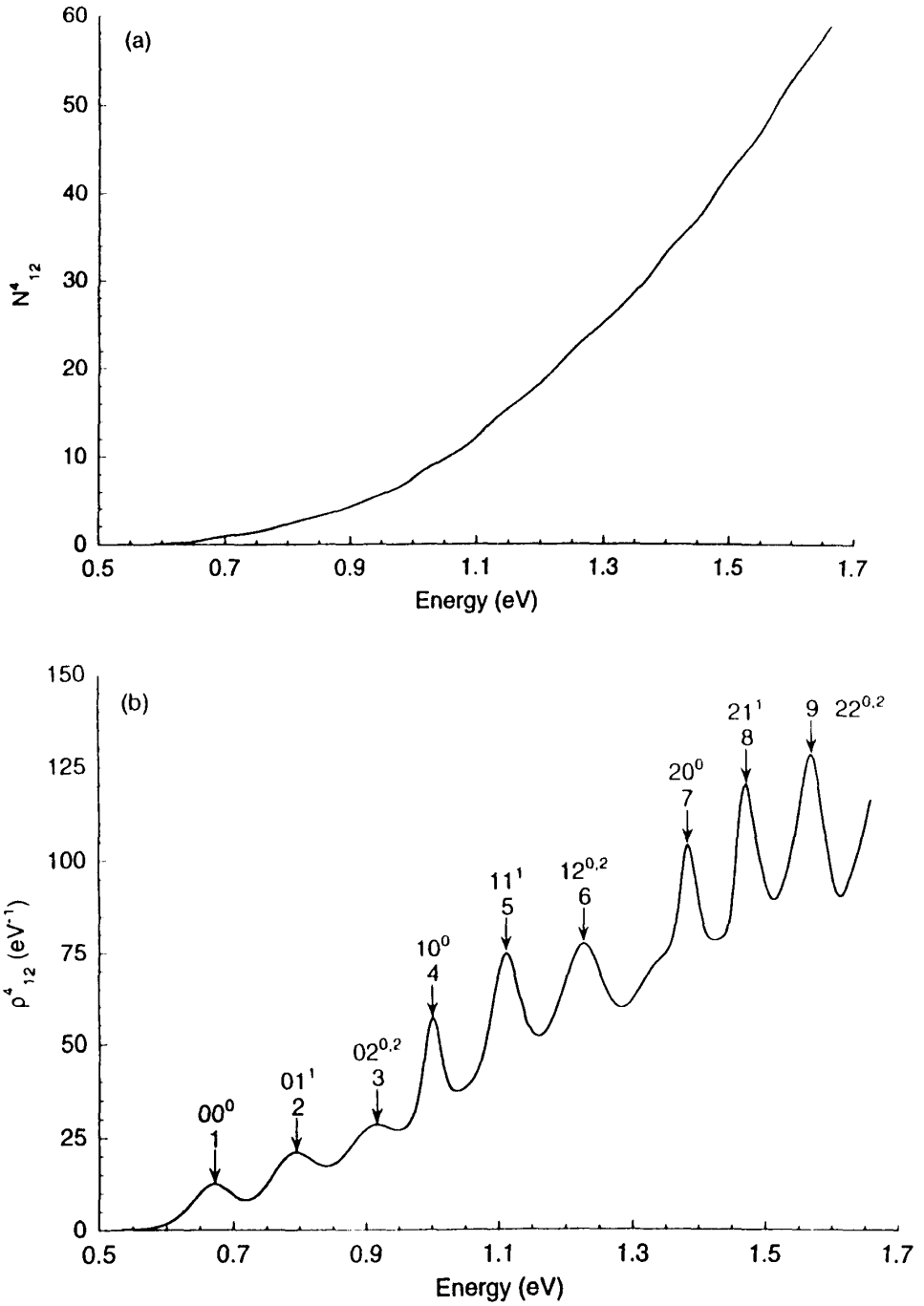

Figure 3 H + H_2, J = 4. (a) Cumulative reaction probability. (b) Density of reactive states. In part b, the peaks are labeled by feature numbers and by the assigned quantum numbers of one of the levels contributing to the peak. See Table 4 for the complete set of assignments.

overlapping. Ignoring K-splitting, transition states with nonzero values of ν_2 (less than or equal to J) have a degeneracy of ν_2 + 1 (66). [The K-splitting is much smaller than the spacing of (ν_1, ν_2) levels.] The density's apparently rising baseline is due to the number of these broad, overlapping features increasing with energy; on top of this background, the prominent features due to low ν_2 can be distinguished. Table 4 shows our assignments of the first nine peaks for J = 4, which were made primarily on the basis

Table 4 Quantized Transition State Spectrum for H + H_2, $J = 4$

Feature	Energy (eV)	States	Sum of degeneracies of these states	Running sum	N^4
1	0.671	$[00^0]$	1	1	1
2	0.794	$[01^1]$	2	3	3
3	0.917	$[02^{0,2}]$	3	6	5½
4	1.002	$[10^0]$, $[03^{1,3}]$	5	11	9½
5	1.113	$[11^1]$, $[04^{0,2,4}]$	7	18	16
6	1.228	$[12^{0,2}]$, $[05^{1,3}]$	7	25	24
7	1.383	$[20^0]$, $[13^{1,3}]$, $[06^{0,2,4}]$	10	35	32
8	1.473	$[21^1]$, $[14^{0,2,4}]$, $[07^{1,3}]$	11	46	40
9	1.570	$[22^{0,2}]$, $[15^{1,3}]$, $[08^{0,2,4}]$	12	58	49½

of the spectroscopic constants and by comparison with the fitted quantal transition state energies E_τ for $J = 0$ and 1. This table illustrates that the running degeneracy sum reaches 25 after the first six features, as compared to 6 for $J = 0$.

The energies of the nine features in Table 4 all correspond closely to the energies of maxima in the vibrationally adiabatic potential curves (8). Table 5 illustrates the agreement between the energies predicted by the spectroscopic constants and maxima, E_{max}, in the quantal density of reactive states.

Fitting the quantal density by a sum of terms $\kappa_\tau \rho_\tau(E)$ is difficult because of the large number of transition states for $J = 4$. However, quantized transition state control of chemical reactivity can be assessed for $J = 4$ without identifying all of the individual contributions to the total density by comparing the accurate values of $N^4(E)$ with those in the next to last column of Table 4. If the transition states were ideal ($\kappa_\tau = 1$), the two numbers would be equal. Up to 1.228 eV, the energy of the sixth peak, the numbers are very close; at 1.228 eV the accurate value of $N^4(E)$ is 24. Thus, the quantized transition states up to 1.228 eV are nearly ideal dynamical bottlenecks. Above 1.228 eV the quantal $N^4(E)$ is somewhat smaller than the predicted value, but even at 1.570 eV the difference is only 15%. This difference may be due to the inaccuracy of Eq. (25) at high ν_2 or to

Table 5 Assignments of Quantized Transition States for H + H_2, $J = 4$

Feature	$E(\nu_1\nu_2)$ (eV)	Assignment	E_{max} (eV)
1	0.671	$[00^0]$	0.671
2	0.783	$[01^1]$	0.794
3	0.899	$[02^{0,2}]$	0.917
4	1.005	$[10^0]$	1.002
5	1.111	$[11^1]$	1.113
6	1.213	$[12^{0,2}]$	1.228
7	1.394	$[20^0]$	1.383
8	1.494	$[21^1]$	1.473
9	1.593	$[22^{0,2}]$	1.570

deviations of κ_τ from unity at high values of the total energy or of v_2. In any case, these results show that transition state control of chemical reactivity is maintained up to high energy and that the individual transition states are relatively good bottlenecks for $J = 4$. This strongly suggests that the detailed trends identified for $J = 0$ and $J = 1$ are general and that thermal rate constants, which depend on a weighted sum of J-specific terms (see Sec. II), are determined by the energy levels of the quantized dynamical bottleneck up to high temperature (>1000 K) (101).

V. $O + H_2$

The $O(^3P) + H_2$ reaction was studied (12–14,102,103) with the Johnson-Winter-Schatz (JWS) London-Eyring-Polanyi-Sato-type (LEPS type) potential energy surface (104,105). This surface was originally parameterized to give reasonably accurate thermal rate constants (104), and its qualitative features are similar to later, more accurate surfaces (12,102–110). We use the JWS potential rather than the more accurate surfaces because the JWS potential has better global analytic behavior in all chemical rearrangements, which is necessary for the reactive scattering calculations reported here. The JWS surface has a collinear saddle point, and the $V_{MEP}(s)$ curve, although asymmetric by a few kcal/mol, has roughly the same shape as that for $H + H_2$ and $D + H_2$.

A. Variational and Supernumerary Transition States

The $O(^3P) + H_2 \rightarrow OH + H$ reaction provides a further test of the generality of analyzing chemical reactivity in terms of quantized transition states. The reaction of O with H_2, like that of H with H_2, is generally free of narrow trapped-state resonances and other long-lifetime dynamical effects. However, the $O + H_2$ reaction is more complicated than the $H + H_2$ reaction in that it is asymmetric (that is, reactants and products are different chemical species), and it has nonsymmetrically related multiple-bottleneck regions. This introduces the possibility of dynamical bottlenecks with different sets of energy levels on the reactant side and on the product side of the region of high-reaction-path curvature (102,107,109,110), and it is especially interesting to see if bottlenecks in both regions, as well as those near the approximately symmetric saddle point, exert observable influence on the reaction.

Vibrationally adiabatic potentials were calculated for $O + H_2$ using the same methods (74–76) as for $H + H_2$. Examples of these curves are shown in Fig. 4. For $v_1 > 0$, where v_1 is the quantum number for the stretching motion transverse to the reaction coordinate, the adiabatic curves for this reaction exhibit several local maxima. However, only the first and last local maximum of each curve are plausibly associated with dynamical bottlenecks because the vibrational coordinates do not adjust adiabatically to reaction coordinate motion in the central region due to the large reaction path curvature (111–113). Of the local maxima in the adiabatic regions, the first one is higher. For example, for $v_1 = 1$, $v_2 = 0$, where v_2 is again the bending quantum number, it is 0.05 eV higher, and for $v_1 = 2$, $v_2 = 0$ it is about 0.09 eV higher than the product-side maximum. The difference increases with v_1. If the reaction were completely vibrationally adiabatic, only the higher (reactant-like) maxima would influence reactivity. Therefore we call dynamical bottlenecks with reactant-like geometries variational transition states and designate them in the usual manner, i.e., $[v_1 v_2^K]$. However, many vibrationally nonadiabatic transitions have nonnegligible reaction probabilities in the exact quantal cal-

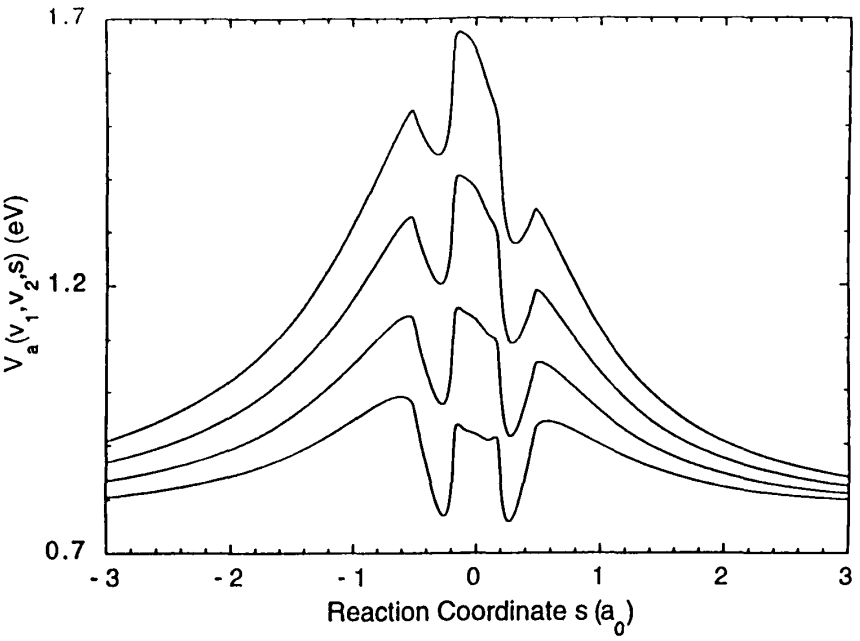

Figure 4 Vibrationally adiabatic potential curves for O + H_2 with $v_1 = 1$, $J = 0$, and $v_2 = 0$, 2, 4, and 6. From the bottom up the curves correspond to the [10^0], [12^0], [14^0], and [16^0] states. (Reprinted with permission from Ref. 14.)

culation. The possibility therefore exists that dynamical bottlenecks with product-like geometries may also have observable influence on the chemical reactivity. We call these supernumerary transition states, and we designate them with the letter *S*, i.e., $S[v_1v_2^K]$, to distinguish them from variational transition states with the same v_1, v_2, and *K*. We further distinguish between two kinds of supernumerary transition states: those of the first kind, whose influence on the total dynamics can be observed; and those of the second kind, whose influence on the total reactive flux is not detectable (14) but which do influence state-to-state reactivity.

B. Total Reactivity

The accurate density of reactive states O + H_2, $J = 0$ is shown in the top left panel of Fig. 5, and results of the quantized transition state theory fit are in Table 6, along with assignments discussed below. The quantal and fitted densities are indistinguishable to plotting accuracy (14), indicating that quantized transition states control the chemical reactivity. The density closely resembles that for the reaction of H with H_2 up to about 1.3 eV. Analogous features are associated with the same sets of quantum numbers through the [06^0] transition state at 1.218 ev.

The fit identified 17 features up to 1.9 eV. The width parameter W_τ generally scales inversely with v_1 and directly with v_2, as expected (14). For many of the states κ_τ is very close to 1.00, and its smallest value is 0.54 (14). Thus many of the quantized transition states are nearly ideal dynamical bottlenecks, and even ones with large bend quantum numbers are quite good.

The maxima in the quantal density of reactive states and in the vibrationally adiabatic curves occur at almost the same energies. Thus, as for the H + H_2 reaction, the

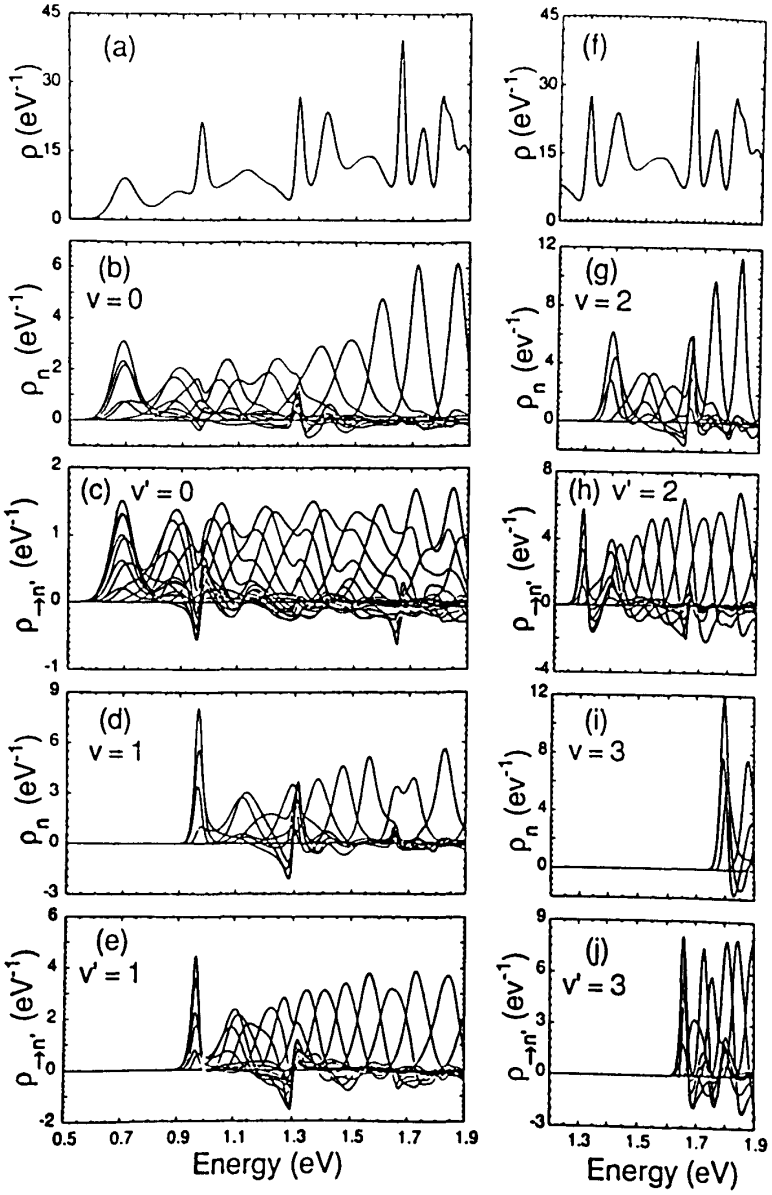

Figure 5 Total, $\rho^J(E)$, and partial, $\rho^J_{vj}(E)$ and $\rho^J_{\rightarrow v'j'}(E)$, densities of reactive states for O + H_2, $J = 0$. (a,f) Total. (b) $v = 0$, $j = 0-15$. (c) $v' = 0$, $j = 0-25$. (d) $v = 1$, $j = 0-12$. (e) $v' = 1$, $j' = 0-22$. (g) $v = 2$, $j = 0-9$. (h) $v' = 2$, $j' = 0-17$. (i) $v = 3$, $j = 0-4$. (j) $v' = 3$, $j' = 0-11$. (Reprinted with permission from Ref. 14.)

accurate quantum mechanical dynamics of O + H_2 is controlled by dynamical bottlenecks that are locally vibrationally adiabatic near quantized transition state energies. The first peak is obviously the [00^0] transition state. The [02^0] transition state was assigned first by Bowman (13), by analyzing our (12) cumulative reaction probabilities, which we made available to him prior to publication. The density has sharp peaks at the energies of both reactant-like and product-like maxima in the $\nu_1 = 2$ and $\nu_1 = 3$ vibrationally adiabatic curves. On this basis we identify the influence of four variational transition states, in particular [00^0], [10^0], [20^0], and [30^0], and two supernumerary transition states, in particular S[20^0] and S[30^0], on the density.

Table 6 Quantized Transition States for O + H_2, $J = 0$

Assignment	E_τ (eV)	κ_τ	W_τ (10^{-2} eV)
[00^0]	0.695	0.96	2.62
[02^0]	0.877	0.89	3.82
[10^0]	0.969	0.62	0.92
[04^0]	1.040	1.00	4.16
[12^0]	1.133	1.00	3.03
[06^0]	1.218	0.54	2.62
S[20^0]	1.306	0.78	0.81
[08^0], [16^0]	1.393	1.00	3.79
[20^0], S[22^0]	1.400	1.01	1.60
[0 10^0], [18^0]	1.501	1.00	3.22
[22^0], S[24^0]	1.564	0.69	2.54
[0 12^0], [1 10^0]	1.619	1.00	5.91
S[30^0]	1.662	0.96	0.68
S[32^0]	1.734	1.00	1.33
[30^0]	1.801	0.63	0.80
S[34^0]	1.829	0.85	1.20
S[36^0]	1.883	1.14	1.82

C. State-Selected Reactivity

Assignment of the remaining fitted features was made [14] largely on the basis of densities of state-selected reaction probability, ρ_n^0 and $\rho_{\to n'}^0$, presented in Fig. 5. Each of the panels (b) through (e) and (g) through (j) displays densities of state-selected reaction probability for a given value of v or v' and for each value of j or j' open up to 1.9 eV.

The first peak in each of the panels corresponds to one of the ground-bend states already identified: [00^0] for $v = 0$ and $v' = 0$, [10^0] for $v = 1$ and $v' = 1$, [20^0] for $v = 2$, S[20^0] for $v' = 2$, [30^0] for $v = 3$, and S[30^0] for $v' = 3$. Note that the first peak for $v' = 2$ ($v' = 3$) channels, identified with a supernumerary transition state, occurs at a lower energy than the first peak for $v = 2$ ($v = 3$) channels, just as the product-like maxima in the vibrationally adiabatic curves are lower than the reactant-like maxima.

The remaining peaks in each panel are associated primarily with bend-excited transition states in the corresponding vibrational manifold. For example, the maxima in the $v = 0$ and $v' = 0$ spectra in Figs. 5b and 5c correspond to transition states [$v_1 = 0$; $v_2 = 0, 2, 4, \ldots, 16^{K=0}$]. Several state-selected spectra, particularly those in the $v = 0$ and $v' = 0$ panels, exhibit double peaks whose maxima nearly overlap with prominent, neighboring peaks in other spectra. This is interesting for two reasons. First, overlapping maxima confirm that a quantized transition state controls reactive flux for the corresponding asymptotic states at energies near the maxima. Second, the existence of two prominent maxima for a single spectrum shows that the asymptotic state couples to two consecutive even-v_2 bend levels of the transition state. The overlapping of peaks also demonstrates that peak maxima do not locate transition state energies exactly, because the overlap is not perfect: relative to the peaks with which they overlap, the individual maxima of a double peak are shifted inward toward the average energy of the double peak.

We note that the peaks in ρ_n^0 and $\rho_{\rightarrow n'}^0$ do not correspond to the opening of asymptotic channels increasing sequentially in j (rotational thresholds). The energy spacing of rotational thresholds would increase linearly with j [the derivative of the $j(j + 1)$ quadratic energy expression is linear in j], where the peaks in Figs. 5b and 5c are evenly spaced, as are the levels of a harmonic oscillator.

The maxima in the vibrationally adiabatic curves at reactant-like and product-like geometries are nearly evenly spaced in energy for a given $v_1 > 0$ stretch manifold, but the latter are more closely spaced than the former (14). Likewise, prominent maxima in the $v = 1$ (Fig. 5d), $v' = 1$ (Fig. 5e), $v = 2$ (Fig. 5g), and $v' = 2$ (Fig. 5h) spectra are also nearly evenly spaced, with the spacing of peaks in the $\rho_n^0(E)$ spectra being larger than the spacing in the corresponding $\rho_{\rightarrow n'}^0$ spectra. (The $v = 3$ and $v' = 3$ spectra begin at too high an energy for the spacing to be judged.) A possible explanation is that the most prominent peaks in ρ_n^0 represent variational transition states, while the most prominent peaks in $\rho_{\rightarrow n'}^0$ represent supernumerary transition states. This would be consistent with the vibrationally adiabatic maxima at reactant-like geometries being less closely spaced than the maxima at product-like geometries (for $v_1 > 0$).

Figure 5 suggests that when both variational and supernumerary transition states influence state-selected dynamics, the former are observed primarily in ρ_n and the latter in $\rho_{\rightarrow n'}$. This is clearly true for the [20^0], S[20^0], [30^0], and S[30^0] transition states in Figs. 5g–j, and the spacing of features suggests that it is also true for bend-excited transition states in the stretch-excited manifolds. This trend is most easily understood by considering that, from the principle of time reversal invariance, quantum mechanical transition probabilities $P_{nn'}$ describe both forward ($n \rightarrow n'$) and reverse ($n' \rightarrow n$) reactions. Thus $\rho_{\rightarrow n'}$ describes both reaction *into* state n' for the *forward* reaction and *out of* state n' for the *reverse* reaction. To understand the state-selected dynamics, we consider the evolution of reactive flux associated with a single asymptotic state. Therefore we consider the forward reaction for ρ_n and the reverse reaction for $\rho_{\rightarrow n'}$. The quantity $\rho_{\rightarrow n'}$, then, tends to be influenced by dynamical bottlenecks for state n' that occur before the region of highly vibrationally nonadiabatic dynamics for the *reverse* reaction, i.e., supernumerary transition states. The quantity ρ_n, on the other hand, tends to be influenced by dynamical bottlenecks on the opposite side of the interaction region (variational transition states) because it describes reaction out of a particular state for the *forward* reaction.

Many but not all of the quantized transition states observed in the densities of state-selected reaction probability are observed as peaks in the total density of reactive states. Some highly bend excited states (e.g., [0 12^0], and [0 14^0]) are observed as peaks only in the state-selected dynamics. If the closely spaced features in the stretch-excited manifolds for $\rho_{\rightarrow n'}^0$ are indicative of supernumerary transition states more closely spaced in energy than the variational transition states (which adiabatic transition state theory also suggests), then only some of the supernumerary transition states, in particular S[20^0], S[22^0], S[24^0], S[30^0], S[32^0], S[34^0], and S[36^0], are observed in the total density, i.e., only some are of the first kind. The other supernumerary transition states identified in the state-selected dynamics are of the second kind.

The interpretation of the accurate quantal results in terms of variational and supernumerary transition states is consistent with model studies of scattering by unsymmetrical one-dimensional Eckart potentials (84). These studies show that both maxima in the unsymmetrical potentials are associated with poles of the scattering matrix, and some of these poles are associated with an increase in the transmission probability, while others are not.

D. Spectroscopic Constants

Spectroscopic constants for the variational transition states were obtained by a fit similar to that used for the H + H_2 reaction. In this case, noting that quantized transition states are associated with poles of the S matrix having the form

$$\bar{E}(v_1, v_2) = E_\tau(v_1, v_2) - i\pi W_\tau(v_1, v_2) \tag{30}$$

we fit both the energies and the widths of the quantized transition states. Equation (30) is equivalent to Eq. (26) except that it has been written in terms of the width parameter W_τ instead of the resonance width Γ (from Eqs. (12), (26), and (28) with v set to zero, $\Gamma = 2\pi W_\tau$). A least-squares fit of the first six O + H_2 levels was made using Eqs. (25) and (30), allowing the spectroscopic parameters to be complex. We constrained x_{11} to be zero because none of the first six states involve $v_1 > 1$. The parameters thus obtained are compared with those obtained by adiabatic transition state theory. The latter were calculated with an analogous least-squares fit in which the real parts of the resonance energy were the maxima in the vibrationally adiabatic curves at reactant-like geometries, and the imaginary parts were obtained from tunneling probabilities for a parabolic approximation to the vibrationally adiabatic curves near their maxima (14).

Table 7 shows that the agreement between the accurate results and adiabatic-transition state theory is quite good for the real parts of E_0, ω_1, and ω_2. The imaginary parts do not match as closely, but the imaginary parts of four of the five spectroscopic constants agree in sign, and in three cases they agree within a factor of about 2.

VI. D + H_2

We have also calculated the density of reactive states for the D + H_2 reaction. These calculations were carried out as part of a converged calculation of the thermal rate constant for the reaction D + H_2 → HD + H over a wide range of temperatures (64). We found in these calculations that rate constants calculated using either the DMBE potential energy surface discussed above or the earlier so-called LSTH potential energy surface (114–116) were in excellent agreement with experiment. In particular the average deviation from experiment (117) over the 250–900 K range is only 5% for both surfaces, which is within the experimental error bars.

Not only the rate constants but also the densities of reactive states are very similar for these two potential energy surfaces; hence we will concentrate here on surveying the results for only one of these surfaces. We arbitrarily chose the LSTH surface for this

Table 7 Spectroscopic Constants (cm^{-1}) for O + H_2, $J = 0$

	Accurate	Adiabatic transition state theory
E_0/hc	3786 − 597*i*	3945 − 971*i*
ω_1	2241 + 507*i*	2326 + 520*i*
ω_2	737 − 307*i*	929 + 75*i*
x_{12}	−45 − 89*i*	−266 − 245*i*
x_{22}	−2 + 43*i*	24 + 88*i*

purpose. In the rest of this section we present an analysis of the role of quantized transition states in the accurate quantal dynamics of the D + H_2 reaction on this surface. We will present results for total angular momenta J = 0, 3, 9, and 15 with H_2 spatial permutation symmetry (S) equal to +1; we show results for parity (P) equal to +1 with J = 0 and 3 and for P = −1 with J = 3, 9, and 15.

First of all we note that the S = +1 and S = −1 symmetry blocks yield almost identical CRPs (64), and this is why we present the results only for S = +1. The density spectrum for D + H_2 with JPS = 0++ is shown as the solid curve in Fig. 6. The heavy dashed curve is the simulated spectrum obtained by fitting the quantal density by a sum of terms as in Eqs. (14) and (15), corresponding to scattering by parabolic barriers. In order to achieve a physical fit we used 13 terms and constrained five of the κ_τ to be equal unity; the resulting fit is quite good. We conclude that quantized transition states control the chemical reactivity globally. As before we label the levels of the transition state as $[\nu_1\nu_2^K]$. For J = 0 only the even-bend states contribute to the CRP. Assignments $[\nu_1\nu_2^K]$ were made on the basis of semiclassically computed vibrationally adiabatic potential maxima and the expected uniformity of the spacings between fitted threshold energies in a given ν_1 or ν_2 progression. The assignments are shown also in Fig. 6. We found evidence for significant influence on the CRP by nine variational transition states and two supernumerary transition states of the first kind at energies below 1.5 eV. Supernumerary transition states in the ν_1 = 2 stretch manifold influence this unsymmetric reaction, just as for O + H_2. The parameters obtained for D + H_2 are shown in Table 8 and may be compared with those for H + H_2 in Table 2.

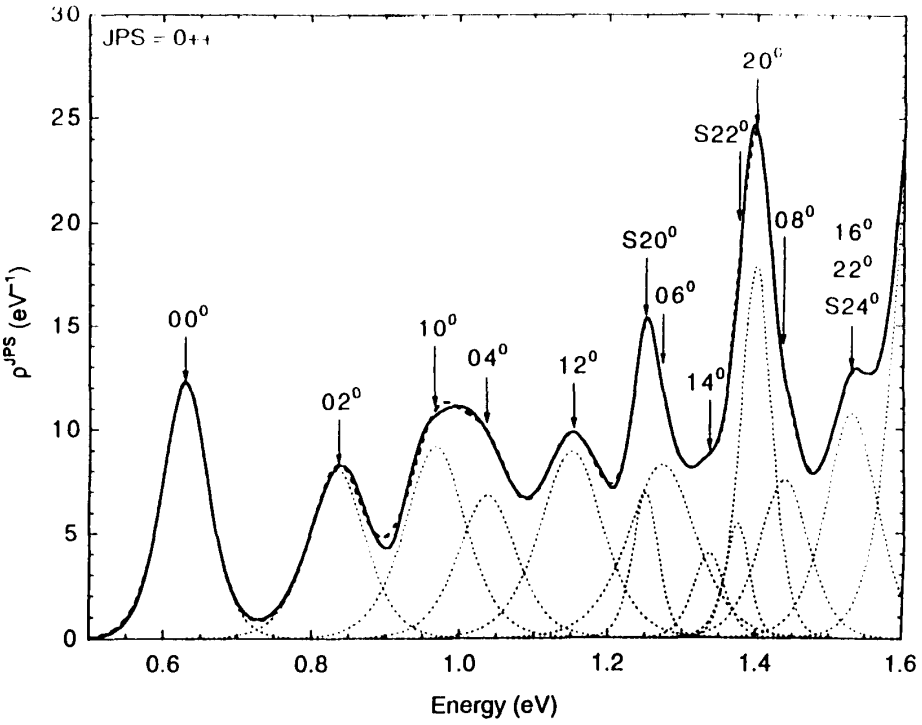

Figure 6 Density of reactive states for D + H_2 with JPS = 0++. The components of the fit are shown as dashed curves, and the assignments are shown above the peaks in the fit. The heavy dashed curve is the sum of the terms in the fit, and the solid curve is the accurate quantal density of reactive states.

Table 8 Quantized Transition States for D + H_2, $J = 0$

Assignment	E_τ (eV)	W_τ (10^{-2} eV)	κ_τ (eV)
[00^0]	0.630	2.04	1.00
[02^0]	0.835	2.51	0.81
[10^0]	0.967	2.72	1.00[a]
[04^0]	1.038	2.59	0.71
[12^0]	1.150	2.81	1.00[a]
S[20^0]	1.250	1.14	0.32
[06^0]	1.273	3.02	1.00[a]
[14^0]	1.336	1.39	0.22
S[22^0]	1.375	1.05	0.23
[20^0]	1.400	1.39	1.00[a]
[08^0]	1.438	2.22	0.67
[16^0], [22^0], S[24^0]	1.529	2.32	1.00[a]
S[30^0]	1.627	2.17	2.84[b]

[a]Constrained to 1.00.
[b]Includes contributions from higher-energy quantized transition states.

Using the E_τ values from Table 8 for the variational transition states [00^0], [02^0], [04^0], [10^0], [12^0], and [20^0] with $J = 0$, and using the positions of the peak maxima for the [00^0] states with $J = 3$ and 15, we obtain spectroscopic constants via fits of the threshold energies to Eq. (25), augmented by an extra term, $-DJ^2(J + 1)^2$. The spectroscopic constants obtained are given in Table 9. These constants predict threshold energies for the [06^0], [08^0], and [14^0] transition states that differ, on average, by only 0.014 eV from the fitted values of E_τ. The value of the rotational constant B is in excellent agreement with the value of 7.04 cm^{-1} obtained from the semiclassical (76) analysis. There is also qualitative agreement between these constants and those [10,16] for H + H_2, given in Sec. IV.A, after taking into account the different reduced masses of the system.

Figure 7 shows the densities of reactive states for $JPS = 0{+}{+}$, $3{+}{+}$, $3{-}{+}$, $9{-}{+}$, and $15{-}{+}$. On each plot we tabulate the energies in eV of the variational transition states predicted by the parameters in Table 9 along with the assignments; and we also list the cumulative reaction probability $N^{JPS}(E)$, summed over both HD product arrangements, at each local minimum. Transition states with $K = 0$ appear only for $(-1)^J P =$

Table 9 Accurate Spectroscopic Constants (cm^{-1}) for D + H_2 Transition States[a]

ω_1	2047
ω_2	882
x_{11}	383
x_{12}	−89
x_{22}	−2
B	7.556
D	0.002

[a]$E_0 = 0.388$ eV.

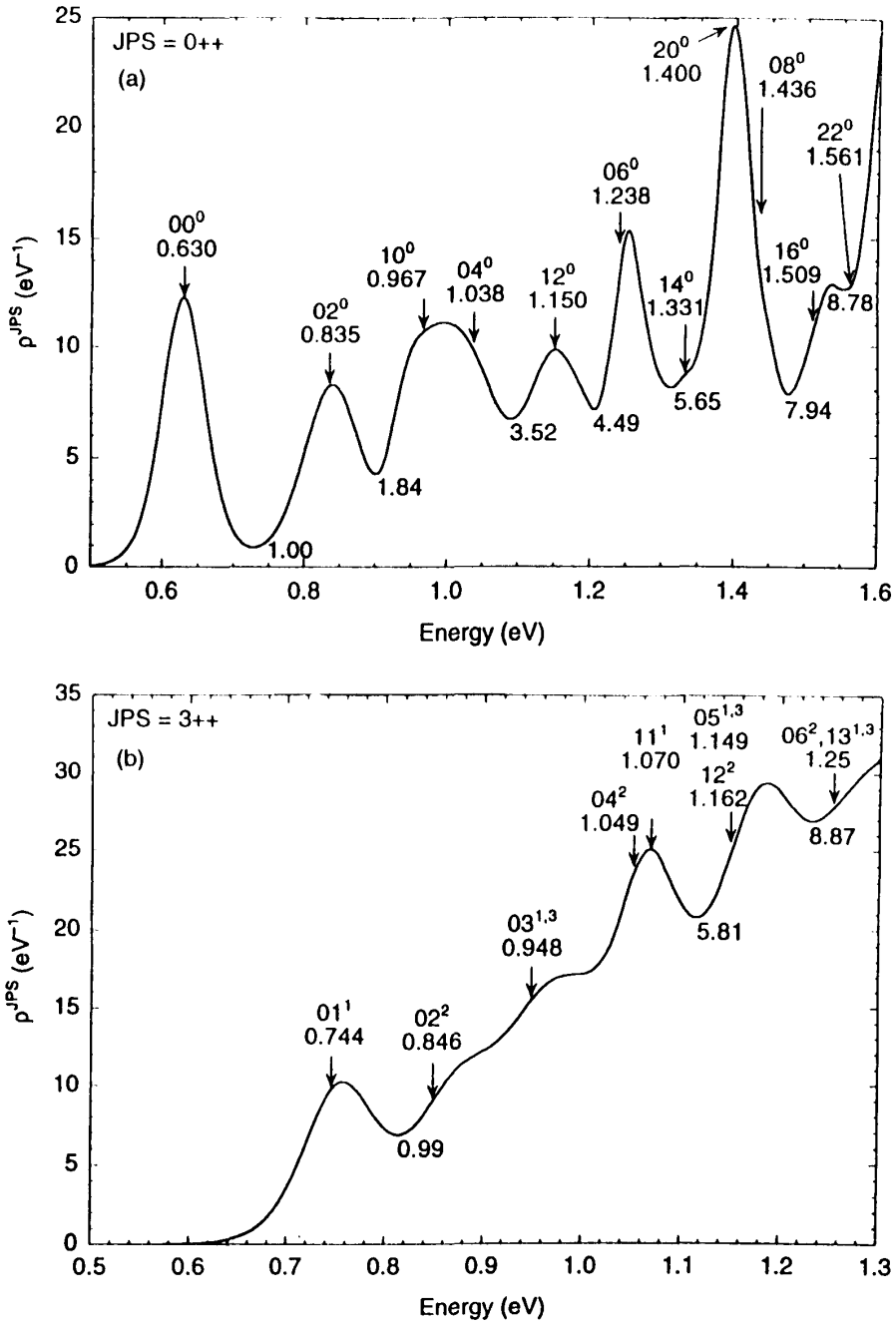

Figure 7 Densities of reactive states $\rho^{JPS}(E)$ for D + H_2 with $S = +1$. (a) $J = 0$, $P = +1$. (b,c) $J = 3$, $P = \pm 1$. (d) $J = 9$, $P = -1$. (e) $J = 15$, $P = -1$. The positions of the variational transition states predicted by the spectroscopic fit are indicated, labeled by their assignments and by their energies in eV, and the local minima of N^{JPS} are labeled by the values of the CRP.

+1, and in particular they are not present in the $JPS = 3++$ spectrum, whereas the $JPS = 3-+$ spectrum has contributions from both zero and nonzero K, based on symmetry arguments given in Sec. IV.B.

The first and most important point that we wish to make on the basis of Fig. 7 is that the quantized transition state structure persists up to high J, despite the increasing density of states due to K degeneracy. This answers affirmatively the most widely asked

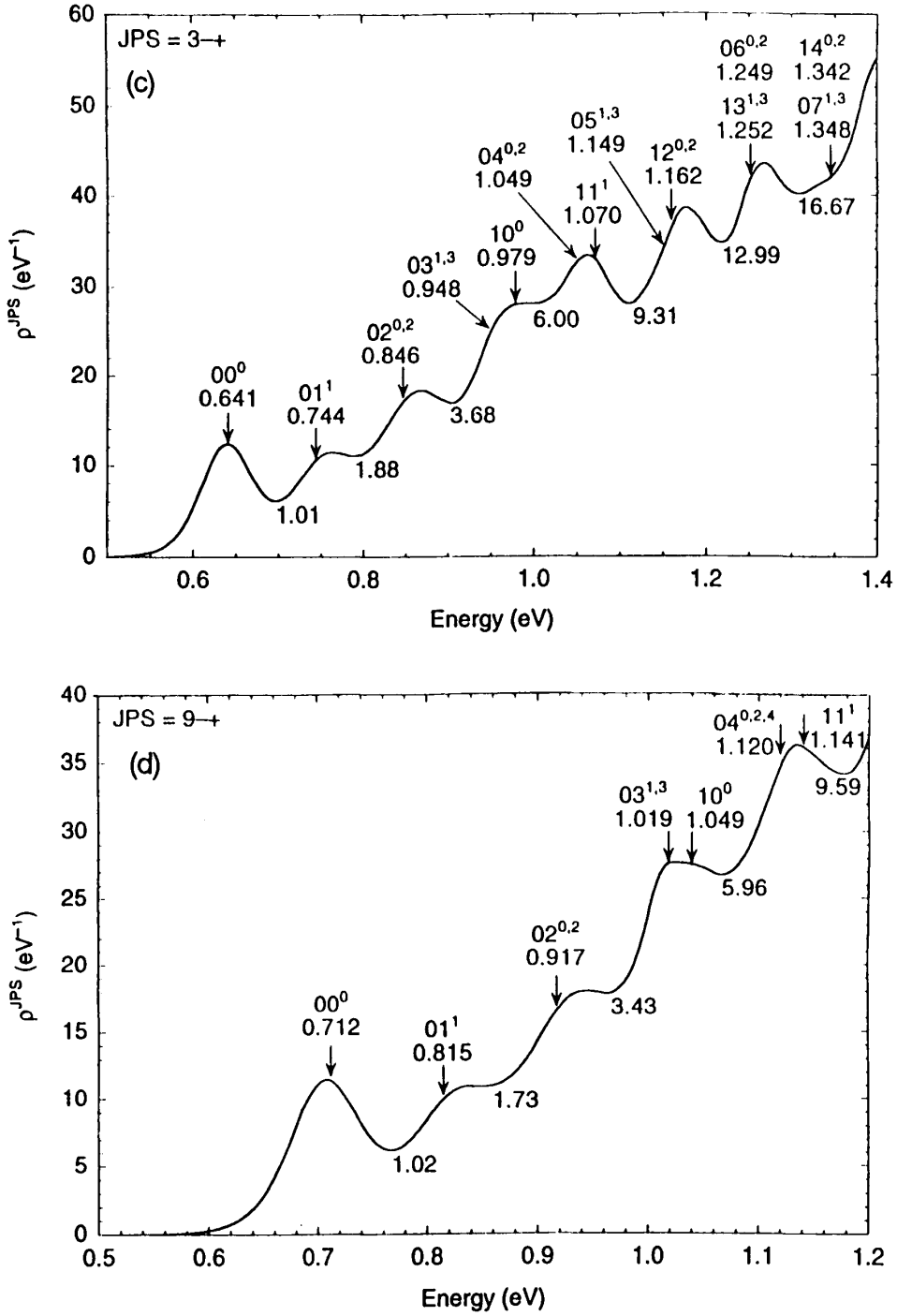

Figure 7 Continued.

question we hear at seminars if we concentrate on low-J examples, namely, can quantized transition state structure be observed at high J?

The values of the CRP at the local minima are a somewhat crude (compared to fitting with the correct line shape) way to estimate the sum of the transmission coefficients of all levels below a given local minimum. In the typical cases with $J = 0-15$, the CRP at the first local minimum is in the range 0.99–1.02. Thus the first transition state, [00^0], is almost always a nearly ideal dynamical bottleneck. The bend states are roughly equally

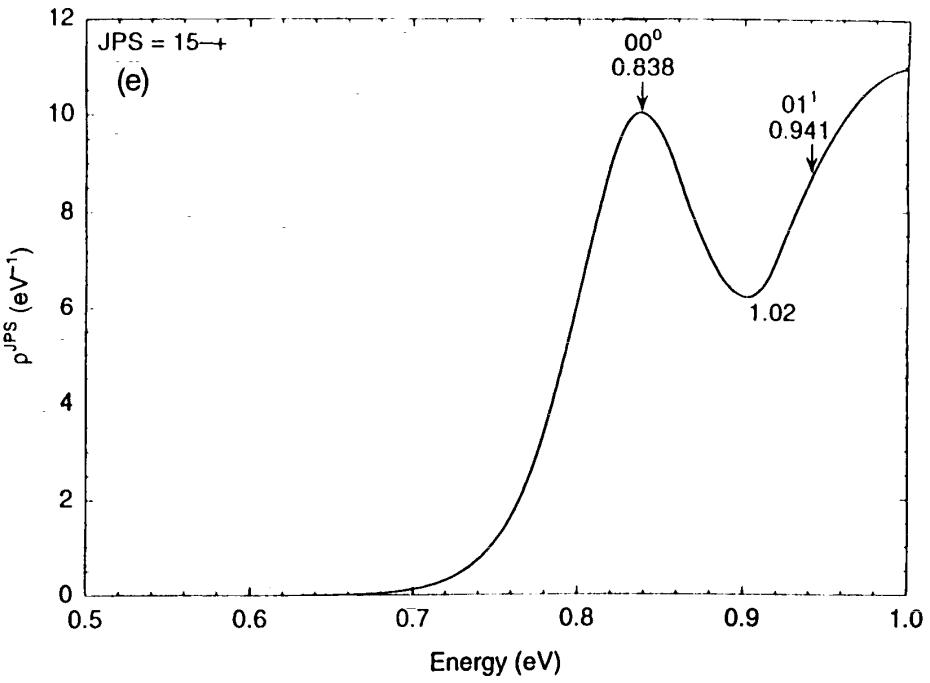

Figure 7 Continued.

spaced in energy. The quantized transition state structures at higher energy are relatively broad and tend to overlap, especially at higher values of J where the different K states can broaden the feature associated with a given ν_1 and ν_2.

Examination of state-selected CRPs for this system (not shown here) indicates that the various initial states can each access several transition states, although some specificity is observed. Much of the state-selected dynamics clearly correlates with the total dynamics. For example, the state-selected densities for various j with $\nu = 0$ have prominent peaks at 0.63, 0.84, and 1.03 eV, while those for $\nu = 1$ have prominent peaks at 0.96 and 1.16 eV.

VII. $F + H_2$

The observation of quantized transition states in $H + H_2$ and $D + H_2$, as discussed in Sec. IV and VI, builds on a long history of the development of theoretical concepts for which these reactions have provided critical early examples (118). The reaction of F with H_2 is another reaction whose detailed understanding has been the subject of many studies over a long period of time. In particular, it is a prototype exothermic chemical reaction, and it has played an important role (119–126) in our appreciation for resonance phenomena. Although resonances were observed theoretically in the $H + H_2$ reaction many years ago (118), resonance effects have been hard to observe experimentally for bimolecular reactions. The $F + H_2$ reaction, though, showed a dependence of the angular scattering pattern on the vibrational quantum number ν' of the HF product that was hard to interpret unless resonance behavior was invoked. In particular, Neumark et al. (125) concluded that "when contrasted with the strong backscattering of HF ($\nu' = 2$) in the reaction $F + p\text{-}H_2$ at 1.84 kcal/mol (0.080 eV relative translational energy, which corresponds to 0.348 eV total energy for $j = 0$) the sharp forward peak of the $\nu' = 3$ product

is the most compelling evidence to date for quantum mechanical dynamical resonance effects in reactive scattering. The shape of the distribution is what one expects when collisions at relatively high impact parameters contribute to the formation of a quasi-bound state followed by selective decay to $v' = 3$ products.'' Early attempts to explain the phenomenon were hindered by incomplete knowledge of the potential energy surface and an inability to perform converged quantum dynamical calculations.

One of the major impediments to understanding the dynamics has been the lack of an accurate potential energy surface, and in fact even the barrier height and saddle point geometry, which are two of the most basic properties of a potential energy surface for a reactive system, have been controversial. Recently, though, three quite different sets of electronic structure calculations (127–131) have converged on similar results for these properties. Furthermore both sets of calculations predict that the bending potential for the saddle point is very soft, and the saddle point may even be (probably is) nonlinear. A global potential energy surface that embodies these new predictions was created and fine tuned by an iterative process involving repeated converged quantum dynamics calculations (126). The new surface is called 6SEC.

Well-converged quantum dynamics calculations were first reported for the $F + H_2$ reaction (for $J = 0$ on an inacccurate potential surface) in 1989 (132), and a combination of large-basis-set electronic structure calculations (127–129), variational transition state theory calculations (126,129), and modifications based on accurate quantum scattering calculations (126) with $J = 0–18$ were used in 1993 to calibrate the 6SEC (126) potential energy surface. Accurate quantum dynamics calculations with $J = 0–21$ (126) give a remarkably realistic reproduction of the energy-dependent experimental (125) angular scattering patterns for the $F + H_2$ reaction for both $v' = 2$ and $v' = 3$, whereas calculations based on intermediate surfaces in the iterative surface fitting process often were very inaccurate for these features due to their inaccurate prediction of high-J resonances ($J \cong 12–17$), which are sensitive tests of surface quality.

Interest in this system is further heightened by photoelectron spectra of FH_2^- in which the final state is a neutral FH_2 system in the transition state region (133–135). The original interpretation (133) of these spectra was that the system made transitions to a resonance state at an energy just below a product asymptote and to continuum states in which probability density accumulated near classical turning points by Franck-Condon transitions to ''scattering wave functions with nearly zero momentum in the Franck-Condon region along the dissociation coordinate.'' The latter were called ''direct'' transitions to emphasize the nonresonant interpretation. The relationship of the observed spectrum to quantized transition states was brought out later though in the work of Kress and Hayes (136), who pointed out the similarity of the observed spectrum to the density of reactive states for the 5SEC (129) potential surface. The 6SEC surface, which is qualitatively similar to (and based on) the 5SEC one in the transition state region, also leads to qualitative agreement with experimental (133) spacings. Werner and co-workers (135), using a surface similar to 6SEC but based on ab initio electronic structure calculations, have carried out a successful direct simulation of the photoelectron spectrum (direct simulations using presumably less accurate surfaces were reported earlier (134)). In light of these results it is of great interest to present the density of reactive states for the $F + H_2$ reaction on the 6SEC surface, which reproduces the state- and energy-dependent angular distributions so well.

For $F + H_2$, we consider both symmetries S (they are calculated separately, taking advantage of the fact that S is a conserved quantum number), and we count both product

arrangements. The resulting cumulative reaction probabilities and densities of reactive states for various sets of the conserved quantum numbers J, P, and S are given in Fig. 8. The curves are labeled similarly to those for D + H_2 except that in the regions between prominent peaks and after the final prominent peak we mark the value of the CRP only at the first local minimum, not at all local minima. The obvious separation of the quantized transition states in both the CRP and density plots is very striking. The energies at the local maxima in the density plot provide a first approximation to the transition state energy levels E_τ, and, for nondegenerate levels, the differences between $N^{JPS}(E)$ at the successive local minima provide a first approximation to the transmission coefficients κ_τ. In some cases these differences are closer to 2 or 3 than to unity, and this indicates a degenerate level or a near degeneracy. In such cases the difference is an approximation to the product of the degeneracy and the average transmission coefficient of the states comprising the degenerate or near-degenerate manifold. (The energies at the local maxima in the CRP plot have no obvious meaning, and in fact it is not even clear why there are local maxima after every rise, but we labeled them for the convenience of the reader.)

The F + H_2 system is characterized by an early, loose transition state whose lowest-frequency motion is best modeled as an internal rotation, in contrast to the tight, linear transition states of the H + H_2, D + H_2, and O + H_2 reactions discussed above, whose low-frequency motion is well modeled as an anharmonic bending vibration. The lowest-energy saddle point on the 6SEC surface is bent, although it is only 0.022 eV lower in energy than the collinear transition state. The marked difference in the character of tight and loose transition states results in striking differences in the corresponding transition state spectra. The hindered-rotor transition-state levels may be labeled by the diatomic reactant's vibrational and rotational quantum numbers, denoted v and j respectively, as well as the magnitude, K, of the projection of J on the atom-to-diatom axis. The projection quantum number is constrained such that (63)

$$[1 - (-1)^j P]/2 \leq K \leq \min(j, J) \tag{31}$$

This may be called a body-frame label set. Alternatively one may use the space-frame labels v, j, and l of the initial collision pair, where l is the orbital angular momentum quantum number of the relative translational motion of FF with respect to H_2. The quantum number l is constrained by (137)

$$|j - J| \leq l \leq |j + J| \tag{32}$$

and

$$(-1)^l = P(-1)^j \tag{33}$$

Neither the (v, j, K) nor the (v, j, l) set of quantum numbers fully separates the motion at the transition state, but these representations provide a basis for discussion.

The asymptotic H_2 eigenstate energies for the 6SEC potential energy surface are given in Table 10, and they illustrate the well-known fact that the energies of pure rotor states are approximately equal to $Bj(j + 1)$, where B is the rotational constant in energy units. Examination of the peak positions in Fig. 8 shows that they fall into clusters whose mean energies are also approximately proportional to $j(j + 1)$, and we present them organized this way in Table 11. The penultimate column of Table 11 displays the internal rotational excitation energies of the extreme energies of each cluster, and we see that they differ from the rotational excitation energies of H_2 in Table 10 by 25–36% for j = 1, 13–14% for j = 2, and less than or equal to 4% for j = 3 and 4. We conclude that

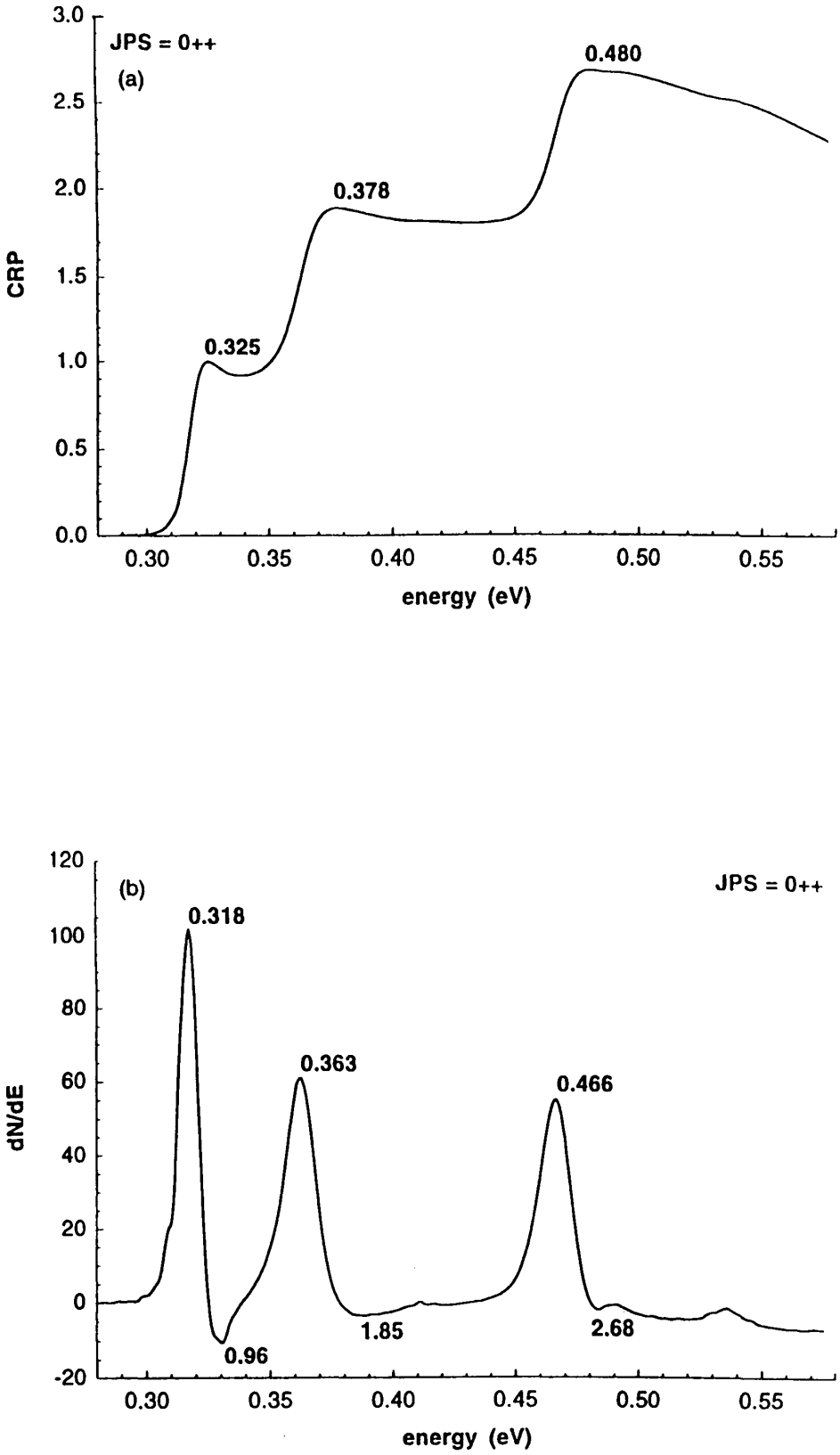

Figure 8 Cumulative reaction probabilities, $N^{JPS}(E)$, and densities of reactive states, $\rho^{JPS}(E)$ in eV^{-1}, for F + H_2 as functions of total energy E. *JPS*: (a,b) 0++, (c,d) 0+−, (e,f) 1−+, (g,h) 1−−, (i,j) 1+−, (k,l) 1++, (m,n) 2++, (o,p) 2+−, (q,r) 2−−, (s,t) 2−+. The energies of maxima and the value of N^{JPS} at selected minima are shown.

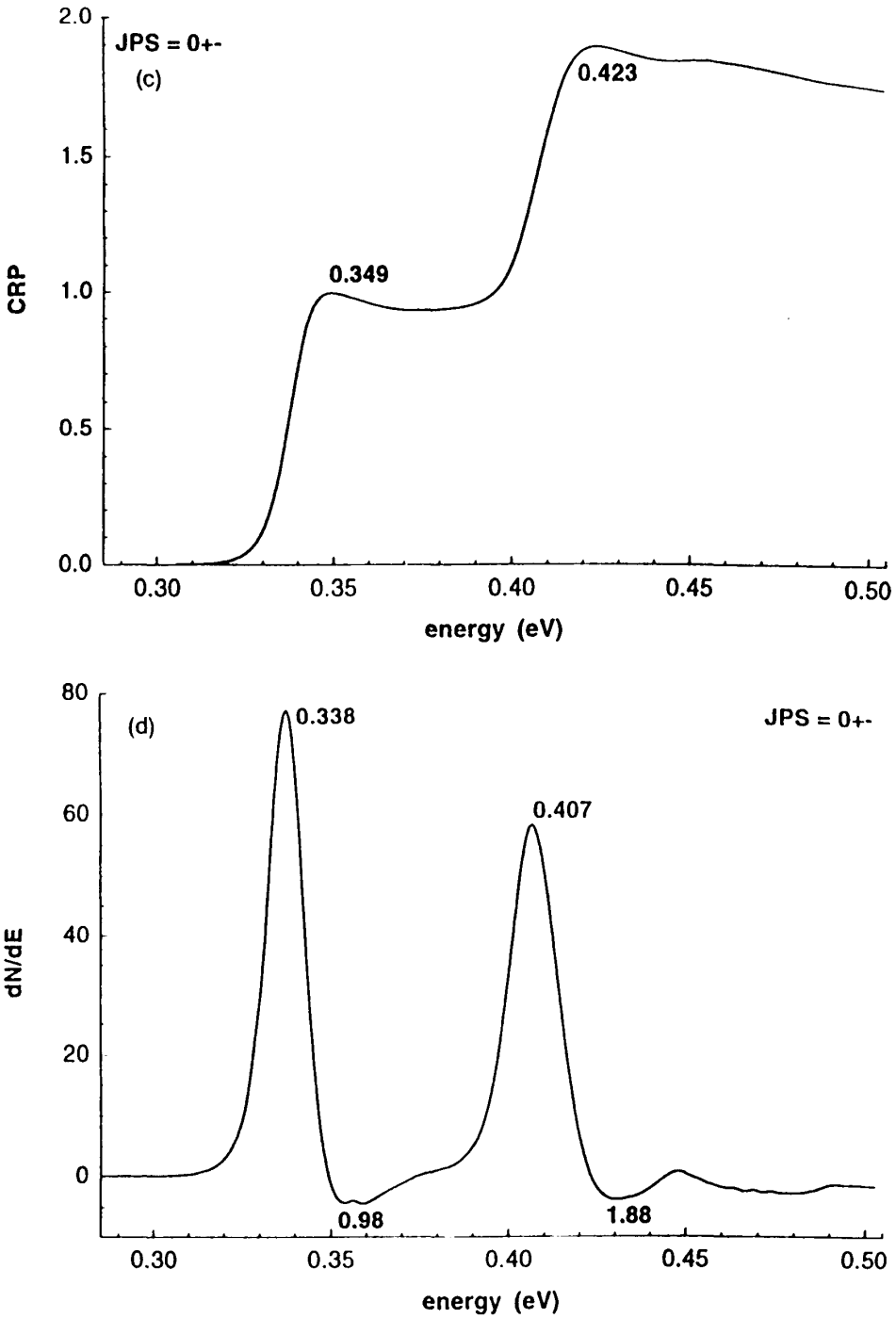

Figure 8 Continued.

because the transition states are so early, j is approximately adiabatic in the region between reactants and transition state. This allows j to be assigned as a good transition state quantum number, similar to the assignment of quantum numbers for some van der Waals complexes (138–140). Table 10 for H_2 and Table 11 for the FH_2 transition state both show the $j(j + 1)$ quadratic dependence on j. Table 10 yields $B \cong 0.0073$ eV for overall rotation of H_2, and Table 11 yields about the same value of B for internal rotation of H_2 in the FH_2 transition state.

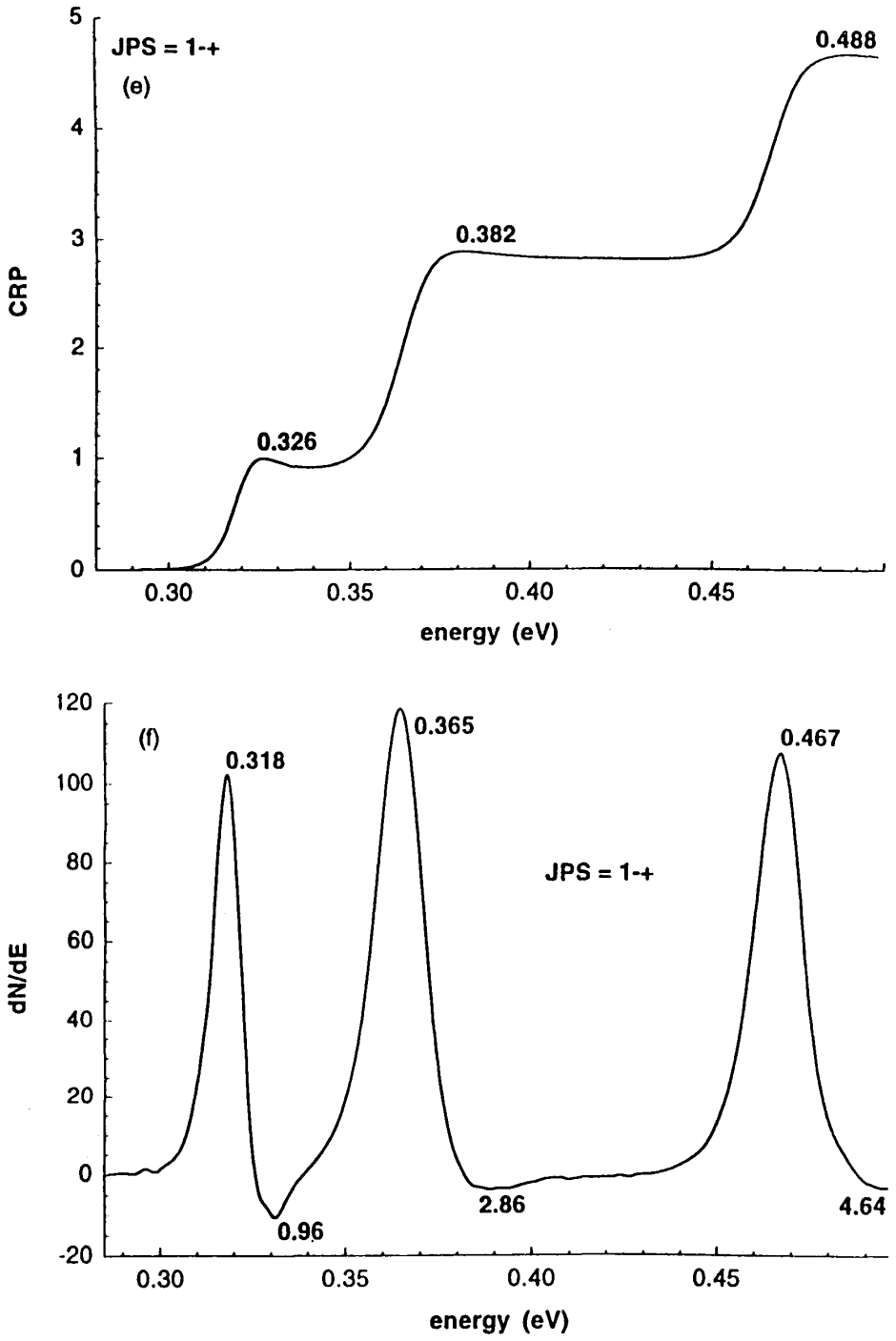

Figure 8 Continued.

In order to further categorize the transition states, we carried out eigenvalue calculations, using a method described elsewhere (141), in which we reduced the dimensionality by fixing the H—H distance at $1.44a_0$ and the F—H_2 distance at $3.17a_0$, approximately the collinear saddle point values. The eigenvalue calculations were carried out with a body-frame basis, first assuming the Hamiltonian is block diagonal in K, then coupling the K blocks. We performed such calculations with $J = 0, 1, 2$, $P = \pm 1$, and $S = -1$. When K was assumed to be a good quantum number, a single basis vector had

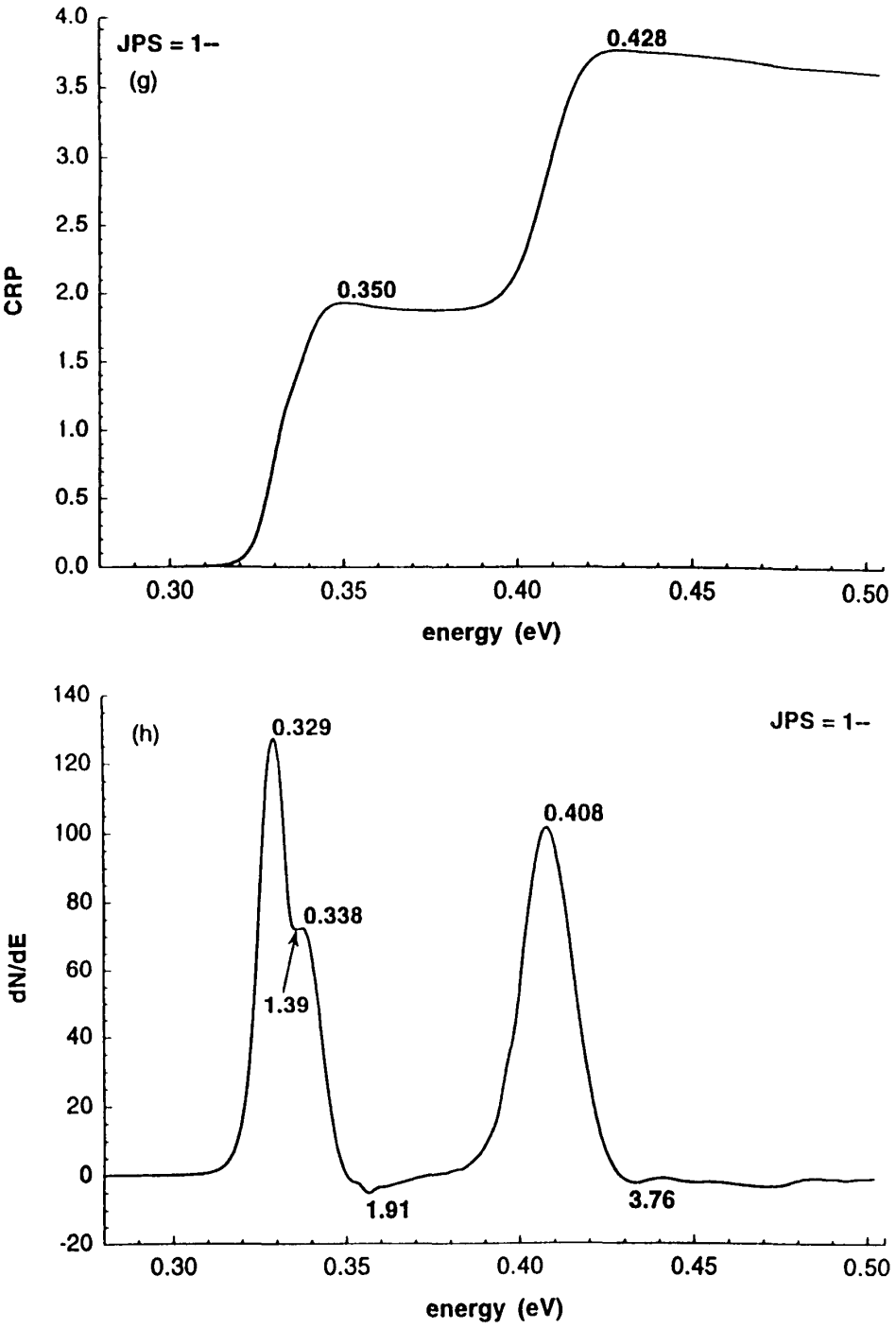

Figure 8 Continued.

a coefficient in the eigenvector greater than or equal to 0.993 in all cases, and for *JPS* = 0+− and 1+−, for which there is only one *K* value, the internal rotational excitation energies of such eigenvalue calculations agree with those in Table 11 within 1 and 5 meV. These results confirm that *j* is a good quantum number.

For *JPS* sets with more than one *K*, we then allowed the *K* blocks to couple. The coupled-*K* internal-rotation excitation energies agree with those in Table 11 with an average absolute deviation of only 7 meV, but the largest coefficient of the uncoupled eigen-

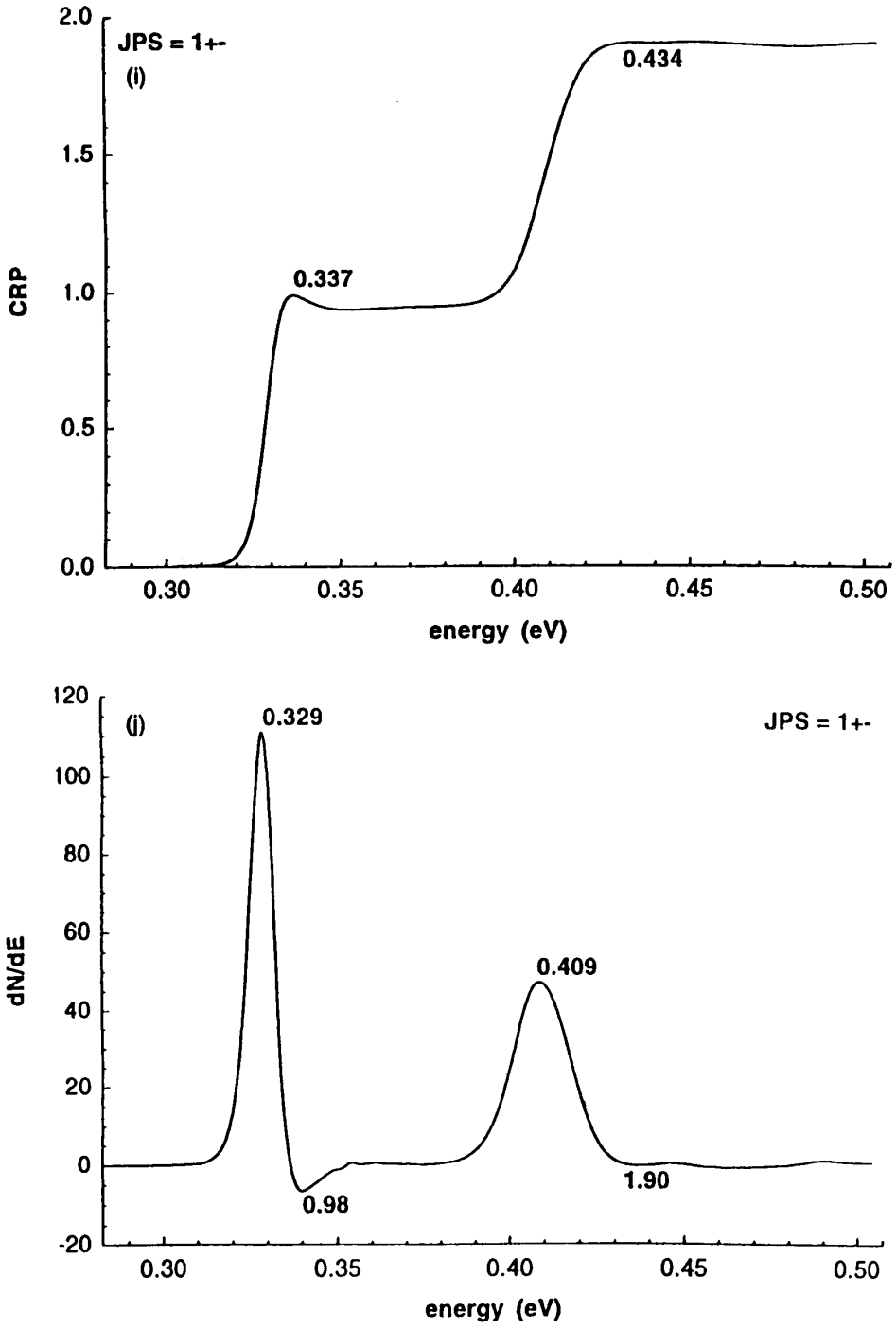

Figure 8 Continued.

states in the various coupled eigenvectors varied from 0.725 to 1.00, with an average value being 0.898, corresponding to a squared coefficient (fractional weight of the basis function in the eigenvector) equal to only 0.806 (i.e., about 81%). Thus, in general K is not a good quantum number, although for the lowest-energy state of each *JPS* block, the largest coefficient in the eigenvector is always at least 0.996. The transition state assignments resulting from this analysis are given in Table 12 (where in this case, we quote

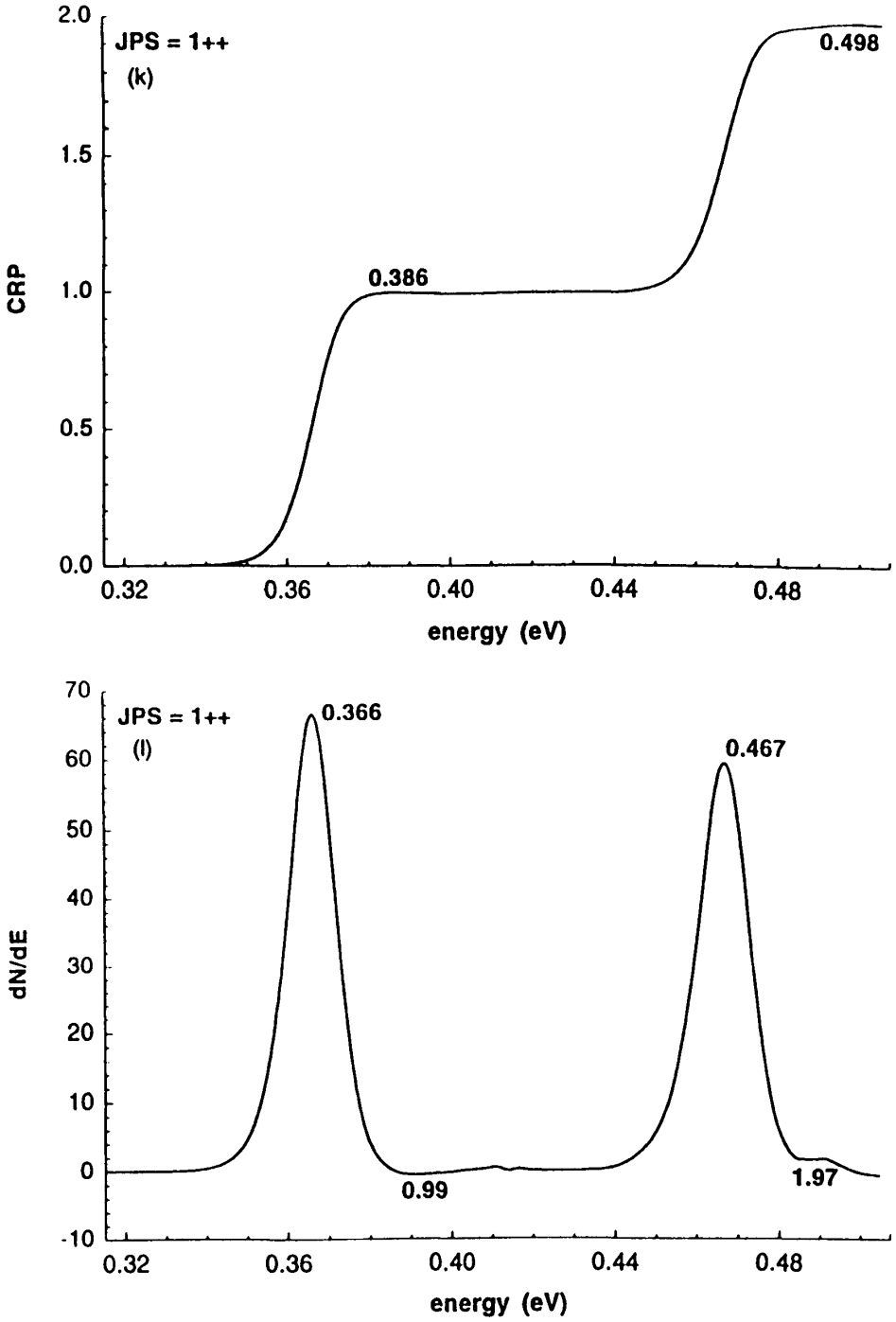

Figure 8 Continued.

the contribution in terms of primitive basis functions rather than uncoupled eigenstates), and these results confirm the j assignments of Table 11.

The levels differing only in K are typically not resolved. However, we can get an idea of the K splitting in two ways. First is the K splitting predicted by the reduced-dimensionality calculations, which is 14–15 meV for $j = 1$ and 4–11 meV for $j = 3$. Second is to look at differences in the energies at which peaks occur in the state-selected

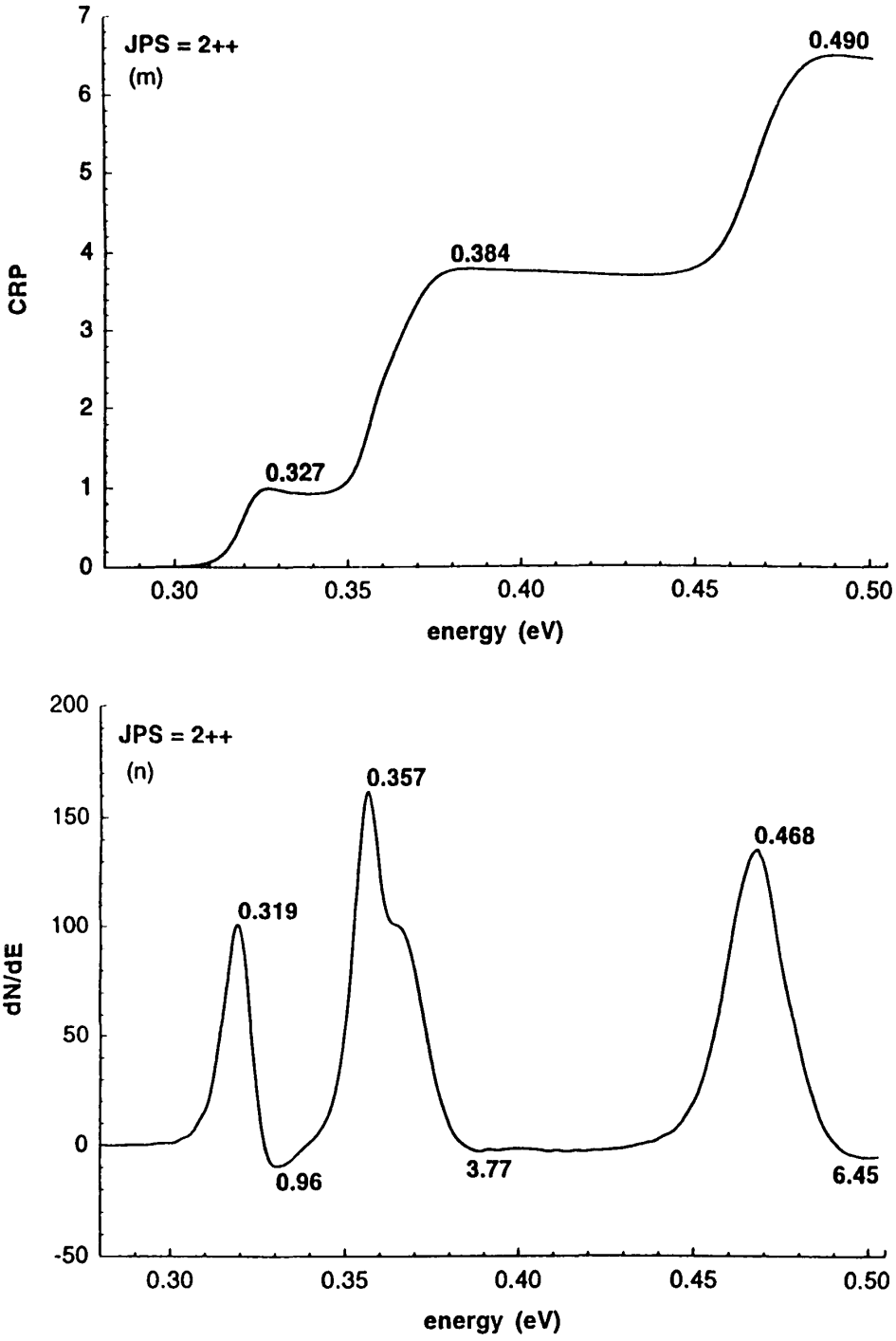

Figure 8 Continued.

densities of reactive states in the body-frame representation. The second method yields ~2–12 meV, depending on the values of J, P, S, and j, which is reasonably consistent with the first method. Since most of the peaks are broader than the estimated splittings, it is not too surprising that the K splittings are not resolved.

The transmission coefficients in the last column of Table 11 are amazing! The average deviation from unity, over 23 values, is only 5%. This is especially striking since

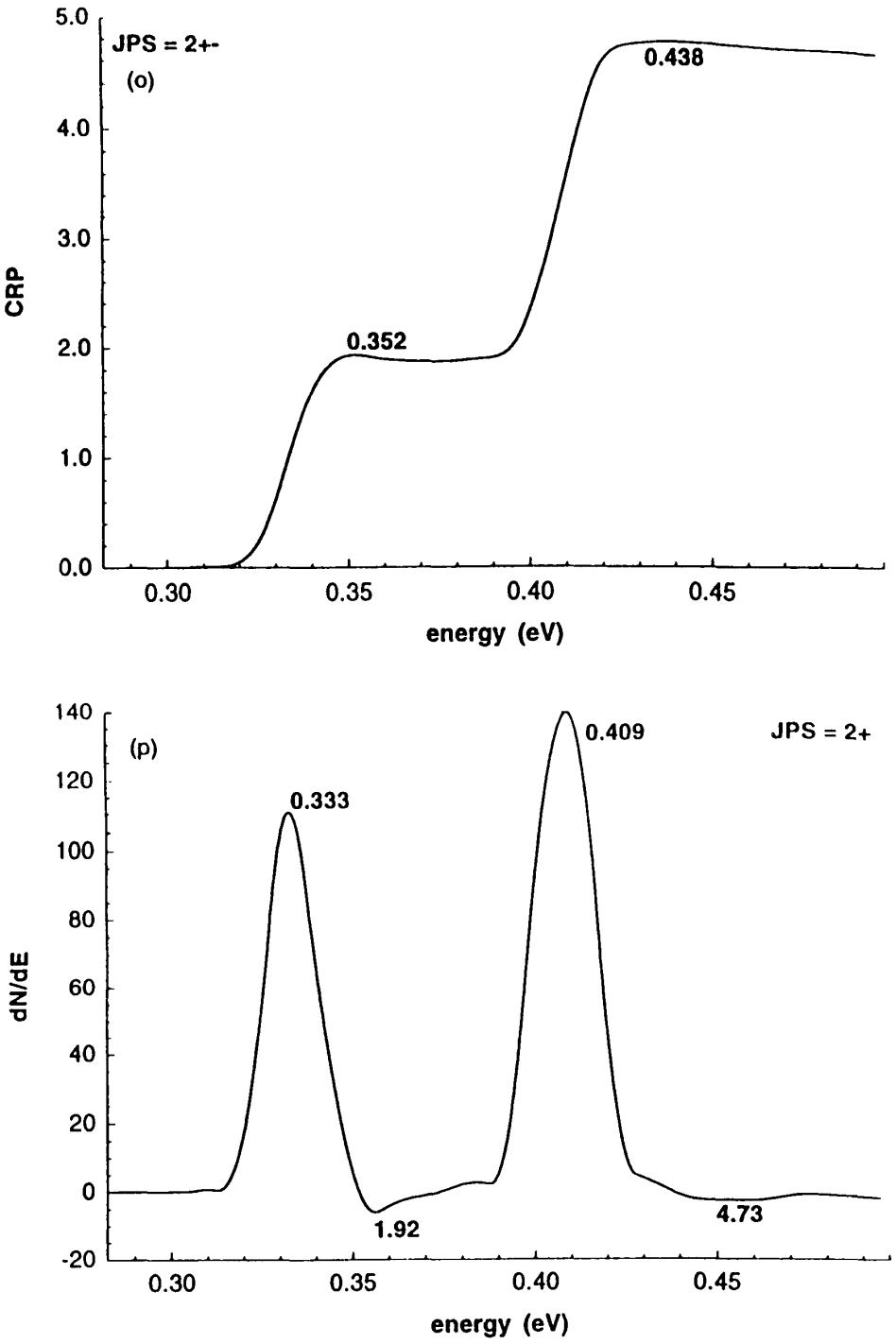

Figure 8 Continued.

the collinear F + H_2 reaction shows a transmission coefficient of about 0.55 averaged over a Boltzmann distribution at 300 K (142), which is by far the largest breakdown of the unit transmission coefficient assumption of any reaction studied to date, out of over 40 cases (143–146). Clearly the mechanism leading to trajectory recrossing (147) in a collinear world is not very significant in the full 3-D world.

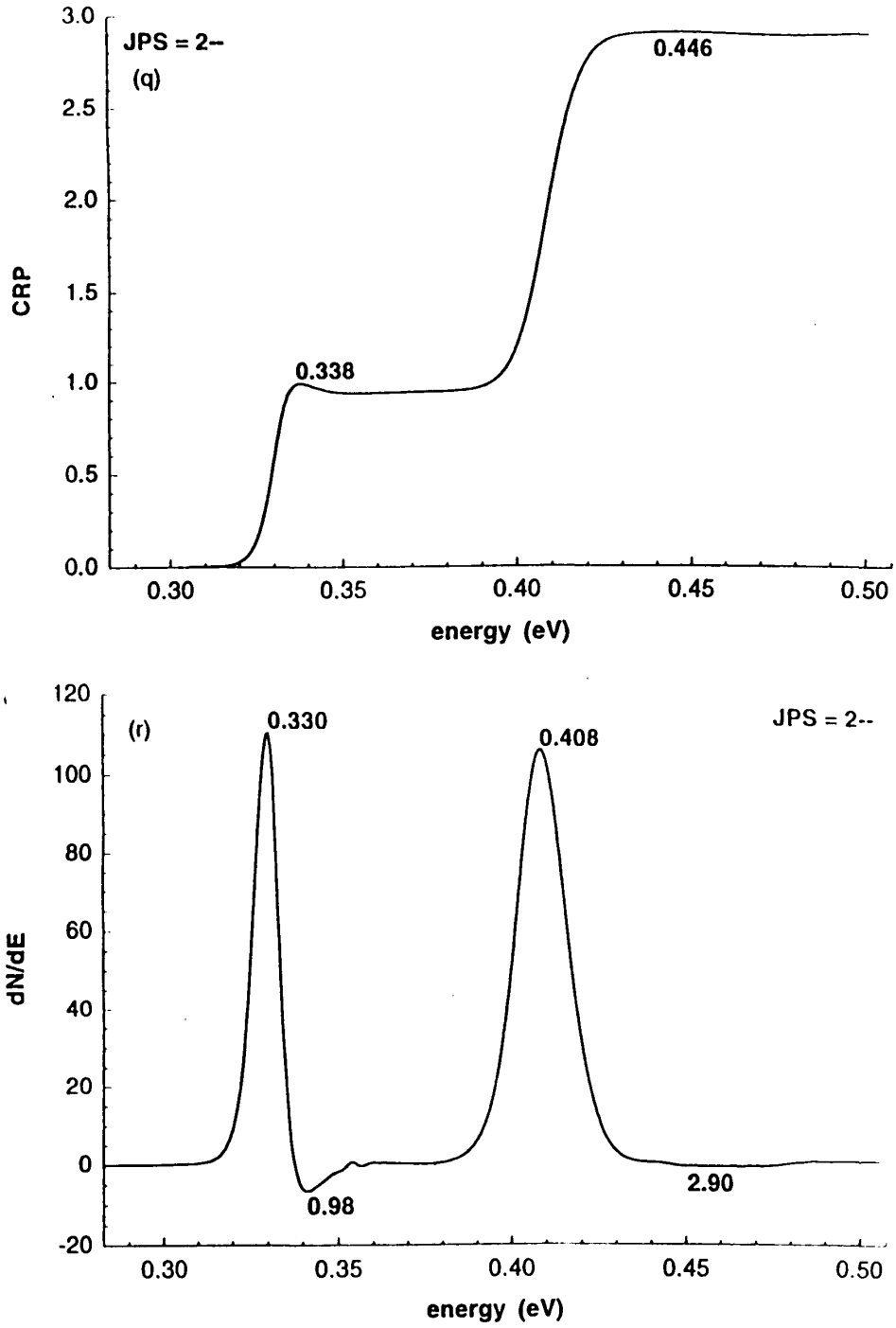

Figure 8 Continued.

VIII. HALOGEN-HYDROGEN HALIDE SYSTEMS

The hydrogen transfer reactions Cl + HCl, I + HI, and I + DI present a more difficult test of quantized transition state control of chemical reactivity. In contrast to the H + H_2, D + H_2, O + H_2, and F + H_2 reactions, the quantized transition state structure in the accurate dynamics of these reactions is almost completely obscured by features that have been attributed to trapped-state resonances and rotational thresholds (17–19). Al-

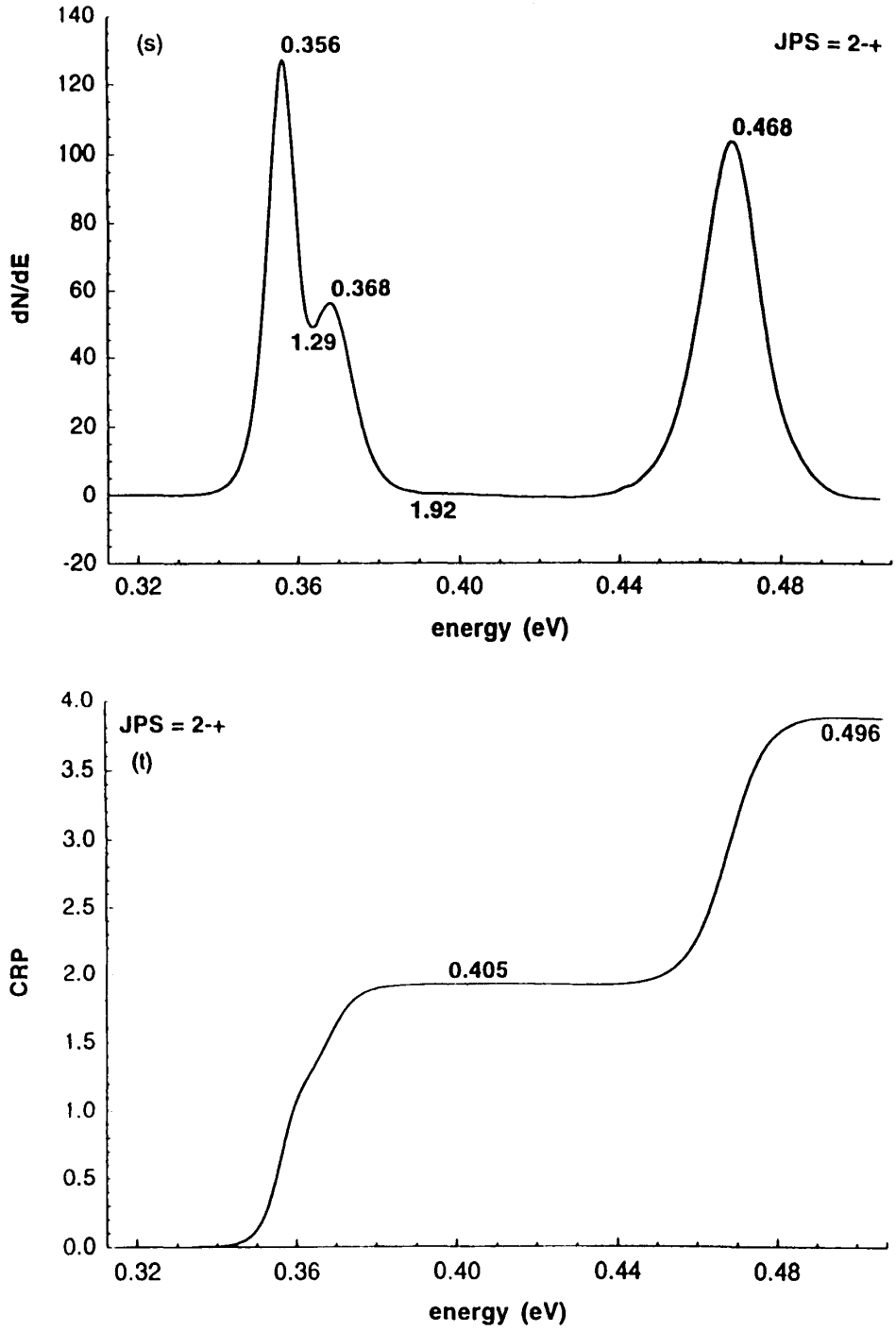

Figure 8 Continued.

though quasibound resonance features and other complicated dependencies of state-to-state reaction probabilities on energy and initial and final states are observable for the reactions discussed above, the cumulative reaction probability for these reactions is remarkably free of such structures and, as discussed above, clearly exhibits the influence of quantized transition states. This is not the case for the halogen-hydrogen halide reactions. However, as we discuss below, the influence of quantized transition states un-

Table 10 Asymptotic H_2 Eigenenergies for the 6SEC Potential Energy Surface for the FH_2 System

j	E_j (eV)	$E_j - E_0$ (meV)	$(E_j - E_0)/j(j+1)$ (meV)
0	0.2687	0.0	—
1	0.2834	14.7	7.4
2	0.3126	43.9	7.3
3	0.3561	87.4	7.3
4	0.4135	144.8	7.2
5	0.4843	215.6	7.2
6	0.5679	299.2	7.1

Table 11 Transition State Level Assignments and Transmission Coefficients for $F + H_2$ on the 6SEC Surface

				Contributing channels[a]				
j	J	P	S	ℓ	K	E_τ (eV)	$E_\tau - 318$ (meV)	κ_τb
0	0	+	+	0	0	0.318		0.96
	1	−	+	1	0	0.318		0.96
	2	+	+	2	0	0.319	0–1	0.96
1	0	+	−	1	0	0.338		0.98
	1	−	−	0,2	0,1	0.329, 0.338		0.95
	1	+	−	1	1	0.329		0.98
	2	+	−	1,3	0,1	0.333, 0.333		0.94
	2	−	−	2	1	0.330	11–20	0.98
2	0	+	+	2	0	0.363		0.89
	1	−	+	1,3	0,1	0.365, 0.365		0.95
	1	+	+	2	1	0.366		0.99
	2	+	+	0,2,4	0,1,2	0.356, 0.356, 0.363		0.92
	2	−	+	1,3	1,2	0.356, 0.368	38–50	0.96
3	0	+	−	3	0	0.407		0.90
	1	−	−	2,4	0,1	0.408, 0.408		0.93
	1	+	−	3	1	0.409		0.92
	2	+	−	1,3,5	0,1,2	0.409, 0.409, 0.409		0.94
	2	−	−	2,4	1,2	0.408, 0.408	89–91	0.96
4	0	+	+	4	0	0.466		0.83
	1	−	+	3,5	0,1	0.467, 0.467		0.89
	1	+	+	4	1	0.467		0.98
	2	+	+	2,4,6	0,1,2	0.468, 0.468, 0.468		0.89
	2	−	+	3,5	1,2	0.468, 0.468	148–150	0.98

[a]We give the labels of the contributing channels using both the space-frame and body-frame representations.
[b]For degenerate or near-degenerate clusters, κ_τ is the average transmission coefficient.

Table 12 Assignments of FH_2 Quantized Transition States[a]

J	P	S	E_r (eV)	Maximum contributor		
				j	K	Fraction
0	+	−	0.338	1	0	0.990
			0.407	3	0	0.988
1	+	−	0.329	1	1	0.990
			0.409	3	1	0.986
1	−	−	0.329	1	1	0.988
			0.338	1	0	0.988
			0.408	3	0	0.532
			0.408	3	1	0.531
2	−	−	0.330	1	1	0.990
			0.408	3	2	0.928
			0.408	3	1	0.918
2	+	−	0.333	1	1	0.982
			0.333	1	0	0.982
			0.409	3	2	0.854
			0.409	3	0	0.519
			0.409	3	1	0.530

[a] E_r values from Table 11; assignments and fractional contributions based on reduced-dimensionality eigenvalue calculations.

derlies the relatively narrow structures that, at first view, are most prominent in the cumulative reaction probabilities for these reactions.

There has been considerable interest by other workers in the resonance structure of reactions of the type X + HX. Many calculations have been performed for such reactions, and it is beyond the scope of this chapter to review them all. We refer the interested reader to other sources (10,11,17–19,148–159) and mention only a few calculations in particular. Quasibound states for collinear reactions of the type X + HX were predicted on the basis of quantum mechanical scattering calculations as early as 1981 (148,150,152), and these states were related to wells in one-dimensional model potentials (148,152). Approximate three-dimensional calculations (156) employing LEPS-type potential energy surfaces (150,152) for ClHCl, IHI, and IDI also located quasibound states, which further model calculations (152,158) were useful in understanding. Accurate three-dimensional quantum mechanical scattering calculations for Cl + HCl (17), I + HI (18), and I + DI (19) were reported by Schatz in 1989. He too employed LEPS-type potential energy surfaces (150,152). The calculated CRPs exhibit an overall increase with energy, on which narrow oscillations are superimposed. The CRP for Cl + HCl exhibits a sharp feature at 0.641 eV that has been interpreted as a trapped-state resonance (17), just below the threshold for reaction of $v = 1$ vibrationally excited reactants. The I + HI and I + DI calculated CRPs also exhibit trapped-state resonance features, in both cases just below the overall threshold to reaction (18,19). On the basis of oscillations in state-selected reaction probabilities, Schatz associated the other oscillations, which occur with roughly the rotational spacing of the reactant diatom, with rotational thresholds for hindered rotor states (17–19).

Experimental evidence for the vibrational structure of XHX transition states has been provided by photoelectron spectroscopy of XHX^- anions with X = Cl, Br, and I (134,160–163). This technique, by inducing photodetachment of an electron from the XHX^- anions, probes the Franck-Condon region, which is believed for these systems to include geometries in the vicinity of the transition state region for the neutral systems. Spectral bands have been interpreted as evidence for trapped-state resonances associated with asymmetric stretch-excited levels of the transition state (160–163), and they are in general agreement with synthetic photoelectron spectra calculated from the scattering computations of Schatz (17–19). In recent experimental spectra (158,162), more closely spaced oscillations have been observed; these are apparently related to rotational thresholds as described by Schatz.

In the rest of this section we discuss our analysis (10,11) of the accurate cumulative reaction probabilities for the halogen-hydrogen halide systems that were published by Schatz (17–19). The CRPs were digitized with an optical scanner, which introduces negligible error. The accurate $N^0(E)$ was fit with cubic splines and convoluted using Eq. (20). Our analysis is based on the observation that the calculated CRPs of Schatz for Cl + HCl, I + HI, and I + DI appeared to have an overall steplike structure reminiscent of that associated with quantized transition states, underlying the narrower features associated with trapped-state resonances and rotational thresholds. Our conclusion that quantized transition states exert broad control of the chemical reactivity for these reactions is not inconsistent with Schatz's description of the narrow trapped-state resonance and rotational threshold features. These different sorts of dynamical features represent different time scales, with the shorter-time (broader) features being more closely related to the traditional concern of chemical kinetics, i.e., reactivity, as discussed below Eq. (23). The relationship of features in the CRP to features in the photoelectron spectrum is not fully worked out yet.

In 1992, Darakjian et al. (164) reported quantum dynamics calculations for the reaction $He + H_2^+ \rightarrow HeH^+ + H$ with $JPS = 0++$. Like the halogen-hydrogen halide reactions, this reaction exhibits a cumulative reaction probability with many narrow resonance structures, spaced about 0.005–0.01 eV apart over the entire energy range. However, it appears that these narrow structures were superimposed on a more coarsely grained, broader structure reminiscent of the steps in the cumulative reaction probability identified with quantized transition states in the $H + H_2$ reaction. Darakjian and coworkers (164) therefore applied an averaging procedure (165,166) to the raw cumulative reaction probability to bring out the quantized transition state structure. When they averaged over an interval of 0.01 eV, the underlying structure appeared with surprising clarity, revealing quantized transition states spaced about 0.07 eV apart. A similar treatment has identified quantized transition state influence of the reaction of Ne with H_2^+ (167–169).

The finite-resolution density of reactive states introduced in Sec. II is especially useful for analyzing the halogen-hydrogen halide reactions because, as stated above, the features due to quantized transition states are partially obscured in these systems by a number of narrow resonances associated with other regions of the potential energy surfaces. Therefore the accurate cumulative reaction probabilities $N^0(E)$ were convoluted with a Gaussian function of variable width F to obtain finite-resolution cumulative reaction probabilities $N^0(E; F)$. Analysis of $dN^0(E; F)/dE$ reveals the influence of quantized transition states underlying the narrower dynamical features of $N^0(E)$.

A. Cl + HCl

Finite-resolution ρ^0 are shown for Cl + HCl in Fig. 9. The value of F was chosen to optimize the separation of scales, smoothing over narrow features while leaving broader structure intact.

The raw $\rho^0(E)$ has many rapid oscillations that are very difficult to interpret. Convolution of $N^0(E)$ for Cl + HCl with a Gaussian having a width parameter F of 0.027 eV (corresponding to Δt = 24 fs) produces a finite-resolution CRP increasing almost monotonically with energy (11) and having clearly recognizable steplike features reminiscent of the H + H_2 and O + H_2 reactions. The corresponding density in Fig. 9 has seven well-defined features and one noticeable shoulder.

Structures suggestive of quantized transition states are discernible even in the unconvoluted $N^0(E)$. The initial rise between 0.40 and 0.45 eV is quite marked, so we assign this feature as [00^0]. Since $N^0(E)$ reaches about 1 by 0.45 eV, the feature corresponds to a nearly ideal dynamical bottleneck. The rapid rise at 0.66–0.67 eV has been shown to be due to a dynamical threshold for formation of vibrationally excited $v' = 1$ products (157), so we assign it as [10^0]. Other features in $N^0(E)$, however, are associated with different kinds of dynamical effects. For example, the sharp peak at 0.647 eV has been identified previously as a trapped-state resonance, and the broader features between 0.5 and 0.6 eV have been associated with rotational thresholds of the asymptotic diatom (17).

The influence of the remaining quantized transition states is identified on the basis of the features in the finite-resolution density $\rho^0(E;0.027)$ in Fig. 9 and the incremental

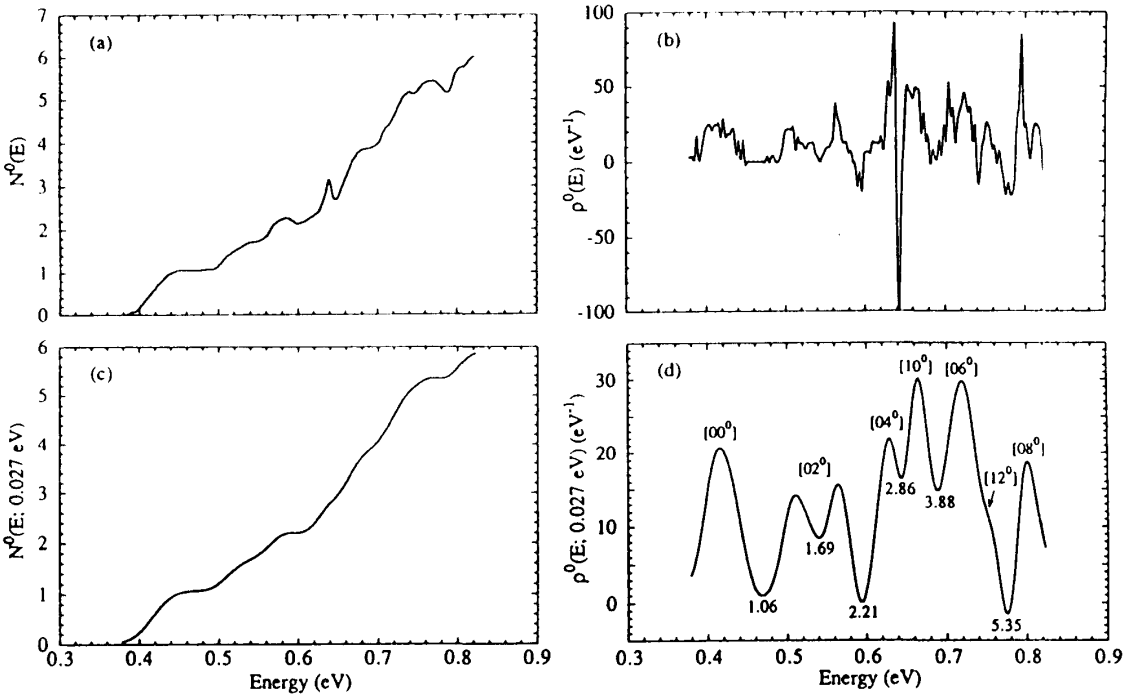

Figure 9 Original and finite-resolution densities of reactive states for the Cl + HCl reaction with J = 0. (a) $N^0(E)$. (b) $\rho^0(E)$. (c) $N^0(E;$ 0.027 eV). (d) $\rho^0(E;$ 0.027 eV). The value of $N^0(E; F)$ is indicated at each minimum in $\rho^0(E; F)$. (Reprinted with permission from Ref. 11, copyright 1992, American Chemical Society.)

rise in $N^0(E;0.027)$ (between the energies of minima between peaks in $\rho^0(E;0.027)$). The first peak corresponds to the initial step in $N^0(E)$ already identified as $[00^0]$; $N^0(E;0.027)$ reaches 1.06 at the minimum following it (0.416 eV). The next two peaks near 0.5 and 0.6 eV are traceable to the rotational thresholds identified in $N^0(E)$. Since $N^0(E;0.027)$ reaches 2.21 at the minimum following them (at 0.594 eV), we conclude that a single quantized transition state is predominantly responsible for the increase in reactive flux over this energy range, and so we assign both of these features as $[02^0]$. One interpretation of the fact that this transition state leads to two peaks rather than one is that there is some intermediate-time structure that is not totally removed by the 0.027-eV-wide averaging procedure. The tail of the next higher feature also contributes to the value of $N^0(E;0.027)$ at 0.594 eV.

Between 0.594 eV and the minimum at 0.775 eV, $\rho^0(E;0.027)$ exhibits three peaks and one shoulder. The peak at 0.665 eV is associated with the rapid rise in $N^0(E)$ already identified as $[10^0]$. Between the minima on either side of this peak, $N^0(E;0.027)$ rises by close to unity (from 2.86 to 3.88). The preceding peak is identified as $[04^0]$, the next even-ν_2 bend state in the ground-stretch manifold. The peak and shoulder following the $[10^0]$ feature are assigned as $[06^0]$ and $[12^0]$, respectively, on the basis of the energy spacing of bend states in the ground-stretch manifold.

Up to 0.735 eV, then, we assign six quantized transition states, and $N^0(E;0.027)$ reaches 5.35. This is in accord with the quantized transition states being good dynamical bottlenecks and exerting predominant control of the chemical reactivity. If our assignments are correct, the average transmission coefficient κ_τ for the six states up to 0.735 eV is 0.89, or 89% of its ideal value.

The remaining feature in the finite-resolution spectrum, at 0.800 eV, is more difficult to assign. On the basis of energy spacings it appears to be $[08^0]$.

It is especially interesting to note that the short- and long-time dynamics of Cl + HCl are sufficiently separated in time scale that an energy resolution of 0.027 eV washes out almost all features due to the latter in $N^0(E)$ and $\rho^0(E)$. The trapped-state resonance responsible for the 0.66–0.67 eV peak in $N^0(E)$ and the rapid oscillation in $\rho^0(E)$ is not discernible in the finite-resolution spectra. Only the broader rotational thresholds near 0.5 and 0.6 eV survive the averaging procedure. These occur on a time scale similar to that of the quantized transition states and cannot as easily be separated.

B. I + HI and I + DI

Raw and finite-resolution spectra for the I + HI reaction are shown in Fig. 10. The method of analysis (11) is similar to that used for Cl + HCl.

The raw $N^0(E)$ exhibits steplike features suggestive of quantized transition states (11). Superimposed on these are wide oscillations which have been identified with rotational thresholds. The corresponding derivative curve shows many rapid oscillations that are difficult to interpret.

In the finite-resolution spectra with a resolution function of 0.027 eV, the rapid oscillations are washed out, as illustrated in Fig. 10. The difference in time scale between the rotational thresholds and the quantized transition states for I + HI is sufficient to separate them with an appropriate resolution function. A vibrationally adiabatic analysis of I + HI predicts the $[10^0]$ threshold at 0.422 eV, which is beyond the energy scale of Fig. 10. Therefore we assign all the features in the finite-resolution density in Fig. 10 to the ground-stretch manifold. By the minimum of $\rho^0(E;0.027)$ at 0.357 eV, $N^0(E;0.027)$

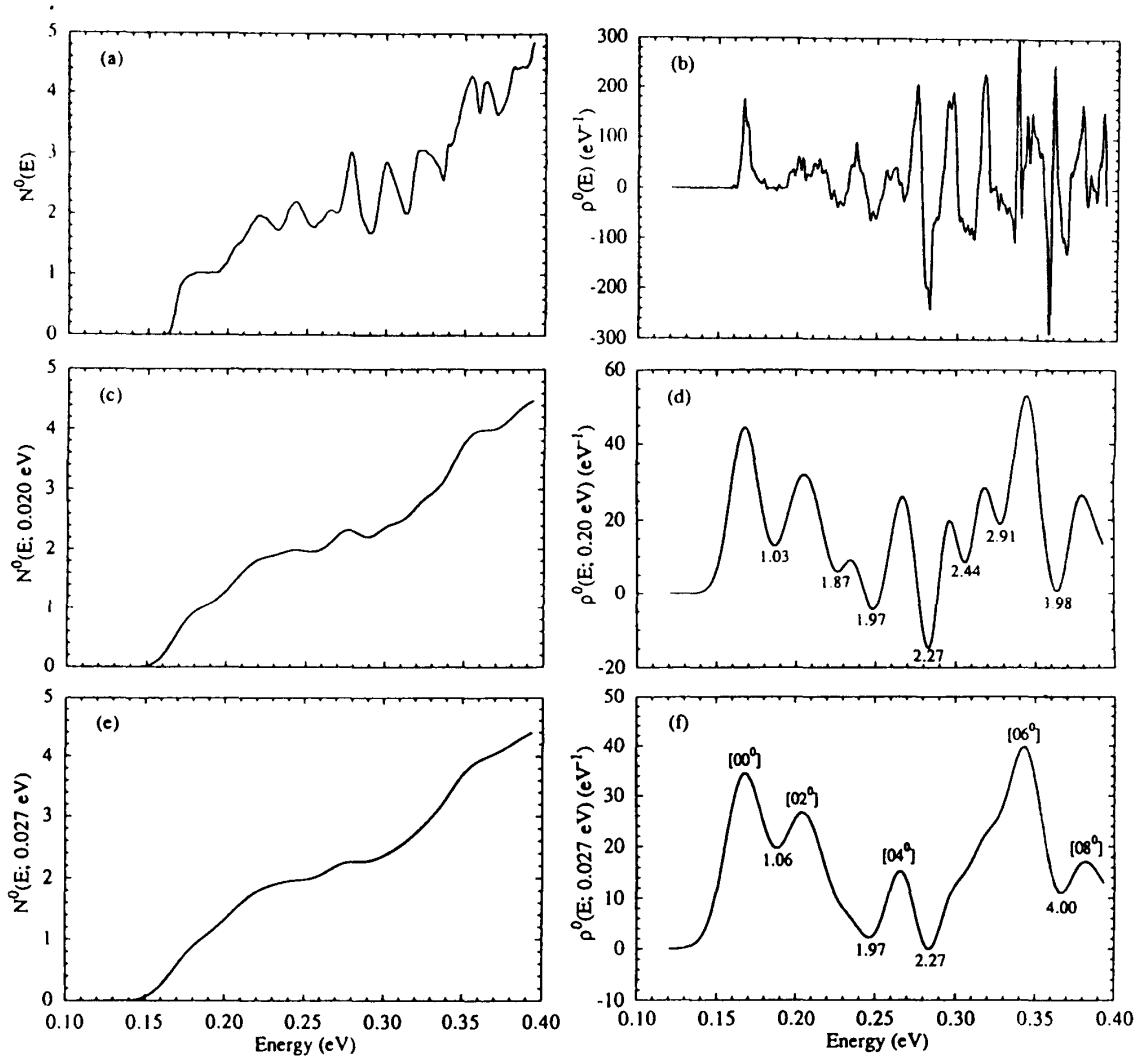

Figure 10 Original and finite-resolution densities of reactive states for the I + HI reaction with $J = 0$. (a) $N^0(E)$. (b) $\rho^0(E)$. (c) $N^0(E; 0.020\text{ eV})$. (d) $\rho^0(E; 0.020\text{ eV})$. (e) $N^0(E; 0.027\text{ eV})$. (f) $\rho^0(E; 0.027\text{ eV})$. The value of $N^0(E; F)$ is indicated at each minimum in $\rho^0(E; F)$. (Reprinted with permission from Ref. 11, copyright 1992, American Chemical Society.)

reaches 4.00. We identify four quantized transition states ([00^0], [02^0], [04^0], and [06^0]) with the four peaks in this range. Thus the four lowest-energy quantized transition states for this reaction gate the flux with apparent unit efficiently (i.e., $\kappa_\tau = 1$), exerting dominant control of the dynamics.

The analysis for I + DI is very similar to that for I + HI and Cl + HCl. With an energy resolution of 0.025 eV, seven quantized transition states were identified up to 0.42 eV, and the average value of κ_τ was 0.8 (11).

C. Spectroscopic Constants for Halogen-Hydrogen Halide Systems

Quantal spectroscopic constants, as defined in Eq. (25), were calculated for the three reactions from fits to assigned peak energies in the finite-resolution density. Vibrationally adiabatic thresholds (the maxima in vibrationally adiabatic curves calculated using the procedure described for H + H_2) were also least-squares fit with Eq. (25). Results are

Table 13 Spectroscopic Constants of ClHCl, IHI, and IDI Quantized Transition States

	E_0 (eV)	ω_1 (cm^{-1})	ω_2 (cm^{-1})	x_{22} (cm^{-1})	x_{12} (cm^{-1})
ClHCl					
quantal	0.231	2010	497	−11.2	
adiabatic	0.271	1920	671	17.4	−269
IHI					
quantal	a	a	235		
adiabatic	6.65(−3)[b]	2200	253	26.8	−154
IDI					
quantal	8.80(−3)	1560	230		
adiabatic	1.72(−2)	1450	192	14.2	−78.5

[a] $E_0 + 0.5hc\omega_1 = 0.139$ eV = 1124 cm^{-1}.
[b] (−3) indicates 10^{-3}.

in Table 13. In general, the quantal and adiabatic values for ω_1 and ω_2 are in good agreement. They differ by 5% (ω_1) and 30% (ω_2) for Cl + HCl, 8% (ω_2) for I + HI, and 7% (ω_1) and 17% (ω_2) for I + DI. (We did not obtain a value for ω_1 for I + HI.) The good agreement of the accurate and adiabatic values supports the quantized transition state assignments for features in the finite-resolution density.

We note that vibrationally adiabatic treatment yields a large magnitude of x_{12} for Cl + HCl, in particular, $x_{12} = -269$ cm^{-1}. This is a consequence of the transition state geometries. The ground-stretch thresholds are at the symmetric saddle point, but the stretch-excited thresholds are displaced toward the asymptotic species. The bending frequencies for these different structures are expected to be quite different, resulting in a large magnitude for x_{12}.

The Cl + HCl quantized transition states have also been studied by Cohen et al. (159), using semiclassical transition state theory based on second-order perturbation theory for cubic force constants and first-order perturbation theory for quartic ones. Their treatment yielded $\omega_1 = 339$ cm^{-1} and $\omega_2 = 508$ cm^{-1}. The former is considerably lower than the values extracted from finite-resolution quantal densities of reactive states and from vibrationally adiabatic analysis, 2010 and 1920 cm^{-1} respectively (11), but the bend frequency ω_2 is in good agreement with the previous (11) values, 497 and 691 cm^{-1} from quantum scattering and vibrationally adiabatic analyses respectively. The discrepancy in the stretching frequency is a consequence of Cohen et al. using second-order perturbation theory in the vicinity of the saddle point rather than the variational transition state. As discussed elsewhere (88), second-order perturbation theory is inadequate to capture large deviations in position of the variational transition state from the saddle point.

IX. OTHER SYSTEMS

A. Rare Gas + H_2^+: Theory

Darakjian et al. (164) computed accurate densities of reactive states for He + $H_2^+ \rightarrow$ HeH^+ + H with $J = 0$. The raw CRP exhibited many rapid oscillations, indicative of narrow trapped-state resonances. By averaging the cumulative reaction probability for

the even spatial permutation symmetry block over a range of 0.02 eV, they obtained a cumulative reaction probability exhibiting four steplike features up to 1.30 eV that were interpreted as quantized transition states. Each of these steps was approximately unity, suggesting that quantized transition states functioning as good dynamical bottlenecks underlie the narrow, trapped-state resonances. Further analysis was provided by Klippenstein and Kress (165); and their density of reactive states (a derivative of an averaged CRP), summed over both symmetry blocks, also shows four clear peaks up to 1.30 eV, and seven peaks (and three shoulders) up to 1.50 eV. The variational transition states in this system are far out in the exit valley, and, as a result, the energy spacings of the steps correlate with product rotational energy spacings.

Kress (167) reported the first converged quantum results for the reaction Ne + $H_2^+ \rightarrow NeH^+ + H$ with $J = 0$. He observed six steps in an averaged cumulative reaction probability and six peaks in the density of reactive states. The spacing is fairly constant and is the range 0.05–0.08 eV. In a follow-up paper (168), Kress and Klippenstein assigned all six states and discussed statistical corrections to variational transition state theory associated with supernumerary transition states. Further analysis and discussion was provided by Kress et al. (169).

B. H + O_2: Theory

Pack and co-workers (166,170) calculated cumulative reaction probabilities for the combustion reaction $H + O_2 \rightarrow OH + O$ with zero total angular momentum. The raw CRP has many narrow resonance features. When the CRP was convoluted with Gaussians, however, the resonance features were sufficiently smoothed that the resulting CRP shows steplike features that the authors interpreted as possibly representing quantized transition states. They noted in particular that the positions and spacings of the steps correspond well with some effective potential barriers in the exit valley. Further calculations on this system were reported by Leforestier and Miller (171). Their CRP curve agrees qualitatively with that of Pack and co-workers, but the energy grid is less fine and the CRP does not display narrow resonance features until after the first two steplike increases in the CRP, from 0 to 1 and from 1 to 2, each of which is quite clean.

C. Li + HF: Theory

Another system where accurate microcanonical rate constants have been calculated is $Li + HF \rightarrow LiF + H$ with $J = 0$ (172). This reaction has variational transition states in the exit valley. Variational transition state theory agrees very well with accurate quantum dynamical calculations up to about 0.15 eV above threshold. After that, deviations are observed, increasing to about a factor of 2 about 0.3 eV above threshold. These deviations were attributed to effective barriers in the entrance valley; these are supernumerary transition states. After Gaussian convolution of the accurate results, only a hint of step structure due to the variational transition states remains. Densities of reactive states, which would make the transition state spectrum more visible, were not published (172).

D. Cl + H_2: Theory

We have also carried out accurate quantum scattering calculations for the reaction $Cl + H_2 \rightarrow HCl + H$, which is about 0.13 eV endothermic in a Born-Oppenheimer sense and about 0.05 eV endothermic when zero-point energy is included. We used the G3 potential

energy surface (173) on which the Born-Oppenheimer barrier height is about 0.34 eV. Thus this is another nearly thermoneutral system of the A + H_2 type, with, however, a barrier height somewhat smaller than that for D + H_2 and O + H_2. For $JPS = 0++$, the CRP rises monotonically and the density of reactive states shows several clearly resolved quantized transition states. The lowest state, $[00^0]$, leads to a well-resolved plateau in the CRP at ~1.0, which is similar to the behavior seen above for H + H_2, D + H_2, and O + H_2. The next two peaks may be assigned to $[02^0]$ and a supernumerary transition state of the first kind with quantum numbers $[10^0]$. The value of the CRP at the local minimum following the third peak in the density is only about 1.8, though. The mere fact that the $[10^0]$ supernumerary transition state is one of the first kind indicates that the fundamental no-recrossing assumption of transition state theory is less valid for this system than for the other A + H_2 systems, and a value of only 1.8 for the CRP at the local minimum preceding the third variational transition state further illustrates the nonideal nature of the dynamics in this system, which will provide an interesting case for further analysis.

E. Experiment

Experimental detection of quantized transition states has been impeded by the difficulty of carrying out experiments in which only one or a few values of the total angular momentum J contribute to the signal. Otherwise the smearing effect of many values of J will tend to hide structure due to quantized transition states. Nevertheless, in the past five years, sophisticated measurements have supplied evidence for the influence of quantized transition states on a number of reactions.

We have already mentioned the interpretation of photodetachment spectra of FH_2^- and XHX^- (X = Cl, Br, I), in terms of quantized transition state resonances. Similar experiments have been carried out for IDI^-, OHF^-, $OHCl^-$, $OHOH^-$, and $HOHOH^-$ (174–177), and these experiments have been interpreted in terms of resonances and other types of vibration-rotation energy level structure associated with the transition state species of the neutral product (10,11,17–19,162,163,174–178). The FH_2^- and FD_2^- photodetachment experiments provide a particularly striking example of the observation of quantized transition states in experimental spectra (133–135). In theoretical work carried out to analyze recent experimental work on photodetachment, in particular for $OHCl^-$ (176), the calculated cumulative reaction probability for the O + HCl reaction showed steps at quantized hindered rotor energies (as well as sharper resonances due to trapped states), but the steps had transmission coefficients considerably smaller than unity.

Photodissociation experiments provide one route to observing the dynamics associated with a single value of J, and as such would be expected (179) to be a good place to look for quantized transition state structure. For the photodissociation of triplet ketene, Lovejoy et al. (180) reported direct observation of a step in the microcanonical rate constant associated with a vibrationally excited transition state, and they interpreted their results using a theoretical framework similar to that used in Sec. IV. Further analysis was provided in later papers (181–183), including a discussion of subthreshold transmission resonances such as have also been predicted theoretically (184,185). The most recent paper from the Moore group (183) exhibits approximately three distinct steps each for photodissociation of CH_2CO and CD_2CO with further structure presumably corresponding to unresolved steps at higher energies. For CH_2CO the first peak was assigned to a

C—C—O bend, and another peak was assigned as a combination of the C—C—O bend with one quantum of hindered rotation.

Another experimental system where steplike structure possibly related to quantized transition states was observed is the work of Wittig and co-workers (186–188) on NO_2 dissociation; these experiments have been further analyzed by Klippenstein and Radivoyevitch (189) and Katagiri and Kato (190), both of whose studies indicate that the interpretation may be more complicated. Wittig and co-workers concluded (187) that the steps observed in the experimental microcanonical rate constants may correspond to overlapping of vibrationally adiabatic thresholds.

Choi et al. measured the *cis-trans* isomerization rate of *trans,trans*-1,3,5,7-octatetraene by exciting its vibronic bands in a supersonic jet and observing fluorescence decay (191). Choi et al. noticed a stepwise increase in the isomerization rate with energy, which they attributed to quantization of the vibrational levels of the transition state for *cis-trans* isomerization of a double bond. This study is especially noteworthy because quantization is observed in a molecule with 48 degrees of freedom. The energy spacing of 80 ± 10 cm^{-1} between the first two steps was tentatively assigned to an in-plane bending vibration of the transition state.

X. CONCLUDING REMARKS

In transition state theory it is assumed that a dynamical bottleneck in the interaction region controls chemical reactivity. Transition state theory relates the rate of a chemical reaction in a microcanonical ensemble to the number of energetically accessible vibrational-rotational levels of the interacting particles at the dynamical bottleneck. In spite of the success of transition state theory, direct evidence for a quantized spectrum of the transition state has been found only recently, and this evidence was found first in accurate quantum mechanical reactive scattering calculations. Quantized transition states have now been identified in accurate three-dimensional quantal calculations for 12 reactive atom-diatom systems. The systems are $H + H_2$, $D + H_2$, $O + H_2$, $Cl + H_2$, $H + O_2$, $F + H_2$, $Cl + HCl$, $I + HI$, $I + DI$, $He + H_2^+$, $Ne + H_2^+$, and $O + HCl$.

In this chapter we reviewed the evidence for the quantized nature of the spectrum of the transition state based on exact quantum mechanical reactive scattering calculations. We discussed fitting the accurate computational results by a model with level-dependent transmission probabilities that include recrossing effects and that account for tunneling and nonclassical reflection based on parabolic effective barriers. We discussed global control of reactivity for both zero and nonzero total angular momentum, and we also discussed the degree of ideality of the individual dynamical bottlenecks. We assigned quantum numbers to individual transition state levels by comparison of the results with maxima in vibrationally adiabatic potential curves. We discussed the relevance of the concept of vibrational adiabaticity for the accurate dynamics. We obtained spectroscopic constants for the quantized transition state by fitting to a truncated Taylor series in the vibrational quantum numbers. We also drew an explicit connection between quantized transition states and quantum mechanical quasibound states, both of which are related to poles of the scattering matrix. In this connection we discussed the relationship of thresholds and resonances. We derived transition state lifetimes for the $H + H_2$ transition states by identifying the lifetimes with the imaginary parts of the resonance energies and relating those imaginary energies to the effective parabolic potentials implied by the fit.

We also noted the reformulation of variational transition state theory in terms of quantum mechanical resonance theory.

We discussed the implications of the O + H_2 reaction's multiple bottleneck regions in terms of variational and supernumerary transition states. We related the observed features to the scattering results for asymmetrical Eckart potentials. We emphasized that global control is maintained to very high energy (1.9 eV) and very high levels of v_2. We demonstrated the influence of quantized transition states at the level of state-selected reaction probability for this reaction.

Next, using D + H_2 as an example, we showed that quantized transition state spectra can be observed and analyzed even for very high total angular momenta, up to 15.

Using F + H_2 as an example, we discussed the correspondence of peaks in the photoelectron spectrum of the negative ion of the transition state with individual quantized transition states for $J = 0-2$. This system is very interesting in that the quantized energy levels show an internal rotation progression, and the average transmission coefficient is 0.95, with all transmission coefficients in the range 0.83–0.98. The ability to assign transmission coefficients to individual levels of the quantized transition state is one of the most remarkable developments of the theoretical analysis of accurate quantal reaction probabilities to date.

We also presented an analysis of halogen-hydrogen halide calculations. We discussed a formalism for probing the reaction at a finite time resolution by convoluting the exact results with a Gaussian function. We demonstrated that quantized transition states dominate the short time dynamics.

Accurate quantal dynamics calculations play important roles in predicting experimentally observable rates, cross sections, and transition probabilities, in elucidating and uncovering quantal phenomena, and in testing approximate dynamics calculations and models. The implementation of quantum mechanical scattering theory for quantal dynamics calculations on bimolecular collisions has become increasingly practical in recent years, especially for reactive collisions (8,12,77,96,101,102,164,166,167,192–220). The use of accurate quantum calculations for transition state spectroscopy, as reviewed in this chapter, provides an especially clear-cut example of where the calculations help us uncover fundamental quantum structures in nature that have a very significant impact even on highly averaged rate phenomena.

ACKNOWLEDGMENTS

The authors are grateful to Yuri Volobuev for participation in early stages of the DH_2 analysis and to Professor Ken Leopold for helpful discussions. The quantum mechanical scattering calculations were supported in part by the National Science Foundation. The variational transition state theory calculations were supported in part by the U.S. Department of Energy, Office of Basic Energy Sciences.

REFERENCES

1. M. M. Kreevoy and D. G. Truhlar, Transition state theory, *Investigation of Rates and Mechanisms of Reactions* (C. F. Bernasconi, ed.) [*Techniques of Chemistry*, 4th ed., A. Weissberger (ed.)], John Wiley & Sons, New York, 1986, Part I, pp. 13–95.

2. G. Herzberg, *Electronic Spectra and Electronic Structure of Polyatomic Molecules* [*Molecular Spectra and Molecular Structure*, Vol. III], Van Nostrand Reinhold, New York, 1966, pp.. 458ff.
3. A. Bohm, *Quantum Mechanics*, 3rd ed., Springer-Verlag, New York, 1993, pp. 452–569.
4. J. Simons, Roles played by metastable states in chemisry, *ACS Symp. Ser. 263*: 3 (1984).
5. *Resonances*, E. Brändas and N. Elander (eds.) [*Lecture Notes in Physics*, Vol. 325], Springer-Verlag, Berlin, 1989.
6. P. D. Kleiber, A. M. Lyyra, K. M. Sando, V. Zafiropulos, and W. C. Stwalley, Reactive collision dynamics by far wing laser scattering: Mg + H_2, *J. Chem. Phys. 85*: 5493 (1986).
7. J. C. Polanyi, M. G. Prisant, and J. S. Wright, Spectroscopy of the transition state (theory). 4. Absorption by $HFH^{\ddagger}$ in H + FH′ → $HFH^{\ddagger}$ → HF + H′, *J. Phys. Chem. 91*: 4727 (1987).
8. D. C. Chatfield, R. S. Friedman, D. G. Truhlar, B. C. Garrett, and D. W. Schwenke, Global control of suprathreshold reactivity by quantized transition states, *J. Am. Chem. Soc. 113*: 486 (1991).
9. D. C. Chatfield, R. S. Friedman, D. G. Truhlar, and D. W. Schwenke, Quantum-dynamical characterization of reactive transition states, *Faraday Discuss. Chem. Soc. 91*: 289 (1991).
10. D. C. Chatfield, R. S. Friedman, G. C. Lynch, and D. G. Truhlar, Discussion remarks, *Faraday Discuss. Chem. Soc. 91*: 398 (1991).
11. D. C. Chatfield, R. S. Friedman, G. C. Lynch, and D. G. Truhlar, Quantized transition-state structure in the cumulative reaction probabilities for the Cl + HCl, I + HI and I + DI reactions, *J. Phys. Chem. 96*: 57 (1992).
12. K. Haug, D. W. Schwenke, D. G. Truhlar, Y. Zhang, J. Z. H. Zhang, and D. J. Kouri, Accurate quantum mechanical reaction probabilities for the reaction O + H_2 → OH + H, *J. Chem. Phys. 87*: 1892 (1987).
13. J. M. Bowman, Comparison of reduced dimensionality and accurate cumulative reaction probabilities for $O(^3P)$ + H_2 (v = 0, 1), *Chem. Phys. Lett. 141*: 545 (1987).
14. D. C. Chatfield, R. S. Friedman, G. C. Lynch, D. G. Truhlar, and D. W. Schwenke, The nature and role of quantized transition states in the accurate quantum dynamics of the reaction O + H_2 → OH + H, *J. Chem. Phys. 98*: 342 (1993).
15. G. C. Lynch, P. Halvick, M. Zhao, D. G. Truhlar, C.-H. Yu, D. J. Kouri, and D. W. Schwenke, Converged three-dimensional quantum mechanical reaction probabilities for the F + H_2 reaction on a potential energy surface with realistic entrance and exit channels and comparisons to results for three other surfaces, *J. Chem. Phys. 94*: 7150 (1991).
16. D. C. Chatfield, R. S. Friedman, D. W. Schwenke, and D. G. Truhlar, Control of chemical reactivity of quantized transition states, *J. Phys. Chem. 96*: 2414 (1992).
17. G. C. Schatz, A three dimensional reactive scattering study of the photodetachment spectrum of ClHCl , *J. Chem. Phys. 90*: 3582 (1989).
18. G. C. Schatz, A three-dimensional quantum reactive scattering study of the I + HI reaction and of the IHI^- photodetachment spectrum, *J. Chem. Phys. 90*: 4847 (1989).
19. G. C. Schatz, A three-dimensional quantum reactive scattering study of the I + DI reaction and of the IDI^- photodetachment spectrum, *J. Chem. Soc. Faraday Trans. 86*: 1729 (1990).
20. B. C. Garrett and D. G. Truhlar, Generalized transition state theory. Classical mechanical theory and applications to collinear reactions of hydrogen molecules, *J. Phys. Chem. 83*: 1052 (1979). Errata: *83*: 3058 (1979): *87*: 4553 (1983).
21. R. A. Marcus, Chemical-reaction cross sections, quasiequilibrium, and generalized activated complexes, *J. Chem. Phys. 45*: 2138 (1966).
22. F. T. Smith, Scattering matrix and chemical reaction rates, *J. Chem. Phys. 36*: 248 (1962).
23. W. H. Miller, Semiclassical limit of quantum mechanical transition state theory for nonseparable systems, *J. Chem. Phys. 62*: 1899 (1975).
24. E. Wigner, Calculation of the rate of elementary association reactions, *J. Chem. Phys. 5*: 720 (1937).

25. J. Horiuti, On the statistical mechanical treatment of the absolute rate of chemical reaction, *Bull. Chem. Soc. Japan 13*: 210 (1938).
26. J. C. Keck, Variational theory of reaction rates, *Adv. Chem. Phys. 13*: 85 (1967).
27. D. G. Truhlar and B. C. Garrett, Variational transition state theory, *Annu. Rev. Phys. Chem. 35*: 159 (1984).
28. S. C. Tucker and D. G. Truhlar, Dynamical formulation of transition state theory: Variational transition states and semiclassical tunneling, *New Theoretical Concepts for Understanding Organic Reactions* (J. Bertrán and I. G. Csizmadia, Eds.), Kluwer, Dordrecht, 1989, p. 291.
29. H. Eyring, The activated complex in chemical reactions, *J. Chem. Phys. 3*: 107 (1935).
30. R. A. Marcus and O. K. Rice, The kinetics of the recombination of methyl radicals and iodine atoms, *J. Phys. Colloid Chem. 55*: 894 (1951).
31. R. A. Marcus, Unimolecular dissociations and free radical recombination reactions, *J. Chem. Phys. 20*: 359 (1952).
32. H. M. Rosenstock, M. B. Wallenstein, A. L. Wahrhaftig, and H. Eyring, Absolute rate theory for isolated systems and the mass spectra of polyatomic molecules, *Proc. Natl. Acad. Sci. USA 38*: 667 (1952).
33. J. L. Magee, Theory of the chemical reaction rate constant, *Proc. Natl. Acad. Sci. U.S.A. 38*: 764 (1952).
34. B. C. Garrett and D. G. Truhlar, Generalized transition state theory. Quantum effects for collinear reactions of hydrogen molecules and isotopically substituted hydrogen molecules, *J. Phys. Chem. 83*: 1079 (1979); Errata: *84*: 682 (1980); *87*: 4553 (1983).
35. D. G. Truhlar, A. D. Isaacson, and B. C. Garrett, Generalized transition state theory, *Theory of Chemical Reaction Dynamics* (M. Baer, ed.), CRC Press, Boca Raton, FL, 1985, Vol. 4, p. 65.
36. E. C. Kemble, *The Fundamental Principles of Quantum Mechanics with Elementary Applications*, Dover, New York, 1958, p. 109.
37. J. J. Sakurai, *Modern Quantum Mechanics*, Addison-Wesley, Redwood City, CA, 1985, pp. 78–80.
38. W. H. Miller, Quantum mechanical transition state theory and a new semiclassical model for reaction rate constants, *J. Chem. Phys. 61*: 1823 (1974).
39. J. W. Tromp and W. H. Miller, New approach to quantum mechanical transition-state theory, *J. Phys. Chem. 90*: 3482 (1986).
40. J. W. Tromp and W. H. Miller, The reactive flux correlation function for collision reactions H + H_2, Cl + HCl, and F + H_2, *Faraday Discuss. Chem. Soc. 84*: 441 (1987).
41. P. N. Day and D. G. Truhlar, Benchmark calculation of thermal reaction rates. II. Direct calculation of the flux autocorrelation function for a canonical ensemble, *J. Chem. Phys. 94*: 2045 (1991).
42. P. N. Day and D. G. Truhlar, Calculation of thermal rate coefficients from the quantum flux autocorrelation function: Converged results and variational quantum transition state theory for O + HD → OD + H and O + HD → OH + D, *J. Chem. Phys. 95*: 5097 (1991).
43. E. J. Heller, Potential surfaces properties and dynamics from molecular spectra: A time-dependent picture, *Potential Energy Surfaces and Dynamics Calculations* (D. G. Truhlar, ed.), Plenum Press, New York, 1981, p. 103.
44. M. J. Seaton, The Hartree-Fock equations for continuous states with applications to electron excitation of the ground configuration terms of O_1, *Philos, Trans. Roy. Soc. London A 245*: 469 (1953).
45. H. S. W. Massey, Theory of the scattering of slow electrons, *Rev. Mod. Phys. 28*: 199 (1956).
46. D. A. Micha, A quantum mechanical model for simple molecular reactions, *Arkiv. Fys. 30*: 411 (1965).
47. W. H. Miller, Coupled equations and the minimum principle for collisions of an atom and a diatomic molecule, including rearrangements, *J. Chem. Phys. 50*: 407 (1969).

48. D. G. Truhlar, J. Abdallah, Jr., and R. L. Smith, Algebraic variational methods in scattering theory, *Adv. Chem. Phys. 25*: 211 (1974).
49. D. G. Truhlar and J. Abdallah, Jr., New methods for calculating scattering cross sections for rearrangement collisions, *Phys. Rev. A 9*: 297 (1974).
50. R. G. Newton, *Scattering Theory of Particles and Waves*, 2nd ed., Springer-Verlag, New York, 1982 (Section 11.3, variational principles; Section 11.2, resonances as poles of the S matrix).
51. G. Staszewska and D. G. Truhlar, Convergence of $\mathscr{L}^2$ methods for scattering problems, *J. Chem. Phys. 86*: 2793 (1987).
52. D. W. Schwenke, K. Haug, D. G. Truhlar, Y. Sun, J. Z. H. Zhang, and D. J. Kouri, Variational basis-set calculations of accurate quantum mechanical reaction probabilities, *J. Phys. Chem. 91*: 6080 (1987).
53. D. W. Schwenke, K. Haug, M. Zhao, D. G. Truhlar, Y. Sun, J. Z. H. Zhang, and D. J. Kouri, Quantum mechanical algebraic variational methods for inelastic and reactive molecular collisions, *J. Phys. Chem. 92*: 3202 (1988).
54. D. W. Schwenke, M. Mladenovic, M. Zhao, D. G. Truhlar, Y. Sun, and D. J. Kouri, Computational strategies and improvements in the linear algebraic variational approach to rearrangement scattering, *Supercomputer Algorithms for Reactivity Dynamics and Kinetics of Small Molecules* (A. Laganà, ed.), Kluwer, Dordrecht, 1989, p. 131.
55. L. Schlessinger, Use of analyticity in the calculation of nonrelativistic scattering amplitudes, *Phys. Rev. 167*: 1411 (1968).
56. Y. Sun, D. J. Kouri, D. G. Truhlar, and D. W. Schwenke, Dynamical basis sets for algebraic variational calculations in quantum-mechanical scattering theory, *Phys. Rev. A 41*: 4857 (1990).
57. Y. Sun, D. J. Kouri, and D. G. Truhlar, A comparative analysis of variational methods for inelastic and reactive scattering, *Nucl. Phys. A508*: 41c (1990).
58. D. W. Schwenke, S. L. Mielke, and D. G. Truhlar, Variational reactive scattering calculations: computational optimization strategies, *Theor. Chim. Acta 79*: 241 (1991).
59. J. Z. H. Zhang, D. J. Kouri, K. Haug, D. W. Schwenke, Y. Shima, and D. G. Truhlar, $\mathscr{L}^2$ amplitude density method for multichannel inelastic and rearrangement collisions, *J. Chem. Phys. 88*: 2492 (1988).
60. D. W. Schwenke and D. G. Truhlar, Localized basis functions and other computational improvements in variational nonorthogonal basis function methods for quantum mechanical scattering problems involving chemical reactions, *Computing Methods in Applied Sciences and Engineering* (R. Glowinski and A. Lichnewsky, Eds.), SIAM, Philadelphia, 1990, p. 291.
61. S. L. Mielke, D. G. Truhlar, and D. W. Schwenke, Improved techniques for outgoing wave variational principle calculations of converged state-to-state transition probabilities for chemical reactions, *J. Chem. Phys. 95*: 5930 (1991).
62. G. J. Tawa, S. L. Mielke, D. G. Truhlar, and D. W. Schwenke, Algebraic variational and propagation formalisms for quantal dynamics calculations of electronic-to-vibrational, rotational energy transfer and application to the quenching of the 3p state of sodium by hydrogen molecules, *J. Chem. Phys. 100*: 5751 (1994).
63. G. J. Tawa, S. L. Mielke, D. G. Truhlar, and D. W. Schwenke, Linear algebraic formulation of reactive scattering with general basis functions, *Advances in Molecular Vibrations and Collision Dynamics*, Vol. 2B (J. M. Bowman, ed.), JAI, Greenwich, CT, 1994, p. 45.
64. S. L. Mielke, G. C. Lynch, D. G. Truhlar, and D. W. Schwenke, *Ab initio* chemical kinetics: Converged quantal rate constants for the D + H_2 systems, *J. Phys. Chem. 98*: 8000 (1994).
65. A. J. C. Varandas, F. B. Brown, C. A. Mead, D. G. Truhlar, and N. C. Blais, A double many-body expansion of the two lowest-energy potential surfaces and nonadiabatic coupling for H_3, *J. Chem. Phys. 86*: 6258 (1987).

66. G. Herzberg, *Infrared and Raman Spectra of Polyatomic Molecules* [*Molecular Spectra and Molecular Structure*, Vol. II], Van Nostrand Reinhold, New York, 1945, pp. 15, 75, 205.
67. M. A. Eliason and J. O. Hirschfelder, General collision theory treatment for the rate of gas phase reactions, *J. Chem. Phys. 30*: 1426 (1959).
68. L. Hofacker, Quantentheorie chemischer Reaktionen, *Z. Naturforsch. 18a*: 607 (1963).
69. D. G. Truhlar, The adiabatic theory of chemical reactions, *J. Chem. Phys. 53*: 2041 (1970).
70. D. G. Truhlar and A. Kuppermann, Exact tunneling calculations, *J. Amer. Chem. Soc. 93*: 1840 (1971).
71. B. C. Garrett, D. G. Truhlar, R. S. Grev, and A. W. Magnuson, Improved treatment of threshold contributions in variational transition-state theory, *J. Phys. Chem. 84*: 1730 (1980). Erratum: *87*: 4554 (1983).
72. R. A. Marcus, On the analytical mechanics of chemical reactions. Quantum mechanics of linear collisions, *J. Chem. Phys. 45*: 4493 (1965).
73. R. A. Marcus, Analytical mechanics and almost vibrationally-adiabatic chemical reactions, *Discussions Faraday Soc. 44*: 7 (1967).
74. B. C. Garrett and D. G. Truhlar, WKB approximation for the reaction-path Hamiltonian: Application to variational transition state theory, vibrationally adiabatic excited-state barrier heights, and resonance calculations, *J. Chem. Phys. 81*: 309 (1984).
75. D. G. Truhlar, Oscillators with quartic anharmonicity: Approximate energy levels, *J. Molec. Spec. 38*: 4151 (1971).
76. B. C. Garrett and D. G. Truhlar, Generalized transition state theory calculations for the reactions D + H_2 and H + D_2 using an accurate potential energy surface: Explanation of the kinetic isotope effect, *J. Chem. Phys. 72*: 3460 (1980).
77. G. C. Lynch, P. Halvick, D. G. Truhlar, B. C. Garrett, D. W. Schwenke, and D. J. Kouri, Semiclassical and quantum mechanical calculations of isotopic kinetic branching ratios for the reaction of O(^{3}P) with HD, *Zeitschrift für Naturforschung 44a*: 427 (1989).
78. B. C. Garrett, D. G. Truhlar, A. J. C. Varandas, and N. C. Blais, Semiclassical variational transition state calculations for the reactions of H and D with thermal and vibrationally excited H_2, *Int. J. Chem. Kin. 18*: 1065 (1986).
79. R. D. Levine and S.-F. Wu, Resonances in reactive collisions: Computational study of the H + H_2 collision, *Chem. Phys. Lett. 11*: 557 (1971).
80. N. Abu-Salbi, D. J. Kouri, M. Baer, and E. Pollak, A study of the quantal time delay matrix in collinear reactive scattering, *J. Chem. Phys. 82*: 4500 (1985).
81. E. Pollak, Periodic orbit analysis of bend level structure of resonances in 3D H + H_2 reactive scattering, *Chem. Phys. Lett. 137*: 171 (1987).
82. O. Atabek, R. Lefebvre, M. Garcia Sucre, J. Gomez-Llorente, and H. Taylor, Quantum localizations over a potential barrier, *Int. J. Quant. Chem. 40*: 211 (1991).
83. R. S. Friedman and D. G. Truhlar, Chemical reaction thresholds are resonances, *Chem. Phys. Lett. 183*: 539 (1991).
84. R. S. Friedman, V. D. Hullinger, and D. G. Truhlar, Quantum mechanical threshold resonances for unsymmetric potential energy barriers, *J. Phys. Chem. 99*: 3184 (1995).
85. A. J. F. Siegert, On the derivation of the dispersion formula for nuclear reactions, *Phys. Rev. 56*: 750 (1939).
86. J. R. Taylor, *Scattering Theory: The Quantum Theory of Nonrelativistic Collisions*, Krieger, Malabar, Florida, 1983, p. 407.
87. M. Zhao and S. A. Rice, Resonance state approach to quantum transition state theory, *J. Phys. Chem. 98*: 3444 (1994).
88. D. G. Truhlar and B. C. Garrett, Resonance state approach to quantum mechanical variational transition state theory, *J. Phys. Chem. 96*: 6515 (1992).
89. W. H. Miller, R. Hernandez, N. C. Handy, D. Jayatilaka, and A. Willetts, *Ab initio* calculation of anharmonic constants for a transition state, with application to semiclassical transition state tunneling probabilities, *Chem. Phys. Lett. 172*: 62 (1990).

90. M. J. Cohen, N. C. Handy, R. Hernandez, and W. H. Miller, Cumulative reaction probabilities for H + H_2 → H_2 + H from a knowledge of the anharmonic force field, *Chem. Phys. Lett. 192*: 407 (1992).
91. H. Feshbach, The unified theory of nuclear reactions. III. Overlapping resonances, *Ann. Phys. (N.Y.) 43*: 410 (1967).
92. H. Feshbach, *Theoretical Nuclear Physics*: *Nuclear Reactions*, John Wiley & Sons, New York, 1992, pp. 164–169, 211–213, 248–249.
93. T. Siedeman and W. H. Miller, Transition state theory, Siegert eigenstates, and quantum mechanical rates, *J. Chem. Phys. 95*: 1768 (1991).
94. V. Ryaboy and N. Moiseyev, Cumulative reaction probability from Siegert eigenvalues: Model Studies, *J. Chem. Phys. 98*: 9618 (1993).
95. A. Kuppermann, Reactive scattering resonances and their physical interpretation: The vibrational structure of the transition state, *Potential Energy Surfaces and Dynamics Calculations* (D. G. Truhlar, ed.), Plenum, New York, 1981, p. 375.
96. S. A. Cuccaro, P. G. Hipes, and A. Kuppermann, Symmetry analysis of accurate H + H_2 resonances for low partial waves, *Chem. Phys. Lett. 157*: 440 (1989).
97. F. T. Smith, Lifetime matrix in collision theory, *Phys. Rev. 118*: 349 (1960).
98. T. Seideman and W. H. Miller, Quantum mechanical reaction probabilities via a discrete variable representation-absorbing boundary condition Green's function, *J. Chem. Phys. 97*: 2499 (1992).
99. W. H. Miller, Beyond transition-state theory: A rigorous quantum theory of chemical reaction rates, *Acc. Chem. Res. 26*: 174 (1993).
100. U. Manthe and W. H. Miller, The cumulative reaction probability as eigenvalue problem, *J. Chem. Phys. 99*: 3411 (1993).
101. D. C. Chatfield, D. G. Truhlar, and D. W. Schwenke, Benchmark calculations of thermal reaction rates. I. Quantal scattering theory, *J. Chem. Phys. 94*: 2040 (1991).
102. J. Z. H. Zhang, Y. Zhang, D. J. Kouri, B. C. Garrett, K. Haug, D. W. Schwenke, and D. G. Truhlar, $\mathscr{L}^2$ Calculations of accurate quantal-dynamical reactive scattering transition probabilities and their use to test semiclassical applications, *Faraday Discuss. Chem. Soc. 84*: 3711 (1987).
103. Y. Sun, C. h. Yu, D. J. Kouri, D. W. Schwenke, P. Halvick, M. Mladenovic, and D. G. Truhlar, Direct calculation of the reactive transition matrix by $\mathscr{L}^2$ quantum mechanical variational methods with complex boundary conditions, *J. Chem. Phys. 91*: 1643 (1989).
104. B. R. Johnson and N. W. Winter, Classical trajectory study of the effect of vibrational energy on the reaction of molecular hydrogen with atomic oxygen, *J. Chem. Phys. 66*: 4116 (1977).
105. G. C. Schatz, A coupled states distorted wave study of the $O(^3P)$ + $H_2(D_2$, HD, DH) reaction, *J. Chem. Phys. 83*: 5677 (1985).
106. D. G. Truhlar, K. Runge, and B. C. Garrett, Variational transition state theory and tunneling calculations of potential energy surface effects on the reaction of $O(^3P)$ with H_2, *Twentieth Symposium (International) on Combustion*, Combustion Institute, Pittsburgh, 1984, p. 585.
107. B. C. Garrett and D. G. Truhlar, Thermal and state-selected rate constant calculations for $O(^3P)$ + H_2 → OH + H and isotopic analogs, *Int. J. Quantum Chem. 29*: 1463 (1986).
108. T. Joseph, D. G. Truhlar, and B. C. Garrett, Improved potential energy surfaces for the reaction $O(^3P)$ + H_2 → OH + H, *J. Chem. Phys. 88*: 6982 (1988).
109. J. M. Bowman and A. F. Wagner, Reduced dimensionality theories of Quantum reactive scattering: Applications to Mu + H_2, H + H_2, $O(^3P)$ + H_2, D_2, and HD, *The Theory of Chemical Reaction Dynamics* (D. C. Clary, ed.), Reidel, Dordrecht, 1986, p. 47.
110. B. C. Garrett, D. G. Truhlar, J. M. Bowman, and A. F. Wagner, Evaluation of dynamical approximations for calculating the effect of vibrational excitation on reaction rates. O + H_2 (n = 0, 1) ↔ OH + H, *J. Phys. Chem. 90*: 4305 (1986).
111. R. D. Levine, Radiationless transitions and population inversions: Two examples of internal conversions, *Chem. Phys. Lett. 10*: 510 (1971).

112. J. W. Duff and D. G. Truhlar, Effect of curvature of the reaction path on dynamic effects in endothermic reactions and product energies in exothermic reactions, *J. Chem. Phys. 62*: 2477 (1975).
113. D. G. Truhlar and D. A. Dixon, Direct-mode chemical reactions: Classical theories, *Atom-Molecule Collision Theory* (R. B. Bernstein, ed.), Plenum, New York, 1979, p. 595.
114. B. Liu, *Ab initio* potential energy surface for linear H_3, *J. Chem. Phys. 58*: 1925 (1973).
115. P. Siegbahn and B. Liu, An accurate three-dimensional potential energy surface for H_3, *J. Chem. Phys. 68*: 2457 (1978).
116. D. G. Truhlar and C. J. Horowitz, Functional representation of Liu and Siegbahn's *ab initio* potential energy calculations for H + H_2, *J. Chem. Phys. 68*: 2466 (1978). Erratum: *71*: 1514 (1979).
117. J. V. Michael and J. R. Fisher, Rate constants for the reaction D + H_2 → HD + H over the temperature range 655–1979 K, by the flash photolysis-shock tube technique, *J. Phys. Chem. 94*: 3318 (1990) and references therein.
118. D. G. Truhlar and R. E. Wyatt, History of H_3 kinetics, *Annu. Rev. Phys. Chem. 27*: 1 (1976).
119. S.-F. Wu, B. R. Johnson, and R. D. Levine, Quantum mechanical computational studies of chemical reactions: III. Collinear A + BC reaction with some model potential energy surfaces, *Mol. Phys. 25*: 839 (1973).
120. T. C. Thompson and D. G. Truhlar, Stabilization calculations and probability densities for the well-studied collisional resonances in collinear F + H_2, F + HD, and F + D_2, *J. Phys. Chem. 88*: 210 (1984).
121. C. C. Marston and R. E. Wyatt, Resonant quasi-periodic and periodic orbits for the three-dimensional reaction of fluorine atoms with hydrogen molecules, *ACS Symp. Ser. 263*: 441 (1984).
122. Z. H. Zhang, N. Abusalbi, M. Baer, D. J. Kouri, and J. Jellinek, Resonance phenomena in quantal reactive infinite-order sudden calculations, *ACS Symp. Ser. 263*: 457 (1984).
123. D. M. Neumark, A. M. Wodtke, G. N. Robinson, C. C. Hayden, and Y. T. Lee, Dynamic resonances in the reaction of fluorine atoms with hydrogen molecules, *ACS Symp. Ser. 263*: 479 (1984).
124. E. F. Hayes and R. B. Walker, Reactive resonances and angular distributions in the rotating linear model, *ACS Symp. Ser. 263*: 493 (1984).
125. D. M. Neumark, A. M. Wodtke, G. N. Robinson, C. C. Hayden, and Y. T. Lee, Molecular beam studies of the F + H_2 reaction, *J. Chem. Phys. 82*, 3045 (1985).
126. S. L. Mielke, G. C. Lynch, D. G. Truhlar, and D. W. Schwenke, A more accurate potential energy surface and quantum mechanical cross section calculations for the F + H_2 reaction, *Chem. Phys. Lett. 213*: 10 (1993). Erratum: *217*: 173 (1994).
127. R. Steckler, D. W. Schwenke, F. B. Brown, and D. G. Truhlar, An improved calculation of the transition state for the F + H_2 reaction, *Chem. Phys. Lett. 121*: 475 (1985).
128. D. W. Schwenke, R. Steckler, F. B. Brown, and D. G. Truhlar, The potential energy surface for the F + H_2 reaction as a function of bond angle in the saddle point vicinity, *J. Chem. Phys. 84*: 5706 (1986).
129. G. C. Lynch, R. Steckler, D. W. Schwenke, A. J. C. Varandas, D. G. Truhlar, and B. C. Garrett, Use of scaled external correlation, a double many-body expansion, and variational transition state theory to calibrate a potential energy surface for FH_2, *J. Chem. Phys. 94*: 7136 (1991).
130. C. W. Bauschlicher, S. P. Walch, S. R. Langhoff, P. R. Taylor, and R. L. Jaffe, Theoretical studies of the potential surface for the F + H_2 → HF + H reaction, *J. Chem. Phys. 88*: 1743 (1988).
131. P. J. Knowles, K. Stark, and H. J. Werner, A full-CI study of the energetics of the reaction F + H_2 → HF + H, *Chem. Phys. Lett. 185*: 555 (1991).
132. C. h. Yu, Y. Sun, D. J. Kouri, P. Halvick, D. G. Truhlar, and D. W. Schwenke, Converged quantum dynamics calculations for the F + H_2 reaction on the well-studied M5 potential-energy surface, *J. Chem. Phys. 90*: 7608 (1989).

133. A. Weaver and D. M. Neumark, Negative-ion photodetachment as a probe of bimolecular transition states: The F + H_2 reaction, *Faraday Discuss. Chem. Soc. 91*: 5 (1991).
134. S. E. Bradforth, D. W. Arnold, D. M. Neumark, and D. E. Manolopoulos, Experimental and theoretical studies of the F + H_2 transition state region via photoelectron spectroscopy of FH_2^-, *J. Chem. Phys. 99*: 6345 (1993).
135. D. E. Manolopoulos, K. Stark, H. J. Werner, D. W. Arnold, S. E. Bradforth, and D. M. Neumark, The transition state of the F + H_2 reaction, *Science 262*: 1852 (1993).
136. J. D. Kress and E. F. Hayes, Assignment of peaks in photodetachment spectra using predicted densities of reactive states: Applications to H_2F^- and D_2F^-, *J. Chem. Phys. 97*: 4881 (1992).
137. A. M. Arthurs and A. Dalgarno, The theory of scattering by a rigid rotator, *Proc. Roy. Soc. Lond. A156*: 540 (1960).
138. S. Bratož and M. L. Martin, Infrared spectra of highly compressed gas mixtures of the type HCl + X. A theoretical study, *J. Chem. Phys. 42*: 1051 (1965).
139. S. V. O'Neil, D. J. Nesbitt, P. Rosmus, H. J. Werner, and D. C. Clary, Weakly bound NeHF, *J. Chem. Phys. 91*: 711 (1989).
140. D. J. Nesbitt, C. M. Lovejoy, T. G. Lindeman, S. V. O'Neil, and D. C. Clary, Slit jet infrared spectroscopy of NeHF complexes: Internal rotor and *J*-dependent predissociation dynamics, *J. Chem. Phys. 91*: 722 (1989).
141. D. W. Schwenke, On the computational of ro-vibrational energy levels of triatomic molecules, *Comp. Phys. Commun. 70*: 1 (1992).
142. B. C. Garrett, D. G. Truhlar, R. S. Grev, A. W. Magnuson, and J. N. L. Connor, Variational transition state theory, vibrationally adiabatic transmission coefficients, and the unified statistical model tested against accurate quantal rate constants for collinear F + H_2, H + F_2, and isotopic analogs, *J. Chem. Phys. 73*: 1721 (1980).
143. D. G. Truhlar, W. L. Hase, and J. T. Hynes, Current status of transition-state theory, *J. Phys. Chem. 87*: 2664 (1983). Additions and corrections: *87*: 5523 (1983).
144. D. G. Truhlar and B. C. Garrett, Dynamical bottlenecks and semiclassical tunneling paths for chemical reactions, *J. Chim. Phys. 84*: 365 (1987).
145. G. C. Lynch, D. G. Truhlar, and B. C. Garrett, Test of the accuracy of small–curvature and minimum–energy reference paths for parameterizing the search for least–action tunneling paths: (H,D) + H′Br → (H,D)Br + H′, *J. Chem. Phy. 90*: 3102 (1989). Erratum: *91*: 3280 (1989).
146. B. C. Garrett and D. G. Truhlar, Critical tests of variational transition state theory and semiclassical tunneling methods for hydrogen and deuterium atom transfer reactions and use of the semiclassical calculations to interpret the overbarrier and tunneling dynamics, *J. Phys. Chem. 95*: 10374 (1991).
147. D. G. Truhlar and B. C. Garrett, General discussion, *Faraday Discuss. Chem. Soc. 84*: 465 (1987).
148. J. A. Kaye and A. Kuppermann, Collinear quantum mechanical properties for the I + HI → IH + H reaction using hyperspherical coordinates, *Chem. Phys. Lett. 77*: 573 (1981).
149. V. K. Babamov and R. A. Marcus, Dynamics of hydrogen atom and proton transfer reaction. Symmetric case, *J. Chem. Phys. 74*: 1790 (1981).
150. J. Manz and J. Römelt, On the collinear I + HI and I + MuI reactions, *Chem. Phys. Lett. 81*: 179 (1981).
151. D. K. Bondi, J. N. L. Connor, B. C. Garrett, and D. G. Truhlar, Test of variational transition state theory with a large-curvature tunneling approximation against accurate quantal reaction probabilities and rate coefficients for three collinear reactions with large reaction–path curvature: Cl + HCl, Cl + DCl, and Cl + MuCl, *J. Chem. Phys. 78*: 5981 (1983).
152. D. K. Bondi, J. N. L. Connor, J. Manz, and J. Römelt, Exact quantum and vibrationally adiabatic quantum semiclassical and quasiclassical study of the collinear reactions Cl + MuCl, Cl + HCl, Cl + DCl, *Mol. Phys. 50*: 467 (1983).

153. D. G. Truhlar, B. C. Garrett, P. G. Hipes, and A. Kuppermann, Test of variational transition state theory against accurate quantal results for a reaction with very large reaction–path curvature and a low barrier, *J. Chem. Phys. 81*: 3542 (1984).
154. J. Manz, Molecular dynamics along hyperspherical coordinates, *Comm. At. Mol. Phys. 17*: 91 (1985).
155. J. Römelt, Calculations on collinear reactions using hyperspherical coordinates, *Theory of Chemical Reaction Dynamics* (D. C. Clary, ed.), Reidel, Dordrecht, 1986, p. 77.
156. J. M. Bowman and B. Gazdy, A reduced dimensionality $\mathscr{L}^2$ simulation of the photodetachment spectra of $ClHCl^-$ and IHI^-, *J. Phys. Chem. 93*: 5129 (1989).
157. G. C. Schatz, D. Sokolovski, and J. N. L. Connor, Influence of transition state resonances on integral cross sections and product rovibrational distributions for the Cl + HCl → ClH + Cl reaction, *J. Chem. Phys. 94*: 4311 (1991).
158. R. B. Metz and D. M. Neumark, Adiabatic three-dimensional simulations of the IHI^-, $BrHI^-$, and $BrHBr^-$ photoelectron spectra, *J. Chem. Phys. 97*: 962 (1992).
159. M. J. Cohen, A. Willetts, and N. C. Handy, Cumulative reaction probabilities for OH + H_2 → H_2O + H and ClH + Cl → Cl + HCl from a knowledge of the anharmonic force field, *J. Chem. Phys. 99*: 5885 (1993).
160. A. Weaver, R. B. Metz, S. E. Bradforth, and D. M. Neumark, Spectroscopy of the I + HI transition-state region by photodetachment of IHI^-, *J. Phys. Chem. 92*: 5558 (1988).
161. R. B. Metz, T. Kitsopoulos, A. Weaver, and D. M. Neumark, Study of the transition state region in the Cl + HCl reaction by photoelectron spectroscopy of $ClHCl^-$, *J. Chem. Phys. 88*: 1463 (1988).
162. R. B. Metz, A. Weaver, S. E. Bradforth, T. N. Kitsopoulos, and D. M. Neumark, Probing the transition state with negative ion photodetachment: The Cl + HCl and Br + HBr reactions, *J. Phys. Chem. 94*: 1377 (1990).
163. S. E. Bradforth, D. W. Arnold, R. B. Metz, A. Weaver, and D. M. Neumark, Spectroscopy of the transition state: Hydrogen abstraction reactions of fluorine, *J. Phys. Chem. 95*: 8066 (1991).
164. Z. Darakjian, E. F. Hayes, G. A. Parker, E. A. Butcher, and J. D. Kress, Direct calculation of collisional properties that require energy derivatives of the S matrix: Results for the reaction He + H_2^+ → HeH^+ + H, *J. Chem. Phys. 95*: 2516 (1991). Erratum: *101*: 9203 (1994).
165. S. K. Klippenstein and J. D. Kress, Comparison of variational Rice-Ramsperger-Kassel-Marcus theory with quantum scattering theory for the He + H_2^+ → HeH^+ + H reaction, *J. Chem. Phys. 96*: 8164 (1992).
166. R. T Pack, E. A. Butcher, and G. A. Parker, Accurate quantum probabilities and threshold behavior of the H + O_2 combustion reaction, *J. Chem. Phys. 99*: 9310 (1993).
167. J. D. Kress, Accurate three-dimensional quantum cumulative reaction probabilities for Ne + H_2^+ → NeH^+ + H, *J. Chem. Phys. 95*: 8673 (1991).
168. J. D. Kress and S. J. Klippenstein, Comparison of variational RRKM theory with quantum scattering theory for the Ne + H_2^+ → NeH^+ + H reaction, *Chem. Phys. Lett. 195*: 513 (1992).
169. J. D. Kress, R. B. Walker, E. F. Hayes, and P. Pendergast, Quantum scattering studies of long-lived resonances for the Ne + H_2^+ → NeH^+ + H reaction, *J. Chem. Phys. 100*: 2728 (1994).
170. R. T Pack, E. A. Butcher, and G. A. Parker, Accurate three-dimensional quantum properties and collision lifetimes of the H + O_2 combustion reaction, *J. Chem. Phys. 102*: 5998 (1995).
171. C. Leforestier and W. H. Miller, Quantum mechanical calculation of the rate constant for the reaction H + O_2 → OH + O, *J. Chem. Phys. 100*: 733 (1994).
172. C. Y. Yang, S. J. Klippenstein, J. D. Kress, R. T Pack, G. A. Parker, and A. Laganà, Comparison of transition state theory with quantum scattering theory for the reaction Li + HF → LiF + H, *J. Chem. Phys. 100*: 4917 (1994).

173. T. C. Allison, S. L. Mielke, G. C. Lynch, D. G. Truhlar, and M. S. Gordon, An improved potential energy surface for the H_2Cl system and its use for calculations of rate constants and kinetic isotope effects, manuscript in preparation.
174. R. B. Metz, S. E. Bradforth, and D. M. Neumark, Transition state spectroscopy of bimolecular reactions using negative ion photodetachment, *Adv. Chem. Phys. 81*: 1 (1992).
175. D. M. Neumark, Transition state spectroscopy of bimolecular chemical reactions, *Annu. Rev. Phys. Chem. 43*: 153 (1992).
176. M. J. Davis, H. Koizumi, G. C. Schatz, S. E. Bradforth, and D. M. Neumark, Experimental and theoretical study of the O + HCl transition state region by photodetachment of $OHCl^-$, *J. Chem. Phys. 101*: 4708 (1994).
177. D. W. Arnold, C. Xu, and D. M. Neumark, Spectroscopy of the transition state: Elementary reactions of the hydroxyl radical studied by photoelectron spectroscopy of O (H_2O) and $H_3O_2^-$, *J. Chem. Phys. 102*: 6088 (1995).
178. G. C. Schatz, Quantum theory of photodetachment spectra of transition states, *J. Phys. Chem. 94*: 6157 (1990).
179. D. G. Truhlar, General discussion, *Faraday Discuss. Chem. Soc. 91*: 395 (1991).
180. E. R. Lovejoy, S. K. Kim, and C. B. Moore, Observation of transition-state vibrational thresholds in the rate of dissociation of ketene, *Science 256*: 1541 (1992).
181. W. H. Green, Jr., C. B. Moore, and W. F. Polik, Transition states and rate constants for unimolecular reactions, *Annu. Rev. Phys. Chem. 43*: 591 (1992).
182. E. R. Lovejoy and C. B. Moore, Structures in the energy dependence of the rate constant of ketene isomerization, *J. Chem. Phys. 98*: 7846 (1993).
183. S. K. Kim, E. R. Lovejoy, and C. B. Moore, Transition state vibrational level thresholds for the dissociation of triplet ketene, *J. Chem. Phys. 102*: 3202 (1995).
184. M. S. Child, Measurable consequences of a dip in the activation barrier for an adiabatic chemical reaction, *Mol. Phys. 12*: 401 (1967).
185. B. C. Garrett, D. G. Truhlar, R. S. Grev, G. C. Schatz, and R. B. Walker, Reaction probabilities, resonances, and thermal rate constants for the collinear reactions H + FH and D + FD on a low-barrier surface: Close-coupling and tunneling calculations, variational transition-state theory, and the unified statistical model, *J. Phys. Chem. 85*: 3806 (1981).
186. G. A. Brucker, S. I. Ionov, Y. Chen, and C. Wittig, Time-resolved studies of NO_2 photoinitiated unimolecular decomposition: step-like variation of $k_{uni}(E)$, *Chem. Phys. Lett. 194*: 301 (1992).
187. S. I. Ionov, G. A. Brucker, C. Jaques, Y. Chen, and C. Wittig, Probing the $NO_2 \rightarrow NO + O$ transition state via time resolved unimolecular decomposition, *J. Chem. Phys. 99*: 3420 (1993).
188. S. I. Ionov, H. F. Davis, K. Mikhaylichenko, L. Valachovic, R. A. Beaudet, and C. Wittig, The density of reactive levels in NO_2 unimolecular decomposition, *J. Chem. Phys. 101*: 4809 (1994).
189. S. J. Klippenstein and T. Radivoyevitch, A theoretical study of the dissociation of NO_2, *J. Chem. Phys. 99*: 3644 (1993).
190. H. Katagiri and S. Kato, The spin-orbit effect on potential surfaces of NO_2 photodissociation, *J. Chem. Phys. 99*: 8805 (1993).
191. Y. S. Choi, T. S. Kim, H. Petek, K. Yoshihara, and R. L. Christensen, Evidence for quantization of the transition state for *cis-trans* isomerization, *J. Chem. Phys. 100*: 9269 (1994).
192. K. Haug, D. W. Schwenke, Y. Shima, D. G. Truhlar, J. Zhang, and D. J. Kouri, $\mathscr{L}^2$ solution of the quantum mechanical reactive scattering problem. The threshold energy for D + $H_2(v = 1) \rightarrow HD + H$, *J. Phys. Chem. 90*: 6757 (1986).
193. Y. C. Zhang, J. Z. H. Zhang, D. J. Kouri, K. Haug, D. W. Schwenke, and D. G. Truhlar, Quantum mechanical calculations of vibrational population inversion in chemical reactions: Numerically exact $\mathscr{L}^2$-amplitude-density study of the H_2Br reactive system, *Phys. Rev. Lett. 60*: 2367 (1988).

194. M. Mladenovic, M. Zhao, D. G. Truhlar, D. W. Schwenke, Y. Sun, and D. J. Kouri, Effect of orbital and rotational angular momentum averaging on branching ratios of dynamical resonances in the reaction H + p-H_2 → o-H_2 + H, *Chem. Phys. Lett. 146*: 358 (1988).
195. M. Mladenovic, M. Zhao, D. G. Truhlar, D. W. Schwenke, Y. Sun, and D. J. Kouri, Converged quantum mechanical calculation of the product vibration-rotation state distribution of the H + p-H_2 reaction, *J. Phys. Chem. 92*: 7035 (1988).
196. M. Zhao, M. Mladenovic, D. G. Truhlar, D. W. Schwenke, O. Sharafeddin, Y. Sun, and D. J. Kouri, Spectroscopic analysis of transition state energy levels: Bending-rotational spectrum and lifetime analysis of H_3 quasibound states, *J. Chem. Phys. 91*: 5302 (1989).
197. M. Zhao, D. G. Truhlar, D. W. Schwenke, and D. J. Kouri, Effect of rotational excitation on state-to-state differential cross sections: D + H_2 → HD + H, *J. Phys. Chem. 94*: 7074 (1990).
198. D. G. Truhlar, D. W. Schwenke, and D. J. Kouri, Quantum dynamics of chemical reactions by converged algebraic variational calculations, *J. Phys. Chem. 94*: 7346 (1990).
199. S. L. Mielke, G. J. Tawa, D. G. Truhlar, and D. W. Schwenke, Quantum photochemistry. Accurate quantum scattering calculations for an electronically nonadiabatic reaction, *Chem. Phys. Lett. 234*: 57 (1995).
200. G. C. Schatz, Quantum reactive scattering using hyperspherical coordinates: Results for H + H_2 and Cl + HCl, *Chem. Phys. Lett. 150*: 92 (1988).
201. W. H. Miller, Recent advances in quantum mechanical reactive scattering theory, Including comparison of recent experiments with rigorous calculations of state-to-state cross sections for the H/D + H_2 → H_2/HD + H reactions, *Annu. Rev. Phys. Chem. 41*: 245 (1990).
202. J. Z. H. Zhang, D. L. Yeager, and W. H. Miller, 3D quantum scattering calculations of the reaction He + H_2^+ → HeH^+ + H for total angular momentum J = 0, *Chem. Phys. Lett. 173*: 489 (1990).
203. J. Z. H. Zhang and W. H. Miller, Quantum reactive scattering via the S-matrix version of the Kohn variational principle: Differential and integral cross sections for D + H_2 → HD + H, *J. Chem. Phys. 91*: 1528 (1989).
204. U. Manthe, T. Seideman, and W. H. Miller, Full-dimensional quantum mechanical calculation of the rate constant for the H_2 + OH → H_2O + H reaction, *J. Chem. Phys. 99*: 10078 (1993).
205. U. Manthe, T. Seideman, and W. H. Miller, Quantum mechanical calculations of the rate constant for the H_2 + OH → H + H_2O reaction: Full-dimensional results and comparison to reduced dimensionality models, *J. Chem. Phys. 101*: 4759 (1994).
206. J. D. Kress, Z. Bačić, G. A. Parker, and R. T. Pack, Quantum effects in the F + H_2 → .HF + H reaction. Accurate 3D calculations with a realistic potential energy surface, *Chem. Phys. Lett. 157*: 484 (1989).
207. Y. S. M. Wu, A. Kuppermann, and B. Lepetit, Theoretical calculation of experimentally observable consequences of the geometric phase on chemical reaction cross sections, *Chem. Phys. Lett. 186*: 319 (1991).
208. Y. S. M. Wu and A. Kuppermann, Prediction of the effect of the geometric phase on product rotational state distributions and integral cross sections, *Chem. Phys. Lett. 201*: 178 (1993).
209. D. Neuhauser, M. Baer, R. S. Judson, and D. J. Kouri, Time dependent three-dimensional body frame quantal wave packet treatment of the H + H_2 exchange reaction on the Liu-Siegbahn-Truhlar-Horowitz (LSTH) surface, *J. Chem. Phys. 90*: 5882 (1989).
210. D. Neuhauser, R. S. Judson, R. L. Jaffe, M. Baer, and D. J. Kouri, Total integral reactive cross sections for F + H_2 → HF + H: Comparison of converged quantum, quasiclassical trajectory and experimental results, *Chem. Phys. Lett. 176*: 546 (1991).
211. M. Gilibert and M. Baer, Exchange processes via electronic nonadiabatic transitions: An accurate three-dimensional quantum mechanical study of the F($^2P_{1/2}$, $^2P_{3/2}$) + H_2 reactive systems, *J. Phys. Chem. 98*: 12822 (1994).

212. D. E. Manolopoulos and D. C. Clary, Quantum calculations on reactive collisions, *Annu. Rep. Prog. Chem. 86*: 95 (1989).
213. D. E. Manolopoulos and R. E. Wyatt, H + H_2 (0, 0) → $H_2(v', j')$ + H integral cross sections on the double many body expansion potential energy surface, *J. Chem. Phys. 92*: 810 (1990).
214. M. D'Mello, D. E. Manolopoulos, and R. E. Wyatt, Quantum dynamics of the H + D_2 → D + HD reaction: comparison with experiment, *J. Chem. Phys. 94*: 5985 (1991).
215. J. M. Launay, Computation of cross sections for the F + $H_2(v = 0, j = 0)$ → FH (v', j') + H reaction by the hyperspherical method, *Theor. Chim. Acta 79*: 183 (1991).
216. J. M. Launay and S. B. Padkjaer, Quantum-dynamical study of the Cl + H_2 → ClH + H reaction, *Chem. Phys. Lett. 181*: 95 (1991).
217. S. E. Branchett, S. B. Padkjaer, and J. M. Launay, Quantum dynamical study of the H + HCl → H_2 + Cl reaction, *Chem. Phys. Lett. 208*: 523 (1993).
218. G. A. Parker, R. T. Pack, and A. Laganà, Accurate 3D quantum reactive probabilities of Li + FH, *Chem. Phys. Lett. 202*: 75 (1993).
219. A. Laganà, R. T. Pack, and G. A. Parker, Li + FH reactive cross sections from $J = 0$ accurate quantum reactivity, *J. Chem. Phys. 99*: 2269 (1993).
220. G. C. Schatz, Influence of atomic fine structure on bimolecular rate constants: The $Cl(^2P)$ + HCl reaction, *J. Phys. Chem. 99*: 7522 (1995).

10

Beyond Transition State Theory: Rigorous Quantum Approaches for Determining Chemical Reaction Rates

WILLIAM H. MILLER
University of California and Lawrence Berkeley National Laboratory, Berkeley, California

I. INTRODUCTION

Transition state theory (TST) (1–3) has historically been the most important and widely used theoretical approach for describing the rates of chemical reactions, and for qualitative pictures and order-of-magnitude estimates one does not expect this situation to change. However a rigorous, quantitative treatment of chemical reaction rates must go beyond TST. A rigorous description, for example, must be based on a quantum mechanical description of the molecular system, but the fundamental assumption (2,3) on which TST is based—namely that the molecular dynamics is "direct," i.e., that no trajectories recross a dividing surface which separates reactants and products (vide infra)—is couched inherently in the language of classical mechanics. There is no unambiguous way to quantize TST, for the various ways of trying to do so invariably require one to introduce additional assumptions about the reaction dynamics. As one tries to eliminate these "additional assumptions" one is driven ultimately to an *exact* quantum treatment of the reaction dynamics which is then no longer a transition state *theory* (i.e., approximation) but simply an exact formulation. It is such exact approaches, those without inherent approximations, that are the subject of this chapter.

One way to determine the rate constant rigorously is to solve the complete state-to-state reactive scattering Schrödinger equation (with approximate scattering boundary conditions) to obtain the S-matrix $\{S_{n_p,n_r}(E, J)\}$ as a function of total energy E and total angular momentum J (where n_r (n_p) label the reactant (product) quantum states), from

which all the state-to-state scattering cross sections can be obtained. Several other chapters in this volume do indeed focus on this state-to-state description of reactive scattering. Averaging these cross sections over the proper distribution of initial quantum states, and summing over all final quantum states, produces the rate constant, but this is in a sense "wasteful" if one seeks only the rate constant itself. Thus we seek not only a rigorous, i.e., *correct*, approach for determining a rate constant, but also one (like TST) that is *direct*, i.e., that avoids having to solve the complete state-to-state reactive scattering problem. The approaches described below are those both *correct* and *direct*, and they will in fact be seen to have qualitative features and interpretations that are reminiscent of TST.

The presentation below first reviews the description of rate constants within the framework of classical mechanics and shows how the transition state approximation arises. The difficulties of quantizing TST are discussed and then fully rigorous quantum approaches presented. Recent applications of these latter to several reactions of interest are presented.

II. CLASSICAL RATE THEORY

Figure 1 shows a schematic depiction of the potential energy surface for a generic bimolecular reaction. Within the realm of classical mechanics the thermal, or equilibrium (i.e., reactants in a Boltzmann distribution), rate constant is given by (1,3,5)

$$k(T) = Q_r(T)^{-1}(2\pi\hbar)^{-f} \int d\mathbf{p} \int d\mathbf{q}\, e^{-\beta H(\mathbf{p},\mathbf{q})} F(\mathbf{p}, \mathbf{q})\chi_r(\mathbf{p}, \mathbf{q}) \tag{1}$$

where $\beta = (kT)^{-1}$, Q_r is the reactant partition function (per unit volume), H is the classical Hamiltonian for the complete molecular system, F is a flux factor, and χ_r is the *characteristic function for reaction*. The flux factor is defined in terms of a *dividing surface*, defined by the equation.

$$f(\mathbf{q}) = 0 \tag{2}$$

which separates reactants (for which $f(\mathbf{q}) < 0$) and products (for which $f(\mathbf{q}) \geq 0$); the flux is then

$$f(\mathbf{p}, \mathbf{q}) = \frac{d}{dt} h[f(\mathbf{q})] \tag{3}$$

where h is the usual Heaviside function

$$h(\xi) = \begin{cases} 1, & \xi > 0 \\ 0, & \xi < 0 \end{cases} \tag{4}$$

Assuming for simplicity that the coordinates and momenta $(\mathbf{q}, \mathbf{p})$ are Cartesian—so that the Hamiltonian is of the form

$$H(\mathbf{p}, \mathbf{q}) = \frac{\mathbf{p}^2}{2m} + V(\mathbf{p}, \mathbf{q}) \tag{5}$$

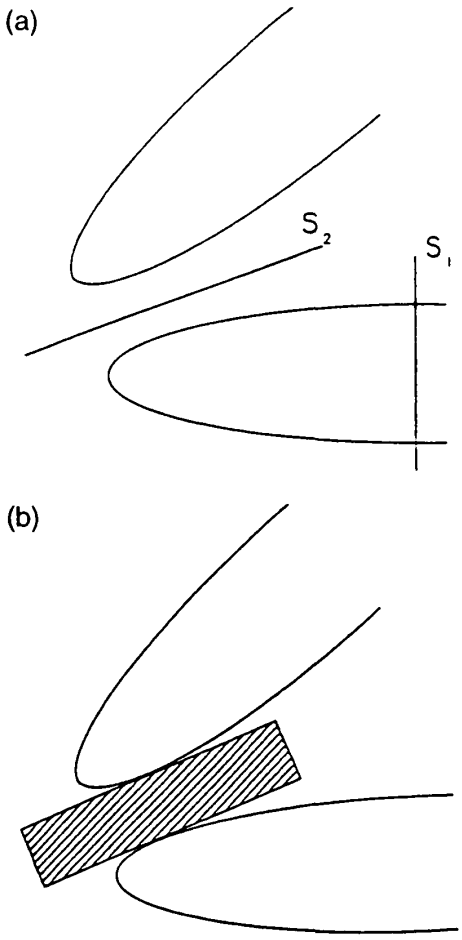

Figure 1 (a) Schematic depiction of the contours of a potential energy surface with two possible choices of the dividing surface (actually a *line* in this two-dimensional case), S_1 in the reactant region and S_2 through the transition state region. (b) Same as (a), but indicating a region of some width about the dividing surface S_2.

Equation (3) for the flux becomes

$$F(\mathbf{p}, \mathbf{q}) = \delta[f(\mathbf{q})] \frac{\partial f}{\partial \mathbf{q}} \cdot \frac{\mathbf{p}}{m} \tag{6}$$

where we used the fact that $h'(\xi) = \delta(\xi)$, the Dirac delta function.

One can define χ_r in several ways (3), but the one that most naturally generalizes to the quantum mechanical case is

$$\chi_r(\mathbf{p}, \mathbf{q}) = \lim_{t \to \infty} h[f(\mathbf{q}(t))] \tag{7}$$

where $\mathbf{q}(t) \equiv \mathbf{q}(t; \mathbf{p}, \mathbf{q})$ is the classical trajectory determined by the initial conditions $(\mathbf{p}, \mathbf{q})$ at time $t = 0$; thus $\chi_r(\mathbf{p}, \mathbf{q}) = 1$ if the trajectory with initial conditions $(\mathbf{p}, \mathbf{q})$ is on the product side of the dividing surface as $t \to \infty$, and is 0 otherwise. All of the *dynamics* of the reaction is thus contained in the characterization function χ_r.

It is useful for some purposes to define the *microcanonical* rate constant $k(E)$,

$$k(E) = [2\pi\hbar\rho_r(E)]^{-1} N(E) \tag{8}$$

where ρ_r is the density of reactant states (per unit energy), and $N(E)$ is the *cumulative reaction probability*,

$$N(E) = 2\pi\hbar(2\pi\hbar)^{-F} \int d\mathbf{p} \int d\mathbf{q}\, \delta[E - H(\mathbf{p}, \mathbf{q})] F(\mathbf{p}, \mathbf{q}) \chi_r(\mathbf{p}, \mathbf{q}) \tag{9}$$

where F and χ_r are as above. Since

$$\int_{-\infty}^{\infty} e^{-\beta E} \delta[E - H(\mathbf{p}, \mathbf{q})] = e^{-\beta H(\mathbf{p},\mathbf{q})} \tag{10}$$

it is easy to see that the thermal rate $k(T)$, Eq. (1), can be expressed in terms of $N(E)$, Eq. (9), as

$$k(T) = [2\pi\hbar Q_r(T)]^{-1} \int_{-\infty}^{\infty} dE\, e^{-\beta E} N(E) \tag{11}$$

For most of this chapter, therefore, $N(E)$ will be focused on as the primary object of interest, and the canonical (i.e., thermal) and microcanonical rates are given in terms of it by Eqs. (11) and (8), respectively. The last section of the chapter, however, discusses an approach for the "direct" determination of the canonical rate $k(T)$ itself.

The calculation implied by Eq. (9) for $N(E)$ (or Eq. (1) for $k(T)$) is therefore to integrate over phase space $(\mathbf{p}, \mathbf{q})$—in practice, usually with Monte Carlo sampling methods—where each phase point $(\mathbf{p}, \mathbf{q})$ serves as the initial conditions for a trajectory that must be run (i.e., numerically integrated) to determine whether χ_r is 1 or 0, i.e., whether or not this phase point contributes to the integral. Because the flux, Eq. (6), contains the factor $\delta[f(\mathbf{q})]$, all trajectories begin on the dividing surface $f(\mathbf{q}) = 0$.

Finally, we note that the rate is independent of the choice of the dividing surface (by virtue of Liouville's theorem) but that a sensible choice for it greatly simplifies the calculation (6). Referring to Fig. 1, it is intuitively clear that using dividing surface S_1 will require trajectories to be run for a much longer time to determine whether they will wind up on the product side as $t \to \infty$ than if dividing surface S_2 is used.

III. TRANSITION STATE THEORY

The fundamental assumption of transition state theory is that of *direct* dynamics, i.e., that all trajectories which cross the dividing surface do so only once (1,3,5). If this is true then a trajectory will be on the product side of the dividing surface at $t \to \infty$ only if it begins at $t = 0$ (on the dividing surface) headed in the product direction, i.e., with positive momentum normal to the dividing surface.

$$\chi_{TST}(\mathbf{p}, \mathbf{q}) = h\left[\frac{\partial f(\mathbf{q})}{\partial(\mathbf{q})} \cdot \frac{\mathbf{p}}{m}\right] \tag{12}$$

which may also be thought of as a short time approximation to the dynamics. The resulting phase-space integral for $N(E)$ which then follows from Eq. (9) is particularly simple if one chooses a *planar* dividing surface; if q_F is the coordinate normal to the dividing plane, then

$$f(\mathbf{q}) = q_F \tag{13}$$

—i.e., $q_F = 0$ defines the dividing surface—and Eq. (9) then reads

$$N_{TST}(E) = 2\pi\hbar(2\pi\hbar)^{-F} \int d\mathbf{q} \int d\mathbf{p}\, \delta\left[E - V(\mathbf{q}) - \frac{\mathbf{p}^2}{2m}\right] \delta(q_F) \frac{p_F}{m} h(p_F) \tag{14}$$

The two delta functions in the integrand allow the integrals over q_F and p_F to be carried out, giving

$$N_{TST}(E) = (2\pi\hbar)^{-(F-1)} \int d\mathbf{p}' \int d\mathbf{q}'\, h[E - H^{\ddagger}(\mathbf{p}', \mathbf{q}')] \tag{15}$$

where $(\mathbf{p}', \mathbf{q}') \equiv (p_k, q_k)$, $k = 1, \ldots, F-1$ are the coordinates and momenta for motion *on* the dividing surface defined by $q_F = 0$, and

$$H^{\ddagger}(\mathbf{p}', \mathbf{q}') = \sum_{k=1}^{F-1} \frac{p_k^2}{2m} + V(\mathbf{q}', q_F = 0) \tag{16}$$

is the Hamiltonian in this reduced space. In words, Eq. (15) says that the cumulative reaction probability is the volume of phase space of the "activated complex" (the $(F-1)$-dimensional system for motion on the dividing surface) with energy less than or equal to E. With Eq. (11), the TST expression for the thermal rate than takes its standard form

$$k_{TST}(T) = \frac{kT}{h} \frac{Q^{\ddagger}(T)}{Q_r(T)} \tag{17}$$

where $Q^{\ddagger}$ is the partition function of the activated complex:

$$Q^{\ddagger}(T) = (2\pi\hbar)^{-(F-1)} \int d\mathbf{p}' \int d\mathbf{q}'\, e^{-\beta H^{\ddagger}(\mathbf{p}', \mathbf{q}')} \tag{18}$$

An important feature of classical transition state theory is that it is an *upper bound* to the correct result for any choice of the dividing surface. That is, since all reactive trajectories must cross the dividing surface, but all trajectories that cross it are not necessarily reactive (because they might recross it at a later time and be nonreactive), any error in the TST approximation, Eq. (12), is to count some nonreactive trajectories as reactive. Thus, while the exact rate expression does not depend on the choice of the dividing surface, the TST rate does, and by virtue of this bounding property the best choice of the dividing surface is the one which makes k_{TST} a *minimum*. This is the *variational* aspect of TST: any parameters which specify the shape or location of the dividing surface are best chosen to minimize the TST rate (7).

Transition state theory is often a very good approximation for the classical rate of a chemical reaction. Pechukas et al. (8), in fact, have shown that TST is *exact* at sufficiently low energy. Figures 2 and 3 show a numerical illustration (9) of this for the standard test reaction $H + H_2 \rightarrow H_2 + H$, for the collinear version of the reaction (Fig. 2) and also in three-dimensional space (Fig. 3).* In both cases TST is essentially exact up to ~0.3 eV above the potential energy barrier, but for higher energies it begins to be

*The functions actually plotted in Figs. 2 and 3 are the ratio of $N(E)$, the reactive flux, to the incident flux (or flux per unit area for the three-dimensional case). These ratios have the more physically meaningful interpretation of an average reaction probability in the collinear case (Fig. 2) and an average reaction cross section in the three-dimensional case (Fig. 3).

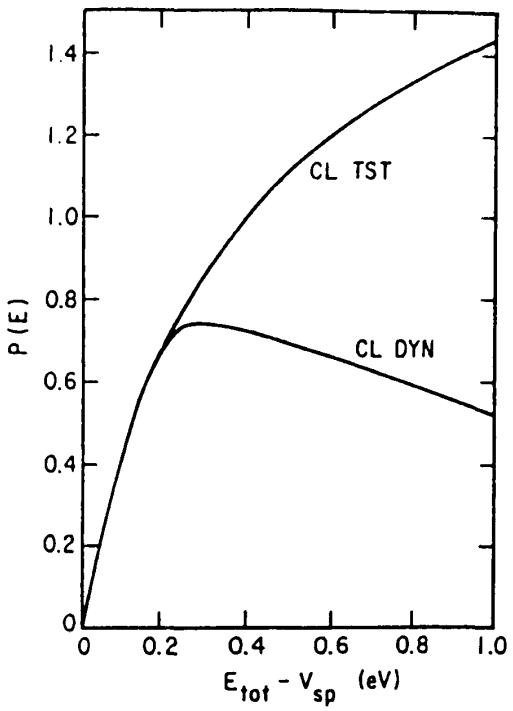

Figure 2 Reaction probability for the collinear H + H_2 reaction on the Porter-Karplus potential surface from a microcanonical classical trajectory calculation (CLDYN) and microcanonical classical transition state theory (CLTST) as a function of total energy above the barrier height (1 eV = 23.06 kcal/mole).

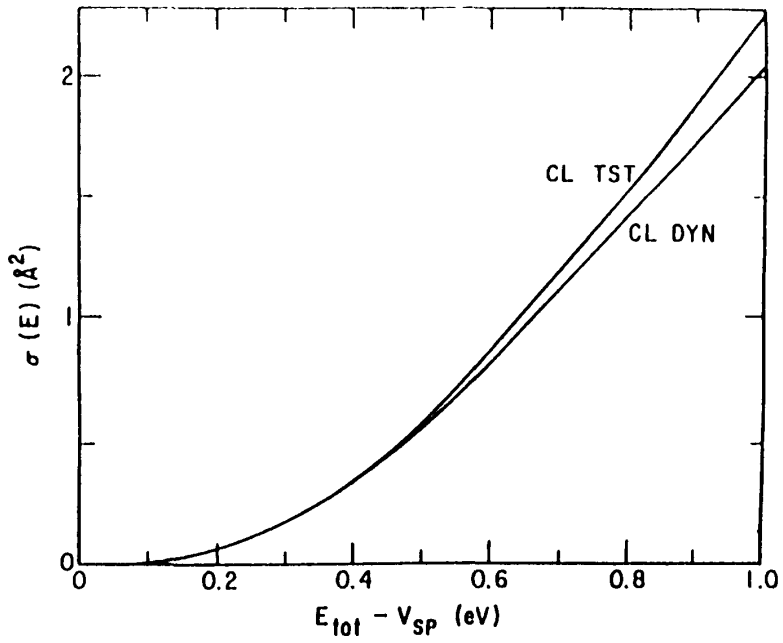

Figure 3 Same as Fig. 2, except that $\sigma(E)$ is the microcanonical reactive cross section for the *three-dimensional* H + H_2 reaction.

increasingly larger than the correct result. That is, as the energy increases there is an increasingly larger fraction of trajectories which "rebound" back across the dividing surface and invalidate the transition state assumption that no trajectories recross it. One also sees that this fraction of TST-violating trajectories is much smaller in three-dimensional space than in one-dimensional.

IV. QUANTUM TRANSITION STATE THEORY

The dynamics of molecular motion must be treated quantum mechanically if one is to have a quantitative description of chemical reactions. Since transition state theory is such a good approximation in classical mechanics—particularly at the lower energies that are most important for determining the thermally averaged rate $k(T)$—one would like to quantize it. Unfortunately there does not seem to be a way to quantize the basic transition state idea without also introducing other approximations. The heuristic argument goes as follows.

The most naive approach to quantizing the TST expression for $N(E)$, Eq. (15), is as follows: the phase-space average becomes a quantum mechanical trace,*

$$N^{(0)}_{\mathrm{QMTST}}(E) = \mathrm{tr}[h(E - \hat{H}^{\ddagger})] = \sum_n h(E - E^{\ddagger}_n) \tag{19}$$

where $\hat{H}^{\ddagger}$ is the Hamiltonian operator in the $(F - 1)$-dimensional space on the dividing surface, and $\{E^{\ddagger}_n\}$ are the eigenvalues (i.e., energy levels) for this bounded motion. The thermal rate constant which results is easily shown from Eq. (11) to be

$$k^{(0)}_{\mathrm{QMTST}}(T) = \frac{kT}{h}\frac{Q^{\ddagger}(T)}{Q_r(T)} \tag{20}$$

but where here $Q^{\ddagger}(T)$ is the *quantum* partition function

$$Q^{\ddagger}(T) = \sum_n e^{-\beta E^{\ddagger}_n} \tag{21}$$

which corresponds to the classical one in Eq. (18).

This zeroth-order approach, however, neglects any quantum mechanical aspect of the reaction coordinate motion (the Fth degree of freedom). If one assumes that the reaction coordinate is separable for the $F - 1$ degrees of freedom on the dividing surface, then the Heaviside function in Eq. (19) is replaced by a one-dimensional tunneling probability.

$$N^{(1)}_{\mathrm{QMTST}}(E) = \sum_n P_F(E - E^{\ddagger}_n) \tag{22}$$

where $P_F(E_F)$ is the tunneling probability for a one-dimensional barrier along the reaction coordinate, as a function of the energy $E_F \equiv E - E^{\ddagger}_n$ in this one degree of freedom. It is easy to show from Eq. (11) that the thermal rate constant corresponding to Eq. (22) is

$$k^{(1)}_{\mathrm{QMTST}}(T) = \kappa(T)\frac{kT}{n}\frac{Q^{\dagger}(T)}{Q_r(T)} \tag{22'}$$

*The quantum mechanical trace of any operator $\hat{A}$ is the sum of its diagonal matrix elements, $\mathrm{tr}(\hat{A}) = \Sigma_i \langle i|\hat{A}|i\rangle$, and is independent of the particular set of basis states $\{|i\rangle\}$ used for this purpose.

where κ, the tunneling correction factor,

$$\kappa(T) = \beta \int_{\epsilon}^{\infty} dE_F\, e^{-\beta E_F} P_F(E_F) \tag{21}$$

results as a multiplicative correction.

The reaction coordinate, however, is clearly *not* separable from the $F - 1$ degrees of freedom on the dividing surface, and at low temperature and for the dynamics of light particles (e.g., hydrogen atoms) the errors resulting from this assumption can be sizable. A *multidimensional* tunneling corrrection (10), one that takes account of coupling between the reaction coordinate and the other degrees of freedom, is thus needed in such cases, and there are a variety of such approximate treatments (11,7) (based primarily on what was learned from semiclassical tunneling calculations (12)). Though many of these are very useful, the only correct multidimensional tunneling correction is to solve the full-dimensional Schrödinger equation, but this is then no longer a "theory" but rather simply the exact quantum result. Unlike classical mechanics, therefore, there is no "rigorous" quantum version of TST—i.e., one that does not make some approximations between couplings of the various degrees of freedom—other than the exact quantum dynamical result.

Before proceeding to consider such rigorous quantum treatments, though, it is useful to note that there does exist a "rigorous" *semiclassical* version of TST.

V. SEMICLASSICAL TRANSITION STATE THEORY

The starting point (13) for semiclassical TST is to note that the classical Hamiltonian can in general be expressed in terms of a set of locally conserved ("good") action variables associated with the transition state (i.e., saddle point) region of the potential energy surface. The first step in SCTST is thus to determine the classical Hamiltonian $H_{cl}(\mathbf{I}) \equiv H_{cl}(I, \ldots, I_F)$ in terms of the F actions $\{I_k\}$. Within a second-order perturbative treatment (14) of the anharmonicity, for example, H_{cl} has the form

$$H_{cl}(\mathbf{I}) = V_0 + \sum_{k=1}^{F} \omega I_k + \sum_{k \le k'=1}^{F} x_{k,k'} I_k I_{k'} \tag{23}$$

where $\{\omega_k\}$ are the normal mode frequencies and $\{x_{k,k'}\}$ are anharmonic constants that are determined by the cubic and quartic force constants of the potential energy surface. If one were considering vibrational motion about a *minimum* on a potential surface, then these actions would be quantized in the usual semiclassical (Bohr-Sommerfeld) fashion:

$$I_k = (n_k + \tfrac{1}{2})\hbar \qquad n_k = 0, 1, \ldots, \tag{24}$$

and Eq. (23) would then yield the vibrational energy levels. For a saddle point H_{cl} has the same form as Eq. (23) (within the perturbative approximation), the only difference being that ω_F, the normal mode frequency associated with the reaction coordinate, is pure imaginary. (Also, of course, one is not thinking of vibrational energy levels in connection with a saddle point but rather the reaction rate through it.) The $F - 1$ actions associated with the bounded degrees of freedom are quantized in the usual semiclassical fashion,

i.e., via Eq. (24), and the action I_F—the one associated with the reaction coordinate—is pure imaginary and defines the generalized barrier penetration integral θ (13).

$$\theta \equiv -\frac{i\pi I_F}{\hbar} \tag{25}$$

θ is determined as a function of total energy E and the $F - 1$ quantum numbers of the activated complex by energy conservation:

$$H_{\text{cl}}\left[I_k = (n_k + \tfrac{1}{2})\hbar,\ I_F = \frac{i\hbar\theta}{\pi}\right] = E \tag{26}$$

i.e., for $\mathbf{n} \equiv \{n_k\}$, $k = 1, \ldots, F - 1$, fixed, one must invert the E-θ relation defined by Eq. (26) to obtain $\theta(E, \mathbf{n})$. Since the dynamics is integrable in terms of the "good" actions, the transmission probability for state $\mathbf{n}$ and energy E has the same form as in one dimension, i.e., $(1 + e^{2\theta})^{-1}$, so the CRP is given by (15)

$$N_{\text{SCTST}}(E) = \sum_{\mathbf{n}} [1 + e^{2\theta(E,\mathbf{n})}]^{-1} \tag{27}$$

The SCTST expression for the thermal rate—which results from Eq. (11) with Eq. (27) for the CRP—can be put in an even more useful form (16), one that avoids having to invert the E-θ relation in Eq. (26). Thus Eqs. (11) and (27) give the thermal rate as

$$k_{\text{SCTST}}(T) = (2\pi\hbar Q_r)^{-1} \sum_{\mathbf{n}} \int_{E_0}^{\infty} dE\ e^{-\beta E}(1 + e^{2\theta(E,\mathbf{n})})^{-1} \tag{28}$$

where E_0 is the reaction threshold and where we have interchanged the order of summation and integration. Since one must integrate over all E in Eq. (28), it is equivalent to change the integration variables from E to θ and integrate over all θ:

$$\begin{aligned}\int_{E_0}^{\infty} dE\ e^{-\beta E}(1 + e^{2\theta(\mathbf{n},E)})^{-1} &= \int_{\infty}^{-\infty} d\theta\ \frac{\partial E(\mathbf{n}, \theta)}{\partial\theta}\ e^{-\beta E(\mathbf{n},\theta)}(1 + e^{2\theta})^{-1} \\ &= \frac{1}{\beta}\int_{-\infty}^{\infty} d\theta\ e^{-\beta E(\mathbf{n},\theta)}\ \frac{1}{2}\ \text{sech}^2(\theta)\end{aligned} \tag{29}$$

where the last line results from an integration by parts. (The surface terms vanish because $E(\theta \to \infty) = E_0$, the reaction threshold, and $E(\theta \to -\infty) = \infty$.) Use of Eq. (29) in Eq. (28) then gives

$$k_{\text{SCTST}}(T) = (2\pi\hbar Q_r\beta)^{-1} \int_{-\infty}^{\infty} d\theta\ \frac{1}{2}\ \text{sech}^2(\theta) \sum_{\mathbf{n}^\ddagger} e^{-\beta E(\mathbf{n}^\ddagger,\theta)} \tag{30}$$

where we have again changed the order of summation and integration. Noting that $(2\pi\hbar\beta)^{-1} = kT/h$, Eq. (30) takes the form of the traditional TST

$$k_{\text{SCTST}}(T) = \frac{kT}{h}\frac{Q^\ddagger(T)}{Q_r(T)} \tag{31a}$$

by defining the reactive partition function of the activated complex (including the tunneling correction factor which is not separable from it) as an average of the fixed θ partition function $Q^{\ddagger}(T, \theta)$ with the weight function $\frac{1}{2}\,\mathrm{sech}^2(\theta)$:

$$Q^{\ddagger}(T) = \int_{-\infty}^{\infty} d\theta\, \frac{1}{2}\, \mathrm{sech}^2(\theta) Q^{\ddagger}(T, \theta) \tag{31b}$$

where

$$Q^{\ddagger}(T, \theta) \equiv \sum_{\mathbf{n}} e^{-\beta E(\mathbf{n}, \theta)} \tag{31c}$$

Applications (16) have demonstrated the usefulness of this formulation of the $k(T)$ calculation.

These SCTST expressions, in both the microcanonical (Eq. (27)) and canonical (Eq. (31)) forms, include coupling between all the degrees of freedom in a uniform manner. For example, even at the perturbative level, Eq. (23), there is an anharmonic coupling between modes of the activated complex $x_{k,k'}$, k and $k' \leq F - 1$) and between the reaction coordinate and modes of the activated complex ($x_{k,F}$, $k \leq F - 1$). This is not a dynamically exact theory, however, because these actions variables are in general only locally "good." For energies too far above or below the barrier V_0 they may fail to exist. This semiclassical theory is thus still a transition state "theory" (i.e., dynamical approximation).

VI. RIGOROUS QUANTUM RATE THEORY

The completely rigorous equilibrium rate constant can also be written in the form of Eq. (11), where for a bimolecular reaction the rigorous expression for the cumulative reaction probability is (17).

$$N(E) = \sum_{n_p} \sum_{n_r} |S_{n_p, n_r}(E)|^2 \tag{32}$$

where n_r (n_p) denote all the quantum numbers of the reactants (products), and the square moduli of the S-matrix elements are the reaction probabilities for the $n_r \rightarrow n_p$ (state-to-state) transition. It is Eq. (32), in fact, which suggests the term "cumulative reaction probability" for $N(E)$: i.e., the *total* reaction probability from initial reactant state n_r is given by

$$P_{n_r}(E) \equiv \sum_{n_p} |S_{n_p, n_r}(E)|^2 \tag{33a}$$

and if one idealized matters by assuming that some initial states are completely reactive and others completely nonreactive, i.e., $P_{n_r} = 0$ or 1, then clearly $N(E)$,

$$N(E) \equiv \sum_{n_r} P_{n_r}(E) \tag{33b}$$

would be the number of reactive states. This interpretation as the "number of reactive states" also comes from transition state theory (cf. Eq. (19)) where there N is the number of states of the activated complex that lie below total energy E, i.e., which have positive kinetic energy in the reaction coordinate at the transition state. In reality, of course, reaction probabilities can take on any values between 0 and 1, but the interpretation of $N(E)$ as the effective number of quantum states which react is still qualitatively useful.

Though Eq. (32) provides a rigorous quantum definition of the cumulative reaction probability, it is not helpful in a practical sense because a complete state-to-state reactive scattering calculation is required to obtain the S matrix. We seek a more direct (and thus presumably more efficient) route to $N(E)$, but without approximation, to which approximations can be incorporated later as needed in specific applications.

A formally exact (and "direct") expression for $N(E)$ can be obtained by quantizing the dynamically exact classical expression, Eq. (9) (with Eq. (7)); the classical phase-space average becomes a quantum trace, and classical functions become operators:

$$N(E) = 2\pi\hbar \text{ tr}[\delta(E - \hat{H})\hat{F}\hat{\chi}_r] \tag{34}$$

where

$$\hat{\chi}_r = \lim_{t\to\infty} h[f(\hat{\mathbf{q}}(t))]$$

and we note that quantum mechanical time evolution is expressed as

$$\hat{\chi}_r = \lim_{t\to\infty} e^{i\hat{H}t/\hbar}\, h[f(\mathbf{q})]\, e^{-i\hat{H}t/\hbar} \tag{35}$$

($\hat{\chi}_r$ is a projection operator that projects onto all states that are on the product side of the dividing surface in the infinite future.) The long-time limit can also be written as the integral of the time derivative:

$$\begin{aligned} \lim_{t\to\infty} h[f(\hat{\mathbf{q}}(t))] &= \int_0^\infty dt\, \frac{d}{dt}\, h[f(\hat{\mathbf{q}}(t))] \\ &= \int_0^\infty dt\, e^{i\hat{H}t/\hbar}\hat{F}e^{-i\hat{H}t/\hbar} \end{aligned} \tag{36}$$

where $\hat{F}$ is the flux operator

$$\hat{F} = \frac{i}{\hbar}\,[\hat{H},\, h(\hat{f}(\mathbf{q}))] \tag{37}$$

Interchanging the order of the trace and the time integral, and noting that the (real part of the) integrand is even, then gives

$$N(E) = (2\pi\hbar)\,\frac{1}{2}\int_{-\infty}^{\infty} dt\, \text{tr}[\delta(E - \hat{H})\hat{F}e^{i\hat{H}t/\hbar}\hat{F}e^{-i\hat{H}t/\hbar}]$$

But the operator $e^{-i\hat{H}t/\hbar}$ can be replaced by the scalar $e^{-iEt/\hbar}$ since this operator sits next to $\delta(E - \hat{H})$ (with a cyclic permutation inside the trace), and with the identity

$$\int_{-\infty}^{\infty} dt\, e^{i(\hat{H}-E)t/\hbar} = 2\pi\hbar\delta(E - \hat{H})$$

one obtains the following result (18):

$$N(E) = \tfrac{1}{2}(2\pi\hbar)^2 \text{ tr}[\hat{F}\delta(E - \hat{H})\hat{F}\delta(E - \hat{H})] \tag{38}$$

Equation (38) is quite a beguiling expression. For example, in the classical expression for $N(E)$, Eq. (9), there is a *statistical* factor $\delta(E - H)$, the flux factor F, and

a *dynamical* factor χ. A similar structure exists in the quantum expression, Eq. (34), where the dynamical factor is the projection operator $\hat{\chi}_r$. The manipulations following Eq. (35), however, lead to the result, Eq. (38), which appears to have *no* dynamical information; i.e., only the statistical operator $\delta(E - \hat{H})$ and flux operator $\hat{F}$ are involved in Eq. (38). This is an example of the fact that dynamics and statistics are inseparably intertwined in quantum mechanics; e.g., a wave function describes the *dynamical motion* of the particles and also their *statistics*. Finally, note that one cannot convert Eq. (38) directly to a corresponding classical expression by replacing the trace by a phase-space average and the operators by the corresponding functions (as one *can* do for Eq. (34)). If one tries, the result is

$$N(E) = \tfrac{1}{2}(2\pi\hbar)^2(2\pi\hbar)^{-F} \int d\mathbf{p} \int d\mathbf{q}\, \delta(E - H(\mathbf{p}, \mathbf{q}))^2 F(\mathbf{p}, \mathbf{q})^2 \tag{39}$$

which appears to be infinite (because of the squares of the delta functions); the factor $\hbar^2$ (which does not divide out in normalization) is 0 in the classical limit, however, so Eq. (39) is simply indeterminant.

The difficult part of Eq. (38) to evaluate is the microcanonical density operator, $\delta(E = \hat{H})$, which is usually (19) expressed in terms of the outgoing wave Green's function (actually an *operator*)

$$\delta(E - \hat{H}) = -\frac{1}{\pi} \operatorname{Im} \hat{G}^{+}(E) \tag{40a}$$

where

$$\hat{G}^{+}(E) = \lim_{\varepsilon \to 0} (E + i\varepsilon - \hat{H})^{-1} \tag{40b}$$

ε is a positive constant which imposes the outgoing wave boundary condition on the Green's function (hence the "+" designation), or it may be thought of as a convergence factor in the expression for G^{+} in terms of the time evolution operator $e^{-i\hat{H}t/\hbar}$:

$$\hat{G}^{+}(E) = (i\hbar)^{-1} \int_0^{\infty} dt\, e^{i(E + i\varepsilon)t/\hbar} e^{-i\hat{H}t/\hbar}$$

the factor $\exp(-\varepsilon t/\hbar)$ in the integrand makes the time integral well behaved in the long time ($t \to \infty$) limit.

The parameter ε in Eq. (40b) usually plays a purely formal role in quantum scattering theory, but it has recently (4a) been pointed out that one may think of it as the *absorbing potential* that a number of persons (20) have used in numerical wave packet propagation calculations to prevent reflections at the edge of the coordinate space grid. In this latter approach one adds a negative imaginary potential to the true potential energy function:

$$V(\mathbf{q}) \to V(\mathbf{q}) - i\varepsilon(\mathbf{q}) \tag{41a}$$

but this is clearly equivalent to adding the positive (operator) ε to E in $E - H$:

$$E - \hat{H} \to E + i\varepsilon(\mathrm{q}) - \hat{H} \tag{41b}$$

Allowing ε to be a (positive) function of coordinates, i.e., a potential energy operator, is better than taking it to be a constant, because it can be chosen to be zero in the physically

relevant region of space and only "turned on" at the edges of this region to impose the outgoing wave boundary condition. Absorbing flux in this manner, and thus not allowing it to return to the interaction region, is analogous in a classical calculation to terminating trajectories when they exit the interaction region.

Figure 4 shows a sketch of the potential energy surface for the generic reaction $H + H_2 \rightarrow H_2 + H$, with the absorbing potential $\varepsilon(\mathbf{q})$ indicated by dashed contours. $\varepsilon(\mathbf{q})$ is zero in the transition state region, where the reaction dynamics (i.e., tunneling, recrossing dynamics, etc.) takes place, and is turned on outside this region. In practice one chooses the interaction region (that between the absorbing potentials) to be as small as possible, so that as small a basis set as possible can be used to represent the operators and evaluate the trace. Choosing it too small, though, will cause the absorbing potentials to interfere with reaction dynamics one is attempting to describe.

With the microcanonical density operator given by Eq. (40) (with some choice for ε), straightforward algebraic manipulations (also using Eq. (37)) lead to the following even simpler form for the cumulative reaction probability (4b):

$$N(E) = 4\ \mathrm{tr}[\hat{G}^{+}(E)^{*}\hat{\varepsilon}_p\hat{G}^{+}(E)\hat{\varepsilon}_r] \tag{42a}$$

where ε_r (ε_p) is the part of the adsorbing potential in the reactant (product) valley, and $\varepsilon \equiv \varepsilon_r + \varepsilon_p$. This expression may be evaluated in any convenient basis set which spans the interaction region and also extends some ways into the absorbing region. The explicit matrix expression is then

$$N(E) = 4\ \mathrm{tr}[(E - i\varepsilon - \mathbf{H})^{-1} \cdot \varepsilon_p \cdot (E + i\varepsilon - \mathbf{H})^{-1} \cdot \varepsilon_r] \tag{42b}$$

It is interesting that in Eq. (42) all reference to a specific dividing surface has vanished; it is implicit that a dividing surface lies somewhere between the reactant and product "absorbing strips" (cf. Fig. 4), but there is no dependence on its specific choice. This is consistent with the earlier discussion that in classical mechanics $N(E)$ is independent of the choice of the dividing surface provided that one actually determines the exact dynamics (cf. Liouville's theorem), as is being done here quantum mechanically.

VII. CUMULATIVE REACTION PROBABILITY AS AN EIGENVALUE PROBLEM

In recent work (21) it has been shown that the most efficient way to evaluate the trace in Eq. (42) is first to symmetrize the operand of the trace,

$$N(E) = \mathrm{tr}[\hat{P}(E)] \tag{43a}$$

where

$$\hat{P}(E) \equiv 4\hat{\varepsilon}_r^{1/2}\hat{G}(E)^{*}\varepsilon_p\hat{G}(E)\hat{\varepsilon}_r^{1/2} \tag{43b}$$

$\hat{P}(E)$ is seen to be a Hermitian operator (or matrix), so that its eigenvalues $\{p_k(E)\}$ are all real, and from Eq. (44a) the CRP is their sum

$$N(E) = \sum_k p_k(E) \tag{44}$$

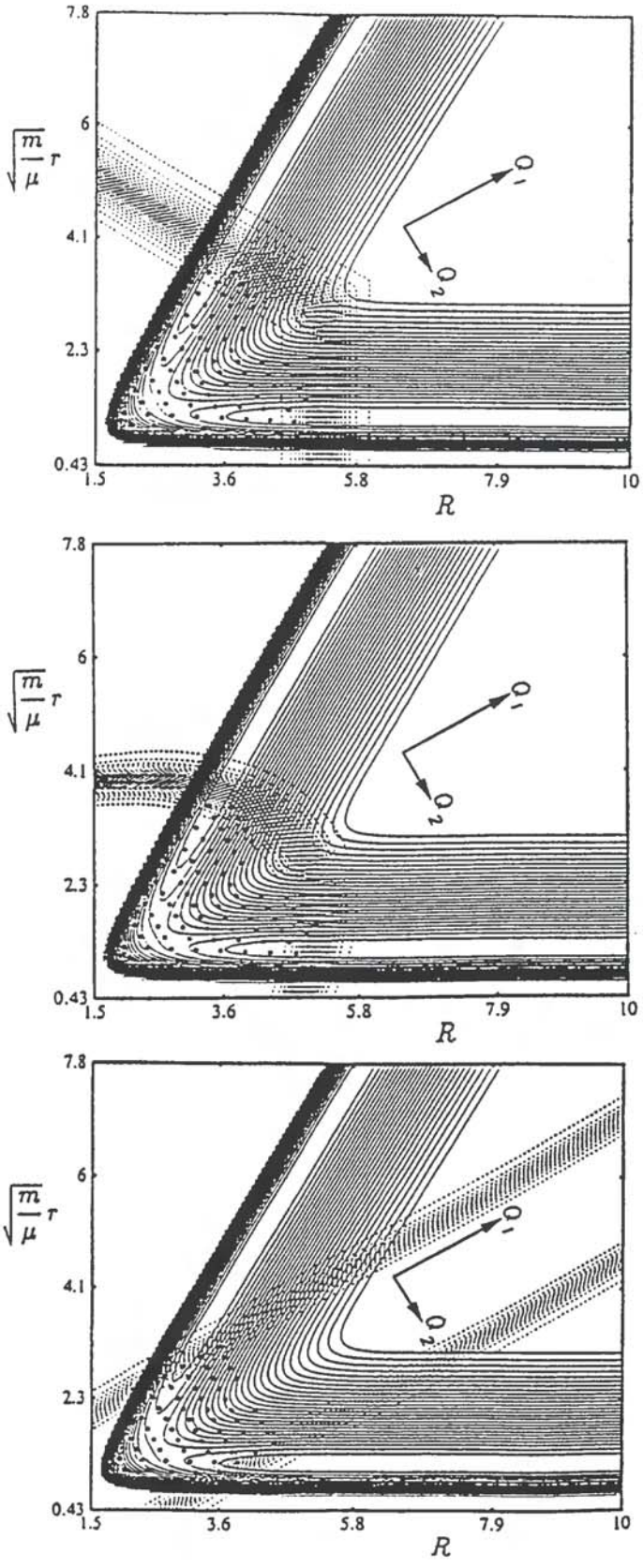

Figure 4 Solid lines are contours of the potential energy surface for the $H + H_2 \rightarrow H_2 + H$ reaction. Broken lines are contours of the absorbing potential (which is zero in the central part of the interaction region and "turned on" at the edge), for three possible choices of it. The points are the grid points which constitute the "basis set" for the evaluation of the quantum trace, Eq. (42).

It is also easy to see that $\hat{P}(E)$ is a positive operator (since it has the form $L^{\dagger}L$), so that its eigenvalues are all positive. It is not as obvious—but can be readily shown—that $\hat{P}(E)$ is also bounded by the identity operator

$$\hat{P}(E) \leq 1 \tag{45a}$$

from which it follows that

$$0 \leq p_k(E) \leq 1 \tag{45b}$$

The eigenvalues $\{p_k\}$ can thus be thought of as *probabilities*, and then Eq. (44) bears an interesting relation to the simple transition state expression, Eq. (22), in which $N(E)$ is given (approximately) as a sum of one-dimensional tunneling (or transmission) probabilities over all states of the activated complex. The *exact* $N(E)$ is given in Eq. (44) as the sum of the "eigenreaction probabilities" $\{p_k\}$, the eigenvalues of the operator $\hat{P}$ defined by Eq. (43b).

Equations (42)–(44) provides the first practical scheme for determining the rate constant for a chemical reaction absolutely *correctly*, but *directly*, i.e., without having to solve the complete reactive scattering problem. This is not a transition state "theory" since calculation of the Green's function, the matrix inverse of $E + i\varepsilon - \mathbf{H}$, is equivalent to solving the Schrödinger equation; i.e., it generates the complete quantum dynamics. Since this is required only in the transition state region (between the reactant and product absorbing strips), one may think of this quantum mechanical calculation as the analog of a classical trajectory calculation which begins trajectories on a dividing surface in the transition state region and follows them for a short time to see which ones are reactive.

VIII. SOME RECENT APPLICATIONS

In recent applications (4,21–23) is has proved useful to employ a set of *grid points* in coordinate space as the basis set in which to evaluate Eqs. (42b) or (43) and (44). These discrete variable (24), pseudospectral (25), or collocation methods (26) are proving quite useful for a variety of molecular quantum mechanical calculations. The primary advantages of such approaches are that (1) no integrals are required in order to construct the Hamiltonian matrix (e.g., the potential energy matrix is diagonal, the diagonal values being the values of the potential energy function at the grid points), and (2) the Hamiltonian matrix is extremely sparse (so that large systems of linear equations can be solved efficiently).

Figure 4c shows the set of grid points and the absorbing potentials which yield accurate results for the standard test problem, the collinear $H + H_2 \rightarrow H_2 + H$ reaction. The important feature to see here is how close the absorbing potentials can be brought in and how localized the grid can be taken about the transition state region. This is the region in which it is necessary to determine the quantum dynamics in order to obtain the correct result for $N(E)$ (and thus $k(T)$). No information about reactant and product quantum states is involved in the calculation.

Figure 5a shows the cumulative reaction probability so obtained (4a) for the collinear $H + H_2$ reaction. Apart from noting that it is correct (by comparison with earlier scattering calculations (27) using Eq. (32)), it is interesting to observe that at the higher energies $N(E)$ is not a monotonically increasing function of energy. This is a signature of transition-state-theory-violating dynamics, i.e., recrossing trajectories in a classical

picture, and the result of a short-lived collision complex that causes resonances in a quantum description.*

For the H + H_2 reaction in three-dimensional space one needs to add in the bending degree of freedom in the transition state region and also allow the three-atom system to rotate. Figure 5b shows the cumulative reaction probability obtained (4b) for zero total angular momentum ($J = 0$), and again it is in complete agreement with results (28) obtained from Eq. (32) via full scattering calculations. Even though collision complexes also form in the three-dimensional version of the H + H_2 reaction, $N(E)$ in Fig. 5b appears (to the eye, at least) to increase monotonically with energy in transition-state-like fashion. This is the quantum mechanical analog of the phenomenon seen above classically (9), where the dynamics behaves more transition-state-like the higher the physical dimension of the system.

A more challenging application (22) is to the reaction

$$H + O_2 \rightarrow OH + O \tag{46}$$

which is one of the most important reactions for modeling the combustion of hydrocarbons. Figure 6 shows a schematic of the potential surface (29), and one sees why this is a more complicated reaction to deal with: the deep well (~2 eV) in the interaction region leads to the formation of a moderately long-lived collision complex, strongly violating the transition state assumption of "direct dynamics." The rigorous quantum methodology described above, however, is nevertheless applicable: absorbing potentials are introduced just outside the interaction region where all the reaction dynamics (tunneling, recrossings, etc.) is determined, and the grid points cover the region in between. Figure 7 shows the cumulative reaction probability for this reaction (for $J = 0$ total angular momentum), and structure resulting from the collision complex is readily observable. Figure 8 shows the thermal rate constant obtained by Boltzmann averaging $N(E)$ via Eq. (11), and in it one sees that all remnants of the resonance structure has vanished. There is excellent agreement with the latest experimental results of Du and Hessler (30).

Full (six)-dimensional calculations for the CRP of the reaction (23)

$$H_2 + OH \rightarrow H + H_2O \tag{47}$$

have also been carried out and are shown in Fig. 9 (for total angular momentum $J = 0$), the first such calculation of the CRP for a four-atom reaction. This reaction is very

---

*$N(E)$ will always increase monotonically with E in a transition state approximation. It is easy to prove this classically, e.g., from Eq. (15). If the dividing surface is held fixed as E varies, then from Eq. (15) one has

$$\frac{d}{dE} N_{TST}(E) = (2\pi\hbar)^{-(F-1)} \int d\mathbf{p}' \int d\mathbf{q}' \, \delta[E - H^{\ddagger}]$$

which is clearly positive. Furthermore, if the dividing surface is parameterized and allowed to vary with energy, the above equation still holds because any parameters in the dividing surface are chosen variationally. Thus, if the dividing surface (and thus the Hamiltonian $H^{\ddagger}$) depends on some parameters $c_1, c_2, \ldots = \{c_k\}$, then the expression for N_{TST} will depend not only on the energy E but also on these parameters, $N_{TST}(E, c_1, c_2, \ldots)$. The values of the c_k's are chosen, however, by the variational condition $0 = (\partial/\partial c_k) N_{TST}(E, \{c_k\})$, which determines specific values $c_k(E)$. Thus, the variationally optimized result for the cumulative reaction probability is $N_{TST}(E, c_1(E), c_2(E), \ldots) \equiv N_{TST}(E)$. Then

$$\frac{d}{dE} N_{TST}(E) = \frac{\partial}{\partial E} N_{TST}(E,\{c_k\}) + \sum_k \partial N_{TST}/\partial c_k \, c_k'(E)$$

but the last terms are all zero because of the variational conditions.

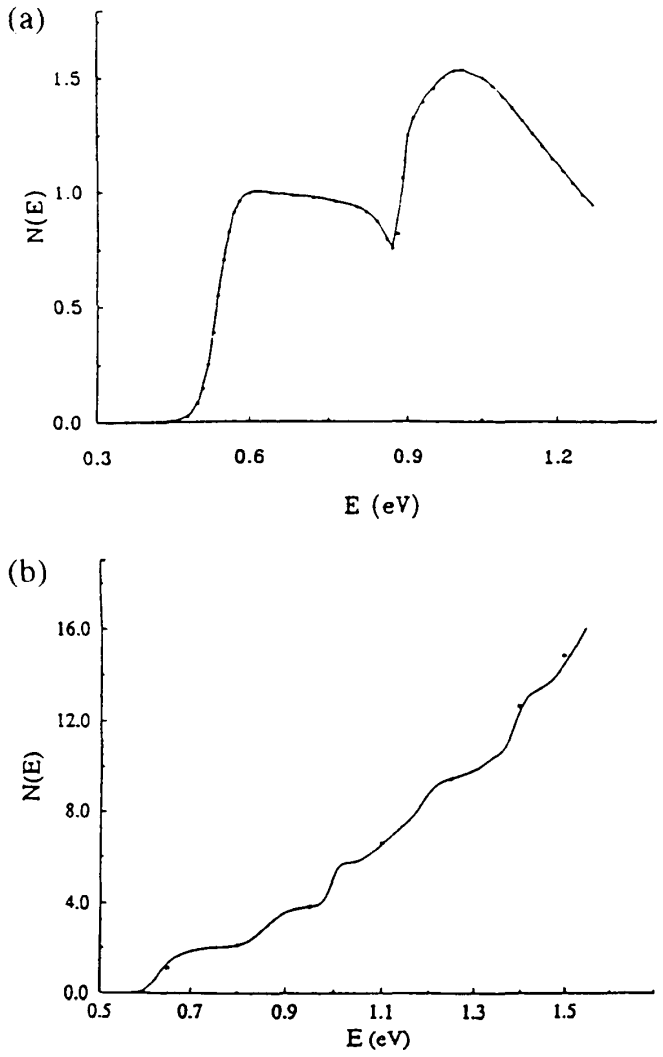

Figure 5 Cumulative reaction probability for the $H + H_2 \rightarrow H_2 + H$ reaction (a) for collinear geometry (Ref. 4a), (b) three-dimensional space for total angular momentum $J = 0$ (Ref. 4b). The solid lines are the present results, and the dots the results of earlier scattering calculations (27 and 29, respectively, for a and b) using Eq. (32).

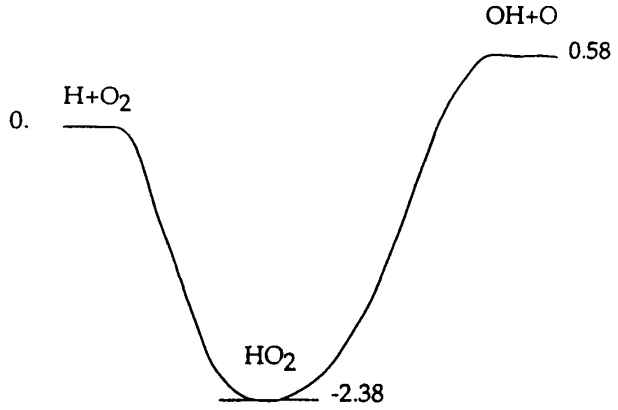

Figure 6 Energetics (in eV) of the H—O—O potential energy surface.

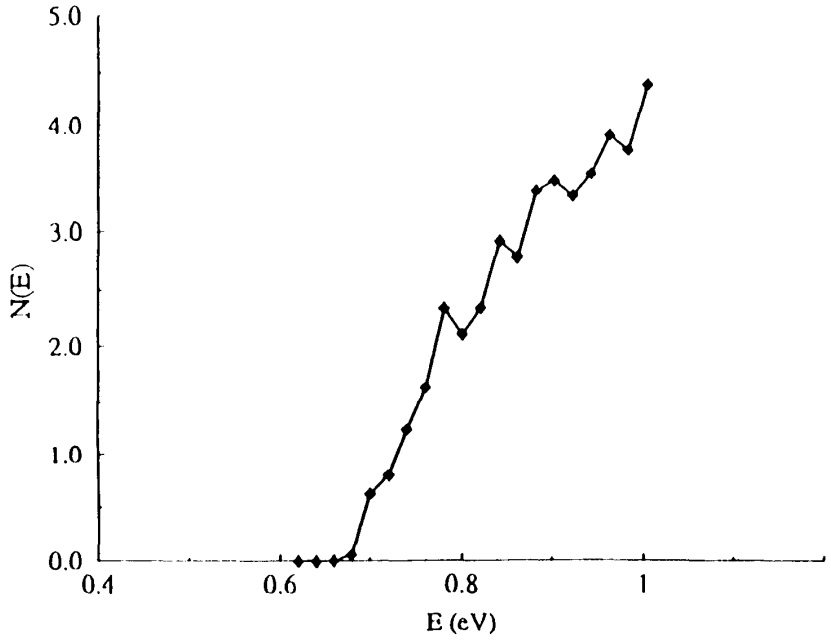

Figure 7 The cumulative reaction probability, for the H + O_2 → OH + O reaction as a function of total energy, for total angular momentum $J = 0$.

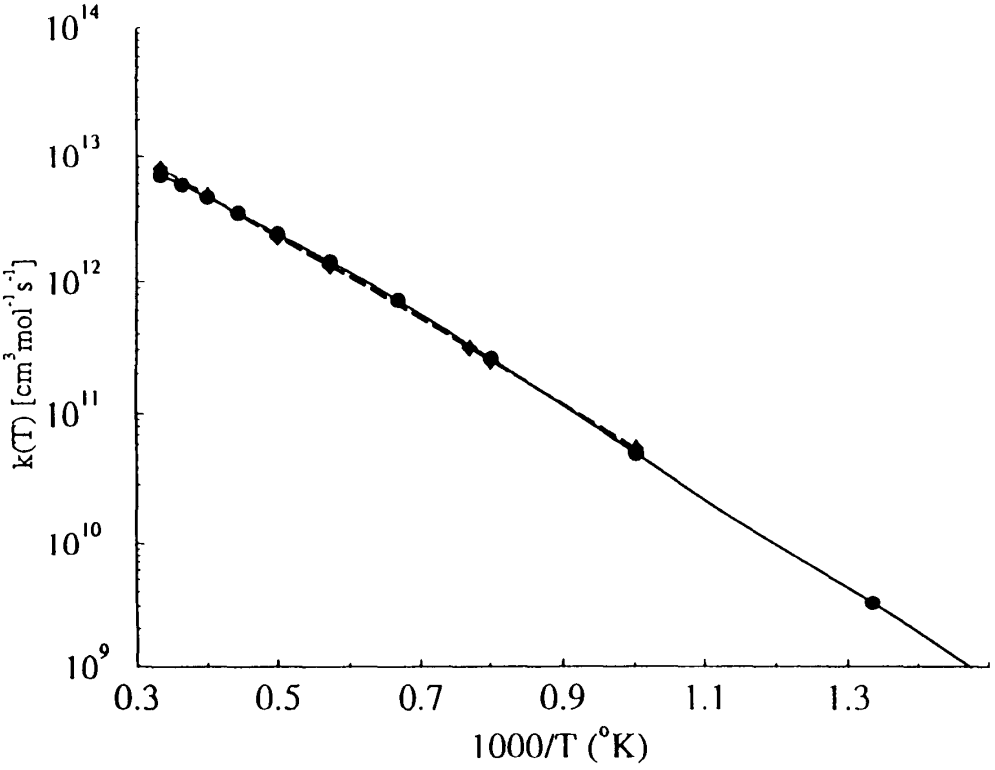

Figure 8 Thermal rate constant for the H + O_2 → OH + O reaction; the solid line is the present theoretical result obtained by Boltzmann averaging $N(E)$ (of Fig. 7) via Eq. (11), and the dashed line is the experimental results of Ref. 8.

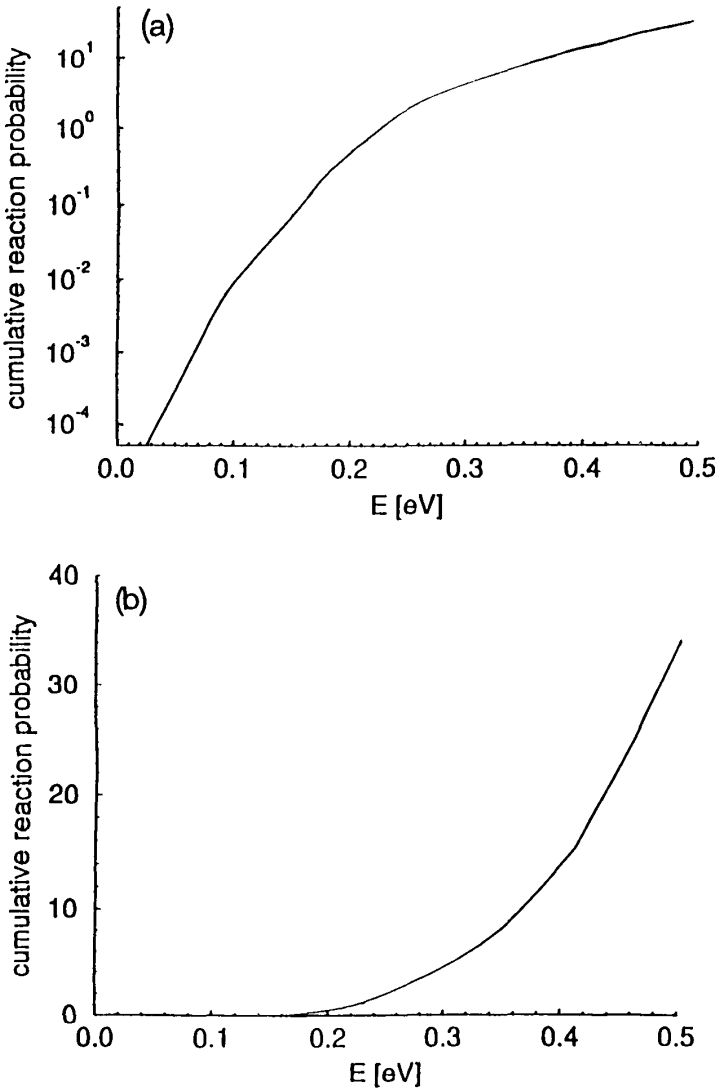

Figure 9 The cumulative reaction probability for the $H_2 + OH \rightarrow H_2O + H$ reaction as a function of total energy, for total angular momentum $J = 0$; (a) logarithmic scale, (b) linear scale.

"transition-state-like" because there is a simple saddle point separating reactants and products. One qualitative feature that one notes, compared for example to the CRP for the three-dimensional $H + H_2$ reaction in Fig. 5b, is that the "stair case structure" that is a holdover from the classical sum of step functions (Eq. (19)) is absent in Fig. 9. This is readily understood by looking at the individual eigenreaction probabilities $\{p_k(E)\}$ in Fig. 10; the higher density of states for the four-atom system results in the "overlap" of the various threshold structures.

Finally, calculations for the CRP have been carried out (31) for the isomerization of ketene:

$$H_2C{=}C'{=}O \leftrightarrow O{=}C{=}C'H_2 \tag{48}$$

where C and C′ indicate carbon isotopes ^{12}C and ^{13}C (so that reactants and products are distinguishable). Figure 11 shows a one-dimensional sketch along the reaction path for this reaction (32), and its most important feature is the existence of a metastable region

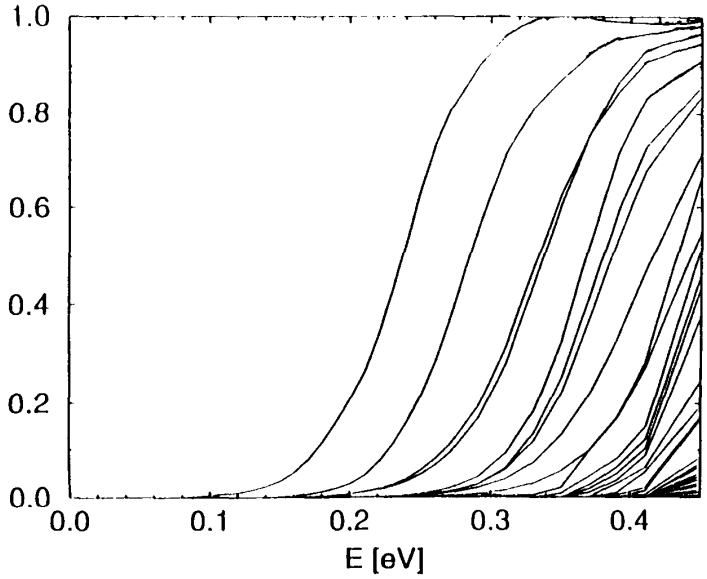

Figure 10 Eigenreaction probabilities $\{p_k(E)\}$ for the H_2 + OH → H_2O + H reaction, as a function of total energy.

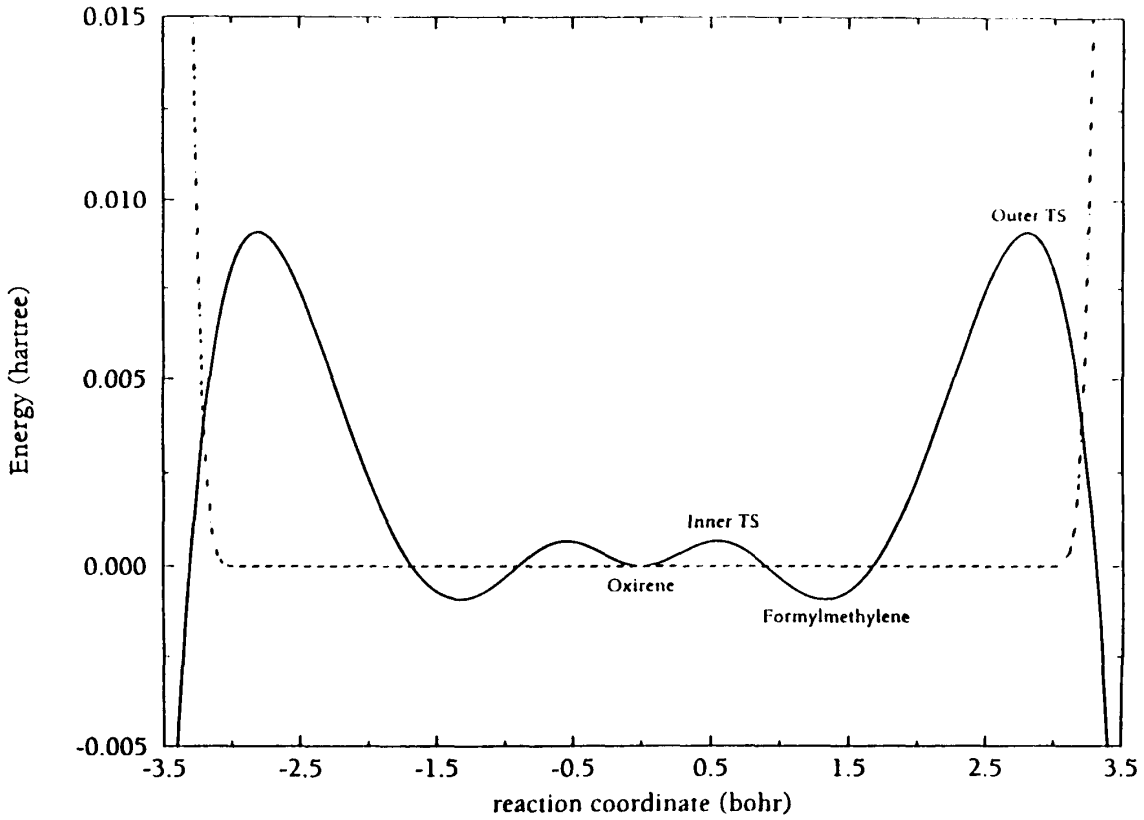

Figure 11 A one-dimensional sketch of the potential energy surface for the isomerization of ketene, $H_2C{=}C'{=}O \rightarrow O{=}C{=}C'H_2$.

about the oxirene geometry

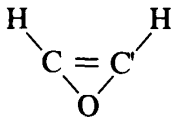

(49)

The reaction thus takes place by the two H atoms and the O atom running around, changing ends of the C=C moity, passing through the oxirene geometry. This is a multidimensional version of tunneling through a double-barrier potential, with the possibility of resonance structure in the energy dependence due to weak quantization of the metastable oxirene species. Recent experiments by Lovejoy and Moore (33) have clearly revealed similar resonance features.

Figure 12 shows preliminary results that have been obtained for the microcanonical rate $k(E)$ (Eq. (8)) as a function of energy E, compared to the experimental values. Though individual features do not match up one-for-one—which is quite beyond the accuracy of the present potential energy surface—the density and widths of the resonance features are in quite good agreement with each other. The calculations definitely lend credence to the validity of the experimental results and their interpretation as metastable resonance structure.

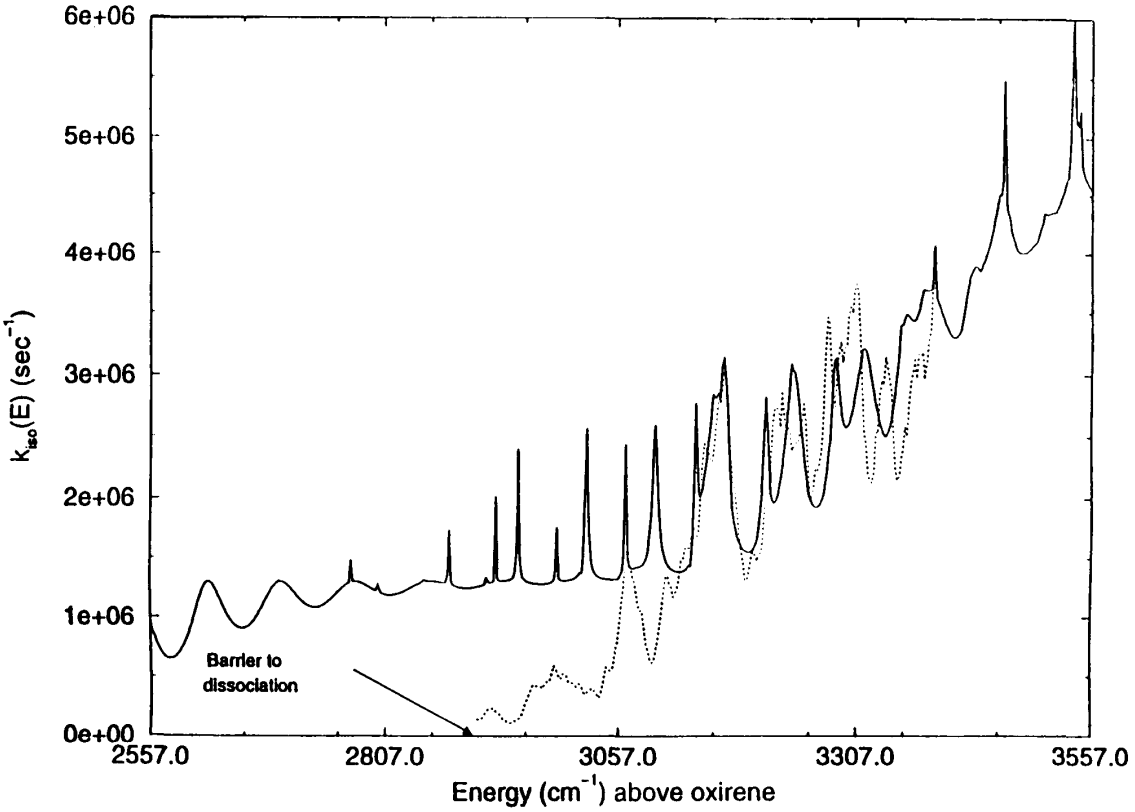

Figure 12 Microcanonical rate constant, $k(E)$, obtained theoretically (solid line) compare to the experimental results of Ref. 33.

IX. DIRECT CALCULATION OF $k(T)$

Most of the above discussion has concentrated on calculation of the cumulative reaction probability, $N(E)$, from which one obtains the microcanonical rate $k(E)$ via Eq. (8) or the canonical rate $k(T)$ by averaging over total energy as in Eq. (11). If one is primarily interested in the thermal rate, however, it would clearly be desirable to be able to calculate it "directly" for a given temperature T and not have to calculate $N(E)$ at many values of E.

This is possible in precisely the same fashion as above for $N(E)$. Thus just as Eq. (34) is the rigorous quantum expression for $N(E)$ that corresponds to the classical expression Eq. (9), the following expression for $k(T)$ is the quantum version which corresponds to the classical expression, Eq. (1), for $k(T)$:

$$k(T) = Q_r(T)^{-1} \lim_{t\to\infty} \mathrm{tr}[e^{-\beta\hat{H}}\hat{F}e^{i\hat{H}t/\hbar}\hat{h}e^{-i\hat{H}t/\hbar}] \tag{50}$$

Since $h^2 = h$, this expression can be symmetrized as

$$k(T) = Q_r(T)^{-1} \lim_{t\to\infty} \mathrm{tr}\,\hat{P}(t) \tag{51a}$$

where

$$\hat{P}(t) = \hat{h}e^{-i\hat{H}t/\hbar}\hat{F}e^{i\hat{H}t/\hbar}\hat{h} \tag{51b}$$

$\hat{P}(t)$ is a manifestly Hermitian operator and is also of low rank, so the trace in Eq. (51a) can be conveniently evaluated by the same tricks used in Eqs. (43)–(45).

This approach is currently under active development (35) and should be of most interest for the case of bimolecular reactions, where one is usually interested in obtaining the thermal rate constant $k(T)$.

X. CONCLUDING REMARKS

Considerable progress has thus been made in the ability to compute a chemical reaction rate *directly*, without having to solve the complete state-to-state reactive scattering problem, but also *correctly*, i.e., without inherent approximation. One does not avoid having to solve the Schrödinger equation, but must only solve it locally, in the transition state region between reactants and products. In this sense the rigorous theory retains a flavor of transition state theory. More specifically, the cumulative reaction probability is most efficiently calculated by determining the eigenreaction probabilities $\{p_k\}$ (Eq. (44)), which are the rigorous analog of the TST transmission probabilities (Eq. (22)).

Even with this progress, though, rigorous calculations of the type described above for $H+O_2$ and $OH+H_2$ are feasible only for relatively small molecular systems (though "small" is somewhat larger than it used to be!). To deal with more complex systems one would like to be able to combine rigorous quantum treatments such as these for the few degrees of freedom most strongly involved in the chemical reaction with an approximate treatment of the (perhaps many) remaining degrees of freedom that are not so intimately involved. One would ideally like this "approximate treatment" to be based on classical mechanics, perhaps in a *semi*classical framework, so that classical trajectory simulation methodology can be brought to bear. Various ideas of this type exist (35,36), and one expects to see progress along these lines.

ACKNOWLEDGMENT

This work has been supported by the Director, Office of Energy Research, Office of Basic Energy Sciences, Chemical Sciences Division, of the U.S. Department of Energy under contract DE-AC03-76SF00098 and also by the National Science Foundation under grant CHE-8920690.

REFERENCES

1. (a) An interesting set of papers by many of the founders of the theory—Wigner, M. Polanyi, Evans, Eyring—is in *Trans. Faraday Soc. 34*: 1–127 (1938). (b) For a reasonably recent review, see D. G. Truhlar, W. L. Hase, and J. T. Hynes, *J. Phys. Chem. 87*: 2664 (1983).
2. E. Wigner, *Trans. Faraday Soc. 34*: 29 (1938).
3. P. Pechukas, *Dynamics of Molecular Collisions*, Part B (W. H. Miller, ed.), Plenum, New York, 1976, chap. 6.
4. (a) T. Seideman and W. H. Miller, *J. Chem. Phys. 96*: 4412 (1992). (b) T. Seideman and W. H. Miller, *J. Chem. Phys. 97*: 2499 (1992). (c) W. H. Miller and T. Seideman, Cumulative and state-to-state reaction probabilities via a discrete variable representation—absorbing boundary condition Green's function, *Time Dependent Quantum Molecular Dynamics: Experiments and Theory* (J. Broeckhove, ed., NATO ARW. (d) W. H. MIller, *Accts. Chem. Res. 26*: 174 (1993).
5. W. H. Miller *Accts. Chem. Res. 9*: 306 (1976).
6. (a) J. C. Keck, *Adv. Chem. Phys. 13*: 85 (1967). (b) J. Horiuti, *Bull. Chem. Soc. Jpn. 13*: 210 (1938).
7. For a review of many applications of this variational feature, see (a) D. G. Truhlar and B. C. Garrett, *Accs. Chem. Res. 13*: 440 (1980). (b) Ann. Rev. *Phys. Chem. 35*: 159 (1984).
8. (a) F. J. McLafferty and P. Pechukas, *J. Chem. Phys. 58*: 1622 (1973). (b) F. J. McLafferty and P. Pechukas, *Chem. Phys. Lett. 27*: 511 (1974).
9. S. Chapman, S. M. Hornstein, and W. H. Miller, *J. Am. Chem. Soc. 97*: 892 (1975).
10. H. S. Johnston and D. Rapp, *J. Am. Chem. Soc. 83*: 1 (1961).
11. (a) R. A. Marcus and M. E. Coltrin, *J. Chem. Phys. 67*: 2609 (1977). (b) Ref. 8b. (c) N. Makri and W. H. Miller, *J. Chem Phys. 91*: 4026 (1989).
12. (a) T. F. George and W. H. Miller, *J. Chem. Phys. 57*: 2458 (1972). (b) S. M. Hornstein and W. H. Miller, *J. Chem. Phys. 61*: 745 (1974).
13. W. H. Miller, *Faraday Disc. Chem. Soc. 62*: 40 (1977).
14. (a) W. H. Miller, R. Hernandez, N. C. Handy, D. Jayatilaka, and A. Willetts, *Chem. Phys. Lett. 172*: 62 (1990). (b) M. J. Cohen, H. C. Handy, R. Hernandez, and W. H. Miller, *Chem. Phys. Lett. 192*: 407 (1992).
15. This is also closely related to the semiclassical periodic orbit (''instanton'') theory; W. H. Miller, *J. Chem. Phys. 62*: 1899 (1975).
16. R. Hernandez and W. H. Miller, *Chem. Phys. Lett. 214*: 129 (1993).
17. W. H. Miller, *J. Chem. Phys. 61*: 1823 (1974).
18. (a) W. H. Miller, S. D. Schwartz, and J. W. Tromp, *J. Chem. Phys. 79*: 4889 (1983). (b) J. W. Tromp and W. H. Miller, *J. Phys. Chem. 90*: 3482 (1986).
19. See, for example, R. G. Newton, *Scattering Theory of Waves and Particles*, Springer-Verlag, Berlin, 1982, p. 176 *et seq.*
20. (a) A. Goldberg and B. W. Shore, *J. Phys. B. 11*: 3339 (1978). (b) C. Leforestier and R. E. Wyatt, *J. Chem. Phys. 78*: 2334 (1983). (c) R. Kosloff and D. Kosloff, *J. Comput. Phys. 63*: 363 (1986). (d) D. Neuhauser and M. Baer, *J. Chem. Phys. 90*: 4351 (1989).
21. U. Manthe and W. H. Miller, *J. Chem. Phys. 99*: 3411 (1993).
22. C. Leforestier and W. H. Miller, *J. Chem. Phys. 100*: 733 (1994).

23. U. Manthe, T. Seideman, and W. H. Miller, *J. Chem. Phys. 99*: 10078 (1993); 101, 4759 (1994).
24. (a) J. V. Lill, G. A. Parker, and J. C. Light, *J. Chem. Phys. 85*: 900 (1986). (b) J. T. Muckerman, *Chem. Phys. Lett. 173*: 200 (1990).
25. (a) R. A. Friesner, *Chem. Phys. Lett. 116*: 39 (1985). (b) R. A. Friesner, *J. Chem. Phys. 85*: 1462 (1986).
26. (a) A. C. Peet and W. H. Miller, *Chem. Phys. Lett. 149*: 257 (1988). (b) W. Yang, A. C. Peet, and W. H. Miller, *J. Chem. Phys. 91*: 7537 (1989).
27. D. K. Bondi, D. C. Clary, J. N. L. Connor, B. C. Garret, and D. G. Truhlar, *J. Chem. Phys. 76*: 4986 (1982); D. K. Bondi and J. N. L. Connor, *J. Chem. Phys. 82*: 4383 (1985).
28. D. C. Chatfield, R. S. Friedman, D. G. Truhlar, B. C. Garrett, and D. W. Schwenke, *J. Am. Chem. Soc. 113*: 486 (1991).
29. M. R. Pastrana, L. A. M. Quintales, J. Brandão, and J. A. C. Varandas, *J. Phys. Chem. 94*: 8073 (1990).
30. H. Du and J. P. Hessler, *J. Chem. Phys. 96*: 1077 (1992).
31. D. Gezelter and W. H. Miller, *J. Chem. Phys. 103*: 7868 (1995).
32. A. P. Scott, R. H. Nobes, H. F. Schaefer III, and L. Radom, *J. Am. Chem. Soc.*, in press.
33. E. R. Lovejoy and C. B. Moore, *J. Chem. Phys. 98*: 7846 (1993).
34. W. H. Thompson and W. H. Miller, *J. Chem. Phys. 102*: 7409 (1995).
35. B. Vekhter, M. A. Ratner, and R. B. Gerber, *J. Chem. Phys. 99*: 7916 (1993).
36. S. Keshavamurthy and W. H. Miller, *Chem. Phys. Lett. 218*: 189 (1994).

11

The Geometric Phase in Reaction Dynamics

ARON KUPPERMANN
California Institute of Technology, Pasadena, California

I. INTRODUCTION

In diatomic systems the potential energy curves of two electronically adiabatic states will only intersect if the states have different symmetries or differ in some other crucial manner. For a polyatomic system, on the other hand, two electronically adiabatic potential energy surfaces (PESs) can intersect even if the corresponding states have the same symmetry and spin multiplicity [1]. This possibility stems from the fact that such systems have more than one independent nuclear coordinate. Let us assume that the spin terms in the system's Hamiltonian can be neglected and that two of its electronically adiabatic PESs display an intersection that is conical. Furthermore, let us require that the corresponding adiabatic electronic wave functions be real and as continuous a function of the nuclear coordinates as possible. Then, if the system is transported around a closed loop in nuclear configuration space (a so-called pseudorotation) that encircles an intersection geometry, those wave functions must change sign [1,2]. Reciprocally, if such an adiabatic electronic wave function changes sign upon a motion of the polyatomic system around a closed loop in nuclear configuration space, somewhere on or inside that loop there must exist a conical intersection. These conical intersections are a generalization of those associated with the Jahn-Teller effect [3].

Conical intersections between electronically adiabatic potential energy surfaces are not only possible but actually quite frequent, if not prevalent, in polyatomic systems. Some examples are triatomic systems whose isolated atoms have ^2S ground states [1,2] such as H_3 and its isotopomers (DH_2, HD_2, HDT, etc.), LiH_2 and its isotopomers, and tri-alkali systems such as Na_3 and LiNaK. Many other kinds of polyatomic molecules also display such intersections. The reason is that they have three or more internal nuclear motion degrees of freedom, and only two independent relations between electronic Ham-

iltonian matrix elements are sufficient for the existence of doubly degenerate electronic energy eigenvalues; as a result, these relations are easy to satisfy [2]. The systems C_2H [4,5], NH_2 [6], NO_2 [7,8], and HO_2 [9,10] represent just a few examples.

The change in sign of the real adiabatic electronic wave functions associated with a pair of intersecting PESs upon a pseudorotation around a conical intersection of the system has consequences for its structure and dynamics. It requires that the corresponding nuclear wave functions undergo a compensating change of sign, known as the geometric phase effect [11]. This change in sign, in turn, profoundly affects the nature of the solutions of the corresponding nuclear motion Schrödinger equation (SE) [12]. For systems whose conical intersection geometry is either an equilateral triangle or close to one, symmetrized hyperspherical coordinates [12] are very convenient for enforcing such sign change.

The objective of this chapter is to discuss the conceptual and methodological issues associated with the influence this effect has on bimolecular state-to-state reaction cross sections. Its organization is as follows. In Sec. II we describe the nature of intersections between electronically adiabatic potential energy surfaces, and in Sec. III we discuss the effect of conical intersections on nuclear wave functions. The symmetrized hyperspherical coordinate methodology for solving the nuclear SE describing scattering processes that occur on the ground electronically adiabatic PES is described in Sec. IV. Systems displaying a conical intersection with the first electronically adiabatic excited state PES are included in this description. The results obtained applying this methodology to the H_3, DH_2, and HD_2 systems are discussed in Sec. V, and concluding remarks are given in Sec. VI. Some of the discussion in Secs. II through V has not appeared in the literature previously.

II. ELECTRONICALLY ADIABATIC POTENTIAL ENERGY SURFACES AND THEIR INTERSECTIONS

A. Definition of Electronically Adiabatic Potential Energy Surfaces

Let us consider a system consisting of electrons and nuclei. Let $\mathbf{r}^{el}$ denote the set of all orbital coordinates of the electrons with respect to a space-fixed (sf) frame, and let $\mathbf{s}^{el}$ be the corresponding spin coordinates. Similarly, let $\mathbf{r}^{nu}$ and $\mathbf{s}^{nu}$ denote the orbital and spin nuclear coordinates. We will consider in this chapter systems for which the electronuclear Hamiltonian $\hat{H}$ does not contain spin-dependent terms. Generalization to spin-dependent Hamiltonians does not present a major conceptual problem, but escapes our present objectives. For the present systems, $\hat{H}$ can be written as

$$\hat{H}(\mathbf{r}^{el}, \mathbf{r}^{nu}) = \hat{T}(\mathbf{r}^{nu}) + \hat{H}^{el}(\mathbf{r}^{el}; \mathbf{r}^{nu}) \tag{1}$$

where $\hat{T}(\mathbf{r}^{nu})$ is the nuclear kinetic energy operator and $\hat{H}^{el}$ is the rest of the Hamiltonian, which does not contain differential operators in $\mathbf{r}^{nu}$ and depends only parametrically on this variable. It is therefore the "fixed nuclei" part of $\hat{H}$.

The time-independent Schrödinger equation for the system is

$$\hat{H}(\mathbf{r}^{el}, \mathbf{r}^{nu})\Psi(\mathbf{r}^{el}, \mathbf{r}^{nu}, \mathbf{s}^{el}, \mathbf{s}^{nu}) = E\Psi(\mathbf{r}^{el}, \mathbf{r}^{nu}, \mathbf{s}^{el}, \mathbf{s}^{nu}) \tag{2}$$

and, in view of the independence of $\hat{H}$ on $\mathbf{s}^{el}$ and $\mathbf{s}^{nu}$, we can write

$$\Psi(\mathbf{r}^{el}, \mathbf{r}^{nu}, \mathbf{s}^{el}, \mathbf{s}^{nu}) = \Psi^{o}(\mathbf{r}^{el}, \mathbf{r}^{nu})\Psi^{s}(\mathbf{s}^{el}, \mathbf{s}^{nu}) \tag{3}$$

where Ψ^o and Ψ^s are, respectively, the orbital and spin parts of the system's eigenfunction. It is convenient to expand Ψ^o according to

$$\Psi^o(\mathbf{r}^{el}, \mathbf{r}^{nu}) = \sum\!\!\!\!\!\!\int_{\mathbf{n}} \Psi_{\mathbf{n}}^{nu,ad}(\mathbf{r}^{nu})\Psi_{\mathbf{n}}^{el,ad}(\mathbf{r}^{el}; \mathbf{r}^{nu}) \tag{4}$$

where the $\psi_{\mathbf{n}}^{el,ad}(\mathbf{r}^{el}; \mathbf{r}^{nu})$ are the orthonormal adiabatic electronic wave functions defined by

$$\hat{H}^{el}(\mathbf{r}^{el}; \mathbf{r}^{nu})\psi_{\mathbf{n}}^{el,ad}(\mathbf{r}^{el}; \mathbf{r}^{nu}) = \varepsilon_{\mathbf{n}}^{ad}(\mathbf{r}^{nu})\psi_{\mathbf{n}}^{el,ad}(\mathbf{r}^{el}; \mathbf{r}^{nu}) \tag{5}$$

subject to appropriate asymptotic conditions. They form a complete set of functions of $\mathbf{r}^{el}$. The quantity $\mathbf{n}$ represents the set of all quantum numbers which stem from the solution of (5) and the symbol $\sum\!\!\!\!\!\!\int_{\mathbf{n}}$ in (4) designates a sum over the discrete values of those quantum numbers and an integration over their continuous values. Equation (4) is usually called the Born-Oppenheimer expansion and each electronic eigenvalue $\varepsilon_{\mathbf{n}}(\mathbf{r}^{nu})$, considered as a function of $\mathbf{r}^{nu}$, is referred to as an electronically adiabatic potential energy function or, more commonly, an electronically adiabatic potential energy surface (PES). For each $\mathbf{r}^{nu}$ they are ordered according to their increasing values. Therefore, if for a given $\mathbf{r}^{nu}$ we have $\varepsilon_{\mathbf{n}'} \geq \varepsilon_{\mathbf{n}}$, the same relation holds for *all* $\mathbf{r}^{nu}$. The PESs play an important role in the description of the motion of the system's nuclei, as described in Sec. III.

Since the coulombic interaction potential between the system's particles which appears in $\hat{H}^{el}$ depends only on their relative distances, the quantities $\varepsilon_{\mathbf{n}}^{ad}(\mathbf{r}^{nu})$ and $\psi_{\mathbf{n}}^{el,ad}$ do not depend on the position of the center of mass of their nuclei. If we define a body-fixed frame attached to the system's nuclei, those quantities also do not depend on the three Euler angles which orient the nuclear frame with respect to a space-fixed one. This means that for an N-nuclei system ($N > 2$), $\varepsilon_{\mathbf{n}}^{ad}(\mathbf{r}^{nu})$ depends in general on $3N - 6$ scalar variables. We will replace in these PESs, and in $\psi_{\mathbf{n}}^{el,ad}$, $\mathbf{r}^{nu}$ by an appropriately chosen set of internal nuclear coordinates $\mathbf{q} \equiv (q_1, q_2, \ldots, q_{3N-6})$. Of particular interest for this chapter are triatomic systems ($N = 3$) involving all nuclear configurations (even when the system is a stable molecule having a collinear equilibrium configuration), and the corresponding PESs have dimension 3. For each additional nucleus that dimension increases by 3, and at present accurate scattering calculations are limited by the speed and fast memory of current high-performance computers to triatomic and tetraatomic systems, the dimensionality of the latter's PES being 6.

B. Intersections between Pairs of Electronically Adiabatic Potential Energy Surfaces

Let us assume that a pair of adjacent (according to the increasing energy criterion) PES $\varepsilon_i^{ad}(\mathbf{q})$ and $\varepsilon_j^{ad}(\mathbf{q})$ intersect at a set of nuclear geometries $\mathbf{q}_0$. The dimensionality of this set, for $N \geq 3$, is in the range zero (if no intersection exists) to $3N - 7$. For example, for triatomic systems and pairs of PESs which do intersect, this intersection can be a line (not necessarily straight) or a two-dimensional surface in the four-dimensional space spanned by the energy ε and the three internal scalar coordinates used to define the nuclear geometry of the system. The locus of the intersection geometries $\{\mathbf{q}_0\}$ in the three-dimensional space spanned by $\mathbf{q}$ must be continuous [13]. It may have finite or infinite extent, but in the former case it must be closed. For triatomic systems this means that it may be an infinitely long line, a closed curve, an infinite surface, or a closed surface.

When a pair of adjacent PESs intersects, it is useful to discuss their shape in the vicinity of their intersection. In some instances, more than two PESs may intersect at certain $\mathbf{q}_0$, but these less frequent cases will not be examined here. Let $\psi_i^{el,ad}$ and $\psi_j^{el,ad}$ be an orthonormal pair of adiabatic electronic wave functions corresponding to the consecutive electronic eigenvalues ε_i^{ad} and ε_j^{ad} respectively. We will now determine a set of conditions for the associated PESs to intersect. To that effect, let us consider an orthogonal transformation relating that pair of adiabatic electronic wave functions to another orthonormal basis pair of electronic functions, ϕ_i^{el} and ϕ_j^{el}, by

$$\begin{aligned}\psi_i(\mathbf{r}^{el};\mathbf{q}) &= \cos\alpha(\mathbf{q})\phi_i(\mathbf{r}^{el};\mathbf{q}) - \sin\alpha\,\phi_j \\ \psi_j(\mathbf{r}^{el};\mathbf{q}) &= \sin\alpha(\mathbf{q})\phi_i(\mathbf{r}^{el};\mathbf{q}) + \cos\alpha\,\phi_j\end{aligned} \tag{6}$$

where α is a real angle, in the 0 to π range, which depends on the internal configuration coordinates $\mathbf{q}$. For notational simplicity, we have dropped the superscripts in the ψ and ϕ. This restricted angular range (rather than the 0 to 2π one) is chosen because a replacement of α by $\alpha + \pi$ is the same as a replacement of ϕ_i and ϕ_j by the equivalent pair $-\phi_i$, $-\phi_j$. Let $\mathbf{H}_\phi$ be the 2 by 2 Hermitian matrix defined by

$$\mathbf{H}_\phi(\mathbf{q}) = \begin{pmatrix} H_{ii} & H_{ij} \\ H_{ji} & H_{jj} \end{pmatrix} \tag{7}$$

where

$$\begin{aligned} H_{nn'}(\mathbf{q}) &= \langle \phi_n(\mathbf{r}^{el};\mathbf{q}) \mid \hat{H}^{el}(\mathbf{r}^{el};\mathbf{q}) \mid \phi_{n'}(\mathbf{r}^{el};\mathbf{q})\rangle_{r^{el}} \\ &= \int \phi_n^*(\mathbf{r}^{el};\mathbf{q})\hat{H}^{el}(\mathbf{r}^{el};\mathbf{q})\phi_{n'}(\mathbf{r}^{el};\mathbf{q})\,d\mathbf{r}^{el} \qquad \mathbf{n}, \mathbf{n}' = \mathbf{i}, \mathbf{j} \end{aligned} \tag{8}$$

In addition, let $\mathbf{H}_\psi$ be the 2 by 2 matrix defined by (7) with the ϕ in (8) replaced by the corresponding ψ. In view of [5] and the orthonormality of the ψ_n we have

$$\mathbf{H}_\psi(\mathbf{q}) = \begin{pmatrix} \varepsilon_i^{ad}(\mathbf{q}) & 0 \\ 0 & \varepsilon_j^{ad}(\mathbf{q}) \end{pmatrix} \tag{9}$$

Choosing $\psi_n(\mathbf{r}^{el};\mathbf{q})$ that are real (which is possible because of the neglect of the spin-dependent terms in the system's Hamiltonian), results in real $\phi_n(\mathbf{r}^{el};\mathbf{q})$ and a $\mathbf{H}_\phi$ that is real and symmetric. In view of (6), $\mathbf{H}_\phi$ and $\mathbf{H}_\psi$ are interrelated by a similarity transformation.

If instead of starting with ψ_i and ψ_j, we select a pair of real normalized basis function $\phi_i(\mathbf{r}^{el};\mathbf{q})$ and $\phi_j(\mathbf{r}^{el};\mathbf{q})$, orthogonal to each other and to the remaining $\psi_n(\mathbf{r}^{el};\mathbf{q})$ ($\mathbf{n} \neq \mathbf{i}, \mathbf{j}$), (6) through (9) still hold and $\mathbf{H}_\phi(\mathbf{q})$ can be calculated from (8). From it we can obtain $\varepsilon_i^{ad}(\mathbf{q})$, $\varepsilon_j^{ad}(\mathbf{q})$ and $\alpha(\mathbf{q})$ subject to the conditions $\varepsilon_j^{ad} \geq \varepsilon_i^{ad}$ and $0 \leq \alpha \leq \pi$, by the expressions

$$\begin{aligned} \sin 2\alpha &= \frac{2H_{ij}}{[(H_{jj} - H_{ii})^2 + 4H_{ij}^2]^{1/2}} \\ \cos 2\alpha &= \frac{H_{jj} - H_{ii}}{[(H_{jj} - H_{ii})^2 + 4H_{ij}^2]^{1/2}} \end{aligned} \qquad 0 \leq 2\alpha < 2\pi \tag{10}$$

$$\begin{aligned} \varepsilon_i^{ad} &= H_{ii}\cos^2\alpha + H_{jj}\sin^2\alpha - H_{ij}\sin 2\alpha \\ &= \tfrac{1}{2}(H_{ii} + H_{jj}) - \tfrac{1}{2}[(H_{jj} - H_{ii})^2 + 4H_{ij}^2]^{1/2} \end{aligned} \tag{11}$$

$$\varepsilon_j^{ad} = H_{ii} \sin^2 \alpha + H_{jj} \cos^2 \alpha + H_{ij} \sin 2\alpha \tag{12}$$

$$= \tfrac{1}{2} (H_{ii} + H_{jj}) + \tfrac{1}{2} [(H_{jj} - H_{ii})^2 + 4H_{ij}^2]^{1/2}$$

These equations yield

$$\varepsilon_j^{ad}(\mathbf{q}) - \varepsilon_i^{ad}(\mathbf{q}) = \{[H_{jj}(\mathbf{q}) - H_{ii}(\mathbf{q})]^2 + 4H_{ij}^2(\mathbf{q})\}^{1/2} \tag{13}$$

A necessary and sufficient set of conditions for the adjacent ε_i^{ad} and ε_j^{ad} PESs to intersect is that at least one value $\mathbf{q}_0$ of $\mathbf{q}$ exist for which

$$H_{jj}(\mathbf{q}_0) = H_{ii}(\mathbf{q}_0) \tag{14}$$

and

$$H_{ij}(\mathbf{q}_0) = 0 \tag{15}$$

For $N > 2$ these relations constitute a system of two equations in the $3N - 6$ real scalar variables represented by $\mathbf{q}$, i.e., three variables for $N = 3$ and 6 variables for $N = 6$, and intersections between PESs are common. For $N = 2$, however, $\mathbf{q}$ is a single scalar variable, the internuclear distance, and diatomic potential energy curve crossings for adiabatic electronic states of the same symmetry and spin multiplicity are very rare, because their existence requires that this distance satisfy two independent conditions [14]. This leads to the noncrossing rule of such curves.

Let $\mathbf{q}_0$ be a solution of (14) and (15). The characteristics of the intersection between $\varepsilon_i^{ad}(\mathbf{q})$ and $\varepsilon_j^{ad}(\mathbf{q})$ depend on the details of the three functions H_{ii}, H_{jj}, and H_{ij} of the $3N - 6$ variables $\mathbf{q}$ (for $N > 2$) in the vicinity of $\mathbf{q}_0$. A convenient approach to the discussion of these characteristics is to expand $\hat{H}^{el}(\mathbf{r}^{el}; \mathbf{q})$ in a power series of a variable $\mathbf{Q}$ which depends on the deviation of $\mathbf{q}$ from $\mathbf{q}_0$ [13,15]. We define this variable by

$$\mathbf{Q} \equiv (Q_1, Q_2, \ldots, Q_{3N-6}) = \mathbf{f}(\mathbf{q} - \mathbf{q}_0) \tag{16}$$

subject to the condition that when $\mathbf{q} = \mathbf{q}_0$, $\mathbf{Q} = \mathbf{0}$. As a result, $\mathbf{q}$ can be considered to be a function of $\mathbf{q}_0$ and $\mathbf{Q}$. The function $\mathbf{f}$ in (16) is arbitrary, and gives desired flexibility to the choice of $\mathbf{Q}$, in that it permits us to select $\mathbf{Q} \neq \mathbf{q} - \mathbf{q}_0$.

The expansion of interest is

$$\hat{H}^{el}(\mathbf{r}^{el}; \mathbf{q}) = \hat{H}^{el}(\mathbf{r}^{el}; \mathbf{q}_0) + \sum_{k=1}^{3N-6} \hat{H}_k^{el}(\mathbf{r}^{el}; \mathbf{q}_0) Q_k + \sum_{k,l=1}^{3N-6} \hat{H}_{kl}^{el}(\mathbf{r}^{el}; \mathbf{q}_0) Q_k Q_l + \cdots \tag{17}$$

where

$$\hat{H}_k^{el}(\mathbf{r}^{el}; \mathbf{q}_0) = \left[\frac{\partial \hat{H}_k^{el}(\mathbf{r}^{el}; \mathbf{q})}{\partial Q_k} \right]_{Q=0} \tag{18}$$

and

$$\hat{H}_{kl}^{el}(\mathbf{r}^{el}; \mathbf{q}_0) = \frac{1}{2} \left[\frac{\partial^2 \hat{H}^{el}(\mathbf{r}^{el}; \mathbf{q})}{\partial Q_k \partial Q_l} \right]_{Q=0} \tag{19}$$

To obtain a similar expansion of the matrix elements $H_{nn'}(\mathbf{q})$ of $\hat{H}^{el}$ we pick as an electronic basis set the two wave functions $\psi_i(\mathbf{r}^{el}; \mathbf{q}_0)$ and $\psi_j(\mathbf{r}^{el}; \mathbf{q}_0)$ which are degenerate solutions of (5) at $\mathbf{q} = \mathbf{q}_0$ and therefore diagonalize $\mathbf{H}_\psi$ at this value of $\mathbf{q}$ but not, in general, at other values. It should be noted that these functions differ from those used in

(6) in that they are independent of $\mathbf{q}$. Nevertheless, it will be a very good approximation to assume that $\psi_i(\mathbf{r}^{el}; \mathbf{q})$ and $\psi_j(\mathbf{r}^{el}; \mathbf{q})$ can be expressed as linear combinations of $\psi_i(\mathbf{r}^{el}; \mathbf{q}_0)$ and $\psi_j(\mathbf{r}^{el}; \mathbf{q}_0)$ for values of $\mathbf{q}$ sufficiently close to $\mathbf{q}_0$. Using this basis set we have

$$\mathbf{H}_\psi(\mathbf{q}) = \begin{pmatrix} H_{ii}(\mathbf{q}) & H_{ij}(\mathbf{q}) \\ H_{ij}(\mathbf{q}) & H_{jj}(\mathbf{q}) \end{pmatrix} \tag{20}$$

where

$$H_{ii}(\mathbf{q}_0) = \varepsilon_i^{ad}(\mathbf{q}_0) = H_{jj}(\mathbf{q}_0) = \varepsilon_j^{ad}(\mathbf{q}_0) \qquad H_{ij}(\mathbf{q}_0) = 0 \tag{21}$$

Expansion of the $H_{\mathbf{nn}'}(\mathbf{q})$ around $\mathbf{q}_0$ leads to an expression similar to (17):

$$H_{\mathbf{nn}'}(\mathbf{q}) = H_{\mathbf{nn}'}(\mathbf{q}_0) + \sum_{k=1}^{3N-6} H_{\mathbf{nn}'}^{(k)}(\mathbf{q}_0)Q_k + \sum_{k,l=1}^{3N-6} H_{\mathbf{nn}'}^{(k,l)}(\mathbf{q}_0)Q_kQ_l + \cdots \qquad \mathbf{n}, \mathbf{n}' = \mathbf{i}, \mathbf{j} \tag{22}$$

where

$$H_{\mathbf{nn}'}^{(k)}(\mathbf{q}_0) = \left[\frac{\partial H_{\mathbf{nn}'}(\mathbf{q})}{\partial Q_k}\right]_{\mathbf{Q}=\mathbf{0}} \tag{23}$$

and

$$H_{\mathbf{nn}'}^{(k,l)}(\mathbf{q}_0) = \frac{1}{2}\left[\frac{\partial^2 H_{\mathbf{nn}'}(\mathbf{q})}{\partial Q_k \partial Q_l}\right]_{\mathbf{Q}=\mathbf{0}} \tag{24}$$

We can calculate the right-hand side of (22) using the definition of $H_{\mathbf{nn}'}(\mathbf{q})$ together with (17). In the vicinity of the intersection of interest it is appropriate to retain in (22) only the lowest-order terms in each of the Q_k ($k = 1, 2, \ldots, 3N - 6$). In addition, in order to explore the point group symmetry properties of $\psi_i(\mathbf{r}^{el}; \mathbf{q}_0)$ and $\psi_j(\mathbf{r}^{el}; \mathbf{q}_0)$ it is desirable to choose for the Q_k coordinates which display simple transformation properties under the operations of that group, such as normal mode coordinates [13,15] or, in some circumstances, symmetrized hyperspherical coordinates [12,16,17]. Such choices lead to simple point group symmetries for the $\hat{H}_k^{el}(\mathbf{r}^{el}; \mathbf{q}_0)$ and $\hat{H}_{kl}^{el}(\mathbf{r}^{el}; \mathbf{q}_0)$ and permit the identification of which $\hat{H}_{\mathbf{nn}'}^{(k)}(\mathbf{q}_0)$ and $\hat{H}_{\mathbf{nn}'}^{(k,l)}(\mathbf{q}_0)$ vanish due to symmetry [18].

A detailed analysis of this kind, using normal mode coordinates, has been made for triatomic systems [13,15,18] for the several possible point groups: D_{3h} (equilateral triangle), C_{2v} (isosceles triangle), $C_{\infty v}$ (linear), $D_{\infty h}$ (linear with a center of symmetry), and C_s (only a plane of symmetry). Choosing for Q_1, Q_2, and Q_3 the symmetric stretch, the bending, and the antisymmetric stretch normal mode coordinates, respectively, all having dimensions of length, the shapes of the PESs in the immediate vicinity of their intersections have been investigated. (It is not implied in this analysis that the nuclear geometries corresponding to these point groups represent stable configurations or that the normal mode coordinates are associated with vibrational motions. In this manner, unstable configurations such as equilateral triangle configurations of the ground electronic state of H_3 are included in these considerations.) These PESs are three-dimensional surfaces in the four-dimensional space defined by the coordinates ε (the adiabatic energy), Q_1, Q_2, and Q_3 (for a fixed $\mathbf{q}_0$). To describe them, it is convenient to specify the nature of their cuts for $Q_1 = 0$, $Q_2 = 0$, and $Q_3 = 0$ respectively. The following shapes have been identified:

(a) For the C_{2v} point group, we take for the electronic basis the A_1 and B_2 electronic state wave functions, both of which are symmetric under reflection through to the plane of the molecule (19), or A_2 and B_1, both of which are antisymmetric under that reflection. There is no mixing between those wave functions for the $Q_3 = 0$ section, and $\varepsilon_{A_1}(Q_1, Q_2, Q_3 = 0)$ and $\varepsilon_{B_2}(Q_1, Q_2, Q_3 = 0)$ or $\varepsilon_{A_2}(Q_1, Q_2, Q_3 = 0)$ and $\varepsilon_{B_1}(Q_1, Q_2, Q_3 = 0)$ are planes that intersect each other along straight one-dimensional lines. For $Q_1 = 0$, $\varepsilon_{A_1}(Q_1 = 0, Q_2, Q_3)$ and $\varepsilon_{B_2}(Q_1 = 0, Q_2, Q_3)$ or $\varepsilon_{A_2}(Q_1 = 0, Q_2, Q_3)$ and $\varepsilon_{B_1}(Q_1 = 0, Q_2, Q_3)$ are the manifolds of a double cone, the mixing angle α in (6) assuming all allowed values in the 0 to π range. This double cone is, in general, not circular, and the intersection between each of these pairs of PES is called a conical intersection. Intersections of this type, in a simple two-degree-of-freedom model, were first described by Teller (20).

(b) For the D_{3h} point group, symmetry imposes the existence of doubly degenerate adiabatic electronic states, which split upon distortions of the triatomic system away from equilateral triangle geometries. This guarantees the existence of intersections between the corresponding PESs, based purely on symmetry arguments. We select $\mathbf{q}_0$ to correspond to such an equilateral triangle configuration and consider a degenerate E' state choosing for the electronic bases functions the two components $\psi^{E'_1}$ and $\psi^{E'_2}$ of this state, both of which are symmetric under reflection through the plane of the molecule. This E' state splits into A_1 and B_2 states when the system is distorted into a C_{2v} configuration. The D_{3h} group is of particular interest for this chapter, since equilateral triangle configurations of the trihydrogen isotopic systems discussed in Sec. V are associated with it. A detailed analysis of (22), taking into account the symmetries of $\psi^{E'_1}$ and $\psi^{E'_2}$ used in the calculation of the $H_{nn'}$ (see (8)), leads to the conclusion that to first order in Q_1, Q_2, and Q_3, (20) is given by

$$\mathbf{H}_{\psi}(\mathbf{q}_0, \mathbf{Q}) = \begin{pmatrix} aQ_1 - bQ_2 & bQ_3 \\ bQ_3 & aQ_1 + bQ_2 \end{pmatrix} \tag{25}$$

where a and $b > 0$ are independent of the Q_k but are functions of $\mathbf{q}_0$ and have dimensions of energy per unit length. The zero of energy was chosen as the degenerate adiabatic energy at $\mathbf{q}_0$. Replacement of (25) into (10) through (12) leads to

$$\sin 2\alpha = \frac{Q_3}{(Q_2^2 + Q_3^2)^{1/2}} \qquad \cos 2\alpha = \frac{Q_2}{(Q_2^2 + Q_3^2)^{1/2}} \qquad 0 \leq 2\alpha < 2\pi \tag{26}$$

$$\varepsilon_i^{ad}(\mathbf{q}_0, \mathbf{Q}) = aQ_1 + b(Q_2^2 + Q_3^2)^{1/2} \tag{27}$$

$$\varepsilon_j^{ad}(\mathbf{q}_0, \mathbf{Q}) = aQ_1 - b(Q_2^2 + Q_3^2)^{1/2} \tag{28}$$

where ε_i^{ad} and ε_j^{ad} are respectively the lower and upper electronically adiabatic PES in the vicinity of the equilateral triangle configuration associated with $\mathbf{q}_0$.

It can be seen from (26) that α is independent of Q_1. If we set either Q_2 or Q_3 equal to zero, ε_i^{ad} and ε_j^{ad} are planes in the corresponding three-dimensional subspaces and intersect along a straight line in the ϵ, Q_1 plane. In addition, α is restricted to the two values $\pi/4$ and $3\pi/4$ for $Q_2 = 0$ and the different two values 0 and $\pi/2$ for $Q_3 = 0$. If, on the other hand, we set $Q_1 = 0$, ε_i^{ad} and ε_j^{ad} become the lower and upper manifold of a circular double cone whose vertex is the origin and whose axis of symmetry is the ε axis. In a coordinate system in which this axis is replaced by an ε/b axis (in order to make its units the same as those of the Q_k), the cone's half-angle is 45°. The intersection

between these two PESs is once more conical. It is important to notice that in this case, if we allow the point $P(Q_1 = 0, Q_2, Q_3)$ in the Q_2, Q_3 plane to traverse a complete circular loop around the axis of the cone, the corresponding nuclear configuration performs a complete pseudorotation around the corresponding $\mathbf{q}_0$ equilateral triangle conical intersection configuration. Such a pseudorotation is depicted in Fig. 1. If we start and end that loop on a point along the positive Q_2 axis, 2α changes continuously from 0 to 2π and, in view of (6), $\psi_i(\mathbf{r}^{el}; \mathbf{q})$ changes from $\psi^{E'1}(\mathbf{r}^{el}; \mathbf{q}_0)$ to $-\psi^{E'1}(\mathbf{r}^{el}; \mathbf{q}_0)$ and $\psi_j(\mathbf{r}^{el}; \mathbf{q}_0)$ from $\psi^{E'2}(\mathbf{r}^{el}; \mathbf{q}_0)$ to $-\psi^{E'2}(\mathbf{r}^{el}; \mathbf{q}_0)$. In other words, $\psi_i(\mathbf{r}^{el}; \mathbf{q})$ and $\psi_j(\mathbf{r}^{el}; \mathbf{q})$ undergo a change in sign as the system traverses a complete loop around the conical intersection axis. This is a very important conclusion, which will be discussed in greater detail in Sec. II.C, and constitutes the basis for the geometric phase effect in D_{3h} systems. It is a consequence of requiring that the $\psi_n(\mathbf{r}^{el}; \mathbf{q})$ be real functions of both $\mathbf{r}^{el}$ and $\mathbf{q}$ and that they vary continuously with $\mathbf{r}^{el}$ and as much as possible with $\mathbf{q}$ also.

(c) For the $C_{\infty v}$ point group, we take for the electronic bases the degenerate components of the Π state of the linear molecule in question. Upon bending, this state splits into A' and A'' states, which are respectively symmetric and antisymmetric with respect to the molecular plane. The intersection between the corresponding PESs is a glancing one.

(d) For the $D_{\infty h}$ point group, we consider the intersection associated with the Σ_g^+ and Σ_u^+ collinear states. For $Q_2 = 0$ we get a double cone for the corresponding PESs. For $Q_3 = 0$, the PESs become intersecting parabolic cylinders. For $Q_1 = 0$, they intersect at a point, and separate linearly in the Q_3 direction and quadratically in the Q_2 direction. This illustrates the fact that the shapes of two intersecting PESs may be quite different for each of the three $Q_k = 0$ sections.

(e) For the C_s point group, if we consider two states of the same symmetry with respect to the molecular plane and the same spin multiplicity, symmetry arguments do

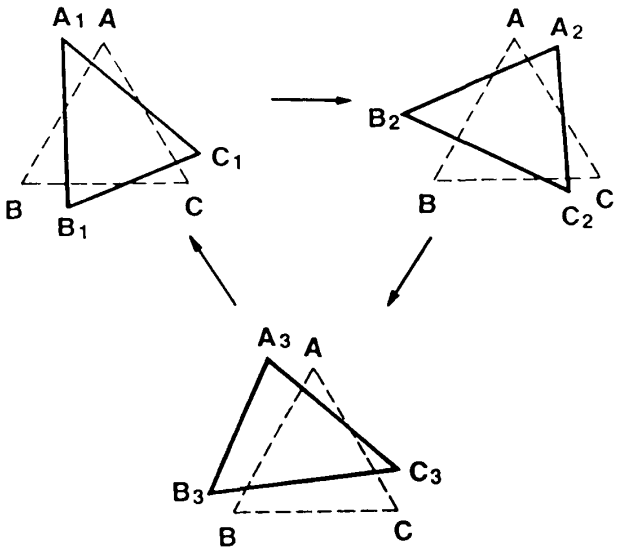

Figure 1 Pseudorotation of a system of three nuclei around an equilateral triangle configuration. The points A, B, C are the vertices of a reference equilateral triangle configuration (dashed). Three nuclei in positions A_1, B_1, C_1 display a nonequilibrium triangle configuration. As these nuclei move around the reference positions A, B, C, to A_2, B_2, C_2, then to A_3, B_3, C_3 and finally back to A_1, B_1, C_1, the system executes a pseudorotation around the reference configuration.

not require that their PESs intersect. Nevertheless, intersections may occur as a result of other considerations, such as those having to do with which atomic orbitals contribute to the electronic wave functions. In particular, conical intersections may and frequently do occur, as further discussed in Sec. II.C [1,2].

An analysis for systems with $N > 3$, based on similar considerations, is possible but seems not to have been done so far.

C. Conical Intersections and the Non-Single-Valuedness of Real Adiabatic Electronic Wave Functions

In Sec. II.B we assumed that an intersection between the two PESs $\varepsilon_i^{ad}(\mathbf{q})$ and $\varepsilon_j^{ad}(\mathbf{q})$ existed, and analyzed some of their possible shapes in the vicinity of their intersection. This analysis was done for triatomic systems in electronically adiabatic states belonging to all possible point groups. In the present section we discuss necessary and sufficient conditions for the existence of *conical* intersections between the PESs of general polyatomic systems, regardless of point group symmetries, and the changes the corresponding adiabatic electronic wave functions undergo when the systems execute pseudorotations around such intersections.

We consider the Hamiltonian matrix (20) satisfying (21) and obtained using the basis functions $\psi_n(\mathbf{r}^{el}; \mathbf{q}_0)$ with $\mathbf{n} = \mathbf{i}, \mathbf{j}$. The variable $\mathbf{Q}$, defined by (16), will be chosen to have dimensions of length, but not otherwise confined to representing normal mode coordinates. Let us consider the value $\overline{\mathbf{Q}}$ of $\mathbf{Q}$ defined by

$$\overline{\mathbf{Q}} = (Q_1, Q_2, Q_3 = 0, \ldots, Q_{3N-6} = 0) \tag{29}$$

and examine the shape of the corresponding PESs in the region of small Q_1 and Q_2. This is equivalent to examining the shapes of cuts of $\varepsilon_n^{ad}(\mathbf{q}_0, \mathbf{Q})$ $(\mathbf{n} = \mathbf{i}, \mathbf{j})$ for $Q_3 = Q_4 = \cdots = Q_{3N-6} = 0$ in the vicinity of the intersection configuration $\mathbf{q}_0$. As in (22), we expand the $H_{nn'}(\mathbf{q}_0, \overline{\mathbf{Q}})$ in a power series of Q_1 and Q_2 and assume that for each of the three elements H_{ii}, H_{jj}, and H_{ij} there exists at least one nonvanishing first-order term. Under these conditions, we drop the higher-order terms and write, in the vicinity of $Q_1 = Q_2 = 0$,

$$\mathbf{H}_\psi(\mathbf{q}_0, \overline{\mathbf{Q}}) = \begin{pmatrix} \varepsilon^{ad}(\mathbf{q}_0) + a_1Q_1 + a_2Q_2 & c_1Q_1 + c_2Q_2 \\ c_1Q_1 + c_2Q_2 & \varepsilon^{ad}(\mathbf{q}_0) + b_1Q_1 + b_2Q_2 \end{pmatrix} \tag{30}$$

where $\varepsilon^{ad}(\mathbf{q}_0)$ is the adiabatic electronic energy of both PESs $\varepsilon_n^{ad}(\mathbf{q}_0, \mathbf{Q})$ $(\mathbf{n} = \mathbf{i}, \mathbf{j})$ for $\mathbf{Q} = \mathbf{0}$, i.e., at the intersection configuration $\mathbf{q}_0$. The coefficients a_k, b_k, and c_k $(k = 1, 2)$ depend on $\mathbf{q}_0$ and have dimensions of energy per unit length. Replacing the matrix elements of (30) into (11) and (12), we get

$$\varepsilon_i^{ad}(\mathbf{q}_0, \overline{\mathbf{Q}}) = \varepsilon^{ad}(\mathbf{q}_0) + \tfrac{1}{2}(a_1 + b_1)Q_1 + \tfrac{1}{2}(a_2 + b_2)Q_2 - W(\mathbf{q}_0, \overline{\mathbf{Q}}) \tag{31}$$

$$\varepsilon_j^{ad}(\mathbf{q}_0, \overline{\mathbf{Q}}) = \varepsilon^{ad}(\mathbf{q}_0) + \tfrac{1}{2}(a_1 + b_1)Q_1 + \tfrac{1}{2}(a_2 + b_2)Q_2 + W(\mathbf{q}_0, \overline{\mathbf{Q}}) \tag{32}$$

where

$$W(\mathbf{q}_0, \overline{\mathbf{Q}}) = \{[(b_1 - a_1)Q_1 + (b_2 - a_2)Q_2]^2 + 4(c_1Q_1 + c_2Q_2)^2\}^{1/2} \tag{33}$$

Let us assume that the coefficients a_k, b_k, and c_k $(k = 1, 2)$ are such that $W(\mathbf{q}_0, \overline{\mathbf{Q}})$ is a function of both Q_1 and Q_2. This implies that $a_k = b_k$ and $c_k = 0$ cannot be valid simultaneously. Under these conditions, let us show that (31) and (32) represent the lower

and upper manifolds of an elliptical double cone in a cartesian space whose axes are Q_1, Q_2 and $\mathscr{E} = \varepsilon^{ad}(\mathbf{q}_0, \overline{\mathbf{Q}})$ and whose vertex occurs at $Q_1 = Q_2 = 0$ and $\mathscr{E} = \varepsilon^{ad}(\mathbf{q}_0)$. The proof is straightforward but algebraically rather laborious, and will only be outlined here. First, inspection of those two expressions shows that this vertex is the only point that the two manifolds have in common. Second, we examine their intersection with a plane Π passing through that vertex, whose equation is given by

$$\mathscr{E} = \varepsilon^{ad}(\mathbf{q}_0) + AQ_1 + BQ_2 \tag{34}$$

where A and B are real constants. Setting the left-hand side of either (31) or (32) equal to $\mathscr{E}$ and eliminating this variable between either of these two expressions and (34) leads to an equation in Q_1 and Q_2 of the form

$$CQ_1^2 + DQ_2^2 + FQ_1Q_2 = 0 \tag{35}$$

This equation represents the projection of that intersection on the Q_1, Q_2 plane, where the C, D and F coefficients are simple real functions of A, B, and of the a_k, b_k, and $c_k (k = 1, 2)$. It can be factored as

$$D(GQ_1 - Q_2)(JQ_1 - Q_2) = 0 \tag{36}$$

where, for certain easily determined ranges of A and B, the constants G and J are real. Expression (36) represents the equations of two straight lines on that plane, passing through the origin $Q_1 = Q_2 = 0$, and which we designate L_1 and L_2. We now consider each of the two vertical planes Π_1 and Π_2 determined by the $\mathscr{E}$ axis and L_1 and L_2 respectively. The intersections of Π_1 and Π_2 with the PESs coincide with the intersections of Π with those surfaces. Let us show that they are two straight lines passing through the vertex. To that effect we consider the two cartesian axes L_1 and $\mathscr{E}$ in the Π_1 plane, with an origin at $Q_1 = Q_2 = 0$. Let x_1 be a cartesian coordinate along L_1. For points on this line, Q_1 and Q_2 are proportional to x_1. Replacing these functions of x_1 into (31) and (32) (with their left-hand side replaced by $\mathscr{E}$) leads to an expression of the form

$$\mathscr{E} = \varepsilon^{ad}(\mathbf{q}_0) + K_1x_1 \tag{37}$$

which is the equation of a straight line on the Π_1 plane passing through the vertex. The same is true if we consider the Π_2 plane, with K_1x_1 replaced by K_2x_2. We conclude that the intersections of the plane Π (defined by (34)) with the pair of PESs given by (31) and (32) is a pair of straight lines passing through the vertex, once the constants A and B are chosen so as to make G and J real. For two special pairs of values of A and B these lines coincide.

To complete the proof that (31) and (32) constitute an elliptical double cone, let us show that their intersections with $\mathscr{E}$ = constant horizontal planes in Q_1, Q_2, $\mathscr{E}$ space are ellipses. Those equations can be put in the form

$$\alpha_1Q_1^2 + \alpha_2Q_2^2 + \alpha_3Q_1Q_2 + \alpha_4Q_1 + \alpha_5Q_2 = [\mathscr{E} - \varepsilon^{ad}(\mathbf{q}_0)]^2 \tag{38}$$

which, upon an appropriate linear transformation from Q_1, Q_2 to Q_1', Q_2', can be rewritten as

$$\frac{(Q_1' - \beta_1)^2}{\gamma_1^2} + \frac{(Q_2' - \beta_2)^2}{\gamma_2^2} = 1 \tag{39}$$

with the real constants β_k, $\gamma_k (k = 1, 2)$ depending on $\mathscr{E} - \varepsilon^{ad}(\mathbf{q}_0)$ and on the a_k, b_k, $c_k (k = 1, 2)$. Expression (39) is the equation of an ellipse in Q_1', Q_2' coordinates. Since

the linear transformation back to Q_1, Q_2 can change the lengths of its axis but cannot change its elliptical shape, we conclude that (38) also represents an ellipse, Q.E.D. In summary, we have proven that given the $\mathbf{H}_\psi(\mathbf{q}_0, Q_1, Q_2, Q_3 = 0, \ldots, Q_{3N-6} = 0)$ Hamiltonian matrix of (30), with the a_k, b_k, $c_k(k = 1, 2)$ coefficients subject to the restrictions specified after (33), the corresponding PESs in the 3D cartesian space defined by Q_1, Q_2, $\mathscr{E}$ constitute an elliptical double cone with a vertex on the $\mathscr{E}$ axis at $\mathscr{E} = \varepsilon(\mathbf{q}_0)$. It should be stressed that no particular point group symmetry property of the $\psi_n(\mathbf{r}^{el}; \mathbf{q}_0)$ $(\mathbf{n} = \mathbf{i}, \mathbf{j})$ which generated (30) was assumed. The only assumption was that its elements were first-order functions of Q_1 and Q_2 in the vicinity of the intersection configuration $\mathbf{q}_0$, which is the most common case for polyatomic systems. By *reduction ad absurdum*, one can also show that if two PESs intersect as an elliptical double cone in Q_1, Q_2, $\mathscr{E}$ space in the vicinity of the intersection configuration $\mathbf{q}_0$, the corresponding 2×2 Hamiltonian matrix $\mathbf{H}_\psi$ generated by the basis functions $\psi_i(\mathbf{r}^{el}; \mathbf{q}_0)$ and $\psi_j(\mathbf{r}^{el}; \mathbf{q}_0)$ has the form (30) with the a_k, b_k, $c_k(k = 1, 2)$ satisfying the conditions specified after (33). We conclude that (30) plus those conditions constitute a necessary and sufficient condition for the intersection of the two PESs $\varepsilon_i^{ad}(\mathbf{q}_0, \overline{\mathbf{Q}})$ and $\varepsilon_j^{ad}(\mathbf{q}_0, \overline{\mathbf{Q}})$ to be conical.

We now examine the changes which the adiabatic electronic wave functions $\psi_n(\mathbf{r}^{el}; \mathbf{q}_0)$ $(\mathbf{n} = \mathbf{i}, \mathbf{j})$ undergo when the system traverses a closed loop in the 2D Q_1, Q_2 space around the origin $Q_1 = Q_2 = 0$ corresponding to the intersection configuration $\mathbf{q}_0$. To that effect, let us define the polar coordinates R, φ (1) by

$$\begin{aligned} Q_1'' &\equiv (b_1 - a_1)Q_1 + (b_2 - a_2)Q_2 = R \cos \varphi \\ Q_2'' &\equiv 2(c_1Q_1 + c_2Q_2) = R \sin \varphi \end{aligned} \tag{40}$$

where

$$R \geq 0 \qquad 0 \leq \varphi < 2\pi \tag{41}$$

We wish to relate φ to the angle $\alpha(\mathbf{q}_0, \overline{\mathbf{Q}})$ defined, in analogy to (6), by

$$\begin{aligned} \psi_i(\mathbf{r}^{el}; \mathbf{q}_0, \overline{\mathbf{Q}}) &= \cos \alpha\ (\mathbf{q}_0, \overline{\mathbf{Q}})\psi_i(\mathbf{r}^{el}; \mathbf{q}_0) - \sin \alpha\ \psi_j(\mathbf{r}^{el}; \mathbf{q}_0) \\ \psi_j(\mathbf{r}^{el}; \mathbf{q}_0, \overline{\mathbf{Q}}) &= \sin \alpha\ (\mathbf{q}_0, \overline{\mathbf{Q}})\psi_i(\mathbf{r}^{el}; \mathbf{q}_0) + \cos \alpha\ \psi_j(\mathbf{r}^{el}; \mathbf{q}_0) \end{aligned} \tag{42}$$

where

$$0 \leq \alpha(\mathbf{q}_0, \overline{\mathbf{Q}}) \leq \pi \tag{43}$$

α is given by (10) with the matrix elements H_{ii}, H_{jj}, and H_{ij} being those in (30). Inverting (40) to obtain Q_1 and Q_2 in terms of R and φ, replacing the results into (30) to obtain the elements of $\mathbf{H}_\psi(\mathbf{q}_0, \overline{\mathbf{Q}})$ as functions of R and φ and finally substituting these elements in the right-hand side of (10) furnishes the simple but very useful result

$$\alpha = \frac{\varphi}{2} \tag{44}$$

A closed loop around the origin on the Q_1'', Q_2'' plane from the initial configuration R, $\varphi = 0$ to the identical final configuration R, $\varphi = 2\pi$ brings the system from a given initial configuration $\mathbf{q}_0$, $\overline{\mathbf{Q}}_0$ to the *same* final configuration. Such a closed loop is called a pseudorotation around the conical intersection configuration $\mathbf{q}_0$ in $\overline{\mathbf{Q}}$ space. A pseudorotation for D_{3h} triatomic systems was depicted in Fig. 1 for the $\overline{\mathbf{Q}} \equiv (Q_1 = 0, Q_2, Q_3)$ space. In general, as φ changes from 0 to 2π, (42) and (44) show that $\psi_i(\mathbf{r}^{el}; \mathbf{q}_0, \overline{\mathbf{Q}})$ changes contin-

uously from $\psi_i(\mathbf{r}^{el}; \mathbf{q}_0)$ to $-\psi_i(\mathbf{r}^{el}; \mathbf{q}_0)$ and $\psi_j(\mathbf{r}^{el}; \mathbf{q}_0, \overline{\mathbf{Q}})$ from $\psi_j(\mathbf{r}^{el}; \mathbf{q}_0)$ to $-\psi_j(\mathbf{r}^{el}; \mathbf{q}_0)$. This means that both $\psi_i(\mathbf{r}^{el}; \mathbf{q}_0, \overline{\mathbf{Q}})$ and $\psi_j(\mathbf{r}^{el}; \mathbf{q}_0, \overline{\mathbf{Q}})$ undergo a discontinuous change in sign across the $\varphi = 0$ line as the system traverses a closed loop in $\overline{\mathbf{Q}}$ space around the conical intersection configuration $\mathbf{q}_0$. This is a generalization of a similar property derived in Sec. II.B for D_{3h} triatomic systems, and is valid for any conical intersection. It shows, as a result, that adiabatic electronic wave functions associated with a conical intersection, if required to be single-valued real continuous functions of $\mathbf{r}^{el}$, as well as real and, to the extent possible, single-valued continuous functions of $\mathbf{q}$, must display discontinuous sign changes across some cut in $\mathbf{q}$ space which contains the locus of the conical intersection geometries $\mathbf{q}_0$. At first blush, this seems to violate the single-valuedness condition imposed by quantum mechanics on wave functions. This is, however, not the case, as the nuclear motion of the system is not included in those adiabatic electronic functions. Once a full wave function, including the description of that motion, is considered, single-valuedness of the electronuclear wave function is recovered, as described in detail in Sec. III.

Longuet-Higgins [2] has also proven an inverse theorem, namely that if a real adiabatic electronic wave function changes sign when a polyatomic system traverses a one-dimensional closed loop on a two-dimensional surface in the $(3N - 6)$-dimensional nuclear configuration space, then the corresponding electronic state must become discontinuous and degenerate with another one at an odd number of points lying on that surface and within that loop. As a consequence, the two corresponding electronically adiabatic potential energy surfaces must intersect conically at each of those points. If the number of those points is even, that change in sign does not take place. One may therefore conclude that a necessary and sufficient condition for two potential energy surfaces $\varepsilon_i^{ad}(\mathbf{q})$ and $\varepsilon_j^{ad}(\mathbf{q})$ to intersect conically at an odd number of points on a two-dimensional surface in nuclear configuration space is that, upon traversing a closed loop on that surface, the corresponding two real adiabatic electronic wave functions $\psi_i(\mathbf{r}^{el}; \mathbf{q})$ and $\psi_j(\mathbf{r}^{el}; \mathbf{q})$ must change sign if required to be continuous along the loop (excluding the loop's end points where the discontinuous change in sign takes place).

D. The Abundance of Conical Intersections

We have seen in Sec. II.B that a necessary and sufficient set of conditions for an intersection between the two adjacent PESs $\varepsilon_i^{ad}(\mathbf{q})$ and $\varepsilon_j^{ad}(\mathbf{q})$ to occur is that at least one configuration $\mathbf{q}_0$ of the system should exist for which the two equations (14) and (15) are satisfied. For $N \geq 3$, they constitute a system of two equations in the $3N - 6 \geq 3$ real scalar variables $q_1, q_2, \ldots, q_{3N-6}$, and it is expected that such equations should have solutions very frequently, and therefore that intersections between pairs of adjacent PESs (double degeneracies) should be quite common in nature, regardless of symmetry properties of the system, i.e., even for unsymmetrical configurations. As a matter of fact, for $N \geq 4$ triple degeneracies (intersections between triplets of adjacent PESs) should also occur quite commonly, since in this case five independent conditions must be satisfied by the $3N - 6 \geq 6$ real (scalar) variables q_i $(i = 1, 2, \ldots, 3N - 6)$ (2).

The next question is how frequently are the intersections between pairs of adjacent electronically adiabatic PESs conical in two-dimensional subspaces of the $(3N - 6)$-dimensional nuclear configuration space $\mathbf{q}$? We have seen that for an intersection to have such a property it suffices that the corresponding 2×2 Hamiltonian matrix $\mathbf{H}_\psi$ have some nonvanishing linear terms, as indicated in (30), with the coefficients of those terms

subject to the mild conditions described after (33). Once more, this should happen quite frequently. We conclude that for $N \geq 3$, conical intersections between pairs of adjacent electronically adiabatic PES should be very common in nature. As a result, it is quite important to determine the effect of such intersections on the dynamics of the corresponding systems. This is the central objective of the present chapter.

III. NUCLEAR WAVE FUNCTIONS AND THE GEOMETRIC PHASE EFFECT FOR CONICAL INTERSECTIONS

A. The Born-Oppenheimer Expansion and the One- and Two-State Approximations

Let the system being considered consist of N nuclei and n electrons. The nuclear position vectors with respect to a laboratory-fixed frame with origin O will be designated by $\mathbf{r}^{nu} \equiv (\mathbf{r}_1^{nu}, \mathbf{r}_2^{nu}, \ldots, \mathbf{r}_N^{nu})$, and the electron position vectors in that same frame by $\mathbf{r}^{el} \equiv (\mathbf{r}_1^{el}, \mathbf{r}_2^{el}, \ldots, \mathbf{r}_n^{el})$. In order to separate the motion of the center of mass $\overline{G}$ of the system, it is convenient to change these variables to the equivalent ones $\mathbf{r}_{\overline{G}}$, $\mathbf{R}'_\lambda \equiv (\mathbf{R}'_{\lambda_1}, \mathbf{R}'_{\lambda_2}, \ldots, \mathbf{R}'_{\lambda_{N-1}})$, and $\mathbf{r}' \equiv (\mathbf{r}'_1, \mathbf{r}'_2, \ldots, \mathbf{r}'_n)$, defined as follows:

a. $\mathbf{r}_{\overline{G}}$ is the position vector of $\overline{G}$ in the laboratory-fixed frame.
b. λ is an arbitrary clustering scheme for the N nuclei [21,22]. Two such clustering schemes are shown in Fig. 2 for four nuclei. Associated with λ, we define the Jacobi relative position vectors $\mathbf{R}'_{\lambda_i}$ $(i = 1, 2, \ldots, N-1)$.
c. Let G be the center of mass of the N nuclei. We define $\mathbf{r}'_1$ as the position vector of electron 1 with respect to G, and G_1 as the center of mass of the subsystem comprised of the N nuclei and electron 1. Similarly, $\mathbf{r}'_2$ is the position vector of electron 2 with respect to G_1 and G_2 is the center of mass of the N nuclei and electrons 1 and 2, etc. Finally, $\mathbf{r}'_n$ is the position vector of the nth electron with respect to G_{n-1} and $G_n \equiv \overline{G}$ is the center of mass of the N-nuclei plus

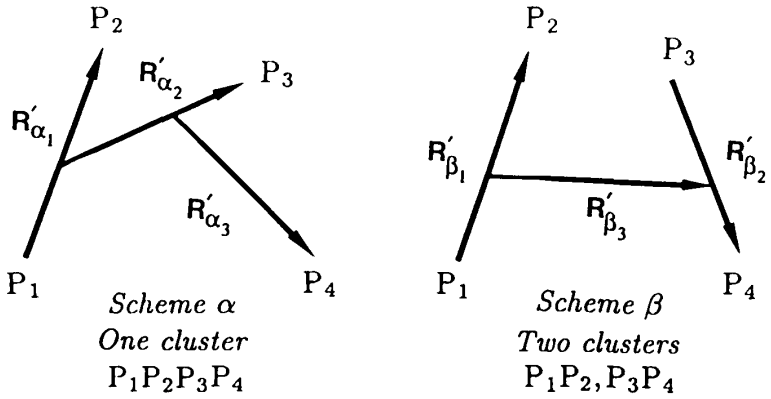

Figure 2 Clustering schemes for a four-nuclei system. The four nuclei P_1, P_2, P_3, P_4 are connected by two distinct sets of Jacobi vectors. In scheme α, vector $\mathbf{R}'_{\alpha_1}$ connects P_1 to P_2, $\mathbf{R}'_{\alpha_2}$ connects the center of mass of P_1P_2 to P_3, and $\mathbf{R}'_{\alpha_3}$ the center of mass of $P_1P_2P_3$ to P_4. This is called a canonical or one-cluster (formed by all four nuclei) scheme. In scheme β, $\mathbf{R}'_{\beta_1}$ is the same as $\mathbf{R}'_{\alpha_1}$, $\mathbf{R}'_{\beta_2}$ connects P_3 to P_4 and $\mathbf{R}'_{\beta_3}$ connects the center of mass of P_1P_2 to that of P_3P_4. This is called a two-cluster (P_1P_2 and P_3P_4) scheme. Both $\mathbf{R}'_{\alpha_3}$ and $\mathbf{R}'_{\beta_3}$ pass through the center of mass of the whole system.

n-electron system. Figure 3 depicts these several vectors for a 3-nuclei plus 4-electron system.

In terms of the variables $\mathbf{r}_{\bar{G}}$, $\mathbf{R}'_{\lambda}$, and $\mathbf{r}'$, the system's total kinetic energy operator $\hat{T}^{\text{tot}}$ is given by

$$\hat{T}^{\text{tot}} = \hat{T}_{\bar{G}} + \hat{T}_{\text{nu}} + \hat{T}_{\text{el}} \tag{45}$$

where the terms in the right-hand side are, respectively, the kinetic energy operators of the center of mass $\bar{G}$, of the nuclei and of the electrons and are given by

$$\hat{T}_{\bar{G}} = \frac{-\hbar^2}{2(M + nm)} \nabla^2_{r_{\bar{G}}} \tag{46}$$

$$\hat{T}_{\text{nu}} = \sum_{i=1}^{N-1} \frac{-\hbar^2}{2\mu_{\lambda_i}} \nabla^2_{\mathbf{R}'_{\lambda_i}} \tag{47}$$

$$\hat{T}_{\text{el}} = \sum_{j=1}^{n} \frac{-\hbar^2}{2\nu_j} \nabla^2_{\mathbf{r}'_j} \tag{48}$$

In these expressions M is the total nuclear mass, m is the mass of one electron, and the μ_{λ_i} and ν_j are effective masses [22] associated with the corresponding coordinates $\boldsymbol{R}'_{\lambda_1}$ and $\mathbf{r}'_j$, with

$$\nu_j = \frac{[M + (j - 1)m]m}{M + jm} \tag{49}$$

Because of the small ratio of the electron mass to the total mass of the nuclei, $\nu_j \cong \nu \cong m$. In addition, the several intermediate centers of mass G_j ($j = 1, 2, \ldots, n - 1$) and the overall system center of mass $\bar{G}$ are very close to the nuclear center of mass G. However, the distinctness of these centers of mass and the differences between the ν_j and

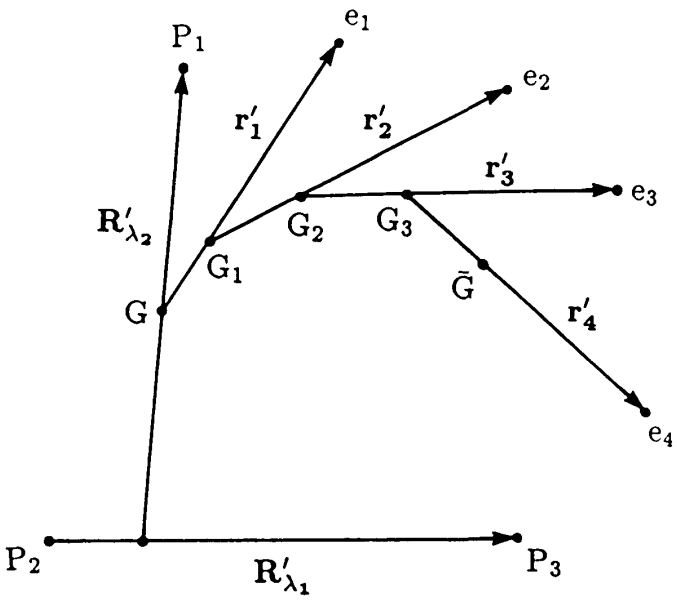

Figure 3 Jacobi vectors for a three-nuclei, four-electron system. The nuclei are P_1, P_2, P_3 and the electrons are e_1, e_2, e_3, e_4.

m are responsible for the so-called mass polarization effect in the electronic spectra of these systems and produces relative shifts in the corresponding energy levels of 10^{-4} or less. In the present considerations we take the G_j ($j = 1, 2, \ldots, n-1$) and $\overline{G} \equiv G_n$ to be distinct from G and the ν_j to be distinct from m, since this does not introduce any formal complications. In the actual scattering calculations described in this chapter these differences are ignored as they introduce relative changes in the several cross sections of the order of 10^{-4} or less, which is beyond the present achievable accuracy in the measurement of such cross sections.

We assume that no external fields act on the system, and therefore that the potential energy function V is independent of $\mathbf{r}_{\overline{G}}$. As a result, we will omit $\hat{T}_{\overline{G}}$ and consider only the system's internal kinetic energy operator $\hat{T}^{\text{int}}$ given by

$$\hat{T}^{\text{int}} = \hat{T}^{\text{int}}_{\text{nu}} + \hat{T}_{\text{el}} \tag{50}$$

We next transform from the Jacobi vectors $\mathbf{R}'_{\lambda_i}$ ($i = 1, 2, \ldots, N-1$) and $\mathbf{r}'_j$ ($j = 1, 2, \ldots, n$) to the mass-scaled Jacobi vectors [22] $\mathbf{R}_{\lambda_i}$ and $\mathbf{r}_j$ defined by

$$\mathbf{R}_{\lambda_i} = \left(\frac{\mu_{\lambda_i}}{\mu}\right)^{1/2} \mathbf{R}'_{\lambda_i} \qquad \mathbf{r}_j = \left(\frac{\nu_j}{\nu}\right)^{1/2} \mathbf{r}'_j \tag{51}$$

where

$$\mu = \left(\frac{1}{M}\prod_{i=1}^{N} M_i\right)^{1/(N-1)} \qquad \nu = m\left(\frac{M}{M + nm}\right)^{1/n} \tag{52}$$

M_i being the mass of nucleus i. In terms of the mass-scaled vectors $\mathbf{R}_\lambda \equiv (\mathbf{R}_{\lambda_1}, \mathbf{R}_{\lambda_2}, \ldots, \mathbf{R}_{\lambda_{N-1}})$ and $\mathbf{r} \equiv (\mathbf{r}_1, \mathbf{r}_2, \ldots, \mathbf{r}_n)$, $\hat{T}^{\text{int}}$ can be expressed as

$$\hat{T}^{\text{int}} = -\frac{\hbar^2}{2\mu}\nabla^2_{\mathbf{R}} - \frac{\hbar^2}{2\nu}\nabla^2_{\mathbf{r}} \tag{53}$$

where

$$\nabla^2_{\mathbf{R}} \equiv \sum_{i=1}^{N-1} \nabla^2_{\mathbf{R}_{\lambda_i}} \qquad \nabla^2_{\mathbf{r}} \equiv \sum_{j=1}^{n} \nabla^2_{\mathbf{r}_j} \tag{54}$$

with $\nabla^2_{\mathbf{R}}$ (and $\nabla^2_{\mathbf{r}}$) being independent of the choice of clustering scheme λ. Equation 53 is a very convenient form for the system's internal kinetic energy operator. The system's internal Hamiltonian, which excludes the kinetic energy operator of its center of mass, is rigorously given by

$$\hat{H}^{\text{int}} = \hat{T}^{\text{int}} + V \tag{55}$$

where, in the absence of spin-dependent terms, V is the coulombic potential energy between all the nuclei and electrons and is completely determined by $\mathbf{R}$ and $\mathbf{r}$.

The system's electronic Hamiltonian is now given by

$$\hat{H}^{\text{el}}(\mathbf{r}; \mathbf{q}) = -\frac{\hbar^2}{2\nu}\nabla^2_{\mathbf{r}} + \mathbf{V}(\mathbf{r}; \mathbf{q}) \tag{56}$$

where, for $N \geq 3$, $\mathbf{q} \equiv (q_1, q_2, \ldots, q_{3N-6})$ is an appropriate set of scalar internal nuclear coordinates considered in Sec. II.A and depends on $\mathbf{R}$ only. The electronically adiabatic wave functions are still defined by (5) but with the space-fixed electronic position vectors

$\mathbf{r}^{el}$ replaced by the mass-scaled Jacobi vectors $\mathbf{r}$ and the space-fixed nuclear coordinates $\mathbf{r}^{nu}$ by the internal nuclear coordinates $\mathbf{q}(\mathbf{R})$:

$$\hat{H}^{el}(\mathbf{r};\mathbf{q})\psi_n^{el,ad}(\mathbf{r};\mathbf{q}) = \varepsilon_n^{ad}(\mathbf{q})\psi_n^{el,ad}(\mathbf{r};\mathbf{q}) \tag{57}$$

Similarly, the Born-Oppenheimer expansion for the orbital wave function is still given by (4), with appropriate variable substitutions:

$$\Psi^0(\mathbf{r},\mathbf{R}) = \sum\!\!\!\!\!\!\int_n \psi_n^{nu,ad}(\mathbf{R})\psi_n^{el,ad}(\mathbf{r};\mathbf{q}) \tag{58}$$

The complete set of adiabatic electronic wave functions are orthonormalized according to

$$\langle \psi_n^{el,ad}(\mathbf{r};\mathbf{q}) \mid \psi_{n'}^{el,ad}(\mathbf{r};\mathbf{q}) \rangle_r = \begin{cases} \delta_{n,n'} & \text{for } \mathbf{n} \text{ and } \mathbf{n}' \text{ discrete} \\ \delta(\mathbf{n}-\mathbf{n}') & \text{for } \mathbf{n} \text{ and } \mathbf{n}' \text{ continuous} \\ 0 & \text{for } \mathbf{n} \text{ discrete and } \mathbf{n}' \text{ continuous, or vice versa} \end{cases} \tag{59}$$

Replacement of (58) into the Schrödinger equation

$$\hat{H}^{int}(\mathbf{r},\mathbf{R})\Psi^0(\mathbf{r},\mathbf{R}) = E\Psi^0(\mathbf{r},\mathbf{R}) \tag{60}$$

(where E differs from the one in (2) in that it excludes the translational energy of the system's center of mass) leads to the following set of coupled equations in the electronically adiabatic representation nuclear wave functions $\chi_n^{ad}(\mathbf{R}) \equiv \psi_n^{nu,ad}(\mathbf{R})$:

$$-\frac{\hbar^2}{2\mu}\nabla_R^2\chi_n^{ad}(\mathbf{R}) + \sum_{n'}\frac{-\hbar^2}{\mu}\mathbf{W}_{n,n'}^{(1)ad}(\mathbf{R})\cdot\nabla_R\chi_{n'}^{ad}(\mathbf{R}) + \sum_{n'}\frac{-\hbar^2}{2\mu}W_{n,n'}^{(2)ad}(\mathbf{R})\chi_{n'}^{ad}(\mathbf{R} = [E - \varepsilon_n^{ad}(\mathbf{q})]\,\chi_n^{ad}(\mathbf{R}) \tag{61}$$

The $\mathbf{W}_{n,n'}^{(1)ad}$ and $W_{n,n'}^{(2)ad}$ are defined by

$$\mathbf{W}_{n,n'}^{(1)ad}(\mathbf{R}) = \langle\psi_n^{el,ad}(\mathbf{r};\mathbf{q})|\nabla_R|\psi_{n'}^{el,ad}(\mathbf{r};\mathbf{q})\rangle_r \tag{62}$$

and

$$W_{n,n'}^{(2)ad}(\mathbf{R}) = \langle\psi_n^{el,ad}(\mathbf{r};\mathbf{q})|\nabla_R^2|\psi_{n'}^{el,ad}(\mathbf{r};\mathbf{q})\rangle_r \tag{63}$$

and are called the first and second-derivative coupling elements respectively. In (61) through (63) ∇_R represents the column vector gradient operator in the $3(N-1)$-dimensional mass-scaled Jacobi nuclear coordinate space and is λ-dependent. In spite of this, the scalar products $\nabla_R^2 = \nabla_R \cdot \nabla_R$ and $\mathbf{W}_{n,n'}^{(1)}(\mathbf{R}) \cdot \nabla_R$ are *not* λ-dependent. The reason is that a $\lambda \rightarrow \lambda'$ arrangement channel transformation is a kinematic rotation [17]. As a result, we may omit any explicit designation of λ in (61). It should be noted that, as a consequence of (59), the matrix whose elements are the $\mathbf{W}_{n,n'}^{(1)ad}(\mathbf{R})$ vectors is skew-hermitian, and therefore its diagonal elements $\mathbf{W}_{n,n}^{(1)ad}(\mathbf{R})$ are pure imaginary quantities. If the $\psi_n^{el,ad}(\mathbf{r};\mathbf{q})$ are chosen to be real, which is usually the case, that matrix is skew-symmetric and those diagonal elements vanish identically.

For values of E corresponding to the unbound nuclear motion continuum, Eq. (61), when associated with appropriate asymptotic conditions, constitutes the scattering equations (for all n) for the system's nuclear motion. These equations are, as pointed out

above, rigorous except for the neglect of spin terms in the Hamiltonian and other relativistic corrections. For light nuclei, such terms are about four orders of magnitude or more smaller than the coulombic ones. If desired, they may be introduced at a later stage by perturbative techniques, as is done for bound states [23]. It should be stressed that the components of $\mathbf{R}$ and $\mathbf{r}$ are those in a cartesian frame whose axes have space-fixed directions, and whose origin is the center of mass $\overline{G}$ of the system. These components are independent of the position of $\overline{G}$ and, as a result, that frame is called space-fixed. Furthermore, the partial derivatives implied in $\nabla_{\mathbf{R}}^2$ should be taken with the space-fixed components of $\mathbf{r}$ maintained constant. However, for computational convenience, $\psi_{\mathbf{n}}^{\mathrm{el,ad}}(\mathbf{r}; \mathbf{q})$ is usually obtained with the components of $\mathbf{r}$ expressed in a body-fixed frame, which is permitted because (57) is invariant under a space-fixed to body-fixed transformation. Under these circumstances it is necessary in the calculation of the coupling elements of (62) and (63) to reexpress $\nabla_{\mathbf{R}}$ in terms of partial derivatives obtained with the body-fixed components of $\mathbf{r}$ maintained constant. This introduces small additional electronic-nuclear motion coupling terms that are also four orders of magnitude or more smaller than the coulombic ones. For scattering problems they can be safely neglected or, if desired, reintroduced perturbatively.

The Born-Oppenheimer expansion (58) is complete, but involves an infinite number of electronically adiabatic states. Under many circumstances this expansion can, however, be dramatically truncated to one or two terms only. For example, let $\varepsilon_{\mathbf{i}}^{\mathrm{ad}}(\mathbf{q})$ be the lowest PES of a given system, and $\varepsilon_{\mathbf{j}}^{\mathrm{ad}}(\mathbf{q})$ the next higher one. The region of nuclear configuration space for which these two PESs come close together is usually quite restricted. Let us consider a bound state energy or a dynamic process at an energy sufficiently below that for which such close approach (or intersection) takes place. Under these circumstances it suffices, to a very good accuracy, to retain only the $\mathbf{n} = \mathbf{i}$ term in (58):

$$\Psi^0(\mathbf{r}, \mathbf{R}) = \chi_{\mathbf{i}}^{\mathrm{ad}}(\mathbf{R})\psi_{\mathbf{i}}^{\mathrm{el,ad}}(\mathbf{r}; \mathbf{q}) \tag{64}$$

This is the so-called one-electronically-adiabatic-state or simply the one-state approximation, and leads to a motion of the system's nuclei restricted to the single PES $\varepsilon_{\mathbf{i}}^{\mathrm{ad}}(\mathbf{q})$. The corresponding wave function $\chi_{\mathbf{i}}^{\mathrm{ad}}(\mathbf{R})$ is determined by

$$\begin{aligned} -\frac{\hbar^2}{2\mu}\nabla_{\mathbf{R}}^2\chi_{\mathbf{i}}^{\mathrm{ad}}(\mathbf{R}) - \frac{\hbar^2}{\mu}\mathbf{W}_{\mathbf{i},\mathbf{i}}^{(1)\mathrm{ad}}(\mathbf{R}) \cdot \nabla_{\mathbf{R}}\chi_{\mathbf{i}}^{\mathrm{ad}}(\mathbf{R}) - \frac{\hbar^2}{2\mu}W_{\mathbf{i},\mathbf{i}}^{(2)\mathrm{ad}}(\mathbf{R})\chi_{\mathbf{i}}^{\mathrm{ad}}(\mathbf{R}) \\ = [E - \varepsilon_{\mathbf{i}}^{\mathrm{ad}}(\mathbf{q})]\chi_{\mathbf{i}}^{\mathrm{ad}}(\mathbf{R}) \end{aligned} \tag{65}$$

together with appropriate asymptotic conditions associated with the bound or scattering states of interest. As pointed out after (63), if $\psi_{\mathbf{i}}^{\mathrm{el,ad}}(\mathbf{r}; \mathbf{q})$ is real $\mathbf{W}_{\mathbf{i},\mathbf{i}}^{(1)\mathrm{ad}}(\mathbf{R})$ vanishes. Equation (65) is much simpler than (61) since in the former $\chi_{\mathbf{i}}^{\mathrm{ad}}(\mathbf{R})$ is not coupled to the remaining $\chi_{\mathbf{n}}^{\mathrm{ad}}(\mathbf{R})$ with $\mathbf{n} \neq \mathbf{i}$. It should be noticed that although $\psi_{\mathbf{i}}^{\mathrm{el,ad}}(\mathbf{r}; \mathbf{q})$ depends on the internal nuclear configuration coordinates $\mathbf{q}$, the $\nabla_{\mathbf{R}}^2$ and $\nabla_{\mathbf{R}}$ operators contain in addition external nuclear coordinates which describe the rotation of the nuclei around their center of mass. Such external coordinates can be chosen to be the Euler angles of an appropriate frame attached to the nuclei (i.e., a body-fixed frame), measured with respect to the space-fixed frame. As a result, the $\nabla_{\mathbf{R}}^2$ and $\nabla_{\mathbf{R}}$ operators in (65) contain terms in these external variables, as well as in the internal ones $\mathbf{q}$.

Within the one-state description it is possible to introduce an additional approximation by neglecting the $\mathbf{W}_{\mathbf{i},\mathbf{i}}^{(1)\mathrm{ad}}$ and $W_{\mathbf{i},\mathbf{i}}^{(2)\mathrm{ad}}$ terms in (65). This approximation is based on the fact that, away from the close approach region between the $\varepsilon_{\mathbf{i}}^{\mathrm{ad}}(\mathbf{q})$ and $\varepsilon_{\mathbf{j}}^{\mathrm{ad}}(\mathbf{q})$ PESs, $\psi_{\mathbf{i}}^{\mathrm{el,ad}}(\mathbf{r}; \mathbf{q})$ is a slowly varying function of $\mathbf{q}$ and its first and second derivatives with

respect to the components of this variable are small. For the usual case in which $\psi_i^{el,ad}(\mathbf{r};\mathbf{q})$ is chosen to be real, $\mathbf{W}_{i,i}^{(1)ad}(\mathbf{R})$ vanishes identically and only $W_{i,i}^{(2)ad}(\mathbf{R})$ needs to be neglected. In this case (65) becomes simply

$$\hat{H}^{nu}(\mathbf{R})\chi_i^{ad}(\mathbf{R}) = -\frac{\hbar^2}{2\mu}\nabla_R^2\chi_i^{ad}(\mathbf{R}) + \varepsilon_i^{ad}(\mathbf{q})\chi_i^{ad}(\mathbf{R}) = E\chi_i^{ad}(\mathbf{R}) \tag{66}$$

where $\hat{H}^{nu}(\mathbf{R})$ is an effective nuclear Hamiltonian. The pair of equations (64) and (66) constitute the usual Born-Oppenheimer electronically adiabatic approximation, which is very accurate and useful for a wide variety of systems and conditions, and is used in the calculations described in this chapter. Its essential assumption is that the coupling of the nuclear motion on the ground state PES of the system to the electronic motion for that state or to the nuclear motion on other PESs can be neglected. The existence of a conical intersection between the $\varepsilon_i^{ad}(\mathbf{q})$ and $\varepsilon_j^{ad}(\mathbf{q})$ PESs requires special consideration, since if $\psi_i^{el,ad}(\mathbf{r};\mathbf{q})$ is allowed to be complex, $\mathbf{W}_{i,i}^{(1)ad}(\mathbf{R})$ diverges at that intersection and cannot be neglected. If, instead, $\psi_i^{el,ad}(\mathbf{r};\mathbf{q})$ is required to be real, $\chi_i^{ad}(\mathbf{R})$ must satisfy special conditions even when it does not penetrate into regions of nuclear configuration space close to that intersection. This matter will be discussed in detail in Sec. III.B and III.C.

If the system can sample regions of nuclear configuration space for which the $\varepsilon_i^{ad}(\mathbf{q})$ and $\varepsilon_j^{ad}(\mathbf{q})$ PESs are close to one another, more terms in (58) must be included. If, however, the system's energy is low enough for the nuclear motion on $\varepsilon_j^{ad}(\mathbf{q})$ not to sample regions for which this surface comes close to the next higher one, it suffices to include the two terms $\mathbf{n} = \mathbf{i}, \mathbf{j}$ in the Born-Oppenheimer expansion:

$$\Psi^0(\mathbf{r},\mathbf{R}) = \chi_i^{ad}(\mathbf{R})\psi_i^{el,ad}(\mathbf{r};\mathbf{q}) + \chi_j^{ad}(\mathbf{R})\psi_j^{el,ad}(\mathbf{r};\mathbf{q}) \tag{67}$$

This is the two- (electronically adiabatic-) state approximation. The corresponding equations for the adiabatic nuclear wave functions χ_i^{ad} and $\chi^{ad}{}_j$ are

$$\begin{aligned}
&-\frac{\hbar^2}{2\mu}\nabla_R^2\chi_i^{ad}(\mathbf{R}) - \frac{\hbar^2}{\mu}[\mathbf{W}_{i,i}^{(1)ad}(\mathbf{R})\cdot\nabla_R\chi_i^{ad}(\mathbf{R}) + \mathbf{W}_{i,j}^{(1)ad}(\mathbf{R})\cdot\nabla_R\chi_j^{ad}(\mathbf{R})] \\
&-\frac{\hbar^2}{2\mu}[W_{i,i}^{(2)ad}(\mathbf{R})\chi_i^{ad}(\mathbf{R}) + W_{i,j}^{(2)ad}(\mathbf{R})\chi_j^{ad}(\mathbf{R})] + \varepsilon_i^{ad}(\mathbf{q})\chi_i^{ad}(\mathbf{R}) = E\chi_i^{ad}(\mathbf{R}) \\
&-\frac{\hbar^2}{2\mu}\nabla_R^2\chi_j^{ad}(\mathbf{R}) - \frac{\hbar^2}{\mu}[\mathbf{W}_{j,i}^{(1)ad}(\mathbf{R})\cdot\nabla_R\chi_i^{ad}(\mathbf{R}) + \mathbf{W}_{j,j}^{(1)ad}(\mathbf{R})\cdot\nabla_R\chi_j^{ad}(\mathbf{R})] \\
&-\frac{\hbar^2}{2\mu}[W_{j,i}^{(2)ad}(\mathbf{R})\chi_i^{ad}(\mathbf{R}) + W_{j,j}^{(2)ad}(\mathbf{R})\chi_j^{ad}(\mathbf{R})] + \varepsilon_j^{ad}(\mathbf{q})\chi_j^{ad}(\mathbf{R}) = E\chi_j^{ad}(\mathbf{R})
\end{aligned} \tag{68}$$

For the usual case in which the $\psi_n^{el,ad}(\mathbf{r};\mathbf{q})$ are chosen to be real, the skew-symmetry property mentioned after (63) simplifies these equations to

$$\begin{aligned}
&-\frac{\hbar^2}{2\mu}\nabla_R^2\chi_i^{ad}(\mathbf{R}) - \frac{\hbar^2}{\mu}\mathbf{W}_{i,j}^{(1)ad}(\mathbf{R})\cdot\nabla_R\chi_j^{ad}(\mathbf{R}) \\
&-\frac{\hbar^2}{2\mu}[W_{i,i}^{(2)ad}(\mathbf{R})\chi_i^{ad}(\mathbf{R}) + W_{i,j}^{(2)ad}(\mathbf{R})\chi_j^{ad}(\mathbf{R})] + \varepsilon_i^{ad}(\mathbf{q})\chi_i^{ad}(\mathbf{R}) = E\chi_i^{ad}(\mathbf{R}) \\
&-\frac{\hbar^2}{2\mu}\nabla_R^2\chi_j^{ad}(\mathbf{R}) + \frac{\hbar^2}{\mu}\mathbf{W}_{i,j}^{(1)ad}(\mathbf{R})\cdot\nabla_R\chi_i^{ad}(\mathbf{R}) \\
&-\frac{\hbar^2}{2\mu}[W_{j,i}^{(2)ad}(\mathbf{R})\chi_i^{ad}(\mathbf{R}) + W_{j,j}^{(2)ad}(\mathbf{R})\chi_j^{ad}(\mathbf{R})] + \varepsilon_j^{ad}(\mathbf{q})\chi_j^{ad}(\mathbf{R}) = E\chi_j^{ad}(\mathbf{R})
\end{aligned} \tag{69}$$

Combined with appropriate asymptotic conditions, these are the nuclear motion equations which must be solved when two electronically adiabatic PESs are involved in the process. As for the one-state approximation, the existence of a conical intersection between the $\varepsilon_i^{ad}(\mathbf{q})$ and $\varepsilon_j^{ad}(\mathbf{q})$ PESs requires that additional restrictions be imposed on χ_i^{ad} and χ_j^{ad}. These will be discussed in Sec. III.B.

Under the conditions of validity of the two-electronically-adiabatic-state approximation it is possible to change from the $\psi_n^{el,ad}(\mathbf{r}; \mathbf{q})$ ($\mathbf{n} = \mathbf{i}, \mathbf{j}$) electronically adiabatic representation to a diabatic one $\psi_n^{el,ad}(\mathbf{r}; \mathbf{q})$ ($\mathbf{n} = \mathbf{i}, \mathbf{j}$) for which the $\nabla_R \cdot \chi_n^d(\mathbf{R})$ terms in the corresponding diabatic nuclear motion equations are significantly smaller than in the adiabatic equation or, for favorable conditions, vanish [24–26]. Such an electronically diabatic representation is usually more convenient for scattering calculations involving two electronically adiabatic PESs, but not for those involving a single adiabatic PES. This matter will be further discussed in Sec. III.B.3 for the case in which a conical intersection between the $\varepsilon_i^{ad}(\mathbf{q})$ and $\varepsilon_j^{ad}(\mathbf{q})$ PESs occurs.

B. The Boundary Condition Description of Nuclear Wave Functions

1. The Electronically Adiabatic Representation

Let us consider initially a system for which the one-state approximation described by (64) and (65) is applicable, and which displays a conical intersection between PESs $\varepsilon_i^{ad}(\mathbf{q})$ and $\varepsilon_j^{ad}(\mathbf{q})$. As seen after (44), the wave function $\psi_i^{el,ad}(\mathbf{r}; \mathbf{q})$ of (64), if required to be real-valued, undergoes a discontinuous change in sign across some cut in $\mathbf{q}$ space containing the locus of conical intersection geometries $\mathbf{q}_0$, which means that $\psi_i^{el,ad}(\mathbf{r}; \mathbf{q})$ is not a single-valued function of the internal nuclear configuration of the system. On the other hand, in this approximation, the orbital electronuclear wave functions $\Psi^0(\mathbf{r}, \mathbf{R})$ of (64) *must*, by the basic principles of quantum mechanics, be a single-valued function of $\mathbf{R}$. For this condition to be fulfilled, it is necessary that the $\chi_i^{ad}(\mathbf{R})$ of that equation also undergo a change in sign across the same cut in the $\mathbf{q}$ subspace of $\mathbf{R}$ space. This constitutes a boundary condition that must be imposed on (65), or in the Born-Oppenheimer approximation, (66), in addition to the usual asymptotic conditions which describe the bound or scattering states of interest. If this extra boundary condition is not imposed, wrong results will be obtained, and the magnitude of the error may be quite large, as described in Sec. V. On the other hand, if this condition is imposed, the results will have the same level of accuracy that the regular one-state approximation would have if the system did not display a conical intersection. As a result, for the situation in which $\psi_i^{el,ad}(\mathbf{r}; \mathbf{q})$ is required to be real, this change of sign is an essential part of the one-state approximation in the presence of a conical intersection. This is true even if the energy of interest is significantly below the minimum conical intersection energy, as clearly demonstrated for H_3 in Sec. V.A. In other words, this is the case even if the coupling elements $\mathbf{W}_{ij}^{(1)}(\mathbf{R})$ and $W_{ij}^{(2)}(\mathbf{R})$ which appear in the first of (69) for the two-state approximation vanish identically. In a geometrical sense, this change of sign of $\chi_i^{ad}(\mathbf{R})$ following a pseudorotation of the system around a conical intersection geometry is not a consequence of the magnitude of its coupling to the upper surface wave function $\chi_j^{ad}(\mathbf{R})$, but represents instead a topological property akin to that displayed by a Möbius strip. This matter is further discussed in Sec. III.D.

We next consider a system for which the one-state approximation is not accurate enough, but for which the two-state approximation described by (67) and (68) is adequate. We further assume that there exists a conical intersection between PESs $\varepsilon_i^{ad}(\mathbf{q})$ and $\varepsilon_j^{ad}(\mathbf{q})$.

Again, as seen after (44), the wave functions $\psi_i^{el,ad}(\mathbf{r};\mathbf{q})$ and $\psi_j^{el,ad}(\mathbf{r};\mathbf{q})$ of (67), if required to be real, must both undergo a discontinuous change in sign across some cut in $\mathbf{q}$ space containing the locus of the conical intersection geometries. As for the one-state approximation, this makes it necessary that both $\chi_i^{ad}(\mathbf{R})$ and $\chi_j^{ad}(\mathbf{R})$ undergo a similar change in sign across that cut, in order for the $\Psi^0(\mathbf{r},\mathbf{R})$ of (67) to be a single-valued function of the nuclear configurations of the system. This means that upon transitioning from the one-state approximation to the two-state one, while retaining the electronically adiabatic representation, the change-of-sign boundary condition on the nuclear wave functions must also be retained. Once more, this is independent of the magnitude of the couplings between these wave functions. The first derivative coupling element $\mathbf{W}_{ij}^{(1)}(\mathbf{R})$ has a pole at conical intersection geometries [27], and in Sec. III.B.2 we describe how to cope with such singularities.

2. The Electronically Diabatic Representation

In addition to the electronically adiabatic representation described by (4) and (5) or, equivalently (57) and (58), other representations can be defined in which the adiabatic electronic wave function basis set used in expansions (4) or (58) is replaced by some other set of functions of the electronic coordinates $\mathbf{r}^{el}$ or $\mathbf{r}$. Let us in what follows assume that we have separated the motion of the center of mass $\overline{G}$ of the system and adopted the Jacobi mass-scaled vectors $\mathbf{R}_\lambda$ and $\mathbf{r}$ defined after (52), and in terms of which the adiabatic electronic wave functions are $\psi_n^{el,ad}(\mathbf{r};\mathbf{q})$ and the corresponding nuclear wave function coefficients are $\chi_n^{ad}(\mathbf{R})$. The symbol $\mathbf{q}(\mathbf{R})$ refers to the set of scalar nuclear position coordinates defined after (56). Let $\{\psi_n^{el,d}(\mathbf{r};\mathbf{q})\}$ label that alternate electronic basis set, which is allowed to be parametrically dependent on $\mathbf{q}$, and for which we will use the designation "diabatic." We now proceed to define such a set. Let $\chi_n^{d}(\mathbf{R})$ be the nuclear wave function coefficients associated with those diabatic electronic wave functions. As a result, we may rewrite (58) as

$$\Psi^0(\mathbf{r};\mathbf{R}) = \sum\!\!\!\!\!\!\int_n \chi_n^{ad}(\mathbf{R})\psi_n^{el,ad}(\mathbf{r};\mathbf{q}) = \sum\!\!\!\!\!\!\int_n \chi_n^{d}(\mathbf{R})\psi_n^{el,d}(\mathbf{r};\mathbf{q}) \tag{70}$$

We assume the $\{\psi_n^{el,d}(\mathbf{r};\mathbf{q})\}$ set to be complete in $\mathbf{r}$ and orthonormalized in a manner similar to [59], with the superscript "ad" replaced by "d." The column vector $\psi^{el,ad}(\mathbf{r};\mathbf{q})$ whose elements are the $\psi_n^{el,d}(\mathbf{r};\mathbf{q})$ are related to the column vector $\psi^{el,d}(\mathbf{r};\mathbf{q})$ whose elements are the $\psi_n^{el,ad}(\mathbf{r};\mathbf{q})$ by a unitary transformation of infinite dimensions:

$$\psi^{el,ad}(\mathbf{r};\mathbf{q}) = \mathbf{A}^*(\mathbf{q})\psi^{el,d}(\mathbf{r};\mathbf{q}) \tag{71}$$

$$\mathbf{A}^\dagger(\mathbf{q})\mathbf{A}(\mathbf{q}) = \mathbf{I} \tag{72}$$

We chose to use $\mathbf{A}^*(\mathbf{q})$ rather than $\mathbf{A}(\mathbf{q})$ in (71) to simplify the form of (73). The diabatic basis set will be completely determined once we select the unitary matrix $\mathbf{A}(\mathbf{q})$. If both $\psi_n^{el,ad}(\mathbf{r};\mathbf{q})$ and $\psi_n^{el,d}(\mathbf{r};\mathbf{q})$ are chosen to be real, $\mathbf{A}(\mathbf{q})$ must be orthogonal. Replacement of (71) into (70) and use of the orthonormality properties of both the adiabatic and diabatic electronic basis sets leads to

$$\chi^{ad}(\mathbf{R}) = \mathbf{A}(\mathbf{q})\chi^{d}(\mathbf{R}) \tag{73}$$

where $\chi^{d}(\mathbf{R})$ and $\chi^{ad}(\mathbf{R})$ are the column vectors whose elements are, respectively, the nuclear wave functions $\chi_n^{d}(\mathbf{R})$ and $\chi_n^{ad}(\mathbf{R})$.

We can recast (61) in the more compact matrix form

$$-\frac{\hbar^2}{2\mu}\nabla_{\mathbf{R}}^2\chi^{ad}(\mathbf{R}) - \frac{\hbar^2}{\mu}\mathbf{W}^{(1)ad}(\mathbf{R})\cdot\nabla_{\mathbf{R}}\chi^{ad}(\mathbf{R}) - \frac{\hbar^2}{2\mu}\mathbf{W}^{(2)ad}(\mathbf{R})\chi^{ad}(\mathbf{R}) = [E\mathbf{I} - \boldsymbol{\varepsilon}^{ad}(\mathbf{q})]\chi^{ad}(\mathbf{R}) \tag{74}$$

where $\mathbf{W}^{(1)ad}$ and $\mathbf{W}^{(2)ad}$ are the matrices whose $\mathbf{n}$ row and $\mathbf{n}'$ column element are respectively the column vector $\mathbf{W}^{(1)ad}_{\mathbf{n},\mathbf{n}'}$ defined by (62) and the scalar $W^{(2)ad}_{i,j}(\mathbf{R})$ defined by (63). These matrices are called respectively the first- and second-derivative coupling matrices. In addition, $\mathbf{I}$ is the identity matrix and $\boldsymbol{\varepsilon}^{ad}$ is the diagonal matrix whose diagonal elements are the $\varepsilon^{ad}_{\mathbf{n}}$. If we replace the right-most side of (70) into (60), we obtain the equation corresponding to (74) for $\chi^d(\mathbf{R})$:

$$-\frac{\hbar^2}{2\mu}\nabla_{\mathbf{R}}^2\chi^{d}(\mathbf{R}) - \frac{\hbar^2}{\mu}\mathbf{W}^{(1)d}(\mathbf{R})\cdot\nabla_{\mathbf{R}}\chi^{d}(\mathbf{R}) - \frac{\hbar^2}{2\mu}\mathbf{W}^{(2)d}(\mathbf{R})\chi^{d}(\mathbf{R}) = [E\mathbf{I} - \boldsymbol{\varepsilon}^{d}(\mathbf{q})]\,\chi^{d}(\mathbf{R}) \tag{75}$$

The $\mathbf{W}^{(1)d}$ and $\mathbf{W}^{(2)d}$ matrices are analogous to their adiabatic counterparts, their elements being defined by

$$\mathbf{W}^{(1)d}_{\mathbf{n},\mathbf{n}'}(\mathbf{R}) = \langle\psi^{el,d}_{\mathbf{n}}(\mathbf{r};\mathbf{q})|\nabla_{\mathbf{R}}|\psi^{el,d}_{\mathbf{n}'}(\mathbf{r};\mathbf{q})\rangle_{\mathbf{r}} \tag{76}$$

and

$$W^{(2)d}_{\mathbf{n},\mathbf{n}'}(\mathbf{R}) = \langle\psi^{el,d}_{n}(\mathbf{r};\mathbf{q})|\nabla^2_{\mathbf{R}}|\psi^{el,d}_{\mathbf{n}'}(\mathbf{r};\mathbf{q})\rangle_{\mathbf{r}} \tag{77}$$

The $\boldsymbol{\varepsilon}^{ad}$ matrix is in general nondiagonal and its elements are defined by

$$\varepsilon^{d}_{\mathbf{n},\mathbf{n}'}(\mathbf{q}) = \langle\psi^{el,d}_{\mathbf{n}}(\mathbf{r};\mathbf{q})|\hat{H}^{el}(\mathbf{r};\mathbf{q})|\psi^{el,d}_{\mathbf{n}'}(\mathbf{r};\mathbf{q})\rangle_{\mathbf{r}} \tag{78}$$

An alternative form of (75) can be obtained by replacing (73) into (74). The result is

$$-\frac{\hbar^2}{2\mu}\nabla_{\mathbf{R}}^2\chi^{d}(\mathbf{R}) - \frac{\hbar^2}{\mu}\mathbf{A}^{\dagger}(\mathbf{q})[\nabla_{\mathbf{R}}\mathbf{A}(\mathbf{q}) + \mathbf{W}^{(1)ad}(\mathbf{R})\mathbf{A}(\mathbf{q})]\cdot\nabla_{\mathbf{R}}\chi^{d}(\mathbf{R}) - \frac{\hbar^2}{2\mu}\mathbf{A}^{\dagger}(\mathbf{q})[\nabla^2_{\mathbf{R}}\mathbf{A}(\mathbf{q}) + 2\mathbf{W}^{(1)ad}(\mathbf{R})\cdot\nabla_{\mathbf{R}}\mathbf{A}(\mathbf{q}) + \mathbf{W}^{(2)ad}(\mathbf{R})\mathbf{A}(\mathbf{q})]\chi^{d}(\mathbf{R}) = [E\mathbf{I} - \mathbf{A}^{\dagger}(\mathbf{q})\boldsymbol{\varepsilon}^{ad}(\mathbf{q})\mathbf{A}(\mathbf{q})]\chi^{d}(\mathbf{R}) \tag{79}$$

Identification of (75) and (79) furnishes the relations between the diabatic and adiabatic coupling matrices.

$$\mathbf{W}^{(1)d}(\mathbf{R}) = \mathbf{A}^{\dagger}(\mathbf{q})[\nabla_{\mathbf{R}}\mathbf{A}(\mathbf{q}) + \mathbf{W}^{(1)ad}(\mathbf{R})\mathbf{A}(\mathbf{q})] \tag{80}$$

$$\mathbf{W}^{(2)d}(\mathbf{R}) = \mathbf{A}^{\dagger}(\mathbf{q})[\nabla^2_{\mathbf{R}}\mathbf{A}(\mathbf{q}) + 2\mathbf{W}^{(1)ad}(\mathbf{R})\cdot\nabla_{\mathbf{R}}\mathbf{A}(\mathbf{q}) + \mathbf{W}^{(2)ad}(\mathbf{R})\mathbf{A}(\mathbf{q})] \tag{81}$$

In addition,

$$\boldsymbol{\varepsilon}^{d}(\mathbf{R}) = \mathbf{A}^{\dagger}(\mathbf{q})\boldsymbol{\varepsilon}^{ad}(\mathbf{q})\mathbf{A}(\mathbf{q}) \tag{82}$$

The unitary transformation matrix $\mathbf{A}(\mathbf{q})$ of (71), (73) and (79) is arbitrary, and can be chosen to make (79) have desirable properties which (74) does not display. In many instances the couplings between consecutive PESs are significant only in the small regions of nuclear configuration space where those PESs are close to each other or

intersect, as discussed in Sec. III.A. Equation (74) can in these cases be truncated at a small number of components of $\chi^{ad}(\mathbf{R})$, usually one or two, for a large number of cases. This is a very desirable property. On the other hand, the first derivative coupling matrix $\mathbf{W}^{(1)ad}(\mathbf{R})$ which appears in that equation varies very rapidly with $\mathbf{q}(\mathbf{R})$ in those small regions, which introduces numerical difficulties in the integration of that equation. In particular, the presence of a conical intersection between two PESs produces a singularity in the corresponding coupling matrix element at the intersection geometries. It is therefore desirable to chose $\mathbf{A}(\mathbf{q})$ so as to minimize this problem, without unduly increasing the number of states used in the corresponding diabatic electronic basis set expansion. A possible approach is to try to find an $\mathbf{A}(\mathbf{q})$ which makes the $\mathbf{W}^{(1)d}(\mathbf{R})$ of (75) and (80) vanish identically. One way to achieve this is to require the $\psi_n^{el,d}(\mathbf{r}; \mathbf{q})$ to be independent of $\mathbf{q}$, as (76) clearly indicates. With this choice we see from (77) that $\mathbf{W}^{(2)d}(\mathbf{R})$ also vanishes identically and (75) acquires the very simple and convenient form

$$-\frac{\hbar^2}{2\mu}\nabla_R^2\chi^d(\mathbf{R}) + \varepsilon^d(\mathbf{q})\chi^d(\mathbf{R}) = E\chi^d(\mathbf{R}) \tag{83}$$

There is, however, a serious shortcoming associated with such a $\mathbf{q}$-independent electronic basis set $\{\psi_n^{el,d}(\mathbf{r})\}$. If we consider, for example, a two-state adiabatic expansion involving only $\psi_i^{el,ad}(\mathbf{r}; \mathbf{q})$ and $\psi_j^{el,ad}(\mathbf{r}; \mathbf{q})$, the corresponding diabatic expansion in the $\psi_n^{el,d}(\mathbf{r}; \mathbf{q})$ must contain a sufficiently large number of terms to represent those two adiabatic electronic wave functions well for all values of the $\mathbf{q}$ sampled by $\chi^{ad}(\mathbf{R})$. This is, in general, an unacceptably large number. In addition, it can be shown [25] that in general no other choice of $\psi_n^{el,d}(\mathbf{r}; \mathbf{q})$ makes $\mathbf{W}^{(1)d}(\mathbf{R})$ vanish for all $\mathbf{R}$.

An alternative approach to the selection of $\mathbf{A}(\mathbf{q})$ is to consider an electronically adiabatic expansion truncated at a small number $\mathcal{N}$ of terms and require $\mathbf{A}(\mathbf{q})$ to be an $(\mathcal{N} \times \mathcal{N})$-dimensional matrix. In this case, neither the adiabatic nor the diabatic electronic basis set is complete, but we assume that the adiabatic expansion in $\mathcal{N}$ terms is sufficiently accurate for our purposes. We now wish to select this $\mathbf{A}(\mathbf{q})$ so as to minimize the effect of the term in (75) containing $\mathbf{W}^{(1)ad}(\mathbf{R})$. Ideally, we would like to force this matrix to vanish identically. Unfortunately, this is not always possible, as we shall now show.

Given a vector $\mathbf{W}(\mathbf{x}) \equiv (W_1(\mathbf{x}), W_2(\mathbf{x}), \ldots, W_{\mathcal{N}}(\mathbf{x}))$ in an $\mathcal{N}$-dimensional space, spanned by cartesian coordinates $\mathbf{x} \equiv (x_1, x_2, \ldots, x_{\mathcal{N}})$, it is always possible to determine another vector $\mathbf{W}_t(\mathbf{x})$ and a function $\Phi(\mathbf{x})$, called the scalar potential of $\mathbf{W}(\mathbf{x})$, subject to the conditions

$$\text{curl } \mathbf{W}_t(\mathbf{x}) = \text{curl } \mathbf{W}(\mathbf{x}) \tag{84}$$

and

$$\nabla_x \cdot \mathbf{W}_t(\mathbf{x}) = 0 \tag{85}$$

such that

$$\mathbf{W}(\mathbf{x}) = \mathbf{W}_l(\mathbf{x}) + \mathbf{W}_t(\mathbf{x}) \tag{86}$$

and

$$\mathbf{W}_l(\mathbf{x}) = \nabla_x\Phi(\mathbf{x}) \tag{87}$$

This is a generalization of the Helmholtz theorem for three-dimensional space [28]. $\mathbf{W}_l(\mathbf{x})$ and $\mathbf{W}_t(\mathbf{x})$ are called the longitudinal and transverse parts of $\mathbf{W}(\mathbf{x})$, respectively. The

scalar potential can be obtained uniquely from the vector

$$\mathbf{V}(\mathbf{x}) = \int \frac{\mathbf{W}(\mathbf{x})}{4\pi|\mathbf{x} - \mathbf{x}'|}\, d\mathbf{x}' \tag{88}$$

by the relation

$$\Phi(\mathbf{x}) = -\nabla_{\mathbf{x}} \cdot \mathbf{V}(\mathbf{x}) \tag{89}$$

$\mathbf{V}(\mathbf{x})$ is a solution of the $\mathcal{N}$-dimensional vector Poisson equation

$$\nabla_{\mathbf{x}}^2 \mathbf{V}(\mathbf{x}) = -\mathbf{W}(\mathbf{x}) \tag{90}$$

Replacement of (78) into (79) and use of the $\mathcal{N}$-dimensional version of Gauss's theorem yields the useful expression [28]

$$\Phi(\mathbf{x}) = -\int \frac{\nabla_{\mathbf{x}'} \mathbf{W}(\mathbf{x})}{4\pi|\mathbf{x} - \mathbf{x}'|}\, d\mathbf{x}' \tag{91}$$

Once $\Phi(\mathbf{x})$ is known we calculate $\mathbf{W}_t(\mathbf{x})$ in terms $\mathbf{W}(\mathbf{x})$ by substituting (87) into (86).

It should be noted that curl $\mathbf{W}(\mathbf{x})$ is, in general, a skew-symmetric tensor $\mathbf{T}(\mathbf{x})$ of rank 2, whose elements T_{ij} are defined by [29]

$$T_{ij}(\mathbf{x}) = \frac{\partial W_i(\mathbf{x})}{\partial x_j} - \frac{\partial W_j(\mathbf{x})}{\partial x_i} \tag{92}$$

Only for $\mathcal{N} = 3$ can this tensor be represented by an axial vector, and in this case another vector $\boldsymbol{A}(\mathbf{x})$, called the vector potential of $\mathbf{W}(\mathbf{x})$, exists [28] such that

$$\mathbf{W}_t(\mathbf{x}) = \text{curl}\, \boldsymbol{A}(\mathbf{x}) \tag{93}$$

and

$$\nabla_{\mathbf{x}} \cdot \boldsymbol{A}(\mathbf{x}) = 0 \tag{94}$$

The explicit expression for this vector potential is

$$\boldsymbol{A}(\mathbf{x}) = \text{curl}\, \mathbf{V}(\mathbf{x}) \tag{95}$$

and in terms of it we can write, for this $\mathcal{N} = 3$ case,

$$\mathbf{W}(\mathbf{x}) = \nabla_{\mathbf{x}}\Phi(\mathbf{x}) + \nabla_{\mathbf{x}} \times \boldsymbol{A}(\mathbf{x}) \tag{96}$$

As a result of (86) and (87), we can, for the general $\mathcal{N}$ case, express the vector $\mathbf{W}_{\mathbf{n},\mathbf{n}'}^{(1)\text{ad}}(\mathbf{R})$ as

$$\mathbf{W}_{\mathbf{n},\mathbf{n}'}^{(1)\text{ad}}(\mathbf{R}) = \nabla_{\mathbf{R}}\Phi_{\mathbf{n},\mathbf{n}'}^{\text{ad}}(\mathbf{R}) + \mathbf{W}_{\mathbf{n},\mathbf{n}'t}^{(1)\text{ad}}(\mathbf{R}) \tag{97}$$

and this relation can be used to put the matrix $\mathbf{W}^{(1)\text{ad}}(\mathbf{R})$ in the form

$$\mathbf{W}^{(1)\text{ad}}(\mathbf{R}) = \nabla_{\mathbf{R}}\Phi^{\text{ad}}(\mathbf{R}) + \mathbf{W}_t^{(1)\text{ad}}(\mathbf{R}) \tag{98}$$

In this equation $\Phi^{(1)\text{ad}}(\mathbf{R})$ and $\mathbf{W}_t^{(1)\text{ad}}(\mathbf{R})$ are the matrices whose elements are the scalars $\Phi_{\mathbf{n},\mathbf{n}'}^{(1)\text{ad}}(\mathbf{R})$ and vectors $\mathbf{W}_{\mathbf{n},\mathbf{n}'t}^{(1)\text{ad}}(\mathbf{R})$ respectively. It should be noticed that, in view of (91) and (62), the scalar potential $\Phi_{\mathbf{n},\mathbf{n}'}^{(1)\text{ad}}(\mathbf{R})$ depends on $\mathbf{R}$ through $\mathbf{q}$ only and can therefore be written as $\Phi_{\mathbf{n},\mathbf{n}'}^{(1)\text{ad}}(\mathbf{q})$. The reason is that $\nabla_{\mathbf{R}} \cdot \mathbf{W}_{\mathbf{n},\mathbf{n}'}^{(1)\text{ad}}(\mathbf{R})$ is a scalar function of $\mathbf{R}$ and must be independent of axes rotations in general, and in particular on the rotation of the space-fixed frame to the body-fixed frame mentioned in the last paragraph of Sec. II.A. The

components of $\mathbf{R}$ in that body-fixed frame are functions of $\mathbf{q}$ only, i.e., the resulting $\mathbf{R}^{bf}(\mathbf{q})$ are independent of the Euler angles that define that rotation. The same is true for $|\mathbf{R} - \mathbf{R}'|$. Replacing in (91) Φ, $\mathbf{x}$, $\mathbf{x}'$ and $\mathbf{W}$ by $\Phi^{(1)ad}_{\mathbf{n},\mathbf{n}'}$, $\mathbf{R}$, $\mathbf{R}'$ and $\mathbf{W}^{(1)ad}_{\mathbf{n},\mathbf{n}'}$ respectively and performing the orthogonal change of integration variables from $\mathbf{R}'$ to $\mathbf{R}'^{bf}$ leads to the dependence of $\Phi^{(1)ad}_{\mathbf{n},\mathbf{n}'}$ on $\mathbf{q}$ just mentioned.

We now return to (79) and try to impose on $\mathbf{A}(\mathbf{q})$ the condition that

$$\nabla_{\mathbf{R}}\mathbf{A}(\mathbf{q}) + \mathbf{W}^{(1)ad}(\mathbf{R})\mathbf{A}(\mathbf{q}) = 0 \tag{99}$$

Let $\{X_i \mid i = 1, 2, \ldots, 3N - 3\}$ be the cartesian components of $\mathbf{R}$ in the sf frame, let

$$[\mathbf{W}^{(1)ad}_{\mathbf{n},\mathbf{n}'}(\mathbf{R})]_i = \left\langle \psi^{el,ad}_{\mathbf{n}}(\mathbf{r};\mathbf{q}) \left| \frac{\partial}{\partial X_i} \right| \psi^{el,ad}_{\mathbf{n}'}(\mathbf{r};\mathbf{q}) \right\rangle_{\mathbf{r}} \qquad i = 1, 2, \ldots, 3N - 3, \quad \mathbf{n}, \mathbf{n}' = 1, 2, \ldots, \mathcal{N} \tag{100}$$

be the corresponding components of the coupling vector $\mathbf{W}^{(1)ad}_{\mathbf{n},\mathbf{n}'}(\mathbf{R})$, and let

$$[\text{curl } \mathbf{W}^{(1)ad}_{\mathbf{n},\mathbf{n}'}(\mathbf{R})]_{ij} = \frac{\partial}{\partial X_j}[\mathbf{W}^{(1)ad}_{\mathbf{n},\mathbf{n}'}(\mathbf{R})]_i - \frac{\partial}{\partial X_i}[\mathbf{W}^{(1)ad}_{\mathbf{n},\mathbf{n}'}(\mathbf{R})]_j \tag{101}$$

be the components of the rank-2 tensor curl $\mathbf{W}^{(1)ad}_{\mathbf{n},\mathbf{n}'}(\mathbf{R})$. If we now write (99) in expanded scalar form, obtain from it the second derivatives $\partial^2\mathbf{A}_{\mathbf{n},\mathbf{n}'}(\mathbf{q})/\partial X_i \partial X_j$ and $\partial^2\mathbf{A}_{\mathbf{n},\mathbf{n}'}(\mathbf{q})/\partial X_j \partial X_i$, and equate these two quantities, we obtain the following necessary condition for (99) to have a solution [24–26]:

$$[\text{curl } \mathbf{W}^{(1)ad}_{\mathbf{n},\mathbf{n}'}(\mathbf{R})]_{ij} = -[\mathbf{W}^{(1)ad}_i(\mathbf{R}), \mathbf{W}^{(1)ad}_j(\mathbf{R})]_{\mathbf{n},\mathbf{n}'} \tag{102}$$

In this expression, $\mathbf{W}^{(1)ad}_k(\mathbf{R})$ ($k = i, j$) is the $\mathcal{N} \times \mathcal{N}$ matrix whose row $\mathbf{n}$ and column $\mathbf{n}'$ element is the k element of the $\mathbf{W}^{(1)ad}_{\mathbf{n},\mathbf{n}'}(\mathbf{R})$ vector, i.e., $[\mathbf{W}^{(1)ad}_{\mathbf{n},\mathbf{n}'}(\mathbf{R})]_k$, and the brackets in its right-hand side denote the commutator of the two matrices within. When $\mathbf{n}$ and $\mathbf{n}'$ are allowed to span the complete infinite set of adiabatic electronic quantum numbers, condition (102) is satisfied [24,26], (99) has a solution, and the resulting $\mathbf{A}(\mathbf{q})$ leads to the $\mathbf{q}$-independent diabatic electronic basis set mentioned in connection with (83). For the small values of $\mathcal{N}$ case being considered here, (102) is in general not satisfied and (98) does not have a solution. On the other hand, the equation obtained by replacing in (99) $\mathbf{W}^{(1)ad}(\mathbf{R})$ by its longitudinal part $\nabla_{\mathbf{R}}\Phi^{(1)ad}(\mathbf{q})$ [see remark after (98)], namely

$$\nabla_{\mathbf{R}}\mathbf{A}(\mathbf{q}) + [\nabla_{\mathbf{R}}\Phi^{(1)ad}(\mathbf{q})]\mathbf{A}(\mathbf{q}) = \mathbf{0} \tag{103}$$

does have solution, since

$$\text{curl } [\nabla_{\mathbf{R}}\Phi^{(1)ad}_{\mathbf{n},\mathbf{n}'}(\mathbf{q})] = \mathbf{0} \tag{104}$$

and

$$[\nabla_{\mathbf{R}}\Phi^{(1)ad}_i(\mathbf{q}), \nabla_{\mathbf{R}}\Phi^{(1)ad}_j(\mathbf{q})] = \mathbf{0} \tag{105}$$

where $\nabla_{\mathbf{R}}\Phi^{(1)ad}(\mathbf{q})$ is the $\mathcal{N} \times \mathcal{N}$ matrix whose row n and column n' element is $\partial\Phi^{(1)ad}_{\mathbf{n},\mathbf{n}'}(\mathbf{q})/\partial X_k$.

Using for $\mathbf{A}(\mathbf{q})$ a solution of (103), replacing it in (79) and taking (98) into account yields

$$-\frac{\hbar^2}{2\mu}\nabla_{\mathbf{R}}^2\boldsymbol{\chi}^{\mathrm{d}}(\mathbf{R}) - \frac{\hbar^2}{\mu}\mathbf{A}^{\dagger}(\mathbf{q})\mathbf{W}_t^{(1)\mathrm{ad}}(\mathbf{R}) \cdot \nabla_{\mathbf{R}}\boldsymbol{\chi}^{\mathrm{d}}(\mathbf{R}) - \frac{\hbar^2}{2\mu}\mathbf{W}^{(2)\mathrm{d}}(\mathbf{R})\boldsymbol{\chi}^{\mathrm{d}}(\mathbf{R}) = [E\mathbf{I} - \boldsymbol{\varepsilon}^{\mathrm{d}}(\mathbf{q})]\boldsymbol{\chi}^{\mathrm{d}}(\mathbf{R}) \tag{106}$$

where $\mathbf{W}^{(2)\mathrm{d}}(\mathbf{R})$ and $\boldsymbol{\varepsilon}^{\mathrm{d}}(\mathbf{q})$ are given by (81) and (82) respectively. Equation (106) is rigorously equivalent to its adiabatic counterpart (74) for a truncation at the same small number $\mathcal{N}$ of states. It still contains, however, a nonvanishing $\nabla_{\mathbf{R}}\boldsymbol{\chi}^{\mathrm{d}}(\mathbf{R})$ term, even though the longitudinal part of $\mathbf{W}^{(1)\mathrm{ad}}(\mathbf{R})$ has been eliminated from its vector coefficient.

In order to obtain a more useful adiabatization, it is customary to introduce into (62) two approximations. The first is to assume that the $\nabla_{\mathbf{R}}\boldsymbol{\chi}^{\mathrm{d}}(\mathbf{R})$ term is negligible compared to the remaining ones. This assumption is justifiable in the neighborhood of a conical intersection, where $\nabla_{\mathbf{R}}\Phi^{(1)\mathrm{ad}}(\mathbf{q})$, the longitudinal part of $\mathbf{W}^{(1)\mathrm{ad}}(\mathbf{R})$, has off-diagonal elements which display a pole at conical intersection geometries [27]. The corresponding off-diagonal elements of $\mathbf{W}_t^{(1)\mathrm{ad}}(\mathbf{R})$ are not singular and become negligible with respect to those of $\nabla_{\mathbf{R}}\Phi^{(1)\mathrm{ad}}(\mathbf{q})$ in that neighborhood. The second is to assume that the $\mathbf{W}^{(2)\mathrm{d}}(\mathbf{R})\boldsymbol{\chi}^{\mathrm{d}}(\mathbf{R})$ term is also negligible compared to the remaining ones. This assumption is rigorously correct for a complete diabatic electronic basis set and is approximately valid for a two-diabatic electronic basis set in the close vicinity of a conical intersection between the $\varepsilon_i^{\mathrm{ad}}(\mathbf{q})$ and $\varepsilon_j^{\mathrm{ad}}(\mathbf{q})$ PESs.

As a result of these considerations, and using the two-electronically-adiabatic real-valued basis set $\psi_i^{\mathrm{el,ad}}(\mathbf{r};\mathbf{q})$ and $\psi_j^{\mathrm{el,ad}}(\mathbf{r};\mathbf{q})$, we can express the orthogonal transformation matrix of (71) and (73) as

$$\mathbf{A}(\beta(\mathbf{q})) = \begin{pmatrix} \cos\beta(\mathbf{q}) & -\sin\beta(\mathbf{q}) \\ \sin\beta(\mathbf{q}) & \cos\beta(\mathbf{q}) \end{pmatrix} \tag{107}$$

where $\beta(\mathbf{q})$ is an unknown angle to be determined from (103) which $\mathbf{A}(\mathbf{q})$ has been required to satisfy. The equation for the two-dimensional vector $\boldsymbol{\chi}^{\mathrm{d}}(\mathbf{R})$ associated with this $\mathbf{A}$ is

$$-\frac{\hbar^2}{2\mu}\nabla_{\mathbf{R}}^2\boldsymbol{\chi}^{\mathrm{d}}(\mathbf{R}) + \boldsymbol{\varepsilon}^{\mathrm{d}}(\mathbf{q})\boldsymbol{\chi}^{\mathrm{d}}(\mathbf{R}) = E\boldsymbol{\chi}^{\mathrm{d}}(\mathbf{R}) \tag{108}$$

where $\boldsymbol{\varepsilon}^{\mathrm{d}}(\mathbf{q})$ is the nondiagonal 2×2 matrix

$$\boldsymbol{\varepsilon}^{\mathrm{d}}(\mathbf{q}) = \tilde{\mathbf{A}}(\beta(\mathbf{q}))\boldsymbol{\varepsilon}^{\mathrm{ad}}(\mathbf{q})\mathbf{A}(\beta(\mathbf{q})) \tag{109}$$

It should be stressed that (108) is not as accurate as the two-electronic-state approximation given by (74) (for $\mathcal{N} = 2$) because usually the latter is valid over the entire region of nuclear configuration space sampled by $\boldsymbol{\chi}^{\mathrm{ad}}(\mathbf{R})$, whereas (108) is only a good approximation in the immediate vicinity of the conical intersection being considered.

We next address the matter of the boundary conditions which the $\boldsymbol{\chi}^{\mathrm{d}}(\mathbf{R})$ must satisfy for such conically intersecting systems. To this effect, we must establish the relation between the diabatic electronic wave functions $\psi_{\mathbf{n}}^{\mathrm{el,d}}(\mathbf{r};\mathbf{q})$, $\mathbf{n} = \mathbf{i}, \mathbf{j}$ and the adiabatic ones $\psi_{\mathbf{n}}^{\mathrm{el,ad}}(\mathbf{r};\mathbf{q}_0)$ at the conical intersection. We know from (75) and the reality of $\mathbf{A}$ that

$$\boldsymbol{\psi}^{\mathrm{el,d}}(\mathbf{r};\mathbf{q}) = \mathbf{A}(\beta(\mathbf{q}))\boldsymbol{\psi}^{\mathrm{el,d}}(\mathbf{r};\mathbf{q}) \tag{110}$$

For the two-state approximation being considered, $\mathbf{W}^{(1)ad}(\mathbf{R})$ is given by

$$\mathbf{W}^{(1)ad}(\mathbf{R}) = \begin{pmatrix} \mathbf{0} & \mathbf{W}^{(1)ad}_{i,j}(\mathbf{R}) \\ -\mathbf{W}^{(1)ad}_{i,j} & \mathbf{0} \end{pmatrix} \tag{111}$$

where $\mathbf{W}^{(1)ad}_{i,j}(\mathbf{R})$ is the $3(N-1)$-dimensional vector

$$\mathbf{W}^{(1)ad}_{i,j}(\mathbf{R}) = \langle \psi^{el,ad}_i(\mathbf{r};\mathbf{q})|\nabla_R|\psi^{el,ad}_j(\mathbf{r};\mathbf{q})\rangle_r \tag{112}$$

and $\mathbf{0}$ is the null vector of equal dimensions. The matrix $\Phi^{(1)ad}(\mathbf{q})$ of (98) and (103) now has the form

$$\Phi(\mathbf{q}) = \begin{pmatrix} \mathbf{0} & \Phi^{(1)ad}_{i,j}(\mathbf{q}) \\ -\Phi^{1)ad}_{i,j}(\mathbf{q}) & \mathbf{0} \end{pmatrix} \tag{113}$$

where $\nabla_R\Phi^{(1)ad}_{i,j}(\mathbf{q})$ is the longitudinal part of $\mathbf{W}^{(1)ad}_{i,j}(\mathbf{R})$ and $\Phi^{(1)ad}_{i,j}(\mathbf{q})$ is a known scalar function of $\mathbf{q}$. It must be remembered that at conical intersection configurations $\mathbf{q}_0$, $\nabla_R\Phi_{n,n'}(\mathbf{q})$ has a pole [27, 30–32] and therefore that (103) should be handled with caution at those configurations. In what follows, such caution has been exercised. Substituting (107) and (113) into (103) results in

$$\nabla_R\beta(\mathbf{q}) = \nabla_R\Phi_{i,j}(\mathbf{q}) \tag{114}$$

which can be integrated to give

$$\beta(\mathbf{q}) = \Phi^{(1)ad}_{i,j}(\mathbf{q}) + K_1 \tag{115}$$

where K_1 is a constant independent of $\mathbf{q}$ (and of $\mathbf{R}$).

Relations (42) and (44) are valid in the close vicinity of a conical intersection. In the notation of Sec. III.A they can be rewritten as

$$\begin{aligned} \psi^{el,ad}_i(\mathbf{r};\mathbf{q}) &= \cos\frac{\varphi(\mathbf{q})}{2}\,\psi^{el,ad}_i(\mathbf{r};\mathbf{q}_0) - \sin\frac{\varphi(\mathbf{q})}{2}\,\psi^{el,ad}_j(\mathbf{r};\mathbf{q}_0) \\ \psi^{el,ad}_j(\mathbf{r};\mathbf{q}) &= \sin\frac{\varphi(\mathbf{q})}{2}\,\psi^{el,ad}_i(\mathbf{r};\mathbf{q}_0) + \cos\frac{\varphi(\mathbf{q})}{2}\,\psi^{el,ad}_j(\mathbf{r};\mathbf{q}_0) \end{aligned} \tag{116}$$

where the parametric dependence of φ on $\mathbf{q}_0$ is implied. Equation (116) can be recast in matrix notation as

$$\boldsymbol{\psi}^{el,ad}(\mathbf{r};\mathbf{q}) = \mathbf{A}[\tfrac{1}{2}\varphi(\mathbf{q})]\boldsymbol{\psi}^{el,ad}(\mathbf{r};\mathbf{q}_0) \tag{117}$$

where $\mathbf{A}[\frac{1}{2}\varphi(\mathbf{q})]$ is the matrix obtained from (106) by replacing $\beta(\mathbf{q})$ by $\frac{1}{2}\varphi(\mathbf{q})$. Combining this expression with (110) and using the orthogonality of $\mathbf{A}$ we get

$$\boldsymbol{\psi}^{el,d}(\mathbf{r},\mathbf{q}) = \tilde{\mathbf{A}}[\beta(\mathbf{q})]\mathbf{A}[\tfrac{1}{2}\varphi(\mathbf{q})]\boldsymbol{\psi}^{el,ad}(\mathbf{r};\mathbf{q}_0) \tag{118}$$

In view of (107) and its $\varphi(\mathbf{q})/2-$ equivalent, and using (115), this expression can be written as

$$\boldsymbol{\psi}^{el,d}(\mathbf{r},\mathbf{q}) = \mathbf{A}\left[\frac{\varphi(\mathbf{q})}{2} - \Phi^{(1)ad}_{i,j}(\mathbf{q}) - K_1\right]\boldsymbol{\psi}^{el,ad}(\mathbf{r};\mathbf{q}_0) \tag{119}$$

We must now obtain a connection between the angles φ and $\Phi^{(1)ad}_{i,j}$. To that effect, we replace (116) into (62), with $\mathbf{n}$, $\mathbf{n}'$ replaced by $\mathbf{i}$, $\mathbf{j}$. Using the orthonormality of the $\psi^{el,ad}_n(\mathbf{r};\mathbf{q}_0)$ ($\mathbf{n} = \mathbf{i}, \mathbf{j}$) and the fact that they are independent of $\mathbf{R}$, we obtain after some

straightforward algebra the relation

$$\mathbf{W}_{i,j}^{(1)ad}(\mathbf{R}) = \tfrac{1}{2}\nabla_{\mathbf{R}}\varphi(\mathbf{q}) \tag{120}$$

where φ depends on $\mathbf{R}$ through $\mathbf{q}$. Together with (97) this expression yields

$$\tfrac{1}{2}\nabla_{\mathbf{R}}\varphi(\mathbf{q}) = \nabla_{\mathbf{R}}\Phi_{i,j}^{(1)ad}(\mathbf{q}) + \mathbf{W}_{i,j}^{(1)ad}(\mathbf{R}) \tag{121}$$

In view of the pole displayed by $\nabla_{\mathbf{R}}\Phi_{ij}^{(1)ad}(\mathbf{q})$ at the conical intersection geometries $\mathbf{q}_0$ [27], we can in the vicinity of such geometries drop the second term in the right-hand side of (121) to get

$$\tfrac{1}{2}\nabla_{\mathbf{R}}\varphi(\mathbf{q}) = \nabla_{\mathbf{R}}\Phi_{i,j}^{(1)ad}(\mathbf{q}) \tag{122}$$

Integration of this expression furnishes

$$\tfrac{1}{2}\varphi(\mathbf{q}) = \Phi_{i,j}^{(1)ad}(\mathbf{q}) + K_2 \tag{123}$$

where K_2 is a constant. This is the desired connection between φ and $\Phi_{i,j}^{(1)ad}$. Replacing it into (119) finally yields

$$\boldsymbol{\psi}^{el,d}(\mathbf{r};\mathbf{q}) = \mathbf{A}(K)\boldsymbol{\psi}^{el,ad}(\mathbf{r};\mathbf{q}_0) \tag{124}$$

where $K = K_2 - K_1$. Although this expression is only valid for $\mathbf{q} \neq \mathbf{q}_0$, it does not display a singular behavior as $\mathbf{q} \to \mathbf{q}_0$. As part of the definition of $\boldsymbol{\psi}^{el,d}(\mathbf{r};\mathbf{q}_0)$, we will require (124) to be valid at $\mathbf{q} = \mathbf{q}_0$ also. If desired, the constant K may be chosen so as to make $\boldsymbol{\psi}^{el,d}(\mathbf{r};\mathbf{q}_0)$ and $\boldsymbol{\psi}^{el,ad}(\mathbf{r};\mathbf{q}_0)$ coincide, in which case $K = 0$ and $\mathbf{A}(K) = \mathbf{I}$, resulting in

$$\boldsymbol{\psi}^{el,d}(\mathbf{r};\mathbf{q}) = \boldsymbol{\psi}^{el,ad}(\mathbf{r};\mathbf{q}_0) \tag{125}$$

Equation (124) is a very important expression, which relates the diabatic electronic wave-functions $\boldsymbol{\psi}^{el,d}(\mathbf{r};\mathbf{q})$, in the *vicinity* of a conical intersection, with the adiabatic electronic wave functions *at* that intersection. It shows that, in that vicinity (which includes the conical intersection geometry itself), the diabatic electronic wave functions are constant with respect to $\mathbf{q}$, i.e., do not change as the nuclear configuration geometry changes. As a result, these wave functions cannot have a discontinuity with respect to $\mathbf{q}$ at, or in the close neighborhood of, a conical intersection, which means that the adiabatic to diabatic transformation defined by (103) removed the discontinuity which was present in the corresponding adiabatic electronic wave functions. Furthermore, as the system is transported across closed loops in nuclear configuration space around but near to conical intersection geometries, the diabatic electronic wave functions cannot change sign, and on the contrary are single-valued and continuous. As we move away from such geometries, into regions for which (124) is no longer valid, no other source of discontinuity exists since we assumed from the beginning that the $\varepsilon_i^{ad}(\mathbf{q})$ and $\varepsilon_j^{ad}(\mathbf{q})$ PESs only had one continuous conical intersection locus in the region of nuclear configuration space sampled by $\chi^{ad}(\mathbf{R})$. Consequently, as $\mathbf{q}$ recedes from $\mathbf{q}_0$, the $\boldsymbol{\psi}^{el,d}(\mathbf{r};\mathbf{q})$ must change continuously and therefore must continue to be single-valued and continuous functions of $\mathbf{q}$. We conclude that these diabatic electronic wave functions have this property not only near $\mathbf{q}_0$ but over that entire region of nuclear configuration space. As a result, the $\chi^{d}(\mathbf{R})$ must also be single-valued continuous functions of $\mathbf{R}$ in that region, and their sign cannot change as the system is transported over closed loops around conical intersection con-

figurations, even when those loops are everywhere far from such configurations. In summary, the boundary conditions which must be satisfied by the $\chi^{d}(\mathbf{R})$ are the usual ones of single-valuedness and continuity, as opposed to the unusual ones associated with the $\chi^{ad}(\mathbf{R})$ involving changes in sign around such loops.

Before concluding this subsection, it should be mentioned that useful diabatizations can be obtained if the adiabatic electronic wave functions are calculated using the DIM (diatomics in molecules) method [33]. In this method, those wave functions are expanded in terms of valence-bond basis functions, and the coefficients of such expansions vary significantly more rapidly with the nuclear coordinates than do the valence-bond bases. When calculating the elements of the first-derivative coupling matrix $\mathbf{W}^{(1)ad}(\mathbf{R})$, it is assumed that only those coefficients vary with the nuclear configuration, i.e., that the valence-bond functions are independent of the nuclear coordinates. This furnishes an approximate $\mathbf{W}^{(1)ad}(\mathbf{R})$, which is then used in lieu of the exact one. It is straightforward to show that this DIM $\mathbf{W}^{(1)ad}(\mathbf{R})$ can be diabatized exactly. Such an approach has been used recently to perform zero total angular momentum partial wave scattering calculations in a two-diabatic-state representation of the $Na(3p\ ^2P) + H_2 \rightarrow Na(3s\ ^2S) + H_2$ or NaH + H process [34], involving two conically intersecting adiabatic PESs, diabatized by Baer's method [24,26].

3. Comparison of the Adiabatic and Diabatic Representations

Let us now compare the characteristics of the electronically adiabatic and diabatic representations for systems displaying a conical intersection, in the one- and two-state approximations.

For the two-state case with real electronic wave functions, the nuclear motion Schrödinger equations are given by (74) and (106) for the adiabatic and diabatic representations, respectively. For this case, all the matrices in those equations have dimensions 2×2 and the $\chi^{ad}(\mathbf{R})$ and $\chi^{d}(\mathbf{R})$ vectors have dimensions 2×1, whereas those appearing in $\mathbf{W}^{(1)ad}$ and $\mathbf{W}^{(1)d}$ have the dimensions of $\mathbf{R}$, namely, $3(N - 1) \times 1$ where N is the number of nuclei in the system. Equation (69) furnishes a more explicit version of (74) and the $\mathbf{A}(\mathbf{q})$ appearing in (106) is given by (107) with $\beta(\mathbf{q})$ obtained from (115). These versions of (74) and (106) are rigorously equivalent, once the appropriate boundary conditions for $\chi^{ad}(\mathbf{R})$ and $\chi^{d}(\mathbf{R})$ discussed in Secs. III.B.1 and III.B.2 are taken into account. The main differences between and characteristics of those equations are the following:

a. Whereas the $\chi^{ad}(\mathbf{R})$ of (74) must change sign upon a pseudorotation of the system around the conical intersection configuration, $\chi^{d}(\mathbf{R})$ is instead continuous.
b. The 2×2 skew-symmetric matrix $\mathbf{W}^{(1)ad}(\mathbf{R})$ is given by (111) and (112), and its off-diagonal elements diverge at the conical intersection geometries. As a result, the $\mathbf{W}^{(1)ad}(\mathbf{R}) \cdot \nabla_{\mathbf{R}}\chi^{ad}(\mathbf{R})$ term appearing in (74) requires very careful handling, if $\chi^{ad}(\mathbf{R})$ samples such geometries.
c. The 2×2 matrix $\mathbf{W}_t^{(1)ad}(\mathbf{R})$, formed by the transverse parts of the elements of $\mathbf{W}^{(1)ad}(\mathbf{R})$, is also skew-symmetric, but its off-diagonal elements do not diverge at the conical intersection. As a result, the $\mathbf{W}_t^{(1)ad}(\mathbf{R}) \cdot \nabla_{\mathbf{R}}\chi^{d}(\mathbf{R})$ term appearing in (106) is well behaved at that intersection, and does not require special handling if $\chi^{ad}(\mathbf{R})$ samples such nuclear configurations.
d. The elements of the $-(\hbar^2/2\mu)\mathbf{W}^{(2)ad}(\mathbf{R})$ and $-(\hbar^2/2\mu)\mathbf{W}^{(2)d}(\mathbf{R})$ matrices appearing in (74) and (106) are relatively small when compared with the diagonal

elements of $\boldsymbol{\varepsilon}^{ad}(\mathbf{q})$ and with all the elements of $\boldsymbol{\varepsilon}^{d}(\mathbf{q})$ respectively, but do not vanish identically. The elements of $\mathbf{W}^{(2)d}(\mathbf{R})$ are, generally, smaller than those of $\mathbf{W}^{(2)ad}(\mathbf{R})$ due to the fact that, as the number $\mathcal{N}$ of states in the representation increases toward infinity, $\mathbf{W}^{(2)d}(\mathbf{R})$ approaches the null matrix but $\mathbf{W}^{(2)ad}(\mathbf{R})$ does not.

e. The diabatic representation nuclear motion equation (108), which is usually used in lieu of (106), with single-valued and continuous $\boldsymbol{\chi}^{d}(\mathbf{R})$, is no longer rigorously equivalent to (74) because of the additional assumptions $\mathbf{W}_t^{(1)ad}(\mathbf{R}) = \mathbf{0}$ and $\mathbf{W}^{(2)d}(\mathbf{R}) = \mathbf{0}$ used in its derivation. However, (108) does not contain a term in $\nabla_{\mathbf{R}}\boldsymbol{\chi}^{d}(\mathbf{R})$, which is of major computational advantage since much more efficient numerical integration methods exist for such equations than for those containing such a term.

Everything considered, it is much more convenient, for the two-electronic-state expansion in systems displaying conical intersections, to use the diabatic equation (108) rather than the adiabatic one (74). When doing so, however, the errors associated with the neglect of the $\mathbf{W}_t^{(1)ad}(\mathbf{R})$ and $\mathbf{W}^{(2)d}(\mathbf{R})$ terms appearing in (106) should be estimated, and if necessary the effect of these terms can be introduced a posteriori by perturbation methods. The same is true for the errors in the coupling elements introduced when using the DIM approach.

By contrast, for the case in which a single electronically adiabatic term in the Born-Oppenheimer expansion is adequate, resulting in (64), the adiabatic representation is the one of choice, as justified below. The nuclear motion Schrödinger equation associated with (64) is (65), which for real adiabatic electronic wave functions has no $\nabla_{\mathbf{R}}\chi_i^{ad}$ term. If we transform to a diabatic representation, we need two diabatic electronic states at least, since none of the four elements of $\boldsymbol{\varepsilon}^{d}(\mathbf{q})$ in (109) is negligible and all these contribute to $\boldsymbol{\varepsilon}_i^{ad}(\mathbf{q})$ [and to $\varepsilon_j^{ad}(\mathbf{q})$]. This is true even when the matrices $\mathbf{W}^{(1)ad}(\mathbf{R})$ and $\mathbf{W}^{(2)ad}(\mathbf{R})$ in (74) or (69) vanish identically and decouple $\chi_i^{ad}(\mathbf{R})$ from $\chi^{ad}{}_j(\mathbf{R})$. In other words, $\chi_i^{d}(\mathbf{R})$ and $\chi^{d}{}_j(\mathbf{R})$ are always coupled, even for conditions under which $\chi_i^{ad}(\mathbf{R})$ and $\chi^{ad}{}_j(\mathbf{R})$ are completely decoupled, which happens frequently when the energy of the system, E, is significantly below the minimum energy of the conical intersection $\varepsilon_i^{ad}(\mathbf{q}_0)$. For the H_3 system, for example, that minimum energy is 2.75 eV above the bottom of the isolated ground electronic state H_2 potential energy curve [30], and collisions for E in the range 0.3 eV to 1.8 eV are of great interest, as will be seen in Sec. V.A. The number of channels which must be used for the two-diabatic-electronic-state representation is, under these conditions, significantly larger than that needed for the one-adiabatic-electronic-state representation, and the computation time for solving the nuclear motion Schrödinger equation increases with the cube of the number of channels involved. As a result, the diabatic representation presents a serious disadvantage with respect to the adiabatic one, for methods for which it is easy to inject the adiabatic representation boundary condition in the calculations, as is the case for the symmetrized hyperspherical coordinate methodology described in Sec. IV. This makes the adiabatic representation the preferred one, as stated above.

C. The Variable Phase Description of Nuclear Wave Functions

As summarized in Sec. III.B.1, the adiabatic electronic wave functions $\psi_n^{el,ad}(\mathbf{r}; \mathbf{q})$ associated with a pair of conically interesting PESs $\varepsilon_i^{ad}(\mathbf{q})$ and $\varepsilon_j^{ad}(\mathbf{q})$, if required to be real, must change sign when the system is transported around a closed loop in internal con-

figuration space $\mathbf{q}$ around a conical intersection configuration $\mathbf{q}_0$. In order to maintain the single-valuedness (and continuity) of the orbital electronuclear wave function $\Psi^0(\mathbf{r}, \mathbf{R})$ of (64) for the one-state approximation, or of (67) for the two-state approximation, the corresponding nuclear-wave-function coefficients $\chi_n^{ad}(\mathbf{R})$ were required to undergo a compensating change in sign, leading to unusual boundary conditions involving discontinuities in those coefficients. An alternative approach to this conical intersection problem is to drop the reality condition on the $\psi_n^{el,ad}(\mathbf{r}; \mathbf{q})$ ($\mathbf{n} = \mathbf{i}, \mathbf{j}$) but require instead that they be single valued. Let us examine this approach, first for the one-state case and next for the two-state case.

The one-state case has been discussed in detail in a pioneering paper by Mead and Truhlar [11], and will be summarized below in a slightly different mathematical language. In the rest of this section, $\bar{\psi}_n^{el,ad}(\mathbf{r}; \mathbf{q})$ will denote adiabatic electronic wave functions which are required to be real and which therefore undergo a discontinuous change of sign upon a pseudorotation of the system around a conical intersection configuration, whereas $\psi_n^{el,ad}(\mathbf{r}; \mathbf{q})$ will be used to describe such wave functions that, rather than being real, are required to be single-valued (and continuous) functions of $\mathbf{q}$. For the one-state approximation these two electronic wave functions are related by

$$\psi_i^{el,ad}(\mathbf{r}; \mathbf{q}) = e^{if(\mathbf{q})}\bar{\psi}_i^{el,ad}(\mathbf{r}; \mathbf{q}) \tag{126}$$

and the corresponding χ_i^{ad} and $\bar{\chi}_i^{ad}$ by

$$\chi_i^{ad}(\mathbf{R}) = e^{\ if(\mathbf{q})}\bar{\chi}_i^{ad}(\mathbf{R}) \tag{127}$$

where $f(\mathbf{q})$ is a real phase angle that is a single-valued and continuous function of $\mathbf{q}$. This function is chosen so as to make $e^{if(\mathbf{q})}$ change sign upon such a pseudorotation, compensating the change of sign in $\bar{\psi}_i^{el,ad}(\mathbf{r}; \mathbf{q})$ and ascertaining the single-valuedness and continuity of $\psi_i^{el,ad}(\mathbf{r}; \mathbf{q})$ with respect to $\mathbf{q}$. Replacement of (126) into (62) and (63) leads straightforwardly to

$$\mathbf{W}_{i,i}^{(1)ad}(\mathbf{R}) = i\nabla_{\mathbf{R}} f(\mathbf{q}) \tag{128}$$

and

$$\mathbf{W}_{i,i}^{(2)ad}(\mathbf{R}) = \bar{\mathbf{W}}_{i,i}^{(2)ad}(\mathbf{R}) - [\nabla_{\mathbf{R}} f(\mathbf{q})]^2 + i\nabla_{\mathbf{R}}^2 f(\mathbf{q}) \tag{129}$$

where

$$\bar{\mathbf{W}}_{i,i}^{(2)ad}(\mathbf{R}) = \langle \bar{\psi}_i^{el,ad}(\mathbf{r}; \mathbf{q}) | \nabla_{\mathbf{R}}^2 | \bar{\psi}_i^{el,ad}(\mathbf{r}; \mathbf{q}) \rangle_{\mathbf{R}} \tag{130}$$

Substitution of the last two expressions into (65) results in the following very important equation for $\chi_i^{ad}(\mathbf{R})$:

$$\begin{aligned} &-\frac{\hbar^2}{2\mu}\nabla_{\mathbf{R}}^2\chi_i^{ad}(\mathbf{R}) - \frac{\hbar^2 i}{\mu}\nabla_{\mathbf{R}} f(\mathbf{q}) \cdot \nabla_{\mathbf{R}\chi i}^{ad}(\mathbf{R}) + \frac{\hbar^2}{2\mu}[(\nabla_{\mathbf{R}} f(\mathbf{q}))^2 - i\nabla_{\mathbf{R}}^2 f(\mathbf{q})]\chi_i^{ad}(\mathbf{R}) \\ &= [E - \varepsilon_i(\mathbf{q}) + \frac{\hbar^2}{2\mu}\bar{W}_{i,i}^{(2)ad}(\mathbf{R})]\chi_i^{ad}(\mathbf{R}) \end{aligned} \tag{131}$$

The quantity $\nabla_{\mathbf{R}} f(\mathbf{q})$ is called a gauge potential because the one-state electronuclear wave function

$$\Psi^o(\mathbf{r}, \mathbf{R}) = \chi_i^{ad}(\mathbf{R})\psi_i^{el,ad}(\mathbf{r}; \mathbf{q}) = \bar{\chi}_i^{ad}(\mathbf{R})\bar{\psi}_i^{el,ad}(\mathbf{r}; \mathbf{q}) \tag{132}$$

is independent of $f(\mathbf{q})$ and is unchanged if an arbitrary function $g(\mathbf{q})$, having the same defining properties as $f(\mathbf{q})$, is added to $f(\mathbf{q})$.

The boundary condition associated with this equation is that $\chi_i^{ad}(\mathbf{R})$ be single-valued (and continuous) everywhere in $\mathbf{R}$ space, since in (64) $\psi_i^{el,ad}(\mathbf{r}; \mathbf{q})$ is now a single-valued (and continuous) function of $\mathbf{q}$. For comparison purposes, let us consider a hypothetical system of N spin-less particles of charge w and global reduced mass μ subject to a mutual magnetic interaction described by a time-independent vector potential $\mathcal{A}(\mathbf{R})$, in addition to a time-independent static interaction described by a potential $V(\mathbf{R})$. The time-independent Schrödinger equation for the corresponding internal wave function $\psi(\mathbf{R})$ is

$$-\frac{\hbar^2}{2\mu}\nabla_R^2\psi(\mathbf{R}) + \frac{iw\hbar}{\mu c}\mathcal{A}(\mathbf{R})\cdot\nabla_R\psi(\mathbf{R}) + \left[\frac{w^2}{2mc^2}\mathcal{A}^2(\mathbf{R})\right] + \frac{iw\hbar}{2\mu c}(\nabla_R\cdot\mathcal{A}(\mathbf{R}))\psi(\mathbf{R}) = [E - V(\mathbf{R})]\psi(\mathbf{R}) \tag{133}$$

where c is the speed of light. Comparison of (133) and (131) indicates that they are mathematically equivalent, as long as

$$\mathcal{A}(\mathbf{R}) = -\frac{c\hbar}{w}\nabla_R f(\mathbf{q}) \tag{134}$$

and

$$V(\mathbf{R}) = \varepsilon_i^{ad}(\mathbf{q}) - \frac{\hbar^2}{2\mu}\overline{W}_{i,i}^{(2)ad}(\mathbf{R}) \tag{135}$$

This means that the use of the phase factor $e^{if(\mathbf{q})}$ is equivalent to the introduction of a pseudomagnetic field between the nuclei, described by a vector potential $\mathcal{A}(\mathbf{R})$ proportional to the gradient of the phase angle. This provides an interesting physical analogy between the motion of the nuclei in the one-state approximation and the motion of the particles in the comparison system. It should be noted that the gauge potential $\nabla_R f(\mathbf{q})$, related to the electromagnetic vector potential $\mathcal{A}(\mathbf{R})$ [11], is quite distinct from and has a different origin than the vector potential associated with (96). In that expression $\mathbf{W}(\mathbf{x})$ is the first-derivative coupling matrix element $\mathbf{W}_{i,j}^{(1)ad}(\mathbf{R})$ of (111) and (112) that couples the nuclear motion on PESs ε_i^{ad} and ε_j^{ad} according to (69). This vector is involved [24,26] in the determination of the adiabatic-to-diabatic transformation matrix $\mathbf{A}(\mathbf{q})$ of (73) via (99), for $\psi_n^{el,ad}(\mathbf{r}; \mathbf{q})$ ($\mathbf{n} = \mathbf{i}, \mathbf{j}$) real, whereas $\nabla_R f(\mathbf{q})$ arises from the single-valuedness condition imposed on $\psi_i^{el,ad}(\mathbf{r}; \mathbf{q})$ when this function is allowed to be complex, and does not involve any coupling to another PES.

We must now select the phase angle $f(\mathbf{q})$. To that effect let us define another angle $\lambda(\mathbf{q})$ having an implied parametric dependent on $\mathbf{q}_0$, by expressions analogous to (10), but with 2α replaced by λ and the $H_{n,n'}$ redefined as

$$H_{n,n'}(\mathbf{q}; \mathbf{q}_0) = \langle\psi_n^{el,ad}(\mathbf{r}; \mathbf{q}_0)|\hat{H}^{el}(\mathbf{r}; \mathbf{q})|\psi_{n'}^{el,ad}(\mathbf{r}; \mathbf{q}_0)\rangle_r \qquad \mathbf{n}, \mathbf{n}' = \mathbf{i}, \mathbf{j} \tag{136}$$

These $H_{n,n'}(\mathbf{q}; \mathbf{q}_0)$ are defined everywhere in $\mathbf{q}$ space, but only in the vicinity of the conical intersection configuration $\mathbf{q}_0$ do they approach the mixing angle $\varphi(\mathbf{q})$ of (116):

$$\lambda(\mathbf{q}) \underset{\mathbf{q}\to\mathbf{q}_0}{\sim} \varphi(\mathbf{q}) \tag{137}$$

As $\varphi(\mathbf{q})$, the angle $\lambda(\mathbf{q})$ increases by 2π upon a pseudorotation of the system around $\mathbf{q}_0$. Therefore, $(n/2)\lambda(\mathbf{q})$, with n an odd integer, is an acceptable choice for $f(\mathbf{q})$. Rather than making $n = 1$, it is more convenient to choose $n = 3$ in order to simplify the introduction of permutation symmetry in systems containing three identical nuclei [11]. As a result,

$$f(\mathbf{q}) = \frac{3}{2}\lambda(\mathbf{q}) \tag{138}$$

is a reasonable selection for this phase angle. It should be stressed, however, that any other choice of $f(\mathbf{q})$ which is a real single-valued continuous function of $\mathbf{q}$ is acceptable, as long as it increases by an odd number times π upon a pseudorotation of the system around $\mathbf{q}_0$. Mathematical or numerical convenience, for a given system, should dictate its selection. From (138) we obtain

$$\nabla_R f(\mathbf{q}) = \frac{3}{2}\frac{\partial \mathbf{q}(\mathbf{R})}{\partial \mathbf{R}}\nabla_q \lambda(\mathbf{q}) \tag{139}$$

where $\partial\mathbf{q}(\mathbf{R})/\partial\mathbf{R}$ is the Jacobian matrix of dimensions $(3N - 3) \times (3N - 6)$ associated with $\mathbf{q}(\mathbf{R})$ and $\nabla_q\lambda(\mathbf{q})$ is a $(3N - 6)$-dimensional vector. A detailed examination of the explicit expression for $\lambda(\mathbf{q})$, mentioned before (136), shows that $\nabla_q\lambda(\mathbf{q})$ has a pole at $\mathbf{q}_0$ and that its curl with respect to $\mathbf{q}$ (which is a $(3N - 6)$-dimensional tensor of rank 2) vanishes everywhere except at $\mathbf{q} = \mathbf{q}_0$, where it displays a δ-function-type behavior.

For systems having three nuclei (i.e., $N = 3$) $\nabla_q\lambda(\mathbf{q})$ is three-dimensional and its curl $\nabla_q \times \nabla_q\lambda(\mathbf{q})$ is an axial vector proportional to the associated pseudomagnetic field. As a result, that field vanishes over the entire $\mathbf{q}$ space except along the line of conical intersection configurations, where it behaves as a δ-function [11]. The associated effect of the conical intersection on the nuclear wave function $\chi_i^{ad}(\mathbf{R})$ has close mathematical similarities to the Aharonov-Bohm effect for the motion of an electron around a very narrowly confined magnetic field [35] and has been called the molecular Aharonov-Bohm effect [11]. According to this effect, interference occurs between paths passing on opposite sides of the field, even though those paths only sample regions of space where the field vanishes. A similar effect exists when a chemical reaction occurs via paths passing around opposite sides of a conical intersection even when those paths do not get close to that intersection [11,36] as further discussed in Secs. V.A and V.B.

The Schrödinger equation satisfied by $\bar{\chi}^{ad}{}_i(\mathbf{R})$ is

$$-\frac{\hbar^2}{2\mu}\nabla_R^2\bar{\chi}_i^{ad}(\mathbf{R}) - \frac{\hbar^2}{2\mu}\bar{W}_{i,i}^{(2)ad}(\mathbf{R})\bar{\chi}_i^{ad}(\mathbf{R}) = [E - \varepsilon_i^{ad}(\mathbf{q})]\bar{\chi}_i^{ad}(\mathbf{R}) \tag{140}$$

subject to the boundary condition that $\bar{\chi}^{ad}{}_i(\mathbf{R})$ must change sign upon pseudorotations of the system around conical intersection configuration. The two equations (131) and (140), together with their respective boundary conditions, are completely equivalent, once (127) is taken into account. Whereas (140) has the unusual pseudorotation boundary condition associated with it, (131) has a nonvanishing first-derivative (i.e., gradient) term whose coefficient diverges at conical intersection configurations. As long as we do not approach such configurations too closely, this divergence does not present numerical problems. However, the corresponding coupled channel equations (see Sec. IV.B) have first-derivative terms which appreciably slow down the most efficient second order matrix differential equation integration methods. All one-state reactive scattering calculations on

systems displaying conical intersections that have been performed so far have used the Born-Oppenheimer version of (140) (i.e., $\overline{\mathbf{W}}^{(2)ad}_{i,i}(\mathbf{R}) = 0$). In addition, (129), also with $\overline{W}^{(2)ad}_{i,i}(\mathbf{R}) = 0$, has been solved for a simple two-mathematical-dimensions model system [37] using a variational method. It appears thus far that, using symmetrized hyperspherical coordinates and propagation methods (see Secs. IV and V), (140) offers a simpler route than (131) for the calculation of the cross sections of simple chemical reactions confined to a ground state electronically adiabatic PES that intersects conically the first excited one. It is this approach that will be described in greater detail in Secs. IV and V.

These considerations can be easily extended to the two-state approximation for conically intersecting PESs. For this case, we set

$$\boldsymbol{\psi}^{el,ad}(\mathbf{r}; \mathbf{q}) = e^{if(\mathbf{q})}\overline{\boldsymbol{\psi}}^{el,ad}(\mathbf{r}; \mathbf{q}) \tag{141}$$

and

$$\boldsymbol{\chi}^{ad}(\mathbf{R}) = e^{-if(\mathbf{q})}\overline{\boldsymbol{\chi}}^{ad}(\mathbf{R}) \tag{142}$$

where $f(\mathbf{q})$ satisfies the same boundary conditions as those for the one-state case, and $\boldsymbol{\psi}^{el,ad}$, $\overline{\boldsymbol{\psi}}^{el,ad}$, $\boldsymbol{\chi}^{ad}$, and $\overline{\boldsymbol{\chi}}^{ad}$ are two-dimensional vectors whose components have subscripts **i** and **j** respectively. Those of $\boldsymbol{\psi}^{el,ad}$ and $\boldsymbol{\chi}^{ad}$ are the ones that appear in (67), with the condition that they both be single-valued continuous functions of **q** and **R** respectively. The vector $\overline{\boldsymbol{\psi}}^{el,ad}$, on the other hand, is required to be real, and as a result changes sign upon pseudorotations of the system around conical intersection configurations. Once $f(\mathbf{q})$ is chosen, (142) is used to define $\overline{\boldsymbol{\chi}}^{ad}(\mathbf{R})$. Since $\boldsymbol{\chi}^{ad}(\mathbf{R})$ is single-valued and $e^{-if(\mathbf{q})}$ changes sign upon such a pseudorotation, so does $\overline{\boldsymbol{\chi}}^{ad}(\mathbf{R})$. Equation (67) can be written in vector notation as

$$\Psi_o(\mathbf{r}; \mathbf{R}) = \tilde{\boldsymbol{\chi}}^{ad}(\mathbf{R})\boldsymbol{\psi}^{el,ad}(\mathbf{r}; \mathbf{q}) = \tilde{\overline{\boldsymbol{\chi}}}^{ad}(\mathbf{R})\overline{\boldsymbol{\psi}}^{el,ad}(\mathbf{r}; \mathbf{q}) \tag{143}$$

The Schrödinger equation satisfied by $\boldsymbol{\chi}^{ad}(\mathbf{R})$ is (74), with $\mathbf{W}^{(1)ad}(\mathbf{R})$ and $\mathbf{W}^{(2)ad}(\mathbf{R})$ being 2×2 matrices whose elements are scalars and $(3N - 6)$-dimensional column vectors respectively. The equation satisfied by $\overline{\boldsymbol{\chi}}^{ad}(\mathbf{R})$ is similar to (74), but with $\boldsymbol{\chi}^{ad}$, $\mathbf{W}^{(1)ad}$ and $\mathbf{W}^{(2)ad}$ replaced respectively by their barred counterparts, $\overline{\boldsymbol{\chi}}^{ad}$, $\overline{\mathbf{W}}^{(1)ad}$ and $\overline{\mathbf{W}}^{(2)ad}$, where

$$\begin{aligned} \overline{W}^{(1)ad}_{n,n'}(\mathbf{R}) &= \langle\overline{\psi}^{el,ad}_{n}(\mathbf{r}; \mathbf{q})|\nabla_R|\overline{\psi}^{el,ad}_{n'}(\mathbf{r}; \mathbf{q})\rangle_r \\ \overline{\mathbf{W}}^{(2)ad}_{n,n'}(\mathbf{R} &= \langle\overline{\psi}^{al,ad}_{n}(\mathbf{r}; \mathbf{q})|\nabla^2_R|\overline{\psi}^{el,ad}_{n'}(\mathbf{r}; \mathbf{q})\rangle_r \qquad \mathbf{n}, \mathbf{n}' = \mathbf{i}, \mathbf{j} \end{aligned} \tag{144}$$

We can express $\mathbf{W}^{(1)ad}$ and $\mathbf{W}^{(2)ad}$ in terms of their barred counterparts and of $f(\mathbf{q})$ by substituting (141) into (62) and (63). The result is

$$\mathbf{W}^{(1)ad}(\mathbf{R}) = \overline{\mathbf{W}}^{(1)ad}(\mathbf{R}) + i[\nabla_R f(\mathbf{q})]\mathbf{I} \tag{145}$$

and

$$\begin{aligned} \mathbf{W}^{(2)ad}(\mathbf{R}) = \overline{\mathbf{W}}^{(2)ad}(\mathbf{R}) &+ 2i[\nabla_R f(\mathbf{q})] \cdot \overline{\mathbf{W}}^{(1)ad}(\mathbf{R}) \\ &+ \{i\nabla^2_R f(\mathbf{q}) - [\nabla_R f(\mathbf{q})]^2\}\mathbf{I} \end{aligned} \tag{146}$$

where **I** stands for the 2×2 identity matrix and $[\nabla_R f(\mathbf{q})] \cdot \overline{\mathbf{W}}^{(1)ad}(\mathbf{R})$ is a 2×2 matrix whose **n, n′** element is $[\nabla_R f(\mathbf{q})] \cdot \overline{\mathbf{W}}^{(1)ad}_{n,n'}(\mathbf{R})$ with **n, n′** = **i, j**. It should be noticed that whereas $\overline{\mathbf{W}}^{(1)ad}(\mathbf{R})$ is real and skew-symmetric, and therefore nondiagonal, and $i[\nabla_R f(\mathbf{q})]\mathbf{I}$ is diagonal, its diagonal elements being pure imaginary quantities. By inserting the last

two expressions into (74) we obtain

$$-\frac{\hbar^2}{2\mu}\nabla_R^2\chi^{ad}(\mathbf{R}) - \frac{\hbar^2}{\mu}\{\overline{\mathbf{W}}^{(1)ad}(\mathbf{R}) + i[\nabla_R f(\mathbf{q})]\mathbf{I}\}\cdot\nabla_R\chi^{ad}(\mathbf{R}) - \frac{\hbar^2}{\mu}\{\overline{\mathbf{W}}^{(2)ad}(\mathbf{R}) + 2i[\nabla_R f(\mathbf{q})]\cdot\overline{\mathbf{W}}^{(1)ad}(\mathbf{R}) + [i\nabla_R^2 f(\mathbf{q}) - (\nabla_R f(\mathbf{q}))^2]\mathbf{I}\}\chi^{ad}(\mathbf{R}) \quad (147)$$
$$= [E\mathbf{I} - \varepsilon^{ad}(\mathbf{q})]\chi^{ad}(\mathbf{R})$$

The boundary condition for this equation is still that $\chi^{ad}(\mathbf{R})$ must be single-valued and continuous. The effect of the conical intersection between the PESs $\varepsilon_i^{ad}(\mathbf{q})$ and $\varepsilon_j^{ad}(\mathbf{q})$ is contained through the $f(\mathbf{q})$ terms. This real phase angle is chosen in the same manner as for the one-state case. No calculations have been reported so far using this approach.

D. Generalization of the Geometric Phase to Other Phenomena

The geometric phase effect associated with chemical reactions [11] and with the motion of electrons in magnetic fields [35] was generalized in 1984 by Berry [38] to systems which are transported around a loop or circuit C in parameter space. If $\hat{H}$ is the system's Hamiltonian and $\mathbf{R}$ a set of parametric variables on which $\hat{H}$ depends, he showed that an eigenstate of $\hat{H}$, when the system is transported slowly (i.e., adiabatically) around C, will acquire a geometrical phase factor $e^{i\gamma(c)}$, independent of time, in addition to the familiar dynamical phase factor. He also derived an explicit general formula for $\gamma(c)$ in terms of the spectrum and eigenstates of $\hat{H}(\mathbf{R})$ over a surface spanning C. The geometric phase angle $\gamma(C)$ is now widely known in the literature as Berry's phase. This phase is an example of a holonmy, the extent to which some variables change when other variables or parameters characterizing a system return to their initial value. Simon [39] subsequently interpreted Berry's phase in terms of the differential geometry concept of fiber bundles. Berry's basic concept was the separation of a system into an internal part, involving rapidly varying internal degrees of freedom, and an external part, involving slowly varying external (i.e., parametric) degrees of freedom. The geometric phase arises from the coupling between the motions of the internal and external parts. For molecular systems, the internal "fast" degrees of freedom are the electronic ones, and the external "slow" ones are the nuclear ones. The geometric phase arises from the coupling between these two kinds of degrees of freedom. The applications of Berry's phase to spectroscopic phenomena has been extensively reviewed [40]. This review also includes references to applications in classical mechanics, field theories, and solid-state physics. The geometric phase constitutes an active field of research in physics and chemistry, and many hundreds of papers in it have been published. The applications of quantum reaction dynamics of interest to this chapter are also evolving very rapidly.

IV. SYMMETRIZED HYPERSPHERICAL COORDINATES FOR TRIATOMIC SYSTEMS AND THE GEOMETRIC PHASE EFFECT

A. Symmetrized Hyperspherical Coordinates

1. Jacobi Body-Fixed Symmetrized Hyperspherical Coordinates

Let us consider a system involving three nuclei A_α, A_β, A_γ having masses M_α, M_β, and M_γ, respectively, and let λ, ν, κ be a cyclic permutation of α, β, γ. The λ-arrangement Jacobi vectors ($\lambda = \alpha, \beta, \gamma$) are defined in Fig. 4 where $G_{A_\nu A_\kappa}$ and G are the centers of

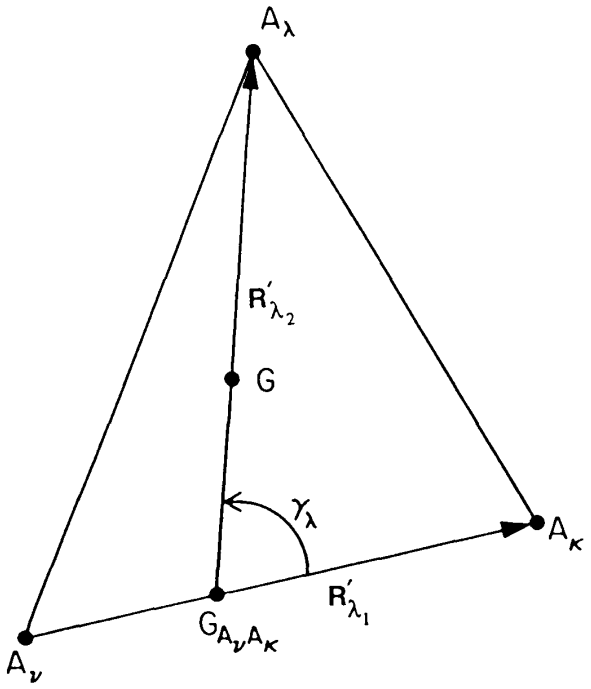

Figure 4 The λ-arrangement Jacobi coordinates for a system of three nuclei A_α, A_β, A_γ. λ, ν, κ is a cyclic permutation of α, β, γ.

mass of $A_\nu A_\kappa$ and $A_\lambda A_\nu A_\kappa$ respectively. The corresponding mass-scaled Jacobi vectors are

$$\mathbf{R}_{\lambda_i} = \left(\frac{\mu_{\lambda_i}}{\mu}\right)^{1/2} \mathbf{R}'_{\lambda_i} \qquad i = 1, 2 \tag{148}$$

where

$$\mu_{\lambda_1} = \frac{M_\nu M_\kappa}{M} \qquad \mu_{\lambda_2} = \frac{M_\lambda (M_\nu + M_\kappa)}{M} \tag{149}$$

are the reduced masses of $A_\nu A_\kappa$ and A_λ, $A_\lambda A_\kappa$, M is the total mass of the nuclei, and μ is the reduced or effective mass of the set of three nuclei and is given by

$$\mu = \left(\frac{M_\alpha M_\beta M_\gamma}{M}\right)^{1/2} \tag{150}$$

We define a system of symmetrized hyperspherical coordinates ρ, ω_λ, γ_λ, where γ_λ is the angle, in the 0 to π range, between the vectors $\mathbf{R}_{\lambda_1}$ and $\mathbf{R}_{\lambda_2}$ and ρ and ω_λ are defined by [16]

$$\rho = (R^2_{\lambda_1} + R^2_{\lambda_2})^{1/2} \tag{151}$$

and

$$\begin{aligned} R_{\lambda_1} &= \rho \sin \frac{\omega_\lambda}{2} \\ R_{\lambda_2} &= \rho \cos \frac{\omega_\lambda}{2} \end{aligned} \qquad 0 \le \omega_\lambda \le \pi \tag{152}$$

The hyperradius ρ is independent of λ [21,22].

Associated with these coordinates we define a system of internal **q**-space mathematical axes $OX_\lambda YZ_\lambda$ in which a general point P has spherical polar coordinates ρ, ω_λ, and γ_λ. The cartesian coordinates of P in this space are

$$\begin{aligned} X_\lambda &= \rho \sin \omega_\lambda \cos \gamma_\lambda \\ Y &= \rho \sin \omega_\lambda \sin \gamma_\lambda \geq 0 \\ Z_\lambda &= \rho \cos \omega_\lambda \end{aligned} \tag{153}$$

where, as shown below, OY and Y are λ-independent. An important property of this space is that there exists a one-to-one correspondence between points P and nuclear configurations of the system [16,41]. The division of ω_λ by 2 in the right-hand side of (152) is essential for this property to be valid. In addition, a $\lambda \rightarrow \nu$ arrangement channel transformation is equivalent to a clockwise rotation of the $OX_\lambda YZ_\lambda$ frame around OY by an angle $2\alpha_{\lambda\nu}$, where $\alpha_{\lambda\nu}$ is the angle in the $\pi/2$ to π range defined by [41]

$$\begin{aligned} \sin \alpha_{\lambda\nu} &= \left[\frac{M_\kappa M}{(M_\lambda + M_\kappa)(M_\nu + M_\kappa)}\right]^{1/2} \\ \cos \alpha_{\lambda\nu} &= -\left[\frac{M_\lambda M_\nu}{(M_\lambda + M_\kappa)(M_\nu + M_\kappa)}\right]^{1/2} \end{aligned} \tag{154}$$

This property stems from the fact that, under $\lambda \rightarrow \nu$ arrangement channel changes of coordinates, the $\mathbf{R}_\lambda \rightarrow \mathbf{R}_\nu$ transformation is a rotation [17,41,42]. As a result, such transformations are called kinematic rotations. The fact that under kinematic rotations $OX_\lambda YZ_\lambda$ is rotated around OY means that this axis is invariant under $\lambda \rightarrow \nu$ transformations, and the same is true for the coordinate Y, as stated above.

Let us now consider the PES ε_i^{ad}, denoted in the rest of this chapter by V. As a consequence of (154), equipotentials of $V(\rho, \omega_\lambda, \gamma_\lambda)$ are rotated without distortion upon such a $\lambda \rightarrow \nu$ transformation [16,17,41] and display the permutation symmetry properties of the system of nuclei. By this we mean that if two of the three nuclei are identical and the third one is distinct, those maps have the symmetry of the S_2 permutation group of two objects, and the OYZ_α plane is a plane of symmetry for AB_2 systems. Similarly, if the three nuclei are identical, these maps have the symmetry of the S_3 permutation group of three objects, which is isomorphic with the C_{3v} point group. These properties of $V(\rho, \omega_\lambda, \gamma_\lambda)$ in the $OX_\lambda YZ_\lambda$ space justify calling ρ, ω_λ, γ_λ the internal λ-arrangement symmetrized hyperspherical coordinates and OX_λ, OY, OZ_λ the corresponding (nonphysical) axes. It should be kept in mind that this space is only the $Y \geq 0$ half-space of the full $OX_\lambda YZ_\lambda$ cartesian space. In Fig. 5 (p. 453) we display schematically an equipotential of $V(\rho, \omega_\lambda, \gamma_\lambda)$, including its $Y < 0$ mirror image for simplicity of display. The set of λ-arrangement-channel hyperspherical coordinates ρ, ω_λ, γ_λ is most useful in regions of the internal configuration space for which A_λ is sufficiently far from $A_\nu A_\kappa$ for this arrangement not to interact with either the $A_\nu + A_\lambda A_\kappa$ or $A_\kappa + A_\lambda A_\nu$ arrangements. For those regions it is convenient to define a Jacobi body-fixed-λ (bfλ) $GX^{bf\lambda}Y^{bf\lambda}Z^{bf\lambda}$ obtained from the physical space-fixed frame $GX^{sf}Y^{sf}Z^{sf}$ by a rotation through Euler angles ϕ_λ, θ_λ, ψ_λ, where θ_λ, ϕ_λ are the polar angles of $\mathbf{R}_{\lambda_2}$ in the latter frame. ψ_λ is the angle in the 0 to 2π range between the $\mathbf{R}_{\lambda_2}$, GZ^{sf}, and $\mathbf{R}_{\lambda_2}$, $\mathbf{R}_{\lambda_1}$ half-planes, whose common edge is $\mathbf{R}_{\lambda_2}$, and measured counterclockwise from the first to the second of these half-planes as viewed from the tip of the $\mathbf{R}_{\lambda_2}$ vector. The $GZ^{bf\lambda}$ axis lies along $\mathbf{R}_{\lambda_2}$ and the $GX^{bf\lambda}Z^{bf\lambda}$ half-plane

with positive $X^{\text{bf}\lambda}$ contains $\mathbf{R}_{\lambda_1}$. As ψ_λ varies, the triatomic plane, which contains $\mathbf{R}_{\lambda_1}$ and $\mathbf{R}_{\lambda_2}$, rotates (i.e., tumbles) around $\mathbf{R}_{\lambda_2}$, and it is called the tumbling angle [43].[1]

The set of six coordinates ρ, Ξ_λ where $\Xi_\lambda \equiv (\phi_\lambda, \theta_\lambda, \psi_\lambda, \omega_\lambda, \gamma_\lambda)$ [44] are called the Jacobi bfλ arrangement channel symmetrized hyperspherical coordinates of nuclear configuration space $\mathbf{R}$. The system's nuclear kinetic energy operator in those coordinates is given by

$$\hat{T}(\mathbf{R}) = -\frac{\hbar^2}{2\mu}\nabla^2_{\mathbf{R}} = \hat{T}_\rho(\rho) + \frac{\hat{\Lambda}^2}{2\mu\rho^2} \tag{155}$$

where $\hat{T}_\rho(\rho)$ is the hyperradial kinetic energy operator

$$\hat{T}_\rho(\rho) = -\frac{\hbar^2}{2\mu}\frac{1}{\rho^5}\frac{\partial}{\partial\rho}\rho^5\frac{\partial}{\partial\rho} \tag{156}$$

and $\hat{\Lambda}^2$ is the grand-canonical angular momentum operator

$$\hat{\Lambda}^2 = \hat{L}^2(\omega_\lambda) + \frac{\hat{j}^2_\lambda}{\sin^2\omega_\lambda} + \frac{l^2_\lambda}{\cos^2\omega_\lambda} \tag{157}$$

In this expression, $\hat{L}^2(\omega_\lambda)$ is the angular momentum operator associated with the hyperangle ω_λ:

$$\hat{L}^2(\omega_\lambda) = -4\hbar^2\frac{1}{\sin^2\omega_\lambda}\frac{\partial}{\partial\omega_\lambda}\sin^2\omega_\lambda\frac{\partial}{\partial\omega_\lambda} \tag{158}$$

and $\hat{j}^2_\lambda$ and $\hat{l}^2_\lambda$ are the angular momentum operators associated with $\mathbf{R}_{\lambda_1}$ and $\mathbf{R}_{\lambda_2}$, respectively, expressed in terms of the angles, ϕ_λ, θ_λ, γ_λ, ψ_λ. The corresponding two vector angular momenta are related to the total orbital angular momentum $\hat{\mathbf{J}}$ of the nuclei by

$$\hat{\mathbf{j}}_\lambda + \hat{\mathbf{l}}_\lambda = \hat{\mathbf{J}} \tag{159}$$

In order to facilitate the introduction of partial wave expansions, it is convenient to express $\hat{\Lambda}^2$ in terms of $\partial/\partial\gamma_\lambda$ and $\hat{\mathbf{J}}$ instead of $\hat{\mathbf{j}}_\lambda$ and $\hat{\mathbf{l}}_\lambda$. Substituting (160) into (158) and utilizing the properties of angular momentum operators eventually leads to the expression

$$\begin{aligned}\hat{\Lambda}^2 = \hat{\mathbf{L}}^2(\omega_\lambda) &+ \frac{4}{\sin^2\omega_\lambda}\left[\frac{-\hbar^2}{\sin\gamma_\lambda}\frac{\partial}{\partial\gamma_\lambda}\sin\gamma_\lambda\frac{\partial}{\partial\gamma_\lambda} + \frac{1}{\sin^2\gamma_\lambda}\hat{J}^{\text{bf}\lambda 2}_Z\right] \\ &+ \frac{1}{\cos^2(\omega_\lambda/2)}\left\{\hat{J}^2 - 2\hat{J}^{\text{bf}\lambda 2}_Z + \left[\cot\gamma_\lambda\hat{J}^{\text{bf}\lambda}_Z - \hbar\left(\cot\gamma_\lambda + \frac{\partial}{\partial\gamma_\lambda}\right)\right]\hat{J}^{\text{bf}\lambda}_- \right. \\ &\left. + \left[\cot\gamma_\lambda\hat{J}^{\text{bf}\lambda}_Z + \hbar\left(\cot\gamma_\lambda + \frac{\partial}{\partial\gamma_\lambda}\right)\right]\hat{J}^{\text{bf}\lambda}_+\right\}\end{aligned} \tag{160}$$

where

$$\hat{J}^{\text{bf}\lambda}_\pm = \hat{J}^{\text{bf}\lambda}_X \pm i\hat{J}^{\text{bf}\lambda}_Y \tag{161}$$

$\hat{J}^{\text{bf}\lambda}_X$, $\hat{J}^{\text{bf}\lambda}_Y$, and $\hat{J}^{\text{bf}\lambda}_Z$ being the components of $\hat{\mathbf{J}}$ in the Jacobi bfλ frame. The reason this expression is convenient is that the Euler angles ϕ_λ, θ_λ, ψ_λ of this frame appear in $\hat{J}^2$, $\hat{J}^{\text{bf}\lambda}_z$, and $\hat{J}^{\text{bf}\lambda}_\pm$ and nowhere else. The action of these operators on the Wigner rotation functions are well known [45], and their explicit expressions in terms of $\partial/\partial\phi_\lambda$, $\partial/\partial\theta_\lambda$

and $\partial/\partial\psi_\lambda$ are not needed. Equations (161), (158) and (155) furnish the nuclear motion Hamiltonian of (66)

$$\hat{H}^{nu}(\mathbf{R}_\lambda) = -\frac{\hbar^2}{2\mu}\nabla^2_{\mathbf{R}} + V(\rho, \omega_\lambda, \gamma_\lambda) \tag{162}$$

in the Jacobi bfλ hyperspherical coordinates.

The volume element $d\mathbf{R}_\lambda$ in these coordinates is

$$d\mathbf{R}_\lambda = [\sin\theta_\lambda\, d\phi_\lambda\, d\theta_\lambda\, d\psi_\lambda]\left(\frac{\rho^5}{8}\right)\sin^2\omega_\lambda \sin\gamma_\lambda\, d\rho\, d\omega_\lambda\, d\gamma_\lambda \tag{163}$$

The factor in brackets is the three-dimensional angular element associated with the Euler angles ϕ_λ, θ_λ, ψ_λ, and the remaining factor is the volume element associated with the internal configuration variables ρ, ω_λ, γ_λ on which the PES V depends. These ρ, Ξ_λ Jacobi symmetrized hyperspherical coordinates have been previously used in reactive scattering calculations for H_3 in its ground adiabatic electronic state, ignoring the presence of the conical intersection with its first electronically excited state [44].

2. Principal Axes of Inertia Symmetrized Hyperspherical Coordinates

Let us define another pair of angles θ, φ_λ in the internal $OX_\lambda Y Z_\lambda$ **q**-space as the spherical polar angles of P with respect to the axes $O\bar{X}_\lambda \bar{Y}_\lambda \bar{Z}$ where $O\bar{X}_\lambda \equiv OZ_\lambda$, $O\bar{Y}_\lambda \equiv OX_\lambda$, and $O\bar{Z} \equiv O\bar{Y}$ [12]. The relation between θ, φ_λ and ω_λ, γ_λ is

$$\begin{aligned} \sin\theta\cos\varphi_\lambda &= \cos\omega_\lambda \\ \sin\theta\sin\varphi_\lambda &= \sin\omega_\lambda\cos\gamma_\lambda \\ \cos\theta &= \sin\omega_\lambda\sin\gamma_\lambda \\ 0 \le \theta \le \pi/2 \qquad & 0 \le \varphi_\lambda < 2\pi \end{aligned} \tag{164}$$

Let, in addition, $GX^{I\lambda}Y^{I}Z^{I\lambda}$ be another body-fixed frame $I\lambda$ whose axes are the principal axes of inertia of the three nuclei, and whose Euler angles with respect to $GX^{sf}Y^{sf}Z^{sf}$ are a_λ, b_λ, c_λ. The senses of those axes are chosen so that the $I\lambda$ system has the same handedness as the sf one and in a manner that results in a one-to-one correspondence between ρ, $\Phi_\lambda \equiv (a_\lambda, b_\lambda, c_\lambda, \theta, \varphi_\lambda)$ and the space-fixed cartesian coordinates of $\mathbf{R}_{\lambda_1}$ and $\mathbf{R}_{\lambda_2}$. Furthermore, the $I\lambda$ axes are labeled so that the corresponding principal moments of inertia lie in the order

$$I^\lambda_Z \le I^\lambda_X \le I_Y \tag{165}$$

The $\mathbf{R}_{\lambda_1}$ and $\mathbf{R}_{\lambda_2}$ vectors lie in the $GX^{I\lambda}Z^{I\lambda}$ plane.[2] Under a $\lambda \to \nu$ arrangement channel transformation φ_λ changes according to

$$\varphi_\nu = \varphi_\lambda + 2\alpha_{\lambda\nu} \mod 2\pi \tag{166}$$

θ and GY^I are unchanged, and the $GX^{I\lambda}$ and $GZ^{I\lambda}$ axes are either unchanged or both change senses. This means that the corresponding Euler angles may at most change by $\pm\pi$ modulo 2π.

The coordinates ρ, $\mathbf{\Phi}_\lambda$ are called the principal axes of inertia symmetrized hyperspherical coordinates. The kinetic energy operator in these coordinates is still given by (155), but $\hat{\Lambda}^2$ is now expressed as [12]

$$\begin{aligned}\hat{\Lambda}^2 = {} & \hat{\Lambda}_0^2(\theta, \varphi_\lambda) + \frac{4\hat{J}_Z^{I\lambda^2}}{\cos^2\theta} \\ & + \frac{1}{\cos^2(\pi/4 - \theta/2)}\left[\frac{\hat{J}^2 - \hat{J}_Z^{I\lambda^2}}{2} + \frac{\hat{J}_+^{I\lambda^2} + \hat{J}_-^{I\lambda^2}}{4} - \hat{J}_Z^{I\lambda^2}\right] \\ & + \frac{1}{\sin^2\theta}\left[\frac{\hat{J}^2 - \hat{J}_Z^{I\lambda^2}}{2} - \frac{\hat{J}_+^{I\lambda^2} + \hat{J}_-^{I\lambda^2}}{4}\right] \\ & - 2\hbar\frac{\cos\theta}{\sin^2\theta}(\hat{J}_+^{I\lambda} - \hat{J}_-^{I\lambda})\frac{\partial}{\partial\varphi_\lambda}\end{aligned} \tag{167}$$

where

$$\hat{\Lambda}_0^2(\theta, \varphi_\lambda) = -4\hbar^2\left(\frac{1}{\sin 2\theta}\frac{\partial}{\partial\theta}\sin 2\theta\frac{\partial}{\partial\theta} + \frac{1}{\sin^2\theta}\frac{\partial^2}{\partial\varphi_\lambda^2}\right) \tag{168}$$

and

$$\hat{J}_\pm^{I\lambda} = \hat{J}_X^{I\lambda} \pm i\hat{J}_Y^{I\lambda} \tag{169}$$

$\hat{J}_X^{I\lambda}$, $\hat{J}_Y^I$, and $\hat{J}_Z^{I\lambda}$ being the components of $\hat{\mathbf{J}}$ in the $I\lambda$ frame. In view of (166), the operator $\partial/\partial\varphi_\lambda$ is invariant under a $\lambda \rightarrow \nu$ transformation. Since the GY^I axis is also invariant, so is $\hat{J}_+^{I\lambda} - \hat{J}_-^{I\lambda}$. Such a transformation either leaves $GX^{I\lambda}$ unchanged or at most changes its sense, which means that $\hat{J}_+^{I\lambda}$ and $\hat{J}_-^{I\lambda}$ are either unchanged or change into $-\hat{J}_-^{I\lambda}$ and $-\hat{J}_+^{I\lambda}$ respectively, leaving $\hat{J}_+^{I\lambda^2} + \hat{J}_-^{I\lambda^2}$ unaltered. Finally, $\hat{J}^2$ and $\hat{J}_Z^{I\lambda^2}$ are also invariant. We conclude that every one of the terms in the right-hand side of (167) is invariant under kinematic rotations. This is particularly useful in the strong interaction region, in which the three nuclei are close together. As for the Jacobi bfλ coordinates, the Euler angles appear only in $\hat{J}^2$, $\hat{J}_Z^{I\lambda}$, and $\hat{J}_\pm^{I\lambda}$ and since results of their operation on Wigner rotation functions are known, we do not need their explicit expressions in terms of $\partial/\partial a_\lambda$, $\partial/\partial b_\lambda$, and $\partial/\partial c_\lambda$. The expression for the volume element in the ρ, $\mathbf{\Phi}_\lambda$ coordinates is

$$d\mathbf{R}_\lambda = [\sin b_\lambda\, da_\lambda\, db_\lambda\, dc_\lambda]\left(\frac{\rho^5}{16}\right)\sin 2\theta\, d\rho\, d\theta\, d\varphi_\lambda \tag{170}$$

These ρ, $\mathbf{\Phi}_\lambda$ coordinates have been used in all integral and differential reaction cross-section calculations which include the effect of the geometric phase reported so far [12,36,46–48]. They are closely related to several sets of coordinates described previously [49–54].

B. Partial Wave Expansion

We wish to solve the Born-Oppenheimer nuclear motion SE [66] for the adiabatic orbital nuclear wave function $\chi^{ad}(\mathbf{R})$ (in which the subscript **i**, referring to the ground adiabatic electronic state of the system, will hereafter be implied), with the Born-Oppenheimer nuclear motion Hamiltonian $\hat{H}^{nu}(\mathbf{R}_\lambda)$ given by (162), (155) and either (160) or (168). To

that effect, we first define an auxiliary nuclear wave function $\chi^{JM\Pi\Gamma}(\mathbf{R}_\lambda)$ by requiring it to be a simultaneous eigenfunction of $\hat{H}^{nu}$, of the square of the total nuclear orbital angular momentum $\hat{\mathbf{J}}$, of its sf Z component $\hat{\mathbf{J}}_Z$, and of the inversion operator $\hat{I}$ of the nuclei through their center of mass G according to the equations

$$\begin{aligned} \hat{H}^{nu}\chi^{JM\Pi\Gamma} &= E\chi^{JM\Pi\Gamma} \\ \hat{\mathbf{J}}^2\chi^{JM\Pi\Gamma} &= J(J+1)\hbar^2\chi^{JM\Pi\Gamma} \\ \hat{\mathbf{J}}_Z\chi^{JM\Pi\Gamma} &= M\hbar\chi^{JM\Pi\Gamma} \\ \hat{I}\chi^{JM\Pi\Gamma} &= (-1)^{\Pi}\chi^{JM\Pi\Gamma} \end{aligned} \tag{171}$$

In these expressions J and M are respectively the quantum numbers associated with $\hat{\mathbf{J}}^2$ and $\hat{\mathbf{J}}_Z$ and $\Pi = 0, 1$ is a parity quantum number which specifies whether $\chi^{JM\Pi\Gamma}$ is symmetric or antisymmetric with respect to inversion through G. In addition, $\chi^{JM\Pi\Gamma}$ is required to transform according to the irreducible representations Γ of the permutation group of identical nuclei of the system. Once the $\chi^{JM\Pi\Gamma}$ are obtained, χ^{ad} can be expressed as a linear combination of these functions, with coefficients chosen so as to enforce the desired asymptotic conditions. This linear combination is called a partial wave expansion, and the $\chi^{JM\Pi\Gamma}$ are called partial waves. In the present chapter, we adopt scattering asymptotic conditions, as we are interested in the calculation of reactive scattering cross sections in the triatomic systems under consideration. To obtain these cross sections, the χ^{ad} never have to be obtained explicitly. Instead, associated to $\chi^{JM\Pi\Gamma}$ a partial wave scattering matrix $\mathbf{S}^{J\Pi\Gamma}$ is calculated and in terms of which the differential and integral cross sections for the system is obtained directly by standard methods [44], with the effect of the Pauli principle for identical nuclei included.

To obtain a solution of Eq. (171) we first define the parity Wigner rotation functions

$$D^{J\Pi}_{M\Omega_\lambda} = \left\{\frac{2J+1}{16\pi^2[1+(-1)^{J+\Pi}\delta_{\Omega_\lambda,0}]}\right\}^{1/2}[D^J_{M\Omega_\lambda} + (-1)^{J+\Pi+\Omega_\lambda}D^J_{M,-\Omega_\lambda}] \tag{172}$$

where $D^J_{M\Omega_\lambda}$ is a Wigner rotation function of the Euler angles (either ϕ_λ, θ_λ, ψ_λ or a_λ, b_λ, c_λ) [45] and $\delta_{\Omega_\lambda,0}$ is the Kronecker symbol. These functions are orthonormalized according to

$$\int D^{J'\Pi'}_{M'\Omega'_\lambda} D^{J\Pi}_{M\Omega_\lambda}\, d\tau = \delta^{J'\Pi'M'\Omega'_\lambda}_{J\Pi M\Omega_\lambda} \tag{173}$$

where $d\tau$ is the three-dimensional angular element for the Euler angles in question and the right-hand-side is a generalized Kronecker symbol which equals 1 if all the superscripts equal their corresponding subscripts and vanishes otherwise. Let us define the symbol $\boldsymbol{\alpha}_\lambda$ which stands for the five principal axes hyperangles $\boldsymbol{\Phi}_\lambda$ in the strong interaction region of internal configuration space or for the Jacobi bfλ ones $\boldsymbol{\Xi}_\lambda$ in the weak interaction region. In either of the coordinate sets ρ, $\boldsymbol{\alpha}_\lambda$ we expand $\chi^{JM\Pi\Gamma}$ according to

$$\chi^{JM\Pi\Gamma n_\lambda\Omega_\lambda}(\rho, \boldsymbol{\alpha}_\lambda) = \frac{1}{\rho^{5/2}}\sum_{n_\lambda\Omega_\lambda} b^{J\Pi\Gamma n'_\lambda\Omega'_\lambda}_{n_\lambda\Omega_\lambda}(\rho;\bar{\rho})\Phi^{JM\Pi\Gamma}_{n_\lambda\Omega_\lambda}(\boldsymbol{\alpha}_\lambda;\bar{\rho}) \tag{174}$$

In this expression, the $\Phi^{JM\Pi\Gamma}_{n_\lambda\Omega_\lambda}(\boldsymbol{\alpha}_\lambda;\bar{\rho})$ form a conveniently defined complete orthonormal basis set in the five hyperangles $\boldsymbol{\alpha}_\lambda$ which depends parametrically on $\bar{\rho}$, and the $b^{J\Pi\Gamma n'_\lambda\Omega'_\lambda}_{n_\lambda\Omega_\lambda}(\rho;\bar{\rho})$ are coefficients which, once calculated, determine $\chi^{JM\Pi\Gamma n'_\lambda\Omega'_\lambda}(\rho;\alpha_\lambda)$. The superscripts $n'_\lambda\Omega'_\lambda$ in (174) were added to indicate that there are as many linearly inde-

pendent solutions of (171) as there are functions $\Phi^{JM\Pi\Gamma}_{n_\lambda\Omega_\lambda}$. The latter are called local hyperspherical surface functions (LHSFs) and are required to be eigenfunctions of $\hat{\mathbf{J}}^2$, $\hat{\mathbf{J}}_Z$, and $\hat{I}$. Since the $D^{J\Pi}_{M\Omega_\lambda}$ have that property, we set

$$\Phi^{JM\Pi\Gamma}_{n_\lambda\Omega_\lambda}(\alpha_\lambda; \bar{\rho}) = D^{J\Pi}_{M\Omega_\lambda}(\alpha^{(1)}_\lambda)\phi^{\Pi\Gamma}_{n_\lambda\Omega_\lambda}(\alpha^{(2)}_\lambda; \bar{\rho}) \tag{175}$$

where $\boldsymbol{\alpha}^{(1)}_\lambda$ stands for the set of three Euler angles contained in $\boldsymbol{\alpha}_\lambda$ and $\boldsymbol{\alpha}^{(2)}_\lambda$ stands for the remaining two hyperangles, i.e., θ, φ_λ for the $I\lambda$ coordinates and ω_λ, γ_λ for the bfλ ones. The functions $\phi^{\Pi\Gamma}_{n_\lambda\Omega_\lambda}$, called two-dimensional LHSFs, are defined as the eigenfunctions of the two-dimensional reference Hamiltonian (12)

$$\begin{aligned}\hat{h}^{\Omega_\lambda}(\boldsymbol{\alpha}^{(2)}_\lambda; \bar{\rho}) &= \frac{1}{2\mu\bar{\rho}^2}\left[\hat{\Lambda}^2_0(\theta, \varphi_\lambda) + \frac{4\Omega^2_\lambda\hbar^2}{\cos^2\theta}\right] + V(\bar{\rho}, \theta, \varphi_\lambda) \\ &= \frac{1}{2\mu\bar{\rho}^2}\left\{\hat{L}^2(\omega_\lambda) + \frac{4}{\sin^2\omega_\lambda}\left[\frac{-\hbar^2}{\sin\gamma_\lambda}\frac{\partial}{\partial\gamma_\lambda}\sin\gamma_\lambda\frac{\partial}{\partial\gamma_\lambda} + \frac{\Omega^2_\lambda\hbar^2}{\sin^2\gamma_\lambda}\right]\right\} \\ &\quad + V(\bar{\rho}, \omega_\lambda, \gamma_\lambda)\end{aligned} \tag{176}$$

i.e.,

$$\hat{h}^{\Omega_\lambda}(\boldsymbol{\alpha}^{(2)}_\lambda; \bar{\rho})\phi^{\Pi\Gamma}_{n_\lambda\Omega_\lambda}(\boldsymbol{\alpha}^{(2)}_\lambda; \bar{\rho}) = \varepsilon^{\Pi\Gamma}_{n_\lambda\Omega_\lambda}(\bar{\rho})\phi^{\Pi\Gamma}_{n_\lambda\Omega_\lambda}(\boldsymbol{\alpha}^{(2)}_\lambda; \bar{\rho}) \tag{177}$$

This expression describes the motion of a particle of mass μ in the internal nuclear configuration space ρ, $\boldsymbol{\alpha}^{(2)}_\lambda$ on a half-sphere of fixed radius $\bar{\rho}$ and subject to the Hamiltonian $\hat{h}^{\Omega_\lambda}$. The eigenfunctions $\phi^{\Pi\Gamma}_{n_\lambda\Omega_\lambda}$ must not diverge anywhere on this hemisphere, and $\boldsymbol{n}_\lambda$ is the quantum number resulting from this boundary condition. $\boldsymbol{n}_\lambda$ is two-dimensional since the underlying problem has two angular degrees of freedom.

In the strong interaction region of configuration space, where we use the internal coordinates θ, φ_λ, (177) is solved by expanding $\phi^{\Pi\Gamma}_{n_\lambda\Omega_\lambda}(\theta, \varphi_\lambda; \bar{\rho})$ in a direct product of two orthonormal basis sets, $\{f^{\Omega_\lambda}_n(\theta; \bar{\rho})\}$ and $\{g^{\Pi\Gamma}_{p_\lambda\Omega_\lambda}(\varphi_\lambda; \bar{\rho})\}$, where n and p_λ are two quantum numbers that span those sets and $\boldsymbol{n}_\lambda \equiv (n, p_\lambda)$. The f and g functions may be chosen to be $\bar{\rho}$-independent linear combinations of simple trigonometric functions in the angles θ and φ_λ respectively [12], or may be chosen instead to be functions reflecting the properties of $V(\bar{\rho}, \theta, \varphi_\lambda)$ so as to minimize the number of terms needed for this expansion to converge. In the weak interaction region of configuration space, where we use the bfλ coordinates ρ, Ξ_λ, we expand the $\phi^{\Pi\Gamma}_{n_\lambda\Omega_\lambda}(\omega_\lambda, \gamma_\lambda; \bar{\rho})$ in the direct product of the basis sets $P^{j_\lambda}_{\Omega_\lambda}(\cos\gamma_\lambda)$ of the associated Legendre functions of $\cos\gamma_\lambda$, and the functions $t^{\Pi\Gamma}_{\nu_\lambda j_\lambda\Omega_\lambda}(\omega_\lambda; \bar{\rho})$ determined by the numerical solution of a one-dimensional eigenfunction equation in ω_λ [12,44]. In this case, $\boldsymbol{n}_\lambda \equiv (j_\lambda, \nu_\lambda)$ and the quantum numbers ν_λ, j_λ, Ω_λ correlate asymptotically with the vibration, rotation, and helicity magnetic quantum numbers of the isolated $A_\nu A_\kappa$ diatom along the direction of the final velocity vector of A_λ with respect to $A_\nu A_\kappa$ [43].

With the $\Phi^{JM\Pi\Gamma}_{n_\lambda\Omega_\lambda}(\boldsymbol{\alpha}^{(2)}_\lambda; \bar{\rho})$ thus completely defined, (174) is inserted into the first of (171). This results in a set of coupled hyperradial second-order ordinary differential equations (called coupled-channel equations) in the coefficients $b^{J\Pi\Gamma n_\lambda\Omega_\lambda}_{n_\lambda\Omega_\lambda}(\rho; \bar{\rho})$, which is cast as a second order differential equation in a matrix $\mathbf{b}^{J\Pi\Gamma}$ of the form

$$-\frac{\hbar^2}{2\mu}\frac{d^2\mathbf{b}^{J\Pi\Gamma}(\rho; \bar{\rho})}{d\rho^2} + \mathbf{V}^{J\Pi\Gamma}(\rho; \bar{\rho})\,\mathbf{b}^{J\Pi\Gamma}(\rho; \bar{\rho}) = E\mathbf{b}^{J\Pi\Gamma}(\rho; \bar{\rho}) \tag{178}$$

where $\mathbf{V}^{J\Pi\Gamma}(\rho; \bar{\rho})$ is an interaction potential matrix that produces coupling in both n_λ and Ω_λ. The Ω_λ part of this coupling is different for the ρ, Φ_λ and ρ, Ξ_λ variables. For the former, the presence of the operators $\hat{J}_\pm^{I\lambda}$ and $\hat{J}_\pm^{I\lambda^2}$ in (167) leads to a pentadiagonal coupling of Ω_λ to $\Omega_\lambda \pm 1$ and $\Omega_\lambda \pm 2$. Since, on the other hand, $\hat{J}_\pm^{bf\lambda}$ but no other power of these operators appears in (160), the Ω_λ part of the coupling in the equations obtained with the ρ, Ξ_λ variables is tridiagonal; i.e., Ω_λ is coupled to $\Omega_\lambda \pm 1$ only. These different degrees of Ω_λ-coupling do not affect the numerical effort needed to solve the corresponding hyperradial equations.

The numerical procedure used in association with the ρ, α_λ coordinates is as follows (12). The internal configuration space is divided into a number of spherical hyperradial sectors. The two-dimensional LHSFs are then determined at the center $\bar{\rho}$ of each sector and used to obtain the coupling matrix $\mathbf{V}^{J\Pi\Gamma}(\rho; \bar{\rho})$ over the entire sector. Equation (178) is transformed into the firstorder nonlinear Bessel-Ricatti matrix differential equation

$$\frac{d\mathbf{f}^{J\Pi\Gamma}(\rho; \bar{\rho})}{d\rho} + [\mathbf{f}^{J\Pi\Gamma}(\rho; \bar{\rho})]^2 + \frac{2\mu}{\hbar^2}[E\mathbf{I} - \mathbf{V}^{J\Pi\Gamma}(\rho; \bar{\rho})] = \mathbf{0} \tag{179}$$

where $\mathbf{f}^{J\Pi\Gamma}(\rho; \bar{\rho})$ is the logarithmic derivative matrix $[(d/d\rho)\mathbf{b}^{J\Pi\Gamma}(\rho; \bar{\rho})][\mathbf{b}^{J\Pi\Gamma}(\rho; \bar{\rho})]^{-1}$. This equation is integrated from the beginning to the end of each sector using the efficient fourth-order logarithmic-derivative method [55–57], and for which the initial $\mathbf{f}^{J\Pi\Gamma}(\rho; \bar{\rho})$ is obtained from the last such matrix at the end of the previous sector. Initially, the ρ, $\mathbf{\Phi}_\lambda$ coordinates are used. The first sector starts at a hyperradius ρ_0 sufficiently small for the WKB solution to be applicable. In this manner, the $\mathbf{f}^{J\Pi\Gamma}$ equation is integrated from ρ_0 to a value ρ_s of the hyperradius for which the interactions between the three different arrangement channels λ have become negligible. At that point one switches to the variables ρ, ω_λ, γ_λ and integrates that equation for each $\lambda = \alpha, \beta, \gamma$ separately to a value ρ_a at which the interactions within the arrangement channels (associated with inelastic and elastic transitions) have also become negligible. It is also necessary to swtich from the $I\lambda$ principal axes of inertia frame to the Jacobi bfλ frame, i.e., from Euler angles a_λ, b_λ, c_λ to Euler angles ϕ_λ, θ_λ, ψ_λ. This can be done either at $\rho = \rho_s$ or at $\rho = \rho_a$. In the former case we use the angular variables Ξ_λ in the weak interaction region $\rho_s \leq \rho \leq \rho_a$, and in the latter we use in that region the mixed set of angular variables a_λ, b_λ, c_λ for the Euler angles and ω_λ, γ_λ for the internal angles. The Euler angles which accomplish the $I\lambda \rightarrow$ bfλ transformation can be obtained from the equations of note 2 and are 0, ε_λ, π where ε_λ is the angle in the 0 to π range determined by

$$\cos \varepsilon_\lambda = \frac{\sqrt{2} \cos(\varphi_\lambda/2) \cos(\pi/4 - \theta/2)}{(1 + \sin \theta \cos \varphi_\lambda)^{1/2}} \tag{180}$$

At ρ_a the $\chi^{JM\Pi\Gamma}(\rho, \Xi_\lambda)$ are matched to asymptotic atom-diatom wave functions expressed in the usual mass-scaled Jacobi coordinates R_{λ_1}, γ_λ, ψ_λ, R_{λ_2}, θ_λ, ϕ_λ. From this asymptotic analysis one obtains the reactance matrix $\mathbf{R}^{J\Pi\Gamma}$ and from it the scattering matrix $\mathbf{S}^{J\Pi\Gamma}$. This is done for all Γ and both parities $\Pi = 0$ and 1 and a sufficient number of partial waves (i.e., values of J) for the resulting cross sections of interest have converged to the desired degree of accuracy.

It should be noted that the $\hat{\Lambda}^2$ operators of (160) and (167) display Eckart singularities [58], but for the results reported in Sec. V these singularities have not produced special difficulties. At higher energies and/or for other systems difficulties may arise and will have to be dealt with accordingly.

C. Basis Sets for Conical Intersection Systems

Let us consider the hyperspherical coordinates ρ, $\mathbf{\Phi}_\lambda$ of Sec. IV.A.2 for which internal configuration three-dimensional space $\mathbf{q}$ is defined by the spherical polar coordinates ρ, θ, φ_λ. Let us further consider a two-dimensional hemispherical cut in this space obtained by making ρ equal to a constant $\bar{\rho}$. Let $\bar{P}$ be the point at which the locus L of conical intersection geometries of the system intersects this hemisphere. In order that the boundary conditions on $\chi^{ad}(\mathbf{R})$ associated with the conical intersection be satisfied, it is sufficient that for every $\bar{\rho}$ related conditions be satisfied by the products of basis functions $f_n^{\Omega_\lambda}(\theta; \bar{\rho}) g_{p_\lambda \Omega_\lambda}^{\Pi\Gamma}(\varphi_\lambda; \bar{\rho})$ used in the determination of the two-dimensional LHSF $\phi_{np_\lambda\Omega_\lambda}^{\Pi\Gamma}(\theta, \varphi_\lambda; \bar{\rho})$. Upon a 6D pseudo-rotation of the system, a_λ, b_λ, c_λ, $\bar{\rho}$, θ, φ_λ change to $(\pi + a_\lambda) \bmod 2\pi$, $\pi - b_\lambda$, $(\pi - c_\lambda) \bmod 2\pi$, $\bar{\rho}$, θ, $\varphi_\lambda + 2\pi$ respectively, while the associated point $P(\rho, \theta, \varphi_\lambda)$ in $\mathbf{q}$ space traverses a closed loop aroung P.[3] To indicate how to take this fact into account, let us consider first the H_3 system, which displays a conical intersection between its ground and first excited electronically adiabatic PESs for equilateral triangular configurations (18). The locus L is for this case the $GY \equiv G\bar{Z}$ axis of that space (see Fig. 5), for which $\theta = 0$. For $\rho = \bar{\rho}$ and arbitrary θ we can define a loop around $\bar{P}$ to be the circle of radius $\bar{\rho} \cos\theta$. As a point P traverses this loop, φ_λ varies from 0 to 2π. In order that the conical intersection boundary condition be satisfied, it suffices to impose on the basis functions $g_{p_\lambda\Omega_\lambda}^{\Pi\Gamma}(\varphi_\lambda)$ the geometric phase (GP) condition

$$g_{p_\lambda\Omega_\lambda}^{\Pi\Gamma}(\varphi_\lambda + 2\pi; \bar{\rho}) = -(-1)^{\Pi} g_{p_\lambda\Omega_\lambda}^{\Pi\Gamma}(\varphi_\lambda; \bar{\rho}) \tag{181}$$

In the absence of such an intersection, the no-geometric-phase (NGP) boundary condition associated with the single-valuedness of $\chi^{ad}(\mathbf{R})$ is instead

$$g_{p_\lambda\Omega_\lambda}^{\Pi\Gamma}(\varphi_\lambda + 2\pi; \bar{\rho}) = (-1)^{\Pi} g_{p_\lambda\Omega_\lambda}^{\Pi\Gamma}(\varphi_\lambda; \bar{\rho}) \tag{182}$$

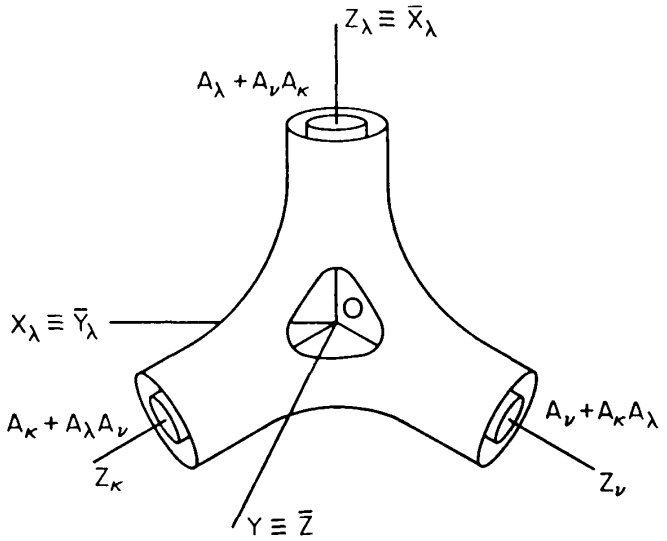

Figure 5 Equipotential energy surface for a system of three atoms in symmetrized internal coordinates. The $OX_\lambda \equiv OY_\lambda$, $OY \equiv OZ$, and $OZ_\lambda = OX_\lambda$ define two related nonphysical internal nuclear coordinate frames and spaces. A point P in those spaces has spherical polar coordinates ρ, ω_λ, γ_λ in the $OX_\lambda YZ_\lambda$ frame and ρ, θ, φ_λ in the $OX_\lambda Y_\lambda Z$ frame.

The formalism and methodologies for these two cases are otherwise exactly the same. As a result, using the symmetrized hyperspherical coordinates ρ, θ, φ_λ, inclusion of the effect of the GP on scattering calculations for H_3 is extremely simple, and is accomplished by imposing a simple boundary condition on the basis set for only one of the six coordinates which describe the nuclear motion of the system. This entails no increase in computational effort.

One possible choice of the $g^{\Pi\Gamma}_{p_\lambda\Omega_\lambda}(\varphi_\lambda;\bar{\rho})$ for H_3 that satisfy (181), for the A_1, A_2 and E irreducible representations of the S_3 permutation group, are the following $\bar{\rho}$-independent functions [12]:

(a) for even Ω_λ:

$$\begin{aligned} g^{0A_1}_{p_\lambda\Omega_\lambda} &= \sin[(3p_\lambda + 3/2)\varphi_\lambda] & g^{1A_1}_{p_\lambda\Omega_\lambda} &= \sin(3p_\lambda\varphi_\lambda) \\ g^{0A_2}_{p_\lambda\Omega_\lambda} &= \cos[(3p_\lambda + 3/2)\varphi_\lambda] & g^{1A_2}_{p_\lambda\Omega_\lambda} &= \cos(3p_\lambda\varphi_\lambda) \\ g^{0E}_{p_\lambda\Omega_\lambda} &= \cos[(3p_\lambda \pm 1/2)\varphi_\lambda] & g^{1E}_{p_\lambda\Omega_\lambda} &= \cos[(3p_\lambda \pm 1)\varphi_\lambda] \end{aligned} \tag{183}$$

(b) for odd Ω_λ:

$$\begin{aligned} g^{0A_1}_{p_\lambda\Omega_\lambda} &= \cos[(3p_\lambda + 3/2)\varphi_\lambda] & g^{1A_1}_{p_\lambda\Omega_\lambda} &= \cos(3p_\lambda\varphi_\lambda) \\ g^{0A_2}_{p_\lambda\Omega_\lambda} &= \sin[(3p_\lambda + 3/2)\varphi_\lambda] & g^{1A_2}_{p_\lambda\Omega_\lambda} &= \sin(3p_\lambda\varphi_\lambda) \\ g^{0E}_{p_\lambda\Omega_\lambda} &= \sin[(3p_\lambda \pm 1/2)\varphi_\lambda] & g^{1E}_{p_\lambda\Omega_\lambda} &= \sin[(3p_\lambda \pm 1)\varphi_\lambda] \end{aligned} \tag{184}$$

In these expressions, p_λ is a nonnegative integer with $3p_\lambda - 1$ and $3p_\lambda - 1/2$ restricted to non-negative values.

If instead we wish (181) to be satisfied, a corresponding choice of the $g^{\Pi\Gamma}_{p_\lambda\Omega_\lambda}(\varphi_\lambda;\bar{\rho})$ is (12)

(a) for even Ω_λ:

$$\begin{aligned} g^{0A_1}_{p_\lambda\Omega_\lambda} &= \cos(3p_\lambda\varphi_\lambda) & g^{1A_1}_{p_\lambda\Omega_\lambda} &= \cos[(3p_\lambda + 3/2)\varphi_\lambda] \\ g^{0A_2}_{p_\lambda\Omega_\lambda} &= \sin(3p_\lambda\varphi_\lambda) & g^{1A_2}_{p_\lambda\Omega_\lambda} &= \sin[(3p_\lambda + 3/2)\varphi_\lambda] \\ g^{0E}_{p_\lambda\Omega_\lambda} &= \cos[(3p_\lambda \pm 1)\varphi_\lambda] & g^{1E}_{p_\lambda\Omega_\lambda} &= \cos[(3p_\lambda \pm 1/2)\varphi_\lambda] \end{aligned} \tag{185}$$

(b) for odd Ω_λ:

$$\begin{aligned} g^{0A_1} &= \sin(3p_\lambda\varphi_\lambda) & g^{1A_1}_{p_\lambda\Omega_\lambda} &= \sin[(3p_\lambda + 3/2)\varphi_\lambda] \\ g^{0A_2}_{p_\lambda\Omega_\lambda} &= \cos(3p_\lambda\varphi_\lambda) & g^{1A_2}_{p_\lambda\Omega_\lambda} &= \cos[(3p_\lambda + 3/2)\varphi_\lambda \\ g^{0E}_{p_\lambda\Omega_\lambda} &= \sin[(3p_\lambda \pm 1)\varphi_\lambda] & g^{1E}_{p_\lambda\Omega_\lambda} &= \sin[(3p_\lambda \pm 1/2)\varphi_\lambda] \end{aligned} \tag{186}$$

The allowed values of p_λ are the same as those for (183) and (184).

Let us now consider the isotopomers of H_3 of the AB_2 type, such as DH_2 and HD_2. The conical intersection line L is for these cases still a straight line, but no longer coincides with OY. It lies instead in the symmetry place OYZ_λ of Fig. 5 for $A_\nu \equiv A_\kappa$ and makes and angle θ_L with OY in the 0 to $\pi/2$ range, given by

$$\cos\theta_L = \frac{[3(1 + 2M_B/M_A)]^{1/2}}{2 + M_B/M_A} \tag{187}$$

For $M_A > M_B$, L tilts toward the positive OZ_λ axis, whereas for $M_A < M_B$ it tilts away from it. For DH_2, θ_L is 11.5° and the tilt is toward OZ_λ, whereas for HD_2 it is 14.5° and the tilt is away from OZ_λ. A loop around OY with constant $\bar{\rho}$ and θ encloses the conical intersection point $\bar{P}$ if $\theta > \theta_L$ but not otherwise. At low energies, χ^{ad} (**R**) does not sample regions for which θ is low, because $V(\bar{\rho}, \theta, \varphi_\lambda)$ is high for such regions. For example, for the DH_2 system and total energies $E \leq 1.8$ eV, χ^{ad} (**R**) is non-negligible only in regions for which $\rho \geq 2$ bohr. For such values of ρ, $V(\rho, \theta = 11.5°, \varphi_\lambda) > 3$ eV. As a result, for these E, regions of **q** space for which $\theta < \theta_L$ are highly classically forbidden, and χ^{ad} (**R**) is essentially zero inside of them. Under these conditions, loops around OY through regions for which χ^{ad} (**R**) is not negligible always enclose conical intersection configurations and must change sign, just as for H_3. Similar considerations are valid for HD_2 for $E \leq 1.6$ eV. We conclude that the use of basis functions $g^{III}_{p\lambda\Omega_\lambda}(\varphi_\lambda; \bar{\rho})$ which satisfy (181) constitutes an accurate way of including the effect of the geometric phase for DH_2 and HD_2 for $E \leq 1.8$ eV and $E \leq 1.6$ eV respectively.

For substantially higher energies, or for less symmetric systems, this methodology must be modified appropriately. One approach is to replace the hyperspherical coordinates θ, φ_λ by new variables $\bar{\theta}$, $\bar{\varphi}_\lambda$ orthogonal to and having the same ranges of definition as the old ones. We impose the condition that loops generated by varying $\bar{\varphi}_\lambda$ over a 0 to 2π range while keeping $\bar{\rho}$ and $\bar{\theta}$ constant always enclose the $\bar{P}$ conical intersection point, independently of the values of $\bar{\rho}$ and $\bar{\theta}$. It is always possible to obtain such $\bar{\theta}$, $\bar{\varphi}_\lambda$. To enforce the conical intersection boundary conditions we use a basis set $\bar{g}^{III}_{p\lambda\Omega_\lambda}(\varphi_\lambda; \bar{\rho})$ which satisfy (181) with φ_λ replaced by $\bar{\varphi}_\lambda$. Similarly, we replace the basis set $f^{\Omega_\lambda}_n(\theta; \bar{\rho})$ by another one, $\bar{f}^{\Omega_\lambda}_n(\bar{\theta}; \bar{\rho})$. The old variables θ, φ_λ are now known functions of the new ones $\bar{\theta}$, $\bar{\rho}_\lambda$. We need to evaluate matrix elements of functions of θ, φ_λ and of differential operators involving these two variables, in the representation formed by the direct product of the new basis sets. The corresponding numerical quadratures can be performed using either θ, φ_λ or $\bar{\theta}$, $\bar{\varphi}_\lambda$ as integration variables. The Hamiltonian is still expressed in the old variables. This approach to treating the GP effect is conceptually sound not only for the H_3 isotopomers, but for other triatomic systems as well, but has not been tried out yet. Regardless of the presence or not of conical intersections, the problems associated with Eckart singularities mentioned at the end of Sec. IV.B must be dealt with for each new system considered.

V. APPLICATIONS TO ISOTOPIC TRIHYDROGEN SYSTEMS

A. H_3

As stated above, the H_3 system displays a conical intersection between its ground and first excited adiabatic electronic states for equilateral triangle geometries [1, 18, 30, 59]. The method used to take this effect into account for reactive scattering on its ground PES has been summarized in Sec. IV, and more details are given elsewhere [12]. We highlight here some of the results obtained performing accurate calculations on this system using the LSTH PES [60, 61].

For relatively low total energies E (in the 0.7 to 1.5-eV range with respect to the bottom of the isolated H_2 diatom well), para → ortho and ortho → para integral and differential cross sections are essentially not affected by the presence of the conical intersection [12]. However, para → para and ortho → ortho differential cross sections are strongly affected, as exemplified in Fig. 6. Inclusion of the GP effect results in a

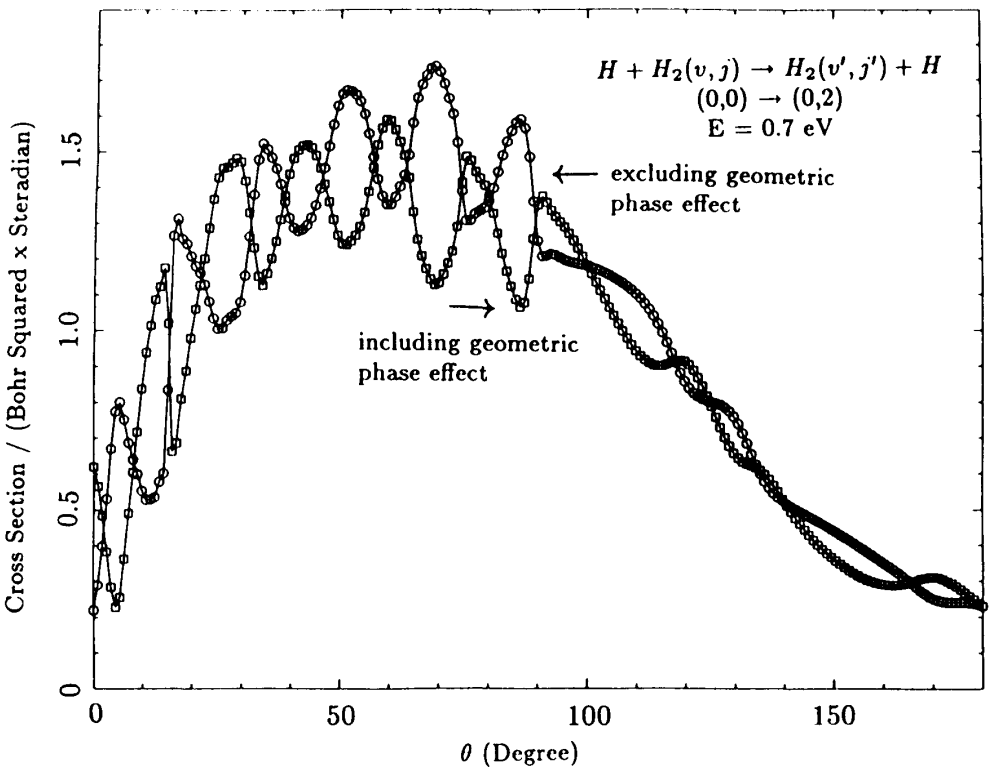

Figure 6 Degeneracy-summed differential cross sections for the H + H_2 (v = 0, j = 0) → H_2 (v' = 0, j' = 2) + H reaction, at a total energy of 0.7 eV, as a function of scattering angle. The squares (circles) correspond to the GP (NGP) calculations. (From Ref. 12).

change of the phase of the oscillations of those cross sections with angle, even for E as low as 0.7 eV. This phenomenon results from interferences between the direct and exchange scattering amplitudes. The calculations show that at this energy, the GP does not change the direct scattering amplitude, but changes the sign of the exchange one, in agreement with a semiclassical model [62]. These results are predictive of what will be found experimentally once measurements of such cross sections are made. These predictions differ from those of all other calculations for this system, since the latter were made without inclusion of the GP effect. Such measurements are highly desirable. The corresponding effect on the degeneracy summed-and-averaged integral cross sections is also significant, enhancing it by about 30% for the H + H_2 (v = 0, j = 0) → H_2 (v' = 1, j' = 2) + H transition at E = 1.2 eV when compared with the corresponding NGP cross section. The existence of such interference effects for triatomic systems between direct and exchange scattering amplitudes is restricted to the case in which the three atoms are identical, such as H_3, D_3, and Li_3.

It should be kept in mind that the lowest conical intersection energy for this system is 2.75 eV [30]. As a result, the effect of the nonadiabatic coupling between the adiabatic ground and first excited electronic states, due to the $\mathbf{W}_{i,j}^{(1)ad}(\mathbf{R})$ and $W_{i,j}^{(2)ad}(\mathbf{R})$ terms of the first of (69), is negligible for the geometries $\mathbf{R}$ sampled at these relatively low energies by $\chi_i^{ad}(\mathbf{R})$ because they are far from the conical intersection geometries. The effect of this conical intersection at such energies is entirely due to the geometric phase and the ensuant boundary conditions; it is present, when the adiabatic electronic wave functions

are real, even when these coupling matrices vanish identically, as was assumed in the present calculations. As such, it is an effect that resembles the Pauli principle for electron exchange, which is also independent of the strength of the interaction between the atoms comprising a molecular system.

For E in the range of 1.8 to 2.3 eV [36], still significantly below the lowest conical intersection energy, large GP effects are also found in para → ortho and ortho → para integral cross sections. In particular, product rotational state distributions can change appreciably, as depicted in Figs. 7 and 8. These distributions are compared to the experimental results of Zare and co-workers for the D + H_2 system [63–66] and to calculations on this system performed without including the GP effect [64]. The differences found for H_3 between the GP and the NGP results mimic surprisingly well the differences between the experimental D + H_2 results and the theoretical NGP ones. The physical mechanism responsible for the GP effect in the H_3 system, as well as in the DH_2 system that is further discussed in Sec. V.B, can be explained with the help of Fig. 9. This figure displays two kinds of exchange paths going from the A + BC region of internal nuclear configuration space to the AB + C one. The first kind (full line) corresponds to a direct approach of A to B, formation of the A–B bond and concurrent rupture of the B–C

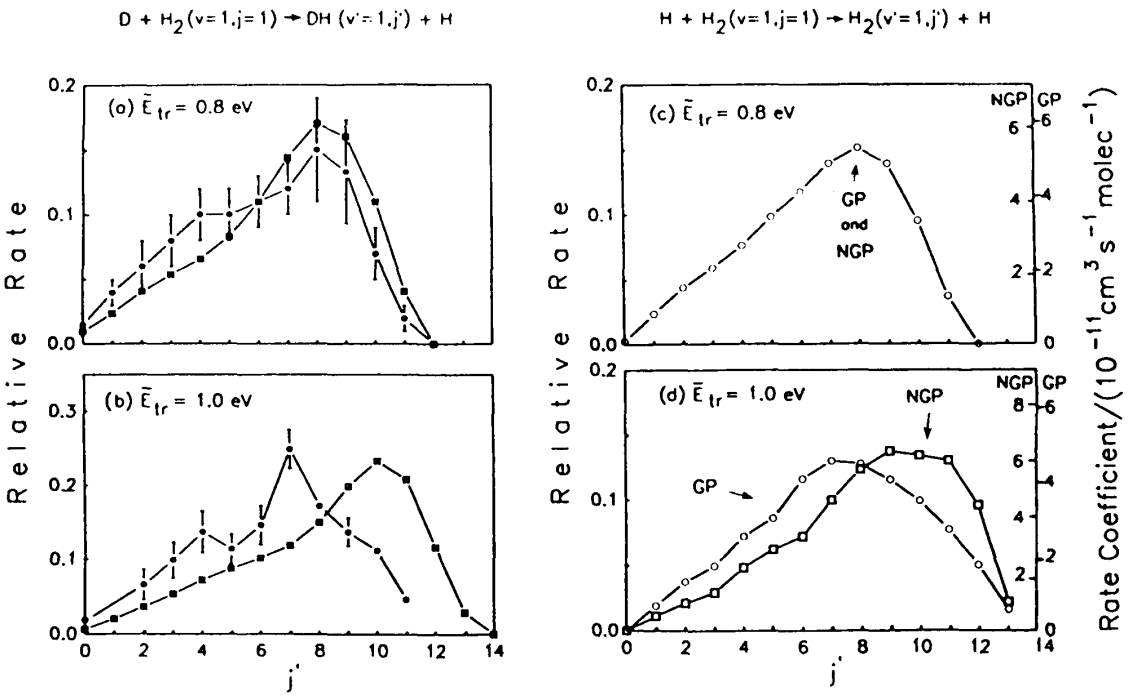

Figure 7 (a) Comparison of theoretical and experimental rates (products of initial relative velocities by integral cross sections) as a function of the product rotational state quantum number j' for D + H_2 (v = 1, j = 1) → DH (v' = 1, j') + H at an average initial relative translational energy E_{tr} = 0.8 eV (average total energy E = 1.6 eV). The solid circles represent the experimental results of Ref. 66. Solid squares are NGP theoretical values of Ref. 64. (b) Same as for panel (a), with E_{tr} = 1.0 eV (E = 1.8 eV) and Ref. 65 for the experimental results. (c) GP and NGP calculations for H + H_2 (v = 1, j = 1) → H_2 (v' = 1, j' = 1) + H at E_{tr} = 0.8 eV (E = 1.6 eV), treating one of the three H atoms as having nuclear spin 1 and excluding direct scattering contributions, for the purpose of comparison with the D + H_2 reaction. (d) Same as for panel (c), with E_{tr} = 1.0 eV (E = 1.8 eV). The open circles (squares) represent the GP (NGP) results. (From Ref. 36.)

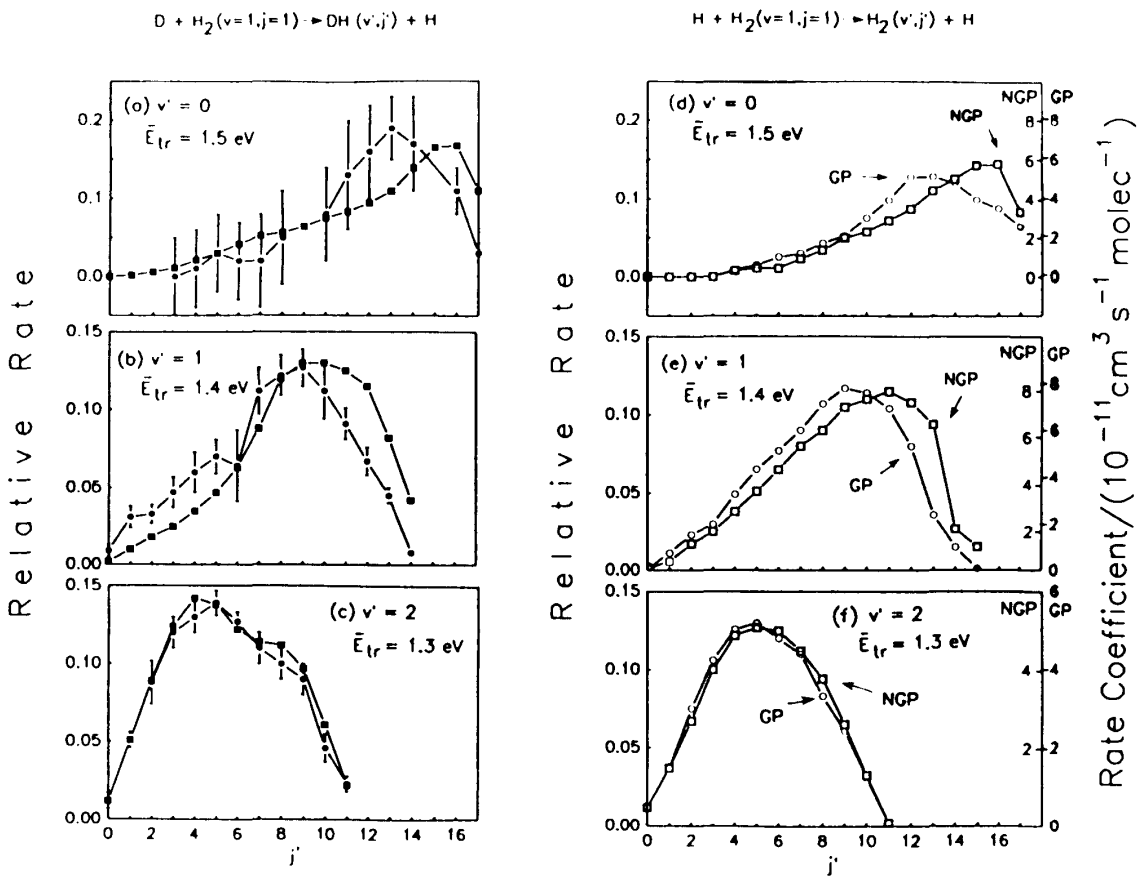

Figure 8 Comparison of experimental rates as a function of the product rotational state quantum number j' for D + H_2 (v = 1, j = 1) → DH (v', j') + H with the theoretical NGP results for this reaction and with the theoretical GP and NGP results for H + H_2 (v = 1, j = 1) → H_2 (v', j') + H at E_{tr} = 1.3 eV, 1.4 eV and 1.5 eV (E = 2.0 eV, 2.1 eV, and 2.2 eV) and for the v' values indicated. The symbols, references and explanations are otherwise the same as those for Fig. 7. (From Ref. 36.)

bond, followed by the motion of C away from the newly formed AB molecule. The second kind (dashed line), which becomes more prevalent as the energy increases, moves around the Y axis, which is, as stated in Sec. IV.C, the locus of H_3 conical intersection configurations. This corresponds to A first approaching the C end of the BC molecule, forming an incipient bond with that atom while relaxing the B–C bond, then strengthening the A–B bond while concomitantly breaking the B–C one, atom C finally receding from AB. The effect of the conical intersection on the semiclassical phases of each of these two kinds of paths is different, and in the case of the dashed path depends on the detailed regions of configuration traversed. As a result, and as depicted in Figs. 10 and 11, the degeneracy-summed-and-averaged state-to-state para → ortho and ortho → para integral cross sections display interferences due to these two kinds of exchange paths. The details of these interferences depend on whether the GP effect is included. It should be noticed that this explanation is qualitative but that the calculations reported [36] were done accurately (benchmark quality) using the methods described in Sec. IV, without any use of paths or of semiclassical approximations.

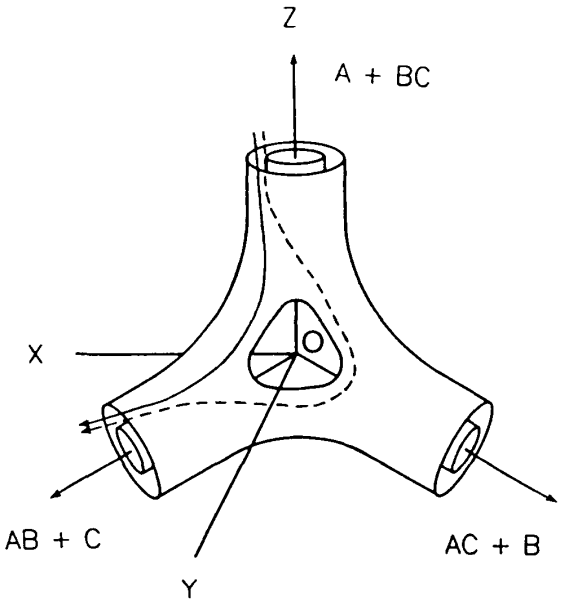

Figure 9 This figure depicts two kinds of semiclassical paths which contribute to the exchange scattering amplitude for a triatomic system ABC. An equipotential energy surface for the ground adiabatic electronic state of H_3 is represented. The *OXYZ* frame is the same as the $OX_\lambda YZ_\lambda$ frame of Fig. 5 with the λ subscript suppressed. The conical intersection configurations for H_3 (equilateral triangles) are represented by points on the *OY* axis. The dashed path partially encircles the conical intersection line, whereas the solid one does not. (From Ref. 36.)

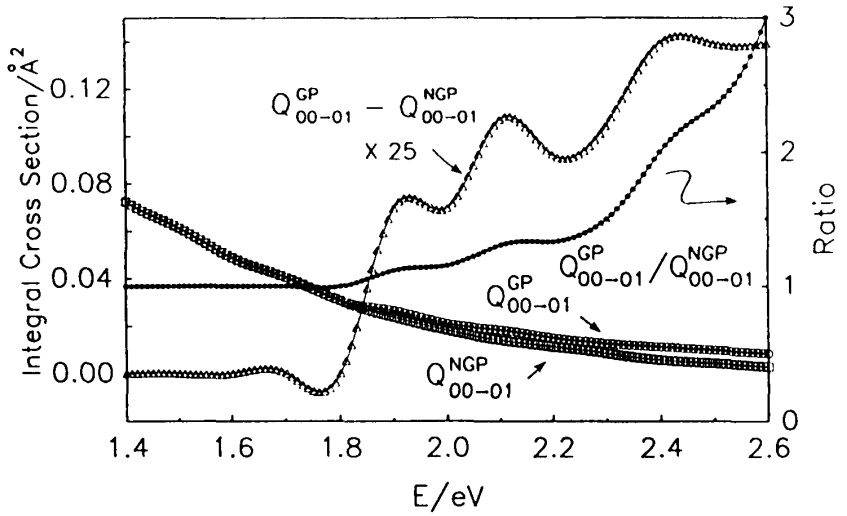

Figure 10 Degeneracy-summed integral cross sections for the H + H_2 (v = 0, j = 0) → H_2 (v' = 0, j' = 1) + H as a function of total energy. The open circles (squares) depict the GP (NGP) results. The open triangles represent the difference between the GP and NGP cross sections, multiplied by a factor of 25 before plotting. The full circles represent their ratio, and correspond to the coordinate scale at the right of the figure. (From Ref. 36.)

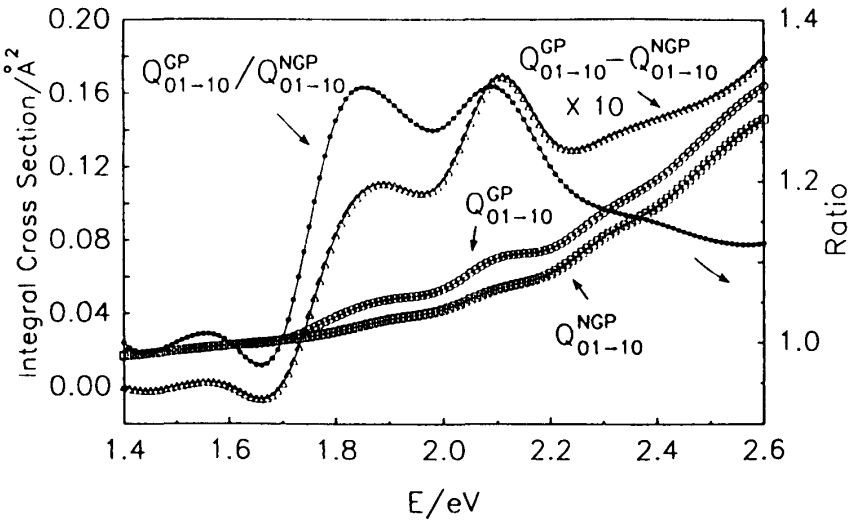

Figure 11 Degeneracy-averaged integral cross sections for the H + H_2 (v = 0, j = 1) → H_2 (v' = 1, j' = 0) + H reaction as a function of total energy. The symbols have the same meaning as in Fig. 10. (From Ref. 36.)

B. DH_2

The same equilateral triangle conical intersection which exists for the H_3 system also exists for its isotopomer DH_2. However, in the mass-scaled internal configuration space $\mathbf{q} \equiv (\rho, \omega_\lambda, \gamma_\lambda) \equiv (\rho, \theta, \varphi_\lambda)$ of Figs. 5 and 9, for $A_\lambda + A_\nu A_\kappa$ and A + BC particularized to D + H_2, $V(\mathbf{q})$ displays S_2 permutation group symmetry, with OYZ of Fig. 9 being a plane of symmetry for A + B_2, rather than S_3 symmetry (isomorphic with C_{3v}) symmetry. The conical intersection line is, as mentioned in Sec. V.A., a straight line in that symmetry plane, making an angle of 11.5° with the OY axis and tilted towards the negative part of the OZ axis. In addition, the angle between the positive OZ axis, which is associated with the asymptotic D + H_2 (A + BC) configuration and its DH + H (AB + C) counterpart is no longer 120° as it was for the H_3 system, but 109° instead, because of the mass-scaling of the Jacobi coordinates given by (51). The Γ irreducible representations of S_2 are A for wave functions symmetric with respect to reflection through OYZ and B for wave functions which are antisymmetric under that reflection.

Accurate GP and NGP calculations for the DH_2 system were performed in the total energy range 0.78 eV ≤ E ≤ 1.8 eV [46], using the LSTH PES [60, 61]. Up to 1440 even-parity and 1260 odd-parity LHSFs were used in (174) for each irreducible representation and total angular momentum, for a total of 5400 LHSFs. The maximum J was 42. Rotational state distribution measurements for the D + H_2 reaction were made by Zare and co-workers [63–66], as indicated in Sec. V.A. For the D + H_2 (v = 1, j = 1) → DH (v' = 1, j') + H process at E = 1.8 eV, there is a significant difference between the experimental results and the NGP calculations [64]. Experiment [65] and both GP and NGP theory [46] are compared in Fig. 12. The NGP results agree with previous ones [64], but show a significant disagreement with the experimental ones, well outside experimental error. The GP results, on the other hand, agree well with experiment, displaying a maximum at j' = 7. The small remaining differences may be due to residual systematic experimental errors, not reflected by the error bars. These results leave little

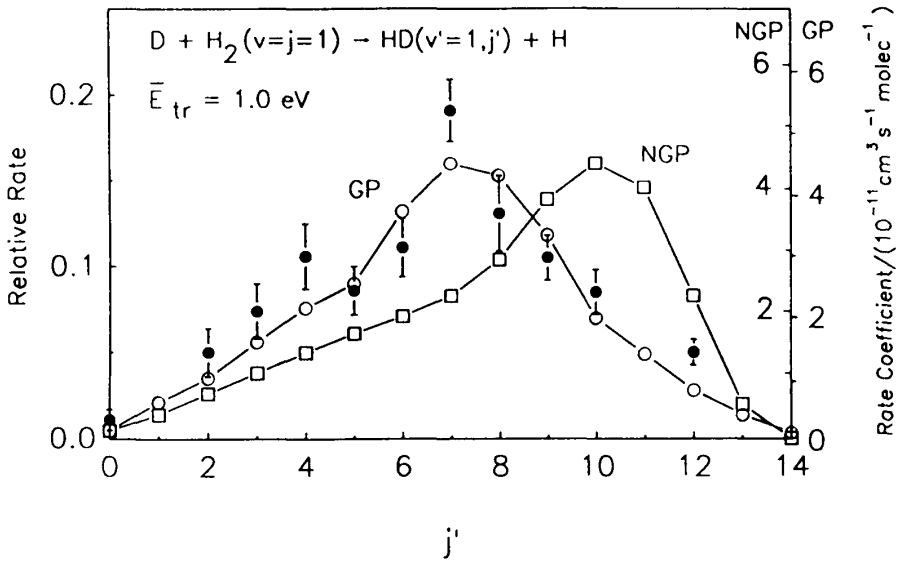

Figure 12 Comparison of theoretical and experimental rates (products of initial relative velocities by integral cross sections) as a function of rotational state quantum number j' for D + H_2 (v = 1, j = 1) → DH (v' = 1, j') + H for an average initial relative translational energy E = 1.0 eV (average total energy E = 1.8 eV). The solid circles display the same experimental results of Ref. 65 depicted in Fig. 7b. The open squares (circles) represent the NGP (GP) calculations. (From Ref. 46.)

doubt that the experiments are essentially correct and that the GP effect plays an important role for this process. Differential cross sections for the D + H_2 (v = 1, j = 1) → DH (v' = 1, j') + H reaction for j' = 5 through 10 are displayed in Fig. 13. As can be seen, large differences between the GP and NGP results occur. This is not surprising, given the differences in the corresponding integral cross sections shown in Fig. 12 and the fact that differential cross sections are usually more sensitive to the details of the dynamics than are integral ones. The GP curves in Fig. 13 are predictive of what the results of measurements, not yet performed, should be. The only source of inaccuracy of the calculations, other than the small and controlable computational errors associated with the numerical methods employed, is the inaccuracy of the LSTH PES used [60, 61]. This PES is estimated to have an absolute accuracy of about 0.5 kcal/mole (0.022 eV) and an accuracy for differences of about 0.2 kcal/mole (0.009 eV) over the entire range of nuclear configurations of interest. Barring the existence of a resonance in the neighborhood of E = 1.8 eV (see Sec. V.C), the GP curves of Fig. 13 are expected to be quite close to those which should result from good state-to-state differential cross-section measurements. Such measurements would be very important for comparing experiment and theory.

C. HD_2

The HD_2 system is computationally a much more difficult one than the isotopically reversed DH_2 one. The reason is that, at a given total energy, there are many more accessible D_2 rovibrational states than there are H_2 ones, requiring therefore a much larger number of channels (i.e., terms) in the LHSF expansion of (174). Recent differential cross-section measurements for the H + D_2 reaction [67, 68] have stimulated accurate

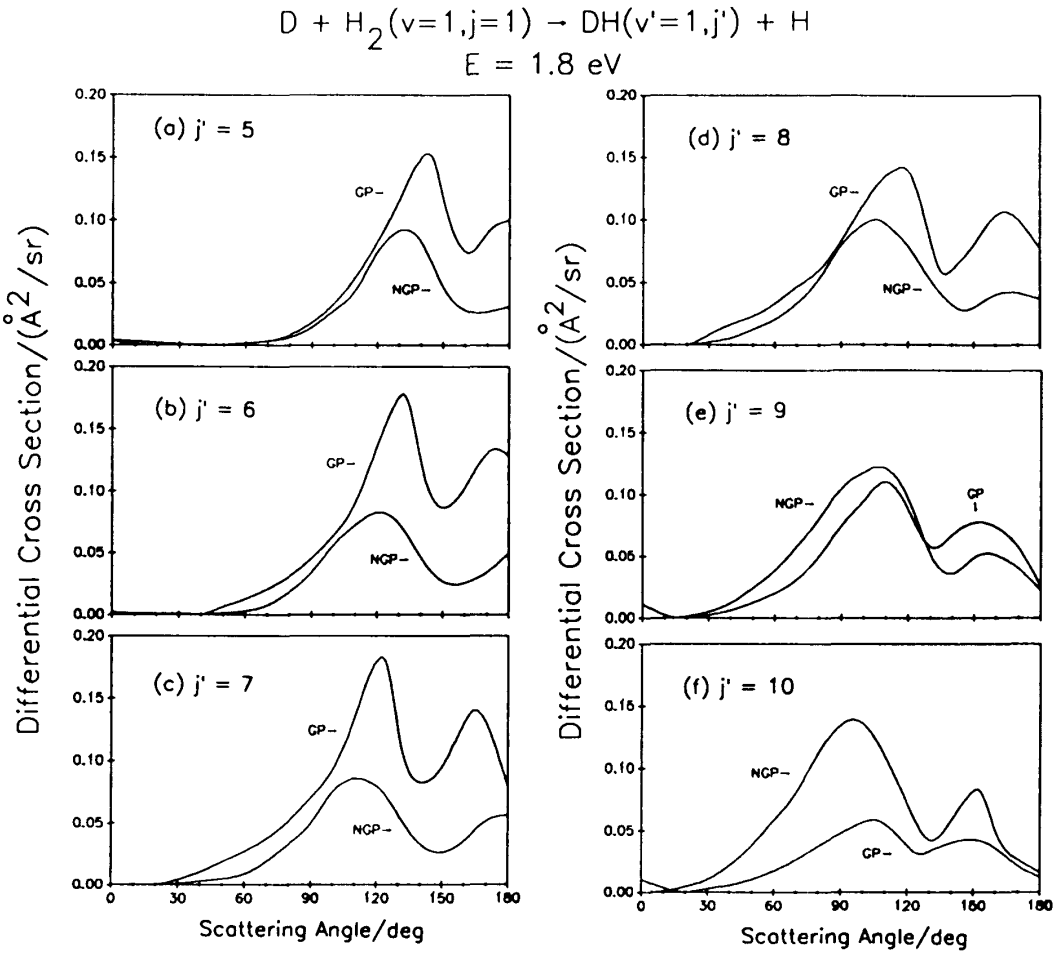

Figure 13 Theoretical GP and NGP differential cross sections at E = 1.8 eV for D + H_2 (v = 1, j = 1) → DH (v' = 1, j') + H. Panels (a) through (f) display the results (multiplied by 5 before plotting) for j' = 5 through 10, respectively. (From Ref. 46.)

GP (and NGP) calculations on this system to be performed over the total energy range 1.42 eV ≤ E ≤ 1.53 eV [47, 48] which encompasses the energies of 1.47 eV [68] and 1.48 eV [67] at which the experiments were performed. The maximum number of channels used in (174) for any of the Π, Γ, and J combinations was 2012, and the maximum value of J was 46, corresponding to a total of approximately 7500 LHSFs. At E = 1.53 eV, there are 1042 v, j, m open states for D_2 and 543 for HD.

The differential cross sections (DCSs) for the H + D_2 (v = 0, j = 0) → HD (v' = 0, j') + D at E = 1.48 eV are given in Fig. 14 as a function of j' and of the scattering angle, both for the GP and NGP cases [47]. These two sets of results differ significantly. In particular, the scattering angles at which the peaks in the NGP DCSs occur increase nearly linearly from 0° to 110° as j' increases from 0 to 12, whereas those for the GP DCS change more slowly as j' varies from 0 to 5 than from 6 to 12. As a result, the sum of these DCSs over all j' shows a clearly discernible peak between 0° and 45° for the GP results, whereas the NGP one is quite flat in this angular range. This is due to the presence, in the GP results, of a Feschbach resonance in the neighborhood of this energy for the LSTH PES, whereas the NGP ones do not display such a resonance, as

$$H + D_2(v=0,j=0) \rightarrow HD(v'=0,j') + D$$

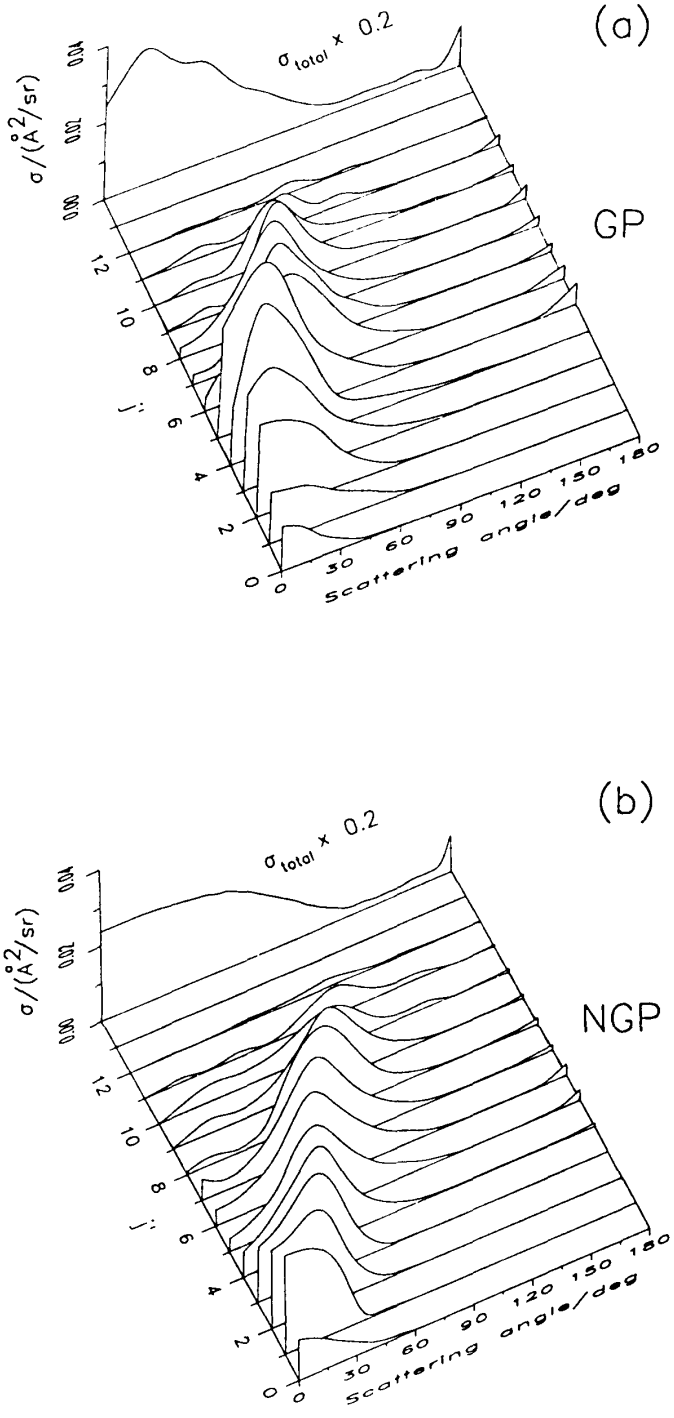

Figure 14 Degeneracy-summed GP and NGP differential cross sections for the H + D_2 (v = 0, j = 0) → DH (v' = 0, j') + D reaction as a function of j' and of the scattering angle between the direction of the initial center-of-mass H atom velocity vector and the final center-of-mass D atom velocity vector. (This is the supplement of the usual scattering angle, and has been chosen to facilitate comparison with experiment.) The total energy is E = 1.481 eV and the initial relative collision energy is E_{tr} = 1.290 eV. The curves labeled total are the sums of these DCSs over all j' and have been multiplied by 0.2 before plotting. (From Ref. 47.)

described below. The LSTH surface is, however, not sufficiently accurate for the resonance energy predicted to be reliable, as further discussed in the rest of this subsection.

The GP and NGP degeneracy-summed differential cross section for the H + D_2 ($v = 0, j = 0$) → HD ($v' = 0, j'$) + D reaction is given as a function of E and of the scattering angle in Fig. 15, for $j' = 4$, 5, and 6 [48]. The GP plots show significantly more structure as a function of E than do the NGP ones. In particular, for $j' = 5$ the GP DCS has a backward peak at $E = 1.484$ eV and scattering angle 163°with a fwhm of 41 meV and a forward one at $E = 1.502$ eV and scattering angle 0° with a fwhm of 21 meV. By contrast, the NGP DCS shows near constancy or only a slow monotonic decrease with energy at all angles over the energy range considered. The energy dependence of the $j' = 5$ GP DCS is strongly suggestive of a resonance, whereas that of the NGP indicates none.

The degeneracy-summed resonance timedelays for the same processes of Fig. 15 are given in Fig. 16, also as a function of E and of the scattering angle. The $j' = 5$ GP plot displays a backward peak of 156 fs and a forward one of 98 fs, whereas the corresponding NGP resonance timedelay is everywhere zero within the accuracy of the plots. This confirms the resonance nature of the structure observed in the $j' = 5$ GP DCS. The absence of a resonance in the NGP calculations does not mean that they cannot in general display such resonances. It means, instead, that the corresponding resonance energy, if it exists, is shifted to an energy outside the range considered in these calculations and/or to a different transition

Some recent calculations have been done (Y.-S.M. Wu and A. Kuppermann, unpublished results) using an improved version of the BKMP PES for the ground adiabatic electronic state of H_3 [69]. We refer here to this as yet unpublished PES as the BKMP2 PES.* Its barrier height is 9.61 kcal/mole, which is 0.2 kcal/mole (0.009 meV) lower than that of the LSTH PES. This value is in excellent agreement with the barrier height of 9.61 kcal/mole also, obtained from an exact quantum Monte Carlo calculation [70] having an absolute error of ± 0.01 kcal/mole. Although the BKMP2 barrier is only 9 meV lower than that of the LSTH PES, the corresponding resonance is shifted downwards in energy by 55 meV, a decrease six times greater than the saddle point energy decrease. The reason is that other features of the PES that are important for determining the resonance energy, such as curvatures in directions transverse to the minimum energy path, are also different. The corresponding timedelays are about 3 times less than the LSTH ones. This very large sensitivity of the resonance energy and timedelay to small changes in the PESs involved is indicative that these resonances have spectroscopic-like characteristics that may permit a determination of the topography of those surfaces. This is an exciting prospect. It also suggests that if by saying that an ab initio PES is chemically accurate we mean that it is capable of predicting dynamic properties of the system within experimental accuracy, then 0.2 kcal/mole (9 meV) can no longer be considered a standard of chemical accuracy, at least for H_3 and its isotopic counterparts. A more appropriate standard of accuracy for this system may be about 0.01 kcal/mole (0.4 meV), a standard just being achieved by the exact quantum Monte Carlo method [70] but not by the presently existing variational molecular quantum mechanics codes.

*The author thanks A. I. Boothroyd, P. G. Martin, and W. J. Keogh for making the new BKMP2 H_3 PES available prior to publication.

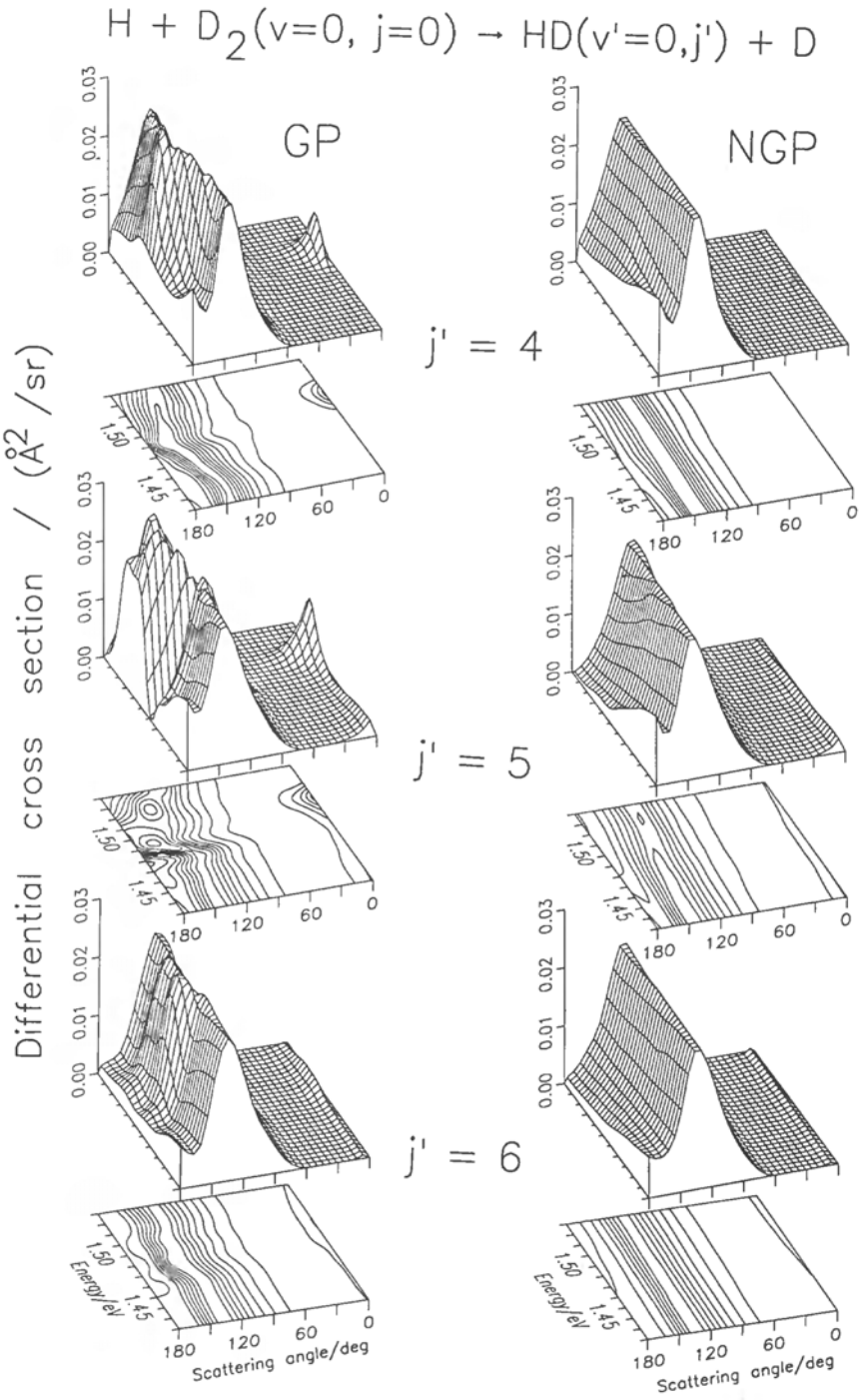

Figure 15 Degeneracy-summed GP and NGP differential cross sections for the H + D_2 (v = 0, j = 0) → HD (v' = 0, j') + D reaction as a function of total energy (measured with respect to the bottom of the isolated D_2 well) and of the center-of-mass scattering angle of the HD molecule product. Results are shown for j' = 4, 5, and 6. The contour lines displayed at the bottom of the plots range from 0.004 to 0.028 Å^2/sr in steps of 0.004 Å^2/sr. (From Ref. 48.)

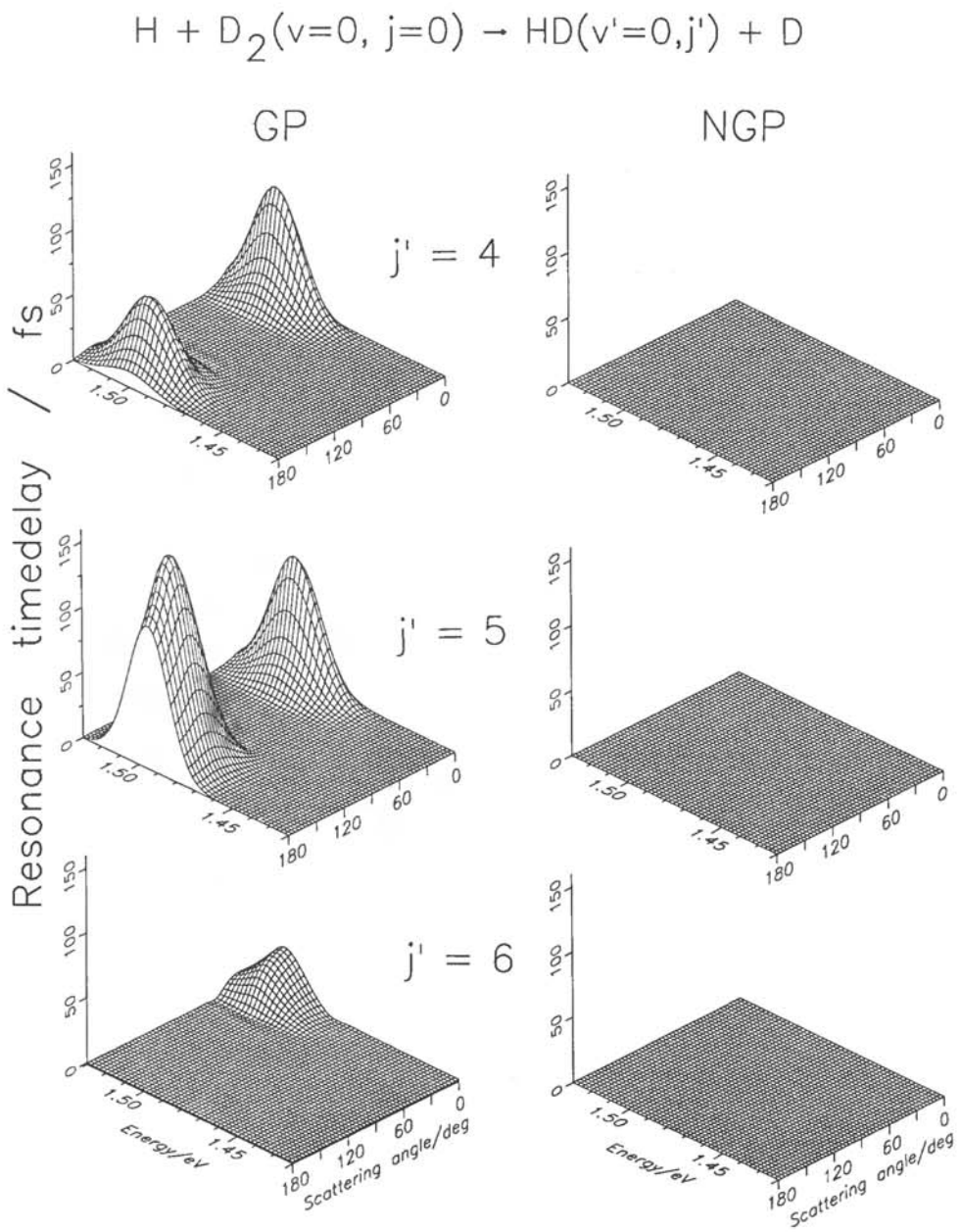

Figure 16 Degeneracy-summed GP and NGP resonance time delays for the H + D_2 (v = 0, j = 0) → HD (v' = 0, j') + D reaction. The horizontal axes and other labels are the same as in Fig. 15. (From Ref. 48.)

VI. CONCLUSIONS

For systems displaying a conical intersection between its ground and first excited adiabatic electronic states, the first-derivative coupling element between those states has a singularity at the conical intersection nuclear geometries. In spite of this, the one-adiabatic-electronic-state approximation still provides an accurate description of the system's nuclear motion, if the total energy is sufficiently below the lowest conical intersection energy for the nuclear motion wave function to be negligible in the vicinity of that

intersection. Special care, however, must be exercised in using such one-state approximation. This can be done by two distinct but equivalent approaches.

1. The system's ground state adiabatic electronic wave function can be forced to be real. In this case, it changes sign discontinuously as the system undergoes pseudorotations around conical intersection geometries. In order that the orbital electronuclear wave function be single-valued, the corresponding nuclear wave function must undergo a compensating discontinuous change in sign upon such pseudorotations, but otherwise the nuclear motion Schrödinger equation (SE) is unaltered. This change of sign boundary condition is called the geometric phase (GP) effect. For triatomic systems whose conical intersection geometry is an equilateral triangle or close to it, the use of symmetrized hyperspherical coordinates in the description of the nuclear motion makes the imposition of this condition very simple, affecting only one of these six coordinates. This kind of boundary condition is very different from the usual one appropriate for systems not displaying a conical intersection, namely, that the corresponding nuclear wave-function (associated with a real electronic wave function) be a single-valued and continuous function of the nuclear coordinates. The conical intersection boundary condition on the nuclear wave function must be enforced even at such low energies that that wave function is negligible even quite far away from the conical intersection geometries; significant errors can result if such a boundary condition is not imposed.

2. The system's ground state adiabatic electronic wave function is allowed to have a nuclear-configuration-dependent complex phase and required to be a single-valued and continuous function of the nuclear coordinates. In this case, the nuclear wave function is also required to be a single-valued and continuous function of those coordinates. The resulting nuclear motion SE differs from the usual one by the appearance of a first-derivative term proportional to the gradient of the phase angle and of a shift in the potential energy function proportional to the diagonal ground state second-derivative coupling matrix element. In addition, that gradient has a pole at the conical intersection configurations. This modified SE is analogous to the one which describes the motion of a charged particle in the presence of a highly localized magnetic field. If the system does not approach too closely any conical intersection geometry, this pole does not present any serious numerical difficulties. The presence of a first derivative term has, however, the disadvantage of slowing down the most efficient methods used for the integration of the systems of second order differential equations that result from the coupled-channel expansion of the nuclear motion SE.

Extensive calculations of state-to-state integral and differential cross sections for the H_3, DH_2, and HD_2 systems at sufficiently low energies for the one-state approximation to be highly accurate have been performed. All of these calculations have employed the first of the two approaches just described, and used the symmetrized hyperspherical coordinate propagation methodology. This methodology is very convenient for enforcing the conical intersection boundary condition when the intersection geometry is close to an equilateral triangle. An analysis of the results obtained shows a large influence of the GP effect, such that its neglect results in very substantial errors. This is specially true for state-to-state differential cross sections, for which the importance of the GP becomes more pronounced at lower energies than it does for the corresponding integral cross sections. For other systems displaying conical intersections, one should not neglect the GP effect without very careful analysis.

As the system's energy increases, the accuracy of the one-state approximation decreases, and it becomes necessary to use the two-state approximation. This can be done

in the adiabatic-electronic-state representation, for which the two approaches described above continue to be valid. In the first, the two adiabatic electronic state wave functions are forced to be real, and as a result both undergo a discontinuous change in sign as the system executes pseudorotations around conical intersection geometries. The corresponding two nuclear wave function coefficients are then also required to change sign discontinuously upon such pseudorotations, resulting in the usual two coupled nuclear motion equations, but with the unusual change of sign boundary condition. These equations involve first derivative coupling terms whose coefficients diverge at conical intersection configurations. Since such configurations are accessible at the energies of interest, this presents a major difficulty. In the second approach a complex phase is introduced and results in coupled nuclear motion equations displaying a pseudomagnetic field. These equations have first-derivative coupling terms whose coefficients diverge at conical intersection configurations just as in the first approach, and present similar difficulties.

An alternative to the adiabatic representation is the diabatic one. In the latter, a suitable transformation is found which eliminates the diverging part of the first-derivative coupling matrix that appears in the first approach just described. The remaining part is usually small, can be neglected initially, and reintroduced perturbatively, if deemed necessary, after the equations omitting it are solved. The diabatic electronic and nuclear wave functions which result from this transformation are single-valued continuous functions of the nuclear coordiantes, i.e., do not change sign upon pseudorotations of the system around the conical intersection. This diabatization approach is the method of choice in the two-state approximation. In attempting to use it in the one-adiabatic-electronic-state approximation, however, it presents the serious disadvantage of generating a system of two nuclear diabatic wave-function equations whose coupling cannot be neglected. This unnecessarily increases in a significant way the computational effort required for solving the nuclear motion problem. The method of choice, in this case, is to retain the real electronically adiabatic one-state representation and use the change-of-sign boundary condition.

All these considerations were made assuming that the spin-containing terms in the system's Hamiltonian vanish. If they do not, but are small, they can be introduced after the fact by perturbative methods.

In conclusion, the conceptual aspects of the geometric phase effect for conically intersecting systems seem now to be well understood. It is important to include this effect not only for bimolecular reactions but also for photodissociation processes occurring in these systems, unless a careful analysis shows it to be nonsignificant.

NOTES

1. The components of $\mathbf{R}_{\lambda_1}$ and $\mathbf{R}_{\lambda_2}$ in the bfλ system are

$$X_{\lambda 1}^{bf\lambda} = R_{\lambda 1} \sin \gamma_\lambda \qquad Y_{\lambda 1}^{bf\lambda} = 0 \qquad Z_{\lambda 1}^{bf\lambda} = R_{\lambda 1} \cos \gamma_\lambda$$
$$X_{\lambda 2}^{bf\lambda} = 0 \qquad Y_{\lambda 2}^{bf\lambda} = 0 \qquad Z_{\lambda 2}^{bf\lambda} = R_{\lambda 2}$$

2. The components of $\mathbf{R}_{\lambda_1}$ and $\mathbf{R}_{\lambda_2}$ in the $I\lambda$ frame are [12]

$$X_{\lambda 1}^{I\lambda} = -\rho \sin(\pi/4 - \theta/2) \cos(\varphi_\lambda/2) \qquad Y_{\lambda 1}^{I\lambda} = 0 \qquad Z_{\lambda 1}^{I\lambda} = \rho \cos(\pi/4 - \theta/2) \sin(\varphi_\lambda/2)$$
$$X_{\lambda 2}^{I\lambda} = \rho \sin(\pi/4 - \theta/2) \sin(\varphi_\lambda/2) \qquad Y_{\lambda 2}^{I\lambda} = 0 \qquad Z_{\lambda 2}^{I\lambda} = \rho \cos(\pi/4 - \theta/2) \cos(\varphi_\lambda/2)$$

   Given their cartesian components in the sf frame, these expressions determine a_λ, b_λ, c_λ uniquely (in their respective ranges of definition) and therefore specify both the directions and the senses of the $I\lambda$ axes.

3. As a result, the function $D_{M\Omega_\lambda}^{II}$ of (175) is multiplied by $(-1)^{II}$ and the products just mentioned must change by a factor of $-(-1)^{II}$.

ACKNOWLEDGMENTS

This work was supported in part by National Science Foundation Grant No. CHE 9311401. Some of it was performed while the author was a visitor in the CNRS group of Jean-Michel Launay and Maryvonne LeDorneuf at the Department of Atoms and Molecules in Astrophysics, Paris Observatory, Meudon, France, during part of 1992. He wishes to thank them for their kind hospitality and the CNRS for support during that visit.

REFERENCES

1. G. Herzberg and H. C. Longuet-Higgins, Intersection of potential energy surfaces in polyatomic molecules, *Discussion Faraday Soc. 35*: 77 (1963).
2. H. C. Longuet-Higgins, The intersection of potential energy surfaces in polyatomic molecules, *Proc. R. Soc. Lond. A 344*: 147 (1975).
3. H. A. Jahn and E. Teller, Stability of polyatomic molecules in degenerate electronic states. I: Orbital degeneracy, *Proc. R. Soc. A 161*: 220 (1937).
4. P. G. Carrick, A. J. Merer, and R. F. Curl, $\tilde{A}^2\Pi \leftarrow \tilde{X}^2\,\Sigma^+$ infrared electronic transition of C_2H, *J.Chem. Phys. 78*: 3652 (1983).
5. W. B. Yan, J. L. Hall, J. W. Stephens, M. L. Richnow, and R. F. Curl, Color center laser spectroscopy of excited C_2H, *J.Chem Phys. 86*: 1657 (1987).
6. C. Petrongolo, G. Hirsch, and R. J. Buenker, Diabatic representation of the $\tilde{A}^2A_1/\tilde{B}^2B_1$ conical intersection in NH_2, *Mol. Phys. 70*: 835 (1990).
7. G. Hirsch, R. J. Buenker and C. Petrongolo, Ab initio study of NO_2. II: Non-adiabatic coupling between the two lowest $^2A'$ states and the construction of a diabatic representation, *Mol. Phys. 70*: 835 (1990).
8. D. C. Robie, M. Hunger, J. L. Bates, and H. Reisler, Product state distributions in the photodissociation of expansion-cooled NO_2 near the $NO(X^2\Pi)v = 1$ threshold, *Chem. Phys. Lett. 193*: 413 (1992).
9. S. P. Walch and R. J. Duchovic, Theoretical characterization of the potential-energy surface for $H + O_2 \leftrightarrow HO_2^* \leftrightarrow OH + O$. III: Computed points to define a global potential-energy surface, *J. Chem. Phys. 94*: 7068 (1991).
10. B. Kendrick and R. T. Pack, Potential energy surfaces for the low-lying $^2A''$ and $^2A'$ states of HO_2: Use of the diatomics in molecules model to fit ab initio data, *J. Chem. Phys. 102*: 1994 (1995).
11. C. A. Mead and D. G. Truhlar, On the determination of Born-Oppenheimer nuclear motion wave functions including complications due to conical intersections and identical nuclei, *J. Chem. Phys. 70*: 2282 (1979).
12. Y.-S M. Wu, A. Kuppermann and B. Lepetit, Theoretical calculation of experimentally observable consequences of the geometric phase on chemical reaction cross sections, *Chem. Phys. Lett. 186*: 319 (1991). There are typographical errors in Table 1 of this reference which have been corrected in (183) through (186).
13. T. Carrington, The geometry of intersecting potential surfaces, *Acc. Chem. Res. 7*: 20 (1974).
14. J. von Neumann and E. P. Wigner, Über das Verhalten von Eigenwerten bei adiabatischen Prozessen, *Z. Phys. 30*: 467 (1929).
15. T. Carrington, Triatomic potential surfaces, *Faraday Discuss. Chem. Soc. 53*: 27 (1972).
16. A Kuppermann, A useful mapping of triatomic potential energy surfaces, *Chem. Phys. Lett. 32*: 374 (1975).
17. A. Kuppermann, A new look at symmetrized hyperspherical coordinates, *Advances in Molecular Vibrations and Collision Dynamics*. (J. Bowman, ed.), JAI Press, Greenwich, CT, 1994, Vol. 2B, p. 117.

18. R. N. Porter, R. M. Stevens, and M. Karplus, Symmetric H_3: A semiemperical and ab initio study of a simple Jahn-Teller system, *J. Chem. Phys. 49*: 5163 (1968).
19. R. S. Mulliken, Report on notation for the spectra of polyatomic molecules, *J. Chem. Phys. 23*: 1997 (1955); *24*: 1118 (1956) (E).
20. E. Teller, The crossing of potential surfaces, *J. Phys. Chem. 41*: 109 (1937).
21. L. M. Delves, Tertiary and general-order collisions, *Nucl. Phys. 9*: 391 (1959).
22. L. M. Delves, Tertiary and general-order collisions, *Nucl. Phys. 20*: 275 (1960).
23. H. Lefebvre-Brion and R. W. Field, *Perturbations in the Spectra of Diatomic Molecules*, Academic Press, New York, 1986, Chap. 2.
24. M. Baer, Adiabatic and diabatic representations for atom-molecule collisions: Treatment of the collinear arrangement, *Chem. Phys. Lett. 35*: 112 (1975).
25. C. A. Mead and D. G. Truhlar, Conditions for the definition of a strictly diabatic electronic basis for molecular systems, *J. Chem. Phys. 77*: 6090 (1982).
26. M. Baer and R. Englman, A study of the diabatic electronic representation within the Born-Oppenheimer approximation, *Mol. Phys. 75*: 293 (1992).
27. C. A. Mead, Electronic Hamiltonian, wave functions, and energies, and derivative coupling between Born-Oppenheimer states in the vicinity of a conical intersection, *J. Chem. Phys. 78*: 807 (1983).
28. P. M. Morse and H. Feshbach, *Methods of Theoretical Physics*, McGraw-Hill, New York, 1953, pp. 52–54, 1763.
29. H. Margenau and G. M. Murphy, *The Mathematics of Physics and Chemistry*, Van Nostrand, New York, 1943, p. 192.
30. A. J. C. Varandas, F. B. Brown, C. A. Mead, D. G. Truhlar, and N. C. Blais, A double many-body expansion of the two lowest-energy potential surfaces and non-adiabatic coupling for H_2, *J. Chem. Phys. 86*: 6258 (1987).
31. T. Packer, L. S. Cederbaum, and H. Köppel, Approximately diabatic states from block diagonalization of the electronic Hamiltonian, *J. Chem. Phys. 89*: 7367 (1988).
32. H. Köppel, W. Domcke, and L.S. Cederbaum, Multimode molecular dynamics beyond the Born-Oppenheimer approximation, *Adv. Chem. Phys. 57*: 59 (1984).
33. J. C. Tully, Diatomics-in-molecules potential energy surfaces. II. Non-adiabatic and spin-orbit interactions, *J. Chem. Phys. 59*: 5122 (1973).
34. D. W. Schwenke, S. L. Mielke, G. J. Tawa, R. S. Friedman, P. Halvick and D. G. Truhlar, Converged quantum mechanical calculations of electronic-to-vibrational, rotational energy transfer probabilities in a system with a conical intersection, *J. Chem. Phys. 203*: 565 (1993).
35. Y. Aharonov and D. Bohm, Significance of electromagnetic potentials in the quantum theory, *Phys. Rev. 115*: 485 (1959).
36. Y.-S.M. Wu and A. Kuppermann, Prediction of the effect of the geometric phase on product rotational state distributions and integral cross sections, *Chem. Phys. Lett. 201*: 178 (1993).
37. X. Wu, R. E. Wyatt, and M. D'Mello, Inclusion of the geometric phase in quantum reactive scattering calculations: A variational formulation, *J. Chem. Phys. 101*: 2953 (1994).
38. M. V. Berry, Quantal phase factors accompanying adiabatic changes, *Proc. R. Soc. Lond. A 392*: 45 (1984).
39. B. Simon, Holonomy, the quantum adiabatic theorem, and Berry's phase, *Phys. Rev. Lett. 51*: 2167 (1983).
40. J. W. Zwanziger, M. Koenig, and A. Pines, Berry's phase, *Ann. Rev. Phys. Chem. 41*: 601 (1990).
41. A. Kuppermann, Accurate quantum calculations of reactive systems, *Theoretical Chemistry-Theory of Scattering: Papers of Honor of Henry Eyring* (D. Henderseon, ed.) Academic Press, New York, 1981, Vol. 6A, p. 79.
42. A. Kuppermann, G. C. Schatz, and M. Baer, Quantum Mechanical Reactive Scattering for Planar Atom Plus Diatom Systems. I: Theory, *J. Chem. Phys. 65*: 4596 (1976).

43. G. C. Schatz and A. Kuppermann, Quantum mechanical reactive scattering for three-dimensional atom plus diatom systems. I: Theory, *J. Chem. Phys. 65*: 4642 (1976).
44. S. A. Cuccaro, P. G. Hipes and A. Kuppermann, Hyperspherical coordinate reactive scattering using variational surface functions, *Chem. Phys. Lett. 154*: 155 (1989).
45. A. S. Davydov, *Quantum Mechanics, 2nd Ed.*, Pergamon Press, Oxford, UK, 1976, p. 151.
46. A. Kuppermann and Y.-S. M. Wu, The geometric phase shows up in chemical reactions, *J. Chem. Phys. 205*: 577 (1993); *213*: 636 (1993) (E).
47. Y.-S. M. Wu and A. Kuppermann, The importance of the geometric phase effect for the $H + D_2 \rightarrow HD + D$ reaction, *Chem. Phys. Lett. 235*: 105 (1995).
48. A. Kuppermann and Y.-S. M. Wu, The quantitative prediction and lifetime of a pronounced reactive scattering resonance, *Chem. Phys. Lett. 241*: 229 (1995); *243*: 586 (1995) (E).
49. F. T. Smith, A symmetric representation for three-body problems. I: Motion in a plane, *J. Math Phys. 3*: 735 (1962).
50. R. C. Whitten and F. T. Smith, Symmetric representation for three-body problems. II: Motion in space, *J. Math. Phys. 9*: 1103 (1968).
51. B. R. Johnson, On hyperspherical coordinates and mapping the internal configurations of a three body system, *J. Chem. Phys. 73*: 5051 (1980).
52. R. T. Pack and G. A. Parker, Quantum reactive scattering in three dimensions using hyperspherical (APH) coordinates. Theory, *J. Chem. Phys. 87*: 3883 (1987).
53. J. M. Launay and M. Le Dourneuf, Hyperspherical close-coupling claculation of integral cross sections for the reaction $H + H_2 \rightarrow H_2 + H$, *Chem. Phys. Lett. 163*: 178 (1989).
54. A. Kuppermann, Reactive scattering with row-orthonormal hyperspherical coordinates. 1: Transformation properties and Hamiltonian for triatomic systems, *J. Phys. Chem. 100*: 2629 (1996).
55. B. R. Johnson, The multichannel log-derivative method for scattering calculations, *J. Comp. Phys. 13*: 445 (1973).
56. B. R. Johnson, The log derivative and renormalized Numerov algorithms, *Algorithms and Computer Codes For Atomic and Molecular Quantum Scattering Theory* (*L. Thomas, ed.*), NRCC Workshop, Lawrence Berkeley Laboratory, Report No. LBL 9501, 1979.
57. D. E. Manolopoulos, An improved log derivative method for inelastic scattering, *J. Chem. Phys. 85*: 6425 (1986).
58. R. T. Pack, Choosing body-fixed axes in arrangement channels approaches to reactive scattering, Advances in Molecular Vibrations and Collision Dynamics (J. Bowman, ed.), JAI Press, Greenwich, CT 1994, Vol. 2A, p. 111.
59. B. Lepetit, Z. Peng, and A. Kuppermann, Calculation of bound rovibrational states on the first electronically excited state of the H_3 system, *Chem. Phys. Lett. 166*: 572 (1990).
60. P. Siegbahn and B. Liu, An accurate three-dimensional potential energy surface for H_3, *J. Chem. Phys. 68*: 2457 (1978).
61. D. G. Truhlar and C. J. Horowitz, Functional representation of Liu and Siegbahn's accurate ab initio potential energy calculations for $H + H_2$, *J. Chem. Phys. 68*: 2466 (1978); *71*, 1514 (1979) (E).
62. C. A. Mead, Superposition of reactive and nonreactive scattering in the presence of a conical intersection, *J. Chem. Phys. 72*: 3839 (1980).
63. D. A. V. Kliner, K. D. Rinen, and R. N. Zare, The $D + H_2$ reaction. Comparison of experimental with quantum-mechanical and quasi-classical calculations, *Chem. Phys. Lett. 166*: 107 (1990).
64. D. Neuhauser, R. S. Judson, D. J. Kouri, D. E. Edelman, N. E. Shafer, D. A. V. Kliner, and R. N. Zare, State-to-state rates for the $D + H_2$ ($v = 1, j = 1$) $\rightarrow$ HD (v', j') + H reaction. Predictions and measurements, *Science 257*: 519 (1992).
65. D. A. V. Kliner, D. E. Adelman, and R. N. Zare, Comparison of experimental and theoretical integral cross sections for $D + H_2$ ($v = 1, j = 1$) $\rightarrow$ HD ($v' = 1, j'$) + H, *J. Chem. Phys. 95*: 1648 (1991).

66. D. E. Adelman, N. E. Shafer, D. A. V. Kliner, and R. N. Zare, Measurement of relative state-to-state rate constants for the reaction D + H_2 (v, j) → HD (v', j') + H, *J. Chem. Phys. 97*: 7323 (1992).
67. T. N. Kitsopoulos, M. A. Buntine, D. P. Baldwin, R. N. Zare, and D. W. Chandler, Reactive-product imaging. The H + D_2 reaction, *Science 260*: 1605 (1993).
68. L. Schnieder, K. Seekamp-Rahn, J. Borkowski, E. Wrede, K. H. Welge, F. J. Aoiz, L. Bañares, M. J. D'Mello, V. J. Herrero, V. Sáez Rábanos, and R. E. Wyatt, Experimental studies and theoretical predictions for the H + D_2 → HD + D Reaction, *Science 269*: 207 (1995).
69. A. I. Boothroyd, W. J. Keogh, P. G. Martin, and M. R. Peterson, An improved H_3 potential energy surface, *J. Chem. Phys. 95*: 4343 (1991).
70. D. L. Diedrich and J. B. Anderson, Exact quantum Monte Carlo calculations of the potential energy surface for the reaction H + H_2 → H_2 + H, *J. Chem. Phys. 100*: 8089 (1994).

12

Nonadiabatic Transitions: Beyond Born-Oppenheimer

HIROKI NAKAMURA

Institute for Molecular Science, Myodaiji, Okazaki, Japan

I. INTRODUCTION

Nonadiabatic transition due to potential curve (or surface) crossing is one of the most important mechanisms to effectively induce electronic transitions (1,2). This is a very interdisciplinary concept and appears in various fields of physics and chemistry, even in biology (1). The most typical examples are, of course, a variety of atomic and molecular processes such as atomic and molecular collisions, chemical reactions, and molecular spectroscopic processes. Attempts have even been made to classify organic chemical reactions by curve-crossing diagrams (3). Other exotic examples are nuclear collisions and reactions in nuclear physics (4,5), dynamic processes on solid surface, energy relaxation and phase transitions in condensed phase physics (6,7), and electron and proton transfer processes in biology (8,9). The ordinate and abscissa in these curve-crossing problems are usually potential energy and spatial coordinate, respectively, although they can, in principle, be anything. In the case of electron transfer the ordinate is free energy; and in the case of atomic and molecular processes in an external field the abscissa is field strength (10). A much more exotic example is the resonant neutrino transfer in the sun, in which the ordinate is effective neutrino mass squared and the abscissa is electron density (11). The multidisciplinarity of nonadiabatic transition can also be easily understood from Fig. 1, which depicts the three simple kinds of two-state curve-crossing problems: inelastic scattering, predissociation or resonant elastic scattering, and perturbed bound state. All these are different physical processes, but the most essential part, i.e., curve crossing in the center, is the same. If this central part is solved, these three problems can be easily formulated.

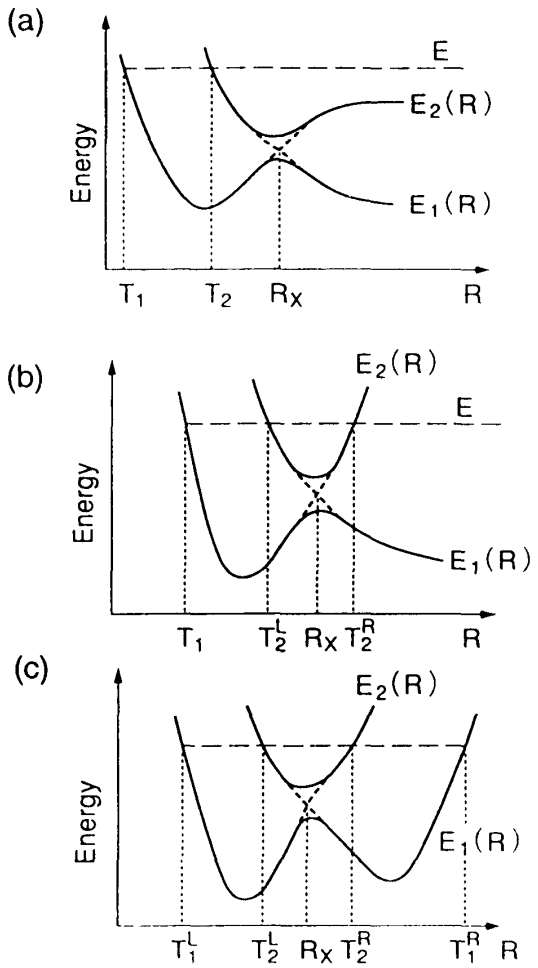

Figure 1 Three typical problems of nonadiabatically coupled two states: (a) inelastic scattering, (b) elastic scattering or predissociation, (c) perturbed bound state or phase transition in condensed medium.

Two-state curve crossing can be classified into the following two cases according to the crossing scheme (see Fig. 2): (1) Landau-Zener (LZ) case, in which the two diabatic potential curves (dotted lines in the figure) have the same signs for the slopes (Fig. 2a), and (2) nonadiabatic tunneling (NT) case, in which the diabatic curves have opposite signs of the slopes (Fig. 2b). These two cases are physically very different, since in the NT case particle transmission (nonadiabatic tunneling) occurs from left to right or vice versa; besides complete reflection occurs at certain discrete energies higher than the bottom of the upper adiabatic potential (solid line). This NT process plays a very important role in various fields. For instance, this can lead to phase transition in a condensed medium, as is schematically shown in Fig. 1c. Figure 3 shows another interesting example of nonadiabatic transition observed experimentally (12). This is photodissociation of bromoacetylchloride. It was observed that the C—Cl bond breakage is more probable than the C—Br bond breakage despite the fact that the potential barrier for the C—Cl breakage is higher than that of the C—Br bond breakage. This is because these potential barriers are not ordinary single potential barriers as in Fig. 3a, but are induced by the nonadiabatic tunneling-type curve crossing and the diabatic coupling in the C—Br bond breakage is

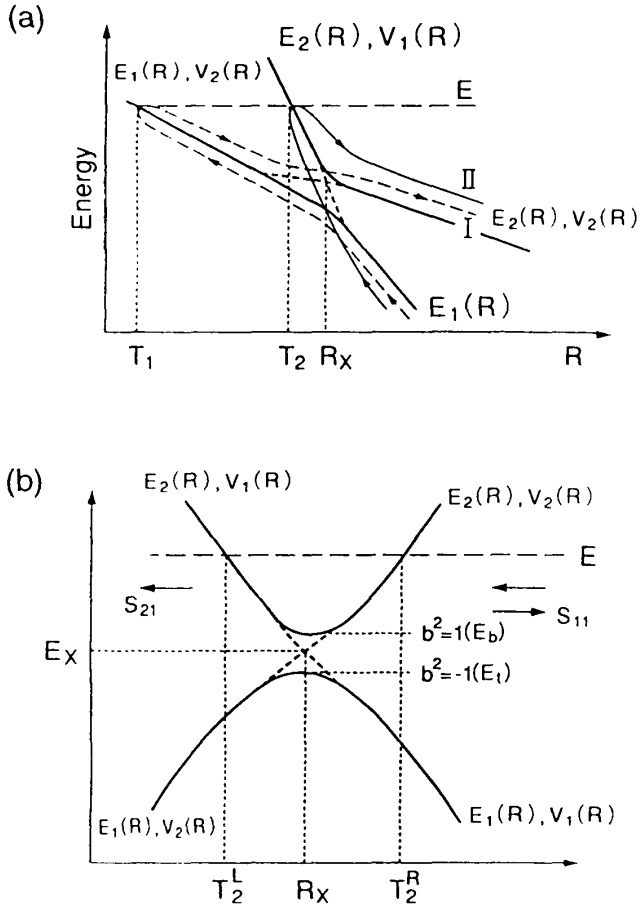

Figure 2 Two basic cases of curve crossing: (a) Landau-Zener (LZ) case, (b) nonadiabatic tunneling (NT) case.

small (see Fig. 3b). Figure 4 clearly demonstrates how different the nonadiabatic tunneling is from ordinary single-potential tunneling. The solid line is the nonadiabatic tunneling (transmission) probability for the following potential system ($V_1(x)$ and $V_2(x)$ are the crossing diabatic potentials, and $V(x)$ is a coupling between the two): $V_1(x) = \alpha(x + a/2)$ for $x \geq -a/2$, 0 for $x \leq -a/2$, $V_2(x) = -\alpha(x - a/2)$ for $x \leq a/2$, $\beta(x - a/2)(x - b + a/2)$ for $a/2 \leq x \leq b - a/2$, 0 for $x \geq b - a/2$, $V(x) = V_0(a/2 - x)(x + a/2)/(a/2)^2$ for $-a/2 \leq x \leq a/2$, 0 otherwise, where $\beta = \alpha/(b - a)$, $\alpha = 2.0$, $a = 0.5$, $b = 1.0$ and $V_0 = 0.05$ in atomic units. The dashed line in Fig. 4 is the probability of tunneling through the lower adiabatic potential $E_1(x) = 0.5\{V_1(x) + V_2(x) - \sqrt{[V_1(x) - V_2(x)]^2 4V^2(x)}\}$ with the coupling to the upper potential completely neglected. The difference between the two curves in Fig. 4 clearly demonstrates the effects of nonadiabatic coupling. If there is no diabatic coupling between $V_1(x)$ and $V_2(x)$, then the transmission probability is exactly zero. Another interesting feature of nonadiabatic tunneling is the complete reflection which occurs at certain discrete energies as is seen in Fig. 4. This will be discussed in more detail in Sec. VI.

In this chapter the basic semiclassical theory of nonadiabatic transition is reviewed and explained. Semiclassical theory has a history of more than 60 years since the pioneering work of Landau (13), Zener (14), and Stückelberg (15) in 1932. Not only a brief historical survey of the theory, but also the most recent theoretical achievements are

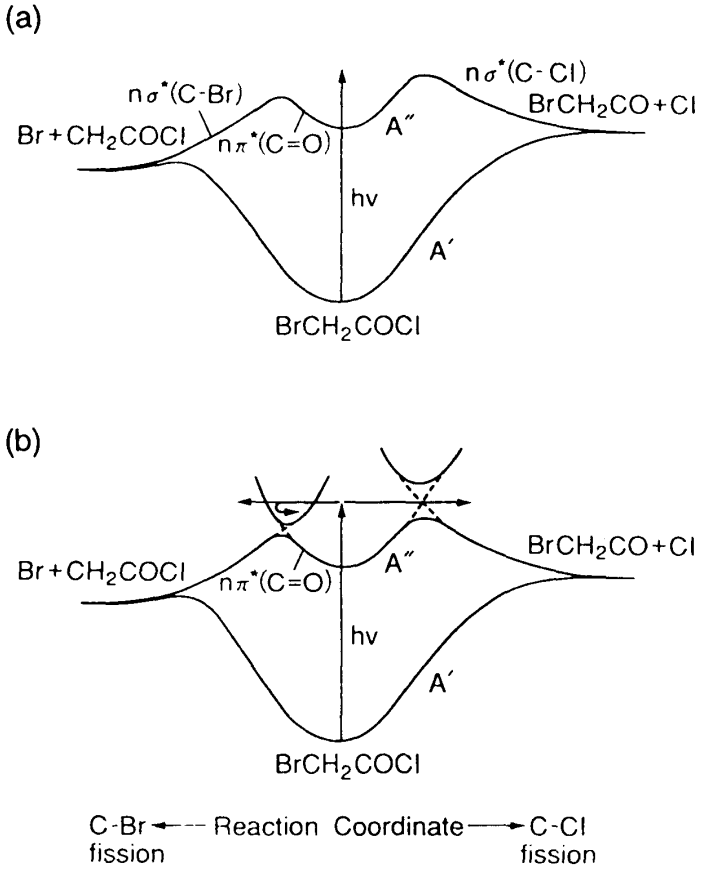

Figure 3 Schematic potential diagram for photodissociation of bromoacetyle chloride. (a) The case when the upper A″ states are neglected. The barrier heights cannot explain the dominant breakage of C—Cl bond. (b) Nonadiabatic tunneling type curve crossing scheme. This can explain the experimental fact. (From Ref. 12.)

described here. The recently developed new theory can provide simple, compact, yet very accurate formulae for one-dimensional two-state curve-crossing problems for the LZ and NT cases (16,17). This can be applied to a variety of problems depicted in Fig. 1, even in the general multistate framework. Furthermore, this sophisticated one-dimensional theory can be incorporated into the trajectory surface hopping (TSH) (18) method, which is often used in the study of multidimensional chemical reactions. Since the theory can give accurate phases due to nonadiabatic transition and can deal even with classically forbidden events, the conventional TSH method could be substantially improved and made more sophisticated.

There is also a noncrossing nonadiabatic transition called the Rosen-Zener-Demkov type (1,2). Figure 5 shows the corresponding potential diagram, in which the two adiabatic potentials are in near resonance at large R. The nonadiabatic transition is not as effective as the crossing case, but this still presents an important mechanism in atomic and molecular processes.

This chapter is organized as follows. Section II interprets the underlying concept of nonadiabatic transition and its interdisciplinarity. Properties of nonadiabatic couplings are summarized. The terms "diabatic," "adiabatic," and "nonadiabatic" are explained. Section III briefly surveys the history of semiclassical theories of nonadiabatic transition

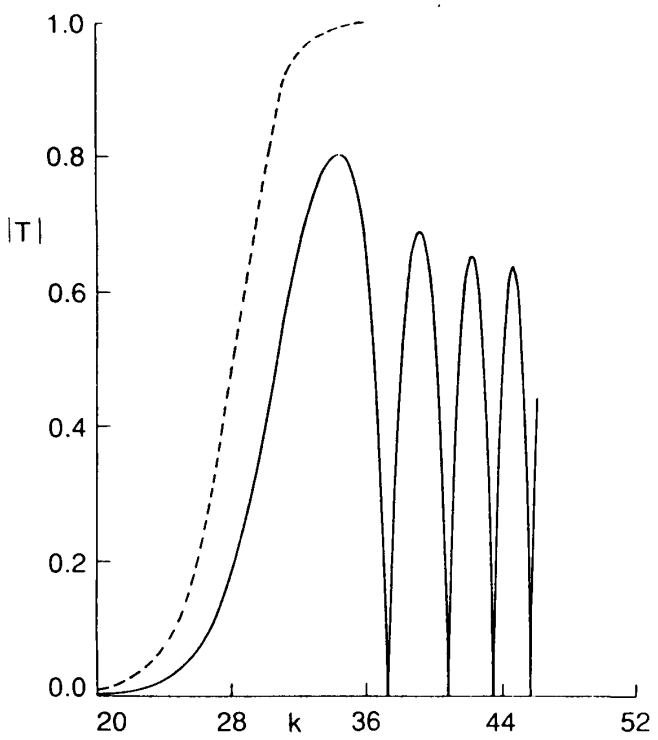

Figure 4 Effects of nonadiabatic coupling on transmission probability. Solid line: nonadiabatic tunneling, dash line: single adiabatic potential tunneling. $|T|^2$ is the probability and k is the wave number. (From Ref. 37.)

due to curve crossing, starting from the work of Landau, Zener, and Stückelberg up to around 1991. The methodologies of these theories are briefly reviewed, since they are quite instructive. The theory of Rosen-Zener-Demkov-type noncrossing nonadiabatic transition is also briefly surveyed. In Sec. IV, by analyzing the total Hamiltonian of the diatomic system, the origins and properties of nonadiabatic radial and rotational (Coriolis) couplings are clarified. It is shown that the new representation called "dynamical state representation" makes a unified treatment of the nonadiabatic transitions possible

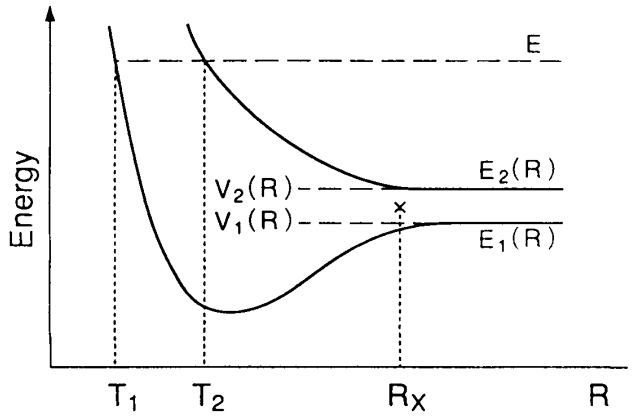

Figure 5 Schematic potential diagram of the Rosen-Zener-Demkov type of nonadiabatic transition.

(1,2,19). The recently developed new theory for the most fundamental linear potential models is also briefly summarized (20–23). Quantum mechanically exact as well as new accurate semiclassical solutions are derived. These give a very convenient basis for deriving the practically useful new semiclassical formulae applicable to general curved potentials. The Rosen-Zener-Demkov-type of problem is also briefly described in Sec. IV. The background mathematics underlying the nonadiabatic transitions is concisely interpreted in Sec. V. This is the Stokes phenomenon of asymptotic solutions of the associated differential equations (24). Readers not interested in the underlying mathematics can skip this section. The newly developed accurate and compact formulae of the scattering matrix applicable to general curved potentials (16,17) are summarized in Sec. VI. Available methodologies for multilevel and multidimensional problems are summarized in Sec. VII. A summary and future perspectives are given in Sec. VIII.

II. WHAT IS "NONADIABATIC TRANSITION"?

If the system under consideration is described by two groups of variables and one (R) changes slowly compared to the other (r), then the state of the system can be well represented by the eigenstates of the motions with respect to the rapidly changing variables (r) obtained at each fixed value of the slowly changing variables (R). This is called "adiabatic approximation" with respect to the parameter R, which defines a set of eigenfunctions and eigenenergies as a function of R, $\{\psi_n(r:R), E_n(R)\}$. If this approximation is good—the adiabaticity holds well—the system stays on the same eigenstate $E_n(R)$. If this is true over the whole range of R, however, no transition occurs and the system is physically not interesting at all. Physically interesting phenomena occur when the adiabaticity breaks down. This happens when two (or more) adiabatic eigenstates come close together in a certain region of the adiabatic parameter R, as in Fig. 1. This close encounter of potential curves is called "avoided crossing" or "pseudocrossing." Nonadiabatic transitions induced by the motion with respect to R occur most effectively at these avoided crossings, because the necessary energy transfer between the different kinds of degrees of freedom is smallest there. Nonadiabatic transition can also be interpreted as follows: The physical characters of the r-motions basically stay the same along the diabatic states, and the change of character proceeds adiabatically when the R-motion is infinitesimally slow. When the R-motion becomes relatively fast, r-motions cannot completely adjust to the R-motion and the nonadiabatic transition is induced at the avoided crossing. Nonadiabatic transitions are thus regarded as one of the origins of various kinds of state changes, namely, the origin of the mutability of the universe.

In the case of electronic transitions in molecular dynamic processes we are interested in the adiabatic parameters R, and the rapidly varying variables r are internuclear coordinates and electron coordinates, respectively. The eigenstates $\{E_n(R)\}$ are nothing but the ordinary Born-Oppenheimer adiabatic potential energy curves (or surfaces). Generally speaking, adiabaticity holds well because of the big mass disparity between the electron and nucleus and the nonadiabatic transitions occur locally at avoided crossings. The "diabatic" states are defined by the diagonal matrix elements $V_j(R) \equiv \langle \varphi_j^{(d)} | H_{\rm el} | \varphi_j^{(d)} \rangle$ of the electronic Hamiltonian $H_{\rm el}$ of the system at fixed R, where $\varphi_j^{(d)}(r:R)$ is a certain approximate electronic wave function. The diabatic states couple to each other by the off-diagonal matrix element (diabatic coupling) $V_{jk}(R) \equiv \langle \varphi_j^{(d)} | H_{\rm el} | \varphi_k^{(j)} \rangle$ ($j \neq k$). As is easily conjectured, this diabatic representation is not unique. On the other hand, adiabatic states can be defined uniquely as the eigenstates of $H_{\rm el}$. Once a diabatic rep-

resentation is given, the corresponding adiabatic states are uniquely obtained simply by diagonalizing the matrix of H_{el} in the diabatic representation. In the two-state approximation, the adiabatic states $\{\psi_n^{(a)}(r:R), E_n(R)\}$ are easily obtained as

$$E_n(R) = \tfrac{1}{2}\{V_1(R) + V_2(R) \pm \sqrt{[V_1(R) - V_2(R)]^2 + 4V^2(R)}\} \tag{1}$$

with $E_2(R) > E_1(R)$ and

$$\begin{pmatrix} \psi_1^{(a)} \\ \psi_2^{(a)} \end{pmatrix} = \begin{pmatrix} \cos\theta & -\sin\theta \\ \sin\theta & \cos\theta \end{pmatrix} \begin{pmatrix} \varphi_1^{(d)} \\ \varphi_2^{(d)} \end{pmatrix} \tag{2}$$

where $V(R) = V_{12}(R)$ and

$$\theta = \frac{1}{2}\tan^{-1}\frac{2V(R)}{V_2(R) - V_1(R)} \tag{3}$$

Since $2V(R)/[V_2(R) - V_1(R)] \to +0\ (-0)$ for $R \ll R_X$ $(R \gg R_X)$, $\psi_1^{(a)} \to \varphi_1^{(d)}$ $(\varphi_2^{(d)})$ and $\psi_2^{(a)} \to \varphi_2^{(d)}$ $(\varphi_1^{(d)})$ for $R \ll R_X$ $(R \gg R_X)$. This switching of states, i.e., the rapid change of the character of electronic state, usually occurs in a localized region at R_x, representing the fundamental feature of avoided crossing.

In the adiabatic representation, H_{el} is diagonal and the transition among the adiabatic states of the same electronic symmetry is induced by the nonadiabatic radial coupling

$$T_{jk}^{rad} = \left\langle \psi_j^{(a)} \middle| \frac{\partial}{\partial R} \middle| \psi_k^{(a)} \right\rangle = \frac{\partial\theta}{\partial R} = \frac{(dV/dR)(V_k - V_j) - Vd(V_k - V_j)/dR}{[E_j(R) - E_k(R)]^2} \tag{4}$$

where the R-dependence of $\varphi^{(d)}$ is assumed to be neglected after the second equal sign. In contrast to the diabatic-to-adiabatic transformation, the adiabatic-to-diabatic transformation cannot be uniquely defined. Nonzero couplings of the form of Eq. (4) always exist among the diabatic states unless we use the R-independent electronic wave functions as basis functions. When R is a one-dimensional parameter, the following Neumann-Wigner noncrossing rule holds among the adiabatic states: Adiabatic states cannot have real crossings on the real axis of R. This can be simply proved as follows: As is easily seen from Eq. (1), $V(R)$ and $V_1(R) - V_2(R)$ should be zero at the same time in order to have a real crossing. This is not possible, in general, if R is a one-dimensional parameter. When the two adiabatic states have different electronic symmetries, such as Σ and Π of a diatomic molecule, real crossing becomes possible because $V(R)$ is zero. When R is an N-dimensional parameter, real potential surface crossing of dimension N-2 is possible for states with the same electronic symmetry.

Adiabatic states with different electronic symmetries couple not by the radial coupling of Eq. (4) but by nonadiabatic rotational (Coriolis) coupling, H_{cor}. For Σ and Π states of a diatomic molecule, the Coriolis coupling matrix element is given by (see Sec. III)

$$T_{jk}^{rot} = -\frac{\hbar^2}{\sqrt{2}\mu R^2}\sqrt{J(J+1)}\,\langle\psi_j^{(a)}(\Sigma)|L_-|\psi_k^{(a)}(\Pi)\rangle \tag{5}$$

with

$$L_- = L_\xi - iL_\eta \tag{6}$$

where L_ξ (L_η) is the x (y) component of the electronic angular momentum operator with the z-axis taken to be the molecular axis, and μ is the mass. The Coriolis coupling is easily seen to have analytical properties very different from those of the radial coupling given by Eq. (4). The former has a second-order pole at $R = 0$, provided the matrix element of L is not equal to zero there, while the latter has a pole of order unity at the complex crossing point $R_\cdot$, where $E_j(R_\cdot) = E_k(R_\cdot)$ (see Eq. (4)). Thus, the semiclassical theories developed for the radially induced nonadiabatic transitions cannot be directly applied to the rotationally induced transitions (25,26). If we move into a new representation, called the "dynamical state" representation, in which the Coriolis couplings are diagonal (1,2,19), then all kinds of nonadiabatic transitions can be treated in a unified way by the theories developed for the radially induced nonadiabatic transitions. This will be discussed in Sec. IV.

Finally, the terms "adiabatic," "diabatic," and "nonadiabatic" are explained from the author's viewpoint. First of all, when we talk about transition in the case of curve-crossing, we have to specify the representation (adiabatic or diabatic). "Nonadiabatic" should be used basically to mean coupling. Thus "nonadiabatic transition" means a transition between adiabatic states induced by nonadiabatic coupling; "nonadiabatic state" is not an appropriate expression. On the other hand, "adiabatic" should be used to mean "state," and "adiabatic transition" should not be used. "Diabatic" should also basically mean "state," but "diabatic transition" can be used to mean a transition due to diabatic coupling in the diabatic state representation.

In addition to the time-independent treatment, time-dependent treatment is often employed because of its convenience. The order of the differential equations can be reduced to half compared to the time-independent case, since the time-dependent Schrödinger equation is a first-order differential equation, i.e., the type of evolution equation. Care should be paid, though, to what the "time" is. If the Hamiltonian is that of the total system including the nuclear motion, then the time is real and nuclear motion is described by the wave packet. Wave packet dynamics are not discussed here. If the Hamiltonian is the electronic one defined at each fixed nuclear configuration, on the other hand, time represents nuclear motion: the internuclear coordinate is assumed to be a certain function of time, or the nuclear motion is described by a certain classical trajectory. This treatment has often been employed to derive various semiclassical theories. Derivations of general time-independent solutions can be made based on the time-dependent treatment, for instance (27). However, time is unidirectional, and the linear potential in time, for instance, is much different from the linear potential in R. The turning point effects cannot be taken into account by the linear potential in time (no reflection effect), because the model assumes high collision energies from the beginning.

III. HISTORICAL SURVEY

The theory of nonadiabatic transition dates back to 1932, when the pioneering works for curve-crossing and noncrossing problems were published by Landau (13), Zener (14), and Stückelberg (15) and by Rosen and Zener (28), respectively. Since then numerous papers by many authors have been devoted to these subjects, especially to curve-crossing problems (1,2,19,29–33). In this section a brief survey to around 1991 is made, which is informative and gives a good introduction to further developments described in subsequent sections.

A. Curve-Crossing Type of Nonadiabatic Transition

Landau discussed the curve-crossing problem by using the complex contour integral method (13,34). In general, the transition probability p in first-order perturbation theory is given by

$$p \simeq \left| \int \chi_1(R) f(R) \chi_2(R)\, dR \right|^2 \tag{7}$$

where $f(R)$ represents the coupling (can be an operator) between the two states and χ_1 (χ_2) is the nuclear wave function in channel 1 (2). Since the nuclear wave functions oscillate rapidly on the real R-axis and the ordinary WKB functions are not applicable in the vicinity of turning points, it is more convenient to move into the complex R-plane. Using the primitive WKB functions for χ_1 and χ_2, and picking up the only main term in the upper half-plane, he obtained the expression

$$p \simeq p_{\mathrm{LS}} \equiv \exp\left[-2\ \mathrm{Im} \int^{R_*} (k_1(R) - k_2(R))\, dR \right] \tag{8}$$

where LS stands for Landau-Stückelberg and

$$k_j(R) = \left\{ \frac{2\mu}{\hbar^2} [E - E_j(R)] \right\}^{1/2} \tag{9}$$

with $E_2(R) > E_1(R)$. If we further assume that the adiabatic potentials $E_j(R)$ are derived from the linear diabatic potentials and the constant coupling between them and that the relative nuclear motion is described by a straight-line trajectory with constant velocity v, we obtain the famous Landau-Zener formula

$$p_{\mathrm{LZ}}^{(0)} = \exp\left[-\frac{2\pi A^2}{\hbar v |\Delta F|} \right] \tag{10}$$

where A is the diabatic coupling and $\Delta F = F_1 - F_2$ is the difference between slopes of the diabatic potentials.

This method, generally called the Landau method, is very instructive and useful because it is quite general. However, the original coupling $f(R)$ in Eq. (7) has disappeared and the preexponential factor is taken to be unity in Eqs. (8) and (10). This is a mystery, but is actually correct in the Landau-Zener model (linear potential, constant coupling, and constant velocity), as was proved by Zener (14). Landau himself probably did not care about the preexponential factor, because the exponent is the most decisive factor in any case. But it is interesting to note that if we employ the adiabatic-state representation (otherwise we cannot obtain the exponents of Eqs. (8) and (10)), the coupling $f(R)$ should be a nonadiabatic coupling and is actually given by

$$f(R) \propto T_{12}^{\mathrm{rad}} \frac{\partial}{\partial R} \qquad \text{(derivative operator!)} \tag{11}$$

where T_{12}^{rad} has a pole of order unity at R_* (see Eq. (4)). If we evaluate the contour integral with the residue of the pole taken into account, we cannot get unity as a preexponential factor, naturally, although the exponent is the same even with the operator Eq. (11). So (8) and (10) are clearly beyond first-order perturbation theory, and the preex-

ponential factor (=unity) is the result of a kind of renormalization based on the above analytical properties.

Zener employed the time-dependent Schrödinger equation in the diabatic representation (14):

$$-i\hbar \frac{d}{dt}\begin{pmatrix} c_1 \\ c_2 \end{pmatrix} = \begin{pmatrix} 0 & V(t)\exp\left[\frac{-i}{\hbar}\int^t (V_1 - V_2)\,dt'\right] \\ V(t)\exp\left[-\frac{i}{\hbar}\int^t (V_1 - V_2)\,dt'\right] & 0 \end{pmatrix} \tag{12}$$

where the total wave function is expanded as

$$\Psi = c_1(t)\exp\left[\frac{i}{\hbar}\int^t V_1(t')\,dt'\right]\varphi_1^{(d)} + c_2(t)\exp\left[-\frac{i}{\hbar}\int^t V_2(t')\,dt'\right]\varphi_2^{(d)} \tag{13}$$

The coefficients $c_1(t)$ and $c_2(t)$ do not depend on the diabatic potentials separately but on the difference $V_1(t) - V_2(t)$, which is assumed to be a linear function of time:

$$V_1(t) - V_2(t) = |\Delta F|vt \tag{14}$$

If we further assume that the diabatic coupling $V(t)$ is constant, then Eq. (12) can be solved exactly in terms of the Weber function. Then the final transition probability is exactly equal to Eq. (10). The linearity in time t is very much different from the linearity in coordinate R and the effects of turning points are completely neglected in the former approximation. In Landau's treatment this corresponds to the assumption of the common straightline classical trajectory with constant velocity. Thus, the Landau-Zener formula Eq. (10) is valid only at collision energies much higher than the crossing point.

Stückelberg did the most elaborate analysis (15). He applied the approximate complex WKB analysis to the fourth-order differential equation obtained from the original second-order coupled Schrödinger equations. In the complex R-plane he took into account the Stokes phenomenon associated with the asymptotic solutions in an approximate way, and finally derived not only the Landau-Zener transition probability p but also the total inelastic transition probability P_{12} as

$$P_{12} \simeq 4p_{LS}(1 - p_{LS})\sin^2 \tau \tag{15}$$

where p_{LS} is the same as Eq. (8),

$$\tau = \int_{T_1}^{Rx} k_1(R)\,dR - \int_{T_2}^{Rx} k_2(R)\,dR \tag{16}$$

and T_j is the turning point on the adiabatic potential $E_j(R)$ (j = 1, 2). Equation (15) contains the effects of turning points and can be interpreted nicely, as described below, in terms of localized nonadiabatic transition at R_X and adiabatic wave propagation along the adiabatic potentials. Since there are two possible (classical) paths for the 1 → 2 inelastic transition (see Fig. 2a), the corresponding scattering matrix elements S_{21} may

be expressed as

$$\begin{aligned} S_{21} &= \sqrt{p_{LS}(1 - p_{LS})}e^{i(\eta_1+\tau_1)}e^{i(\eta_2-\tau_2)} \\ &\quad - \sqrt{p_{LS}(1 - p_{LS})}e^{i(\eta_1-\tau_1)}e^{i(\eta_2+\tau_2)} \\ &= 2ie^{i(\eta_1+\eta_2)}\sqrt{p_{LS}(1 - p_{LS})}\sin\tau \end{aligned} \tag{17}$$

with

$$\tau = \tau_1 - \tau_2 \tag{18}$$

where the first (second) term in the first equation of Eq. (17) corresponds to path I (II) in Fig. 2a, η_j represents the elastic scattering phase shift by the potential $E_j(R)$ (j = 1, 2), and τ_j is the phase integral from T_j to R_X along $E_j(R)$ (j = 1, 2). Thus, $P_{12} = |S_{21}|^2$ is equal to Eq. (15). This idea of decomposing the whole process into sequential events of nonadiabatic transitions and adiabatic wave propagations is very physical and constitutes the basis of semiclassical theory (1,2).

Figure 6 clearly demonstrates the insufficiency of the simple Landau-Zener formula (10). This figure depicts the results for the linear potential model (in R), in which, as will be shown in the next section, the quantum mechanically exact analytical solutions have been obtained. The following two parameters can describe this model completely:

$$a^2 = \frac{\hbar^2}{2\mu}\frac{F(F_1 - F_2)}{8A^3} \quad \text{and} \quad b_2 = (E - E_X)\frac{F_1 - F_2}{2FA} \tag{19}$$

with

$$F = \sqrt{F_1|F_2|} \tag{20}$$

where E_X is the energy at crossing point, and $F_1 > 0$ and $F_1 > F_2$ are assumed without loss of generality. These parameters effectively represent the coupling strength and the collision energy; $a^2 \simeq 1$ corresponds to intermediate coupling strength. This figure clearly shows that Eq. (10) is usable only at high energies. After the pioneering works mentioned above a great deal of effort has been made by many authors in order to correct the

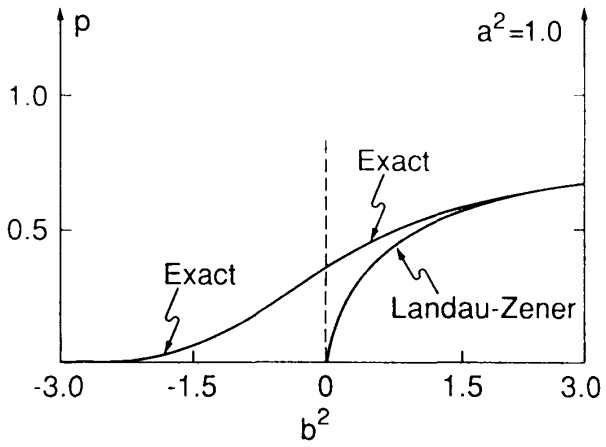

Figure 6 Landau-Zener transition probability in the linear potential model of the LZ type with a^2 = 1.0. a^2 and b^2 are defined by Eq. (19). Landau-Zener means the result of Eq. (10).

defects of these simple theories. Readers can refer to many review articles and books (1,2,19,29–33).

The best formulas up to about 1991 may be summarized as follows: The 2 × 2 scattering matrix corresponding to Fig. 2a is given by

$$S = P_{\infty X} O_X P_{XIX} I_X P_{X\infty} \tag{21}$$

where $P_{A\cdots B}$ is a diagonal matrix representing the adiabatic wave propagation from B to A, and I_X (O_X) is a nondiagonal matrix expressing the nonadiabatic transition at crossing point R_X in the incoming (outgoing) segment. These matrices are explicitly given as

$$[P_{\infty X}]_{nm} = [P_{X\infty}]_{nm} = \delta_{nm} \exp\left\{ i \int_{R_X}^{\infty} [k_n(R) - k_n(\infty)]\, dR - i k_n(\infty) R_X \right\} \tag{22a}$$

$$[P_{XIX}]_{nm} = \delta_{nm} \exp\left[2i \int_{T_n}^{R_X} k_n(R)\, dR + \frac{i\pi}{2} \right] \tag{22b}$$

$$I_X = \begin{pmatrix} \sqrt{1 - p_{LS}}\, e^{i\phi_S} & \sqrt{p_{LS}}\, e^{i\sigma_0} \\ -\sqrt{p_{LS}}\, e^{-i\sigma_0} & \sqrt{1 - p_{LS}}\, e^{-i\phi_S} \end{pmatrix} \tag{22c}$$

and

$$O_X = \tilde{I}_X \qquad \text{(transpose of } I_X\text{)} \tag{22d}$$

where

$$p_{LS} = \exp(-2\delta) \tag{23}$$

$$\sigma_0^{LS} + i\delta = \int_{R_X}^{R_\bullet} [k_1(R) - k_2(R)]\, dR \tag{24}$$

and

$$\phi_S(\delta) = \frac{\delta}{\pi} \ln\left(\frac{\delta}{\pi}\right) - \frac{\delta}{\pi} - \frac{\pi}{4} - \arg \Gamma\left(i \frac{\delta}{\pi}\right) \tag{25}$$

The phase $\phi_S(\delta)$ is called the Stokes phase. This Stokes phase correction ϕ_S is equal to $\pi/4(0)$ in the limit of zero (infinitely strong) diabatic coupling, i.e., in the limit of $\delta = 0$ ($\delta = \infty$). Thus the total inelastic transition probability $P_{12} = |S_{21}|^2$ is given by

$$P_{12} \simeq 4 p_{LS}(1 - p_{LS}) \sin^2(\sigma + \phi_S) \tag{26}$$

with

$$\sigma = \sigma_0^{LS} + \tau \tag{27}$$

The elastic scattering phase shift η_n is given by

$$\exp(2i\eta_n) = (P_{\infty X} P_{XIX} P_{X\infty})_{nm} \tag{28}$$

With the phase corrections σ_0^{LS} and ϕ_S, Eq. (21) works quite well, but still cannot be free from the following defects: (1) δ requires the analytic continuation of $E_n(R)$'s into the complex R-plane and the complex contour integral in Eq. (24), which is not easy for experimentalists to use. (2) The formula works only at energies higher than E_X, although Eq. (23) works better than the original Landau-Zener formula (Eq. (10)). At energies slightly lower than E_X some empirical modification was introduced to δ, but no analyti-

cal formula had actually been developed to cover the whole range of energies lower than E_X.

In the NT case (Fig. 2b), the semiclassical idea of sequential events of nonadiabatic transition and adiabatic wave propagation can be utilized at energies higher than the bottom of the upper adiabatic potential. The S-matrix in this case is

$$S_{nm} = S^R_{nm} \exp[i(\eta^{NT}_n + \eta^{NT}_m)] \tag{29}$$

with

$$\eta^{NT}_n = \lim_{R \to \pm\infty} \left[\pm \int_{R_X}^{R} k_1(R')\, dR' \mp k_1(R)R + \frac{\pi}{4} \right] \qquad \text{for } n = \begin{pmatrix} 1 \\ 2 \end{pmatrix} \tag{30}$$

where S^R is called the reduced scattering matrix and is given by

$$S^R_{11} = \frac{p_{LS}}{1 + (1 - p_{LS})e^{2i\psi_{LS}}} e^{2i\gamma_2(T^L_2, R_X) - 2i\sigma^{LS}_0} \tag{31a}$$

$$S^R_{22} = \frac{p_{LS}}{1 + (1 - p^{LS})e^{2i\psi_{LS}}} e^{2i\gamma_2(R_X, T^R_2) + 2i\sigma^{LS}_0} \tag{31b}$$

and

$$S^R_{12} = S^R_{21} = \frac{2(1 - p_{LS})^{1/2}}{1 + (1 - p_{LS})e^{2i\psi_{LS}}} \cos \psi_{LS}\, e^{i\gamma_2(T^L_2, T^R_2)} \tag{31c}$$

where

$$\psi_{LS} = -\phi_S(\delta) + \gamma_2(T^L_2, T^R_2) \tag{32}$$

and

$$\gamma_n(a, b) = \int_a^b k_n(R)\, dR \tag{33}$$

The physical processes in this NT case are quite different from those in the LZ case: The diagonal (off-diagonal) elements of S-matrix represent reflection (transmission) with channel 1 (2) designating the wave on the right (left) side of the potential barrier. The denominator in Eqs. (31) represents trapping by the upper adiabatic potential. Another very interesting feature is "complete reflection ($S_{12} = S_{21} = 0$)," which occurs at certain discrete energies where $\cos \psi_{LS} = 0$ is satisfied. This will be discussed in more detail in Sec. VI. Again, Eqs. (31) are valid only at energies higher than the bottom (E_b) of the upper adiabatic potential and no accurate formulas are available at energies lower than that.

B. Noncrossing Type of Nonadiabatic Transition

Another kind of radially induced nonadiabatic transition is the Rosen-Zener-Demkov type (1,2). In contrast to the curve-crossing case, the two diabatic potentials have very weak R-dependence (actually, their difference is assumed to be constant in the basic model) and the diabatic coupling has a strong (~exponential) R-dependence (see Fig. 5). The nonadiabatic transition is not as effective as the curve-crossing case, but this case also presents an important transition, especially when the two potentials are near resonance asymptotically.

The name Rosen-Zener came from their original work on the time-dependent theory of the double Stern-Gerlach experiment (28). This problem is totally different from our present subject, but the mathematical basis corresponds to the problem of nonadiabatic transition: the corresponding potential difference and diabatic coupling are constant and hyperbolic secant function of time, respectively. They solved the time-dependent Schrödinger equation exactly. In 1963, Demkov (35) discussed the near-resonant change transfer process again in the time-dependent formalism and obtained essentially the same formula as that of Rosen and Zener. He assumed a constant energy difference and the exponential function for the coupling. The overall inelastic transition probability $P_{12} = |S_{21}|^2$ is

$$P_{12} \simeq \operatorname{sech}^2\left(\frac{\pi\Delta}{2\hbar\beta v}\right)\sin^2\left(\frac{2V_0}{\pi\beta v}\right) \tag{34}$$

where Δ is the difference (constant) of the two diabatic potentials, and β and V_0 are the exponent and the preexponential factor of the diabatic coupling. Although the adiabatic potentials have no conspicuous avoided crossing, the nonadiabatic transition occurs quite locally at $R_X = \mathrm{Re}(R_\cdot)$, where the adiabatic potentials start to diverge (see Fig. 5). $R_\cdot$ is the complex crossing point closest to the real axis. In this case there are an infinite number of complex crossing points which are distributed with equal distance in parallel with the imaginary axis, but it suffices to take into account the only one closest to the real axis. As the noncrossing of potential curves implies, there is no switching of the character of the electronic state, and the nonadiabatic transition probability does not approach unity but rather one-half at the high-energy limit. The nonadiabatic transition probability p_{RZ} by one passage of R_X is obtained from Eq. (34) as

$$p_{RZ}^{(0)} = \left[1 + \exp\left(\frac{\pi\Delta}{\hbar\beta v}\right)\right]^{-1} \tag{35}$$

The same semiclassical idea of decomposing the whole process into sequential events of nonadiabatic transition and adiabatic wave propagation can be applied together with the complex phase integral for nonadiabatic transition. Thus the scattering matrix can be expressed in the same way as Eqs. (21)–(22b). The difference from the Landau-Zener case appears in the matrices I_X and O_X ($=\tilde{I}_X$) as

$$I_X = \begin{pmatrix} \sqrt{1 - p_{RZ}} & \sqrt{p_{RZ}}e^{i\sigma_0^{LS}} \\ -\sqrt{p_{RZ}}e^{-i\sigma_0^{LS}} & \sqrt{1 - p_{RZ}} \end{pmatrix} \tag{36}$$

with

$$p_{RZ} = [1 + \exp(2\delta)]^{-1} \tag{37}$$

where σ_0^{LS} and δ are defined by Eq. (24). The total inelastic transition probability is

$$P_{12} \simeq 4p_{RZ}(1 - p_{RZ})\sin^2\sigma = \operatorname{sech}^2\delta\,\sin^2\sigma \tag{38}$$

where σ is defined by Eq. (27). The Stokes phase ϕ_S does not appear in this noncrossing case (19).

C. Nonadiabatic Transition Due to Coriolis Coupling

There is another kind of nonadiabatic transition, induced by Coriolis interaction (or rotational coupling (1,2)), that has a very different character from radially induced non-

adiabatic transitions. The transitions are not localized at the crossing point even in the adiabatic representation, because the Coriolis coupling is proportional to R^{-2} and is most dominant at the turning point, not at the crossing point (see Eq. (5)). The theories developed for the curve-crossing and the noncrossing cases cannot be applied directly to this case. However, if we introduce a new representation in which Coriolis coupling is diagonal, then we can make them applicable. More detailed discussions are given in the next section.

IV. DYNAMICAL STATE REPRESENTATION AND QUANTUM MECHANICAL SOLUTIONS OF BASIC ONE-DIMENSIONAL MODELS

In this section it is clearly demonstrated that radially and rotationally induced nonadiabatic transitions can be treated in a unified way by introducing the dynamical state representation. Then the most fundamental quantum mechanical models are discussed for the curve-crossing and noncrossing cases.

A. Dynamical State Representation

Let us start with the Hamiltonian $\tilde{H}$ of a diatomic molecule, which is given in the body-fixed coordinate system as (the mass polarization and relativistic effects are disregarded)

$$\begin{aligned}\tilde{H} &= -\frac{\hbar^2}{2\mu}\frac{1}{R^2}\left(\frac{\partial}{\partial R}R^2\frac{\partial}{\partial R}\right) + \frac{\hbar^2}{2\mu R^2}(\mathcal{J} - \mathcal{L})^2 + H_{\text{el}} \\ &= -\frac{\hbar^2}{2\mu}\frac{1}{R^2}\left(\frac{\partial}{\partial R}R^2\frac{\partial}{\partial R}\right) + H_{\text{rot}} + H_{\text{cor}} + H' + H_{\text{el}}\end{aligned} \tag{39}$$

where

$$H_{\text{rot}} = -\frac{\hbar^2}{2\mu R^2}(\mathcal{J}^2 - 2\Lambda^2) \tag{40a}$$

$$H_{\text{cor}} = -\frac{\hbar^2}{2\mu R^2}(\mathcal{L}_+\mathcal{U}_+ + \mathcal{L}_-\mathcal{U}_-) \tag{40b}$$

and

$$H' = \frac{\hbar^2}{2\mu R^2}\mathcal{L}^2 \tag{40c}$$

Here, $\mathcal{J}$ ($\mathcal{L}$) is the total (electronic) angular momentum operator, R is the internuclear distance as before, μ is the reduced mass, and Λ is the component of $\mathcal{L}$ along the molecular axis. The ladder operators $\mathcal{L}_\pm$ and $\mathcal{U}_\pm$ are explicitly given as follows:

$$\mathcal{L}_\pm = \mathcal{L}_\xi \pm i\mathcal{L}_\eta \tag{41}$$

and

$$\mathcal{U}_\pm = \mp\frac{\partial}{\partial\Theta} + \frac{i}{\sin\Theta}\frac{\partial}{\partial\Phi} + L_\zeta\cot\Theta \tag{42}$$

where $\mathcal{L}_\xi$, $\mathcal{L}_\eta$, and $\mathcal{L}_\zeta$ are the components of $\mathcal{L}$ in the body-fixed coordinate system with the ζ axis along the molecular axis, and (Θ, Φ) are the ordinary angle variables to define

the molecular axis orientation in the space-fixed coordinate system. Note that the Schrödinger equation $\tilde{H}\tilde{\Psi} = E\tilde{\Psi}$ and the Hamiltonian $\tilde{H}$ can be transformed to

$$H\Psi = E\Psi \tag{43a}$$

and

$$H = R\tilde{H}R^{-1} = -\frac{\hbar^2}{2\mu}\frac{\partial^2}{\partial R^2} + H_{\text{rot}} + H_{\text{cor}} + H' + H_{\text{el}} \tag{43b}$$

with

$$\Psi = R\tilde{\Psi} \tag{43c}$$

The ordinary Born-Oppenheimer adiabatic states are defined by the eigenvalue problem of H_{el}:

$$H_{\text{el}}\psi_n^{(a)}(\mathbf{r}:R|\Lambda) = E_n(R:\Lambda)\psi_n^a(\mathbf{r}:R|\Lambda) \tag{44}$$

Nonadiabatic transitions among these states are induced by either the first term of Eq. (43b) or H_{cor}. The states of the same Λ are coupled by T^{rad} given by Eq. (4). Transitions between the states of different electronic symmetries (different $|\Lambda|$) are induced by the Coriolis coupling H_{cor} and have quite different properties from the radially induced transitions. In order to look into this in more detail, let us introduce the electronic-rotational basis functions defined as

$$\Phi_n^{J\pm}(\mathbf{r}) = \frac{1}{\sqrt{2}}\{\psi_n^{(a)}(\mathbf{r}:R|\Lambda^+) \pm \psi_n^{(a)}(\mathbf{r}:R|\Lambda^-)\}Y(\hat{R}:J\Lambda) \qquad \text{for } \Lambda \neq 0 \tag{45a}$$

and

$$\Phi_n^{J\pm}(\Sigma) = \psi_n^{(a)}(\mathbf{r}:R|\Sigma^+)Y(\hat{R}:J\Sigma) \qquad \text{for } \Lambda = 0 \tag{45b}$$

where $\Lambda^{\pm} = \pm|\Lambda|$ and $Y(\hat{R}:J\Lambda)$ is the eigenfunction of H_{rot}:

$$H_{\text{rot}}Y(\hat{R}:J\Lambda) = [J(J+1) - 2\Lambda^2]Y(\hat{R}:J\Lambda) \tag{46}$$

These functions $\Phi_n^{J\pm}$ are the eigenfunctions of $H_{\text{el}} + H_{\text{rot}}$:

$$(H_{\text{el}} + H_{\text{rot}})\Phi_n^{J\pm}(\Lambda) = \left\{E_n^{\Lambda}(R) + \frac{\hbar^2}{2\mu R^2}[J(J+1) - 2\Lambda^2]\right\}\Phi_n^{J\pm}(\Lambda) \tag{47}$$

There is no coupling between the two manifolds $\{\Phi_n^{J+}(\Lambda)\}$ and $\{\Phi_n^{J-}(\Lambda)\}$. Now, the Coriolis (or nonadiabatic rotational) coupling matrix element within each manifold is

$$\begin{aligned} T_{1,2}^{\text{rot}}(\Lambda_1, \Lambda_2) &= \langle\Phi_1^{J\pm}(\Lambda_1)|H_{\text{cor}}|\Phi_2^{J\pm}(\Lambda_2)\rangle \\ &= -\frac{\hbar^2}{2\mu R^2}\{\lambda_-(J, \Lambda_2^+)\delta(\Lambda_1^+, \Lambda_2^+ - 1)\langle\psi_1^{(a)}(\Lambda_1^+)|\mathcal{L}_-|\psi_2^{(a)}(\Lambda_2^+)\rangle \\ &\quad + \lambda_+(J, \Lambda_2^+)\delta(\Lambda_1^+, \Lambda_2^+ + 1)\langle\psi_1^{(a)}(\Lambda_1^+)|\mathcal{L}_+|\psi_2^{(a)}(\Lambda_2^+)\rangle\} \\ &\quad \text{for } \Lambda_1, \Lambda_2 \neq 0 \end{aligned} \tag{48}$$

where

$$\lambda_{\pm}(J, \Lambda) = \sqrt{(J+\Lambda)(J \pm \Lambda + 1)} \tag{49}$$

If one of the states is a Σ-state, then

$$T^{\text{rot}}_{1,2}(\Sigma, \Pi) \equiv \langle \Phi^J_1(\Sigma) | H_{\text{cor}} | \Phi^{J\pm}_2(\Pi) \rangle \tag{50}$$
$$= \begin{cases} -\dfrac{\hbar^2}{\sqrt{2}\mu R^2} \sqrt{J(J+1)}\, \langle \psi^{(a)}_1(\Sigma) | L_- | \psi^{(a)}_2(\Pi^+) \rangle & \text{for } + \\ 0 \quad \text{for } - \end{cases}$$

The Coriolis coupling is usually not very strong unless the nuclear kinetic energy is very high, but it plays an important role because it couples the states which cannot be coupled by T^{rad}. In spectroscopic problems, this coupling is called "heterogeneous perturbation," in contrast to "homogeneous perturbation" for the radial coupling case (36). As can be easily conjectured from Eqs. (4) and (48) (or (50)), the two kinds of nonadiabatic transition have quite different properties from each other. In the radially induced case the coupling has a pole of order unity at the complex crossing point $R_\cdot$, where $\Delta E(R_\cdot) = E_1(R_\cdot) - E_2(R_\cdot)$ has a zero with order one-half (see Eqs. (1) and (4)). This analytical property underlies the curve-crossing problem and is the reason why the preexponential factor of the Landau-Zener transition probability is exactly unity. The Coriolis coupling, on the other hand, has a pole of order 2 at $R = 0$, and the corresponding potential curves $E^\Lambda_n(R)$ can have a real curve crossing at finite R or at $R = 0$ (united-atom degeneracy).* This suggests that the semiclassical theories developed for the radial coupling problem cannot be directly applied to the Coriolis coupling problem. However, this problem can be solved by introducing a new representation, called "dynamical state" representation (1,2,19).

The dynamical states (DS) are defined as the eigenstates of the total Hamiltonian of Eq. (43b) with the first term excluded; i.e.,

$$H_{\text{dyn}} \Psi^{J\pm}_n(\mathbf{r}, \bar{R}:R) \equiv (H_{\text{el}} + H_{\text{rot}} + H_{\text{cor}} + H') \Psi^{J\pm}_n(\mathbf{r}, \bar{R}:R) \tag{51}$$
$$= W^{J\pm}_n(R) \Psi^{J\pm}_n(\mathbf{r}, \bar{R}:R)$$

where $\Psi^{J\pm}_n$ may be expanded in terms of electronic-rotational basis functions as

$$\Psi^{J\pm}_n(\mathbf{r}, \bar{R}:R) = \sum_\Lambda C^{J\Lambda\pm}_n \Phi^{J\pm}_n(\mathbf{r}, \bar{R}:R|\Lambda) \tag{52}$$

Transitions among dynamical states are exclusively induced by the radical coupling given by Eq. (4) with $\psi^{(a)}$'s replaced by the relevant DS's $\Psi^{J\pm}_n$. In this representation Λ is not a good quantum number anymore, and the Neumann-Wigner noncrossing rule applies to all dynamical states. The analytical properties of the coupling and energy difference ΔW in this representation are the same as those of the original radial coupling problems, and thus the semiclassical theories developed for the latter can now be applied in a unified way to any transitions in the new representation. This idea can be, in principle, generalized to more complicated systems by using the hyperspherical coordinate system (1,2). The analytical properties of the various nonadiabatic transitions are summarized in Table 1. Numerical examples of the DS representation can be found in Refs. 1 and 2.

*When the relevant two electronic states $E^\Lambda_n(R)$ correlate to the same atomic orbital in the united-atom limit $R \to 0$, $\Delta E(R) \propto R^2$ and the electronic matrix element of $\mathcal{L}_+$ (or $\mathcal{L}_-$) in Eq. (48) is not equal to zero at $R = 0$.

Table 1 Analytical Properties of Various Nonadiabatic Transitions

Coupling scheme	Potential energy difference $\Delta E \propto$	Coupling
Radial		
(curve crossing and noncrossing)	$(R - R_\cdot)^{1/2}$	$(R - R_\cdot)^{-1}$
$R_\cdot$: complex		
Rotational		
(a) crossing at finite $R = R_\cdot$	$R - R_X$	R^{-2}
(b) no crossing	constant	
(c) united-atom degeneracy	R^2	
Any transition	Dynamical state representation	
($R_\cdot$: complex)	$(R - R_\cdot)^{1/2}$	R^{-1}

Note that the radial coupling T^{rad} loses its personality in the complex R-plane, especially at $R \sim R_\cdot$. From Eqs. (2) and (3) we can easily show

$$T_{12}^{\text{rad}} = \left\langle \psi_1^{(a)} \left| \frac{\partial}{\partial R} \right| \psi_2^{(a)} \right\rangle \cong \frac{\partial \theta}{\partial R} \cong \frac{i}{4} \frac{1}{R - R_\cdot} \tag{53}$$

This holds irrespective of the forms of $V_1(R)$, $V_2(R)$, and $V(R)$. Furthermore, the radial coupling should satisfy the following condition even on the real axis in the case of curve crossing:

$$\int_{-\infty}^{\infty} T_{12}^{\text{rad}}\, dR = \frac{\pi}{2} \tag{54}$$

As a reflection of these properties, direct information on T^{rad} is not required in the semiclassical analytical theory, as demonstrated in the previous section. That information is replaced by the analytical continuation of the adiabatic potentials into the complex R-plane (see Eq. (24)). In order to carry out the quantum mechanical numerical calculations, however, we always stay on the real R-axis and we require explicit information on the nonadiabatic couplings. Even in the diabatic representation, which is often employed because of its convenience, nonadiabatic couplings are necessary to obtain the diabatic couplings. The quantum mechanical calculations are usually made by solving the coupled differential equations derived from an expansion of the total wave function in terms of the electronic wave functions.

B. Linear Potential Model—Curve-Crossing Case

The most fundamental quantum mechanical model of curve crossing is the linear potential model (in coordinate R), in which the diabatic crossing potentials $V_1(R)$ and $V_2(R)$ are linear functions of R and the diabatic coupling $V(R)$ is constant ($=A$). The basic coupled Schrödinger equations are (29)

$$-\frac{\hbar^2}{2\mu} \frac{d^2 \varphi_1^{(d)}}{dR^2} + [V_1(R) - (E - E_X)]\varphi_1^{(d)} = -A\varphi_2^{(d)} \tag{55a}$$

and

$$-\frac{\hbar^2}{2\mu}\frac{d^2\varphi_2^{(d)}}{dR^2} + [V_2(R) - (E - E_X)]\varphi_2^{(d)} = -A\varphi_1^{(d)} \tag{55b}$$

where

$$V_j(R) = -F_j(R - R_X) \qquad (j = 1, 2) \tag{56}$$

Without loss of generality, it is assumed that $F_1 > 0$ and $F_1 > F_2$ as before. The LZ case (see Fig. 2a) corresponds to $F_1F_2 > 0$, and the NT case (see Fig. 2b) to $F_1F_2 < 0$. Transformations

$$\varphi_j^{(d)} = \frac{1}{2\pi}\int_{-\infty}^{\infty} u_j(k)e^{ikR}\,dR \qquad (j = 1, 2) \tag{57}$$

$$u_j(k) = \frac{2}{|f_j|}A_j(k)\exp\left[\frac{i}{f_j}\left(\epsilon k - \frac{k^3}{3}\right)\right] \qquad (j = 1, 2) \tag{58}$$

and

$$B(\xi) = A_1(k)\exp\left[\frac{i}{2}\left(\frac{a^2\xi^3}{3} - b^2\xi\right)\right] \qquad \text{(LZ case)} \tag{59a}$$

or

$$B(\xi) = A_1(k)\exp\left[-\frac{i}{2}\left(\frac{a^2\xi^3}{3} - b^2\xi\right)\right] \qquad \text{(NT case)} \tag{59b}$$

lead to

$$\frac{d^2B(\xi)}{d\xi^2} + q(\xi)B(\xi) = 0 \tag{60}$$

with

$$q(\xi) = \begin{cases} \dfrac{1}{4} - ia^2\xi + \dfrac{1}{4}(a^2\xi^2 - b^2)^2 & \text{(LZ case)} \quad (61a) \\ -\dfrac{1}{4} + ia^2\xi + \dfrac{1}{4}(a^2\xi^2 - b^2)^2 & \text{(NT case)} \quad (61b) \end{cases}$$

where

$$\epsilon = \frac{2\mu}{\hbar^2}(E - E_X), \quad f_j = \frac{2\mu}{\hbar^2}F_j, \quad \alpha = \frac{2\mu A}{\hbar^2}, \quad \xi = \frac{2\alpha k}{f} \tag{62}$$

$$a^2 = \frac{f(f_1 - f_2)}{8\alpha^3}, \quad b^2 = \frac{\epsilon(f_1 - f_2)}{2\alpha f} \tag{63}$$

and

$$f = (f_1|f_2|)^{1/2} \tag{64}$$

The quantities a^2 (≥ 0) and b^2 ($-\infty < b^2 < \infty$) are the same basic parameters as before (see Eq. (19)), representing the effective coupling strength and the collision energy re-

spectively. In the NT case $b^2 = 1$ (-1) corresponds to the bottom (top) of the upper (lower) adiabatic potential (see Fig. 2b).

The most fundamental physical quantity is the reduced scattering matrix S^R defined from the ordinary scattering matrix S as (see Eq. (29))

$$S_{mn} = S^R_{mn} \exp[i(\eta_m + \eta_n)] \tag{65}$$

where η_m and η_n are the elastic scattering phase shifts which diverge in the present linear potential model. The off-diagonal (diagonal) elements represent transmission (reflection) in the NT case (see Fig. 2b). From the solution of Eq. (60) the functions $A_j(k)$ are obtained by Eqs. (59) and

$$A_2(k) = 2i \exp\left[\pm i\left(\frac{a^2}{3}\xi^3 - b^2\xi\right)\right]\frac{dA_1}{d\xi} \qquad \text{(upper sign for LZ, lower sign for NT)} \tag{66}$$

Then the reduced scattering matrices are defined by

$$\begin{pmatrix} A_1(\infty) \\ A_2(\infty) \end{pmatrix} = S^R_{\mathrm{LZ}} \begin{pmatrix} A_1(-\infty) \\ A_2(-\infty) \end{pmatrix} \qquad \text{(LZ case)} \tag{67a}$$

and

$$\begin{pmatrix} A_1(\infty) \\ A_2(-\infty) \end{pmatrix} = S^R_{\mathrm{NT}} \begin{pmatrix} A_1(-\infty) \\ A_2(\infty) \end{pmatrix} \qquad \text{(NT case)} \tag{67b}$$

Thus the key point is to obtain the connections of the asymptotic solutions of Eq. (60) at $\xi \to \pm\infty$. The underlying mathematics to carry this out analytically is the Stokes phenomenon of asymptotic solutions of differential equations and is explained briefly in Sec. V. This is very important mathematics for the general semiclassical theory and various physical phenomena. It is interesting that the apparent small differences in $q(\xi)$ of Eqs. (61) between the LZ and NT cases make a big difference mathematically and physically. The mathematical differences are not detailed here, but the physical differences are obvious, as pointed out in the Introduction.

Recently, Zhu and Nakamura carefully analyzed the Stokes phenomenon of Eq. (60) and succeeded in deriving not only quantum mechanically exact, but also new semiclassical expressions of S^R. The quantum mechanically exact solutions in the LZ case (20–23) are

$$S^R = \begin{pmatrix} 1 + U_1U_2 & -U_2 \\ -U_2 & 1 - U_1^*U_2 \end{pmatrix} \tag{68}$$

with

$$U_2 = \frac{2i \operatorname{Im} U_1}{1 + |U_1|^2} \tag{69}$$

$$P_{12} = |S^R_{21}|^2 = 4p(1 - p)\sin^2(\arg U_1) \tag{70}$$

and

$$p = \frac{1}{1 + |U_1|^2} \tag{71}$$

where $U_1(a^2, b^2)$ is a complex quantity (Stokes constant) and given as an infinite series (20), and p represents the Landau-Zener transition probability for one passage of the crossing point. In addition to the unitarity, the reduced scattering matrix satisfies the properties $S^R_{11} = (S^R_{22})$ and $S^R_{12} = S^R_{21}$ = pure imaginary. These properties can be proved from the symmetries of the differential equations satisfied by $A_j(k)$'s. Equation (70) is a familiar expression for inelastic scattering probability in the semiclassical theory; but this is an exact expression.

For the NT case we have

$$S^R = \frac{1}{1 + U_1 U_2} \begin{pmatrix} 1 & U_2 \\ U_2 & 1 \end{pmatrix} \tag{72}$$

with

$$U_2 = \frac{2i \text{ Im}(U_1)}{|U_1|^2 - 1} \tag{73}$$

$$P_{12} = |S^R_{21}|^2 = \frac{4(\text{Im } U_1)^2}{(|U_1|^2 - 1)^2 + 4(\text{Im } U_1)^2} \tag{74a}$$

$$= \frac{2 \sin^2(\arg U_1)}{2 \sin^2(\arg U_1) + p^2/2(1 - p)} \qquad \text{for } b^2 \geq 1 \tag{74b}$$

and

$$p = 1 - |U_1|^2 \qquad \text{for } b^2 \geq 1 \tag{75}$$

where $U_1(a^2, b^2)$ is also a complex quantity (Stokes constant) given by an infinite series (20), and p represents the Landau-Zener transition probability which has the physical meaning of nonadiabatic transition for one passage of crossing point only at energies higher than the bottom of the upper adiabatic potential. In the same way as in the LZ case, the reduced scattering matrix can be proven to satisfy the relations $S^R_{11} = S^R_{22}$ and $S^R_{12} = S^R_{21}$. Equation (74b) has also the same form as that in the semiclassical theory, but this is a quantum mechanically exact expression. The same notations U_1 and p as in the LZ case are used, but they are naturally different. Also note that Eq. (74a) is valid at any energy, but Eq. (74b) is valid only at $b^2 \geq 1$. It is very interesting that complete reflection occurs at

$$\arg U_1 = l\pi \qquad (l = 0, 1, \ldots) \tag{76}$$

This suggests an interesting theoretical possibility of molecular switching (37). Although the infinite series for U_1 are quite complicated, they have provided us with a unique opportunity to investigate and improve the validity of various semiclassical solutions.

The new semiclassical analysis has been carried out in Refs. 21 and 22 for the LZ and NT cases, respectively. The formulae obtained there are compact and yet more accurate than those available before. They are further rewritten and improved in Ref. 23 so that they can practically cover the whole range of a^2 (coupling strength) and can be easily extended to general curved potentials. This was made possible by replacing the diabatic parameters a^2 and b^2 by adiabatic parameters at relevant places and by introducing some empirical corrections. The results are not given here, but the final results applicable to general curved potentials are summarized in Sec. VI.

C. Noncrossing Model

The simplest model is the following: the diabatic potentials are constant with $V_2 - V_1 = \Delta > 0$ and the diabatic coupling is $V_0 e^{-\beta(R-R_X)}$, where $\Delta = 2V_0$. Recently, Osherov and Voronin obtained the quantum mechanically exact analytical solution for this model in terms of the Meijer function (38). In the adiabatic representation this system presents a three-channel problem at $E > V_2 > V_1$, since there is no repulsive wall at $R \ll R_X$ in the lower adiabatic potential. They have obtained the analytical expression of a 3×3 transition matrix. Adding a repulsive potential wall at $R \ll R_X$ for the lower adiabatic channel and using the semiclassical idea of independent events of nonadiabatic transition at R_X and adiabatic wave propagation elsewhere, they derived the overall inelastic nonadiabatic transition probability P_{12} as follows:

$$P_{12} = \frac{\sinh(\pi k_1/\beta)\sinh(\pi k_2/\beta)\sin^2 \tau}{[\cosh^2\{\pi(k_1 - k_2)/2\beta\}][\cosh^2\{\pi(k_1 + k_2)/2\beta\} - \sin^2\tau]} \tag{77}$$

where $k_j = k_j(R = \infty)$ and τ is the phase difference between the two adiabatic potentials from turning point to R_X, corresponding to Eq. (16). At high collision energy we have

$$k_1 - k_2 \simeq \frac{\Delta}{\hbar\beta v} \tag{78}$$

where v is the velocity. Then Eq. (77) leads to

$$P_{12} \simeq \operatorname{sech}^2\left(\frac{\pi\Delta}{2\hbar\beta v}\right)\sin^2 \sigma \tag{79}$$

which agrees with the Rosen-Zener-Demkov formula in Eq. (34).

V. MATHEMATICAL BACKGROUND

The very basic mathematics, i.e., Stokes' phenomenon, which underlies semiclassical theory, is briefly explained in this section by taking the Airy function as an example. The Stokes constant and connection matrix in the case of the Weber function are provided, since the Weber function is useful in many applications. Finally, the Stokes phenomenon of the linear curve-crossing model discussed in Sec. IV is explained briefly.

A. What Is Stokes' Phenomenon?

Let us consider the Airy differential equation

$$\frac{d^2w(z)}{dz^2} - h^2 z w(z) = 0 \tag{80}$$

where h is a certain large positive parameter. The WKB type of asymptotic solutions in the complex z-plane are

$$(\cdot, z) = z^{-1/4} \exp\left(h \int^z z^{1/2}\, dz\right) = z^{-1/4} \exp(\tfrac{2}{3} hz^{3/2}) \tag{81a}$$

and

$$(z, \cdot) = z^{-1/4} \exp\left(-h \int^z z^{1/2}\, dz\right) = z^{-1/4} \exp(-\tfrac{2}{3} hz^{3/2}) \tag{81b}$$

These are called standard WKB solutions. A general solution in the asymptotic region is, of course, given by a linear combination of these two solutions,

$$w(z) \simeq A(\cdot, z) + B(z, \cdot) \tag{82}$$

where A and B are arbitrary constants. Can this be a single-valued function in the whole asymptotic region with the same coefficients A and B? The answer is no. This is obvious, since Eq. (80) is nothing but the Schrödinger equation with the linear potential h^2x at zero total energy. Equation (82) represents a running wave at $x = \mathrm{Re}(z) < 0$, but includes the unphysical exponentially growing wave in the classically forbidden region $x = \mathrm{Re}(z) > 0$. This suggests that the coefficients should be changed from region to region.

What does this mean? The functions (81) are multivalued functions with branch point at $z = 0$. This branch point comes from the zero of the coefficient of Eq. (80). This is called the transition point of order unity. There emanate two kinds of lines from $z = 0$: One is defined by $\mathrm{Im}(z^{3/2}) = 0$ and is called Stokes' line, and the other ($\mathrm{Re}(z^{3/2}) = 0$) is called the anti-Stokes line. Figure 7 shows these lines (dashed line for Stokes and solid line for anti-Stokes) together with a branch cut (wave line). The two solutions (81) are approximate, and one is exponentially large (dominant) and the other is exponentially small (subdominant). Thus, the coefficient of the subdominant solution is affected by the error of the dominant solution. This effect can be taken into account by assigning a constant T (Stokes' constant) to each Stokes line, across which the coefficient A of the subdominant solution is changed to $A + BT$ with B the coefficient of the dominant solution. The Stokes constant is assigned to the Stokes line because the dominant (subdominant) solution becomes most dominant (subdominant) there. Thus, the asymptotic solutions have to be changed from sector to sector in the complex z-plane. This is called Stokes' phenomenon (24,39). Across the anti-Stokes line the dominancy changes, namely the dominant (subdominant) solution becomes subdominant (dominant). When we cross the branch cut counterclockwise, the solution $(\cdot, z)$ $[(z, \cdot)]$ changes to $-i(z, \cdot)$ $[-i(\cdot, z)]$. According to these rules, the solution given by Eq. (82) in region 1 of Fig. 7 changes as follows:

$$\begin{aligned}
&\text{region 1} && A(\cdot, z) + B(z, \cdot)_s && \text{(83a)}\\
&\text{region 2} && A(\cdot, z) + B(z, \cdot)_d && \text{(83b)}\\
&\text{region 3} && (A + BT_1)(\cdot, z)_s + B(z, \cdot)_d && \text{(83c)}\\
&\text{region 4} && (A + BT_1)(\cdot, z)_d + B(z, \cdot)_s && \text{(83d)}\\
&\text{region 5} && (A + BT_1)(\cdot, z)_d + [B + T_2(A + BT_1)](z, \cdot)_s && \text{(83e)}\\
&\text{region 6} && -i(A + BT_1)(z, \cdot)_d - i[B + T_2(A + BT_1)](\cdot, z)_s && \text{(83f)}\\
&\text{region 7} && -i(A + BT_1)(z, \cdot)_s - i[B + T_2(A + BT_1)](\cdot, z)_d && \text{(83g)}\\
&\text{region 1} && -i\{(A + BT_1) + T_3[B + T_2(A + BT_1)]\}(z, \cdot)_s && \\
& && -i[B + T_2(A + BT_1)](\cdot, z)_d && \text{(83h)}
\end{aligned}$$

Since the solution of Eq. (83h) should coincide with that of Eq. (83a) for arbitrary A and B, we can easily derive

$$T_1 = T_2 = T_3 = i \tag{84}$$

Now, we have the single-valued general solution valid in the whole asymptotic region. For instance, we can obtain the following connection formula for the physical solution on the real axis:

$$(\cdot, x) - i(x, \cdot) \qquad (x < 0) \leftrightarrow -i(x, \cdot) \qquad (x > 0) \tag{85}$$

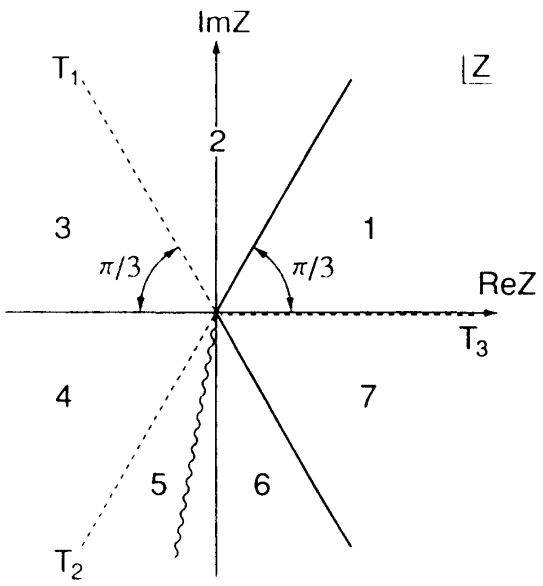

Figure 7 Stokes and anti-Stokes lines for the Airy function. ____: Stokes line, ... : anti-Stokes line, ~~~: branch cut.

The ordinary Airy function $A_i(z)$ corresponds to this solution with $A = 0$. Equation (85) represents the famous connection formula for the WKB solutions crossing the turning point. As can now be easily understood, once we know all the Stokes constants the connections among asymptotic solutions are known and the physical quantities, such as the scattering matrix, can be derived. However, the Airy function is exceptionally simple and the Stokes constants are generally not known except for some special cases (40).

When the coefficient of the differential equation is an nth-order polynomial, the $n + 2$ Stokes lines run radially in the asymptotic region. There are thus $n + 2$ unknown Stokes constants, but only three independent conditions are obtained from the single-valuedness as demonstrated for the Airy function.

B. The Weber Function

The Weber equation

$$\frac{d^2w(z)}{dz^2} + h^2(z^2 - \epsilon^2)w(z) = 0 \tag{86}$$

presents a very basic model in quantum mechanics. There are two first-order transition points $z = \pm\epsilon$ and four Stokes lines in the asymptotic region, as shown in Fig. 8. Asymptotic solutions of Eq. (86) on arg $z = 0$ and π are expressed in ordinary WKB functions as

$$w(z) \underset{z\to+\infty}{\to} Aq^{-1/4}(z)\exp\left[i\int_0^z q^{1/2}(z)\,dz\right] + Bq^{-1/4}(z)\exp\left[-i\int_0^z q^{1/2}(z)\,dz\right] \tag{87a}$$

and

$$w(z) \underset{z\to-\infty}{\to} Cq^{-1/4}(z)\exp\left[i\int_0^z q^{1/2}(z)\,dz\right] + Dq^{-1/4}(z)\exp\left[-i\int_0^z q^{1/2}(z)\,dz\right] \tag{87b}$$

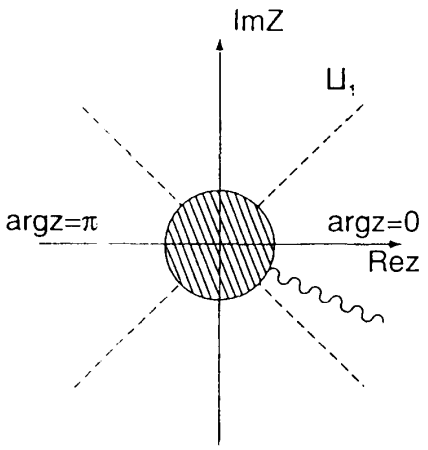

Figure 8 Stokes and anti-Stokes lines in the asymptotic region for the Weber function: ____: Stokes line, : anti-Stokes line, ~~~: branch cut.

where

$$q(z) = h^2(z^2 - \epsilon^2) \tag{88}$$

The standard WKB solutions are

$$(\cdot, z) = z^{-1/2} \exp[iP_W(z)] \tag{89a}$$

and

$$(z, \cdot) = z^{-1/2} \exp[-iP_W(z)] \tag{89b}$$

with

$$P_W(z) = \tfrac{1}{2}h(z^2 - \epsilon \ln z) \tag{90}$$

The asymptotic solutions of (87) are rewritten as

$$\phi_W(z) \underset{z\to+\infty}{\to} A'(\cdot, z) + B'(z, \cdot) \tag{91a}$$

and

$$\phi_W(z) \underset{z\to-\infty}{\to} C'(\cdot, z) + B'(z, \cdot) \tag{91b}$$

The primed coefficients are connected by

$$\begin{pmatrix} C' \\ D' \end{pmatrix} = \begin{pmatrix} 1 & U \\ -(1 + e^{2\pi\beta})/U & e^{-2\pi\beta} \end{pmatrix} \begin{pmatrix} A' \\ B' \end{pmatrix} \tag{92}$$

where U is the Stokes constant on the Stokes line $\arg z = \pi/4$, which is given by

$$U = i \frac{\sqrt{2\pi}}{\Gamma(1/2 - i\beta)} e^{-\pi\beta/2} e^{-i\beta \ln(2h)} \tag{93}$$

and

$$\beta = \tfrac{1}{2}h\epsilon^2 \tag{94}$$

Since the phase integrals in Eqs. (87) and (89) are related by

$$\pm i \int_0^z q^{1/2}(z)\, dz \underset{z\to\pm\infty}{\to} \pm iP_W(z) + \delta_\pm^W \tag{95}$$

where

$$\delta_+^W = ih(-\tfrac{1}{4}\epsilon^2 - \tfrac{1}{2}\ln 2 + \tfrac{1}{2}\epsilon^2 \ln\sqrt{e^{\pi i}\epsilon^2}) \tag{96a}$$

and

$$\delta_-^W = -\delta_+^W + \frac{\pi}{2} h\epsilon^2 \tag{96b}$$

we can obtain the connection matrix between the coefficients in Eqs. (87) as

$$F(\beta) = \begin{pmatrix} \dfrac{\sqrt{2\pi}\exp[\pi\beta/2 - i\beta + i\beta\ln(e^{\pi i}\beta)]}{\Gamma(1/2 + i\beta)} & ie^{\pi\beta} \\ -ie^{\pi\beta} & \dfrac{\sqrt{2\pi}\exp[\pi\beta/2 + i\beta - i\beta\ln(e^{\pi i}\beta)]}{\Gamma(1/2 - i\beta)} \end{pmatrix} \tag{97}$$

with

$$\begin{pmatrix} C \\ D \end{pmatrix} = F(\beta)\begin{pmatrix} A \\ B \end{pmatrix} \tag{98}$$

Next, let us consider Eq. (86) with h replaced by ih' ($h' > 0$) and the connection matrix along the Stokes lines $\arg z = \pm\pi/2$. The phase integrals in Eqs. (87) are replaced by

$$\pm i \int_0^z q^{1/2}(z)\, dz \to \mp \int_0^z q^{1/2}(z)\, dz \tag{99}$$

where $q(z)$ on the right side is defined also by Eq. (88) with h replaced by h'. Using the same procedure, one can obtain the connection matrix $H(\beta)$:

$$H(\beta) = \begin{pmatrix} \dfrac{\sqrt{2\pi}\cos(\pi\beta)}{2\Gamma(1/2 - \beta)} e^{\beta - \beta\ln\beta} & -\sin(\pi\beta) \\ \sin(\pi\beta) & \dfrac{\sqrt{2\pi}}{\Gamma(1/2 + \alpha)} e^{-\beta + \beta\ln\beta} \end{pmatrix} \tag{100}$$

with

$$\begin{pmatrix} C \\ D \end{pmatrix} = H(\beta)\begin{pmatrix} A \\ B \end{pmatrix} \tag{101}$$

where β is given by Eq. (94) with h replaced by h'.

C. Linear Potential Crossing

In this section the mathematical procedure is briefly outlined for deriving the exact expressions of the reduced scattering matrices and of the Stokes constants in the linear curve-crossing problems and for devising new semiclassical approximations to them.

1. General Properties and Exact Solutions (20,41)

Let us first consider the general second-order differential equation with quartic polynomial coefficient function:

$$\frac{d^2w(z)}{dz^2} + q(z)w(z) = 0 \tag{102}$$

where

$$q(z) = a_4z^4 + a_2z^2 + a_1z + a_0 \qquad (a_4 > 0) \tag{103}$$

The standard WKB solutions are

$$(\cdot, z) = z^{-1} \exp[ip(z)] \tag{104a}$$

and

$$(z, \cdot) = z^{-1} \exp[-ip(z)] \tag{104b}$$

with

$$p(z) = \frac{i}{3}\sqrt{a_4}z^3 + \frac{i}{2\sqrt{a_4}}a_2z + \frac{i}{2\sqrt{a_4}}a_1 \ln(z) \tag{105}$$

For later convenience, the following transformation of variables is introduced:

$$\zeta = \frac{2}{3}(-a_4)^{1/2}z^3 \qquad \text{and} \qquad w(z) = \frac{u(\zeta)}{z} \tag{106}$$

Then Eq. (102) becomes

$$\frac{d^2u(\zeta)}{d\zeta^2} + Q(\zeta)u(\zeta) = 0 \tag{107}$$

with

$$Q(\zeta) = -1/4 + Q_0\zeta^{-2/3} + Q_1\zeta^{-1} + Q_2\zeta^{-4/3} + Q_4\zeta^{-2} \tag{108}$$

There are six Stokes lines in the asymptotic region of z as shown in Fig. 9. In the ζ-plane they coincide with the real axis, since $\arg \zeta = 3 \arg z + \pi/2$.

Using the transformation in Eq. (106), we can obtain the simple relations between the Stokes constant U_j in the z-plane and the Stokes constant T_j in the ζ-plane for $j = 1-6$. Using the symmetry of the differential equation (107) with Eq. (108), we can derive the interrelations among T_j's as

$$T_{j+1} = \bar{T}_j e^{-2\pi iQ_1} \qquad (j = 1, 3, 5) \tag{109a}$$

and

$$T_{j+1} = \bar{T}_j e^{2\pi iQ_1} \qquad (j = 2, 4) \tag{109b}$$

where the overbar means the following transformation:

$$\zeta \to \zeta e^{-\pi i}, \quad Q_0 \to \omega^2Q_0, \quad Q_1 \to \omega^3Q_1, \quad \text{and} \quad Q_2 \to \omega^4Q_2 \tag{110}$$

with $\omega = e^{-\pi i/3}$. Finally, by transforming Eq. (107) into coupled integral equations and utilizing the asymptotic expansion of the incomplete gamma function, the analytical ex-

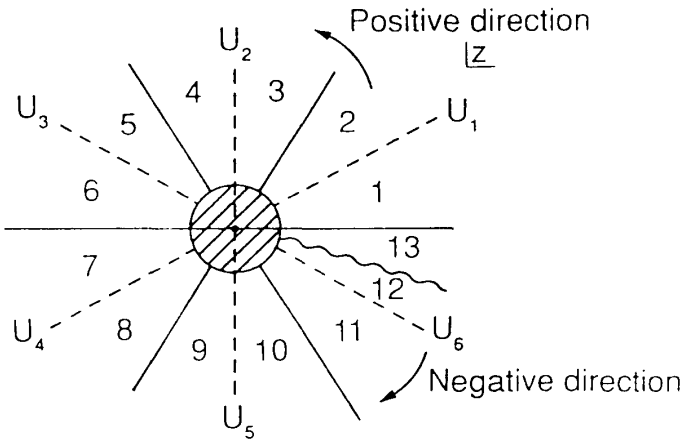

Figure 9 Stokes (dashed) and anti-Stokes (solid) lines for the differential equation (102) with Eq. (103). (From Ref. 41.)

pression of T_1 is obtained in the form of a convergent infinite series. This enables us to derive analytical expressions of all the Stokes constants T_j. The procedure to derive T_1 and the result are quite complicated and thus omitted here. The results obtained can be directly applied to linear curve-crossing problems, the basic differential equations of which are given by Eqs. (60) and (61). The reduced scattering matrices for the LZ and NT cases are expressed in terms of the only Stokes constant U_1 as given in Eqs. (68) and (72) (20).

2. Approximate Expressions of the Stokes Constant U_1 (20–23)

In order to derive approximate analytical expressions of U_1, we need to know the distribution of the four transition points in the complex z-plane. The transition points are zero points of the following quartic polynomials (see Eqs. (61)):

$$z^4 - 2\frac{b^2}{a^2}z^2 \mp i\frac{4}{a^2}z + \left(\frac{b^2}{a^2}\right)^2 \pm \frac{1}{a^4} = 0 \tag{111}$$

where the upper (lower) sign corresponds to the LZ (NT) case. In the LZ case the four transition points t_j ($j = 1-4$) are given as follows (see Figs. 2 and 3 of Ref. 20):

$$t_{1,2} = \pm x_1 + iy \qquad t_{3,4} = \mp x_2 - iy \tag{112}$$

where

$$x_1^2 = y^2 + \frac{b^2}{a^2} + \frac{1}{a^2 y} \qquad (x_1 > 0) \tag{113a}$$

$$x_2^2 = y^2 + \frac{b^2}{a^2} - \frac{1}{a^2 y} \qquad (x_2^2 \text{ real}) \tag{113b}$$

and y is a positive solution (there is only one) of

$$y^6 + \frac{b^2}{a^2}y^4 - \frac{1}{4a^4}y^2 - \frac{1}{4a^4} = 0 \tag{113c}$$

In the NT case the situation is much more complicated than the LZ case, and Eqs. (113) are replaced by

$$x_1^2 = y^2 + \frac{b^2}{a^2} - \frac{1}{a^2 y} \tag{114a}$$

$$x_2^2 = y^2 + \frac{b^2}{a^2} + \frac{1}{a^2 y} \tag{114b}$$

and

$$y^6 + \frac{b^2}{a^2} y^4 + \frac{1}{4a^4} y^2 - \frac{1}{4a^2} = 0 \tag{114c}$$

where $y > 0$, but both x_1^2 and x_2^2 can be negative. The distribution of the t_j's is classified into six cases (see Figs. 4 and 5 of Ref. 20).

Next, we consider the two limiting cases in order to derive compact analytical expressions for U_1. The first is the case that the two pairs of transition points (t_1, t_4) and (t_2, t_3) are well isolated from each other along the real axis and can be treated separately. Roughly speaking, this corresponds to $b^2 \gg 1$ in both the LZ and NT cases. The connection matrix L which connects the coefficients of the asymptotic solutions are $z \to \pm\infty$ and is directly related to scattering matrix can be well approximated by

$$L = F_1 F_0 F_2 \tag{115}$$

where F_j ($j = 1, 2$) are obtained from the Weber equation with F_1 (F_2) corresponding to $\mathrm{Re}(z) < 0$ (> 0) (see Eq. (97)), and F_0 represents the connection between the two pairs of transition points and is given by

$$F_0 = \begin{pmatrix} e^{-i\Phi} & 0 \\ 0 & e^{i\Phi} \end{pmatrix} \tag{116}$$

where

$$\Phi = \int_{-x_0}^{x_0} q^{1/2}(z)\, dz \tag{117}$$

and

$$x_0 = \frac{x_1 + x_2}{2} = \begin{cases} \dfrac{1}{\sqrt{2a}} \sqrt{b^2 + \sqrt{b^4 + 1}} & \text{(LZ case)} \qquad (118a) \\ \dfrac{1}{\sqrt{2a}} \sqrt{b^2 + \sqrt{b^4 - 1}} & \text{(NT case)} \qquad (118b) \end{cases}$$

From this procedure we obtain the explicit expression for U_1.

The second limiting case is that the pairs (t_1, t_2) and (t_3, t_4) are well separated along the imaginary axis, which is a Stokes line. This corresponds roughly to $b^2 \ll -1$ (see case (a) in Fig. 1 and case (e) in Figs. 4 and 5 of Ref. 20). The connection matrix G which connects the coefficients of the asymptotic solutions at $z \to \infty e^{\pm \pi i/2}$ can be well approximated as

$$G = H_1 H_0 H_2 \tag{119}$$

where H_j ($j = 1, 2$) are again obtained from the Weber equation with H_1 (H_2) corresponding to $\mathrm{Im}\, z < 0$ (> 0) (see Eq. (100)), and H_0 represents the connection between the two

pairs and is

$$H_0 = \begin{pmatrix} e^{-i\tilde{\Phi}} & 0 \\ 0 & e^{i\tilde{\Phi}} \end{pmatrix} \tag{120}$$

where

$$\Phi = \int_{-iy}^{iy} q^{1/2}(z)\, dz \tag{121}$$

The above connection is made on the Stokes line and one-half of the Stokes constants are assigned to the Stokes line according to the Jeffrey's connection formula (24). This procedure leads to the explicit approximate expression of U_1.

The first limiting case has been treated by using basically the same idea by many authors (29,32), but the present analysis is most accurate and gives much better results. The second limiting case has never been treated properly before. The formulas obtained in the analysis have covered a very wide range of a^2 and b^2 due to careful analysis, and can be easily modified to cover practically the whole range of a^2 and b^2 except for $|b^2| \leq 1$ in the NT case, where the four transition points cannot be separated into any pairs. This case requires a totally different analysis, which is not described here (23,42).

VI. NEW THEORETICAL DEVELOPMENTS: BEYOND THE LANDAU-ZENER-STÜCKELBERG THEORY

Recently, a new semiclassical theory has been developed for the general two-state curve-crossing problems (16,17). This theory is applicable to the LZ and NT cases of general curved potentials, regardless of the coupling strength and energy. This does not require any sophisticated calculus, such as complex contour integrals like Eq. (24) and complicated special functions, so it is very convenient even for general nonspecialist users. Furthermore, compact and accurate formulas have been derived for the Landau-Zener transition probability p. These are as simple as, and yet far better than, the famous Landau-Zener formula $p_{LZ}^{(0)}$ of Eq. (10). They are simply expressed in terms of the basic parameters a^2 and b^2 (see Eqs. (19) and (63)) for $E \geq E_X$ ($E \geq E_b$) in the LZ (NT) case (see Fig. 2), but are still applicable to the general curved potentials. At $E \leq E_X$ in the LZ case another compact and accurate formula has been obtained for the Landau-Zener transition probability. At $E \leq E_b$ in the NT case a compact and accurate expression has been derived for the nonadiabatic tunneling (transmission) probability. Finally, the basic parameters a^2 and b^2 can be reexpressed only in terms of the corresponding adiabatic potentials; thus nonunique diabatization procedure is not required when only adiabatic potentials are available. the new semiclassical theory outlined above is summarized in this section. This makes possible a complete set of solutions for the general two-state curve-crossing problems.

A. Nonadiabatic Tunneling Case (16)

The reduced scattering matrix S^R given by Eqs. (72) and (73) is the one in the diabatic representation. In the adiabatic representation we have

$$S^{R(a)} = \frac{1}{1 + U_1 U_2} \begin{pmatrix} e^{i\Delta_{11}} & U_2 e^{i\Delta_{12}} \\ U_2 e^{i\Delta_{12}} & e^{i\Delta_{22}} \end{pmatrix} \tag{122}$$

where U_2 is given by Eq. (73) and the additional phases Δ_{ij} are defined below. The elastic scattering phases $\eta^{(a)}{}_j$ in the adiabatic representation are defined as

$$\eta_1^{(a)} = \lim_{R>>X_1} \left(\int_{X_1}^{R} k_1(R)\, dR - k_1(R)R + \frac{\pi}{4} \right) \tag{123a}$$

and

$$\eta_2^{(a)} = \lim_{R<<X_2} \left(-\int_{X_2}^{R} k_1(R)\, dR + k_1(R)R + \frac{\pi}{4} \right) \tag{123b}$$

where the reference points $X_{1,2}$ are defined in each energy region. Another interesting and useful achievement is that the basic diabatic parameters a^2 and b^2 defined by Eqs. (19) (see Eq. (63) also) can be reexpressed in terms of the adiabatic potentials as (see Fig. 10)

$$a^2 = \frac{(1 - \gamma^2)\hbar^2}{\mu(R_b - R_t)^2(E_b - E_t)} \tag{124}$$

and

$$b^2 = \frac{E - (E_b + E_t)/2}{(E_b - E_t)/2} \tag{125}$$

with

$$\gamma = \frac{E_b - E_t}{E_2[(R_b + R_t)/2] - E_1[(R_b + R_t)/2]} \qquad (0 < \gamma \leq 1) \tag{126}$$

Another important matrix in the NT case is the transfer matrix N which connects the waves on the right side of the barrier to those on the left side. This matrix is obtained

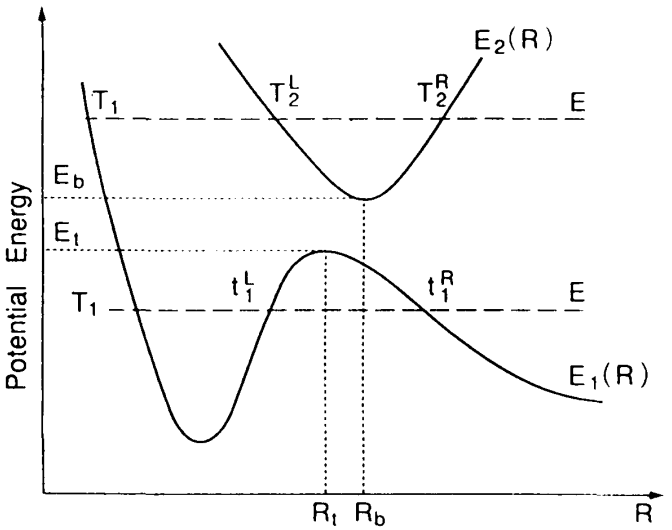

Figure 10 Two-state curve crossing in the NT case. Adiabatic potential parameters to express a^2 and b^2 (see Eqs. (124) and (125)).

from the reduced scattering matrix S^R as

$$N_{11} = \frac{1}{S_{12}^{R(a)*}}, \quad N_{22} = N_{11}^*, \quad N_{12} = \frac{S_{22}^{R(a)}}{S_{12}^{R(a)*}}, \quad \text{and} \quad N_{21} = N_{12}^* \tag{127}$$

In the following three subsections the Stokes constant U_1 and other basic quantities are presented. Finally in Sec. VI.A.4, the interesting phenomenon of complete reflection is further interpreted.

1. $E \leq E_t$ $(b^2 \leq -1)$

The Stokes constant U_1 is expressed as

$$\text{Re } U_1 = \sin(2\sigma_{ZN})\left\{\frac{g_1}{4}\left[B\left(\frac{\sigma_{ZN}}{\pi}\right)\right]^{1/2}\exp(-\delta_{ZN}) + \frac{\exp(\delta_{ZN})}{[B(\sigma_{ZN}/\pi)]^{1/2}}\right\} \tag{128a}$$

and

$$\text{Im } U_1 = \cos(2\sigma_{ZN})\left\{\frac{(\text{Re } U_1)^2}{\sin^2(2\sigma_{ZN})} + \frac{1}{\cos^2(\sigma_{ZN})}\right\}^{1/2} - \frac{1}{2\sin(\sigma_{ZN})}\left|\frac{\text{Re } U_1}{\cos(\sigma_{ZN})}\right| \tag{128b}$$

where

$$\sigma_{ZN} = (1 - g_2)\frac{\pi}{16a|b|}\frac{[6 + 10(1 - b^{-4})^{1/2}]^{1/2}}{1 + (1 - b^{-4})^{1/2}} \tag{129}$$

$$B(X) = \frac{2\pi X^{2X}e^{-2X}}{X\Gamma^2(X)} \tag{130}$$

$$\delta_{ZN} = \int_{t_1^I}^{t_1^R} |k_1(R)|\, dR \tag{131}$$

$$g_1 = \frac{2a}{1 + a} \tag{132}$$

and

$$g_2 = 0.32 \times 10^{-2/a^2}\exp(-\delta_{ZN}) \tag{133}$$

The additional phases Δ_{ij} in Eq. (122) are given by

$$\Delta_{12} = \Delta_{11} = \Delta_{22} = \frac{-2\sigma_{ZN}}{1 - g_2} \tag{134}$$

The reference points $X_{1,2}$ to define the elastic scattering phases (Eqs. (123)) are $X_1 = t_1^R$ and $X_2 = t_1^I$ (see Fig. 10). The factors g_1 and g_2 are introduced empirically in order to cover the whole range of coupling strength. These are unity and zero, respectively, in the original formulation. The overall transmission (nonadiabatic tunneling) probability P_{12} is explicitly expressed as (see Eq. (74))

$$P_{12} = |S_{21}^{R(a)}|^2 = \frac{B(\sigma_{ZN}/\pi)\exp(-2\delta_{ZN})}{[1 + (g_1/4)B(\sigma_{ZN}/\pi)\exp(-2\delta_{ZN})]^2 + B(\sigma_{ZN}/\pi)\exp(-2\delta_{ZN})} \tag{135}$$

The factor $e^{-2\delta_{ZN}}$ is nothing but the Gamov factor, and the function $B(\sigma_{ZN}/\pi)$ clearly indicates the effect of nonadiabatic coupling on the tunneling. In the strong diabatic coupling limit, $a^2 \to 0$ and $B(\sigma_{ZN}/\pi) \to 1$; thus P_{12} coincides with the well-known formula for single-potential tunneling.

2. $E_t \leq E \leq E_b \quad (|b^2| \leq 1)$

The Stokes constant U_1 is

$$U_1 = \frac{i[(1 + W^2)^{1/2}e^{i\phi} - 1]}{W} \tag{136}$$

with

$$\phi = \sigma_{ZN} + \arg \Gamma\left(\frac{1}{2} + i\frac{\delta_{ZN}}{\pi}\right) - \frac{\delta_{ZN}}{\pi}\ln\left(\frac{\delta_{ZN}}{\pi}\right) + \frac{\delta_{ZN}}{\pi} - g_3 \tag{137}$$

and

$$W = \frac{1}{a^{2/3}}\int_0^\infty \cos\left(\frac{t^3}{3} - \frac{b^2}{a^{2/3}}t - \frac{1}{2a^{2/3}}\frac{1}{g_4 + a^{1/3}t}\right) dt \tag{138}$$

where

$$\sigma_{ZN} = -\frac{1}{a}\left[0.057(1 + b^2)^{0.25} + \frac{1}{3}\right](1 - b^2)(5 + 3b^2)^{1/2} \tag{139}$$

$$\delta_{ZN} = \frac{1}{a}\left[0.057(1 - b^2)^{0.25} + \frac{1}{3}\right](1 + b^2)(5 - 3b^2)^{1/2} \tag{140}$$

$$g_3 = 0.34\frac{a^{0.7}(a^{0.7} + 0.35)}{a^{2.1} + 0.73}(0.42 + b^2)\left(2 + \frac{100b^2}{100 + a^2}\right)^{0.25} \tag{141}$$

and

$$g_4 = \left|\frac{1 - (0.37 - 0.08b^2)b^2a^{-2/3}}{1 + 0.56a^{-2/3}}\right| \tag{142}$$

The parameters σ_{ZN} and δ_{ZN} are the empirical expressions of the quantities

$$\sigma = \mathrm{Im}\left(\int_{R_1^{(2)}}^{R_2^{(2)}} k_2(R)\, dR\right) \tag{143}$$

and

$$\delta = \mathrm{Im}\left(\int_{R_1^{(1)}}^{R_2^{(1)}} k_1(R)\, dR\right) \tag{144}$$

where $R_{1,2}^{(j)}$ are the complex turning points on the adiabatic potential $E_j(R)$. The factors g_3 and g_4, which are zero and unity respectively in the original formulation, are the empirical corrections. The additional phases Δ_{ij} in Eq. (122) are

$$\Delta_{12} = \sigma_{ZN} \tag{145a}$$

$$\Delta_{11} = \sigma_{ZN} - \sigma_0^{ZN} \tag{145b}$$

and

$$\Delta_{22} = \sigma_{ZN} + 2\sigma_0^{ZN} \tag{145c}$$

with

$$\sigma_0^{ZN} = -\frac{1}{3}(R_t - R_b)k_1(R_t)(1 + b^2) \tag{146}$$

where R_t (R_b) is the position of the top (bottom) of the lower (upper) adiabatic potential (see Fig. 10). The reference points $X_{1,2}$ to define $\eta_j^{(a)}$'s of Eqs. (123) are $X_{1,2} = R_t$. The overall nonadiabatic tunneling (transmission) probability is equal to

$$P_{12} = |S_{21}^{R(a)}|^2 = \frac{W^2}{1 + W^2} \tag{147}$$

3. $E \geq E_b$ $(b^2 \geq 1)$

We have the following expression for the Stokes constant:

$$U_1 = i(1 - p_{ZN})^{1/2} \exp(i\psi_{ZN}) \tag{148}$$

where p_{ZN} is the Landau-Zener transition probability given by

$$p_{ZN} = \exp\left[-\frac{\pi}{4ab}\left(\frac{2}{1 + (1 - b^{-4}g_5)^{1/2}}\right)^{1/2}\right] \tag{149}$$

and ψ_{ZN} is the phase corresponding to ψ_{LS} of Eq. (31) and is

$$\psi_{ZN} = \sigma_{ZN} - \phi_S(\delta_{ZN}) - g_6 \tag{150a}$$

with

$$\sigma_{ZN} = \gamma_2(T_2^L, T_2^R) \tag{150b}$$

The factors g_5 and g_6, which are unity and zero respectively in the original formulation, are again the empirical corrections in order to cover the whole range of coupling strength and are defined by

$$g_5 = 0.72 - 0.62a^{1.43} \tag{151}$$

and

$$g_6 = \frac{0.23a^{1/2}}{a^{1/2} + 0.75} 40^{-\gamma_2(T_1^L, T_2^R)} \tag{152}$$

The phase integral γ_2 and the Stokes phase correction ϕ_S are defined by Eq. (25) and Eq. (25), respectively. The nonadiabatic transition parameter δ_{ZN} is the counterpart of σ_{ZN} at $E \leq E_t$ and is

$$\delta_{ZN} = \frac{\pi}{16ab} \frac{\{6 + 10[1 - b^{-4}]^{1/2}\}^{1/2}}{1 + [1 - b^{-4}]^{1/2}} \tag{153}$$

The Landau-Zener transition probability p_{ZN} is as simple as the famous Landau-Zener formula $p_{LZ}^{(0)}$ of Eq. (10) but much better. Note that $p_{LZ}^{(0)}$ is expressed in terms of a^2 and b^2 as

$$p_{LZ}^{(0)} = \exp\left(-\frac{\pi}{4ab}\right) \tag{154}$$

The additional phases Δ_{ij} in Eq. (122) are

$$\Delta_{12} = \gamma_2(T_2^L, T_2^R) \tag{155a}$$

$$\Delta_{11} = 2\gamma_2(T_2^L, R_b) - 2\sigma_0^{ZN} \tag{155b}$$

and

$$\Delta_{22} = 2\gamma_2(R_b, T_2^R) + 2\sigma_0^{ZN} \tag{155c}$$

with

$$\sigma_0^{ZN} = \frac{R_b - R_t}{2}\left\{k_1(R_t) + k_2(R_b) + \frac{1}{3}\frac{[k_1(R_t) - k_2(R_b)]^2}{k_1(R_t) + k_2(R_b)}\right\} \tag{156}$$

The reference points $X_{1,2}$ in the definition of $\eta_j^{(a)}$ of Eqs. (123) are the same as in the case $E_t \leq E \leq E_b$; i.e., $X_{1,2} = R_t$. The overall nonadiabatic tunneling (transmission) probability P_{12} is equal to

$$P_{12} = |S_{21}^{R(a)}|^2 = \frac{4\cos^2\psi_{ZN}}{4\cos^2\psi_{ZN} + p_{ZN}^2/(1 - p_{ZN})} \tag{157}$$

The reduced scattering matrix derived before 1991, i.e., Eqs. (31), has essentially the same form as the new one here except that ψ_{ZN}, p_{ZN}, and σ_0^{ZN} have simpler, improved expressions.

4. Complete Reflection

As is clear from Eq. (157), the transmission probability P_{12} becomes zero when the following condition is satisfied:

$$\psi_{ZN} = \gamma_2(T_2^L, T_2^R) - \phi_S = \left(l + \frac{1}{2}\right)\pi, \qquad l = 0, 1, 2, \ldots \tag{158}$$

where for simplicity the empirical correction g_6 is omitted. This is a very interesting phenomenon, because the complete reflection of wave occurs in a simple potential like the one shown in Fig. 2b at certain discrete energies which satisfy Eq. (158). This phenomenon was proved by exact quantum mechanics outlined in Sec. IV in the linear potential model (20). This occurs at $\mathrm{Im}(U_1) = 0$. The condition of (158) is similar to the simple Bohr-Sommerfeld quantization condition but with an extra correction term ϕ_S due to nonadiabatic coupling whose value is in the interval $(0, \pi/4)$. A numerical example can be seen in Fig. 4. The width of the complete reflection dip depends on the coupling and the shape of the potential naturally and can be expressed analytically, but we do not go into the details here.

This phenomenon implies, however, the following intriguing possibilities (37): (1) bound state in the continuum and (2) switching of transmission in a periodic system. These are explained very briefly. If we put two noninteracting potentials of the type of Fig. 2b, bound states can exist between the two potential units at the energies which satisfy the condition of complete reflection, Eq. (158). In addition, the following quantization condition is, of course, required:

$$\gamma_1(R_t^{(1)}, R_t^{(2)}) + \frac{1}{2}[\arg S_{11}^{R(a)} + \arg S_{22}^{R(a)}] = s\pi, \qquad s = 1, 2, \ldots \tag{159}$$

where $R_t^{(j)}$ represents the top of the lower adiabatic potential at the jth potential unit. This condition can be compatible with Eq. (158)—a bound state in continuum is theoretically possible. The second interesting possibility is molecular switching. In a system composed of N identical potential units, complete resonant transmission is possible at certain discrete energies. These energies constitute a conduction band in the $N \to \infty$ limit. If we create an impurity in this system, say by changing the diabatic coupling in one of the potential units, then complete transmission is not possible anymore; besides this impurity creates a new series of complete reflection dips (37). So, if we could change one of the potential units in a reversible way and make one of the new complete reflection dips coincide with one of the original complete transmission peaks, then we could control the transmission theoretically in principle. More detailed analysis can be made, but is omitted here, since this deviates a bit from the main theme of this chapter.

B. Landau-Zener Case

The reduced scattering matrix in the adiabatic representation is (cf. Eq. (72))

$$S^{R(a)} = \begin{pmatrix} (1 + U_1U_2)e^{-2i\sigma} & -U_2 \\ -U_2 & (1 - U_1^*U_2)e^{2i\sigma} \end{pmatrix} \tag{160}$$

where U_2 is defined by Eq. (69). The phase σ is given below in the subsections. The elastic scattering phases are

$$\eta_1^{(a)} = \lim_{R\to\infty} \left[\int_{T_1}^{R} k_1(R)\, dR - k_1(R)R + \frac{\pi}{4} \right] \tag{161a}$$

and

$$\eta_2^{(a)} = \lim_{R\to\infty} \left[\int_{T_2}^{R} k_2(R)\, dR - k_2(R)R + \frac{\pi}{4} \right] \tag{161b}$$

where T_j is the turning point on the adiabatic potential $E_j(R)$ (see Fig. 2a). The reduced scattering matrix elements are explicitly given as

$$S_{11}^{R(a)} = [p_{ZN} + (1 - p_{ZN})e^{2i\psi_{ZN}}]e^{-2i\sigma_{ZN}} \tag{162a}$$

$$S_{22}^{R(a)} = [p_{ZN} + (1 - p_{ZN})e^{-2i\psi_{ZN}}]e^{2i\sigma_{ZN}} \tag{162b}$$

and

$$S_{12}^{R(a)} = S_{21}^{R(a)} = -2i\sqrt{p_{ZN}(1 - p_{ZN})}\sin\psi_{ZN} \tag{162c}$$

where p_{ZN} is the Landau-Zener transition probability defined by Eq. (71) and

$$\psi_{ZN} = \arg(U_1) \tag{163}$$

As in the NT case, the basic diabatic parameters a^2 and b^2 defined by Eqs. (19) can be reexpressed in terms of the adiabatic potentials as given below, so a nonunique diabatization procedure is not required. These parameters are

$$a^2 = \sqrt{d^2 - 1}\, \frac{\hbar^2}{\mu(T_2^{(0)} - T_1^{(0)})^2[E_2(R_0) - E_1(R_0)]} \tag{164}$$

and

$$b^2 = \sqrt{d^2 - 1}\,\frac{E - [E_2(R_0) + E_1(R_0)]/2}{[E_2(R_0) - E_1(R_0)]/2} \tag{165}$$

with

$$d^2 = \frac{[E_2(T_1^{(0)}) - E_1(T_1^{(0)})][E_2(T_2^{(0)}) - E_1(T_2^{(0)})]}{[E_2(R_0) - E_1(R_0)]^2} \tag{166}$$

where R_0 is the position at which $E_2(R) - E_1(R)$ becomes a minimum (see Fig. 11):

$$E_2(T_2^{(0)}) = E_1(T_1^{(0)}) = E_X \tag{167}$$

and

$$E_X = \frac{1}{2}[E_2(R_0) + E_1(R_0)] \tag{168}$$

The best recommended formulas are two sets: one is valid at $E \geq E_X$ and the other at $E \leq E_X$. These are explicitly presented in the following subsections.

1. $E \geq E_X$ $(b^2 \geq 0)$

The Stokes constant is simply

$$U_1 = \left(\frac{1}{p_{ZN}} - 1\right)^{1/2} e^{i\psi_{ZN}} \tag{169}$$

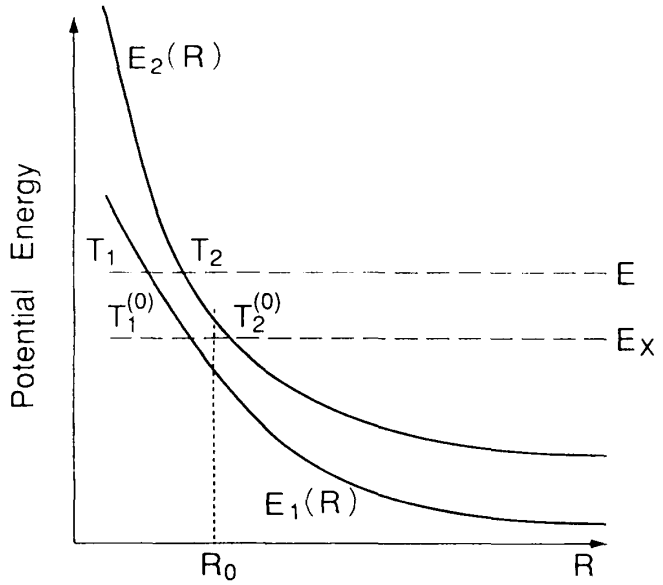

Figure 11 Two-state curve crossing in the LZ case. Adiabatic potential parameters to express a^2 and b^2 (see Eqs. (164) and (165)).

with

$$p_{ZN} = \exp\left[-\frac{\pi}{4ab}\left(\frac{2}{1+\sqrt{1+b^{-4}h_1}}\right)^{1/2}\right] \tag{170}$$

$$\psi_{ZN} = \sigma_{ZN} - \frac{\delta_\psi}{\pi} + \frac{\delta_\psi}{\pi}\ln\left(\frac{\delta_\psi}{\pi}\right) - \arg\Gamma\left(i\frac{\delta_\psi}{\pi}\right) - \frac{\pi}{4} \tag{171}$$

and

$$\delta_\psi = \delta_{ZN}(1 + h_2) \tag{172}$$

where

$$h_1 = 0.7 + 0.4a^2 \tag{173}$$

and

$$h_2 = \frac{5\sqrt{a}}{\sqrt{a} + 0.8}\,10^{-\sigma_{ZN}} \tag{174}$$

The factors h_1 and h_2, which are unity and zero in the original formulation, are empirical corrections in order to cover the whole range of coupling strength. The famous Landau-Zener formula is equal to Eq. (154), and the formula (170) is as simple as, but far better than, Eq. (154). Figure 12 demonstrates this fact. Since the exact p can be calculated only in the linear potential model, Fig. 12 is the result for that model. Equation (170) can work well for general curved potentials, since nonadiabatic transition is very well localized at the avoided crossing point. The phase integrals σ_{ZN} and δ_{ZN} are explicitly

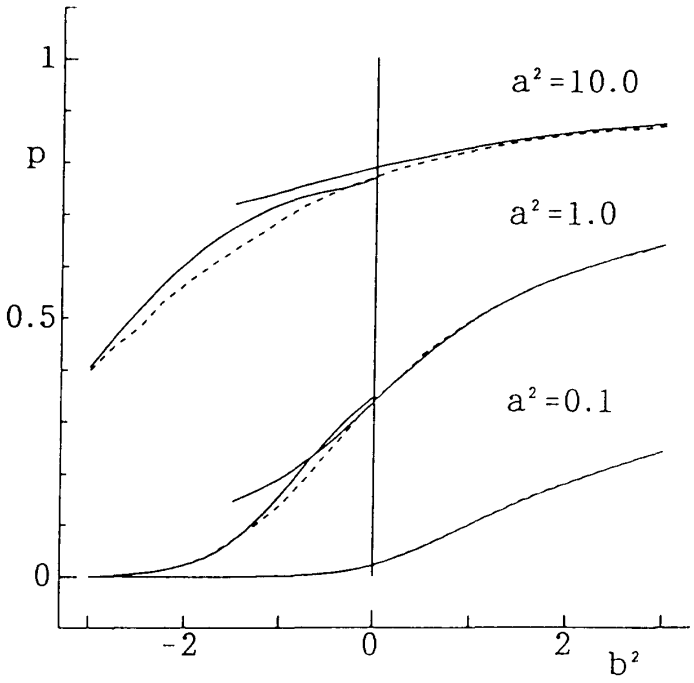

Figure 12 The Landau-Zener transition probability p in the LZ case. Dashed line: exact, solid line: Eqs. (170) and (183). (From Ref. 23.)

expressed as

$$\sigma_{ZN} = \int_{t_1}^{T_1^{(0)}} k_1(R)\, dR - \int_{t_2}^{T_2^{(0)}} k_2(R)\, dR + \sqrt{\frac{b^2}{a^2}} + \frac{1}{2a} R + \frac{1}{\sqrt{2}a} \frac{1}{(b^4 + 1)^{1/4}} \frac{R_0 - (T_1^{(0)} + T_2^{(0)})/2}{T_2^{(0)} - T_1^{(0)}} \sqrt{\frac{d^2}{d^2 - 1}} \sqrt{1 + \frac{b^2}{\sqrt{b^4 + 1}}} \tag{175}$$

and

$$\delta_{ZN} = \frac{1}{2a} I - \frac{1}{\sqrt{2}a} \frac{1}{(b^4 + 1)^{1/4}} \frac{R_0 - (T_1^{(0)} + T_2^{(0)})/2}{T_2^{(0)} - T_1^{(0)}} \sqrt{\frac{d^2}{d^2 - 1}} \sqrt{1 - \frac{b^2}{\sqrt{b^4 + 1}}} \tag{176}$$

where

$$R = \left[\frac{2}{B^2} + \frac{B^2 + 4|b^2| + \sqrt{2|b^2|}B}{2} \right]^{1/2} \tag{177}$$

$$\left[\frac{\pi B^2}{4} - \frac{\sqrt{|b^2|/2}}{B} - \frac{B^2}{2} \sin^{-1}\left(\frac{\sqrt{2|b^2|}}{B} \right) \right] \tag{178}$$

$$I = \frac{\sqrt{2}\pi}{4B^2} \sqrt{B^2 + \frac{0.24}{B^2}}$$

with

$$B = \sqrt{|b^2| + \sqrt{b^4 + 1}} \tag{179}$$

These expressions might look messy at a glance, but they do not involve any complex calculus and complicated special functions, and they are very convenient for practical applications. The essential points in deriving these expressions are as follows: The linear potential approximation was applied to the complex phase integral, but was minimized by introducing the real reference points $T_j^{(0)}$'s instead of R_X (see Eq. (24) and Fig. 11). The complex phase integral in the linear potential model was further approximated by the explicit simple functions including I and R in the above expressions. The deviations from the linear potential model were also estimated to give the last terms in Eqs. (175) and (176).

2. $E \leq E_X$ $(b^2 \leq 0)$

The Stokes constant is expressed as

$$\text{Re } U_1 = \cos(\sigma_{ZN}) \left\{ \sqrt{B\left(\frac{\sigma_{ZN}}{\pi}\right)} e^{\delta_{ZN}} - h_3 \sin^2(\sigma_{ZN}) \frac{e^{-\delta_{ZN}}}{\sqrt{B(\sigma_{ZN}/\pi)}} \right\} \tag{180a}$$

and

$$\text{Im } U_1 = \sin(\sigma_{ZN})\left\{B\left(\frac{\sigma_{ZN}}{\pi}\right)e^{2\delta_{ZN}} - h_3^2 \sin^2(\sigma_{ZN})\cos^2(\sigma_{ZN}) \frac{e^{-2\delta_{ZN}}}{\sqrt{B(\sigma_{ZN}/\pi)}} + 2h_3 \cos^2(\sigma_{ZN}) - h_4\right\}^{1/2} \tag{180b}$$

with

$$h_3 = 1.8a^{0.46}e^{-\delta_{ZN}} \tag{181}$$

and

$$h_4 = \frac{3\sigma_{ZN}}{\pi\delta_{ZN}} \ln(1.2 + a^2) - \frac{1}{a^2} \tag{182}$$

The function $B(X)$ is the same as Eq. (130). The factors h_3 and h_4, which are unity in the original formulation, are the empirical corrections introduced in order to cover the whole range of coupling strength.

The Landau-Zener transition probability p_{ZN} can be explicitly given as

$$p_{ZN} = \left[1 + B\left(\frac{\sigma_{ZN}}{\pi}\right)e^{2\delta_{ZN}} - h_4 \sin^2(\sigma_{ZN})\right]^{-1} \tag{183}$$

This is the first result ever obtained and yet works well over the whole range of coupling strength, as demonstrated in Fig. 12. As is easily conjectured, this probability includes the effects not only of the nonadiabatic transition presented by σ_{ZN} but also of the tunneling from the turning point to the avoided crossing point represented by δ_{ZN}. The phase integrals σ_{ZN} and δ_{ZN} are explicitly given as follows:

$$\sigma_{ZN} = \frac{1}{2a} I + \frac{1}{\sqrt{2}a} \frac{1}{(b^4 + 1)^{1/4}} \frac{R_0 - (T_1^{(0)} + T_2^{(0)})/2}{T_2^{(0)} - T_1^{(0)}} \sqrt{\frac{d^2}{d^2 - 1}} \sqrt{1 + \frac{b^2}{\sqrt{b^4 + 1}}} \tag{184}$$

and

$$\delta_{ZN} = \int_{T_1}^{T_1^{(0)}} |k_1(R)|\, dR - \int_{T_2}^{T_2^{(0)}} |k_2(R)|\, dR + \sqrt{\frac{|b^2|}{a^2}} + \frac{1}{2a} R - \frac{1}{\sqrt{2}a} \frac{1}{(b^4 + 1)^{1/4}} \frac{R_0 - (T_1^{(0)} + T_2^{(0)})/2}{T_2^{(0)} - T_1^{(0)}} \sqrt{\frac{d^2}{d^2 - 1}} \sqrt{1 - \frac{b^2}{\sqrt{b^4 + 1}}} \tag{185}$$

where R, I, and d^2 are given by Eqs. (177), (178), and (166), respectively.

C. Numerical Applications

In order to demonstrate the validity and usefulness of the formulas in this section, numerical examples are shown in Figs. 13–16. The NT case is shown in Figs. 13 and 14 for the overall transmission probability $P_{12} = |S_{12}^R|^2$ and the phase arg S_{12}, respectively

(16). The potentials employed are (in a.u.)

$$V_1(x) = 0.5e^{7.5x}, \quad V_2(x) = 0.5e^{-3.75x}, \quad \text{and} \quad V(x) = \frac{3}{2\sqrt{2}} V_0 e^{-2.5x^2} \tag{186}$$

The LZ case is shown in Figs. 15 and 16 for the inelastic transition probability $P_{12} = |S_{12}^R|^2$ and the phase arg S_{11}, respectively (17). The potentials are

$$V_1(x) = 1.5e^{-3/10Kx} - 0.5, \qquad V_2(x) = e^{-5Kx/K+1)}$$

and

$$V(x) = \frac{\sqrt{2K}}{\sqrt{K+1}} e^{-2.5x^2} \qquad \text{with } K = 1.2 \tag{187}$$

The coupling parameters V_0 in Eqs. (186) and (187) are varied so that the parameter a^2 defined by Eq. (19) covers the three regimes: 10.0 (weak), 1.0 (intermediate), and 0.1 (strong). The adiabatic approximation means that a^2 and b^2 are estimated from the adiabatic potentials by Eqs. (124)–(125) and (164)–(165).

VII. METHODOLOGIES FOR MULTILEVEL AND MULTIDIMENSIONAL PROBLEMS

In this section the present status of the methodologies is briefly summarized for the multilevel curve crossing and multidimensional problems, and a new method is proposed for the latter. The accurate one-dimensional two-state theory described in the previous section enables us to treat certain classes of multilevel and multidimensional problems with high accuracy. The diagrammatic technique is useful for the former, and the latter can be challenged by incorporating the theory into the framework of the trajectory surface hopping (TSH) method (18) and/or the decoupling scheme of classical S-matrix theory (43–45). These are discussed in the following subsections.

A. Diagrammatic Technique

As frequently mentioned, the various dynamic processes can be decomposed into sequential basic events such as wave propagation and nonadiabatic transition. The conceivable basic elements (or events) are (1) wave propagation along the potential without any transition, (2) wave reflection at the turning point, (3) single-potential barrier penetration and reflection, (4) nonadiabatic transition at the crossing point, (5) nonadiabatic tunneling at energies lower than the bottom of the upper adiabatic potential, and (6) noncrossing type of nonadiabatic transition. These are expressed in Figs. 17–21.

When we write the semiclassical wave function on the adiabatic potential $E_n(R)$ as

$$\psi_n(R) \simeq -V_n' \varphi_n^{(+)}(R:a) + V_n'' \varphi_n^{(-)}(R:a) \tag{188}$$

with

$$\varphi_n^{(\pm)}(R:a) = \sqrt{\frac{\mu}{2\pi k_n(R)}} \exp\left[\pm i \int_a^R k_n(R)\, dR \right] \tag{189}$$

the connections of the coefficients are given as follows for each basic element.

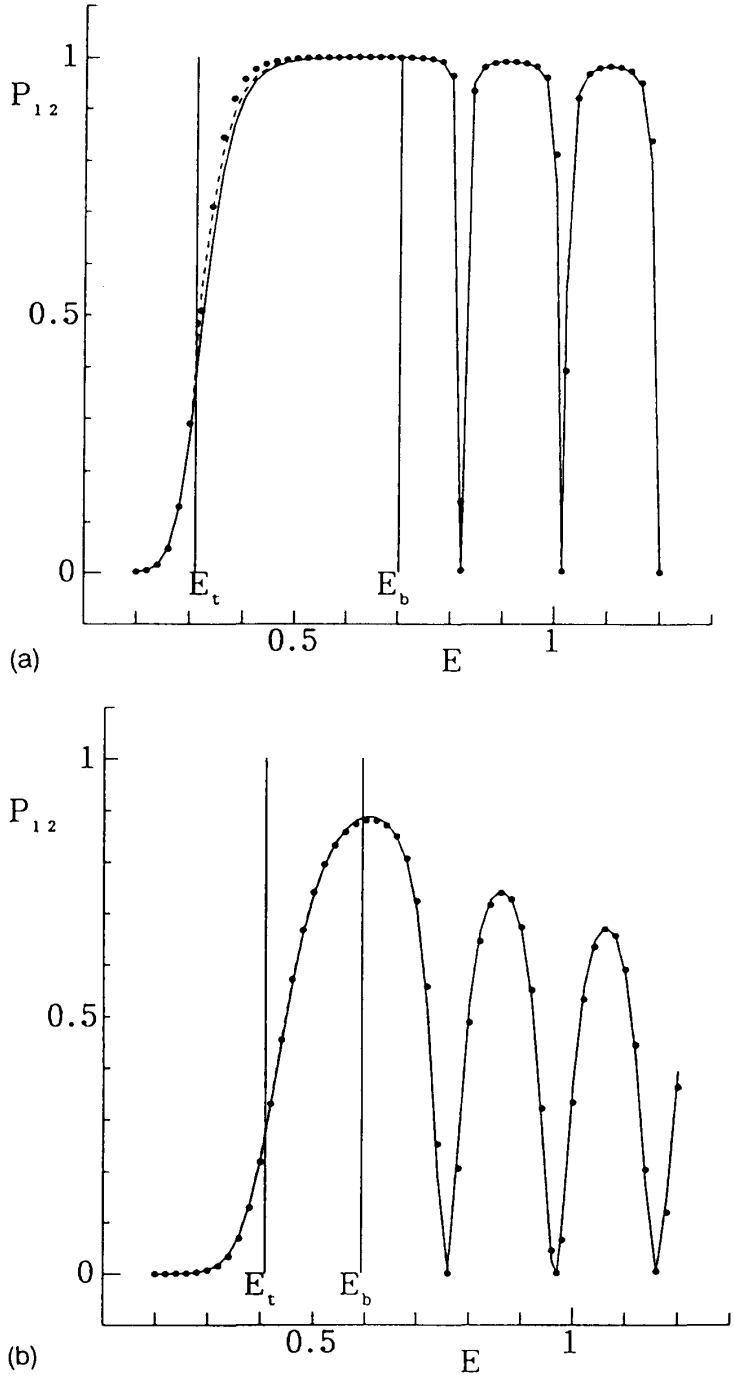

Figure 13 Nonadiabatic tunneling (transmission) probability $P_{12} = |S_{12}|^2$ as a function of energy for the potential (186). ·: exact, : present semiclassical (adiabatic), — — —: present semiclassical (diabatic). (a) a^2 (dia) = 0.1, (b) a^2 = 1.0 and (c) a^2 = 10. (From Ref. 16.)

1. Wave Propagation (see Fig. 17)

$$\mathcal{U} = \begin{pmatrix} e^{i\gamma_n(a,b)} & 0 \\ 0 & e^{-i\gamma_n(a,b)} \end{pmatrix} \mathcal{V} \equiv P_{ab}\mathcal{V} \qquad (a < b) \tag{190}$$

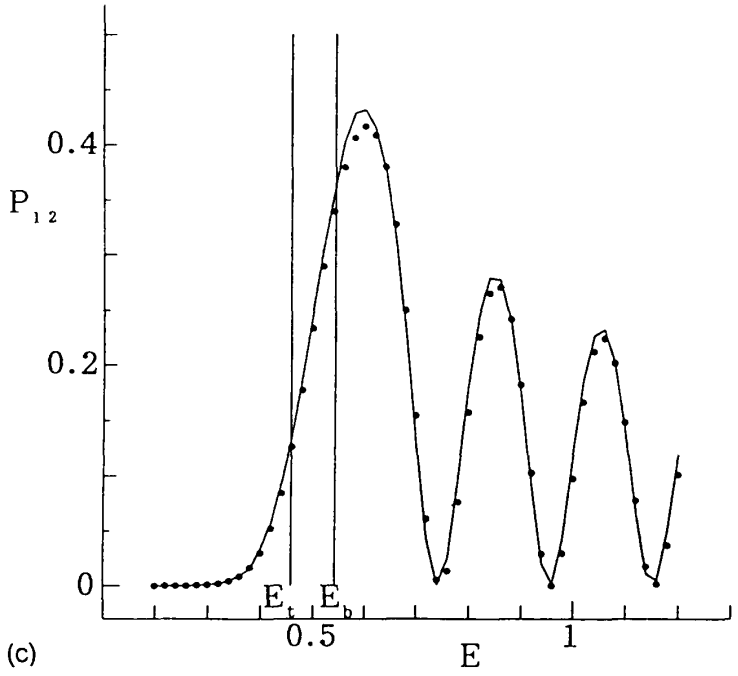

(c)

where $\gamma_n(a, b)$ is defined by Eq. (33), $\mathcal{V}$ is a column vector with components V' and V'', and $\mathcal{U}$ is a similar vector which represents the wave function with b as a reference point.

2. Wave Reflection at Turning Point (Fig. 18)

$$\mathcal{V} = \begin{pmatrix} e^{\pi i/1} & 0 \\ 0 & e^{-\pi i/4} \end{pmatrix} \begin{pmatrix} A \\ A \end{pmatrix} \equiv Q \begin{pmatrix} A \\ A \end{pmatrix} \tag{191}$$

where A simply represents the wave amplitude. When the turning point is on the right side, the signs of $\pi i/4$ should be interchanged.

3. Single-Potential Barrier Penetration and Reflection (Fig. 19)

$$\mathcal{U} = M\mathcal{V} \equiv Q \begin{pmatrix} \sqrt{1 + e^{2\pi\epsilon}}\, e^{-i\phi} & ie^{\pi\epsilon} e^{i\theta} \\ -ie^{\pi\epsilon} e^{-i\theta} & \sqrt{1 + e^{2\pi\epsilon}}\, e^{i\phi} \end{pmatrix} Q^* \mathcal{V} \tag{192}$$

where

$$\epsilon = \begin{cases} \pi \displaystyle\int_a^b |k(R)|\, dR & \text{for } E < E_t \qquad (193a) \\ \dfrac{1}{\pi i} \displaystyle\int_{R_+}^{R_-} k(R)\, dR & E > E_t, \qquad (193b) \end{cases}$$

$$\theta = \begin{cases} 0 & \text{for } E < E_t \qquad (194a) \\ \displaystyle\int_{R_+}^{R_t} k(R)\, dR + \int_{R_-}^{R_t} k(R)\, dR & E > E_t, \qquad (194b) \end{cases}$$

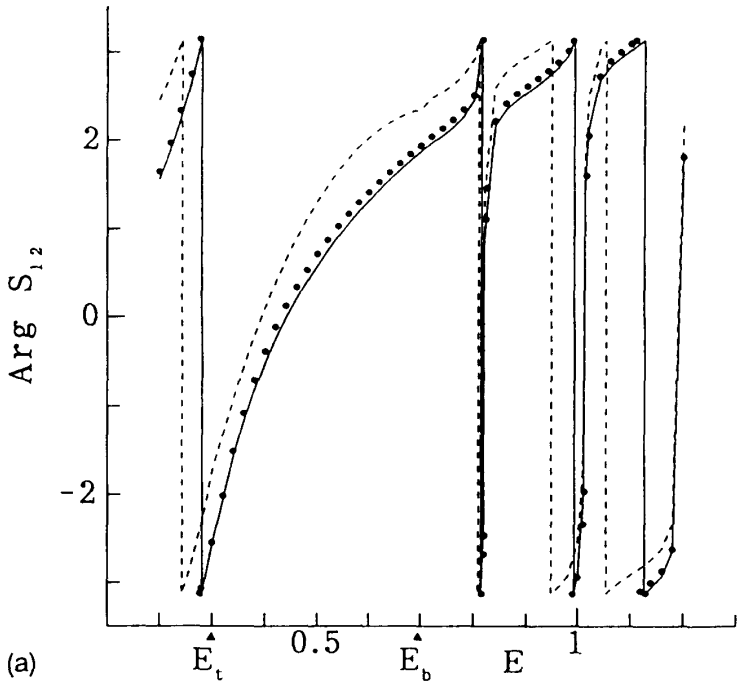

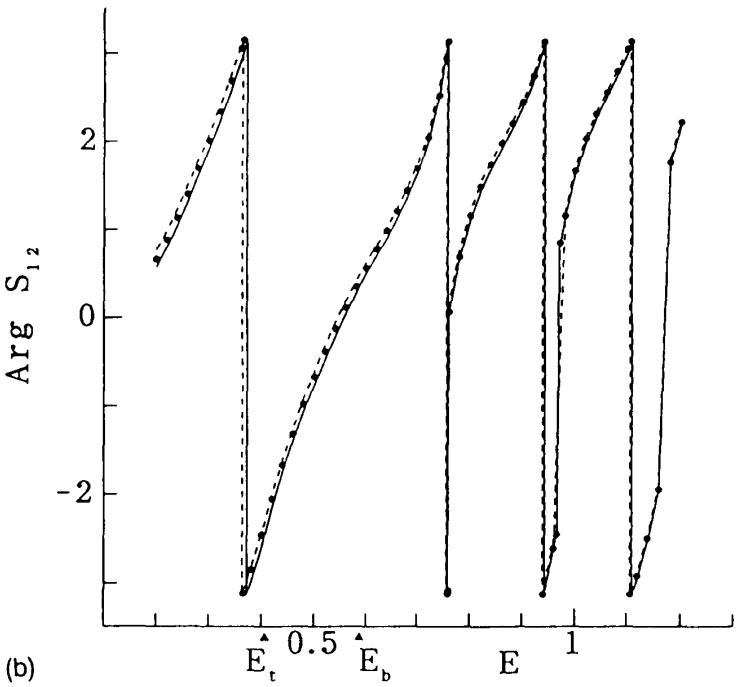

Figure 14 ArgS_{12} as a function of energy in the NT case for the potential (186). ·: exact, ...: present semiclassical (adiabatic), — — —: present semiclassical (diabatic). (a) a^2 (dia) = 0.1, (b) a^2 = 1.0 and (c) a^2 = 10. (From Ref. 16.)

$$\phi = \arg \Gamma\left(\frac{1}{2} + i\epsilon\right) - \epsilon \ln|\epsilon| + \epsilon \tag{195}$$

$R_\pm$ are the complex turning points and E_t is the barrier top. When $E > E_t$, Q should be replaced by the unit matrix.

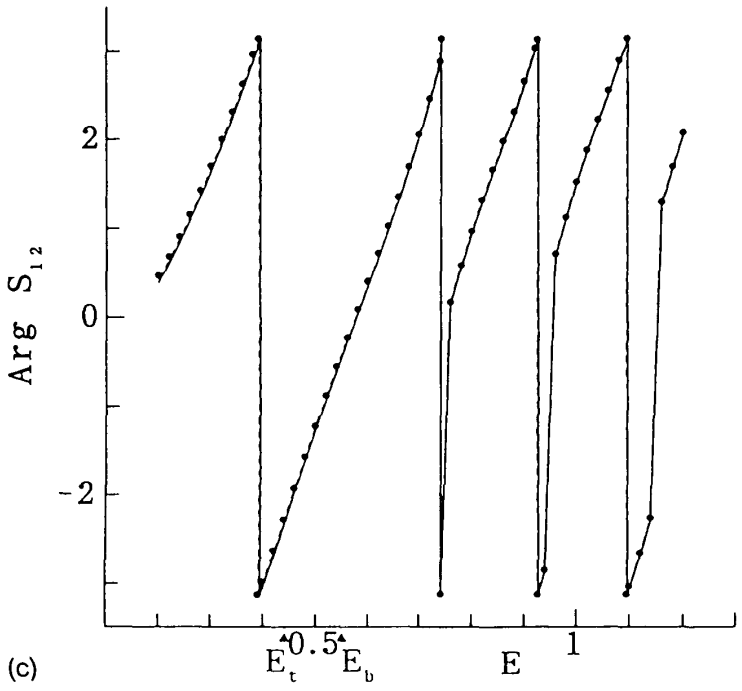

(c)

4. Nonadiabatic Transition at Crossing Point (Fig. 20)

The matrices I_X and $O_X = I_X'$ (transpose of I_X) introduced before take care of this by

$$\mathcal{U}'' = I_X \mathcal{V}'' \qquad \text{and} \qquad \mathcal{V}' = O_X \mathcal{U}' \tag{196}$$

where $\mathcal{V}'$ is a column vector with components V_1' and V_2', and the other vectors have similar meanings. From the new theory in Sec. VI we can now recommend the best formulas for I_X and O_X as follows: In the NT case at $E \geq E_b$ (see Fig. 10),

$$I_X^{\mathrm{NT}} = \begin{pmatrix} \sqrt{1 - p_{\mathrm{ZN}}}\, e^{i(\sigma_{\mathrm{ZN}} - \psi_{\mathrm{ZN}})} & \sqrt{p_{\mathrm{ZN}}}\, e^{i\sigma_0^{\mathrm{ZN}}} \\ -\sqrt{p_{\mathrm{ZN}}}\, e^{-i\sigma_0^{\mathrm{ZN}}} & \sqrt{1 - p_{\mathrm{ZN}}}\, e^{-i(\sigma_{\mathrm{ZN}} - \psi_{\mathrm{ZN}})} \end{pmatrix} \tag{197}$$

where the various quantities are defined in Sec. VI.A.3. The derivation of Eq. (197) is given in the appendix. In the LZ case at $E \geq E_X$ (see Fig. 11),

$$I_X^{\mathrm{LZ}} = \begin{pmatrix} \sqrt{1 - p_{\mathrm{ZN}}}\, e^{-i(\sigma_{\mathrm{ZN}} - \psi_{\mathrm{ZN}})} & -\sqrt{p_{\mathrm{ZN}}}\, e^{i\sigma_0^{\mathrm{ZN}}} \\ \sqrt{p_{\mathrm{ZN}}}\, e^{-i\sigma_0^{\mathrm{ZN}}} & \sqrt{1 - p_{\mathrm{ZN}}}\, e^{i(\sigma_{\mathrm{ZN}} - \psi_{\mathrm{ZN}})} \end{pmatrix} \tag{198}$$

where the various quantities are defined in Sec. VI.B.1. σ_0^{ZN} represents the third ~ fifth terms in Eq. (175). At $E \leq E_X$ in the LZ case we have

$$\mathcal{V}' = Q S^{R(a)} \mathcal{V}'' \tag{199}$$

where $S^{R(a)}$ is given by Eqs. (162) and (163) with Eqs. (180)–(185).

5. Nonadiabatic Tunneling at $E \leq E_b$ (Fig. 21)

The vector of wave function is

$$\mathcal{U} = QNQ^* \mathcal{V} \tag{200}$$

where N is a transfer matrix defined by Eq. (127) from the reduced scattering matrix $S^{R(a)}$, which is defined by Eq. (122) with various quantities given in Secs. VI.A.2 and VI.A.3.

6. Noncrossing-Type Nonadiabatic Transition (Fig. 20)

We need I_X and O_X (= I_X') matrices, which are given in Sec. III.B (see Eq. (36)).

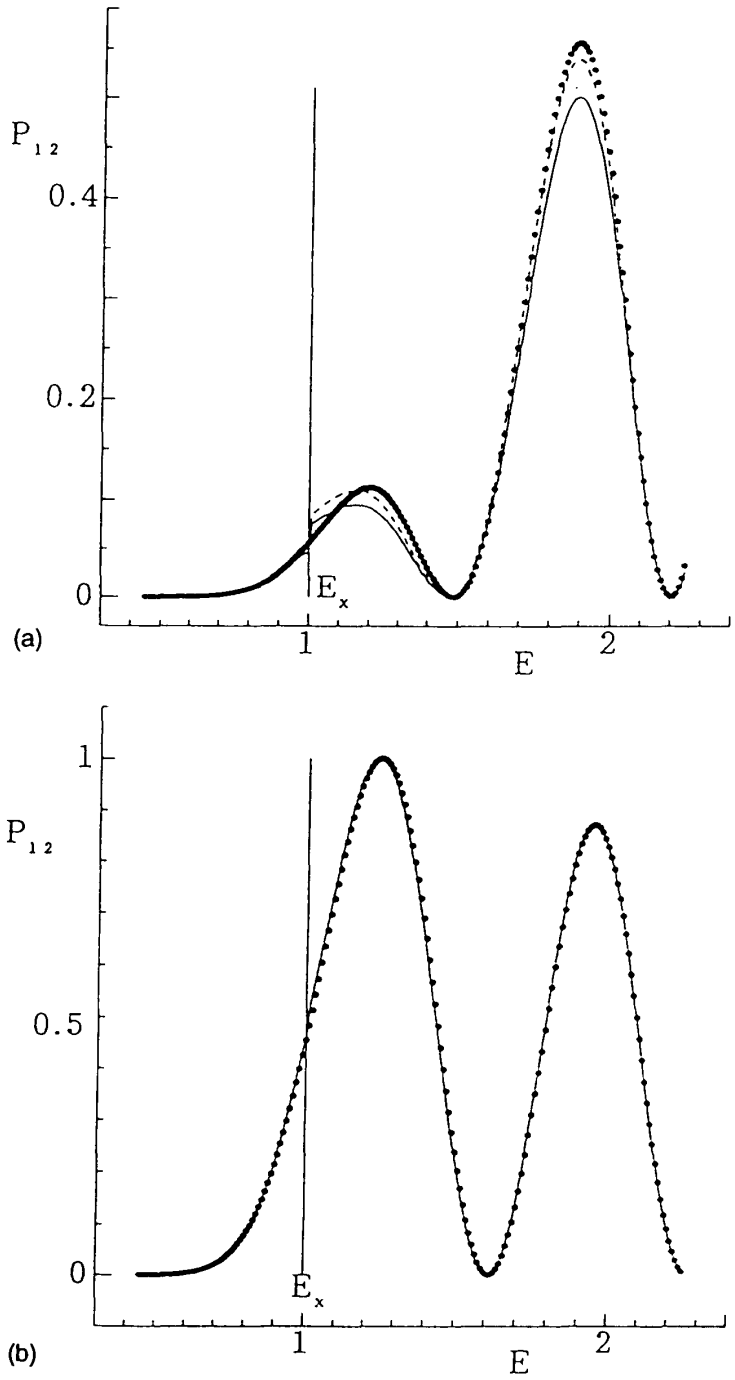

Figure 15 Transition probability $P_{12} = |S_{12}|^2$ against energy in the LZ case for the potential (187). ·: exact, : present semiclassical (adiabatic), — — —: present semiclassical (diabatic). (a) a^2 (dia) = 0.1, (b) a^2 = 1.0 and (c) a^2 = 10. (From Ref. 17.)

Now, various kinds of curve-crossing problems be diagrammatically expressed by assembling the basic elements given above and solved by combining the appropriate matrices. One of the simplest examples is the two-state inelastic scattering depicted in Fig. 1a, the corresponding diagram of which is simply given by Fig. 22. The scattering matrix is expressed in the form of Eq. (21).

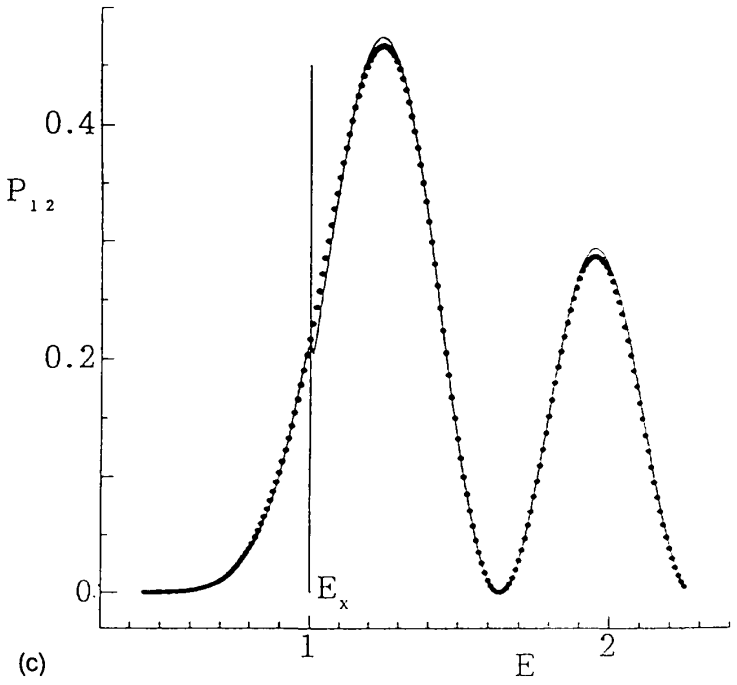

B. Multichannel Curve-Crossing Problem

The most accurate method for multilevel curve crossing problems is, of course, to solve the close-coupling differential equations numerically. This is not the subject here, however; instead, we discuss the applications of the two-state semiclassical theory and the diagrammatic technique. With these tools we can deal with various problems such as inelastic scattering, elastic scattering with resonance, photon impact process, and perturbed bound state in a unified way. The overall scattering matrix S, for instance, can be defined as

$$\mathcal{V}' = S\mathcal{V}'' \tag{201}$$

where $\mathcal{V}'$ ($\mathcal{V}''$) is the column vector composed of the coefficients which represent the asymptotically outgoing (incoming) waves. If all channels are open, the S-matrix is simply expressed by an equation like Eq. (21). If all channels are closed, we have

$$\mathcal{V}' = Q^{2\mathcal{D}}\mathcal{V}'' \tag{202}$$

which leads to a secular equation to determine eigenvalues.

Here, we consider an example shown in Fig. 23a, which includes both open and closed channels. The corresponding diagram is depicted in Fig. 23b (2). When closed channels are included, it is convenient to construct the following χ matrix in terms of which the S-matrix is expressed as (2)

$$S = P_{\infty R_0}\{\chi_{oo} - \chi_{oc}(\chi_{cc} - P^{*}_{R_0 T^R R_0})^{-1}\chi_{co}\}P_{R_0\infty} \tag{203}$$

where the subscript o (c) means open (closed), and χ_{oc} represents the open channel–closed channel block of the whole χ-matrix, and so on. The suffix T^R represents the right-side, i.e., outer, turning point T_n^R, and R_0 is an appropriately chosen position larger

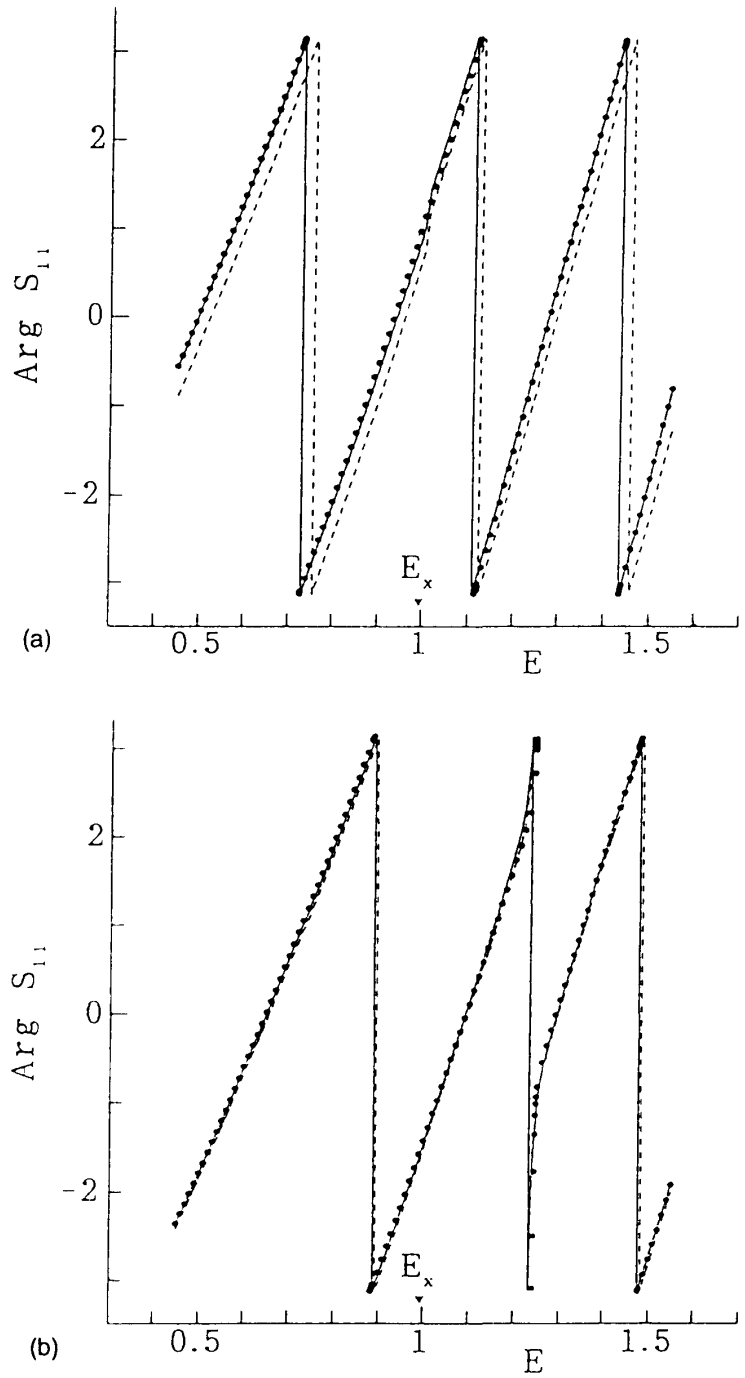

Figure 16 ArgS_{12} against energy in the LZ case for the potential (187). ·: exact, : present semiclassical (adiabatic), — — —: present semiclassical (diabatic). (a) a^2 (dia) = 0.1, (b) a^2 = 1.0 and (c) a^2 = 10. (From Ref. 17.)

than the rightmost basic element (diagram) and smaller than T^R if the latter exists. R_0 can be taken to be either dependent on or independent of the channel number. The matrices $P_{\infty R_0} = P_{R_0\infty}$ and $P_{R_0 I^R R_0}$ are the same as those defined by Eqs. (22) except that the integration limits in $P_{R_0 I^R R_0}$ are interchanged since $R_0 < T_0$. These matrices span either open channels or closed channels. Now, the matrix χ in the case of Fig. 23 can be simply

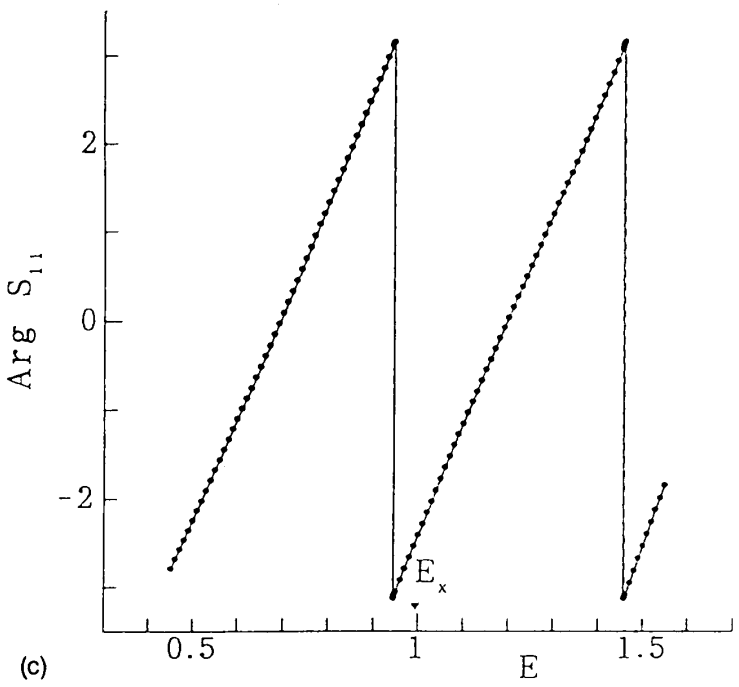

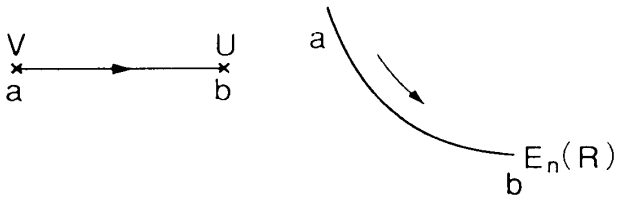

Figure 17 Diagram for wave propagation from a to b along the potential $E_n(R)$.

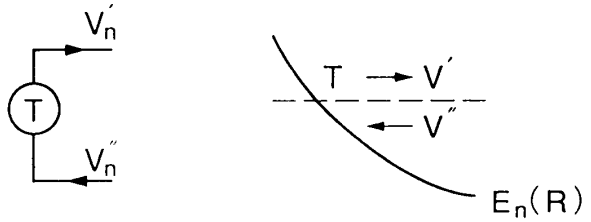

Figure 18 Diagram for wave reflection at the turning point T.

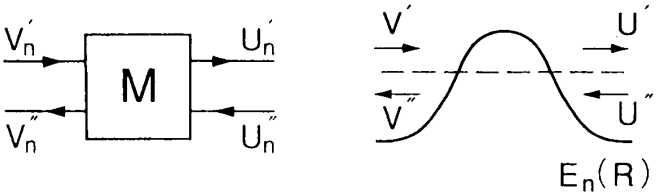

Figure 19 Diagram for single-potential barrier penetration and reflection.

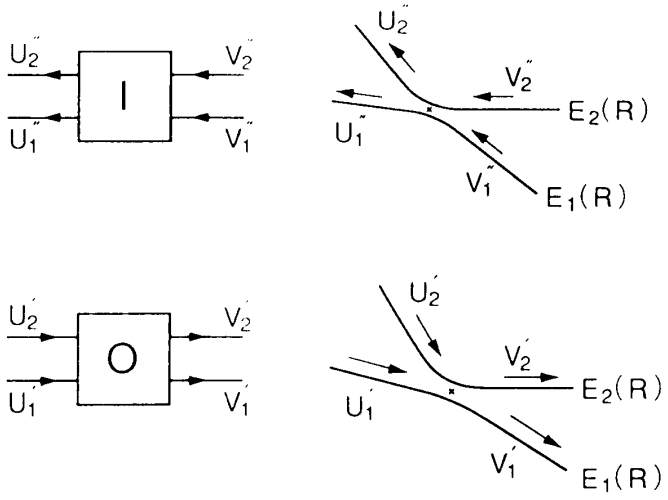

Figure 20 Diagram for nonadiabatic transition.

expressed as

$$\chi = P_{C_1R_0} O_{C_1} P'_{C_1C_2} O_{C_2} P'_{C_2TC_2} I_{C_2} P'_{C_1C_2} I_{C_1} P_{C_1R_0} \tag{204}$$

where the matrices P_{AB}, I_X, and O_X are the same as before (see Eq. (190)) except that I_X and O_X are now 3×3 matrices having off-diagonal elements only between the channels coupled by curve crossing. The matrices $P'_{C_1C_2}$ and $P'_{C_2TC_2}$ are defined as

$$[P'_{C_1C_2}]_{nm} = \begin{cases} \delta_{nm} \exp\left[i \int_{R_{C_1}}^{R_{C_2}} k_n(R)\, dR \right] & \text{for } n, m = 1, 2 \\ \delta_{nm} \exp\left[i \int_{R_{C_1}}^{T_3} k_3(R)\, dR \right] & \text{otherwise} \end{cases} \tag{205}$$

and

$$[P'_{C_2TC_2}]_{nm} = \begin{cases} \delta_{nm} \exp\left[2i \int_{T_n'}^{R_{C_2}} k_n(R)\, dR + \dfrac{\pi i}{2} \right] & \text{for } n, m = 1 \\ \delta_{nm} & \text{otherwise} \end{cases} \tag{206}$$

where the (3,3) element of $P'_{C_1C_2}$ can be put in $P'_{C_2TC_2}$ with the exponent doubled.

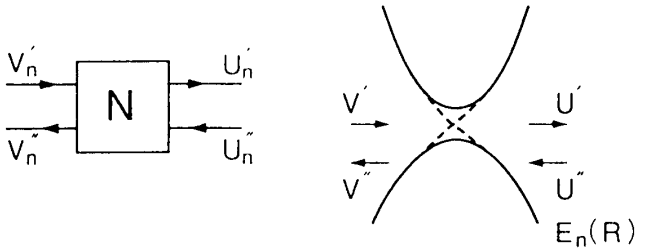

Figure 21 Diagram for nonadiabatic tunneling.

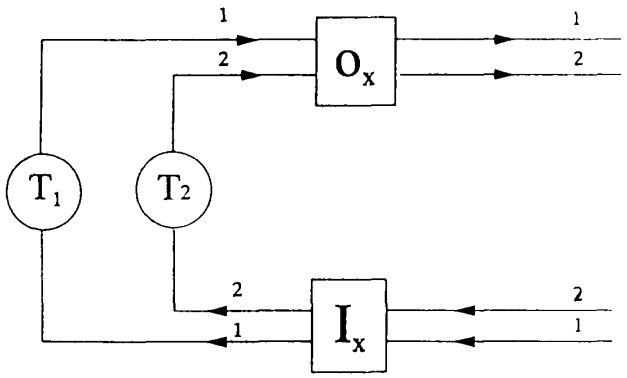

Figure 22 Diagram corresponding to Fig. 1a.

In this formulation the effects of closed channels can be straightforwardly incorporated into the S-matrix. Resonances in the scattering clearly correspond to the complex solutions of

$$\det[\chi_{cc} - P^*_{R_0 T^R R_0}] = 0 \tag{207}$$

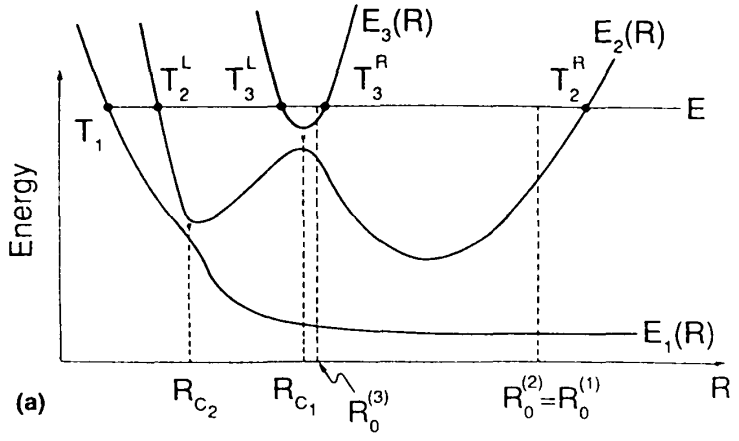

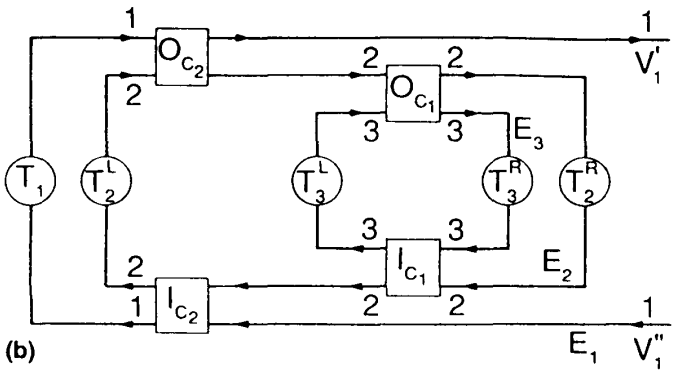

Figure 23 Model three-state potential curve diagram (a) and its corresponding diagram (b). (From Ref. 2, reprinted by permission of John Wiley and Sons Inc.)

The above method can handle the general cases which involve tunneling and nonadiabatic tunneling, since the basic matrices are available now. Numerical application has not yet been made with the newly developed formulas described in Sec. VI. However, the encouraging results obtained before with the old version of the two-state theory indicate that the method should work well (1,2,46). If the two-state theory is accurate enough and the phases due to nonadiabatic transition are treated properly, the method works surprisingly well even when the avoided crossings are located close together in such a way that the nonadiabatic couplings overlap.

C. Multidimensional Problem

It is very important to develop a good theory applicable to multidimensional problems, since most of the physical phenomena intrinsically occur in multidimensional space (47). In general, a real surface intersection of dimension $N - 2$ is possible, when the potential energy surfaces of the same electronic symmetry are functions of N variables. There are basically three kinds of surface crossings (48): (1) avoided crossing, (2) conical intersection, and (3) glancing intersection. In the first case, the diabatic surfaces cross with each other along a line called the "seam," and the adiabatic surfaces have the shape of a hyperbolic cylinder oriented along the seam. In the direction perpendicular to the seam, we have the scheme of one-dimensional avoided crossing. In the case of conical intersection, the adiabatic surfaces are discontinuous at the crossing point. Along the lines passing near the crossing point, the ordinary one-dimensional avoided crossing scheme holds. The Jahn-Teller problem is a famous example of this (49). The effects of the geometrical phase due to conical intersection (Berry phase) have attracted much attention recently (50). In the glancing intersection case corresponding to the Renner-Teller problem (49), the two adiabatic surfaces are continuous even at the point of contact, and the curve-crossing type of analysis is not adequate.

There is no real multidimensional analytical semiclassical theory of nonadiabatic transition. The Stokes phenomenon of partial differential equations has not yet been mathematically established as far as the author knows. Maslov and Fedoriuk have developed semiclassical mechanics in multidimensional space, but it is still restricted to the regular regime without tunneling and chaotic behavior (51). Presently available and practically useful methodologies are (1) reduction to one-dimensional multilevel problems and (2) the TSH method. In the first case the total wave function is expanded in terms of internal states and the coupled ordinary differential equations are derived (52). The most accurate results are obtained by solving the equations numerically. For numerical convenience the adiabatic-to-diabatic transformation is usually employed, although this cannot be exact. The transformation matrix is obtained from the line integral of nonadiabatic couplings. We do not go into the details here and the reader should refer to the literature (52). In some cases the one-dimensional multilevel curve-crossing problems can be solved by using the one-dimensional two-state theory, as explained in the previous subsection.

Another practical method is TSH (18), in which ordinary classical trajectories are run until they come close to the surface crossing region where the trajectories are jumped to the other surface with probability given by the Landau-Zener formula. This method is simple and convenient, but suffers from the following drawbacks: all phases are completely neglected and only the probabilities (not the probability amplitudes) are handled; the detailed balance is not necessarily satisfied; and nonadiabatic transitions at energies

lower than the crossing point are ignored. Besides, the Landau-Zener formula does not work at energies near the crossing point. Since classical trajectory constitutes a curvilinear one-dimensional space and we now have compact and accurate formulas at hand which can be used whatever the energy and coupling strengths are, the TSH method can be very much improved. We can actually implement the decoupling scheme (42) of the Miller-George classical S-matrix theory (44,45). The phase along the classical trajectory and the phase due to nonadiabatic transition can be incorporated into the classical S-matrix. It may be true that in many cases the effects of phases are smeared out and the random-phase approximation works pretty well, but this cannot always be the case. Besides, we cannot know in advance whether this is true. Since we can estimate the phase accurately now, it is certainly much better to carry out the calculations with the effects of phase included. The initial condition for the trajectory after hopping is somewhat problematic, but the conventional choice is considered to be reasonable and acceptable (18). That is, only the momentum component perpendicular to the crossing seam is changed by an amount corresponding to the adiabatic potential energy difference. The nonadiabatic transition probability does not have to be evaluated by the complex contour integral, since simple and accurate formulas are now available for the Landau-Zener transition probability and for nonadiabatic tunneling (transmission) probability regardless of the energy and coupling strength. The double-end boundary condition in the original classical S-matrix theory guarantees the detailed balance, but is very difficult to be satisfied in practical calculations. The condition can be relaxed by defining the reaction probability for the transition $n_1 \rightarrow n_2$ as

$$P_{n_2,n_1} = \int_{n_2-1/2}^{n_2+1/2} d\bar{n}_2 \int_{n_1-1/2}^{n_1+1/2} d\bar{n}_1 \, |S_{\bar{n}_2,\bar{n}_1}|^2 \tag{208}$$

where $S_{\bar{n}_2,\bar{n}_1}$ is the scattering matrix with $\bar{n}_j$ (j = 1, 2) designating the continuous action variables, and n_j (j = 1, 2) are the corresponding quantum numbers (integers) (44,45). Equation (208) still preserves the detailed balance. Furthermore, if we use the dynamical state representation described in Sec. IV, then any kind of coupling can be handled in a unified way. This is very significant in Coriolis coupling because the transition due to this coupling is not localized in the Born-Oppenheimer representation and we cannot apply the idea of surface hopping at surface crossings. In the DS representation the surface-hopping procedure can be straightforwardly utilized. Thus, the method proposed above, which may be called a "semiclassical surface-hopping method," can remedy all the drawbacks of TSH and should be able to significantly improve it and the decoupling scheme of classical S-matrix theory. Practical applications are strongly desired.

VIII. SUMMARY

The significance of nonadiabatic transition in a wide range of physics and chemistry was emphasized and explained. This is a very inter- and multidisciplinary concept which plays a crucial role in the state or phase change in various fields, being an origin of the mutability of the universe (1,2). The semiclassical theory of nonadiabatic transition has been developed by many authors (19,29–33) since the pioneering work of Landau (13), Zener (14), and Stückelberg (15). A brief historical survey of the theory was presented for curve-crossing and noncrossing cases. Nonadiabatic transition due to Coriolis cou-

pling was also touched upon. The basic one-dimensional models are interpreted and their unified theoretical treatments are demonstrated.

Recent new developments of the one-dimensional two-state theory for the curve-crossing nonadiabatic transitions were summarized (16,17). These present a complete set of solutions for the two fundamental physically different cases: Landau-Zener (LZ) case, in which the two diabatic potential curves cross with the same sign of slopes, and the nonadiabatic tunneling (NT) case, in which the two curves cross with the opposite sign of slopes. The formulae of S-matrix are compact and accurate and can cover practically the whole range of coupling strength and energy. In particular, the new formulae for the Landau-Zener transition probability are as simple as the famous Landau-Zener formula but are far better. A compact expression for the nonadiabatic tunneling (transmission) probability is also available. Based on the physical idea that a whole dynamic process can be decomposed into sequential events of localized nonadiabatic transmission at avoided crossing and adiabatic wave propagation along adiabatic potentials, present semiclassical theory can be applied to all kinds of problems, such as those depicted in Fig. 1. Now, the theory presents a complete picture of the two-state curve crossing problems for the first time since Landau (13), Zener (14), and Stückelberg (15).

Thus, problems such as the nonadiabatic transition at energies lower than the crossing point, which cannot be treated by the old version of semiclassical theory, can now be accurately handled by the new theory. The new theory can be usefully incorporated into the framework to deal with the multilevel curve-crossing and multidimensional problems. For instance, a new implementation was proposed for the TSH method (18) and the decoupling scheme of classical S-matrix theory (43). This implementation is expected to significantly improve these methods, and its practical applications are strongly desired. The mathematical background of the semiclassical theory of nonadiabatic transition, namely, the Stokes phenomenon of asymptotic solutions of differential equations, was explained briefly by taking some simple examples. This background contains very important basic mathematics for semiclassical theory in general.

Since the one-dimensional theory of curve crossing is practically complete now, we have to challenge the multidimensional problems. The simplest challenge is, of course, applications of the new one-dimensional theory to various practical reaction processes, as explained above. This would be very useful to clarify the mechanisms of various dynamics. The real challenge is, however, developing multidimensional theory. There must be certain phenomena embedded which are intrinsically multidimensional and cannot be interpreted by one-dimensional theory. Another useful development is a generalization of the theory of Osherov and Voronin (38) for the quantum Rosen-Zener-Demkov model to make it applicable to general curved potentials. Finally, complete reflection in the nonadiabatic type of curve crossing is a very intriguing phenomenon and should be further investigated. The possibility of molecular switching based on this phenomenon should also be analyzed further (37).

ACKNOWLEDGMENTS

The new theoretical developments described in Sec. VI were done in collaboration with Dr. C. Zhu. This work was supported in part by a Grant-in-Aid for Scientific Research on Priority Area "Theory of Chemical Reactions" from the Ministry of Education, Science and Culture of Japan.

APPENDIX: DERIVATION OF EQ. (197)

Using the diagrammatic technique explained in Sec. VII.A, we can obtain the reduced scattering matrix $S^{R(a)}$ for the nonadiabatic tunneling at $E \geq E_b$ (see Fig. 2b) as

$$S^{R(a)} = -i\begin{pmatrix} \dfrac{O_{12}L_l^2 I_{21}}{1 - O_{22}L_l^2 I_{22}L_r^2} & O_{11} + \dfrac{O_{12}L_l^2 I_{22}L_r^2 O_{21}}{1 - O_{22}L_l^2 I_{22}L_r^2} \\ I_{11} + \dfrac{I_{12}L_r^2 O_{22}L_l^2 I_{21}}{1 - O_{22}L_l^2 I_{22}L_r^2} & \dfrac{I_{12}L_r^2 O_{21}}{1 - O_{22}L_l^2 I_{22}L_r^2} \end{pmatrix} \tag{A1}$$

where I_{ij} and O_{ij} are the (i, j) elements of the matrices I_X^{NT} and O_X^{NT} (= transpose of I_X^{NT}), and $L_l = \gamma_2(T_2^L, R_b)$ and $L_r = \gamma_2(R_b, T_2^R)$ with the phase integral γ_2 defined by Eq. (33). Putting the unitary matrix I_X^{NT} in the form

$$I_X^{NT} = \begin{pmatrix} \sqrt{1 - p_{ZN}}e^{i\alpha} & \sqrt{p_{ZN}}e^{i\beta} \\ -\sqrt{p_{ZN}}e^{-i\beta} & \sqrt{1 - p_{ZN}}e^{-i\alpha} \end{pmatrix} \tag{A2}$$

and comparing Eq. (A1) with the reduced scattering matrix $S^{R(a)}$ derived in Sec. VI.A.3, we obtain

$$\alpha = L_l + L_r - \psi_{ZN} = \sigma_{ZN} - \psi_{ZN} \tag{A3}$$

and

$$\beta = \sigma_0^{ZN} \tag{A4}$$

where σ_{ZN}, ψ_{ZN}, and σ_0^{ZN} are defined by Eqs. (150*b*), (150*a*), and (156), respectively. This completes the derivation of Eq. (197).

REFERENCES

This is not a comprehensive list; mainly review articles and books are cited.

1. H. Nakamura, What are the basic mechanisms of electronic transitions in molecular dynamic processes?, *Int. Rev. Phys. Chem. 10*: 123 (1991).
2. H. Nakamura, Semiclassical approach to charge-transfer processes in ion-molecule collisions, *State-Selected and State-to-State Ion-Molecule Reaction Dynamics.* Part 2: *Theory, Advances in Chemical Physics LXXXII* (M. Baer and C. Y. Ng, eds.), Wiley, New York, 1992, p. 243.
3. S. S. Shaik and P. C. Hiberty, Curve crossing diagrams as general models for chemical reactivity and structure, *Theoretical Models of Chemical Bonding.* Part 4 (Z. B. Maksic, ed.), Springer-Verlag, Berlin, 1991, p. 269.
4. B. Imanishi and W. von Oertzen, Molecular orbitals of nucleons in nucleus-nucleus collisions, *Phys. Rep. 155*: 29 (1987).
5. A. Thiel, The Landau-Zener effect in nuclear molecules, *J. Phys. G 16*: 867 (1990).
6. A. Yoshimori and M. Tsukada (eds.), *Dynamical Processes and Ordering on Solid Surfaces*, Springer-Verlag, Berlin, 1985.
7. R. Engleman, *Non-Radiative Decay of Ions and Molecules in Solids*, North-Holland, Amsterdam, 1979.
8. J. R. Bolton, N. Mataga, and G. McLendon (eds.), *Electron Transfer in Inorganic, Organic, and Biological Systems, Advances in Chemistry Series 228*, American Chemical Society, Washington, DC, 1991.
9. D. DeVault, *Quantum-Mechanical Tunneling in Biological Systems*, Cambridge University Press, Cambridge, 1984.

10. D. Kleppner, M. G. Littman, and M. L. Zimmerman, Rydberg atoms in strong fields, *Rydberg States of Atoms and Molecules* (R. F. Stebbings and F. B. Dunning, ed.), Cambridge University Press, Cambridge, 1983, p. 73.
11. B. Schwarzschild, Conversion in matter may account for missing solar neutrinos, *Phys. Today June*: 17 (1986).
12. P. W. Kash, G. C. G. Waschewsky, L. J. Butler, and M. M. Francl, Distance dependence of nonadiabaticity in the branching between C—Br and C—Cl bond fission following $^1[n(O), \pi^*(C{=}O)]$ excitation in bromo-propionyl chloride, *J. Chem. Phys. 99*: 4479 (1993).
13. L. D. Landau, Zur theorie der Energieübertragung bei Stössen. II, *Phys. Zts. Sowjet. 2*: 46 (1932).
14. C. Zener, Nonadiabatic crossing of energy levels, *Proc. Roy. Soc. A137*: 696 (1932).
15. E. C. G. Stückelberg, Theorie der unelastischen Stösse zwischen atomen, *Helv. Phys. Acta. 5*: 369 (1932).
16. C. Zhu and H. Nakamura, Theory of nonadiabatic transition for general two-state curve crossing problems. I: Nonadiabatic tunneling case, *J. Chem. Phys. 101*: 10630 (1994).
17. C. Zhu and H. Nakamura, Theory of nonadiabatic transition for general two-state curve crossing problems. II: Landau-Zener case, *J. Chem. Phys. 102* (1995).
18. S. Chapman, The classical trajectory-surface-hopping approach to charge-transfer processes, *State-Selected and State-to-State, Ion-Molecule Reaction Dynamics.* Part 2: *Theory, Advances in Chemical Physics LXXXII* (M. Baer and C. Y. Ng, eds.), Wiley, New York, 1992, p. 423.
19. D. S. F. Crothers, A critique of Zwaan-Stueckelberg phase integral techniques, *Adv. Phys. 20*: 405 (1971).
20. C. Zhu, H. Nakamura, N. Re, and V. Aquilanti, The two-state linear curve crossing problems revisited. I: Analysis of Stokes phenomenon and expressions for scattering matrices, *J. Chem. Phys. 97*: 1892 (1992).
21. C. Zhu and H. Nakamura, The two-state linear curve crossing problems revisited. II: Analytical approximations for the Stokes constant and scattering matrix: The Landau-Zener case, *J. Chem. Phys. 97*: 8497 (1992).
22. C. Zhu and H. Nakamura, The two-state linear curve crossing problems revisited. III: Analytical approximations for Stokes constant and scattering matrix: Nonadiabatic tunneling case, *J. Chem. Phys. 98*: 6208 (1993).
23. C. Zhu and H. Nakamura, Two-state linea curve crossing problems revisited. IV: The best analytical formulas for scattering matrices, *J. Chem. Phys. 101*: 4855 (1994).
24. J. Heading, *An Introduction to Phase Integral Methods*, Methuen, London, 1962.
25. A. Russek, Rotationally induced transitions in atomic collisions, *Phys. Rev. A4*: 1918 (1971).
26. U. Wille and R. Hippler, Mechanisms of inner-shell vacancy production in slow ion-atom collisions, *Phys. Rep. 132*: 129 (1986).
27. H. Nakamura, What are the basic mechanisms of electronic transitions in molecular dynamic processes?, *Int. Rev. Phys. Chem. 10*: App. A (1991).
28. N. Rosen and C. Zener, Double Sterm-Gerlach experiment and related collision phenomena, *Phys. Rev. 40*: 502 (1932).
29. M. S. Child, *Molecular Collision Theory*, Academic Press, London, 1974.
30. J. C. Tully, Nonadiabatic processes in molecular collisions, *Dynamics of Molecular Collisions.* Part B (W. H. Miller, ed.), Plenum, New York, 1976, p. 217.
31. B. C. Eu, *Semiclassical Theories of Molecular Scattering*, Springer-Verlag, Berlin, 1984.
32. E. E. Nikitin and S. Ya. Umanskii, *Theory of Slow Atomic Collisions*, Springer-Verlag, Berlin, 1984.
33. M. S. Child, *Semiclassical Mechanics with Molecular Applications*, Clarendon, Oxford, 1991.
34. L. D. Landau and E. M. Lifshitz, *Quantum Mechanics Nonrelativistic Theory*, Pergamon, New York, 1965.
35. Yu N. Demkov, Charge transfer at small resonance defects, *JETP 18*: 138 (1964).

36. G. Herzberg, *Molecular Spectra and Molecular Structure.* I: *Spectra Diatomic Molecules*, D. Van Nostrand, Princeton, 1950.
37. H. Nakamura, Nonadiabatic tunneling in one-dimensional finite periodic potential system, *J. Chem. Phys. 97*: 256 (1992).
38. V. I. Osherov and A. I. Voronin, Exact analytical solution of the quantum Rosen-Zener-Demkov model, *Phys. Rev. A49*: 265 (1994).
39. M. A. Evgrafov and M. V. Fedoryuk, Asymptotic behavior as $\lambda \to \infty$ of the solution of the equation $w''(z) - p(z, \lambda)w(z) = 0$ in the complex z-plane, *Russ. Math. Surv. 21*: 1 (1996).
40. Y. Sibuya, *Global Theory of a Second-Order Linear Ordinary Differential Equation with a Polynomial Coefficient*, North-Holland, Amsterdam, 1975.
41. C. Zhu and H. Nakamura, Stokes constants for a certain class of second-order ordinary differential equations, *J. Math Phys. 33*: 2697 (1992).
42. C. Zhu and H. Nakamura, Numerical method for the two-state linear curve crossing: non-adiabatic tunneling case, *Comp. Phys. Comm. 74*: 9 (1993).
43. A. Kormonicki, T. F. George, and K. Morokuma, Decoupling scheme for a semiclassical treatment of electronic transitions in atom-diatom collisions: real valued trajectories and local analytic continuation, *J. Chem. Phys. 65*: 48 (1976).
44. W. H. Miller, Classical-limit quantum mechanics and the theory of molecular collisions, *Advances in Chemical Physics XXV* (I. Prigogine and S. A. Rice, eds.), Wiley, New York, 1974, p. 69.
45. W. H. Miller, The classical S-matrix in molecular collisions, *Advances in Chemical Physics XXX* (I. Prigogine and S. A. Rice, eds.), Wiley, New York, 1975, p. 77.
46. H. Nakamura, Semiclassical treatment of nonadiabatic transitions: multilevel curve crossing and nonadiabatic tunneling problems, *J. Chem. Phys. 87*: 4031 (1987).
47. R. L. Whetten, G. S. Ezra, and E. R. Grant, Molecular dynamics beyond the adiabatic approximation: new experiments and theory, *Ann. Rev. Phys. Chem. 36*: 277 (1985).
48. M. Desouter-Lecomte, B. Leyh-Nihant, M. T. Praet, and J. C. Lorquet, Nonadiabatic unimolecular reactions of polyatomic molecules, *J. Phys. Chem. 89*: 214 (1985).
49. H. C. Longuet-Higgins, Some recent developments in the theory of molecular energy levels, *Adv. Spectrosc. 2*: 429 (1961).
50. A. Shapere and F. Wilczek (eds.), *Geometric Phases in Physics*, World Scientific, Singapore, 1989.
51. V. P. Maslov and M. V. Fedoriuk, *Semiclassical Approximation in Quantum Mechanics*, Reidel, Boston, 1981.
52. M. Baer, Quantum mechanical treatment for charge-transfer processes in ion-molecule collisions, *State-Selected and State-to-State Ion-Molecule Reaction Dynamics.* Part 2: *Theory, Advances in Chemical Physics* LXXXII (M. Baer and C. Y. Ng, eds.), Wiley, New York, 1992, p. 187.

13

Application of Semiclassical Dynamics to Chemical Reactions

GERT D. BILLING and N. BALAKRISHNAN

H. C. Ørsted Institute, University of Copenhagen, Copenhagen, Denmark

NIKOLA MARKOVIĆ

Göteborg University, Göteborg, Sweden

I. INTRODUCTION

The dynamics of the nuclei, contrary to that of the electronic motion, is often well described by classical mechanics. Thus, classical trajectory calculations are often used successfully for calculating rate constants or state-averaged cross sections (1). However, some quantum mechanical effects are present even in nuclear dynamics. These have essentially to do with tunneling and resonances, but they also appear when state-resolved cross sections are sought after. Tunneling is obviously a quantum effect and resonances are inherently connected with the quantum nature of the system. Whereas tunneling is absent in classical mechanics, the effect of resonances can sometimes be accounted for, at least approximately. The failure of classical mechanics to produce good state-resolved quantities can have several reasons: The quantum rotational and/or vibrational spacing can be large, making it difficult if not impossible to adequately assign a state to a given continuous classical vibrational or rotational action (the boxing problem). Also the motion may be quantum by nature; i.e., the particular event is dynamically classically forbidden. This "problem" was particularly visible in the classical S-matrix (2) formulation of the scattering problem. Recently also the "geometric phase" problem connected with conical intersections of electronic states has added to the quantum nature of the nuclear dynam-

ics (3). Thus these findings have led to attempts to solve reactive three- and four-center scattering problems exactly, i.e. quantum mechanically. For a three-particle system the problem becomes a four-dimensional one, keeping in mind that the center of mass motion and conservation of total angular momentum and its projection can be introduced as five "constraints." Likewise the four-particle problem becomes a seven-dimensional one. To treat these problems exactly by either state or grid expansion or hybrid methods is of course a tremendous undertaking and at least one which would be carried out only if the underlying potential energy surface was very accurate. Also the exact quantum methods in principle yield more information than what is needed even for comparison with the most detailed experiments. Furthermore, the need for considering the influence of the surroundings—be it "spectator" atoms not participating in the rearrangement process, catalytic, or solvent effects on the reaction—calls for attempts to use a more approximate dynamical methodology. Here several possibilities exist: time-dependent multiconfiguration self-consistent (MCSCF) methods (4), Feynman path integral formulations (5), reduced dimensionality quantum mechanics (6), or mixed quantum-classical formulations, the subject of this chapter. The mixed quantum-classical formulation can also be introduced in reaction path theory—a theory based on an approximate Hamiltonian, where only the dynamics in the vicinity of the reaction path is included in the description. The introduction of approximate Hamiltonians in which the spectator modes are treated approximately (as a harmonic heat bath) are expected to be the only possible avenue for large systems or reactions in condensed phases. The semiclassical approaches described here have been used for atom-diatom reactions such as $D + H_2$ (7), $D^+ + H_2$ (8), $O + O_2$ (9) and diatom-diatom systems such as $H_2 + OH$ in the gas phase (18); but they have also been used for more complicated reactions such as S_N2 reactions in the gas phase (10) and in liquids (11).

II. QUANTUM-CLASSICAL METHODOLOGY

The quantum-classical method, sometimes called the classical path method, has been widely used in inelastic scattering problems (for a recent review see (12)). This was done by expanding the wave function in eigenstates of the asymptotic Hamiltonian, i.e., in vibrational/rotational product-type eigenfunctions and treating the relative motion within a trajectory approach. By inserting the wave function into the time-dependent Schrödinger equations (TDSE), one obtains a set of coupled equations for the expansion coefficients. However, the methodology can of course be generalized such that internal motions, such as rotational and soft vibrational motions, are also treated by classical dynamics. In any case, the quantum-classical method assumes that the degrees of freedom in question can be divided into classical and quantum subsets. Since the two dynamics (classical and quantum) have different natures, it is not obvious how the dynamics of the two parts should be coupled. In the past several suggestions have appeared. Here we deal only with the coupling, which is defined through a separability scheme obtained using a single configuration approach combined with a search for the optimum trajectory.

A. The Separability Assumption

It is possible to define a classical path theory by introducing a single configuration type of approximation. Consider, e.g., a system with two degrees of freedom r and R where the first is the vibrational and the second the translational degree of freedom. Thus we

assume that the wave function can be approximated by

$$\Psi(r, R, t) = \psi(r, t)\Phi(R, t) \tag{1}$$

This is expected to be a good approximation if the two degrees of freedom are not strongly coupled. The wave function $\psi(r, t)$ is expanded in a basis set $\phi_n(r)$ where $\phi_n(r)$ are eigenfunctions to the asymptotic Hamiltonian $H_0(r)$; i.e.,

$$H_0(r)\phi_n(r) = E_n\phi_n(r) \tag{2}$$

The total Hamiltonian is

$$H(r, R) = -\frac{\hbar^2}{2\mu}\frac{\partial^2}{\partial R^2} + H_0(r) + V(r, R) \tag{3}$$

where μ is the reduced mass and $V(r, R)$ is the interaction potential. In order to introduce a classical-like motion in the R coordinate, the wave function $\Phi(R, t)$ is approximated by a Gaussian wave packet (GWP):

$$\Phi(R, t) = \exp\left(\frac{i}{\hbar}(\gamma(t) + P(t)(R - R(t)) + A(t)(R - R(t))^2)\right) \tag{4}$$

where Re $\gamma(t)$ is a phase factor, Im $\gamma(t)$ is defined by the normalization condition, $R(t)$ is a "trajectory," $P(t)$ is a momentum, and $A(t)$ is a width parameter of the wave packet. The GWP is centered around $R(t)$ in coordinate space and around $P(t)$ in momentum space; i.e. the distribution in momentum space is

$$F(P_l) = 2\hbar\sqrt{\pi g(-t)}\exp(-g(-t)(P(-t) + P_l)^2) \tag{5}$$

where the initial momentum $P(-t)$ is negative and

$$g(t) = \frac{\text{Im } A(t)}{2\hbar \mid A(t) \mid^2} \tag{6}$$

Thus $R(-t) = R_0$ and $P(-t) = -P_0$ denote the center of the Gaussian distribution in coordinate and momentum space respectively. Note that the time axis is defined such that the turning point for the motion along R is reached at $t = 0$, the system is initialized at $-t$ and analyzed at $+t$, where $t \to \infty$.

The potential $V(r, R)$ is now expanded in a power series around the "reference path" $R(t)$, and the above trial function is inserted in the time-dependent Schrödinger equation. By equating terms with equal powers of $\Delta R = R - R(t)$ the coupled equations to be solved in this mixed quantum-GWP formulation become

$$i\hbar\dot{a}_n(t) = E_n a_n(t) + \sum_m \langle\phi_n \mid V(R(t), r) \mid \phi_m\rangle\, a_m(t) \tag{7}$$

$$\dot{R}(t) = \frac{P(t)}{\mu} \tag{8}$$

$$-\dot{P}(t) = \langle\psi \left| \frac{\partial V(R(t), r)}{\partial r} \right| \psi\rangle \tag{9}$$

$$-\dot{A}(t) = \frac{1}{2}\langle\psi \left| \frac{\partial^2 V(R(t), r)}{\partial r^2} \right| \psi\rangle \tag{10}$$

$$\dot{\gamma}(t) = \frac{P(t)^2}{\mu} + \frac{i\hbar A(t)}{\mu} \tag{11}$$

where $a_n(t)$ are expansion coefficients for the wave function $\psi(r, t)$ and the angle brackets indicate integration over r-space.

B. The Optimum Trajectory Approach

The product-type wave function assumed in the previous section is the appropriate asymptotic wave function. However, if we solve the coupled equations (7)–(11), we assume that the asymptotic product form also holds later. This is of course an approximation to the true situation. We also notice that if the time dependent Schrödinger equation had been solved exactly we would have obtained a solution for a Gaussian distribution of energies or momenta centered around P_0. The probability for a given transition at a given initial energy would have been obtained by projecting onto outgoing plane waves and dividing by the incoming flux at the same energy; i.e., considering the energy E we have

$$E = E_I + \frac{P_I^2}{2\mu} = E_F + \frac{P_F^2}{2\mu} \tag{12}$$

and the transition probability for the transition $I \rightarrow F$ is obtained as

$$P_{I\rightarrow F} = \frac{P_F}{P_I} \frac{|\langle \exp(-ik_F R)\phi_F(r)|\ \Psi(R, r, t)\rangle|^2}{|\langle \exp(ik_I R)\phi_I(r)|\ \Psi(R, r, -t)\rangle|^2} \tag{13}$$

where $k_I = P_I/\hbar$. The denominator can be evaluated to give $F(P_I)$. It is important to notice that the transition probability $P_{I\rightarrow F}$ in principle is independent of P_0, i.e., where the center of the wave packet is located and also of the initial width of the GWP. In practice, there will (for numerical reasons) be a slight dependence since all momenta are not represented with the same weight. If the dynamics is not solved exactly but is approximated by introducing a product-type wave function there will, however, usually be a strong dependence of the initial momentum in $P_{I\rightarrow F}^{\mathrm{SCF}}$ defined as

$$P_{I\rightarrow F}^{\mathrm{SCF}}(P_0, \alpha_0) = \frac{P_F}{P_I} |\ a_F\ |^2 \sqrt{\frac{g(t)}{g(-t)}} \exp(-g(t)(P(t) - P_F)^2 + g(-t)(-P_0 + P_I)^2) \tag{14}$$

where α_0 is related to the width, σ of the GWP at the turning point, $\alpha_0 = \hbar/4\sigma^2$, and a_F the amplitude for being in state F at time t. a_F is obtained by solving Eqs. (7). It is convenient and completely general to parameterize at the turning point using Im $A(t = 0) = \alpha_0$ and Re $A(t = 0) = 0$. In the exact quantum treatment of the problem one would require that the probability is independent of the two parameters P_0 and α_0. But we can obtain a classical path theory by defining an optimum momentum P_0^* such that

$$\left.\frac{\partial P_{I\rightarrow F}}{\partial \alpha_0}\right|_{P_0=P_0^*} = 0 \tag{15}$$

i.e., P_0^* is computed variationally (16). If the scattering problem had been treated exactly, then the transition probability is independent of both the momentum P_0 and the width parameter α_0; i.e., they are parameters which can be chosen arbitrarily, at least in principle. Thus Eq. (15) holds if the scattering problem is treated exactly (i.e., quantum mechanically). If the scattering problem is not treated exactly, then the probability will of course depend on the two parameters, but since P_0 is a parameter we can define a momentum P_0^* for which the result is at least independent of α_0.

C. Higher-Order Correction Terms

The above results were obtained using a product-type trial wave function and then invoking the quantum mechanical "boundary" conditions in order to obtain a way of defining the parameter P_0. If the intermolecular potential is quadratic in the coordinate R, then the TDSE can be exactly fulfilled by the trial function (1) (13). Since the potential is not quadratic, the trial function can only be a good approximation in a short time interval, and hence correction terms have to be included. This can be done formally by using the trial function (16)

$$\Psi(r, R, t) = \psi(r, t)\Phi(R, t) \sum_n \epsilon_n(t)(R - R(t))^n \tag{16}$$

If we, as before, expand the potential in a power series around the reference trajectory, $R(t)$, and equate terms of the same power we obtain a set of coupled equations for the expansion coefficients $\epsilon_n(t)$. It has recently been demonstrated that inclusion of these "higher-order correction" terms does improve the agreement between the exact quantum and the semiclassical transition probabilities for inelastic collision problems (14).

III. INELASTIC SCATTERING WITH ABSORBING BOUNDARIES

Total reaction probabilities and cross sections can be obtained from a wave packet treatment of the vibrational coordinates of the reactants by adding an absorbing potential, i.e., a negative imaginary potential (15) at large bond distances. The potential absorbs the part of the wave packet entering the reactive channels. Thus the total reaction probability can then be calculated from the flux over the boundaries placed in the reactant valley (see Fig. 1) or by projecting the scattered wave packet onto the inelastic channels and subtracting the total inelastic probability from unity. This methodology was introduced in order to study inelastic processes near the dissociation limit in the $Ar+Ar_2^*$ excimer system (17) and was later extended to diatom-diatom systems (18). The semiclassical wave packet approach involves propagation of wave packets in one and two dimensions (see below). The classical and quantum systems are coupled through an effective Hamiltonian.

A. Atom-Diatom Cases

Consider an atom A colliding with a diatomic molecule BC. The mixed quantum classical Hamiltonian for the system is

$$H(r; R, P_R, j,\gamma) = \hat{H}_0(r; j) + H_1(R, \gamma, P_R, j) + H_2(r; R, \gamma) \tag{17}$$

where r is the BC bond distance, R is the distance from the center of mass of the diatomic molecule to A, P_R is the corresponding momentum, γ is the angle between the r and R axes, and j is the rotational action. We treat the vibrational motion quantum mechanically

$$\hat{H}_0 = -\frac{\hbar^2}{2m}\frac{\partial^2}{\partial r^2} + \frac{j(t)^2}{2m}\left(\frac{1}{r^2} - \frac{1}{r_{eq}^2}\right) \tag{18}$$

where m is the reduced mass of the diatom and r_{eq} is the equilibrium value of the bond distance. The Hamiltonian H_1 depends only on the classical variables:

$$H_1(R, \gamma, P_R, j) = \frac{j^2}{2mr_{eq}^2} + \frac{1}{2\mu}\left(P_R^2 + \frac{l^2}{R^2}\right) + V_{eff}(R, \gamma) \tag{19}$$

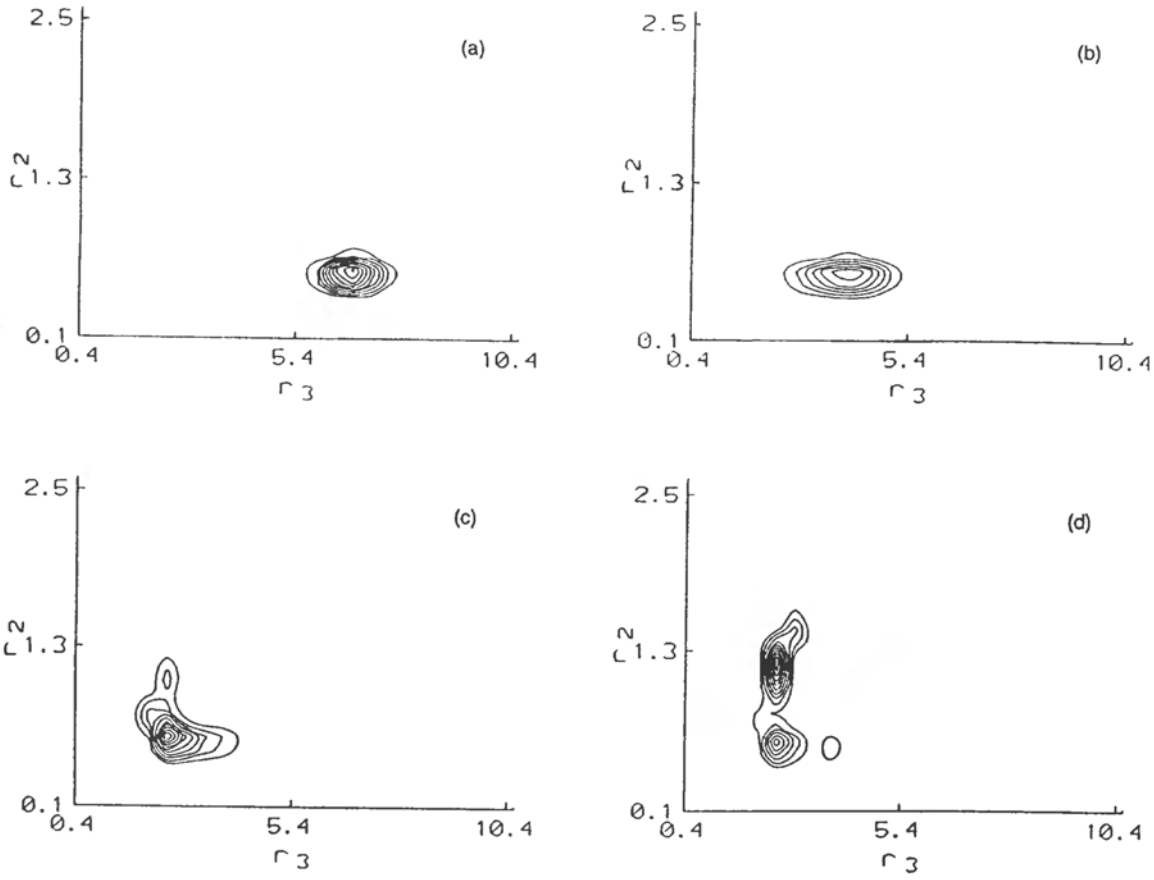

Figure 1 Contour map of the wave packet, i.e., $\int dr_1 \mid \psi(r_1, r_2, r_3) \mid^2$ as a function of r_2 and r_3 for $H_2 + OH \rightarrow H_2O + H$. r_2 is the HH, r_1 is the OH bond distance, and r_3 is the center of mass distance. The reactive flux is measured over the r_2 distance. The contour maps are shown after (a) 20 fs, (b) 60 fs, (c) 80 fs, and (d) 100 fs.

where μ is the reduced mass of the relative center of mass motion, l is the orbital angular momentum, and V_{eff} is an effective potential,

$$V_{\text{eff}}(R, \gamma) = \langle \psi \mid V(R, r, \gamma) \mid \psi \rangle \tag{20}$$

where the angle brackets indicate integration over the quantum coordinate r. The above separation in $\hat{H}_0$ and H_1 enables an expansion of the perturbation term in (18) around r_{eq} and gives through Eq. (19) a Hamiltonian for a rigid rotor moving in an effective potential. This problem is solved using classical mechanics.

Finally we have

$$H_2 = V(R, r, \gamma) - V_{\text{eff}}(R, \gamma) \tag{21}$$

The wave function $\psi(r, t)$ is initialized to a particular bound state of the diatomic molecule; i.e.,

$$\psi(r, t_0) = \phi_n(r) \tag{22}$$

where $\phi_n(r)$ is a vibrational eigenfunction of BC.

The time evolution is followed by solving the time-dependent Schrödinger equation

$$i\hbar \frac{\partial \psi(r, t)}{\partial t} = H(r; t)\psi(r, t) \tag{23}$$

where we have indicated that the Hamiltonian is time dependent through the classical variables. The above equation is solved using expansion on a grid in r; i.e., the wave function is represented only at a certain number of discrete values of r. The kinetic energy term can be evaluated by the fast Fourier transform (FFT) methodology (19) and the solution to Eq. (23) obtained using one of the time-propagation methods available (second-order differencing (SOD) (19), split operator (20), Chebyshev expansion (21), or Lanczos iterative reduction technique (22)). The advantage of using a grid method for the solution of the TDSE is that we can easily account for bond-breaking events (here dissociation) by adding an optical potential (15) at large values of r on the grid:

$$V_{\text{opt}}(r) = \begin{cases} -if(r), & r \geq r^* \\ 0, & r < r^* \end{cases} \tag{24}$$

After the collision the wave function is projected onto the bound states of the diatomic molecule and the inelastic transition probabilities are obtained as

$$P_{n \to m} = | \langle \psi(r, t \to \infty) | \phi_m(r) \rangle |^2 \tag{25}$$

The dissociation probability can be obtained as either

$$P_d = 1 - \sum_m P_{n \to m} \tag{26}$$

or by computing the flux over a boundary placed just before the absorbing potential.

$$P_d = \frac{\hbar}{m} \int_{t_0}^{\infty} dt \, \text{Im}\left[\psi(r, t)^* \frac{\partial}{\partial r} \psi(r, t) \right] \tag{27}$$

where Im denotes the imaginary part of $[\cdot\cdot]$. The time dependence of the Hamiltonian $H(r; t)$ is obtained through the classical variables, by solving Hamiltons equations of motion using the Hamiltonian H_1:

$$\dot{R} = \frac{\dot{P}_R}{\mu} \tag{28}$$

$$\dot{P}_R = \frac{l^2}{\mu R^3} - \frac{\partial V_{\text{eff}}}{\partial R} \tag{29}$$

$$\dot{q}_j = \frac{j}{m r_{\text{eq}}^2} + \frac{\partial V_{\text{eff}}}{\partial \gamma} \frac{\partial \gamma}{\partial j} \tag{30}$$

$$\frac{dj}{dt} = -\frac{\partial V_{\text{eff}}}{\partial \gamma} \frac{\partial \gamma}{\partial q_j} \tag{31}$$

$$\dot{q}_l = \frac{l}{\mu R^2} + \frac{\partial V_{\text{eff}}}{\partial \gamma} \frac{\partial \gamma}{\partial l} \tag{32}$$

$$\frac{dl}{dt} = -\frac{\partial V_{\text{eff}}}{\partial \gamma} \frac{\partial \gamma}{\partial q_l} \tag{33}$$

where we can use that (24)

$$\cos \gamma = - \cos q_l \cos q_j + \frac{j^2 + l^2 - J^2}{2lj} \sin q_j \sin q_l \tag{34}$$

where J is the total angular momentum, q_l and q_j are angles conjugated to the classical actions l and j. Since we absorb part of the wave function by the optical potential, we should use the normalized effective potential $V_{\text{eff}}/ \langle \psi \mid \psi \rangle$ in the classical equations of motion above.

B. Diatom-Diatom Cases

For two diatomic molecules we can use the same approach as above, since by forming a triatomic molecule through a reaction between two diatomics, we break one bond and hence the flux over that bond is related to the total reaction probability; i.e., we are interested in computing the reaction cross section for the reaction

$$\text{AB} + \text{CD} \rightarrow \text{ABC} + \text{D} \tag{35}$$

Introducing the three vectors $\mathbf{R}_i$ (i = 1, 2, 3), where $\mathbf{R}_1$ is the vector from A to B, $\mathbf{R}_2$ the vector from C to D, and $\mathbf{R}_3$ the vector from the center of mass of AB to that of CD, we can define the mass-scaled coordinates as

$$r_i = \sqrt{\frac{\mu_i}{\mu}} R_i \tag{36}$$

where μ_1 is the reduced mass of AB, μ_2 the reduced mass of CD, μ_3 the reduced mass of the relative motion, and $\mu = (\mu_1\mu_2\mu_3)^{1/3}$, we get the following form of the kinetic energy operator:

$$\hat{H} = - \frac{\hbar^2}{2\mu} \sum_i^3 \left(\frac{\partial^2}{\partial r_{ix}^2} + \frac{\partial^2}{\partial r_{iy}^2} + \frac{\partial^2}{\partial r_{iz}^2} \right) \tag{37}$$

Introducing spherical polar coordinates we have

$$\hat{T} = - \frac{\hbar^2}{2\mu} \sum_i^3 \left[\frac{\partial^2}{\partial r_i^2} + \frac{2}{r_i} \frac{\partial}{\partial r_i} + \frac{1}{r_i^2} \left(\frac{\partial^2}{\partial \theta_i^2} + \cot \theta_i \frac{\partial}{\partial \theta_i} + \frac{1}{\sin^2 \theta_i} \frac{\partial^2}{\partial \phi_i^2} \right) \right] \tag{38}$$

The non-Hermitian term with $\partial/\partial r_i$ can be removed by transformation of the wave function with a factor $1/r_1r_2r_3$ (18). In the semiclassical framework we can treat the two vibrational coordinates r_1 and r_2 quantum mechanically; i.e., the kinetic part of the quantum Hamiltonian becomes

$$\hat{H}_q = - \frac{\hbar^2}{2\mu} \left(\frac{\partial^2}{\partial r_1^2} + \frac{\partial^2}{\partial r_2^2} \right) \tag{39}$$

and the initial wave function is just a product vibrational function, $\psi(r_1, r_2, t = 0) = \phi_n(r_1)\phi_m(r_2)$. By introducing an absorbing potential in the r_2 coordinate at large r_2 distances and recording the flux over a grid point just before the absorbing potential, we can determine the total reaction probability for a given trajectory in classical phase space. Another way of obtaining the total reaction probability is to project the wave packet

$\psi(r_1, r_2, t)$ onto the asymptotic nonreactive product states:

$$P_{nm}^{\mathrm{NR}} = \int dr_1\ dr_2\ \psi(r_1, r_2, t)\phi_n(r_1)\phi_m(r_2) \tag{40}$$

and obtain the reaction probability as

$$P_{n_0m_0}^{R} = 1 - \sum_{nm} P_{nm}^{\mathrm{NR}} \tag{41}$$

The classical equations of motion are solved using the effective Hamiltonian

$$H_{\mathrm{sc}}^{\mathrm{eff}} = \frac{\langle\ \psi\ |\ \hat{H}_{\mathrm{sc}}\ |\ \psi\ \rangle}{\langle\ \psi\ |\ \psi\ \rangle} \tag{42}$$

where

$$\hat{H}_{\mathrm{sc}} = \hat{H}_q + \frac{p_{r_3}^2}{2\mu} + \sum_i^3 \frac{1}{2\mu r_i^2}\left(p_{\theta_i}^2 + \frac{1}{\sin^2\theta_i}\,p_{\phi_i}^2\right) + V(r_i, \theta_i, \phi_i) \tag{43}$$

The Hamiltonian is normalized with $\langle\ \phi\ |\ \phi\ \rangle$ because the wave function in the product channel is adsorbed by an imaginary potential.

The reaction rate constant is obtained by averaging the cross section over initial Boltzmann distributions of the rotational energies of the two diatomic molecules and the translational energy for the relative motion:

$$\begin{aligned} k_{n_0m_0}(T) = {} & \sqrt{\frac{8kT}{\pi\mu_3}} \int_0^\infty d(\beta\ E_{\mathrm{kin}})\beta\ E_{\mathrm{kin}}\ \exp(-\beta\ E_{\mathrm{kin}}) \\ & \frac{1}{Q_{\mathrm{rot},1}} \sum_{j_1} (2j_1 + 1)\ \exp(-\beta\ E_{\mathrm{rot},1}) \\ & \frac{1}{Q_{\mathrm{rot},2}} \sum_{j_2} (2j_2 + 1)\ \exp(-\beta\ E_{\mathrm{rot},2}) \\ & \frac{\pi}{k_{n_0j_1m_0j_2}^2} \sum_{l} (2l + 1)\ \frac{1}{N}\ P_{n_0m_0}^{R}(j_1j_2l) \end{aligned} \tag{44}$$

where $Q_{\mathrm{rot},i}$ $(i = 1, 2)$ are rotational partition functions:

$$Q_{\mathrm{rot},i} = \frac{\hbar^2}{2I_i} \tag{45}$$

where I_i are the moment of inertia, j_i are the rotational and l the orbital angular momenta, N is the number of "trajectories" in the classical phase space, and $P_{n_0m_0}^{R}(j_1j_2l)$ is the reaction probability obtained from the wave function propagated for the specific selected trajectory. Letting

$$\frac{\hbar^2 k_{n_0j_1m_0j_2}^2}{2\mu_3} = E_{\mathrm{kin}} \tag{46}$$

and the energy available for the classical degrees of freedom $U = E_{\text{rot},1} + E_{\text{rot},2} + E_{\text{kin}} = (E - E_{n_0 m_0})$, we can define an "average cross section" as

$$\langle \sigma_{n_0 m_0}(U, T_0) \rangle = \frac{\pi \hbar^6}{8\mu_3 (kT_0)^3 I_1 I_2} \int_0^{l_{\max}} dl\ (2l + 1) \times \int_0^{j_{1,\max}} dj_1\ (2j_1 + 1) \int_0^{j_{2,\max}} dj_2\ (2j_2 + 1) P^R_{n_0 m_0} \tag{47}$$

where T_0 is an arbitrary reference temperature (to get the unit Å^2) which drops out when the cross sections are used to calculate rate constants. The average cross section is evaluated by a Monte Carlo technique. Thus, the rotational and orbital angular momenta and their conjugate angles are picked randomly, and the integral (47) is approximated by a sum:

$$\langle \sigma_{n_0 m_0}(U, T_0) \rangle = \frac{1}{N} \sum_{\xi(i)} F_{n_0 m_0}(\{\xi(i)\}) \tag{48}$$

where N is the number of trajectories, $l = \xi_1 l_{\max}$, $m_l = l \cos(\pi \xi_2)$, $j_1 = \xi_3 j_{1,\max}$, $m_{j1} = j_1 \cos(\pi \xi_4)$, $j_2 = \xi_5 j_{2\max}$, $m_{j2} = j_2 \cos(\pi \xi_6)$, $\beta_l = 2\pi \xi_7$, $\beta_{ml} = 2\pi \xi_8$, $\beta_{j1} = 2\pi \xi_9$, $\beta_{j2} = 2\pi \xi_{10}$, $\beta_{mj1} = 2\pi \xi_{11}$, and $\beta_{mj2} = 2\pi \xi_{12}$. The function $F(\ )$ is defined by

$$F_{n_0 m_0}(\{\xi(i)\}) = \frac{\pi \hbar^6}{8\mu_3 (kT_0)^3 I_1 I_2} l_{\max} j_{1,\max} j_{2,\max} (2l_{\max} \xi_1 + 1)(2j_{1,\max} \xi_3 + 1) \times (2j_{2,\max} \xi_5 + 1) P^R_{n_0 m_0}(\{\xi_i\}) \tag{49}$$

where the random variables ξ_i are picked between 0 and 1. The rate constant is now obtained as

$$k'_{n_0 m_0}(T) = \sqrt{\frac{8kT}{\pi \mu_3}} \left(\frac{T_0}{T}\right)^3 \int_0^\infty d(\beta U)\ \exp(-\beta U)\ \langle \sigma_{n_0 m_0}(U, T_0) \rangle \tag{50}$$

Thus, this wave packet version of the atom-diatom and diatom-diatom inelastic scattering theory (23) is able in a simple manner to give information on the total reaction probabilities. The methodology described above can easily be extended to three quantum degrees of freedom, treating, e.g., the r_3 motion quantally (see (25)). Figure 1 visualizes the result of such a propagation for the $H_2 + OH \rightarrow H_2O + H$ reaction. The figure shows how the flux increases in the reactive channel (large r_2). The flux over a boundary at $r_2 = 1.12$ Å is recorded before the wave function is absorbed by an imaginary potential starting at $r_2 = 1.36$ Å.

IV. HYPERSPHERICAL COORDINATE APPROACH

In the previous section we have introduced a semiclassical methodology which is capable of giving total reaction probabilities and cross sections. If one is interested in state-to-state resolved quantities, it is necessary to introduce a coordinate system in which reactant and product channels are described in the same manner, i.e., so that the separation into a quantum and a classical part does not discriminate between the channels. The reason is that it is not possible to construct a proper wave function for the product channel from a quantum-classical method in which a mixture of classical and quantum coordinates is

used in the reactant channel. Fortunately such coordinates do exist, namely hyperspherical coordinates (26).

A. The Four-Atom Case

One way of constructing hyperspherical coordinates for a four-atom system is to consider the three vectors $\mathbf{R}_i$ (see Fig. 2) and introduce first the usual angles (θ_i, ϕ_i) such that

$$R_{ix} = R_i \sin\theta_i \cos\phi_i \tag{51}$$

$$R_{iy} = R_i \sin\theta_i \sin\phi_i \tag{52}$$

$$R_{iz} = R_i \cos\theta_i \tag{53}$$

Next we consider the vector (R_1, R_2, R_3) for which we can introduce polar coordinates η_1 and η_2 such that

$$R_1 = \rho \sin\eta_2 \sin\eta_1 \tag{54}$$

$$R_2 = \rho \sin\eta_2 \cos\eta_1 \tag{55}$$

$$R_3 = \rho \cos\eta_2 \tag{56}$$

We can then transform to hyperspherical coordinates by expressing the three Jacobi vectors (see Fig. 2) in the following manner:

$$R_{1x} = \rho \sin\eta_2 \sin\eta_1 \sin\theta_1 \cos\phi_1 \tag{57}$$

$$R_{1y} = \rho \sin\eta_2 \sin\eta_1 \sin\theta_1 \sin\phi_1 \tag{58}$$

$$R_{1z} = \rho \sin\eta_2 \sin\eta_1 \cos\theta_1 \tag{59}$$

$$R_{2x} = \rho \sin\eta_2 \cos\eta_1 \sin\theta_2 \cos\phi_2 \tag{60}$$

$$R_{2y} = \rho \sin\eta_2 \cos\eta_1 \sin\theta_2 \sin\phi_2 \tag{61}$$

$$R_{2z} = \rho \sin\eta_2 \cos\eta_1 \cos\theta_2 \tag{62}$$

$$R_{3x} = \rho \cos\eta_2 \sin\theta_3 \cos\phi_3 \tag{63}$$

$$R_{3y} = \rho \cos\eta_2 \sin\theta_3 \sin\phi_3 \tag{64}$$

$$R_{3z} = \rho \cos\eta_2 \cos\theta_3 \tag{65}$$

Thus the hyperspherical coordinates are defined implicitly from the Jacobi vectors, which in turn can be chosen differently than is done here (e.g., $\mathbf{R}_2$ from the center of mass of AB to atom C, and $\mathbf{R}_3$ from the center of mass of ABC to atom D). We see that the hyperradius ρ defines the "size" of the system, since

$$\rho^2 = R_1^2 + R_2^2 + R_3^2 \tag{66}$$

Introducing the reduced mass as

$$\mu = \left(\frac{m_1 m_2 m_3 m_4}{m_1 + m_2 + m_3 + m_4}\right)^{1/3} \tag{67}$$

we obtain the following Hamiltonian:

$$\hat{H} = -\frac{\hbar^2}{2\mu}\frac{1}{\rho^8}\frac{\partial}{\partial\rho}\left(\rho^8\frac{\partial}{\partial\rho}\right) + \frac{1}{2\mu\rho^2}(\hat{\mathcal{L}}_1^2 + \hat{\mathcal{L}}_2^2) - \frac{\hbar^2}{2\mu}\sum_{i=1}^{3}\frac{\hat{\ell}_i^2}{R_i^2} \tag{68}$$

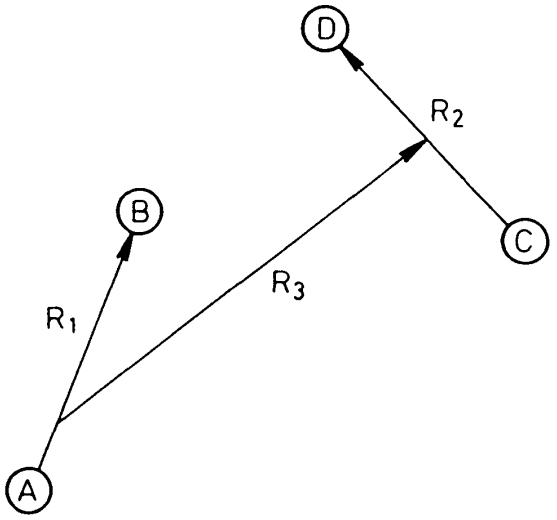

Figure 2 Jacobi vectors for a four-center reaction.

where

$$\hat{\mathscr{L}}_1^2 = -\frac{4\hbar^2}{\sin^2\eta_2}\frac{1}{\sin^2(2\eta_1)}\frac{\partial}{\partial(2\eta_1)}(\sin^2 2\eta_1)\frac{\partial}{\partial(2\eta_1)} \tag{69}$$

$$\hat{\mathscr{L}}_2^2 = -\frac{\hbar^2}{\sin^5\eta_2\cos^2\eta_2}\frac{\partial}{\partial\eta_2}\left(\sin^5\eta_2\cos^2\eta_2\frac{\partial}{\partial\eta_2}\right) \tag{70}$$

$$\hat{\ell}_i^2 = \frac{\partial^2}{\partial\theta_i^2} + \frac{1}{\sin^2\theta_i}\frac{\partial^2}{\partial\phi_i^2} + \cot\theta_i\frac{\partial}{\partial\theta_i} \tag{71}$$

The volume element is

$$\rho^8\sin^2\eta_1\cos^2\eta_1\cos^2\eta_2\sin^5\eta_2\,d\rho\,d\eta_1\,d\eta_2\prod_{i=1}^{3}\sin\theta_i\,d\theta_i\,d\phi_i \tag{72}$$

A mixed quantum-classical approach can now be obtained by treating the rotational motion of the three vectors $\mathbf{r}_i$ classically and the three variables ρ, η_1, and η_2 quantally. In order to further simplify the Hamiltonian in this case, we introduce the transformed wave function

$$\tilde{\Psi} = \frac{1}{2}\rho^4\sin(2\eta_1)\sin^{5/2}\eta_2\cos\eta_2\,\Psi \tag{73}$$

With this transformation, the Hamiltonian for $\tilde{\Psi}$ becomes

$$-\frac{\hbar^2}{2\mu}\frac{\partial^2}{\partial\rho^2} - \frac{\hbar^2}{2\mu\rho^2}\frac{1}{\sin^2\eta_2}\frac{\partial^2}{\partial\eta_1^2} - \frac{\hbar^2}{2\mu\rho^2}\frac{\partial^2}{\partial\eta_2^2} + V_{ex} + V_{pot} + H_{clas} \tag{74}$$

where the "extra" potential is due to the coordinate transformations

$$V_{ex} = \frac{7}{4}\frac{\hbar^2}{\mu\rho^2} + \frac{\hbar^2}{8\mu\rho^2}\left(\frac{15\cos^2\eta_2 - 16}{\sin^2\eta_2}\right) \tag{75}$$

The "classical" Hamiltonian H_{clas} becomes just

$$H_{\text{clas}} = \frac{1}{2\mu}\sum_{i}^{3}\frac{1}{r_i^2}\left(p_{\theta_i}^2 + \frac{1}{\sin^2\theta_i}p_{\phi_i}^2\right) \tag{76}$$

In the exact formulation of the problem it is convenient to introduce a coupled wave packet approach, in which some of the degrees of freedom are described by wave packet dynamics and the remaining by a basis set expansion. In order to reduce the dimensionality of the problem the conservation of total angular momentum J and its projection M should be explicitly included by introducing appropriate coupling between angular momenta. Thus the wave function can be expanded as

$$\begin{aligned}\tilde{\Psi} = \sum \xi_\alpha^{JM}(\rho, \eta_1, \eta_2, t)Y_{j_1m_1}(\theta_1, \phi_1)Y_{j_2m_2}(\theta_2, \phi_2)Y_{lm}(\theta_3, \phi_3)\,(-1)^{j_1-j_2+m_{12}}(-1)^{j_{12}-l+M} \\ \times\sqrt{(2j_{12}+1)(2J+1)}\begin{pmatrix} j_1 & j_2 & j_{12} \\ m_1 & m_2 & -m_{12}\end{pmatrix}\begin{pmatrix} j_{12} & l & J \\ m_{12} & m & -M\end{pmatrix}\end{aligned} \tag{77}$$

where $\alpha = (j_1m_1j_2m_2lmj_{12}m_{12})$ is a collective quantum number. The summation is subject to the selection rules of the 3-j symbols $\begin{pmatrix}\cdot & \cdot & \cdot \\ \cdot & \cdot & \cdot\end{pmatrix}$ (27), i.e., $m_1 + m_2 = m_{12}$ and $m_{12} + m = M$. This and conservation of J and M reduce the dimensionality of the problem from 11 to 7. We notice that j_{12} and l take values over $|\, j_1 - j_2 \,| \le j_{12} \le j_1 + j_2$ and $|\, j_{12} - l \,| \le J \le j_{12} + l$, respectively. The wave packet is ξ_α is initialized as

$$\xi_\alpha(\rho, \eta_1, \eta_2, t) = \phi_{n_1 j_1}(r_1)\phi_{n_2 j_2}(r_2)F(r_3, t)\;|\;J(r_1, r_2, r_3 \mid \rho, \eta_1, \eta_2)\;|^{1/2} \tag{78}$$

where ϕ are vibrational wave functions and $F(r_3, t)$ is a translational wave packet. The Jacobian for the transformation from (r_1, r_2, r_3) to (ρ, η_1, η_2) is

$$J(r_1, r_2, r_3 \mid \rho, \eta_1, \eta_2) = \rho^2 \sin\eta_2 \tag{79}$$

The exact solution will then involve the propagation of a large number of coupled 3D wave packets. How many depends of course upon the energy, but around 1000 would, for most purposes, be a minimum. Hence a reduction of the complexity is required. This can be achieved either by decoupling approximations or by introducing a quantum-classical description.

B. The Three-Atom Case

In the three-atom case we introduce the hyperspherical coordinates: the hyperradius ρ and the two hyperangles θ and ϕ specifying the size and shape of the ABC triangle, and the three Euler angles α, β, and γ giving the orientation of the triangle in space. The connection to ordinary Jacobi coordinates is obtained through the equations

$$\gamma^2 = \frac{d_1^2}{2}\rho^2(1 + \sin\theta\cos\phi) \tag{80}$$

$$R^2 = \frac{1}{2d_1^2}\rho^2(1 - \sin\theta\cos\phi) \tag{81}$$

$$\cos\eta = -\frac{\sin\theta\sin\phi}{\sqrt{1 - \sin^2\theta\sin^2\phi}} \tag{82}$$

where r is the BC bond distance, R is the distance from A to the center of mass of BC, η is the angle between r and R, and d_1 is a constant dependent on the mass combination in the reactant channel. The angle γ' together with an angle ξ specify the orientation of the diatomic molecule BC in a body-fixed coordinate system with the z-axis along the R-axis. The Hamiltonian for the three-body problem can be expressed in terms of hyperspherical coordinates as (28)

$$\hat{H} = -\frac{\hbar^2}{2\mu}\frac{\partial^2}{\partial\rho^2} + \frac{2}{\mu\rho^2}\hat{L}^2(\theta, \phi) + \frac{1}{\mu\rho^2}\left[\frac{\hat{J}_x^2}{1 - \sin\theta} + \frac{\hat{J}_y^2}{1 + \sin\theta} + \frac{\hat{J}_z^2}{2\sin^2\theta}\right] - \frac{2\cos\theta\,\hat{J}_z\hat{P}_\phi}{\mu\rho^2\sin^2\theta} + V(\rho, \theta, \phi) + \Delta V(\rho, \theta) \tag{83}$$

where

$$\mu = \sqrt{\frac{m_A m_B m_C}{m_A + m_B + m_C}} \tag{84}$$

$$\hat{J}_z = -i\hbar\frac{\partial}{\partial\gamma} \tag{85}$$

$$\hat{P}_\phi = -i\hbar\frac{\partial}{\partial\phi} \tag{86}$$

$$\hat{L}^2(\theta, \phi) = -\hbar^2\left[\frac{\partial^2}{\partial\theta^2} + \frac{1}{\sin^2\theta}\frac{\partial^2}{\partial\phi^2}\right] \tag{87}$$

$$\Delta V(\rho, \theta) = -\frac{\hbar^2}{2\mu\rho^2}\left[\frac{1}{4} + \frac{4}{\sin^2 2\theta}\right] \tag{88}$$

By introducing $\hat{J}^2 = \hat{J}_x^2 + \hat{J}_y^2 + \hat{J}_z^2$, we can rewrite the third and fourth terms of Eq. (83) as

$$\frac{\hat{J}^2 - \hat{J}_z^2}{\mu\rho^2\cos^2\theta} + \frac{\hat{J}_z^2 - 4\cos\theta\,\hat{J}_z\hat{P}_\phi}{2\mu\rho^2\sin^2\theta} + \frac{\sin\theta}{\mu\rho^2\cos^2\theta}\frac{1}{2}[\hat{J}_+^2 + \hat{J}_-^2] \tag{89}$$

where $\hat{J}_+$ and $\hat{J}_-$ are raising and lowering operators (26), (28). These operators couple the K quantum states, K being the projection quantum number on a body-fixed axis. It is possible to decouple these states by making either a decoupling approximation (i.e., to keep K constant) or to invoke a classical treatment of the corresponding classical action $P_\gamma = \hbar K$, where P_γ is the momentum conjugate to the angle γ. Thus, the latter two variables are treated "classically"; i.e., they are allowed to vary according to classical mechanical rules. The mixed quantum-classical Hamiltonian is now

$$\hat{H} = -\frac{\hbar^2}{2\mu}\frac{\partial^2}{\partial\rho^2} + \hat{H}_0(\rho, \theta, \phi) + \hat{H}_1(\rho, \theta, \phi, t; J) \tag{90}$$

where

$$\hat{H}_0 = \frac{2}{\mu\rho^2}\hat{L}^2(\theta, \phi) + V(\rho, \theta, \phi) + \Delta V(\theta, \rho) \tag{91}$$

$$\hat{H}_1 = \frac{P_\gamma(P_\gamma - 4\cos\theta\,\hat{P}_\phi)}{2\mu\rho^2\sin^2\theta} + \frac{P_J^2 - P_\gamma^2}{\mu\rho^2\cos^2\theta}(1 + \sin\theta\cos 2\gamma) \tag{92}$$

If also the motion along the hyperradius is treated classically, then the first term in Eq. (90) is replaced by $P_\rho^2/2\mu$. The variables ρ and γ are those which are most classical (i.e., slow motions), whereas θ and ϕ are more quantum mechanical. This can also be seen by introducing the asymptotic mapping

$$\theta = \frac{\pi}{2} - \frac{x}{\rho} \sin \eta \tag{93}$$

$$\phi = \phi_0 + \frac{x}{\rho} \cos \eta \tag{94}$$

where ϕ_0 is a channel-dependent angle and the internuclear diatom distance r is related to x through the equation

$$r = \frac{d_i x}{2} \tag{95}$$

where d_i is a constant depending on the mass combination in the various arrangement channels. The asymptotic ($\rho \to \infty$) Hamiltonian becomes

$$\begin{aligned} \hat{H} \to \frac{P_\rho^2}{2\mu} - \frac{2\hbar^2}{\mu}\left[\frac{\partial^2}{\partial x^2} + \frac{1}{x}\frac{\partial}{\partial x} - \frac{1}{4x^2}\right] + V(x) \\ - \frac{2\hbar^2}{\mu x^2}\left[\frac{\partial^2}{\partial \eta^2} + \frac{1}{4 \sin^2 \eta} + \frac{1}{4}\right] + \frac{P_J^2 - P_\gamma^2}{\mu x^2 \sin^2 \eta}(1 + \cos(2\gamma)) \end{aligned} \tag{96}$$

The eigenfunctions are

$$\phi_{vj}(x, \eta; \nu) = \frac{1}{\sqrt{x}} \sqrt{\sin \eta} g_{vj}(x) P_j^\nu(\cos \eta) \tag{97}$$

where P_j^ν is an associated Legendre polynomial with a continuous value of ν:

$$\nu = \frac{\cos \gamma}{\hbar} \sqrt{P_J^2 - P_\gamma^2} \tag{98}$$

For large values of j we can approximate the Legendre function and obtain (29)

$$\phi_{vj} \sim \sqrt{\frac{2}{\pi x}}\, g_{vj}(x) \frac{\Gamma(j + 1 + \nu)}{\Gamma\left(j + {}^3/_2\right)} \cos\left(\left(j + \frac{1}{2}\right)\eta - \frac{\pi}{4} + \frac{\nu\pi}{2}\right) \tag{99}$$

Thus the asymptotic quantum states are labeled by the vibrational and rotational quantum numbers, whereas the projection quantum number is treated classically. We have in the above Hamiltonian indicated that it depends upon time through the classical variables. Thus the quantum mechanical problem consists of propagating the solution to the TDSE

$$i\hbar \frac{\partial \Psi(\theta, \phi, t)}{\partial t} = \hat{H}\Psi(\theta, \phi, t) \tag{100}$$

The classical equations of motion are solved using an effective potential

$$V_{\text{eff}} = \langle \Psi \mid \hat{H} \mid \Psi \rangle \tag{101}$$

In order to obtain state-resolved probabilities, the wave function should be projected onto the eigenfunctions (97). If the analysis is carried out (approximately) using the eigenfunctions $P_j(\cos \eta)$ (i.e., setting $\nu = 0$), then the Hamiltonian $\hat{H}_1$ should be modified to

$$\hat{H}_1 - \frac{P_J^2 - P_\gamma^2}{\mu x^2} (1 + \cos 2\gamma) \tag{102}$$

to prevent asymptotic coupling. This is achieved by replacing $1/\cos^2 \theta$ by $1/\cos^2 \theta - 1/(\theta - \pi/2)^2$ in Eq. (92).

1. One Classical Degree of Freedom

If the angle γ and the momentum P_γ are treated classically, then the quantum-dynamical problem becomes a three-dimensional one and the solution for $J = 0$ becomes exact. Furthermore, to treat larger J-values does not become more complicated. We notice that for initial $\nu = 0$ value we have $P_J = P_\gamma$ or $\gamma = \pi/2$ initially. In the first case we have P_γ = constant throughout the calculation, since $\partial H_{\text{eff}}/\partial\gamma = 0$, where H_{eff} is defined by

$$\begin{aligned} H_{\text{eff}}(P_\gamma, \gamma, t) = \langle \Psi \left| -\frac{\hbar^2}{2\mu}\frac{\partial^2}{\partial\rho^2} + \hat{H}_0(\rho, \theta, \phi) \right| \Psi \rangle \\ + \frac{P_\gamma^2}{2\mu} \langle \Psi \left| \frac{1}{\rho^2 \sin^2 \theta} \right| \Psi \rangle - \frac{2P_\gamma}{\mu} \langle \Psi \left| \frac{\cos \theta \hat{P}_\phi}{\rho^2 \sin^2 \theta} \right| \Psi \rangle \\ + \frac{P_J^2 - P_\gamma^2}{\mu} \left(\langle \Psi \left| \frac{1}{\rho^2 \cos^2 \theta} \right| \Psi \rangle + \cos 2\gamma \langle \Psi \left| \frac{\sin \theta}{\rho^2 \cos^2 \theta} \right| \Psi \rangle \right) \end{aligned} \tag{103}$$

In principle we can consider γ as a classical variable, which can be selected randomly in $[0, 2\pi]$. Thus the value of P_γ should be given according to Eq. (98). Recall that K and therefore P_γ can take positive as well as negative values. For negative values the term $P_\gamma P_\phi$ in Eq. (92) changes sign. This term is responsible for coupling even and odd states with respect to reflection around $\phi = 0$. Thus in order to preserve the symmetry of a given initial state during the propagation, an appropriate linear combination of K quantum states has to be taken. Actually a given initial vib-rot state is expanded as follows:

$$\psi_{\text{initial}} = \sum_{K=-J}^{K=J} \Phi_K(\rho, \theta, \phi) \sqrt{\frac{2J + 1}{8\pi^2}} D^{J*}_{MK}(\alpha, \beta, \gamma) \tag{104}$$

where D^J_{MK} is a rotation matrix element (27). In the semiclassical approximation these individual K-components can be propagated separately, remembering that a given K value yields some constraint (according to Eq. (98)) upon the initial γ value. In the coplanar approximation we set $P_J = P_\gamma$; hence the term with γ disappears, and we consider only one K value for each J. For the relative motion we can introduce an initial Gaussian wave packet to cover a range of energies in one calculation (30). For the rotationally averaged quantities this coplanar method gave good results, but for the rotational resolved cross sections reasonable results were obtained only when the wave packet was projected onto Arthurs-Dalgarno states asymptotically (30); i.e., instead of using the asymptotic rotational eigenfunctions $Y_{jm}(\eta, \xi)$ labeled by the rotational angular momentum and the

projection quantum number m, the jl labeled states

$$\mathcal{Y}_{jl}^{JM} = (-1)^{j-l-M}\sqrt{\frac{(2J+1)(2l+1)}{4\pi}} \times \sum_m \begin{pmatrix} j & l & J \\ m & 0 & -m \end{pmatrix} Y_{jm}(\eta, \xi)D^J_{-M,-m}(\Phi', \Theta', 0) \tag{105}$$

are used. Here the angles Φ' and θ' specify the orientation of R. The reason for the better projection obtained using these states (see Figs. 3 and 4) is that l is a "better" (more preserved) quantum number than m in these coplanar calculations.

The quantum-mechanical part of the problem is reduced to propagating the solution to a time-dependent Schrödinger equation in three dimensions;

$$i\hbar \frac{\partial\Psi(\rho, \theta, \phi, t)}{\partial t} = \hat{H}\Psi(\rho, \theta, \phi, t) \tag{106}$$

where $\hat{H}$ is given by Eq. (90). This can be done by expanding the wave function in a basis set of eigenfunctions to the Hamiltonian (91);

$$\Psi(\rho, \theta, \phi, t) = \sum_n a_n(\rho, t)\phi_n(\theta, \phi; \rho) \tag{107}$$

where the "adiabatic" eigenfunctions depend parametrically on ρ

$$\hat{H}_0\phi_n(\theta, \phi; \rho) = E_n(\rho)\phi_n(\theta, \phi; \rho) \tag{108}$$

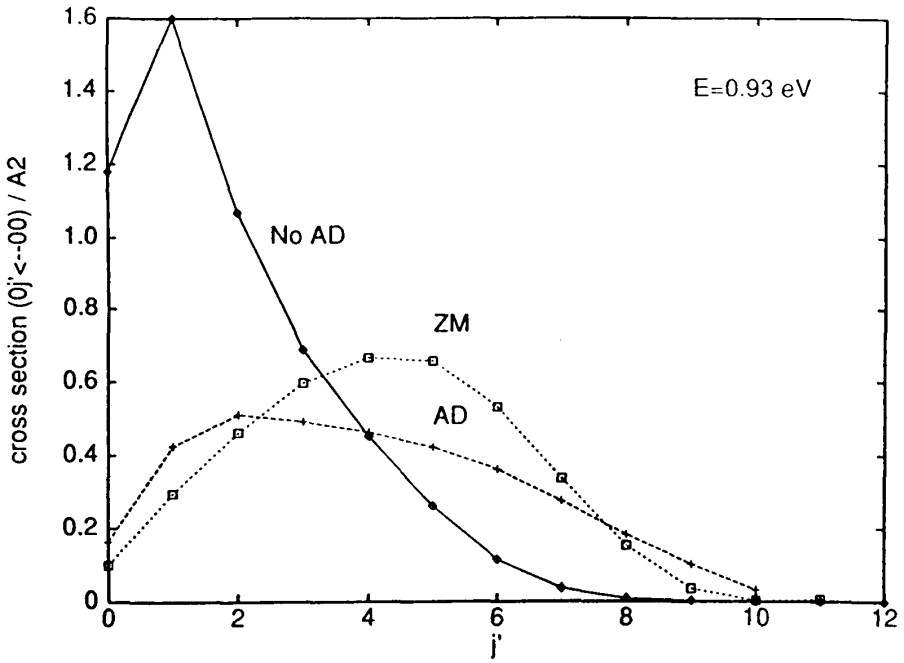

Figure 3 Comparison of exact (ZM) (35) and semiclassical coplanar cross sections for the reaction D + $H_2(v = 0, j = 0) \rightarrow DH(v' = 0, j')$ + H at total energy 0.93 eV. The AD results are obtained using projection on Arthur-Dalgarno asymptotic states (105). The (No AD) results are obtained projecting onto the asymptotic states (97).

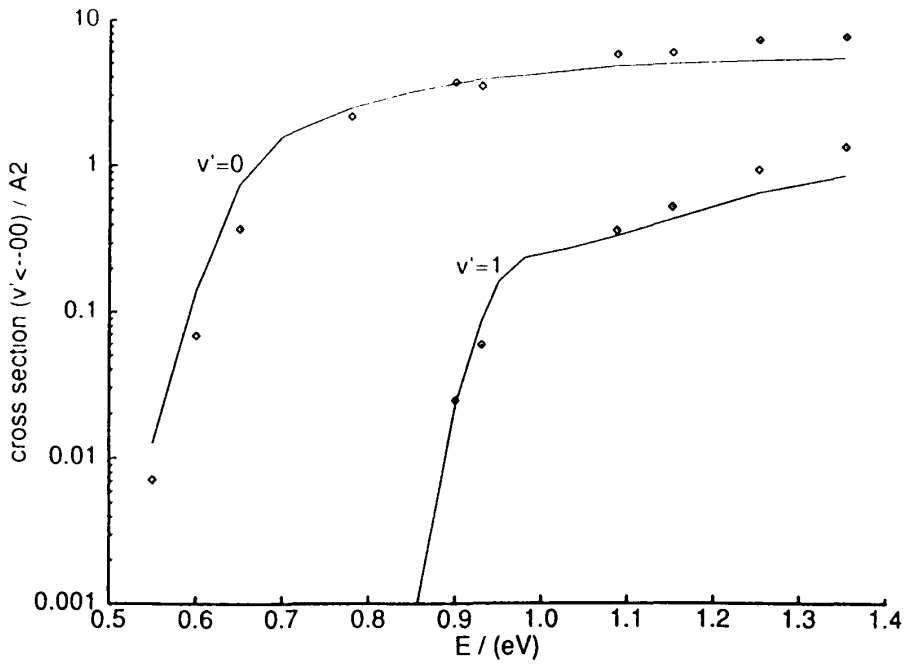

Figure 4 Rotational summed cross sections, i.e., cross sections for the reaction D + $H_2(v = 0, j = 0) \rightarrow DH(v') + H$ for $v' = 0, 1$. Solid lines indicate the exact values from (35) and the semiclassical values are (◇).

The above equation can be solved in suitable ρ ranges, and basis sets are switched when propagating the solution to the Schrödinger equation through the ρ range by taking appropriate overlaps between the ranges (31). This methodology is most convenient if the time-independent Schrödinger equation is solved or if the ρ motion is also treated classically (see below). If we consider an initial Gaussian wave packet for the relative motion, (i.e., have a distribution in ρ space), it is more convenient to consider a grid representation of the wave packet (i.e., to propagate the time-dependent Schrödinger equation on a 3D grid). This can be done by evaluating the kinetic energy terms using either an FFT or a discrete-variable representation (DVR) (32) method combined with a time-propagation method such as the Lanczos reduction technique (22). In this method, the outgoing wave packet is mapped onto asymptotic eigenstates at a given value of the hyperradius ρ* in a region where the reactive coupling has ceased. Thus we calculate

$$c_{vj}(t;\ \rho^*) = \langle \phi_{nj}(\theta,\ \phi;\ \rho^*) \mid \Psi(\rho^*,\ \theta,\ \phi) \rangle \tag{109}$$

If the collision is described in a mixed quantum-classical representation, it is not possible to map onto Jacobi coordinates (i.e., the 4D space (R, r, η, ξ)) since the wave function is known only in a 3D space. However, the θ, φ coordinates can be expressed through the asymptotic mapping (94) in terms of the variables r and η at a given value of ρ. The asymptotic propagation can then be performed in mixed Jacobi-hyperspherical coordinates, i.e., in the coordinates ρ, r, η (see (33) and Appendix A).

2. Two Classical Degrees of Freedom

The other slow motion which is a candidate for a classical mechanical treatment is the motion along the hyperradius ρ; i.e., the quantum mechanical problem is reduced to a two-dimensional one in the hyperangles θ and φ. This corresponds asymptotically as we

have seen to a quantum mechanical treatment of the vibrational and rotational motions. Again, the quantum mechanical problem can be solved by using either a wave packet propagation method on a 2D grid or solving a set of coupled equations in the expansion coefficients $a_n(t)$. In this case, the wave function is expanded in the eigenfunctions $\phi_n(\theta, \phi; \rho(t))$ as

$$\Psi(\theta, \phi, t) = \sum_n a_n(t)\phi_n(\theta, \phi; \rho(t)) \tag{110}$$

From the TDSE we then obtain (34)

$$\dot{a}_m(t) = -\sum_n a_n(t) \exp(i\Delta_{nm}(t)) \times \left[\dot{\rho} \left\langle \phi_m \left| \frac{\partial}{\partial \rho} \right| \phi_n \right\rangle\right] + \frac{i}{\hbar} \langle \phi_m \mid \hat{H}_1 \mid \phi_n \rangle \tag{111}$$

where

$$\Delta_{nm}(t) = \frac{1}{\hbar} \int_{-\infty}^{t} dt' \, [E_m(\rho(t')) - E_n(\rho(t'))] \tag{112}$$

The classical equations of motion become

$$\dot{\gamma} = \frac{\partial H_{sc}}{\partial P_\gamma} \tag{113}$$

$$\dot{P}_\gamma = -\frac{\partial H_{sc}}{\partial \gamma} \tag{114}$$

$$\dot{\rho} = \frac{\partial H_{sc}}{\partial P_\rho} \tag{115}$$

$$\dot{P}_\rho = -\frac{\partial H_{sc}}{\partial \rho} - \frac{\mu}{P_\rho} \frac{\partial H_{sc}}{\partial t} \tag{116}$$

where

$$\frac{\partial H_{sc}}{\partial t} = -\dot{\rho} \sum_{nm} a_n^*(t) \exp(i\Delta_{nm}(t))[D(\rho, t), B(\rho)]a_m(t) \tag{117}$$

and

$$D_{nm}(t) = \langle \phi_n \mid \hat{H}_1 \mid \phi_m \rangle + E_n\delta_{nm} \tag{118}$$

$$B_{nm} = \left\langle \phi_n \left| \frac{\partial}{\partial \rho} \right| \phi_m \right\rangle \tag{119}$$

where the brackets indicate integration over the quantum variables. As mentioned, it is often more convenient to introduce a wave packet propagation scheme instead of the state expansion technique. From a technical viewpoint the wave packet methodology is easily programmed and 2D wave packets are readily propagated.

V. NONADIABATIC MULTISURFACE PROBLEMS

The treatment of multisurface problems is conveniently carried out using either the 2D or the 3D quantum treatments. Since the FFT evaluation of the kinetic energy is the

time-limiting step, the computational effort increases only about linearly with the number of surfaces if the diabatic representation is used. The reason is that in the diabatic representation the "kinetic" energy part is diagonal and, hence, the Fourier transforms are carried out on each surface wave function separately. In the adiabatic representation, on the other hand, the potential is "diagonal" and coupling occurs through the kinetic energy part of the Hamiltonian.

Thus we have (in the 2D quantum case) the following set of equations:

$$i\hbar \frac{\partial}{\partial t}\begin{bmatrix}\Psi_1^d\\ \Psi_2^d\end{bmatrix} = \frac{2}{\mu\rho^2}\hat{L}^2(\theta, \phi)\begin{bmatrix}\Psi_1^d\\ \Psi_2^d\end{bmatrix} + \begin{bmatrix}V_{11} + \Delta V & V_{12}\\ V_{21} & V_{22} + \Delta V\end{bmatrix}\begin{bmatrix}\Psi_1^d\\ \Psi_2^d\end{bmatrix} \tag{120}$$

where two diabatic surfaces have been considered, ΔV is the extra potential, and V_{12} is the nonadiabatic coupling term. The equations are of course extendable to any number of diabatic states. The effective potential for the classical variables is obtained as

$$V_{\text{eff}}(\rho) = \left\langle [\Psi_1^d \quad \Psi_2^d]\begin{bmatrix}V_{11} + \Delta V & V_{12}\\ V_{21} & V_{22} + \Delta V\end{bmatrix}\begin{bmatrix}\Psi_1^d\\ \Psi_2^d\end{bmatrix}\right\rangle \tag{121}$$

and the effective Hamiltonian for the classical degrees of freedom is

$$\begin{aligned} H_{\text{eff}} = {} & \frac{P_\rho^2}{2\mu} + V_{\text{eff}}(\rho) + \frac{2}{\mu\rho^2}\langle|\, \hat{L}^2(\theta, \phi)\,|\rangle + \frac{P_\gamma^2}{2\mu\rho^2}\left\langle\left|\frac{1}{\sin^2\theta}\right|\right\rangle \\ & - \frac{2P_\gamma}{\mu\rho^2}\left\langle\left|\frac{\cos\theta\,\hat{P}_\phi}{\sin^2\theta}\right|\right\rangle \\ & + \frac{P_J^2 - P_\gamma^2}{\mu\rho^2}\left\langle\left|\frac{1}{\cos^2\theta}\right|\right\rangle + \frac{P_J^2 - P_\gamma^2}{\mu\rho^2}\cos 2\gamma\left\langle\left|\frac{\sin\theta}{\cos^2\theta}\right|\right\rangle \end{aligned} \tag{122}$$

where $\langle|\ |\rangle$ denotes expectation value. Transformation to the adiabatic representation is obtained by diagonalizing the potential matrix at each grid point. In this manner the time-dependent probability of a given channel can be calculated by "grid summation." In Fig. 5 we show the time-dependent evolution of the channel probabilities for the reaction

$$D^+ + H_2 \rightarrow \begin{cases} D^+ + H_2 \\ H^+ + H\,D \\ H_2^+ + D \\ H\,D^+ + H \end{cases} \tag{123}$$

The calculation includes three diabatic potential energy surfaces obtained using the diatomic in molecules (DIM) method (36). Using this 2D quantum treatment in hyperspherical coordinates the nonadiabatic problem can be solved also for problems involving more than three diabatic surfaces.

VI. LARGE SYSTEMS

For large systems (systems with more than four atoms) it is necessary to use methods which reduce the coordinate space for which we have to know the potential energy surface. Since chemical reactions are at most three or four-center reactions, the obvious partitioning is to treat the motion of the three or four atoms defining the reaction center by some of the methods described and the remaining motion using a small-amplitude description identical to the one used in the reaction path Hamiltonian method. In the

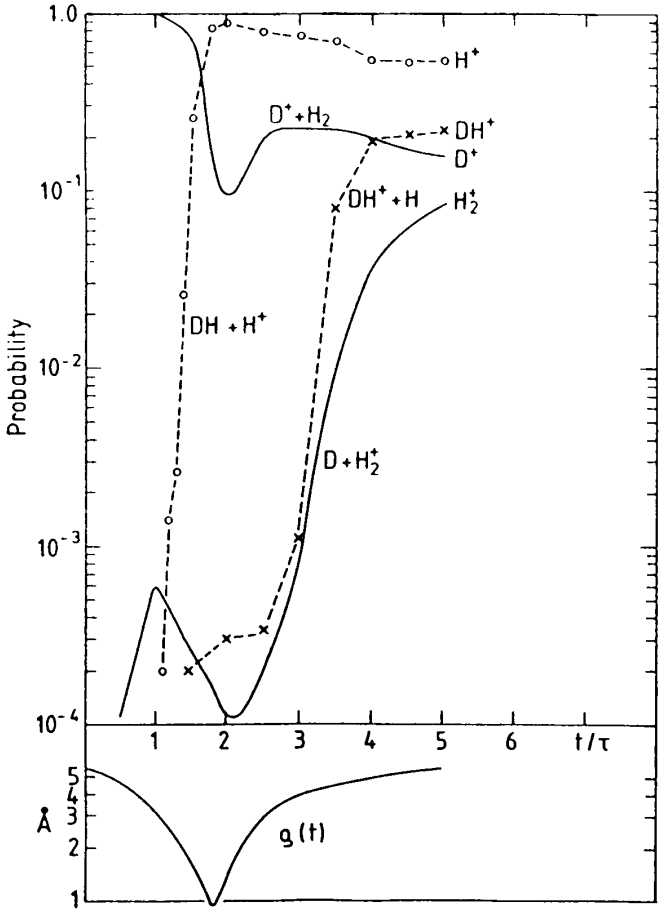

Figure 5 Reaction and charge transfer probabilities for a 2D quantum treatment of the $D^+ + H_2$ system. The lower panel shows the hyperradius $\rho(t)$. The time unit $1\ \tau = 10^{-14}$ s.

reaction path method the motion along the path is projected out and treated as a translational motion (quantally or classically), whereas the motion "perpendicular" to the path is treated within a harmonic description. The reaction path Hamiltonian can be written as (37), (38):

$$H = \frac{p_s^2}{2N} + H^0_{\text{vib}} + V_0(s) + H^0_{\text{rot}} - \frac{p_s}{N} \sum_{kk'} p_k Q_{k'} B_{kk'} \tag{124}$$

where

$$N = 1 + 2 \sum_k B_{kl} Q_k + \sum_{kk'} \bar{C}_{kk'} Q_k Q_{k'} \tag{125}$$

and

$$\bar{C}_{kk'} = C_{kk'} - \sum_l B_{lk} B_{lk'} \tag{126}$$

p_s is the momentum for the motion along the reaction path s,

$$H^0_{\text{vib}} = \sum_k \frac{1}{2} (p_k^2 + \omega_k^2 Q_k^2) \tag{127}$$

Q_k is the vibrational (normal mode) coordinates for the vibrational motion perpendicular to the reaction path, p_k are the corresponding momenta, $V_0(s)$ is the potential along the path and

$$H^0_{\text{rot}} = \frac{1}{2} \sum_{\alpha} \frac{P^2_{\alpha}}{I^e_{\alpha\alpha}(s)} \tag{128}$$

is the Hamiltonian for the overall rotational motion of the reaction-path complex. The equilibrium principal moments of inertia $I^e_{\alpha\alpha}(s)$ depend upon the reaction path coordinate through the position vectors of the ith atom $a_i(s)$:

$$I^e_{\alpha\alpha}(s) = \sum_i m_i(a^2_{i\beta} + a^2_{i\gamma}) \tag{129}$$

where $\alpha, \beta, \gamma = x, y, z$. The vibrational modes are coupled through the Coriolis-like coupling elements $B_{kk'}$ and $C_{kk'}$. The vibrational motion k is coupled to the reaction path motion by the Coriolis term B_{kF}. Also the Coriolis coupling terms are functions of s. They are defined through the eigenvectors obtained by solving the normal mode eigenvalue problem for the perpendicular vibrational motion and the vector associated with the motion along the reaction path (see (39) for details). Denoting these eigenvectors by $\mathbf{l}_{ik}$ and $\mathbf{l}_{iF}$, where i is the particle number, k is the vibrational mode, and F denotes the reaction path degree of freedom, we have

$$B_{kF} = \sum_i \frac{d}{ds} \mathbf{l}_{ik} \cdot \mathbf{l}_{iF} \tag{130}$$

$$B_{kk'} = \sum_i \frac{d}{ds} \mathbf{l}_{ik} \cdot \mathbf{l}_{ik'} \tag{131}$$

$$C_{kk'} = \sum_i \frac{d}{ds} \mathbf{l}_{ik} \cdot \frac{d}{ds} \mathbf{l}_{ik'} \tag{132}$$

The reaction path dynamics can be solved with a quantum mechanical treatment of the vibrational motion together with either a classical description of the reaction path motion and the rotational motion of the reaction complex, or a quantum mechanical treatment of the reaction path motion can be introduced using wave packet propagation along the reaction path. In this method the momentum p_s is replaced by its quantum mechanical counterpart $\hat{p}_s$ (40). We notice that the reaction path formulation retains terms up to second order in the vibrational motion perpendicular to the path. Hence it is consistent to expand the factor $1/N$ to second order. In this manner the Hamiltonian can be brought in a form where it can be solved formally by introducing a second quantization description of the vibrational degrees of freedom (41). This expansion of $1/N$ is advantageous from a computational point of view. The reason being that the factor N can become numerically small in actual calculations if the excitation of the vibrational motions is large, which in turn forces the momentum p_s to become small. The consequence is that the motion along the reaction path stops or becomes numerically difficult to integrate (42). In the expanded version a similar coupling would cause above-the-barrier reflection of the trajectory.

If only the perpendicular vibrational motion is quantized, then the operator-algebraic treatment of the quantum mechanical part of the system can be introduced and, hence, the effective Hamiltonian, which couples the reaction path motion and the quantum degrees of freedom, can be given a very compact form. Thus, the effective Hamil-

tonian for the rotational motion and the reaction path motion is obtained as the expectation value of the total Hamiltonian:

$$H_{\text{eff}} = \langle \Psi \mid H(p_s, s, P_\alpha, \hat{P}_k, Q_k) \mid \Psi \rangle \tag{133}$$

where Ψ is the wave function for the vibrational degrees of freedom. The final result is

$$\begin{aligned} H_{\text{eff}} = &\frac{1}{2}p_s^2 + V_0(s) + H_{\text{rot}} + \hbar \sum_k \left(n_k^0 + \frac{1}{2} + \rho_k(t) \right) \tilde{\omega}_k(s) \\ &+ \sum_k (W_k^- P_k^+ - W_k^+ P_k^-) + \sum_{k>l} \{F_{kl}^+ (n_k^0 Q_{kl} + n_l^0 Q_{lk}^* + \alpha_l^+ \alpha_k^-) + \text{c.c.}\} \end{aligned} \tag{134}$$

where

$$\rho_k = P_k^+ P_k^- + \sum_l n_l^0 Q_{lk} Q_{lk}^* \tag{135}$$

The first term in Eq. (134) is the kinetic energy along the reaction path. The kinetic energy can go to zero if the coupling to the other degrees of freedom, the rotational motion and the perpendicular vibrational motion (fourth term in Eq. (134)), is strong or if the potential $V_0(s)$ has a barrier. The last two terms are the expectation values of the linear and quadratic coupling terms. Thus the quantum and classical motions are coupled self-consistently to each other. The individual terms are shown as a function of time in Fig. 6 for the H_2 + OH system.

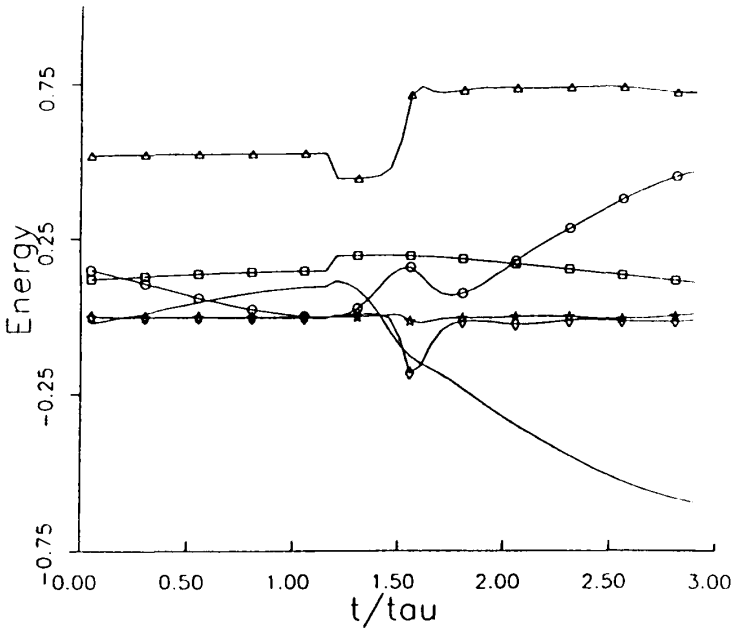

Figure 6 Energies entering the reaction path Hamiltonian for the H_2 + OH → H_2O + H reaction. The upper curve (△) is the energy in the perpendicular vibrational modes, the kinetic energy along the reaction path $p_s^2/2$ is indicated by (○), the potential energy $V_0(s)$ by the solid line, the rotational energy by (□), the effective potential arising from the linear coupling term (second to last term in Eq. (134)) by (◇) and from the quadratic terms (last term in Eq. (134)) by (★). The small discontinuity at t = 1.2 τ (10^{-14} s) is due to the way the tunneling through the barrier is carried out. The initial kinetic energy is 0.20, rotational angular momentum $J = 10\hbar$ and vibrational states v = 0. Energies are in units of 100 kJ/mol.

The modulated vibrational frequency (in Eq. (134)) is defined by

$$\tilde{\omega}_k(s) = \omega_k(s) + \frac{1}{2}\frac{p_s^2 \tilde{C}_{kk}}{\omega_k(s)} \tag{136}$$

where

$$\tilde{C}_{kl} = 4B_{kl'}B_{l'k'} - C_{kl} + \sum_{k'} B_{k'k}B_{k'l} \tag{137}$$

The quantities $P_k^{\pm}$ are given as

$$P_k^{+} = \alpha_k + \sum_l Q_{lk}\alpha_l^{+} \tag{138}$$

where

$$\alpha_k^{+} = -\frac{1}{\hbar}\int dt \left(F_k^{+} + \sum_l F_l^{+} Q_{lk}\right) \tag{139}$$

and $\alpha_k^{-} = (\alpha_k^{+})^*$. The functions α_k^{+} are obtained as integrals over the linear forces

$$F_k^{\pm} = f_k \exp(\pm i\theta_k) \tag{140}$$

where the linear force couples the perpendicular vibrational degrees of freedom to the motion along the reaction path and the rotational motion:

$$f_k = -p_s^2 B_{kl'}(s)b_k(s) - b_k(s)\sum_{\alpha\beta}\frac{P_\alpha P_\beta a_k^{\alpha\beta}}{I_{\alpha\alpha}^e I_{\beta\beta}^e} \tag{141}$$

$$\theta_k = \int \tilde{\omega}(s)\, dt \tag{142}$$

$$b_k(s) = \sqrt{\frac{\hbar}{2\omega(s)}} \tag{143}$$

and

$$a_k^{\alpha\alpha} = 2\sum_i \sqrt{m_i}(a_{i\beta}l_{ik}^{\beta} + a_{i\gamma}l_{ik}^{\gamma}) \tag{144}$$

$$a_k^{\alpha\beta} = 2\sum_i \sqrt{m_i}(a_{i\beta}l_{ik}^{\alpha} + a_{i\alpha}l_{ik}^{\beta}) \tag{145}$$

The functions $W_k^{\pm}$ are defined by

$$W_k^{\pm} = F_k^{\pm} + \sum_{j=1}^{M} F_j^{\pm} Q_{jk}^{\pm} \tag{146}$$

where $M = 3N - 7$, the number of perpendicular vibrations. Finally the functions Q_{kl} are obtained from the solution to the coupled equations

$$i\hbar\dot{\mathbf{R}} = \mathbf{AR} \tag{147}$$

where $\mathbf{R}(t_0) = \mathbf{I}$ (unit matrix). The elements of the matrix $\mathbf{A}$ are connected to the quadratic forces. Thus,

$$A_{kl} = F_{kl}^{+} \qquad \text{for } k > l \tag{148}$$

$$A_{kl} = F_{kl}^{-} \qquad \text{for } l < k \tag{149}$$

$$A_{kk} = 0 \tag{150}$$

where

$$F_{kl}^{\pm} = f_{kl} \exp(\pm i(\theta_k - \theta_l)) \tag{151}$$

and

$$f_{kl} = b_k b_l \left(\frac{1}{2} p_s^2 \tilde{C}_{kl} - \frac{i}{2} p_s(\omega_k + \omega_l) B_{kl} + p_s \sum_{k'} B_{k'l} \sum_{\alpha} \frac{P_\alpha \xi_{kk'}^{\alpha}}{I_{\alpha\alpha}^{c}(s)} \right) \tag{152}$$

$$\xi_{kk'}^{\alpha} = \sum_{i} (l_{ik}^{\beta} l_{ik'}^{\gamma} - l_{ik}^{\gamma} l_{ik'}^{\beta}) \tag{153}$$

Thus the numerical work is reduced to the calculation of the $2M$ integrals $\alpha_k^{\pm}$ involving the linear forces and the $M \times M$ coupled equations for the quadratic forces. The motion along the reaction path is governed by the effective Hamiltonian (134). The motion is coupled self-consistently to the excitation of the rotational motion of the complex and the excitation of the $3N$-7 "perpendicular" vibrational degrees of freedom. If the reaction path dynamics is solved by classical mechanics, it is necessary to introduce a tunneling probability if energies are below the barrier for reaction. Coupling between the reaction path motion and the other degrees of freedom will change the location of the turning point for the motion along s. The tunneling probability can be estimated using simple expressions known from WKB theory (see, e.g., (43)), namely,

$$P_{\text{tunn}} = \frac{1}{1 + \exp(2I(s_1, s_2))} \tag{154}$$

where (40)

$$I(s_1, s_2) = \frac{1}{\hbar} \int_{s_1}^{s_2} ds \sqrt{\frac{2[H'_{\text{eff}} - E]}{1 + 2\epsilon(s, t)}} \tag{155}$$

The two turning points are determined by $H'_{\text{eff}}(s_i) = E$, H'_{eff}, and $\epsilon(s, t)$ are defined by

$$H_{\text{eff}} = H'_{\text{eff}} + \frac{1}{2} p_s^2 (1 + 2\epsilon(s, t)) \tag{156}$$

where we neglect the linear terms in p_s entering the second-order term in Eq. (134). In practice the tunneling integral is calculated by tracing the reaction path through the barrier using integration in complex time (see Fig. 7).

The semiclassical solution of the reaction path dynamics has been used to treat simple collinear atom-diatom, diatom-diatom systems in 3D and also S_N2 reactions (42).

VII. DISCUSSION

The semiclassical treatment of inelastic scattering processes is well developed (see, e.g., Refs. (12) and (23). It is therefore obvious to attempt to use the machinery available

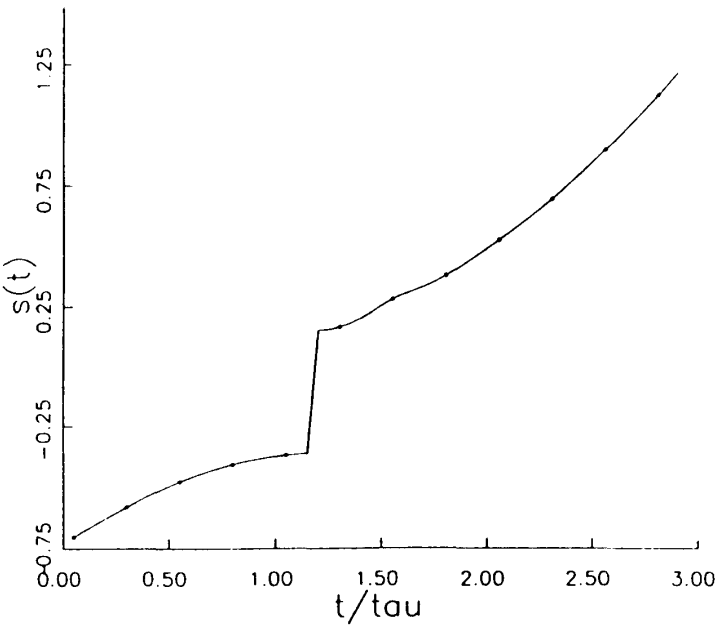

Figure 7 The reaction path $s(t)$ in units of $\sqrt{amu}$Å as a function of time in units of τ (10^{-14} s). At t = 1.2 the integration is carried out in complex time in order to tunnel through the barrier.

from inelastic scattering on reactive processes as well. This avenue has been followed here, first, by introducing absorbing boundary conditions in an "inelastic" formulation of the problem (see Sec. III) and then by the introduction of hyperspherical coordinates, which essentially transforms the reactive problem to an inelastic one.

From the semiclassical approach to inelastic scattering (23) we know that a classical treatment of the motion in the translational degree of freedom, as, e.g., the motion along the hyperradius ρ, requires an energy mapping procedure (at least if state-to-state information is needed). This is necessary in order to relate the total energy of the system to the conserved semiclassical energy. An approach for this based on a Gaussian wave packet derivation of the equations is outlined in Sec. II. This procedure has so far only been tested for inelastic processes, and it is likely that the zeroth-order solution to the problem given in Sec. II.B is not sufficient for reactive scattering problems but that higher-order correction terms (Sec. II.C) are important. The reason is that the motion along the hyperradius ρ is strongly coupled to the other degrees of freedom; i.e., the separability assumption is not valid. This problem is avoided by treating ρ quantally and by introducing only a classical treatment of the angle γ. The price to be paid is that 3D wave packets have to be propagated. However, this scheme, which is exact for J = 0, still introduces a significant reduction in the complexity of the problem.

For larger systems it is necessary to introduce approximate Hamiltonians. The system is divided into rigid and nonrigid parts. The nonrigid part is projected out of the total Hamiltonian and the dynamics treated exactly. The rigid part can be approximated by a set of forced oscillators. The reaction path method is but one way of achieving this goal. Here only one degree of freedom—the motion along the reaction path—is treated exactly. However, the methodology can in principle be extended to any number of degrees of freedom (44).

The semiclassical method described in this chapter is flexible in the sense that the number of degrees of freedom treated quantum mechanically can be increased if the computational capability increases. Furthermore it is posssible to improve the description of the degrees of freedom treated "classically" by adding higher-order correction terms to the Gaussian wave packet description. This latter possibility is, however, not fully explored at present.

Finally the introduction of the second quantization scheme for treatment of the forced boson problem and combining it with exact dynamical treatment of a few degrees of freedom makes it feasible to deal with the dynamics of large systems.

APPENDIX A

Asymptotically, hyperspherical coordinates become inadequate since the energetically allowed space contains fewer and fewer grid points. It is therefore necessary to map the wave function onto other coordinates (e.g., Jacobi coordinates). However, in the semiclassical treatment of the problem this is not possible since the wave function is known only in a restricted phase space, i.e., in either (θ, ϕ) or (ρ, θ, ϕ) space. It is therefore necessary either to carry out the projection in these coordinates by using variable grid methodology or to introduce a mixed Jacobi-hyperspherical coordinate treatment. This latter procedure is possible since we can express the Hamiltonian as

$$\hat{H} = \hat{H}_a + \frac{1}{\rho^2}\hat{H}_b + \frac{1}{\rho^4}\hat{H}_c + \cdots + W \tag{157}$$

where

$$\hat{H}_a = -\frac{\hbar^2}{2\mu}\frac{\partial^2}{\partial\rho^2} + \hat{H}_{0,as}(x, \eta) + \frac{P_j^2 - P_{e\gamma}^2}{\mu x^2 \sin^2\eta}[1 + \cos 2\gamma] \tag{158}$$

$$\hat{H}_b = -\frac{\hbar^2}{2\mu}\left(\frac{19}{12} + 4\hat{O}_1\right) + \frac{P_\gamma^2}{2\mu} - \frac{2i\hbar P_\gamma}{\mu}\hat{O}_2 + \frac{P_j^2 - P_\gamma^2}{\mu}\left[\frac{1}{3} - \frac{1}{6}\cos 2\gamma\right] \tag{159}$$

$$\hat{H}_c = x^2 \sin^2\eta\left[-\frac{\hbar^2}{2\mu}\left(\frac{16}{15} + \frac{8}{3}\hat{O}_1\right) + \frac{P_\gamma^2}{2\mu} - \frac{10i\hbar P_\gamma}{6\mu}\hat{O}_2 + \frac{P_j^2 - P_\gamma^2}{\mu}\left[\frac{1}{15} - \frac{7}{120}\cos 2\gamma\right]\right] \tag{160}$$

and

$$W = V(x, \eta, \rho) - V_{\text{morse}}(r(x)) \tag{161}$$

$$\hat{H}_{0,as} = -\frac{2\hbar^2}{2\mu}\left(\frac{\partial^2}{\partial x^2} + \frac{1}{x}\frac{\partial}{\partial x} - \frac{1}{4x^2}\right) - \frac{2\hbar^2}{\mu x^2}\left(\frac{\partial^2}{\partial\eta^2} + \frac{1}{4\sin^2\eta} + \frac{1}{4}\right) \tag{162}$$

$$\hat{O}_1 = x^2 \sin^2\eta\left(\cos^2\eta\frac{\partial^2}{\partial x^2} + \frac{\sin^2\eta}{x}\frac{\partial}{\partial x} + \frac{\sin^2\eta}{x^2}\frac{\partial^2}{\partial\eta^2} + \frac{2\sin\eta\cos\eta}{x^2}\frac{\partial}{\partial\eta} - \frac{2\sin\eta\cos\eta}{x}\frac{\partial^2}{\partial x\partial\eta}\right) \tag{163}$$

$$\hat{O}_2 = x\sin\eta\left(\cos\eta\frac{\partial}{\partial x} - \frac{\sin\eta}{x}\frac{\partial}{\partial\eta}\right) \tag{164}$$

where V_{morse} is a Morse potential.

REFERENCES

1. See, e.g., R. N. Porter and L. M. Raff, Classical trajectory methods in molecular collisions, *Dynamics of Molecular Collisions*, Part B (W. H. Miller, ed.), Plenum Press, New York, 1976.
2. W. H. Miller, *Adv. Chem. Phys. 25*: 69 (1974).
3. Y.-S. Wu and A. Kuppermann, *Chem. Phys. Lett. 195*: 178 (1992); Y.-S. Wu, B. Lepetit, and A. Kuppermann, *Chem. Phys. Lett. 186*: 319 (1991).
4. See, e.g., N. Makri and W. H. Miller, *J. Chem. Phys. 87*: 5781 (1987); Z. Kotler, A. Nitzan and R. Kosloff, *Chem. Phys. Lett. 153*: 483 (1988); H.-D. Meyer, U. Manthe, and L. S. Cederbaum, *Chem. Phys. Lett. 165*: 73 (1990).
5. P. Pechukas, *Phys. Rev. 181*: 166, 174 (1969).
6. D. C. Clary, *J. Chem. Phys. 95*: 7298 (1991); *96*: 3656 (1992); *J. Phys. Chem. 98*: 10678 (1994); J. M. Bowman and D. Wang, *J. Chem. Phys. 96*: 7852 (1992); D. Wang and J. M. Bowman, *J. Chem. Phys. 98*: 6235 (1993).
7. N. Marković, G. D. Billing, and J. T. Muckerman, *Chem. Phys. Lett. 172*: 509 (1990); N. Marković and G. D. Billing, *J. Chem. Phys. 97*: 8201 (1992); *Chem. Phys. 173*: 385 (1993); G. D. Billing and N. Marković, *J. Chem. Phys. 99*: 2674 (1993).
8. N. Marković and G. D. Billing, *Chem. Phys. 191*: 247 (1995).
9. M. Chajia and M. Jacon, *J. Chem. Phys. 101*: 271 (1994).
10. G. D. Billing, *Chem. Phys. 159*: 109 (1992); *161*: 245 (1992).
11. G. D. Billing and K. V. Mikkelsen, *Chem. Phys. 182*: 249 (1994).
12. G. D. Billing, *Int. Rev. Phys. Chem. 13*: 309 (1994).
13. E. J. Heller, *J. Chem. Phys. 62*: 1544 (1975).
14. G. D. Billing, *Chem. Phys. 189*: 523 (1994).
15. See, e.g., D. Neuhauser and M. Baer, *J. Chem. Phys. 90*: 4351 (1989).
16. G. D. Billing, *J. Chem. Phys. 99*: 5849 (1993).
17. L. Goubert, G. D. Billing, E. Desoppere, and W. Wieme, *Chem. Phys. Lett. 219*: 360 (1994).
18. N. Balakrishnan and G. D. Billing, *J. Chem. Phys. 101*: 2785 (1994); *Chem. Phys. Lett. 233*: 145 (1995).
19. D. Kosloff and R. Kosloff, *J. Comput. Phys. 52*: 35 (1983).
20. M. D. Feit, J. A. Fleck, Jr., and A. Steiger, *J. Comput. Phys. 47*: 412 (1982).
21. H. Tal-Ezer and R. Kosloff, *J. Chem. Phys. 81*: 3967 (1984).
22. T. J. Park and J. C. Light, *J. Chem. Phys. 85*: 5870 (1986).
23. G. D. Billing, *Comp. Phys. Rep. 1*: 223 (1984).
24. W. H. Miller, *J. Chem. Phys. 54*: 5386 (1971).
25. N. Balakrishnan and G. D. Billing, *Chem. Phys. 189*: 499 (1994).
26. B. R. Johnson, *J. Chem. Phys. 79*: 1906, 1916 (1983).
27. See, e.g., D. M. Brink and G. R. Satchler, *Angular Momentum*, Oxford University Press, 1968.
28. G. D. Billing and N. Marković, *J. Chem. Phys. 99*: 2674 (1993). N. Marković and G. D. Billing, *J. Chem. Phys. 100*: 1085 (1994).
29. I. S. Gradshteyn and I. M. Ryzhik, *Table of Integrals, Series and Products*, Academic Press, New York, 1965.
30. N. Marković and G. D. Billing, *Chem. Phys. 173*: 385 (1993).
31. See, e.g., B. Lepetit and J. M. Launay, *Chem. Phys. Lett. 151*: 287 (1988).
32. See, e.g., J. V. Lill, G. A. Parker, and J. C. Light, *Chem. Phys. Lett. 89*: 483 (1982); J. C. Light, I. P. Hamilton, and J. V. Lill, *J. Chem. Phys. 82*: 400 (1985); J. T. Muckerman, *Chem. Phys. Lett. 173*: 200 (1990); D. T. Colbert and W. H. Miller, *J. Chem. Phys. 96*: 1982 (1992); *Numerical Grid Methods and Their Application to Schrödinger's Equation*, NATO ASI Series (C. Cerjan, ed.), Kluwer, Boston, 1993.
33. N. Marković and G. D. Billing, *J. Chem. Phys. 97*: 8201 (1992).
34. J. T. Muckerman, R. D. Gilbert, and G. D. Billing, *J. Chem. Phys. 88*: 4779 (1988).
35. J. Z. H. Zhang and W. H. Miller, *J. Chem. Phys. 91*: 1528 (1989).

36. J. C. Tully and R. K. Preston, *J. Chem. Phys. 55*: 562 (1971); Ch. Schlier, U. Nowotny and E. Teloy, *Chem. Phys. 111*: 401 (1987).
37. W. H. Miller, N. C. Handy, and J. E. Adams, *J. Chem. Phys. 72*: 99 (1980).
38. G. D. Billing, *Chem. Phys. 89*: 199 (1984).
39. G. D. Billing, *Chem. Phys. 135*: 63 (1990).
40. G. D. Billing, *Chem. Phys. 161*: 245 (1992).
41. G. D. Billing, *Chem. Phys. 67*: 35 (1982).
42. G. D. Billing, *Chem. Phys. 159*: 109 (1992).
43. M. S. Child, *Molecular Collision Theory*, Academic Press, London, 1974.
44. G. D. Billing (in preparation).

14

Nonlinear Classical Dynamics and Unimolecular Reactions

JOHN S. HUTCHINSON

Rice University, Houston, Texas

I. INTRODUCTION

A chemical reaction is, at the most fundamental level, a rearrangement of the atoms of the reactant molecules. In the simplest case of unimolecular reaction, this rearrangement can be viewed as the limit of very high amplitude vibrational motion. For example, a unimolecular dissociation reaction is simply the extension of a bond stretch vibration to the point of fragmentation. Similarly, a cis-trans isomerization reaction is the result of a very high amplitude torsional vibration.

The question of how these unimolecular events occur is one of the most intriguing fundamental questions in chemistry. What vibrational motions precede and produce this high-amplitude motion in the reaction coordinate? Such extreme vibrational motion must require high-energy excitation of the vibrational mode leading to reaction. Thus the question of how a reaction occurs has been viewed as equivalent to the question of how a large amount of vibrational energy becomes accumulated in a single, concerted vibrational motion leading to the unimolecular transition state.

It is worth asking at the outset what we expect in terms of answers to these questions. Over the past three decades, a great deal of research (1–5) has been directed at revealing the details of the high-energy vibrations and unimolecular reactions of isolated molecules, each study generally representing a different view of what it means to ask "how does a unimolecular reaction occur?" Given the diversity of the literature in this field, it is even worth wondering whether a cogent answer to this question exists. In this chapter, we will present one view of an answer to these questions based on some recent progress in the development of models of unimolecular reactions. Our focus will be on

the specific fundamental questions of the vibrational dynamics and associated energy transfer dynamics which lead to reaction: how and why is sufficient vibrational energy transferred into the reaction coordinate to surmount the reaction barrier? And, what vibrational motions precede the reactive event and why?

A. Historical View

One way to approach the processes of a unimolecular reaction is to treat it statistically. This is the approach taken in transition state theory (6), or in its most common form Rice-Ramsberger-Kassel-Marcus (RRKM) theory (7). The underlying assumption of RRKM theory is that, as a consequence of the dynamics of molecular oscillations, all vibrational states of an isolated molecule are equally probable. Therefore, the rate of unimolecular reaction, with activation energy E_a at a given total molecular energy E, is determined only by the number of states available at the transition state with energy equal to or less than the available energy at the transition state, $E - E_a$, and by the total number of all vibrational states at or near the total energy. The former number is the state count $N(E - E_a)$, and the latter number is the density of vibrational states, $G(E)$. The rate of reaction is taken to the proportional to the probability of randomly selecting a vibrational state at the transition state:

$$k_{\mathrm{RRKM}}(E) = \frac{1}{h}\frac{N(E - E_a)}{G(E)} \tag{1}$$

The fundamental assumption of RRKM theory, that of equal a prior state probabilities, has a variety of consequences. In particular, it is clear that the rate of reaction depends only on the total energy of the molecule, E. k_{RRKM} is therefore independent of how the molecule is activated to that energy, and is independent of the initial distribution of the energy. For example, the rate of reaction is the same whether the energy is initially localized in a single bond or vibrational mode or obeys a thermal distribution. Similarly, there is no dependence of the reaction rate on the particular vibrations undergone by the molecule subsequent to excitation during its lifetime. RRKM theory predicts that the rate constant should not vary with the initially prepared vibrational state or with the distributions of energy in that state.

This consequence is directly verifiable in a variety of experiments. The most significant of these are the chemical activation studies (8–13) reported in the 1960s and 1970s. The principle idea of these studies is to prepare a highly excited molecule by two or more different chemical means and then to compare the rates and branching ratios of unimolecular reactions derived from these different preparations. This is illustrated by a comparison of the unimolecular reactions of methylcyclopropane following preparation from two reactions:

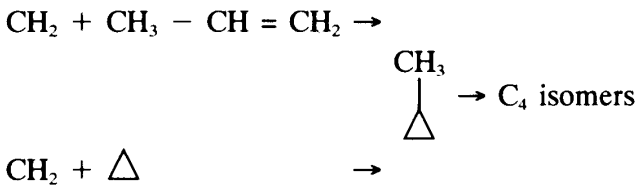

(2)

The first reaction presumably produces methylcyclopropane with vibrational energy in the ring, whereas the second reaction should produce the molecule with excitation closer to the side chain. However, Butler and Kistiakowsky (8) found no quantitative

difference in the branching ratios of the various C_4 isomers produced by reaction arising from the two different activations. This reveals an independence of reaction rate from the preparation of the excited state, consistent with the assumptions of RRKM theory. Evidently, the relaxation of the initial "local" vibrational excitation is complete on a time scale which is short compared to that of the unimolecular reaction. Chemical activation studies on a wide variety of molecules have resulted in this same conclusion (1).

During the late 1970s and throughout the 1980s, direct experimental comparisons of state selected unimolecular reaction rates with RRKM predictions became possible via laser photochemical studies (3,14,15). Quite reasonably, an observed agreement between experimental and RRKM rate constants has been generally taken as evidence that unimolecular reactions proceed via chaotic or even ergodic dynamics. Typical of these studies is the photodissociation of *t*-butyl hydroperoxide by direct single photon excitation of a high overtone state of the O—H stretch (16). Such a "local mode excitation" would appear to offer a significant nonthermal accumulation of energy in a mode adjacent to the reactive O—O bond, and thus possibly produce an unusually fast reaction. In particular, we might expect the dissociation to occur before the RRKM assumption of equal probability in all vibrational states might be obeyed. Nevertheless, Zare and coworkers (16) observed photochemical reaction rates in very close agreement with the predictions of RRKM theory. This result is again consistent with the view of very rapid redistribution of the available vibrational energy. (As a note, research in our group has also shown that the initial excitation in such "local mode overtone" processes is not at all local anyway (17–19).) Similar results were also observed in a very large number of increasingly sophisticated photochemical studies of unimolecular reaction rates in comparison with RRKM predictions (16,20–29).

A somewhat more "direct" observation of the rate of intramolecular mode–mode energy transfer is provided by a myriad of studies of spectroscopic line widths for states of high vibrational energy. Using photoacoustic detection, Bray and Berry (30) first reported bands corresponding to the excitation of a local C—H bond in benzene to high overtone levels (e.g., ν = 5 to 9). The observed widths of these bands are typically 60 to 100 cm^{-1}, dependent upon the excitation level. Such broad bands can be interpreted as consistent with and uncertainty principle broadening due to intramolecular vibrational relaxation (IVR) on the scale of 50 to 100 fs, or 5 to 10 vibrational periods of a C—H oscillator. Similar measurements were reported from a large number of groups, using a variety of techniques, on a wide range of molecules with light atom–heavy atom bond mode excitation (e.g., H—N, H—O, H—C, H—Si). In each case, the time scale of IVR is observed to be a fraction of a picosecond, consistent with the RRKM hypothesis that energy redistribution should be complete on a time scale very short compared to the lifetime of the reaction (3,15,30–38).

This RRKM picture of rapid IVR prior to unimolecular reaction has been heavily studied theoretically. There is an obvious implication in the RRKM assumptions that, since all vibrational states are equally probable, then the vibrational dynamics leading up to the reaction must be entirely random, implying that the events leading up to the reaction are nonselective and unpredictable. That is, the reaction is a random event, occurring at a random and unpredictable time. If this were true, then the only available answer to the question of how the reaction occurs would be "it happens to happen."

Consequently, much of the research in unimolecular dynamics has been devoted to observing and explaining both rapid intramolecular flow of vibrational energy and the possibility of "chaos" in the vibrational dynamics. The literature on these two related

subjects is enormous, and the reader is referred to several compilations and reviews (5,39,40). In summary, these studies have shown that, above a certain threshold total energy, molecular vibrations are expected to be chaotic. Specifically, classical trajectories for these vibrations are dynamically unstable, and time-invariant phase space structures (''tori'') are not observed. Similarly, calculations of vibrational energy flow in model molecular coupled oscillator systems reveal that such energy flow is expected to be very rapid indeed. The predicted time scales are reasonably in agreement with those observed in spectral linewidth studies.

B. Overview

In this paper, we return to the fundamental questions posed in the opening paragraphs of this introduction. Specifically, we will present one view, based on research in our group over the past decade, of an answer to the questions of how and why localized vibrational excitations rapidly become delocalized, and how and why a delocalized distribution of vibrational energy becomes significantly localized in a unimolecular reaction coordinate, producing fragmentation or isomerization. We consider these two questions in this order, noting here at the outset that the answers are, surprisingly, not related to one another.

II. NONLINEAR RESONANCE AND INTRAMOLECULAR VIBRATIONAL RELAXATION

A. Nonlinear Resonance

In the context considered here, a ''resonance'' is a near match of frequency between two coupled oscillations. Such a resonance will produce energy transfer from one of the oscillators to the other. A ''nonlinear resonance'' is a resonance arising from the nonlinearity of the restoring force in one or both of the oscillators, or in other words, due to the anharmonicity of one or both of the oscillators. For a harmonic oscillator, of course, the frequency of oscillation is independent of the energy or amplitude of the oscillation. Molecular vibrational modes, however, are both anharmonic, particularly at energies sufficient for unimolecular reaction, and the energy dependence of the oscillator frequency is critical to mode-mode energy transfer.

In many cases, the potential energy associated with stretching a single bond in a molecular can be accurately represented by the Morse potential

$$V_M(S) = D(1 - e^{-\alpha S})^2 \tag{3}$$

where S is the displacement of the bond length from its equilibrium value, D is the bond dissociation energy, and α is a parameter related to the harmonic frequency Ω of the bond via

$$\alpha = \Omega \left(\frac{\mu}{2D}\right)^{1/2} \tag{4}$$

The dependence of the frequency of a Morse oscillator on its energy can be seen clearly by transforming the Hamiltonian to action-angle variables (41) (J, θ), as defined by

$$S = \frac{1}{\alpha} \ln \frac{1 - \rho \sin \theta}{1 - \rho^2} \tag{5}$$

$$P = (2\mu D\rho^2)^{1/2} \frac{(1 - \rho^2)^{1/2} \cos\theta}{1 - \rho^2 \sin\theta} \tag{6}$$

where

$$\rho = \left(\frac{\Omega J}{D} - \frac{\Omega^2 J^2}{4D^2}\right) \tag{7}$$

and Ω is the harmonic frequency of the Morse oscillator. These transformations yield a Hamiltonian which is independent of the angle coordinate:

$$H = \Omega J - \frac{\Omega^2 J^2}{4D} \tag{8}$$

Hence, the action J is a constant of the vibrational motion and is a measure of the bond mode energy. The anharmonic, energy-dependent frequency ω of this bond mode can be found from Eq. (8) and Hamilton's equations:

$$\omega = \frac{d\theta}{dt} \tag{9}$$

$$= \frac{\partial H}{\partial J} \tag{10}$$

$$= \Omega\left(1 - \frac{\Omega J}{2D}\right) \tag{11}$$

$$= \Omega\left(1 - \frac{E}{D}\right)^{1/2} \tag{12}$$

Equation (12) clearly reveals that the frequency of the Morse oscillator decreases monotonically with increasing excitation energy.

The significance of this nonlinear frequency dependence for vibrational energy transfer was generally established many years ago by Chirikov (42,43) and Ford (44,45) and was established in the context of molecular mode–mode energy flow by Oxtoby and Rice, (46) Jaffé and Brumer, (47) Sibert et al. (48), and Hutchinson et al. (49). We can illustrate with a simple model for the stretching vibrations in an ABA molecule (e.g., H_2O), as studied by Sibert et al. (48) and consisting of two identical Morse oscillators, coupled kinetically.

Expressed in terms of the bond displacements and momenta (S_j, P_j), the Hamiltonian for this model is

$$H = H_1(S_1, P_1) + H_2(S_2, P_2) - \frac{P_1 P_2}{m_B} \tag{13}$$

where

$$H_j = \frac{P_j^2}{2\mu_{AB}} + V_M(S_j) \tag{14}$$

m_B is the mass of the central atom, and μ_{AB} is the reduced mass of the AB bond. The energy in each bond can be calculated from H_j, revealing the details of the mode to mode transfer of energy. For a large range of intermediate energies, two very distinct types of dynamics are found, dependent upon the initial conditions. In the first type,

illustrated in Fig. 1a, the total vibrational energy is initially distributed significantly unequally, and the initial disparity in mode energies is maintained throughout the dynamics. Considering Eq. (12) the difference in energies initially produces a substantial difference in the nonlinear frequencies of the modes. Hence, due to the nonlinearity of the oscillators, there is no resonance in this case, and the extent of energy transfer is minimal and incomplete. The initially localized excitation remains localized.

The second type of dynamics is illustrated in Fig. 1b. In this case, the initial energies of the two modes are comparable, and a substantial quantity of energy exchanges periodically between them. Now, there is no localization of energy. Since the mode energies are comparable, then, via Eq. (12) the nonlinear frequencies of the two modes are also comparable. Hence, the energy transfer in Fig. 1b is a result of the nonlinear resonance between the two modes for these conditions.

Chirikov analysis quantitatively reveals the coupling responsible for the resonant energy transfer. Equation (13) can be transformed to action-angle coordinates via Eqs. (5) and (6), with the result

$$H = \Omega J_1 - \frac{\Omega_1^2 J_1^2}{4D} \tag{15}$$

$$+ \Omega J_1 - \frac{\Omega_1^2 J_1^2}{4D} \tag{16}$$

$$- \frac{P_1(\theta_1, J_1)P_2(\theta_2, J_2)}{m_B} \tag{17}$$

The coupling H_{12} arising from the P_1P_2 term can be analyzed by expansion in a Fourier series in the angle coordinates:

$$H_{12} = \sum_n \sum_m V_{nm} \cos(n\theta_1 - m\theta_2) \tag{18}$$

All of the terms in this series are high frequency and thus have minimal effect on the values of the actions J_1 and J_2, unless for some particular choice of n and m for the current energy distribution,

$$n \frac{d\theta_1}{dt} - m \frac{d\theta_2}{dt} = n\omega_1 - m\omega_2 \approx 0 \tag{19}$$

where ω_j is the nonlinear energy-dependent frequency of the jth mode given by Eq. (12). In the case of the prototype ABA molecule at intermediate energies, only the V_{11} coefficient (on the $n = m = 1$ term) is sufficiently large to be of significance in the energy transfer dynamics. Furthermore, this term is a high-frequency term unless the frequencies of the two modes are "close enough." This, in turn, requires that the energies of the modes not be too different from one another. This accounts for the differences in the dynamics in Figs. 1a,b.

How close do the frequencies have to be to permit complete energy transfer as in Fig. 1b? The answer is defined by the "resonance width," which can be determined by the Chirikov analysis. Similarly, Chirikov analysis can be used to predict the time scale for the energy exchange between the modes (48). Hence, nonlinear resonance analysis gives a very complete picture of the periodic exchange of energy between two modes, as shown in Fig. 1b.

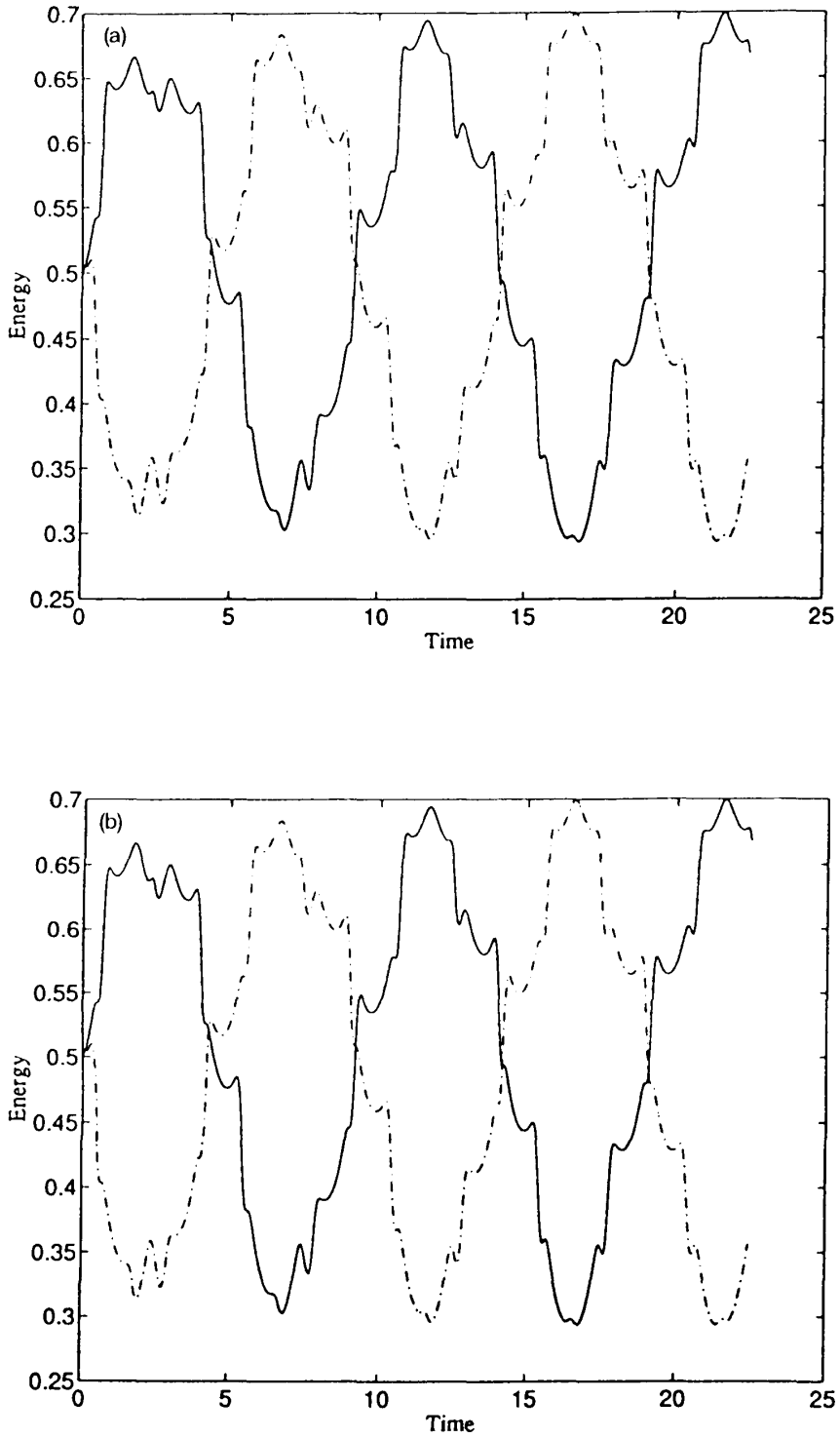

Figure 1 Individual mode energies, H_j, from Eq. (14) for the coupled Morse oscillator system in Eq. (13) as functions of time measured in harmonic vibrational periods. Each figure represents a single trajectory. The total energy in each trajectory is D, the dissociation energy of a single mode. (a) Localization of the excitation. The two modes are not in nonlinear resonance. (b) Quasi-periodic exchange of the excitation. The two modes are in nonlinear resonance.

B. IVR via Sequential Nonlinear Resonance

It is debatable whether the energy flow depicted in Fig. 1b represents intramolecular vibrational energy relaxation. In the first place, this energy exchange is periodic or very nearly so. Hence, recurrence of the initial energy distribution is observed, and "relaxation" does not occur. In the second place, the energy exchange dynamics depicted in Fig. 1b are more apparent than real, in that the distribution of energy in the normal modes is constant. Thus, the energy flow observed is a consequence of the relatively arbitrary partitioning of the Hamiltonian represented by Eq. (13).

One way to view the periodicity on Fig. 1b is to note that the dynamics can be understood via a single "isolated" resonance. Aperiodic energy transfer requires multiple or "overlapping" resonances acting simultaneously. This can occur in either of two ways. First, for the prototype ABA molecule but at higher energies than those illustrated in Fig. 1, a different class of energy transfer dynamics can be observed: energy can remain localized in one mode for an extended period, and then significant energy exchange occurs. Muller (50) showed that this high-amplitude, aperiodic exchange can be understood via Chirikov analysis. Specifically, for sufficiently high energy, the series in Eq. (18) cannot be effectively reduced to a single low-frequency term. Rather, one must include the 1-1, 1-2, and 2-1 terms in the coupling H_{12} to reproduce these dynamics. This is because the resonance width of the 1-1 resonance overlaps the resonance widths of the 1-2 and 2-1 resonances. In other words, for a particular range of energy distributions, the oscillators are both 1-1 and 1-2 resonance simultaneously. The result of the overlap of resonances is energy transfer which is aperiodic (50).

Secondly, and in chemical terms, somewhat more significantly, overlapping resonances can occur because of the participation of more than two modes in the energy exchange. Hutchinson et al. (49) demonstrated how nonlinear resonance analysis can be applied to describe intramolecular energy relaxation in vibrational models with more than two modes. The concept is illustrated in Fig. 2. In the left column are hypothetical harmonic (i.e., zero-energy) frequencies of a system with four coupled oscillators, all nonlinear. Assume we have a localized excitation in the highest-frequency mode. Then, due to nonlinearity, the frequency of this mode is reduced, according to Eq. (12), thus putting this mode into near resonance with one of the other three modes. Energy transfers from the excited mode to the unexcited mode, and as a consequence, the frequency of the excited mode rises as its energy is depleted. The result is that the high-frequency mode comes into near resonance with the next highest frequency mode. Subsequent energy transfer into this mode occurs. Most notably, however, the energy initially transferred into the lower-frequency mode is now "trapped," since this mode is no longer in resonance with the excited mode. As a result, the energy which was initially in the highest-frequency mode is now "irreversibly" relaxed to other modes, at least to the extent that the time scale for recurrence of the initial localization is extremely long.

This mechanism of nonlinear resonances acting in sequence has been used to account for IVR in a variety of molecules, including benzene and substituted benzenes (51), alkanes (52), peroxides (53), and other molecules. In addition, the quantum mechanical correspondence to sequential nonlinear resonance has been developed (54–56). Most recently, very high level quantum dynamical calculations of IVR processes have been presented (57), involving extremely large numbers of quantum states, and these calculations have reinforced the utility of the basic classical picture presented in Fig. 2.

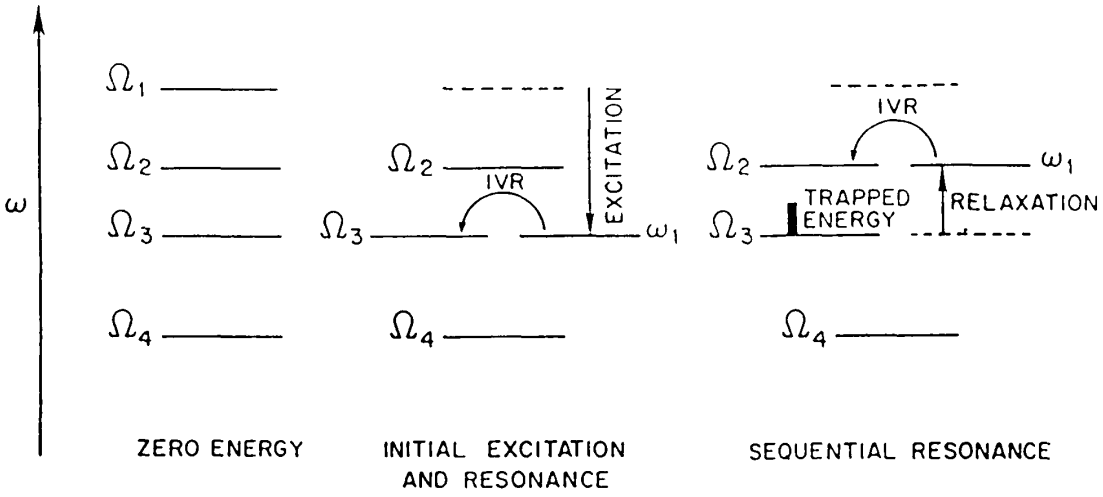

Figure 2 Schematic mechanism for relaxation of an initially excited anharmonic mode via sequential nonlinear resonance. In the first column, labeled "Zero Energy," the frequencies of a hypothetical set of normal modes are plotted vertically. In a typical molecule, the highest frequency modes correspond to CH or OH stretching, and these modes are strongly anharmonic. Thus, upon "Initial Excitation," the frequency of the highest mode is reduced according to Eq. (12). This possibility creates a near resonance with one of the unexcited normal modes, as shown. The result will be energy transfer (labeled "IVR" in the diagram) analogous to the nonlinear resonant energy exchange dynamics of Fig. 1b. A result of the energy transfer is relaxation of the Ω_1 mode, causing an increase in the frequency of this mode. This creates a new nonlinear resonance with a second, higher-frequency normal mode, resulting in further energy transfer. The first resonance is now detuned, and the energy initially deposited into that normal mode is "trapped." The initial localization of energy thus appears to have irreversibly relaxed.

In conclusion, then, the dynamics by which a highly excited local vibration relaxes its energy into other modes in the molecule is well understood. The energy exchange mechanism is dominated by the role of nonlinear resonances.

III. DYNAMICS OF UNIMOLECULAR REACTIONS

A. Energy Transfer During Unimolecular Reaction

One of the hallmarks of the sequential nonlinear resonance mechanism presented above is "mode–specificity." That is, vibrational energy is transferred into specific modes at specific points in the relaxation process. An intriguing question is whether it is possible to use this mode-specific energy transfer to initiate a unimolecular reaction with similar specificity. This was attempted in a variety of experiments, with mixed success, in the late 1970s and early 1980s. Typical of these experiments is the *t*-butyl hydroperoxide photodissociation study (16) mentioned in the Introduction. Recall that a large amount of vibrational energy was "deposited" in the local O—H stretching mode via direct one-photon absorption. One might speculate that this energy could relax mode–specifically into the weak adjacent O—O bond, thus initiating fragmentation with an unusually fast rate. However, it is observed experimentally that the rate of photodissociation is not

significantly different from that expected from a thermal (random) energy distribution. Thus, the localized energy excitation must relax to a thermal distribution very rapidly without initiating the unimolecular reaction in the process, and the accumulation of energy in the reaction coordinate must occur via some other mechanism than a sequential nonlinear resonance.

There are two questions posed in these conclusions. The second is our old question, still unanswered in this chapter, of how the reaction occurs—or equivalently, of how a large local accumulation of energy in the reaction coordinate occurs. The first is a new question: why can the reaction coordinate not be activated by nonlinear resonance with the locally excited mode?

The answer was first discussed by Uzer and Hynes (58) in a simple two-mode model and was developed later by Holme and Hutchinson (59) in a realistic molecular study. In the experiments reported, the mode excited is virtually always a high-frequency hydrogen-carbon, hydrogen-oxygen, or hydrogen-nitrogen stretch, whereas the reaction coordinate mode is usually comparatively low frequency. Referring then to Fig. 2, the excited mode is like Ω_1 and the reaction coordinate is, for example, like Ω_3. Under appropriate conditions, then, resonant transfer of energy from the excited mode to the reaction coordinate is possible and is indeed observed. However, Fig. 2 illustrates that a consequence of this resonance energy transfer is the "detuning" of the resonance: following only a small transfer of energy, ω_1 has increased so that the modes Ω_1 and Ω_3 are no longer in resonance. Furthermore, although it is not shown in Fig. 2, the frequency of the reaction coordinate will decrease as it gains energy, and this effect exacerbates the detuning of the reaction coordinate from the activated mode. Both Uzer and Hynes and Holme and Hutchinson demonstrated that this detuning destroys any hypothetical mode–specificity, in agreement with most experimental observations.

An interesting puzzle is posed by this discussion: since the reaction coordinate frequency decreases with increasing excitation and since this effect results in the interruption of resonant energy transfer from other activated modes, how does the reaction coordinate ever receive sufficient energy to overcome the energy barrier at the transition state? This argument would make it seem that, in the process of activating a cold reaction coordinate to the reaction level, "you can't get there from here." Of course, reactions do occur, so another mechanism besides nonlinear resonance must contribute.

In the remainder of this section we illustrate the actual process of reaction coordinate activation and unimolecular reaction from several reactions studied in our group. To summarize what we will see, each reaction occurs via an "impulsive" activation of the reaction coordinate. The impulsive energy transfer is very large scale, occurs very abruptly, is aperiodic, and does not appear to be related to frequency resonance conditions. This large-scale energy transfer results from very large couplings, arising from fairly specific, correlated oscillations among two or more vibrational modes.

B. Dissociation of Hydrazoic Acid

Hydrazoic acid (HN_3) can dissociate into diatomic fragments, HN and N_2 by undergoing a singlet to triplet electronic transition (60,61). The transition can be viewed as the result of an electronic surface crossing between the ground state of the HN_3 parent molecule with an excited state which correlates to the ground $^1\Sigma_g$ state of the N_2 product and the ground $^3\Sigma$ state of the HN product. The crossing occurs when the central N—N bond of

the parent is extended to a length of $3.5a_o$, an event which requires an energy of 12,700 cm^{-1} (1.52 eV or 147 kJ/mol).

The dissociation has been studied photochemically by exciting the dipole active HN stretch with infrared multiphoton pumping and with one-photon local mode overtone excitation. From the discussions above, it is clear that we are primarily concerned in this chapter with the vibrational events which produce the activation of the N–N reaction coordinate and not with the electronic events which determine whether the curve crossing occurs. Hence, we have focused on the events on the ground electronic surface of the parent molecule which lead to an extension of the N–N bond to $3.5a_o$.

Julien (62) constructed a realistic potential energy surface to describe the vibrations in all six degrees of freedom for hydrazoic acid. This semiempirical surface correctly predicts normal mode frequencies, observable anharmonicities, and the activation energy at $3.5a_o$. An ensemble of 100 trajectories was generated with initial energy of 19,380 cm^{-1} in the H–N stretch and zero-point energy in all other normal modes. The initial momenta for each trajectory were scaled so that the total energy of each trajectory is exactly 21,500 cm^{-1}. Each trajectory was followed until the transition state was reached, up to a maximum time of 10 ps. Prior to this time, 83 of the trajectories reacted.

For those trajectories which reacted, we were primarily interested in the dynamics by which they approached the transition state. To focus on these details in the last few vibrations prior to reaction, we defined a time origin $t = 0$ as the time at which the inner turning point of the N–N stretch was last reached prior to reaction. (Thus, each trajectory hits the inner turning point of the N–N vibration for the last time at $t = 0$). We then averaged over the ensemble, as a function of time, the energy in each local mode and in each normal mode, and the value of each local mode coordinate and momentum.

Focusing first of the average energy versus time, we see in Fig. 3 that the requisite energy for reaction arrives in the N–N bond just prior to reaction. This burst of energy comes from a temporary large buildup in the terminal N–N bond. This large-scale, aperiodic transfer of energy is illustrative of the "impulsive" energy transfer which we have observed as being responsible for reaction. The reaction coordinate remains cold for a very long period, and then, immediately prior to reaction, receives a rapid impulse of energy sufficient to surmount the reaction barrier. We note that this energy transfer is not reminiscent of the nonlinear resonant exchange of energy in Fig. 1b, nor is it predictable from a simple examination of the nonlinear frequencies of the interacting oscillators.

What produces this impulse? It should not be surprising that such a large-scale energy transfer is a rather unique event, since it must require an unusually large mode–mode coupling. In fact, because of this, the dynamics leading to the transition state are rather specific.

To establish this, we examine the averages of the local mode coordinates as functions of time, again referenced to $t = 0$ at the last inner turning point. This time, we also superimpose on the averages $\pm 2\sigma$ (the standard deviations). In Fig. 4, we clearly see that there are very significant oscillations in the average of the terminal N–N stretch. Evidently, each trajectory undergoes very nearly the same oscillations in the nonreactive N–N stretch on the approach to the transition state in the reactive N–N stretch. The standard deviations establish that there is very little departure of the trajectories from this path. Therefore, the reaction occurs as a consequence of a very specific dynamic event, involving a strong correlation between the two N–N stretching modes. We have also shown that, during this final period, the vibrations are unusually dynamically stable.

Figures 3 and 4 provide at least preliminary answers to the questions of how the reaction occurs and how the reaction coordinate becomes activated. In Sec. IV, we will provide a more complete description of the details of the reaction, including the underlying explanation of why these events take place.

However, before undertaking that analysis, we note that the results discussed here are representative of our observations of all the unimolecular reactions we have studied. In each case, the reaction coordinate is activated by an impulse just prior to reaction, and the vibrational dynamics approaching the transition state are highly specific and uniquely stable. We illustrate a few of these reactions here.

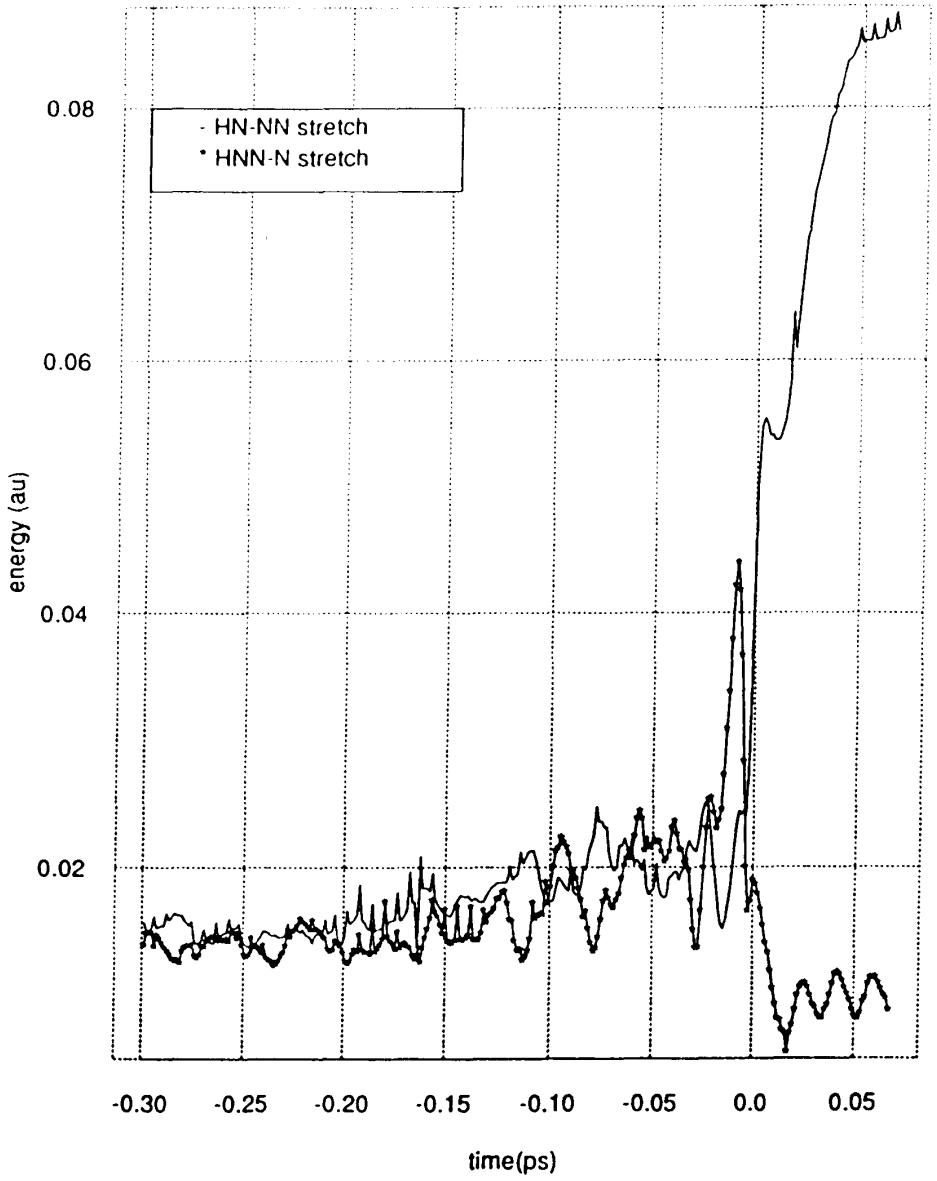

Figure 3 Ensemble average bond energies of the two NN stretching modes or hydrazoic acid. Trajectories have been aligned so that $t = 0$ is the last inner turning point of the central NN stretch prior to dissociation for every trajectory. Note the "impulse" in the energy transfer, activating the reaction coordinate.

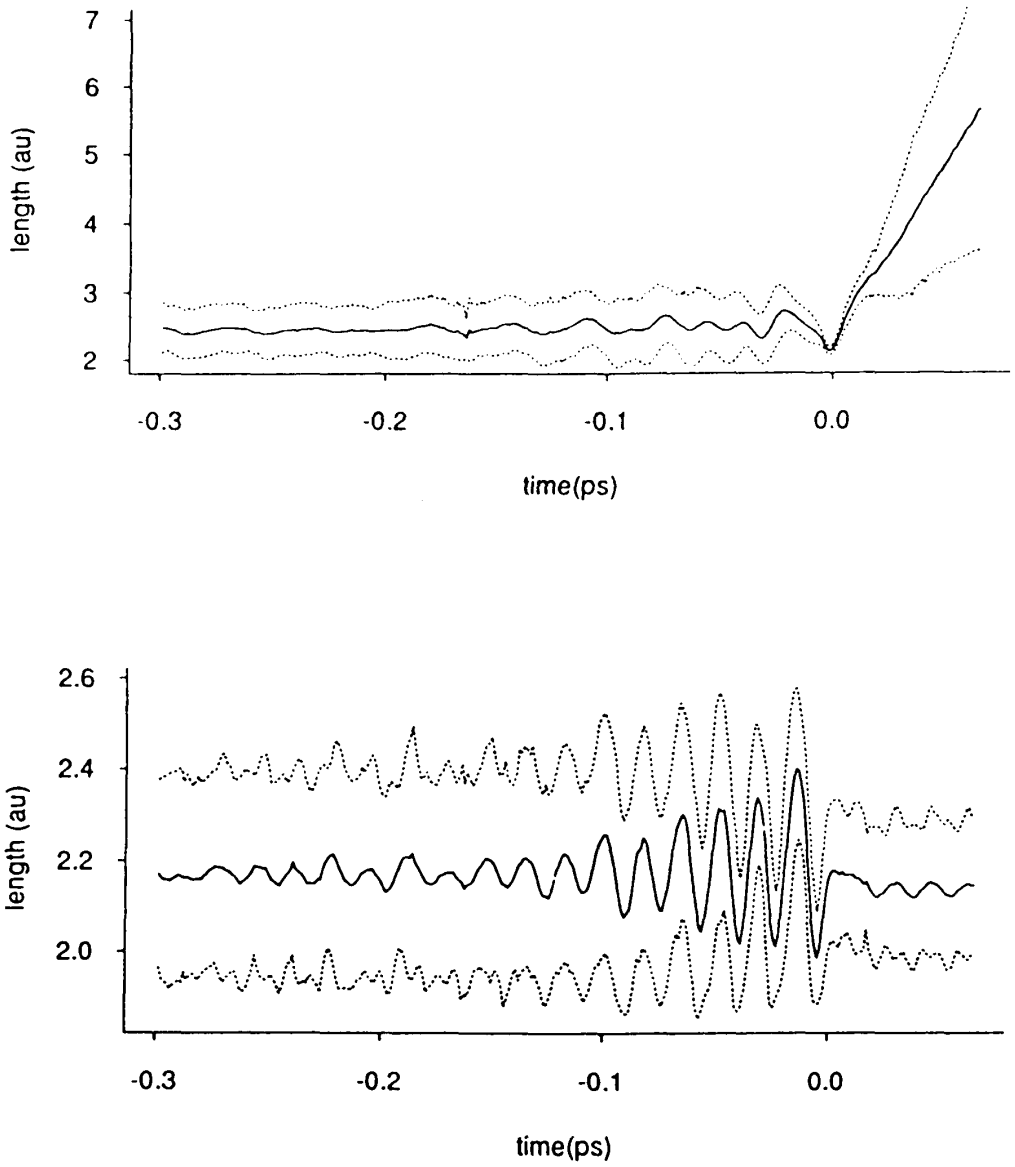

Figure 4 Averages and standard deviations ($\pm 2\sigma$) of selected local mode coordinates of hydrazoic acid. The upper frame is the central NN (reaction coordinate) stretch and the lower frame is the terminal NN (non-reactive) stretch. As in Fig. 3, all trajectories have been aligned so that t = 0 is the last inner turning point of the central NN stretch prior to dissociation. Note that the coordinate average of the terminal NN stretch oscillates with high amplitude during the last brief period prior to reaction, representing a narrow pathway in coordinate space leading to the reaction.

C. Dissociation of Hydrogen Peroxide

The central O—O bond in hydrogen peroxide has a dissociation energy of 17,350 cm^{-1}, an amount of energy which can be more than achieved by excitation of the $\nu = 6$ overtone of an O—H bond. As a consequence, there have been a number of experimental and theoretical studies of overtone induced dissociation of hydrogen peroxide.

Again, our purpose here is an understanding of the events which activate the O—O stretch and which therefore lead to the reaction. These events were first analyzed by Uzer et al. (53), who developed a model potential energy function for vibrational of

HOOH in all six degrees of freedom. The results presented here, from calculations in our own group, were first reported by them.

We calculated 100 trajectories with a large initial excitation in each of the two H—O bond stretching modes. Each trajectory was integrated until the central O—O stretch extended to a length of $7a_o$, arbitrarily taken to be the point of reaction, or until 10 ps. We then analyzed the dynamics of the 84 reactive trajectories using the same approach described above for hydrazoic acid. Specifically, we defined the $t = 0$ time origin for each trajectory to the time when the inner turning point of the O—O stretch was last achieved. Using this definition, we ensemble averaged the local mode energies, coordinates, and momenta as functions of time.

Once again, we find that the reaction coordinate is activated by impulsive energy transfer. Furthermore, as illustrated in Fig. 5, this transfer results from highly specific oscillatory motions. Most notably, the two H—O—O bending modes follow a very specific path in which a carefully phased symmetric bending motion occurs (53). It is worth remembering that the data in Fig. 5 represent ensemble averages. Therefore, since the average displays significant oscillation, each trajectory in the ensemble follows the same path, to a fair degree of precision, during the final few vibrational periods before the O—O bond breaks. The effect of this pathway is to produce a very large kinematic coupling between the bending modes and the O—O stretch. In particular, each outer turning point of the symmetric bending forces the stretch to an extreme inner turning point, thus elevating its energy.

It is interesting to note that, in these two very similar molecules undergoing similar reactions, the vibrational pathway leading to reaction is very different. In particular, both hydrogen peroxide and hydrazoic acid are four atom molecules undergoing fragmentation of the central bond. However, in hydrazoic acid, one of the terminal stretching modes is critical in correlating with and activating the reaction coordinate vibration. In Fig. 5, we see that, in hydrogen peroxide, the nonreactive O—H stretches play no role in the critical dynamics leading to reaction. In particular, any phase of the O—H stretch will lead to reaction. The explanation of the differences is presented with the analysis in Sec. IV.

D. Isomerization of Diimide

To illustrate reactive vibrational dynamics in a very different type of unimolecular reaction, we consider the trans-cis isomerization of diimide (HNNH). The central N—N bond is a double bond, so the barrier to isomerization from trans to cis is quite high, 192 kJ/mol. Spears (63,64) developed a model to describe the high-energy vibrations of diimide in all six degrees of freedom. We demonstrated that nonlinear resonance interactions are critical to the dynamics of mode–mode energy transfer into and out of the torsional vibration (63). We also found, however, that these resonant interactions were detuned before the excitation of the torsional mode was sufficient to achieve isomerization.

How then does the reaction occur? As before, the activation of the reaction coordinate occurs via impulsive energy transfer, in this case in quantities as great as 100 kJ/mol in a single vibrational period.

To analyze the reactive dynamics responsible for this enormous transfer of energy, we defined the time origin $t = 0$ as the point in each trajectory where the torsional vibration reached the top of the transition barrier, where the dihedral angle $\tau = \pi/2$. We then averaged each local mode coordinate over an ensemble of reactive trajectories as a

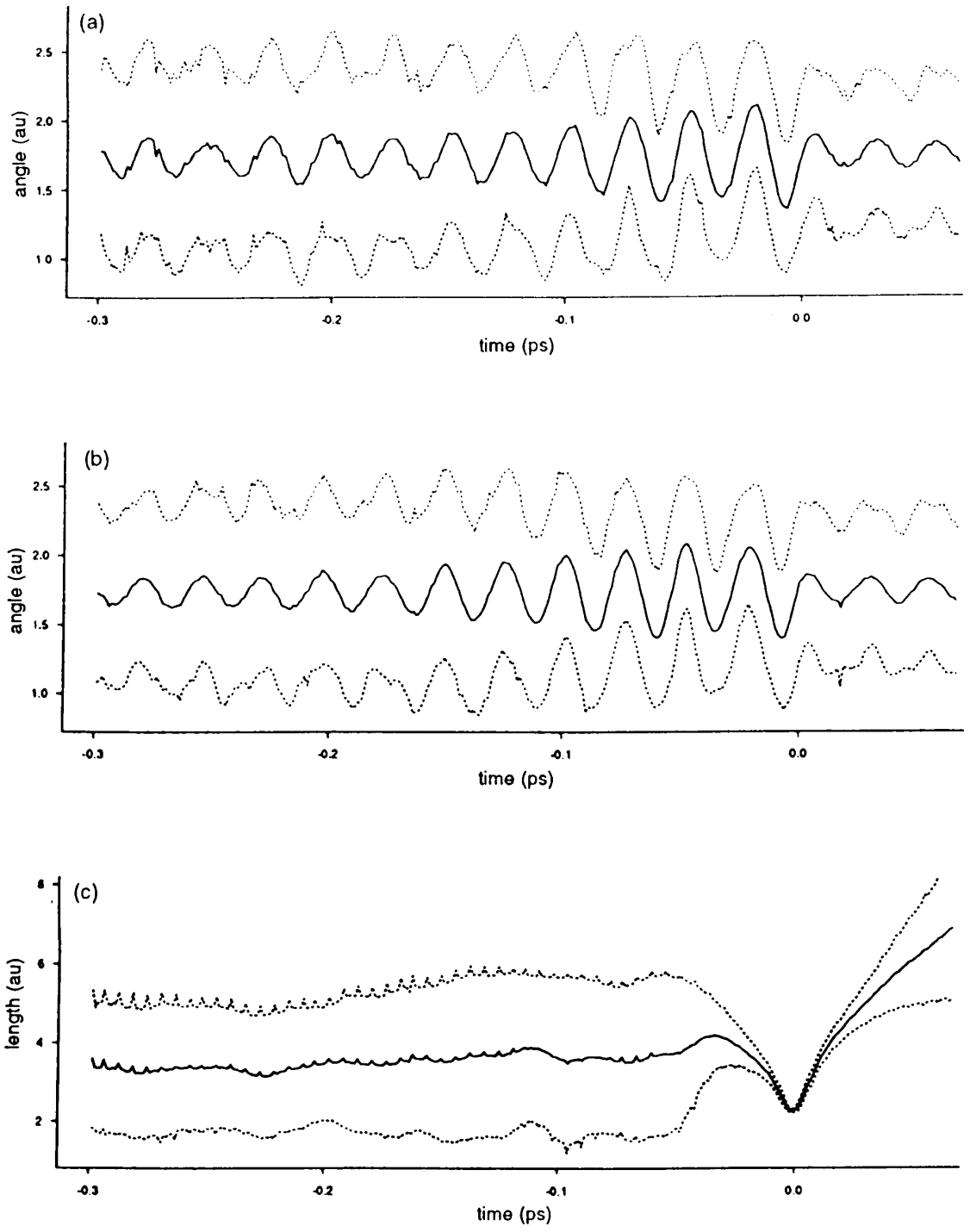

Figure 5 Averages and standard deviations ($\pm 2\sigma$) of selected local mode coordinates of hydrogen peroxide: (a) one of the OOH bend angles; (b) the other OOH bend angle; (c) the central OO stretch. As in Fig. 4, all trajectories have been aligned so that $t = 0$ is the last inner turning point of the central OO stretch prior to dissociation. A narrow pathway in coordinate space leading to the reaction is again observed.

function of time. The results are displayed in Fig. 6. Note that the H—N stretching modes follow a specific path producing a symmetric stretching motion for a brief period immediately prior to the reaction. As in the other reactions, the large-amplitude oscillations in the averages and the small standard deviations about the averages reveal that, to fair precision, each trajectory which reacts does so by following the same path.

Spears (64) demonstrated that the effect of this pathway was to generate exceptionally large couplings between the stretching modes and the torsional reaction coordinate. In particular, the reduction of the internal moment of inertia for internal rotation (torsion) during the inner turning point of the symmetric stretch produces a large internal Coriolis coupling.

IV. PHASE-SPACE ANALYSIS OF UNIMOLECULAR REACTION DYNAMICS

We began this chapter by asking both "how" and "why" questions about unimolecular reactions. The previous section provides a clear answer to the question of "how" a unimolecular reaction occurs, at least for the reactions we have studied to date. Two conclusions arise: evidently, each reaction does have a fairly specific vibrational path which leads to the reactive transition state, but also evidently, that path may be different for each reaction.

If we are to predict, or at least to understand, the reactive vibrational pathway for any given unimolecular reaction, then we must develop an understanding of "why" the reaction follows that path. To do so, we now adopt a very different approach to analyzing the reactive dynamics (65). We note at the outset that this analysis is based on theoretical developments and insights first provided by De Leon and co-workers (66–70).

A. Sampling Reactive Dynamics from the Transition State

Each trajectory which reacts, by definition, must pass through the transition state. In the simplest cases, the transition state will be the point along the reaction coordinate where the potential energy is a local maximum, i.e., the top of the barrier to reaction. In other cases, the location of the transition state is less obvious, and in all cases the definition of the transition state is arbitrary. Nevertheless, we can always find a region through which all trajectories must pass in order to reach the product region. Now, if every trajectory follows very nearly the same specific path to reach the transition state, then this path may be observed by starting trajectories at the transition state and running them "backwards" in time, back in the direction of the reactants.

We therefore adopt the approach of selecting initial conditions by sampling the entire energetically accessible phase space at the transition state and running each of these trajectories backward in time (65). Most of these trajectories (indeed, in most systems, all of these trajectories) will relax the initial excitation in the reaction coordinate, thus becoming "trapped," highly excited states of the reactant molecule. Since these are the states we previously sampled, we should observe exactly the same dynamics effects discussed in the previous section. As we shall see, we will also gain considerably greater insight.

We select as our system for study here a reduced model of the dissociation of hydrazoic acid. As described above, Julien et al., observed that only the two N—N stretches were relevant to the critical dynamics of the reaction, so we consider only these

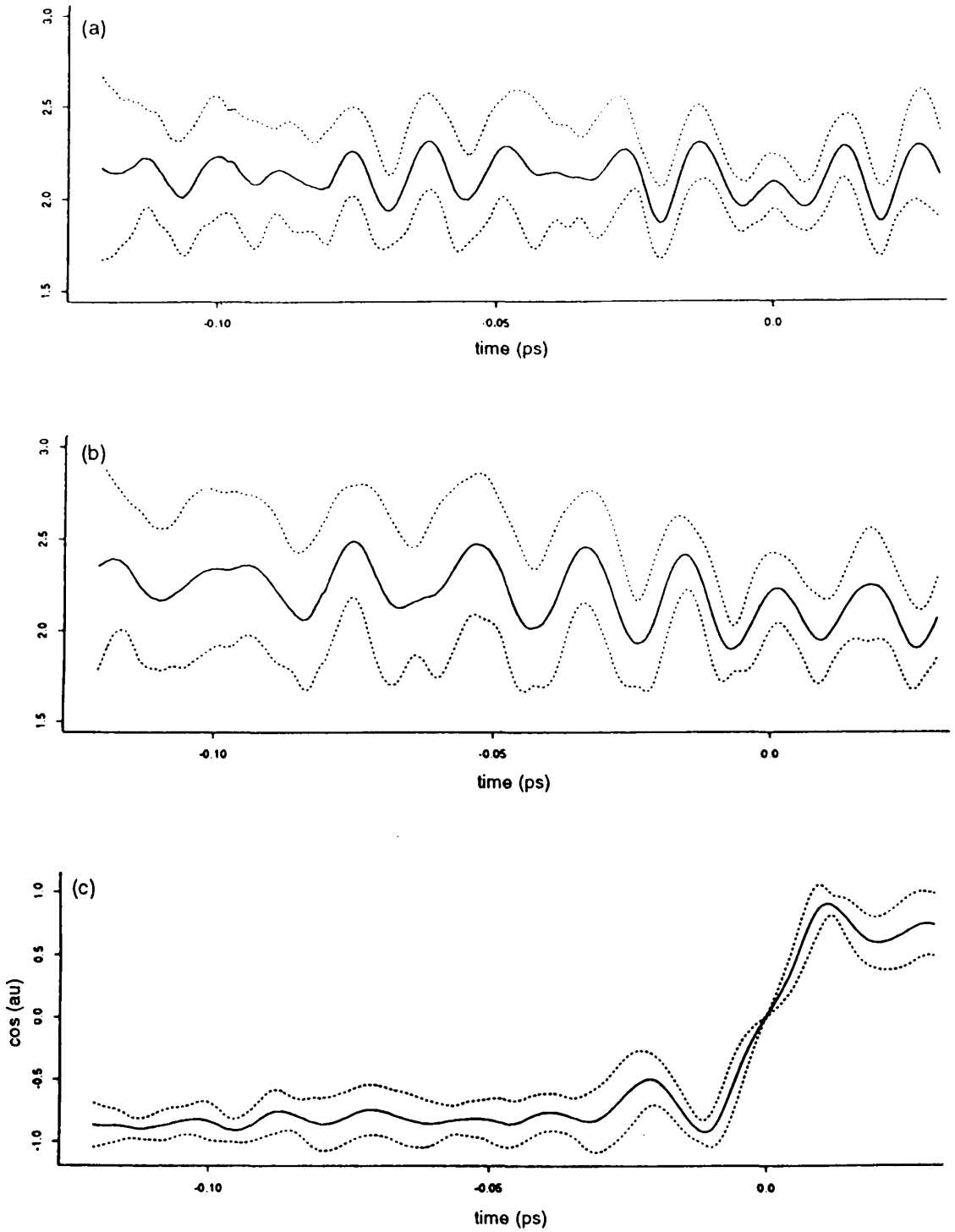

Figure 6 Averages and standard deviations ($\pm 2\sigma$) of selected local mode coordinates of diimide: (a) one of the NH stretches; (b) the other HN stretch; (c) the cosine of the dihedral angle for the torsional mode (reaction coordinate). In this case, all trajectories have been aligned so that $t = 0$ is the time of barrier crossing for the trans-cis isomerization. A narrow pathway in coordinate space leading to the reaction is again observed.

two modes in our model. The full six-mode model is thus reduced to a coupled Morse oscillator system:

$$H = H_1 + H_2 + T_{12} + V_{12} \tag{20}$$

where

$$H_j = \frac{p_j^2}{2\mu_j} + D_j(1 - e^{-\alpha_j(r_j - r_j^0)})^2 \tag{21}$$

$$T_{12} = -\frac{p_1 p_2}{m_N} \tag{22}$$

$$V_{12} = \frac{F_{12}}{\alpha_1 \alpha_2}(1 - e^{-\alpha_1(r_1 - r_1^0)})(1 - e^{-\alpha_2(r_2 - r_2^0)}) \tag{23}$$

r_1 is the nondissociative N—N bond and r_2 is the N—N reaction coordinate. We have taken the NNN bond angle to be fixed in the linear position, not far from its equilibrium value of 171.3°. The equilibrium geometry is at $(r_1^0, r_2^0) = (2.143a_0, 2.349a_0)$. Since the singlet-triplet crossing discussed in Sec. III occurs at $r_2 = 3.5a_0$, we regard this as the transition state and we begin trajectories there. The barrier to reaction is 147 kJ/mol, and we consider an ensemble of trajectories with total fixed energy equal to 160 kJ/mol. The excess energy is available to be partitioned as either excess energy in the reaction coordinate (i.e., in kinetic energy) or in the nonreactive mode.

To sample the accessible regions of phase space near the transition state, we systematically vary the amount of excess energy in the reaction coordinate by varying p_2. We find it convenient to group initial states into families, each "family" containing a set of trajectories with fixed p_2. All trajectories in a family have approximately the same amount of excess energy in r_2. The initial conditions for one particular family of trajectories are plotted in Fig. 7. It is worth remembering that, for a one-dimensional oscillator with a fixed total energy, the possible states form approximately an ellipse in phase space, and what is observed in Fig. 7 is approximately that ellipse. Each point on the ellipse represents a different initial phase of the r_1 mode, and we sample all phases between 0 and 2π. The dashed line in Fig. 7 represents the total energy boundary: points in phase space outside of that boundary exceed the total fixed energy at the transition state. We sample all of the accessible energy by varying p_2, and sampling all initial phases at each p_2.

B. Specific Dynamics and Impulsive Energy Transfer

We propagate the set of initial conditions above backwards in time to examine the dynamics which lead to the transition state. We then ensemble average both the bond length coordinates and the bond mode energies as functions of time. The results are shown in Figs. 8 and 9. In these figures, $t = 0$ is again taken to be the time that each trajectory visits the last inner turning point in r_2.

Considering first the averages of the bond lengths in Fig. 8, we note that, in the absence of mode–mode coupling, the average of r_1 would remain fixed at the equilibrium value of $2.143a_0$, since we have sample all phase around this value. Furthermore, the standard deviation of r_1 about this value should remain large, since we continue to sample the entire range of available r_1 values. Indeed, for the last half-vibrational period in r_2 prior to reaction, this is about what is observed for r_1. However, for times prior to this

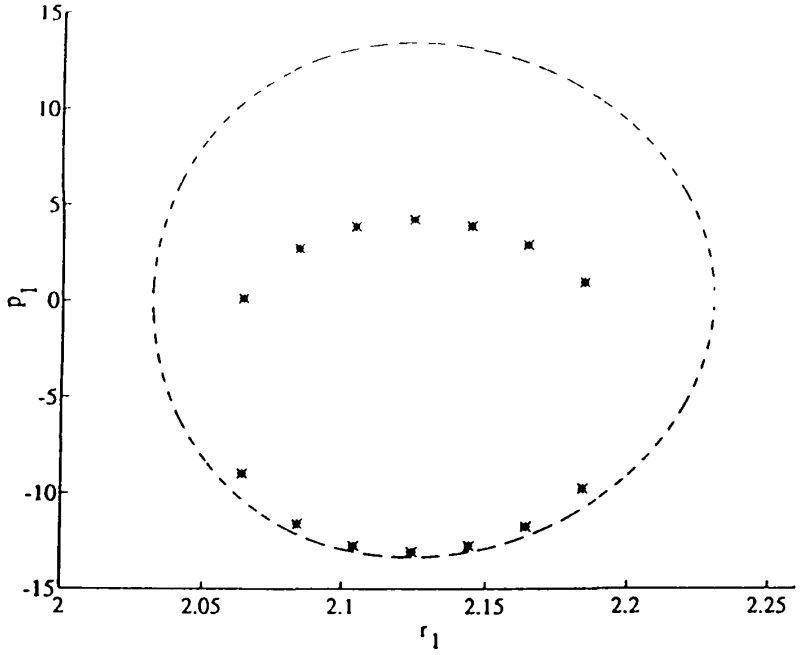

Figure 7 A sample family of trajectories for the two-mode hydrazoic acid model. Each asterisk marks the location of the initial conditions for a single trajectory. Each trajectory in this family begins at the transition state with $p_2 = -8.905$ au.

point, we observe large-amplitude oscillations in the ensemble average, with very small standard deviations, and these oscillations persist for several periods. For yet earlier times, the oscillations in the average are more damped, and the standard deviations are much larger. These results agree essentially perfectly with those presented in Sec. III.A, although those results were for the randomly selected initial conditions far from the transition state for a model with six degrees of freedom.

It is worth reflecting on the content of Fig. 8 for some time, particularly in light of the fact that these trajectories were run "backwards." That is, we have shown time advancing in the direction of the reaction, so that the trajectories reach the transition state at the far right of these plots. However, the dynamics were actually run in reverse, right to left. Therefore, we start with a set of trajectories which sample of all phases of r_1, but very quickly the dynamics cause the trajectories to coalesce to a small range of r_1 values, all with about the same phase. The trajectories oscillate in phase for several periods before sampling all phases again. In *forward* time, then, a randomly selected set of trajectories will coalesce in phase to oscillate with a particular phase for several vibrational periods prior to reaction.

We therefore ask the question, what physical effects cause a set of trajectories, which sample all phases, to very rapidly align themselves into approximately a single phase? Similarly, we may ask, why is this behavior required for reaction to occur?

An important clue is given in Fig. 9, which provides the ensemble averages as functions of time for the individual mode energies and the mode–mode couplings. The first feature to notice is the impulsive exchange of energy out of the nonreactive mode (H_1) into the reaction coordinate (H_2) very near to $t = 0$. The second feature is that this exchange results from a very large increase in the kinetic coupling (T_{12}) just prior to $t = 0$, and that the potential coupling is largely irrelevant to these dynamics. As we have

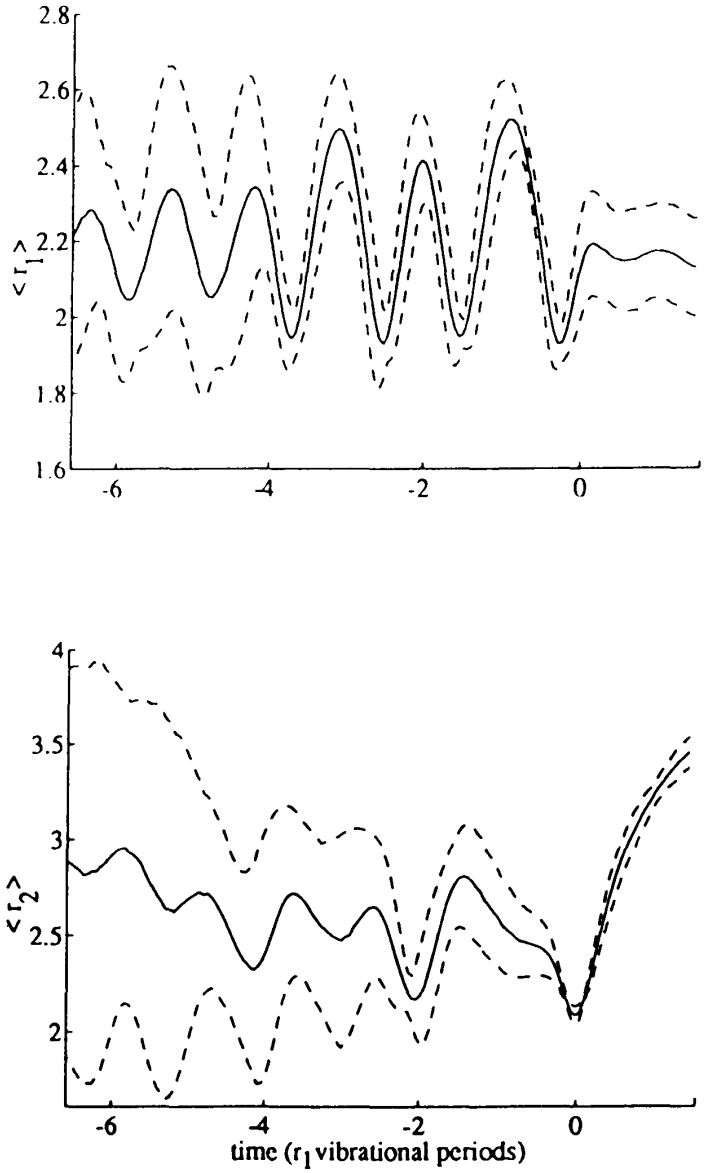

Figure 8 Ensemble averages of the coordinate for local modes r_1 and r_2 in the two-mode model of dissociation of hydrazoic acid. The trajectories in this ensemble were all initially started at the transition state of the reaction and run backwards in time.

seen, the impulsive transfer of energy is necessary for activation of the reaction coordinate. This burst of energy flow requires a very large coupling, as seen in Fig. 9. As we shall see, this large coupling places a major constraint on where the reactive trajectories may go.

C. Reactive Cylinders in Phase Space

A key to understanding the dynamics presented in Figs. 8 and 9 is found in analyzing the structure of the vibrational phase space generated by the set of trajectories started at the transition state. This approach was considered in significant detail by De Leon and his group in an excellent series of papers (66–69).

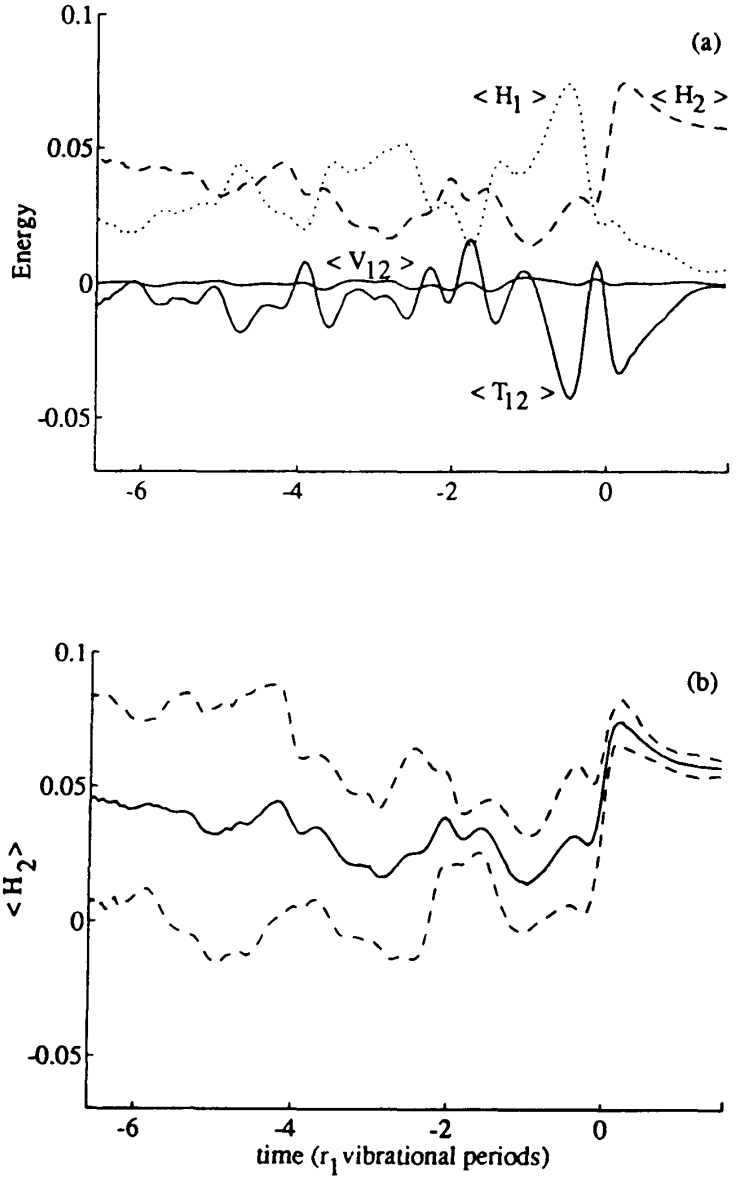

Figure 9 Average energies in modes 1 and 2 and average kinetic coupling, T_{12}, and potential coupling, V_{12}, for the two-mode hydrazoic acid model at a total energy of 0.0610 au. Impulsive energy transfer accompanied by high-amplitude spikes in T_{12} occurs near the last inner turning point in r_2.

Consider a single family of trajectories as in Fig. 7. If this were a one-dimensional oscillator, then these trajectories would evolve in phase space simply by oscillating about the closed curve which joins them. In a two-dimensional system without mode–mode coupling, this would be unchanged. However, if this motion were plotted as a function of, for example, motion along the reaction coordinate (again assuming no coupling), then the closed curve in Fig. 7. would be extended in the two-mode phase space to form a simple right cylinder, with cross section given by the closed curve. Although it is somewhat difficult to visualize, in the full four-dimensional phase space for a two-mode system, the topology of the structure generated by the motion of the trajectories initiated at the transition state is that of a cylinder.

For systems with coupling between the reaction coordinate and one or more other degrees of freedom, De Leon showed that the structure generated by the trajectories in phase space remains that of a cylinder, provided only that the coupling is not too large. To determine whether a system actually generates such a cylinder, one needs to see the motion in the multidimensional phase space. Since this is difficult to imagine, let alone draw, De Leon et al. used the standard method of a surface-of-section of the phase space. For a two-degree-of-freedom system, we simply slice the four-dimensional space by taking a surface corresponding to a fixed value of one coordinate. We then plot the value of the coordinate and momentum for the other coordinate each time the trajectory crosses this surface. If the trajectories move on the surface of a cylinder in the four-dimensional phase space, then the surface will "slice" this cylinder, producing cross sections which are closed curves.

We have applied this analysis to the families of trajectories described previously for our two-mode model of hydrazoic acid. Following De Leon and co-workers, we choose to plot (r_1, p_2) each time the trajectory crosses the surface $r_1 = r_1^0$ with $p_2 > 0$. Since each trajectory makes multiple passes through this surface, then we denote the point of each passage by the number of that pass. Typical results are shown for two families trajectories in Fig. 10. We see clearly that all of the trajectories in a single family, on a single pass, form a cluster of points on intersection with the surface. The most notable of these clusters is the collection of 2's and 3's in the upper left of each figure. These points for a single family clearly form a closed curve representing the cross section of a cylinder. Other such closed curves are also present, although not as obvious. It appears, in fact, that the cylinder persists for six or seven vibrational periods in r_1, crossing this surface in different regions on each pass through $r_1 = r_1^0$. Also of note is the fact that the cylinder cross sections in Fig. 10a fit "inside" the corresponding cross sections in Fig. 10b. The different families of trajectories produce concentric cylinders, with the families with larger p_2 (and smaller E_1) inside the trajectories with smaller p_2.

A more revealing view of this cylinder is provided in Fig. 11. Here we have plotted the (r_1, p_1) surface, as in Fig. 7 but now as a function of the distance traveled in r_2, which we have calculated as the r_2 arc length. Two families of trajectories are shown, representing the extremes in p_2. One is the "perimeter family." This is the set of trajectories with the maximum amount of energy in the r_1 mode at the transition state; i.e., $p_2 = 0$. These trajectories would form the set at the energy boundary in Fig. 7. These trajectories are represented by the dashed lines, sweeping out the tornado-like figure. The other family has a single member, and is the trajectory where p_2 is the maximum allowed by the total energy constraint. This trajectory lies at the center of all of the other concentric families and is therefore regarded as the "central trajectory." It is represented by the solid line in Fig. 11.

The cylinder leading to the transition state is very obvious in this figure. There are several points to observe: first, at the bottom of the figure, where the r_2 arc length is 0, is the transition state. All trajectories at the transition state lie within the boundary of the perimeter family at this point. Second, as the trajectories leave the transition state, they remain clustered as they were at the transition state, sweeping out a cylinder in the phase space. Third, the cylinder "moves" as it evolves, following a somewhat twisted path in the phase space, predictable from the path of the central trajectory. Viewed in terms of (r_1, p_1), the trajectories of the perimeter family oscillate around the outside of the cylinder. As r_2 propagates, the trajectories then "wind" around the outside of the cylinder.

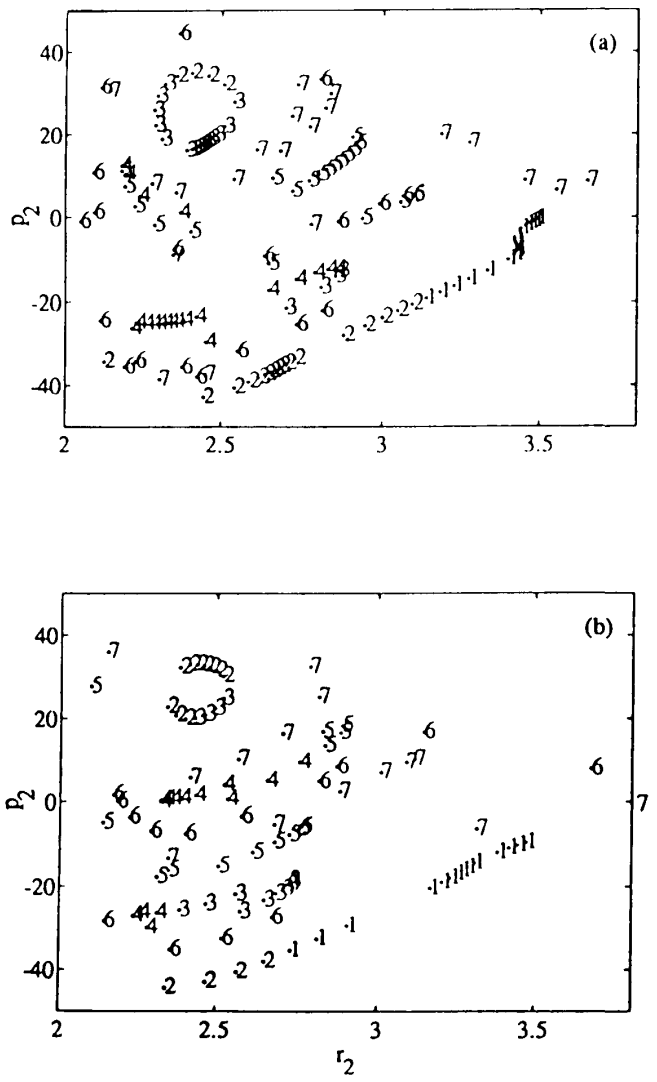

Figure 10 Phase space surfaces of section at $r_1 = r_1^0$, $p_1 > 0$ for trajectories of the two-mode hydrazoic acid model at a total energy of 0.0610 au. Each frame is for a different "family" of initial states: (a) $p_2 = 0$ au; (b) $p_2 = -8.905$ au. Each number indicates the passage of a trajectory through this surface; i.e., a 2 indicates the second pass of that trajectory. Note that trajectories cluster together by passage number.

Two significant conclusions can be drawn from this figure. First, since all trajectories at the transition state evolve through the cylinder in Fig. 11, then any trajectory which is to reach the transition state in forward time *must enter and follow the cylinder.* As such, De Leon dubbed this the "reaction cylinder." Second, since the reaction cylinder oscillates as it approaches the transition state, then an average of the value of r_1 for the trajectories in the cylinder must oscillate as well. This accounts for the oscillations observed in the time dependence of the ensemble average of r_1 just prior to reaction.

Furthermore, this phase-space perspective reveals that there is even stronger correlation among the reactive mode and the nonreactive mode than is evident in the ensemble averages. Specifically, the variations from the ensemble average represented by the standard deviations are not random. Rather, they represent the organized distribution of phases about the cylinder as the trajectories wind around the cylinder.

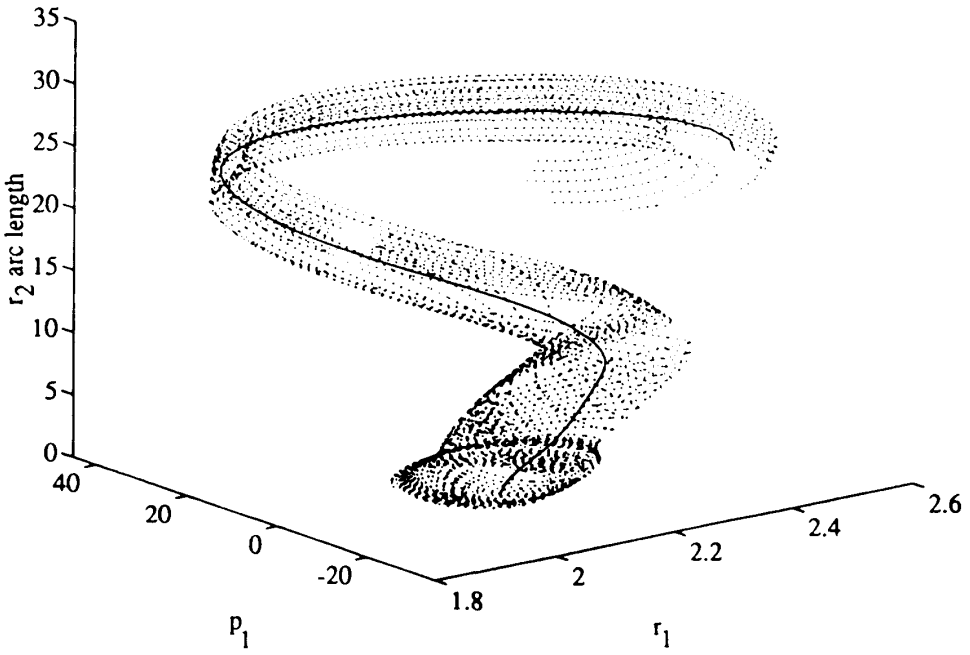

Figure 11 Phase-space surface p_1 versus r_1 versus r_2 arc length for the trajectories in the perimeter family (dotted lines) and for the central trajectory (solid line) of the two-mode hydrazoic acid model at a total energy of 0.0610 au. The reaction cylinder is conspicuous as these trajectories move through phase space.

D. Energetic Constraints on Reactive Motion

Our question now becomes, why does the cylinder follow the specific path that it does? We already have a preliminary answer to this question: very large mode–mode couplings are required for activation of the reaction coordinate, so trajectories approaching the transition state must pass through a relatively restricted window in phase space to achieve these couplings.

Viewed in reverse time starting from the transition state, this answer is less satisfying. We note that all trajectories at the transition state follow the specific path dictated by the cylinder, which carries the ensemble into the region of large mode-mode coupling, as in Fig. 8. But how did the trajectories (or the cylinder) know to go to that region, a priori of having been there? What is it that directs the cylinder to head for the region of largest coupling? These are nontrivial questions, for they go directly to our understanding of "why" the reaction occurs in the way that it does.

We have mentioned one key feature of the energetics of the reaction, that being that the mode–mode coupling involving the reactive mode and at least one other mode must become very large immediately prior to reaction. This is necessary to induce the impulsive transfer of energy which activates the reaction coordinate. A second key feature, however, has not been mentioned. Note the time of the impulsive energy transfer in Fig. 9, and recall that $t = 0$ defines the time at which the trajectories last hit the inner turning point of the reaction coordinate. The energy transfer is essentially complete at $t = 0$, one-half of a vibrational period *prior* to the time at which that energy is required to surmount the activation barrier. During that last half–vibration, the energy in the reaction coordinate does not vary by much: to a reasonable approximation, the reaction coordinate is adiabatic during its last half–vibration.

This approximate adiabaticity imposes a significant constraint on the approach of each trajectory to the transition state. Consider a single trajectory at the transition state with energy E_2 in the reaction coordinate. As r_2 moves "downhill" toward the minimum, we know now that this energy remains comparatively constant. In fact, at $r_2 = r_2^\circ$, E_2 must all be converted to kinetic energy, so at this point, $p_2 = \sqrt{2\mu_2 E_2}$ must be a large momentum. Referring back to the two-mode Hamiltonian in Eq. (13), we thus take $H = E$, $H_2 = E_2$, and substitute in $r_2 = r_2^\circ$ and $p_2 = \sqrt{2\mu_2 E_2}$. The resultant equation can be solved to find the allowed values of p_1 as a function of the value of r_1 when the trajectory passes through the minimum in r_2.

$$p_1 = \mu_1 \left[\frac{p_2}{m_N} \pm \left(\left[\frac{p_2}{m_N} \right]^2 + \frac{2}{\mu_1} [E - E_2 - V_1(r_1) - V_{12}(r_1, r_2)] \right)^{1/2} \right] \tag{24}$$

This curve is plotted in Fig. 12 for the same total energy as in the previous results and a fixed value of $E_2 = 178$ kJ/mol. Also shown in this figure are actual trajectory intersections with this (r_1, p_1) surface of section at $r_2 = r_2^\circ$, trajectories in the perimeter family. The trajectories again are arranged in a closed curve, indicating a cross section of a cylinder. We note that the boundary of this empirically observed cylinder is very well predicted by the simple result in Eq. (24).

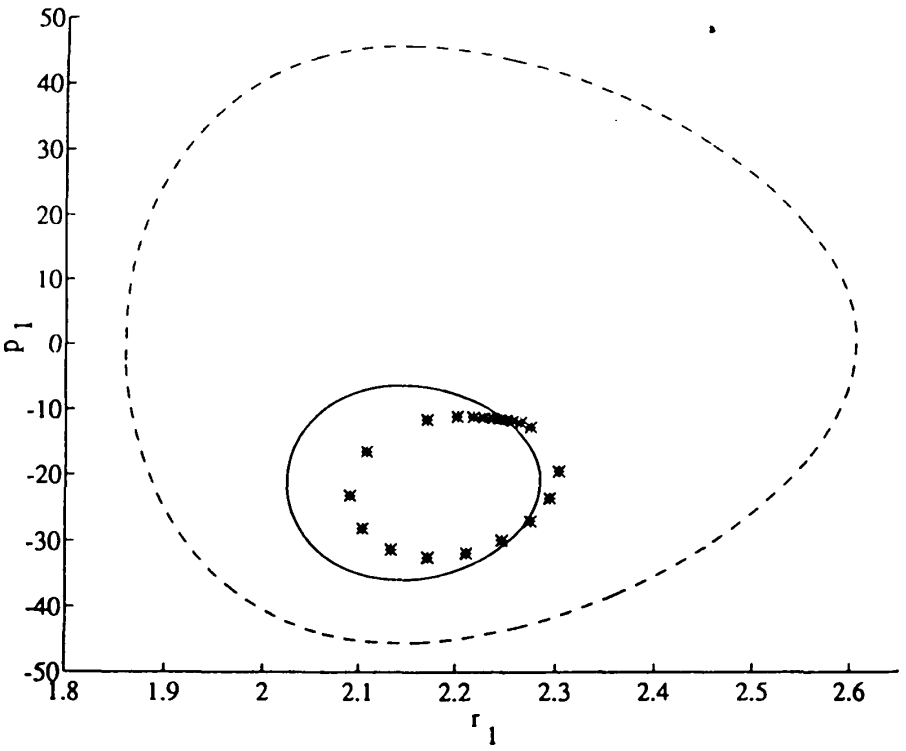

Figure 12 Phase-space surface of section p_1 versus r_1 at $r_2 = r_2^\circ$ at a total energy of 0.0610 au. The dashed line is the total energy boundary. The asterisks indicate the points where the trajectories of the perimeter family pass through this surface after leaving the transition state. The solid line is the constraint determined by Eq. (24) for a fixed $E_2 = 0.0700$ au. Equation 24 accurately predicts both the location and distribution of the trajectories as they pass through this surface and thus describes the location of the reactive cylinder in phase space.

Our conclusion is that the reaction cylinder follows the specific path through phase space that we observe as a consequence of the constraints imposed on the dynamics by the near-adiabaticity of the reaction coordinate during its last half-vibration before reaction. Trajectories leaving the transition state in the reverse direction must pass through a very narrow window in phase space because that is the only region consistent with the constraints of fixed total energy and approximately fixed energy in the reaction coordinate. This narrow window defines a fairly narrow range of permissible phases of the nonreactive mode at the time where $r_2 = r_2^0$, or in other words, the two modes must be phase correlated prior to the reaction, as we have observed.

We therefore have a fairly detailed description of both "how" and "why" this particular unimolecular reaction occurs. In forward time, the approach to the transition state is highly constrained, in that only a narrow path, accessible via a careful phasing of a nonreactive mode with the reactive mode, is consistent with the constraints of large reactive mode energy, fixed total energy, and large mode–mode couplings.

V. CONCLUSIONS

At the beginning of this chapter, we wondered whether a cogent answer exists to the questions of "how" and "why" a unimolecular reaction occurs. The remainder of this chapter has been devoted to describing research aimed at such an answer. Of course, cogency is in the eye and mind of the reader, and whether we have defined a satisfactory answer is a matter of opinion. However, specifically referring only the unimolecular fragmentation reaction of hydrazoic acid, the answer to the question of how the reaction occurs seems clearly provided by the detailed dynamics shown in Figs. 8 and 9. And the answer to the question of why the reaction occurs this way seems clearly provided by the constraint in Eq. (24).

A second but equally important question is that of what shall be done with the answer now that we have it. Here we approach the answer from two different perspectives.

First, it seems desirable, even *prima facie*, that we develop an intuition of how chemical reactions occur. For example, molecular orbital theory provides a fair amount of detailed intuition about the energetics of chemical reactions, i.e., when do we expect large activation barriers, when do we expect concerted reactions, what is the effect of an electrophilic substituent on reaction product distributions, etc. A similar intuition has not been available concerning the role of dynamics in chemical reactivity. It is reasonable, as a chemist, to ask how one could enhance energy transfer specifically into the reaction coordinate, thus to make the reaction more efficient and to produce better reaction yields with fewer byproducts.

Indeed, the many reported laboratory attempts at "mode–specific" photochemistry were directed at such control over the energy flow during unimolecular reaction. It is understandable, *post hoc*, why these attempts failed, given a lack of knowledge about the events involved in the flow of energy into the reaction coordinate. It is hoped that the type of results discussed herein may enhance our intuition about reactive events, and thus enhance the success of mode–specific chemistry. For example, it seems apparent that current efforts to control chemical reactivity via coherent laser pulse shaping would be strengthened by a knowledge of what vibrations must be excited.

Second, at a more practical level, a knowledge of the vibrational events which precede reaction should simplify application of transition state theories to reaction rate

calculations (68,71). In fact, several authors have used a knowledge of the structure of vibrational phase space to construct dynamically based, rather than statistically based, theories of unimolecular reaction rates (71–75). Most notably, De Leon has developed a "reactive island" kinetic theory based on the existence of the reaction cylinder, and has used this to account for non-RRKM kinetics of model unimolecular reactions (69,70). We hope and expect that the details of reactive vibrational motions presented here will contribute further to those developments.

ACKNOWLEDGMENTS

The author wishes to recognize and thank his students, who were responsible entirely for the work presented herein. These include, specifically, T. A. Holme, J. R. Fair, K. R. Wright, L. G. Spears III, J. Jiang, V. Julien, A. Patel, Y. Jones, and R. P. Muller. This work was supported in part by a grant from the Robert A. Welch Foundation of Houston, Texas. Acknowledgment is made to the donors of the Petroleum Research Fund, administered by the American Chemical Society, for partial support of this research.

REFERENCES

1. I. Oref and B. S. Rabinovitch, *Acc. Chem. Res. 12*:166 (1979).
2. C. S. Parmenter, *Faraday Discuss. Chem. Soc. 75*:7 (1983).
3. F. F. Crim, *Ann. Rev. Phys. Chem. 35*:657 (1984).
4. R. A. Marcus, *J. Chem. Soc., Faraday Trans. 2 84*:1237 (1988) and references therein.
5. W. L. Hase (Ed.), *Intramolecular and Nonlinear Dynamics*, JAI Press, 1991.
6. J. I. Steinfield, J. S. Francisco, and W. L. Hase, *Chemical Kinetics and Dynamics*, Prentice Hall, 1989.
7. P. A. Robinson and K. A. Holbrook, *Unimolecular Reactions*, Wiley, 1972.
8. J. N. Butler and G. B. Kistiakowsky, *J. Am. Chem. Soc. 82*:759 (1960).
9. R. E. Harrington, B. S. Rabinovitch, and H. M. Frey, *J. Chem. Phys. 33*:1271 (1960).
10. E. A. Hardwidge, B. S. Rabinovitch, and R. C. Ireton, *J. Chem. Phys. 58*:340 (1973).
11. F. H. Dorer and R. S. Rabinovitch, *J. Phys. Chem. 69*:1952 (1965).
12. K. C. Kim and D. W. Setser, *J. Phys. Chem. 78*:2166 (1974).
13. B. E. Holmes and D. W. Setser, *J. Phys. Chem. 79*:1320 (1975).
14. D. S. King, *Adv. Chem. Phys. 50*:105 (1982).
15. M. J. Berry, Vibrational photochemistry and photophysics, in *Proceedings of the Robert A. Welch Foundation Conferences on Chemical Research*, XXVIII, p. 133, Welch Foundation, 1984.
16. D. W. Chandler, W. E. Farneth, and R. N. Zare, *J. Chem. Phys. 77*:4447 (1982).
17. T. A. Holme and J. S. Hutchinson, *J. Chem. Phys. 84*:5455 (1986).
18. J. S. Hutchinson, *J. Chem. Phys. 85*:7087 (1986).
19. J. S. Hutchinson and K. T. Marshall, *J. Chem. Soc. Faraday Trans. II 84*:1535 (1988).
20. M-C. Chuang, J. E. Baggott, D. W. Chandler, W. E. Farneth, and R. N. Zare, *Faraday Discuss. Chem. Soc. 75*:301 (1983).
21. J. M. Jasinski, J. K. Frisoli, and C. B. Moore, *J. Chem. Phys. 79*:1312 (1983).
22. J. M. Jasinski, J. K. Frisoli, and C. B. Moore, *Faraday Discuss. Chem. Soc. 75*:289 (1983).
23. J. M. Jasinski, J. K. Frisoli, and C. B. Moore, *J. Phys. Chem. 87*:2209 (1983).
24. E. S. McGinley and F. F. Crim, *J. Chem. Phys. 85*:5748 (1986).
25. B. D. Cannon and F. F. Crim, *J. Chem. Phys. 75*:1752 (1981).
26. T. M. Ticich, T. R. Rizzo, H-R. Dübal, and F. F. Crim, *J. Chem. Phys. 84*:1508 (1986).
27. N. F. Scherer, F. E. Doany, A. H. Zewail, and J. W. Perry, *J. Chem. Phys. 84*:1932 (1986).

28. M-C. Chuang and R. N. Zare, *J. Chem. Phys. 82*:4791 (1985).
29. T. D. Kunz, Ph.D. thesis, Rice University, 1986.
30. R. G. Bray and M. J. Berry, *J. Chem. Phys. 71*:4909 (1979).
31. K. V. Reddy, D. F. Heller, and M. J. Berry, *J. Chem. Phys. 76*:2814 (1982).
32. M. E. Long, R. L. Swofford, and A. C. Albrecht, *Science 191*:183 (1976).
33. R. L. Swofford, M. E. Long, and A. C. Albrecht, *J. Chem. Phys. 65*:179 (1976).
34. H. L. Fang and R. L. Swofford, *J. Chem. Phys. 72*(12):6382 (1980).
35. J. S. Wong and C. B. Moore, *J. Chem. Phys. 77*:603 (1982).
36. G. J. Scherer, K. K. Lehmann, and W. Klemperer, *J. Chem. Phys. 78*:2817 (1983).
37. L. J. Butler, T. M. Ticich, M. D. Likar, and F. F. Crim, *J. Chem. Phys. 85*:2331 (1986).
38. E. S. McGinley and F. F. Crim, *J. Chem. Phys. 85*:5741 (1986).
39. T. Uzer, *Phys. Rep. 199*:73 (1991).
40. *J. Chem. Soc. Faraday Trans. II 84* (1988) contains a series of articles of this subject.
41. H. Goldstein, *Classical Mechanics*, Addison-Wesley, 1980.
42. B. V. Chirikov, *Phys. Rep. 52*:263 (1979).
43. F. N. Izrailev and B. V. Chirikov, *Sov. Phys. Dokl. 11*:30 (1966).
44. J. Ford, *Adv. Chem. Phys. 24*:155 (1973).
45. J. Ford, *J. Math. Phys. 2*:387 (1961).
46. D. W. Oxtoby and S. A. Rice, *J. Chem. Phys. 65*:1676 (1976).
47. C. Jaffé and P. Brumer, *J. Chem. Phys. 73*:5646 (1980).
48. E. L. Sibert III, W. P. Reinhardt, and J. T. Hynes, *J. Chem. Phys. 77*(7):3583 (1982).
49. J. S. Hutchinson, W. P. Reinhardt, and J. T. Hynes, *J. Chem. Phys. 79*(9):4247 (1983).
50. R. P. Muller, J. S. Hutchinson, and T. A. Holme, *J. Chem. Phys. 90*:4582 (1989).
51. E. L. Sibert III, J. T. Hynes, and W. P. Reinhardt, *J. Chem. Phys. 81*(3):1135 (1984).
52. J. S. Hutchinson, J. T. Hynes, and W. P. Reinhardt, *J. Phys. Chem. 90*(16):3528 (1986).
53. T. Uzer, J. T. Hynes, and W. P. Reinhardt, *J. Chem. Phys. 85*(10):5791 (1986).
54. J. S. Hutchinson, E. L. Sibert III, and J. T. Hynes, *J. Chem. Phys. 81*(3):1314 (1984).
55. J. S. Hutchinson, J. T. Hynes, and W. P. Reinhardt, *Chem. Phys. Lett. 108*(4):353 (1984).
56. E. L. Sibert III, W. P. Reinhardt, and J. T. Hynes, *J. Chem. Phys. 81*(3):1115 (1984).
57. C. Iung and R. E. Wyatt, *J. Chem. Phys. 99*:2261 (1993).
58. T. Uzer and J. T. Hynes, *Chem. Phys. Lett. 113*:483 (1985).
59. T. A. Holme and J. S. Hutchinson, *J. Chem. Phys. 83*:2860 (1985).
60. M. H. Alexander, H.-J. Werner, T. Hemmer, and P. J. Knowles, *J. Chem. Phys. 93*:3307 (1990).
61. B. R. Foy, M. P. Casassa, J. C. Stephenson, and D. S. King, *J. Chem. Phys. 89*:608 (1988).
62. V. Julien, A. Patel, Y. Jones, J. Jiang, and J. S. Hutchinson, *J. Phys. Chem. 97*:7011 (1993).
63. L. G. Spears, Jr., and J. S. Hutchinson, *J. Chem. Phys. 88*:240 (1988).
64. L. G. Spears, Jr., and J. S. Hutchinson, *J. Chem. Phys. 88*:250 (1988).
65. J. R. Fair, K. R. Wright, and J. S Hutchinson, *J. Phys. Chem. 99*:14707 (1995).
66. N. De Leon and C. C. Marston, *J. Chem. Phys. 91*:3405 (1989).
67. N. De Leon, M. A. Mehta, and R. Q. Topper, *J. Chem. Phys. 94*:8310 (1991).
68. N. De Leon, *J. Chem. Phys. 96*:285 (1992).
69. N. De Leon, *Chem. Phys. Lett. 189*:371 (1992).
70. N . De Leon and S. Ling, *J. Chem. Phys. 101*:4790 (1994).
71. M. J. Davis and R. T. Skodje, *Adv. Classical Traj. Meth. 1*:77 (1992).
72. M. J. Davis and S. K. Gray, *J. Chem. Phys. 84*:5389 (1986).
73. R. T. Skodje and M. J. Davis, *J. Chem. Phys. 88*:2429 (1988).
74. S. K. Gray, S. A. Rice, and M. J. Davis, *J. Phys. Chem. 90*:3470 (1986).
75. R. E. Gillilan and G. S. Ezra, *J. Chem. Phys. 94*:2648 (1991).

15

The Classical Trajectory Approach to Reaction Dynamics

HOWARD R. MAYNE

University of New Hampshire, Durham, New Hampshire

I. INTRODUCTION

The classical trajectory approach corresponds to many people's intuitive feeling about how atoms behave during the course of a collision. Each atom is thought of as a structureless point moving deterministically as a function of time under the influence of the forces between that atom and its neighbors. After the dust has settled, one can examine each of the product fragments to determine how many atoms are in each fragment, how much energy each fragment contains, how fast the species are retreating from each other, and how the (conserved) total angular momentum is distributed among the fragments.

In reality, of course, atoms obey quantum mechanics rather than classical mechanics. As you will discover in other chapters in this book, great advances have been made recently in the quantum mechanical treatment of molecular systems. However, one should realize just how much care has to go into the selection of correct coordinates and the necessity to choose appropriate systems for quantum mechanical study. For arbitrarily large systems, or for systems containing several heavy atoms, quantum methods are not yet readily applicable. It is in such cases that classical mechanical approaches can be utilized with profit. Furthermore, even in systems for which quantum mechanical treatments are now feasible, comparisons with classical data often help researchers to isolate those phenomena which arise solely in the quantum mechanics, yielding fundamental insight into the two different dynamics. In the classical approach, the motion of each atom is calculated by numerically solving the classical differential equations of motion (1), either second order with respect to time in the positions, $\mathbf{x}$ (Newton's law), or,

equivalently, first order with respect to time in both the positions, **x**, and the momenta, **p** (Hamilton's equations). Given any set of initial values for the position and momentum of each atom, there is a huge array of computational techniques (2,3) available for solving these equations. Current computational power has greatly increased the speed with which such equations can be solved and the number of atoms which can be dealt with. The resulting output, $\mathbf{x}(t)$, is referred to as the classical trajectory originating from the given initial conditions. The $\mathbf{x}(t)$ and its time derivative $\dot{\mathbf{x}}(t)$ (or, equivalently, $\mathbf{p}(t)$) suffice to determine the potential energy, the kinetic energy and the angular momentum possessed by each atom.

Of course, for the computational output to have any use to the chemical community, the systems must be chosen to provide answers to some chemical problems. It is here that more specialized techniques are required. First, the interaction potential between the atoms must be, in some sense at least, "realistic." In principle, the potential energy should be computed for all possible geometries (or enough to interpolate between) of the nuclei by solving the full electronic Schrödinger equation for each geometry. This is clearly impractical for most cases, and often unnecessary, depending on the system under study. For a few-electron system like H_3, for which extremely detailed experimental data exist, then a potential of high quality is clearly crucial. On the other hand, if one wants to study the feasibility of iodine atom recombination within a cluster of argon atoms, simplifications in the potential can (and must) be made.

Furthermore, the initial conditions chosen must also be appropriate to the chemical system being modeled. If the goal is to correlate the outcome of the dynamics with the initial quantum numbers of the molecules involved, then an algorithm must be produced which generates initial positions and momenta within the molecule which mimic the attributes of those quantum labels. If a simulation requires modeling a large cluster at a given temperature, again techniques are required to produce and to sample the appropriate initial classical coordinates.

In this chapter, we will briefly sketch out the preliminary theory needed to understand and carry out gas-phase classical trajectory calculations. For the sake of compactness, more sophisticated algorithms will be touched on only qualitatively, and the reader is referred to the original literature. No claim to completeness is made here; rather a (necessarily biased) selection of the armory of available techniques will be given, together with a (necessarily incomplete) review of the strengths and weaknesses of the classical trajectory approach. Finally a sample of results from various research areas will be presented.

There have been several earlier reviews of the classical trajectory approach (3–10). For a particularly thorough treatment of the methods of calculating cross sections for atom plus diatom reactions, the reader is referred to the paper of Truhlar and Muckerman (7). An encyclopedic review of techniques and applications through 1983 is given by Raff and Thompson (8). The most recent review of applications is by Mayne (10). The first real use of the trajectory method in the literature remains an outstanding example of its use (11).

At this point, it might be appropriate to point out that the term "molecular dynamics" is now sometimes used as synonymous with classical trajectory calculations, albeit usually when fairly large systems are being modeled. This is somewhat different from the more traditional usage (12,13) in statistical mechanics in which the classical equations of motion are solved to produce time-averaged properties of (typically) equilibrium systems.

II. CLASSICAL EQUATIONS OF MOTION

The most typical approach is via the classical Hamiltonian for an N-atom system:

$$H(\mathbf{x}_1, \ldots, \mathbf{x}_N; \mathbf{p}_1, \ldots, \mathbf{p}_N) = \sum_{i=1}^{N} \frac{\mathbf{p}_i \cdot \mathbf{p}_i}{2m_i} + V(\mathbf{x}_1, \ldots, \mathbf{x}_N) \tag{1}$$

where $\mathbf{x}_i$ are the positions (typically Cartesian), $\mathbf{p}_i$ are the momenta for the ith atom, and m_i is the mass of the ith atom. The first term of the r.h.s. of Eq. (1) is the kinetic energy, the second the potential energy. If, indeed, Cartesian coordinates are employed, then $\mathbf{p}_i = m_i\dot{\mathbf{x}}_i$ (when other coordinates are used, we shall explicitly mention this in the text). If the calculation is carried out in the full three dimensions, then the $\mathbf{x}$ and $\mathbf{p}$ are 3-vectors: $\mathbf{x}_i = (x_i, y_i, z_i)$, $\mathbf{p}_i = (p_{x_i}, p_{y_i}, p_{z_i})$.

The positions and momenta obey Hamilton's equations:

$$\dot{\mathbf{x}}_i = \nabla_{\mathbf{p}_i} H = \frac{p_i}{m_i} \tag{2}$$

$$\dot{\mathbf{p}}_i = -\nabla_{\mathbf{x}_i} H = -\nabla_{\mathbf{x}_i} V \tag{3}$$

In terms of the (x, y, z) components of the positions and momenta, this is

$$\begin{aligned} \dot{x}_1 &= \frac{p_{x_1}}{m_1} \\ \dot{y} &= \frac{p_{y_1}}{m_1} \\ &\cdot \\ &\cdot \\ &\cdot \\ \dot{p}_{z_N} &= -\frac{\partial V}{\partial z_n}(x_1, \mathbf{y}_1, \ldots, \mathbf{z}_N) \end{aligned} \tag{4}$$

As mentioned, given the current coordinates and momenta, $(\mathbf{x}(t), \mathbf{p}(t)) = x_1, y_1, \ldots, Z_n; p_{x_1}, p_{y_1}, \ldots, p_{z_n})$, and their time derivatives, $(\dot{\mathbf{x}}(t), \dot{\mathbf{p}}(t)) = (\dot{x}_1, \dot{y}_1, \ldots, \dot{z}_n; \dot{p}_{x_1}, \dot{p}_{y_1}, \ldots, \dot{p}_{z_n})$, then the values of $(\mathbf{x}(t + \delta t), \mathbf{p}(t + \delta t))$ at some future (or past) time can be computed. The choice of computational algorithm for this depends on the problem at hand. For instance, special techniques are required if the equations are "stiff"; that is, if the typical time scale of motion in some modes is much shorter than in others. The criteria for choice are discussed in several excellent reviews (2,3,8).

The potential is often (although not invariably) parametrized in terms of interatomic distances. To illustrate how the calculation is carried out, refer to Fig. 1a, which shows the coordinates needed to describe the collision of two diatomic molecules. The interatomic distances, r_{ij}, are given by

$$\begin{aligned} r_{ij} &= |\mathbf{r}_{ij}| = |\mathbf{x}_i - \mathbf{x}_j| \qquad (i < j) \\ &= [(x_i - x_j)^2 + (y_i - y_j)^2 + (z_i - z_j)^2]^{1/2} \end{aligned} \tag{5}$$

Typically, the potential will be written as $V(r_{12}, r_{13}, r_{14}, r_{23}, r_{24}, r_{34})$. Therefore, in the calculation of Hamilton's equations (Eq. (4)), chain rule terms appear. For instance, for the system in Fig. 1a, the coordinate $\mathbf{x}_1$ is involved in the three distances, r_{12}, r_{13}, r_{16}.

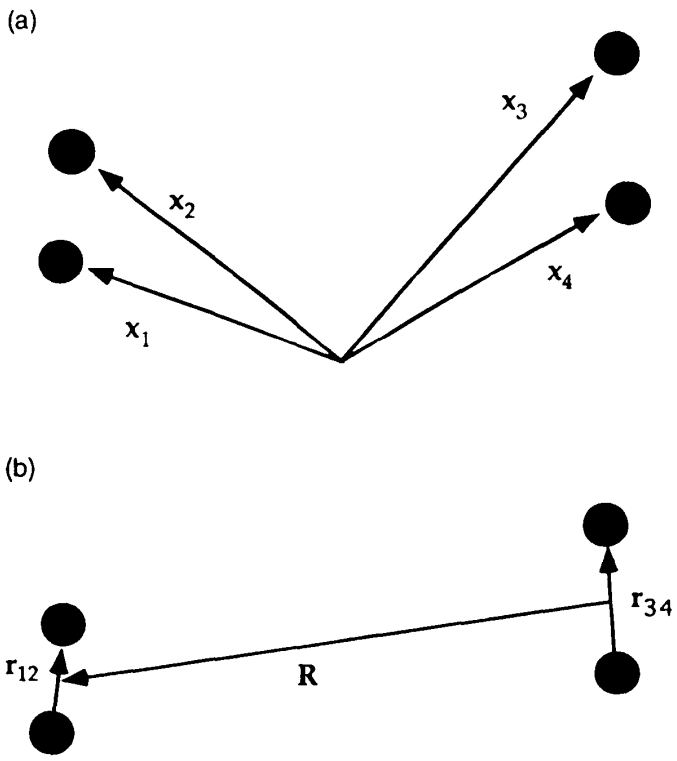

Figure 1 (a) Cartesian coordinates for two diatomic molecules, 12 and 34. (b) Jacobi coordinates for the same two molecules.

Therefore,

$$\dot{p}_{x_1} = -\frac{\partial V}{\partial x_1} = -\left(\frac{\partial V}{\partial r_{12}} \cdot \frac{\partial r_{12}}{\partial x_1} + \frac{\partial V}{\partial r_{13}} \cdot \frac{\partial r_{13}}{\partial x_1} + \frac{\partial V}{\partial r_{14}} \cdot \frac{\partial r_{14}}{\partial x_1}\right) \tag{6}$$

with, for instance,

$$\frac{\partial r_{12}}{\partial x_1} = \frac{x_1 - x_2}{r_{12}} \tag{7}$$

Note, too, that

$$\frac{\partial r_{12}}{\partial x_2} = \frac{x_2 - x_1}{r_{12}} = -\frac{\partial r_{12}}{\partial x_1} \tag{8}$$

Using Cartesian coordinates, there are 24 equations of motion for this four-atom system.

In Fig. 1b we show an alternative coordinate system for the same four atoms. In the absence of an external force, the center of mass remains stationary. There is therefore no need to include the $\mathbf{R}_{oc}$ coordinate in the motion. The dynamics reduces to 18 equations of motion in three coordinates, $\mathbf{r}_{12}$, $\mathbf{r}_{34}$, and $\mathbf{R}$. These are called the Jacobi coordinates. Instead of the masses of the individual atoms appearing in the Hamiltonian, we now have the reduced masses, μ_{12}, μ_{34}, and μ:

$$\mu_{12} = \frac{m_1 m_2}{m_1 + m_2}; \qquad \mu_{34} = \frac{m_3 m_4}{m_3 + m_4}; \qquad \mu = \frac{(m_1 + m_2)(m_3 + m_4)}{m_1 + m_2 + m_3 + m_4} \tag{9}$$

The Hamiltonian becomes

$$H = \frac{\mathbf{p}_{r12} \cdot \mathbf{p}_{r12}}{2\mu_{12}} + \frac{\mathbf{p}_{r34} \cdot \mathbf{p}_{r34}}{2\mu_{34}} + \frac{\mathbf{p}_R \cdot \mathbf{p}_R}{2\mu} + V(\mathbf{r}_{12}, \mathbf{r}_{34}, \mathbf{R}) \tag{10}$$

The "bond" vectors $\mathbf{r}_{12}$ and $\mathbf{r}_{34}$ are particularly suited to the usual parametrization of the potential. However, the "translational" coordinate $\mathbf{R}$ is a little less "natural" for the potential. Since we require $\mathbf{r}_{12}$, $\mathbf{r}_{34}$, and $\mathbf{R}$ to be independent variables, in order to apply the chain rule, we must express $\mathbf{r}_{13}$ and $\mathbf{r}_{24}$ in terms of the three independent variables:

$$\mathbf{r}_{13} = \frac{m_2}{m_1 + m_2}\mathbf{r}_{12} + \mathbf{R} + \frac{m_4}{m_3 + m_4}\mathbf{r}_{34}$$
$$\mathbf{r}_{24} = -\frac{m_1}{m_1 + m_2}\mathbf{r}_{12} + \mathbf{R} - \frac{-m_3}{m_3 + m_4}\mathbf{r}_{34} \tag{11}$$

Thus, the price to be paid for the reduction in the number of equations of motion is a slight increase in the complexity of the equations needed to evaluate the $\mathbf{r}_{ij}$, and hence the potential. Potential derivatives including $\mathbf{R}$ would appear in the following way:

$$\frac{\partial V}{\partial R_x} = \frac{\partial V}{\partial r_{13}}\frac{\partial r_{13}}{\partial R_x} + \frac{\partial V}{\partial r_{24}}\frac{\partial r_{24}}{\partial R_x} \tag{12}$$

with

$$\frac{\partial r_{13}}{\partial R_x} = \frac{1}{r_{13}} \tag{13}$$

and so on.

This particular choice of coordinates seems eminently reasonable for a diatom-diatom collision. On the other hand, let us say that a reaction occurs and the products are a triatom and an atom (see Fig. 2). The Cartesian coordinates are now as appropriate as before, whereas the Jacobi coordinates are rather less useful for visualization purposes. However it must be emphasized that the trajectory can still be integrated in these conditions. (In general, you will see in the remainder of this book that the choice of coordinates is crucial in quantum mechanical calculations; it is far less important in classical mechanics.) In general, it is worthwhile using Jacobi coordinates for three- and four-atom systems.

III. INITIAL AND FINAL CONDITIONS

Choosing the appropriate initial values of the positions and the momenta for each trajectory is not a trivial problem. First, imagine that the colliding species are rigid bodies. As can be clearly seen in Fig. 3, the outcome of the collisions in Figs. 3a,b will be very different. In the former, the molecules are oriented so that their bonds are parallel, the collision will be almost "head on," and the speed with which the species collide (indicated by the size of the arrow) is high. By contrast, in Fig. 3b, the bonds of the molecules are perpendicular to each other, the collision is glancing, and the collision speed is low. We consider each of these conditions on the following page.

(a)

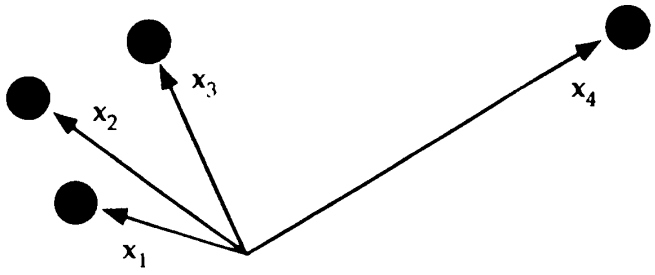

(b)

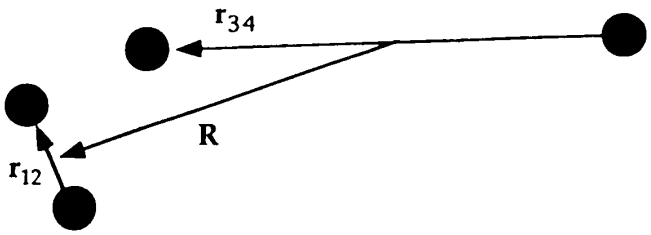

Figure 2 (a) Cartesian coordinates for 123 + 4 reactive products of reaction between diatoms in Fig. 1. (b) Jacobi coordinates of same species.

(a)

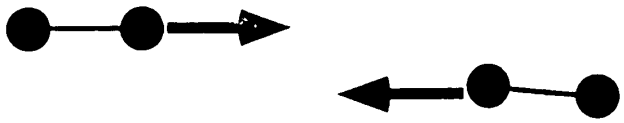

(b)

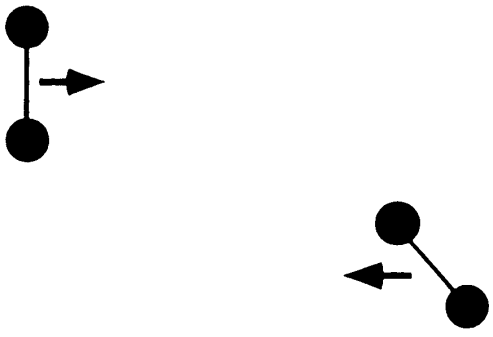

Figure 3 Possible collision conditions for two diatomic molecules: (a) head on, hard collision, with diatom bonds almost parallel; (b) glancing, soft collision, with bonds almost perpendicular.

A. Collision Speed and Impact Parameter

The speed with which the reactant molecules collide is obtained from the collision energy. (If thermal rate constants are to be obtained, many values of the collision energy must be sampled (see below).) Referring to Fig. 2, we see that if $R = |\mathbf{R}|$ is sufficiently large, the potential energy reduces to the sum of the diatomic potentials in the 12 and 34 molecules, $V(\mathbf{r}_{12}, \mathbf{r}_{34}, \mathbf{R}) \rightarrow V(r_{12}) + V(r_{34})$. The internal energy of the 12 (34) diatom is then

$$\varepsilon_{k\ell} = \frac{1}{2\mu_{k\ell}} \mathbf{P}_{k\ell} \cdot \mathbf{P}_{k\ell} + V(r_{k\ell}) \tag{14}$$

where $k\ell = 12$ (34). Thus the intermolecular translation energy is, from Eq. (10), $E_T = (1/2\mu)\mathbf{p}_R \cdot \mathbf{p}_R$. It is convenient to assume the initial relative motion is along the z axis. Thus, the initial $\mathbf{p}_R$ vector is $(0, 0, -(2\mu E_T)^{1/2})$, where the minus sign ensures that the molecules approach each other.

Next we consider the starting values for the intermolecular position vector $\mathbf{R}$. In the absence of any intermolecular potential, the 34 diatom would move past the 12 diatom with constant speed along the z axis. Clearly the closest distance of approach of the diatoms will be $(R_x^2(t = 0) + R_y^2(t = 0)^{1/2}$. This distance is referred to as the "impact parameter," b. It is convenient (but not necessary) to place the $\mathbf{R}$ vector initially in the (x, y) plane. Thus the initial choice for $\mathbf{R}$ is $(b, 0, z_0)$ where z_0 is some distance chosen so that the starting value of $R = (b^2 + z_0^2)^{1/2}$ is sufficiently large that the intermolecular potential is negligible. For applications in which the collision process of interest continues out to large impact parameters, z_0 can be chosen to be a function of b, with $z_0(b)$ decreasing so that the trajectory does not run an unnecessarily long time. For instance, if the intermolecular potential is negligible for $R \geq R_c$ then $z_0(b) = (R_c^2 - b^2)^{1/2}$ is a reasonable choice.

The angular momentum of the relative intermolecular motion is given by $\mathbf{L} = \mathbf{R} \times \mathbf{p}_R$. If the initial values suggested here are used, then $\mathbf{L} = (0, b(2\mu E_T)^{1/2}, 0)$. This form is particularly convenient for monitoring conservation of angular momentum during the collision.

Note that even if the trajectory is not to be integrated in Jacobi coordinates, the Hamiltonian has to be expressed in terms of an intermolecular coordinate at some point to set up the intermolecular motions correctly. These coordinates can then be transformed back into the coordinates used for the integration.

B. Internal Coordinates

The selection of the coordinates and momenta within each reactant fragment is not a simple task if it is to be done rigorously. Just how much rigor is required is a function of the problem being studied.

We begin the discussion by considering a simple problem. If the fragment is considered to be a rigid body, then its orientation is determined by the use of Euler angles (1). Define some convenient Cartesian coordinate systems $\mathbf{X} = (X, Y, Z)$ centered at the fragment's center of mass and fixed within the fragment. The rigid-body fragment can be rotated into any new orientation in a space-fixed coordinate frame centered at the fragment's center of mass, $\mathbf{x} = (x, y, z)$. Since the dynamics will be run in a space-fixed coordinate system, but the internal "features" of a fragment are described using a body-fixed system, this is an important step. This transformation is effected by the repeated

action of rotation about the body-fixed axes (8). We define the rotation matrix for rotation in a counterclockwise direction about the Z axis, $R_Z(\alpha)$, by

$$\mathbf{R}_Z(\alpha) = \begin{pmatrix} \cos\alpha & \sin\alpha & 0 \\ -\sin\alpha & \cos\alpha & 0 \\ 0 & 0 & 1 \end{pmatrix} \tag{15}$$

$\mathbf{R}_Y(\alpha)$ is defined analogously.

Now the new coordinates are given by (8)

$$\mathbf{x} = \mathbf{R}_Z(-\phi)\mathbf{R}_Y(\theta)\mathbf{R}_Z(-\eta)\mathbf{X} \tag{16}$$

where $0 \leq \phi \leq 2\pi$, $0 \leq \eta \leq 2\pi$, and $0 \leq \theta \leq \pi$.

For instance, if we are concerned with a diatomic molecule, it is convenient to set the bond initially along the Z axis. Thus, $\mathbf{X} = (0, 0, r_e)$, where r_e is the equilibrium bond length. After the transformation, the space-fixed coordinates are r_e (sin θ cos ϕ, sin θ sin ϕ, cos θ), corresponding to the usual spherical polar coordinates.

The momenta can be transformed analogously:

$$\mathbf{p}_x = \mathbf{R}_Z(-\phi)\mathbf{R}_Y(\theta)\mathbf{R}_Z(-\eta)\mathbf{p}_X \tag{17}$$

Thus, if the diatom is rotating, then we can choose the momentum, p_0, to be in any direction perpendicular to the Z axis, say along Y. The transformed momentum is

$$\begin{aligned} p_x &= p_0(-\cos\theta\cos\phi\sin\eta - \sin\phi\cos\eta) \\ p_y &= p_0(-\cos\theta\sin\phi\sin\eta + \cos\phi\cos\eta) \\ p_z &= p_0(\sin\theta\sin\eta) \end{aligned} \tag{18}$$

The above conditions are the usual initial conditions for carrying out calculations on a rigid rotor (14). In most cases, once the $\mathbf{X}$ and $\mathbf{p}_X$ for each atom in a fragment have been selected within the fragment, Eqs. (16) and (17) can be used to transform the coordinates.

Choosing the value of p_0 to be used is an interesting problem in itself. Quantum mechanically, the expectation value of the square of angular momentum is $\hbar^2 j(j+1)$, where the integer j is the rotational quantum number. Classically, of course, there is no need to restrict any variable to discrete values. However, the practice is generally to carry out the trajectory calculation with variables such as the energy and the angular momentum restricted to quantum mechanical values. When this is done, the calculations are often termed *quasi*classical trajectory calculations. The choice of $p_0 = \hbar\sqrt{j(j+1)}/r_e$ in Eqs. (18) reproduces both the quantum mechanical angular momentum and the rigid rotor energy for a given value of j.

C. Monte Carlo Selection of Initial Conditions

Before we proceed to the more complicated case of nonrigid species, it is perhaps appropriate to discuss the selection of initial conditions for rigid body trajectories. Whether a particular event (for instance, a rearrangement reaction) occurs during a given trajectory is clearly a function of the initial conditions for that trajectory. Each trajectory constitutes a binary trial, having the possible outcomes: 1 (event occurs); or 0 (event does not occur). Clearly, sufficient individual tries have to be made that the result is statistically significant. To do this one must sample over the "uninteresting" variables.

One can do this in two possible ways. One is to sample systematically. For instance, if one is interested is understanding in great detail how the reactivity of a planar collision

varies with the orientation of one of the diatoms, then one could observe the outcome as a function of θ_2, for fixed b, θ_1.

However, for the calculation of observables, usually far more dimensions have to be sampled. In such cases systematic sampling of each variable in turn is impractical. It is here that Monte Carlo methods are usually employed. For instance, the cross section for reaction at fixed collision energy of an atom with an initially rigid diatom is given by (7,8,14)

$$\sigma^R(E_T) = 2\pi \int_0^\infty db\, b \int_0^\pi \sin\theta\, d\theta \int_0^{2\pi} d\phi \int_0^{2\pi} d\eta\, P^R(b, \theta, \phi, \eta) \tag{19}$$

where $P^R(b, \theta, \phi, \eta)$ is the probability of the reaction occurring at given (b, θ, ϕ, η). This is handled in the Monte Carlo approach by sampling over initial (b, θ, ϕ, η) points, recording the binary outcome (one or zero) originating from each initial point, then approximating the integral as a sum. In the absence of prior information about the outcome of a collision, it is traditional to randomly sample each variable "flat" (that is, with each value having the same likelihood of being selected) on its interval.

The integrals over ϕ and η are already of this form. Thus we choose

$$\phi = 2\pi\xi_\phi, \qquad \eta = 2\pi\xi_\eta \tag{20}$$

where the ξ are random numbers which are themselves "flat" on the interval [0, 1]. (For most applications, the random number generators supplied with most FORTRAN or C compilers work quite adequately.)

On the other hand, θ, although it has to be sampled on the interval 0 to π, has its contributions to the integral not weighted evenly. So rather than sample θ flat on $[0, \pi]$, then weight each trajectory by the sin θ selected, the variable is transformed. This can be done by making the substitution $\alpha = -\cos\theta$. Then $\int_0^\pi \sin\theta\, d\theta \rightarrow \int_{-1}^1 d\alpha$. Therefore, the θ is selected using

$$\alpha = 2\xi_\alpha - 1 \tag{21}$$

or equivalently

$$\cos\theta = 2\xi_{\cos\theta} - 1 \tag{22}$$

For the impact parameter integral, some decisions need to be made. Again it is required that the variable be sampled flat from some distribution. Unfortunately, b has the upper limit of ∞. The simplest way to accommodate this is to use one's knowledge of the interaction potential (or some preliminary dynamical calculations) and determine a reasonable cut off value, $b_{\max}$. Then $2\pi \int_0^{b_{\max}} db\, b \rightarrow \pi \int_0^{b_{\max}^2} d\alpha$, where $\alpha = b^2$. This is,

$$b = \sqrt{\xi_b}\, b_{\max} \tag{23}$$

One possible problem with this approach is that it weights high-impact parameters much more than low ones, whereas often the events of interest occur at low-impact parameters. One way around this is to utilize importance sampling for the impact parameter (7,8,15). This would be the preferred approach if some prior knowledge of $P^R(b)$ is available. An alternative approach is to calculate the probability at fixed b values, then perform a numerical weighted quadrature to obtain the cross section. The latter can be used if there is very little initial information available, especially when the dynamics are expensive to run.

Other variables may not be as easy to transform onto a flat interval as were those above. For instance, if a rotational state is to be selected for a diatomic rigid rotor whose energy is given by $E_j = Bj(j + 1)$. The weighting of each j state in a canonical distribution at temperature T is

$$w(j) = (2j + 1)e^{-E_j/k_BT} \tag{24}$$

where k_B is the Boltzmann constant. (We have assumed that odd and even j states have equal statistical weighting.) The rigid rotor partition function is given by

$$q_j(T) = \sum_{j=0}^{\infty} (2j + 1)e^{-E_j/k_BT} \tag{25}$$

For widely spaced rotational levels, it is inappropriate to approximate the sum with an integral. Our task, then, is to choose an initial value of j for each trajectory, given that each j has an associated probability, $p(j) = w(j)/q_j$. This can be done by realizing that the cumulative probability, $p_j^{\text{cum}} = \Sigma_{j=0}^{j'} p(j)$, tends to unity as $j' \to \infty$. That is, one can select a random number, ξ, flat on [0, 1] and look up the j' value whose p^{cum} is closest to ξ.

An alternative method, which is much more powerful for selecting from a set of many variables, but is mostly clearly understood with one variable, is the von Neumann rejection technique (15). First choose some $j_{\max}$, such that $j > j_{\max}$ is highly unlikely at the temperature of interest. Now select a j on the interval 0 to $j_{\max}$,

$$j = \xi_1 j_{\max} \tag{26}$$

and determine $p(j) = w(j)/q_j$. Now select a fresh random number, ξ_2. If $p(j) > \xi_2$ then that j value (suitably rounded to an integer) is accepted; if not, it is rejected, another j value is selected, and a new comparison carried out. This continues until an acceptable value of j is obtained. The power of this method is that there is no need to "invert" from cumulative probability function to the independent variables. While this inversion is trivial for a single variable, it is usually infeasible in many variables.

D. Initial Conditions for Nonrigid Species

In reality, even if a molecular species is at absolute zero, it will contain vibrational zero-point energy quantum mechanically. How to build this into a classical trajectory calculation is one of the enduring problems in this field.

Let us first consider a diatomic molecule, for instance one with a harmonic potential in its vibrational ground state. One possibility is to start the calculation with the diatom at its equilibrium bond length; that is, with $r = r_e$. Indeed, if rotational excitation is the only process of interest, molecules are often treated as rigid bodies with their bonds frozen at their equilibrium bond lengths. These lengths can be maintained throughout the collision by the use of Lagrange multipliers (8,14).

On the other hand, the energy of the harmonic vibrational eigenstates is well known:

$$\epsilon_v = (v + 1/2)\hbar\omega \tag{27}$$

where v is the vibrational quantum number and ω is the angular frequency of the oscillator. In order that the classical and quantum calculations have the same total energy, this vibrational energy has to be put into classical vibrational motion of the diatom.

However, it is clear that the probability density distributions of the classical and quantum oscillations are quite different, particularly for low values of v: the quantum oscillation has the largest probability density near $r = r_e$; the classical probability density (the "residence time") is greatest at the turning points.

Therefore, whether the zero-point vibrational energy for collisions which originate in the vibrational ground state should be included or not has been the matter of some debate. Some authors (16) have maintained that the classical probability density distribution during reactive collisions resembles that of a quantum wave packet more closely if the zero-point energy (ZPE) is excluded. On the other hand, a very large number of calculations of reactive bimolecular reactions involving diatoms (4–8,10) have shown that agreement with experiment and with quantum calculations is much better if ZPE is included. Similarly, it has been shown (17,18) that clusters behave too rigidly if dynamics are initiated with the cluster at its minimum potential energy geometry. Better agreement with experimental data has been obtained if at least some ZPE is included.

The usual practice with a diatom, then, is to add kinetic energy in r, such that the total energy in the diatom is equal to the vibrational energy eigenvalue for the selected vibrational quantum number, ϵ_v. Now both r and p_r must be appropriately chosen, such that

$$\epsilon_v = \frac{p_r^2}{2\mu} + V(r) \tag{28}$$

where μ is the reduced mass of the diatom.

The harmonic oscillator model ($V = kx^2/2$) for a diatom is an instructive example. Following the spirit of the quasiclassical method, once the vibrational quantum number is determined the oscillator is assigned the energy corresponding to the quantum mechanical energy eigenvalue (eq. (29)). Newton's equation for the harmonic oscillator is

$$\frac{d^2x}{dt^2} + \omega^2 x = 0 \tag{29}$$

where $x = r - r_e$ and $\omega^2 = k/\mu$, where k is Hooke's law constant.

The general solution of the differential equation is elementary and is

$$x = x_0 \sin(\omega t + \delta) \tag{30}$$

where x_0 is the outer turning point of the vibrational motion and is equal to $(2\varepsilon_v/k)^{1/2}$. The motion has period $2\pi/\omega$. However, note that each x value is visited twice each period. Therefore at time $t = 0$, x can be selected by setting $\delta = \pi\xi$, where ξ is flat on [0, 1]. Clearly then $r = r_e + x$. The initial momentum is found using

$$\dot{x} = \pm(2\varepsilon_v/\mu - \omega^2 x^2)^{1/2} \tag{31}$$

Clearly $\dot{x}$ is double valued for each x. The sign can be chosen using a random number:

$$\text{sign} = \begin{cases} + & \text{if } \xi - 0.5 > 0 \\ - & \text{if } \xi - 0.5 < 0 \end{cases} \tag{32}$$

Then $p_r = \mu\dot{x}$.

We now show that the value of x selected above is the same as would be chosen from a Monte Carlo method. The probability of finding the oscillator within dx of x is inversely proportional to $\dot{x}$ (the slower x is traversed, the more chance of finding the system near that x value).

That is,

$$p(x)\,dx \propto \frac{dx}{\omega x_0 \cos(\omega t + \delta)} = \frac{dx}{\omega(x_0^2 - x^2)^{1/2}} \tag{33}$$

The cumulative probability function, $P^{\text{cum}}(x')$, is then

$$\begin{aligned} P^{\text{cum}}(x') &= \int_{-x_0}^{x'} dx\,(x_0^2 - x^2)^{-1/2} \Big/ \int_{-x_0}^{x_0} dx\,(x_0^2 - x^2)^{-1/2} \\ &= 1 - \pi^{-1} \arccos\left(\frac{x'}{x_0}\right) \end{aligned} \tag{34}$$

By equating $P^{\text{cum}}(x)$ with a random number, ξ, and performing elementary manipulation we obtain

$$x = -x_0 \sin \pi\xi \tag{35}$$

which is the same result as above with an unimportant sign change.

For more realistic models of the diatom potential, for instance a Morse function, the dynamics is more complicated. For a nonrotating Morse potential, the necessary analytical equations have been worked out (8). For a rotating diatom, however, the problem is more complex. The best approach in this case is one based on the concept of action-angle variables for periodic motions (1). Porter et al. (19) give one recipe. More recently, Eaker (20) has proposed a method based on a Fourier analysis (21) of the motion.

For polyatomic molecules, the problem is more complicated. For small-amplitude motion, certainly one can decompose the motion into independent harmonic (normal mode) motion and treat each of these as was done for a single oscillator. If the system has significant anharmonicity, then the "good" action-angle variables must first be found. Such techniques are available in the literature (8,21–25).

For large molecules or clusters, however, different approaches are necessary. These are beautifully reviewed in the paper by Raff and Thompson (8); we refer the interested reader there for more details.

The most comprehensive trajectory code which is commercially available is VENUS, from the group of Hase (26). This code is extremely well documented.

E. Final Conditions

After the collision is considered complete, the final conditions must be considered. First, a strictly qualitative outcome (such as whether reaction has occurred or not) is usually easily determined. Other clearly classical variables such as relative product speeds and scattering angles are fairly obviously defined.

In Cartesian coordinates, the center of mass of a fragment containing n atoms is

$$\mathbf{x}^{\text{c.m.}} = \sum_{i=1}^{n} m_i \mathbf{x}_i \Big/ \sum_{i=1}^{n} m_i \tag{36}$$

The velocity of the center of mass is clearly

$$\dot{\mathbf{x}}^{\text{c.m.}} = \sum_{i=1}^{n} m_i \dot{\mathbf{x}}_i \Big/ \sum_{i=1}^{n} m_i = \sum_{i=1}^{n} \mathbf{p}_i \Big/ \sum_{i=1}^{n} m_i \tag{37}$$

The relative velocity between two fragments, ℓ and k, is simply $\dot{\mathbf{x}}_{\ell k} = \dot{\mathbf{x}}_{\ell}^{\text{c.m.}} - \dot{\mathbf{x}}_{k}^{\text{c.m.}}$.

Scattering angles are usually measured relative to some initial velocity vector, $\mathbf{v}_0$ (for instance, the relative velocity of the colliding diatoms considered in Sec. III.A). Then $\theta_\ell = \arccos(\dot{\mathbf{x}}_{\ell}^{\text{c.m.}} \cdot \mathbf{v}_0 / |\dot{\mathbf{x}}_{\ell}^{\text{c.m.}}| \, |\mathbf{v}_0|)$.

It is less obvious how to assign quantum variables. While, for instance, the total classical angular momentum of a collision fragment is clearly defined, in the case of small fragments product rotational quantum numbers are typically sought. The standard procedure for linear molecules is to assume rigid rotor conditions and to solve the usual correspondence principle relations to obtain the quasiclassical product quantum numbers (restricted to integer values).

The quasiclassical recipe is followed as before, setting

$$\mathbf{J} = |\mathbf{r} \times \mathbf{p}_r| = \hbar\sqrt{\tilde{j}(\tilde{j} + 1)} \tag{38}$$

which is solved to yield

$$\tilde{j} = \sqrt{\left(\frac{J}{\hbar}\right)^2 + \frac{1}{4}} - \frac{1}{2} \tag{39}$$

where the tilde indicates that the classical calculation will not necessarily yield an integer value for j.

For nonlinear molecules, the situation is more complex (24).

For a diatom (as for a separable vibrational mode in a polyatomic) the product vibrational quantum number is found from the Bohr-Sommerfeld quantization conditions: namely that $\oint p_r \, dr = (v + 1/2)h$ for bound motions (27). That is, if the momentum is followed over one half-period the product vibrational action can be calculated:

$$\tilde{v} + \frac{1}{2} = \frac{1}{\pi h} \int_{r_-}^{r_+} \left(2\mu\left(\varepsilon - V(r) - \frac{J^2}{2\mu r^2}\right)\right)^{1/2} dr \tag{40}$$

Here r_+ and r_- are the outer and inner turning points of the vibrational motion. J is the magnitude of the rotational angular momentum, $|\mathbf{r} \times \mathbf{p}_r|$. The tilde over the v emphasizes that the quasiclassical value of the vibrational quantum number will, in general, not be an integer.

For polyatomics, the approach of Schatz et al. (22–25) provides the most practical techniques.

F. Observables

Observables, such as cross sections and rate constants, can be extracted from the output of the trajectory calculations. Again, the event of interest must be clearly defined. For instance, in an AB + CD collision, the event of interest may be reaction to ABC + D whether this has occurred is relatively easily determined. As was outlined in Sec. III.C, each trajectory which satisfies the condition is weighted with 1, else 0. The event of interest, however, could be more detailed. If, for instance, one wished to compare with quantum (or experimental) results in which the process AB(v = 0, j = 0) + CD(v = 0,

$j = 0) \rightarrow AB(v', j') + CD(v'', j'')$ were studied, the appropriate classical events must be defined. Typically, product vibrational and rotational (noninteger) quantum numbers $(\tilde{v}, \tilde{j})$ are "binned" to the nearest integer values. (Occasionally, the rotational quantum numbers are additionally restricted to odd or even values (8,14).)

The integral cross section for this process is then $\sigma_{00,00\rightarrow v'j',v''j''}(E_r)$, and it is given by an equation analogous to Eq. (19), with sampling over the angles θ, ϕ, η for both AB and CD, and the vibrational phases of each diatom as well as the impact parameter. The reaction cross section now becomes (5–8)

$$\sigma^R(E_T) \approx \pi b_{\max}^2 \frac{N^R}{N} \tag{41}$$

where N^R is the number of reactive trajectories sampled over the initial conditions, and N is the total number of trajectories sampled.

If a sufficiently large number of trajectories is run, the standard deviation in the cross section is approximately given by (5–8)

$$s = \sigma^R \times \left(\frac{N - N^R}{NN^R}\right)^{1/2} \tag{42}$$

Another observable of interest is the differential cross section. Typically the product attribute scanned is the scattering angle, θ, between the initial velocity vector and the c.m. velocity vector of some fragment of interest. This measure (5–8,14) is

$$\frac{d^2\sigma^{event}(\theta)}{d\omega^2} = \frac{\pi b_{\max}^2 P^{event}(\theta)}{2\pi \sin\theta} \tag{43}$$

As with v and j, the angle variable is also typically "binned" (7,8,14).

Rate constants can be obtained directly by Monte Carlo sampling the initial energies for a canonical distribution. Alternatively, cross sections at several energies can be carried out, and the rate constant at temperature T obtained by taking the appropriate integral (5–8) over the translational energy:

$$k^{event}(T) = \left(\frac{2}{k_B T}\right)^{3/2} \frac{1}{(\pi\mu)^{1/2}} \int_0^\infty dE_T\, E_T \sigma^{event}(E_T) \exp\left(\frac{-E_T}{k_B T}\right) \tag{44}$$

IV. CAVEATS

A. Tunneling

One major caveat concerning the usefulness of trajectory calculations is the problem of tunneling. That is, whenever a classical trajectory approaches a potential energy barrier with less energy than the energy of the barrier maximum, the trajectory is completely reflected. By contrast, a quantum mechanical system with the same energy will have a nonzero probability of transmission through the barrier. In bimolecular reactions, the fact that trajectories are somewhat less adiabatic than is quantum dynamics somewhat compensates for the lack of tunneling (28). Occasionally, techniques have been devised to incorporate some form of tunneling into a trajectory calculation (29–31). Clearly, the greatest danger from inaccuracy due to tunneling is in a system in which there are multiple barriers which must be overcome consecutively.

B. Adiabatic Leak

Another, potentially far more devastating, weakness in classical mechanical methods is the problem of "adiabatic leak" (32–38). The difficulty arises from the fact that in quantum mechanics, bound modes are constrained to contain at least the ZPE for that mode. Classical mechanics has no such restrictions. Even if ZPE is initially put into a mode in classical mechanics, it can "leak" out during the course of a trajectory. Thus it is quite possible to have (in the simplest case) a diatomic molecule as the product of a reactive trajectory containing less energy than the vibrational ZPE. This is clearly unphysical.

Various strategies for dealing with this problem have been proposed. The simplest is to throw out those reactive trajectories which exhibit unphysical product energies (this can be total internal energy, vibrational energy, even rotational energy) (39–43). There is a disadvantage to this, however. Since the number of reactive trajectories is typically less than the number of unreactive trajectories, this method results in a decrease in the number of trajectories sampled from the reactive part of the initial phase space. This has the result of, in most cases, lowering the reaction probability below that for comparable quantum calculations. Recently, Varandas (43) has proposed an improved procedure in which the relative weightings of the trajectories sampled in the reactive and nonreactive portions of phase space are adjusted to reflect this. In all these approaches Hamilton's equations are numerically solved in the usual way with the normal quasiclassical initial conditions, and the statistical weighting of individual trajectories is adjusted *after* the trajectory is complete. Varandas refers to these as "nonactive" methods.

More subtle than the lack of ZPE in bound modes *after* the collision is the problem of ZPE *during* the collision. For instance, as a trajectory passes over a saddle point in a reactive collision, all but one of the vibrational (e.g., normal) modes are bound. Each of these bound modes is subject to quantization and should contain ZPE. In classical mechanics, however, there is no such restriction. This has been most clearly shown in model studies of reactive collisions (28,35), in which it could be seen that the classical threshold for reaction occurred at a lower energy than the quantum threshold, since the classical trajectories could "pass under" the quantum mechanical vibrationally adiabatic barrier to reaction. However, this problem is conspicuous only near threshold, and may even compensate somewhat for the lack of tunneling exhibited by quantum mechanics. One approach in which ZPE for local modes was added to the potential energy (44) has had some success in improving reaction threshold calculations.

This phenomenon of ZPE leak can, however, have drastic consequences in studies of energy flow within molecules and unimolecular decomposition. There the problem is that classical mechanics does not "lock up" the ZPE energy in the correct modes (as quantum mechanics does), and hence that the (conserved) energy is free to be elsewhere. In particular, if that energy is free to cross barriers, then energy flow can be unrealistically (again, in comparison to quantum mechanics) fast. One striking consequence is the observation of cold $(HF)_n$ clusters evaporating via the transfer of ZPE from HF internal vibration to intermolecular modes (38).

Attempts to deal with this aspect of the ZPE problem have been referred to (43) as "active" methods. The earliest proposed techniques were those of Miller et al. (45) and Bowman et al. (46). These methods were essentially the same. They both introduced a constraint into the dynamics which reflects back trajectories attempting to enter that region of the phase space which would allow that mode to have less than its ZPE. A

similar method has been suggested by Varandas and Marques (40). One difficulty with these approaches is that, although they conserve total energy, they fail to conserve angular momentum (since at the reflection point, momenta **p** are switched to $-\mathbf{p}$). A technique which ameliorates this problem has been suggested by Lim and McCormack (47), who replace the reflecting hard wall in phase space with a sticky wall, which deflects the dynamics out of the forbidden, sub-ZPE region, but adjusts the new momenta and positions so that angular momentum remains conserved. Peslherbe and Hase (48) have recently reconsidered the concept of simply transforming $\mathbf{p} \rightarrow -\mathbf{p}$ at the point the trajectory enters a quantum mechanically "forbidden" region of phase space. One conclusion they came to is that, if the appropriate coordinates are carefully chosen, then both linear and angular momentum can be simultaneously conserved.

Recently, a ZPE-preserving method based on taking the classical limit of the Hamiltonian has been proposed (49). The trajectory so formed is referred to as the reference trajectory. The trajectories using the full Hamiltonian are then shifted with respect to the reference, and cannot, by construction, lose ZPE.

An alternative philosophy is to construct a classical trajectory which is not a solution of an initial value problem. Such constrained trajectories would no longer obey Hamilton's equations, but would extremize the classical action subject to certain dynamical constraints (50–52).

More testing of these approaches is certainly required before any final pronouncements on their worth can be made. One important contribution to assessing the ideas was that of Sewell et al. (53). For a system of coupled oscillators, they showed that the constraints of Miller et al. and Bowman et al. (45,46) may induce physically undesirable effects. In particular, they gave an example of a trajectory in the quasiperiodic regime being transformed into a chaotic one by the action of the constraints.

On the other hand, a recent study of energy flow in CH_3OOCH_3 (54) reported qualitative agreement with RRKM analysis and with experimental rate constants, using the Miller et al. (45) method.

C. Electronic Nonadiabaticity

Another assumption made in the straightforward application of classical mechanics to atomic motions is the Born-Oppenheimer approximation. That is, for each atomic geometry there is a single electronic potential energy surface under whose influence the atoms move. In reality, there are geometries at which more than one surface can play a role. The simplest such case is where two potentials (in the so-called diabatic picture) cross each other.

In those cases where the dynamics cannot be adequately described by motion on a single adiabatic potential-energy surface, additional dynamical assumptions must be made. The pioneering technique is the trajectory surface hopping (TSH) method (55,56) of Tully and co-workers. In these calculations, the classical trajectories are integrated on an adiabatic potential energy surface (typically generated by diatomics in molecules, DIM (57)) until they reach the vicinity of an avoided crossing. At this point, the probability of the trajectory hopping to another adiabatic surface is determined using a local Landau-Zener probability. When a hop occurs, the momenta must be adjusted to conserve energy (58). Both the hopping and nonhopping trajectories are then further integrated on the appropriate adiabatic surface until they either hop again or reach the asymptotic region.

If many hops occur along a single trajectory, different strategies (55,56,59) have been devised to avoid the necessity of following an excessive number of trajectories.

There are several variations to this basic technique. Determining the exact location of the avoided crossing has been the subject of some discussion (60,61). Blais and Truhlar (62) avoid the local hop criterion by computing the semiclassical probability for each surface along the trajectory (63). Whenever the probability of being on the current surface drops below 0.5, a random number is generated to determine whether a hop should occur, and to which surface. The technique has been applied to quenching of Na* by H_2 (62,63) and the $H_2^+ + H_2$ system (64). A similar procedure was proposed and tested by Parlant and Gislason (65). Dunne et al. (66) have proposed a method in which the Liouville equation for the electronic density matrix is computed along the trajectory. Several of these approaches have been critically compared (67).

Recently the surface-hopping technique has been extended to cope with electronic transitions in molecular dynamics simulations. Tully (68) has presented a general theory and a specialization (69) to proton transfer reactions in solution.

V. APPLICATIONS

A. Gas-Phase Bimolecular Reactions

Classical trajectory calculations on A + BC and AB + CD reactions through 1990 have been reviewed previously (10).

The $H + H_2$ reaction is now able to be treated with great accuracy by a variety of quantum mechanical methods, many of which will be described elsewhere in this book. Occasionally, though, classical calculations are still done in order to explore the origin of features of dynamics. In a series of papers, Aoiz et al. (70–73) have carried out extremely detailed calculations on this system. Some discrepancy between cross sections into different rotational states was noted. Otherwise agreement was surprisingly good between classical and quantum mechanics. Persky and Kornweitz (74) have observed oscillations in the $\sigma^R(E_T)$ for $D + H_2$ ($v = 1$) reactions.

The $F + H_2$ reaction continues to be of interest (75–80). Calculations on $F + D_2$ have been carried out recently on an extremely accurate potential surface (78) and are in remarkably good agreement with crossed beam experiments. Branching between the products in F + HD has been explored (79,80). The $F + H_2$ reaction was recently revisited using an improved surface. Kornweitz et al. (82) have probed steric effects in O + HCl. "Peripheral" chemical reactions have also been modeled (83). Collision-induced dissociation in $Rg + X_2$ was recently studied (84).

The reactions containing the atoms H, N, and O have been investigated (85). Systems like this, in which the surface possesses deep wells which lead to long-lived complexes, are still beyond the reach of quantum mechanical methods. Similar long-lived three atom systems, of interest in combustion, are those containing OOH (86,87). The atmospherically important reactions $N + NO \rightarrow N_2 + O$ and $N + O_2 \rightarrow NO + O$ have been studied (88–91).

Various other complex-forming reactions have also been investigated using the trajectory method. For instance, the effect of translational energy on the interhalogen reaction F + ICl has been addressed (92). Complex formation in the $Br + I_2$ reaction has been studied both by simulations and experiment (93). The differential cross section was the chief focus of a study of the reaction $Cl + ICH_3 \rightarrow ClI + CH_3$ (where the CH_3

was treated as a pseudoatom (94). The effects of collision energy, rotational state, and orientation on the $O(^3P) + I_2$ reaction have been explored (95,96). The reaction of $O(^1D)$ with H_2 (also complex forming) has been studied using trajectory surface hopping on DIM surface (97).

A review of four-atom reaction dynamics was recently published (98). Classical trajectory treatments include those on the $OH + H_2 \rightarrow H_2O + H$ reaction (or its reverse) (99–109) and the OH + CO reaction (110,111). Further calculations on the H_3O and HOCO systems have been carried out by Schatz (112) as well as calculations on H_4^+ and NHNO.

All the above calculations were carried out on relatively accurate potential energy surfaces. An interesting high-energy calculation of $N_2 + O_2$ using model surfaces was recently presented, in which reaction and dissociation channels were accessible (113).

The reaction $O + O_3 \rightarrow 2O_2$ was recently studied (114).

B. Ion-Molecule Reactions

A common prototype system for ion-molecule reactions is:

$$O^+ + H_2 \rightarrow OH^+ + H$$

One reason for this is that a single potential energy surface appears to be important in the dynamics. Using a model potential surface, González et al. (115) found good agreement with experimental values of $\sigma^R(E_T)$ at low collision energies. The effect of reactant rotation in $O^+ + H_2$ and isotopic variants has been examined (116).

Single surface QCT calculations have also been carried out on $B^+ + H_2 \rightarrow BH^+ + H$ (117). Agreement of $\sigma^R(E_T)$ with experiment was generally good.

The surface-hopping trajectory approach has been applied to reaction and collision-induced dissociation in $He + HD^+$ (118).

Extensive classical trajectory calculations of the S_N2 reaction

$$Cl^- + CH_3Cl \rightarrow CH_3Cl + Cl^-$$

reaction have been carried out (119–123). One important finding (119) was that vibration in the reactant C—Cl bond-enhanced reaction.

C. Unimolecular and Addition Reactions

Because of the many atoms involved in most unimolecular reactions of interest, classical mechanics is still, in many cases, the method of choice. The potential problems were discussed in Sec. IV.

Because the reaction has been the subject of considerable experimental activity, the overtone-induced dissociation of H_2O_2 has been frequency studied (124,125). In a model study based on HOO dissociation, Uzer and co-workers (126) compared classical and quantum dynamics.

Detailed comparisons of classical dynamics with statistical models have been carried out for systems as varied as N_2O predissociation (127), evaporation of $(Ar)_n$ clusters (128–130), and Al_3 dissociation (131).

The more exothermic "Coulomb explosion" of $(Ar)_n^{2+}$ has also been investigated by classical dynamics (132).

The *cis/trans* isomerization of HONO has been the subject of several studies in the gas phase (133–135) and in a Xe matrix (136). Raff (137–139) has investigated the dynamics of organic addition reactions in Ar matrices.

Thompson, Raff, and co-workers have carried out several gas-phase studies of disilane dissociation (140,141) and bond fission reactions (142,143).

Classical trajectories have also been used to study ring inversion in RDX (hexahydro-1,3,5-trinitro-1,3,5-triazine) in both the gas phase and a Xe bath (144).

Other systems studied include isomerization in malonaldehyde, using a model incorporating tunneling (30), and N inversion in aziridine (145).

In an interesting study, Chang et al. (146), have proposed the use of power spectra (Fourier transforms of $r(t)$) as a diagnostic tool for nonstatistical behavior in unimolecular decomposition.

The addition reaction $H + CH_3 \rightarrow CH_4$ has been investigated both in the gas phase (147) and in an inert gas cluster (18).

D. Clusters

Recently there has been considerable interest in experimentally studying gas-phase reactions in which atomic or molecular clusters are involved (148–154). One obvious motivation for this work is that inert species can act as a "solvent," and insight can be gained into the role that solvent molecules play in solution phase reactions. Such phenomena include "caging," in which the solvent sterically hinders the separation of reactants, and energy stabilization, in which a metastable species can become stable by losing internal energy to the solvent heat sink. Experimental studies which directly address such problems have recently been carried out. Lineberger and co-workers (152) studied the photodissociation and recombination of I_2 in mass-selected clusters, allowing them to investigate caging as a function of the number of molecules in the cluster. They showed that the caging efficiency increases dramatically as the solvent molecules form the first solvent "shell." Lallement et al. (153) considered the steric effects of solvation in the exchange reaction between Ba and N_2O solvated in argon. Naaman and co-workers (154) looked at the recombination reaction $O + CO \cdot R_n \rightarrow CO_2 + nR$, where R is a noble gas atom. Both groups found that the reactivity was dramatically affected by the number of noble gas atoms. In particular, the ability of the solvent to act as a "chaperone," removing excess energy from the CO_2, increased dramatically with the number of noble gas atoms. A trajectory model of this type of reaction using a single cluster atom has been carried out (155).

Clearly, the modeling of such systems is a many-body problem. At the very best, the solvent molecule motion will have to be treated using classical mechanics; if there are too many heavy species, the heavy particles may have to be treated as a thermal bath. The most widely applied methods of coupling the motion of the "primary" system (in which the equations of motion for each particle is solved numerically) and the thermal bath are the generalized Langevin (156) and the Langevin techniques (157,158). Typically, for few heavy reactant species, a full classical mechanical treatment will be employed. In some cases, however, reactants which contain light atoms have been treated using quantum mechanics, with the light atom dynamics usually solved in the mean field of the heavy species. A review of some of the methods employed has been recently published (149).

Trajectory simulations of intracluster reactions have been carried out. In a recent molecular dynamics study, Landman and co-workers (159) showed that gas-phase attachment reactions involving either $[Na_4Cl_3]^+$ or $[Na_{14}Cl_{12}]^{+2}$ and a Cl^- anion can be catalyzed by solvating the sodium chloride fragment in an argon cluster, which serves as a local heat reservoir. Hu and Hase (30,160,161) investigated the use of microclusters to simulate caging and other effects in association reactions. Hu and Martens (162,163) considered the specific case of iodine recombination in an argon microcluster and were able to demonstrate clearly the role which the evaporation of the Ar cluster plays in stabilizing the product I_2.

The simulation of dissociation of Br_2^- in $(Ar)_n$ and $(CO_2)_n$ clusters has been carried out (164). The calculations clearly show the "caging" of the solvent shell reported in the Lineberger experiments (152).

Clusters as "reactants" have also been studied. The fragmentation of Ar_{29} and Ne_{29} clusters in Xe^+ was simulated by Kolibiar et al. (165). The evaporation of Ar from an $(Ar)_{n-1}$ Xe^+ cluster after Ar impact has also been investigated (165). The formation of small doubly charged *p*-diffuorobenzene clusters is another example (167).

In a somewhat different vein, Cleveland and Landman (168) reported that the impact of the relatively large cluster of 561 argon atoms with a crystal surface results in the formation of a shock-wave-like region within the cluster and causes considerable damage to the surface.

There have been other classical dynamical simulations of the impact of clusters with surfaces, in which the emphasis was on the behavior within the cluster at impact. Even et al. (169) demonstrated that there were shock waves produced within the cluster. Other workers (170,171) have shown that diatomics can be efficiently dissociated on a very short time scale within such clusters. They suggest that this could open up a new area of "thermal femtochemistry."

Other groups have investigated the evaporation dynamics of clusters on impact with a surface (172–177). It has been suggested (177) that the fragmentation pattern might serve as a probe of cluster shape for small clusters.

In an interesting recent paper, McCoy et al. (178) looked at the classical dynamics in an $(HCl)_2$ dimer following excitation of one HCl bond.

E. Collisions at Solid Surfaces

The literature on dynamics at the gas-solid interface is vast (see, for instance (179–184)). The choice of topics considered here in some detail will clearly be highly subjective. We will focus on those studies which have most in common with the other topics in this chapter and in the entire volume. We will restrict ourselves to the following areas: (a) physisorption dynamics, (b) dissociative chemisorption of H_2 on metals, (c) Eley-Rideal processes, (d) photochemistry of adsorbed molecule, and (e) cluster-catalyzed chemisorption.

1. Physisorption

In an extremely detailed series of papers, Prisant and co-workers have examined the buildup of physisorbed layers of chlorine and bromine on rare gas surfaces (185–187). This series of papers is also noteworthy for the quality of the computer graphics employed in its presentation.

The sticking of atoms and molecules on Ar(s) using Langevin methods has been investigated (188).

In an interesting study, Hase et al. (189) looked at the effect of the lattice properties of a (111) diamond surface on the association of a gas-phase H atom with that surface. The authors emphasize the importance of ZPE in the lattice in a full understanding of the dynamics.

Adams (190) has modeled the adsorption of CO onto metals using collisions of CO with small metal clusters. The reverse process of desorption for NO on surfaces has been modeled by Hasselbrink (191).

2. Dissociative Chemisorption of Hydrogen on Metal Surfaces

The study of dissociative chemisorption of gas-phase molecules on metal surfaces is important to the understanding of a myriad of processes such as heterogeneous catalysis, electrode reactions, and corrosion, to name but a few (179–181). Recent advances in molecular beam, laser, and surface detection technologies have made it possible to study the reactions of monoenergetic molecular beams with clean, well-characterized metal surfaces.

The dissociative chemisorption of H_2 on metals,

$$H_2(g) + S \rightarrow 2H - S$$

(where S represents the surface) is among the most-studied classes of gas-surface reactions. The H_2-metal systems provide prototypical examples of the dissociative chemisorption process.

A great deal of experimental (192–195) and theoretical (196–210) work has been carried out on the effect of the translational and vibrational energy of the reactant molecule on dissociative chemisorption at metal surfaces and clusters (211). For example, such studies often reveal whether or not dissociative chemisorption has an activation barrier and, if so, the magnitude of the barrier to reaction. The relative efficacies of translation (T) and vibration (V) in promoting dissociative chemisorption have been examined. In particular (220), it has been found that V can be as effective as T in overcoming the barrier to reaction in the activated dissociative chemisorption of H_2 on Cu(111). These findings are in agreement with theoretical studies which employ a PES where the barrier to reaction occurs after the H—H bond begins to stretch (222,223). Borrowing from the nomenclature of gas-phase reaction dynamics, these results are taken as evidence of a late barrier to reaction in the dissociative chemisorption of H_2 on Cu(111).

Several gas-phase studies (35,223) (mostly theoretical in nature) have predicted a much richer structure in the reaction probability in gas-phase reactions as a function of rotational energy (R), in contrast to the monotonic rise in the reactivity observed with increasing T or V. It has been suggested (223) that this more complicated rotational dependence might be unfolded to yield even more intricate details of the reaction PES than those revealed by T and V dependence data.

As in the gas phase, the role of R in dissociative chemisorption on metal surfaces has received less attention than that of T and V. The principal reason for this is that experiments which directly measure the effect of R on these reactions are not yet feasible. The only experimental results which address the role of rotation in dissociative chemisorption come from rotational state measurements in recombinative desorption studies. It is possible for individual atoms chemisorbed on a surface to diffuse on about the

surface. Recombinative desorption, the reverse process of dissociative chemisorption, occurs when two such atoms join to form a gas-phase molecule:

$$2H\text{—}S \rightarrow H_2(g) + S \quad (3)$$

In one experiment (224), Zare and co-workers measured the j distributions of H_2 and D_2 desorbed from the Cu(110) and Cu(111) surfaces. They found that although these distributions had a mean rotational energy somewhat less than $k_B T_s$ (where k_B is the Boltzmann constant and T_s is the surface temperature), they did not deviate significantly from a Boltzmann distribution. Since the measured rotational state distributions seemed to have enhance populations at low j, application of the principle of detailed balancing led Zare and co-workers to propose that rotation might slightly hinder dissociative chemisorption.

However, a subsequent recombinative desorption study by Michelsen, Rettner, and Auerbach (225) has presented results suggesting that the role of R in dissociative chemisorption may, in fact, be quite complex. In this study, the velocity distributions of D_2 molecules desorbed from the Cu(111) surface were measured for a wide range of distinct rovibrational (v, j) states (with v = 0, 1, and 2 and j = 0 to 14). It was found that the mean translation energy first increased with j, reached a maximum at j = 5 and then decreased with higher j values. Application of detailed balancing to these data indicates that R inhibits the dissociative chemisorption of D_2 on Cu(111) at low j, but enhances reactivity at high j. This trend is remarkably similar to that observed in the study of gas-phase reactions (see above). A theoretical study of H_2 on Ni(100) (226) showed remarkable qualitative agreement with these experiments. These dynamical calculations indicate dissociative chemisorption is highly dependent upon the angular momentum quantum number, m_j, which determines the orientation of the molecule's plane of rotation with respect to the surface.

3. Eley-Rideal Processes

Eley-Rideal chemisorption processes are of the following type:

$$AB(g) + S \rightleftharpoons A\text{—}S + B(g)$$

They have recently begun to be the object of some study (227,228). In a combined experimental and theoretical study, Williams et al. (229) demonstrated the direct "pickup" of relatively large adsorbed hydrocarbon species by polycyclic hydrocarbon ions. Chang et al. (230) have studied the abstraction of H atoms from diamond by H(g): $H(g) + H(ad) \rightarrow H_2(g)$.

In a high-energy flat-surface study using a LEPS-type potential, Beauregard and Mayne investigated isotope effects for HD(g) + W(001) (231).

4. Photochemistry of Adsorbed Species

Recently, there has been interest in performing photochemistry on species adsorbed on a surface. Typically a layer of, for instance, HBr is physisorbed. A small fraction of these molecules are subsequently photolyzed by a laser. In the gas phase, photodissociation processes are best understood using the Franck-Condon principle, and quantum mechanical models (232). However, on a surface, the substrate must be explicitly accounted for. Because of the many-body nature of the process, classical mechanics is a natural choice. The resulting atoms move rapidly over the surface, colliding with both substrate and adsorbate (233–235).

5. Cluster-Catalyzed Chemisorption

Recently we presented the first theoretical study of the enhancement of a chemisorption reaction via cluster-surface collision (176,236). In that work the possibility of enhancing the prototypical gas-semiconductor chemisorption reaction of H_2 on Si(111) (1 × 1) by dissolving the H_2 in a small noble gas cluster was investigated. The reaction has a dynamic threshold of roughly of 0.4 eV translational energy. However, reaction could be induced at a H_2 collision energy of 0.1 eV for a microcluster containing four or more Ar atoms. It is clear that the clustering of the solvent atoms allows an energy pooling effect, transferring enough energy to the H_2 that it can overcome the barrier to reaction. This is reminiscent of Ceyer's work (237) in which physisorbed species were induced to overcome a barrier to chemisorption by bombardment with noble gas atoms; in this case the bombarding species are carried in situ.

REFERENCES

1. H. Goldstein, *Classical Mechanics*, Addison-Wesley, Reading, MA, 1965.
2. See, for example, W. H. Press, S. A. Teukolsky, W. T. Vetterling and B. P. Flannery, *Numerical Recipes*, 2nd ed., Cambridge University Press, New York, 1992.
3. D. L. Bunker, *Meth. Comput. Phys. 10*:287 (1971).
4. R. N. Porter, *Ann. Rev. Phys. Chem. 25*:287 (1971).
5. J. C. Polanyi and J. L. Schreiber, *Physical Chemistry, an Advanced Treatise*, Vol. 6A (W. Jost, ed.), Academic Press, New York, 1974, p. 383.
6. R. N. Porter and L. M. Raff, *Modern Theoretical Chemistry* (W. H. Miller, ed.), New York, Plenum, 1976, p. 1.
7. D. G. Truhlar and J. T. Muckerman, *Atom-Molecule Collision Theory* (R. B. Bernstein, ed.), Plenum, New York, 1979, p. 505.
8. L. M. Raff and D. L. Thompson, *Theory of Chemical Reaction Dynamics*, Vol. 3, (M. Baer, ed.), CRC Press, Boca Raton, 1985, p. 1.
9. D. M. Hirst, *A Computational Approach to Chemistry*, Blackwell, Oxford, 1990.
10. H. R. Mayne, *Int. Rev. Phys. Chem. 10*:107 (1991).
11. M. Karplus, R. N. Porter, and R. D. Sharma, *J. Chem. Phys. 43*:3259 (1965).
12. M. P. Allen and D. J. Tildesley, *Computer Simulations of Liquids*, Clarenden Press, Oxford, 1987.
13. J. M. Haile, *Molecular Dynamics Simulation*, Wiley, New York, 1992.
14. M. D. Pattengill, *Atom-Molecule Collision Theory* (R. B. Bernstein, ed.), Plenum, New York, 1979, p. 359.
15. M. H. Kalos and P. A. Whitlock, *Monte Carlo Methods*, Vol. 1, New York, 1986.
16. G. Torres-Vega and J. H. Frederick, *J. Chem. Phys. 93*:8862 (1990).
17. T. Uzer, B. D. McDonald, Y. Guan, and D. L. Thompson, *Chem. Phys. Lett. 152*:405 (1988).
18. X. Hu and W. L. Hase, *Z. Phys. D. 25*:27 (1992).
19. R. N. Porter, L. M. Raff, and W. M. Miller, *J. Chem. Phys. 63*:2214 (1975).
20. C. W. Eaker, *J. Chem. Phys. 90*:105 (1989).
21. C. W. Eaker, G. C. Schatz, N. DeLeon, and E. J. Heller, *J. Chem. Phys. 81*:5913 (1984).
22. G. C. Schatz, *Top. Current Phys. 90*:105 (1983).
23. C. W. Eaker and G. C. Schatz, *J. Chem. Phys. 81*:2394 (1984).
24. R. J. Duchovic and G. C. Schatz, *J. Chem. Phys. 84*:2239 (1986).
25. G. C. Schatz, *Comp. Phys. Commun. 51*:135 (1988).
26. W. L. Hase, R. J. Duchovic, X. Hu, K. F. Lim, D.-H. Lu, K. N. Swamy, S. R. Vande Linde, and R. J. Wolf; VENUS, Quantum Chemistry Program Exchange, Indiana University.
27. H. A. Kramers, *Z. Phys. 39*:828 (1926).

28. G. C. Schatz, *Chem. Res. 87*:81 (1987).
29. S. Keshavamurthy and W. H. Miller, *Chem. Phys. Lett. 205*:96 (1993).
30. Y. Guo, T. D. Sewell, and D. L. Thompson, *Chem. Phys. Lett. 224*:470 (1994).
31. Y. Qin and D. L. Thompson, *J. Chem. Phys. 100*:6445 (1994).
32. J. M. Bowman and A. Kuppermann, *J. Chem. Phys. 59*:6524, (1973).
33. K. T. Lee, J. M. Bowman, A. F. Wagner, and G. C. Schatz, *J. Chem. Phys. 76*:3563 (1982).
34. G. C. Schatz, *J. Chem. Phys. 79*:5386 (1983).
35. H. R. Mayne, *Chem. Phys. Lett. 130*:249 (1986).
36. L. L. Gibson, G. C. Schatz, M. A. Ratner, and M. J. Davis, *J. Chem. Phys. 86*:3263 (1987).
37. D.-H. Lu and W. L. Hase, *Chem. Phys. Lett. 142*:198 (1987).
38. H. Sun, R. O. Watts, and U. Buck, *J. Chem. Phys. 96*:1810 (1992).
39. A. J. C. Varandas, J. Brandão, and M. R. Pastrana, *J. Chem. Phys. 96*:5137 (1992).
40. A. J. C. Varandas and J. M. C. Marques, *J. Chem. Phys. 97*:4050 (1992).
41. G. Nyman, *Chem. Phys. 173*:159 (1993).
42. A. J. C. Varandas, *J. Chem. Phys. 99*:1076 (1993).
43. A. J. C. Varandas, *Chem. Phys. Lett. 225*:18 (1994).
44. G. C. Schatz, *J. Chem. Phys. 79*:5386 (1983).
45. W. H. Miller, W. L. Hase, and C. L. Darling, *J. Chem. Phys. 91*:2863 (1989).
46. J. M. Bowman, B. Gradzy, and Q. Sun, *J. Chem. Phys. 91*:2859 (1989).
47. K. F. Lim and D. A. McCormack, *J. Chem. Phys. 102*:1705 (1995).
48. G. H. Peslherbe and W. L. Hase, *J. Chem. Phys. 100*:1179 (1994).
49. M. Ben-Nun and R. D. Levine, *J. Chem. Phys. 101*:8768 (1994).
50. J. D. Doll, T. L. Beck, and D. L. Freeman, *Int. J. Quant. Chem. Symp. 23*:73 (1989).
51. A. E. Cho, J. D. Doll, and D. L. Freeman, *Chem. Phys. Lett. 229*:218 (1994).
52. R. E. Gillilan and K. R. Wilson, *J. Chem. Phys. 97*:1757 (1992).
53. T. D. Sewell, D. L. Thompson, J. D. Gezeltzer, and W. H. Miller, *Chem. Phys. Lett. 193*: 512 (1992).
54. F. E. Budenholzer, M. Y. Chang, and K. C. Huang, *J. Phys. Chem. 98*:12501 (1994).
55. R. K. Preston and J. C. Tully, *J. Chem. Phys. 54*:4297 (1971).
56. J. C. Tully and R. K. Preston, *J. Chem. Phys. 55*:562 (1971).
57. P. J. Kuntz, *Atom-Molecule Collision Theory* (R. B. Bernstein, ed.), New York, Plenum, 1979, p. 505.
58. W. H. Miller and T. F. George, *J. Chem. Phys. 56*:5637 (1972).
59. J. R. Stine and J. T. Muckerman, *J. Chem. Phys. 65*:3975 (1976).
60. C. A. Mead and D. G. Truhlar, *J. Chem. Phys. 84*:1055 (1986).
61. J. R. Stine and J. T. Muckerman, *J. Chem. Phys. 84*:1056 (1986).
62. N. C. Blais and D. G. Truhlar, *J. Chem. Phys. 79*:1334 (1983).
63. D. G. Truhlar, J. W. Duff, N. C. Blais, J. C. Tully, and B. C. Garrett, *J. Chem. Phys. 77*: 764 (1982).
64. J. R. Stine and J. T. Muckerman, *J. Chem. Phys. 91*:459 (1987).
65. G. Parlant and E. A. Gislason, *J. Chem. Phys. 91*:4416 (1989).
66. L. J. Dunne, J. N. Murrell, and J. G. Stamper, *Chem. Phys. Lett. 112*:497 (1984).
67. C. W. Eaker, *J. Chem. Phys. 87*:4532 (1987).
68. J. C. Tully, *J. Chem. Phys. 93*:1061 (1990).
69. S. Hammes-Schiffer and J. C. Tully, *J. Chem. Phys. 101*:4657 (1994).
70. F. J. Aoiz, V. J. Herrero, and V. Sáez Rábanos, *J. Chem. Phys. 97*:7423 (1992).
71. F. J. Aoiz, V. J. Herrero, O. Puentedwa, and V. Sáez Rábanos, *Chem. Phys. Lett. 198*:321 (1992).
72. F. J. Aoiz, H. K. Buchenau, V. J. Herrero, and V. Sáez Rábanos, *J. Chem. Phys. 100*:3789 (1994).
73. F. J. Aoiz, L. Bañares, M. J. D'Mello, V. J. Herrero, V. Sáez Rábanos, L. Schneider, and R. E. Wyatt, *J. Chem. Phys. 101*:5781 (1994).

74. A. Persky and H. Kornweitz, *Chem. Phys. Lett. 184*:479 (1991).
75. F. J. Aoiz, V. J. Herrero, M. M. Nogueira, and V. Sáez Rábanos, *Chem. Phys. Lett. 204*:359 (1993).
76. F. J. Aoiz, L. Bañares, V. J. Herrero, and V. Sáez Rábanos, *Chem. Phys. Lett. 218*:422 (1994).
77. F. J. Aoiz, L. Bañares, V. J. Herrero, and V. Séz Rábanos, *Chem. Phys. 187*:227 (1994).
78. F. J. Aoiz, L. Bañares, V. J. Herrero, V. Séz Rábanos, K. Stark, and H.-J. Werner, *J. Phys. Chem. 98*:10655 (1994).
79. F. J. Aoiz, V. J. Herrero, M. M. Nogueira, and V. Sáez Rábanos, *Chem. Phys. Lett. 211*:72 (1993).
80. G. W. Johnston, H. Kornweitz, I. Schechter, A. Persky, B. Katz, R. Bersohn, and R. D. Levine, *J. Chem. Phys. 94*:2749 (1991).
81. W. Jakubetz and P. J. Kuntz, *Chem. Phys. 179*:241 (1994).
82. H. Kornweitz, A. Persky, I. Schechter, and R. D. Levine, *Chem. Phys. Lett. 169*:489 (1990).
83. M. Ben-Nun, M. Brouard, J. P. Simons, and R. D. Levine, *Chem. Phys. Lett. 210*:423 (1993).
84. M. Ben-Nun, T. Raz, and R. D. Levine, *Chem. Phys. Lett. 220*:291 (1994).
85. R. Guadagnini, G. C. Schatz, and S. P. Walch, *J. Chem. Phys. 102*:784 (1995).
86. G. Nyman and J. Davidsson, *J. Chem. Phys. 92*:2415 (1990).
87. V. Klimo, M. Bitterová, S. Biskupič, and J. Urban, *Chem. Phys. 173*:367 (1993).
88. M. Gilibert, A. Aguilar, M. González, F. Mota, and R. Sayós, *J. Chem. Phys. 97*:5542 (1992).
89. M. Gilibert, A. Aguilar, M. González, and R. Sayós, *J. Chem. Phys. 99*:1719 (1993).
90. M. Gilibert, A. Aguilar, M. González, and R. Sayós, *Chem. Phys. 172*:99 (1993).
91. M. Gilibert, A. Aguilar, M. González, and R. Sayós, *Chem. Phys. 178*:287 (1993).
92. I. Urrecha, I. Serna, and J. Iturbe, *Chem. Phys. 154*:85 (1991).
93. I. R. Sims, M. Gruebelz, E. D. Potter, and A. H. Zewail, *J. Chem. Phys. 97*:4127 (1992).
94. L. Bañares, M. Menéndez, J. C. Whitehead, J. G. Muga, and A. Gonzalez-Ureña, *Chem. Phys. 146*:139 (1990).
95. A. M. Kosmas and R. J. Williams, *Chem. Phys. 140*:413 (1990).
96. A. M. Kosmas, *Chem. Phys. Lett. 187*:512 (1991).
97. P. J. Kuntz, B. I. Niefer, and J. J. Sloan, *Chem. Phys. 151*:77 (1991).
98. D. C. Clary, *J. Phys. Chem. 98*:10678 (1994).
99. G. C. Schatz and H. Elgersma, *Chem. Phys. Lett. 73*:21 (1980).
100. G. C. Schatz, *Chem. Phys. Lett. 74*:1133 (1981).
101. G. C. Schatz, M. C. Colton, and J. L. Grant, *J. Phys. Chem. 88*:2971 (1984).
102. O. Rashed and N. J. Brown, *J. Chem. Phys. 82*:5506 (1985).
103. N. J. Brown and O. Rashed, *J. Chem. Phys. 85*:4348 (1986).
104. J. A. Harrison and H. R. Mayne, *J. Chem. Phys. 87*:3698 (1987).
105. J. A. Harrison and H. R. Mayne, *J. Chem. Phys. 88*:7424 (1988).
106. K. Kudla and G. C. Schatz, *Chem. Phys. Lett. 193*:507 (1992).
107. K. Kudla and G. C. Schatz, *J. Chem. Phys. 98*:4644 (1993).
108. K. Kudla and G. C. Schatz, *Chem. Phys. 175*:71 (1993).
109. K. S. Bradley and G. C. Schatz, *J. Phys. Chem. 98*:3788 (1994).
110. K. Kudla, G. C. Schatz, and A. F. Wagner, *J. Chem. Phys. 95*:1635 (1991).
111. D. C. Clary and G. C. Schatz, *J. Chem. Phys. 99*:4578 (1993).
112. G. C. Schatz, *J. Phys. Chem. 99*:516 (1995).
113. T. Raz and R. D. Levine, *Chem. Phys. Lett. 226*:47 (1994).
114. A. J. C. Varandas and A. C. Pais, *Theoretical and Computational Models for Organic Chemistry* (S. J. Formosinho, I. G. Czismadia, and L. G. Arnant, eds.), Kluwer, Dordrecht, 1991, p. 55.
115. M. González, M. Gilibert, A. Aguilar, and R. Sáyos, *J. Chem. Phys. 98*:2927 (1993).
116. M. González, M. Gilibert, A. Aguilar, and R. Sayós, *Chem. Phys. Lett. 204*:578 (1993).

117. V. Klimo and J. Tiňo, *Chem. Phys. 159*:141 (1992).
118. K. Dong, E. A. Gislason, and M. Sizun, *Chem. Phys. 179*:143 (1994).
119. S. R. Vande Linde and W. L. Hase, *J. Am. Chem. Soc. 111*:2349 (1989).
120. S. R. Vande Linde and W. L. Hase, *J. Phys. Chem. 94*:6148 (1990).
121. S. R. Vande Linde and W. L. Hase, *J. Chem. Phys. 93*:7962 (1990).
122. Y. J. Cho, S. R. Vande Linde, L. Zhu, and W. L. Hase, *J. Chem. Phys. 96*:8275 (1992).
123. W. L. Hase and Y. J. Cho, *J. Chem. Phys. 98*:8626 (1993).
124. C. Getino, B. G. Sumpter, and J. Santamaria, *Chem. Phys. 145*:1 (1990).
125. S. Chapman and T. Uzer, *Adv. Class Traj. Meth. 1*:345 (1991).
126. E. Yurtsever, H. Günay, and T. Uzer, *J. Chem. Phys. 99*:1135 (1993).
127. D. K. Sahm and D. L. Thompson, *Chem. Phys. Lett. 210*:175 (1993).
128. S. Weerasinghe and F. G. Amar, *Z. Phys. D20*:167 (1991).
129. S. Weerasinghe and F. G. Amar, *J. Chem. Phys. 98*:4967 (1992).
130. C. E. Román and I. L. Garzan, *Z. Phys. D20*:163 (1991).
131. G. Peslherbe and W. L. Hase, *J. Chem. Phys. 101*:8535 (1994).
132. A. Goldberg, I. Last, and T. F. George, *J. Chem. Phys. 100*:8277 (1994).
133. Y. Qin and D. L. Thompson, *J. Chem. Phys. 96*:1992 (1992).
134. Y. Guan and D. L. Thompson, *Chem. Phys. 139*:147 (1989).
135. C. C. Chambers and D. L. Thompson, *Chem. Phys. Lett. 218*:166 (1993).
136. P. M. Agrawal, D. L. Thompson, and L. M. Raff, *J. Chem. Phys. 101*:9937 (1994).
137. L. M. Raff, *J. Chem. Phys. 93*:3160 (1990).
138. L. M. Raff, *J. Chem. Phys. 95*:8901 (1991).
139. L. M. Raff, *J. Chem. Phys. 97*:7459 (1992).
140. P. M. Agrawal, D. L. Thompson, and L. M. Raff, *J. Chem. Phys. 92*:1069 (1990).
141. H. W. Schranz, L. M. Raff, and D. L. Thompson, *J. Chem. Phys. 95*:106 (1991).
142. T. D. Sewell and D. L. Thompson, *J. Chem. Phys. 93*:4077 (1990).
143. T. D. Sewell, H. D. Schranz, D. L. Thompson, and L. M. Raff, *J. Chem. Phys. 95*:8089 (1991).
144. E. P. Wallis and D. L. Thompson, *J. Chem. Phys. 99*:2661 (1993).
145. H. Gai and D. L. Thompson, *Chem. Phys. Lett. 160*:119 (1990).
146. X. Y. Chang, T. D. Sewell, L. M. Raff, and D. L. Thompson, *J. Chem. Phys. 97*:7354 (1992).
147. X. Hu and W. L. Hase, *J. Chem. Phys. 95*:8073 (1991).
148. *The Chemical Physics of Atomic and Molecular Clusters*, Proc. Enrico Fermi Int. Summer School (G. Scoles, ed.), Elsevier Science, Amsterdam, 1990.
149. R. B. Gerber, A. B. McCoy, and A. Garcia-Vela, *Ann. Rev. Phys. Chem. 45*:275 (1994).
150. A. W. Castleman and S. Wei, *Ann. Rev. Phys. Chem. 45*:685 (1994).
151. R. Naaman, *Adv. Chem. Phys. 70*:181 (1988).
152. J. R. Papanikolas, J. R. Gord, N. E. Levinger, D. Ray, V. Vorsa, and W. C. Lineberger, *J. Phys. Chem. 95*:8028 (1991).
153. A. Lallement, J. Cuvellier, J. M. Mestdagh, P. Meynadier, P. de Pujo, O. Sublemonier, J. P. Visticot, J. Berlande, and X. Biquard, *Chem. Phys. Lett. 189*:182 (1992).
154. J. Nieman, J. Shwartz, and R. Naaman, *Z. Phys. D1*:231 (1986).
155. Y. Hurwitz, Y. Ruditz, R. Naaman, and R. B. Gerber, *J. Chem. Phys. 98*:2941 (1993).
156. J. C. Tully, *J. Chem. Phys. 73*:1975 (1980).
157. R. R. Lucchese and J. C. Tully, *J. Chem. Phys. 80*:3451 (1984).
158. A. E. DePristo and H. Metiu, *J. Chem. Phys. 90*:1229 (1989).
159. H.-P. Kaukonen, U. Landman, and C. L. Cleveland, *J. Chem. Phys. 95*:4997 (1991).
160. X. Hu and W. L. Hase, *J. Phys. Chem. 96*:7535 (1992).
161. X. Hu and W. L. Hase, *J. Chem. Phys. 98*:7826 (1993).
162. X. Hu and C. C. Martens, *J. Chem. Phys. 97*:8805 (1992).
163. X. Hu and C. C. Martens, *J. Chem. Phys. 98*:8551 (1993).

164. L. Perera and F. G. Amar, *J. Chem. Phys. 90*:7354 (1989).
165. M. Kolibiar, M. Foltin, and T. D. Märk, *Chem. Phys. Lett. 219*:252 (1994).
166. M. Ichihasi, Y. Otaki, and T. Kondow, *Chem. Phys. Lett. 189*:353 (1992).
167. S. Martrenchard-Barra, C. Jouvet, C. Lardeux-Dedonder, and D. Solgadi, *Chem. Phys. Lett. 215*:291 (1993).
168. C. L. Cleveland and U. Landman, *Science 257*:355 (1992).
169. U. Even, I. Schek, and J. Jortner, *Chem. Phys. Lett. 202*:303 (1993).
170. I. Schek, T. Raz, R. D. Levine, and J. Jortner, *J. Chem. Phys. 101*:8596 (1994).
171. T. Raz, I. Schek, M. Ben-Nun, U. Even, J. Jortner, and R. D. Levine, *J. Chem. Phys. 101*: 8606 (1994).
172. G.-Q. Xu, S. L. Bernaseki, and J. C. Tully, *J. Chem. Phys. 88*:3376 (1988).
173. G.-Q. Xu, R. J. Holland, S. L. Bernasek, and J. C. Tully, *J. Chem. Phys. 90*:3831 (1989).
174. J. B. C. Pettersson and N. Marković, *Chem. Phys. Lett. 201*:621 (1993).
175. N. Marković and J. B. C. Pettersson, *J. Chem. Phys. 100*:3911 (1994).
176. J. N. Beauregard and H. R. Mayne, *J. Chem. Phys. 99*:6667 (1993).
177. J. A. Niesse, J. N. Beauregard, and H. R. Mayne, *J. Phys. Chem. 98*:8600 (1994).
178. A. B. McCoy, Y. Hurwitz, and R. B. Gerber, *J. Phys. Chem. 97*:12516 (1993).
179. G. A. Somorjai, *Chemistry in Two Dimensions: Surfaces*, Cornell University Press, Ithaca, NY, 1981.
180. A. Zangwill, *Physics at Surfaces*, Cambridge University Press, New Rochelle, NY, 1988.
181. A. E. DePristo and A. Kara, *Adv. Chem. Phys. 77*:163 (1990).
182. R. B. Gerber, *Chem. Rev. 87*:43 (1987).
183. S. T. Ceyer, *Ann. Rev. Phys. Chem. 39*:479 (1988).
184. D. W. Brenner and B. J. Garrison, *Adv. Chem. Phys. 74*:281 (1989).
185. A. J. Trayanov and M. G. Prisant, *J. Chem. Phys. 94*:2352 (1991).
186. K. M. Christoffel, A. L. Trayanov, and M. G. Prisant. *J. Chem. Phys. 101*:4418 (1994).
187. A. L. Trayanov and M. G. Prisant, *J. Chem. Phys. 101*:4433 (1994).
188. Z. A. Insepov and A. M. Zhankadamova, *Z. Phys. D20*:145 (1991).
189. C. Accary, P. Barbarat, W. L. Hase, and K. C. Hass. *J. Phys. Chem. 97*:9934 (1993).
190. J. E. Adams, *J. Chem. Phys. 92*:1849 (1990).
191. E. Hasselbrink, *Chem. Phys. Lett. 170*:329 (1990).
192. A. Hodgson, J. Moryl, and H. Zhao, *Chem. Phys. Lett. 182*:152 (1991).
193. C. T. Rettner, D. J. Auerbach, and H. A. Michelsen, *Phys. Rev. Lett. 68*:1164 (1992).
194. C. T. Rettner, D. J. Auerbach, and H. A. Michelsen, *Phys. Rev. Lett. 68*:2547 (1992).
195. C. T. Rettner, H. A. Michelsen, and D. J. Auerbach, *Faraday Discuss. 96*:17 (1993).
196. J. H. McCreery and G. Wolken, Jr., *J. Chem. Phys. 65*:1310 (1976).
197. J. H. McCreery and G. Wolken, Jr., *Chem. Phys. Lett. 39*:478 (1976).
198. A. Gelb and M. J. Cardillo, *Surf. Sci. 59*:128 (1976).
199. A. Gelb and M. J. Cardillo, *Surf. Sci. 64*:197 (1977).
200. A. Gelb and M. J. Cardillo, *Surf. Sci. 75*:199 (1978).
201. G. F. Tantardini and M. Simonetta, *Surf. Sci. 105*:517 (1981).
202. G. F. Tantardini and M. Simonetta, *Chem. Phys. Lett. 87*:420 (1982).
203. C.-Y. Lee and A. E. DePristo, *J. Chem. Phys. 85*:4161 (1986).
204. A. Kara and A. E. DePristo, *J. Chem. Phys. 92*:5653 (1990).
205. A. Kara and A. E. Depristo, *J. Chem. Phys. 88*:5240 (1988).
206. C. Y. Lee and A. E. DePristo, *J. Chem. Phys. 87*:1401 (1987).
207. A. Forni and G. F. Tantardini, *J. Chem. Soc. Faraday Trans. 87*:1447 (1991).
208. A. Forni, M. C. Desjonquères, D. Spanjaard, and G. F. Tantardini, *Surf. Sci. 169/170*, 201 (1992).
209. A. Forni, M. C. Desjonquères, D. Spanjaard, and G. F. Tantardini, *Surf. Sci. 274*:161 (1992).
210. S. Holloway and B. Jackson, *Chem. Phys. Lett. 172*:40 (1990).
211. R. C. Mowrey and B. I. Dunlap, *Int. J. Quant, Chem. 25*:641 (1991).

212. M. R. Hand and S. Holloway, *J. Chem. Phys. 91*:7209 (1989).
213. D. Halstead and S. Holloway, *J. Chem. Phys. 93*:(1990) 2859.
214. U. Nielson, D. Halstead, S. Holloway, and J. K. Norskov, *J. Chem. Phys. 93*:2879 (1990).
215. G. R. Darling and S. Holloway, *J. Chem. Phys. 93*:9145 (1990).
216. G. R. Darling and S. Holloway, *Chem. Phys. Lett. 191*:396 (1992).
217. B. Jackson and H. Metiu, *J. Chem. Phys. 86*:1026 (1987).
218. C. M. Chiang and B. Jackson, *J. Chem. Phys. 87*:1026 (1987).
219. A. J. Cruz and B. Jackson, *J. Chem. Phys. 94*:5715 (1991).
220. B. E. Hayden, in *Dynamics of Gas-Surface Interactions*, (C. T. Rettner and M. N. R. Ashfold, eds.), Royal Society of Chemistry, London, 1991, p. 137.
221. H. G. Yu and J. Y. Cheng, *Chem. Phys. Lett. 226*:183 (1994).
222. B. Jackson, *J. Phys. Chem. 93*:7699 (1989).
223. J. A. Harrison, L. J. Isakson, and H. R. Mayne, *J. Chem. Phys. 91*:6906 (1989).
224. G. D. Kubiak, G. O. Sitz, and R. N. Zare, *J. Chem. Phys. 83*:2538 (1985).
225. H. A. Michelsen, C. T. Rettner, and D. J. Auerbach, *Phys. Rev. Lett. 69*:2678 (1992).
226. J. N. Beauregard and H. R. Mayne, *Chem. Phys. Lett. 205*:515 (1993).
227. M. Persson and B. Jackson, *J. Chem. Phys. 102*:1078 (1995).
228. C. T. Rettner, *Phys. Rev. Lett. 69*:383 (1992).
229. E. R. Williams, G. C. Jones, L. Fang, R. N. Zane, B. J. Garrison, and D. W. Brenner, *J. Am. Chem. Soc. 114*:3207 (1992).
230. X. Y. Chang, M. Perry, J. Peploski, D. L. Thompson, and L. M. Raff, *J. Chem. Phys. 99*: 4748 (1993).
231. J. N. Beauregard and H. R. Mayne, *Chem. Phys. Lett. 193*:115 (1992).
232. M. N. R. Ashfold and J. E. Baggott, *Molecule Photodissociation Dynamics*, Royal Society of Chemistry, London, 1987.
233. V. J. Barclay, D. B. Jack, J. C. Polanyi, and Y. Zeiri, *J. Chem. Phys. 97*:9458 (1992).
234. V. J. Barclay, W.-M. Hung, J. C. Polanyi, G. Zhang, and Y. Zeiri, *Faraday Discuss. 96*:129 (1993).
235. V. J. Barclay, D. B. Jack, J. C. Polanyi, and Y. Zeiri, *J. Phys. Chem. 97*:12541 (1993).
236. J. N. Beauregard and H. R. Mayne, *Surf. Sci. Lett. 280*:L253 (1993).
237. J. D. Beckerle, Q. Y. Yang, A. D. Johnson, and S. T. Ceyer, *J. Chem. Phys. 86*:7235.

16

Theory of Activated Rate Processes

ELI POLLAK

Weizmann Institute of Science, Rehovot, Israel

> I feel it necessary to explain from the very beginning why I have preferred to give a series of theoretical lectures. . . . The theoretical side of physical chemistry is and will remain the dominant one.
>
> Arrhenius (1)

I. INTRODUCTION

Activated rate processes are ubiquitous in condensed matter physics and chemistry. Their characteristic feature is the existence of an energy barrier separating the initial and final state. The system can undergo the necessary change only if it has sufficient energy to cross the barrier. It must be *activated* in order to react. The activation is usually effected by an external medium, such as a liquid solvent or a solid, which is in thermal equilibrium at temperature T. The second property is that one is probing a *rate process*. The change from reactants to products is accompanied by an exponential decay in time of reactants, such that a rate constant may be defined as the characteristic inverse time of the exponential decay.

The theory of activated rate processes originates with Arrhenius (2), who, inspired by van't Hoff, demonstrated that the temperature dependence of the rate of change of optical isomers is characterized by an *activation energy* $E^{\ddagger}$. Forty years of intensive research on activated reactions culminated with Eyring's famous paper on the absolute rate theory (3) and the deceptively simple expression

$$\Gamma = \Gamma_0 e^{-E^{\ddagger}/k_B T} \tag{1}$$

where Γ_0 is known as the *prefactor*, whose dimensions are time^{-1} and k_B is Boltzmann's constant. Perhaps Eyring's main contribution to chemistry and physics was his demon-

stration that the transition state theory (TST) formula (1) is applicable to a wide variety of chemical and physical processes, ranging from exchange reactions to catalysis and diffusion (4). An interesting review of the early history of the development of the theory may be found in Ref. 5.

Eyring's use of the word "absolute" was probably not meant to imply divine inspiration but rather the fact that Eyring's TST enabled estimation not only of the activation energy but also of the magnitude of the rate. Classical TST, developed by Wigner (6) and Eyring, gave insight into the prefactor. The theory was applied extensively to thermal gas-phase reactions where collisions lead to preparation of thermally equilibrated reactants, but reaction proceeds without influence of any external medium.

Although the applicability of the rate expression to experiment was amply demonstrated, its theoretical foundation remained quite unclear for a long period of time. This was especially so for reactions in condensed phases. Perhaps the most critical question discussed in scientific gatherings (7,8) and textbooks (9) was the identity of the "activation energy" $E^{\ddagger}$. Is this the energetic barrier separating reactants and products on the potential energy surface, or is it a free energy? It was only in 1978 that Chandler (10) provided a classical microscopic justification for the use of TST in condensed-phase reactions and showed that it really is the free energy of activation.

A very different approach to the theory of activated rate processes was suggested by Kramers in his seminal paper of 1940 (11). In contrast to TST, which at best allows for the solvent to modify the free energy of activation, Kramers suggested that the solvent (or other medium) applies a frictional force on the reacting solute. The frictional force dissipates energy from the system to the bath; this is counteracted by a random force which arises from fluctuations in the bath. The friction and the random fluctuations are related by a fluctuation dissipation relation. The existence of friction and random fluctuations causes two opposing effects. In the low friction limit, Kramers argued that without any external source of energy reaction cannot occur. Reactants must cross an energy barrier, and without any source of energy they will not have the necessary energy. The interaction of the solvent with the solute is the mechanism of energy transfer. In this *underdamped* regime, any increase in the damping strength implies an increase in the fluctuational force and will result in an increase in the reaction rate.

In the limit of moderate to strong damping, the frictional force is substantial enough to cause a fast exchange of energy between solute and solvent so that the solute is maintained in thermal equilibrium. However, the frictional force makes it difficult for the particles to move and the rate is limited by the *spatial diffusion* of the particle across the barrier separating reactants and products. As the damping increases, the diffusion time increases and the rate decreases. In Kramers' theory, friction plays a critical role. The dependence of the rate on the friction is described in terms of a bell-shaped function. Only its maximum value is given by a TST expression which does not include any dependence of the rate on friction. Kramers' modification of the rate expression in the spatial diffusion limit is often (erroneously, see below) referred to as a dynamical recrossing correction induced by the solvent.

Kramers modeled the interaction in terms of a one-dimensional Langevin equation (LE):

$$m\ddot{q} + \frac{dw(q)}{dq} + m\gamma\dot{q} = \xi(t) \tag{2}$$

where the reacting solute has mass m, coordinate q, and feels a potential $w(q)$. The dots denote time derivatives, the random force $\xi(t)$ is Gaussian with zero mean, and its correlation function is related to the damping constant γ through the second fluctuation dissipation theorem:

$$\langle \xi(t)\xi(t') \rangle = mk_B T 2\gamma\delta(t - t') \tag{3}$$

where $\delta(x)$ is the Dirac delta function.

Kramers derived an expression for the rate in the underdamped and spatial diffusion limits. He did not derive a uniform expression for the rate valid for all values of the damping strength. This is the Kramers turnover problem, which was solved only in the late eighties by Pollak, Grabert, and Hänggi (12) and is known as PGH theory.

Kramers' paper spurred an enormous amount of research on the theory of activated rate processes, especially in the physics community, as evidenced in numerous textbooks; see, for example, Refs. 13 and 14. However, as noted by Landauer (15) in his subjective description of the history of noise activated escape from metastable states, up till the end of the seventies, the physical chemistry community largely ignored the theory of rates introduced by Kramers. The first experimental measurements of viscosity effects on activated rate processes were performed on the isomerization of *trans*-stilbene to *cis*-stilbene by Fischer and co-workers in 1968 (16). These authors were not aware of Kramers' work and interpreted their results in terms of the free volume necessary for isomerization to occur. Since then, experimental work has proliferated; see, for example, the recent textbook (17).

Kramers' model is simplistic. It is one-dimensional and assumes that the friction is Markovian—uncorrelated in time. A multidimensional generalization of Kramers' problem in the spatial diffusion limit was proposed and solved by Langer (18). The multidimensional energy diffusion limit was solved by Matkowsky, Schuss, and coworkers (19,20). A multidimensional turnover theory has been recently formulated (21).

When thinking of any condensed medium, it is evident that in many cases the time scales of solvent motion may be of the same order as time scales of the reacting system. It is also reasonable to assume that the magnitude of the frictional force depends on the solute coordinate. For example, in surface diffusion, one would expect that the frictional force is stronger, the closer the diffusing atom is to the surface. One therefore generalizes Kramers' problem (22) and introduces a time- and space-dependent friction function $(dg(q)^2/dq)\gamma(t)$. The time-dependent part $\gamma(t)$ is usually characterized by two parameters, a damping strength γ and a memory time τ. The space-dependent function $g(q)$ is taken to have unit derivative ($g(q) = q$) at the barrier top of the potential $w(q)$. One then replaces the Langevin equation (2) with a space- and time-dependent friction generalized Langevin equation (STGLE) (22):

$$m\ddot{q} + \frac{dw(q)}{dq} + m\int^{t} dt' \frac{dg[q(t)]}{dq}\gamma(t - t')\frac{dg[q(t')]}{dq}\dot{q}(t') = \frac{dg[q(t)]}{dq}\xi(t) \tag{4}$$

The Gaussian random force $\xi(t)$ has zero mean but is correlated such that

$$\langle \xi(t)\xi(t') \rangle = mk_B T\gamma(t - t') \tag{5}$$

In case that there is no space dependence of the friction ($g(q) = g$ for all q) we will refer to Eq. (4) as the GLE. The GLE reduces to the Langevin equation (2), when the friction function is ohmic; that is, the friction function is a Dirac δ function in time (cf. Eq. (3)).

Kramers' approach to rate theory in the underdamped and spatial-diffusion-limited regimes spurred extensions which were applicable to the much more complex STGLE. Grote and Hynes (23) used a parabolic barrier approximation to derive the rate expression for the GLE in the spatial diffusion limit. Carmeli and Nitzan derived expressions for the rate of the GLE (24) and the STGLE (25) in the underdamped limit. The overdamped limit for the rate in the presence of delta correlated friction was solved using the mean first passage time expression (26,27). A turnover theory, valid for space- and time-dependent friction, has only been recently presented by Haynes, Voth, and Pollak (28,29).

Until the mid-eighties it was generally accepted that the STGLE was a reasonable representation of the dynamics which allowed for dynamically induced corrections to the rate predicted by the TST method. Kramers' theory was considered to be complementary but essentially different from TST. It was well understood that the STGLE is a continuum limit of a Hamiltonian in which the solute interacts nonlinearly with a harmonic bath (22,30). In fact the STGLE was originally derived from the Hamiltonian form. Only in 1985 did I realize that the Kramers-Grote-Hynes solution for the rate of the GLE in the spatial diffusion limit may be derived from TST by allowing the bath to influence the choice of the dividing surface between reactants and products (31). The use of TST methods and consideration of the dynamics of the Hamiltonian equivalent form of the STGLE opened up a new approach to the theory of activated rate processes. Most notably, the TST method allows one to remove previous restriction of the theoretical treatments to the STGLE. TST may be applied to a general Hamiltonian with anharmonic baths (32). The implications of the TST approach are still under intensive investigation as of this writing.

The results of over 50 years of study of rate theory in condensed phases may be summarized in terms of a compact and deceptively simple formula for the rate

$$\Gamma = \Upsilon \kappa_{sd} \Gamma_{1D} \tag{6}$$

Here Γ_{1D} is the so called one-dimensional TST estimate for the rate and is mainly determined by the one-dimensional potential of mean force $w(q)$. The *depopulation factor* Υ becomes much smaller than unity in the underdamped limit and is important when the rate is limited by the energy diffusion process. In the spatial-diffusion-limited regime, the depopulation factor Υ is unity but the *spatial diffusion factor* κ_{sd} becomes much smaller than unity. The major theme of this review is theoretical methods for estimating the depopulation and spatial diffusion factors.

It is impossible to do justice within the limited extent of one chapter to all theoretical developments. For example, I will omit methods relating to the Fokker-Planck equation representation of the dynamics. This includes the method of adiabatic elimination discussed extensively in Ref. 33 or the approach based on the Rayleigh quotient, developed by Talkner (34,35). There are a number of reviews, monographs, and special journal issues devoted to the theory of activated rate processes (5,13,14,36–40), the interested reader is urged to consult them. I will also omit any quantum theory of activated rate processes. The thread which connects the material presented in this chapter will be the use of the Hamiltonian equivalent form of the STGLE and more general forms to derive the classical theory of activated rate processes.

A brief review of some of the basic concepts and numerical methods used for the study of classical reaction dynamics in condensed phases is presented in Sec. II. Of central importance is the reactive flux method (5,10,37,41) without which it would be

impossible to obtain numerical results for reactions with high (reduced) barriers ($E^{\ddagger}/k_BT$). We also review the methods used to model and solve the dynamics in terms of the STGLE. Finally we present the Hamiltonian equivalent formulation of the STGLE.

If the potential $w(q)$ is a purely parabolic barrier potential, then the associated GLE may be solved analytically by a normal mode transformation. The parabolic barrier approximation plays a central role in the theory of activated rate processes and is discussed in some detail in Sec. III. The parabolic barrier approximation leads to the concept of *optimized planar dividing surfaces* (32, 42). Section IV is devoted to the variational TST method and its application to STGLE's using optimized planar dividing surfaces. The applicability of the variational TST method to the general case, in which the bath is also anharmonic is reviewed in Sec. V. Sections III–V summarize the main ingredients necessary for a theory for the spatial diffusion factor κ_{sd}.

The theory for the depopulation factor Y for the GLE and the STGLE is discussed in Sec. VI. Multidimensional generalizations for the depopulation and the spatial diffusion factors are presented in Sec. VII. Extension of the theory to include motion on periodic potentials and surface diffusion is given in Sec. VIII. We end with a discussion of future directions and topics which remain unsolved at this point.

II. BASIC CONCEPTS AND NUMERICAL METHODS

A. The Rate Constant

In any activated rate process one assumes the existence of reactants, labeled a, and products, labeled b. The fact that one is dealing with a *rate process* implies, as mentioned, that the time evolution of normalized reactant (n_a) and product (n_b) populations, $n_a(t) + n_b(t) = 1$, may be described by the coupled set of master equations:

$$\dot{n}_a(t) = -\Gamma_a n_a(t) + \Gamma_b n_b(t) \tag{7}$$

$$\dot{n}_b(t) = \Gamma_a n_a(t) - \Gamma_b n_b(t) \tag{8}$$

where the rates Γ_a and Γ_b are the decay rates for the reactant and product channels respectively. This review deals exclusively with the theory of these decay rates. Detailed balance implies that the forward and backward rates are related ($\beta \equiv 1/k_BT$):

$$e^{-\beta E_a}\Gamma_a = e^{-\beta E_b}\Gamma_b \tag{9}$$

If initially one starts only with reactants ($n_a(0) = 1$) then the solution of this coupled set of equations is

$$n_a(t) = \frac{1}{\Gamma_a + \Gamma_b}\left(\Gamma_b + \Gamma_a e^{-(\Gamma_a+\Gamma_b)t}\right) \tag{10}$$

By following the time dependence of the reactant population and using the condition of detailed balance, Eq. (9), one can extract the desired rates. This methodology has been implemented successfully in a number of simulations; see for example Ref. 43. Alternatively, one can compute the mean first passage time for all trajectories initiated at reactants and thus obtain the rate, cf. Ref. 44.

These direct methods are usually very expensive. When the barrier separating reactants and products is large relative to k_BT the trajectory will spend a time of the order of $e^{E^{\ddagger}/k_BT}$ before escaping and even with modern day computers, such integration times rapidly become inaccessible.

B. The Reactive Flux Method

The major advantage of the reactive flux method is that it enables one to initiate trajectories at the barrier top instead of at reactants or products. In this way, one saves all the wasted computer time waiting for the particle to escape from the well to the barrier.

The method is based on the validity of Onsager's regression hypothesis (45,46) which assures that fluctuations about the equilibrium state decay on the average with the same rate as macroscopic deviations from equilibrium. It is therefore sufficient to know the decay rate of equilibrium correlation functions, and one need not determine explicitly the decay rate of the macroscopic population as in the previous subsection.

The relevant correlation function in our case is related to population fluctuations. Without loss of generality, one assumes the existence of a reaction coordinate q such that reactants, labeled a, are defined by the region $q < q^{\ddagger}$ and products, labeled b, are defined by the region $q > q^{\ddagger}$. Following the discussion in Ref. 5, one defines the characteristic function of reactants (products) $\theta_a(q)$ ($\theta_b(q)$) as

$$\theta_a(q) = 1 \qquad \text{for } q < q^{\ddagger} \tag{11}$$

$$\theta_a(q) = 0 \qquad \text{for } q > q^{\ddagger} \tag{12}$$

and a similar definition is made for θ_b. At equilibrium $\langle \theta_a \rangle \equiv \theta_{a,\mathrm{eq}}$ and similarly $\langle \theta_b \rangle \equiv \theta_{b,\mathrm{eq}}$.

The fluctuation in population $\delta\theta_i \equiv \theta_i - \theta_{i,\mathrm{eq}}$, $i = a, b$ decays (after a short induction time τ_{ind}) with the same rate Γ as the population itself, such that (for $t > t'$):

$$\frac{\langle \delta\theta_i[q(t)]\delta\theta_i[q(t')]\rangle}{\langle \delta\theta_i^2 \rangle} = e^{-(\Gamma_a + \Gamma_b)(t - t')}, \qquad i = a, b \tag{13}$$

Taking the time derivative of Eq. (13) with respect to t and setting $t' = 0$ one easily finds that the *reactive flux* obeys

$$\frac{\langle \delta\theta_i[q(0)]\dot{\theta}_i[q(t)]\rangle}{\langle \delta\theta_i^2 \rangle} = -(\Gamma_a + \Gamma_b)e^{-(\Gamma_a + \Gamma_b)t}, \qquad i = a, b \tag{14}$$

Finally, using the fact that the derivative of a step function is a Dirac delta function, the fact that the time t at which the relation (14) is first obeyed is much much shorter than $1/\Gamma$ (because of the high barrier) and using detailed balance one finds the desired formula:

$$\Gamma_i = \frac{\langle \delta[q(0)]\dot{q}\theta_i[q(t)]\rangle}{\langle \theta_i(q)\rangle}, \qquad i = a, b \tag{15}$$

This central result implies that at time $t = 0$ one can initiate trajectories *anywhere* and after a short initiation time the reactive flux will reach a plateau value, which relaxes exponentially, but at a very slow rate.

There is an additional advantage to the reactive flux method. In the limit of very short times, the coordinate $q(t)$ will be in the reactants region if its velocity at time $t = 0$ is in the direction of the reactants. Therefore the zero time limit of the reactive flux expression is just the one-dimensional TST estimate for the rate. This means that if one wants to study corrections to TST all one needs to do numerically is compute the transmission coefficient κ defined as the plateau value of the time-dependent transmission

coefficient:

$$\kappa_a(t) = \frac{\langle \delta[q(0)]\dot{q}\theta_a[q(t)]\rangle}{\langle \delta[q(0)]\dot{q}\theta_a[-\dot{q}(0)]\rangle} \tag{16}$$

In this form it becomes evident that the transmission coefficient is just the plateau value of the average of a unidirectional thermal flux. To obtain the dynamical corrections to TST there is no need to know the TST rate itself. Numerically it may be actually easier to compute the transmission coefficient $\kappa_a(t)$ than the magnitude of the one-dimensional TST rate. The 1D TST rate may be obtained only after extensive Monte Carlo averaging. A small error in the activation energy can easily mask the correction term, which is just a prefactor.

C. Numerical Modeling of the STGLE

The space- and time-dependent generalized Langevin equation (4) is a phenomenological equation. The exact numerical dynamics for any given simulation is not identical to the numerical solution of an STGLE. However, the numerical solution of the equations of motion of a system of hundreds or thousands of particles is in many senses a black box. One may get some numbers, but the dynamics is so complicated that there is very little useful additional information. On the other hand, because so much more is known about the solution of STGLEs it is very useful to try and map the complex dynamics onto an STGLE.

There are three main ingredients that enter the STGLE. These are the potential of mean force $w(q)$, the time-dependent friction $\gamma(t)$, and its spatial dependence as expressed in terms of the function $g(q)$. Practical schemes used to determine each of these will be described in this subsection. The Hamiltonian of the full system may be written without loss of generality in terms of Cartesian coordinates as

$$H = T_{\text{sys}} + T_b + V \tag{17}$$

where T denotes kinetic energy and V potential energy. It is useful to use mass-weighted Cartesian coordinates. If m_i is the mass of the ith particle and $\tilde{x}_i$ the x component of the coordinate, the mass-weighted component becomes $x_i = m_i^{1/2}\tilde{x}_i$. The reaction coordinate q is also mass weighted. Effectively this implies that everywhere (see, for example, Eqs. (4) and (5)) the particle mass $m = 1$.

The reaction coordinate q is a priori not uniquely defined. Usually, however, one has some reasonable feeling for a good guess. For example, in a symmetric exchange reaction this could be the antisymmetric stretch, or in an isomerization reaction it could be a torsional angle. The reaction coordinate q is not necessarily a Cartesian coordinate; however, it may be written as $q = f(\underline{x})$, where $\underline{x}$ denotes the collection of all mass-weighted coordinates of all particles in the simulation. The potential of mean force is then, by definition,

$$w(q) = -k_B T \ln(L \cdot \langle \delta[q - f(\underline{x})]\rangle_{\text{coord}}) \tag{18}$$

where the brackets denote the thermally weighted average over all coordinates:

$$\langle g(q, \underline{x})\rangle_{\text{coord}} \equiv \frac{Tr_{\text{coord}} g(q, \underline{x}) e^{-V/k_B T}}{Tr_{\text{coord}} e^{-V/k_B T}} \tag{19}$$

and Tr_{coord} denotes integration over all coordinates. The length scale L is

$$L \equiv \int dq\, e^{-w(q)/k_B T} \tag{20}$$

The integrations implied in Eq. (18) may be done with Monte Carlo methods or molecular dynamics. Both methods have been used; see for example Refs. 47–49.

The potential of mean force will typically have two wells, corresponding to reactants and products, separated by a barrier. To set the notation, we denote the location of the reactant well, the barrier, and the product well by q_a, $q^\ddagger$, and q_b, respectively. One usually expects that the dynamics will be governed by the behavior of the system around the barrier top. Thus the standard procedure (48,49) for generating a GLE is to restrict the system to the barrier top $q = q^\ddagger$ and determine the force autocorrelation function of all other degrees of freedom. The force is just ∇V, so by using molecular dynamics constrained to the barrier top one can compute the force autocorrelation function $\langle \nabla V(t) \cdot \nabla V(0) \rangle$. One then models the true dynamics in terms of a GLE in which the time-dependent friction function is determined through the fluctuation dissipation relation, Eq. (5).

This procedure has been criticized by Berne and co-workers (50–52). They have shown that the friction function generated in this manner at values of the reaction coordinate different from the barrier top may be quite different from that generated at the barrier top. If the GLE description were accurate, the friction function should be independent of the reaction coordinate. This deficiency may be compensated by using the coordinate dependence of the force correlation function to generate the STGLE (29). One first evaluates the coordinate-dependent friction function

$$\eta(t - t'; q) \equiv \frac{1}{k_B T} \langle \delta F(t) \delta F(t') \rangle_q \tag{21}$$

where $\langle \delta F(t) \delta F(t') \rangle_q$ is the bath averaged autocorrelation function for the fluctuating force exerted by the bath modes at the clamped value of the reaction coordinate. The time-dependent friction function $\gamma(t)$ (cf. Eq. (4)) is defined to be

$$\gamma(t) \equiv \eta(t, q = q^\ddagger) \tag{22}$$

If the STGLE is a "good" description of the dynamics, then the function $g(q)$ may be shown to be

$$g(q) = \eta(0; q^\ddagger)^{-1/2} \int_{q^\ddagger}^{q} dq'\, \eta(0; q')^{1/2} \tag{23}$$

To date this procedure has not yet been implemented for a realistic simulation, but one would expect it to give a more accurate representation of the true dynamics. Even this construction is not foolproof; the true bath is not Gaussian as implied by the STGLE. There is also some arbitrariness in the prescription since, in principle, one could use any time t and not necessarily the $t = 0$ value of the friction function $\eta(t; q)$ in Eq. (23). Only if the system were exactly described by the STGLE would this arbitrariness be removed.

The remaining missing ingredient is the kinetic energy associated with the reaction coordinate. By using mass-weighted coordinates one notes that if the reaction coordinate

is a linear combination of atomic coordinates then the effective mass remains unity. If it is a nonlinear function, the effective mass will, in principle, be a function of the coordinate and more care must be used. It is not difficult to generalize the STGLE to include a coordinate-dependent mass.

D. Numerical Solution for the STGLE

Numerical solution of the Langevin equation is relatively straightforward. At each integration step one generates via a random number generator the Gaussian random force and includes it in a finite difference representation of the LE (usually using some version of a Verlet algorithm) to integrate the equation of motion. The GLE or STGLE with memory friction is tougher, since in principle it is necessary to keep a record of all former steps in order to proceed to the next one. It is also necessary to sample the random force such that it obeys the fluctuation dissipation relation, Eq. (5).

There are two straightforward ways to overcome this obstacle. One is discretization of the STGLE in terms of its Hamiltonian representation. The Hamiltonian dynamics of each oscillator is local in time. The random force is replaced by uncorrelated random initial conditions for each oscillator. This discretization has been used successfully by various authors (28,53–55), although it has its limitations (28,55). As the damping strength increases one needs to use an increasingly finer grid of oscillators, and at some point this becomes prohibitively expensive.

A different way is to represent the time dependence in terms of a series of exponentials. For the GLE it has been shown (56–59) that each exponential term leads to an additional degree of freedom, but the ensuing random force is Gaussian and delta correlated. The same holds for the STGLE (60). Here, we will show how this works for a single exponential term; generalization to more terms is straightforward.

The exponential form for the friction function is

$$\gamma(t) = \frac{\gamma}{\tau} e^{-t/\tau} \tag{24}$$

where γ is the damping strength and τ is the memory time. One introduces an auxiliary variable z and the two-dimensional potential

$$V(q, z) = w(q) + \frac{1}{2}\frac{\gamma}{\tau}[z - g(q)]^2 \tag{25}$$

where $g(q)$ leads to the spatial dependence of the friction; cf. Eq. (4). It is then a matter of straightforward algebra (60) to show that the STGLE is equivalent to the two coupled equations of motion:

$$\ddot{q} + \frac{\partial V(q, z)}{\partial q} = 0 \tag{26}$$

$$\gamma\dot{z} + \frac{\partial V(q, z)}{\partial z} = N(t) \tag{27}$$

where $N(t)$ is a Gaussian random force with zero mean and is delta correlated:

$$\langle N(t)N(t')\rangle = 2k_B T\gamma\delta(t - t') \tag{28}$$

It is now straightforward to integrate these equations of motion since the memory term has disappeared via the auxiliary variable z. Extensive use of this trick has been made for the GLE; see for example Ref. 59.

The fact that the STGLE with exponential memory friction can be written as a set of coupled Langevin equations means that one can also write a Fokker-Planck operator for the system and then use the known properties of Fokker-Planck operators (13,34) to derive rate expressions and other interesting results.

E. The Hamiltonian Equivalent

As shown by Zwanzig (22) the STGLE (Eq. (4)) may be derived from a Hamiltonian in which the mass-weighted reaction coordinate q is coupled *nonlinearly* to a harmonic bath:

$$H = \frac{1}{2}p_q^2 + w(q) + \sum_j \left[\frac{1}{2}p_{x_j}^2 + \frac{1}{2}\left(\omega_j x_j - \frac{c_j g(q)}{\omega_j}\right)^2\right] \tag{29}$$

The jth harmonic bath mode is characterized by the mass-weighted coordinate x_j, momentum p_{x_j} and frequency ω_j.

The exact equation of motion for each of the bath oscillators is

$$\ddot{x} + \omega_j^2 x_j = c_j g(q) \tag{30}$$

and is seen to have the form of a forced harmonic oscillator equation of motion. It may be solved in terms of the time dependence of the reaction coordinate and the initial value of the oscillator coordinate and momentum. This solution is then placed into the exact equation of motion for the reaction coordinate

$$\ddot{q} + \frac{dw(q)}{dq} + \sum_j \frac{c_j^2}{\omega_j^2} g(q)\frac{dg(q)}{dq} = \frac{dg(q)}{dq}\sum_j c_j x_j \tag{31}$$

After integration by parts, one obtains an STGLE with the following identification:

$$\gamma(t) = \sum_j \frac{c_j^2}{\omega_j^2}\cos(\omega_j t) \tag{32}$$

and

$$\xi(t) = \sum_j c_j\left(\left[x_j(0) - \frac{c_j g(q(0))}{\omega_j^2}\right]\cos(\omega_j t) + \frac{p_{x_j}(0)}{\omega_j}\sin(\omega_j t)\right) \tag{33}$$

Equation (32) indicates how one may achieve the continuum limit of the Hamiltonian form. One notes that if the friction function $\gamma(t)$ appearing in the STGLE is a periodic function with period τ then Eq. (32) is just the cosine Fourier expansion of the friction function. The frequencies ω_j are integer multiples of the fundamental frequency $2\pi/\tau$ and the coefficients c_j are just the appropriate Fourier expansion coefficients.

In practice, the friction function $\gamma(t)$ appearing in the STGLE is not periodic but a decaying function. However, one may use it to construct the periodic function $\gamma(t;\tau) \equiv \sum_{n=-\infty}^{\infty}\gamma(t - n\tau)\theta(t - n\tau)\theta[(n+1)\tau - t]$ where $\theta(x)$ is the unit step function. The continuum limit is obtained when the period τ goes to ∞. In any numerical discretization of the STGLE care must always be taken not to extend the dynamics beyond the chosen value of the period τ, as beyond this time one is following the dynamics of a system which is considerably different from the continuum STGLE.

It is very useful to define a spectral density which "measures" the density of bath modes coupled to the reaction coordinate in a given frequency range. It is defined as

$$J(\omega) = \frac{\pi}{2} \sum_j \frac{c_j^2}{\omega_j} [\delta(\omega - \omega_j) - \delta(\omega + \omega_j)] \tag{34}$$

One also notes that the friction function is just the cosine Fourier transform of the spectral density:

$$\gamma(t) = \frac{2}{\pi} \int_0^\infty d\omega \frac{J(\omega)}{\omega} \cos(\omega t) \tag{35}$$

Finally, the Laplace transform of the time-dependent friction is given in discretized form as

$$\hat{\gamma}(s) \equiv \int_0^\infty dt\, e^{-st} \gamma(t) = \sum_j \frac{c_j^2}{\omega_j^2} \frac{s}{\omega_j^2 + s^2} \tag{36}$$

III. THE PARABOLIC BARRIER AND THE GLE

The parabolic barrier plays a special role in rate theory. The GLE (with space-independent friction) may be solved analytically using Laplace transforms. The two-dimensional Fokker-Planck equation derived from the Langevin equation may be solved analytically, as was done by Kramers in his famous paper of 1940. In this section we present some of the analytic results for the parabolic barrier dynamics. These results are important from both a conceptual and a practical point of view. Later we shall see how one returns to the parabolic barrier case as a source of comprehension, approximation, etc.

Results presented here will be derived from the Hamiltonian representation. Although almost all of them may be derived using other methods, I find that the Hamiltonian approach is the simplest in the sense that memory friction is as easy to handle as ohmic friction. The central building block for the parabolic barrier case is the normal mode transformation of the Hamiltonian, discussed in detail in Sec. III.A. In Sec. III.B the normal mode transformation is used to construct normal mode free-energy surfaces.

The Langevin equation, in which the time-dependent friction is ohmic, plays a special role in the theory of activated rate processes. Kramers originally formulated the problem in terms of ohmic friction. In most applications in chemistry the friction will not be ohmic; however, the ohmic case is the simplest to analyze. Apart from the historic importance, the analytical simplicity helps in understanding and analyzing more difficult cases of space- and time-dependent friction. A summary of important results for the parabolic barrier and ohmic friction is presented in Sec. III.C.

The separability of the Hamiltonian in the normal mode form implies that the dynamics is in some sense trivial. One must only consider the continuum limit of a collection of independent harmonic oscillators and a single parabolic barrier. As described in Sec. III.D, this simple dynamics leads to some important relations between the Hamiltonian approach and the more standard stochastic theories. Multidimensional generalization of the parabolic barrier case will be discussed briefly in Sec. VIII.

A. The Normal Mode Transformation

When the potential of mean force is a parabolic barrier

$$w(q) = -\frac{1}{2}\omega^{\ddagger 2}q^2 \tag{37}$$

and the friction function is space independent, the equivalent Hamiltonian is a quadratic form in all coordinates—system and bath. This means that it may be diagonalized using a normal mode transformation (61).

The orthogonal transformation matrix **U** (62) diagonalizes the parabolic barrier Hamiltonian such that it has one negative eigenvalue $-\lambda^{\ddagger 2}$ and positive eigenvalues λ_j^2, $j = 1, \ldots, N, \ldots$ with associated coordinates and momenta $\rho, p_\rho, y_j, p_{y_j}$, $j = 1, \ldots, N, \ldots$:

$$H = \frac{1}{2}\left[p_\rho^2 + \sum_j p_{y_j}^2 - \lambda^{\ddagger 2}\rho^2 + \sum_j \lambda_j^2 y_j^2\right] \equiv T + V_{pb} \tag{38}$$

where we have used the notation V_{pb} to denote all potential terms of the Hamiltonian. There is a one-to-one correspondence between the unperturbed frequencies $\omega^\ddagger, \omega_j, j = 1, \ldots, N, \ldots$ (cf. Eq. (29)) and these normal mode frequencies. The diagonalization of the potential has been carried out explicitly in Refs. 62–64. One finds that the unstable mode frequency $\lambda^\ddagger$ is the lowest positive solution of the equation

$$\lambda^{\ddagger 2} + \lambda^\ddagger \hat{\gamma}(\lambda^\ddagger) = \omega^{\ddagger 2} \tag{39}$$

known as the Kramers-Grote-Hynes (KGH) equation (11,23). In contrast to the KGH methodology, or the derivation of the equation by Hänggi and Mojtabai (65) which is based on a mean first passage time approach, the derivation of the KGH equation from the Hamiltonian equivalent has the advantage of identifying the solution of the KGH equation as a physical barrier frequency.

The vector of normal mode coordinates is obtained by an orthogonal transformation from the old coordinates:

$$\begin{pmatrix} \rho \\ \underline{y} \end{pmatrix} = \mathbf{U}\begin{pmatrix} q \\ \underline{x} \end{pmatrix} \tag{40}$$

This transformation implies that

$$q = u_{00}\rho + \sum_j u_{j0}y_j \tag{41}$$

and that

$$\rho = u_{00}q + \sum_j u_{0j}x_j \tag{42}$$

One can show (12,62) that the matrix element u_{00} may be expressed in terms of the Laplace transform of the time-dependent friction and the barrier frequency $\lambda^\ddagger$:

$$u_{00}^2 = \left(1 + \frac{1}{2}\left[\frac{\hat{\gamma}(\lambda^\ddagger)}{\lambda^\ddagger} + \frac{\partial\hat{\gamma}(s)}{\partial s}\bigg|_{s=\lambda^\ddagger}\right]\right)^{-1} \tag{43}$$

One also finds the simple relations (62)

$$u_{0j} = u_{00} \frac{c_j}{\omega_j^2 + \lambda^{\ddagger 2}} \tag{44}$$

for the stable mode transformation coefficients.

Two central identities have been derived for the orthogonal transformation matrix elements and associated frequencies. The first identity (64) uses the determinant of the force constant matrix $\mathbf{K}$ to show that for any value of the parameter ϵ:

$$\begin{aligned} \det(\mathbf{K} + \epsilon^2\mathbf{I}) &= (-\lambda^{\ddagger 2} + \epsilon^2) \prod_j (\lambda_j^2 + \epsilon^2) \\ &= [-\omega^{\ddagger 2} + \epsilon^2 + \epsilon\hat{\gamma}(\epsilon)] \prod_j (\omega_j^2 + \epsilon^2) \end{aligned} \tag{45}$$

Specifically for $\epsilon = 0$ one finds that the product of the normal mode frequencies is identical to the product of the original frequencies.

The second identity is based on the inverse of the force constant matrix. One finds for any ϵ (66) that

$$\frac{u_{00}^2}{-\lambda^{\ddagger 2} + \epsilon^2} + \sum_j \frac{u_{j0}^2}{\lambda_j^2 + \epsilon^2} = [-\omega^{\ddagger 2} + \epsilon^2 + \epsilon\hat{\gamma}(\epsilon)]^{-1} \tag{46}$$

This allows one to define a normal mode friction function (12) (note that the definition here differs from that of Refs. 12 and 67 by a factor of u_{00}^2):

$$K(t) = \sum_j u_{j0}^2 \cos(\lambda_j t) \tag{47}$$

whose Laplace transform may be related via Eq. (46) to the Laplace transform of the time-dependent friction:

$$\frac{\hat{K}(\epsilon)}{\epsilon} = \sum_j \frac{u_{j0}^2}{\lambda_j^2 + \epsilon^2} = [-\omega^{\ddagger 2} + \epsilon^2 + \epsilon\hat{\gamma}(\epsilon)]^{-1} - \frac{u_{00}^2}{-\lambda^{\ddagger 2} + \epsilon^2} \tag{48}$$

It becomes then also evident that one can define a spectral density of the normal modes $I(\lambda)$ (67) in analogy to the spectral density $J(\omega)$ (cf. Eq. (34)):

$$I(\lambda) \equiv \frac{\pi}{2} \sum_j \frac{u_{j0}^2}{\lambda_j} [\delta(\lambda - \lambda_j) - \delta(\lambda + \lambda_j)] \tag{49}$$

Since $\delta(\lambda) = (1/\pi)\int_0^\infty dt \cos(\lambda t)$ one may relate the spectral density of the normal modes to the Laplace transform of the friction function $K(t)$ (67):

$$I(\lambda) = \frac{1}{\lambda} \mathrm{Re}[\hat{K}(i\lambda)] \tag{50}$$

The Laplace transform of the friction function $K(t)$ is known in the continuum limit (cf. Eq. (48)) so that one may now directly relate the spectral density of the normal modes $I(\lambda)$ to the spectral density $J(\omega)$. One finds

$$I(\lambda) = \frac{J(\lambda)}{(\omega^{\ddagger 2} + \lambda\ \mathrm{Im}\ \hat{\gamma}(i\lambda) + \lambda^2)^2 + J^2(\lambda)} \tag{51}$$

where we used the relation $J(\omega)/\omega = \mathrm{Re}\ \hat{\gamma}(i\omega)$ (cf. Eqs. (35) and (36)).

B. Collective Modes and a Free-Energy Surface

The parabolic barrier case demonstrates that the effect of the medium is to replace the original reaction coordinate q by a collective mode ρ along which the dynamics is trivial. It is useful to define a *collective bath mode* σ orthogonal to the unstable mode ρ as

$$\sigma \equiv \frac{1}{u_l} \sum_j u_{j0} y_j \tag{52}$$

where the parameter u_l is a normalization constant:

$$u_l^2 \equiv 1 - u_{00}^2 \tag{53}$$

With this form it is evident that

$$q = u_{00}\rho + u_l\sigma \tag{54}$$

and that the collective modes ρ and σ are orthogonal to each other.

As we shall see later it is of interest to obtain the free-energy surface in the collective modes ρ and σ. By definition (see also Eq. (18)) the free-energy surface is ($\beta \equiv 1/k_B T$):

$$W_{pb}(\rho, \sigma) \equiv -\frac{1}{\beta} \ln\left[A \cdot \left\langle \delta(\rho - \rho')\delta\left(\sigma - \frac{1}{u_l}\sum_j u_{j0} y_j\right)\right\rangle_{\text{coord}}\right] \tag{55}$$

where the brackets denotes an average with respect to all coordinates weighted by the canonical distribution $e^{-\beta V_{pb}}$ (cf. Eq. (38)). The normalization A has the units of a surface:

$$A = \int d\rho\, d\sigma\, e^{-\beta W(\rho,\sigma)} \tag{56}$$

Of course, in the case of a purely parabolic barrier, the integration over ρ in this definition will diverge, but this is not important. The free-energy surface is always defined up to an arbitrary constant.

Using the Fourier resolution of the Dirac δ function:

$$\delta\left(\sigma - \frac{1}{u_l}\sum_j u_{j0} y_j\right) = \frac{1}{2\pi}\int d\kappa\, e^{i\kappa(\sigma - (1/u_l)\sum_j u_{j0} y_j)} \tag{57}$$

the integrations over the bath coordinates in Eq. (55) reduce to simple Gaussian integrals. The resulting expression for the free-energy surface of the parabolic barrier is

$$W_{pb}(\rho, \sigma) = \frac{1}{2}[-\lambda^{\ddagger 2}\rho^2 + \Omega^2\sigma^2] \tag{58}$$

where the collective bath mode frequency Ω is found to be

$$\Omega^2 = \frac{1}{u_l^2}\sum_j \frac{u_{j0}^2}{\lambda_j^2} = \frac{1}{u_l^2}\left(\frac{u_{00}^2}{\lambda^{\ddagger 2}} - \frac{1}{\omega^{\ddagger 2}}\right) \tag{59}$$

The second equality on the right-hand side follows directly from Eq. (46) for $\epsilon = 0$. This allows the collective bath mode frequency to be expressed in terms of the Laplace transform of the time-dependent friction (cf. Eqs. (39) and (43)), so it is well defined in the continuum limit.

C. The Special Case of Ohmic Friction

As mentioned in the Introduction, ohmic friction is (Dirac) δ correlated:

$$\gamma(t) = 2\gamma\delta(t) \tag{60}$$

where γ is the damping constant. Ohmic friction is also the $\tau \to 0$ limit of exponential time-dependent friction, cf. Eq. (24). The spectral density for Ohmic friction (cf. Eqs. (34) and (35)) is

$$J(\omega) = \gamma\omega \tag{61}$$

The KGH equation (Eq. 39) is quadratic with two solutions. The positive solution gives the unstable mode barrier frequency:

$$\lambda^{\ddagger} = \left(\frac{\gamma^2}{4} + \omega^{\ddagger 2}\right)^{1/2} - \frac{\gamma}{2} \tag{62}$$

The modulus of the negative solution is

$$\lambda_{+} = \left(\frac{\gamma^2}{4} + \omega^{\ddagger 2}\right)^{1/2} + \frac{\gamma}{2} \tag{63}$$

and appears later in the normal mode friction function $K(t)$ (cf. Eq. (47)).

The projection matrix element u_{00} (cf. Eq. (43)) is

$$u_{00}^2 = \left(1 + \frac{\gamma}{2\lambda^{\ddagger}}\right)^{-1} \tag{64}$$

The ohmic normal mode friction function is found to be

$$K(t) = \frac{u_{00}^2}{2\lambda^{\ddagger}} \left(\lambda_{+} e^{-\lambda_{+}|t|} - \lambda^{\ddagger} e^{-\lambda^{\ddagger}|t|}\right) \tag{65}$$

Note that in contrast to the ohmic friction, the normal mode friction function has memory. The corresponding spectral density of normal modes $I(\lambda)$ (cf. Eq. (49)) decays as λ^4, in a sense it is much better behaved than the ohmic spectral density $J(\omega)$, which increases without bound with ω. Finally, the collective bath mode frequency, Ω (cf. Eq. (59)),

$$\Omega^2 = \omega^{\ddagger 2} \tag{66}$$

is identical to the barrier frequency.

D. Dynamics and the Relation to Stochastic Theories

Although the normal mode representation is very useful, the physically observable coordinate is usually the system coordinate q. In the Langevin representation of the dynamics, the trajectory $q(t)$ is characterized by a random force which affects its motion. In the equivalent Fokker-Planck representation of Langevin dynamics, all dynamical information lies in the joint probability distribution function that the particle at time t has position and velocity q, v, given that at time $t = 0$ its position and velocity were q', v'.

In the Hamiltonian representation, any trajectory is deterministic; the random element comes from averaging over initial conditions. However, there is a clear connection between these representations. If the dynamics in the Hamiltonian representation is known, it can be used to generate the probability distribution function in the physical

space. The advantage of the Hamiltonian representation is that one can construct this distribution function also for arbitrary memory friction. This, in contrast to the Fokker-Planck equation in the phase space of the particle which is defined for ohmic friction.

In this subsection we will provide a few examples demonstrating the utility of the Hamiltonian approach (68). For the parabolic barrier, everything is known because of the separability of the problem. The time dependence of the unstable mode is given in terms of the initial conditions as

$$\rho(t) = \rho(0)\cosh(\lambda^{\ddagger}t) + \frac{p_\rho(0)}{\lambda^{\ddagger}}\sinh(\lambda^{\ddagger}t) \tag{67}$$

The equivalent equation for the momentum $p_\rho(t)$ is obtained by differentiation with respect to time. Similarly for any of the stable modes one has

$$y_j(t) = y_j(0)\cos(\lambda_j t) + \frac{p_{y_j}(t)}{\lambda_j}\sin(\lambda_j t) \tag{68}$$

The relation between the physical coordinate and momentum q, p_q and the normal modes is known (cf. Eq. (41)), so one can express any function of the particle coordinate and momentum in terms of the time dependence of the normal modes and their initial conditions. It follows that the average of *any* time-dependent function of the coordinates and momenta, given initial conditions in the physical space $\langle f[q(t), p_q(t); q(0), p_q(0)]\rangle$, can be determined by averaging over the initial conditions of the normal modes under suitable constraints.

The central relation needed is

$$\begin{aligned}
&\langle f[q(t), p_q(t); q(0) = q', p_q(0) = p_q']\rangle \\
&\quad = \int dq\, dp_q\, \mathrm{Tr} e^{-\beta H}\delta\left[q - u_{\infty 0}\rho(t) - \sum_j u_{j0}y_j(t)\right]\delta\left[p_q - u_{\infty 0}p_\rho(t) - \sum_j u_{j0}p_{y_j}(t)\right] \\
&\quad \times f[q, p_q; q', p_q']\delta\left[q' - u_{\infty 0}\rho(0) - \sum_j u_{j0}y_j(0)\right]\delta\left[p_q' - u_{\infty 0}p_\rho(0) - \sum_j u_{j0}p_{y_j}(0)\right] \\
&\quad \div \mathrm{Tr} e^{-\beta H}\delta\left[q' - u_{\infty 0}\rho(0) - \sum_j u_{j0}y_j(0)\right]\delta\left[p_q' - u_{\infty 0}p_\rho(0) - \sum_j u_{j0}p_{y_j}(0)\right]
\end{aligned} \tag{69}$$

The Tr operation is over the phase space of the initial conditions of the normal modes. The volume element is $d_\rho(0)\, dp_\rho(0)\, \Pi_j\, dy_j(0)\, dp_{y_j}(0)$. The Hamiltonian H is the full Hamiltonian conveniently expressed in terms of the normal modes as in Eq. (38).

The denominator of Eq. (69) is readily evaluated:

$$\begin{aligned}
&\mathrm{Tr} e^{-\beta H}\delta\left[q' - u_{00}\rho(0) - \sum_j u_{j0}y_j(0)\right]\delta\left[p_q' - u_{00}p_\rho(0) - \sum_j u_{j0}p_{y_j}(0)\right] \\
&\quad = \prod_j \frac{2\pi}{\beta\omega_j} e^{(-\beta/2)(p_q^2 - \omega^{\ddagger 2}q^2)}
\end{aligned} \tag{70}$$

Technically, the integration over the initial conditions is usually effected by using the Fourier representation of the δ function as already done above (cf. Eq. (57)).

As a first example, we consider the momentum correlation function $\langle p_q(t)p_q(0)\rangle$ thermally averaged over all initial configurations of the particle and the phase space of the bath. Since the correlation function is quadratic in all variables, it is convenient to

immediately integrate over the appropriate δ functions in Eq. (69) and perform the Gaussian averages. One finds

$$\langle p_q(t)p_q(0)\rangle = \frac{1}{\beta}\left[u_{00}^2 \cosh(\lambda^{\ddagger}t) + K(t)\right] \tag{71}$$

thus connecting between the normal mode friction function $K(t)$, (cf. Eq. (47)) and the velocity autocorrelation function. The divergence with time is natural; Eq. (71) gives the velocity correlation function for a purely parabolic barrier for which eventually the particle will find itself at an infinite distance from the barrier with an infinite velocity. Taking the Laplace transform of Eq. (71) and using Eq. (48), one recovers the standard result for the velocity correlation function in terms of the Laplace transform of the friction:

$$\int_0^{\infty} dt\ e^{-st}\ \langle p_q(t)p_q(0)\rangle = \frac{1}{\beta}\,\frac{s}{-\omega^{\ddagger 2} + s^2 + s\hat{\eta}(s)} \tag{72}$$

As a second example, it is instructive to derive the Kramers stationary flux function which serves as a basis for practical application in the Rayleigh quotient variational method (34,35). In principle there are an infinity of stationary flux functions, as any function in phase space which is constant along a classical trajectory will be stationary. Kramers imposed in addition the boundary condition that the flux is associated with particles that were initiated in the infinite past in the reactant region. Following Pechukas (69), one defines (68) the characteristic function of phase points in phase space χ_r, which is unity on all phase space points of a trajectory which was initiated in the infinite past at reactants and is zero otherwise. By definition χ_r is stationary. The distribution function associated with the characteristic function χ_r projected onto the physical phase space is then

$$F_r(\tilde{q}, \tilde{p}) = \frac{\mathrm{Tr}\delta(q - \tilde{q})\delta(p_q - \tilde{p}_q)\chi_r e^{-\beta H}}{\mathrm{Tr}\delta(q - \tilde{q})\delta(p_q - \tilde{p}_q)e^{-\beta H}} \tag{73}$$

For the parabolic barrier, the separability in the normal modes implies that the characteristic function is given simply as

$$\chi_r = \theta(p_\rho - \lambda^{\ddagger}\rho) \tag{74}$$

where $\theta(x)$ is the unit step function. It is then a matter of some straightforward algebra, using also Eq. (70), to find that

$$F_r(\tilde{q}, \tilde{p}) = \frac{1}{\sqrt{\pi}} \int_{-\infty}^{[(\beta/2)(\lambda^{\ddagger}/\hat{\gamma}(\lambda^{\ddagger}))]^{1/2}(\tilde{p} - (\omega^{\ddagger 2}/\lambda^{\ddagger})\tilde{q})} e^{-y^2}\, dy \tag{75}$$

It is easy to show that for ohmic friction this reduces to Kramers' function. Note though that we have immediately derived the generalization of Kramers' function which is valid for arbitrary memory friction. By demonstrating that Kramers' function is the projection onto the physical phase space of Pechukas' characteristic function, we have actually shown that Kramers' function may be interpreted as the probability for reaction at the given system phase space point. This interpretation was subsequently further developed by Kohen and Tannor (70).

The same approach has been used in Ref. 68 to derive an eigenfunction of the Fokker-Planck operator as well as the stochastic separatrix in phase space (71–73). The dynamics in the normal mode representation was also used in conjunction with the re-

active flux method and perturbation theory to derive finite barrier corrections to the rate in the presence of a nonlinear system potential (74).

IV. VTST WITH PLANAR DIVIDING SURFACES

A. The Parabolic Barrier Limit

One of the major advantages of the Hamiltonian formalism is that it allows one to apply TST to dissipative systems. Originally, TST was formulated for classical systems in which a given point in the full phase space uniquely defines a trajectory. Since Hamilton's equations of motion are linear with respect to time, two trajectories sharing the same point in phase space are identical. This is also known as the noncrossing rule in phase space. When the STGLE is considered in the phase space of the system (q, p_q), the noncrossing rule is no longer valid. The random force implies that knowledge of the trajectory at one point in the system phase space is not sufficient for uniquely determining its history. The Hamiltonian formulation of the GLE helps in overcoming this problem by increasing the space and considering trajectories in the combined phase space of system and bath. One first applies TST to the discretized Hamiltonian system and only at the end takes the continuum limit.

A central concept in TST is the dividing surface. It is defined as a surface that divides the full space into two disjoint subsets—the reactants and products phase space. The dividing surface has the property that any trajectory going from reactants to products or vice versa must cross it. The fundamental idea of TST is that by "sitting" on the dividing surface and counting all those trajectories that move from reactants to products one will at worst provide an overestimate of the reactive flux. At worst, trajectories could recross the dividing surface and then the net forward flux is lowered. For a detailed discussion of recrossings in TST see for example Ref. 75. TST thus provides an upper bound for the reaction rate. This upper bound depends on the dividing surface used, varying it to minimize the reactive flux leads to variational transition state theory (VTST).

The TST expression (3,6,69,76,77) for the escape rate is

$$\Gamma = \frac{\int dp_q\ dq\ \Pi_j\ dp_j\ dx_j\ \delta(f)(\vec{\nabla} f \cdot \mathbf{p})\theta(\vec{\nabla} f \cdot \mathbf{p})e^{-\beta H}}{\int dp_q\ dq\ \Pi_j\ dp_j\ dx_j\ \theta(-f)e^{-\beta H}} \tag{76}$$

The Dirac delta function $\delta(f)$ localizes the integration onto the dividing surface $f = 0$. The gradient of the dividing surface (∇f) is in the full phase space, $\mathbf{p}$ is the generalized velocity vector in phase space with components $\{\dot{q}, \dot{p}_q; \dot{x}_j, \dot{p}_j;\ j = 1, \ldots, N\}$, and $\theta(y)$ is the unit step function which restricts the flux to be in one direction only. The term $\nabla f \cdot \mathbf{p}$ is proportional to the velocity perpendicular to the dividing surface. The numerator is the unidirectional flux, and the denominator is the partition function of reactants.

The choice for the transition state implicit in Kramers' original paper (11) is the barrier top along the system reaction coordinate q. The dividing surface takes the form $f = q - q^{\ddagger}$ and the rate expression reduces to the "one-dimensional" result

$$\Gamma_{1D} = (2\pi\beta)^{-1/2} \frac{e^{-\beta w(q^{\ddagger})}}{\int dq\ \theta(-q)e^{-\beta w(q)}} \simeq \frac{\omega_a}{2\pi} e^{-\beta E^{\ddagger}} \tag{77}$$

where we assume that the barrier of the potential of mean force $w(q)$ is located at $q = q^{\ddagger}$ and $E^{\ddagger}$ is the difference between the barrier and well energies of the potential of mean force.

Kramers' (11) correction to the one-dimensional TST rate came from consideration of the properties of the Fokker-Planck equation in the vicinity of the barrier in the presence of ohmic friction. As noted in the previous section, if one considers only the parabolic barrier limit, the Fokker-Planck equation may be solved analytically. Grote and Hynes (23) and Hänggi and Mojtabai (65) generalized Kramers' result to include the case of memory friction and the GLE. A different approach (31) would be to consider the Hamiltonian equivalent, Equation (29), for space-independent coupling ($g(q) = q$ in Eq. (29)) in the parabolic barrier limit.

Truncating the potential of mean force as a parabolic barrier allows diagonalization of the Hamiltonian, as discussed in the previous section. Motion is separable along the generalized reaction coordinate ρ. TST will therefore be exact (in the parabolic barrier limit) if one chooses the dividing surface $f = \rho - \rho^{\ddagger}$. Inserting this choice into the TST expression for the rate (31) leads to the well-known KGH expression for the rate in the spatial diffusion limit:

$$\Gamma_{pb} = \frac{\lambda^{\ddagger}}{\omega^{\ddagger}} \Gamma_{1D} \tag{78}$$

This derivation of the KGH expression demonstrates the equivalence with TST. The prefactor is not a result of any dynamics but is derived from the equilibrium distribution. The effect of the medium is to modify the reaction coordinate and thus the partition function of all perpendicular degrees of freedom at the barrier top. The choice of the system coordinate for the dividing surface may be a poor one, since the medium will cause many recrossings of this dividing surface. An explicit estimate of these recrossings has been presented in Ref. 78. However, by choosing the dividing surface $f = \rho - \rho^{\ddagger}$, all the recrossings disappear, and TST is exact. The rate is just the ratio of thermal partition functions at the barrier and the well.

B. Planar Dividing Surfaces

The parabolic barrier result is suggestive. It shows that the best dividing surface may be considered as a collective mode which is a linear combination of the system coordinate and all bath modes. A natural generalization of the parabolic barrier result would be to choose the dividing surface as a linear combination of *all* coordinates but to optimize the coefficients even in the presence of nonlinearity in the potential of mean force and a space-dependent coupling. Such a general dividing surface is by definition a planar dividing surface in the configuration space of the system and the bath since it defines a hyperplane. The general form of a planar dividing surface is

$$f = a_0 q + \sum_j a_j x_j \tag{79}$$

where the coefficients are normalized according to

$$a_0^2 + \sum_j a_j^2 = 1 \tag{80}$$

One may now define a potential of mean force $w[f]$ along the generalized coordinate f as

$$w[f] = -k_B T \ln\left(L_f \cdot \left\langle \delta\left[f - a_0 q - \sum_j a_j x_j \right] \right\rangle_{\text{coord}} \right) \tag{81}$$

where the length scale L_f is

$$L_f \equiv \int df\, e^{-\beta w[f]} \tag{82}$$

and the averaging is over all coordinates, with the thermal weighting $e^{-\beta V}$ where the potential V is the sum of all potential terms of the Hamiltonian, Eq. (29).

The fact that the generalized coordinate f is a linear combination of all bath modes and that the potential is quadratic in the bath variables allows one to express the potential of mean force $w[f]$ in terms of a single quadrature over the system coordinate q. The detailed derivation is presented in Ref. 42, the main technical trick being the usual use of the Fourier representation of the Dirac δ functions. The resulting expression is

$$e^{-\beta w[f]} = \left(\frac{\beta A^2}{2\pi}\right)^{1/2} \int_{-\infty}^{\infty} dq\; e^{(-\beta[(1/2)A^2(qC(q)-f)^2 + w(q)])} \tag{83}$$

where $w(q)$ is the potential of mean force along the system coordinate. The collective frequency, A, and the collective coupling function, $C(q)$, in Eq. (83) are

$$A^{-2} = \sum_j \frac{a_j^2}{\omega_j^2} \tag{84}$$

and

$$C(q) = a_0 + \frac{g(q)}{q} \sum_j \frac{a_j c_j}{\omega_j^2} \tag{85}$$

With these preliminaries it is easy to see that the TST expression for the rate using the planar dividing surface reduces to the "simple" result

$$\Gamma[f] = \Gamma_{1D} e^{-\beta[w[f] - w(q^\ddagger)]} \tag{86}$$

Optimal planar dividing surface VTST is thus reduced to finding the *maximum* of the free energy $w[f]$. Here we note that the major difference between the space-dependent friction problem and the space-independent friction problem is that in the latter the coupling constant C is also dependent on the system coordinate q since $g(q) \neq q$ in the general case.

One must now vary the free energy $w[f]$ with respect to the location f as well as with respect to the transformation coefficients $\{a_0, a_j;\ j = 1, \ldots, N\}$. This leads to the optimal planar dividing surface estimate for the rate of reaction. The details follow closely those given in Appendix B of Ref. 42. Varying with respect to the location f one finds the maximum at

$$f^\ddagger = \langle qC(q) \rangle \tag{87}$$

where the brackets denote the averaging

$$\langle (\cdots) \rangle \equiv \frac{\displaystyle\int_{-\infty}^{\infty} dq (\cdots) \exp(-\beta[\tfrac{1}{2}A^2(qC(q) - f^\ddagger)^2 + \omega(q)])}{\displaystyle\int_{-\infty}^{\infty} dq\, \exp(-\beta[\tfrac{1}{2}A^2(qC(q) - f^\ddagger)^2 + \omega(q)])} \tag{88}$$

Using the notation

$$d_j \equiv \frac{\langle c_j g(q)[qC(q) - f^{\ddagger}]\rangle}{\langle q[qC(q) - f^{\ddagger}]\rangle} \tag{89}$$

one finds that the variation of the free energy with respect to the transformation coefficients a_j, $j = 1, \ldots, N$, gives

$$a_j = a_0 \frac{d_j}{\omega_j^2 + \lambda^{\ddagger 2}}, \qquad j = 1, \ldots, N \tag{90}$$

Here $\lambda^{\ddagger}$ is referred to as the generalized barrier frequency; its magnitude will be determined by variation of the free energy with respect to the coefficient a_0.

Using the normalization of the transformation coefficients it is noted that a_0 is parametrically dependent on the magnitude of the generalized barrier frequency:

$$a_0^2 = \left[1 + \sum_j \frac{d_j^2}{(\omega_j^2 + \lambda^{\ddagger 2})^2}\right]^{-1} \tag{91}$$

Similarly, the collective frequency A and the collective coupling function $C(q)$ are parametrically dependent only on $\lambda^{\ddagger}$:

$$A^{-2} = a_0^2 \sum_j \frac{d_j^2}{\omega_j^2(\omega_j^2 + \lambda^{\ddagger 2})^2} \tag{92}$$

$$C(q) = a_0\left[1 + \frac{g(q)}{q} \sum_j \frac{d_j c_j}{\omega_j^2(\omega_j^2 + \lambda^{\ddagger 2})}\right] \tag{93}$$

Varying the free energy with respect to a_0 gives the necessary remaining equation for the barrier frequency:

$$a_0 = A^2\beta\langle q(qC(q) - f^{\ddagger})\rangle \tag{94}$$

To complete the optimal planar dividing surface VTST, it is necessary to express all quantities in the continuum limit. It is useful to define an *average spatial enhancement* coefficient ξ as

$$\xi \equiv \frac{\langle g(q)[qC(q) - f^{\ddagger}]\rangle}{\langle q[qC(q) - f^{\ddagger}]\rangle} \tag{95}$$

For space-independent friction $g(q) = q$ so that the average spatial enhancement coefficient is unity. Any deviation of ξ from unity is thus due to the effect of the space dependence of the friction. One now finds that the jth transformation coefficient is

$$a_j = a_0 \xi \frac{c_j}{\omega_j^2 + \lambda^{\ddagger 2}} \tag{96}$$

In other words, space dependence of the coupling will change the effective strength of the coupling of each mode from c_j to ξc_j, hence the term *average spatial enhancement* for ξ. This quantity is the essential ingredient in understanding the impact of spatially dependent friction on a barrier crossing problem.

With these preliminaries, one may express all relevant parameters in terms of the Laplace transform of the time-dependent friction. Specifically,

$$C(q) = a_0\left[1 + \xi\frac{g(q)}{q}\frac{\hat{\eta}(\lambda^\ddagger)}{\lambda^\ddagger}\right] \tag{97}$$

The effective frequency is

$$A^2 = \frac{\lambda^{\ddagger 2}}{a_0^2(1 + \xi^2\hat{\eta}(\lambda^\ddagger)/\lambda^\ddagger) - 1} \tag{98}$$

and the normalization condition is

$$a_0^2 = \left[1 + \frac{1}{2}\xi^2\left(\frac{\hat{\eta}(\lambda^\ddagger)}{\lambda^\ddagger} + \frac{\partial\hat{\eta}(s)}{\partial s}\bigg|_{s=\lambda^\ddagger}\right)\right]^{-1} \tag{99}$$

The barrier frequency is then determined from minimization of the free energy; cf. Eqs. (83) and (86).

In practice, the numerical solution of the resulting transcendental equation for the generalized barrier frequency ($\lambda^\ddagger$) and the location ($f^\ddagger$) may be challenging. After minimizing with respect to all transformation coefficients, except a_0, the rate remains a function of two independent variables, a_0 and $f^\ddagger$. Equation (99) allows one to replace a_0 by the reactive frequency $\lambda^\ddagger$ as the independent variable. Instead of now solving the transcendental equations resulting from variation with respect to the two variables it is simpler to find the maximum of the free energy numerically. One fixes the barrier location $f^\ddagger$ and varies the barrier frequency to find its minimal value as a function of $f^\ddagger$. One then varies $f^\ddagger$ to find the minimal rate. Even with this procedure it is still necesssary to solve one transcendental equation to find the average spatial enhancement ξ (cf. Eq. (95)) at each value of the pair $\lambda^\ddagger$, $f^\ddagger$. More details on the numerical minimization may be found in Refs. 29 and 43. A simplification arises for the case a symmetric potential and a symmetric coupling function, $g(q)/q$. The symmetry implies that $f^\ddagger = a_0 q^\ddagger$ is a solution of Eq. (87) and so one is left with only one independent variable, the barrier frequency.

The optimal planar dividing surface VTST has been used to study a variety of problems. A study of space-independent but exponential time-dependent friction was presented in Ref. 43. The major interesting result was the prediction of a memory suppression of the rate of reaction which occurs when the memory time and the inverse damping time ($1/\gamma$) are of the same order. When this happens, the time it takes the particle to diffuse over the barrier is similar to the memory time and the particle "feels" the nonlinearity in the potential of mean force. This leads to substantial reduction of the rate relative to the parabolic barrier estimate.

A study of the effects of space-dependent friction and time-dependent friction was presented in Ref. 29. One finds that when the friction is stronger in the well than at the barrier, the spatial enhancement factor becomes substantially larger than unity, again leading to a substantial reduction of the rate relative to the parabolic barrier estimate. In all cases, the effects become smaller as the barrier height measured in units of k_BT becomes larger. Comparison with molecular dynamics simulations shows that the optimal planar dividing surface estimate for the rate is essentially exact.

A planar dividing surface might seem to lead to divergences in the case of a cubic potential of mean force. This question has been dealt with at length in Ref. 79. By introducing a kink into the planar dividing surface one can remove the divergence. In

practice, unless the barrier is very small, the kink has hardly any effect on the location of the barrier or the barrier frequency $\lambda^{\ddagger}$.

V. VTST FOR CONDENSED PHASES

A. Reduction to Two Degrees of Freedom

In the previous section we demonstrated how variational transition state theory may be usefully applied to systems described by a space- and time-dependent generalized Langevin equation. The harmonic nature of the bath implicit in the STGLE led to a compact analytical expression for the optimized planar dividing surface result. Except for very low temperatures, most reactive systems cannot be described in terms of a harmonic bath. In this section we demonstrate how the VTST formalism may be applied to general condensed phase reactive systems. For a recent review, see Ref. 80.

The Hamiltonian describing the system and the bath will have the form

$$H = \frac{p_q^2}{2} + \sum_j \frac{p_{x_j}^2}{2} + V_q(q) + V_x(\underline{x}) + V_i(q, \underline{x}) \tag{100}$$

The notation is similar to the one used for the STGLE (cf. Eq. (29)). We assume the existence of N bath degrees of freedom and the summation is over all of them. The notation $\underline{x}$ denotes the vector $x_1, x_2, \ldots, x_N$. This form of the Hamiltonian is applicable to systems in 3D as long as one considers the motion in Cartesian coordinates.

The potential V has three parts. The "gas-phase" system potential is denoted by V_q, the potential of interaction between all bath degrees of freedom is denoted V_x and the interaction potential between the system and the bath is denoted V_i. We have assumed that the system is one-dimensional for the sake of simplicity. In principle, the system coordinate q may be generalized to M degrees of freedom which would describe the molecular motion of a molecule with M degrees of freedom in the gas phase. The potentials are not restricted to being harmonic.

The potential of mean force $w(q)$ is defined as in Eqs. (18) and (20). It is characterized by reactant and product wells at $q = q_a$ and $q = q_b$ respectively and a barrier at $q = q^{\ddagger}$. The TST expression for the rate is given in Eq. (76). The standard choice for the transition state, is the barrier top of the potential of mean force. As discussed in the previous section, this choice leads to the one-dimensional TST estimate for the rate Γ_{1D}, given in Eq. (77). It should be stressed that this one-dimensional estimate, derived by Chandler (10), is already very useful. The potential of mean force includes in it an averaging over all system and bath modes excluding the reaction coordinate. It will in general be quite different from the "gas-phase potential" $V_q(q)$ and so will include solvation effects on the barrier height.

This derivation indicates though how to include more subtle effects of the environment. There is nothing that limits one to the dividing surface $f = q - q^{\ddagger}$. The only restriction on the dividing surface is that any reactive trajectory must cross it. A generalization would be to allow the dividing surface to be curved and thus depend on two coordinates. The best choice for these two collective modes is not obvious a priori. It is here that the power of VTST will be used very effectively. The variational principle which says that the best dividing surface is the one that minimizes the flux will be used to determine the optimal choice of these two coordinates. The program for this section is thus as follows:

a. Define two collective modes ρ, σ and a dividing surface $f = f(\rho, \sigma)$ which is a function of these two modes only.
b. Define a free-energy surface $W(\rho, \sigma)$, which is the two-degrees-of-freedom generalization of the potential of mean force $w(q)$.
c. Derive the VTST expression for the rate based on the restricted dividing surface and show that the effects of the bath are now incorporated through the free-energy surface $W(\rho, \sigma)$.

Motivated by the optimized planar dividing surface VTST presented in the previous section (81), it is natural to define the two orthogonal collective modes ρ, σ as

$$\rho \equiv a_0 q + \sum_j a_j x_j \tag{101}$$

$$\sigma \equiv a_1 q - \frac{a_0}{a_1} \sum_j a_j x_j \tag{102}$$

The transformation coefficients a_j are independent of any of the coordinates and are normalized as in Eq. (80). The momenta conjugate to the two collective modes are

$$p_\rho = a_0 p_q + \sum_j a_j p_{x_j} \tag{103}$$

$$p_\sigma = a_1 p_q - \frac{a_0}{a_1} \sum_j a_j p_{x_j} \tag{104}$$

With these definitions, the system coordinate may be written as the linear combination

$$q = a_0 \rho + a_1 \sigma \tag{105}$$

In the following the coordinate ρ will denote the generalized reaction coordinate (the analog of the coordinate f in the previous section) and the coordinate σ the collective bath mode.

The free-energy surface $W(\rho, \sigma)$ is defined as

$$W(\rho, \sigma) \equiv -\frac{1}{\beta} \ln \frac{S \int dq \, \Pi_j dx_j \, \delta(\rho - a_0 q - \Sigma_j a_j x_j) \delta(\sigma - a_1 q + (a_0/a_1) \Sigma_j a_j x_j) e^{-\beta V}}{\int dq \, \Pi_j dx_j \, e^{-\beta V}} \tag{106}$$

Here S is a normalization constant with the dimension of an area:

$$S \equiv \int d\rho \, d\sigma \, e^{-\beta W(\rho, \sigma)} \tag{107}$$

The free-energy surface $W(\rho, \sigma)$ is related to the potential of mean force $w(q)$. With some straightforward manipulation of Eqs. (18) and (106) one can prove the identity

$$\frac{e^{-\beta w(q)}}{\int dq \, e^{-\beta w(q)}} = \frac{\int d\rho \, d\sigma \, \delta(q - a_0 \rho - a_1 \sigma) e^{-\beta W(\rho, \sigma)}}{\int d\rho \, d\sigma \, e^{-\beta W(\rho, \sigma)}} \tag{108}$$

The dividing surface is assumed to be a function of the two collective modes, that is $f = f(\rho, \sigma)$. We will see that this implies that the reactive flux (the numerator in Eq. (76)) can be expressed in terms of a two-degree-of-freedom Hamiltonian whose potential energy surface is the free-energy surface $W(\rho, \sigma)$.

The restriction that the dividing surface is in the (ρ, σ) configuration space implies that the momentum perpendicular to the dividing surface may be expressed solely in terms of the generalized coordinates and their associated momenta:

$$\nabla f \cdot \mathbf{p} = \frac{\partial f}{\partial \rho} p_\rho + \frac{\partial f}{\partial \sigma} p_\sigma \tag{109}$$

Introducing the identity

$$1 = \int dp_\rho \, dp_\sigma \, \delta\left(p_\rho - a_0 p_q - \sum_j a_j p_{x_j}\right) \delta\left(p_\sigma - a_1 p_q + \frac{a_0}{a_1} \sum_j a_j p_{x_j}\right) \tag{110}$$

into the numerator and denominator of Eq. (76) enables explicit integration over the system momentum p_q and all bath momenta p_{x_j}. The integration over the system and bath coordinates may also be formally solved by introducing an analogous identity for the coordinates ρ, σ and using the definition of the free-energy surface $W(\rho, \sigma)$. This leads to the result

$$\Gamma_a = \frac{\beta}{2\pi} \frac{\int dp_\rho \, d\rho \, dp_\sigma \, d\sigma \, \delta[f(\rho, \sigma)](\nabla f \cdot \mathbf{p})\theta(\nabla f \cdot \mathbf{p}) e^{-\beta H(\rho,\sigma)}}{\int d\rho \, d\sigma \, e^{-\beta W(\rho,\sigma)}} \tag{111}$$

Here, **p** denotes the generalized velocity vector only in the two (collective mode)-degrees-of-freedom phase space and $H(\rho, \sigma)$ denotes the effective two-degrees-of-freedom Hamiltonian:

$$H(\rho, \sigma) \equiv \tfrac{1}{2}(p_\rho^2 + p_\sigma^2) + W(\rho, \sigma) \tag{112}$$

Equations (111) and (112) generalize Chandler's one-dimensional result. The TST upper bound for the rate may be obtained as the variational solution of an effective two-degrees-of-freedom problem in which the potential is a two-degrees-of-freedom free-energy surface.

We shall see that the introduction of two collective modes suffices to account for the so-called dynamic friction effects. In other words, the dynamic friction is in fact not dynamic at all but is accounted for in terms of a free-energy surface. To reach this goal we still lack a number of elements. The transformation coefficients have yet to be defined and one needs to solve for the optimal dividing surface. Both these goals are attained by making explicit use of the variational property of transition state theory.

B. Nonlinear Kramers-Grote-Hynes Theory

Kramers' result for the rate in the spatial diffusion limit and its later generalization was based on solution of the Langevin equation for a parabolic barrier. The reasoning was that in this limit the rate-determining step is the rate of diffusion across the barrier so that only the barrier region is important and one can well approximate it as parabolic. The mathematical formulation of this reasoning was that as long as the temperature was low enough such that $\beta[w(q^\ddagger) - w(q_a)] \gg 1$, a steepest descent estimate for the rate is quite accurate. This estimate involves only the second derivative of the potential about the barrier top. We will use the same approach to estimate the rate using the free-energy surface in two degrees of freedom.

We assume that the free-energy surface has a saddle point at $\rho^\ddagger$, $\sigma^\ddagger$ and that its parabolic expansion is

$$W(\rho, \sigma) \simeq W(\rho^\ddagger, \sigma^\ddagger) + \tfrac{1}{2}W_{\sigma\sigma}(\sigma - \sigma^\ddagger)^2 - \tfrac{1}{2}W_{\rho\rho}(\rho - \rho^\ddagger)^2 \tag{113}$$

Here we have imposed the condition that the generalized coordinates are the normal modes of the saddle point. This is not a restriction, since these coordinates are linear combinations of the original physical coordinates, so any additional linear combination is permitted. We have also explicitly assumed that ρ is the reaction coordinate and σ is the stable mode so that $W_{\rho\rho}$ and $W_{\sigma\sigma}$ are positive.

The relationship between the potential of mean force and the free-energy surface as given in Eq. (108) leads to some important identities. The parabolic expansion for the potential of mean force is denoted

$$w(q) \simeq w(q^\ddagger) - \tfrac{1}{2}\omega^{\ddagger 2}(q - q^\ddagger)^2 \tag{114}$$

Insertion of the parabolic expansion (Eq. 113) for the free-energy surface and the potential of mean force (Eq. 114) into Eq. (108) and equating coefficients for q^2, q^1, q^0 leads respectively to the following three identities:

$$\frac{1}{\omega^{\ddagger 2}} = \frac{a_0^2}{W_{\rho\rho}} - \frac{a_f^2}{W_{\sigma\sigma}} \tag{115}$$

$$q^\ddagger = a_0\rho^\ddagger + a_f\sigma^\ddagger \tag{116}$$

$$\frac{e^{\beta w(0)}}{L} = \left(\frac{2\pi}{\beta}\frac{\omega^{\ddagger 2}}{W_{\rho\rho}W_{\sigma\sigma}}\right)^{1/2}\frac{e^{-\beta W(\rho^\ddagger,\sigma^\ddagger)}}{S} \tag{117}$$

The first identity relates the saddle point frequencies to the parabolic barrier frequency. It results from the condition that the collective modes are normal modes of the free-energy surface such that $W_{\rho\sigma} = 0$. The second identity means that the saddle point of the free-energy surface necessarily lies on the subspace $q = q^\ddagger$ of the full coordinate space and the third identity relates the barrier height at the saddle point to the barrier height of the potential of mean force.

The separability of the two modes in the parabolic expansion of the free-energy surface implies that the optimal dividing surface is just $f = \rho - \rho^\ddagger$. Inserting this form into the rate expression (Eq. (111)) leads, after some straightforward manipulation and use of the identities in Eqs. (115) and (117), to the important result

$$\Gamma_{a_{II}} = \left[\frac{W_{\rho\rho}}{\omega^{\ddagger 2}}\right]^{1/2}\Gamma_{a_{1D}} \tag{118}$$

The addition of the extra degree of freedom leads to a correction to the one-dimensional result in the form of a prefactor which is just the reduced barrier frequency at the saddle point. This result is very general. The KGH expression for the rate in the spatial diffusion limit (Eq. (78)) is just a special case in which the bath modes are harmonic and the coupling between the system and the bath is bilinear. However, Eq. (118) is much more general, in fact it is not yet completely defined since we have not yet shown how to determine the transformation coefficients a_0, a_j, $j = 1, \ldots, N$.

C. Optimizing the Transformation Coefficients

In view of the variational property of transition state theory it is evident that within the parabolic barrier estimate for the rate, the optimal transformation coefficients are those that minimize the parabolic barrier frequency $W_{\rho\rho}^{1/2}$ of the free-energy surface, subject to the constraint that the coefficients a_j are normalized.

Using the definition of the free-energy surface (Eq. 106) one finds after some manipulation the following expression for $W_{\rho\rho}$:

$$W_{\rho\rho} = \beta[\langle (L_\rho V)^2\rangle - \langle L_\rho V\rangle^2] - \langle L_\rho^2 V\rangle \tag{119}$$

where the operator L_ρ is defined as

$$L_\rho \equiv a_0 \frac{\partial}{\partial q} + \sum_j a_j \frac{\partial}{\partial x_j} \tag{120}$$

and the brackets denote the *centroid* average:

$$\langle F\rangle \equiv \frac{\int \Pi_j dx_j \; F\delta(\Sigma_n \; a_j x_j) e^{-\beta V}}{\int \Pi_j dx_j \; \delta(\Sigma_j \; a_j x_j) e^{-\beta V}} \tag{121}$$

where F and V are evaluated at $q = q^\ddagger$, which is the expansion point.

In anticipation of the final result, it is useful to define a bath force constant matrix **K** whose elements are

$$K_{jk} \equiv \langle V_{x_j x_k}\rangle - \beta[\langle V_{x_j} V_{x_k}\rangle - \langle V_{x_j}\rangle\langle V_{x_k}\rangle] \tag{122}$$

Here V_{x_j} denotes partial differentiation with respect to the variable x_j. This matrix is symmetric and so may be diagonalized with an orthogonal transformation matrix **O** leading to a new set of bath coordinates z_j, $j = 1, \ldots, N$, such that

$$x_k = \sum_j o_{jk} z_j \tag{123}$$

The eigenvalues of the matrix **K** will be denoted ω_j^2, $j = 1, \ldots, N$. It is also useful to transform from the original coefficients a_j to new coefficients a_j' using the same orthogonal transformation:

$$a_j' = \sum_j a_k o_{jk} \tag{124}$$

To complete the notation, the coupling coefficients c_j are defined as

$$c_j \equiv \langle V_{z_j q}\rangle - \beta[\langle V_{z_j} V_q\rangle - \langle V_{z_j}\rangle\langle V_q\rangle], \qquad j = 1, \ldots, N \tag{125}$$

and a "barrier frequency" ω_q is

$$\omega_q^2 \equiv \beta[\langle V_q V_q\rangle - \langle V_q\rangle\langle V_q\rangle] - \langle V_{qq}\rangle \tag{126}$$

With this notation, the second derivative of W may be written in the illuminating form:

$$W_{\rho\rho} = a_0^2\omega_q^2 - 2a_0 \sum_j a_j' c_j - \sum_j a_j'^2 \omega_j^2 \tag{127}$$

Using the method of Lagrange multipliers, it is now necessary to find the stationary points of the function $L(a_0, \underline{a}')$:

$$L(a_0, \underline{a}') = W_{\rho\rho} + \mu\left(1 - a_0^2 - \sum_j a_j'^2\right) \tag{128}$$

In principle one should also add the constraint that the collective modes are orthogonal (Eq. 113); however, minimizing the negative eigenvalue in an unconstrained form automatically leads to orthogonality.

The variation is quite complicated since the various quantities appearing in Eq. (128) such as c_j and ω_j are themselves functions of the coefficients a_j'. The averages are constrained (cf. Eq. (121)) to the centroid defined by the a_j''s. To circumvent this complication one may use a self-consistent-field approach. Given an initial choice of the coefficients, one varies the Lagrangian in Eq. (128), ignoring the dependence of the c_j's, and the frequencies ω_j and ω_q on the transformation coefficients, to find a new set of transformation coefficients. The new set is then used to generate a new set of c_j's, etc., and the procedure is repeated until convergence is obtained.

Using this self-consistent approach, the variation of the Lagrangian with respect to a_j' gives the by-now familiar result

$$a_j' = \frac{c_j}{\omega_j^2 + \mu} \tag{129}$$

Imposing the condition of normalization gives an expression for a_0^2:

$$a_0^2 = \left[1 + \sum_j \frac{c_j^2}{(\omega_j^2 + \mu)^2}\right]^{-1} \tag{130}$$

and it will not come as a surprise to find that variation with respect to a_0 gives a Grote-Hynes relation for the Lagrange multiplier μ:

$$\mu = \frac{\omega_q^2 + \Sigma_j\, c_j^2/\omega_j^2}{1 + \Sigma_j\, c_j^2/\omega_j^2(\omega_j^2 + \mu)} \tag{131}$$

To summarize, using the definition of the coupling coefficients c_j and bath frequencies ω_j as defined from Eqs. (122)–(125) one can construct the time-dependent friction function:

$$\gamma(t) \equiv \sum_j \frac{c_j^2}{\omega_j^2} \cos(\omega_j t) \tag{132}$$

such that the renormalized barrier frequency is a solution of the Grote-Hynes equation:

$$\mu = \frac{\omega_q^2 + \gamma(0)}{1 + \hat{\gamma}(\mu^{1/2})/\mu^{1/2}} \tag{133}$$

thus completing the generalization of the KGH theory to nonlinear system bath interactions and anharmonic baths. Insofar as the parabolic barrier approximation holds, or if the nonlinear part of the free energy surface is positive definite, this result will give a rigorous upper bound for the classical rate of reaction.

D. Summary

Numerical implementation of the theory presented in the previous section to a realistic system proceeds via the following steps:

a. Identify a reaction coordinate q, this will usually be a bond coordinate of the reacting molecular species.

b. Compute via standard Monte Carlo methods the potential of mean force $w(q)$ and extract the barrier height, location, and frequency.
c. Make an initial choice for the transformation coefficients a_j as delineated below.
d. Using standard Monte Carlo methods evaluate the centroid averages of the first and second derivatives of the full potential at the barrier ($q = q^{\ddagger}$).
e. Diagonalize the resulting force constant matrix to obtain the values of the frequencies (ω_j's) and coupling coefficients c_j.
f. Construct the new set of transformation coefficients a_j' and use them as input back in step d.
g. Repeat steps d–f until convergence is obtained.
h. Construct the time-dependent friction function and solve the Grote-Hynes equation to obtain an optimized estimate for the reaction rate and collective modes.

The initial guess for the transformation coefficients needed in step c may be guided from the structure of the generalized Langevin equation. It is reasonable to demand that this initial choice be such that in the limit that a GLE is a valid description of the dynamics it gives the exact GLE result. A choice that meets this criterion is to define the initial coupling coefficients through the relation

$$c_{j0} \equiv \left\langle \frac{\partial^2 V}{\partial x_j \partial q} \right\rangle_{q=0} \tag{134}$$

and the initial frequencies as

$$\omega_{j0}^2 \equiv \left\langle \frac{\partial^2 V}{\partial x_j^2} \right\rangle_{q=0} \tag{135}$$

In these last two definitions the averages are taken to be *simple* thermal averages at the barrier instead of centroid averages. With this initial guess one will find (after some manipulation) that if the GLE is a true representation of the Hamiltonian then one single iteration converges to the KGH estimate for the rate.

The VTST method has been recently implemented for the model S_N2 reaction $Cl^- + CH_3Cl \rightarrow ClCH_3 + Cl^-$ in water. An extensive numerical study of this model was described by Bergsma et al. and Gertner et al. in Refs. 48 and 49. They used the reactive flux formulation to estimate the numerically exact rate constant. They also tested the GLE model for the reaction dynamics. As mentioned in Sec. II.C they represented the time-dependent friction function as the force autocorrelation function when the reacting system is clamped at the top of the barrier of the potential of mean force.

The VTST study of this same system has been described in detail in Refs. 82 and 83. The main results are that there is excellent agreement between the VTST predictions for the rate constants and the numerically exact results based on the reactive flux method. Convergence of the iteration method described in this section is very fast, at worst one needed five iterations, typically, two or three were sufficient. The friction function generated by the VTST method was in excellent agreement with the ad hoc procedure used in Refs. 48 and 49, this was attributed to the relatively fast time scale of the reaction, such that only the near vicinity of the barrier really contributes to the friction function.

The VTST method also allows one to determine the dynamical source of the friction and its range. It was found that the largest contribution comes from solvent translational modes, solvent rotational modes have a small effect, solvent stretch modes can be com-

pletely neglected. By inspecting the optimized transformation coefficients, the VTST method provides information on the range over which the solvent significantly perturbs the reaction dynamics. For the specific models used, it was found that inclusion of 64 water molecules is marginally sufficient. Molecules at a distance greater than 11 Å from the reaction center have a negligible influence on the magnitude of the frictional force although they could affect the potential of mean force. Finally, for the same model, the VTST method also demonstrated that solute stretch, rotational, and translational modes have a negligible effect on the rate constant.

VI. ENERGY DIFFUSION AND PGH THEORY

A. Preliminaries

As mentioned in the Introduction, in the underdamped case, the rate is limited by the energy diffusion process while the spatial diffusion factor κ_{sd} is unity. Transition state theory, using a dividing surface in configuration space grossly overestimates the rate since it assumes that reactive trajectories are thermally distributed. In the energy-diffusion-limited regime, the exchange of energy between the particle and the bath is slow, and once the particle has sufficient energy to react it does so. The population of reacting particles with energy above the top of the barrier is severely depleted relative to the canonical distribution. In this limit, one must consider the dynamics, a thermal equilibrium theory such as TST is insufficient (even if one chooses a dividing surface in energy space (78, 84)).

Kramers solved the problem in the underdamped limit but could not find a uniform formula valid for all damping strengths. A major step forward was made by Melnikov and Meshkov (85,86), who derived a more general solution for the Fokker-Planck equation representation of the Langevin equation. Their solution provided a uniform expression for the rate leading from the energy-diffusion-limited expression to the one-dimensional TST expression. They did not derive an expression that led directly to the KGH result. The turnover problem was finally solved by Pollak, Grabert, and Hänggi (PGH) (12) and included the case of memory friction. In this section we will outline the PGH turnover theory. More details as well as extensions dealing with quantum effects may be found in Refs. 12 and 67.

At first we limit ourselves to the case of space-independent friction. A central feature in PGH theory is that the dynamics is considered in the normal modes of the parabolic barrier. This ensures that if the particle reaches the parabolic barrier of the unstable mode with enough energy, it will immediately cross it. The same is not true when considering the dynamics in the system coordinate for which the motion is not separable even in the barrier region. Another important factor in PGH theory is that in contrast to all previous approaches, the energy-diffusion-limited regime is not characterized by a small damping constant ($\gamma/\omega^{\ddagger} \ll 1$), but by a weak coupling between the unstable parabolic barrier normal mode ρ and the other stable modes.

The potential of mean force may always be written as

$$w(q) = w(q^{\ddagger}) - \tfrac{1}{2}\omega^{\ddagger 2}(q - q^{\ddagger 2})^2 + w_1(q) \tag{136}$$

where $w_1(q)$ is termed the *nonlinearity* of the potential of mean force. Recalling the definition of the collective mode σ (cf. Eq. (52)), assuming (without loss of generality) that $q^{\ddagger} = 0$ and using the fact that the system coordinate q is a linear combination of ρ

and σ (cf. Eq. (54)) one finds that the exact equation of motion for the unstable mode is

$$\ddot{\rho} - \lambda^{\ddagger 2}\rho = -u_{00}w_1'(u_{00}\rho + u_l\sigma) \tag{137}$$

Evidently, if $u_l = 0$ (cf. Eq. (53)), the motion of the unstable mode is decoupled from the rest of the stable modes. In this limit, the escape rate would be zero since the particle cannot escape from the well without receiving the necessary energy from its surrounding. The small parameter which identifies the energy-diffusion-limited regime is thus u_l.

Note that when the damping constant $\gamma \to 0$ also $u_l \to 0$, as may be seen from inspection of Eqs. (43) and (53). It is important to realize that in the presence of memory friction, there exist limits such that $u_l \to 0$ but $\lambda^{\ddagger} \neq \omega^{\ddagger}$ (12). Claims to the contrary not withstanding (87), using u_l as the perturbation parameter leads therefore to a more general theory for the depopulation factor than any theory based on the weak damping limit which is defined by a small damping constant.

The energy E of the unstable mode is defined as

$$\begin{aligned} E &= \tfrac{1}{2}p_\rho^2 + V(\rho) \\ V(\rho) &\equiv -\tfrac{1}{2}\lambda^{\ddagger 2}\rho^2 + w_1(u_{00}\rho) \end{aligned} \tag{138}$$

When the particle is in the close vicinity of the barrier one may ignore the nonlinear part of the potential w_1. If the energy $E > 0$ the particle will cross the barrier, if $E < 0$ it will be reflected.

Following Kramers we imagine injecting particles at a constant rate near the bottom of the well and removing them when they reach the adjacent well or the continuum. The system will approach a steady-state probability W with a constant flux across the barrier. If the barrier height is sufficiently large with respect to k_BT then close to the bottom of the well the probability W will be identical to the thermal distribution. If equilibrium is maintained for all energies, then in the vicinity of the barrier, the distribution W (normalized to one particle in the well) takes the form

$$W(\rho, p_\rho) = \frac{\beta\omega_a}{2\pi}\frac{\lambda^{\ddagger}}{\omega^{\ddagger}}e^{-\beta(E+E^{\ddagger})} \tag{139}$$

For $E < 0$, let $f(E)\,dE\,dt$ denote *the probability to find the system within the time interval dt, with a mode energy between E and E + dE at a turning point of the* ρ *mode.* For a thermal distribution W, near the barrier top, one finds that

$$f_{eq}(E) = \frac{\beta\omega_a}{2\pi}\frac{\lambda^{\ddagger}}{\omega^{\ddagger}}e^{-\beta(E+E^{\ddagger})} \tag{140}$$

For $E > 0$ the system crosses the barrier. In this case, $f(E)\,dE\,dt$ will denote the probability to find the system at the barrier $\rho = 0$, within the time interval dt and with energy between E and $E + dE$. The thermal distribution for positive energies is identical in form to that given in Eq. (140).

The rate of transitions out of the well is by definition

$$\Gamma = \int_0^\infty dE\, f(E) \tag{141}$$

since all particles reaching the barrier with positive energy in the unstable mode escape. This is a crucial point. If the particle reaches the barrier with positive energy in the system coordinate q it does not necessarily escape. For finite damping, the bath may cause the particle to recross the barrier. But the unstable mode ρ is rigorously separated in the barrier region from all other modes as long as the energy of the escaping particle does not deviate too much from the barrier energy. *The recrossing problem does not occur in the normal mode representation.*

The rate formula Eq. (141) is exact. Approximations enter because the nonequilibrium probability $f(E)$ is not known exactly. Note though that in the equilibrium limit, replacing $f(E)$ by $f_{eq}(E)$ in Eq. (141) immediately leads to the KGH estimate for the rate. In the strong coupling limit, energy diffusion is fast and equilibrium is maintained throughout. In this limit, PGH theory reduces to the correct spatial diffusion limited expression.

The distribution $f(E)$ is determined by the dynamics. Suppose the particle with energy E' is reflected from the barrier. It will move to the well and will at some later time return to the barrier region with energy E. The distribution $f(E)$ is determined by the conditional probability $P(E|E')\,dE$ that a system leaving the barrier region with energy E' in the ρ mode returns to the barrier with an energy between E and $E + dE$. In the steady state (67), one will find that the distribution of particles $f(E)$ at energy E is related to the distribution at energy E' by the relation

$$f(E) = \int_{-E^{\ddagger}}^{0} dE'\ P(E|E')f(E') \tag{142}$$

This equation is of central importance in PGH theory. Deep in the well, the unstable mode is strongly coupled to the other modes and equilibrium is maintained. This is the boundary condition needed to solve the integral equation. It also allows one to replace the lower limit of the integration by $-\infty$ provided that the barrier height is large with respect to k_BT.

B. The Conditional Probability Kernel $P(E|E')$

All the dynamics of the energy diffusion process are included in the probability kernel. The energy loss and energy fluctuations of the particle are determined with the aid of perturbation theory. The zeroth-order (in u_l) equation of motion for the unstable mode is

$$\ddot{\rho} + V'(\rho) = 0 \tag{143}$$

The exact equation of motion for the jth stable oscillator is

$$\ddot{y} + \lambda_j^2 y_j^2 = -u_{j0}w_1'(u_{00}\rho + u_l\sigma) \tag{144}$$

The first-order perturbation theory equation of motion for the jth stable oscillator is obtained by setting $u_l = 0$ in the argument of w_1' in Eq. (144). This reduces the equation to that of a forced oscillator, where the forcing function is

$$F(t) \equiv -w_1'[u_{00}\rho(t)] \tag{145}$$

and is determined by the unperturbed motion of the unstable ρ mode, as in Eq. (143).

The energy of the jth oscillator at time t is

$$E_j(t) = \tfrac{1}{2}[p_j^2(t) + \lambda_j^2 y_j^2(t)] \tag{146}$$

The total energy of the bath is

$$E_B(t) = \sum_j E_j(t) \tag{147}$$

It is a matter of some algebra, using the known solution for forced harmonic oscillators (cf. Ref. 12) to show that the oscillator energy at time t is given in terms of the initial conditions of the bath as

$$E_B(t) = E_B(0) - \Delta(t) + \delta(t) \tag{148}$$

The *systematic* energy loss $\Delta(t)$ (which is positive definite; cf. Ref. 12) is found to be

$$\Delta(t) = \frac{1}{2}\int_0^t dt' \int_0^t dt'' \, F(t')K(t' - t'')F(t'') \tag{149}$$

where $K(t)$ is the friction kernel defined in Eq. (47) and the force F has been defined in Eq. (145). The *random* energy loss $\delta(t)$ is dependent on the initial conditions of the bath:

$$\delta(t) = \int_0^t dt' \sum_j u_{j0}[p_{y_j}(0)\cos(\lambda_j t') - \lambda_j y_j(0)\sin(\lambda_j t')]F(t') \tag{150}$$

The energy gained (or lost) by the bath is also the energy lost (or gained) by the stable mode. Averaging over all initial conditions of the bath will thus lead to an explicit expression for the conditional probability kernel:

$$P(E(t)|E') = \langle \delta[E(t) - E' + \Delta(t) - \delta(t)] \rangle \tag{151}$$

where the average is over the canonical distribution of initial conditions of the bath $\exp(-(\beta/2)\Sigma_j [p_{y_j}^2(0) + \lambda_j^2 y_j^2(0)])$ and $\delta[\ ]$ is the Dirac δ function. Since the fluctuating part of the energy loss is linear in the initial conditions of the bath and they are Gaussian distributed one readily obtains (using the Fourier representation of the Dirac δ function) that the conditional probability kernel is a Gaussian:

$$P(E(t)|E') = \left(\frac{\beta}{4\pi\Delta(t)}\right)^{1/2} \exp\left(-\beta\frac{[E - E' + \Delta(t)]^2}{4\Delta(t)}\right) \tag{152}$$

C. The Depopulation Factor

The main contribution to the systematic energy loss $\Delta(t)$ comes from motion in the region of the well. When the particle is close to the barrier top, the forcing function $F(t)$ is negligibly small. Since the well depth is large when compared to $k_B T$, the energy loss $\Delta(t)$ taken over one period of motion will be quite insensitive to the energy. To leading order therefore it may be taken as a constant. It is then convenient to evaluate it at the barrier energy, for which the period of motion of the unperturbed particle is infinite. This allows one (67) to conveniently rewrite the energy loss as

$$\Delta = \frac{1}{2\pi}\int_{-\infty}^{\infty} d\lambda \, \lambda I(\lambda)|\tilde{F}(\lambda)|^2 \tag{153}$$

$$\tilde{F}(\lambda) \equiv \int_{-\infty}^{\infty} e^{i\lambda t} F(t) \tag{154}$$

Henceforth the notation Δ without the argument will be used exclusively to denote the energy loss associated with the infinite period orbit at the barrier energy. The spectral density of the normal modes $I(\lambda)$ has been defined in Eq. (49) and is easily expressed in terms of the usual spectral density $J(\omega)$ as in Eq. (51). For many one-dimensional potentials, the infinite period trajectory is known analytically so that also the Fourier-transformed force $\tilde{F}(\lambda)$ is known analytically. Finding the energy loss reduces then to at most a single quadrature.

Given the energy loss, the depopulation factor is found by solution of the integral equation, Eq. (142). A clear description of the necessary algebra may be found in the appendix of Ref. 67; here we just write the final result:

$$\Upsilon = \Upsilon(\Delta) \equiv \exp\left(\frac{1}{2\pi}\int_{-\infty}^{\infty} dx\, \frac{\ln[1 - e^{-\beta\Delta(x^2+1/4)}]}{x^2 + 1/4}\right) \tag{155}$$

When the energy loss is small in comparison to k_BT one finds that the depopulation factor reduces to $\Upsilon \sim \beta\Delta$ and one recovers the usual estimate for the rate in the energy diffusion limit. When the energy loss is large compared to k_BT, the depopulation factor approaches unity exponentially fast, $\Upsilon \sim 1 - (2/\sqrt{\pi\beta\Delta})e^{-\beta\Delta/4}$.

The result given in Eq. (155) is correct for a single-well potential. For a double-well potential in which the energy loss in each of the two wells is Δ_a, Δ_b, one must revise the integral equation to take into consideration the flux returning from each one of the wells. As shown by Melnikov (85,86), this then leads to the deceptively simple result for the depopulation factor:

$$\Upsilon = \frac{\Upsilon(\Delta_a)\Upsilon(\Delta_b)}{\Upsilon(\Delta_a + \Delta_b)} \tag{156}$$

It is important to realize the limitations of PGH theory. The derivation depends on three central conditions:

(a) First-order perturbation theory, $u_l^2 \ll 1$.
(b) The energy loss is mainly determined by the dynamics at the barrier energy.
(c) A large reduced barrier height $E^{\ddagger} \gg k_BT$.

The first condition is usually not too stringent. One will often find that although $u_l^2 \ll 1$ the energy loss Δ can become much larger than unity. At this point the depopulation factor becomes unity and the energy loss mechanism is no longer of any importance. The second condition is critical. In the presence of memory friction it may happen that the bottleneck for the energy diffusion process is at energies substantially lower than the barrier height, as demonstrated recently by Tucker and co-workers (88). In this case PGH theory must be substantially modified; see, for example, the discussion in Ref. 78. The large reduced barrier is also important. Finite barrier corrections have been discussed recently by Melnikov (89). Moreover, in the presence of memory friction, even when the perturbation parameter is small it may happen that the effective barrier for the unstable mode motion will become very small and this will again cause a breakdown of PGH theory. Such examples as well as a more detailed discussion of these points may be found in Ref. 12.

We have discussed here in detail the aspects of the turnover theory that lead to an expression for the rate constant. The same methodology may be also used to obtain more detailed information on the distribution $f(E)$ of particles hitting the barrier. Specifically

one can obtain an analytic expression for the average energy of escaping particles (86, 90). In the underdamped limit, one finds that the average energy is $\sqrt{\Delta} \ll \sqrt{k_B T}$ in agreement with earlier predictions of Büttiker et al. (92). As mentioned, particles with energy above the barrier get depleted and the distribution is very different from the thermal distribution. More details about the distribution may be found in Ref. 91.

D. Turnover Theory for Space- and Time-Dependent Friction

It is possible to extend the PGH treatment to the more general case of space- and time-dependent friction. The methodology would consist of first finding the optimized planar dividing surface which minimizes the number of recrossings, as described in Sec. V. One would then treat this coordinate as the unstable normal mode and repeat the PGH treatment. However, in many cases, when the damping is weak there is hardly any difference between the unstable mode and the system coordinate, while in the moderate damping limit, the depopulation factor rapidly approaches unity. Therefore, *if the memory time in the friction is not too long*, one can replace the more complicated (but more accurate) PGH perturbation theory, with a simpler theory in which the small parameter is taken to be c_j/ω_j^2 for each of the bath modes.

In such a theory, the zeroth-order equation of motion for the system coordinate is

$$\ddot{q} + \frac{dw(q)}{dq} = 0 \tag{157}$$

The first-order equations of motion for each of the bath oscillators take the form (cf. Eq. (29)):

$$\ddot{x}_j + \omega_j^2 q = c_j g(q) \tag{158}$$

where $g(q)$ is now a time-dependent forcing function whose time dependence is determined by the zeroth-order motion of the system coordinate q as in Eq. (157).

It is then a matter of some algebra, following the same steps as in PGH theory to find that the energy loss from the particle to the bath, taken over the infinite period motion of the particle at the barrier energy is

$$\Delta = \frac{1}{2} \int_{-\infty}^{\infty} \int_{-\infty}^{\infty} dt\, dt'\, \dot{g}(t)\gamma(t - t')\dot{g}(t') \tag{159}$$

where the dot denotes time differentiation. Given the energy loss, the depopulation factor is taken as in Eq. (155) for the single-well case and Eq. (156) for the double-well potential.

This version of the turnover theory for space- and time-dependent friction has been tested successfully against numerical simulation data, for a number of cases, in Refs. 28 and 29.

VII. MULTIDIMENSIONAL TURNOVER THEORY

A. Preliminaries

A multidimensional system is one in which the Hamiltonian describing the dynamics of the particle in the absence of friction has more than one degree of freedom. For simplicity, we will consider two degrees of freedom, denoting the reaction coordinate as q and a

perpendicular coupled mode by z. Each of the modes is coupled to the other via an interaction potential $w(q, z)$ and may be also coupled separately to a bath, described by independent friction functions and random forces.

The existence of two (or more) modes leads to a much richer physics than in the one-dimensional case. In the weak damping limit, a critical parameter is the extent of coupling between the two modes. If the coupling is stronger than the coupling of each mode to the bath, then there will be efficient energy transfer between the modes and the spectator mode will be able to "feed" energy into the reaction coordinate. In such a case, one would expect the two-dimensional rate to be larger than the one-dimensional (93–96). If though the coupling is weaker than the coupling to the baths then one would expect the multidimensional dynamics to reduce to an effective one-dimensional case. A complete turnover theory should be able to reduce correctly to all these limits and provide solutions also for intermediate regimes.

In the moderate and strong damping regimes, a critical parameter is the friction anisotropy, the ratio of damping strengths in the two modes. Berezhkovskii and Zitserman (97–99) have shown that depending on the coupling between the modes and the friction anisotropy, one can obtain regimes in which the "standard" solution, which is based on a parabolic expansion around the saddle point of the multidimensional potential energy surface fails. A turnover theory which deals uniformly with all these cases is described in this section.

The extension of Kramers' solution in the spatial diffusion limit to the multidimensional case was given by Langer (18) for ohmic friction and by Nitzan (38,93) and Grote and Hynes (94) for memory friction. Similarly, the extension of Kramers' energy diffusion result to the multidimensional case, when the coupling between the two modes is "strong" was given by Matkowsky, Schuss, and co-workers (19, 20), Borkovec and Berne (95,96), and Nitzan (38). A uniform expression for the rate which goes smoothly from the weak damping energy diffusion limited regime to the strong damping spatial-diffusion-limited regime, when the coupling between the modes is strong, has been derived only recently (21). Here we will sketch these most recent results and their extension to cases of weak and intermediate coupling between two modes.

The equations of motion of the particle are two coupled GLEs:

$$\ddot{q} + \frac{\partial w(q, z)}{\partial q} + \int^{t} dt' \, \gamma_q(t - t')\dot{q}(t') = \xi_q(t) \tag{160}$$

$$\ddot{z} + \frac{\partial w(q, z)}{\partial z} + \int^{t} dt' \, \gamma_z(t - t')\dot{z}(t') = \xi_z(t) \tag{161}$$

The notation $\dot{q}$ denotes the time derivative, and $\gamma_q(t)$ and $\gamma_z(t)$ are the time-dependent friction forces acting upon q and z respectively. The Gaussian random forces ξ_q, ξ_z are uncorrelated, with zero mean and obey the respective fluctuation dissipation relations:

$$\langle \xi_i(t)\xi_i(t') \rangle = \frac{1}{\beta} \gamma_i(t - t'), \qquad i = q, z \tag{162}$$

The potential w is assumed to have a well at q_0, z_0 and a barrier at $q = z = 0$.

In the Kramers turnover theory (12,67), the expression for the rate, valid for all values of the damping is still given as a product of three factors as in Eq. (6). As discussed in the previous section, the depopulation factor is determined uniquely by the reduced energy loss parameter $\delta \equiv \beta\Delta$ (12,67), the explicit dependence is given in Eq.

(155). One of the main differences between the one-dimensional and the multidimensional turnover theory comes from the change between the one-dimensional and multidimensional energy loss mechanism.

The Hamiltonian representation (42) of the two coupled GLEs is

$$H = H_{qz} + \frac{1}{2}\sum_j \left[p_{q_j}^2 + \left(\omega_{q_j}x_j - \frac{c_{q_j}}{\omega_{q_j}}q\right)^2\right] + \frac{1}{2}\sum_j \left[p_{z_j}^2 + \left(\omega_{z_j}y_j - \frac{c_{z_j}}{\omega_{z_j}}z\right)^2\right] \tag{163}$$

where H_{qz} is the Hamiltonian governing the system when it is decoupled from the bath

$$H_{qz} = \tfrac{1}{2}(p_q^2 + p_z^2) + w(q, z) \tag{164}$$

the (mass scaled) bath momenta and coordinates are denoted p_{q_j}, x_j, p_{z_j}, y_j. As usual, each bath mode is characterized by a harmonic frequency (ω_{q_j}, ω_{z_j}) and bilinear coupling coefficient to the reaction coordinate c_{q_j} or the perpendicular mode c_{z_j}. The Hamiltonian representation for the time-dependent frictions is

$$\gamma_i(t) = \sum_j \frac{c_{ij}^2}{\omega_j^2}\cos(\omega_j t), \qquad i = q, z \tag{165}$$

and we have used the same notation for the bath frequencies since they are identical for each bath, provided one uses the same discretization.

B. The Multidimensional Energy Loss

As a first step, we will assume that the two modes of the particle (q, z) are strongly coupled. As in the one-dimensional case, the important quantity which is needed for solution of the integral equation is the conditional probability kernel $P(E|E')$. This kernel describes the probability that the particle will start at the barrier with some well-defined energy E' in the system coordinates and momenta (all other degrees of freedom are thermalized), will go to the reactants zone and return to the barrier with energy E. Note that in the multidimensional case the energy of the particle, is defined as the energy in both modes.

As in PGH theory, one is interested in the energy loss to the bath only when the energy along the reaction coordinate is close to the barrier top (within k_BT). Any larger range will induce corrections which are of the order of the inverse barrier height ($1/\beta E^{\ddagger}$) which may be neglected. The energy loss is evaluated, using perturbation theory, as the energy transferred from the particle modes to all other modes. We are interested in the energy loss to the bath for a particle initiated at the barrier top returning to it at time t.

The *exact* equations of motion for the bath modes in the Hamiltonian representation of the GLE are

$$\ddot{x}_j + \omega_j^2 x_j = c_{q_j} q \tag{166}$$

$$\ddot{y}_j + \omega_j^2 y_j = c_{z_j} z \tag{167}$$

These equations are forced oscillator equations of motion whose solution in terms of the time dependence of q, z is well known. As in the weak damping version of PGH theory

described at the end of the previous section, these equations may be solved perturbatively. Since the damping is weak, the coupling coefficients c_{q_j} and c_{z_j} may be assumed to be small. One then solves the uncoupled dynamics of the system as determined by Hamilton's equations of motion derived for the uncoupled Hamiltonian H_{qz} (which we will denote as $q_0(t)$, $z_0(t)$) and uses these time-dependent solutions as known forcing functions for the bath equations of motions.

Any trajectory is determined by the initial conditions. At time $t = 0$ the initial values of the system coordinates and momenta are denoted as $p_q(0)$, $q(0)$, $p_z(0)$, $z(0)$. Each bath mode has initial values of the coordinates and momenta which correspond to an initial energy $E_{q_j}(0)$, $E_{z_j}(0)$:

$$E_{q_j}(0) = \frac{1}{2}\left[p_{q_j}(0)^2 + \left(\omega_j x_{q_j}(0) - q(0)\frac{c_{q_j}}{\omega_j}\right)^2\right] \tag{168}$$

and an analogous definition holds for E_{z_j}. The total energy of each of the two baths at time t is:

$$E_{B_i}(t) \equiv \sum_j E_{i_j}(t), \qquad i = q, z \tag{169}$$

Following the same perturbation theory as in PGH and integrating by parts leads to the result that at any later time t the total change in energy of the two baths $\Delta E(t)$ may be decomposed into systematic ($\Delta_j(t)$, $j = q, z$) and random components ($\delta_j(t)$, $j = q, z$):

$$\begin{aligned}\Delta E(t) &\equiv E_{B_q}(t) - E_{B_q}(0) + E_{B_z}(t) - E_{B_z}(0) \\ &= \Delta_q(t) + \Delta_z(t) + \delta_q(t) + \delta_z(t)\end{aligned} \tag{170}$$

The systematic energies gained by the baths are

$$\Delta_q(t) = \frac{1}{2}\int_0^t dt' \int_0^t dt'' \, \gamma_q(t' - t'')\dot{q}_0(t')\dot{q}_0(t'') \tag{171}$$

$$\Delta_z(t) = \frac{1}{2}\int_0^t dt' \int_0^t dt'' \, \gamma_z(t' - t'')\dot{z}_0(t')\dot{z}_0(t'') \tag{172}$$

The random components of the energy loss are given in terms of the initial conditions of the baths as

$$\delta_q(t) = -\int_0^t dt' \, q_0(t') \sum_j c_{q_j}\left[\frac{p_{q_j}(0)}{\omega_j}\sin(\omega_j t') + \left(x_j(0) - q(0)\frac{c_{q_j}}{\omega_j^2}\right)\cos(\omega_j t')\right] \tag{173}$$

and an analogous equation may be written down for δ_z.

The initial conditions of the bath are taken from a canonical distribution ($e^{-\beta H}$). The Hamiltonian equivalent is quadratic in the bath variables. Therefore the random components of the energy loss are Gaussian, with zero mean and their variance is just twice the systematic energy loss and the probability kernel is identical in form to the one-dimensional case.

There remains though an essential difference between the one-dimensional and the multidimensional case. In the latter case the total energy loss $\Delta(t)$ defined as

$$\Delta(t) = \Delta_q(t) + \Delta_z(t) \tag{174}$$

depends on the initial conditions of the system coordinates. The rate, however, is determined by trajectories whose energy is in the immediate vicinity ($\pm k_b T$) of the barrier. The velocity of these trajectories at the barrier is therefore very small, and the main contribution to the energy loss comes from the motion far from the barrier in the region of the well. Since we are assuming that the two degrees of freedom in the region of the well are strongly coupled, any trajectory $q(t)$, $z(t)$ will be ergodic. It is this assumption of strong coupling which simplifies the problem and leads to the conclusion that the energy loss of all trajectories will be identical.

The actual evaluation of the energy loss is based on explicit use of the ergodic theorem. The quantity Δ_t is defined as the energy lost per unit time by the particle during its traversal in the region of the well:

$$\Delta_t = \frac{1}{t}\,\Delta(t) \tag{175}$$

When the two modes are strongly coupled, the energy lost per unit time will be for all practical purposes *independent* of the precise initial conditions of the unperturbed trajectory initiated at the barrier. During the traversal of the well region, because of the strong coupling between the modes, the path will be chaotic, and so each trajectory explores the same region in phase space. In different wording, the energy loss per unit time is a time average over a chaotic trajectory. The ergodic theorem allows it to be replaced by a phase-space average.

Defining the friction-weighted velocity correlation function as

$$C_{\gamma\gamma}(t',\,E) \equiv \frac{\mathrm{Tr}\delta(E - H_{qz})[\dot{q}\gamma_q(t')\dot{q}(t') + \dot{z}\gamma_z(t')\dot{z}(t')]}{\mathrm{Tr}\delta(E - H_{qz})} \tag{176}$$

where the Tr operation is over the q, z phase space, we find that the energy loss per unit time is just the time integral (zero Laplace component) of the correlation function. Since the energy loss per unit time is (to leading order in $k_B T/E^{\ddagger}$) independent of the energy we may replace the microcanonical average in Eq. (176) by a canonical average over all energies *greater than the barrier top* and denote the thermally averaged function as $C_{\gamma\gamma}(t, \beta)$. We may safely assume that this correlation function decays faster than the time it takes the particle to return to the barrier and so may interchange integration limits in Eqs. (171) and (172) to find

$$\Delta_t = \int_0^{\infty} dt\; C_{\gamma\gamma}(t,\,\beta) \tag{177}$$

The energy loss itself is the product of the time it takes the particle to return to the barrier and the energy loss per unit time. This time, on the average is just the inverse of the RRKM unimolecular, canonical dissociation rate:

$$t(\beta) = k_{\mathrm{RRKM}}^{-1}(\beta) = \frac{\text{density}}{\text{flux}} = \frac{\mathrm{Tr}e^{-\beta H_{qz}}\theta(-H_{qz})}{\mathrm{Tr}e^{-\beta H_{qz}}\delta(q)\dot{q}\theta(-\dot{q})} \tag{178}$$

The final expression for the (reduced) energy loss is thus

$$\delta = \beta t(\beta)\Delta_t \tag{179}$$

At this point, the energy loss is given in terms of quantities which are determined purely by the uncoupled dynamics of H_{qz} and the time-dependent friction functions.

To make contact with previous approaches to the multidimensional turnover problem it is useful to consider the special case of ohmic friction for both modes such that

$$\gamma_i(t) = 2\gamma_i\delta(t), \qquad i = q, z \tag{180}$$

The energy loss per unit time reduces to the relatively simple expression

$$\Delta_t = \langle \gamma_q p_q^2 + \gamma_z p_z^2 \rangle_{qz} \tag{181}$$

where the average is a trace over the thermal distribution $e^{-\beta H_{qz}}\theta(-H_{qz})$ in the well region. Combining this result with Eqs. (178) and (179) gives

$$\delta = \beta \frac{\langle \gamma_q p_q^2 + \gamma_z p_z^2 \rangle_{qz}}{\langle \delta(q)\dot{q}\theta(-\dot{q}) \rangle_{qz}} \tag{182}$$

A simple estimate of this expression is obtained by approximating the potential in the well region as purely parabolic with frequencies ω_q, ω_z such that the frequency along the perpendicular mode is the same at the well and the barrier. One then finds that

$$\delta \sim \pi \frac{\gamma_q + \gamma_z}{\omega_q} (\beta E^{\ddagger})^2 \tag{183}$$

In the underdamped limit, for which the energy loss $\delta \ll 1$ the depopulation factor $\Upsilon \simeq \delta$ and the expression for the rate

$$\Gamma \sim \frac{1}{2} (\beta E^{\ddagger})^2 (\gamma_q + \gamma_z) e^{-\beta E^{\ddagger}} \tag{184}$$

is identical to the estimate derived by Matkowsky and Schuss (19,20) and Borkovec and Berne (96).

In the one-dimensional case, the depopulation factor in the underdamped limit is linearly proportional to $\beta E^{\ddagger}$ while in the two-degrees-of-freedom case studied here, it is quadratic. The rate increases much faster with damping in the multidimensional case. The reason is that both modes are activated by their respective baths. Since they are strongly coupled, the spectator mode z will supply the energy it picks up from its bath to the reaction coordinate thus enhancing the possibility of activation. The added enhancement of the rate in the underdamped limit is critically dependent on the strong coupling between the modes.

The multidimensional theory presented here has been applied successfully to some numerical simulation data in Ref. 21. The theory is not limited to two degrees of freedom and is easily generalized to any number of strongly coupled degrees of freedom. In practice though, a typical multidimensional reacting system will have some modes which are strongly coupled and others which are not. Thus the challenge is to adapt the present theory also to the case of weak to moderate coupling of modes. This has been done (100) recently by computing the energy loss numerically. Instead of estimating it by using the ergodic theorem, one can run a thermal ensemble of trajectories initiated at the barrier top in the direction of reactants and compute the energy loss using Eqs. (171), (172), and (174). The resulting energy loss will approach the one-dimensional result when the modes are uncoupled and will reduce to the multidimensional result described in this subsection when the modes are strongly coupled.

Note that the present formulation of the turnover theory has used the weak coupling perturbation theory and has not based itself on the normal modes of the system and the

bath at the barrier top. This was done for the sake of convenience. As in the one-dimensional case, the use of the normal modes would give a better theory since it deals correctly with the recrossing problem. However, a multidimensional theory using the normal modes is substantially more complex than the present formulation and remains to be worked out in all its details.

C. The Spatial Diffusion Limit

The "standard" approach for deriving a rate expression in the spatial diffusion limit is the multidimensional generalization of the one-dimensional parabolic barrier expression for the rate (cf. Eq. (78)). Assuming that the largest parameter of the problem is the reduced barrier height ($E^{\ddagger}/k_BT$) one may approximate the rate by considering only the dynamics in the vicinity of the saddle point of the multidimensional potential energy surface. Keeping only quadratic terms leaves one with a quadratic form of the Hamiltonian which may be diagonalized. The rate is then given by the usual TST formula as the ratio of equilibrium flux at the barrier to the density of reactants (cf. Eq. (76)).

The force constant matrices at the barrier and well are denoted respectively $\mathbf{K}^{\ddagger}$ $\mathbf{K}_0$. As shown in Ref. 42 diagonalization of the barrier force constant matrix leads to a barrier frequency $\lambda^{\ddagger}$ which is the positive solution of the equation

$$\det[\lambda^{\ddagger 2}\mathbf{I} + \lambda^{\ddagger}\underline{\hat{\gamma}}(\lambda^{\ddagger}) + \mathbf{K}^{\ddagger}] = 0 \tag{185}$$

where $\mathbf{I}$ is the identity matrix and $\underline{\hat{\gamma}}$ is a diagonal matrix, whose elements are $\hat{\gamma}_i(\lambda^{\ddagger})$, $i = q, z$. The hat notation indicates as usual the Laplace transform of the respective time-dependent frictions. This equation is the multidimensional generalization of the one-dimensional KGH equation for the barrier frequency (cf. Eq. (39)). The rate in the spatial diffusion limit is then found to be (18,93,94,101)

$$\Gamma_{sd} = \frac{1}{2\pi}\left(\frac{\det[\mathbf{K}_0]}{|\det[\mathbf{K}^{\ddagger}]|}\right)^{1/2}\lambda^{\ddagger}e^{-\beta E^{\ddagger}} \tag{186}$$

This is the "standard" expression for the multidimensional rate.

In recent years, it has become evident that this standard treatment may be restricted in its applicability. Limitations of the standard treatment in the presence of anisotropic friction have been discussed by a number of authors (97–99,101–110). It has been shown that introduction of large anisotropy in the friction coefficients can lead to qualitatively new physics. The particle may prefer to avoid the saddle point rather than escape through it. The activation energy may become dependent on the friction anisotropy, which can lead to a lowering of the apparent activation energy. The extent of these effects depends both on the details of the potential energy surface as well as the friction anisotropy.

In this section we will demonstrate application of the optimal planar dividing surface VTST to the spatial diffusion limit in the multidimensional case. It has been shown in Refs. 42 and 111 that such a theory reduces both to the standard as well as the nonstandard solution obtained for anisotropic friction. When the friction anisotropy becomes larger than the reduced barrier height, it is no longer true that one can assume that only the saddle point region of the potential determines the rate. In the optimal planar dividing surface VTST formalism, the dividing surface is not restricted to the saddle point and one does not need this assumption. The full potential comes into play and the resulting theory is more general.

In the multidimensional case, the optimal planar dividing surface in configuration space has the form

$$f = a_0 q + \sum_j a_j x_j + b_0 z + \sum_j b_j y_j \tag{187}$$

which is an obvious generalization of the one-dimensional planar surface (cf. Eq. (79)). The coefficients a_0, b_0, a_j, b_j, $j = 1, \ldots, N$, are the components of the unit vector ∇f perpendicular to the dividing surface and hence normalized:

$$a_0^2 + \sum_j a_j^2 + b_0^2 + \sum_j b_j^2 = 1 \tag{188}$$

The potential $w = w(q, z)$ is a function of two variables, without loss of generality we shall let q denote the "fast" variable and z the slow one ($\gamma_z \gg \gamma_q$). We will also assume that the potential of mean force $w(q)$ acting on the q coordinate is a double-well potential. By definition,

$$w(q) = -\frac{1}{\beta} \ln\left[\frac{1}{L}\int dz\, e^{\beta w(q,z)}\right] \tag{189}$$

where the length scale L is

$$L \equiv \int dq\, e^{\beta w(q)} \tag{190}$$

The one-dimensional estimate for the rate constant from the reactants well, located at $q = q_a$, $z = z_a$, is obtained as usual (cf. Eq. (77)) by choosing the simple dividing surface $f = q$ where we have assumed that the barrier of the potential of mean force $w(q)$ is located at $q = 0$. In analogy with Eq. (81) one may define a potential of mean force along the generalized coordinate f. Since f is linear in the bath modes and the Hamiltonian is quadratic, one may obtain an explicit result for the potential of mean force $w[f]$ which is an obvious generalization of Eqs. (83)–(85):

$$e^{\beta w[f]} = \left(\frac{\beta A^2}{2\pi L^2}\right)^{1/2} \int_{-\infty}^{\infty} dq\, dz\, e^{(-\beta[(1/2)A^2(Cq+Dz-p_0)^2 + w(q,z)])} \tag{191}$$

The parameters A, C, and D are

$$A^2 = \sum_j \left(\frac{a_j^2}{\omega_j^2} + \frac{b_j^2}{\omega_j^2}\right) \tag{192}$$

$$C = a_0 + \sum_j \frac{a_j c_j}{\omega_j^2} \tag{193}$$

$$D = b_0 + \sum_j \frac{b_j d_j}{\omega_j^2} \tag{194}$$

The TST expression for the rate, Eq. (76), using the dividing surface f reduces again to the "simple" result, which generalizes Eq. (86):

$$\Gamma = \Gamma_{1D} e^{-\beta[w[f] - w(0)]} \tag{195}$$

Optimizing the VTST expression for the rate is thus again a search for the *maximum* of the free energy $w[f]$.

A transmission coefficient P_{00} may be defined as the ratio of the rate constant Γ to the one-dimensional TST estimate Γ_{1D}. Seeking the optimal planar dividing surface is identical to varying the expression for the transmission coefficient with respect to the coefficients a_0, b_0, $[a_j, b_j]$, $j = 1, \ldots, N$, determining the spatial orientation of the dividing surface, and with respect to the location f, determining the distance of the dividing surface from the origin. These variations are to be carried out subject to the restriction imposed by the normalization condition, Eq. (188). The result of this variational procedure is that all the coefficients a_j, b_j are proportional to a_0 and b_0 respectively:

$$a_j = a_0 \frac{c_j}{\omega_j^2 + \lambda^{\ddagger 2}} \tag{196}$$

$$b_j = b_0 \frac{d_j}{\omega_j^2 + \lambda^{\ddagger 2}} \tag{197}$$

Here we have introduced the barrier frequency $\lambda^{\ddagger}$ which is defined by the equation

$$\lambda^{\ddagger 2} = A^2(a_0 C + b_0 D - 1) \tag{198}$$

The results for the transformation coefficients, Eqs. (196) and (197), enable us to express the various parameters in terms of the barrier frequency, the Laplace transforms of the two time-dependent friction kernels, and the coefficients a_0 and b_0. The explicit relations are

$$C = a_0\left[1 + \frac{\hat{\gamma}_q(\lambda^{\ddagger})}{\lambda^{\ddagger}}\right] \tag{199}$$

$$D = b_0\left[1 + \frac{\hat{\gamma}_z(\lambda^{\ddagger})}{\lambda^{\ddagger}}\right] \tag{200}$$

and the frequency A^2 is

$$A^2 = \frac{\lambda^{\ddagger 2}}{a_0 C + b_0 D - 1} \tag{201}$$

Variation with respect to the distance f leads to the equation

$$f^{\ddagger} \equiv C\langle q \rangle + D\langle z \rangle \tag{202}$$

where we have introduced the convenient notation

$$\langle q^n z^m \rangle \equiv \frac{P_{nm}}{P_{00}} \tag{203}$$

$$P_{nm} \equiv \left(\frac{\beta A^2}{2\pi L^2}\right)^{1/2} \int_{-\infty}^{\infty} dq\, dz\, q^n z^m e^{(-\beta[(1/2)A^2(Cq+Dz-p_0)^2 + w(q,z) - w(0)])} \tag{204}$$

The result for $f^{\ddagger}$ allows us to immediately deduce that if the potential $w(q, z)$ is symmetric with respect to inversion of q and z, then $f^{\ddagger} = 0$; i.e., the dividing surface passes through the saddle point.

Variation with respect to a_0 and b_0 now leads to two coupled equations

$$\beta A^2[C\langle (q - \langle q \rangle)^2 \rangle + D\langle (qz - \langle q \rangle\langle z \rangle) \rangle] = a_0 \tag{205}$$

$$\beta A^2[C\langle (zq - \langle z \rangle\langle q \rangle) \rangle + D\langle (z - \langle z \rangle)^2 \rangle] = b_0 \tag{206}$$

At this point we are left with four unknown quantities (a_0, b_0, $f^\ddagger$ and $\lambda^\ddagger$). We are also left with four equations, three of which are Eqs. (202), (205), and (206), and the fourth is the normalization condition

$$1 = a_0^2\left[1 + \frac{1}{2}\left(\frac{\hat{\gamma}_q(\lambda^\ddagger)}{\lambda^\ddagger} + \left.\frac{\partial\hat{\gamma}_q(s)}{\partial s}\right|_{s=\lambda^\ddagger}\right)\right] + b_0^2\left[1 + \frac{1}{2}\left(\frac{\hat{\gamma}_z(\lambda^\ddagger)}{\lambda^\ddagger} + \left.\frac{\partial\hat{\gamma}_z(s)}{\partial s}\right|_{s=\lambda^\ddagger}\right)\right] \tag{207}$$

One can find the optimal planar dividing surface and estimate the rate constant for arbitrary time-dependent friction. The approach can be extended to include space- and time-dependent friction (29) and is not restricted to two degrees of freedom. Optimal planar dividing surface VTST is powerful enough to handle the interesting limits of anisotropic friction. Depending on the potential and the anisotropy, one finds both saddle point avoidance in asymmetric systems and a lowering of the activation energy. The interested reader is urged to consult Refs. 42 and 111.

VIII. THEORY OF ACTIVATED SURFACE DIFFUSION

The turnover theory presented in Sec. VII dealt with a single-well or a double-well potential. The diffusion of a particle on a surface is usually associated with motion on a periodic lattice. In principle, the adsorbed particle moves in a three-dimensional space. One coordinate (z) is in a direction vertical to the surface, two other coordinates (x, y) are along the surface plane. As argued in Ref. 112, one should often expect to find the frequency along the vertical axis to be substantially larger than typical frequencies of motion along the plane. This allows for a Born-Oppenheimer like separation of the vertical motion from motion along the plane, reducing the problem to an effective two-dimensional one.

For metal atoms on metal surfaces, one expects that the friction on the adatom will come from acoustic phonons, this leads to the conclusion that the friction will be ohmic (112)–(115). One can estimate the magnitude of the friction coefficient from measured quantities such as sound velocity in the crystal, temperature dependence of the diffusion coefficient, lattice geometry, and crystal density (112)–(114). One usually finds that the friction coefficient is small, $\gamma/\omega \sim 0.1$, where ω is a characteristic frequency of the adatom on the surface. This implies that the magnitude of the energy loss parameter will typically be of the order of unity or higher, depending on the barrier height and on the surface temperature. In other words, typically, atomic surface diffusion occurs in a parameter range which is about the turnover region in Kramers theory. It is therefore of practical interest to apply the turnover theory also to surface diffusion.

We will consider only one-dimensional surface diffusion. The potential $w(q)$ is assumed to be periodic with a spacing a between wells. In the spatial diffusion limit, the particle might escape from a well, get trapped in an adjacent well, and after a long time escape with equal probability in either direction. In this case, the diffusion coefficient is proportional to the product of the spatial diffusion rate of escape from the well and the distance squared between the wells (116):

$$D_{sd} = \tfrac{1}{2}\Gamma_{sd}a^2 \tag{208}$$

In the underdamped limit, the average energy of a particle that escapes above a barrier is proportional to the square root of the energy loss ($\delta = \beta\Delta$) as the particle moves from one barrier to the next (92). Since $\sqrt{\delta} \gg \delta$ when $\delta \ll 1$, the particle will move a long distance before being retrapped in one of the wells. The diffusion coefficient will grow as the damping becomes weaker. In this section we will describe the adaptation of the turnover theory to this problem (117), giving a uniform expression for the diffusion coefficient as well as the hopping distribution to different sites, valid for all damping strengths.

The time evolution of the system is assumed to be governed by the GLE (cf. Eq. (4)). The periodic potential $w(q)$ is characterized by the frequencies ω_0, $\omega^\ddagger$ at the wells and barriers respectively, with a barrier height $E^\ddagger$ and distance a between adjacent wells. The particle is assumed to be initially in one of the wells, labeled 0. The boundary conditions are such that the energy distribution of the particle deep down in the 0th well is thermal ($\sim e^{-\epsilon}$, where $\epsilon \equiv E/k_BT$ is the reduced energy and is 0 at the barrier top) and no particles will be found at the bottom of any of the other wells.

When the coupling between the particle and the bath is not weak the rate for hopping out of the well is determined by the rate of spatial diffusion over the barrier top. For high enough barriers (cf. Eq. (78))

$$\Gamma_{sd} = \frac{\omega_0}{\pi} e^{-\beta E^\ddagger} \frac{\lambda^\ddagger}{\omega^\ddagger} \tag{209}$$

The difference between the periodic potential and the single- or double-well potentials in the spatial diffusion limit, is that in the periodic potential the particle may escape from either side of the well. The spatial diffusion rate is therefore twice as large.

The starting point for the evaluation of the turnover expression for the escape rate (117) is an equation for the stationary flux of particles exiting each well at either barrier. The number of particles per unit energy and per unit time hitting the right (left) barrier of the jth well with positive (negative) velocity is denoted by f_j^+ (f_j^-). The reflection symmetry of the potential and the boundary conditions about the zeroth well implies that $f_j^+(\epsilon) = f_{-j}^-(\epsilon)$.

As the particle traverses from one barrier to the next, its energy changes. The conditional Gaussian probability kernel $P(\epsilon|\epsilon')$ that the particle changes its energy from ϵ' to ϵ is the same Gaussian as in Eq. (152) and is determined by the energy loss parameter δ. The average energy loss from the particle to the bath (δ) as the particle traverses from one well to the next is given in terms of the friction function and the unperturbed orbit of the particle at the barrier energy:

$$\delta \equiv \beta\Delta = \beta \frac{m}{2} \int_{-\infty}^{\infty} dt \int_{-\infty}^{\infty} dt' \, \dot{q}(t)\gamma(t - t')\dot{q}(t') \tag{210}$$

Note that here we are using the weak damping limit for the energy loss rather than the PGH result (Eq. (149)) obtained by considering the unperturbed motion in the unstable normal mode. This choice is not purely for the sake of convenience. When transforming to normal modes, the effective potential along the unstable normal mode is no longer periodic. As one jumps from one barrier to the next, one must change from one unstable mode to the next and this complicates the problem. Using the weak damping version of perturbation theory and considering the unperturbed motion in the system coordinate circumvents this problem.

The unperturbed orbit of the particle is the solution of the unperturbed equation of motion $m\ddot{q} + dw(q)/dq = 0$ at the barrier energy such that at time $t = -\infty$ the particle is initiated at the first barrier and it reaches the adjacent barrier at $t = \infty$. Equation (210) may be rewritten as an integral in the frequency domain:

$$\delta = \frac{1}{4\pi} \beta m \int_{-\infty}^{+\infty} d\omega \, |\tilde{\dot{q}}(\omega)|^2 \tilde{\gamma}(\omega) \tag{211}$$

where the tilde stands for the Fourier transform of the corresponding value ($\tilde{x}(\omega) = \int dt \, x(t)\exp(-i\omega t)$).

The steady-state equation for the fluxes, which gives the fundamental integral equation which must be solved, is

$$f_j^+(\epsilon) = \int_{-\infty}^{\infty} d\epsilon' \, P(\epsilon|\epsilon')[\theta(-\epsilon')f_j(\epsilon') + \theta(\epsilon')f_{j-1}^+(\epsilon')] \tag{212}$$

where $\theta(x)$ is the unit step function. The boundary conditions for the fluxes are

$$f_j^+(\epsilon) \simeq \delta_{j0} \frac{\omega_0}{2\pi} e^{\epsilon}, \qquad \epsilon \to -\infty \tag{213}$$

where δ_{j0} is the Kronecker δ function.

The number of particles per unit time which are trapped in the jth well (Γ_j) is given by the difference between the incoming and outgoing fluxes of the jth well:

$$\Gamma_j = \int_{-\infty}^{\infty} d\epsilon \, \theta(\epsilon)[f_{j-1}^+(\epsilon) + f_{j+1}(\epsilon) - f_j(\epsilon) - f_j^+(\epsilon)] \tag{214}$$

The rate of escape from the zeroth well Γ is

$$\Gamma = -\Gamma_0 \tag{215}$$

The probability of being trapped at the jth well is

$$P_j = \frac{\Gamma_j}{\Gamma} \tag{216}$$

such that the mean-squared path length is

$$\langle l^2 \rangle = a^2 \sum_{j=-\infty}^{\infty} j^2 P_j \tag{217}$$

The diffusion coefficient for the one-dimensional problem is just the rate of escape multiplied by half the mean-squared path length (115):

$$D = \frac{1}{2} \Gamma \langle l^2 \rangle = \frac{1}{2} a^2 \sum_{j=-\infty}^{\infty} j^2 \Gamma_j \tag{218}$$

The integral equations may be solved by Fourier transforms. Details are given in Refs. 67, 86, and (117), so we just give the operative results. For the Gaussian probability kernel one finds that

$$\tilde{P}(is) = \exp[\delta(s^2 + \tfrac{1}{4})] \tag{219}$$

A function $G(is, k)$ is defined as

$$G(is, k) \equiv \frac{1 - \tilde{P}^2(is)}{1 + \tilde{P}^2(is) - 2\tilde{P}(is)\cos(k)} \tag{220}$$

The result for the partial rates is

$$\Gamma_j = -\Gamma_{sd} \frac{1}{\pi} \int_0^{2\pi} dk \, \sin^2\left(\frac{k}{2}\right)\cos(jk) \times \exp\left[\frac{1}{\pi} \int_0^{\infty} d\tau \, \frac{\ln[G(\tau - i/2, k)]}{\tau^2 + 1/4}\right] \tag{221}$$

The expression for the diffusion coefficient simplifies considerably because of the infinite summation over the partial rates (cf. Eqs. (216) and (218)):

$$\frac{D}{D_{sd}} = \Upsilon^{-1} \exp\left[\frac{1}{\pi} \int_0^{\infty} d\tau \, \frac{\ln[1 + \tilde{P}(\tau - i/2)]}{\tau^2 + 1/4}\right] \tag{222}$$

where $D_{sd} \equiv \frac{1}{2}a^2\Gamma_{sd}$ is the diffusion coefficient in the spatial diffusion limit and is independent of the reduced energy loss δ. The "depopulation factor" Υ in Eq. (222) is a function of δ only, the dependence has been given explicitly in Eq. (155). Equations (155), (221), and (222) provide a uniform expression for the partial rates, the decay rate and the diffusion coefficient in terms of the reduced energy loss δ and the rate expression in the spatial diffusion limit. The mean-squared traversal distance may be obtained directly from the rate and the diffusion coefficient via Eq. (218).

In some experiments (118) the spatial probability distribution of the initially localized particle was measured at the early stages of evolution. At long times the evolution is universal, controlled by the diffusion equation and the shape of the distribution is Gaussian. At the early stage, however, the shape of the distribution depends on the particle jump length between successive trappings.

It is possible to derive the time-dependent probability distribution allowing any jump length (113). The location of the particle on the lattice is denoted by two indices l, m, such that the location of the particle at time $t = 0$ is at $l = m = 0$. The probability distribution $w_{l,m}(t)$ for the particle to be at the l, m site at time t is determined by the following master equations:

$$\frac{d}{dt} w_{l,m}(t) = \sum_{j=-\infty}^{\infty} \Gamma_j^1 w_{l-j,m} + \sum_{j=-\infty}^{\infty} \Gamma_j^2 w_{l,m-j} \tag{223}$$

Here we assume that the particle can jump independently along two lattice directions with the transition rates Γ_j^1 and Γ_j^2, $j = 0, \pm 1, \ldots$. It is understood that the rates Γ_0^1 and Γ_0^2 are negative (cf. Eqs. (214) and (215)), allowing for escape from the l, m site. The escape rate Γ from the site is thus $\Gamma = -(\Gamma_0^1 + \Gamma_0^2)$. The initial condition for the distribution is

$$w_{l,m}(t = 0) = \delta_{l,0} \cdot \delta_{m,0} \tag{224}$$

Explicit expressions for the rates Γ_j have been given above (cf. Eq. (221)).

The translational invariance of the surface allows us to solve the master equation (223) by Fourier transforms. One finds that

$$\hat{w}(\mathbf{k}, t) = e^{-(\hat{\Gamma}^1(k_1) + \hat{\Gamma}^2(k_2))t} \tag{225}$$

where

$$\hat{w}(\mathbf{k}, t) = \sum_{l,m} w_{l,m}(t) e^{i(k_1 l + k_2 m)} \tag{226}$$

and

$$\hat{\Gamma}^{1,2}(k) = \sum_{l} \Gamma_l^{1,2} e^{ikl} \tag{227}$$

From Eq. (225) it follows that

$$w_{l,m}(t) = w_l^1(t) w_m^2(t) \tag{228}$$

where

$$w_l^{1,2}(t) = \frac{1}{2\pi} \int_0^{2\pi} dk\, e^{-\hat{\Gamma}^{1,2}(k)t} e^{-ikl} \tag{229}$$

Using the known expression for the rates Γ_l (Eq. (221)), one can show that

$$\frac{\hat{\Gamma}(k)}{\Gamma_{vd}} = 2 \sin^2\left(\frac{k}{2}\right) \exp \left[\frac{1}{\pi} \int_0^{+\infty} ds \frac{\ln \dfrac{1 - \exp[-2\delta(s^2 + 1/4)]}{1 + \exp[-2\delta(s^2 + 1/4)] - 2\cos(k)\exp[-\delta(s^2 + 1/4)]}}{s^2 + \dfrac{1}{4}} \right] \tag{230}$$

Equations (228), (229), and (230) give the explicit solution for the time evolution of the probablity distribution $w_{l,m}$.

The average jump length squared, is a function of the reduced energy loss parameter δ (117). For a large energy loss ($\delta \gg 1$), the particle can jump only to the nearest-neighbor well and the distribution quickly approaches the Gaussian distribution. In the underdamped limit ($\delta \ll 1$) long jumps are the rule (117), and the spatial distribution deviates strongly from the Gaussian distribution in the early stages of evolution. The evolution of the spatial distribution for the case of small δ has been considered in Ref. (119).

The theory of surface diffusion described thus far (see also Ref. 117) is one-dimensional. It suggests that the interaction between the two surface degrees of freedom of the adsorbed particle may also be neglected. This is a severe assumption. As seen in the previous section if the coupling between the modes is strong, the average energy lost by the particle is much larger than estimated from a one-dimensional model. One would expect that in such a case, multiple hopping is highly unlikely and the diffusion occurs via independent single hops. We note though that a multidimensional turnover theory of surface diffusion remains to be developed more fully.

IX. SUMMARY

The classical theory of activated rate processes has been developed rather extensively during the past decade. This chapter has outlined progress made using the Hamiltonian equivalent approach for the dynamics of the GLE. The one-dimensional theory has matured in a sense. Some of the important open questions such as the derivation of a

turnover theory have been answered. Although the major developments have been presented, there are some important additions which have not been discussed at any length, for example the derivation of finite barrier corrections to the rate constant in the spatial diffusion (74) and the energy diffusion limits (89). The VTST method has been used to solve the barrier crossing problem in the presence of a cusped potential (120), a problem that has been of some interest in previous work, see for example Refs. 121 and 122.

Not all one-dimensional problems have been satisfactorily solved. Some of the shortcomings and open problems have been mentioned elsewhere in this chapter, here we summarize a few. An important question has to do with the effects of memory. The work of Tucker (88,123) has pointed out the deficiencies of PGH theory when there is a severe mismatch between the characteristic frequency of the system and the frequency spectrum of the bath. The assumption of PGH theory that the rate-determining step in the weak coupling regime is gaining the barrier energy, proves to be wrong. If the system frequency at the well bottom is larger than the characteristic bath frequency then energy relaxation will be faster as the frequency of the system is lowered. As the energy is increased the frequency is lowered so that the bottleneck is not at the barrier top. The formulation of a turnover theory valid for this limit is an open problem.

Although, as mentioned, the VTST method has been used for the cusped potential problem, the solution is not complete. Of special interest are finite barrier corrections terms for the rate in the moderate damping limit. Previous expansions based themselves on the solution for a parabolic barrier, which is not valid for this case. Similarly, only the weak damping version of the turnover theory is applicable, since the unstable normal mode does not exist.

The case of a periodic potential is also of interest. In PGH theory one considers motion of the unstable normal mode. When the potential is periodic, there are an infinite number of unstable modes, each shifted from the other by a constant term. The potential in any one of these coordinates is no longer periodic. The adaptation of PGH theory outside the weak damping regime is still an open problem.

The periodic potential poses some other interesting challenges. For example, what happens when the potential is periodic but characterized by two different barrier heights within one period? The periodic potential poses also some practical numerical problems in the underdamped limit. Since the particle traverses over very long distances, numerical convergence for direct integration of the Langevin equation is not simple; see for example Ref. 91.

The multidimensional case poses much more severe problems. Especially when the coupling between the modes of the system is moderate such that chaotic and regular dynamics coexist in the unperturbed system, one encounters difficulties. The multidimensional case is of practical relevance when considering surface diffusion phenomena.

Perhaps though the most severe criticism of the whole theory is that, to date, applications and breakthroughs with respect to experimental observations have not been plentiful. The original introduction of memory friction by Grote and Hynes was useful conceptually and some experimental results have been analyzed in terms of non-Markovian spectral densities, see for example Ref. 123. However, beyond a parametrization, there is to date no general "good" theory for microscopic friction. Application of VTST to simulations of "realistic" reactions in liquids is perhaps a first step but has not yet really clarified this issue.

Ideally, the least one would hope for is characterization of different solvents in terms of two parameters, taken as a damping constant and a memory time. A systematic

classification does not exist. One of the central problems plaguing any application to realistic systems is that the frictional effects appear as a prefactor, which is often masked by the exponential part. A small error in activation energy leads to large errors in the prefactor. Another aspect is that in many molecular dynamics simulations the magnitude of the friction exerted on the reaction coordinate was typically not too large.

There have been extensive experiments on the isomerization of stilbene and its derivatives (125, 126), none of which to date have received any serious theoretical numerical analysis. In this experiment, changes in pressure have caused changes of orders of magnitude in the rate. It is time that a serious molecular dynamics study of this system be undertaken. This might also be useful in understanding the importance of multidimensional effects, since typically, in an isomerization of a big molecule, one could expect that more than one angle participates strongly in the isomerization process.

Perhaps the most fruitful and simple application of the theory is in the case of surface diffusion (127). Although some numerical studies have been published, the analysis in terms of the GLE has been lacking. The turnover theory for surface diffusion has only been recently formulated, one could expect that in the coming few years applications of the theory to numerical simulation studies would lead to a deeper understanding of its importance and validity (128). The theory can also be applied to reactions in clusters. After all, in some senses, any molecular dynamics simulation is equivalent to a reaction in a cluster. Investigation as a function of cluster size would help in identifying the changes occurring as one moves from the gas to the liquid phase.

As mentioned in the Introduction, this review has been limited to the classical theory of activated rate processes. The quantum theory has been extensively developed in the past decade and deserves a review on its own.

ACKNOWLEDGMENT

I would like to thank my colleagues Professors A.M. Berezhkovskii, H. Grabert, P. Hänggi, M. Kozhushner, A. M. Levine, I. Rips, P. Talkner, and G. A. Voth, Dr. A. M. Frishman, and students Y. Georgievskii, G. Gershinski, and E. Hershkowits whose stimulation, criticism, and support were a necessary ingredient in much of the work reviewed in this paper. Special thanks are due to Professor A. M. Levine for his careful reading of an early version of the manuscript. A major portion of this chapter was written while I was on sabbatical leave at the PSI Institute in Villigen, Switzerland. It would not have been written without the gracious hospitality of Professor P. Talkner and the support of the Julius Baer Stiftung.

REFERENCES

1. S. Arrhenius, in *Theories of Solutions*, Oxford University Press, London, 1912, p. xx.
2. S. Arrhenius, *Z. Phys. Chem. (Leipzig) 4*: 226 (1889).
3. H. Eyring, *J. Chem. Phys. 3*: 107 (1935).
4. S. Glasstone, K. J. Laidler, and H. Eyring, *The Theory of Rate Processes*, McGraw-Hill, New York, 1941.
5. P. Hänggi, P. Talkner, and M. Borkovec, *Rev. Mod. Phys. 62*: 251 (1990).
6. E. P. Wigner, *J. Chem. Phys. 5*: 720 (1937).
7. E. A. Guggenheim and J. Weiss, *Trans. Faraday Soc. 34*: 68 (1938).
8. *The Transition State*, Chemical Society, Burlington House, London, 1962. Discussion on the paper by H. Eyring et al.

9. K. J. Laidler, *Theories of Chemical Reaction Rates*, McGraw-Hill, New York, 1969, p. 76.
10. D. J. Chandler, *J. Chem. Phys. 68*: 2959 (1978).
11. H. A. Kramers, *Physica 7*: 284 (1940).
12. E. Pollak, H. Grabert, and P. Hänggi, *J. Chem. Phys. 91*: 4073 (1989).
13. H. Risken, *The Fokker-Planck Equation*, Springer Series in Synergetics, Vol. 18, 2nd ed., Springer-Verlag, Berlin, 1989.
14. C. W. Gardiner, *Handbook of Stochastic Methods*, Springer, New York, 1983.
15. R. Landauer, *Noise in Nonlinear Dynamical Systems*. Vol. 1. *Theory of Continuous Fokker-Planck Systems* (F. Moss and P. V. E. McClintock, eds.), Cambridge University Press, Cambridge, 1989, p. 1.
16. D. Gegiou, K. A. Muszkat, and E. Fischer, *J. Am. Chem. Soc. 90*: 12 (1968).
17. G. R. Fleming and P. Hänggi (eds.), *Activated Barrier Crossing*, World Scientific, New York, 1993.
18. J. S. Langer, *Ann. Phys. (N.Y.) 54*: 258 (1969).
19. B. J. Matkowsky, Z. Schuss, and E. Ben-Jacob, *SIAM J. Appl. Math. 42*: 835 (1982).
20. B. J. Matkowsky, Z. Schuss, and C. Tier, *SIAM J. Appl. Math. 43*: 673 (1983).
21. E. Pollak and E. Hershkowitz, *Chem. Phys. 180*: 191 (1994).
22. R. Zwanzig, *J. Stat. Phys. 9*: 215 (1973).
23. R. F. Grote and J. T. Hynes, *J. Chem. Phys. 73*: 2715 (1980).
24. B. Carmeli and A. Nitzan, *Phys. Rev. Lett. 49*: 423 (1982).
25. B. Carmeli and A. Nitzan, *Chem. Phys. Lett. 102*: 517 (1983).
26. S. H. Northrup and J. T. Hynes, *J. Chem. Phys. 68*: 3203 (1978).
27. B. Gavish, *Phys. Rev. Lett. 44*: 1160 (1980).
28. G. R. Haynes, G. A. Voth, and E. Pollak, *Chem. Phys. Lett. 207*: 309 (1993).
29. G. R. Haynes, G. A. Voth, and E. Pollak, *J. Chem. Phys. 101*: 7811 (1994).
30. A. O. Caldeira and A. J. Leggett, *Ann. Phys. (N.Y)* 149: 374 (1983).
31. E. Pollak, *J. Chem. Phys. 85*: 865 (1986).
32. E. Pollak, *J. Chem. Phys. 95*: 533 (1991).
33. P. Grigolini, *Adv. Chem. Phys. 62*: 1 (1985).
34. P. Talkner, *Ber. Bunsenges. Phys. Chem. 95*: 327 (1991).
35. P. Talkner, *Chem. Phys. 180*: 199 (1994).
36. S. A. Adelman, *Adv. Chem. Phys. 53*: 61 (1983).
37. B. J. Berne, M. Borkovec, and J. E. Straub, *J. Phys. Chem. 92*: 3711 (1988).
38. A. Nitzan, *Adv. Chem. Phys. 70*: part 2, 489 (1988).
39. Special Issue of *Ber. Bunsenges. Phys. Chem. 95*: 225–443 (1991), edited by P. Hänggi and J. Troe.
40. Special issue of *Chem. Phys. 180*: 109–355 (1994).
41. J. A. Montgomery, D. Chandler, and B. J. Berne, *J. Chem. Phys. 70*: 4056 (1979).
42. A. M. Berezhkovskii, E. Pollak, and V. Yu. Zitserman, *J. Chem. Phys. 97*: 2422 (1992).
43. A. M. Frishman and E. Pollak, *J. Chem. Phys. 98*: 9532 (1993).
44. S. Linkwitz, H. Grabert, E. Turlot, D. Estéve, and M. H. Devoret, *Phys. Rev. A 45*: R3369 (1992).
45. L. Onsager, *Phys. Rev. 37*: 405 (1931).
46. L. Onsager, *Phys. Rev. 38*: 2265 (1931).
47. J. Chandrasekhar, S. F. Smith, and W. L. Jorgensen, *J. Am. Chem. Soc. 106*: 3049 (1984); *107*: 154 (1985).
48. J. P. Bergsma, B. J. Gertner, K. R. Wilson, and J. T. Hynes, *J. Chem. Phys. 86*: 1356 (1987).
49. B. J. Gertner, K. R. Wilson, and J. T. Hynes, *J. Chem. Phys. 90*: 3537 (1989).
50. J. E. Straub, M. Borkovec, and B. J. Berne, *J. Phys. Chem. 91*: 4995 (1987).
51. J. E. Straub, M. Borkovec, and B. J. Berne, *J. Chem. Phys. 89*: 4833 (1988).
52. J. E. Straub, B. J. Berne, and B. Roux, *J. Chem. Phys. 93*: 6804 (1990).
53. J. B. Straus and G. A. Voth, *J. Chem. Phys. 96*: 5460 (1992).

54. J. B. Straus, J. M. Gomez Llorente, and G. A. Voth, *J. Chem. Phys. 98*: 4082 (1993).
55. M. Topaler and N. Makri, *J. Chem. Phys. 101*: 7500 (1994).
56. M. C. Wang and G. E. Uhlenbeck, *Rev. Mod. Phys. 17*: 323 (1945).
57. L. Ermak and H. Buckholz, *J. Comput. Phys. 35*: 169 (1980).
58. B. Carmeli and A. Nitzan, *Chem. Phys. Lett. 106*: 329 (1984).
59. J. E. Straub, M. Borkovec, and B. J. Berne, *J. Chem. Phys. 84*: 1788 (1986).
60. E. Pollak and A. M. Berezhkovskii, *J. Chem. Phys. 99*: 1344 (1993).
61. E. B. Wilson, Jr., J. C. Decius, and P. C. Cross, *Molecular Vibrations*, McGraw-Hill, New York, 1955.
62. A. M. Levine, M. Shapiro, and E. Pollak, *J. Chem. Phys. 88*: 1959 (1988).
63. E. Pollak, *Phys. Rev. A 33*: 4244 (1986).
64. E. Pollak, *Chem. Phys. Lett. 127*: 178 (1986).
65. P. Hänggi and F. Mojtabai, *Phys. Rev. A 26*: 1168 (1982).
66. A. M. Levine, W. Hontscha, and E. Pollak, *Phys. Rev. A 40*: 2138 (1989).
67. I. Rips and E. Pollak, *Phys. Rev. A 41*: 5366 (1990).
68. E. Pollak, A. M. Berezhkovskii, and Z. Schuss, *J. Chem. Phys. 100*: 334 (1994).
69. P. Pechukas, *Dynamics of Molecular Collisions B*, (W. H. Miller, ed.), Plenum, New York, 1976, p. 269.
70. D. Tannor and D. Kohen, *J. Chem. Phys. 100*: 4932 (1994).
71. D. Ryter, *Physica A 142*: 103 (1987).
72. D. Ryter, *J. Stat. Phys. 49*: 751 (1987).
73. M. M. Klosek, B. J. Matkowsky, and Z. Schuss, Ber. Bunsenges, *Phys. Chem. 95*: 331 (1991).
74. E. Pollak and P. Talkner, *Phys. Rev. E 47*: 922 (1993).
75. E. Pollak, *Theory of Chemical Reaction Dynamics*, Vol. 3, (M. Baer, ed.), CRC Press, Boca Raton, FL, 1985, p. 123.
76. J. C. Keck, *Adv. Chem. Phys. 13*: 85 (1967).
77. W. H. Miller, *J. Chem. Phys. 61*: 1823 (1974).
78. E. Pollak and P. Talkner, *Phys. Rev. E, 51*: 1868 (1995).
79. A. M. Frishman, A. M. Berezhkovskii, and E. Pollak, *Phys. Rev. E. 49*: 1216 (1994).
80. E. Pollak, *Activated Barrier Crossing* (G. R. Fleming and P. Hänggi, eds.), World Scientific, New York, 1993, p. 5.
81. Chronologically, the VTST for condensed phases presented in this section was derived in Ref. 32, and motivated the optimized planar dividing surface VTST presented in the previous section and in Ref. 42.
82. G. Gershinski and E. Pollak, *J. Chem. Phys. 101*: 7174 (1994).
83. G. Gershinski and E. Pollak, *J. Chem. Phys. 103*: 8501 (1995).
84. E. Pollak, *Mod. Phys. Lett. 5*: 13 (1991).
85. V. I. Melnikov and S. V. Meshkov, *J. Chem. Phys. 85*: 1018 (1986).
86. V. I. Melnikov, *Phys. Rept. 209*: 1 (1991).
87. H. Dekker and A. Maassen van den Brink, *Phys. Rev. E 49*: 2559 (1994).
88. S. K. Reese, S. C. Tucker, and G. K. Schenter, *J. Chem. Phys., 102*: 104 (1995).
89. V. I. Melnikov, *Phys. Rev. E 48*: 3271 (1993).
90. E. Pollak, J. S. Bader, B. J. Berne, and P. Talkner, *Phys. Rev. Lett. 70*: 3299 (1993).
91. J. S. Bader, B. J. Berne, and E. Pollak, *J. Chem. Phys., 102*: 4037 (1995).
92. M. Büttiker, E. P. Harris, and R. Landauer, *Phys. Rev. B 28*: 1268 (1983).
93. A. Nitzan, *J. Chem. Phys. 86*: 2734 (1987).
94. R. F. Grote and J. T. Hynes, *J. Chem. Phys. 74*: 4465 (1981); *75*: 2191 (1981).
95. B. J. Berne, *Chem. Phys. Lett. 107*: 131 (1984).
96. M. Borkovec and B. J. Berne, *J. Chem. Phys. 82*: 794 (1985).
97. A. M. Berezhkovskii and V. Yu. Zitserman, *Physica A 166*: 585 (1990).
98. A. M. Berezhkovskii and V. Yu. Zitserman, *Chem. Phys. 157*: 141 (1991).

99. A. M. Berezhkovskii and V. Yu. Zitserman, *J. Phys. A 25*: 2077 (1992).
100. E. Hershkowits and E. Pollak, to be published.
101. A. Nitzan and Z. Schuss, *Activated Barrier Crossing* (G. R. Fleming and P. Hänggi, eds.), World Scientific, New York, 1993, p. 42.
102. S. H. Northrup and J. A. McCammon, *J. Chem. Phys. 78*: 987 (1983).
103. M. Berkowitz, J. D. Morgan, J. A. McCammon and S. H. Northrup, *J. Chem. Phys. 79*: 5563 (1983).
104. N. Agmon and J. J. Hopfield, *J. Chem. Phys. 78*: 6947 (1983); *79*: 2042 (1983); *80*: 592 (1984).
105. N. Agmon and R. Kosloff, *J. Phys. Chem. 91*: 1988 (1987).
106. N. Agmon and S. Rabinovich, *Ber. Bunsenges. Phys. Chem. 95*: 278 (1991).
107. N. Agmon and S. Rabinovich, *J. Chem. Phys. 97*: 7270 (1992).
108. M. M. Klosek, B. J. Matkowsky, and Z. Schuss, *Ber. Bunsenges. Phys. Chem. 95*: 331 (1991).
109. B. Carmeli, V. Mujica, and A. Nitzan, *Ber. Bunsenges. Phys. Chem. 95*: 319 (1991).
110. A. M. Berezhkovskii and V. Yu. Zitserman, *Physica A 187*: 519 (1992).
111. A. M. Berezhkovskii, A. M. Frishman, and E. Pollak, *J. Chem. Phys. 101*: 4778 (1994).
112. G. DeLorenzi and G. Jacucci, *Surface Sci. 164*: 526 (1985).
113. Y. Georgievskii, M. A. Kozhushner, and E. Pollak, *J. Chem. Phys., 102*: 6908 (1995).
114. M. A. Kozhushner, A. S. Prostnev, M. O. Rozovskii, and B. R. Shub, *Phys. Stat. Sol. (b) 136*: 557 (1986).
115. R. Tsekov and E. Ruckenstein, *J. Chem. Phys. 100*: 1450 (1994).
116. J. D. Doll and A. F. Voter, *Annu. Rev. Phys. Chem. 38*: 413 (1987).
117. Y. Georgievskii and E. Pollak, *Phys. Rev. E 49*: 5098 (1994).
118. M. Lovisa and G. Ehrlich, *J. Phys. (Paris) 50*: C8-279 (1989).
119. A. S. Prostnev, M. A. Kozhushner, and B. R. Shub, *Khimich. Phis. (Chem. Phys.) 5*: 85 (1986).
120. E. Pollak, *J. Chem. Phys. 93*: 1116 (1990).
121. D. F. Calef and P. G. Wolynes, *J. Phys. Chem. 87*: 3387 (1983).
122. H. Dekker, *Physica A 136*: 124 (1986).
123. S. C. Tucker, *J. Chem. Phys. 101*: 2006 (1994).
124. B. Bagchi and D. W. Oxtoby, *J. Chem. Phys. 78*: 2735 (1983).
125. J. Troe, *Ber. Bunsenges. Phys. Chem. 95*: 228 (1990).
126. J. Schroeder and J. Troe, *Activated Barrier Crossing* (G. R. Fleming and P. Hänggi, eds.), World Scientific, New York, 1993, p. 206.
127. Y. Georgievskii and E. Pollak, *Surface Sci. Lett.*, in press.
128. G. Gershinsky, Y. Georgievskii, E. Pollak and G. Betz, *Surface Sci.*, in press.

Index

A

B

Start of Citation[PU]Marcel Dekker, Inc.[/PU][DP]1996[/DP]End of Citation

C

E

Start of Citation[PU]Marcel Dekker, Inc.[/PU][DP]1996[/DP]End of Citation

G

Start of Citation[PU]Marcel Dekker, Inc.[/PU][DP]1996[/DP]End of Citation

O

Start of Citation[PU]Marcel Dekker, Inc.[/PU][DP]1996[/DP]End of Citation

S

T

Z